THIESEL 2020

Thermo-and Fluid Dynamic Processes
in Direct Injection Engines
8th – 11th September

UNIVERSITAT POLITÈCNICA DE VALÈNCIA
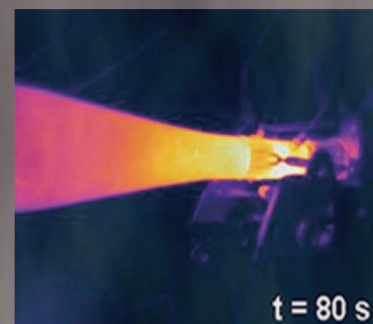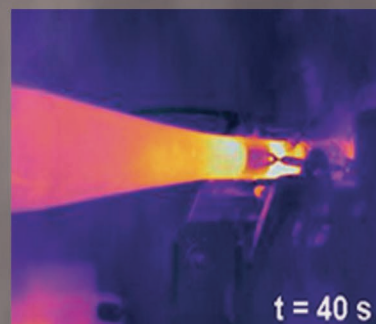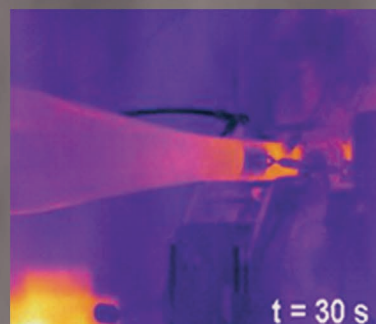
motores térmicos

t = 0 s

t = 30 s

t = 40 s

t = 80 s

The contents of this publication have been approved by the Conference Scientific Committee and in accordance to the procedure set out in
http://www.cmt.upv.es/Thiesel.aspx

THIESEL 2020

Thermo-and Fluid Dynamic Processes
in Direct Injection Engines
8th - 11th September

COMMITTEES

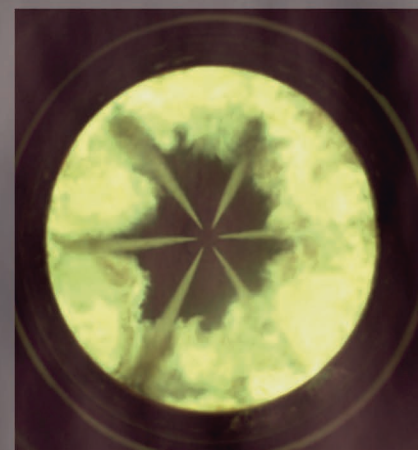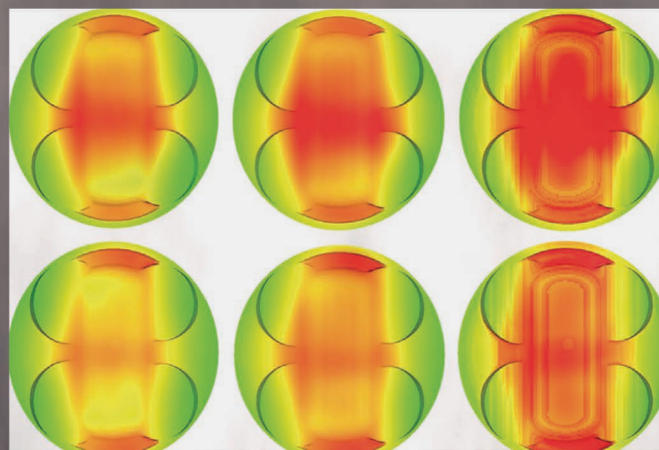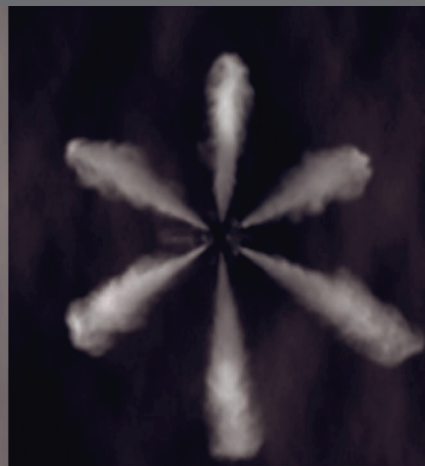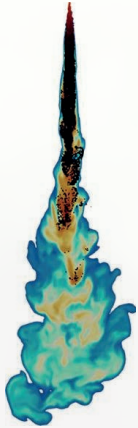### EUROPEAN ORGANISING COMMITTEE

Prof. F. PAYRI
CMT. Universitat Politècnica de València (SPAIN)

Prof. J.M. DESANTES
CMT. Universitat Politècnica de València (SPAIN)

Dr. C. ANGELBERGER
IFP Energies Nouvelles (FRANCE)

Prof. T. KOCH
IFKM. Karlsruher Institut für Technologie (GERMANY)

OVERSEAS ORGANISING COMMITTEE

Prof. R. REITZ
University of Wisconsin - Madison (U.S.A.)

Prof. J. SENDA
Doshisha University (JAPAN)

Dr. P. MILES
Sandia National Laboratories (U.S.A.)

Prof. C. BAE
KAIST (KOREA)

CONFERENCE COORDINATOR

Dr. X. MARGOT
CMT. Universitat Politècnica de València (SPAIN)

ADVISORY COMMITTEE

Dr. P. ADOMEIT	FEV (Germany)
Dr. A. AMER	SAUDI ARAMCO (Saudi Arabia)
Prof. O. ARMAS	Universidad de Castilla-La Mancha (Spain)
Mr. I. BALLOUL	Volvo Powertrain France (France)
Prof. J. BENAJES	Universitat Politècnica de València (Spain)
Dr. R. BURKE	University of Bath (U.K.)
Dr. P.-O. CALENDINI	Aramco Fuel Research Center (France)
Dr. G. COMA	Renault (France)
Dr. A. COSTALL	Imperial College London (U.K.)
Dr. P. GASTALDI	Aramco Fuel Research Center (France)
Dr. N. GUERRASSI	Delphi Automotive Systems (Luxemburg)
Dr. S. GUILAIN	Renault (France)
Dr. J. KASHDAN	IFP Energies Nouvelles (France)
Dr. M. KOIKE	Toyota R&D Labs (Japan)
Dr. C. KRUEGER	Daimler (Germany)
Prof. M. LAPUERTA	Universidad de Castilla-La Mancha (Spain)
Prof. L. LE MOYNE	ISAT (France)
Dr. P. LÖFHOLM	Wärtsilä (Finland)
Mr. P. MALLET	Renault (France)
Dr. X. MARGOT	Universitat Politècnica de València (Spain)
Prof. F. MAROTEAUX	Université de Versailles (UVSQ) (France)
Prof. F. MILLO	Politecnico di Torino (Italy)
Dr. A. MOHAMMADI	Toyota Motor Europe (Belgium)
Prof. E. MURASE	Kyushu University (Japan)
Dr. H. NAKAMURA	HORIBA Europe (Germany)
Prof. H. OGAWA	Hokkaidou University (Japan)
Prof. A. ONORATI	Politecnico di Milano (Italy)
Prof. H. PITSCH	RWTH Aachen (Germany)
Dr. P. PRIESCHING	AVL (Austria)
Dr. F. RAVET	Renault (France)
Prof. C. ROUSSELLE	Polytech' Orléans (France)
Mr. O. SALVAT	PSA Peugeot Citroën (France)
Dr. K. SENECAL	Convergent Science (U.S.A.)
Dr. C. SOTERIOU	Consulting Engineer (U.K.)
Prof. F. TINAUT	Universidad de Valladolid (Spain)
Mr. T. TOMODA	Toyota Motor Corporation (Japan)
Prof. A. TORREGROSA	Universitat Politècnica de València (Spain)
Dr. B. VAGLIECO	Istituto Motori (Italy)
Dr. O. VARNIER	Jaguar Land Rover (U.K.)
Dr. A. VASSALLO	Punch Torino SpA (Italy)
Mr. A. WARD	Ricardo (U.K.)
Dr. A. WIMMER	LEC (Austria)
Mr. M. WINTERBOURN	Delphi Technologies (U.K.)

Table of Contents

Alternative Fuels

New Combustion Concepts

Injection + Combustion

CO2 Reduction

Emission Abatement

Posters Abstracts

Index of authors

Effect of advanced biofuels on WLTC emissions of a Euro 6 diesel vehicle with SCR under different climatic conditions

J.J. Hernández[(*)]; J. Rodríguez-Fernández; M. Lapuerta; A. Calle-Asensio; A. Ramos; J. Barba.

Universidad de Castilla-La Mancha, Escuela Técnica Superior de Ingeniería Industrial, Avda. Camilo José Cela s/n, 13071 Ciudad Real, Spain.

[(*)] Authors for correspondence:
E-mail: JuanJose.Hernandez@uclm.es
Telephone: +(34) 926 295 300 (Ext 3880)

Abstract. Hydrotreated vegetable oil (HVO), a glycerol-derived biofuel (blended with diesel fuel at 20% v/v, Mo·bio®) and biodiesel produced through the esterification of residual free fatty acids from the palm oil industry (pure and blended with diesel fuel at 20% v/v), all of them considered as advanced biofuels as defined in the Directive EU/2018/2001, were tested in a Euro 6 diesel vehicle equipped with ammonia-SCR. Tests were carried out in a chassis dyno at warm (24ºC) and cold (-7ºC) ambient conditions following the current certification procedure for light-duty vehicles (WLTC). Together with gaseous and particle emissions, the efficiency of the SCR when changing the fuel was analysed. In general, fuel properties were relevant only at warm conditions. Engine mechanical/thermal losses and a worsened combustion process masked the effect of the fuel at -7 ºC. Because of the lower EGR rate, NO_x emissions upstream of the SCR were higher at cold temperature, mainly during the low and the extra-high speed phases of the WLTC. CO and THC emissions were only important at the beginning of the cycle and at -7 ºC. HVO presented advantages regarding these compounds, while the worse cloud point of biodiesel led to higher emissions. As expected, engine-out NO_x emissions were very sensitive to the EGR rate, HVO showing a slightly better behaviour because of its high cetane number. The SCR efficiency was mainly affected by the exhaust gas temperature (higher values under warm conditions), although fuel-derived effects were also significant. In fact, a more appropriate NO_2/ NO_x ratio at the catalyst inlet for HVO (which promotes the fast reduction reaction) and a higher hydrocarbon concentration at the low-speed phase for B20 (which are consumed later in NO_x reduction reactions) contributed to a lower tail-pipe NO_x emissions at -7 ºC when these fuels were used. The oxygen content of biodiesel-based fuels (B100 and B20) led to lower particle number with respect to diesel fuel, although the EGR rate also played a significant role (as in case of Mo·bio®). Despite of its nil aromatic content, the higher EGR rate and the extremely superior autoignition trend of HVO led to higher particle number under high engine load and warm conditions (which promote local richer premixed conditions downstream of the lift-off length of the fuel jet).

1. Introduction

The impact of pollutant emissions derived from road transport on human health and environment has been a priority concern for governments and institutions during the last decades. In Europe, the last Euro 6 emissions regulation has become much more stringent, mainly regarding nitrogen oxides (NO_x). The limit established for this compound in light-duty diesel vehicles decreased from 180 mg/km in Euro 5 to 80 mg/km in Euro 6 [1]. This change has forced vehicle manufacturers to use complex after-treatment systems for reducing tailpipe NO_x beyond the values that can be achieved with internal measures such as exhaust gas recirculation or advanced injection strategies. Two different options are currently used, lean NO_x trap (LNT) and selective catalytic reduction (SCR). Because of its easier implementation in light-duty vehicles (since it does not require an additional dosing system), the former was most popular during Euro 6b. With the entry into force of Euro 6c and Euro 6d-temp [2], the certification driving cycle changed to the Worldwide harmonized Light-duty vehicles Test Cycle (WLTC), sometimes complemented with real driving emissions (RDE), which are tougher in terms of dynamics, load and duration than the previous New European Driving Cycle (NEDC). In order to adapt to these new requirements, manufacturers started to increase the use of ammonia-SCR due to its higher efficiency on NO_x

conversion (near 95% within a temperature range between around 200 and 350 ºC [3]) once the light-off temperature of the catalyst is reached. The acceptable performance of LNT at low temperature together with the greater conversion efficiencies of SCR at high engine loads are pushing towards the combined used of both systems in new vehicle developments [4].

Simultaneously, the use of renewable fuels as substitutes of conventional fossil fuels has been strongly promoted in the last years. The recent EU Renewable Energy Directive (2018/2001) [5] establishes a contribution of renewable energy of 14% in rail and road transport by 2030, encouraging the use of biofuels with non-crop and waste origin (with a contribution of at least 3.5% and multiple counting), usually denoted as advanced biofuels. Conventional biodiesel, a mixture of fatty acid methyl esters (FAME) with properties limited in standard EN 14214 [6], is obtained from transesterification of vegetable oils or animal fats and it has been the most widely used biofuel in diesel vehicles. It must be blended (with ratios depending on the feedstock and the production process) with diesel fuel to fulfil the standard EN 590 [7]. A more sustainable way (with enhanced lifecycle GHG emissions) to produce FAME is based on the esterification of residual free fatty acids from industrial processes [8]. This latter method allows for avoiding the formation of glycerine, the most abundant residue derived from transesterification processes. Glycerine represents around 10% by wt. of the obtained products [9] and somehow conditions the viability of the biodiesel industry (its low purity and the excess of this compound regarding pharmaceutical applications limit its alternative uses). Some pioneering industrial initiatives evaluate the revalorization of this waste to produce fatty acid glycerol esters (FAGE) through transesterification-transketalization reactions with triglycerides [10]. FAGE must be blended with FAME or diesel fuel because of its weak cold flow behaviour and viscosity [11]. Although there is still a significant lack of information regarding the use of FAME from esterification of residual fatty acids and FAME/FAGE blends in diesel engines, similar properties to conventional biodiesel, even higher oxygen-content, lead to a reduction in particulate matter (PM), carbon monoxide (CO) and total hydrocarbons (THC) [12][13][14].

Other promising alternative to conventional diesel fuel are paraffinic fuels like gas-to-liquid (GTL) or hydrotreated vegetable oil (HVO), the latter being more attractive since it can be produced in current oil refineries with minor changes in the production facilities and it has renewable origin. HVO is manufactured through a hydrotreating process of different oils [15]. This biofuel has a cetane number and an energy content significantly higher than diesel fuel [16], which has been proved to contribute to important CO_2 savings [17]. Regarding pollutant emissions, although they are very dependent on the type of engine and the engine mapping [18][19], reductions in particulate matter emissions are usually reported [20][21] while NO_x trends are not so clear[22].

The combination of modern De NO_x aftertreatment devices and a higher expected contribution of advanced biofuels in diesel-type fuels is a new challenge for engine/vehicle manufacturers and for the biofuels industry. The engine mapping, which has been optimized for operation with conventional diesel fuel, could be optimized to the use of these new promising biofuels. This optimization involves the regulation and control of the after-treatment operating conditions, such as the LNT regeneration frequency and/or the urea injection strategy in the SCR. Moreover, there is yet a significant lack of information on the effect of advanced biofuels during real driving operation at cold temperature, which will be required in future EU regulations to check the reliability of aftertreatment at adverse climatic conditions [23]. Thus, the main target of this work is to evaluate, in comparison with conventional diesel fuel, the effect of three different advanced biofuels (HVO, FAME from an esterification process and a FAGE-FAME blend) on the performance and regulated emissions (gaseous compounds and particles) of a Euro 6b light-duty diesel vehicle equipped with an ammonia-SCR device. Tests have been carried out following the WLTC procedure at two ambient temperatures, 24 ºC (as established in the current certification regulation) and −7 ºC (representative of cold conditions). As a novelty, by comparing NO_x emission upstream and downstream of the SCR, the catalyst efficiency was calculated for each phase of the cycle. Therefore, this paper provides important information which can be used for optimizing the after-treatment system over the whole cycle of a diesel vehicle equipped with SCR and fuelled with advanced biofuels.

2. Experimental

2.1 Vehicle and experimental setup

Driving tests were carried out using a Peugeot 3008 1.6 BlueHDi, a light-duty vehicle equipped with a direct injection diesel engine (model DV6 FC) which is representative of the current market in Europe (it belongs to the SUV-crossover segment). The exhaust gas aftertreatment system allows to fulfil the emission limits specified in the EU standard Euro 6b [1] and it consists of a diesel oxidation catalyst (DOC) for oxidizing CO and unburnt hydrocarbons (THC), an ammonia selective catalytic reduction

(SCR) device for the removal of NO_x and a regenerative wall-flow diesel particulate filter (DPF) for eliminating soot. This vehicle uses cooled high-pressure exhaust gas recirculation (EGR) to reduce engine-out NO_x emissions. A scheme of the engine and the exhaust system configuration is shown in Fig. 1, while the main vehicle characteristics are shown in Table 1.

Table 1. Vehicle characteristics

Engine	DV6 FC 1.6 BlueHDi
Cylinders	4
Valves per cylinder	2
Displacement	1560 cm^3
Compression ratio	17:1
Transmission	Manual 6 gears
Rated Power	88 kW / 4000 rpm
Rated Torque	300 Nm / 1750 rpm
EGR system	High-Pressure EGR (Cooled)
Aftertreatment system	DOC + SCR + DPF
EU emissions standard	Euro 6b
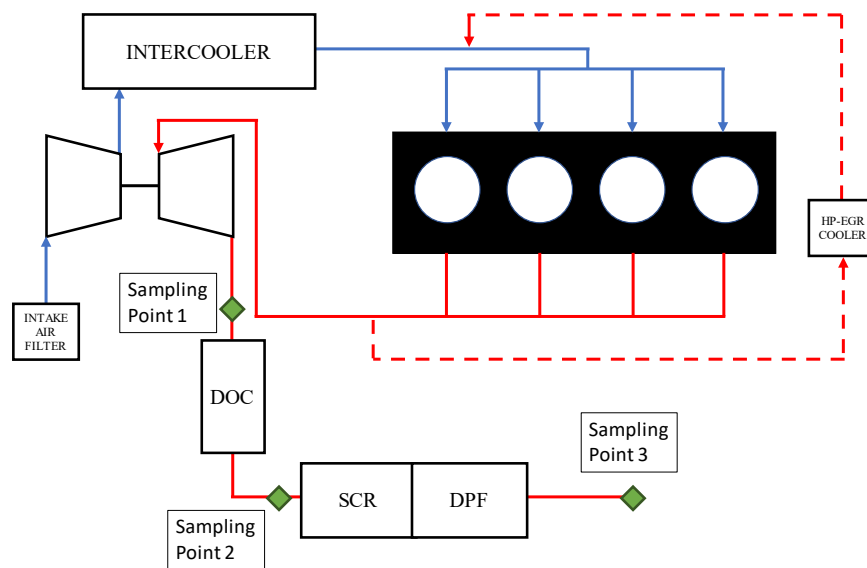
Fig. 1. Engine and exhaust system configuration scheme

Gaseous emissions were measured upstream and downstream of the SCR system (sampling points 2 and 3 in Fig. 1) in order to study the behaviour of this catalyst when changing the fuel. The upstream composition was analysed using a MEXA-ONE C1 equipment, which incorporates a chemiluminescence detector (CLD) for NO and NO_x, a non-dispersive infrared (NDIR) sensor for CO and CO_2 and a flame ionization detector (FID) for THC. Tailpipe emissions (point 3 in Fig. 1) were measured with a Horiba OBS 1300 analyser, which includes two different modules: a MEXA 70 NO_x with a zirconia sensor for NO_x measuring and a MEXA 1170 HNDIR based on NDIR for CO and CO_2 determination. THC emission at this point was quantified with an Amluk FID 2010. Regarding particles, they were measured upstream of the DPF (point 1 in Fig. 1) with an Engine Exhaust Particle Sizer (EEPS) spectrometer manufactured by TSI. The accuracy of the different analysers is shown in Table 2.

Some engine operating parameters, which significantly affect emissions (such as the relative position of the EGR valve and the SCR-inlet temperature), were obtained from the electronic control unit (ECU) through OBD-II connection and using INCA PC software (with its corresponding ODX-Link). The instantaneous fuel consumption was calculated from the carbon balance (CO_2, CO and THC) by using the method proposed in EU directive 1151/2017 [2]. A Kistler Kibox device allowed for evaluating the combustion process (ignition delay time, combustion phasing and duration) through thermodynamic diagnosis. This analyser uses three different signals: the instantaneous in-cylinder pressure (obtained

through a piezoelectric sensor model Z17090sp149 located in the glow plug gap of cylinder 1), the engine crank angle and the energizing current of the fuel injector (measured with a current clamp).

Table 2. Accuracy of the emission analysers

Module	Measuring Method	Accuracy
MEXA ONE-C1	CLD	± 5 ppm NO_x
	NDIR	± 0.0025% CO (v/v)
		± 0.1% CO_2 (v/v)
	FID	± 15 ppm HC
MEXA 720 NO_x	Zirconia sensor	± 30 ppm NO_x
MEXA 1170 HNDIR	NDIR	± 0.02% CO (v/v)
		± 0.32% CO_2 (v/v)
Amluk FID 2010	FID	± 20 ppm HC

All driving tests were carried out in a two-wheels drive (2WD) chassis dynamometer following the World-harmonized Light-duty vehicle Test Cycle (WLTC) Class 3B. The roller has a diameter of 159.1 cm with the driving wheels placed over it. The installation allows to test vehicles up to 165 kW. The inertias and rolling resistances were simulated through the coast-down parameters and a blower synchronized with the vehicle speed is placed in the front of the car to provide frontal cooling air. This facility is placed inside a climatic chamber which can set the ambient temperature between -20 and 40 ºC and the relative air humidity between 30 and 80% (the latter only when ambient temperature is higher than 15 ºC).

2.2 Fuels and methodology

Together with a conventional diesel fuel used as reference (supplied by Repsol and free of biodiesel), three different advanced biofuels were selected for this work. Biodiesel composed of fatty acid methyl esters (FAME), not produced through a conventional transesterification method but through an esterification process of residual fatty acids coming from the palm oil industry, was supplied by Masol Iberia. Hydrotreated vegetable oil (HVO) was provided by NESTE. Both fuels fulfilled the corresponding EU standards regarding fuels quality, EN 14214 [6] and EN 15940 [24] for FAME and HVO respectively. Finally, a novel biofuel consisting of a blend of FAME (70% v/v), fatty acid glycerol esters (FAGE, 27% v/v) and acetals (produced during FAGE production and used for improving cold flow properties, 3% v/v) was also tested. This blend was provided by Inkemia-IUCT with the commercial name of o·bio®. The FAGE content came from transesterification-transketalization reactions of the residual glycerine resulting from the FAME production process by using waste cooking oil as feedstock. More detailed information about this latter fuel can be found in reference [11]. According to the classifications provided in Directive (EU) 2018/2001 [5], these biofuels can be considered as advanced biofuels.

Vehicle tests were performed at two different temperatures, 24 ºC and -7 ºC. Two replicates of the WLTC were carried out to check repeatability (results shown in the next section include the average of both replicates as well as error bars indicating the maximum and minimum values). A preconditioning test with no emissions measurement (following also the WLTC) [25], followed by an 8 hour-duration soaking process, was performed when changing the fuel or the ambient temperature in order to guarantee reliability (same initial conditions).

The main properties of the fuels tested are shown in Table 3. Diesel fuel and HVO were checked neat at both temperatures. Neat biodiesel (B100) was tested at 24 ºC but it was blended with the reference fuel (20% v/v, denoted by B20) at -7 ºC because of its bad cold flow properties at this temperature. Similarly, a blend of o·bio® (20% v/v) and diesel fuel (named as Mo·bio® from now on) was also tested at both temperatures.

Table 3. Fuel properties

Property	Diesel	Biodiesel 20 % v/v (B20)	Biodiesel 100 % v/v (B100)	HVO 100 % v/v (HVO100)	Mo·bio
Density at 15 °C (kg/m³)	829	840	876	780	843
Kinematic viscosity at 40 °C (cSt)	2.92	3.00	5.08	3.21	3.01
Lower Heating Value (MJ/kg)	43.0	41.8	36.9	44.3	41.2
Lubricity (µm)	330	195	186	416	189
Cloud Point (ºC)	-22.1	-6.8	13.1	-32.5	-12.9
Cold filter plugging point (ºC)	-24	-9	12	-44	-16
Derived cetane number	58.29	62.47	66.94	80.06	56.98
T10 (ºC)	227.4	230.1	322.8	258.8	229.6
T50 (ºC)	259.3	273.8	325.3	276.7	269.2
T90 (ºC)	291.6	321.4	334.3	289.4	329.0
C (% w/w)	86.23	84.14	76.24	85.00	83.58
H (% w/w)	13.77	13.48	12.38	15.00	13.38
O (% w/w)	0.00	2.38	11.38	0.00	3.04
Average molecular formula	$C_{13.57}H_{25.99}$ [1]	$C_{14.58}H_{28.04}O_{0.31}$ [3]	$C_{18.06}H_{35.19}O_2$ [2]	$C_{14.17}H_{30.02}$ [1]	$C_{14.66}H_{27.95}O_{0.4}$ [3]
Stoichiometric air to fuel ratio	14.60	14.16	12.51	14.88	14.01

[1] Calculated from the C and H content (provided by the fuel supplier) and the molecular weight, calculated with software ASPEN
[2] Calculated from the ester profile, supplied by the fuel producer
[3] Calculated from the formula of the blended components, weighting the number of C, H and O atoms by the molar fraction

3. Results

3.1 Vehicle efficiency and combustion analysis

The fuel consumption for the different phases of the WLTC procedure is shown in Fig. 2 (at both ambient temperatures), while Fig. 3 shows the energy consumption calculated from the former and the heating value of the fuels tested. The energy consumption is inversely related to the engine thermal efficiency. As expected, fuel consumption increased at -7 ºC due to higher mechanical and heat losses as well as to a less efficient combustion process, especially during the low-speed phase of the driving cycle. Regarding the type of fuel, biodiesel-based fuels (B100, B20 and Mo·bio®), mainly neat biodiesel, exhibited higher fuel consumption consistently with their heating values. In the same way, the high energy content of HVO led, in general, to the best fuel economy. Differences between fuels were less noticeable at cold temperature since the above-mentioned constraints limiting the engine efficiency (mechanical/heat losses and incomplete combustion) masked the effect of the fuel properties. It is valuable to remark that, under warm climatic conditions, B100 and B20 caused higher thermal efficiencies because of an improved combustion process, this effect not being perceptible for Mo·bio® due to its lower cetane number. Moreover, the important decrease in the EGR rate (see Fig. 4, which shows the relative EGR valve

opening (%)) when B100 is used also contributed to an enhanced engine efficiency for this fuel. HVO provided some benefits under conditions for which autoignition is a key phenomenon, such as the warm-up period of the engine (low speed phase) at cold ambient temperature. At these conditions, the cetane number and volatility of the fuel played a significant role.
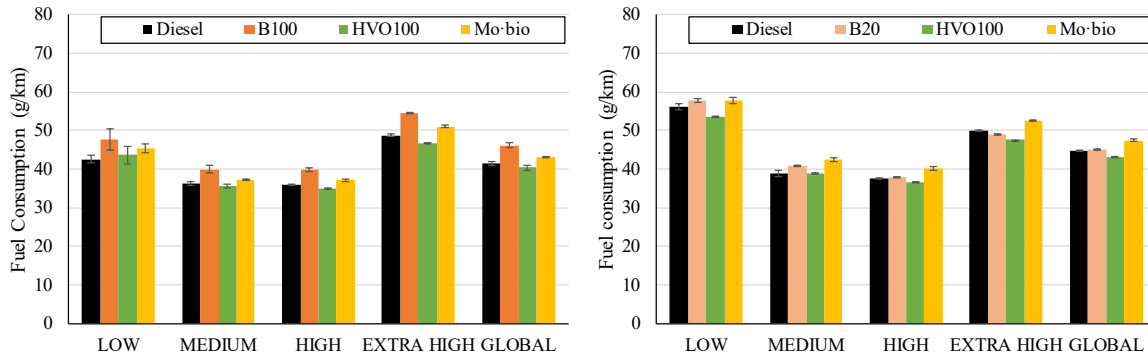
Fig. 2. Specific fuel consumption at 24 ºC (left) and -7 ºC (right)
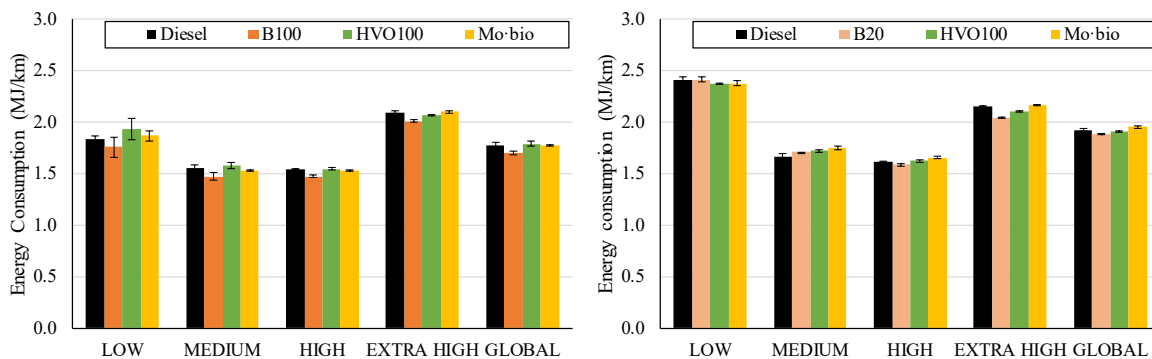
Fig. 3. Specific energy consumption at 24 ºC (left) and -7 ºC (right)

Since the effect of EGR on engine-out NO_x emissions is very relevant [26], Figure 4 also allowed for isolating the influence of the fuel from that of the EGR rate (at least from a qualitative point of view). As observed, cold ambient temperature did not permit high EGR ratios, especially during the first part of the cycle, in order to guarantee an appropriate combustion process. Once the engine is hot enough, the EGR rate increased, reaching even similar values than those at 24 ºC during the extra-high speed phase. Average EGR valve opening values were around 11 and 5 % at 24 and -7 ºC, respectively. No significant differences in the EGR rates were observed between fuels excepting B100 at 24 ºC, for which, as mentioned before, the higher fuel consumption (Fig. 2) led to a decrease in this ratio.
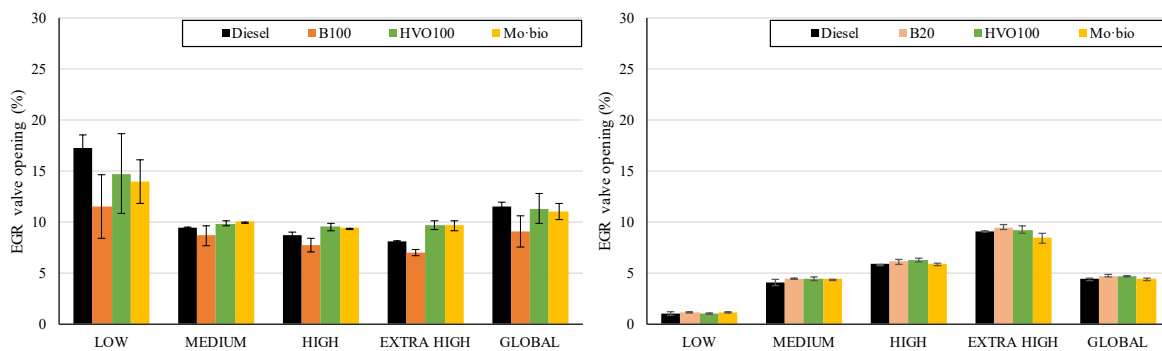
Fig. 4. EGR valve opening at 24 ºC (left) and -7 ºC (right)

Information about the combustion phasing and duration (derived from the combustion diagnosis), which is highly conditioned not only by the type of fuel but also by the injection strategy, was required to justify the engine-out pollutant emissions level. The engine mapping involved two pilot and a main injection events. The timing of the first pilot injection (in crank angle degrees (CAD) before top dead centre (TDC)), which is shown in Fig. 5 for both temperatures, was used in this work as representative for the start of the injection. The injection was advanced at -7 ºC during the low-speed phase to compensate the higher fuel consumption resulting from the lower engine efficiency. As the cycle progresses, the start of injection became similar at both temperatures. Only when the heating value of the fuel is low enough, as it is the case of B100, and the ambient temperature is high enough for the fuel properties to play a differentiating role (24 ºC), the injection timing was somewhat affected by the fuel. An opposite though much less visible trend was observed for HVO, with a slightly lower fuel consumption.
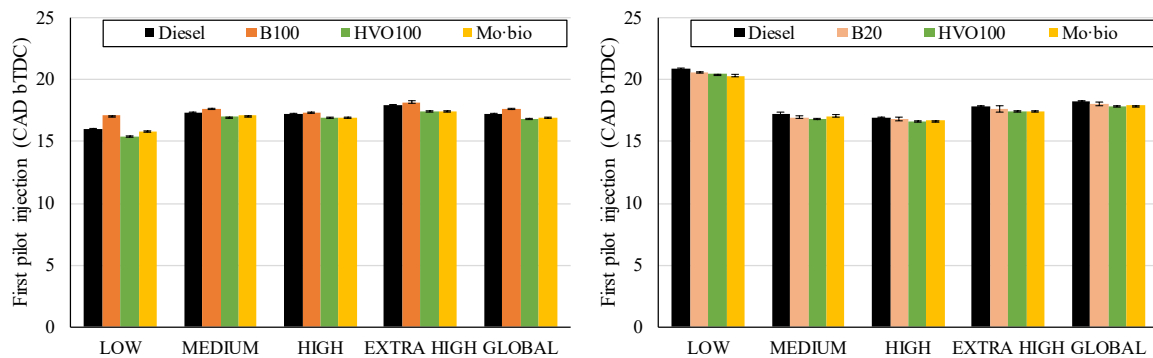
Fig. 5. Start of injection at 24 ºC (left) and -7 ºC (right)

Ignition delay values shown in Fig. 6 were calculated as the crank angle interval between the first pilot injection and the start of the combustion (defined as the angle for which 5% of the total apparent heat has been released). The overall higher values at 24 ºC were probably consequence of the higher EGR rates, since the autoignition time is very sensitive to the in-cylinder oxygen concentration [27]. The cetane number of HVO was very relevant mainly during the warm-up period of the engine under both climatic conditions, showing the shortest ignition delay. The poorer physical properties of biodiesel and Mo·bio®, mainly the viscosity in case of B100 and the volatility for the latter, retarded autoignition (although the higher cetane number of Mo·bio® partially compensate this trend). This behaviour was evident at 24 ºC although, once again, the in-cylinder thermodynamic conditions dominated over the fuel properties under cold ambient temperature, unless the fuel composition clearly favoured ignition (as it is the case of HVO). Differences between fuels diminished during the final parts of the cycle, when the engine temperature was high enough.
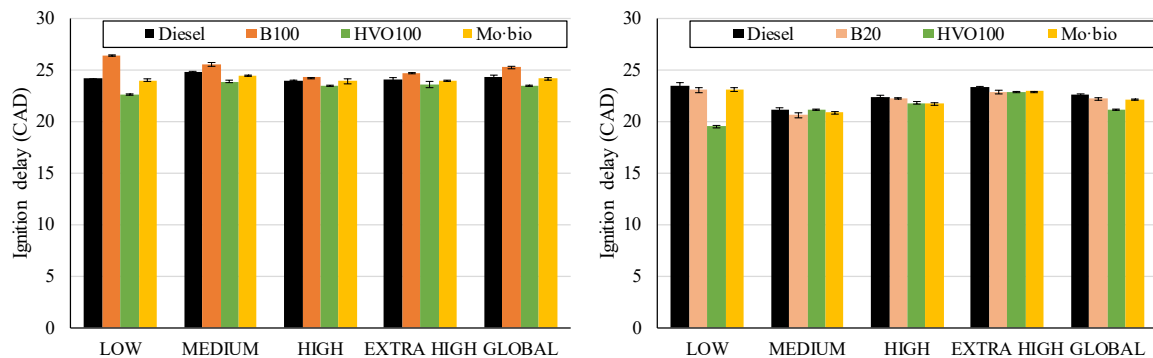
Fig. 6. Ignition delay at 24 ºC (left) and -7 ºC (right)

Figures 7 and 8 show, respectively, the combustion duration (defined as the crank angle interval between the start of combustion and the angle for which 90% of the total heat was released), and the crank angle for which 50% of the total apparent heat release was reached (usually denoted as CA50). No important differences were observed between climatic conditions, since the lower in-cylinder

temperature at -7 ºC (which would hinder the combustion development) counteracts the also lower EGR rate (this condition enhancing combustion). The higher combustion velocity of oxygen-containing fuels (B100, B20 and Mo·bio®) [28] led to a faster combustion process. Oppositely, the paraffinic structure of HVO slightly extended the combustion duration [29][30]. The combination of the mentioned parameters (injection timing, ignition delay and combustion duration) led to the combustion phasing (CA50) indicated in Fig. 8. No relevant differences between fuels were detected since longer ignition delays are usually linked with quicker combustion processes and/or advanced injection timings. Regarding the ambient temperature, the slightly advanced injection and the shorter ignition delay at -7 ºC moved combustion closer to TDC.
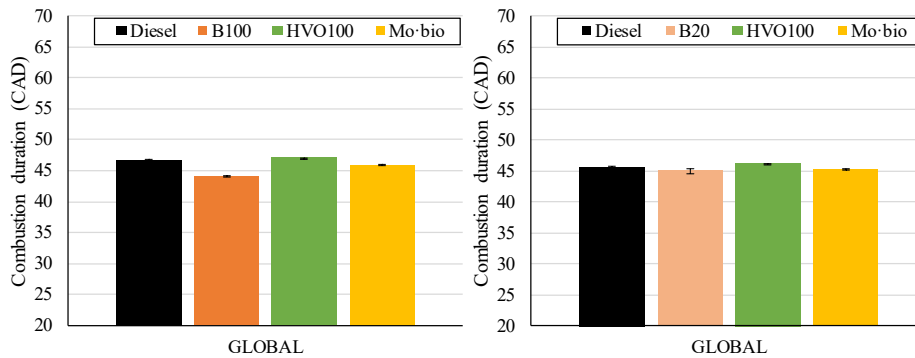
Fig. 7. Combustion duration at 24 ºC (left) and -7 ºC (right)
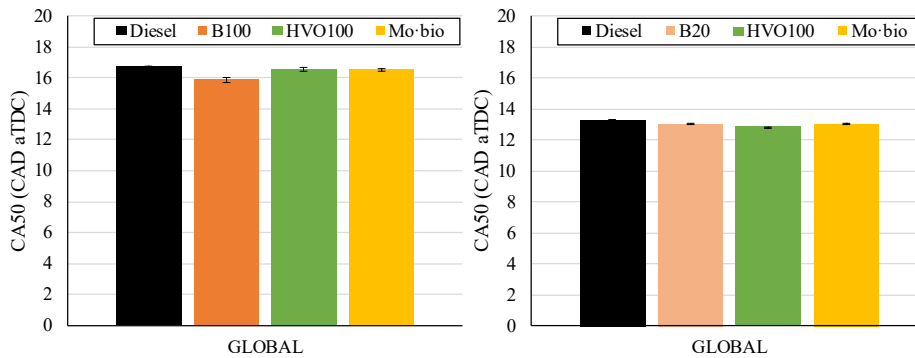
Fig. 8. CA50 at 24 ºC (left) and -7 ºC (right)

The exhaust gas temperature, which strongly affects the conversion efficiency of the SCR (shown later), is a consequence of the energy consumption and the combustion phasing and duration. The instantaneous evolution of this parameter is shown in Fig. 9 upstream of the SCR (point 2 in Fig. 1). The higher EGR rate, the also higher intake air temperature and the slightly delayed combustion process at 24 ºC dominated over the lower energy consumption, thus leading to a higher thermal level in the exhaust gas when compared to -7 ºC.
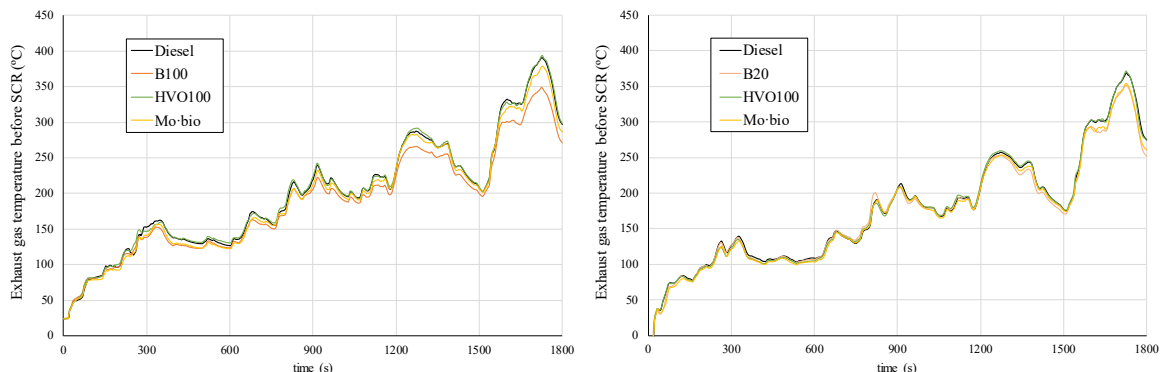
Fig. 9. Exhaust gas temperature upstream of SCR at 24 ºC (left) and -7 ºC (right)

Neat biodiesel exhibited lower exhaust gas temperatures because mainly its lower EGR rate. Furthermore, an improved combustion efficiency (Figure 3) and a slightly earlier combustion process (Figure 8), the latter causing a more intense cooling of the burnt gas during expansion, also contributed to this result.

3.2 Gaseous emissions

As explained before, gaseous emissions were measured upstream (after the DOC) and downstream (after the DPF) of the SCR system. In case of CO emissions, only downstream values are shown in Fig. 10 because of the negligible effect of the SCR catalyst on this compound [31]. As observed, tailpipe CO emissions were very small and only noticeable during the first instants of the low speed phase of the cycle, because the light-off temperature of the DOC was not reached yet. Obviously, this effect is more significant at -7 ºC. Variations between fuels were small excepting HVO at cold temperature because, as previously commented, its higher combustion efficiency (Figure 3) together with its more appropriate volatility (which favours evaporation) caused a lower engine-out CO level. Figure 11 shows THC emissions upstream and downstream of the SCR. These emissions were also very low and followed the same trend as CO with ambient temperature. In this case, at cold temperature, not only HVO stood out from the rest of fuels (with the smaller THC amount) but also B20, which displayed a sharp THC peak at the beginning of the cycle. The worse cloud point of this latter fuel, close to the tested temperature, prompted this behaviour. In addition, the higher oxygen content of Mo·bio® (Table 3) also provided benefits with respect to B20. It should be noted that, under these conditions, the THC concentration after the SCR was lower than that at the inlet of the catalyst. This trend has been reported in other works as consequence of a chemical use of hydrocarbons by the SCR. At low exhaust gas temperature conditions (cold ambient and/or low speed phase of the cycle, as shown in Fig. 9) unconverted THCs are adsorbed and stored in the porous structure of the SCR. Later, when the temperature increases enough, they are released and consumed during the NO_x reduction paths [32][33] as a reducing agent in combination with ammonia.
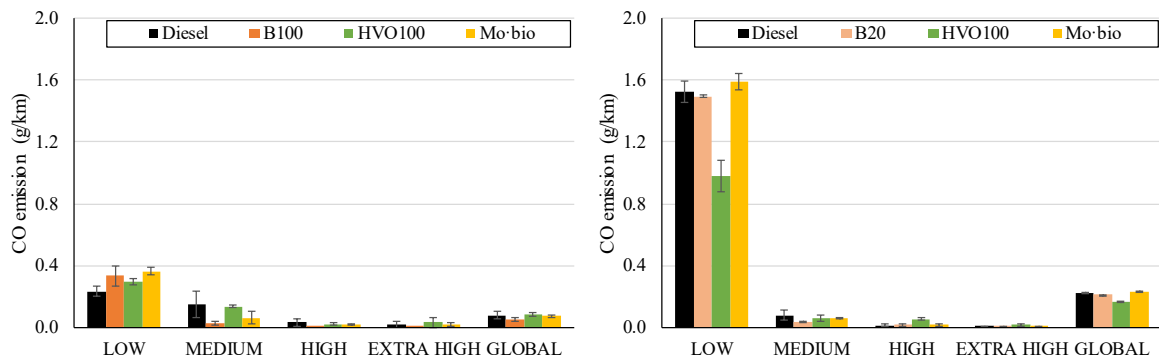
Fig. 10. Specific CO emission at 24 ºC (left) and -7 ºC (right)
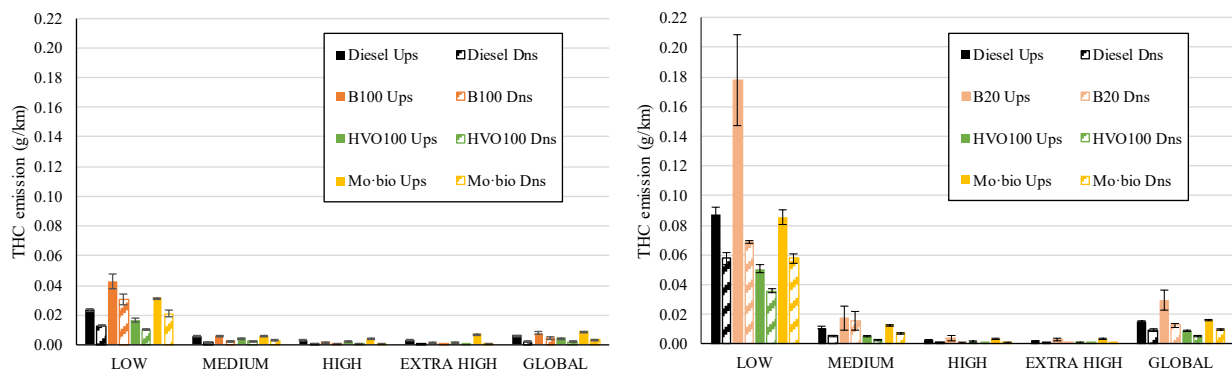
Fig. 11. Specific THC emission upstream (Ups) and downstream (Dns) of the SCR at 24 ºC (left) and -7 ºC (right)

Figure 12 shows the specific NO$_x$ emission upstream of the SCR at both temperatures. The lower EGR valve opening, together with a minor contribution of a more centred combustion process (see CA50 in Fig. 8), caused an increase in NO$_x$ emissions at – 7 ºC. Moreover, higher fuel consumptions at the low speed (to compensate engine losses) and at the extra-high speed (to comply with the higher engine power requirement) phases also contributed to higher NO$_x$. Regarding fuel-related effects, the smaller EGR rate and the shorter combustion duration with biodiesel increased NO$_x$ formation under warm conditions. Additionally, the higher equivalence ratio (derived from a higher fuel consumption) when biodiesel-type fuels are used could be the main reason for their also higher NO$_x$ emission at -7 ºC. While the superior autoignition trend of HVO reduced NO$_x$ at warm temperature by diminishing the premixed combustion fraction, no clear explanation was found to explain the best performance of diesel fuel at cold temperature. It is valuable to mention that the very high sensitivity of NO$_x$ emissions to the EGR rate limits somehow the achievement of more precise conclusions.
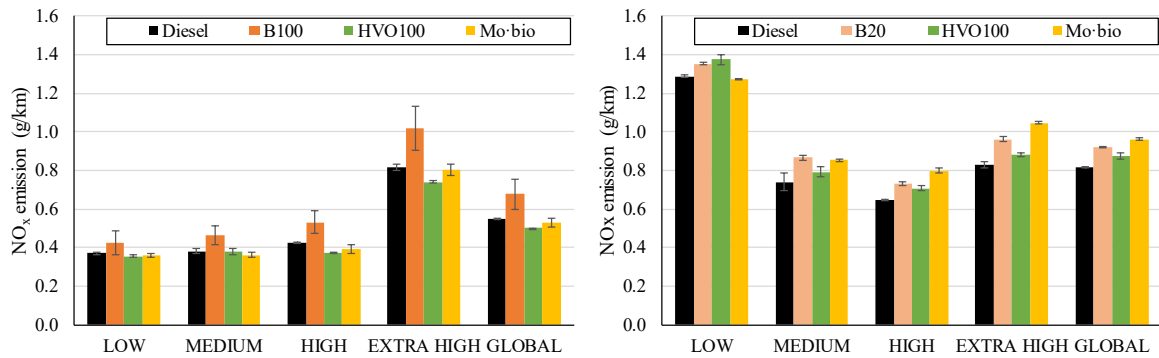
Fig. 12. Specific NO$_x$ emission upstream of the SCR at 24 ºC (left) and -7 ºC (right)

The SCR efficiency, shown in Fig. 13, was calculated from the NO$_x$ emission upstream and downstream of the system. Three reasons contributed to better efficiencies at warm conditions: a more appropriate catalyst temperature (the main parameter affecting the NO$_x$ conversion rate in this type of catalysts), the lower inlet NO$_x$ concentration and an adequate NO$_2$/ NO$_x$ ratio (shown in Fig. 14).
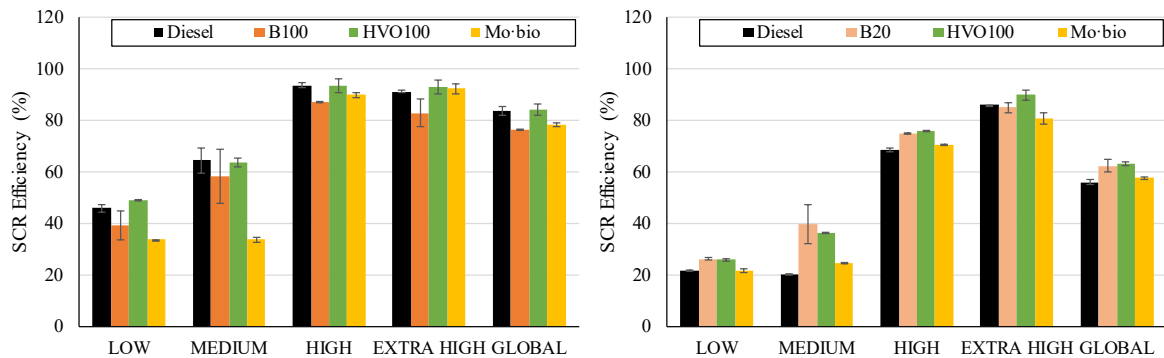
Fig 13. SCR efficiency at 24 ºC (left) 410 and -7 ºC (right)
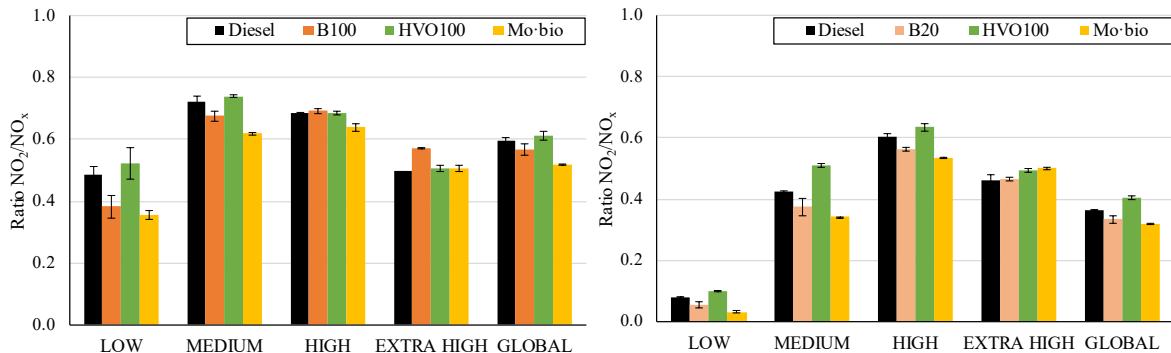
Fig. 14. NO$_2$ to NO$_x$ ratio upstream SCR at 24 ºC (left) and -7 ºC (right)

In fact, it has been widely reported that NO_2/NO_x ratios below 0.5 hinder the fast reduction reaction ($NH_3 + 1/2\ NO + 1/2\ NO_2 = N_2 + 3/2\ H_2O$), which highly boosts the NO_x removal rate [34]. This could be the reason for the highest SCR efficiency at cold temperature when HVO was used. The acceptable conversion efficiencies of B20 at -7 ºC were maybe due to the previous mentioned THC accumulation in the catalyst substrate during the low speed phase. These hydrocarbons were released in the subsequent phases of the cycle, thus supporting NO_x reduction reactions. Since the exhaust gas temperature at 24 ºC (Figure 9) was lower for B100 and Mo·bio®, in addition to the higher NO_x amount at the SCR inlet, it was not surprising the worse conversion level when using these fuels.

3.3 Particle emissions

Particle number emissions were measured upstream of the DPF using an EEPS, which allows for counting particles with diameters between 5.6 and 560 nm and provides the number concentration as function of the diameter. Since EU regulation 1151/2017 [2] only considers particles larger than 23 nm, this value was taken as the lower limit during the tests. In general, particle number was only relevant when the fuel consumption was substantial, i.e. during the extra high-speed phase at both climatic conditions and the low-speed phase at – 7ºC. As widely reported, the oxygen content of biodiesel-based fuels (B100 and B20) led to lower particle number with respect to diesel fuel. However, Mo·bio®, which has higher oxygen content than B20, caused similar or even higher particle number emissions than diesel fuel at the extra-high speed phases. Although this trend could be explained by a larger EGR rate (Figure 4) at warm conditions, no clear explanation was found at -7 ºC. Because of its nil aromatic content, HVO caused lower particle number emissions than diesel fuel excepting the extra-high speed phase at 24 ºC, for which HVO produced much more soot. Together with the difference in the EGR rate between these fuels at this condition (Figure 4), maybe not enough to justify the important increase in soot emissions with HVO, the significant autoignition reactivity of this fuel (favoured at warm temperature and high engine loads) could also contribute to the formation of soot precursors because of richer conditions downstream of the lift-off length during the transient fuel jet evolution. The local equivalence ratios of the premixed combustion taking place at this location have been widely reported to greatly affect engine-out soot emissions, as initially documented by Dec [35] and widely checked in subsequent works [36][37]. In fact, although unusual, some authors have observed an increase in soot emission when using HVO under some engine conditions because of this phenomenon [38].
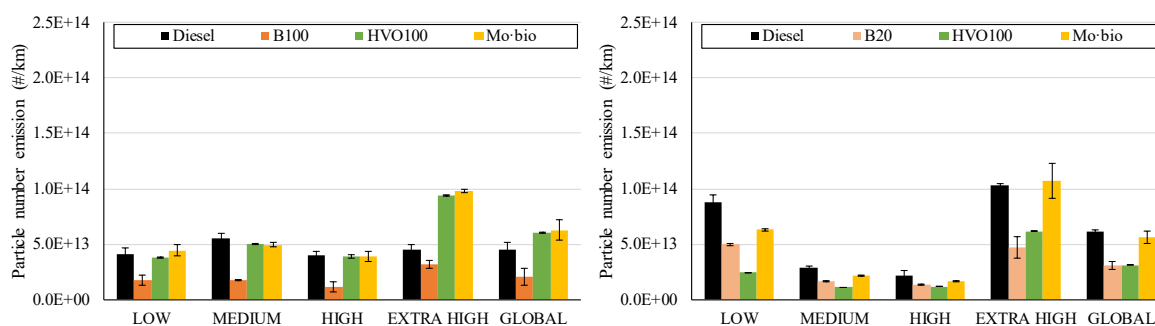
Fig. 15. Specific particle number emissions at 24 ºC (left) and -7 ºC (right)

Conclusions

Tests in a chassis dyno with a Euro 6 diesel vehicle equipped with ammonia-SCR following the WLTC at 24 and -7 ºC were performed. Three advanced biofuels (HVO, a glycerol-derived biofuel and biodiesel from the esterification of residual free fatty acids) were used in order to evaluate fuel-derived effects when compared to conventional diesel fuel. Although results showed that the engine operating conditions (mainly the EGR rate), the driving cycle phase and the ambient temperature played a more important role than that of fuel type on pollutant emissions and SCR efficiency, some fuel-related conclusions were obtained mostly under warm climatic conditions. This allows to conclude that even though the biofuels tested can be used directly in modern diesel vehicles, some engine mapping modification would let for lowering pollutant emissions. This latter aspect is especially important nowadays because of the expected greater presence of these compounds in future diesel-type fuels as well as more restrictive upcoming certification limits. The main following conclusions can be drawn:

- Biodiesel fuels, B100 and B20, caused higher thermal efficiencies (more noticeable at warm temperature) due to their oxygen content and, in the former case, to the lower EGR rate. HVO (with a high cetane number and volatility) showed benefits in terms of thermal efficiency under conditions for which autoignition became relevant, such as the warm-up period at cold ambient temperature.

- The combination between injection timing (more advanced for biodiesel-type fuels because of their higher fuel consumption), ignition delay (lower for HVO because of its high cetane number) and combustion duration (shorter for oxygen-containing fuels) led to similar combustion location (CA50) for all the fuels. The more advanced combustion phasing at -7 ºC was caused by the lower EGR rate at this condition.

- Once the light-off temperature of the DOC was reached (after the first period of the low speed phase, especially at -7 ºC), CO and THC emissions were insignificant. While, in general, HVO presented the lowest values, the high cloud point of B20 caused significant THC emissions at cold ambient temperature. Regarding NO_x emissions, the very strong impact of EGR on this compound makes difficult to clearly isolate the effect of the fuel composition. Nevertheless, it seems that the autoignition trend of HVO allowed for reducing NO_x due to the decrease in the premixed combustion ratio.

- The SCR efficiency was not only affected by the catalyst temperature and the NO_x concentration at the catalyst inlet (both higher at warm temperature), but also by the NO_2/ NO_x ratio (closer or higher to the optimal value of 0.5 at 24 ºC). The latter reason (which favours the fast reduction reaction) could cause the best performance observed for HVO at cold temperature. THC-supported reduction reactions also contributed to the acceptable conversion efficiencies of B20 at this climatic condition.

- Noticeable particle number emissions were associated to high fuel consumptions (extra high-speed phase at both climatic conditions and low-speed phase at -7ºC). The EGR rate appeared again as a significant parameter governing soot emission. However, HVO, which was expected to reduce soot because of its nil aromatic content, led to significant emissions under high engine loads at warm temperature. In addition to a higher EGR rate, a richer local premixed combustion after the lift-off length of the fuel jet also promoted this latter result.

Acknowledgements

References

[1]. UN. 2008 Commission Regulation (EC) No 692/2008 of 18 July 2008 implementing and amending Regulation (EC) No 715/2007 of the European Parliament and of the Council on type-approval of motor vehicles with respect to emissions from light passenger and commercial vehicles (Euro 5 and Euro 6) and on access to vehicle repair and maintenance information (OJ L 199 28.7.2008, p.1).

[2]. UN 2017 Commission Regulation (EU) 2017/1151 of 1 June 2017 supplementing Regulation (EC) No 715/2007 of the European Parliament and of the Council on type-approval of motor vehicles with respect to emissions from light passenger and commercial vehicles (Euro 5 and Euro 6) and on access to vehicle repair and maintenance information, amending Directive 2007/46/EC of the European Parliament and of the Council, Commission Regulation (EC) No 692/2008 and Commission Regulation (EU) No 1230/2012 and repealing Commission Regulation (EC) No 692/2008 (OJ L 175, 7.7.2017, p. 1).

[3]. Mohan S, Dinesha P, Kumar S. NO_x reduction behaviour in copper zeolite catalysts for ammonia SCR systems: A review. Chemical Engineering Journal. 2020;384.

[4]. Wittka T, Holderbaum B, Dittmann P, Pischinger S. Experimental Investigation of Combined LNT + SCR Diesel Exhaust Aftertreatment. Emission Control Science and Technology 2015;1(2):167-182.

[5]. European Parliament. Directive (EU) 2018/2001 of the European Parliament and of the Council of 11 December 2018 on the Promotion of the Use of Energy from Renewable Sources. 2018. Available online: https://eur-lex.europa.eu/legal-content/EN/TXT/?uri=uriserv:OJ.L_.2018.328.01.0082.01.ENG (accessed on 15 March 2020).

[6]. EN 14214:2013. Liquid petroleum products – Fatty acid methyl esters (FAME) for use in diesel engines and heating applications – Requirements and tests methods. European Committee for Standardization, 2013.

[7]. EN 590:2014 Automotive fuels - Diesel - Requirements and test methods.

[8]. El Kinawy OS, Zaher FA. Studies on esterification kinetics of short chain alcohols with fatty acids to produce biodiesel fuel. Energy Sources, Part A: Recovery, Utilization and Environmental Effects. 2012;34(7):662-670.

[9]. Khayoon MS, Hameed BH. Synthesis of hybrid SBA-15 functionalized with molybdophosphoric acid as efficient catalyst for glycerol esterification to fuel additives. Applied Catalysis A: General. 2012;433-434:152-161.

[10]. Lapuerta M, Rodríguez-Fernández J, Estevez C, Bayarri N. Properties of fatty acid glycerol formal ester (FAGE) for use as a component in blends for diesel engines. Biomass and Bioenergy. 2015;76:130-140.

[11]. Lapuerta M, González-García I, Céspedes I, Estévez C, Bayarri N. Improvement of cold flow properties of a new biofuel derived from glycerol. Fuel. 2019;242:794-803.

[12]. Lapuerta M, Rodríguez-Fernández J, García-Contreras R. Effect of a glycerol-derived advanced biofuel -FAGE (fatty acid formal glycerol ester)- on the emissions of a diesel engine tested under the New European Driving Cycle. Energy. 2015;93:568-579.

[13]. Silitonga AS, Masjuki HH, Mahlia TMI, Ong HC, Chong WT. Experimental study on performance and exhaust emissions of a diesel engine fuelled with Ceiba pentandra biodiesel blends. Energy Conversion Management. 2013;76:828-836.

[14]. Nabi MN, Akhter MS, Shahadat MMZ. Improvement of engine emissions with conventional diesel fuel and diesel-biodiesel blends. Bioresource Technology. 2006;97(3):372-378.

[15]. Sonthalia A, Kumar N. Hydroprocessed vegetable oil as a fuel for transportation sector: A review. Journal of the Energy Institute. 2019;92(1):1-17.

[16]. No S.-Y. Application of hydrotreated vegetable oil from triglyceride based biomass to CI engines - A review. Fuel. 2014;115:88-96.

[17]. Torres-Ortega CE, Gong J, You F, Rong B-. Optimal synthesis of integrated process for coproduction of biodiesel and hydrotreated vegetable oil (HVO) diesel from hybrid oil feedstocks. Computer Aided Chemical Engineering. 2017;40:673-678.

[18]. Omari A, Pischinger S, Bhardwaj OP, Holderbaum B, Nuottimäki J, Honkanen M. Improving Engine Efficiency and Emission Reduction Potential of HVO by Fuel-Specific Engine Calibration in Modern Passenger Car Diesel Applications. SAE International Journal of Fuels and Lubricants 2017;10(3).

[19]. Dimitriadis A, Seljak T, Vihar R, Žvar Baškovič U, Dimaratos A, Bezergianni S, et al. Improving PM-NOx trade-off with paraffinic fuels: A study towards diesel engine optimization with HVO. Fuel. 2020;265.

[20]. Murtonen T, Aakko-Saksa P, Koponen P, Lehto K, Sarjovaara T, Happonen M et al. Emission reduction potential with paraffinic renewable diesel by optimizing engine settings or using oxygenate. In SAE 2012 International Powertrains, Fuels and Lubricants Meeting, FFL 2012, Malmo, Sweden, 18-20 September 2012. SAE Technical Papers. SAE International. 2012. 2012-01-1590.

[21]. Aatola H, Larmi M, Sarjovaara T, Mikkonen S. Hydrotreated vegetable Oil (HVO) as a renewable diesel fuel: Trade-off between NOx, particulate emission, and fuel consumption of a heavy duty engine. SAE International Journal of Engines. 2009;1(1):1251-1262.

[22]. Dimitradis A, Natsios I, Dimaratos A, Katsaounis D, Samaras Z, Bezergianni S, Letho K. Evaluation of a Hydrotreated Vegetable Oil (HVO) and Effects on Emissions of a Passenger Car Diesel Engine. Frontiers in Mechanical Engineering. 2018; 4, 7.

[23]. Bielaczyc P, Szczotka A, Woodburn J. The effect of a low ambient temperature on the cold-start emissions and fuel consumption of passenger cars. Proceedings of the Institution of Mechanical Engineers, Part D: Journal of Automobile Engineering. 2011;225(9):1253-1264.

[24]. EN 15940:2016. Automotive fuels – Paraffinic diesel fuel from synthesis or hydrotreatment – Requirements and methods. European Committee for Standardization, 2016.

[25]. UNECE Regulation 15. Global technical regulation on Worldwide harmonized Light vehicles Test Procedures (WLTP), 2019. https://www.unece.org/fileadmin/DAM/trans/main/wp29/wp29r-1998agr-rules/GTR15-am5-For_Registry_EN.pdf. (accessed on 15 March 2020).

[26]. Jain A, Singh AP, Agarwal AK. Effect of split fuel injection and EGR on NO$_x$ and PM emission reduction in a low temperature combustion (LTC) mode diesel engine. Energy. 2017;122:249-264.

[27]. Lapuerta M, Sanz-Argent J, Raine RR. Ignition characteristics of diesel fuel in a constant volume bomb under diesel-like conditions. Effect of the operation parameters. Energy and Fuels. 2014;28(8):5445-5454.

[28]. Öztürk E. Performance, emissions, combustion and injection characteristics of a diesel engine fuelled with canola oil-hazelnut soapstock biodiesel mixture. Fuel Processing Technology. 2015;129:183-191.

[29]. Li Y, Xu H, Cracknell R, Head R, Shuai S. An experimental investigation into combustion characteristics of HVO compared with TME and ULSD at varied blend ratios. Fuel. 2019;255: 115757.

[30]. Armas O, García-Contreras R, Ramos A. On-line thermodynamic diagnosis of diesel combustion process with paraffinic fuels in a vehicle tested under NEDC. Journal of Cleaner Production. 2016;138:94-102.

[31]. Smith MA, Depcik C, Hoard J, Bohac S, Assanis D. The effects of CO, H2, and C3H6 on the SCR reactions of an Fe zeolite SCR catalyst. In SAE 2013 World Congress and Exhibition; Detroit, MI; United States; 16 April 2013 through 18 April 2013; Code 97364. SAE Technical Papers 2013;2.

[32]. Selleri T, Nova I, Tronconi E, Schmeisser V, Seher S. The impact of light and heavy hydrocarbons on the NH3-SCR activity of commercial Cu- and Fe-zeolite catalysts. Catalysis Today. 2019;320:100-111.

[33]. Traa Y, Burger B, Weitkamp J. Zeolite-based materials for the selective catalytic reduction of NO$_x$ with hydrocarbons. Microporous and Mesoporous Materials. 1999;30(1):3-41.

[34]. Forzatti P, Nova I, Tronconi E. New "enhanced NH3-SCR" reaction for NO$_x$ emission control. Industrial and Engineering Chemistry Research. 2010;49(21):10386-10391.

[35]. Dec JE. A conceptual model of di diesel combustion based on laser-sheet imaging. In International Congress and Exposition; Detroit, MI; United States; 24 February 1997 through 27 February 1997; Code 90577. SAE Technical Paper. 1997.

[36]. Payri R, Gimeno J, Cardona S, Ayyapureddi S. Experimental study of the influence of the fuel and boundary conditions over the soot formation in multi-hole diesel injectors using high-speed color diffused back-illumination technique. Applied Thermal Engineering. 2019;158.

[37]. Donkerbroek AJ, Boot MD, Luijten CCM, Dam NJ, ter Meulen JJ. Flame lift-off length and soot production of oxygenated fuels in relation with ignition delay in a DI heavy-duty diesel engine. Combustion and Flame. 2011;158(3):525-538.

[38]. Zubel M, Bhardwaj OP, Heuser B, Holderbaum B, Doerr S, Nuottimäki J. Advanced Fuel Formulation Approach using Blends of Paraffinic and Oxygenated Biofuels: Analysis of Emission Reduction Potential in a High Efficiency Diesel Combustion System. SAE International Journal of Fuels and Lubricants. 2016;9(3):481-492.

Renewable Energy to Power through Net-Zero-Carbon Methanol

R. Durrett[1] and M. Potter[1]

[1]GM Global Research and Development, Warren, Michigan, USA.

E-mail: russell.durrett@gm.com
Telephone: +(1) 586 879 5828

Abstract. Net-Zero-Carbon (NZC) Fuels are synergistic with a growing capacity of renewable energy generation. NZC Liquid Fuels represent an interesting option to accelerate the displacement of fossil fuels in applications or regions where full electrification is challenging or impossible. Within the family of liquid fuels, methanol represents a particularly efficient option for converting renewable energy to a liquid NZC fuel. Furthermore, a compression ignition internal combustion engine provides an efficient path for conversion of energy stored in methanol to power.

This paper will compare the use of neat methanol to Diesel fuel, using n-heptane as a surrogate, via a combined 1-D and 3-D modelling effort in order to evaluate the likely direction of methanol combustion technology for future NZC transportation. Preliminary results suggest that a methanol fueled compression ignition engine will provide excellent fuel conversion efficiency and significant system cost reduction opportunities.

Notation

BMEP	Brake Mean Effective Pressure
BTE	Brake Thermal Efficiency
CNL	Combustion Noise Level
CR	Compression Ratio
EGR	Exhaust Gas Recirculation
LHV	Lower Heating Value
MEOH	Methanol
PCP	Peak Cylinder Pressure
PMEP	Pumping Mean Effective Pressure
NZC	Net Zero Carbon

1. Introduction

In response to concerns regarding climate change, governments and private entities are putting in place initiatives to reduce the CO2 footprint of the economy through both regulations and voluntary sustainability objectives. While sectors of the economy begin to address the mix of energy sources consumed within their operations, the overall demand for energy in some sectors is anticipated to grow. Using the United States commercial truck sector as an example, anticipated energy use for light commercial vehicles in 2020 will be 0.89 quads and grow to 1.07 quads by 2050. Anticipated energy use for freight over the same period will grow from 5.87 quads to 6.09 quads [1]. While electrification of portions of the transportation sector will be an important part of the global path to sustainability, many important participants are exploring a range of transportation energy options within their sustainability plans [2].

1.1 The Case for Methanol as an Energy Carrier

A range of investigators has considered the dynamics of the global energy market. As these investigations proceed, it becomes increasing apparent that a range of energy carriers will likely serve the global economy [3]. While the volume of fossil energy products traded will need to decline substantially over the next decades, renewable energy carriers are likely to replace them, leveraging the legacy methods of distribution. One key driver is the relative location of renewable energy production versus the location of energy consumption. Again, using the example of the United States, Figure 1 shows that the central

continent serves as the primary source of renewable solar and wind capacity, while high density populations occur along the coasts and in the Great Lakes basin [4, 5]. Moving electrical energy long distances can be a challenge. One study indicates the cost of long-distance energy transmission via the electrical grid is an order of magnitude more costly than transport via chemical energy [6].
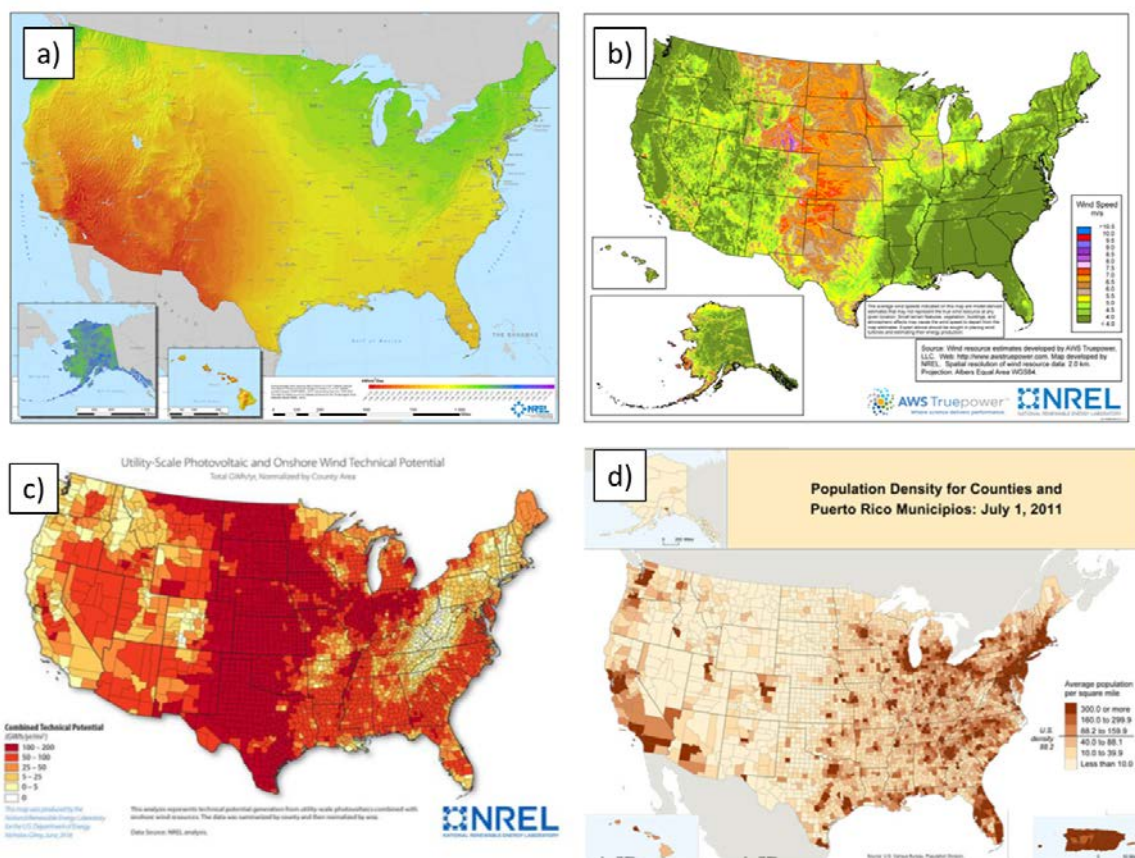
Fig. 1. Renewable energy resources and population distribution, a) solar energy intensity, b) wind energy intensity, c) combined wind and solar intensity, d) population distribution

While it is widely accepted that light duty personal transportation accommodates electrified vehicles well and that local pick-up and delivery is amenable to electrification, other applications may benefit from chemical energy carriers that are more aligned with the operating profile of various fleets and commercial operations. Major fleets exemplify the range of low CO2 options integrated into a comprehensive commercial operation. Very large fleets have had the financial scale to experiment with a range of technologies. The results of those experiments suggest a range of energy carriers will be used well into the next decades. It is noteworthy that e-fuels now are considered along with the more established renewable Diesel, renewable jet fuel, renewable natural gas and electrification as a component of a future transport energy mix [7].

Methanol is a prime candidate as a global energy carrier. It is already widely traded on a global basis as a commodity for a range of industrial and consumer product uses [8]. It is safe, relative to conventional energy carriers, as it has low toxicity, disperses quickly in the event of an accidental release, and biodegrades rapidly in soil or water. The methods and capacity of transport are already well established in the global economy. Methanol can be synthesized from a range of carbon sources including: industrial carbon capture, direct CO2 capture, agricultural waste, and municipal waste, to name a few. When the synthesis process combines these carbon streams with renewable electricity, a fully carbon neutral energy carrier can be the result.

1.2 The Case for Methanol as a Diesel Fuel

Given that methanol is a primary precursor for many of the chemical fuels currently considered as alternatives to fossil fuels [9], it is useful to consider use of methanol directly, thereby eliminating the energy consumption associated with further processing. Methanol is already used in China as fuel for spark

ignition engines and is being considered for use as a blending agent by some investigators for European spark ignition applications [8][10].

An effective way to introduce alternative fuel technology is through fleet applications as has been done with CNG, LNG and LPG. Since fleet operation technology choices are primarily driven by total cost of ownership, vehicle cost and efficiency are important factors driving their vehicle purchases. One way to align financial motivation with societal needs, is to provide cost effective CO_2 reduction technologies to the market.

The case of the Southern California Rapid Transit Authority methanol bus program in the last decades of the 20th century confirms that methanol can serve as a renewable and low emission fuel for Diesel fleet applications [11]. Engine manufacturers participating in the transit bus program provided a useful technical roadmap for re-establishing methanol as a renewable fuel [12, 13].

1.3 The Case for Our Study

In this regard, the authors explored the use of methanol in a contemporary light duty/light commercial Diesel engine configuration. The 0.4L to 0.5L unitary displacement covers a broad range of engine applications ranging from 1.2L to 4.0L offerings. Therefore, the findings from this investigation can be applicable to a wide range of commercial vehicles, particularly in the last mile delivery category, service sector, and vehicles for skilled trades.

In the context of compression ignition applications, the authors see potential for a range of characteristics that might provide opportunities for continued investigation. The low viscosity and fast vaporization of methanol may allow lower pressure fuel systems to be used. Methanol may provide an opportunity to significantly simplify the Diesel typical intake charge system. Research regarding the use of alcohols as reductant fluids in HC-SCR systems has shown significant promise [14]. It is possible that a HC-SCR system using methanol for a reductant would allow a single fluid to serve as both fuel and NOx reductant. Taken in combination, it is reasonable to imagine that a compression ignition engine, optimized for methanol, could be significantly more cost effective for commercial vehicles than a contemporary Diesel fueled engine, thereby facilitating the growth of sustainable energy in the global economy.

2. Fuel, Engine, and Model Description

For the 3-D modeling work, n-heptane was used as a surrogate for Diesel fuel. The model fuel was n-heptane but the comparisons are to a production Diesel engine, so the terms 'n-heptane' and 'Diesel' are both used to refer to the fuel. Several key properties of the fuels are shown in Table 1. Some of the properties of methanol related to CI engine operation are widely known. Methanol has poor ignition quality as shown by the very low cetane number and its energy density on a volume basis is significantly lower than that of hydrocarbon fuels. However, one beneficial quality of methanol is that it requires about 5% less air to produce a given energy release in comparison to n-heptane or Diesel fuel. The lower air requirement will aid in reducing the peak cylinder pressure as well as in reducing the air flow requirements and the pumping work.

In an actual Diesel engine application, methanol would require a lubricity additive similar to that used in [15] in order to protect the fuel injection system. The effect of a lubricity additive on the combustion was not modeled in this study but is assumed to be insignificant.

Table 1. Fuel Properties

Property	N-Heptane	Methanol
Cetane Number	53.8	~5
Density (g / liter)	0.684	0.786
Lower Heating Value (MJ / kg)	44.6	20.09
Energy Density (MJ / liter)	30.5	15.8
Stoichiometric A/F ratio	15.14	6.46
Energy Released per kg Air for Stoichiometric Combustion (MJ / kg air)	2.95	3.11

The engine chosen for this study was a typical light-duty 4-stroke turbocharged compression ignition engine. This type of engine was chosen because it serves the light duty vehicle market as well as commercial and delivery vehicles. Millions of engines of this type are in use around the world.

The 1-D simulations were performed with GT-Power v7.4 [16]. The model chosen for this study was based on one of the example models included with the software (the 'Diesel_VGT_EGR' example) with some slight modifications to accommodate methanol as the fuel. This model was deemed to be a good generic representation of engines in the market, and it contains no proprietary information. The entire engine system was modeled including an inlet airbox and an exhaust aftertreatment system. The model included a turbocharger with a variable geometry turbine and a cooled, high pressure loop EGR system with an EGR control valve and a cooler bypass valve. The main modifications to the model consisted of increasing the compression ratio, changing the fuel to methanol, and increasing the nozzle flow area to maintain a similar injection duration as in the baseline Diesel. The DI-Jet combustion model was implemented in the example engine model so it was used, but the goal of the 1-D modeling was to provide boundary conditions for the 3-D modeling, so the use of the DI-Jet model had little consequence on the overall results. Some key parameters of the model are shown in Table 2.

Table 2. Engine and Operating Parameters for the 1-D Simulations

Total Displacement	2.0 liters
Displacement per Cylinder	0.5 liter
Compression Ratio – Diesel	15.5
Compression Ratio – methanol	19.0
Ambient Pressure	100 kPa
Ambient Temperature	300 K

The 3-D simulations were performed using CONVERGE v2.3 [17]. The model was developed as part of a previous study on Diesel engines by Gao et al [18] and the referenced paper provides many details on the development of the CFD model and its validation. For this study, the only changes to the model were the fuel, the bowl geometry and the nozzle flow area. Only the closed portion of the cycle was simulated with the initial conditions provided by the 1-D model. The 3-D model had a displacement of 0.4L per cylinder compared to 0.5L per cylinder for the 1-D model. To accommodate this difference, the mass of fuel and air provided by the 1-D model was scaled appropriately and the initial temperature and pressure were kept the same. A sector mesh geometry was modeled using a 1/8 sector of the cylinder. The injection rate was based on a current Diesel state of the art high pressure common rail fuel system using 3 injection pulses – 2 pilot events and a single main event. The injection rate shape and duration was kept the same for the methanol cases as for the n-heptane cases. The nozzle area was doubled, as shown in Table 3, to accommodate the larger injected quantity of methanol. A skeletal chemistry mechanism was used for the n-heptane combustion representing the Diesel cases with 144 species and 900 reactions [19, 20]. The methanol cases used a reduced mechanism with 32 species and 167 reactions obtained from the Sandia chemistry website [21]. Additional parameters of the 3-D model are shown in Table 3.

Table 3. Engine and Operating Parameters for the 3-D Simulations

Displacement per Cylinder	0.4 liter
Initial Crank Angle	138 CAD BTDC
Final Crank Angle	141 CAD ATDC
Compression Ratio – Diesel	15.5
Compression Ratio – methanol	19.0
Nozzle Geometry	8 hole, 155 degree
Nozzle Diameter – Diesel	116 microns
Nozzle Diameter – methanol	164 microns

Five engine operating conditions were chosen for this investigation as shown in Table 4. The conditions include a light load point (1), two mid load points (2 and 3), the peak torque point (4) and the peak power point (5).

Table 4. Key Point Operating Conditions

Condition	Speed (RPM)	BMEP (bar)
1	1250	2
2	2000	8
3	1500	14
4	2000	20
5	4000	19

One of the goals of the study was to develop an engine configuration for methanol that would ensure robust operation at reasonable ambient temperature without a glow plug. For a CI engine operating on methanol, it is assumed a glow plug will be available for startup and for operation at cold ambient conditions. The glow plug could also be used as a backup to ensure operation at any condition, but it is desirable to be able to operate a fully warmed up engine over the majority of its operating domain without the need for a glow plug. No attempt was made to model the effect of a glow plug in the CFD model since that was considered outside the scope of this investigation.

The combustion chamber bowl used for the n-heptane cases was based on a current production light duty Diesel design as exemplified in [22]. The Diesel bowl is a re-entrant type bowl as shown in Figure 2.
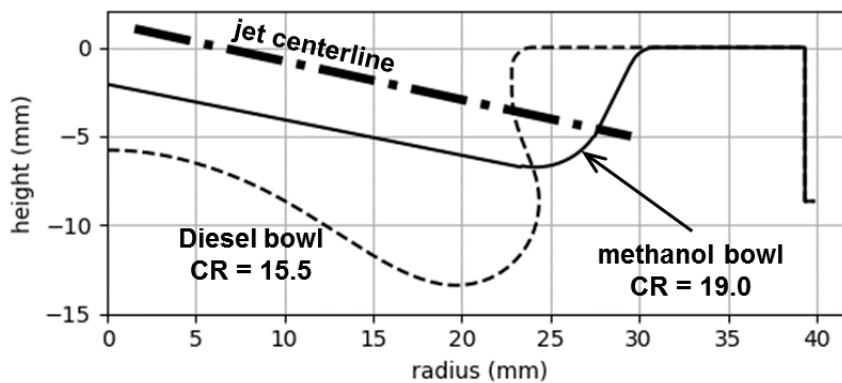
Fig. 2. Comparison of Diesel and Methanol Bowl Profiles

A goal of the study was to use a combination of increased compression ratio and uncooled external EGR to achieve reliable ignition of methanol without the use of a glow plug as described above. A set of preliminary CFD modeling runs using methanol with the original CR = 15.5 Diesel bowl quickly confirmed that the compression ratio had to be increased as expected. The effect of compression ratio on the ignitability of methanol was then investigated by scaling the Diesel bowl to test compression ratios in the range from 18 to 21. A compression ratio of 19 was chosen because it was the minimum value that ensured ignition and combustion efficiency > 99% at the three highest load operating conditions with no uncooled EGR. At the two lowest load conditions, uncooled external EGR was used to increase the trapped gas temperature. The 1-D engine model predicted that slightly over 50% external EGR was available at Condition 1 and up to 25% was available at Condition 2. Thus CR = 19 combined with using uncooled EGR at low load conditions was chosen for methanol to provide the desired ignition quality while minimizing the increase in peak cylinder pressure. Since the EGR was used primarily to aid ignition at low loads, the EGR cooler was not needed and could be removed from the engine. This results in a simplification and cost reduction opportunity for the methanol engine.

Another result of the compression ratio testing using the scaled Diesel bowl was the discovery that the re-entrant bowl design did not work well for methanol. The reason for this was not investigated extensively, but images from the CFD model showed a very rich region in the recirculation zone of the bowl which prevented complete combustion of the fuel. Instead, an entirely different bowl design was chosen for the methanol cases. The historical literature shows that direct injection methanol fueled compression ignition engines were typically designed using open bowls. Figure 3 shows a bowl design for a heavy duty, methanol CI engine from Detroit Diesel [23]. Similar bowl designs are shown in Obert [24] for low viscosity, low cetane number fuels such as methanol and gasoline. The bowl used for the methanol cases in the current study, shown in Figure 2, is very similar to the designs developed in these
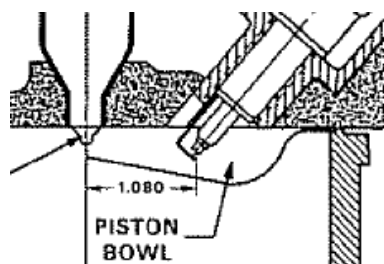
Fig. 3. Historical Methanol CI Engine Bowl Design

earlier methanol engine studies. It is an open bowl design with the surface of the bowl's central cone parallel to the fuel jet centerline and an outer bowl surface oriented to sweep the spray plume up into the squish area as the piston moves down in the cylinder. The open bowl design performed much better with methanol as will be described later. Additionally, the open bowl design is simpler and easier to manufacture than the re-entrant bowl and it would be much better suited to the application of a thermal barrier coating since the surface of the open bowl is more accessible for spraying or pressing on a thermal barrier coating.

3. Modeling Results

One of the advantages of using methanol as a CI engine fuel is the ability to use lower relative air/fuel ratio (lambda) than with Diesel because of the low sooting tendency of methanol. The lower lambda values will be useful for reducing the peak cylinder pressure which is important because of the increased compression ratio required for methanol. The low sooting tendency will also allow the use of EGR for NOx control. One of the key questions addressed in this study was the effect of reducing the air/fuel ratio all the way down to the stoichiometric condition to observe the tradeoff between the brake thermal efficiency and emissions. If the engine could be operated at the stoichiometric condition, a simple 3-way catalyst aftertreatment system could be used resulting in a simpler, lower cost system.

Sweeps of lambda and EGR were modeled at the key points in order to explore the effects of varying these parameters. Figure 4 shows the conditions that were modeled. At the 3 highest load conditions, the EGR rate was varied from 0 up to approximately 10% and lambda was varied from approximately 1.0 to 1.2 or the highest lambda value that could be achieved with the air handling system. For condition 2 (2000 RPM / 8 bar BMEP), the EGR rate was varied between 15 and 25% and lambda was varied from approximately 1.0 to 1.2 or the highest lambda value that could be achieved. At this condition, a minimum of 15% uncooled EGR was required to ensure robust ignition of the methanol. For condition 1 (1250 RPM / 2 bar BMEP), the EGR rate was varied between 45 and 50% and the lambda values, which were between 1.9 and 2.3, resulted from leaving the intake system un-throttled and the turbine wastegate fully closed. At this condition, a minimum of 40% uncooled EGR was required to ensure robust ignition of the methanol.
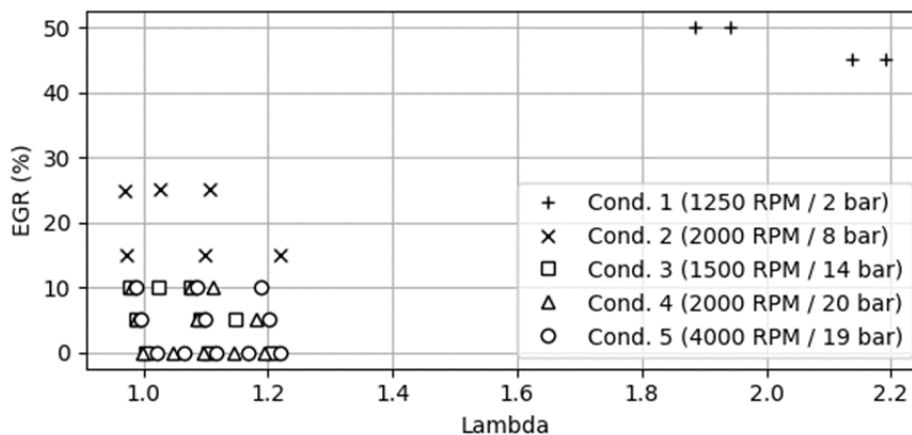
Fig. 4. Lambda and External EGR

Figure 5 shows the combustion efficiency vs. lambda for all operating conditions and all lambda and EGR combinations. For lambda values of about 1.15 and higher, the combustion efficiency for the methanol fueled engine is excellent. For lambda values below 1.15, the combustion efficiency falls, reaching a value of about 94% for stoichiometric operation. The level of EGR does not seem to have a significant effect on this trend; the dominant effect comes from the change in lambda. This trend is true for all of the methanol fueled operating conditions that were investigated.

One question that arises is whether a change in the combustion chamber configuration (the bowl shape, number of spray holes or the hole orientation) or the injection strategy could improve the combustion efficiency for the cases with lambda below 1.15. It is likely that there is a more optimal combination but that optimization was beyond the scope of the present study.
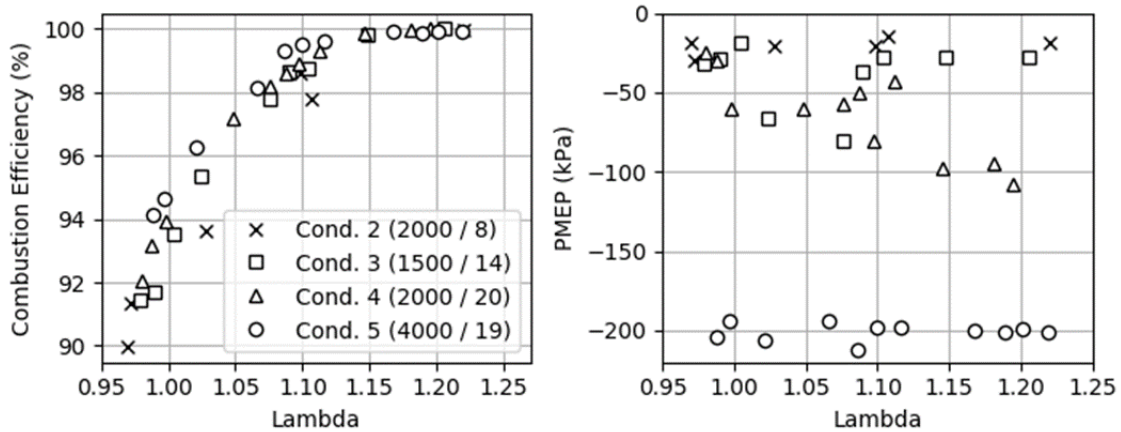
Fig. 5. Combustion Efficiency vs. Lambda for All Operating Conditions

The PMEP for all of the cases is also shown in Figure 5. The PMEP values, obtained from the 1-D model, show a trend of lower PMEP at lower lambda values for conditions 4 (2000 RPM / 20 bar BMEP) where significant boost pressure is required. For the other conditions there is not a significant change in PMEP with lambda. For condition 5 (4000 RPM / 19 bar BMEP) the wastegate is either fully opened or near fully opened.

For the calculation of Brake Thermal Efficiency (BTE) and other brake specific values in the paper, a BMEP value was needed. The BMEP was calculated using the IMEP calculated by the 3-D model combined with the PMEP and FMEP from the 1-D model. BTE for the different cases is shown in Figure 6. In this paper all discussion of efficiency and fuel consumption will be done using BTE. Due to the significant difference in the energy density between methanol and Diesel fuel, BSFC numbers are not directly comparable whereas BTE numbers are comparable. The combustion efficiency is the primary factor affecting the BTE. The pumping work has a secondary effect. As with the combustion efficiency, the BTE is best for the higher range of lambda values. BTE is relatively flat above lambda = 1.10 and falls for lower lambda values. At the stoichiometric condition, the BTE is approximately 6% lower than the peak values, or about 2 to 2.5 percentage points.
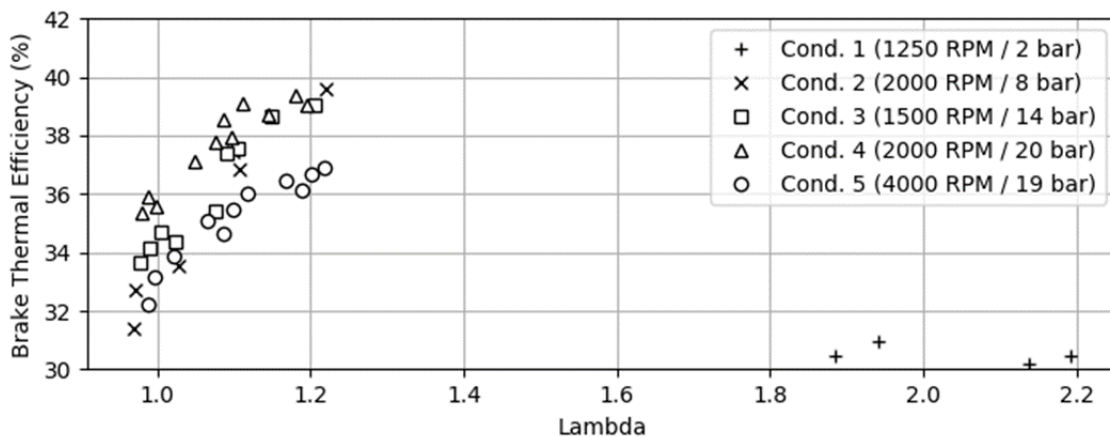
Fig. 6. Brake Thermal Efficiency vs. Lambda

Predicted values of BTE vs BSNOx are shown in Figure 7. Each of the individual lines in the figure represent sweeps of lambda at a given EGR rate. The specific EGR rate for each sweep is shown by the line format. BTE at each condition increases as lambda is increased as shown by the arrow. The lowest BTE point on each curve is near the stoichiometric condition. The main conclusion from this figure is that the EGR rate has the dominant effect on the NOx emissions. The lambda value and the engine's operating condition have secondary effects on the NOx. Even decreasing lambda all the way down to stoichiometric has less effect on NOx than adding an additional 5% EGR. For conditions 1 and 2 the BSNOx values were all below 1 g/kW-hr due to the higher EGR levels required to ensure robust ignition of the methanol.
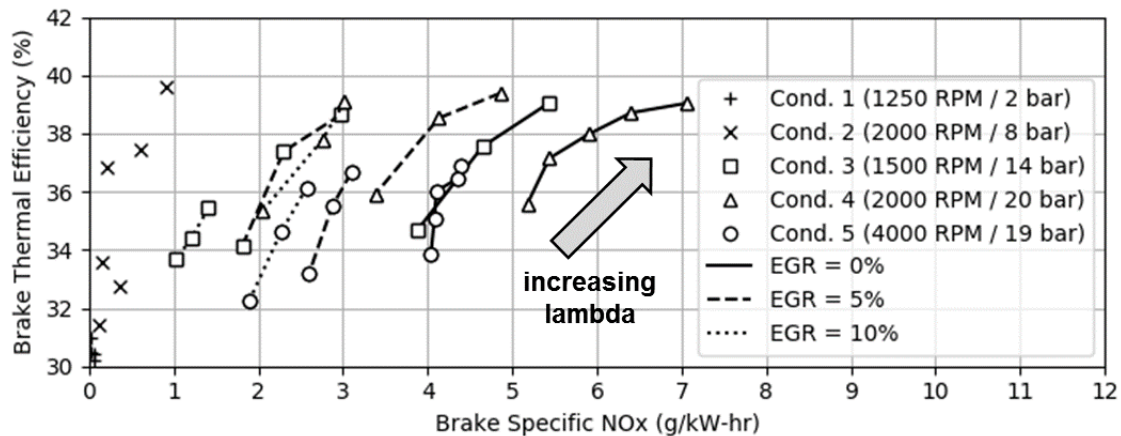
Fig. 7. Brake Thermal Efficiency vs. Brake Specific NOx

4. Comparison of Methanol to Diesel Results

The BTE values for the methanol cases were better than the BTE values for the n-heptane (Diesel) cases for all operating conditions. In order to explain this, a comparison will be made between the heat release rates for an exemplary case with the different fuels. Figure 8 shows the heat release rate for both fuels at condition 3 (1500 RPM / 14 bar BMEP). The injection rate profile, which came from the baseline Diesel engine, was the same for both fuels. It utilized 2 pilot injections which together contained a total of 10% of the fuel and a main injection containing 90% of the fuel.

For the n-heptane case in Figure 8, the fuel from each injection event ignited shortly after it was injected and the HRR shows evidence of the 2 pilot injections and the main injection. For the methanol case, the fuel injected in both pilot events had a significantly longer ignition delay and the combustion of the fuel from the 2 pilot events merged into a single premixed burn event which was better placed from an efficiency point of view (i.e. less over-advanced). The main event fuel for the methanol case ignited shortly after the start of injection, just like the n-heptane case, and for both fuels there is evidence of a diffusion burning period and a burnout "tail" period after the end of injection. The tail of the HRR is significantly shorter for the methanol case resulting in better overall HRR placement and a more effective expansion process. The combination of the less advanced pilot HR location and the shorter tail on the main HR event results in higher indicated work for the methanol case which translates into improved BTE. Conditions 2, 4, and 5 also showed similar differences between the methanol and n-heptane cases. For condition 1 the burn was mostly premixed for both of the fuels due to the low load.
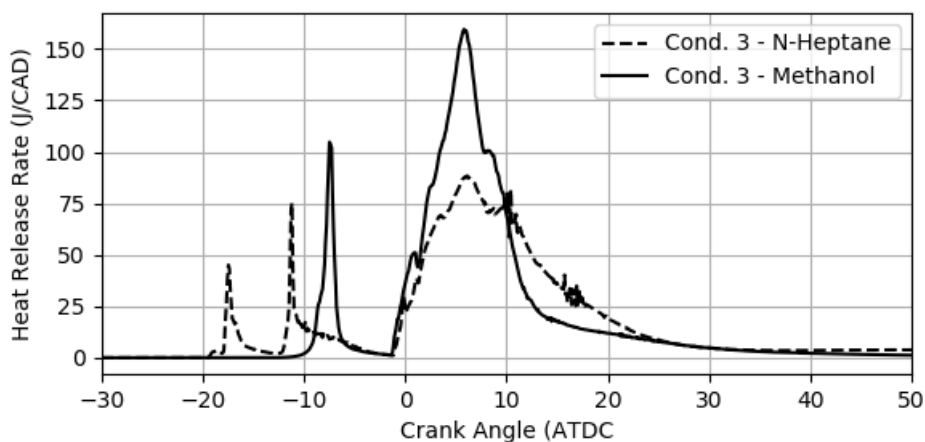
Fig. 8. Heat Release Rate for 1500 RPM / 14 bar BMEP Condition

One consequence of the significantly shorter tail on the methanol heat release rate was that the combustion phasing could be retarded relative to the n-heptane case. Retarding the combustion phasing is an effective way to reduce the peak cylinder pressure with little or no effect on the BTE. Combustion retard sweeps were performed for all of the methanol cases to find a more optimal phasing. Another

consequence of the faster end of combustion burnout was that the injection pressure could be reduced for the high load methanol cases without any significant detrimental effects. It was possible to reduce the peak injection pressure to 1600 bar or less for all of the cases. This capability to use a lower peak injection pressure rating for the fuel system will aid in simplifying and reducing the cost of a methanol CI engine.

Table 5 shows a summary of the results for the methanol and n-heptane cases using optimal lambda, EGR, and injection timing values. All of the methanol cases have peak injection pressure below 1600 bar as described above. The upper part of the table has values for the n-heptane (Diesel) cases and the lower part of the table has values for the methanol cases. As previously described, the methanol engine used uncooled EGR at conditions 1 (50% EGR) and 2 (15% EGR) to aid ignition. No uncooled EGR was required at the higher load conditions (3-5) to aid ignition, but 5% EGR was used for conditions 3 and 4 to bring the NOx level down similar to the Diesel cases.

The peak cylinder pressures for the methanol cases are higher than for the n-heptane cases at all conditions due to a combination of higher compression ratio and shorter burn duration. Overall a methanol engine will need approximately 20 bar higher cylinder pressure capability than a Diesel in order to operate at all of the conditions considered for this study. The combustion noise level with methanol is higher than with n-heptane but not significantly. At the 2000 RPM / 8 bar BMEP condition the CNL with methanol is 3 dBa higher but at the other conditions important to the drive cycle the CNL is within 1 dBa. It is possible that the CNL could be reduced by optimizing the methanol injection strategy, but this was not attempted in this investigation.

The predicted NOx values were very low for the methanol conditions with high EGR rates and similar or slightly lower than the n-heptane predictions at the conditions with low or no EGR. Finally, the BTE with methanol was higher than with n-heptane as discussed above.

Table 5. Summary of Methanol and N-Heptane (Diesel) Results

Fuel	RPM / BMEP	λ	Inj. Pr. (bar)	EGR (%)	PCP (bar)	CNL (dBA)	BSNOx (g/kW-hr)	BTE (%)	
n-heptane	1250 / 2	2.31	340	40	55	74	1.0	28.4	
n-heptane	2000 / 8	1.74	720	8	91	82	4.4	37.6	
n-heptane	1500 / 14	1.22	1520	0	137	84	4.8	35.2	
n-heptane	2000 / 20	1.20	1450	0	155	88	4.7	35.9	
n-heptane	4000 / 19	1.20	2470	0	162	92	7.2	31.1	

Fuel	RPM / BMEP	λ	Inj. Pr. (bar)	EGR (%)	PCP (bar)	CNL (dBA)	BSNOx (g/kW-hr)	BTE (%)	BTE diff (%)
MEOH	1250 / 2	1.95	430	50	65	74	0.0	31.0	9%
MEOH	2000 / 8	1.22	1000	15	110	85	0.9	39.6	5%
MEOH	1500 / 14	1.15	1370	5	153	85	3.0	38.7	10%
MEOH	2000 / 20	1.18	1410	5	183	89	4.9	39.4	10%
MEOH	4000 / 19	1.22	1590	0	180	94	4.4	36.9	18%

The fuel consumption comparison between a baseline Diesel engine and a methanol fueled engine will be made using a simplified estimate of drive cycle emissions for the WLTP cycle. The weighting factors for the 5 key point operating conditions are shown in Table 6. The weightings are based on a 1.6L engine in a 1600 kg vehicle and they represent fuel percentage burned over the cycle.

Table 6. Weighting Factors for WLTP Drive Cycle Estimates

Condition	Speed (RPM)	BMEP (bar)	Weight (%)
1	1250	2	21
2	2000	8	29
3	1500	14	37
4	2000	20	13
5	4000	19	0

The predicted cycle weighted results are shown in Table 7. Comparing the methanol fueled engine results to the baseline Diesel, the BSNOx averaged over the WLTP cycle was reduced by approximately 60%. Average BTE over the cycle was improved by over 8%. An additional consideration is

that there was no optimization performed on the bowl shape, injector nozzle or injection rate shape for the methanol engine in this study. It would be interesting for a future study to perform this optimization in order to see what additional benefits could be achieved.

Table 7. WLTP Cycle Weighted Estimates

	Diesel	Methanol
Cycle average BSNOx (g/kW-hr)	4.01	1.61
Cycle average BTE (%)	34.5	37.4

Although this study did not include experimental validation of the results, the significant NOx reduction that is observed is consistent with experimental results from prior production applications using M100 methanol fuel [12, 13]. Other similarities to previous heavy duty Diesel-to-methanol conversion studies include; compression ratio increase of approximately 25% over the baseline Diesel, lower airflow requirement for methanol relative to Diesel, similar brake thermal efficiency for Diesel and methanol, reduced NOx and PM emissions with methanol. Also interesting to note is that the previous studies, which used 2-stroke engines, were able to use hot internal residual gas to aid ignition and minimize the use of glow plugs similar to the use of hot external EGR in the current study.

The final results of this study show that the performance and emissions of a compression ignition engine fueled with methanol can be equal to or better than a comparable Diesel fueled engine. The use of methanol also allows several cost and complexity saving modifications to the engine. The high pressure loop EGR system can be simplified by removing the EGR cooler since only uncooled EGR is required. The fuel injection system will be required to deliver more fuel, approximately twice the volume compared to Diesel fuel, but the pressure rating of the fuel system can be lower. The study shows that 1600 bar peak injection pressure is probably sufficient. Finally, the piston design and fabrication process can be simplified due to the much simpler bowl shape. The application of a thermal barrier coating to the piston crown would also be simpler and more feasible due to accessibility of the surface.

The study also shows that it would probably be possible to run the methanol engine at stoichiometric conditions due to the very low sooting tendency of the fuel. In the discussion of BTE above, it was shown that dropping the air/fuel ratio from lambda = 1.15 down to lambda = 1.0 resulted in an efficiency decrease of about 6%. If this BTE decrease was applied to the drive cycle estimates shown in Table 7, the cycle BTE for the stoichiometric methanol engine would be similar to the cycle BTE of the baseline Diesel engine. The lowest cost operating strategy would then be a function of the relative costs of the lean vs. stoichiometric aftertreatment systems and the cost of the NZC methanol fuel.

5. Conclusions

The intent of this investigation has been to invigorate interest in net-zero-carbon (NZC) methanol as a transportation fuel for commercial on-road applications. As described earlier in this paper, methanol has been successfully implemented in the recent past for on-road compression ignition engines and it has the attributes to be a valuable addition to the range of renewable fuel alternatives in the future.

Observation from this modeling demonstrate the following:

- Ignition can be achieved with a combination of increased compression ratio (CR = 19.0) and uncooled external EGR.
- Brake Thermal Efficiency with methanol is equivalent or better than with conventional Diesel fuel.
- Engine out NOx levels with methanol are, in general, lower than with conventional Diesel fuel.
- These results have been achieved with a simple injection strategy and minimal optimization.
- No substantial technology or costly adaptions are required to achieve the results shown within this paper, under normal operating conditions.

The results of this study demonstrate that methanol can be implemented in a contemporary Diesel engine architecture with little adaptation. While the details associated with startability, durability, and the broader issues of production applications are not addressed here, the experience of past implementations show that these issues are not insurmountable.

The implications of these results are as follows:

- Methanol has potential to reverse the growing cost of conventional engines through simplification of systems such as the intake charge/EGR system, the fuel injection system and the engine's aftertreatment system.
- The system simplification along with much more favorable soot behavior may translate into reduced maintenance and warranty cost for fleets and vehicle manufacturers.
- Future investigations regarding aftertreatment solutions for methanol engines would be beneficial to understand the full "power system" implications of methanol in the scope of on-road commercial vehicle applications. Further cost reductions might be identified using methanol as the on-board NOx reductant or using a substantially different aftertreatment architecture leveraging stochiometric combustion.

This could be achieved using a fuel with a NZC footprint using chemical production technologies and distribution infrastructures that are already available in the global market. While this paper represents a brief exploratory investigation, the authors believe further study of methanol as a NZC fuel for sustainable compression ignition internal combustion engines should be a topic of substantial interest for the research community as it prepares for sustainable commerce. With that in mind the authors see the potential for a range of research activities that could enhance understanding of methanol as a commercial fuel. This exploration of the potential benefits of using methanol as a sustainable e-fuel for transportation applications shows that methanol is an excellent candidate fuel for further investigation.

References

1. U.S. Energy Information Administration, Annual Energy Outlook 2019, https://www.eia.gov/outlooks/aeo/pdf/aeo2019.pdf, 2019.
2. Sondhi, K., "PepsiCo Fleet Sustainability Strategies," 2018 Green Truck Summit presentation, 2018.
3. Schmidt, J., Gruber, K., Klingler, M., Klöckl, C., Camargo, L. R., Regner, P., Turkovka, O., Wehrle, S., Wetterlund, E., "A new perspective on global renewable energy systems: why trade in energy matters," Energy Environ. Sci. 2019,12,2022, 2019.
4. NREL, "Renewable Energy Technology Resource Maps and Technical Potential for the United States," https://www.nrel.gov/gis/re-potential.html, 2012.
5. US Census Bureau, "Population Density for Counties and Puerto Rico Municioios: July 1, 2011," https://www.census.gov/history/www/reference/maps, 2011.
6. Lyubovsky, M., "Shifting the paradigm: Synthetic liquid fuels offer vehicle for monetizing wind and solar energy," Journal of Energy Security, http://ensec.org, 2017.
7. McDonald, M., "The Evolution Toward Zero," 2020 Green Truck Summit presentation, http://www.worktruckshow.com/gtspresentations, 2020.
8. Bromberg, L., Cheng, W. K., "Methanol as an alternative transportation fuel in the US: Options for sustainable and/or energy-secure transportation," US Department of Energy Alternative Fuels Data Center report https://afdc.energy.gov/files/pdfs/mit_methanol_white_paper.pdf, 2010.
9. Tan, E. C. D., Talmadge, M., Dutta, A., Hensley, J., Schaidle, J., Biddy, M., Humbird, D., Snowden-Swan, L. J., Ross, J., Sexton, D., Yap, R., Lukas, J., "Process Design and Economics for the Conversion of Lignocellulosic Biomass to Hydrocarbons via Indirect Liquefaction," National Renewable Energy Laboratory publication: https://www.nrel.gov/docs/fy15osti/62402.pdf, 2015.
10. Eni, "Eni and FCA have developed A20, a new fuel that pairs emission reduction with energy efficiency," Eni press release April 3 April 2019 https://www.eni.com/assets/documents/press-release/migrated/2019/04/PR_Eni_FCA_ENG.pdf, 2019.
11. Stammer, L. B., "RTD Gives Methanol Buses High Marks," Los Angeles Times, https://www.latimes.com/archives/la-xpm-1990-12-28-me-7359-story.html, 1990.
12. Miller, S. P., Savonen, C.L., "Development Status of Detroit Diesel Corporation Methanol Engine," SAE paper 901564, 1990.
13. Miller, S. P., "DDC 's Production 6V92TA Methanol Bus Engine," SAE paper 911631, 1991.
14. Viola, M., "HC-SCR Catalyst Performance in Reducing NOx Emissions from a Diesel Engine Running Heavy Duty Transient Test Cycles with Diesel Fuel and Ethanol as the Reductants," SAE paper 2009-01-2775, 2009.

15. Lopez, J., García-Oliver, J. M., García, A., Domenech, V., "Gasoline effects on spray characteristics, mixing and auto-ignition processes in a CI engine under Partially Premixed Combustion conditions," Applied Thermal Engineeering, vol. 70, 996-1006, 2014.

16. GT-Power, Engine Simulation Software, Gamma Technologies, https://www.gtisoft.com/gt-suite-applications/.../gt-power-engine-simulation-software/

17. Richards, K. J., Senecal, P. K., and Pomraning, E., 2016, "CONVERGE v2.3 Manual," Convergent Science, Inc., Madison, WI.

18. Gao, G., Grover, R. O. Jr., Gopalakrishnan, V., Diwaker, R., Elwasif, W., Edwards, K. D., Finney, C. E. A., Whitesides, R. A., "Steady-State Calibration of a Diesel Engine in Computational Fluid Dynamics Using a Graphical Processing Unit-Based Chemistry Solver," ASME Journal of Engineering for Gas Turbines and Power, Vol. 140 / 102802, October, 2018.

19. Patel, A., Kong, S. C., and Reitz, R. D., "Development and Validation of a Reduced Reaction Mechanism for HCCI Engine Simulations," SAE paper 2004-01-0558, 2004.

20. Diwakar, R., and Singh, S., "NOx and soot reduction in diesel engine premixed charge compression ignition combustion: a computational investigation," International Journal of Engine Research, vol. 9(3): pp 195-214, 2008.

21. https://www.sandia.gov/TNF/chemistry.html

22. Boretto, G., Golisano, R., Scotti, M., Antonioli, P., Frank, R., Rovatti, G., "The first of a new generation of diesel engines from General Motors – the efficient and powerful 1.6 liter Euro6 Midsize Diesel Engine," 34th International Vienna Motor Symposium 2013

23. Toepel, R. R., Bennethum, J. E., Heruth, R. E., "Development of Detroit Diesel Allison 6V-92TA Methanol Fueled Coach Engine", SAE Paper 831744, 1983.

24. Obert, E. F., Internal Combustion Engines and Air Pollution, 1973.

An Optical Investigation of Combustion and Soot Formation in a Single Cylinder Optical Diesel Engine for Different e-Fuels and Piston Bowl Geometries

J.V. Pastor[1], A. García[1], C. Micó[1], F. Lewiski[1], A. Vassallo[2] and F.C. Pesce[2]

[1]CMT – Motores Térmicos. Universitat Politècnica de València. Camino de Vera s/n, E-46022 Valencia, Spain.

E-mail: angarma8@mot.upv.es
Telephone: +(34) 963 876 574
Fax: +(34) 963 877 659

[2]Punch Torino S.p.A., Corso Castelfidardo, 36, 10129 Torino TO, Italia- formetely employees of General Motors Global Propulsion Systems

E-mail: francesco_concetto.pesce@punchtorino.com
Telephone: +(39)011 438 2437

Abstract. The emissions reduction in internal combustion engines (ICE) is one of the greatest technical challenges of society. Although new technologies for mobility are emerging, the ICE will still have a key role in transport over the next decades. Diesel engines are challenging in terms of pollutant emissions, in particular nitrogen oxides (NOx) and particles. In fact, the last one represents 50% of total emissions of this kind of engine. In this context, new hardware technologies as well as new renewable fuels have shown great potential to reduce soot emissions without affecting engine efficiency (CO2 emissions). For this reason, the impacts of using e-fuels (OMEX and FT-diesel) and different piston bowl geometries (re-entrant, stepped lip and wave-stepped lip bowl) on soot formation and combustion development were analyzed in a single cylinder optical diesel engine. First, an in-cylinder flow characterization and a preliminary flame movement analysis were performed by applying optical techniques such as particle image velocimetry (PIV) and natural luminosity. In addition, an analysis of combustion process, as well, as soot formation was carried out by means of natural luminosity, OH* chemiluminescence and 2 color pyrometry. The e-fuels showed a remarkable reduction in soot formation (especially OMEX). Regarding the bowl geometries evaluated, stepped lip and wave-stepped lip presented a faster late soot oxidation in comparison with the re-entrant geometry. Under extreme soot conditions, differences were also observed between the wave-stepped lip and the stepped lip. A faster soot oxidation was observed for the first one. In general, the application of new hardware (bowl geometries) as well as new kind of fuels in diesel engines have presented a great potential in order to diminish the soot emissions.

1. Introduction

The air pollutant emissions and its reduction have been one of the main topics discussed during the last decades. Regarding internal combustion engines, the strict emissions legislations have forced the transport industry to find innovative and more efficient technologies for the current engines. In specific for compression ignition engine, the biggest challenge is focused on the reduction of soot-NOX trade off. In order to reduce the NOx and soot emissions, as well as, improve the efficiency, new fuel sources[1][2], combustion concepts[3][4] and hardware [5][6] have been applied and tested in compression ignition engines.

Regarding new technologies of hardware, a special attention has been paid to the development of new piston bowl geometries. In diesel engines, the combustion chamber geometry has a direct impact on the flow of the squish zone and swirl movement, as well as, on the spray-wall interactions[7]. In this way, it is evident that the geometry of piston has an important role on the combustion process, fuel-air mixture and pollutant emissions in diesel engines[8]. Re-entrant pistons are the typical bowl design applied in light and medium duty engines, which have usually a high swirl number (SR>1). This bowl geometry has the main objective of creating a re-circulation flow towards the piston center by supporting the swirl movement generated inside the cylinder[9]. In this piston geometry, the fuel jets interact with

the air flow and bulk flow structures are formed by the jet deflection at the combustion chamber walls [10][11]. These bulk flow structures are also very important because they generate turbulence that enhances small-scale mixing and increases the burning rate [12]. In this way, different variations of re-entrant piston have been developed and tested. Several studies have reported a comparison between the re-entrant and stepped lip geometry[7][13][14][15]. The results have shown a great reduction of the soot emissions by using the stepped lip bowl. Bush et al [16] have performed experiments in an optical and metallic engine by using the re-entrant and stepped lip bowl geometries. The emissions measurements from the metallic version reported a significant reduction of soot with a slight reduction in NOx as well. The Mercedes-Benz recently launched an engine with stepped lip bowl. The company reported reduction of particulate emissions and improvements of air utilization[15].

Regarding new fuel sources, Synthetic fuels (e-fuels) have proven to be an attractive solution for emissions reduction[1]. Among the different kind of e-fuels, fischer-Tropsch (FT) diesel and OMEX have a great potential for replacing the fossil diesel. FT diesel is composed by different n-alkanes molecules and it can be obtained from different natural resources e.g. biomass [17]. OMEX or oxymethylene dimethyl ethers are formed by a CH3-O-(CH2-O)x-CH3 chemical structure, where x can be in the range of 1 to 5 [18]. These molecules present a high oxygen content without direct carbon bonds (C-C), which provide low soot emissions. In addition, OMEX can be used directly in diesel engines without the necessity of modifying the injection system. This fuel can be obtained from methanol and formaldehyde[19]. In general, the studies involving FT diesel, pure or blended with diesel, have found a reduction of soot emissions in comparison with the fossil diesel [20][21][22]. Schaberg et al [23] used an optical diesel engine fueled with Fischer-Tropsch and analyzed the soot formation and combustion characteristics by means of OH* chemiluminescence and two color spectroscopy. The FT diesel presented a soot reduction in comparison with the fossil diesel. For the OMEX combustion, different kind of studies have reported positive results in terms of soot, HC and CO emission reductions[24][25]. Omari et al [1] tested pure OME3-5 and blends with diesel. The soot emissions for the blends always presented lower soot emissions than the fossil diesel. In addition, for the pure OME3-5, the soot emissions were almost zero. An optical investigation in a constant volume vessel with blends of OMEX and diesel was performed by Ianuzzi et al [18]. They have found a significant reduction of soot formation as the quantity of OMEX was increased in the blend.

Considering these two very attractive possibilities for decreasing emissions and reducing the fossil diesel dependence, the present work aims firstly to measure and analyze the flow pattern inside of a re-entrant bowl. The second objective was focused on testing and analyzing the combustion process and in-cylinder soot formation of the two mentioned e-fuels (FT diesel and OMEX), as well as, three different piston geometries (re-entrant, stepped lip and stepped lip-wave) as shown in Fig. *1*. For this purpose, a single-cylinder optical diesel engine, based on GM 1.6 L, has been used. The In-cylinder flow characterization was measured by using a particle image velocimetry (PIV) system. For a qualitative analysis of the soot formation and combustion process evolution, the natural luminosity has been registered. In addition, OH* chemiluminescence has been used for the identification of high temperature reaction zones. Finally, the soot formation has been quantified by using the 2-color pyrometry technique.
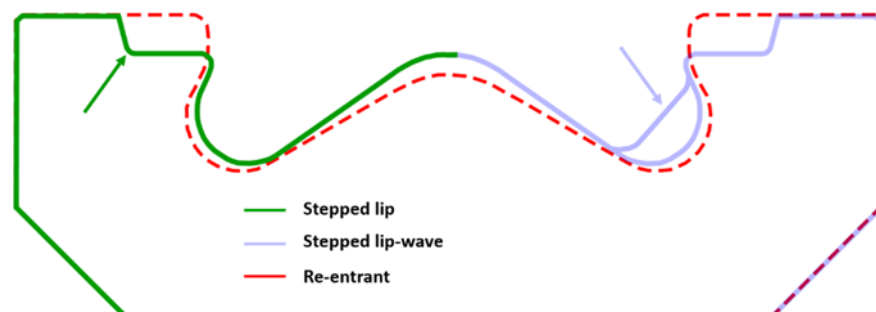
Fig. 1. Sketch of the different piston geometries

2. Test Facility

2.1 Optical Engine

All optical techniques and studies performed in the current paper were performed in a Bowditch designed single-cylinder optical diesel engine. It is derived from a GM 1.6 L commercial diesel engine. The engine is equipped with three optical access. The first one is from the bottom of a transparent piston which is formed by real bowl shape as shown in   Fig. *2*. The other two accesses are located in the upper part of the liner, where two quartz windows are installed. The fire deck has four valves per cylinder and a centrally located Denso solenoid injector with 8 hole-nozzle. In order to guarantee a good effective compression ratio and diminish as much as possible the air leakage (blow by), synthetic rings were used in the piston. These rings expand as the in-cylinder temperature increases.

A common rail system, which is electronically controlled, it was installed in the engine. The control is performed by using a DRIVVEN ® control unit. The start of energizing (SOE), number of injections and number of skip fire cycles can be easily set by means this device.

An AVL GH13P glow plug piezoelectric transductor which was coupled to a Kistler 4603B10 charge amplifier was used for measuring the instantaneous in-cylinder pressure. In addition, instantaneous intake and exhaust pressure were also measured by means of piezorresistive transducers (Kistler/4603B10). The pressure signals were recorded by a Yokogawa DL708E. A home-developed acquisition system, which is called SAMARUC, collects the signal from the different low frequency sensors and controls the electric dynamometer brake.
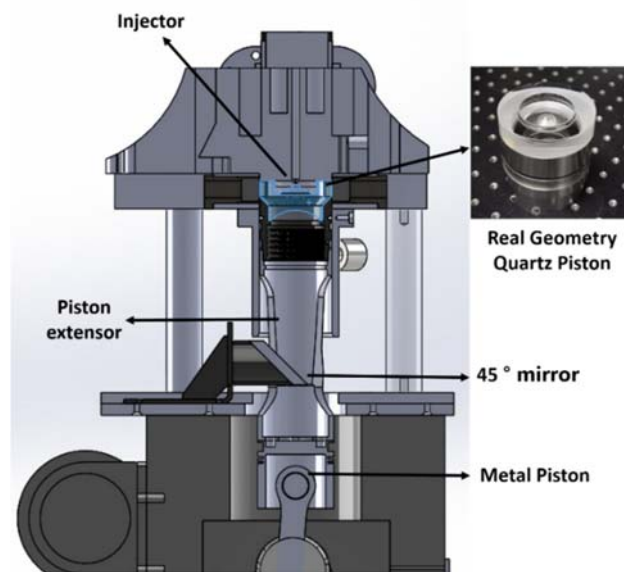
Fig. 2. Optical engine assembly

Table 1. Engine characteristics

Engine type	4 stroke, direct injection
Number of cylinders [-]	1
Number of Valves [-]	4
Bore [mm]	80
Stroke [mm]	80.1
Displacement [l]	0.402

2.2 Test cell

The optical engine is installed in a test cell equipped with all facilities necessary for its control, data acquisition and operation. A scheme of the test cell setup can be seen in Fig. *3*. A scroll compressor is

responsible for supplying the intake air flow. A dryer and a heat exchanger are mounted in the compressor line in order to control the humidity and temperature of the air. An air heater, which is located just before the intake port, is used in order to provide a constant intake air temperature. In order to reduce the pressure pulses in the intake and exhaust line, two settling chambers, one for intake and another for the exhaust, were mounted. An exhaust backpressure valve controls the exhaust pressure. For the current work, the exhaust pressure was kept always 200 mbar higher than the intake pressure with the objective to promote real engine operating conditions. For the tests with fuel injection under non-reactive conditions (i.e PIV measurements), the intake air was mixed with nitrogen in order to achieve the desired oxygen concentration during the tests. The flow mass of nitrogen is controlled by means of PID valve. Table 2 shows the accuracy of the different elements of the test cell.
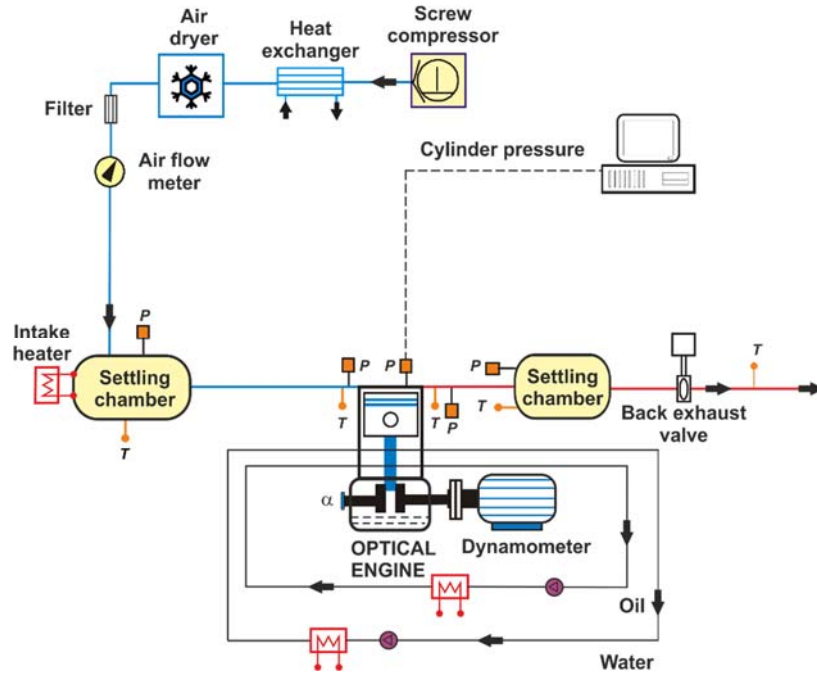
Fig. 3- Test Cell scheme

Table 2. Information of measurement instruments

Variable	Device	Manufacturer / model	Accuracy
In-cylinder pressure	Piezoelectric transducer	AVL / GH13P	±1.25 bar
Intake/exhaust pressure	Piezorresistive transducers	Kistler / 4603B10	±25 mbar
Temperature in settling chambers and manifolds	Thermocouple	TC direct / type K	±2.5 °C
Crank angle, engine speed	Encoder	AVL / 364	±0.02 CAD
Air mass flow	Air flow meter	Sensyflow / FTM700-P	< ±1%

3. In-cylinder flow measurements

The first step of the present work was focused on the in-cylinder flow characterization. From this first step, it was tried to identify the in-cylinder flow pattern inside a real bowl shape under motored conditions and how the spray injection affects this flow under non-reactive conditions. In addition, it was identified the zones with higher Turbulent Kinetic Energy (TKE) inside the piston in order to define appropriate injection strategies for this kind of bowl geometry. For the in-cylinder flow measurement, the PIV optical technique was applied in the optical engine.

3.1 Optical techniques

A standard PIV system was used for the instantaneous two-dimensional velocity field measurement. A double-head 15 Hz pulsed ND:YAG laser was applied as the light source to illuminate the seeding particles present in the intake air. Each pulse laser has 135 mJ at 532 nm. To be possible measuring a specific plan inside the combustion chamber, the laser spot was transformed into a laser sheet by means of a Plano-concave cylindrical lens. For the laser sheet width and thickness adjustment a set of additional Plano-concaves lenses were used in the optical assembly. The laser thickness was kept around of 1 mm, as well as, the width was around 50 mm, which is the mirror width used to reflect the laser sheet toward the piston bottom. The laser sheet was positioned in the middle of the combustion chamber with a vertical orientation, entering through the bottom of piston as shown in Fig. *4*.

The intake air seeding is performed with solid particles of Aluminum Oxide (Al_2O_2). Liquids synthetic particles were tested but they vaporize at the compression stroke. A cyclone introduced and dispersed the particles in the intake system. By means this device, the particles with a diameter higher than 5 microns are kept in suspension due to a centrifugal movement. A positive pressure difference between the cyclone and the intake manifold system was maintained to ensure a continuous particle supply.

The laser light scattered by the seeding particles was recorded with a straddle camera of 4 megapixels (Powerview Plus 4MP by TSI). Time elapsed between the two consecutive laser shots was set between 10 μs and 15 μs. Taking into account that the second frame has a much higher exposure time than the first one (camera characteristics), a narrow band pass filter 532 nm was used for reducing the external light interference.
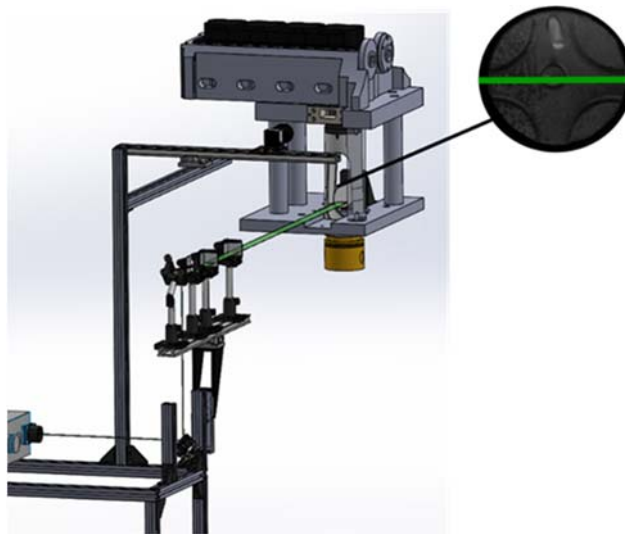
Fig. 4- PIV system

3.2 PIV Data Processing

Image processing

The tests were performed by recording 50 engine cycles for each operating conditions. A couple of background images without particles in the intake air were taken before starting each test. These backgrounds images were subtracted of the images with particles for removing the piston surface reflections. As the piston and side windows curvatures induce radial and axial optical distortions, an image distortion correction is necessary for the correct analysis of the PIV measurements.

For this purpose, a specific algorithm was applied to perform the image correction. First of all, the code identifies the contour bowl and only this region is extracted for the analysis. After the measurable area is isolated, a piece-wise linear transformation is applied in the distorted image. To allow the code to perform the correction, a pair of calibration target images (with and without distortion) were used. The images were captured using a geometric template which is shown in Fig. *5*.
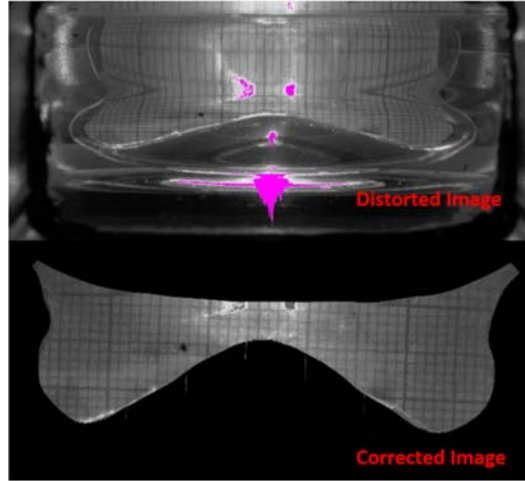
Fig. 5- Distorted image and corrected one

Velocity Field Processing

A commercial PIV software (Insight 3G by TSI) have been used for processing the images. For two consecutively captured frames the software applies a cross-correlation function. Velocity fields were computed based on the displacement of a particle group, which was found within a considered interrogation window. The magnification of the images was around 34 pix/mm with a maximum particle between consecutive images of 8.5 pixels (25%). For this work, the interrogation window was varied from 88 x 88 pixels to 44 to 44 pixels.

Turbulent Kinetic Energy (TKE) analysis

For the TKE analysis, the weight of TKE in relation to the total energy of the fluid was quantified. The methodology used compares the flow pattern with and without injection. Firstly, the TKE was calculated using equation 1:

$$TKE = \frac{1}{2}\frac{1}{N}\sum_{j=1}^{N}\left(\left(u_j - \bar{u}\right)^2 + \left(v_j - \bar{v}\right)^2\right) \tag{1}$$

The ensemble-averaged "u" and "v" components were calculated by equation 2, where N is the number of cycles considered.

$$\bar{u} = \frac{1}{N}\sum_{j=1}^{N}u_j \tag{2}$$

Additionally, the energy related with the mean velocity, i.e. the Mean Kinetic Energy (MKE), was calculated according to equation 3:

$$MKE = \frac{1}{2}(\bar{u}^2 + \bar{v}^2) \tag{3}$$

It was assumed that the total energy of the fluid is the addition of the energy related with the mean velocity (MKE) and the turbulence (TKE). From this, TKE is normalized (TKE*) with respect to the total energy as expressed in equation 4:

$$TKE^* = \frac{TKE}{TKE + MKE} \tag{4}$$

3.3 Test matrix for PIV measurements

Tests were performed at motored and injection under non-reactive conditions. The engine speed was 1200 RPM, with intake pressure of 1.5 bar and exhaust pressure of 1.7 bar. The intake temperature was kept at 50 °C. The injection pressure was set to 400 bar, with an injection duration of 700 µs and a start of energizing of -30 °aTDC. The different laser timings that were performed for both motored and injection conditions are shown in table 3. In Fig. **6** is shown the laser timings used before TDC in reference to the fuel mass flow rate. In addition, the natural luminosity image, which was attached in figure, indicates that the laser sheet does not cross the spray anywhere.

Table 3- PIV measurements settings

RPM	Pintake [bar]	T_Intake [°C]	Pinj [bar]	ET [us]	SOE [°aTDC]	PIV [CAD]
1200	1.5	50	400	700	-30	-25; -20; -15;
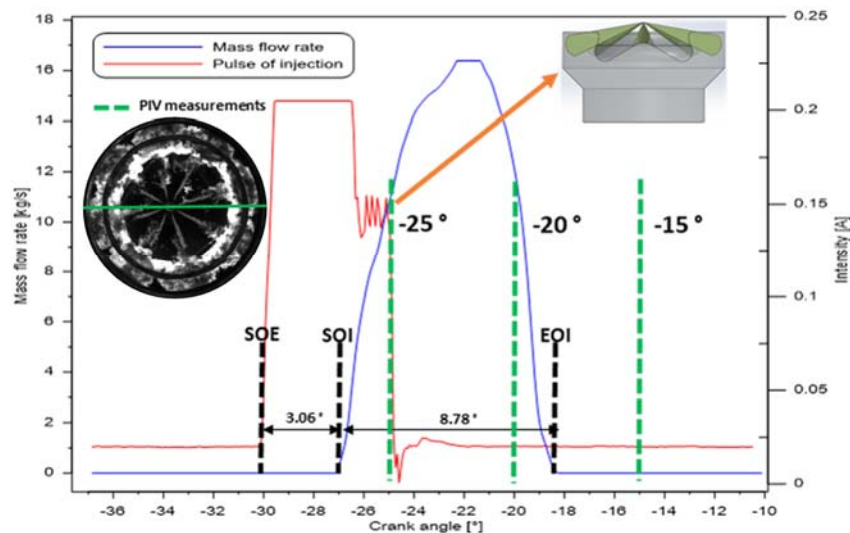
Fig. 6- Laser timings in reference to the fuel mass flow rate

3.4 In-cylinder flow velocity at motored and injection conditions

The flow velocity evolution inside the bowl at motored and injection conditions are shown in Fig. **7**. For the motored case is possible to appreciate that velocities inside the bowl decrease as the piston approaches to TDC.
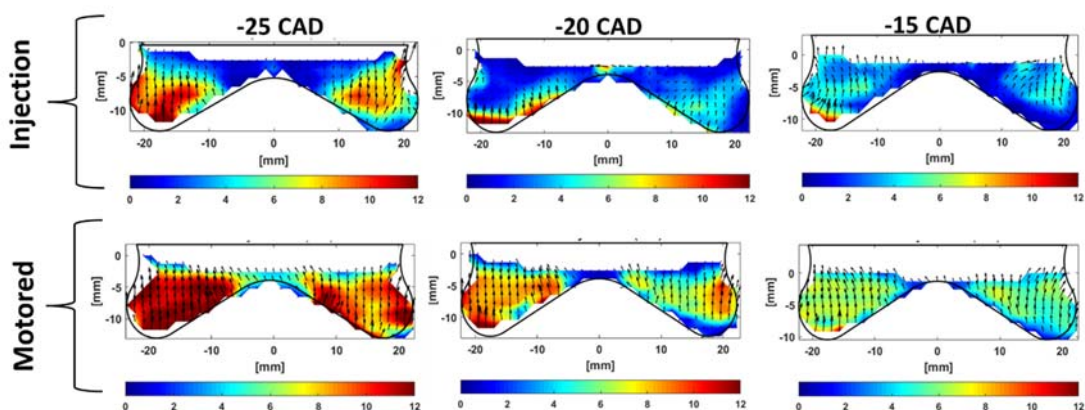
Fig. 7- Mean flow velocity field at motored and injection conditions

In addition, the figure shows that the highest velocities are located at the periphery of the bowl, decreasing from the outer to the center. At 15 CAD, the deflection of some vectors located at periphery indicate the flow from squish zone is entering into the bowl. When fuel injection is added, the flow filed is modified. Thus, the second part of the PIV analysis is performed injecting fuel during the cycle. Early SOE (at -30 CAD) is chosen in order to make possible to perform PIV measurements after the injection while seeing the entire bowl. At 25 CAD the effect of the injection is already noticed in the upper part of the bowl. The sprays seem to cause a deceleration of the velocity field while injection event is still occurring. This effect continues until -20 CAD, where the region with low velocity is bigger. The effect of the injection seems to be absent at -15 CAD, when the injection process ends, and the velocity field increases slightly.

3.5 TKE* analysis at motored and injection conditions

TKE is normalized in relation to the total energy of the fluid (TKE*), as the criterion defined previously. Fig. *8* shows a comparison of TKE* between motored and injection conditions. The figure reveals that for the injection case the turbulence represents a greater amount of the total fluid energy compared to the motored case. It means that despite the motored case presenting higher velocities, the weight of the TKE in relation to the total fluid energy is lower than for the injection case. The turbulence for the single injection case is much higher than motored case. The effect of the injection is clear in the first two images, where the turbulence increases around the zone of the spray. This is the zone that the velocities are lower. After the injection ends, at -15 CAD, the TKE* starts to dissipate inside the bowl.
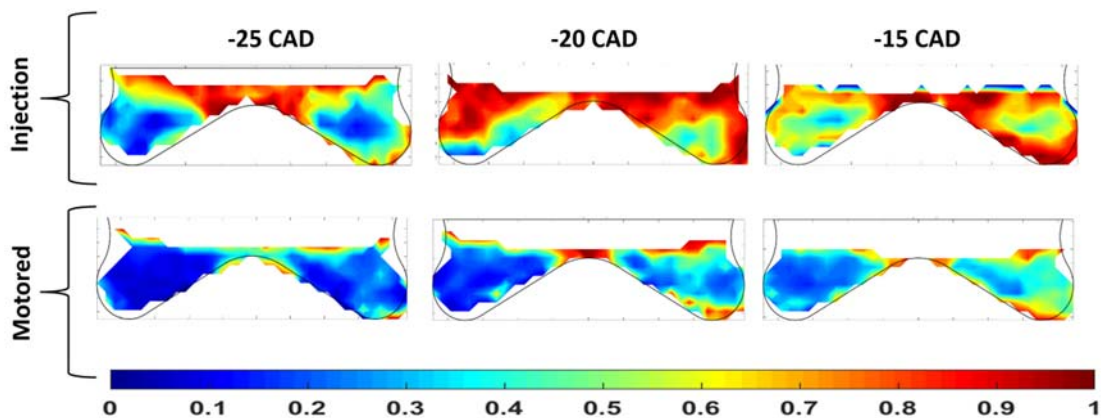
Fig. 8- TKE distribution inside the bowl at motored and injection conditions

4. Piston bowl geometries and e-fuels effects on soot reduction

The first step of the current work helped in the comprehension about the in-cylinder flow behavior in a piston with real bowl shape. This comprehension was very useful for the second work step, where different bowl geometries, together with e-fuels, were studied. In general, the second step was focused on the soot reduction by means of two different alternatives. The first one is centered on the hardware modification with new piston geometry proposals. The second alternative solution for soot reduction was centered in the use of renewable fuels, where the potential of e-fuels were tested.

4.1 Piston geometries

For the current work, three different bowl geometries were tested in the optical engine. A piston with reentrant geometry, which is represented in Fig. *9*a, was tested as the baseline. Besides, a kind of hybrid design combining two bowl geometries in the same piston was developed. One half of the piston, represented in Fig. *9*b, was formed only by the stepped lip geometry. The other one was composed by the stepped lip and wave geometry. The main purpose of the hybrid piston was to compare performance of two bowl geometries in the same combustion cycle, diminishing the effects of the cycle to cycle variation.
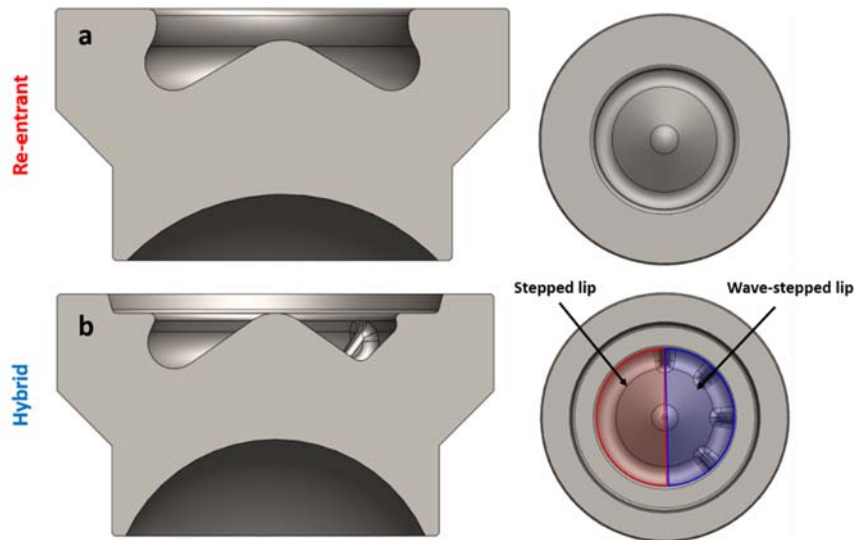
Fig. 9- Bowl geometries: a) Re-entrant. b) Hybrid

4.2 e-fuels properties

The main properties of the fuels studied in this work are presented in table 4. Commercial diesel (EN 590 diesel) was considered the reference fuel in the study. Fischer-Tropsch (FT) diesel and Oxymethylene ether (OMEX) were used without mixing. Cetane number for FT diesel and OMEX is clearly higher than for the commercial diesel, indicating that their ignitability is higher[26]. OMEX presents the lowest viscosity between the three tested fuels, which directly implies in an improvement of the spray quality[27]. Finally, regarding the Lower Heating Value (LHV), FT diesel and commercial diesel have very similar values. However, OMEX's LHV is less than the half of the commercial diesel's. This has a direct impact in fuel consumption.

Table 4. Fuel properties

	EN 590 diesel	FT diesel	OMEX
Density [kg/m3] (T= 15 °C)	842	832	1067
Viscosity [mm2/s] (T= 40 °C)	2.929	3.25	1.18
Cetane number [-]	55.7	75.5	72.9
Carbon content [% m/m]	86.2	85.7	43.6
Hydrogen content [% m/m]	13.8	14.3	8.82
Oxygen content [% m/m]	0	0	47.1
Lower heating value [MJ/kg]	42.44	44.2	19.04

4.3 Optical techniques

For both analyses performed in the current work, piston geometry and e-fuels, three optical techniques have been applied simultaneously in order to identify and analyze the differences in the combustion process. The optical setup is presented in Fig. *10*. They were positioned in order to record the flame radiation that comes from the main optical access (piston bottom). A 45° mirror is positioned just below the piston in order to reflect all flame radiation from the combustion chamber to the optical system. A dichroic mirror was used to reflect the UV radiation to the intensified camera (ICCD), which was positioned parallel to the engine's crankshaft. After the dichroic mirror, which is transparent for the visible range (up to 750nm), a beam splitter was positioned to separate flame radiation between two high speed cameras (550nm and 660 nm). One of them was equipped with a 660 nm filter, which is used for both 2-color measurements as well as for the natural luminosity imaging. The other one was equipped with a 550 nm filter, which was used for 2-color pyrometry. In this case, the Natural luminosity (NL) images have been used in order to provide general information about the combustion process evolution. They correspond to hot soot radiation, which is the dominant source of luminosity in diffusive combustion. The OH* chemiluminescence signal was used in order to identify the near-stoichiometric high temperature

combustion zones inside the different pistons and with the different e-fuels. These zones are characterized for high concentration of excited-state OH*. 2-color pyrometry is used in this work in order to quantify the soot concentration inside the three bowl geometries tested, as well as, for each e-fuel. In this method, soot thermal radiation was detected for two specific wavelengths. From its combination, the soot surface temperature and optical density is determined.
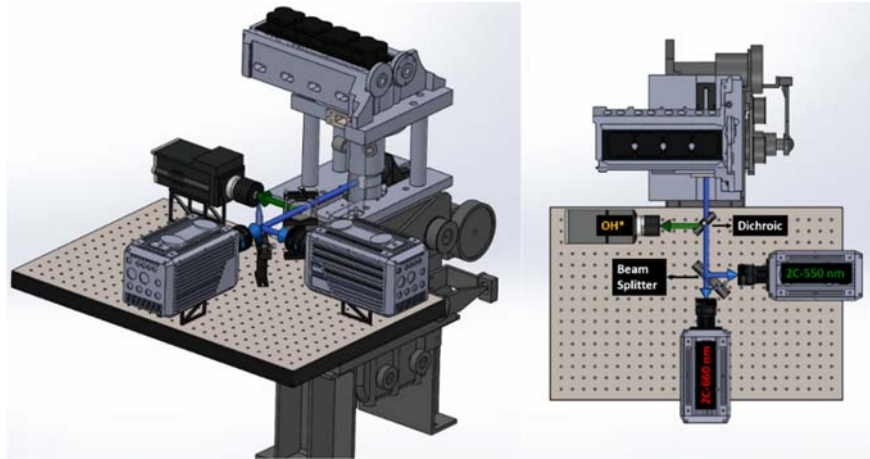
Fig. 10- Optical setup

4.4 Image post-processing

A specific methodology for the image analysis was developed in order to present time and spatially resolved KL2C measurements in a single map. In this way, the combustion images were divided in zones by applying two different criteria: sector zones and radial zones. For the sector analysis, the whole piston image is divided in 5° angular sectors in the azimuth direction as shown in Fig. *11*(a). For every sector an average KL is calculated. For the radial analysis, the piston image is divided in rings, as shown in Fig. *11*(b), with a difference of 0.5 mm between the internal and external radius. For each ring a mean radius is calculated as well as the average KL2C.
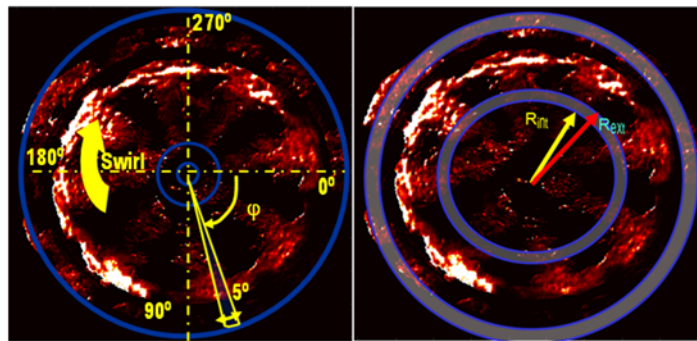
Fig. 11- (a) Methodology for the sector analysis. (b) Methodology for the radial analysis

Taking into account that the tests for the e-fuels were performed with the re-entrant piston, the methodology were applied for the entire piston bore, including the squish zone. In contrast, for the analysis comparing the different bowl geometries, only the bowl part was considered. In addition, for the hybrid piston analysis, an additional methodology was applied in order to isolate two different piston regions, one represented by the stepped lip side and another one by the stepped lip-wave side. The piston was divided into two zones with exactly the same size, as shown in Fig. **12**.
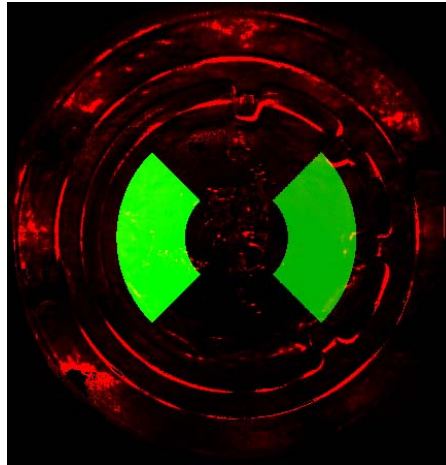
Fig. 12- Regions considered for the radial and sector analysis using the hybrid piston

4.5 Test matrix

For the piston geometry study, the experiments were performed with commercial diesel fuel at 7.5 bar IMEP. The engine speed was kept constant at 1250 rpm. Considering that the two pistons do not have the same compression ratio, different intake pressures and temperatures were used in order to maintain the same IMEP and mass of fuel injected per cycle, as well as the same maximum in-cylinder pressure (Pmax). Four injections per cycle (pilot 1, pilot 2, main and post) were configured to mimic a commercial injection strategy. The injection pressure used was 800 bar. For the e-fuels analysis, the same engine load (7.5 bar IMEP), as well as the same injection strategy for diesel were used. In this case, each e-fuel was tested with four injections, being 2 pilots, main and post injection. Due to the different LHV for each fuel, the engine load was adjusted by increasing the pulse duration of the main injection. All e-fuel tests (FT-diesel and OMEX) were performed only with the re-entrant piston. The analysis for the piston shape effect (hybrid and re-entrant piston) was performed with diesel. Test matrix is represented in table 5.

Table 5- Engine operating conditions for the tests with pistons and e-fuels

Inj. Pattern	Engine Speed	Piston	IMEP (bar)	$\dot{m}_{air}$ (g/s)	Pint (Bar)	Tint (°C)	Toil (°C)	Tcool (°C).	Fuel
Mult	1250	Re-entrant Hybrid	7.5	8.08 8.5	2.15 2.35	90 120	60	15-25	diesel; FT diesel; OMEX diesel

4.6 Piston geometry analysis: Flame movement

Details regarding flame movement are reported in Fig. *13* for 7.5 bar IMEP. The left side represents the re-entrant piston while the right side represents the hybrid piston. As it has been described previously, this one includes the others two bowl geometries: stepped lip without waves (left side) and stepped lip-wave (right side). At 7.7 CAD, in Fig. *13*, main injection is occurring and the spray is interacting with the bowl wall. At this instant, major differences can be detected when comparing the wave side with the other two geometries. When the sprays collide with the bowl wall, the wave protrusions avoid the flame to spread tangentially and redirects it toward the bowl center (red line area), minimizing the flame-flame collisions, providing a pathway for the oxygen supply to flame front and generating less fuel rich zones. In contrast, without waves, flame-flame collisions are observable close to the bowl wall. Focusing on the hybrid piston, at 11.9 CAD (end of main injection) different flame structures can be seen for each piston geometry. The red line represents the area reached by the flame inside the bowl with waves, while the orange line represents the area occupied by the flame at the side without waves. When both are compared, it is possible to see that the orange area is much smaller than the red one. Therefore, it can be stated that the flame in the stepped lip side without waves seems to remain concentrated at the periphery of the bowl. This behavior has been related with effect of the stepped lip, splitting the spray/flame into two parts (one inside the bowl and the other into the squish area) and reducing the momentum of

the spray. Besides, the flame-flame collisions when not using wave protrusions and the resulting stagnations have been considered also a potential cause. In the case of the wave-stepped lip, the reverse flow forces the flame to move towards the bowl center. For the re-entrant geometry, even though the flame goes toward the center due to higher spray momentum, the existence of strong flame-wall and flame-flame interaction can promote the formation of fuel rich zones.
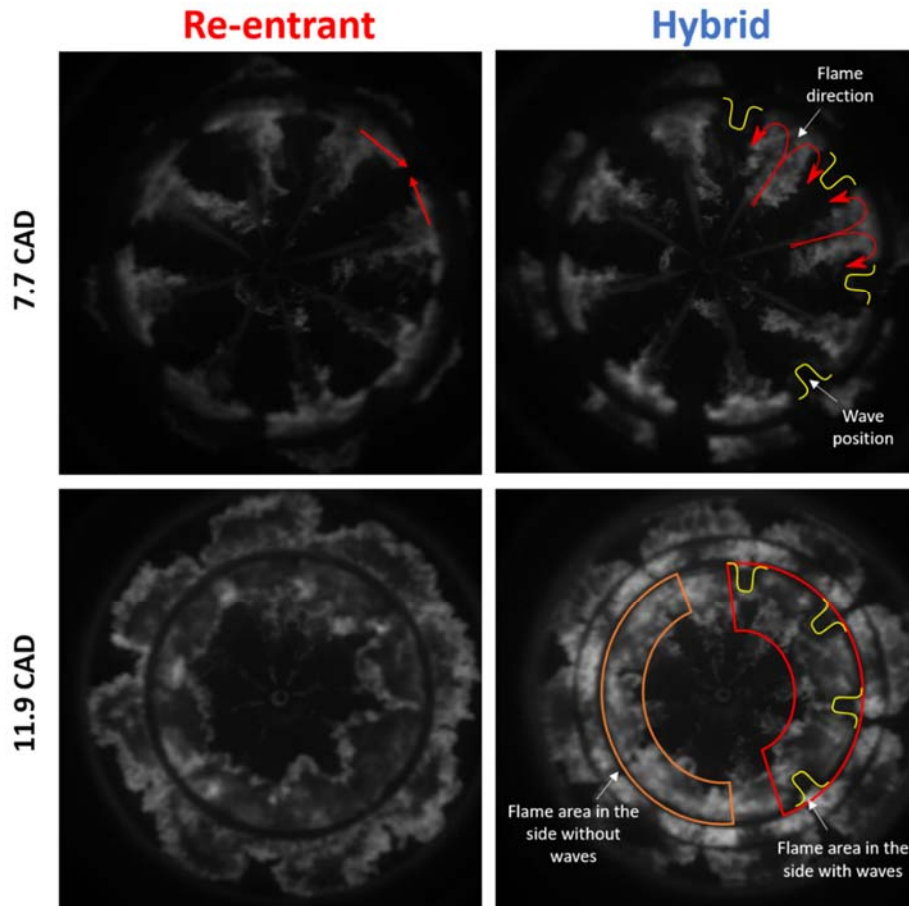
Fig. 13- flame behavior for different bowl templates

4.7 Piston geometry analysis: *Soot formation*

In Fig. **14**, the temporal evolution of mean KL and the accumulated light intensity at 7.5 bar IMEP are shown. In addition, the Fig. **15** shows the 2C pyrometry and OH* chemiluminescence measurements for the same engine conditions at specific CADs. The graphs indicate an important higher peak soot formation for the re-entrant piston. Furthermore, a slower soot oxidation can be seen for the re-entrant one during the late cycle oxidation. In addition, the accumulated light intensity also presents the later soot oxidation for the re-entrant piston than the stepped lip and stepped lip-wave bowls. From the accumulated intensity curve is clear that wave side is promoting a higher peak in comparison with the side without waves. However, during the late combustion phase, a faster oxidation can be appreciated for the stepped lip-wave side. The Fig. **15** shows, for specific piston positions, the spatial distribution of KL inside of each bowl geometry as well as the OH* chemiluminescence. In general, the zones with low OH* intensity correspond to the high soot concentration zones in the re-entrant piston. In contrast, lower soot concentration can be seen for the hybrid piston, corroborating with the OH* images, where its intensity is higher than re-entrant piston. At 10.11 CAD it is possible to appreciate the non-presence of OH* intensity in the zones which are located closer to the wave protrusions. These same zones, for the KL images, present higher soot concentration. This rapid increase of soot formation for this region could be induced by the bigger quartz contact surface present for the side with wave protrusions. The heat transfer characteristic of quartz and the wall temperature could be the factor that contribute for this soot formation. When the flame goes toward the center and starts to interact with the other flame, the soot

is rapidly oxidized. This is represented at 14.61 CAD, where the OH* intensity increased. The final combustion cycle (37.74 CAD) seems to be faster for the hybrid piston due to the fact that soot cloud, as well as OH*signal can still be seen inside the re-entrant bowl.
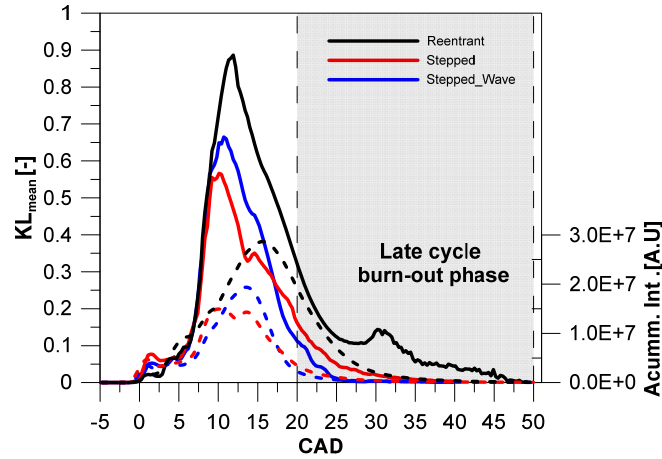
Fig. 14-Temporal evolution of mean KL and accumulated intensity
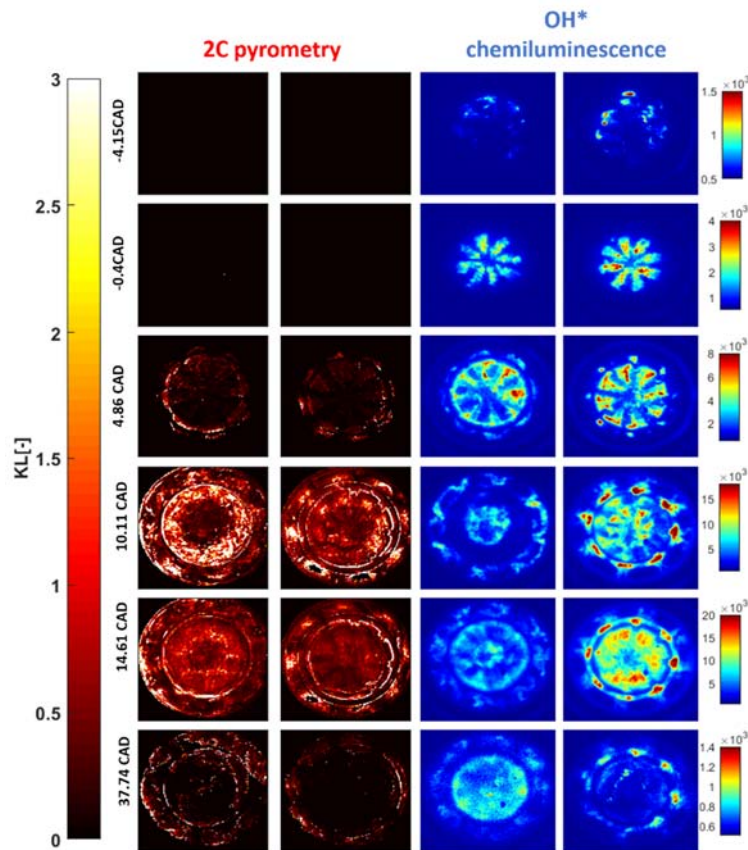
Fig. 15 – 2 color and OH* measurements at 7.5 bar IMEP

The radial maps are presented for each bowl geometry in Fig. *16*. The re-entrant piston starts the soot formation from the bowl periphery. As the flame goes toward the piston center, the soot oxidation process also takes place. The soot oxidation, in comparison with the other two geometries, present a smoother transition of the KL values, indicating a slower oxidation process. In addition, the re-entrant piston also presents bigger areas with high soot concentration than the stepped lip and stepped lip-wave piston. A general reduction of soot formation is clear for the stepped lip and stepped lip-wave

bowls in comparison with the re-entrant one. This significant soot reduction is thanks to the stepped lip, as the great differences of soot production can be appreciated between the re-entrant and hybrid piston. The differences between stepped lip and stepped lip-wave seems to be less sensible but they can still be highlighted. A fast and efficient oxidation is promoted by the stepped lip bowl during the first stages of the combustion process. The stepped lip-wave side promotes initially a higher quantity of soot formation, when the flame interacts with the wall, as previously explained. However, during the final stage of combustion, the oxidation rate for the stepped lip bowl seems to decrease. From 15 CAD until 25 CAD, the soot cloud for the stepped lip bowl presents higher KL value than the stepped lip-wave geometry.
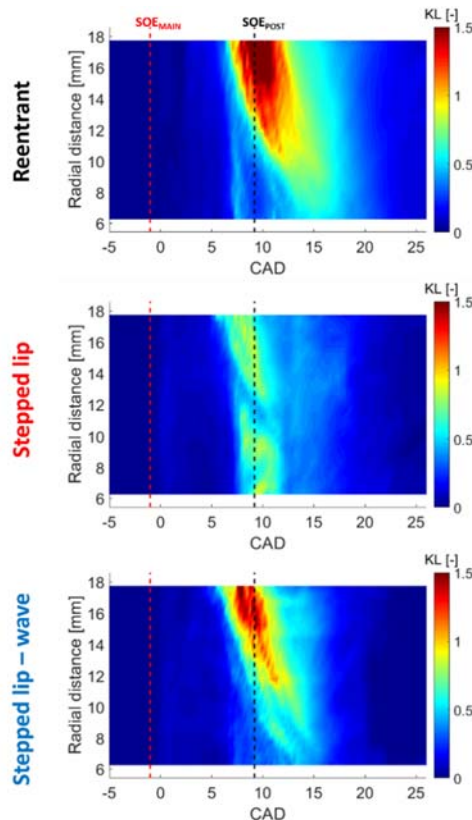
Fig. 16- Radial maps of KL values at 7.5 bar IMEP

4.8 e-fuels analysis: natural luminosity and OH* chemiluminescence

The combustion evolution at 7.5 bar IMEP is presented in Fig. *17* by means of natural luminosity images. The lower range of light intensity showed for the OMEX, which has its maximum at 400, suggests less soot formation for this fuel.
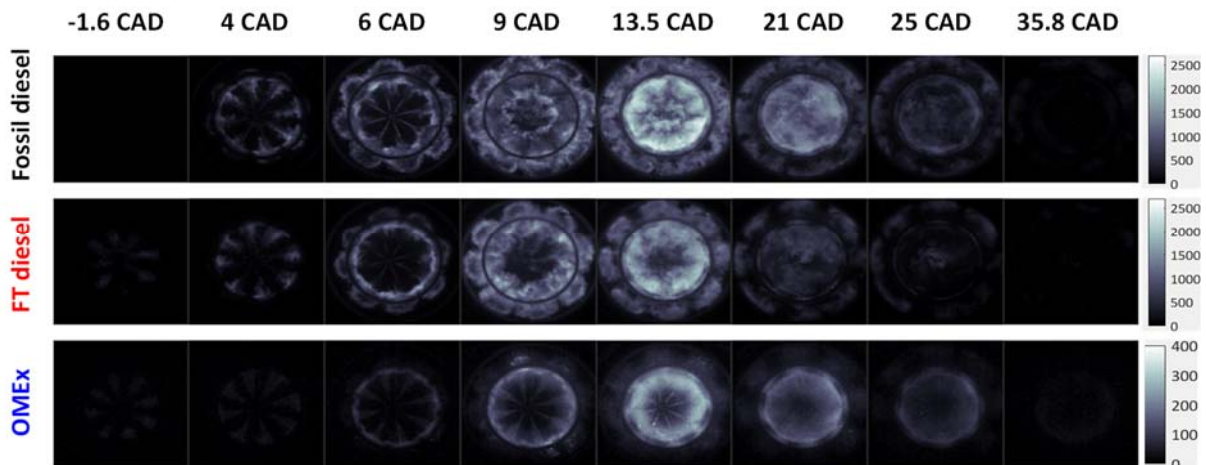
Fig. 17- Natural Luminosity for the tests with e-fuels and fossil diesel at 7.5 bar IMEP

At 9 CAD, some dark regions can be seen for the fossil diesel images. These regions have already been reported by some authors as cold soot regions[28]. In contrast, this effect is not observable for the FT diesel which suggests the existence of hotter soot. From 21 CAD until 25 CAD, the images represent the late-cycle soot oxidation for the 3 fuels. FT diesel seems to oxidize faster than fossil diesel as the NL intensity decreases faster.

The OH* chemiluminescence for the tested fuels at 7.5 bar IMEP can be seen in Fig. *18*. At -1.6 CAD no natural luminosity was observed. However, some OH* radiation is detected. This image is representing the pilot 2 combustion. Higher OH* chemiluminescence can be seen for the FT diesel during this period. At 4 CAD, the three fuels tested show high signal intensity in the periphery for both OH* and NL intensity. This indicates that in this region both near-stoichiometric and fuel rich zones coexist, as reported in previous works[29]. At 9 CAD, the dark zones cited in the NL images correspond also to low OH* intensity. This indicates that the cold soot is attenuating the OH* signal. Fossil diesel presents less area with OH* radiation than the FT diesel and consequently larger dark zones in the NL images. In addition, although OMEX presented the lowest NL intensity, the OH* measurements show the highest intensity. The high amount of oxygen in the OMEX diminishes fuel rich zones and increases the near-stoichiometric zones as well as the presence of OH* in excited state.
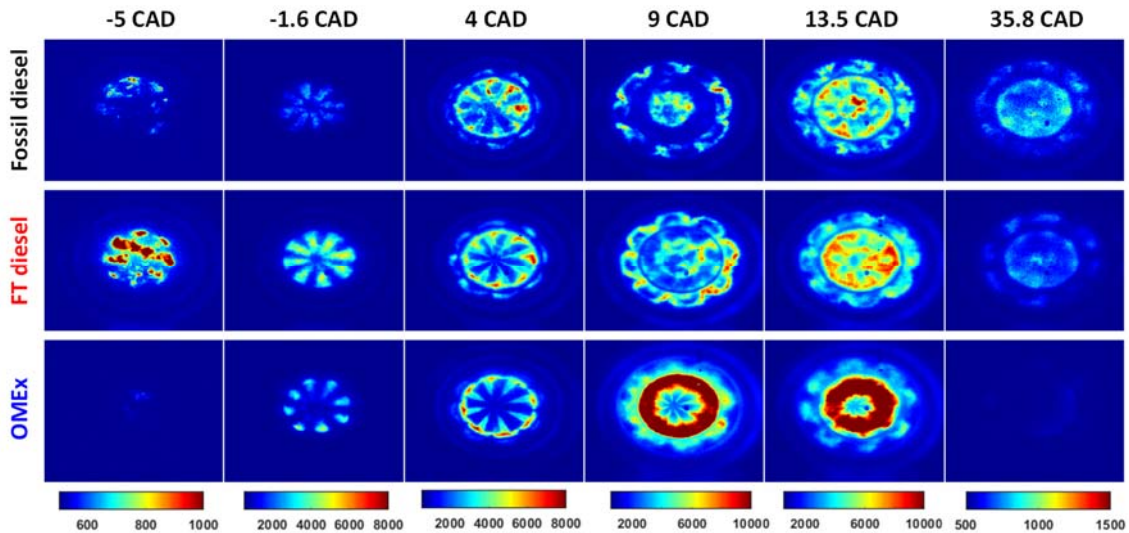
Fig. 18- OH* chemiluminescence images for the tests with e-fuels and fossil diesel at 7.5 bar IMEP

At 35.8 CAD, during the final stages of combustion, the OH* signal confirms that OMEX combustion ends earlier as low OH* signal is observed in comparison with the other two fuels. Furthermore, fossil diesel has the higher OH* intensity for this instant, indicating a slower soot oxidation process in comparison with the FT diesel

4.9 e-fuels analysis: Soot formation

In Fig. *19* is shown the 2C pyrometry measurements at 7.5 bar IMEP. The OMEX emitted light with wavelength below 450 nm, as no light was registered by the two cameras (450 nm and 660 nm) and consequently no KL factor was calculated. This is another factor that indicates no formation of soot during the OMEX combustion process. In relation to the fossil diesel and FT diesel, where the KL factor could be calculated, the images are presented for the same crank positions already shown previously for the NL and OH* images. From 4 CAD until 6 CAD, the soot formation (KL) starts to increase. The periphery region of the bowl, where previously NL and OH* showed highest intensity, also presents the highest soot area. At 9 CAD, the regions with the highest soot concentration correspond to the regions where NL and OH* signals for commercial diesel were weak. This effect reinforces the idea that the cold soot cloud attenuates the OH* signals. For this instant, FT diesel presents KL values slightly lower than commercial diesel, which means less soot production.
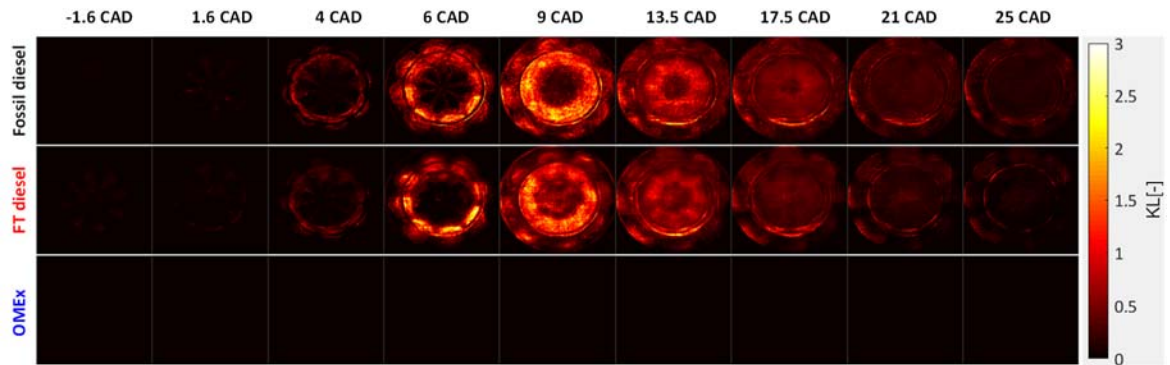
Fig. 19- KL images for the tests with e-fuels and fossil diesel at 7.5 bar IMEP

In Fig. *20* is shown the evolution of the mean KL for each CAD during the combustion process. The commercial diesel starts to increase earlier in the cycle than FT diesel. Furthermore, it is clear that for the first one, the maximum KL value is slightly higher. In addition, during the oxidation process, FT diesel seems to oxidize faster, in agreement with NL and OH* observations. The KL curve for OMEX is zero, as no light intensity was registered by the 2C cameras.
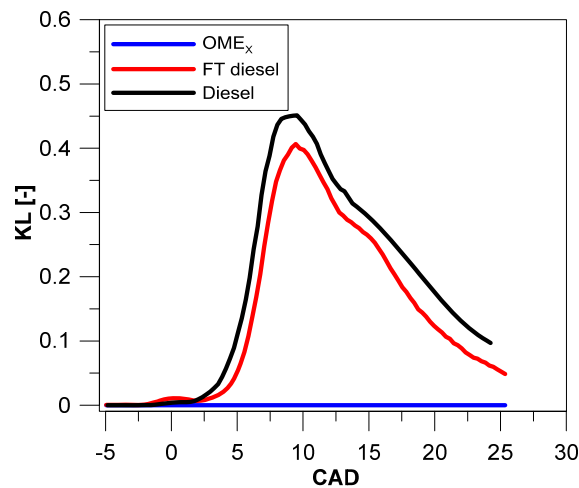
Fig. 20-Temporal evolution of mean KL for tests with e-fuels and fossil diesel at 7.5 bar IMEP

The sector and radial maps are presented in Fig. *21*. For the sector maps (Fig. *21*-left), it is possible to see that commercial diesel present larger areas with high KL values than FT diesel. In addition, from the map is possible to appreciate that the FT diesel achieves lower KL values before than commercial diesel due to the less soot generated inside the cylinder and the faster oxidation. The radial maps (Fig. *21*-right) show that the periphery of the bowl, around 15 mm from the injector, has the highest soot KL. As the piston moves far from the TDC, the highest soot KL areas move toward the center of the piston while decreasing its value. FT diesel achieves low KL (below 0.5) at around of 6mm of radius, while commercial diesel reaches these values closer to bowl center. It evidences again the faster soot oxidation for the FT diesel. Another difference is located in the squish zone, which comprehends from 18mm to 26 mm. For this region, the soot concentration is lower for the FT diesel.
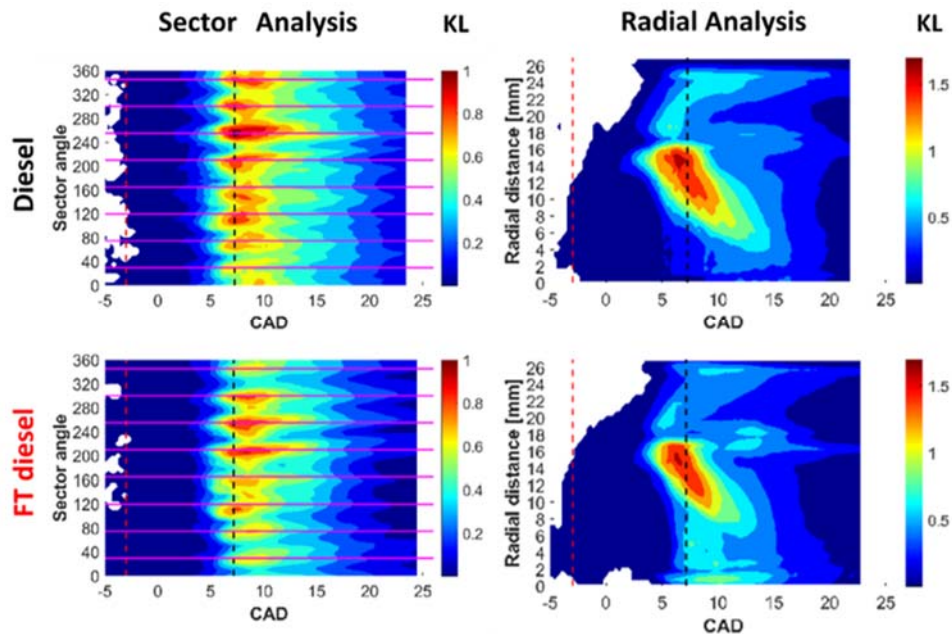
Fig. 21- Radial and Sector KL maps for the tests with e-fuels and fossil diesel at 7.5 bar IMEP

Conclusions

In the first part of the paper, the in-cylinder flow velocity inside of a real bowl geometry was measured and analyzed. In the second part, it was evaluated the combustion process and soot formation of two different e-fuels, as well as three different piston geometries by using three different optical techniques. Main conclusions can be highlighted as follows:
In relation to the in-cylinder flow measurements:

- When the injection event ends, a slight decrease of TKE* can be seen inside the bowl. This reiterates the effect of the fuel injection on the in-cylinder flow.
- Bulk gas velocity and mean kinetic energy of the in-cylinder air decrease when the injection is occurring. This effect is evidenced when the injection ends and the velocity starts to increase again inside the bowl.
- TKE* presents higher values in the injection cases than in motored ones, indicating that the turbulence caused by the injection event could help to improve the fuel air-mixing.

In relation to the different bowl geometries:

- The wave protrusions induce a reverse flow of the flames towards the bowl center. The flame-flame collision is smoothed when the flame is driven by this geometry, avoiding frontal collision as it happens in the side without the protrusions and re-entrant piston.
- The zones with high soot concentration correspond to the zones where the OH* intensity is weak or nonexistent. This indicates that the soot cloud is attenuating the OH* signal.
- A significant soot reduction, as well as a faster soot oxidation could be appreciated for the stepped lips and stepped lip-wave geometries in comparison with the re-entrant bowl. In addition, the mean KL and accumulated intensity curves showed a faster soot oxidation for the stepped lip-wave side during the late cycle oxidation.

In relation to the e-fuels:

- Although the NL intensity for the OMEX is lowest between the three fuels, it presents the highest OH* intensity. The high amount of oxygen can increase the local zones near of stoichiometric conditions and increases the OH* intensity. Furthermore, the very low soot formation permits a better visualization of the OH* chemiluminescence that is not possible to see for the case with FT diesel and fossil diesel.

- The image of OH* chemiluminescence at 35.8 CAD prove the shortest combustion duration for the OMEX. Furthermore, it is clear that FT diesel presents a faster oxidation than commercial diesel.
- FT diesel presents lower soot emissions than commercial diesel at 7.5 bar IMEP.
- Radial map presents lower KL values in the squish zone when FT diesel was used. Furthermore, the FT diesel flame oxidizes the soot farther from the center than commercial diesel.

Acknowledgments

References

[1] Omari A, Heuser B, Pischinger S, Rüdinger C. Potential of long-chain oxymethylene ether and oxymethylene ether-diesel blends for ultra-low emission engines. Appl Energy 2019;239:1242–9. doi:10.1016/j.apenergy.2019.02.035.

[2] Kim YD, Yang CW, Kim BJ, Moon JH, Jeong JY, Jeong SH, et al. Fischer–tropsch diesel production and evaluation as alternative automotive fuel in pilot-scale integrated biomass-to-liquid process. Appl Energy 2016;180:301–12. doi:10.1016/j.apenergy.2016.07.095.

[3] Benajes J, García A, Monsalve-Serrano J, Lago Sari R. Experimental investigation on the efficiency of a diesel oxidation catalyst in a medium-duty multi-cylinder RCCI engine. Energy Convers Manag 2018;176:1–10. doi:10.1016/j.enconman.2018.09.016.

[4] Geng C, Liu H, Chen B, Yao M, Ran X, Yang Z, et al. A comparative study on partially premixed combustion (PPC) and reactivity controlled compression ignition (RCCI) in an optical engine. Proc Combust Inst 2018;37:4759–66. doi:10.1016/j.proci.2018.06.004.

[5] Busch S, Zha K, Kurtz E, Warey A, Peterson R. Experimental and Numerical Studies of Bowl Geometry Impacts on Thermal Efficiency in a Light-Duty Diesel Engine. SAE Tech Pap Ser 2018;1:1–12. doi:10.4271/2018-01-0228.

[6] Leach F, Ismail R, Davy M, Weall A, Cooper B. The effect of a stepped lip piston design on performance and emissions from a high-speed diesel engine. Appl Energy 2018;215:679–89. doi:10.1016/j.apenergy.2018.02.076.

[7] Zha K, Busch S, Warey A, Peterson RC, Kurtz E. A Study of Piston Geometry Effects on Late-Stage Combustion in a Light-Duty Optical Diesel Engine Using Combustion Image Velocimetry. SAE Int J Engines 2018;11:783–804. doi:10.4271/2018-01-0230.

[8] . CSB. Effects of Piston Bowl Geometry on Combustion and Emission Characteristics on Diesel Engine: a Cfd Case Study. Int J Res Eng Technol 2016;05:81–93. doi:10.15623/ijret.2016.0507015.

[9] Eismark J, Andersson M, Christensen M, Karlsson A, Denbratt I. Role of Piston Bowl Shape to Enhance Late-Cycle Soot Oxidation in Low-Swirl Diesel Combustion. SAE Int J Engines 2019;12. doi:10.4271/03-12-03-0017.

[10] Tanov S, Johansson B, Richter M, Wang Z, Wang H. Effects of Injection Strategies on Fluid Flow and Turbulence in Partially Premixed Combustion (PPC) in a Light Duty Engine. SAE Tech Pap Ser 2015;1. doi:10.4271/2015-24-2455.

[11] da Costa RBR, Gomes CA, Valle RM, Franco RL, Huebner R. PIV Measurements of In-Cylinder Tumble Flow in a Motored Single Cylinder Optical Research Engine. SAE Tech Pap Ser 2016;1. doi:10.4271/2015-36-0305.

[12] Miles PC, Collin R, Hildingsson L, Hultqvist A, Andersson Ö. Combined measurements of flow structure, partially oxidized fuel, and soot in a high-speed, direct-injection diesel engine. Proc Combust Inst 2007;31 II:2963–70. doi:10.1016/j.proci.2006.07.231.

[13] Adachi Y, Shimokawa K. COMBUSTION CHAMBER STRUCTURE FOR DIRECT NUECTION DESEL ENGINE. US 8,156,927 B2, 2012.

[14] Neely GD, Sasaki S, Sono H. Investigation of alternative combustion crossing stoichiometric air fuel ratio for clean diesels. SAE Tech Pap 2007. doi:10.4271/2007-01-1840.

[15] Pment DEV, Engines D. OM 654 – Launch of a New Engine Family by Mercedes-Benz n.d.:18–25.

[16] Busch S, Zha K, Perini F, Reitz R, Kurtz E, Warey A, et al. Bowl Geometry Effects on Turbulent Flow Structure in a Direct Injection Diesel Engine. SAE Tech Pap 2018;2018–Septe.

doi:10.4271/2018-01-1794.

[17] Hao B, Song C, Lv G, Li B, Liu X, Wang K, et al. Evaluation of the reduction in carbonyl emissions from a diesel engine using Fischer-Tropsch fuel synthesized from coal. Fuel 2014;133:115–22. doi:10.1016/j.fuel.2014.05.025.

[18] Iannuzzi SE, Barro C, Boulouchos K, Burger J. Combustion behavior and soot formation/oxidation of oxygenated fuels in a cylindrical constant volume chamber. Fuel 2016;167:49–59. doi:10.1016/j.fuel.2015.11.060.

[19] Pellegrini L, Marchionna M, Patrini R, Beatrice C, Del Giacomo N, Guido C. Combustion Behaviour and Emission Performance of Neat and Blended Polyoxymethylene Dimethyl Ethers in a Light-Duty Diesel Engine. SAE Tech Pap Ser 2012;1. doi:10.4271/2012-01-1053.

[20] Lapuerta M, Armas O, Hernández JJ, Tsolakis A. Potential for reducing emissions in a diesel engine by fuelling with conventional biodiesel and Fischer-Tropsch diesel. Fuel 2010;89:3106–13. doi:10.1016/j.fuel.2010.05.013.

[21] Gill SS, Tsolakis A, Dearn KD, Rodríguez-Fernández J. Combustion characteristics and emissions of Fischer–Tropsch diesel fuels in IC engines. Prog Energy Combust Sci 2011;37:503–23. doi:10.1016/J.PECS.2010.09.001.

[22] Jiao Y, Liu R, Zhang Z, Yang C, Zhou G, Dong S, et al. Comparison of combustion and emission characteristics of a diesel engine fueled with diesel and methanol-Fischer-Tropsch diesel-biodiesel-diesel blends at various altitudes. Fuel 2019;243:52–9. doi:10.1016/j.fuel.2019.01.107.

[23] Schaberg P, Botha J, Schnell M, Hermann HO, Pelz N, Maly R. Emissions performance of GTL diesel fuel and blends with optimized engine calibrations. SAE Tech Pap 2005. doi:10.4271/2005-01-2187.

[24] Liu H, Wang Z, Li Y, Zheng Y, He T, Wang J. Recent progress in the application in compression ignition engines and the synthesis technologies of polyoxymethylene dimethyl ethers. Appl Energy 2019;233–234:599–611. doi:10.1016/j.apenergy.2018.10.064.

[25] Omari A, Heuser B, Pischinger S. Potential of oxymethylenether-diesel blends for ultra-low emission engines. Fuel 2017;209:232–7. doi:10.1016/j.fuel.2017.07.107.

[26] Liu H, Wang Z, Wang J, He X. Improvement of emission characteristics and thermal efficiency in diesel engines by fueling gasoline/diesel/PODEn blends. Energy 2016;97:105–12. doi:10.1016/j.energy.2015.12.110.

[27] Chen H, Su X, Li J, Zhong X. Effects of gasoline and polyoxymethylene dimethyl ethers blending in diesel on the combustion and emission of a common rail diesel engine. Energy 2019;171:981–99. doi:10.1016/j.energy.2019.01.089.

[28] Roberts G, Lind T, Eagle W, Musculus MP, Andersson Ö, Rousselle C. Mechanisms of Post-Injection Soot-Reduction Revealed by Visible and Diffused Back-Illumination Soot Extinction Imaging. SAE Tech Pap Ser 2018;1:1–20. doi:10.4271/2018-01-0232.

[29] Jakob M, Hülser T, Janssen A, Adomeit P, Pischinger S, Grünefeld G. Simultaneous high-speed visualization of soot luminosity and OH * chemiluminescence of alternative-fuel combustion in a HSDI diesel engine under realistic operating conditions. Combust Flame 2012;159:2516–29. doi:10.1016/j.combustflame.2012.03.004.

Influence of the Diesel Pilot Injector Configuration on Ethanol Combustion and Performance of a Heavy-Duty Direct Injection Engine

N. Giramondi[1], A. Jäger[2], D. Norling[2] and A. Christiansen Erlandsson[3]

[1]KTH Royal Institute of Technology. Brinellvägen 83, 11428 Stockholm. Sweden.

E-mail: nicolagi@kth.se
Telephone: +46 8 790 6857

[2]Scania CV AB. 15187 Södertälje. Sweden.

E-mail: ander.jager@scania.com | daniel.norling@scania.com
Telephone: +46 8 553 51863 | +46 8 553 81533

[3]KTH Royal Institute of Technology. Stockholm, Sweden. DTU Technical University of Denmark. Lyngby, Denmark.

E-mail: ace@itm.kth.se
Telephone: +46 8 790 7893

Abstract. Thanks to its properties and production pathways, ethanol represents a valuable alternative to fossil fuels, with potential benefits in terms of CO_2, NO_x and soot emission reduction. The resistance to autoignition of ethanol necessitates an ignition trigger in compression-ignition engines for heavy duty applications, which in the current study is a diesel pilot injection. The simultaneous direct injection of pure ethanol as main fuel and diesel as pilot fuel through separate injectors is experimentally investigated in a heavy-duty single cylinder engine at a low and a high load point. The influence of the nozzle hole number and size of the diesel pilot injector on ethanol combustion and engine performance is evaluated based on an injection timing sweep using three diesel injector configurations. The tested configurations have the same geometric total nozzle area for one, two and four diesel sprays. The amount of ethanol injected is swept within a range between $80 - 90\%$ and $91 - 98\%$ on an energy basis at low and high load, respectively. The results show that mixing controlled combustion of ethanol is achieved with all tested diesel injector configurations and that the maximum combustion efficiency and variability levels are in line with conventional diesel combustion. The one-spray diesel injector is the most robust trigger for ethanol ignition, as it allows to limit combustion variability and to achieve higher combustion efficiencies compared to the other diesel injector configurations. However, the two- and four-spray diesel injectors lead to higher indicated efficiency levels. The observed difference in the ethanol ignition dynamics is evaluated and compared to conventional diesel combustion. The study broadens the knowledge on ethanol mixing-controlled combustion in heavy-duty engines at various operating conditions, providing the insight necessary for the optimization of the ethanol-diesel dual-injection system.

1. Introduction

In an effort to decarbonize the transport sector, new CO_2 emission standards have been introduced for heavy-duty vehicles in the European Union and other major markets [1]. From a well-to-wheel perspective, the introduction of low-carbon fuels like ethanol as fossil fuel substitutes in heavy-duty engines has the potential to decrease carbon emissions within short time frames compared to electrification [2], as they can be used in the existing fleet with relatively limited hardware modifications. Ethanol is liquid at ambient conditions bringing benefits in terms of transportation, storage and handling [3]. However, the reduced lower heating value compared to diesel [4] necessitates higher fuel storage capacity. The challenge to introduce ethanol as fuel for heavy-duty transport lays in the resistance to autoignition, as extensively studied by Siebers and Edwards [5]. Under heavy-duty engine conditions, ethanol autoignition is not influenced by pressure and occurs only at temperatures above 950 K [5]. In-cylinder temperatures above 1100 K are necessary for achieving ethanol ignition delays comparable to diesel, and for limiting in-cylinder pressure rise rates [5]. Ethanol has a single-stage ignition characteristics with no low or intermediate temperature heat release [6]. For this reason, ethanol combustion phasing is highly sensitive to the engine inlet conditions [6] when used in premixed combustion concepts, posing challenges with combustion controllability during transient engine operation [7]. It is thereby beneficial to use ethanol as

fuel for compression ignition engines with diesel-like operation. To this end, engine hardware modifications to the injection and combustion systems are required.

Siebers and Edwards [5] stated that a minimum compression ratio of 23:1 is necessary to ensure in-cylinder conditions suitable for ethanol autoignition throughout the whole engine operating range including cold start. Scania has developed an ethanol (ED95) engine with a compression ratio of 28:1 relying on the use of ignition improvers [8]. The same engine was used by Aakko-Saksa et al. [9] for tests using methanol additized with ignition and lubricity improvers. Compared to the ED95 baseline, similar engine performance and THC emissions, lower CO and aldehydes emissions but higher emissions of semi-volatile particles originated from the methanol additives were reported [9]. Shamun et al. [10] investigated the use of pure methanol on a research engine derived from the Scania ethanol engine with a slightly lower compression ratio of 27:1. The study opened up to the possibility to run the engine on pure methanol throughout the whole load range, while limiting the injection parameters within narrow ranges at high load in order to avoid excessive in-cylinder peak pressures [10].

An alternative to the use of high compression ratios for using ethanol in heavy-duty compression-ignition engines is increasing the engine intake temperature, as implemented in the high-temperature stoichiometric compression-ignition engine [11] investigated by Blumreiter et al. [12]. This concept relies on (i) the thermal insulation of the combustion chamber by means of a thermal barrier coating, (ii) direct injection of alcohol fuel in a stoichiometric proportion, and (iii) exhaust gas recirculation. Stable diesel-like combustion of ethanol was reported for a broad engine operating range. Combustion completeness was favored by the high in-cylinder temperatures sustained thanks to the effect of the thermal barrier coating. This effect balanced the otherwise rapid charge cooling driven by the low in-cylinder mass due to the stoichiometric air-fuel ratio [12].

Caterpillar modified a diesel engine to run on pure methanol by installing a glow-plug ignition-assist system [13]. Comparable power output, lower particulate matter and NOx emissions during transient operation were achieved, however, higher hydrocarbon emissions and fuel consumption were also reported [14]. The injector nozzle tip [13] had secondary spray holes located along the injector axis to enable fuel spray impingement against a pin mounted on the piston. The resulting secondary fuel cloud allowed to bridge the gap between the igniting methanol sprays close to the spray-plug and the rest of the fuel sprays. The optical study of Mueller and Musculus [15] on glow-plug assisted ignition of methanol in a heavy-duty engine at a medium load point subsequently confirmed that methanol ignition propagates from spray to spray after being triggered in the spray clouds close to the glow-plug.

Another solution for achieving mixing-controlled combustion of alcohol fuels in compression ignition engines is the adoption of a dual-injection system and the use of a separate pilot injection of diesel as an ignition trigger. The first implementation of this dual-fuel combustion concept dates back to the study of Seko et al. [16] on a methanol-diesel engine with two separate injectors mounted on a swirl chamber. A maximum diesel substitution ratio of 94% on a volume basis was reported with no methanol misfire. Equivalent engine performance for steady-state operation and noise emissions as well as lower NO_x and particulate emissions compared to the diesel engine baseline were observed. However, an increase in the formaldehyde and CO emissions was also reported [16]. Dual-injection systems for the introduction of methanol in ship engines with diesel-like operation were developed by Wärtsilä [17] and MAN Diesel & Turbo [18], however, limited information on performance, emissions and combustion characteristics has been published. Saccullo et al. [19] studied the simultaneous direct injection of methanol and diesel in a heavy-duty engine at a medium load-speed point. Stable methanol combustion with comparable performance, lower NOx and soot emissions compared to the diesel baseline were achieved with substitution ratios of diesel up to 96.6% on an energy basis [19].

In a previous experimental study [20], the simultaneous direct injection of ethanol and diesel pilot through separate injectors was investigated in a single cylinder engine, targeting mixing-controlled combustion of ethanol. The influence of the dual-injection parameters on ethanol combustion characteristics, engine performance and NO_x emissions was evaluated by comparison with dual-injections of diesel and conventional diesel combustion. However, the dual-injector configuration was kept fixed.

Despite the additional complexity of the second injection system, the separate injection of pure ethanol and diesel as an ignition trigger allows the achievement of diffusive combustion of ethanol in a diesel-like process [20] without pre-heating the intake air or using ignition improvers. The limit on ethanol ratio at high engine loads due to the excessive in-cylinder pressure rise rates observed with premixed ethanol combustion concepts [3] is also overcome [20]. Moreover, dual-injections of fuels with different reactivity enable heat-release rate shaping [21] and the enhancement of engine performance within a broad engine load range [20].

The current study extends the investigation of ethanol-diesel direct injection in a heavy-duty engine focusing on the influence of the diesel injector nozzle hole diameter and number on ethanol ignition, combustion characteristics and engine performance at low and high load. More specifically,

three custom-made diesel injector nozzle tips with different number of sprays and a non-symmetric spray pattern were manufactured and tested in the dual-injector system. As a result, an insight into the interaction between diesel and ethanol sprays during ignition and the subsequent impact on engine performance is provided. Dong et al. [22] investigated the influence of the nozzle hole number of the diesel pilot injector on combustion of premixed port injected ethanol. However, given the different combustion concept investigated in [22], comparisons with the results reported in this study can hardly be drawn. Based on the outcome of this study, it will be possible to optimize the design of the ethanol-diesel dual-injection system. Moreover, the experimental dual-fuel combustion data will be used to validate the CFD model adopted in a preliminary simulation study [23].

2. Experimental set-up

Experiments are carried out on a single cylinder metal engine derived from a Scania D12 in-line engine with specifications listed in Table 1. The engine is equipped with a dual-injector system allowing the simultaneous direct injection of pure ethanol and diesel for triggering ignition, as displayed in Fig. 1. The physical properties of the two fuels used in this study are listed in Table 2.

The dual-injector system consists of two solenoid injectors connected to separate rail pressure systems: a heavy-duty Scania injector mounted along the piston centerline and a Bosch light-duty injector with a custom-made nozzle tip mounted in the access hole for the flush-mounted pressure transducer in the cylinder head. The start of injection (SOI), injection duration and pressure of ethanol and diesel can be set independently. In fact, the two injection events are separately controlled using a LabView based control system for the diesel fuel system and an in-house control system for ethanol fuel system, both processing the same encoder signal with 0.1 CAD resolution. Fuel consumption is calculated based on the time variation of fuel mass measured with two separate fuel scales for ethanol and diesel. The piston has a standard bowl geometry for diesel combustion with an additional recess machined in order to accommodate the side injector nozzle tip. The nominal compression ratio is 19.4, compared to an estimated effective compression ratio of 17.7 - 18.2. This difference is caused by the additional crevice volume resulting from the design modification for the side injector installation on the cylinder head, and may also be enhanced by in-cylinder gas blow-by through the side injector seal.

Table 1. Specifications of engine geometry and operation [20]

Nominal compression ratio	19.4:1
Number of valves	4
Swirl number	1.7
Stroke	154 mm
Bore	127 mm
Connecting rod	255 mm
Intake valve closure	136 CAD BTDC
Exhaust valve opening	118 CAD ATDC

Table 2. Physical properties of diesel and ethanol [20]

Fuel	Diesel	Ethanol
Type	MK1 B0	E100
Density at 15°C [kg/m^3]	805.0	794.0
Vapor pressure [kPa]	2.3	16.2
Lower Heating Value [MJ/kg]	42.76	25.58
Kinematic viscosity at 40°C [mm^2/s]	2.242	1.082
Water content [mg/kg]	<30	1290.0
Cetane Number [-]	57.6	12.0

Table 3. Details of the side injector nozzle tip geometry

Configuration	Hole number	Spray hole diameter
A	1	280 µm
B	2	200 µm
C	4	140 µm

Configuration A	Configuration B	Configuration C
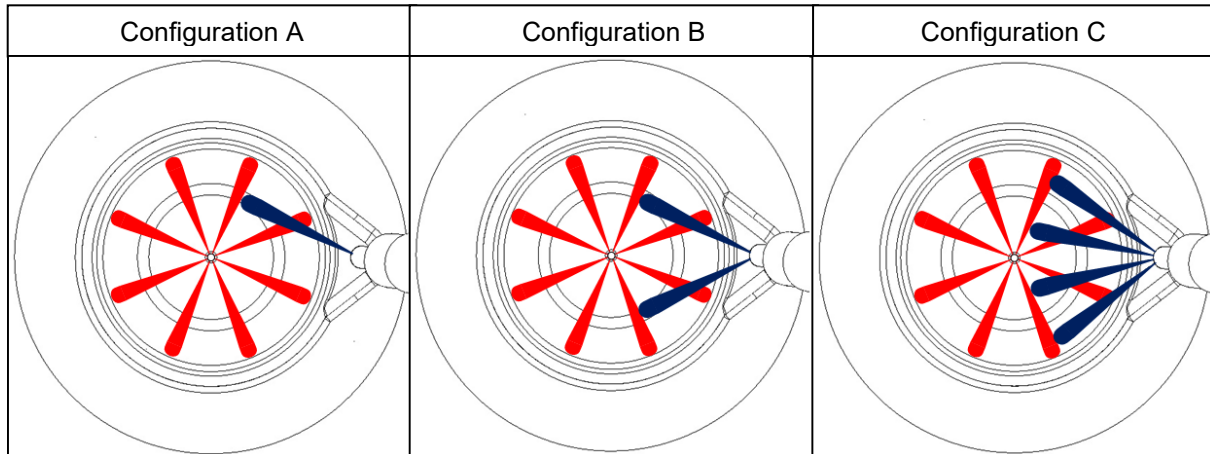
Fig. 1. Schematic of the dual-injector system with the ethanol central injector and three different diesel side injector configurations

CAD-resolved in-cylinder pressure is measured via a channel-mounted pressure transducer. Pollutant emissions are sampled using a Horiba gas analyzer, recording the concentration of CO and HC in the exhaust stream on a dry-basis. A lambda sensor records the concentration of residual oxygen in the exhaust stream, based on which the in-cylinder trapped mass of air is estimated. The intake pressure is measured with a pressure transducer located in the intake manifold whereas the exhaust backpressure is kept atmospheric and measured with a transducer located on a pressure vessel along the exhaust stream. Time-resolved intake and exhaust temperatures are measured with K-type thermocouples mounted on the intake and exhaust manifolds, respectively.

2.1 Side injector configurations

In order to evaluate the interaction between diesel and ethanol sprays, the ethanol central injector with eight fuel sprays is retained while three different diesel injector configurations are tested. The schematic of the nozzle tip geometry of the three side injector configurations is shown in Figure 1. All the configurations have a non-axisymmetric spray pattern and the same total nozzle area, i.e. the injection mass flow rate is approximately the same at a given rail pressure. However, the spray liquid penetration varies given the difference in the orifice diameters [24]. Specifications of the nozzle hole diameter and number are provided in Table 3.

The orientation of the single diesel spray of configuration A coincides with the orientation of one of the sprays of configuration B, however, the corresponding hole area is double. Moreover, the single diesel spray of configuration A is oriented along the direction of the in-cylinder swirl motion. The minimum angular distance between the diesel spray centerlines and the cylinder head sealing surface is approximately equal for all injector configurations and it was set to avoid spray impingement against the cylinder head. The clocking of the main ethanol injector is carried out in order for the centerline connecting the nozzle tips of the ethanol and diesel injectors to bisect the adjacent ethanol sprays, consistently with the preliminary simulation study [23].

It should be noted that the two-spray diesel injector shown in Fig. 1 (configuration B) was the configuration used in the previous experimental study [20] referenced in the introduction section. The differences in the ethanol ignition and combustion characteristics observed while decreasing (configuration A) and increasing (configuration C) the number of sprays of the diesel pilot injector compared to

the baseline configuration (configuration B) are described in the following sections and represent the main contribution of this study.

3. Results

In order to evaluate the influence of the spray hole number and size of the diesel injector on ethanol combustion and engine performance, the same set of test points is repeated using the three different side injector configurations displayed in Fig. 1. The engine conditions investigated in the preliminary study [20] are replicated when using the different side injector configurations in order to ensure a systematic comparison between them. A sweep of the SOI of ethanol and diesel as well as of ethanol-diesel ratio is carried out at a low and a high load point. The boost pressure is kept at 1.2 and 2.3 bar absolute while the targeted fuel energy injected corresponds to an equivalent amount of diesel of 60 and 180 mg at low and high load, respectively. All tests are carried out keeping an atmospheric exhaust backpressure, a rail pressure of ethanol and diesel equal to 1200 bar and an engine speed of 1200 RPM.

Dual-fuel combustion characteristics and performance are compared to conventional diesel combustion. Standard diesel engine tests were preliminary carried out by injecting only diesel through the main injector without operating the side injector. The amount of diesel injected was set to match the overall fuel energy of the dual-fuel test points. The SOI of the single main injection was varied while keeping the rail pressure, engine speed, boost and exhaust pressure at the same levels as in the dual-fuel experiments. The resulting average gross indicated mean effective pressure was equal to 5.9 and 18.6 bar at low and high load, respectively.

The main-pilot separation (MPS) [23] – i.e. dual-injection parameter defined as the difference between the ethanol and diesel SOI shown in Eq. 1 – is varied in this study.

$$MPS \: [CAD] = SOI_{ethanol} - SOI_{diesel} \qquad (1)$$

It should be noted that the above SOIs correspond to the start of the switch-on voltage signal for the injection actuation. The ethanol injector is kept unchanged throughout the tests, therefore the delay between energizing start time and actual start of ethanol injection is approximately equal for all test points – except for limited variations due to differences in the in-cylinder pressure. Moreover, the electronic components and the moving mechanical parts of the three diesel injectors in Figure 1 are the same. Hence, also the delay between energizing start time and actual start of diesel injection is assumed to be equal for all the test points. Diesel is injected before ethanol – i.e. the MPS is positive – in most of the cases. However, a subset of test points with negative MPS is also considered. The percentage of ethanol injected is expressed as the ratio between the ethanol fuel energy and the overall fuel energy injected:

$$Ethanol \: ratio \: [\%] = \frac{m_{inj,ethanol} \: LHV_{ethanol}}{m_{inj,ethanol} \: LHV_{ethanol} + m_{inj,diesel} \: LHV_{inj,diesel}} *100 \qquad (2)$$

Only ethanol ratios above 80% are considered, as this study is aimed at minimizing the amount of diesel injected while keeping stable and complete ethanol combustion.

The CAD resolved apparent rate of heat release (ARoHR) is adopted to evaluate the ignition and combustion characteristics of ethanol:

$$ARoHR \: [J/CAD] = \frac{\gamma}{\gamma - 1} \: p \: \frac{dV}{dCAD} + \frac{1}{\gamma - 1} \: V \: \frac{dp}{dCAD} \qquad (3)$$

In Eq. 3:

- γ is the ratio of the specific heats of the in-cylinder gasses estimated based on the average in-cylinder temperature using the correlation of Brunt and Platts [25];
- V is the in-cylinder volume computed as a function of the combustion chamber geometry [26];
- p is the ensemble average of the filtered in-cylinder pressure of the sampled engine cycles.

The in-cylinder pressure trace of each engine cycle is first filtered with a low-pass filter to exclude the resonance frequency of the channel into which the pressure transducer is mounted. Then, the average of 100 engine cycles is computed and pegged against the average inlet pressure.

A longer ignition delay allows more time for the fuel-air mixing process, leading to a faster heat release at the start of combustion. For this reason, the peak of ARoHR is used as an indicator of the ethanol degree of premixing. The calculation of the start of combustion (SOC) of ethanol based on the
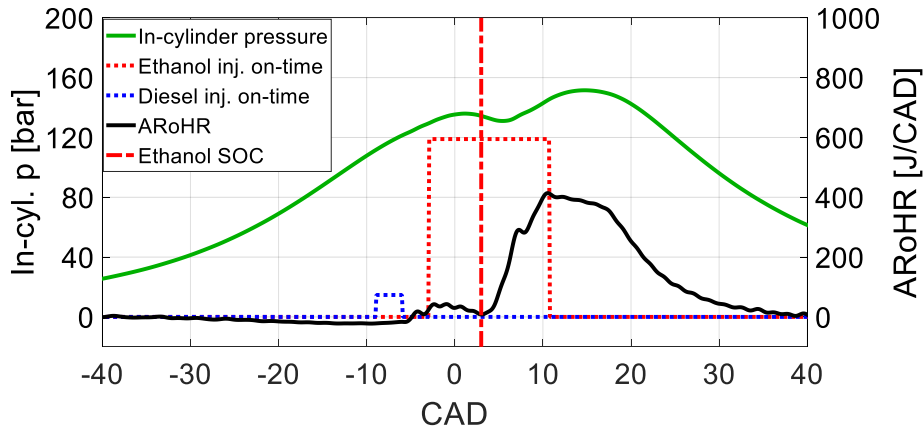
Fig. 2. Ethanol SOC for a representative dual-fuel case at high-load

cumulative rate of heat release was found to be inconsistent for the test points with low main-pilot separations – i.e. when the two injection events of ethanol and diesel overlap. Therefore, ethanol SOC is calculated as the zero of the first derivative of the ARoHR with respect to CAD preceding the main ARoHR peak [20]. As an example, Fig. 2 shows the ethanol SOC against in-cylinder pressure and ARoHR for a representative case at high load.

Ethanol ignition delay is computed as the difference between the SOC and SOI of ethanol. In order to exclude the uncertainty in the identification of the end of the late combustion phase, the end of combustion is assumed at CA90, i.e. after 90% of the cumulative apparent heat is released. Ethanol combustion duration is then calculated as the difference between EOC and SOC.

In this study, the influence of the low pressure cycle on combustion and engine performance is not investigated. The engine work output is expressed in terms of gross indicated mean effective pressure ($IMEP_{gross}$), given by the work output of the compression and combustion stroke – i.e. the gross indicated work – divided by the cylinder swept volume:

$$IMEP_{gross} = \frac{1}{V_{sw}} \int_{V_{BDC, Start\ of\ compression}}^{V_{BDC, End\ of\ expansion}} p\ dV \qquad (4)$$

The engine performance is evaluated based on the gross indicated efficiency ($\eta_{Ind, gross}$), that is the ratio between the gross indicated work and the injected fuel energy:

$$\eta_{Ind, gross} = \frac{\int_{V_{BDC, Start\ of\ compression}}^{V_{BDC, End\ of\ expansion}} p\ dV}{m_{ethanol}\ LHV_{ethanol} + m_{diesel}\ LHV_{diesel}} \qquad (5)$$

Additional parameters used to evaluate the cyclic variability and completeness of ethanol combustion are the coefficient of variation (COV) of $IMEP_{gross}$ and combustion efficiency, respectively. The COV of $IMEP_{gross}$ is the ratio between the standard deviation and the average of the indicated mean effective pressures of the 100 engine cycles sampled for each test point. Combustion efficiency is estimated based on HC and CO engine out emissions, following the approach of Johansson [26][20]. The HC emission measurements are corrected to account for the lower response of flame ionization detector (FID) to oxygenated species [27][20].

An energy balance analysis is carried out for some of the test-cases in order to assess how residual enthalpy of the exhaust gases, in-cylinder heat transfer and blow-by losses impact the gross indicated efficiency. The following set of equations is implemented to calculate exhaust enthalpy, indicated work output, heat transfer and blow-by losses:

$$Q_{Exh} = m_{Exh}\ c_{p_{Exh}}\ (T_{Exh} - T_{Int}) \qquad (6)$$

$$W_{Ind, gross} = IMEP_{gross}\ V_{sw} \qquad (7)$$

$$Q_{Heat\ loss, blow-by} = Q_{Fuel} - (Q_{Exh} + W_{Ind, gross}) \qquad (8)$$

The exhaust mass (m_{Exh}) is estimated based on the in-cylinder trapped mass at IVC and EVO and the overall injected fuel mass, respectively. The in-cylinder trapped mass is in turn computed based on the mass of injected fuel and the measured air-excess in the exhaust stream. The heat capacity at constant pressure (c_p) of the exhaust flow is calculated assuming dry air composition and using a polynomial expression [28] as a function of the temperature measured at exhaust port.

3.1. Influence of the diesel injector configuration at low load

At low load, a three-level full-factorial sweep of diesel SOI, ethanol SOI and ethanol ratio is carried out within ranges of -15 – -6 CAD, -9 – -3 CAD and 80 – 90%, respectively, for a total of 27 test points for each injector configuration. It should be noted that the reported ethanol ratios correspond to the values targeted during the tests – 80%, 85% and 90% – computed based on preliminary fuel injection quantity measurements. Considering all the 81 sampled test points at low load, the mean deviation of the ethanol ratios from the target values is 1.6 percentage points. This deviation is unlikely to affect the conclusions drawn in this study, given the observed limited impact of the ethanol ratio on combustion characteristics and engine performance.

Figure 3 shows the dual-injection strategy, in-cylinder pressure and ARoHR of three reference test cases with a main-pilot separation increasing from case (a) to (c). The slight pressure difference at the end of the compression stroke observed between the different side-injector cases can be explained by fluctuations in the mass of intake air. In all the cases displayed, diesel pilot ignition can be identified as a distinct event preceding the ignition of ethanol. Using the one-spray injector, the combustion of the diesel pilot starts slightly later compared the other diesel injector cases. When the ethanol and diesel

Fig. 3. Dual-fuel combustion characteristics at low load with different side injector configurations at increasing main-pilot separations from case (a) to (c). In-cylinder pressure, apparent rate of heat release, diesel and ethanol injection on-time are highlighted in green, black, blue and red, respectively

injection events are overlapped – e.g. in Fig. 3.a – the one-spray diesel injection provides a stronger source of ethanol ignition. In fact, a higher peak ARoHR and a shorter late combustion phase are observed. With a long main-pilot separation – e.g. in Fig. 3.b and Fig. 3.c – the ARoHR traces tend to overlap, i.e. ethanol ignition and combustion characteristics are comparable for all diesel injector configurations. The only difference observed in such cases is that the ARoHR trace of the one-spray diesel injector falls slightly below the ARoHR traces of the other two diesel injector configurations, as opposed to what observed in Fig. 3.a. The differences in the ethanol ignition and combustion characteristics observed when increasing the MPS from case a to c in Fig. 3 are further explained based on the combustion efficiency trends addressed later in this section.

The confidence intervals for the diesel baseline data highlighted in Fig. 4 – Fig. 6 are calculated based on nine sampled data points assuming a student's t distribution with eight degrees of freedom, consistent with the previous experimental study [20]. The same approach is adopted for the diesel baseline data at high load displayed in Fig. 9 – Fig. 11. In the same figures, two-term exponential functions are fitted to the experimental data for facilitating the comparison between the trends obtained with different diesel injector configurations. Figure 4 highlights the difference in cyclic combustion variability observed between the three side injector configurations. The main-pilot separation has a strong influence on the COV of IMEP at low load with cyclic combustion variability growing at low MPSs. In addition, combustion variability increases when using diesel injectors with a higher number of sprays. The region of high combustion variability of the one-spray diesel injector is limited to a main-pilot separation equal to -3 CAD, whereas using the two-spray diesel injector leads to a higher combustion variability already at a main-pilot separation of 0 CAD. Main-pilot separations below -1 CAD could not even be tested with the four-spray diesel injector due to an excessive decrease in the engine power output and increase in unburned fuel emissions. Test cases with unburned hydrocarbon emissions higher than 5000 ppm on a dry basis – the upper range limit of the HC emission analyzer – were disregarded.

Fig. 4. Combustion variability of the dual-fuel cases as a function of the main pilot separation at low load with different side injector configurations. The confidence interval for the diesel baseline is represented by the horizontal lines
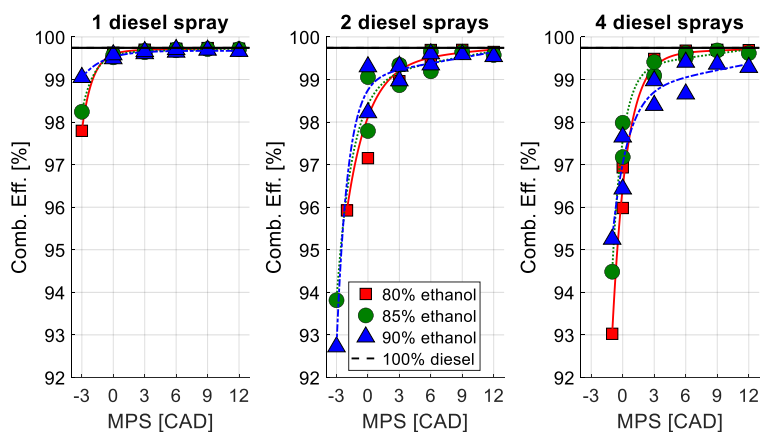
Fig. 5. Combustion efficiency of the dual-fuel cases as a function of the main pilot separation at low load with different side injector configurations. The confidence interval for the diesel baseline is represented by the horizontal lines

Fig. 6. Gross indicated efficiency of the dual-fuel cases as a function of the main pilot separation at low load with different side injector configurations. The confidence interval for the diesel baseline is represented by the horizontal lines
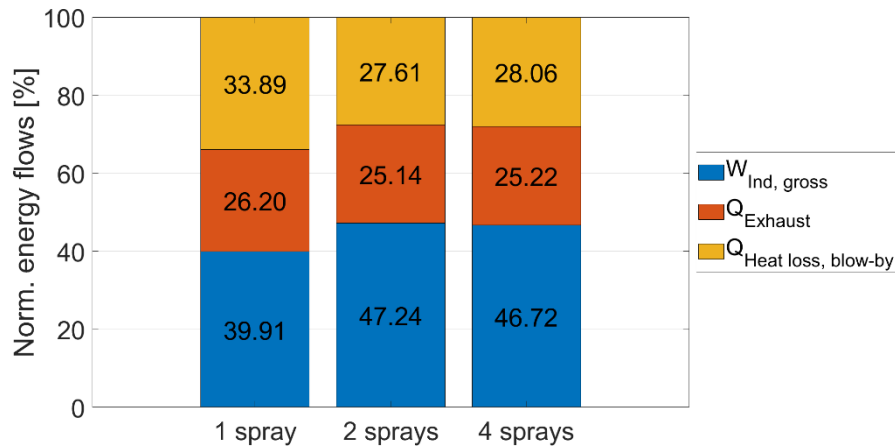
Fig. 7. Energy balance analysis for a reference dual-fuel case at low load with different side injector configurations

The observed cyclic combustion variability is accompanied by partial misfire of ethanol, as confirmed by the combustion efficiency trends displayed in Fig. 5. With a decreasing number of diesel sprays of the side injector, partial misfire of ethanol at low main-pilot separations is mitigated. As an example, partial misfire and incomplete combustion of ethanol is limited to a maximum of 2.2% of the total fuel charge with the one-spray diesel injector, compared to a maximum of 7.3% observed with the two-spray injector at the same main-pilot separation (-3 CAD). The higher combustion efficiency levels obtained with the one-spray diesel injector at low main-pilot separations explain the higher peak in-cylinder pressure and ARoHR of the corresponding case in Fig. 3.a: ethanol ignition is more effective and combustion more complete compared to other injector cases. On the other hand, with any side injector, ethanol-diesel combustion efficiency at high main-pilot separations is comparable to conventional diesel combustion, except for a slight decrement observed in the four-spray injector cases at high ethanol ratios. Extending the main-pilot separation promotes favorable in-cylinder conditions for compression ignition of ethanol at low load [20]. Under these conditions, ethanol combustion completeness is achieved with any of the tested diesel injector configurations. This explains the similarity between ARoHR traces of the different injector cases in Fig. 3.b-c.

Combustion efficiency losses at low main-pilot separations cause a comparable gross indicated efficiency drop, as highlighted in Fig. 6. However, the efficiency levels obtained with the one-spray injector are lower by 5-9 percentage points compared to the two- and four-spray diesel injectors and fall well below the average efficiency value of the conventional diesel combustion baseline. Hence, despite being the most robust trigger for ethanol ignition, the one-spray diesel injection leads to a severe performance deterioration for all investigated test points at low load.

The energy balance analysis carried out for a representative test case at low-load is displayed in Fig. 7. The energy contributions are computed based on Eqs. (6) – (8) and normalized to the fuel energy input. The selected test case has the longest main-pilot separation (12 CAD) and the minimum ethanol-diesel

ratio among the tested values, corresponding to the region with the highest combustion efficiency in Fig. 5. In this way, the analysis is not affected by different amounts of unburned fuel between the different side injector cases. Moreover, the variation of CA50 between the different side injector cases lays within 1.4 CAD. The energy balance analysis shows that the indicated efficiency drop observed with the one-spray diesel injector is caused by higher heat transfer losses, given the limited variations in the exhaust enthalpy between side injector cases. Differences in the duration of the late combustion phase at low load may also play a role in the gross indicated efficiency drop observed for the one-spray injector cases in Fig. 6.

3.2. Influence of the diesel injector configuration at high load

Following the approach described for the low-load cases, a set of 27 test cases is carried out for each side injector configuration at high load. A three-level full-factorial sweep of diesel and ethanol SOI as well as of the ethanol ratio is performed within ranges of -9 – -5 CAD, -7 – -3 CAD and 91 – 98%, respectively. Considering the 81 test points sampled at high load, the mean deviation of the ethanol ratio from the corresponding target values – 91%, 96% and 98% – is 0.5 percentage points. The SOI ranges are narrower compared to low load, in order to avoid exceeding the mechanical limit for the in-cylinder pressure equal to 200 bar.

The main-pilot separation has a strong impact on ethanol ignition characteristics, especially with the one-spray diesel injector. With this injector configuration, a 2 CAD increase in the separation between main and pilot injections causes a sharp decrease in the degree of premixing of ethanol at the moment of ignition, as the set of representative test cases in Fig. 8 shows. Ethanol ignition propagation
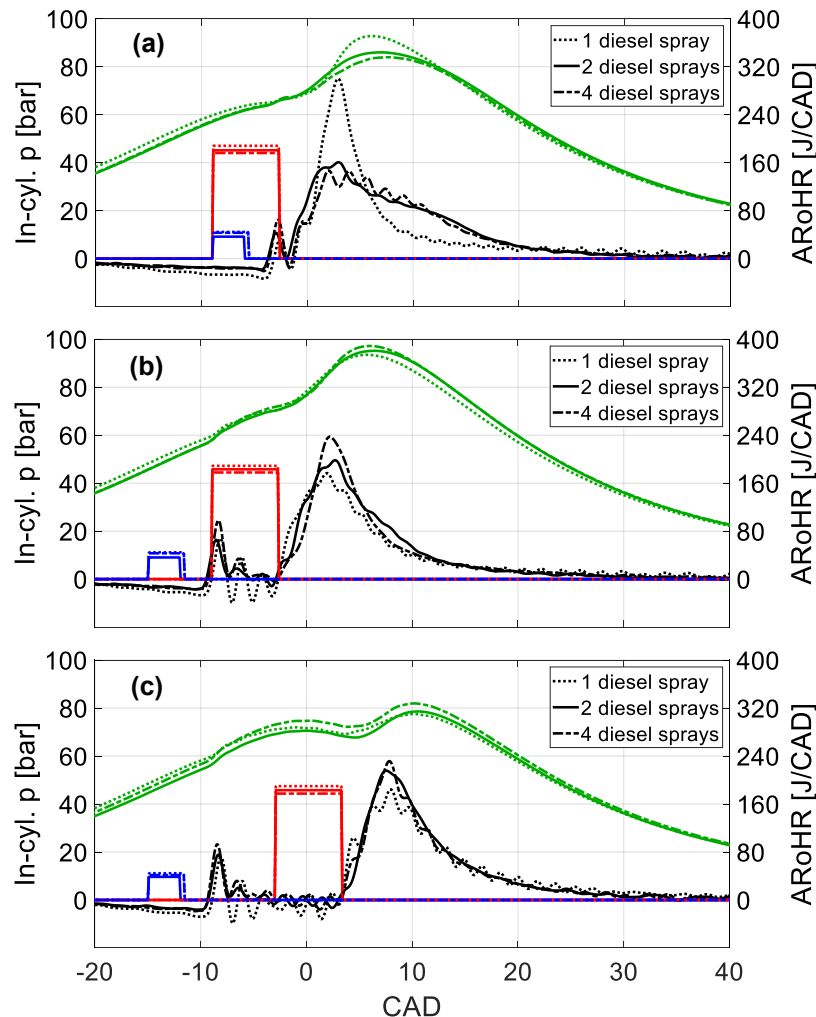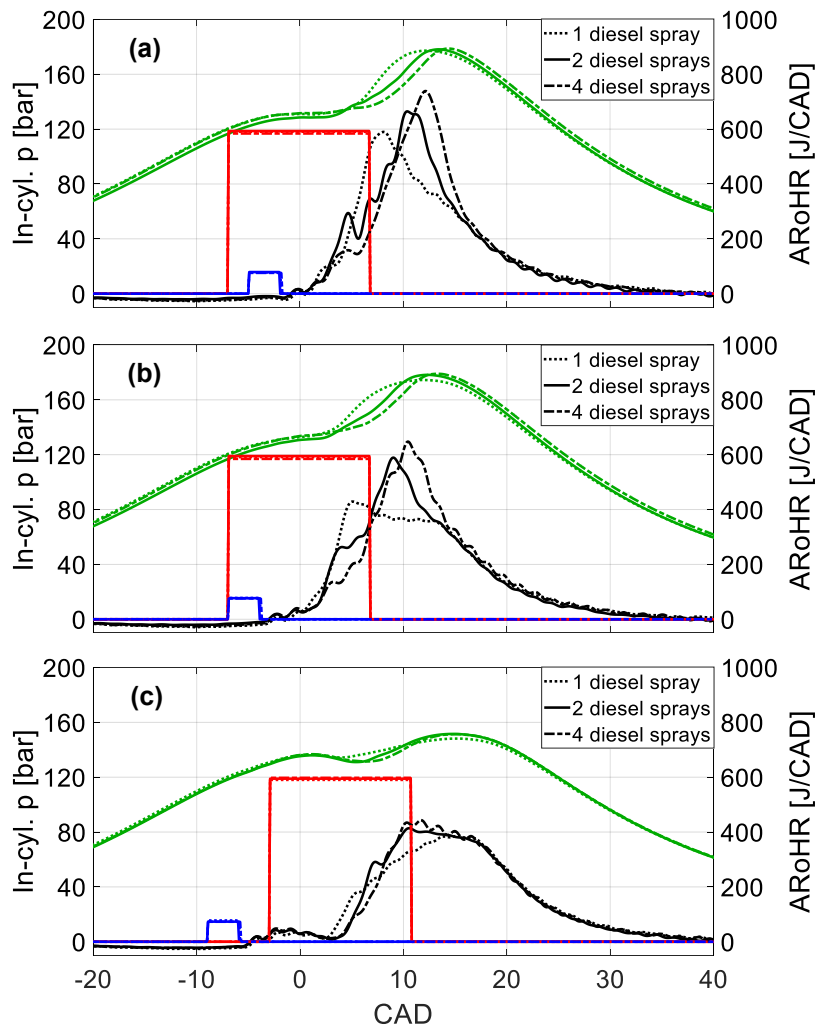

Fig. 8. Dual-fuel combustion characteristics at high load with different side injector configurations at increasing main-pilot separations from case (a) to (c). In-cylinder pressure, apparent rate of heat release, diesel and ethanol injection on-time are highlighted in green, black, blue and red, respectively

limits the overall combustion rate when using the one-spray diesel injector, as confirmed by the plateau observed in the corresponding ARoHR trace in Fig. 8.b as well as by the shallow ARoHR increase in Fig. 8.c. Moreover, Fig. 8.c shows that a shorter ethanol ignition delay is obtained using the one-spray diesel injector, despite the longer air-fuel mixing time required by the larger diesel spray liquid core. The differences in the ethanol ignition dynamics between different side injector cases are not reflected on the end of ethanol combustion, as the ARoHR tails of all side injector cases overlap at any main-pilot separation. The ethanol combustion characteristics observed with the two- and four-spray diesel injectors are similar. Moreover, with a sufficiently long main-pilot separation, the ARoHR peaks are comparable for all side injector cases, as displayed in Fig. 8.c. This is evidence that ethanol mixing-controlled combustion can be achieved using any of the tested diesel injectors and that, with a sufficiently long main-pilot separation, the influence on ethanol combustion characteristics of the nozzle hole number and size of the diesel injector is more limited.

Figure 9 shows the dependence of the ethanol ignition delay on the separation between ethanol and diesel injection for a set of test points with an ethanol ratio of 91%. At negative main-pilot separations, the ethanol ignition delay is almost coincident for all side injector cases. Moreover, an increase in the main-pilot separation leads to shorter ethanol ignition delays. It should be noted, however, that the decrease in the ethanol ignition delay is steeper for the one-spray diesel injector cases, consistent with the ARoHR trends shown in Fig. 8.

The duration of ethanol combustion as a function of the main-pilot separation is displayed in Fig. 10 for the same set of cases shown in Fig. 9. The one-spray diesel injector cases are characterized by the longest ethanol combustion durations, as they have the shortest ethanol ignition delays while the tail of the ARoHR overlaps with the other injector cases, as shown in Fig. 8. It should be also noted that the trends of ethanol combustion duration in Fig. 10 mirror the trends of ethanol ignition delay in Fig. 9. This is evidence that the impact of the diesel injector configuration on the ethanol late combustion phase at high load is limited: a decrease in the ethanol ignition delay drives a comparable increase in the overall combustion duration. Moreover, regardless of the side injector configuration used, ethanol combustion duration is sharply shorter compared to the average combustion duration of the diesel baseline. A faster air-fuel mixing rate driven by the higher volatility of ethanol compared to diesel may explain this difference [20].
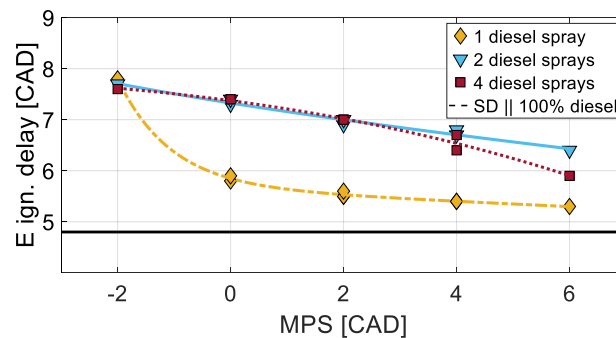
Fig. 9. Ethanol ignition delay as a function of the main pilot separation at high load. The confidence interval for the diesel baseline is represented by the horizontal lines
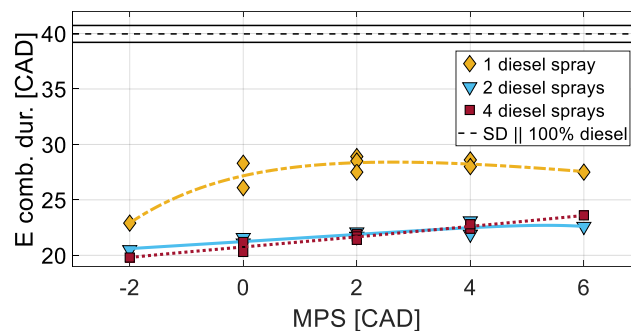
Fig. 10. Ethanol combustion duration as a function of the main pilot separation at high load. The confidence interval for the diesel baseline is represented by the horizontal lines
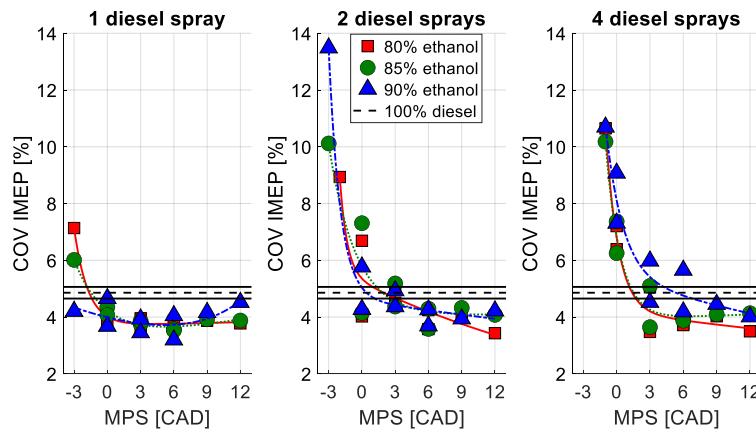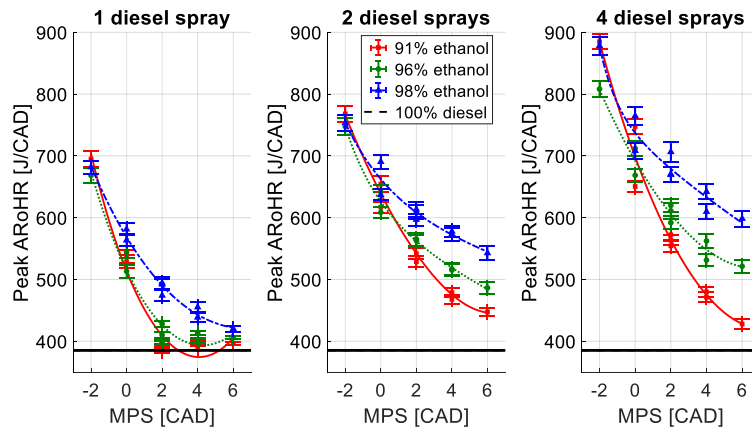
Fig. 11. Peak ARoHR of the dual-fuel cases as a function of the main pilot separation at high load with different side injector configurations. The confidence interval for the diesel baseline is represented by the horizontal lines
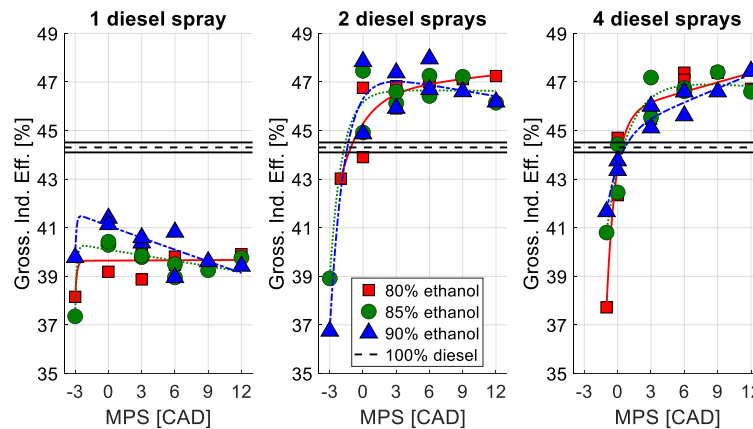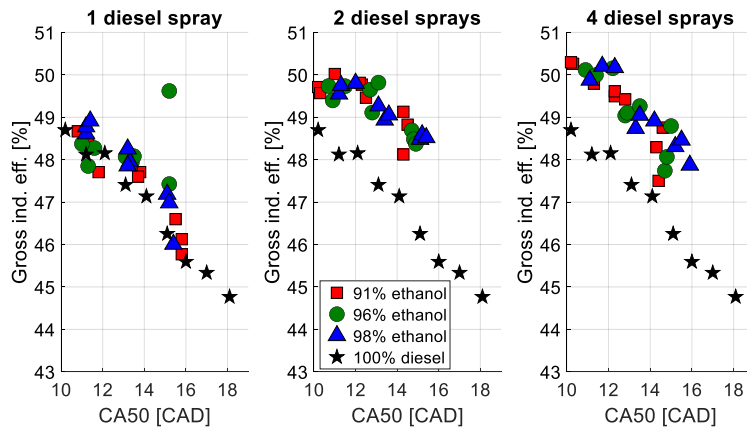

Fig. 12. Gross indicated efficiency of the dual-fuel and diesel baseline cases as a function of combustion phasing at high load

The degree of premixing of ethanol estimated based on the ARoHR peak shows a strong dependence on multiple factors, as shown in Fig. 11. An increase in the main-pilot separation causes a sharp decrease in the ARoHR peak, with any diesel injector configuration used. Lower quantities of diesel injected – i.e. higher ethanol ratios – lead to a higher degree of premixing of ethanol. Moreover, the ARoHR peaks in Fig. 11 translate upwards while increasing the number of sprays of the diesel injector. Hence, an increase in the nozzle hole number of the diesel side injector – and a corresponding decrease in nozzle hole size – leads to a higher degree of premixing of ethanol. This means that the one-spray diesel injector allows to achieve mixing-controlled combustion of ethanol for the broadest range of main-pilot separations among the tested diesel injector configurations.

As observed at low load, differences in performance arise when comparing the results obtained with the three diesel injectors. Figure 12 shows the gross indicated efficiency of the different side injector cases as a function of CA50, compared to the efficiency of the standard diesel baseline cases. The combustion phasing range of the three sets of dual-fuel cases is narrower compared to the diesel baseline, in accordance with the shorter combustion durations displayed in Fig. 10. The shorter combustion durations may contribute to an increase in the work output, with a more limited effect when using the one-spray diesel injector. In fact, the two- and four-spray injector cases have comparable efficiencies, reaching values higher by 1-2 percentage points compared to the diesel baseline. Instead, the gross indicated efficiencies of the one-spray injector cases are in line with the diesel baseline. Hence, the ethanol ignition dynamics driven by the one-spray diesel injector causes a performance penalty also at high load.

4. Discussion

The high peak ARoHR observed at negative main-pilot separations at high load can be explained in light of the results of the study performed by Kokjohn et al. [29] on reactivity controlled compression ignition (RCCI) combustion of iso-octane and n-heptane. A sharp increase in the peak ARoHR was observed [29] in a test case characterized by a high gradient of local equivalence ratio between the high reactivity fuel – within spray plumes having a locally rich or stoichiometric fuel concentration before ignition – and the low reactivity fuel – having a lean and homogeneous concentration across the combustion chamber. Hence, in the present study, the decrease in the main-pilot separation drives a shift of the ethanol-diesel combustion regime from mixing-controlled towards RCCI.

The steeper increase in the degree of premixing of ethanol at low main-pilot separations at high load and the sharper drop in combustion efficiency at low load observed when increasing the number of diesel sprays of the side injector can be further explained based on the study of Lü et al. [30]. The effect of in-cylinder blending of n-heptane and short-chain alcohols on homogeneous charge compression ignition (HCCI) combustion characteristics was investigated in a diesel engine at a low and a medium load point [30]. With ethanol/n-heptane ratios above 20%, an increase in the engine-out HC emissions and a severe engine performance deterioration was reported [30]. By injecting diesel through a higher number of smaller spray holes, the fuel-air mixing process is favored and diesel is more evenly distributed across the piston bowl volume. In this way, the dilution of premixed diesel and ethanol is favored, with a potential inhibiting effect on the ignition of the high reactivity fuel, as observed in [30]. This effect is more limited when using the one-spray diesel injector, as the whole pilot fuel charge is enclosed within a single thicker spray plume. The above hypothesis is consistent with the shorter ignition delays and lower degree of premixing of ethanol obtained with the one-spray diesel injector at high load, as well as with the higher combustion efficiencies at low load compared to the other two diesel injector configurations.

The study on the ignition of n-heptane/n-butanol blends of Zhang et al. [31] explained the inhibiting effect of short-chain alcohols on ignition based on the competition between the production of OH radicals and stable aldehydes at low temperature. The conclusions drawn in [30] and [31] are consistent with the study on autoignition characteristics of butanol/ and ethanol/n-heptane blends performed by Saisirirat et al. [32], that confirmed the inhibiting effect of the alcohol fuel fraction on the ignition of n-heptane. The longer ignition delays of the alcohol/n-heptane blends were explained based on a lower production of OH radicals, limiting the chain branching reactions [32].

In the study of Dong et al. [22] referenced in the introduction, ignition kernels were identified in the stoichiometric region of the high-reactivity fuel sprays. Similarly, in the present study, ethanol combustion is likely to start within the ethanol spray plumes adjacent to the igniting diesel sprays. The study of Mueller and Musculus [15] on glow plug assisted ignition of methanol describes a similar ignition dynamics. Methanol ignition occurs within the spray plumes close to the glow plug located in one hemisphere of the combustion chamber, and it is followed by combustion propagation towards the adjacent fuel sprays [15]. In the current study, only a few ethanol sprays are close to the igniting diesel spray when using the one-spray diesel injector. As a result, the ethanol spray-to-spray ignition propagation is slower, in accordance with the longer combustion durations observed at high load. Such ignition dynamics would also explain the lower gross indicated efficiencies observed with the one-spray diesel injector. In fact, combustion of the ethanol sprays distant from the igniting diesel spray may occur closer to the piston surface – given the longer time for ethanol-air mixing – causing higher heat losses.

A longer penetration of diesel sprays evenly distributed across the piston bowl may promote fast mixing-controlled combustion of ethanol by triggering the simultaneous ignition of a higher number of ethanol sprays. This can be achieved either by increasing the spray hole diameter and the total nozzle area of the diesel side injector while keeping the number of sprays fixed, or by increasing the diesel injection pressure. The former solution would allow to increase the spray liquid penetration – dependent on the nozzle hole diameter rather than on the injection pressure [24] – while limiting the diesel spray dilution effect previously described. The latter solution would allow to extend the diesel spray vapor penetration [33] thanks to higher spray velocities. Hardware changes such as the reduction of the distance between the ethanol and diesel injector nozzle tips should also be considered, in order to promote fast and simultaneous ignition of all the ethanol sprays.

The experimental data on ethanol-diesel direct injection will enable the calibration and validation of the CFD model adopted in the computational study [23] for the preliminary investigation of the ethanol-diesel dual-injection concept. Specifically, the in-cylinder pressure and apparent rate of heat release of a set of test points will be used as target parameters to evaluate the predictive capability of the simulation model. In fact, an acceptable prediction of the in-cylinder pressure and ARoHR traces is required for a detailed evaluation of the interaction between diesel and ethanol sprays during ignition.

5. Conclusion

The diesel injector nozzle hole diameter and number have a strong influence on the characteristics of direct injected ethanol combustion at low and high load, with a subsequent impact on engine performance.

At low load, there is a trade-off between combustion stability and completeness – achieved with a diesel injector with a lower number of spray holes and a larger hole diameter – and engine performance – enhanced using a diesel injector with a higher number of spray holes and a smaller hole diameter. With the dual-injector configuration adopted in this study, a diesel injector with at least two sprays evenly distributing the pilot fuel charge across the piston bowl volume as well as a minimum separation between ethanol and diesel injections are needed in order to avoid the deterioration of either combustion or indicated efficiency.

At high load, there is an analogous trade-off between ethanol degree of premixing and engine performance. The separation between pilot and main injections and/or the relative amount of diesel injected shall increase in order to limit the degree of premixing of ethanol when using a diesel injector with a higher number of smaller holes. The one-spray diesel injector allows to achieve mixing-controlled combustion of ethanol for the broadest range of injection timings and ethanol ratios. However, a diesel injector with at least two sprays is needed in order to shorten ethanol combustion duration and achieve higher indicated efficiencies.

The insight into the influence of the diesel injector nozzle tip geometry on ethanol combustion and engine performance lays the ground for the optimization of the dual-injector system and the dual-fuel direct injection strategy.

References

1. The International Council on Clean Transportation (ICCT), "CO2 Standards for Heavy-Duty Vehicles in the European Union," https://theicct.org/sites/default/files/publications/CO2 HDV EU Policy Update 2019_04_17.pdf, accessed Mar. 2020.

2. Senecal, P.K. and Leach, F., "Diversity in transportation: Why a mix of propulsion technologies is the way forward for the future fleet," *Results Eng.* 4(November):100060, 2019, doi:10.1016/j.rineng.2019.100060.

3. Sarjovaara, T., Alantie, J., and Larmi, M., "Ethanol dual-fuel combustion concept on heavy duty engine," *Energy* 63:76–85, 2013, doi:10.1016/j.energy.2013.10.053.

4. Wu, H., Nithyanandan, K., Lee, T.H., Lee, C.F.F., and Zhang, C., "Spray and combustion characteristics of neat acetone-butanol-ethanol, n-butanol, and diesel in a constant volume chamber," *Energy and Fuels* 28(10):6380–6391, 2014, doi:10.1021/ef5013819.

5. Siebers, D. and Edwards, C.F., "Autoignition of Methanol and Ethanol Sprays under Diesel Engine Conditions," *SAE Technical Paper 870588*, 1987, doi:10.4271/870588.

6. Sjoberg, M. and Dec, J.E., "Ethanol autoignition characteristics and HCCI performance for wide ranges of engine speed, load and boost," *SAE Int. J. Engines* 3(1):84–106, 2010, doi:10.4271/2010-01-0338.

7. Dempsey, A.B., Walker, N.R., Gingrich, E., and Reitz, R.D., "Comparison of Low Temperature Combustion Strategies for Advanced Compression Ignition Engines with a Focus on Controllability," *Combust. Sci. Technol.* 186(2):210–241, 2014, doi:10.1080/00102202.2013.858137.

8. Velazquez, S., Melo, E.H., Moreira, J.R., Apolinario, S.M., and Coelho, S.T., "Ethanol Usage in Urban Public Transportation - Presentation of Results," *SAE Technical Paper 2010-36-0130*, 2010, doi:10.4271/2010-36-0130.

9. Aakko-Saksa, P.T., Westerholm, M., Pettinen, R., Söderström, C., Roslund, P., Piimäkorpi, P., Koponen, P., Murtonen, T., Niinistö, M., Tunér, M., and Ellis, J., "Renewable Methanol with Ignition Improver Additive for Diesel Engines," *Energy and Fuels* 34(1):379–388, 2020, doi:10.1021/acs.energyfuels.9b02654.

10. Shamun, S., Ha, C., Murcak, A., Andersson, Ö., and Tunér, M., "Experimental investigation of methanol compression ignition in a high compression ratio HD engine using a Box-Behnken design," *Fuel* 209:624–633, 2017, doi:10.1016/j.fuel.2017.08.039.

11. Edwards, C.F., Johnson IV, B.H., and Roberts, G.B., "Stoichiometric High-Temperature Direct-Injection Compression-Ignition Engine," US 9,903,262, 2018.

12. Blumreiter, J., Johnson, B., Magnotti, G., Longman, D., Som, S., and National, A., "Mixing-Limited Combustion of Alcohol Fuels in a Diesel Engine," *SAE Technical Paper 2019-01-0552*, 2019, doi:10.4271/2019-01-0552.

13. Bailey, J.M., "Ignition-Assisted Fuel Combustion System," US 4,548,172, 1985.

14. Richards, B.G., "Methanol-fueled caterpillar 3406 engine experience in on-highway trucks," *SAE Technical Paper 902160*, 1990, doi:10.4271/902160.

15. Mueller, C.J. and Musculus, M.P., "Glow plug assisted ignition and combustion of methanol in an optical di diesel engine," *SAE Technical Paper 2001-01-2004*, doi:10.4271/2001-01-2004.

16. Seko, T., Hori, M., Suto, H., and Kobayashi, S., "Methanol diesel engine and its application to a vehicle," *SAE Technical Paper 840116*, 1984, doi:10.4271/840116.

17. Haraldson, L., "Heavy Duty Engines," https://www.ieabioenergy.com/wp-content/uploads/2014/05/P10-Heavy-duty-engines-Haraldson.pdf, accessed Feb. 2020.

18. MAN B&W, "Using Methanol Fuel in the MAN B&W ME-LGI Series," https://www.mandieselturbo.com/docs/default-source/shopwaredocuments/using-methanol-fuel-in-the-man-b-w-me-lgi-series.pdf, accessed Feb. 2020.

19. Saccullo, M., Benham, T., and Denbratt, I., "Dual Fuel Methanol and Diesel Direct Injection HD Single Cylinder Engine Tests," *SAE Technical Paper 2018-01-0259*, 2018, doi:10.4271/2018-01-0259.

20. Giramondi, N., Jäger, A., Krishnan Mahendar, S., and Erlandsson, A., "Combustion Characteristics, Performance and NOx Emissions of a Heavy-Duty Ethanol-Diesel Direct Injection Engine," *SAE Technical Paper 2020-01-2077. To be published on September 15, 2020 by SAE International in United States*.

21. Boretti, A., "Advantages of converting Diesel engines to run as dual fuel ethanol-Diesel," *Appl. Therm. Eng.* 47:1–9, 2012, doi:10.1016/j.applthermaleng.2012.04.037.

22. Dong, S., Wang, Z., Yang, C., Ou, B., Lu, H., Xu, H., and Cheng, X., "Investigations on the effects of fuel stratification on auto-ignition and combustion process of an ethanol/diesel dual-fuel engine," *Appl. Energy* 230(August):19–30, 2018, doi:10.1016/j.apenergy.2018.08.082.

23. Giramondi, N., Mihaescu, M., Christiansen Erlandsson, A., and Jäger, A., "CFD-Driven Preliminary Investigation of Ethanol-Diesel Diffusive Combustion in Heavy-Duty Engines," *SAE Technical Paper 2019-01-2192*, 2019, doi:10.4271/2019-01-2192.

24. Siebers, D.L., "Liquid-phase fuel penetration in diesel sprays," *SAE Technical Paper 980809*, doi:10.4271/980809.

25. Brunt, M.F.J. and Platts, K.C., "Calculation of Heat Release in Direct Injection Diesel Engines," *SAE Technical Paper 1999-01-0187*, 1999, doi:10.4271/1999-01-0187.

26. Johansson, B., "Combustion Engines," Department of Energy Sciences, Lund University, ISBN 9789176230954, 2014.

27. Kar, K. and Cheng, W.K., "Speciated Engine-Out Organic Gas Emissions from a PFI-SI Engine Operating on Ethanol/Gasoline Mixtures," *SAE Int. J. Fuels Lubr.* 2(2):91–101, 2010, doi:10.4271/2009-01-2673.

28. Burcat, A. and Branko, R., "Third millennium ideal gas and condensed phase thermochemical database for combustion with updates from active thermochemical tables," *Tech. Rep.* ANL-05/20(September):ANL-05/20 TAE 960, 2005, doi:10.2172/925269.

29. Kokjohn, S., Reitz, R.D., Splitter, D., and Musculus, M., "Investigation of Fuel Reactivity Stratification for Controlling PCI Heat-Release Rates Using High-Speed Chemiluminescence Imaging and Fuel Tracer Fluorescence," *SAE Int. J. Engines* 5(2):248–269, 2012, doi:10.4271/2012-01-0375.

30. Lü, X., Ji, L., Zu, L., Hou, Y., Huang, C., and Huang, Z., "Experimental study and chemical analysis of n-heptane homogeneous charge compression ignition combustion with port injection of reaction inhibitors," *Combust. Flame* 149(3):261–270, 2007, doi:10.1016/j.combustflame.2007.01.002.

31. Zhang, J., Niu, S., Zhang, Y., Tang, C., Jiang, X., Hu, E., and Huang, Z., "Experimental and modeling study of the auto-ignition of n-heptane/n-butanol mixtures," *Combust. Flame* 160(1):31–39, 2013, doi:10.1016/j.combustflame.2012.09.006.

32. Saisirirat, P., Togbé, C., Chanchaona, S., Foucher, F., Mounaim-Rousselle, C., and Dagaut, P., "Auto-ignition and combustion characteristics in HCCI and JSR using 1-butanol/n-heptane and ethanol/n-heptane blends," *Proc. Combust. Inst.* 33(2):3007–3014, 2011, doi:10.1016/j.proci.2010.07.016.

33. Payri, R., Gimeno, J., Viera, J.P., and Plazas, A.H., "Needle lift profile influence on the vapor phase penetration for a prototype diesel direct acting piezoelectric injector," *Fuel* 113:257–265, 2013, doi:10.1016/j.fuel.2013.05.057.

Assessment of Auto-Ignition Tendency of Gasoline, Methanol, Toluene and Hydrogen Fuel Blends in Spark Ignition Engines

T. Franken[1], L. Seidel[2], L. C. Gonzalez Mestre[1], K. P. Shrestha[1], A. Matrisciano[3] and F. Mauss[1]

[1]Brandenburg University of Technology Cottbus-Senftenberg, Cottbus, Germany.

E-mail: tim.franken@b-tu.de
Telephone: +(49) 160 97738595

[2]LOGE Deutschland GmbH, Cottbus, Germany.

E-mail: lars.seidel@logesoft.com

[3]Chalmers University of Technology, Goteborg, Sweden.

E-mail: andmatr@chalmers.se

Abstract. State of the art spark ignited gasoline engines achieve thermal efficiencies above 46 % e.g. due to friction optimized crank trains, high in-cylinder tumble flow and direct fuel injection. Further improvements of thermal efficiency are expected from lean combustion, higher compression ratio and new knock-resistant fuel blends. One of the limitations to these improvements are set by the auto-ignition in the end gas, which can develop to knocking combustion and severely damage the internal combustion engine. The auto-ignition is enhanced by high cylinder gas temperatures and reactive species in the end gas composition.

Quasi-dimensional Stochastic Reactor Model simulations with detailed chemistry allow to consider the thermochemistry properties of surrogates and complex end gas compositions. Based on the detailed reaction scheme and surrogate model, an innovative tabulated chemistry approach is utilized to generate dual-fuel laminar flame speed and combustion chemistry look-up tables. This reduces the simulation duration to seconds per cycle, while the loss in accuracy compared to solving the chemistry "online" is marginal. The auto-ignition events predicted by the tabulated chemistry simulation are evaluated using the Detonation Diagram developed by Bradley and co-workers. This advanced methodology for quasi-dimensional models evaluates the resonance between the shock wave and reaction-front velocity from auto-ignition in the end gas and determines if it is a harmful developing detonation or normal deflagration.

The aim of this work is to evaluate the auto-ignition characteristics of different fuel blends. The Stochastic Reactor Model with tabulated chemistry is applied to perform a numerical analysis of the auto-ignition of the fuel blends and operating conditions. Experimental measurements of a single cylinder research engine operated with RON95 E10 fuel are used to train and validate the simulation model. The RON95 E10 fuel is blended with Methanol, Hydrogen and Toluene. The knock tendency based on the evaluation of auto-ignition events of the different fuel blends are analysed for three operating points at 1500 *rpm* 15 *bar* IMEP, 2000 *rpm* 20 *bar* IMEP and 2500 *rpm* 15 *bar* IMEP with advanced spark timings.

1. Introduction

The research of alternative fuels for internal combustion engines covers aspects of fuel properties, production processes and availability of resources [1, 2]. One of the most straight forward approaches on producing alternative fuels with available resources, is the combination of excess wind or solar electric energy to produce Hydrogen (H_2) and Carbon Dioxide (CO_2) from the atmosphere or flue gases from industry processes [3, 4]. The captured H_2 can be directly burned in an internal combustion engine or further processed to produce Methane (CH_4) or Methanol (CH_3OH) [5, 6]. These fuels can be directly burned in internal combustion engines, too, or further processed to long-chained hydrocarbon fuels. The research group of Gschwend et al. [7] investigated the properties of 50 alternative fuels for spark ignition (SI) engine applications. They stated that tank-to-wheel CO_2 emissions are reduced for 2,2,3-Trimethylbutane, Butanol and Propanol isomers. While the lowest volumetric fuel consumption is found

for 2-Phenylethanol and Anisole. However, some alternative fuels who show favourable properties for SI engine combustion, raise the threat of health for the environment. Yokoo et al. [8] investigated different fuel mixtures regarding their performance for lean combustion in SI engines. They stated that fuels like Anisole, Furan and Nitromethane are beneficial to extend the lean burn limit of two different internal combustion engines.

The focus of this work is set on Methanol, Toluene (C_7H_8) and Hydrogen mixed with a RON95 E10 surrogate as alternative fuels. The detailed chemistry of these fuels is well established and is applied to investigate the auto-ignition in the end gas. The analysis of the exhaust emissions is not considered since it would exceed the scope of this work. In the subsequent paragraphs selected properties of the fuels are reviewed that are beneficial for efficient SI engine operation. In **Table 1** some properties of the investigated fuels are summarized. The RON95 E10 surrogate is composed of iso-Octane, n-Heptane, Toluene and Ethanol (see **Table 3**). Ethanol and Methanol show the highest vaporization enthalpy (h_{vap}) at 300 K and smallest lower heating value (LHV). Toluene has the highest Research Octane Number (RON) and Motored Octane Number (MON), wherefore it is generally blended in gasoline fuels to reduce the knock tendency. Hydrogen shows the largest LHV value of the investigated fuels.

Table 1: Comparison of fluid properties [9, 10]. (*Determined at 300 K temperature)

Fluid	ρ_{Norm} [m³/kg]	h_{vap} [kJ/kg] *	LHV [MJ/kg]	RON [-]	MON [-]
Iso-Octane	692	363	44.4	100	100
n-Heptane	684	364	44.6	0	0
Ethanol	789	919	26.7	111	94
Methanol	791	1166	19.9	109	89
Toluene	867	412	40.6	116	102
Hydrogen	-	-	120.1	-	-

In **Fig. 1** the predicted laminar flame speeds of the investigated fuels using the detailed Ethanol Toluene Reference Fuel (ETRF) reaction scheme from the LOGEfuel package [11] are outlined. Detailed investigations of the reaction scheme performance can be found in the publications by Shrestha et al. [12, 13, 14, 15]. Hydrogen shows a significant higher laminar flame speed, which is why it is often considered in fuel blends to enhance the combustion. The laminar flame speed for Methanol is found to be slightly higher compared to RON95 E10 and Toluene. The research group of Ranzi et al. [16] published an extensive summary of laminar flame speeds for different alkanes, cyclo-alkanes, aromatics, alcohols and methyl ethers. They reported similar laminar flame speed ranges of Toluene and Methanol as it is shown in **Fig. 1**. Veloo et al. [17] compared the laminar flame speed of Methane, Ethane, Ethanol and Methanol and reported that Methanol shows the highest flame speeds at stoichiometric and rich conditions. Mannaa et al. [18] performed an investigation of various Primary Reference Fuel (PRF), Toluene Reference Fuel (TRF), gasoline mixtures and neat species and its effect on the structure of the flame.
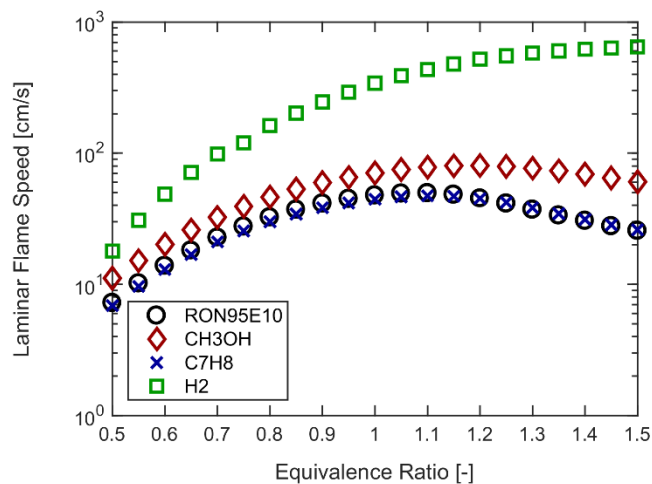
Fig. 1: Comparison of predicted laminar flame speeds for different equivalence ratios for RON95 E10, Methanol, Toluene and Hydrogen at 30 bar and 600 K using an ETRF reaction scheme [11, 12, 13, 14, 15].

They outlined that the laminar flame speed of Toluene is in the same range as iso-Octane, PRF and TRF mixtures at stoichiometric conditions. The increase of Hydrogen fraction in a Hydrogen – Carbon Monoxide – Air mixture is investigated by Dong et al. [19]. The increase of Hydrogen fraction increases the laminar flame speed for lean, stoichiometric, and rich mixture conditions.

The predicted ignition delay times of RON95 E10, Methanol, Toluene and Hydrogen at 10 *bar* and ϕ=1 are outlined in **Fig. 2**. At low temperatures it is shown that the ignition delay times of Methanol, Toluene and Hydrogen are larger compared to RON95 E10. At high temperatures the ignition delay time of Toluene is similar to RON95 E10, while Methanol and Hydrogen show lower ignition delay times. Fieweger et al. [20] investigated the auto-ignition process of PRF mixtures, iso-Octane, n-Heptane and Methanol at elevated pressures and stoichiometric conditions. They showed that at high pressures of 40 *bar* and low temperatures the ignition delay time of Methanol is longer compared to iso-Octane, n-Heptane and PRF mixtures. At higher temperatures, the ignition delay times of Methanol are found in the same range as for n-Heptane. Burke et al. [21] performed an experimental campaign to measure the ignition delay times of different Methanol – Oxygen – Nitrogen – Argon mixtures. They stated that with an increasing fraction of Methanol in the mixture the ignition delay time is decreasing for temperatures between 833 *K* to 952 *K*. The influence of Toluene on the ignition delay time is outlined in the work from Andrae et al. [22]. They showed that the ignition delay times of Toluene are higher compared to TRF mixtures and n-Heptane at 30 *bar* and 50 *bar* pressures and stoichiometric conditions. Kéromnès et al. [23] measured the ignition delay time of Hydrogen and syngas mixtures at higher pressures. With increasing Hydrogen content in the syngas mixture, the ignition delay time is decreasing for different pressures and temperatures.
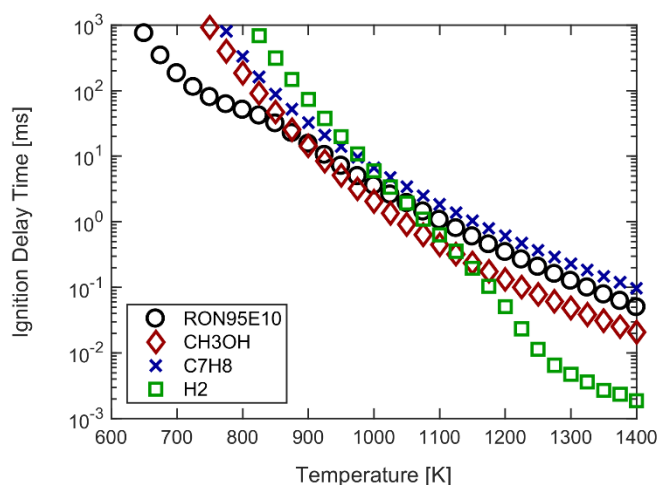
Fig. 2: Comparison of predicted ignition delay times for different temperatures for RON95 E10, Methanol, Toluene and Hydrogen at 10 bar and ϕ=1 using an ETRF reaction scheme [11, 12, 13, 14, 15].

The vapor-liquid saturation pressure and temperature of RON95 E10, Methanol and Toluene is compared in **Fig. 3**. Toluene shows a similar vaporization characteristic as the RON95 E10 surrogate, while Methanol behaves significantly different. The normal boiling point of Methanol is at 337.6 *K*, while the boiling point of Toluene is at 383.7 *K*. The vaporization of Methanol has a significant effect on the auto-ignition characteristic in the end gas and shows an impact on the determination of the MON values as it is discussed by Spausta [24] and Seidel [25].

In this work, the auto-ignition in the end gas for RON95 E10, Methanol, Toluene and Hydrogen mixtures is evaluated using the quasi-dimensional (QD) Stochastic Reactor Model (SRM) with tabulated chemistry and the Detonation Diagram developed by Bradley et al. [26, 27]. Netzer et al. [28, 29, 30, 31, 32] carried out extensive studies on the application of the Detonation Diagram with detailed chemistry to investigate the effect of different RON-MON sensitive fuels and operating conditions on the auto-ignition in SI engines. The Detonation Diagram method allows to evaluate different modes of auto-ignition that can occur in a SI engine and is established as a strong tool for knock analysis.

In the following section the fundamentals of the numerical method are introduced to provide an overview of the applied sub-models. Next, the experiments of the single cylinder research engine and QD-SRM model training are outlined. Finally, the simulation results are analysed and the effects of Methanol, Toluene and Hydrogen on the auto-ignition are discussed.
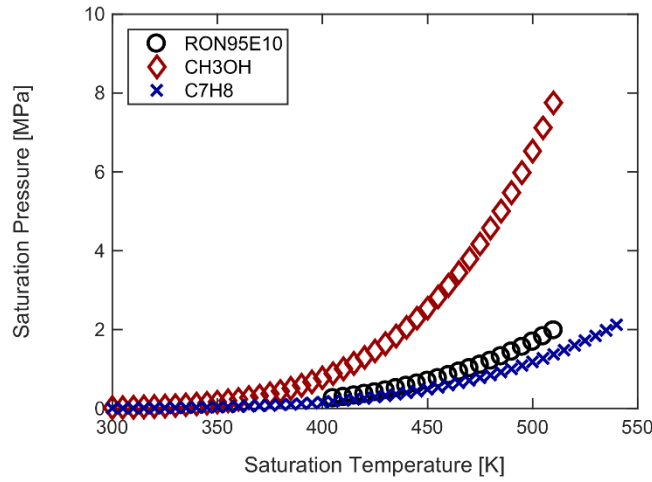
Fig. 3: Comparison of the vapor-liquid saturation of RON95 E10, Methanol and Toluene [9].

2. Methodology

2.1 Stochastic Reactor Model

The QD-SRM is based on a probability density function (pdf) approach for reactive flows [33, 34, 35]. The transport equation (1) of the pdf contains on the left side the accumulation term and various source terms $Q_i(\psi)$. These source terms include the piston work, convective heat transfer, chemical reactions, direct injection, and vaporization. Therein, Φ is a vector of random variables, ψ is its realization in the sample ψ-space and t is the time. The term on the right-hand side P_2 describes the molecular mixing due to turbulence and is in a non-closed form.

$$\frac{\partial}{\partial t} F_{\Phi}(\psi, t) + \frac{\partial}{\partial \psi_i}\big(Q_i(\psi) F_{\Phi}(\psi, t)\big) = P_2 F_{\Phi}(\psi, t) \tag{1}$$

The Curl mixing model [36] is incorporated to close the term P_2 in equation (2). The mixing model contains the turbulent mixing time τ, to account for turbulence-chemistry interaction [37, 38], the training parameter C_{Φ} and the decay parameter β, which is set to 1.

$$P_2 F_{\Phi}(\psi, t) = \frac{C_{\Phi} \beta}{\tau} \cdot \left[\int_{\Delta\psi} F_{\Phi}(\psi - \Delta\psi, t) F_{\Phi}(\psi + \Delta\psi) d(\Delta\psi) - F_{\Phi}(\psi, t) \right] \tag{2}$$

The turbulent mixing time is calculated using the QD K-k turbulence model developed by Dulbecco et al. [39]. The model solves equations for kinetic energy in equation (3) and turbulent kinetic energy in equation (4).

$$\frac{dK}{dt} = 0.5 \cdot C_{tke} \cdot \frac{\dot{m}_{in}}{m_{total}} \cdot v_{in}^2 + C_{inj} \cdot \frac{dK_{inj}}{dt} + K \cdot \frac{\dot{m}_{out}}{m_{total}} + C_{comp} \cdot K \cdot \frac{\dot{\rho}}{\rho} - P_k - K \cdot \left(\frac{\dot{\rho}}{\rho} + \frac{\dot{V}}{V}\right) \tag{3}$$

$$\frac{dk}{dt} = 0.5 \cdot (1 - C_{tke}) \cdot \frac{\dot{m}_{in}}{m_{total}} \cdot v_{in}^2 + C_{inj} \cdot \frac{dk_{inj}}{dt} + k \cdot \frac{\dot{m}_{out}}{m_{total}} + C_{comp} \cdot k \cdot \frac{\dot{\rho}}{\rho} + P_k$$
$$- k \cdot \left(\frac{\dot{\rho}}{\rho} + \frac{\dot{V}}{V}\right) - C_{diss} \cdot \varepsilon \tag{4}$$

In these equations, $\dot{m}_{in}$ is the intake valve mass flow, m_{total} is the trapped cylinder mass, t is the time in seconds, v_{in} is the intake valve flow velocity, K_{inj} is the kinetic energy from the direct injection, $\dot{m}_{out}$ is the exhaust valve mass flow, $\dot{\rho}$ is the change of density, ρ is the density, $\dot{V}$ is the change of cylinder volume and V is the instantaneous cylinder volume. The dissipation ε in equation (5) is derived from the turbulent kinetic energy and integral length scale l_I, which is based on the instantaneous cylinder volume and calculated in equation (6).

65

$$\varepsilon = \frac{2}{3} \cdot \frac{k^{\frac{3}{2}}}{l_I} \tag{5}$$

$$l_I = C_{len} \cdot V^{\frac{1}{3}} \tag{6}$$

The term P_k is a production term for turbulent kinetic energy from tumble motion decay. The equation is outlined in (7).

$$P_k = 0.3307 \cdot C_\beta \cdot l_I \cdot k^{\frac{1}{2}} \cdot \frac{K}{\Delta^2} \tag{7}$$

Therein, Δ is a measure for the size of the tumble vortex and is calculated by $\Delta = min(C_{\Delta,1} \cdot V^{\frac{1}{3}}, C_{\Delta,2} \cdot min(h_{cyl}, d_{bore}))$, with the piston-head distance h_{cyl} and the cylinder bore d_{bore}. The turbulent mixing time is finally calculated using equation (8).

$$\tau = \frac{k}{\varepsilon} \tag{8}$$

The parameters C_{inj}, C_{comp}, C_{tke}, C_{diss}, C_{len}, C_β, $C_{\Delta,1}$, $C_{\Delta,2}$ and C_Φ are model constants and need to be trained for the respective engine.
To solve the pdf transport equation the gas within the cylinder is discretized in notional particles, each containing its own composition and temperature (see **Fig. 4**).
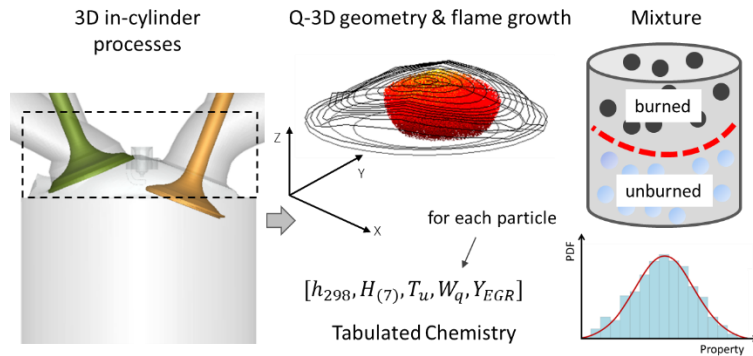
Fig. 4: Concept of the two-zone SRM for spark-ignition engines [37].

The QD-SRM uses a two-zone approach and the auto-ignition in the end gas and chemistry in the burned zone for emission formation are retrieved from the pre-compiled look-up tables. The flame front propagates based on turbulent flame speed s_T, which is calculated retrieving the laminar flame speed s_L from the pre-compiled look-up tables. The turbulent flame speed is calculated with equation (9) based on the model by Peters et al. [40].

$$\frac{s_T}{s_L} = 1 + C \cdot \left(\frac{u'}{s_L}\right)^m \tag{9}$$

Therein, C and m are model constants. u' is the turbulence intensity and is calculated based on the scalar mixing time. Additionally, the flame front is traced based on a polygonal approach to account for flame-wall-interactions (see Q-3D geometry & flame growth in **Fig. 4**) [41]. The values of the model constants are outlined in **Table 2**. Those constants were tested in previous works for different gasoline engines and are not changed during the present work. The QD-SRM accounts for cycle-to-cycle variations in the cylinder gas composition and temperature induced by stochastic mixing and stochastic heat transfer processes [42]. The Woschni heat transfer correlation in equation (10) with base parameters and wall temperatures of 450 K is used to calculate the heat transfer coefficient α [43].

$$\alpha = C_{pre} \cdot d^{-0.2} \cdot p^{0.8} \cdot T^{-0.53} \cdot \left[C_1 \cdot c_m + C_2 \frac{V \cdot T_0}{p_0 \cdot V_0} \cdot (p - p_{mot}) \right] \qquad (10)$$

Therein, C_{pre}, C_1 and C_2 are model constants, d is the engine bore, p is the cylinder pressure, T is the cylinder temperature, c_m is the mean piston speed, p_{mot} is the motored cylinder pressure and V is the cylinder volume. The index 0 highlights parameters at reference conditions. The heat transfer model constants are tested in previous works for different gasoline engines and are not changed during the present work. The QD-SRM model setup is shown in **Table 2**.

Table 2: QD-SRM model setup.

Parameter	Value
Number of Particles	500
Time Step Size	0.5 °CA
Number of Cycles	30
C_{pre}	1.0
C_1	2.28
C_2	0.0065
C	2.5
m	0.9

2.2 Tabulated Chemistry

The tabulated chemistry is based on the detailed ETRF reaction scheme from the LOGEfuel package [11] consisting of 690 species and 8278 reactions. The detailed reaction scheme is validated for different experiments and for engine relevant conditions [12, 13, 14, 15], which is highlighted for one set of experiments from Jerzembeck et al. [44] in **Fig. 5** using the RON95 E10 surrogate from **Table 4**.
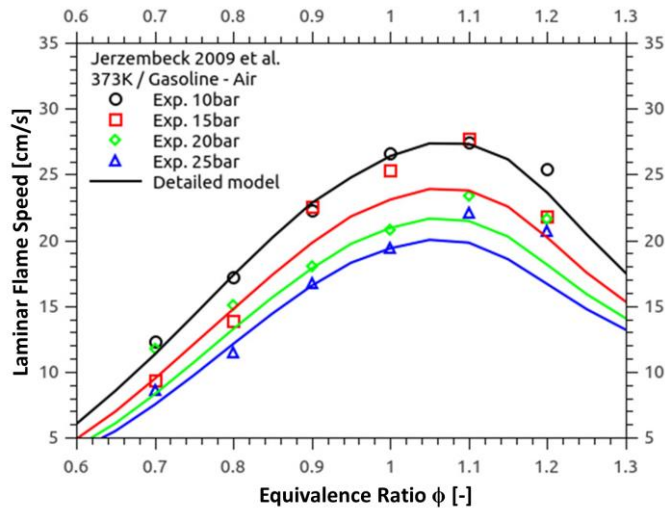
Fig. 5: Comparison of predicted laminar flame speeds using the detailed reaction scheme from the LOGEfuel package [11] and experiments with gasoline as fuel from Jerzembeck et al. [44] at 373 K and different pressures, with air as oxidizer. Measurement accuracy is within ±4 cm/s. The symbols highlight the experiments and the lines show the simulations.

A dual fuel approach for the surrogate and second fuel is used. The composition of the first fuel stream is outlined in **Table 3** in liquid volume fraction. The second fuel stream is composed of Methanol, Toluene or Hydrogen.

Table 3: Surrogate composition in liquid volume fraction for the reference ETRF fuel.

Fuel	Iso-Octane	n-Heptane	Ethanol	Toluene
RON95 E10	0.44	0.141	0.101	0.318

The comparison of the properties of the experimental RON95 E10 fuel and the surrogate are outlined in **Table 4**. The QD-SRM is trained and validated for single cylinder engine experiments using the RON95 E10 fuel.

Table 4: Comparison of the properties of the experimental RON95 E10 fuel and the surrogate.

	Experiment	Surrogate
RON	96.7	96.7
MON	85.8	87.4
C:H:O	6.6:12.8:0.21	6.3:11.8:0.21
Density	748.7 *kg/m³*	756.4 *kg/m³*
LHV	41.78 *MJ/kg*	41.14 *MJ/kg*

The laminar flame speeds and the combustion chemistry are stored in a pre-compiled look-up table (see table ranges in **Table 5** and **Table 6**) using the software LOGEtable [10]. The table ranges are optimized to reduce the size of the tables but to keep a high resolution of auto-ignition sensitive conditions, e.g. the Negative Temperature Coefficient (NTC) region. During the simulation, laminar flame speeds and chemistry sources are retrieved from the look-up tables based on the current thermodynamic conditions.

Furthermore, a progress variable approach is used for the chemistry table look-up [45, 46, 47, 48]. The progress variable C is defined as follows in equation (11).

$$C = \frac{h_{298} - h_{298,u}}{h_{298,max} - h_{298,u}} \tag{11}$$

Therein, h_{298} is the latent enthalpy calculated at 298 *K*, and summed over all species, subscript u denotes unburned state, and subscript max denotes the most reacted state, which is assumed to be where the maximum chemical heat is released.

Table 5: Laminar flame speed dual fuel table specifications.

Parameter	Range	Steps
Temperature	350 – 1400 *K*	50 *K*
Pressure	1 – 150 *bar*	1 .. 10 *bar*
Equivalence Ratio	0.5 – 1.5	0.05
Fuel Fraction	50 – 100 %	10 %
EGR	0 – 40 %	10 %

Table 6: Combustion chemistry dual fuel table specifications.

Parameter	Range	Steps
Temperature	250 – 1400 *K*	10 .. 50 *K*
Pressure	1 – 200 *bar*	5 .. 20 *bar*
Equivalence Ratio	0.2 – 4.0	0.2 .. 0.25
Fuel Fraction	50 – 100 %	10 %
EGR	0 – 10 %	10 %

2.3 Resonance Theory

The resonance theory for the QD-SRM is introduced by Netzer [28]. Based on syngas (mixtures of H_2/CO) experiments and One-Dimensional (1D) CFD simulations, Bradley et al. [26] developed the Detonation Diagram in **Fig. 6**.
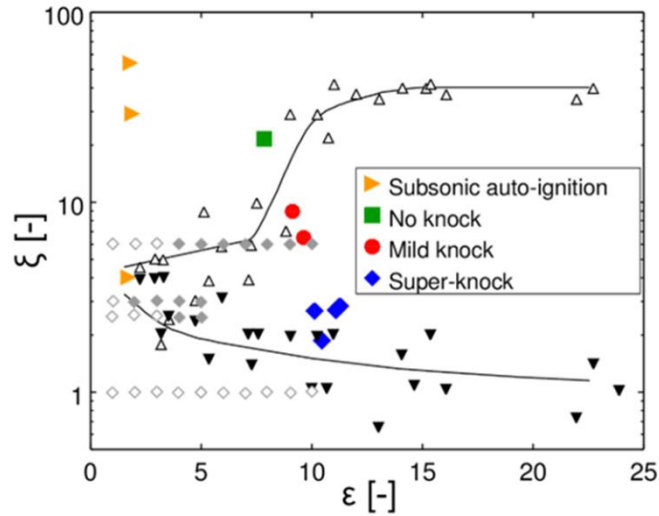
Fig. 6: Detonation Diagram; Full (▼) and hollow triangles (∆) and lines: experiments and simulations by Bradley et al. [26]; Full (♦) and hollow (◊) diamonds one-dimensional simulations by Peters et al. [49]: hollow symbols: no detonation, filled symbols: developing detonation; Full symbols (▶, ■, ●, ♦) LES engine simulations by Bates et al. [50].

The Detonation Diagram evaluates the characteristics of the auto-ignition in the end gas with two dimensionless parameters. ξ is the ratio of the speed of sound a and the apparent reaction-front velocity u [27] in equation (12). The apparent reaction-front velocity can be calculated using the temperature gradient over the travel distance x and the gradient of the ignition delay time τ.

$$\xi = \frac{a}{u} = a\frac{\delta T}{\delta x}\frac{\delta \tau}{\delta T} \tag{12}$$

With the help of the resonance parameter ξ, the characteristic of the auto-ignition event can be separated into different modes. If $u < s_L$, a normal flame occurs driven by heat conduction and diffusion, which is called deflagration [51, 52]. If $s_L < u < a$, a subsonic auto-ignition occurs, which is harmless for the engine. If $u > a$, thermal explosion is observed, which usually does not occur under conventional SI engine operating conditions. To form a developing detonation, u and a must be of the same order of magnitude ($u \approx a$). The order of magnitude increases with higher reactivity of the mixture and is calculated with the reactivity parameter ε in equation (13).

$$\varepsilon = \frac{l}{a \cdot \tau_e} \tag{13}$$

Here, l is the length of the constant temperature gradient kernel before the auto-ignition occurs and τ_e is the excitation time, which is the time between 5 % to maximum heat release of the auto-ignition event. The denominator describes how far the sound wave travels during the ignition event. Evaluated with the length of the constant temperature gradient, ε is a non-dimensional length, which can be interpreted as the dimensionless ignition kernel size. With higher ε and increasing kernel size accordingly, the range of conditions that lead to a developing detonation are getting wider. The limits of the different modes of reaction-front propagation in **Fig. 6** are experimentally and numerically obtained for syngas [26]. To make it applicable for engine conditions, Peters et al. [49] evaluated the regime limits for n-heptane and iso-octane. Since, these modes are chemically dependent on the high temperature chemistry, they appear in the same range for all reviewed fuels. Bates et al. [50] applied this evaluation method to 3D Large Eddy Simulation (LES) and characterized typical areas in the Detonation Diagram that cover engine operating conditions from harmless subsonic auto-ignition over non-knock and mild-knock to super-knock.

Kalghatgi and Bradley [53] investigated pre-ignition and super-knock events for a turbo-charged SI engine. To evaluate the severity of an auto-ignition event based on the Detonation Diagram they proposed the equation (14), which relates the dimensionless expression of the overpressure to the resonance parameter.

$$\frac{p(t)_{max}}{p} \sim \left(\frac{1}{\xi}\right)^2 \tag{14}$$

Subsequently, they calculated $\xi = 8.8$ and $\varepsilon = 9.1$ for an auto-ignition, which is classified as heavy knock. Those values are used in this work for the definition of the knock limit.

3. Experiments

The experiments are conducted on a single cylinder research engine at the TU Berlin. The single cylinder engine is built up for fundamental investigations of port and direct water injection in the FVV project "Water Injection in SI engines" [54]. The engine specifications are depicted in **Table 7**.

Table 7: Technical specifications of single cylinder research engine.

Parameter	Value
Bore	71.9 mm
Stroke	82 mm
Compression Ratio	10.75 : 1
Number of Valves	4
Fuel Injection	Central Direct

The engine experiments are conducted using a central direct fuel injection. The position of the injector is shown in **Fig. 7**. More details on the experimental campaign can also be found in the work of Kauf et al. [55].
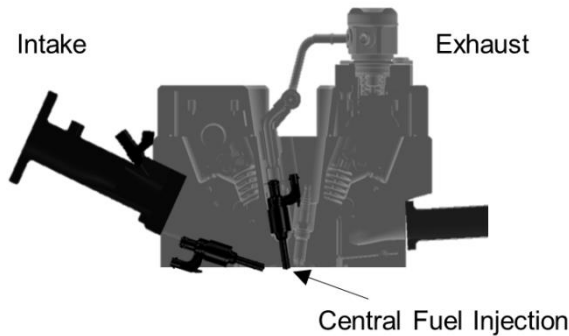
Fig. 7: Position of the central fuel injection of the single cylinder research engine at TU Berlin [55].
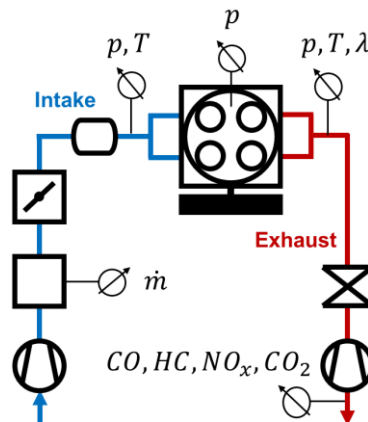
Fig. 8: Single cylinder research engine testbench scheme from TU Berlin [54].

The engine is equipped with low-pressure and high pressure sensors to measure the cylinder and manifold pressures of 250 consecutive cycles. The simplified testbench scheme and positions of the pressure (p), temperature (T), air-fuel ratio (λ), mass flow ($\dot{m}$) sensors and emission analyzers are

shown in **Fig. 8**. The intake system consists of a compressor unit to set the boost pressure, a Sensyflow for air mass flow measurement, a throttle, a mixing tank and two intake runners. The exhaust system consists of two exhaust runners, an exhaust orifice to control the back pressure, a diffusor, and an exhaust ventilation.

4. Model Training

The 1D-QD-SRM model training strategy is outlined in **Fig. 9**. First, the air path system parameters of the 1D model are trained to fit the simulated intake system pressure frequency ($f_{p,intake}$) and amplitude ($A_{p,intake}$) and exhaust system pressure frequency ($f_{p,exhaust}$) and amplitude ($A_{p,exhaust}$). This is done by adjusting the discharge coefficients of the throttle ($C_{D,throttle}$), the intake and exhaust ports ($C_{D,port}$) and the exhaust orifice ($C_{D,orifice}$). Second, the fired operating points are used to fit the closed cycle in-cylinder pressure of the experiments. A multi-objective genetic optimization process is applied using modeFRONTIER [56]. The objectives of the optimization are to minimize the sum of least squares of cylinder pressure ($\varepsilon_{Pressure}$), maximum cylinder pressure (ε_{PCP}), crank angle of maximum cylinder pressure (ε_{PCPCA}) and CO emissions at exhaust valve opening (EVO) ($\varepsilon_{CO,EVO}$). The QD-SRM turbulence model parameters C_Φ and C_{inj} are the optimization input parameters. Subsequently, the QD-SRM model parameters are validated using the remaining fired operating points. More information about the model training and validation results can be found in the work published by Franken et al. [57].
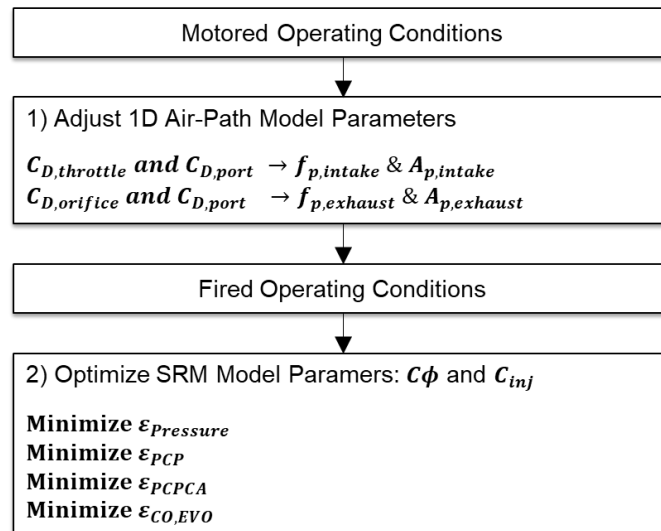
Fig. 9: QD-SRM model training procedure.

The final model parameters of the QD-SRM turbulence model in equation (3) and (4) are shown in **Table 7**. Mostly the same turbulence model parameters are used, as reported by Dulbecco et al. [39].

Table 8: QD-SRM turbulence model parameters.

Parameter	Value
C_{inj}	0.005
C_{comp}	0.67
C_{tke}	0.85
C_{diss}	1.0
C_{len}	0.3
C_β	0.25
$C_{\Delta,1}$	0.073
$C_{\Delta,2}$	0.1313
C_Φ	4.65

5. Results and Discussion

In this work the effect of Methanol, Toluene and Hydrogen addition to the RON95 E10 surrogate in a SI engine is investigated with the focus on auto-ignition in the end gas. While the effect of vaporization enthalpy is considered of those fuels, the air, RON95 E10 and fuel mixture is assumed to be homogeneously mixed to simplify the problem. In the future the effect of inhomogeneous mixtures on the auto-ignition in a SI engine will be investigated. Further, it is assumed that the different fuel blends do not affect the flame-turbulence interaction and one set of model parameters is used for all fuel blends to calculate the turbulent flame speed in equation (9).

First, the QD-SRM model training results are outlined for the measured motored and fired operating points in **Table 9**.

Table 9: QD-SRM engine operating points used for auto-ignition analysis.

OP	Speed	IMEP	λ	ST
1	1500 *rpm*	15 *bar*	1.0	-4.4 °*CA*
2	2000 *rpm*	20 *bar*	1.0	1.5 °*CA*
3	2500 *rpm*	15 *bar*	1.0	-9.7 °*CA*

Second, the spark timing of the three operating points is adjusted to achieve center of combustion at 8 °*CA*, which is defined as Maximum Break Torque (MBT). To keep the IMEP and air-to-fuel ratio (λ) constant during the parameter variations, the charge pressure is modified (see **Fig. 10**). Third, the fuels Methanol (CH_3OH), Toluene (C_7H_8) and Hydrogen (H_2) are added to the surrogate and the auto-ignition is evaluated using the Detonation Diagram. Hereby, Methanol and Toluene are added to the fuel blend to suppress auto-ignition, while Hydrogen is added to advance center of combustion.

Fired Operating Conditions

Apply Methanol, Toluene and Hydrogen

$$p_{boost} \& \dot{m}_{fuel} \quad \rightarrow IMEP = IMEP_{set} \& \lambda = 1$$
$$\theta_{spark}, H_2 \quad \rightarrow MBT$$
$$CH_3OH, C_7H_8 \quad \rightarrow \varepsilon < \varepsilon_{max} \& \xi > \xi_{min}$$
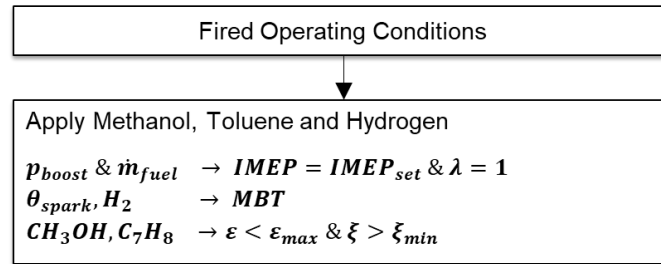
Fig. 10: QD-SRM strategy to adjust the operating point to MBT at the knock limit.

The amount of Methanol, Toluene and Hydrogen addition is quantified based on mass using the fuel fraction (FF) definition in equation (15). Therein, m_i describes the absolute mass of the additional fuel (Methanol, Toluene or Hydrogen) and $m_{RON95E10}$ describes the absolute mass of the base fuel (RON95 E10). The sum of the two masses equals to the total mass of fuel in the cylinder.

$$FF_i = \frac{m_i}{m_{RON95E10}} \cdot 100\% \tag{15}$$

5.1 Training Results

In **Fig. 11** the in-cylinder pressure and heat release rate of the experiments are compared to the QD-SRM training results. The simulation closely matches the pressure during the high pressure phase and valve opening time. Some deviations are found for the operating point at 2000 *rpm* and 20 *bar* IMEP, where the simulation predicts an earlier start of combustion. The exhaust emissions are not the focus of this work, but a comparison with the measured exhaust emissions of the trained model can be found in the publication by Franken et al. [57] and [58].
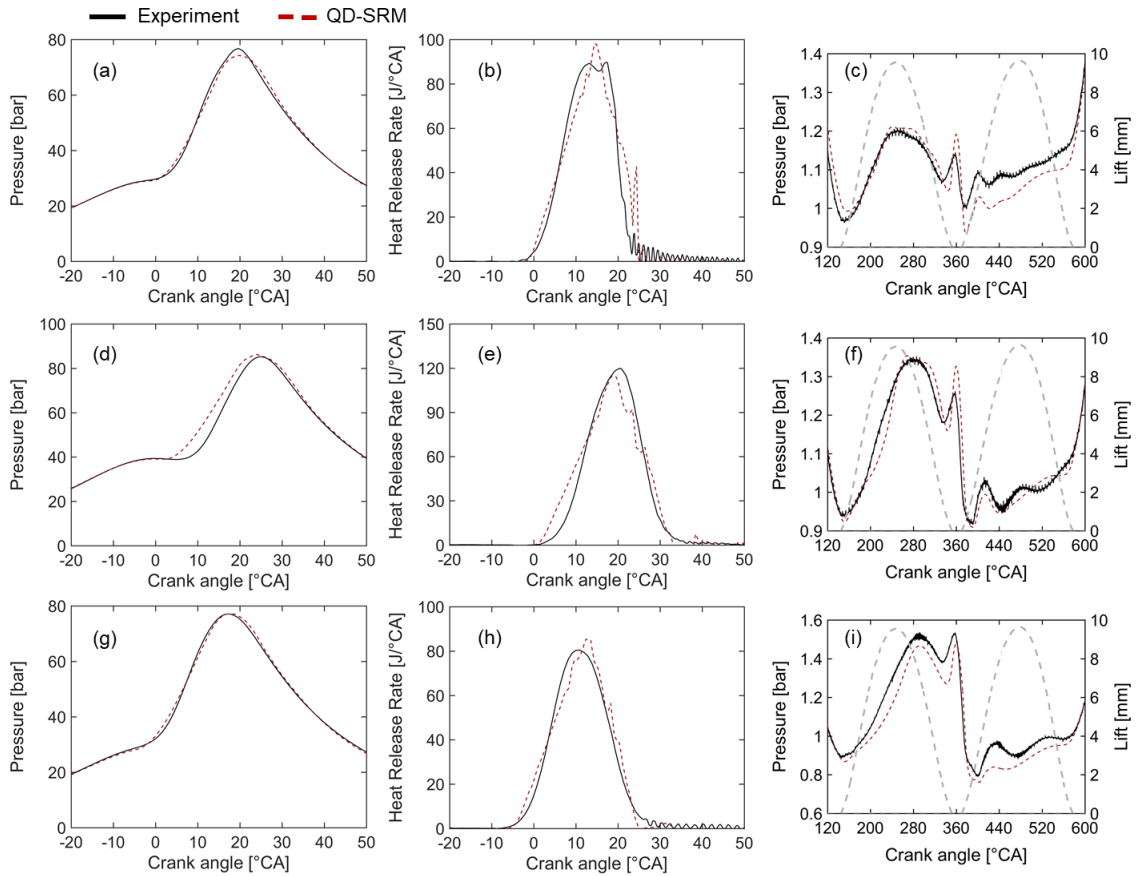
Fig. 11: QD-SRM simulation results of in-cylinder pressure, heat release rate and pressure during valve opening compared to the experiments for three fired operating points: (a) – (c) 1500 rpm 15 bar IMEP, (d) – (f) 2000 rpm 20 bar IMEP and (g) – (i) 2500 rpm 15 bar IMEP. Fired TDC is at 0 °CA.

5.2 Spark Timing Sweep

In **Fig. 12** the simulation results of a spark timing sweep for all three operating points are outlined. With the advanced spark timing the peak cylinder pressure (PCP) is increased up to 100 *bar* to 130 *bar* and the center of combustion is shifted towards MBT (8 *°CA*). The heat release rate (Norm. u-RoHR) in **Fig. 12 (b), (e) and (f)** is normalized by the mass of the air-fuel mixture in the end gas to exclude the effect of changing end gas mass. The maximum heat release rates of 9×10^5 *J/kg/°CA* to 10×10^5 *J/kg/°CA* are found for 1500 *rpm* 15 *bar* IMEP and 2000 *rpm* 20 *bar* IMEP since these operating points are found by experiments and simulations to be at the knock limit. Further, the strong increase of the heat release rate cause a strong rise in the temperature in the end gas from 1000 *K* to 2500 *K*.

The Detonation Diagram in **Fig. 13 (a) to (c)** shows the change of the auto-ignition strength for different spark timings and operating points. The resonance parameter and reactivity parameter are averaged for 30 stochastic cycles of the QD-SRM simulation to obtain a statistical stable result. The auto-ignition at the latest spark timing is found to be in deflagration mode for all operating points, where the reaction front of the auto-ignition propagates at laminar flame speed [51]. With advanced spark timing the combustion of the air-fuel mixture is promoted and auto-ignition in the end gas occurs at higher local temperatures. As a result, the mixture becomes more reactive and the reaction front propagates at subsonic conditions. For the operating points at 1500 *rpm* 15 *bar* IMEP and 2000 *rpm* 20 *bar* IMEP it is predicted that the auto-ignition develops to a detonation (knocking combustion) with a spark timing shift between 4 *°CA* to 6 *°CA* compared to the base spark timing. For 2500 *rpm* 15 *bar* IMEP the spark timing shift is found between 6 *°CA* and 8 *°CA* since this operating point is not at the knock limit.

Fig. 12: QD-SRM simulation results of in-cylinder pressure, normalized heat release rate in the end gas and temperature in the end gas for a spark timing sweep: (a) – (c) 1500 rpm 15 bar IMEP, (d) – (f) 2000 rpm 20 bar IMEP and (g) – (i) 2500 rpm 15 bar IMEP. Fired TDC is at 0 °CA.

Fig. 13: QD-SRM simulation results of the detonation diagram for a spark timing sweep: (a) 1500 rpm 15 bar IMEP, (b) 2000 rpm 20 bar IMEP and (c) 2500 rpm 15 bar IMEP.

The MBT spark timing is determined for all three operating points. For 1500 *rpm* 15 *bar* IMEP a spark timing of -9.4 °*CA* is found, for 2000 *rpm* 20 *bar* IMEP a spark timing of -8.5 °*CA* is found and for 2500 *rpm* 15 *bar* IMEP a spark timing of -14.7 °*CA* is found. The addition of Methanol and Toluene is investigated in the subsequent sections to reduce the strength of auto-ignition at MBT. Further, the addition of Hydrogen is investigated to promote combustion and achieve MBT operating conditions.

5.3 Effect of Methanol Addition

In **Fig. 14** the simulation results of different Methanol fuel fractions for different operating conditions are shown. The increasing amount of Methanol fraction in the fuel blend shows a decreasing trend for the normalized heat release rate and temperature in the end gas. On the one hand side, this is caused

Fig. 14: QD-SRM simulation results of in-cylinder pressure, normalized heat release rate in the end gas and temperature in the end gas for a Methanol fuel fraction sweep: (a) – (c) 1500 rpm 15 bar IMEP, (d) – (f) 2000 rpm 20 bar IMEP and (g) – (i) 2500 rpm 15 bar IMEP. Fired TDC is at 0 °CA.

Fig. 15: QD-SRM simulation results of the detonation diagram for a Methanol fuel fraction sweep: (a) 1500 rpm 15 bar IMEP with vaporization enthalpy, (b) 2000 rpm 20 bar IMEP with vaporization enthalpy, (c) 2500 rpm 15 bar IMEP with vaporization enthalpy, (d) 1500 rpm 15 bar IMEP without vaporization enthalpy, (e) 2000 rpm 20 bar IMEP without vaporization enthalpy and (f) 2500 rpm 15 bar IMEP without vaporization enthalpy.

by the higher vaporization enthalpy of Methanol compared to RON95 E10 (see **Table 1**), and on the other hand side by the changed reactivity of the end gas mixture. The decreased auto-ignition heat release rate is in good agreement with the higher RON value of Methanol (see **Table 1**).

The detonation diagram in **Fig. 15 (a) to (c)** supports this trend because the auto-ignition is moved from the developing detonation to subsonic auto-ignition and deflagration mode. For 1500 *rpm* 15 *bar* IMEP it is found that the addition of 10 % to 30 % Methanol fuel fraction to the fuel blend is required to obtain non-knocking combustion. For 2000 *rpm* 20 *bar* IMEP the Methanol fuel fraction in the fuel blend is determined with 50 % to 80 %.

The effect of the vaporization enthalpy of Methanol on auto-ignition is outlined in **Fig. 15 (d) to (f)**. For the simulation results shown, the vaporization enthalpy of Methanol is neglected and only the effect of changed reactivity due to different end gas mixtures is accounted for. The addition of 10 % to 50% Methanol fuel fraction to the mixture showed an increasing reactivity for 1500 *rpm* 15 *bar* IMEP operating conditions. For 2500 *rpm* 15 *bar* IMEP the 10 % to 100 % Methanol fuel fraction addition increased the reactivity and reaction front velocity. Overall, the vaporization enthalpy of Methanol is found to have a strong effect on the shift of auto-ignition from a developing detonation to deflagration since it reduces the local temperature at which auto-ignition occurs. Those effects are also supported by earlier works (e.g. Spausta [24] and Seidel [25] and works cited therein) who outlined the large deviation of RON and MON values for Methanol and Ethanol due to vaporization at elevated temperatures in the MON test.

5.4 Effect of Toluene Addition

The simulation results for in-cylinder pressure, normalized heat release rate and temperature in the end gas are depicted in **Fig. 16 (a) to (i)**. The increase of Toluene fuel fraction in the fuel blend reduces the normalized heat release rate and temperature in the end gas. This is an effect of the larger ignition delay time of Toluene compared to RON95 E10 as shown in **Fig. 2**.

The Detonation Diagram in **Fig. 17** shows that even a small amount of Toluene in the gas mixture has a large effect on the auto-ignition in the end gas. At 1500 *rpm* 15 *bar* IMEP the addition of 0 % to 10 % Toluene fuel fraction to the fuel blend shifts the auto-ignition to subsonic conditions.
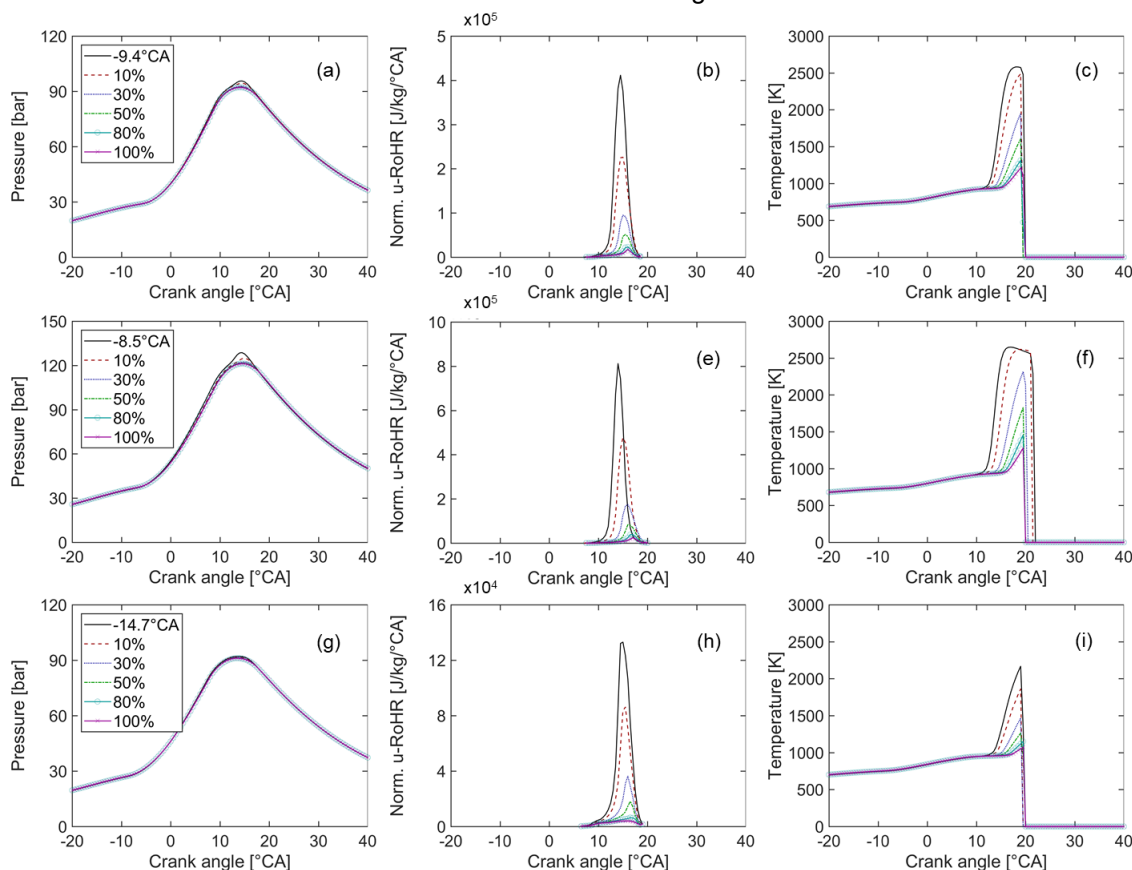
Fig. 16: QD-SRM simulation results of in-cylinder pressure, normalized heat release rate in the end gas and temperature in the end gas for a Toluene fuel fraction sweep: (a) – (c) 1500 rpm 15 bar IMEP, (d) – (f) 2000 rpm 20 bar IMEP and (g) – (i) 2500 rpm 15 bar IMEP. Fired TDC is at 0 °CA.
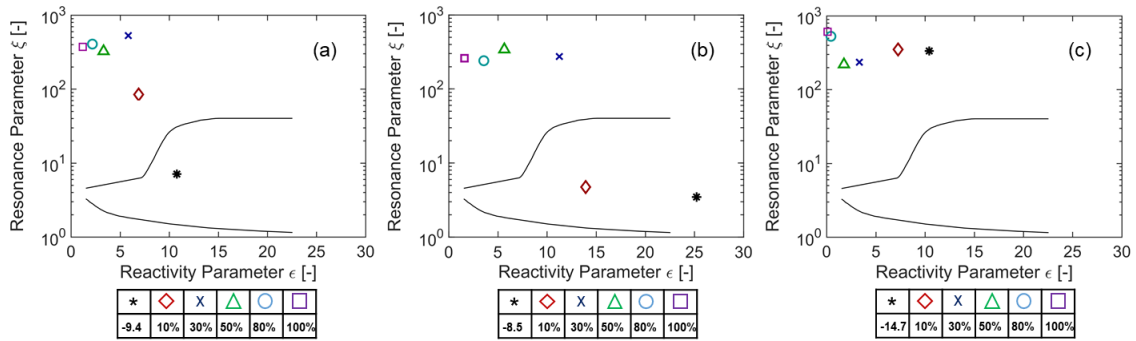
Fig. 17: QD-SRM simulation results of the detonation diagram for a Toluene fuel fraction sweep: (a) 1500 rpm 15 bar IMEP with vaporization enthalpy, (b) 2000 rpm 20 bar IMEP with vaporization enthalpy and (c) 2500 rpm 15 bar IMEP with vaporization enthalpy.

At 2000 *rpm* 20 *bar* IMEP the addition of 10 % to 30 % Toluene fuel fraction to the fuel blend moves the auto-ignition out of the knocking combustion region. While the 2500 *rpm* 15 *bar* IMEP operating point is not knock limited at MBT operation, it also shows a reduced heat release rate in the end gas with increased amount of Toluene.

While Toluene is quite effective in reducing the auto-ignition in the end gas compared to Methanol, it has to be pointed out that higher amounts of aromatics in the fuel blend increase the formation of HC and soot emissions [59].

5.5 Effect of Hydrogen Addition

The simulation results of Hydrogen addition to the fuel blend are shown in **Fig. 18 (a) to (i)**. The charge pressure is increased for cases with higher Hydrogen fuel fraction in the fuel blend to keep the
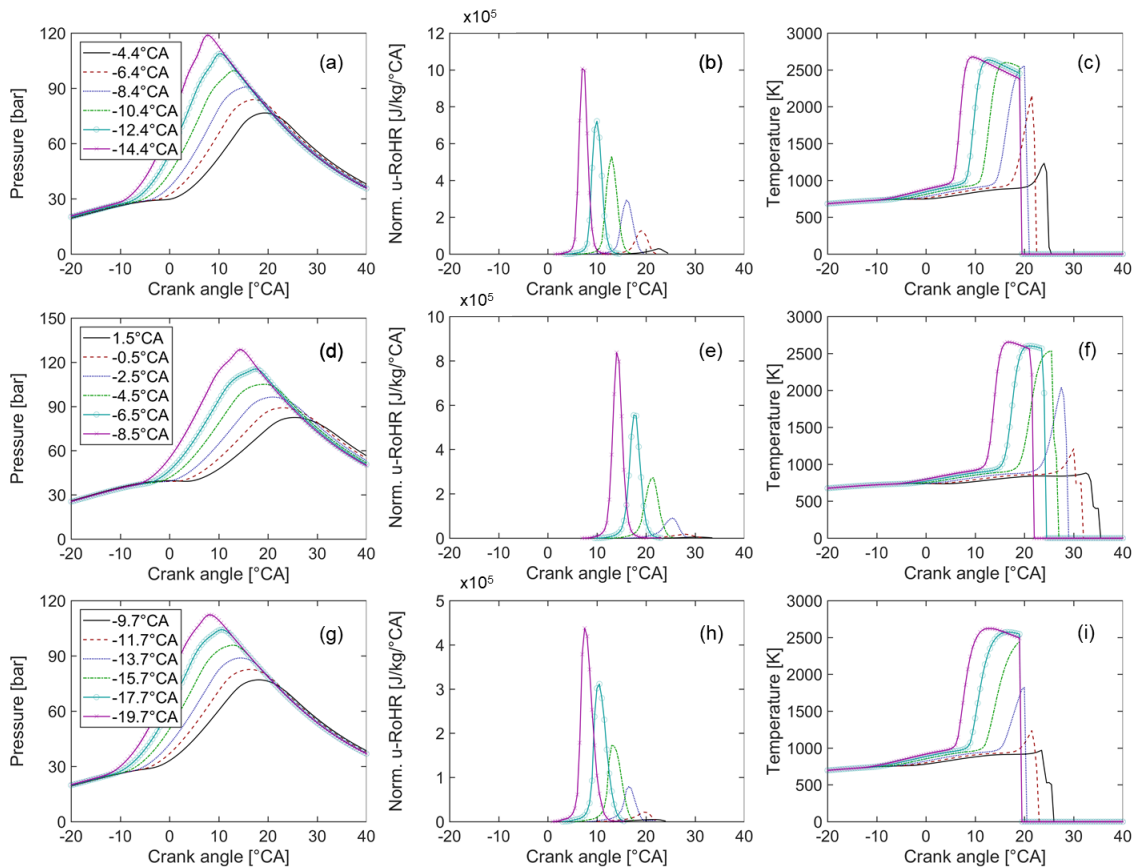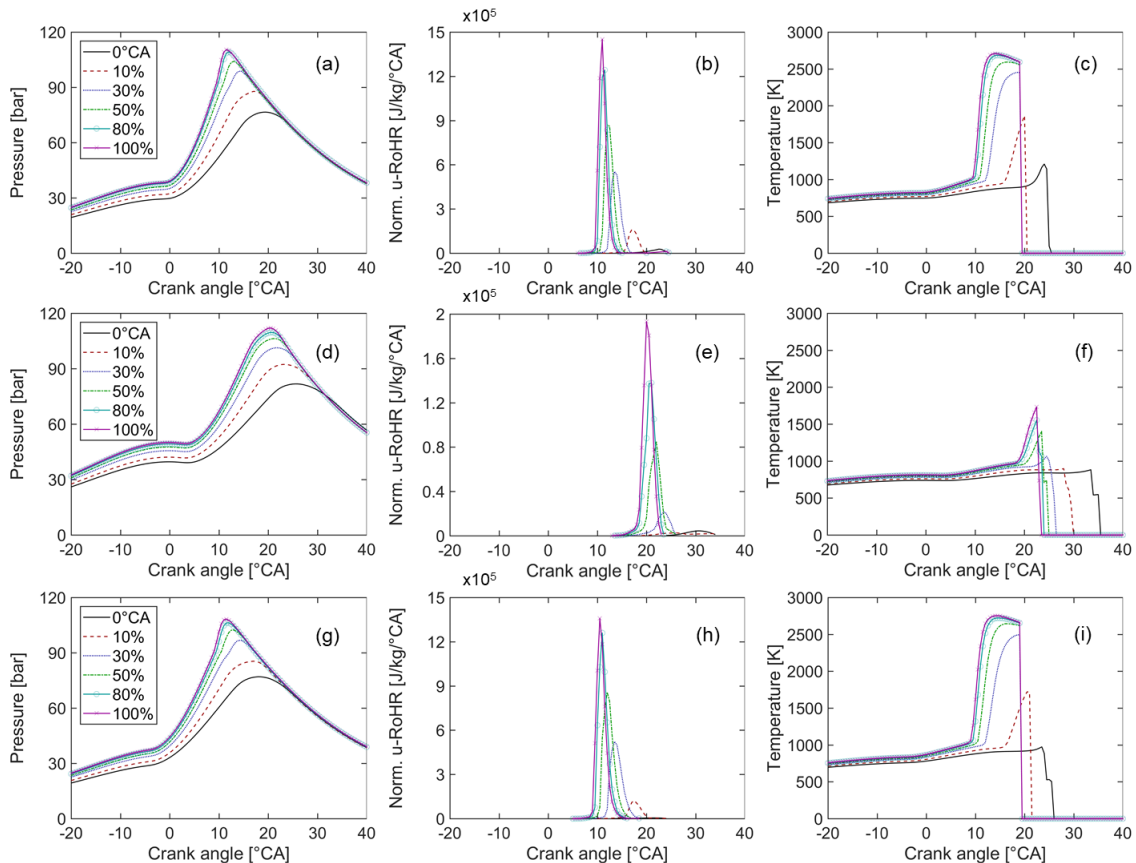

Fig. 18: QD-SRM simulation results of in-cylinder pressure, normalized heat release rate in the end gas and temperature in the end gas for a Hydrogen fuel fraction sweep: (a) – (c) 1500 rpm 15 bar IMEP, (d) – (f) 2000 rpm 20 5bar IMEP and (g) – (i) 2500 rpm 15 bar IMEP. Fired TDC is at 0 °CA.

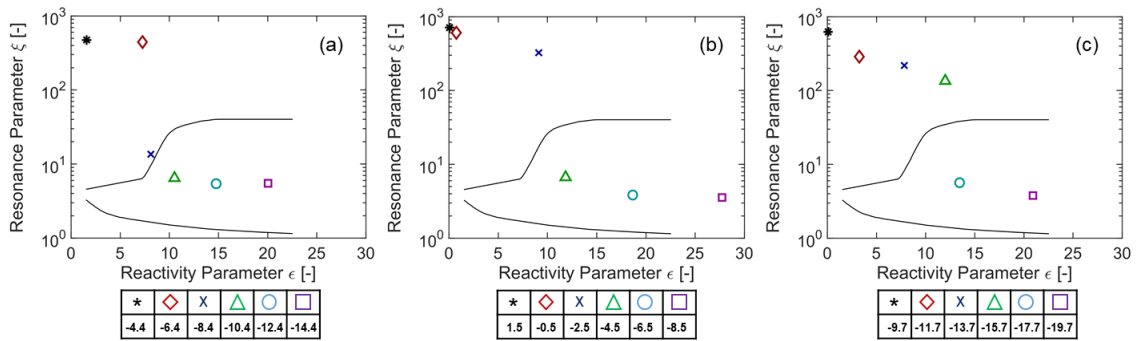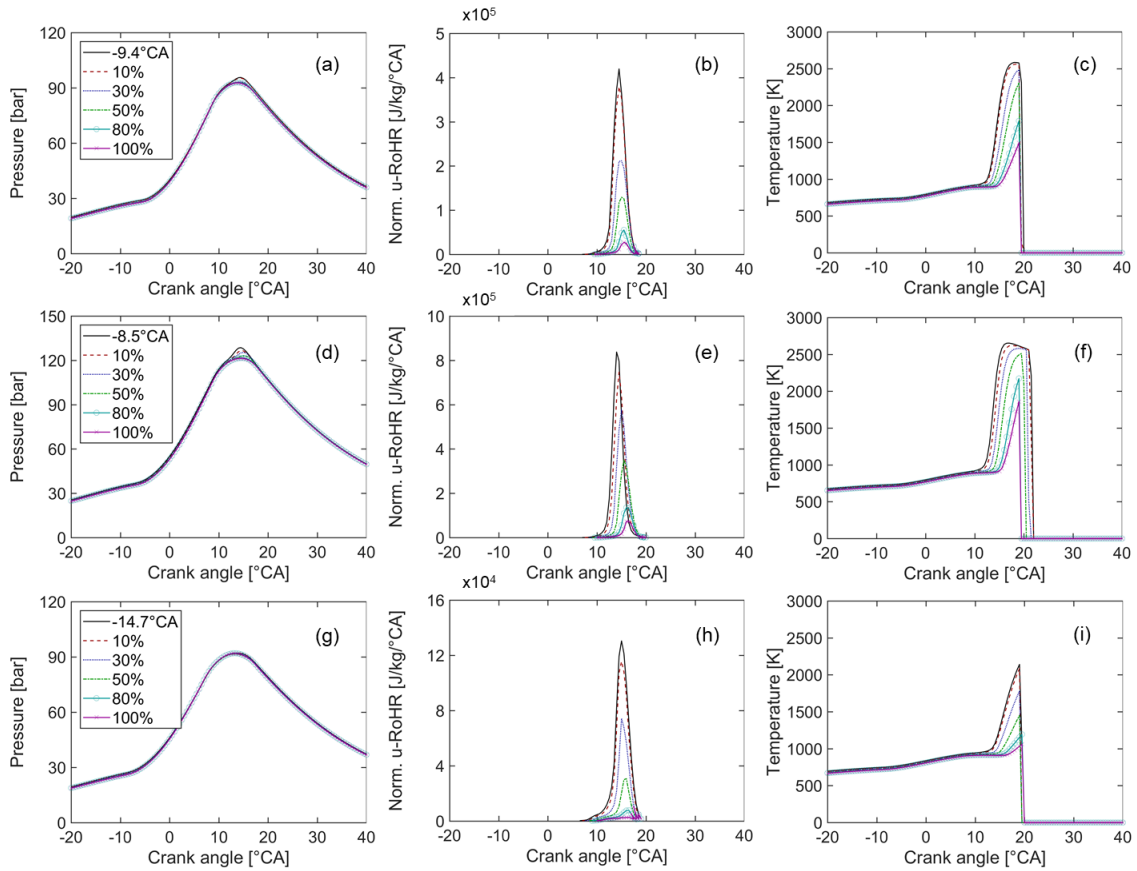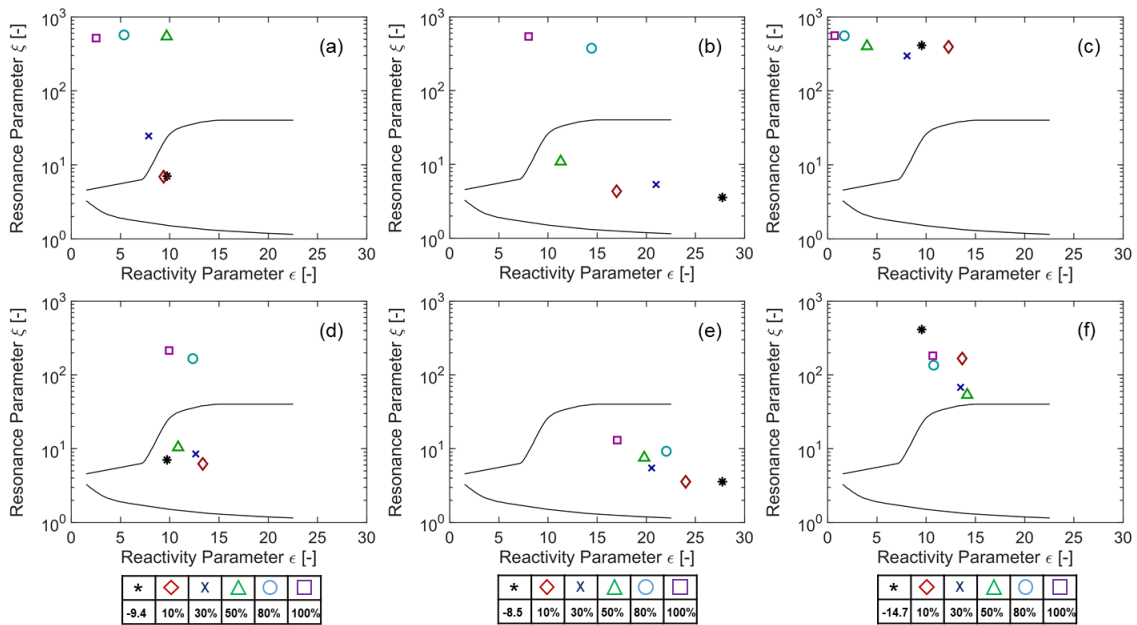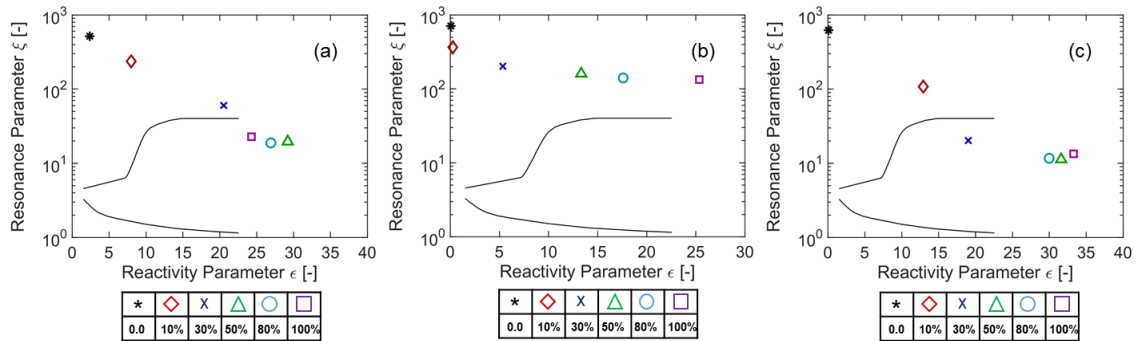**Fig. 19:** QD-SRM simulation results of the detonation diagram for a Hydrogen fuel fraction sweep: (a) 1500 rpm 15 bar IMEP, (b) 2000 rpm 20 bar IMEP and (c) 2500 rpm 15 bar IMEP.

IMEP constant. The laminar flame speed is significantly increased with more Hydrogen fuel fraction in the fuel blend and the gradient of cylinder pressure during flame propagation becomes larger due to the higher laminar flame speeds. Further, the addition of Hydrogen to the fuel blend increases the reactivity of the gas mixture and the auto-ignition heat release rate is increased with increasing Hydrogen fuel fraction. Due to the late spark timing of the operating point at 2000 *rpm* 20 *bar* IMEP the normalized heat release rate is not increasing as much as for the other two operating points since the temperature is already decreased at that crank angle in the expansion stroke.

The detonation diagram in **Fig. 19 (a) to (c)** highlights the increasing reactivity of the gas mixture due to higher Hydrogen fuel fraction. For the operating point at 1500 *rpm* 15 *bar* IMEP and 2500 *rpm* 15 *bar* IMEP the addition of 30 % to 50 % Hydrogen fuel fraction to the fuel blend leads to a developing detonation. At 2000 *rpm* 20 *bar* IMEP the addition of Hydrogen shows an increasing reactivity of the mixture but due to the lower temperature at which auto-ignition occurs, the reaction front velocity and pressure wave are not accelerated as much as for the other two operating points, wherefore the resonance parameter stays at a higher level. The reversed auto-ignition trend at 1500 *rpm* and 15 *bar* IMEP and 2500 *rpm* and 15 *bar* IMEP for 80 % and 100 % Hydrogen fuel fraction in the fuel blend, is because of decreasing local temperature and pressure at the advanced crank angles at which auto-ignition occurs.

6. Conclusions

This work outlines the assessment of different RON95 E10, Methanol, Toluene and Hydrogen blends regarding its effect on the auto-ignition modes in the end gas of a SI engine. It illustrates a novel simulation approach to jointly assess engine operating conditions and fuel blends and its effect on knocking combustion. The methodology is based on numerical investigations using the QD-SRM, dual-fuel tabulated chemistry look-up tables and the detonation diagram. The following conclusions are drawn based on the simulation results:

- The vaporization enthalpy of Methanol has a strong effect on the decreasing auto-ignition tendency of RON95 E10 and Methanol fuel blends. The engine can be operated at MBT at 1500 *rpm* and 15 *bar* IMEP, with 10 % to 30 % Methanol fuel fraction in the fuel blend and at 2000 *rpm* 20 *bar* IMEP, with 50 % to 80 % Methanol fuel fraction in the fuel blend.
- Toluene is highly effective in reducing the auto-ignition tendency for all operating conditions due to the longer ignition delay times. In contrast to Methanol the heat of vaporization is not the major factor, but the fuel chemistry, in particular the absence of a low temperature regime for Toluene. Compared to Methanol, only small additional amounts of Toluene in the fuel blend are needed to operate at MBT without knocking combustion. At 1500 *rpm* 15 *bar* IMEP up to 10 % additional Toluene fuel fraction are needed in the fuel blend and at 2000 *rpm* 20 *bar* IMEP 10 % to 30 % additional Toluene fuel fraction in the fuel blend are needed.
- The addition of Hydrogen decreases the burn duration, increases the PCP and increases the reactivity of the mixture in the end gas. The addition of 30 % Hydrogen fuel fraction in the fuel blend at 1500 *rpm* 15 *bar* IMEP corresponds to 6 °*CA* advancement of the spark timing. At 2500 *rpm* 15 *bar* IMEP the addition of 30 % Hydrogen fuel fraction in the fuel blend corresponds to 8 °*CA* to 10 °*CA* advancement of the spark timing.
- The QD-SRM simulation with tabulated chemistry and knock analysis takes 9 seconds for one engine cycle on 1 Intel Multi-Core i7-7820HQ CPU @ 2.90 GHz.

The future work consists of the following work steps:
- Extend the analysis for lean operation and increased compression ratios.
- Extend the analysis for different reaction mechanisms.
- Extend the analysis for other fuel blends.

References

[1]   J. Farrell, J. Holladay und R. Wagner, „Fuel Blendstocks with the Potential to Optimize Future Gasoline Engine Performance," NREL TP-5400-69009, 2018.

[2]   U. Kramer, S. Stollenwerk, F. Ortloff, X. Sava, A. Janssen, S. Eppler, H. Schüle, A. Döhler, R. Otten, M. Lohrmann, L. Menger, S. Barth, W. Kübler und R. Thee, „Climate-neutral driving in 2050: Options for the complete defossilization of the transport sector," Forschungsvereinigung Verbrennungsmotoren, Frankfurt am Main, 2019.

[3]   J. Vancoillie, J. Demuynck, L. Sileghem, M. Van De Ginste, S. Verhelst, L. Brabant und L. Van Hoorebeke, „The potential of methanol as a fuel for flex-fuel and dedicated spark-ignition engines," *Applied Energy, Vol. 102,* pp. 140-149, 2013.

[4]   J. Vancoillie, J. Demuynck, L. Sileghem, M. Van De Ginste und S. Verhelst, „Comparison of the renewable transportation fuels, hydrogen and methanol formed from hydrogen, with gasoline - Engine efficiency study," *International Journal of Hydrogen Energy,* Bd. 37, pp. 9914-9924, 2012.

[5]   K. Mueller, F. Rachow, V. Guenther und D. Schmeißer, „Methanation of Coke Oven Gas with Nickel-based catalysts," *International Journal of Environmental Science, Vol. 4,* pp. 73-79, 2019.

[6]   F. Rachow, M. Hagendorf, K. Mueller und D. Schmeißer, „Synthesis of Methanol from CO2 for Power-to-Liquid applications," in *Verhandlungen der Deutschen Physikalischen Gesellschaft*, Bad Honnef, 2017.

[7]   D. Gschwend, P. Soltic, A. Wokaun und F. Vogel, „Review and Performance Evaluation of Fifty Alternative Liquid Fuels for Spark-Ignition Engines," *Energy & Fuels, Vol. 33,* pp. 2186-2196, 2019.

[8]   N. Yokoo, Y. Miyamoto, K. Nakata, K. Obata, G. Aoki und M. Watanabe, „Research of Fuel Components to Enhance Engine Thermal Efficiency," Society of Automotive Engineers of Japan, Vol. 50, 2019.

[9]   E. W. Lemmon, M. L. Huber und M. O. McLinden, „NIST Standard Reference Database 23," U.S. Secretary of Commerce, 2013.

[10]   LOGE AB, „LOGEtable v2.0," 2020. [Online]. Available: https://logesoft.com. [Zugriff am 30 April 2020].

[11]   LOGE AB, „LOGEfuel," 2020. [Online]. Available: https://logesoft.com. [Zugriff am 30 April 2020].

[12]   K. P. Shrestha, L. Seidel, T. Zeuch und F. Mauss, „Detailed Kinetic Mechanism for the Oxidation of Ammonia Including the Formation and Reduction of Nitrogen Oxides," *Energy & Fuels, Vol. 32,* pp. 10202-10217, 2018.

[13]   K. P. Shrestha, L. Seidel, T. Zeuch und F. Mauss, „Kinetic Modeling of NOx Formation and Consumption during Methanol and Ethanol Oxidation," *Combustion Science and Technology, Vol. 191,* pp. 1628-1660, 2019.

[14]   K. P. Shrestha, N. Vin, O. Herbinet, L. Seidel, F. Battin-Leclerc, T. Zeuch und F. Mauss, „Insights into nitromethane combustion from detailed kinetic modeling – Pyrolysis experiments in jet-stirred and flow reactors," *Fuel, Vol. 261,* 2020.

[15]   K. P. Shrestha, S. Eckart, A. M. Elbaz, B. R. Giri, C. Fritsche, L. Seidel, W. L. Roberts, H. Krause und F. Mauss, „A comprehensive kinetic model for Dimethyl ether and Dimethoxymethane oxidation and NOx interaction utilizing experimental laminar flame speed measurements at elevated pressure and temperature," *Combustion and Flame,* to be published.

[16]   E. Ranzi, A. Frassoldati, R. Grana, A. Cuoci, T. Faravelli, A. P. Kelley und C. K. Law, „Hierarchical and comparative kinetic modeling of laminar flame speeds of hydrocarbon and oxygenated fuels," *Progress in Energy and Combustion Science,* Bd. 38, pp. 468-501, 2012.

[17]   P. S. Veloo, Y. L. Wang, N. Egolfopoulos und C. K. Westbrook, „A comparative experimental and computational study of methanol, ethanol, and n-butanol flames," *Combustion and Flame,* Bd. 157, pp. 1989-2004, 2010.

[18]   O. Mannaa, M. S. Mansour, W. L. Roberts und S. H. Chung, „Laminar burning velocities at elevated pressures for gasoline and gasoline surrogates associated with RON," *Combustion and Flame,* Bd. 162, pp. 2311-2321, 2015.

[19]   C. Dong, Q. Zhou, Q. Zhao, Y. Zhang, T. Xu und S. Hui, „Experimental study on the laminar flame speed of hydrogen/carbon monoxide/air mixtures," *Fuel,* Bd. 88, pp. 1858-1863, 2009.

[20]   K. Fieweger, R. Blumenthal und G. Adomeit, „Self-Ignition of SI Engine Model Fuels: A Shock Tube Investigation of High Pressure," *Combustion and Flame,* Bd. 109, pp. 599-619, 1997.

[21]   U. Burke, W. K. Metcalfe, S. K. Burke, A. K. Heufer, P. Dagaut und H. J. Curran, „A detailed chemical kinetic modeling, ignition delay time and jet-stirred reactor study of methanol oxidation," *Combustion and Flame,* Bd. 165, pp. 125-136, 2016.

[22]   J. C. G. Andrae, P. Björnbom, R. F. Cracknell und G. T. Kalghatgi, „Autoignition of toluene reference fuels at high pressures modeled with detailed chemical kinetics," *Combustion and Flame,* Bd. 149, pp. 2-24, 2007.

[23]   A. Keromnes, W. K. Metcalfe, K. A. Heufer, N. Donohoe, A. K. Das, C.-J. Sung, J. Herzler, C. Naumann, P. Griebel, O. Mathieu, M. C. Krejci, E. L. Petersen, W. J. Pitz und H. J. Curran, „An experimental and detailed chemical kinetic modeling study of hydrogen and syngas mixture oxidation at elevated pressures," *Combustion and Flame,* Bd. 160, pp. 995-1011, 2013.

[24]   F. Spausta, Eigenschaften und Untersuchungen der flüssigen Treibstoffe. Die gasförmigen Treibstoffe., Wien: Springer-Verlag, 1953.

[25]   L. Seidel, Development and Reduction of a Multicomponent Reference Fuel for Gasoline, Cottbus: BTU Cottbus-Senftenberg, 2017.

[26]   D. Bradley, C. Morley, X. J. Gu und D. R. Emerson, „Amplified Pressure Waves During Autoignition: Relevance to CAI Engines," *SAE Technical Paper, 2002-01 -2868,* 2002.

[27]   X. J. Gu, D. R. Emerson und D. Bradley, „Modes of Reaction Front Propagation from Hot Spots," *Combustion and Flame,* Bd. 133, pp. 63-74, 2003.

[28]   C. Netzer, Simulation and Assessment of Engine Knock Events, Cottbus: BTU Cottbus-Senftenberg, 2019.

[29]   C. Netzer, L. Seidel, M. Pasternak, C. Klauer, C. Perlman, F. Ravet und F. Mauß, „Engine Knock Prediction and Evaluation Based on Detonation Theory Using a Quasi-Dimensional Stochastic Reactor Model," *SAE Technical Paper, 2017-01-0538,* 2017.

[30]   C. Netzer, L. Seidel, M. Pasternak, H. Lehtiniemi, C. Perlman, F. Ravet und F. Mauss, „Three-Dimensional Computational Fluid Dynamics Engine Knock Prediction and Evaluation based on Detailed Chemistry and Detonation Theory," *International Journal of Engine Research,* Bd. 19, Nr. 1, pp. 33-44, 2018.

[31]   C. Netzer, L. Seidel, F. Ravet und F. Mauss, „Assessment of the Validity of RANS Knock Prediction using the Resonance Theory," *International Journal of Engine Research,* 2019.

[32]   C. Netzer, L. Seidel, F. Ravet und F. Mauss, „Impact of the Surrogate Formulation on 3D CFD Engine Knock Prediction using Detailed Chemistry," *Fuel,* Bd. 254, 2019.

[33]   M. Kraft, Stochastic Modeling of Turbulent Reacting Flow in Chemical Engineering, VDI Verlag, 1998.

[34]   M. Tuner, Stochastic Reactor Models for Engine Simulations, Lund: Lund University, 2008.

[35]   M. Pasternak, Simulation of the Diesel Engine Combustion Process Using the Stochastic Reactor Model, Berlin: LOGOS, 2016.

[36]   R. L. Curl, „Dispersed Phase Mixing: I. Theory and Effects in Simple Reactors," *A.I.Ch.E. Journal,* Bd. 9, Nr. 2, pp. 175-181, 1962.

[37]   M. Pasternak, F. Mauss, M. Sens, M. Riess, A. Benz und K. G. Stapf, „Gasoline Engine Simulations using Zero-Dimensional Spark Ignition Stochastic Reactor Model and Three-Dimensional Computational Fluid Dynamics Engine Model," *International Journal of Engine Research,* Bd. 17, Nr. 1, p. 76–85, 2016.

[38]   M. Sens, A. Benz, M. Riess, F. G. Lage, X. S. Bjerkborn, F. Mauss und M. Pasternak, „Multiple Spark Plug Approach: Potential for Future Highly Diluted Spark Ignited Combustion," in *SIA Powertrain*, Versailles, 2015.

[39]   A. Dulbecco, S. Richard, O. Laget und P. Aubret, „Development of a Quasi-Dimensional K-k Turbulence Model for Direct Injection Spark Ignition (DISI) Engines Based on the Formal Reduction of a 3D CFD Approach," *SAE Technical Paper, 2016-01-2229,* 2016.

[40]   N. Peters, Turbulent Combustion, Cambridge: Cambridge University Press, 2000.

[41]   S. Bjerkborn, K. Frojd und C. Perlman, „A Monte Carlo Based Turbulent Flame Propagation Model for Predictive SI In-Cylinder Engine Simulations Employing Detailed Chemistry for Accurate Knock Prediction," *SAE Technical Paper 2012-01-1680,* 2012.

[42]   T. Franken, C. Klauer, M. Kienberg, A. Matrisciano und F. Mauß, „Prediction of Thermal Stratification in an Engine-like Geometry using a 0D Stochastic Reactor Model," *International Journal of Engine Research,* 2019.

[43]   G. Woschni, „A Universally Applicable Equation for the Instantaneous Heat Transfer Coefficient in the Internal Combustion Engine," *SAE Technical Paper, 670931,* 1967.

[44]   S. Jerzembeck, N. Peters, P. Pepiot-Desjardins und H. Pitsch, „Laminar Burning Velocities at High Pressure for Primary Reference Fuels and Fasoline: Experimental and Numerical Investigation," *Combustion and Flame,* Bd. 156, Nr. 2, pp. 292-301, 2009.

[45]   H. Lehtiniemi, A. Borg und F. Mauß, „Combustion Modeling of Diesel Sprays," *SAE Technical Paper, 2016-01-0592,* 2016.

[46]   H. Lehtiniemi, F. Mauß, M. Balthasar und I. Magnusson, „Modeling Diesel Spray Ignition using Detailed Chemistry with a Progress Variable Approach," *Combustion Science and Technology,* Bd. 178, pp. 1977-1997, 2006.

[47]   A. Matrisciano, T. Franken, C. Perlman, A. Borg, H. Lehtiniemi und F. Mauss, „Development of a Computationally Effcient Progress Variable Approach for a Direct Injection Stochastic Reactor Model," *SAE Technical Paper, 2017-01-0512,* 2017.

[48]   A. Matrisciano, A. Borg, C. Perlman und H. Lehtiniemi, „Soot Source Term Tabulation Strategy for Diesel Engine Simulations with SRM," *SAE Technical Paper, 2015-24-2400,* 2015.

[49]   Peters, N., Kerschgens, B. and Paczko, G., „Super-Knock Prediction Using a Refined Theory of Turbulence," *SAE International Journal of Engines, ,* Bd. 6, Nr. 2, pp. 953-967, 2013.

[50]   L. Bates, D. Bradley, G. Paczko and N. Peters, "Engine hotpots: Modes of Auto-Ignition and Reaction Propagation," *Combustion and Flame,* vol. 166, pp. 80-85, 2016.

[51]   Y. B. Zeldovich, „Regime Classification of an Exothermic Reaction with Nonuniform Initial Conditions," *Combustion and Flame,* Bd. 39, pp. 211-214, 1980.

[52]   D. Bradley, „Autoignitions and Detonations in Engines and Ducts," *Philosophical Transactions of the Royal Society,* Bd. 370, pp. 689-714, 2012.

[53]   G. T. Kalghatgi und D. Bradley, „Pre-ignition and 'Super-Knock' in Turbocharged Spark-Ignition Engines," *SAE International Journal of Engines,* Bd. 13, Nr. 4, pp. 399-414, 2015.

[54]   M. S. Gern, M. Kauf, M. Bargende, F. Mauss und A. C. Kulzer, „Water Injection in SI Engines," FVV, Frankfurt am Main, 2020.

[55]   M. Kauf, M. Gern und S. Seefeldt, „Evaluation of Water Injection Strategies for NOx Reduction and Charge Cooling in SI Engines," *SAE Technical Paper, 2019-01-2164,* 2019.

[56]   ESTECO, „modeFRONTIER User Guide 2018R1," 2018. [Online]. Available: https://www.esteco.com/modefrontier.

[57]   T. Franken, F. Mauss, L. Seidel, M. S. Gern, M. Kauf, A. Matrisciano und A. C. Kulzer, „Gasoline engine performance simulation of water injection and low-pressure exhaust gas recirculation using tabulated chemistry," *International Journal of Engine Research,* 2020.

[58]   T. Franken, L. Seidel, A. Matrisciano, F. Mauss, A. C. Kulzer und F. Schuerg, „Analysis of the Water Addition Efficiency on Knock Suppression for Different Octane Ratings," *SAE Technical Paper, 2020-01-0551,* 2020.

[59]   G. Karavalakis, D. Short, D. Vu, R. Russell, M. Hajbabaei, A. Asa-Awuku und T. D. Durbin, „Evaluating the Effects of Aromatics Content in Gasoline on Gaseous and Particulate Matter Emissions from SI-PFI and SIDI Vehicles," *Environmental Schience & Technology,* Bd. 49, pp. 7021-7031, 2015.

Optical Investigations on the Jet Propagation of an Actively Fuelled Pre-Chamber Ignition System with Highspeed Schlieren Imaging

T. Russwurm[1,2], A. Peter[1], L. Weiß[1,2], S. Rieß[1,2], M. Wensing[1,2]

[1]LTT – Lehrstuhl für Technische Thermodynamik. Friedrich-Alexander University Erlangen-Nürnberg FAU. Am Weichselgarten 8, 91058 Erlangen, Germany.

E-mail: tim.russwurm@fau.de
Telephone: +(49) 9131 85 20182

[2] Erlangen Graduate School in Advanced Optical Technologies (SAOT)

Abstract. Pre-chamber ignition systems can be an enabler for combustion processes with diluted charge (lean or high EGR-rate) and thus increase the thermal efficiency of SI engines. A pre-chamber is a small volume with multiple transfer bores to the main cylinder that replaces the spark plug. Inside an active pre-chamber, external scavenging provides a mixture with high flammability even at high dilution in the combustion chamber which is ignited by a spark plug. Following the ignition, hot reactive gases penetrate the cylinder through the transfer bores and provide high ignition energy at multiple sites. Thereby, the combustion duration is reduced significantly, so even with highly diluted charges stable combustion is ensured.

To understand the pre-chamber ignition system isolated from cylinder conditions, highspeed schlieren imaging with a framerate of 50 kHz was used to analyse the jets from the pre-chamber. These measurements were performed inside a constant pressure vessel under highly controlled pressure and temperature conditions. Due to the weak image-to-noise ratio intensive image processing is necessary to extract the major jet parameters like penetration depth and propagation speed. It can be shown that the pre-chamber geometry has a major influence on the jet propagation as well as the body temperature of the pre-chamber. The gas temperature in the constant volume vessel has minor influence. Optical investigations showed to be a useful tool to improve the understanding of the combustion process. The accuracy of simulation models can be improved by calibration to optical data recorded under highly controlled conditions.

1. Introduction

Internal combustion engines for passenger cars in the next stage will need to have higher thermal efficiency in order to contribute to the reduction of CO_2 emissions. In addition to carbon emissions, pollutant emissions such as NO_x must also be kept at a very low level to counteract air pollution. One way to get closer to these goals in SI engines is to burn lean or diluted mixtures and increase the compression ratio. The latter directly affects the efficiency of the gasoline engine process, while diluted mixtures affect the isentropic exponent of the cylinder charge in addition. Charge dilution also lowers the combustion temperature and reduces the throttling losses in part-load operation. Currently, further increase of the compression ratio is limited by the tendency to knock at high loads, increased combustion speed in the full load area mitigates knock limitations.

Active pre-chamber ignition systems can enable combustion processes with highly diluted mixtures. Here, a small separate chamber connected to the cylinder via several transfer ports replaces the spark plug. In this chamber a small amount of ignitable mixture is prepared and ignited by a spark. This produces hot gases which penetrate the cylinder, increase the turbulent kinetic energy and ignite the cylinder charge at several points. This chemical reaction provides considerably more ignition energy than a spark, so that reliable ignition of lean mixtures with small cyclic fluctuations is possible. The challenge with this system is to create good ignition conditions in the pre-chamber. After ignition, the pre-chamber contains mainly residual gas. The gas exchange in the pre-chamber is much worse than in the cylinder. Therefore, the active pre-chamber is equipped with a separate refuelling line to remove the residual gases from the previous cycle. When the main cylinder is operated with lean mixture, a rich mixture from the pre-chamber fuelling line leads to near stochiometric conditions in the pre-chamber and thus to good ignition conditions.

Research on the field of pre-chamber ignition systems can be found back in the 1970s, where the first major investigations are documented [1,2]. The first investigations are from Gussak et. al., already identifying the basics of the geometrical design of active-pre-chamber systems [3,4]. They found that a pre-chamber volume of 1…3 % of the compression volume showed the most promising results. Furthermore, the cross section of the transfer ports should be between 0.02 and 0.04 cm^2/cm^3, referring to the pre-chamber volume. Yamaguchi et al. could identify four different ignition processes from pre-chamber systems, depending on the geometrical design of the transfer ports and their cross section [5]. Next to these early works focusing on the general process, detailed investigations on natural gas engines can be found at Shah et. al. [6–8], also analysing the influence of the pre-chamber volume and transfer port cross section. Kettner et. al. focus on SI engines using a bowl-shaped piston surface and direct injection to fuel the pre-chamber [9]. Toulson and Attard et. al. investigated the pre-chamber geometry as well as different fuels from hydrogen to liquid gasoline in context of their active pre-chamber combustion process called Turbulent Jet Ignition (TJI) [10–14].
Recent work focuses on passenger-car applications [15]. Sens et. al. shows an increased lean operation limit of $\lambda = 2.1$ at 6 bar load and 1500 rpm engine speed with an active pre-chamber. Another investigation on passenger car sized engines can be found at Stadler et. al., where a pre-chamber with six orifices could be operated in the entire engine map [16].

This work focuses on optical investigations of the jet propagation outside the pre-chamber and their influence on the combustion process. The pre-chamber is therefore analysed in a constant pressure vessel with highspeed-schlieren technique, without fuel outside the active pre-chamber, so the primary reaction is visible separately. The influence of the pre-chamber geometry and the temperature of both gas and pre-chamber body is addressed. In addition, the results are compared to full engine measurements using the same pre-chamber.

2. Investigated pre-chamber geometries

Three different pre-chamber geometries are compared. All of them feature six transfer bores with a diameter of 1.0 mm. The pre-chamber volume and the length of the transfer bores are varied.

Table 1. Geometrical pre-chamber characteristics

Pre-Chamber	Volume /cm^3	Bore length /mm
VK1-1	1.34	1.9
VK3	1.70	1.9
VK4	1.70	4.5

The pre-chamber is manufactured from a copper alloy as shown earlier [17]. It is equipped with a spark plug with integrated pressure transducer - Kistler 6113B - to investigate the pressure inside the pre-chamber. In the pre-chamber body, a self-developed magnetic check valve is integrated to seal the pre-chamber fuel line from the combustion pressure.

3. Full engine measurements

The authors showed that active pre-chamber ignition systems can be used to enable lean engine operation by using the gasoline-vapour air-mixture in the fuel tank [18,19]. The engine test results concerning the pre-chamber geometry of the samples that are investigated both in the constant pressure vessel and at the engine test bench are summarized in the following.

3.1 Methodology

The pre-chamber Ignition system was investigated in a production four-cylinder engine. To save prototypes only one cylinder is fired while the remaining are blocked with an aluminium plate in the intake. As operating point, a challenging low-load point with high relevance for fuel consumption in WLTP driving cycle of a medium class passenger car is selected. Detailed information on the engine geometrics and the operating point are listed in Table 2.

The active pre-chamber fuelling is provided by a special fuel system that uses the gasoline vapour air mixture above the liquid level in a fuel tank to enrich the pre-chamber. A special test system was built up for engine research. This system contains a 20 L fuel tank with integrated coolant pipes to control the fuel temperature. By defining the temperature, the HC-concentration in the gas phase can

be variated as the vapour pressure of the gasoline fuel is temperature dependent. This vapour is sucked out by a fuel resistant vacuum pump and compressed to 2.5 bar. The HC-concentration is measured as well as the mass flow. The latter is done by a coriolis mass flow sensor that can measure independently from the composition. Together with the HC-concentration, the fuel mass in the pre-chamber is calculated and considered for efficiency measurements. The dosing is done by a solenoid valve as the one used in common MPI fuel injection systems. Both the injection timing and the injection duration to control the mass flow are implemented in the engine control unit. For the application in a passenger car, different concepts for the generation of the gasoline-vapour-air-mixture are possible [20,21].

Table 2. Geometrical engine characteristics and investigated engine operating point

Engine characteristics		Operating point	
Displacement volume per cylinder	450 ccm	Fuel pressure gasoline	100 bar
Stroke	84.1 mm	Load IMEP	4.5 bar
Bore	82.5 mm	Speed	1500 rpm
Rod length	148 mm	Center of combustion	8° CA a. TDCF
Compression ratio	9.6	PC scavenging pressure	2.5 bar
Valves per cylinder	4	HC concentration in the PC fueling line	45 wt.%
Intake valve diameter	33.9 mm		
Exhaust valve diameter	28.0 mm		
Injector position	side		

3.2 Results

Three different pre-chamber geometries were compared in full engine measurements. The selected HC-concentration of 45 % (equals λ = 0.1) in the pre-chamber fuelling line showed good performance in lean operation. The mixture in the pre-chamber at ignition is composed of both the active fuel purging from the pre-chamber injector and the mixture from the main combustion chamber. Due to the pressure limitations in the fuelling system the active scavenging requires low cylinder pressure and is therefore timed around bottom dead center. The injected very rich composition is diluted with lean mixture from the cylinder, entering the pre chamber by the transfer ports during compression stroke. The trapped fuel mass and residual gases in the pre-chamber are not easy to evaluate, so the calculation of a pre-chamber lambda at ignition timing is complex. The injected fuel mass was therefore adapted to the pre-chamber volume and optimized regarding fuel consumption and combustion stability in a previous step. Objective of this measurement is to compare the same pre-chamber geometry both in full engine operation and in the constant volume vessel as shown later to find a link between the optical measurements and the behaviour in full engine operation.

In Fig. **1** the three different pre-chamber geometries from Table 1 are compared. The combustion duration and the combustion stability are plotted. In the middle diagram the center of combustion is additionally shown. In general, the ignition timing is adapted to keep the MFB50% stable at 8 °CA. However, when no stable engine combustion was possible, the ignition angle was retarded accepting later combustion. The threshold for combustion stability selected in this operating point is a coefficient of variance of 0.04. It becomes clear that the choice of geometric parameters of the pre-chamber has an immense influence on the combustion process. Especially the longer bores have a negative influence on the combustion duration. With VK4, featuring the longer transfer holes, the ignition timing had to be retarded for reasonable stability.

With the small pre-chamber volume (VK1-1), shorter combustion durations and lower cyclical fluctuations under extremely lean conditions can be observed. In the lean range with lambda greater than 1.60 the center of combustion can still be kept constant. Although the burn time increases in the same way as in VK3, the overall increase is smaller, so that the critical combustion duration is only reached at Lambda 1.90. From this point on, no further dilution while maintaining the stability is possible. It seems that this pre-chamber can supply higher ignition energy to the cylinder despite its smaller volume. So, the combination of transfer hole diameter and pre-chamber volume represent the most suitable combination studied.
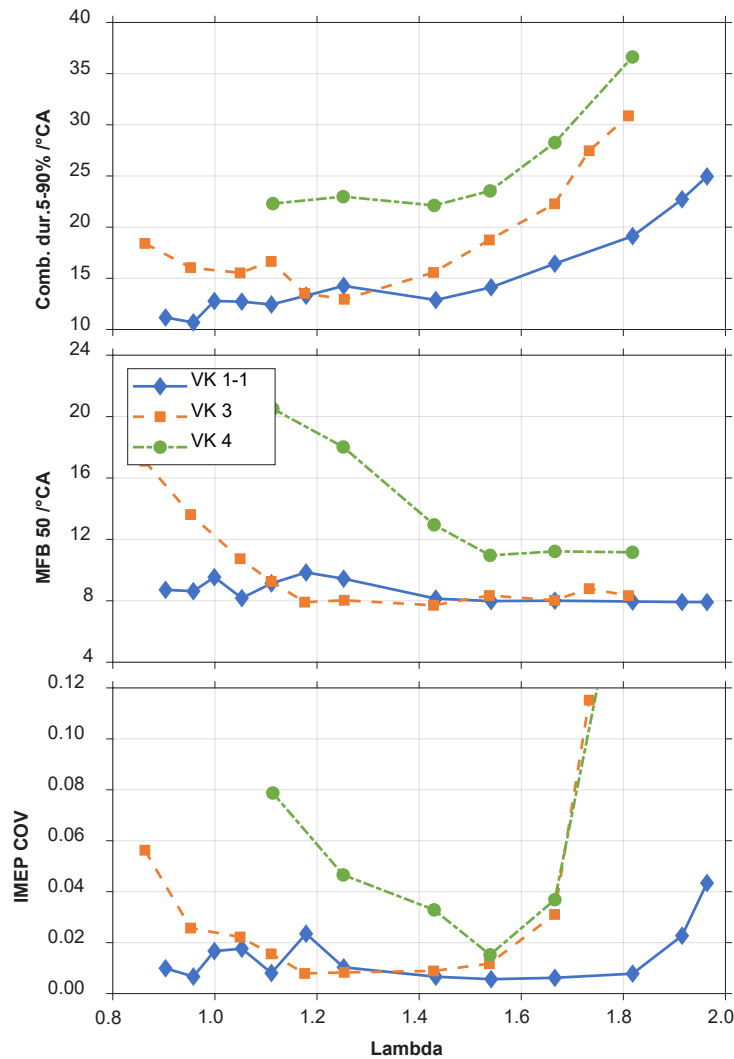
Fig. 1. Investigation of three different pre-chamber geometries in a variation of exhaust-lambda at 4.5 bar IMEP engine load and 1500 rpm engine speed.

4. Highspeed Schlieren Imaging

4.1 Methodology

The optical investigations on the primary ignition processes take place in a constant pressure chamber using highspeed schlieren technique to visualize the gas jets that exit the pre-chamber. Since these penetrate into the combustion chamber when used in the engine, they are decisive for the stability of the ignition. By using the chamber with constant pressure and temperature, the propagation of the gas jets can be analysed under different conditions. Only the pre-chamber is enriched with fuel, outside the pre-chamber there is pure air in contrast to engine operation. The primary reaction can therefore be observed separately.

4.1.1 Constant pressure vessel

The optical measurements are executed at the high temperature and high pressure ignition and combustion chamber "OptiVeP" at FAU (see Fig. **2**). In the cubic shaped vessel, pure air is entered in all four top corners and directly electrically heated up to 300 °C. The ambient gas flow streams with a constant flow velocity of around 30 mm/s through the test region and exits at the bottom corners. There, the scavenged gas is cooled down to around room temperature. Compared to velocities of the flames exiting the pre-chamber, the gas flow velocity through the vessel can be neglected. The permanent scavenging

allows experiments in a frequency of 1 Hz. The ambient pressure is held constant to 10 bar. A back-pressure control valve enables an independent adjustment of temperature and pressure. Further information about the vessel functionality and operation conditions are summarized in [22].
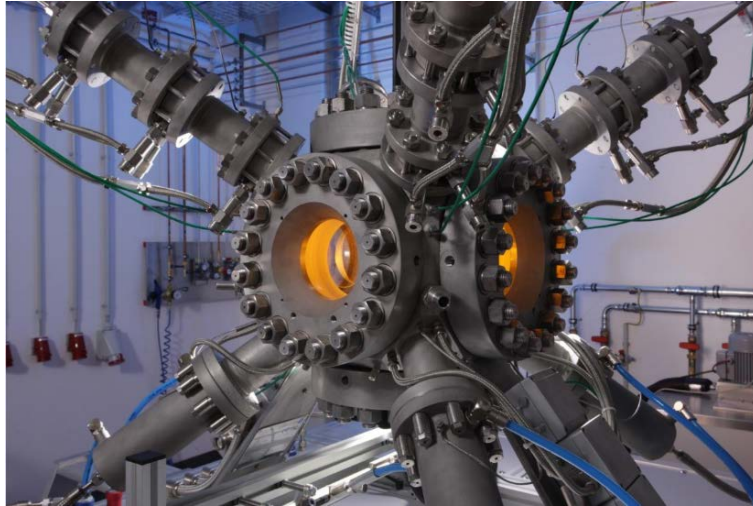
Fig. 2. High pressure and combustion chamber "OptiVep"

The chamber is optically accessible on five sides, where round quartz-glass windows are mounted with a diameter of 125 mm. The sixth side contains the pre-chamber slot which is connected on the bottom side of the vessel. The exiting flame jets penetrate under an elevation angle of 60° from the main axis, thus the optical detection and illumination is practiced through the top window.

4.1.2 Pre-chamber scavenging system for constant pressure vessel

Due to the lack of pressure gradients, the pre-chamber fuelling system used during the full engine experiments is not suitable for the investigations in the constant pressure chamber. The pressure of the gasoline-vapour-air-mixture in this system is limited to a maximum of 4 bar absolute by the precipitation of condensate.
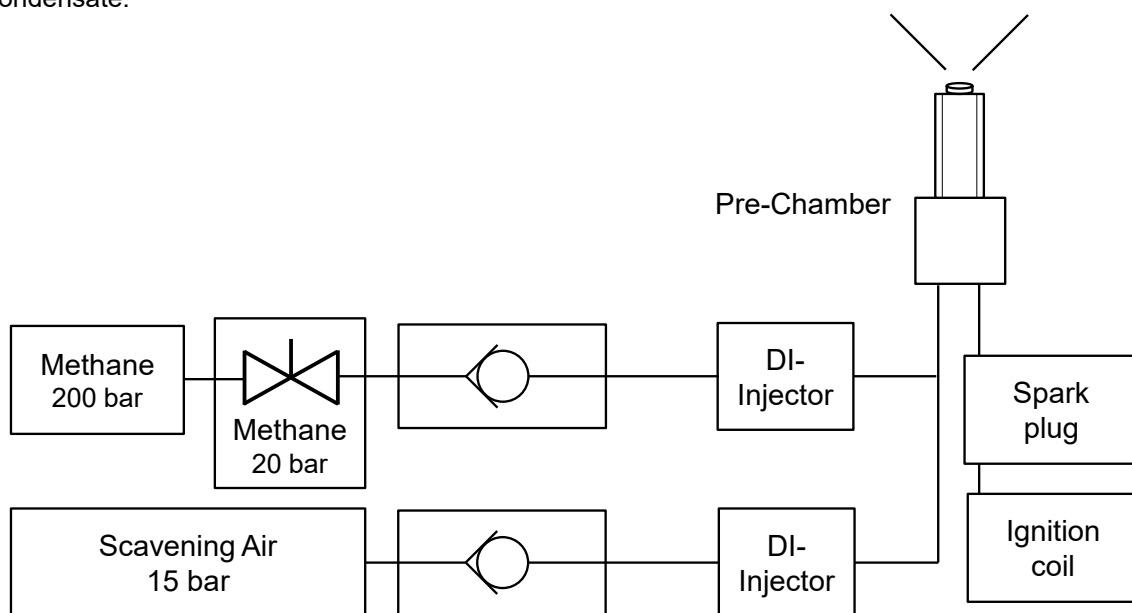
Fig. 3. Pre-chamber fueling system for investigations in the constant pressure vessel using methane as substitute fuel for pre-chamber enrichment

As the chamber should represent engine conditions at ignition timing, the pressure is set to 10 bar. Furthermore, the pre-chamber must be scavenged with air to reach equal conditions for each recorded ignition sequence. A special fuel system for these experiments was developed. In Fig. **3** the function of this fuel system is shown schematically. Instead of the gasoline vapour methane is used as fuel to avoid condensation problems. To purge the burnt residual gas from the pre-chamber between ignitions, additional compressed air is injected into the pre-chamber. The dosing of the fuel and the scavenging air is realized by means of one single injector each. In this study, conventional injectors for direct petrol injection are used. To make sure that no gas is pressed back to the gas supply each pipeline is equipped with an additional check valve. The ignition in the pre-chamber is done by a conventional spark plug together with a power stage that can be triggered externally. This power stage has an integrated ignition coil to supply high voltage to the spark plug. Thus, the ignition timing can be synchronized accurately to the camera. The scavenging injector with air is actuated several times to make sure that all residual gas is removed, then the methane injector injects the fuel with only one injection prior to the ignition. The opening duration and thus the amount of rich gas supplied is adapted to the pre-chamber volume.

4.1.3 Optical Setup
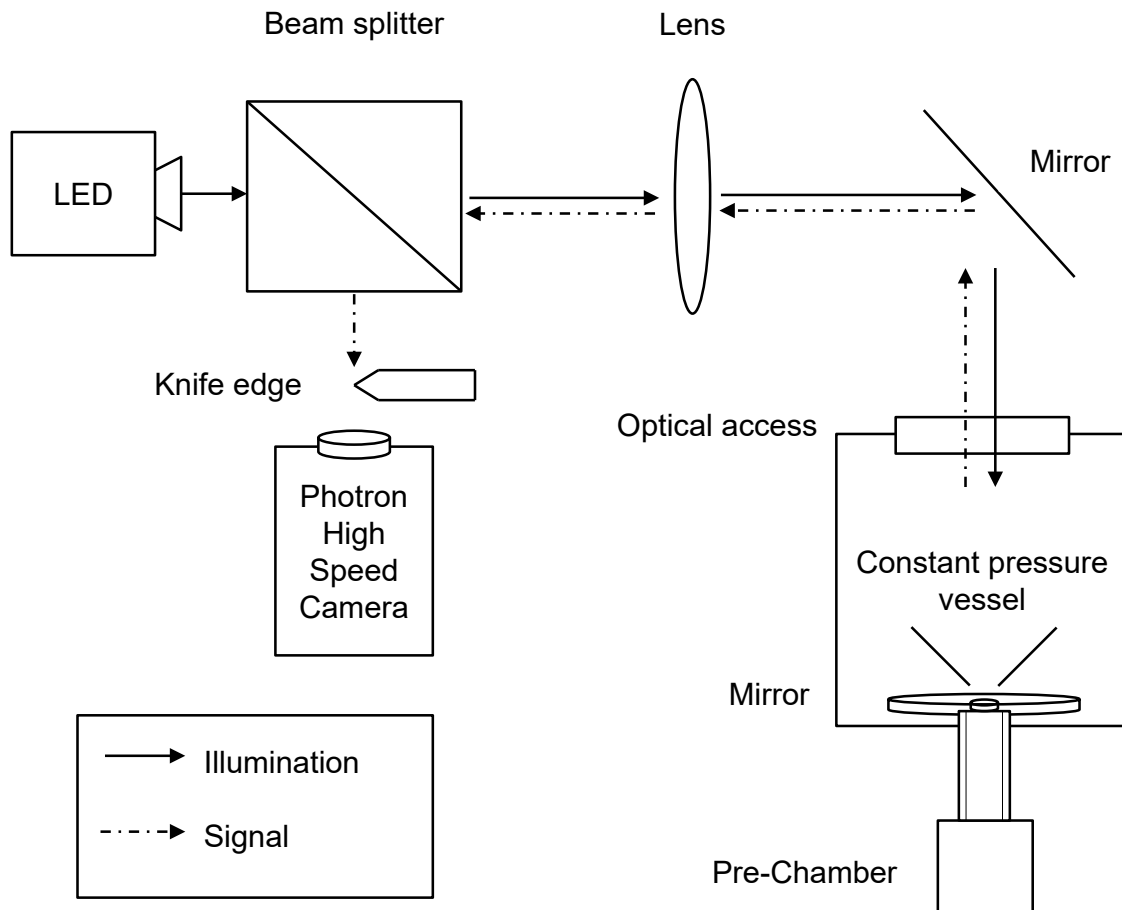
Fig. 4: Schematic sketch of the optical schlieren setup applied at the constant pressure vessel

For the optical characterisation of the pre-chamber, highspeed schlieren imaging is applied. The technique enables to visualize discontinuities of the refractive index in the test area via parallelized light [23]. In a gaseous atmosphere, gradients in the density of the medium can be visualized as they are interconnected in the Gladstone-Dale relation (1). Here, the refractive index n, the species-specific Gladstone-Dale constant k, and the density ρ are linked.

$$n-1 = k\rho \qquad (1)$$

Temperature *T* and pressure *p* influence on the density as known from the ideal gas law (2).

$$\frac{p}{\rho} = RT \qquad\qquad (2)$$

Together with the gas constant *R*, this imaging method can separate areas with different temperature, pressure and gas composition.

As shown in Fig. **4**, the light emitted by a LED-array (Hardsoft IL-106G) is passing a cubic beam splitter and subsequently collimated by a 5" lens to a parallelized bundle of light beams. With a mirror under 45 degree angle, the beam is guided into the vessel from the top window. A polished silica waver, which is exposed inside the hot ambient atmosphere of the vessel, reflects the light back. Thereby, the light is traveling twice through the vessel and the flame volume. After defocusing on the same way back, the beam splitter reflects the returning light into the camera. In this assembly, the beam splitter works like the knife edge because strongly refracted light beams in the expanding bundle are blocked at the beam splitter holder. For detection a Photron SA-Z camera is used. The frame rate is set to 50 kHz, which means a single picture every 20 µs. Designated geometrical flame characteristics are penetration depth and the derived propagation speed of the flame jet which is explained in the following section in detail.

4.2 Image processing

Next to the experiment itself, a major part of this work is the image processing of the recorded highspeed video. As schlieren images visualize a change in refractive index, the contrast between the signal from the pre-chamber jets to the environment is very low. Especially in hot chamber conditions the temperature gradient gets small, resulting in a low signal to noise ratio. Since the gradient is decisive, the relatively large holes compared to the outflowing mass have a negative influence on the signal intensity. Furthermore, the gases in the transfer hole are cooled down by the high thermal conductivity of the copper, resulting in lower temperatures of the exiting gases. To evaluate mayor penetration parameters of the jets, image processing is required to eliminate the background. An Example for a raw image is shown in Fig. **5**.
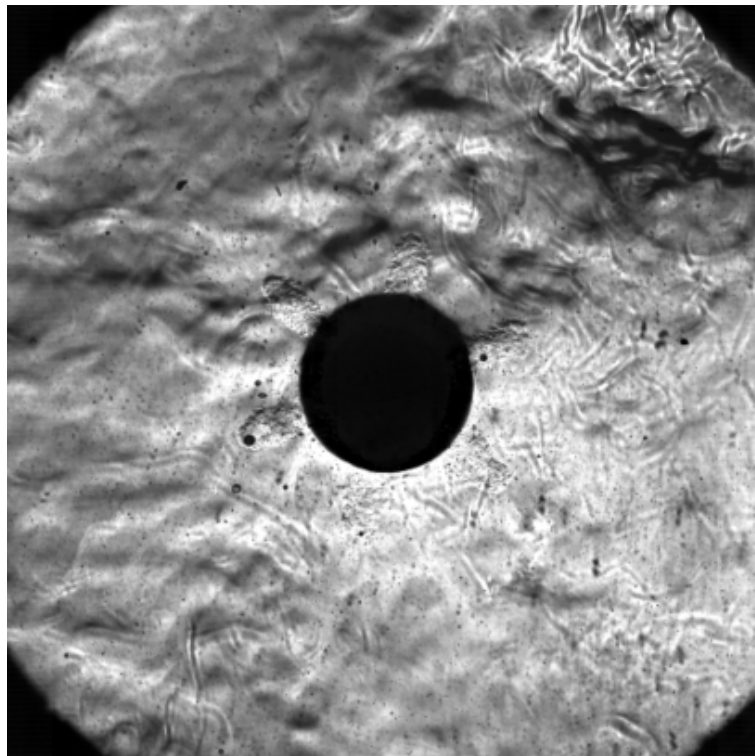
Fig. 5. Example for a raw image of VK3 at 10 bar and 300 °C Chamber conditions

The separate steps of image processing are shown in Fig. **6**. In the first step from the raw image to picture 2, each image is divided pixel by pixel by the image directly preceding it. In this way, the background signal, which changes much more slowly, can be eliminated. Here the postprocessing can benefit from the high imaging rate of 50 kHz. In the second step, the image is multiplied with the image itself to increase the contrast. This is necessary to get a high contrast picture to separate the signal from the remaining background. Therefore, the Otsu method is used [24]. This method uses a user calibrated threshold to distinguish between signal and background. It is a histogram-based procedure, that divides the image into two classes. The difference between the pixel-values inside one class is minimized while the difference between the two classes is maximized. This way, pixels in the background class can be identified and defined as no signal. The result is shown in picture 4. In this picture the exiting jets in front of the surface of the waver can already be seen very well. The last step is the subtraction of a predefined mask. The mask excludes all area outside the waver, where no signal is possible. This mask is generated automatically by analysing the sum of all raw pictures from one ignition sequence. The result of the image processing can be seen in picture 5. It shows the jets with a strong contrast. The boundary of each jet is clearly separable, the structures within one jet can still be recognized. In order to adapt to the different background signals resulting from the different chamber conditions, the number of multiplications and the threshold values of the Otsu separation are adjusted.

The result of this image processing is analysed with an in-house developed code to extract major spray properties from highspeed schlieren or shadowgraphy video sequences. As this code was developed for the analysis of sprays from liquid fuels, the image processing shown in Fig. **6** is necessary in a prior step to get accurate results.

1: Raw image   **2: After division**   **3: After multiplication**

4: After Otsu separation   **5: After mask subtraction**
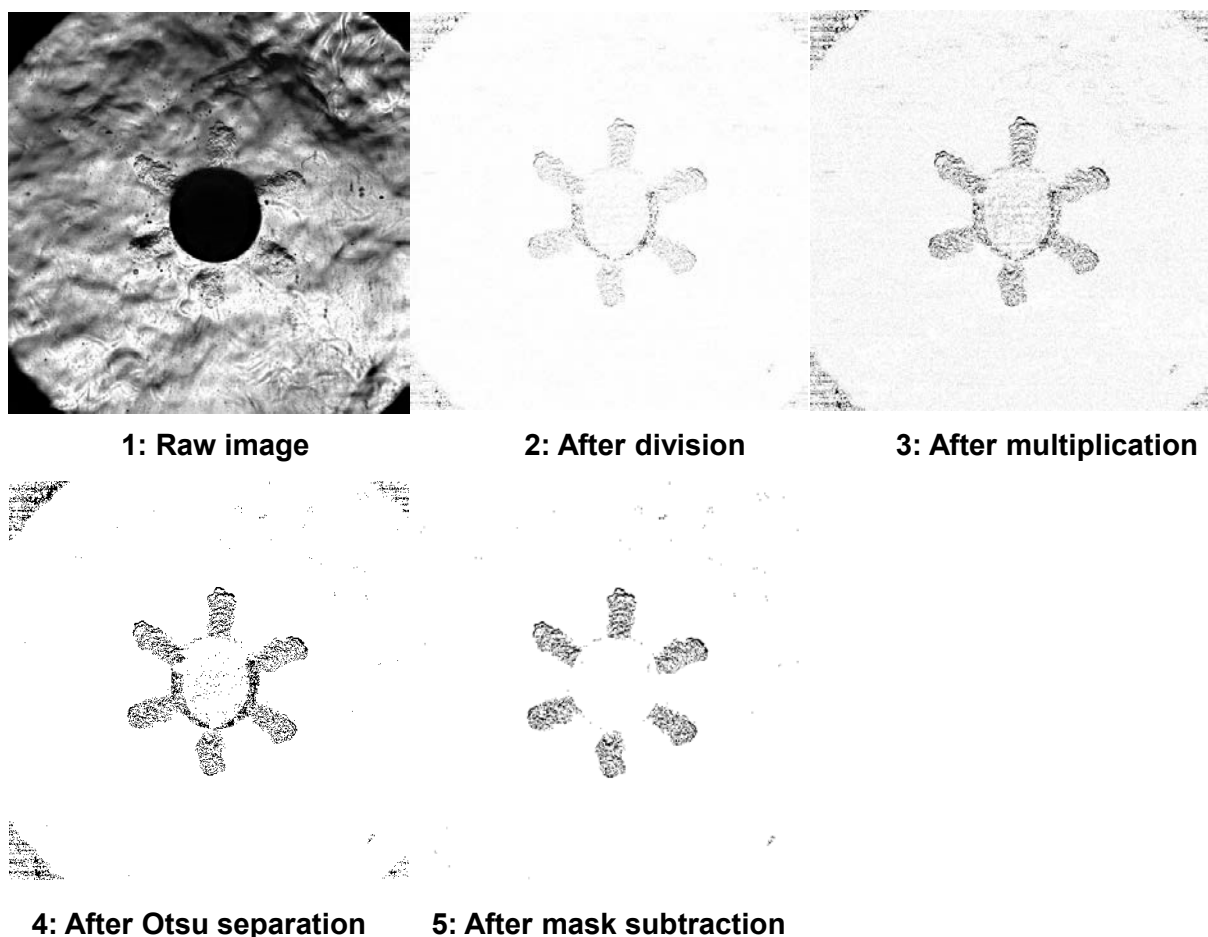
Fig. 6. Partial steps of image processing from the raw image to the result image. Example is VK3 at 10 bar and 200°C

4.3 Results

The following chapter charts the results of the highspeed schlieren images. As parameter for comparison, the penetration depth and the calculated propagation speed of the jet front is used. The values are

processed with the in-house developed MATLAB-based spray evaluation tool "LTT Spray analysis", which determines the mean value from ten successive ignitions with identical boundary conditions. Shot-to-shot variations are addressed in Chapter 4.3.4.

4.3.1 Influence of the pre-chamber geometry

One major question of this work is to evaluate, whether it is possible to use tests in the constant pressure vessel to predict the performance of different pre-chamber geometries in engine operation.

Fig. 7 charts the penetration depth and the propagation speed of the three different investigated pre-chamber geometries. The abscissa depicts the time of the first visible signal leaving the transfer ports. Electrical ignition in the pre-chamber is at -1.25 ms referring to this timescale. This delay is constant for all measurements. The penetration depth over time does not show remarkable differences between the respective geometries. However, the propagation speed is different in the course of the penetration. These diagrams can be compared with Fig. 1, where the geometries are compared in engine operation. Engine operation shows rising combustion speed especially in lean operation from VK4 to VK3 and further to VK1-1. The penetration speed of the respective pre-chamber between 1000 µs and 1500 µs shows the same order of the geometric variants. This leads to the conclusion that, when focusing on the primary reaction, especially a high penetration velocity shortly after the jet exit the pre-chamber is advantageous for the combustion process. This parameter is clearly distinguishable in the highspeed schlieren imaging. Further pre-chamber development based on this primary propagation speed is possible. The generated data in experiments in the constant pressure vessel can predict the engine performance of the investigated pre-chamber.
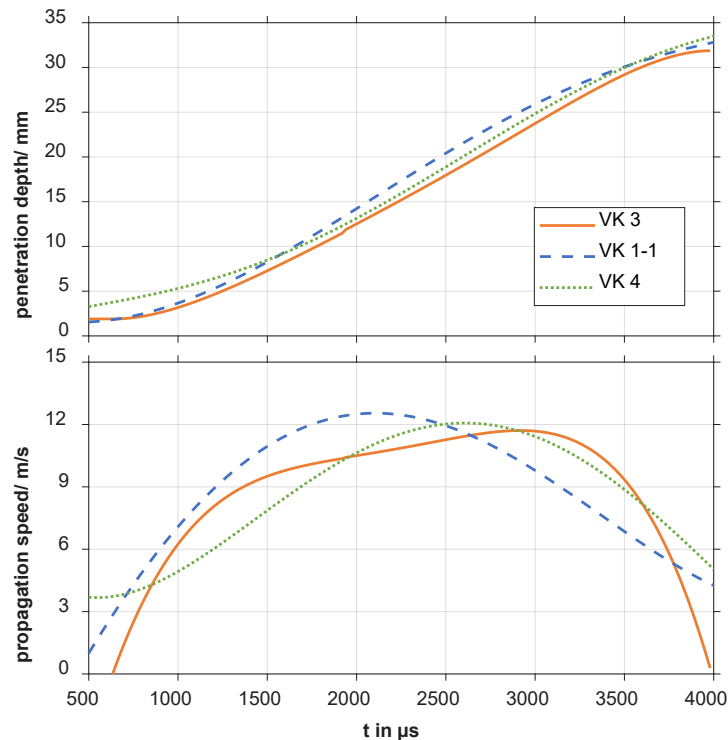
Fig. 7. Penetration depth and propagation speed for three different pre-chamber geometries at 10 bar 200 °C chamber conditions

4.3.2 Influence of the gas temperature in the vessel

One interesting parameter that can be investigated in the constant pressure chamber is the gas temperature inside the vessel. Fig. 8 illustrates the difference between 100 °C, 200 °C and 300 °C at constant 10 bar pressure. In this variation, VK1-1 was used at all temperatures. As expected, the propagation speed rises with higher temperatures. The most significant difference is detected with 300 °C. However, the general behavior, represented by the curvature of both penetration depth and propagation speed is quite the same at all temperatures. Principal statements over the jet propagation can already be done at lower temperatures, which facilitate the image processing.
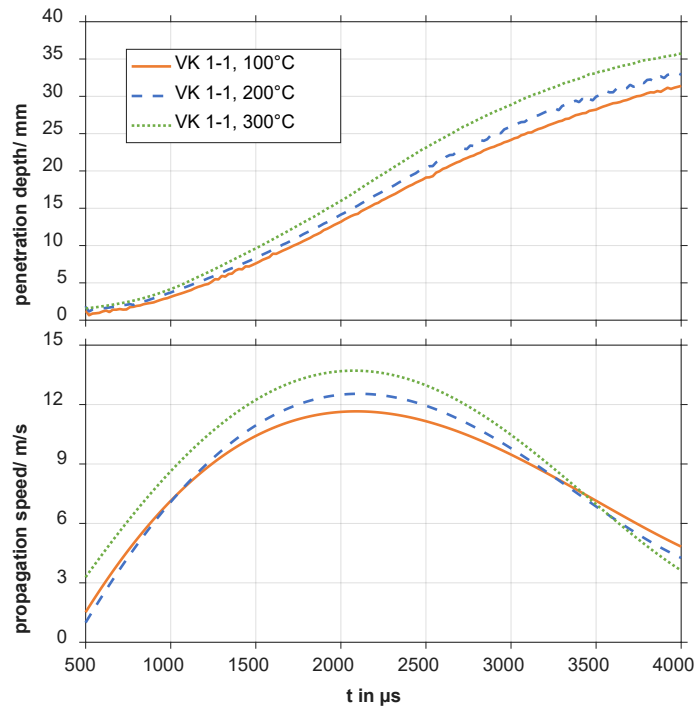
Fig. 8. Penetration depth and propagation speed for three different gas temperatures inside the constant pressure vessel at 10 bar with VK1-1

4.3.3 Influence of the pre-chamber body temperature

Another interesting dependency can be found regarding the flange temperature. The propagation speed is increased significantly in the first section between 500 and 1500 µs. From that time on, the speed is on a similar level for both flange temperatures. Thus, the jets at higher temperature of 90 °C reach around 5 mm more penetration than with 60 °C flange temperature in the corresponding time.

In the last sequence of the ignition, the difference decreases. In general, the behavior is very much alike, the higher temperature leads to a shift towards earlier timings. The maximum propagation
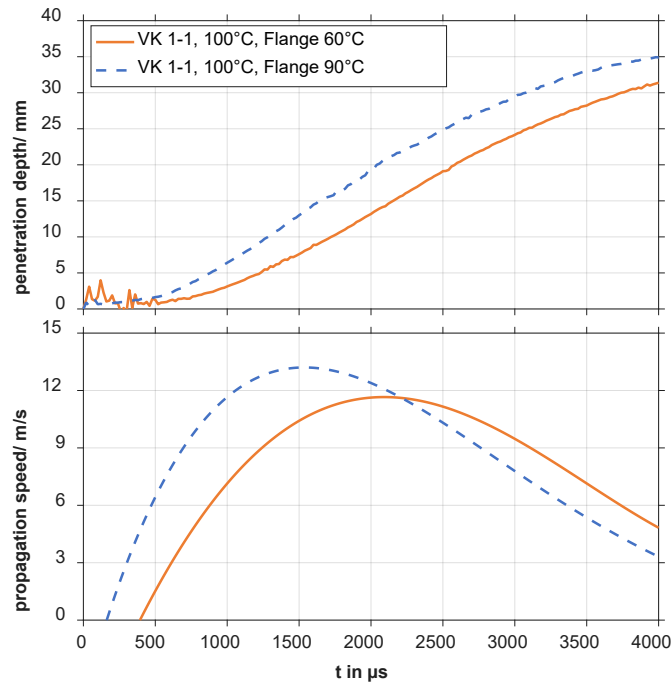
Fig. 9. Penetration depth and propagation speed for two different flange temperatures at 10 bar and 100 °C gas conditions with VK1-1

speed is only 1.5 m/s higher but more than 500 µs earlier. Especially after 1 ms, the time which is most important for the ignition process as shown earlier, the speed is 5 m/s more. It can be concluded that the pre-chamber body temperature has a huge influence on the cylinder ignition, especially with copper as pre-chamber material. However, the shape of the penetration curve remains the same, so if the target of an investigation is to compare for example different pre-chamber geometries, the absolute value of the flange temperature is not highly relevant as long as it is kept constant during the entire investigation.

4.3.4 Shot-to-shot variations

For the evaluation of the calculated penetration values, a closer look into the shot-to-shot variations is recommended. In this investigations, ten consecutive ignition events were evaluated. The previous chapters show the mean value of these ten single shots. In Fig. **10**, all ten recorded ignition events with VK3 at 200 °C gas temperature and 10 bar are compared. For this purpose, the image was extracted from each sequence after 3.4 ms and displayed side by side in the graphic. In addition, the cylinder bore radius of the engine used in chapter 3 and the diameter of the bore of the mirror is shown again. It gets clear, that there are remarkable differences between the single shots. While ignitions 1, 2, 6, 7 and 9 are very similarly developed, ignition 3 shows almost no signal. The latter also shows hardly any signal in the further course of time. In this case, no strong ignition in the pre-chamber has taken place. Ignitions 5, 8 and 10 are not yet developed to the diameter of the bore. Here, a temporal offset results, which shifts the mean value of the propagation towards later times. In contrast to this is ignition 4, which has already clearly exceeded the diameter corresponding to the engine bore. The ignition sequence at this point has been faster.

Resulting of these differences, the reduction of shot to shot variations and their influence on the calculated propagation curve is an important objective of following investigations. The execution of the experiments still offers potential for improved scavenging of the pre-chamber to minimize the influence of the previous shot on the ignition. To extract very bad ignitions like sequence 3, the pressure raise in the pre-chamber can be evaluated in advance and shots with too low signal can be treated separately during the image processing. Additionally, the number of recorded sequences can be increased to get a broader database for statistics. A connection between engine combustion stability and shot-to-shot variations in the chamber experiment is not trivial due to the changes in scavenging and fuelling of the pre-chamber.
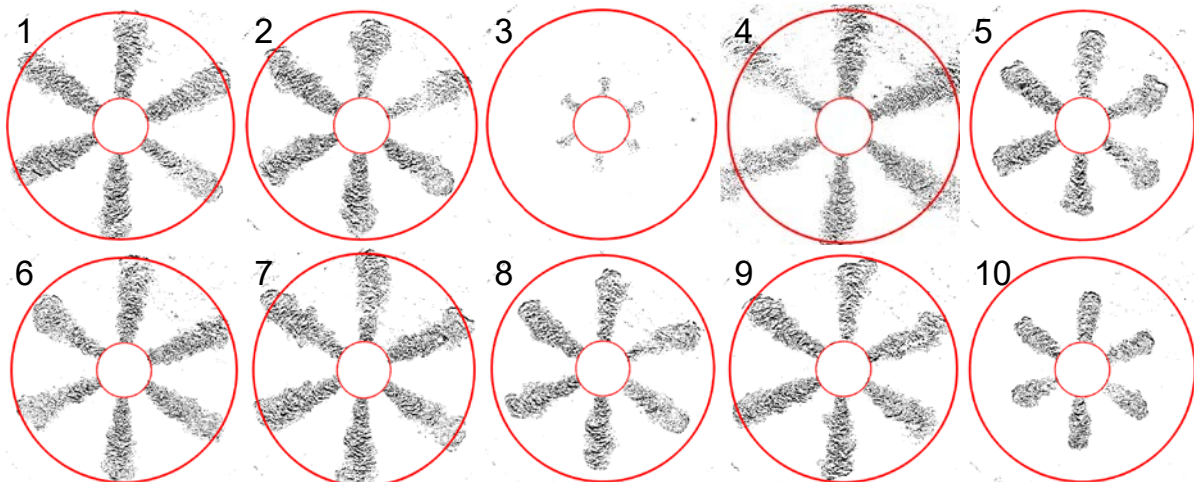
Fig. 10. Images after 3.4 ms of 10 consecutive ignition events with VK3 at 200 °C, 10 bar to illustrate the shot-to-shot variations

5. Conclusions

Active pre-chamber ignition systems can be an enabler for lean combustion processes with increased thermal efficiency and low NO_x emissions. Especially in part load operation, the authors could demonstrate in earlier publications a gain in efficiency of more than 12 % compared to stochiometric operation while keeping the NO_x raw emissions below 20 ppm. For further development of this system, insights into the subsystems are important. The jets emerging from the pre-chamber can be examined in a constant pressure chamber. The latter provides a known environment without the influence of the mixture

in the main combustion chamber. Highspeed schlieren technique enables the evaluation of the jets. In this work, a framerate of 50 kHz results in high temporal resolution. However, due to the low signal to noise ratio, advanced image processing is needed to extract major geometrical parameters from the emerging jets. The measurements showed shot-to-shot variations. A methodic way to reduce this influence can be an increased number of recorded ignitions. The number of ten sequences selected here should be exceeded in future measurements.

A variation of the pre-chamber geometry was evaluated both in engine operation and investigated in the constant pressure chamber. By comparison of these two measurement techniques, the penetration speed of the reactive jets in the sector between 5 mm and 15 mm penetration shows a relation to engine performance in this study. This section of the penetration has major influence on the combustion duration of the entire combustion process in the engine cylinder. The pre-chamber ignition system was evaluated at different gas temperatures and with different flange temperatures to control the temperature of the pre-chamber body. These investigations show faster penetration with increasing temperature, where the body temperature has more influence than the gas temperature. At the same time it could be demonstrated that the general behavior of the penetration is only minor dependent from the temperature, so a comparison of different pre-chamber geometries can be done at reduced ambient temperatures to reduce the background noise.

Optical investigations showed to be a useful tool to improve the understanding of the combustion process. Due to the controlled conditions in the chamber, the primary reaction can be observed in detail. This information is valuable to calibrate simulation models of active pre-chamber combustion processes isolated from the ignition reaction in the cylinder.

Acknowledgements

References

1. J. D. Dale and A. K. Oppenheim, "Enhanced Ignition for I. C. Engines with Premixed Gases," in *SAE International Congress and Exposition*, SAE Technical Paper Series (SAE International, Warrendale, PA, United States, 1981).

2. W. U. Roessler and A. Muraszew, *Evaluation of Prechamber Spark Ignition Engine Concepts. EPA-650/2-75-023* (1975).

3. L. A. Gussak, V. P. Karpov, and Y. V. Tikhonov, "The Application of Lag-Process in Prechamber Engines. SAE Paper 790692," in *Passenger Car Meeting & Exposition*, SAE Technical Paper Series (SAE International, Warrendale, PA, United States, 1979).

4. L. A. Gussak, M. C. Turkish, and D. C. Siegla, "High Chemical Activity of Incomplete Combustion Products and a Method of Prechamber Torch Ignition for Avalanche Activation of Combustion in Internal Combustion Engines. SAE Paper 750890," in *SAE Automobile Engineering and Manufacturing Meeting*, SAE Technical Paper Series (SAE International, Warrendale, PA, United States, 1975).

5. S. Yamaguchi, N. Ohiwa, and T. Hasegawa, "Ignition and burning process in a divided chamber bomb," Combustion and Flame **59**, 177–187 (1985).

6. A. Shah, P. Tunestal, and B. Johansson, "Scalability Aspects of Pre-Chamber Ignition in Heavy Duty Natural Gas Engines. SAE Paper 2016-01-0796," in *SAE 2016 World Congress and Exhibition*, SAE Technical Paper Series (SAE International, Warrendale, PA, United States, 2016).

7. A. Shah, P. Tunestal, and B. Johansson, "Effect of Pre-Chamber Volume and Nozzle Diameter on Pre-Chamber Ignition in Heavy Duty Natural Gas Engines. SAE Paper 2015-01-0867," in *SAE 2015 World Congress & Exhibition*, SAE Technical Paper Series (SAE International, Warrendale, PA, United States, 2015).

8. A. Shah, "Improving the Efficiency of Gas Engines using Pre-chamber Ignition. Doctoral Thesis," (2015).

9. M. Kettner, J. Eichmeier, S. Hensel, and A. Velji, *BPI-Verfahren für Benzin-Direkteinspritzung II. Abschlussbericht* (2007).

10. W. P. Attard and H. Blaxill, *A Lean Burn Gasoline Fueled Pre-Chamber Jet Ignition Combustion System Achieving High Efficiency and Low NOx at Part Load. SAE Paper 2012-01-1146* (SAE International, 2012).

11. W. P. Attard and H. Blaxill, *A Gasoline Fueled Pre-Chamber Jet Ignition Combustion System at Unthrottled Conditions. SAE Paper 2012-01-0386* (SAE International, 2012).

12. W. P. Attard and H. Blaxill, *A Single Fuel Pre-Chamber Jet Ignition Powertrain Achieving High Load, High Efficiency and Near Zero NOx Emissions. SAE Paper 2011-01-2023* (SAE International, 2011).

13. E. Toulson, H. C. Watson, and W. P. Attard, "Gas Assisted Jet Ignition of Ultra-Lean LPG in a Spark Ignition Engine. SAE Paper 2009-01-0506," in *SAE World Congress & Exhibition*, SAE Technical Paper Series (SAE International, Warrendale, PA, United States, 2009).

14. E. Toulson, H. C. Watson, and W. P. Attard, "The Effects of Hot and Cool EGR with Hydrogen Assisted Jet Ignition. SAE Paper 2007-01-3627," in *Asia Pacific Automotive Engineering Conference*, SAE Technical Paper Series (SAE International, Warrendale, PA, United States, 2007).

15. M. Sens, E. Binder, A. Benz, L. Krämer, K. Blumenröder, and M. Schultalbers, "Pre-Chamber Ignition as a Key Technology for Highly Efficient SI Engines – New Approaches and Operating Strategies," in *39. Internationales Wiener Motorensymposium 2018* .

16. A. Stadler, M. Wessoly, S. Blochum, M. Härtl, and G. Wachtmeister, "Gasoline Fueled Pre-Chamber Ignition System for a Light-Duty Passenger Car Engine with Extended Lean Limit," SAE Int. J. Engines **12**, 323–339 (2019).

17. M. Schumacher and M. Wensing, "A Gasoline Fuelled Pre-Chamber Ignition System for Homogeneous Lean Combustion Processes," in *SAE 2016 International Powertrains, Fuels & Lubricants Meeting*, SAE Technical Paper Series (SAE International, Warrendale, PA, United States, 2016).

18. M. Schumacher, T. Russwurm, and M. Wensing, "Pre-chamber Ignition System for Homogeneous Lean Combustion Processes with Active Fuelling by Volatile Fuel Components," in *Ignition Systems for Gasoline Engines* (expert, 2018), pp. 292–310.

19. T. Russwurm, M. Schumacher, and M. Wensing, "Pre-chamber Ignition system for Homogenous Lean Combustion Processes with Active Fuelling by Volatile Fuel Components," in *Motorische Verbrennung und alternative Antriebskonzepte. Aktuelle Probleme und moderne Lösungsansätze (XIV. Tagung) : Tagung des Haus der Technik e.V. Essen, 13.-14. März 2019*, Berichte zur Energie- und Verfahrenstechnik BEV (2019), pp. 275–286.

20. M. Schumacher, Verfahren zum Betrieb eines Verbrennungsmotorsystems und Verbrennungsmotorsystem, DE: 10 2019 210 069.4 .

21. M. Schumacher, Verfahren zum Betrieb eines Verbrennungsmotorsystems für ein Kraftfahrzeug und Verbrennungsmotorsystem für ein Kraftfahrzeug, DE: 10 2016 219 875.0 .

22. S. Riess, L. Weiss, A. Peter, J. Rezaei, and M. Wensing, "Air entrainment and mixture distribution in Diesel sprays investigated by optical measurement techniques," International Journal of Engine Research **19**, 120–133 (2018).

23. G. S. Settles, *Schlieren and shadowgraph techniques. Visualizing phenomena in transparent media*, Softcover reprint of the hardcover 1st edition 2001 (Springer, 2001).

24. N. Otsu, "A Threshold Selection Method from Gray-Level Histograms," IEEE Transactions on Systems, Man, and Cybernetics, 62–66 (1979).

CFD Simulation-based Predesign of an Advanced Gas-diesel Combustion Concept

H. Winter[1], K. Aßmus[1], C. Redtenbacher[1], D. Dimitrov[1], A. Wimmer[1,2]

[1] LEC GmbH, Inffeldgasse 19, Graz, Austria.

E-mail: hubert.winter@lec.tugraz.at
Telephone: +(43) 316 873-30145

[2] Institute of Internal Combustion Engines and Thermodynamics, Inffeldgasse 19, Graz University of Technology, Graz, Austria

E-mail: wimmer@ivt.tugraz.at
Telephone: +(43) 316 873-30001

Abstract. The greenhouse gas saving potential of using gaseous fuels with high methane content (e.g., natural gas) in internal combustion engines instead of conventional liquid fossil fuels is considerable due to the comparatively low emission of carbon dioxide. However, to fully exploit this potential, it is of utmost importance to keep methane slip at a very low level. In contrast to mixture aspirated gas engines and diesel-gas engines, the gas-diesel combustion concept provides the opportunity to avoid methane slip nearly completely since the gaseous fuel is directly injected into the combustion chamber at the end of the high-pressure phase of the engine cycle, resulting in mixing-controlled combustion with low emission of unburned hydrocarbons.

LEC GmbH has developed an advanced high-speed large engine concept based on the gas-diesel combustion process. An effective and reliable virtual design methodology was applied for the concept development. The methodology comprehensively combines 3D CFD and 1D simulation tools for the combustion concept predesign with experiments on a single-cylinder research engine for the concept validation. A major challenge in the virtual design of this dual fuel combustion process is the large number of degrees of freedom that result in particular from the use of a fully flexible combined gas/diesel injector. This paper describes in detail the role of 3D CFD simulation in this approach, which allows precise prediction of the optimal geometries and operating strategies for high-efficiency and low-emission engine operation.

Notation

BMEP	*Brake Mean Effective Pressure*
CA	*Crank angle*
CFD	*Computational Fluid Dynamics*
CNG	*Compressed Natural Gas*
CR	*Compression Ratio*
DOI	*Duration of Injection*
EAR	*Excess Air Ratio*
ECFM	*Extended Coherent Flame Model*
ECFM-3Z	*Extended Coherent Flame Model - 3 Zones*
FEP	*Fame Engine Plus*
FMEP	*Friction Mean Effec tive Pressure*
GSTB	*Linear solver type*
HRR	*Heat Release Rate*
LEC IRAS	*LEC Injection Rate Analysis System*
MCE	*Multi-cylinder Engine*
PDF	*Probability Density Function*
SCE	*Single-cylinder Engine*
SOI	*Start of Injection*

1. Introduction

Fuel properties have a significant influence on the characteristics of the combustion process within an internal combustion engine as well as on the resulting emissions and thus directly on the environment. The use of gaseous fuels with a high methane content (e.g., natural gas) instead of conventional liquid fossil fuels results in comparatively low CO_2 emissions (cf. [5] [7] [22]), making it possible to reduce significant greenhouse gas emissions from a global perspective.

Monovalent gas engines and diesel-gas engines that follow the Otto principle are attractive solutions that exploit this potential. They are well known for their beneficial particulate and nitrogen oxide emission behavior at high efficiency, cf. [21] [22]. However, these quantity-controlled combustion concepts are operated with external mixture formation and are therefore conceptually prone to knocking combustion. Thus, they react very sensitively to changes in the methane number and they inevitably emit a small amount of unburned methane, which contributes to the greenhouse gas effect.

Gas-diesel engines [15] based on the diesel cycle directly inject the gaseous fuel into the combustion chamber during the high-pressure phase of the engine cycle. Ignition is triggered by the injection of a small amount of diesel fuel. With optimal design of this combustion process, the emission of partly burned and unburned hydrocarbons can be almost completely avoided. Due to the knock resistance of the gas-diesel combustion concept, low-quality gases can be used at high compression ratios and therefore with high thermal efficiency combined with remarkable transient operation behavior, cf. [19]. If gases with low methane numbers that are currently being flared or gases from regenerative sources are exploited, the additional greenhouse gas saving potential is enormous and would result in an economic advantage, cf. [1] [10] [12] [17] [24].

These advantages combined with the expansion of the gas infrastructure and technological progress have recently led to an increased utilization of the gas-diesel combustion process in various applications in the medium-speed and low-speed large engine sector, cf. [9] [11] [14]. However, the application of the gas-diesel combustion process in a large high-speed engine is a challenge in terms of fuel injection, as two diesel injectors have to be accommodated in the cylinder head where space is limited. Thus, Woodward L'Orange GmbH has developed an advanced high-pressure gas-diesel injector in one housing that can be installed compactly in a thermodynamically favorable position in the center of the cylinder head, cf. [3] [4] [19] [25].

At LEC GmbH, an advanced high-speed gas-diesel combustion concept based on this new injector technology was developed for a large engine with a displacement of ≈ 6 dm³. An effective and reliable virtual design methodology was applied for the concept development. The methodology comprehensively combines 3D CFD and 1D simulation tools for the combustion concept predesign with experiments on a single-cylinder research engine (SCE) for the concept validation. A major challenge in the virtual design of the dual fuel combustion process is the large number of degrees of freedom that result in particular from the use of the fully flexible gas/diesel injector. Furthermore, the optimal interaction of the injection jets with the piston bowl is critical in order to achieve a minimum emission level.

The applied virtual design methodology was introduced in [3]. An overview was given of the roles of 3D CFD and 1D simulation and the interaction between the simulation tools and the test facilities was described. Selected results of measures for minimizing the emissions of CH_4 and CO while increasing efficiency were discussed. Building upon the information in [3], this paper describes in detail the role of 3D CFD simulation in the approach, which can be seen as the essential basis for precise predesign of the geometries and operating strategies for high-efficiency and low-emission engine operation.

2. Virtual Design Methodology

This section provides an overview of the requirements and boundary conditions for developing the gas-diesel combustion concept in the virtual design process. The interaction of the applied development tools is summarized and the setup of the 3D CFD model is explained in detail. Furthermore, the simulation concept including the defined assessment criteria is discussed.

2.1 Requirements and boundary conditions

The main objective in the design of the gas-diesel combustion process was to achieve minimal emissions, especially a very low level of climate-relevant CH_4 emissions, while keeping fuel consumption low. The development was based on an existing high-speed engine platform with a displacement of

≈ 6 dm³.   Table *1* summarizes the engine-related specifications that define the boundary conditions for the development process. The investigation focused on the engine operating point at the nominal speed of 1500 rpm and the nominal brake mean effective pressure (BMEP) of 22 bar. Compression ratio (CR) and valve timing were transferred from experiences with diesel combustion concepts and set constant for the investigations with the gas-diesel concept.

Table 1: Engine-related specifications

Nominal speed	1500 rpm
Nominal BMEP	22 bar
Displacement	≈ 6 dm³
Compression ratio	16:1
Number of inlet/exhaust valves	2/2
Valve timing	Moderate Miller intake valve timing
Swirl/tumble	≈ 0/0

Further boundary conditions are associated with the use of a combined gas-diesel injector from Woodward L'Orange GmbH. As described in more detail in [19] and [25], with this multi-needle injector technology, diesel fuel and gaseous fuel are able to be injected flexibly and independently of each other. On the diesel side, the injector is equipped with the tried and tested wide range injector technology, which allows energetic diesel fractions of 1 – 100% in full load operation, cf. [13] [20]. Although the injector design provides great flexibility for the layout of the diesel and gas nozzles, the design of the gas path, which is equipped with three simultaneously controlled gas needles, restricts the possible number of gas nozzle holes. With the triangular mounting sleeve contour design, either three, six, or nine gas nozzle holes can be arranged in a suitable way, whereby the nine-hole design has proven to be advantageous with regard to efficiency and emissions in the investigations of a high-speed gas-diesel concept in [3] and [19]. Fig. *1* provides an overview of the possible arrangements of the gas nozzle holes, which are positioned around the diesel nozzle.
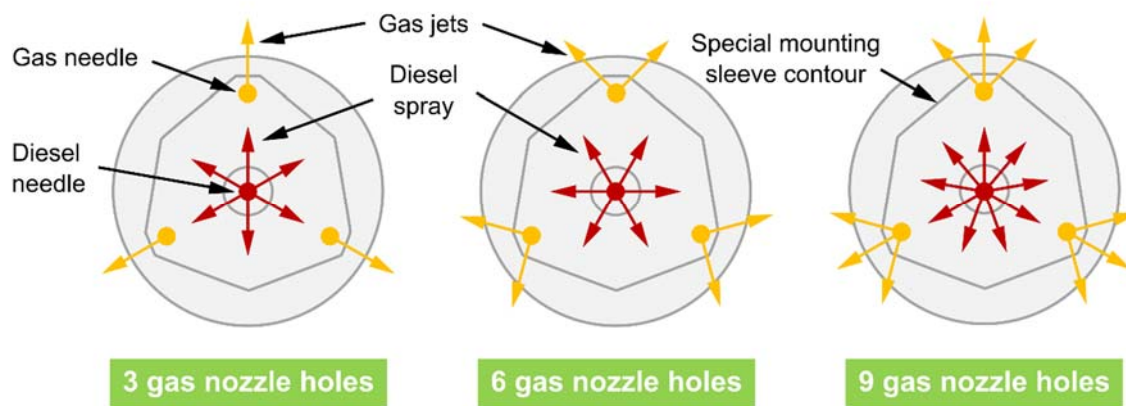
Fig. 1. Schematic illustration of injector design variants with 3, 6, and 9 gas nozzle holes (bottom view)

In all the investigations performed, the gas nozzle and the diesel nozzle are each equipped with the same number of nozzle holes (six or nine). The following Table 2 summarizes additional boundary conditions and limitations related to the gas-diesel injector.

Table 2. Gas-diesel injector boundary conditions

	Gas nozzle	*Diesel nozzle*
Amount of nozzle holes	3/6/9	6–10
Diameter of nozzle holes	basis ± 0.2 mm	basis ± 0.07 mm
Nozzle hole orientation angle	basis ± 15°	basis ± 7.5°
Injection pressures	Up to 600 bar (CNG)	Up to 2200 bar

2.2 Overall simulation approach

In [3], the roles and the interaction of the simulation tools in the virtual design methodology were discussed in detail. This section provides a compact summary of them.

Comprehensive 3D CFD simulation-based investigations of combustion chamber and nozzle geometries as well as injection strategies were performed to optimize the high-pressure phase of the gas-diesel combustion concept. Especially the two high-pressure injections of diesel pilot and gas became accessible for detailed CFD investigations of the phenomena of mixture formation, ignition, and combustion. Since only the high-pressure phase was investigated in detail using 3D CFD simulation, further boundary conditions such as gas injection rate profile, boost pressure, or exhaust gas back pressure initially remain unspecified. Several initial assumptions were made which were then modified in combination with multiple 1D simulations. Besides this aspect, the possibility to enhance the accuracy of the 3D CFD simulation process values at the beginning and at the end of the calculation makes the 1D simulation an important complementary tool in this simulation approach. As described in detail in [3], conditions such as boost pressure or exhaust gas back pressure were calculated alongside further engine performance data with a 1D simulation model of a multi-cylinder gas-diesel engine (MCE) equipped with one-stage turbocharging. In addition, a 1D sub model rendered the newly developed high-pressure gas supply system as well as the gas path inside the injector accessible for gas supply pre-design studies. For the calibration of the injector model, injection rates measured by the manufacturer were available. Hence, a more realistic injection rate profile than the trapezoidal gas injection rate initially assumed in the CFD simulation model was made accessible for further 3D CFD simulations.

Based on each current simulation model design and boundary condition status, the 3D CFD simulation provided heat release rates (HRR) and pollutant compositions like mass fractions of CH_4, CO and NO as an input for the 1D simulation with a 1D MCE model, cf. [3]. Based on this information, the 1D MCE model was able to determine key values like the initial and final condition in the combustion chamber, the injection rates for diesel and gas as well as the expected excess air ratio (EAR) for the desired indicated mean effective pressure. Followed up by an iterative process with two to three data exchanges between 3D CFD and 1D simulation, the boundary conditions of both simulation tools were able to be successfully aligned with each other. In the 1D MCE model, a gas injector and a diesel injector were modeled for each cylinder to consider the cylinder charge increase due to the injected fuel during the high-pressure phase of the combustion process. The NO_x concentration in the cylinder was calculated with a separate model using an extended Zeldovich mechanism, cf. [16]. A two-zone combustion model provided the temperature of the burned zone for simulation of post-flame reactions, cf. [18]. For an accurate estimate of overall engine efficiency and specific emission values, the corresponding 3D CFD results were transferred to the 1D model.

Finally, the validation of the simulation results was performed by a twofold experimental approach, cf. [19]. First, the injector was thoroughly investigated on the LEC injection rate analysis system (LEC IRAS) to determine the gas injection behavior. Second, SCE testing was successfully carried out to validate the injector under operational conditions as discussed in detail in [3] and [19].

2.3 Setup of the 3D CFD model

A detailed analysis of the gas-diesel combustion process requires a well-considered setup of the simulation model. The following section outlines the selection of suitable models used, cake sizes, grid, and topology in more detail. Fig. *2* provides an example of the fuel injection modeling of a 40° cake of the combustion chamber. The gas supply including the gas nozzle was depicted in three dimensions. At the position of the gas valve, the gas mass flow was provided as a mass flow boundary condition received
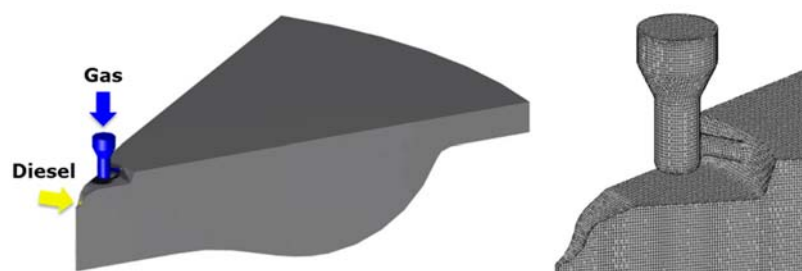
Fig. 2. Fuel injection modeling with a 40° cake model of the combustion chamber

from a 1D submodel. The size and shape of the dead volume behind the gas valve was mapped as realistically as possible in coordination with the injector manufacturer and in combination with the 1D model. As the project progressed, the size was successively reduced, which is important for reducing HC and CO emissions, cf. [3]. The diesel pilot spray was depicted with the implemented AVL FIRE spray module [2]. The main models are the Lagrangian particle tracking model, the Dukowicz [6] evaporation model, and the Wave breakup model [23].

2.3.1 Selection of a suitable combustion model

In an earlier diploma thesis [8], different combustion models were examined for their principle suitability for dual fuel combustion. Based on these results, a preliminary study was performed to investigate the suitability of common combustion models available in FIRE (extended coherent flame model (ECFM), three-zone extended coherent flame model (ECFM-3Z), multi-scalar probability density function model (PDF), cf. [2]) for high-pressure gas injection. In principle, the PDF model and the ECFM model cannot handle the two different fuels diesel and methane. However, the ECFM model provides the option of replacing the diesel pilot with methane in the event of small pilot quantities and converting the material values accordingly to represent a dual fuel system. In the test, it was not possible to ignite the gas jet with the pilot under realistic combustion chamber temperatures. The ECFM-3Z model can deal with the two fuels but has problems with high injection pressures and crashed easily when the gas jets started burning. Even if both the combustion model itself and flow-mechanical aspects can be considered as the cause of the crash, this was not further investigated within the scope of this work and the investigations with this combustion model were discontinued. The most promising choice was the detailed chemistry approach. In contrast to the other models, this model can handle the high-pressure conditions as well as the interaction between the two fuels. It should be noted that the linear GSTP solver was used for all equations of this model. In addition, central differencing for momentum and continuity and upwind for turbulence and energy were applied as discretization schemes, while during the compression phase a constant time step of 0.5 °CA and during the combustion phase a time step of 0.1 °CA was investigated. Table 3 briefly summarizes the results of the model selection process.

Table 3. Suitable combustion models

	ECFM	ECFM-3Z	PDF	Detailed Chemistry
Dual fuel	no	yes	no	yes
Inflammation	for pilot share <1%	yes	no	yes
Combustion	not for realistic temperatures	unstable	no	yes

To ensure that the diesel pilot ignites correctly under the prevailing conditions, the model was validated on the basis of a constant pressure combustion chamber as well as measurements on the SCE in monovalent diesel operation, cf. [13]. Based on the general gas phase reactions module, a mechanism developed by the Engine Research Center at the University of Wisconsin was used (29 species, 52 reactions), cf. [2]. Since this is a highly reduced mechanism, the computing times were reduced to a tolerable level. Thus, a large number of variations were able to be carried out using cake models as discussed in the next subsection. Since NO formation is not included in this mechanism, a separate model was used for its calculation: the Heywood NO model, cf. [2]. The CH_4 and CO emissions were taken directly from the reaction mechanism. The turbulence model was the k zeta-f model, cf. [2].

2.3.2 Models applied (cake sizes), grid, and topology

Different models were applied during the development process; all of them are designed as moving grids to represent the piston movement and shown in Fig. *3* in top dead center (TDC) position. The use of cake models serves to minimize the computing time. Depending on the requirements of the specific tasks, different cake sizes but also a model of the entire combustion chamber were used. The selection of the cake sizes correlates with the nozzle hole arrangements of the gas-diesel injector. Since the gaseous fuel is ignited by a small amount of diesel fuel, the simulation model has to be able to represent two different fuels that interact within the combustion chamber. The high-pressure gradients during gas injection create an additional challenge that the combustion model must manage. The number of mesh cells in the different models range from 0.6 million (40° model) to 2.8 million (360° model).

Fig. 3. Optimization task-specific cake models

The interaction between only one gas jet and one diesel spray was investigated with a 40° cake model for a 9-hole gas nozzle and a 60° cake model for a 6-hole gas nozzle (cf. Fig. **3**, left). Thus, it was possible to determine fundamental influences from the vertical orientation of the jets to each other with regard to optimal ignition of the gas jet. In addition, initial estimates of the required hole diameters, the interaction of the gas jet with the piston geometry, and possible injection strategies were obtained. These models were essentially based on a hexahedral topology with orthogonal orientation and alignment of the middle meridian plane in which the two nozzles were located. These models were created with the automatic mesh generator Fame Engine Plus (FEP) [2] and executed with a boundary layer to better describe the wall heat transfer which is based on the standard wall function model. To evaluate the overall interaction between different aligned diesel and gas jet groups (cf. [3]), the model was extended to a 120° cake. As a result, it became possible to investigate the influence of the horizontal orientation of all jets and to determine suitable diesel and gas nozzle diameters. In this case, the simple orthogonal cell topology as used for the 40° and 60° cake models was no longer sufficient. Therefore, a hybrid topology was used. The area directly adjacent to the injector was created in accordance to the simple orthogonal cell topology with the automatic grid generator FEP. The remaining area was covered with a rotationally symmetric topology that takes the orientation of the gas jets into account. The two model parts are connected at an ellipsoid surface with Hybrid Connect [2]. Fig. **4** shows the difference between the two cell topologies using the example of the 120° cake model.
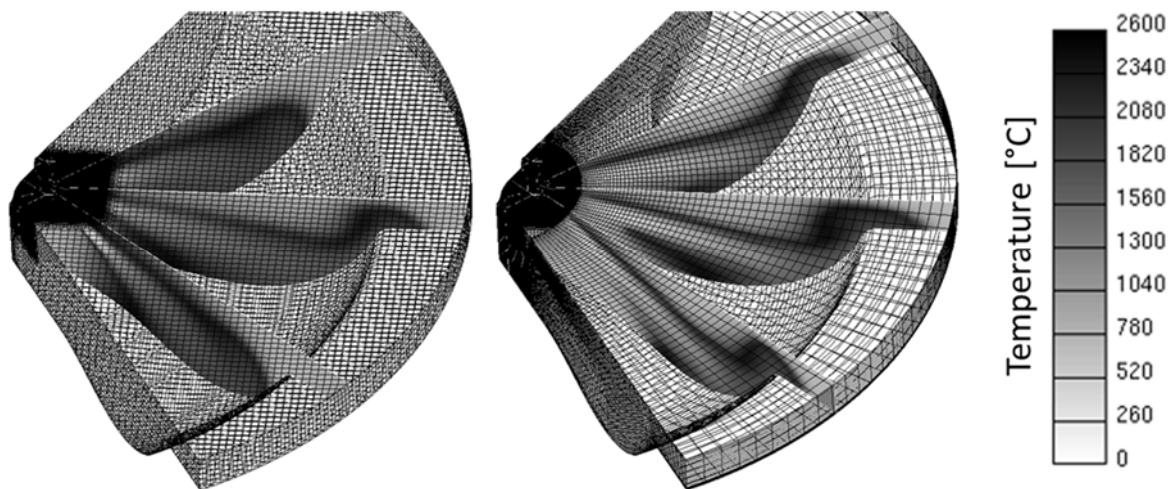
Fig. 4. Comparison of a simple orthogonal cell topology (left) and a rotationally symmetric mesh cell topology (right): example result for temperature gradients during gas-diesel combustion

The mesh on the left was created with the same method as for the 40°/60° cake models. The mesh on the right is from the hybrid model. At the ellipsoidal interface, the topology of the hybrid grid changes to a rotationally symmetric topology. In vertical direction the grid was kept fixed until just below the injector tip, so that the injection was not affected by the grid movement. In the area of the piston some layers were left equidistant and moved as a whole. In the remaining volume between injector and piston, the buffer layer was designed as a moving part. In addition, three meridian sections through the gas nozzle axis are shown. Here the temperatures after the start of combustion are depicted. A comparison of the temperature simulation results from both grid topologies also indicates a greatly reduced penetration depth if the jet flow direction is not orthogonal to the mesh cells, as shown on the left side of Fig. **4**. The result generated with the rotationally symmetric mesh cell topology (Fig. **4** right) shows a more realistic jet penetration characteristic. The difference between the results of both cell topologies is caused by cross diffusion. In contrast with the hybrid grid, all jets are evenly distributed regardless of their orientation. In order to investigate the influence of the symmetry boundary conditions

that apply to the cake models, a 360° model was created that employs a hybrid mesh similar to the one in the 120° cake model.

2.4 Simulation concept and assessment criteria

The following methodology and assessment criteria were defined in order to simulate the combustion process according to the engine and injector-related boundary conditions described in section 2.1. At the beginning, some additional assumptions like BMEP, CR, or Diesel pilot fraction had to be made since there were no empirical values available for this type of combustion process in this engine size. This was necessary in order to complete the list of required boundary conditions for the simulation model so that it worked within the desired load range. Building upon this baseline setup, several simulative parameter studies were carried out. To assess the simulation results, only relative comparisons were made and trend statements were derived.

At the point where the gas valve is positioned (cf. Fig. *2*), a mass flow boundary condition was specified. In comparison to a pressure boundary condition, this is more stable on the one hand and easier to handle on the other hand. At the beginning, trapezoidal injection rate curves were used. These were later replaced by gradients from the 1D submodel. To evaluate the gas rail pressure, the calculated maximum pressure at the boundary condition was determined. Since only the high-pressure cycle was calculated with 3D CFD, the integral of p*dV in this crank angle range was used to pre-assess engine efficiency. To ensure operation within the engine peak pressure limits, the peak pressure of the combustion process can easily be determined by 3D CFD simulation. Since the combustion process interacts closely with the injector geometry and injection strategy as well as with the shape of the combustion chamber, the simulated flame propagation was considered in relation to the average rate of heat release and exhaust gas species. CH_4, CO, and NO were determined at the end of the calculation and provide information about the quality of the combustion process. After the basic injection strategy, the beneficial diesel amount and a basic geometric concept for the injector were set. Several simulations with different injection timings were carried out for each variant. The above-mentioned values were displayed in NO fraction trade-offs to evaluate the combustion concept. Thus, relative comparisons between the simulation results could be made.

3. 3D CFD-based combustion concept optimization

The 3D CFD-based combustion concept optimization process was a highly comprehensive task which will be discussed in two subsections: one on the investigation of the ignition process and one on the investigation of the main combustion process. In the gas-diesel combustion concept, the ignition of the gas mixture is triggered by diesel pilot combustion. The aim is to ensure stable ignition of the gas with the smallest possible amount of diesel. In addition, reliable ignition should be ensured over a wide range of operating points. Starting at ignition, the flame front should spread as quickly and evenly as possible across the gas jets. The combustion characteristic highly depends on the type of combustion strategy. In principle, two main strategies were investigated on the LEC: diesel injection before gas injection and vice versa.

3.1 Investigation of the ignition process

In this section, the basic design of the combustion concept with regard to the injection strategy is first determined and from this the basic injection timings and injection durations are preselected. After the basic strategy is chosen, the possibilities for igniting the gas jet with the burning pilot diesel spray are examined both geometrically and with regard to the time sequence. The main focus is on the orientation of the gas jet and diesel spray angles relative to each other primarily in the vicinity of the injector during ignition and in the first phase of combustion in the free area, where the jets are still hardly influenced by the piston geometry. In addition, the share of diesel required for stable ignition is already determined here. The optimum diesel share that was found was kept constant for all the following investigations.

3.1.1 Sequence of gas and diesel injections

In principle, the hardware used allows both fuels to be injected independently of each other. In the following, two sequences are discussed in detail. In the case that the gas injection starts before the

diesel pilot injection, the injected gas has the opportunity and time to mix with hot air of the combustion chamber before it is ignited by the diesel spray (hereafter *Sequence 1*). Thus, a significant amount of gas is premixed before ignition occurs. Another possibility is to inject the gas after starting the diesel pilot injection, i.e. the gas jet is ignited by the more or less burned diesel spray (called *Sequence 2*). There is less of an opportunity for the gas jet to premix with the compressed air inside of the combustion chamber. In this case the subsequent fuel conversion is expected to be more similar to the diesel combustion process and will occur in a large extent in a mixture-controlled combustion.

Sequence 1. Initially a 60° cake model with a flat piston was used. The compression ratio was assumed to be 16:1 and an EAR of 2 was chosen while the energetic diesel fraction was assumed to be 5%. The qualitative injection curve of the diesel was derived from an existing diesel engine. For the gas mass flow, trapezoidal curves with an injection duration (DOI) of 60° crank angle were assumed, which were shifted in time by degrees crank angle. The absolute fuel quantities were estimated based on an existing gas engine with the desired nominal load. The left-hand side of Fig. *5* shows three shifted gas mass flow curves over the crank angle as well as the mass flow curve of the injected diesel fuel. Start of injection (SOI) for gas is from a base variant shifted by +/- 10 °CA. SOI for diesel is constantly 30 °CA after SOI for gas of the base variant. The graph on the right depicts the corresponding cylinder pressure curves. As also mentioned by Takasaki et al. in [26], earlier gas injection leads to a more pronounced premixing of the cylinder charge and a more significant increase in cylinder pressure. A high level of nitrogen oxides and an increased tendency to knocking combustion would also result from this strategy. As a consequence, a reduced compression ratio becomes necessary which results in a poorer diesel pilot atomization and an unexploited efficiency potential.
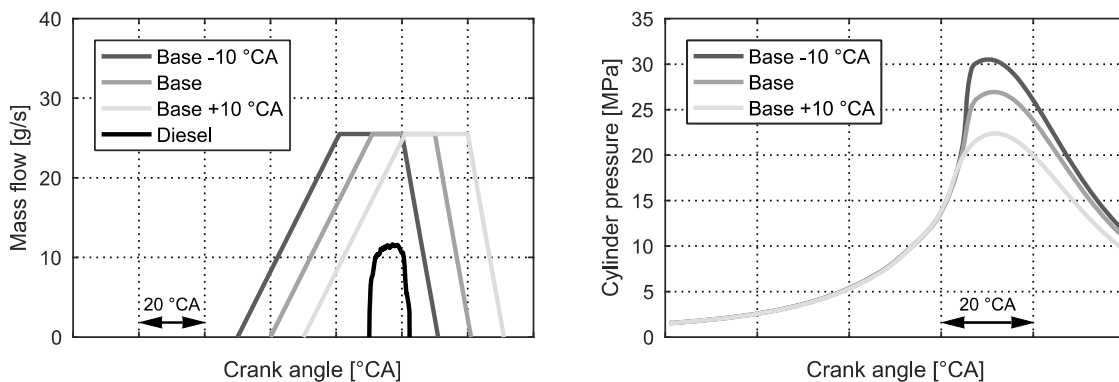
Fig. 5. Gas and diesel injection rates (left) and corresponding cylinder pressures (right) for sequence 1

The results have also revealed that a flat piston has an unfavorable effect on flame propagation in the vicinity of the liner. In addition, the mixture formation of the gas is unfavorable for later injection. Since an improvement in mixture formation can be achieved with 9 jets compared to 6 jets, the next investigations were carried out with 9 jets. Therefore, a 40° model corresponding to nine nozzle holes was used for the next variants, and a moderate piston bowl [3] replaced the flat piston.

Sequence 2. Starts the gas injection closer to the start of diesel injection as shown in Fig. *6* (left), combustion at a significantly lower pressure level becomes possible. Therein the mass flow boundary conditions for a 40° cake model with a moderate piston bowl are shown analogous to sequence 1. The pilot diesel fraction remained at 5%, but the injection time was reduced to less than 2.5 °CA to correspond to more recent data from the injector manufacturer. As the exact lift curve was in the initial phase of the project unknown, a trapezoidal curve was assumed for the diesel injection rate, too. SOI for the gas was starting from a base version by +4 °CA and -2 °CA. DOI of gas injection was reduced to approx. 30 °CA. Here again, the observations coincide with those in [26] and shows a way smoother combustion in Fig. *6* (right) without any proneness to knocking combustion.
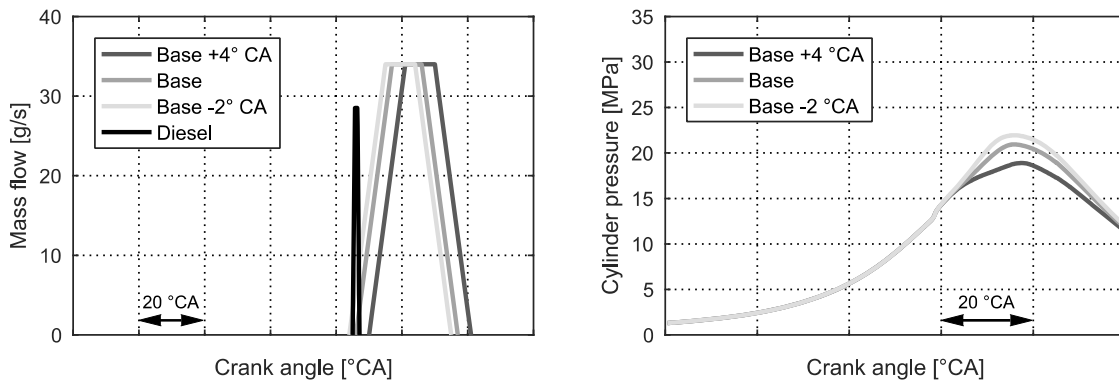
Fig. 6. Gas and diesel injection rates (left) and corresponding cylinder pressures (right) for sequence 2

Affected by the injection sequence a small pressure increase is visible in the rising flank of the cylinder pressure plot which is triggered by the diesel pilot combustion. Afterwards the main combustion of the subsequently injected gas occurs at a significantly lower pressure and temperature level as at sequence 1. Consequently, this strategy seems to be more feasible to keep the engine out NO_x emissions on a lower level than sequence 1. In addition, the peak pressure can also be kept within the defined pressure limit while maintaining the chosen compression ratio. All in all, sequence 2 was favored and investigated further.

3.1.2 Relative orientation of gas and diesel spray angles

All subsequent discussed investigations were based on the 120° cake model, which allows the interactions between adjacent gas jets and diesel sprays to be observed. Fig. *7* and Fig. *8* provide an overview of these activities. On the left of Fig. *7*, the 120° cake model is presented schematically from above with the kind of alignment of the diesel and gas jets of a 9-nozzle injector. The dotted white lines represent the gas jets while the solid lines represent the diesel jets. The black lines indicate that the diesel spray alignment is the same as of the gas jet (aligned). The grey lines show the orientation of diesel jets that are positioned between the gas jets (displaced). The graph on the right shows the simulated, normalized rates of heat release (SOI for diesel was 2 °CA earlier than SOI for gas). When the diesel pilot spray axis is located between the axis of the gas jets, the ignition delay increases because the diesel flames must first spread in the direction of the gas jet. In the event that the diesel spray axis and the gas jet axis are aligned, combustion occurs much earlier. Thus, the injection of the diesel pilot spray can occur later and at a higher temperature so better conditioning is possible. With regard to the emissions, a key fact of our assessment criteria, the aligned variant shows less occurrence of HC and NO emission. Therefore, all further investigations were carried out with an aligned setup.
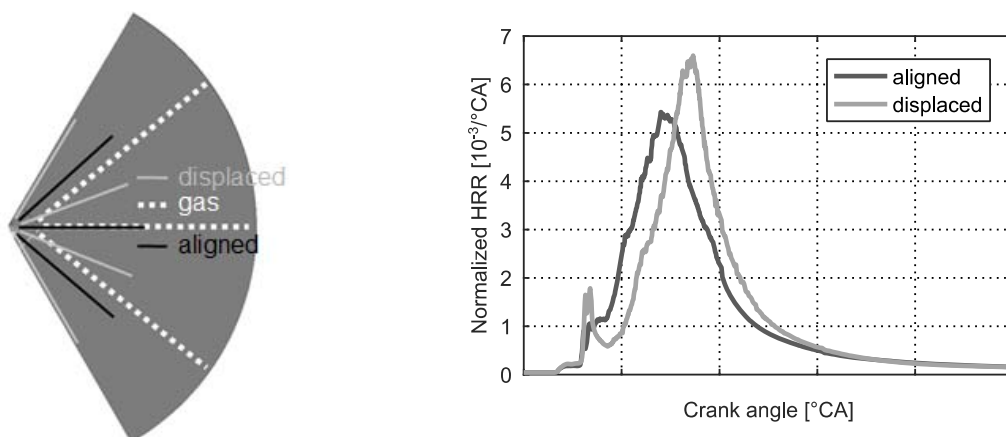
Fig. 7. Influence of the orientation of the Diesel spray to the gas jet: visualization (left) and corresponding HRR (right) at baseline SOI and Diesel spray angle, cf. Fig. **8**
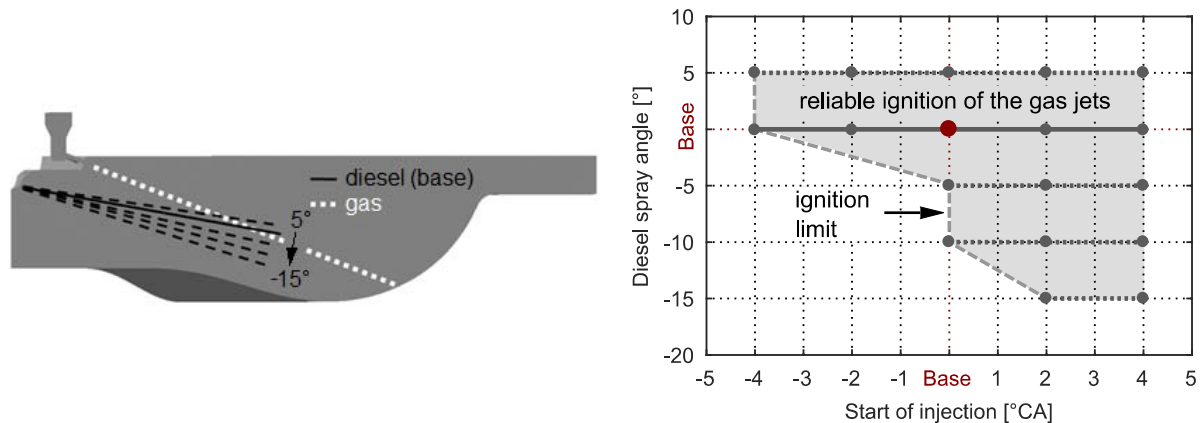
Fig. 8. Visualization of Diesel spray angle variation (left) and ignition limits for selected spray angles (right)

Once the orientation in the circumferential direction was clarified, the orientation of the diesel pilot spray axis was varied in relation to the gas jet axis. In Fig. **8**, the inclination angles of the gas jet and the variations of the diesel pilot spray are shown on the meridian section of the 120° cake model with a baseline piston bowl, cf. [3]. The dotted white line shows the orientation of the gas jet. The solid black line represents the baseline spray angle of the diesel spray. The dashed black line shows the angle variations in 5° steps. In these simulations, starting from a basic configuration (SOI 0°), the injection mass flow profiles for both the diesel and gas jets were shifted in 2 °CA steps to earlier and later timing. In the diagram on the right, the flammable operating points that were still stable were depicted over SOI to allow the display of the operating range. By reducing the diesel spray angle, the operating range is significantly decreased. Of course, a later SOI than displayed in the diagram is possible independently of the Diesel spray angle, however, it is not appropriate from a thermodynamic point of view.

In summary, the combustion process offers various degrees of freedom to directly influence the ignition process. While the sequence of fuel injection can have a significant influence on the proneness to knocking combustion, peak pressure and the formation of pollutants, a clean fine tuning of the jet angle from gas to diesel with regard to thermodynamically favorable ignitability is of central importance. With respect to the subsequent main combustion process, in addition to the parameters that can be directly influenced by the injector design and trigger profile, of course, a suitable matching with the piston bowl is indispensable.

3.2 Investigation of the main combustion process

In this subsection, the further optimization process of the pre-designed injector configuration and the defined injection strategy is discussed with regard to the main combustion process. The optimization of the injection parameters is shown in relation to the required injector cross-sections and in consideration of the available gas pressure provided by the high-pressure gas supply system. Furthermore, the investigation process of the interaction of the gas jet with the combustion chamber geometry is presented.

3.2.1 Injection parameter optimization

Only the basic relationships for the injector design have been examined thus far. To optimize the injection parameters, first the gas pressure is determined in combination with the injection duration. The diameter of the nozzle hole is the corresponding adjustment value in order to achieve the optimum combination of the two parameters. Since the injection timing has a considerable effect on the gas pressure and on the combustion behavior, the timing was varied to allow assessment of the effective efficiency-NO_x behavior in the trade-off.

The pressure gradient between the gas supply boundary condition (cf. Fig. **2**) and the combustion chamber is primarily determined by the gas mass flow and the gas nozzle cross section. If the back pressure increases due to the combustion in the main combustion chamber, a higher pressure also occurs at the boundary section. If the injection time is extended, the mass flow changes while the overall injected gas mass remains unaffected. This also means that a lower pressure difference is required for injection. However, this also reduces the burning speed. The aim of the preliminary design is to show

the relation between gas nozzle cross-section, required gas injection pressure, gas injection duration, and overall combustion behavior.

Based on the previous findings, a matrix of nozzle cross section and injection duration has now been calculated on the basis of the 40° cake model with a moderate piston bowl and spray angles defined above. The 40° cake model was chosen because the accuracy is sufficient for these investigations and it is possible to keep the computing time low. Fig. *9* shows the relationship between these variations.
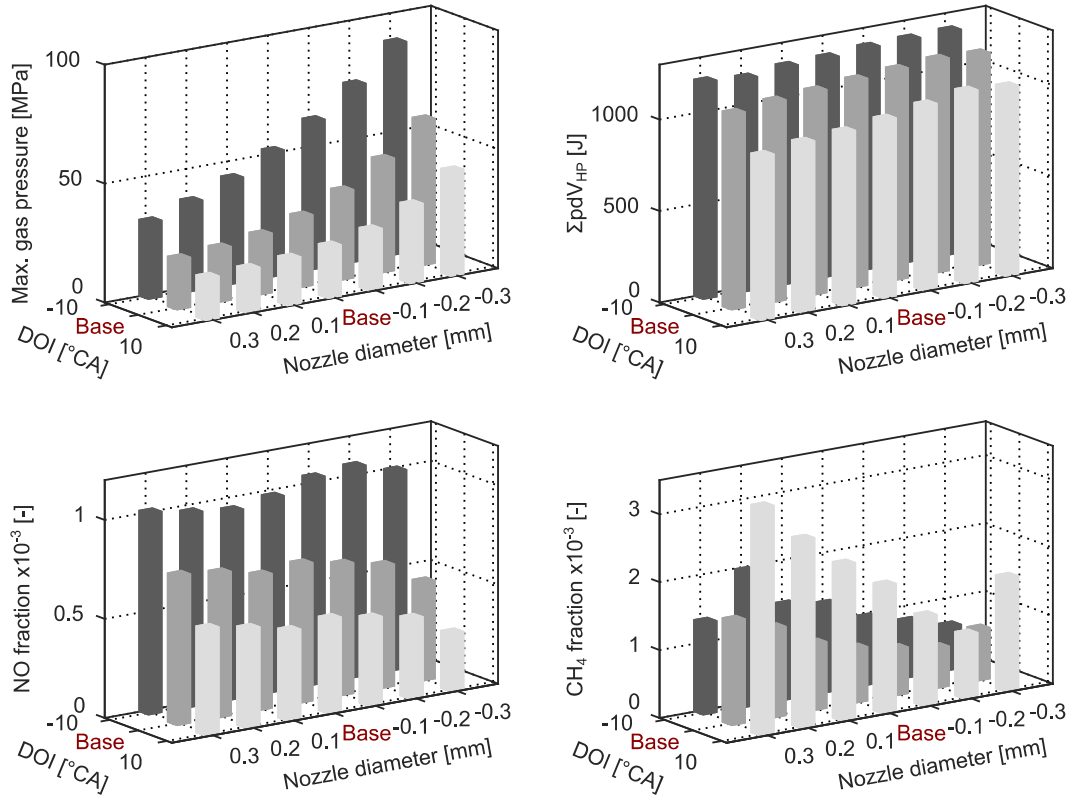
Fig. 9. Correlations for operating behaviour

On the abscissa, the nozzle diameter is varied from a baseline variant by +/-0.3 mm in 0.1 mm steps. The ordinate represents the injection duration from the baseline variant by +/-10 °CA. The upper left diagram graphs the maximum gas pressure at the gas inlet position where the boundary condition was set. It clearly shows the increase with a smaller cross section as well as with a shorter injection time. The upper right diagram displays the $\sum$pdV[1]. In principle, this value increases until the diameter is reduced for 0.2 mm. With a further reduction, a decrease can be observed. In any case, the $\sum$pdV increases as the injection time shortens. In the lower left diagram are the NO fractions at the end of calculation. During long injection periods, however, a bigger diameter results in lower $\sum$pdV values and higher NO occurrences. This indicates an unfavorable mixture formation of the flame jets. Is the baseline injection time reduced by 10 °CA, the pressure is already high enough that sufficient mixture formation can take place in all cases. This results in high $\sum$pdV values overall as well as NO values which only changes slightly in relation to the diameter. In the lower right diagram, the CH_4 mass fraction at end of calculation is presented. When the diameter is reduced from +0.3 mm to -0.2 mm relative to the baseline variant, the CH_4 amount at end of calculation decreases continuously. This can be explained by the better mixture formation as well as by the increased penetration depth as the cross section become smaller. From -0.2 mm to -0.3 mm, the CH_4 fraction increases again. This is most likely due to the amount of gas stored in the dead volume, which only flows into the combustion chamber late after combustion during the expansion phase, with the result that unburned hydrocarbons remain in the combustion chamber after combustion (cf. [3] and Fig. *11*). When taking the shortest injection time (-10 °CA) into consideration, a clear CH_4 decrease trend towards smaller nozzle diameters can be seen with exception of the biggest investigated nozzle diameter at +0.3 mm. In general, this can be explained by the

---

[1] Since we only work with discrete values, $\sum$pdV represents the cumulative work transferable from the burned fuel to the piston.

intensive interaction of the gas jet with the piston bowl. In the case of the shortest injection time, the gas jet is deflected upwards by the piston too strongly so that insufficient mixing with oxygen occurs. In the case of the longest gas injection duration (+10 °CA), insufficient time remains to complete the combustion after end of injection and an increase in unburned hydrocarbons is the result. In this case, the baseline variant is a favorable compromise for the investigated piston bowl shape. Based on these findings, the most favorable parameter set consists of a nozzle diameter of 0.2 mm smaller than the basis one, combined with the basis injection duration. This parameter set results in a gas pressure of approximately 40 MPa while reserves still remain for engine control.

3.2.2 Interaction of the gas injection with the piston bowl

The interaction of the jets with the combustion chamber geometry and the piston bowl shape in particular are considered based on the basic injector cross sections that have been determined, aligned diesel and gas nozzles in combination with sequence 2. Thus, a remarkable potential for reduced emission of pollutants could be achieved. Preliminary investigations have shown that the combustion behavior especially in the late phase of the combustion is significantly dependent on the mixing of the gas jets with the air inside of the combustion chamber. This mixture formation can be improved by both the number of gas jets and the jet interaction strategy with the piston bowl shape, cf. [3]. In this context, the switch from six to nine nozzles has provided advantages in principle, but a greater impact is made by the geometric design of the piston bowl shape. Using CFD, a jet splitting bowl (see [3] for further details) with the contour shown in Fig. *10* was developed on the basis of nine nozzles that split the gas jets. As a consequence, injected natural gas is better mixed with air in the entire combustion chamber as a basis for an improved flame propagation. The selection of nine instead of six nozzles as well as the optimized piston bowl shape has already been presented and discussed in detail in [3] and will not be further examined here. Briefly summarized, the influence of the interaction of spray angle and piston bowl geometry is significant. A comprehensive optimization of jet and spray angles in combination with the piston bowl design enables at least a significant reduction of HC and CO emissions. Based on these results, this paper shows further sensitivity investigations with regard to the optimization of the spray angle. Such a configuration requires the precisely gas jet orientation towards the jet splitting bowl. The extent to which a change in angle affects the combustion behavior and the formation of unburned species is explained below.

Fig. *10* shows the meridian sections of the 120° cake model with the optimized piston bowl shape. Based on the nozzle configuration and injection strategy discussed above, the spray angle was varied together for both diesel and gas jets by 10° relative to a baseline configuration. The meridian sectional view is shown of the CO mass fraction 5 °CA after TDC and complemented by CH_4 mass fraction at 80 °CA after TDC for three angles of the gas and diesel jets axles. The optimal difference in the angle between the diesel and gas jets shown above was maintained and the inclination of the jets varied together (from left to right, spray angles baseline +10° to baseline -10°). An increased spray angle to baseline +10° (top left), the jet hits the piston on top of the jet splitting rib and is unfortunately deflected towards the liner. At 80 °CA (center left), a remarkable CO cloud can be observed in the combustion chamber which remains nearly unburned. In the other case with a 10° steeper angle (baseline -10°), the jet is deflected too strongly downwards into the piston bowl. The gas-air mixture in this section becomes too low in oxygen and result in increased unburned species at end of combustion. In the case of the baseline variant (center middle), the gas jet impinges the jet splitting rib ideally and is deflected to similar parts to areas in the center of the piston bowl and near the fire deck, thereby preventing the direct flow of the gas jets to the liner. As a consequence, optimal use is made of the air in the combustion chamber. The well exploited jet guidance significantly reduces the CO and CH_4 concentrations. The meridian sections are able to illustrate the basic behavior. However, only a sectional view of the combustion chamber is shown. To ensure that the behavior shown in this view corresponds to the rest of the combustion chamber and to quantify the results, an evaluation of the entire combustion chamber was carried out within eight, so called "ring sections" at the end of the calculation, cf. [3]. Thus, it was possible to determine the local radial distribution of the pollutant's CO and CH_4 in the whole combustion chamber and to confirm the observed effects finally.

A significant part of the HC and CO emissions is caused by the storage of fuel gas in the injector dead volume, a small space after the injector valve towards the end of the gas nozzles, cf. [3]. Towards the end of combustion, (visible at 80 °CA after TDC) the stored gas flows into the main combustion chamber as an effect of expansion. Only a small part of it continues to burn, while the rest remains partly and completely unburned as additional CO and CH_4 in the exhaust regardless of the bowl design. Fig. *10* shows the phenomenon (top left section in each subfigure).
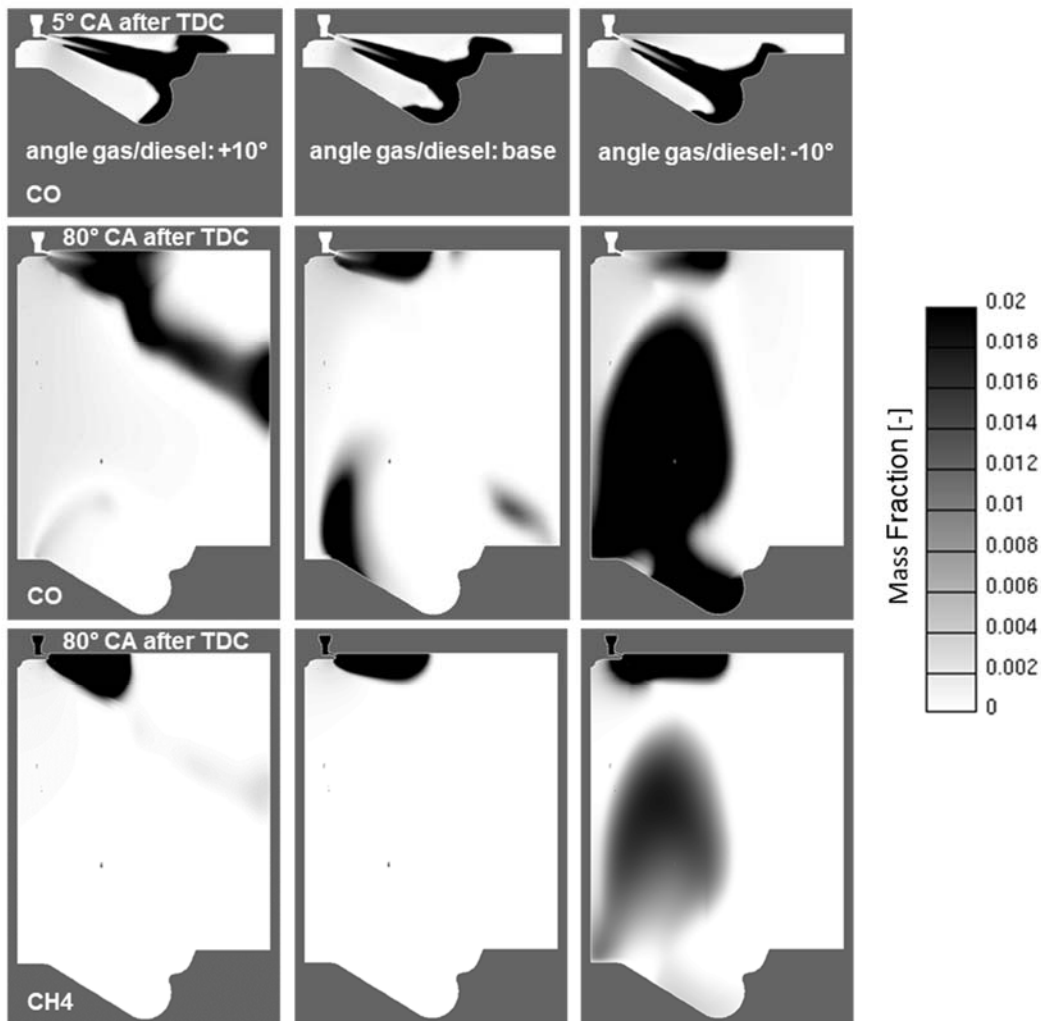
Fig. 10. CO mass fraction @ 5 °CA after TDC and CO and CH$_4$ fraction @ 80 °CA after TDC for different jet/spray angles

As discussed in [3], the detailed evaluation of species remaining in the combustion chamber at the end of the calculation has shown that the post-flow of unburned gas from the injector dead volume makes up a significant proportion of the total unburned exhaust gas mass. Since this proportion is reduced only by decreasing the size of the injector dead volume, it should be kept as small as possible.

While Fig. *10* shows the effects only in one sectional plane for only one SOI, a more comprehensive assessment can be figured out by evaluating the results of a SOI variation for each discussed jet/spray angle variant within the entire combustion chamber. In each case, starting with a basic timing (base), further investigations were carried out at +/-2 and +/-4 °CA and the results for CO and CH$_4$ were plotted in relation to NO$_x$, cf. Fig. *11*. Both diagrams show the mass fractions of the three variants after the end of calculation over the NO mass fraction. The variant with the basis spray angle (black) corresponds to the vertically centrally pictured sectional view in Fig. *10* and provides the lowest values for CO and CH$_4$. In this case, the jet alignment towards the jet splitting rib is most successful. The visualized trends for CO and CH$_4$ at increased/decreased jet/spray angle can be clearly found within the trade-offs in Fig. *11*, independent of the chosen SOI. In addition, the basis variant has also the most robust performance in comparison to the variations in injection timing. All in all, this application appears to be more sensitive to smaller spray angles than to larger ones. One potential explanation for this observation seems to be the higher oxygen occurrence close to the liner in comparison to the piston bowl area since the amount of oxygen present increases with the square of the radius.
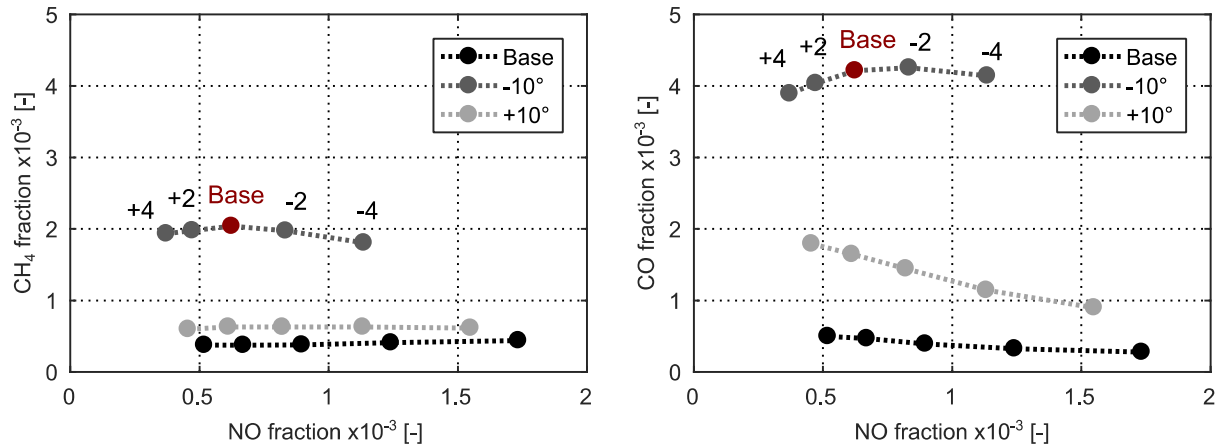
Fig. 11. Emission trade-offs from diesel and gas spray angle variations with the jet splitting bowl

With regard to the main combustion process, the highly sensitive relationship between nozzle hole diameter, DOI, gas pressure, ∑pdV and exhaust gas species was discussed in detail in this section. The development of a basic understanding of these interrelationships was of central importance for the understanding of the combustion process and the further pre-design process. In addition, the CFD simulation outlined the remarkably positive effect on reduction of unburned species by a well-tuned interaction behavior between gas injection and piston bowl.

3.2.3 Experimental Validation

The experimental validation of the results from the simulation-based predesign process was performed by both an intensive investigation of the injector in the LEC IRAS (cf. [19]) and an intensive investigation of the whole combustion concept on the SCE as discussed in detail in [3] and [19]. In order to show to what extent the precalculated trends from 3D CFD simulation could be confirmed by measurements, selected measurement results based on the boundary conditions in Table 4 will be briefly discussed below.

Table 4. Boundary conditions for SCE measurements

Speed	1500 rpm	*Pilot diesel fraction*	3 %
IMEP	24 bar	*Diesel rail pressure*	1300 bar
Excess air ratio	2.1	*Gas rail pressure*	400/500 bar
Manifold air temperature	45 °C	*Methane number*	≈ 89 (natural gas)

Fig. *12* shows, on the basis of the percentual energetic fraction of unburned species (ΔW_{UB}) at 80 °CA after TDC related to the given reference point, selected results of injection timing variations with the baseline piston bowl at 40 MPa gas pressure and with the optimized piston bowl at 40 MPa and 50 MPa gas pressure depending on the brake specific NOx emissions (BSNO$_X$)[2]. From this result, three predictions of the 3D CFD simulation can already be confirmed:

- the positive effect of an optimized piston bowl shape
- the necessity of a precise gas jet impingement on the jet splitting rib
- the positive effect of an increased gas injection pressure

The comparison of the baseline piston bowl and the optimized piston bowl at 40 MPa gas injection pressure shows independent of the injection timing a tremendous benefit in ΔW_{UB} of up to 50 %. Quite low NOX emissions can be achieved by retarding the injection timing, but at the cost of less precised gas jet impingement on the jet splitting rib due to the progressive downward movement of the piston. As a result, an increasing part of the gas jet flows across the piston crown to the liner and lowering efficiency

---

[2] Brake specific emissions are calculated based on the SCE's indicated specific emissions and estimated friction mean effective pressure (FMEP) of the MCE, because the FMEP of the SCE is not representative

due to an increased amount of unburned species as well as retarded combustion phasing. Analogous to the discussed observations to the interaction of the gas injection with the piston bowl, Fig. *12* confirms that clearly for BSNOX levels lower than 5 g/kWh. From this point, the jet splitting rib is no longer hit properly and ΔW_{UB} increases immediately.
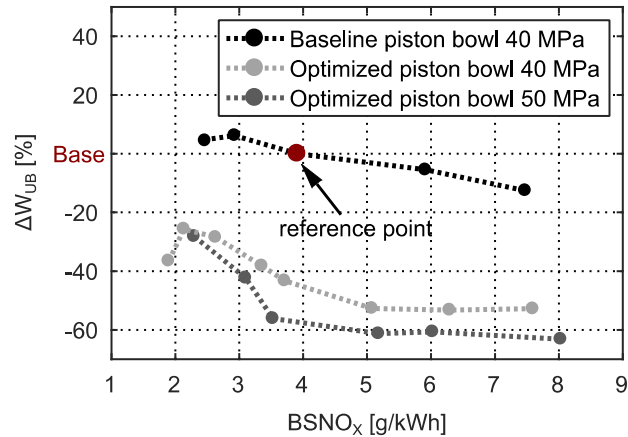
Fig. 12. Difference in energetic fraction of unburned species related to the marked reference point

Based on the observations related to Fig. *9*, the measurement also shows for the same combustion chamber geometry, ΔW_{UB} can be further reduced by an increased injection pressure. In addition, the necessity of a precise gas jet impingement on the jet splitting rib becomes also visible, just at later injection timings and BSNOX levels lower than 3.5 g/kWh. Here the jet splitting rib can be reached until later injection timings due to the higher gas jet velocity, which explains the later and also consequently steeper increase in ΔW_{UB}. The benefits given by both the optimized piston bowl shape and the increased injection pressure are mainly related to the improved mixing behavior within the combustion chamber. For further details please refer to [3] and [19].

4. Conclusion

With this paper a CFD based methodology for the pre-design of an advanced high-speed large engine concept based on the gas-diesel combustion process for reduction of greenhouse gas emissions is presented. In order to achieve these properties, however, extensive preliminary design work is necessary. Therefore, LEC GmbH developed an effective and reliable virtual design methodology that was applied to predesign an advanced high-speed gas-diesel combustion concept that uses a combined high-pressure gas-diesel injector. This paper described in detail the role of 3D CFD simulation in this approach.

Along with the selection and generation of suitable boundary conditions, the combustion model plays a decisive role in the correct description of the combustion process. Therefore, the setup of the 3D CFD model was discussed in detail as well as the models used (cake sizes), grid, and topology. The importance of the last was demonstrated by comparing a simple orthogonal cell topology and a rotationally symmetric mesh cell topology with a focus on the significantly different penetration depths. Assessment criteria to assess the generated simulation results were introduced and examined by selected examples to the 3D CFD based combustion concept optimization process. This process was also highly important in the prediction of a promising hardware setup for subsequent SCE tests with regard to engine-out emissions for future emission legislation. The engine-out emissions are directly related to the combustion process, which in turn affects the required boundary conditions. Overall, the detailed chemistry approach that was chosen and the highly reduced mechanism provided a suitable basis for the description of all these complex relationships. The choice of cake models for the required accuracy permitted the computing times to be kept within a tolerable range of accuracy. However, the choice of cell size and topology is significant and requires experience. The knowledge generated in advance from simulation was of great help in starting up the engine, whereby much experimental tuning work was able to be avoided. Thus, it was shown that this methodology allows a considerable part of the development of a new combustion process to be completed in advance with simulation, thereby considerably reducing time, costs, and engine-out emissions. Subsequently measurements on the SCE have confirmed the chosen method with the models used.

Acknowledgements

References

[1] AEsoy, V.; Magne Einang, P.; Stenersen, D. et al.: "LNG-Fuelled Engines and Fuel Systems for Medium-Speed Engines in Maritime Applications", in: "SAE International Powertrains, Fuels and Lubricants Meeting", SAE Technical Paper Series, Paper No. 2011-01-1998, Detroit, USA, 2011.

[2] AVL-List GmbH: "FIRE Manual V2014", Graz, 2014.

[3] Aßmus, K.; Redtenbacher, C.; Winter, H.; et al.: "Simulation Based Predesign and Validation of a Diesel Ignited High-pressure Gas Direct Injection Combustion Concept", in: Leipertz, A. (ed.): 14th International Congress "Engine Combustion and Alternative Concepts – ENCOM 2019", Berichte zur Energie- und Verfahrenstechnik (BEV), Vol. 19.1, ESYTEC, Erlangen 2019, pp. 83-94.

[4] Bärow, E.; Willmann, M.; Aßmus, K.; et al.: "Operating Experience with a Combined High-Pressure Gas-Diesel Platform Injector", in: Eichlseder, H.; Wimmer, A. (ed.): "17. Tagung Der Arbeitsprozess des Verbrennungsmotors" (= VKM-THD Mitteilungen, Volume 103-1), Graz, 2019, pp. 141-153.

[5] Beutler, M.; Naumann, M.: "Erdgas – Ein alternativer Kraftstoff für den Verkehrssektor – Teil 1: Allgemeine technische Aspekte, Kostenabschätzung und Energiekettenbetrachtung", in: "ATZ Automobiltechnische Zeitschrift", Vol. 100, Issue 9, 1998, pp. 648-656.

[6] Dukowicz, J.: "A particle-fluid numerical model for liquid sprays", in: "Journal of Computational Physics", Vol. 35, Issue 2, 1980, pp. 229-253.

[7] Fischer, C.; Mareske, A.: "Energietechnik und Wirtschaft", in: Grote, K.-H.; Feldhusen, J. (ed.): "DUBBEL - Taschenbuch für den Maschinenbau", Vol. 22, 2007.

[8] Gabelar, W.: "3D CFD Simulation einer Dual-Fuel-Verbrennung bei Großgasmotren", diploma thesis, Graz University of Technology, Graz, 2013.

[9] Grochowina, M.; Hertel, D.; Tartsch, S. et al.: "Ignition of Diesel Pilot Fuel in Dual-Fuel Engines", in: "Proceedings of the ASME 2018 Internal Combustion Engine Division Fall Technical Conference", Bd. 1: "Large Bore Engines; Fuels; Advanced Combustion", ICEF2018, Paper No. ICEF2018-9671, San Diego, USA, 2018, pp. 515–528.

[10] Harrington, J.; Munshi, S.; Nedelcu, C. et al.: "Direct Injection of Natural Gas in a Heavy-Duty Diesel Engine", in: "Spring Fuels & Lubricants Meeting & Exhibition", SAE Technical Paper Series, Paper No. 2002-01-1630, Reno, USA, 2002.

[11] Imhof, D.; Tsuru, D.; Tajima, H. et al.: "High-pressure natural gas injection (GI) marine engine research with a Rapid Compression Expansion Machine", in: "CIMAC World Congress on Combustion Engine", Paper No. 12, Shanghai, China, 2013.

[12] Kaufman, Y. J.; Tanré, D.; Boucher, O.: "A satellite view of aerosols in the climate system", in: "Nature international journal of science", Vol. 419, Issue 6903, 2002, pp. 215–223.

[13] Kiesling, C .; Redtenbacher, C.; Kirsten, M. et al.: "Detailed Assessment of an Advanced Wide Range Diesel Injector for Dual Fuel Operation of Large Engines Paper No. 78, CIMAC Congress 2016, Helsinki, 2016.

[14] Laursen, R. S.: "ME-LGI for use as genset engines", in: "Proceedings for the 8th Motorship Gas Fuelled Ships Conference", Viking Line, Helsinki Port, 2017.

[15] Merker, G. P.; Teichmann, R.: "Funktionsweise von Verbrennungsmotoren", in: Merker, G. P.; Teichmann R. (ed.): "Grundlagen Verbrennungsmotoren", Vol. 7, 2014.

[16] Pattas, K.; Häfner, G.: "Stickoxidbildung bei der ottomotorischen Verbrennung", in: " MTZ Motortechnische Zeitschrift", Vol. 34, Issue No. 12, 1973, pp. 397-404.

[17] Paro, D.: "Gas diesels can draw fuel from the well." In: "The Motor Ship", 1995.

[18] Pischinger, R.; Klell, M.; Sams, T.: "Thermodynamik der Verbrennungskraftmaschine", (= technical book series: List, H. (ed.): "Der Fahrzeugantrieb"), 3rd edition, Vienna, 2009, pp. 248 ff, 338 ff.

[19] Redtenbacher, C.; Aßmus, K.; Lurf, G. et al.: "Detailed Assessment of an Innovative Combined Gas-Diesel Injector for Diesel Ignited High-pressure Gas Direct Injection Combustion Concepts", in: "CIMAC World Congress on Combustion Engine", Paper No. 179, Vancouver, Kanada, 2019.

[20] Redtenbacher, C.; Kiesling, C.; Malin, M. et al.: "Potential and Limitations of Dual Fuel Operation of High Speed Large Engines", in: "Proceedings of the ASME 2016 Internal Combustion Fall Technical Conference, ICEF2016", Paper No. ICEF2016-9359, Greenville, 2016.

[21] Redtenbacher, C.; Malin, M.; Kiesling, C.; et al.: "Gas- und Dual Fuel-Brennverfahren – Die Besseren Brennverfahren für Großmotoren? ", contribution at conference: "16. FAD-Konferenz", Dresden, 2018.

[22] Redtenbacher, C.; Kiesling, C.; Wimmer, A. et al.: "Dual Fuel Brennverfahren – Ein zukunftsweisendes Konzept vom PKW- bis zum Großmotorenbereich?", in: Lenz, H. P. (ed.): "37th International Vienna Motor Symposium 28-29 April 2016. Volume 2: second day" (= Fortschritt-Berichte VDI Reihe 12, Nr. 799), Düsseldorf, 2016, pp. 403-428.

[23] Reitz, R.D.: "Mechanisms of Atomization Processes in High-Pressure Vaporizing Sprays", in: "Atomization and Spray Technology", Vol. 3, No. 4, 1987, pp. 309-337.

[24] Rüger, C.: "Die Wege von Staub", Springer Spektrum, Berlin, 2016.

[25] Senghaas, C.: " New Injector Family for High-Pressure Gas and Low-Caloric Liquid Fuels", in: "CIMAC World Congress on Combustion Engine", Paper No. 119, Vancouver, Kanada, 2019.

[26] Takasaki, K.; Imhof, D.; Ishibashi, R. et al.: "Untersuchung des Brennverfahrens mit Hochdruckdirekteinspritzung von Erdgas durch Visualisierung", in: Eichlseder, H.; Wimmer, A. (ed.): "14. Tagung Der Arbeitsprozess des Verbrennungsmotors" (= VKM-THD Mitteilungen, Volume 96-1), Graz, 2013, pp. 96-109.

RCCI in Heavy Duty Engines

F. Eise, L. Heinz, U. Wagner and T. Koch

IFKM – Institute of Internal Combusion Engines. Karlsruhe Institute of Technology. Rintheimerqueralle 2, 76131 Karlsruhe Germany

E-mail: eise@kit.edu
Telephone: +(49) 721/60842319

Abstract. The simultaneous reduction of fuel consumption and pollutant emissions, namely NO_x and soot, is the predominant goal in modern engine development. In this context, low temperature combustion (LTC) concepts are believed to be the most promising approaches to resolve the above mentioned conflict of goals. Dual fuel, Natural Gas (NG)-diesel in Reactivity Controlled Compression Ignition (RCCI) is a promising high efficient combustion concept that combines EURO-VI engine-out NO_x and PM emissions with 25% CO_2 reduction compared to mono-fuel diesel and natural gas reference.

Main challenges are:
- CH_4 emission reduction: to meet EURO-VI tailpipe target of 0.5 g/kWh;
- Increasing load range: up to 23 bar BMEP;
- Combustion control to enable transient and robust operation under real-world conditions

Different natural gas-fuelled concepts exist. Stoichiometric natural gas SI combustion is widely accepted because of its maturity and simple aftertreatment. Driven by fuel costs and CO_2 emission targets, also conventional dual fuel concepts are introduced, in which natural gas is blended in standard diesel combustion. Depending on the injection timing of the diesel pilot injection, the process is either called liquid spark or RCCI. Conventional dual fuel concepts produce significant NO_x emissions as outcome of the diesel combustion. In RCCI the well homogenized mixture of the diesel pilot and the natural gas result in much cooler room ignition, controlled by injection timing and diesel injection amount.

So far, Single Point Injection and Port Fuel Injection of natural gas are applied in Natural Gas-Diesel RCCI. In this paper, the novel Direct-Injection (DI) Natural Gas technology is studied to reduce in-cylinder CH_4 emission and maximize thermal efficiency. On a heavy duty single cylinder engine the NO_x and soot engine out emissions below the EURO-VI targets have been undergone with ease. Efficiency in all investigated loadpoints is on a high level, even the challenging lowload area. Yet the CH_4-Emissions are about 50% over the target. This "CH_4-Slip" called CH_4-Emissions, result mostly from unburnt fuel. It was expected to result from the quenching area due to stopped flame propagation. A new RCCI-Pistonshape is introduced with raised compression as no knock occurs at all. This shape establishes no quenching and raised in cylinder temperatures to improve CH_4 combustion. The result from four most relevant variables are discussed in this paper. All these measurements are compared at the A50 loadpoint, which was predefined as 6300J/cycle injected fuel energy.

Notation

ATDC	*After top dead center*
BMEP	*Break mean effective pressure*
CA	*Crankshaft angle*
CFD	*Computational fluid dynamics*
CHI (χ)	*Energetic ratio*
CNG	*Compressed natural gas*
DI	*Direct injection*
EGR	*Exhaust gas recirculation*
EPS (ε)	*Compression ratio*
ETA (η)	*Thermal efficiency*
FID	*Flame ionization detector*
FSN	*Filter Smoke Number*
HRF	*High reactivity fuel*
IMEP	*Indicated mean effective pressure*
LAMBDA (λ)	*Air–fuel equivalence ratio*
LRF	*Low reactivity fuel*
LTC	*Low temperature combustion*

BMEP	Mean effective pressure
RCCI	Reactivity Controlled Compression Ignition
SOI	Start of Injection
TDC	Top dead center
W_CNG	Start of CNG injection
W_Diesel	Start of Diesel injection
X50	center of mass conversion
mf_CH$_4$	Methane slip / Effective methane emission
mf_NOx_g_e	Effective NO$_x$ emission

1. Introduction

Intensified environmental requirements necessitate further improvements of combustion processes in heavy duty engines. NO$_x$ and soot formation in particular are typically associated with conventional diesel engines. While further improvement of combustion efficiency in DI-Diesel engines leads to higher combustion temperatures and therefore an increase in NO$_x$ formation, research is beginning to focus on new strategies for low temperature combustion to achieve further improvements in thermal efficiency and simultaneously minimize the formation of pollutants.

A promising approach is the implementation of a homogeneous compression charge ignition which makes it possible to achieve diesel engine-like thermal efficiency with gasoline engine-like emissions [1]. In HCCI the combustion process is initiated by an increase in chemical radicals during the compression process. Combustion starts simultaneously in multiple areas of the combustion chamber and proceeds without flame propagation, avoiding local temperature peaks that lead to thermal NO$_x$ formation. Furthermore, the heat release rate is not limited by the speed of flame propagation which makes it possible to approach idealized Otto cycle. Figure 1 shows the model concept of ignition by exothermic centers. These exothermic centers, which can be described as elements of stoichiometric fuel air mixtures, continuously exchange heat with their environment. Keeping some distance between these centers can be beneficial for the prevention of local temperature peaks and therefore thermal NO$_x$-formation. On the other hand, the temperature of the surrounding gas must be high enough to initiate the decay of fuel molecules. A common way to achieve these temperatures is through the use of hot recirculated exhaust gas.
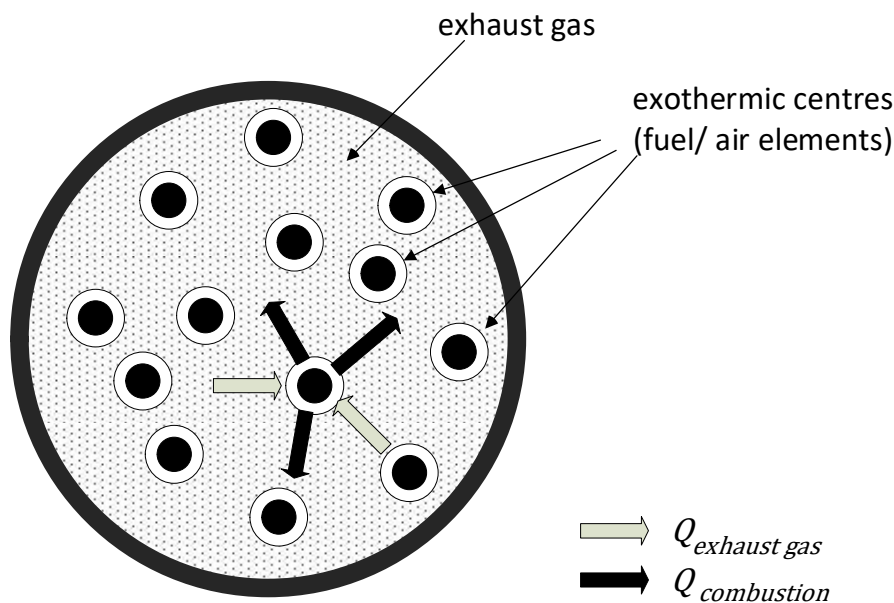
Fig. 1. Combustion control by auto ignition in exothermic centers, redrawn from [2]

To control the auto-ignition process, the rate of chemical decay can be influenced by increasing or lowering the intake charge temperature or varying the engines compression ratio. In comparison to conventional gasoline or diesel engines in which the ignition timing follows a trigger event such as spark timing or the beginning of diesel fuel injection, the control of HCCI is more difficult. Especially in cold

start situations or at low loads, the required temperature for auto ignition cannot be achieved. At high loads on the other hand, the operation range is limited by the engine's resistance to high in-cylinder pressure. In general, the main Challenges of HCCI operation are the inability to reach high loads and the complex control of combustion timing [3].

A possible method to achieve the benefits of homogeneous auto-ignition over a wider operating range is the use of reactivity-controlled compression ignition (RCCI). A more efficient control over combustion processes has the potential to lower both fuel consumption and pollutant formation compared to HCCI [4].

In RCCI, Auto-ignition is controlled by varying the energetic ratio χ (CHI) of two different fuels which makes it possible to effectively control combustion phasing without negative implications on NO_x emissions [5].

$$\chi = \frac{H_{u,LRF}}{H_{u,LRF} + H_{u,HRF}}$$

A chemically homogeneous base mixture of a low reactivity fuel (LRF) is mixed with a small amount of high reactivity fuel (HRF), injected during compression stroke. By increasing the amount of high reactivity fuel, combustion can be initiated even at low loads, while lowering the reactivity increases knock-resistance at high loads. While the LRF delivers the majority of chemical energy, the injection strategy of HRF has a huge impact on ignition-timing and heat release behavior. Controlling injected mass and injection timing of HRF provides two additional degrees of freedom. Early Injection-timing increases the degree of homogenization while a late injection strategy causes a stratification of HRF. Eichmeier distinguishes between stratified diesel combustion, partly stratified diesel combustion and premixed diesel combustion [6]. An overview of the emission and combustion characteristics of these different operation strategies can be seen in Figure 2.
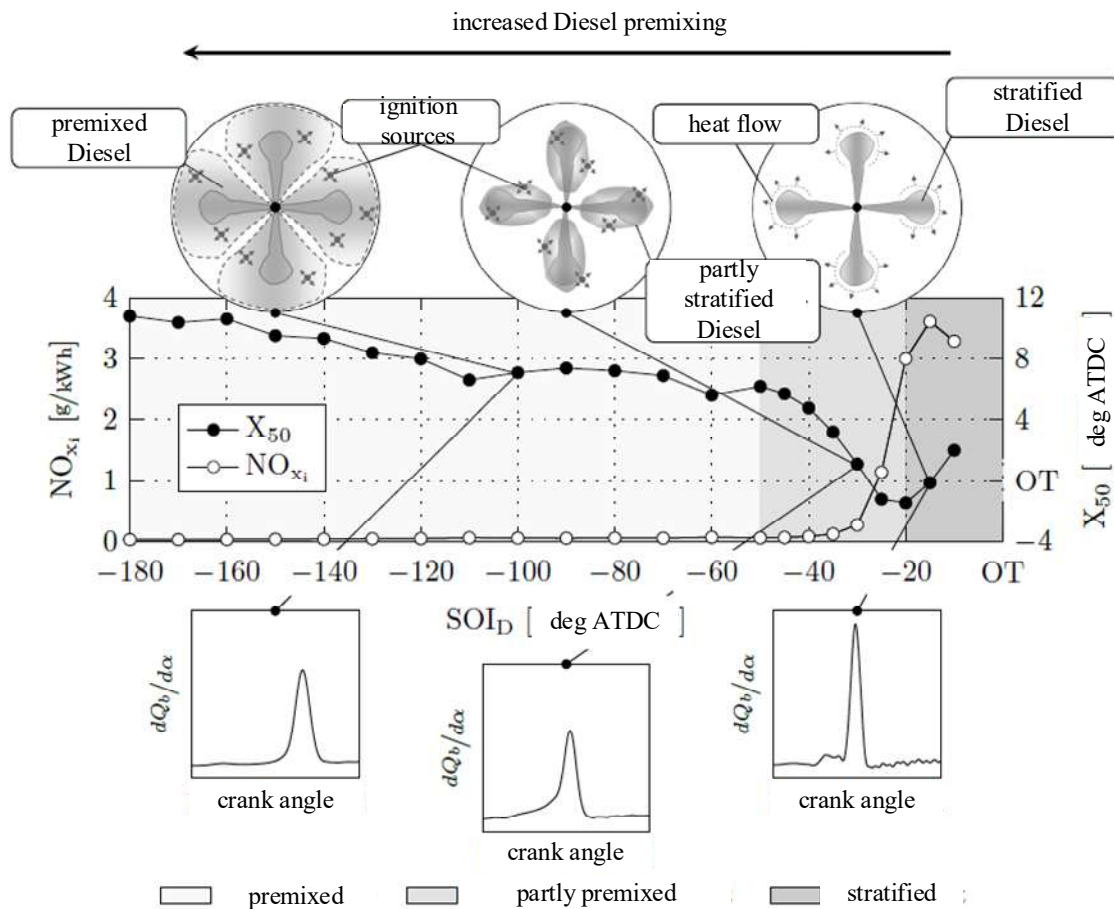
Fig. 2. Influence of HRF injection timing (SOI) on emissions and combustion behavior, PMI=10bar [6]

Stratified diesel combustion is characterized by high soot and NO_x formation due to the combustion of rich mixture parts and local temperature peaks. Heat release typically occurs in a pronounced two stage combustion. In the first stage, areas of rich diesel mixture oxidize under high soot formation. The resulting heat release leads to abrupt combustion of lean mixture after a short delay. Because of strong pressure oscillations combined with adverse emission characteristics, operating points with stratified diesel combustion should be avoided.

Shifting Diesel SOI earlier, the start and center of combustion move in the same direction until earlier start of injection does not lead to an earlier combustion. At this point, lower temperature and pressure levels cause an increase of ignition delay time. Areas containing HRF are larger and diesel concentrations in these areas are decreasing. These operating points of partly stratified diesel are characterized by an inverse behavior of SOI and start of combustion. Earlier injection causes an increase in ignition delay and therefore a later center of combustion. Homogenization increases while combustion temperatures decline. NO_x and soot formation are sinking until earlier injection causes a rise of unburned hydrocarbon concentration in exhaust gas [7].

In research carried out at the University of Wisconsin, RCCI has shown significant reduction in NO_x and soot emission in combination with an improvement in indicated efficiency. Simulations by Kokjohn et al. showed an efficiency improvement due to reduction of heat transfer and improved combustion control. [8]

2. Test procedure and equipment

2.1 Testbench
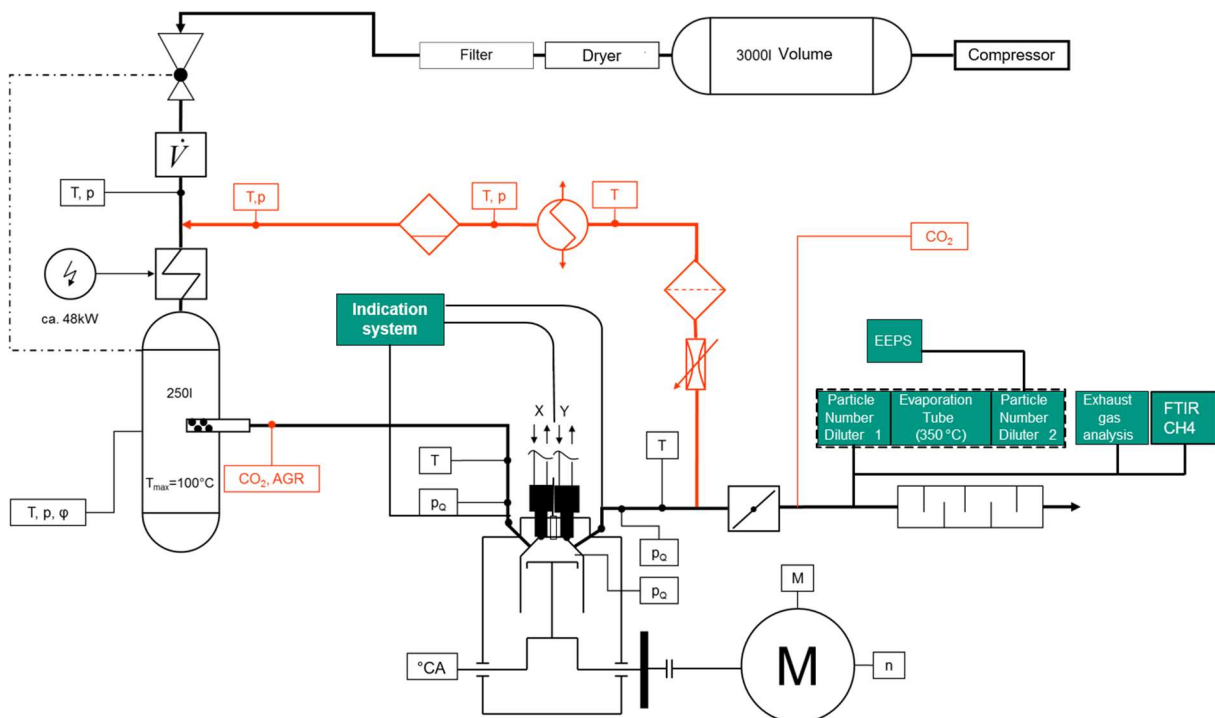
Fig. 3. Single Cylinder Testbench Scheme at KIT

The testbench of a single cylinder heavy duty engine used in this study is shown in Figure 3. The 4-quadrant electrical dynamometer starts and controls the engine. The base engine is built on the Daimler OM472 with adapted cylinder head to introduce a Dual-Fuel injection system. CNG and a liquid fuel (Diesel) are direct injected into the chamber by a second-generation needle in needle Westport HPDI² injector, the successor of the first generation HPDI injector. Full engine data is shown in Table 1. Cooling and lubrication are supplied externally and controlled to a maximum temperature deviation of 2K. Dry charge air supply is provided by the testlab and preheated to a desired engine intake mixture temperature with a deviation of 0.5K. Cooled high pressure EGR is introduced by using a backpressure flap in the exhaust and a standard EGR-Valve. EGR and charge air are mixed in dampening devices to ensure a homogenous mixture and to reduce the pressure fluctuations at the volume flow rate metering. The

EGR rate is calculated by ABB URAS, balancing the CO_2 amount in the inlet and exhaust. CNG-Rail pressure is adapted to match Diesel-Rail pressure by an external compressor station while constantly measuring gas quality. Intake, exhaust and incylinder pressure traces are recorded in the loop by Kistler Kibox indication system at a resolution of 0.1°CA.

Emissions are sampled with different 45° cut midstream probes. Soot is measured with AVL-Smokemeter as FSN. Particle Number concentration is counted in a Condensation Particle Counter AVL APC. The Particle Size Distribution is classified with an TSI EEPS. The gaseous emissions are analyzed in the AVL AMA 4000 with a 2 channel FID to separate the CH_4-Slip from the rest of the remaining hydrocarbons.

Table 1. Testbench data

ELIN Dyno	330kW, 4-Quadrant
Base engine	Daimler OM472
Bore x stroke	139 x 163mm
Injection System	Westport HPDI²
Railpressure	300bar CNG / Diesel
Charge air pressure	Up to 10bar
Intake temperature	20°C - 100°C
External cooled EGR	0% - 50%

2.2 Methodology

The measurement data from the automation System FEV Morphee 3 is averaged over a 60s period. Before sampling a stabilizing criteria and gas transportation time have to be complied. On trigger 100 consecutive cycles are taken out of the Indication systems ring buffer. Those two datasets are combined in Matlab and postprocessed. The indicated data is averaged and based on the fast heat release model, the necessary characteristics are calculated. The net indicated pressure IMEPn from this calculation is used in this study as the base engine power output. The break effective power can be misleading since friction losses, charge air and other media supply are externally on the single cylinder. Still other external devices like the backpressure flap influence the IMEPn too. In the shown sweeps the backpressure (P3) is taken from a turbocharger map and set to 150mbar. To improve comparability of the combined dataset, specific values are calculated and attached to it. One way is to use the EG88 directive for heavy duty gasoline engines. This directive is chosen since the main energy source in this study is CNG and the ignition process is controlled with the second fuel or often called pilot. In the means of, the main energy source is ignited by a different source. Secondary this directive supplies the method to calculate results comparable to EURO-VI legislation limits. For detailed combustion analysis a GT-Power single cylinder model is used. Woschni-Huber is used as the wall heat transfer model and external parameters are automatically setup for the cases in the Matlab routine. The setup then sets the boundary conditions for a Three-Pressure-Analysis (TPA) in GT-Power using the above mentioned three pressure traces. Single cycle events are parsed in Kibox Cockpit.

The sweeps presented in this study are calibrated on the energy amount injected per cycle. On the reference engine, load points were selected and the injected energy per cycle was calculated. This energy amount was always kept same for the comparing load points. As a result, an increased efficiency leads to a raised IMEPn. For the investigation of global effects, the center of mass conversion (X50) or the phasing was kept constant. Most of the diagrams are presented with the X50 at 8°ATDC. When necessary single parameter sweeps with X50 variations complement those sets.

As shown in the introduction and as Nieman et al [5] discussed, combustion losses on lean operated CNG engines result mainly from bulk losses in the squish region, crevice losses and blow-through losses. Since the base engine is derived from the standard diesel OM472 the shape of the combustion chamber is not optimized for Dual-Fuel mode. The base engine application for CNG ignited by a spark plug uses CNG port injection. CNG is distributed equally over the whole combustion chamber and a homogeneous mixture is achieved. While using the base camshaft configuration this results in some points in blow-through losses. This issue is directly solved by introducing CNG-DI and injection timings after the exhaust valve is closed. Still the injection in the overlap is part of the testing to show the constraints.

The combustion chamber shape is optimized in a three-step approach. Start is a port fuel and sparkplug adapted omega shape bowl with the compression ratio ε=13.1. The squish height here is 1mm. Following the previous work of Eichmeier et al the bean shaped RCCI bowl is introduced with the compression ratio ε=13.5. The squish region is significantly reduced with the new shape. Especially the squish height of now 7mm is expected to reduce bulk losses. The third step is lowering the distance

between cylinder head and piston by 1,7mm. This raises ε to 15.4. On every shape and compression ratio the same sweeps are, if possible, performed to compare results. Both bowl shapes are displayed in Figure 4.
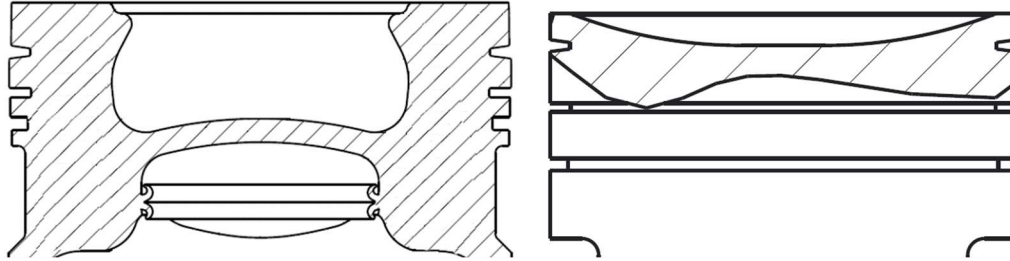
Fig. 4. Left stock port fuel piston ε=13.1, right RCCI piston ε=13.5 / 15.4

3. Results

Starting conservative on a low reactive mixture RCCI with CNG-DI is achieved. To avoid engine damage a switch from liquid spark to RCCI is performed at the 7,5bar BMEP loadpoint. By forwarding Pilot SOI the combustion phasing is forwarded close to an X50 of 0°ATDC. Going further from this point delays the phasing again and partial to full RCCI is reached. Most significant sign is the drop in NO_x emissions since combustion temperature decreases. Then the load is set to 10bar BMEP which equals 6300J/Cycle injected. All the shown sweeps are on this 6300J/cycle mode and referred to as A50. Filter Smoke Number (FSN) is measured but due to the homogenous mixture and the high CNG share it is always below FSN=0.04. After first optimizations it is below FSN=0.02 and won't be shown in the diagrams. Instead particle number measurements are introduced and shown if necessary. For every specific emission there is two main trends that influence the results aside from the raw emission in ppm. Reducing exhaust mass flow, reduces the specific value. While reducing thermal efficiency increases the specific emissions since the power output is reduced. The railpressure for Diesel and CNG is set to 300bar.

3.1 Fuel to air Ratio λ

One of the first project sweeps in RCCI mode is shown in figure 5 on the left side. At CHI=0,91 it is possible to stabilize the combustion. These λ variations are performed by reducing the charge air pressure (P2) and holding the fuel Energy at 6300J/cycle and the EGR-Rate at 30%. At P2=2500mbar the mixture is diluted to λ=2. By reducing P2 the dilution decreases and λ=1.1 is reached at P2=1450mbar. NO_x Emissions for lean combustion are at almost 0g/kWh equal to 2ppm and stay below 0.5g/kWh or 60ppm till λ=1.4. For rich mixture the NO_x threshold of 0.5g/kWh is exceeded. More striking is the CH_4-Slip (mf_CH_4). Operating at λ=2 results in 15% unburnt CNG emitted. Even at λ=1.1 emitting 5g/kWh means 2% of the CNG injected is not ignited. λ≤1 is not feasible due to an increasing number of cycles not igniting at all. In succession emitting the complete cylinder load into the exhaust and endangering the testbench. The efficiency already over 40% is promising, especially considering the amount of unburnt fuel. Figure 5 on the right shows the same sweeps but now optimized with CHI=0,83, T2=60°C and EGR=35%. Most significant change is the reduced CH_4-Slip (mf_CH_4) of 0.8g/kWh and the Pilot SOI (W_Diesel) that is forwarded to -70°ATDC. Even for λ=2 the CH_4-Slip with 2.5g/kWh is way below the start and the efficiency remains around 44%.
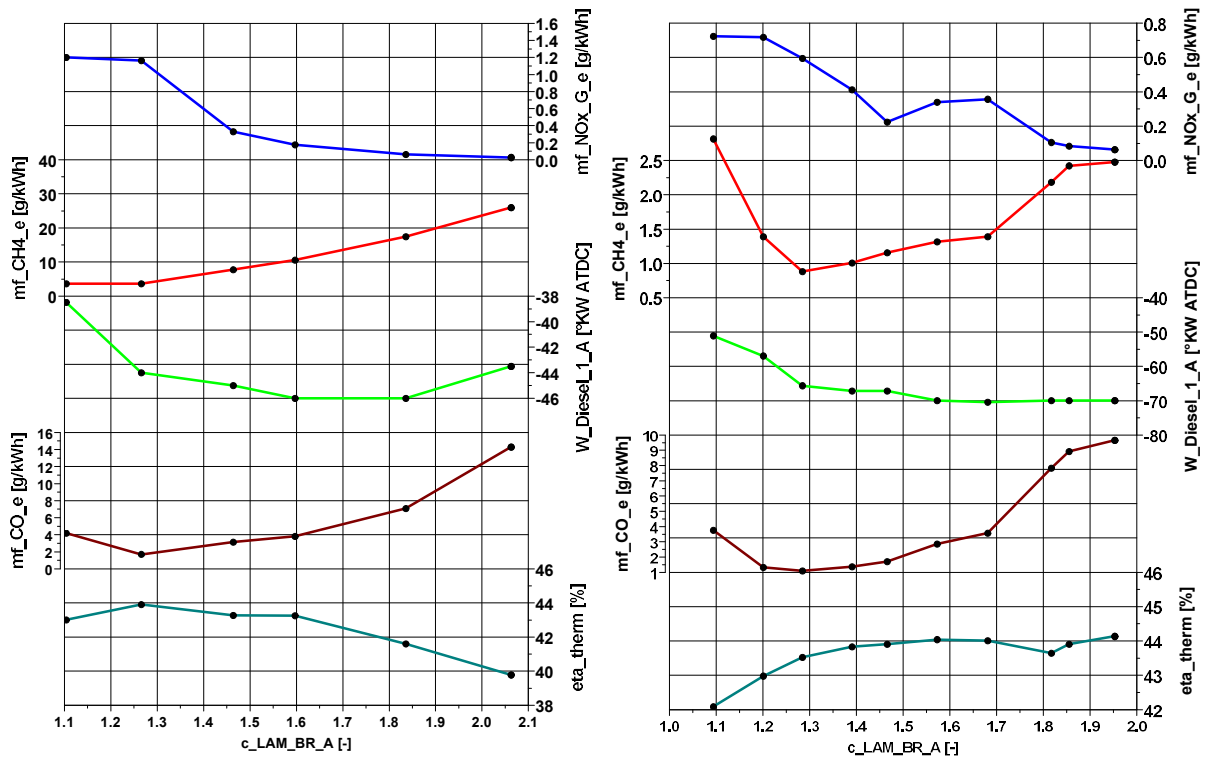
Fig. 5. λ-variation left at CHI=0.91, right optimized at CHI=0.83; P2=1450-2500mbar, 6300J/Cycle, ε=13.1

3.2 CNG Start of Injection

The major advantage of CNG-DI instead of PI is expected to be the degree of freedom for the injection timing and the in-cylinder mixture formation. A variation of the CNG start of injection (W_CNG) at ε=13.1
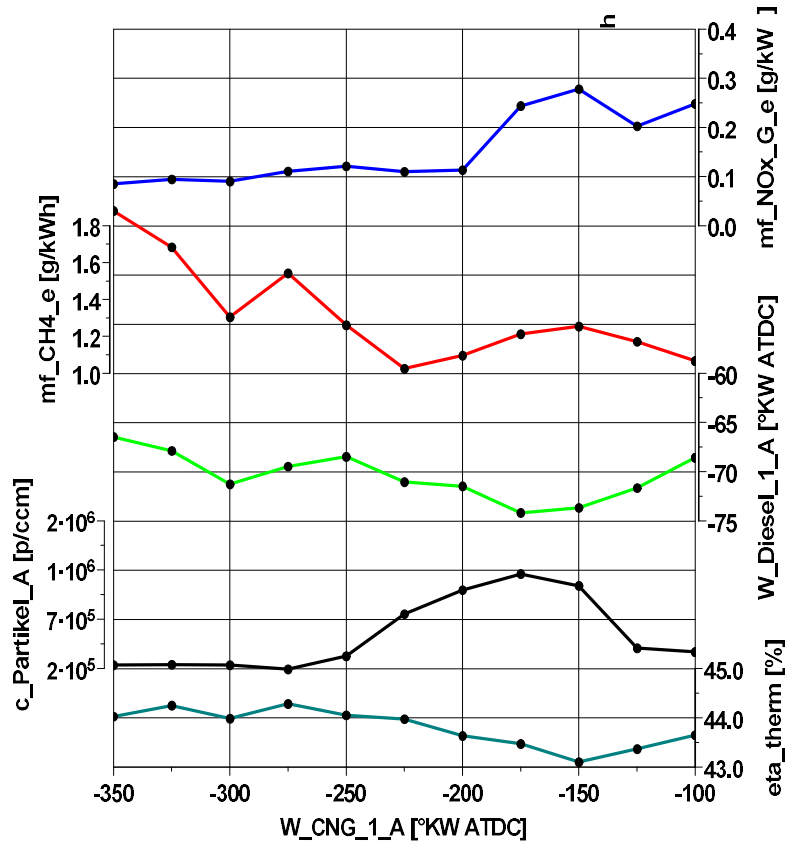
Fig. 6. CNG SOI sweep; λ=1.5, P2=2100mbar, EGR=35%, 6300J/Cycle, ε=13.1 stock bowl

and stock bowl is shown in figure 6. As seen before the region around λ=1.5 is a good compromise and is chosen for the shown figure. First to notice is the NO$_x$ maximum (mf_NO$_x$) 40% below the EURO-VI-Target. At CNG-SOI -200°CA ATDC and earlier NO$_x$ emissions stay at 0.1g/kWh. With Pilot SOI earlier then -65°CA ATDC the diesel spray homogenizes and the combustion temperature is low. This is achieved by reducing CHI to 0,83. The trends for the Diesel share and the Pilot SOI are discussed later in Figure 7. CH$_4$-Slip for early CNG-SOI is a result of the combination of the injector setup and valve timing. The CNG-jets are injected at an angle of 20° close to the flat cylinder head at a pressure of 300bar. Jets hitting the not fully closed exhaust valve can lead to emitted fresh load. Injecting later reduces the slip until a plateau starting -225°CA is reached. Retarding the CNG injection further stabilizes the slip between 1-1.2g/kWh or 400 to 500ppm. At late injections from -100°CA and further the process becomes instable. The injected diesel amount is fluctuating cycle to cycle and the phasing control is lost. This leads to high pressure rise rates at early X50 and misfire on the other side. A concentrated mixture only in the bowl is not possible to achieve on this setup. The efficiency only decreases for the earliest Pilot SOI that are necessary at the late CNG angles. Forwarding Pilot SOI was crucial here because the mixture became more reactive. For the further data shown -250°CA CNG SOI is used in the next sweeps.

3.3 Energetic CNG to Diesel share CHI

As there are unexplained issues with the CNG-SOI it is believed, that for certain points CNG is trapped in the squish and crevice region. Secondary it is possible that the low reactive CNG is separated from the pilot Diesel at late Pilot SOI. Only the CNG inside the bowl would be able to react and the flame would not ignite the volume in the squish region. Following this approach the diesel share is increased from 6% to 22%. The improved reactivity leads to a faster heat release and forwards the combustion phasing. As the phasing will be kept constant the Pilot SOI is forwarded. The Diesel stratification is reduced and the two fuels mix better. As long as stratification decreases along with the increasing Diesel share, NO$_x$ Emissions stay at the ultra low level as expected for RCCI. Figure 7 a variation over CHI, the contrary of the Diesel share illustrates this.
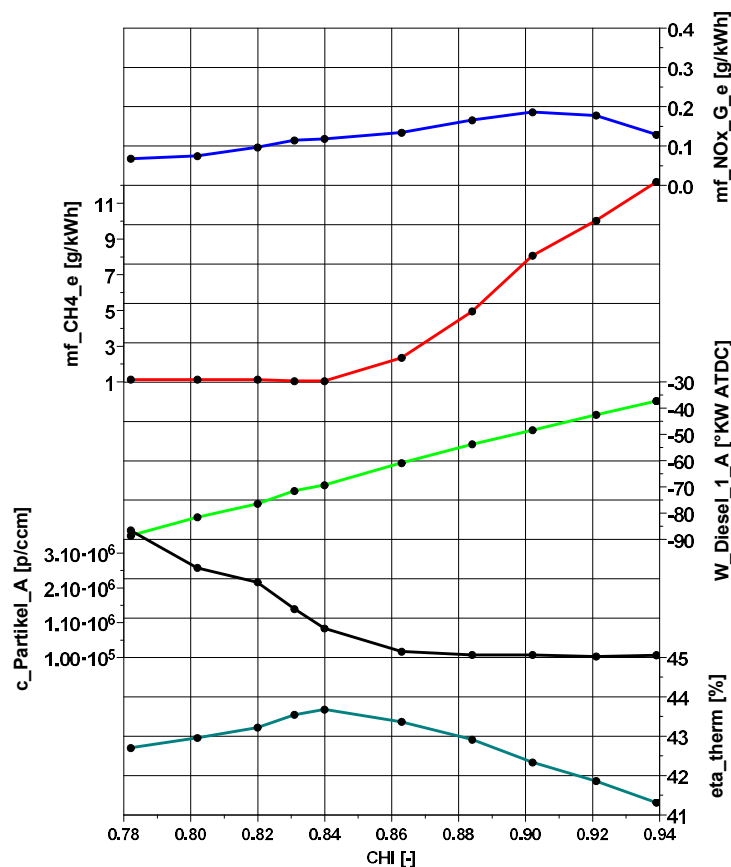
Fig. 7. CHI variation; λ=1.5, P2=2100mbar, EGR=35, 6300J/Cycle, ε=13.1 stock bowl

The Methane emissions decrease linear to reach the minimum of 0.9g/kWh at CHI 0.84. After this point more diesel only reduces efficiency. The pressure analysis shows a loss in combustion efficiency about 1% from CHI=0.84 to 0.78. The fact that the CH_4-Slip can't be reduced further shows that bulk losses are at their possible minimum with this setup. Especially the homogenised Diesel which is also in the squish region at the early SOIs helps to burn the trapped CNG in the later burn phase. The additional Diesel close to the walls not being burned completely at CHI<0.84 is the reason for efficiency loss, since CH_4-Slip is not increasing again. As Eichmeier et al discribed the CO emissions are also increasing. A big influence of CHI on the crevice losses is not expected. The new piston bowl with reduced squish heigt and fireland seem more promising. The burn duration is reduced from more than 40°CA to 20°CA and the pressure rise rates are still below the engine limits. Heat release traces are analysed in the next chapter. In figure 6 and 7 the rising particle number (c_Partikel) for Pilot SOIs earlier as -70°CA is recognisable. Analysis with the particle spectrometer EEPS show a growing peak for particles smaller than 30nm. In combination with CFD Simulations at VKA Aachen the assumption of Diesel hitting the cylinder walls and piston are underlined. To try to avoid this effect testing was done with separated pilot injections too. The result is an instable combustion. The energising time for the small Diesel amounts are too short and the needle stays in the ballistic region on this special injector. Subsequent optical investigations are supposed to improve the understanding of the particle trend better.

All of the seen phenomena lead to the introduction of the RCCI piston with a bigger squish height, lower fireland and a bean shape bowl.

3.4 Stock bowl compared to RCCI bowl

Figure 8 compares the above discussed results of ε=13.1 stock bowl in dashed lines and the ε=13.5 RCCI bowl. Fully matching ε was not possible due to constrution constrains but the difference is still in an accetable range. Expectedly on both sweeps the NO_x emission follows the same trend and stays on the same level. Only in the CNG-SOI sweep on the right at -100°CA the value is twice as high. The explanation can be found in the Pilot SOI. Injecting CNG at -100°CA and Diesel at -80°CA is at the edge of the injector control on this setup. In both diagrams the Pilot SOI follows the same trend and is forwarded between 5 to 10°CA. Reduced heat losses at the improved surface to volume ratio and the raised compression ratio make this necessary to keep the phasing constant at 8°CA ATDC. The new shape diminishes the influence of the CNG SOI on the Methane slip. The best point at -300°CA is only 0.2g/kWh or 100ppm below the worst point at -150°CA. Before the difference was around 1g/kWh or 400ppm. While being on the same level the best point on the new piston now is shifted to mixing with the entering charge air through the open inlet valves and fully homogenising. This behavior is reproducable over all the testing done with the new shape.

In Figure 8 on the left the most important change is the reduced Methane slip even for the high CHI region. The curve is flattened and mf_CH_4=1g/kWh is reached at CHI=0,86 instead of 0,84. The minimum of 0,9g/kWh can't be improved in this sweep. After this point introducing more diesel again only reduces combustion efficiency. On top more diesel reduces the sensitivity to Pilot SOI changes due to the early injections. Changing CHI is then the best solution to influence the X50 phasing.

The improved ignition of the CNG load is visible in the thermal efficiency which is always above 44%. From the point on where most of the CNG is combusting at CHI 0,9 and lower it is even over 45%. To make it comparable the efficiency was improved for 2 percentage points or 6% in total. This is directly achieved by changing the combustion chamber shape.

As seen in figure 9 the heat release for the RCCI bowl compared to the stock bowl is of the same shape. The low temperature reaction at -23°CA is at the same position only the combustion of the main load differs. The heterogenous spots ignite around the same angle (-12°CA) as on the stock bowl. Even though the incylinder pressure is around 1bar higher in that point. Yet the ignition delay on the more homogeneous rest mixture is longer and the main load then burns with a high heat release rate in a shorter duration. Thus, resulting in the same phasing. As a consequence, the peak pressure rises by 12bar to 130bar. The pressure rise rates are still within the engine limits.

In detail it can be seen that on the stock bowl the heat release flattens at 20°CA and cylinder load is still converting. On very high CHI this phase is prolonged and overlapped by a propagating flame up to 60°CA. This point is assumed to result from the squish region which will be verified in CFD and optical investigations. On the RCCI bowl with the increased squish height this phenomenon is barely visible.
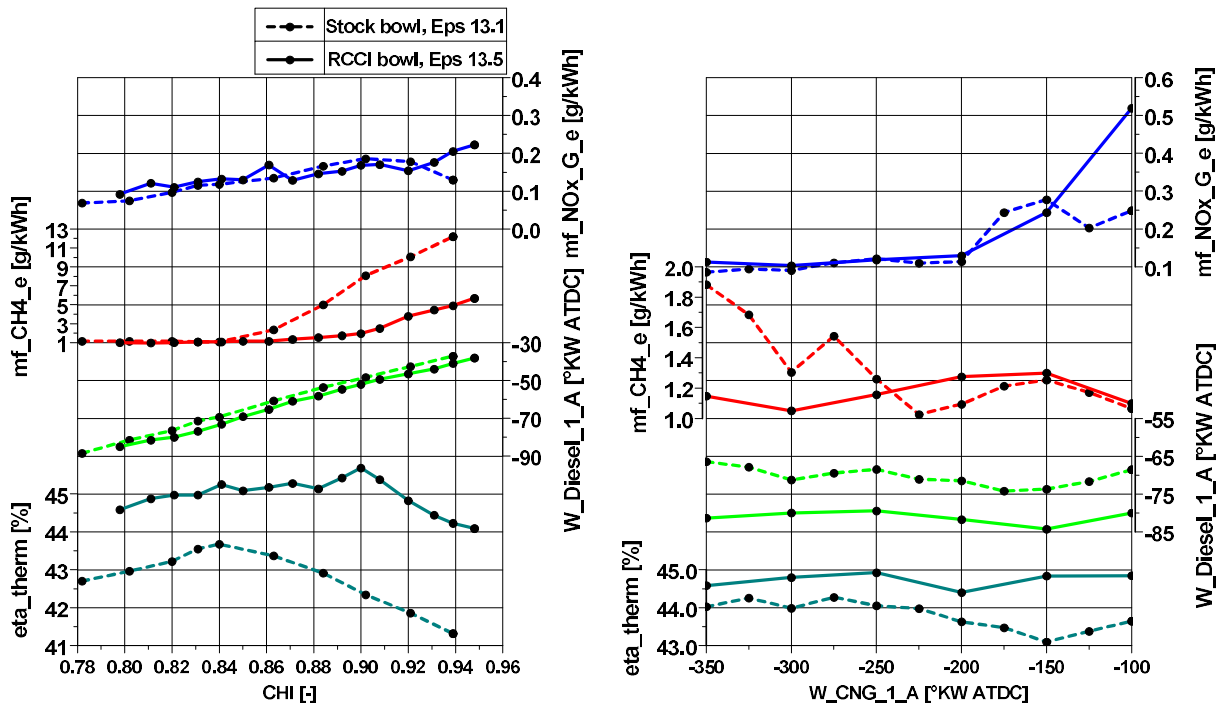
Fig. 8. CHI variation left, CNG SOI sweep right; Comparison of stock and RCCI bowl; λ=1.5, P2=2100mbar, EGR=35%, 6300J/Cycle, ε=13.1 / 13.5
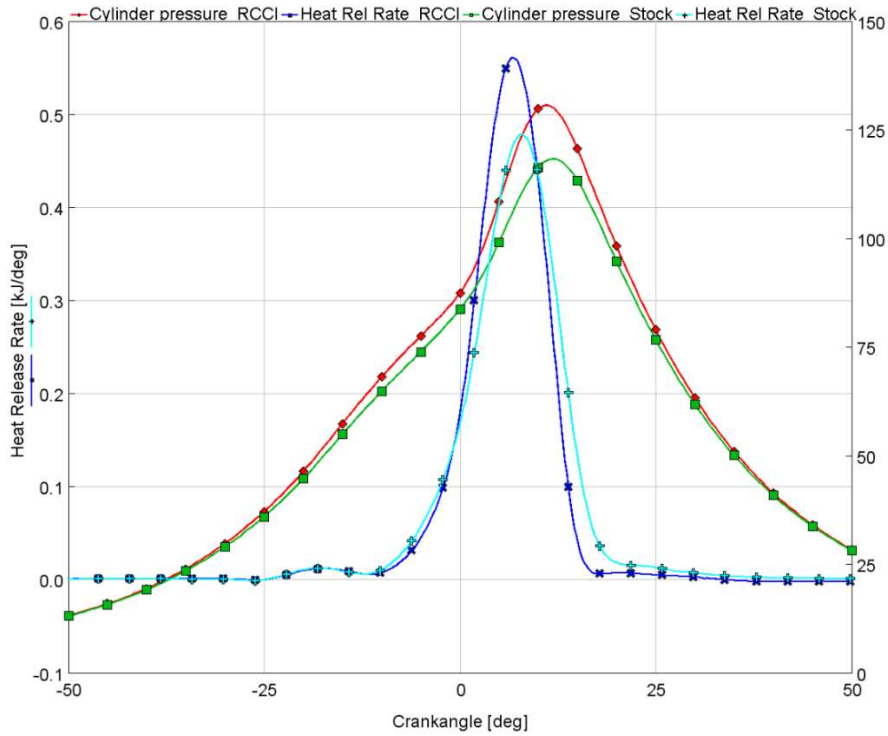
Fig. 9. Pressure and heat release trace over crankangle; λ=1.5, P2=2100mbar, EGR=35, CHI=0.83 6300J/Cylce, ε=13.1 stock and RCCI bowl with ε=13.5

3.5 Compression Ratio 15.5 and RCCI piston

In Figure 10 the CHI sweeps from the last two figure are displayed in comparison with the last setup. The cylinder is lowered by 1.7mm with the same RCCI piston. The resulting compression ratio is 15.5. This third setup is displayed dashed and with triangle markers. Again NO_x emissions are below 50% of the EURO-VI threshold and decrease with the increasing homogeneous Diesel distribution. Especially since the Pilot SOI has to be even earlier than -100°CA to control the combustion phasing. In detail it can be seen that the 15.5 setup has the lowest specific NO_x Emissions.

From the start at CHI=0.94 CH_4 emissions (mf_CH_4) are below the level achieved with the stock bowl at CHI=0.86. After CHI =0,88 there is no further improvement with the high compression. Main reason is the high reactivity leading to overstepping the engine limits for pressure rise rate. Also, beyond this point phasing control is limited. At the Pilot SOI of -100 to -120°CA the influence of changes to the phasing from the SOI is reduced dramatically. At ε=13.5 and a reactive mixture, changing Pilot SOI by 3°CA results in at least 1°CA phasing change. In this case changing the Pilot SOI by 20°CA results in almost 0 change on the phasing. Other effects like fluctuating EGR-Rates or a change in the load temperature dictate the combustion. As a consequence, the cycle to cycle deviation can suddenly increase in a way of not igniting cycles and then forwarding the phasing to 5°CA ATDC. In that moment engine limits are overstepped by 50% and the only useful and fast influence at hand is to increase CHI.

With an efficiency of more than 46% in a partial load point even high CHI seems sufficient. This high CHI region with CH_4-emissions under 2g/kWh and the yet highest measured efficiency is the direct consequence of the raised compression ratio. Regarding only the efficiency, CHI 0.93 has a good controllability, is enough homogenized but still stratified and needs less than 50% Diesel fuel compared to ε=13. Below CHI 0,9 the advantage is weakened. The CH_4-Slip stays on the same level but the combustion efficiency is reduced. Especially the here not shown CO emissions rise from this point on. This CO trend is visible for both compression ratios and it starts with the Pilot SOI of 75°CA and earlier. Possible flame / spray - wall interactions have to be examined closer on the optical setup.
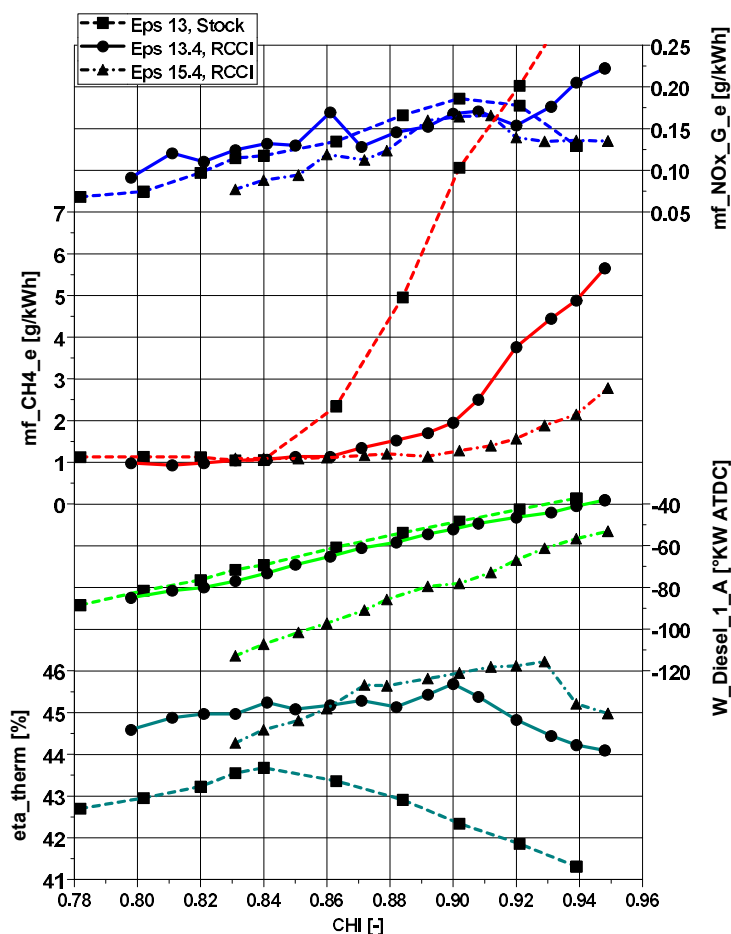
Fig. 10. CHI sweep; λ=1.5, P2=2100mbar, EGR=35, 6300J/Cycle, ε=13.1 stock and RCCI bowl ε=13.5/15.5

4. Conclusions

The data from the FVV Project "RCCI in Heavy Duty Engines" has shown the potential of RCCI with CNG / Diesel DI². Selected sweeps of the main parameters are displayed in this study. A cooled EGR-Rate of 35% is used which suppresses in combination with the early Diesel injections the NO_x formation. Less EGR is possible but then the Diesel SOI has to be retarded which leads to a more stratified Diesel inside the engine. Those rich regions ignite hotter forming more NO_x. At the correct EGR-Rate the inversed energetic Diesel share CHI does not influence the NO_x formation anymore. Increasing the Diesel share even reduces the NO_x emissions since the Pilot SOI has to be forwarded to keep the combustion phasing constant between 7 and 8°CA ATDC. NO_x emissions stay below the EURO-VI target for almost all tests using this strategy.

Lambda in the area of 1.3 to 1.5 shows the best results especially concerning the CH_4-Slip. The sweeps shown are measured at λ=1.5. Lower lambda has shown potential due to the reduced exhaust massflow but for high epsilon it was not possible to control the reactivity. For the comparability only λ=1.5 is displayed. By introducing sufficient Diesel the CH_4 emissions are minimized and more Diesel only reduces the efficiency. For higher compression ratios this Diesel amount is reduced, the trends stay the same and the overall Methane emissions are reduced. This is also the result of the improved combustion chamber layout and the increasing reactivity. As seen in figure 9 the heat release is higher and faster for the RCCI bowl

The used CNG has a Methane share of about 92% and has shown in this highly diluted process a demand of CHI in the region of 0,84 to be combusted by the homogenized but rich enough Diesel spots in the chamber. The EURO-VI target for methane emissions is not fully reached yet but with 0.75g/kWh in sight. The homogenization is enabled by Pilot SOIs between -80 and -60°CA. Those wide spread rich reaction spots ignite simultaneous all over the cylinder and in combination with the high methane number no knock occurred over all the testing. The only issue for the hardware can be the high pressure rise rates. This is mostly the case at the ε=15.5 sweeps which also need Pilot SOI earlier than -100°CA. With the lost phasing control this high compression ratio is excluded from further testing.

In figure 11 an overview of the best points of the sweeps is shown to close this paper. The most interesting figures are pointed out, namely the efficiency and the Methane emissions. In every point NO_x and soot emissions are below the targets. On the fullload points the limiting factor is the pressure rise rate. CHI=0,94 is the lowest possible. At 1000rpm and CHI=0.98 even 25bar BMEP are possible and realized but this testing is still ongoing.
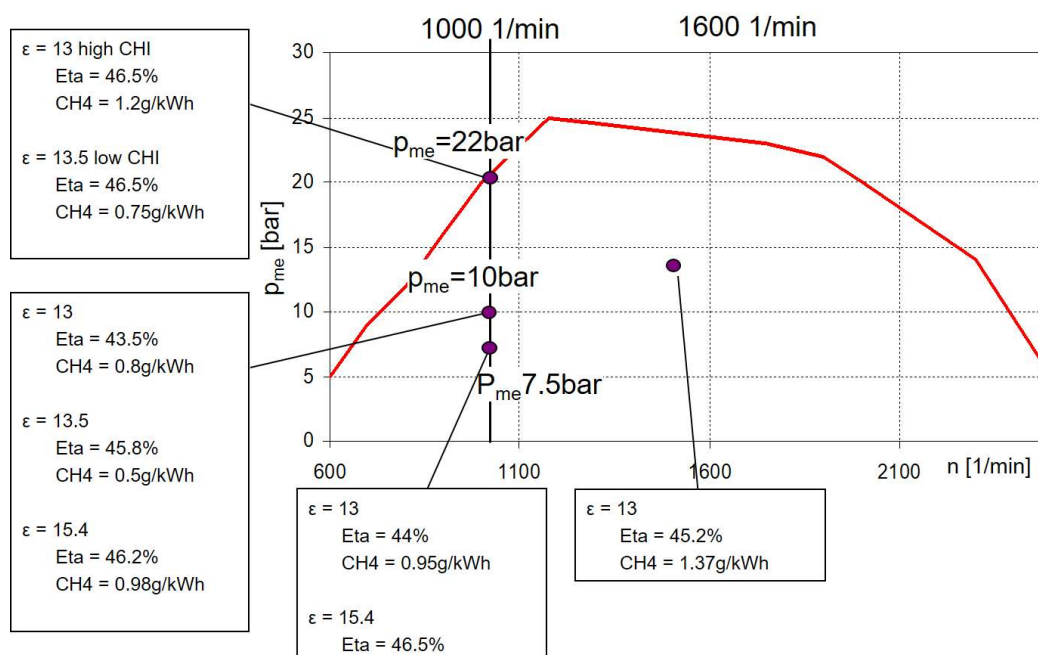
Fig. 11. Engine map with achieved best points in the project

Acknowledgement

References

[1] A. Kulzer, T. Nier und R. Karrelmeyer, A Thermodynamic Study on Boosted HCCI: Experimental Results, Detroit: SAE International, 2011.

[2] C. Stan und P. Guibert, „Verbrennungssteuerung durch Selbstzündung - Teil1: Thermodynamische Grundlagen," MTZ - Motortechnische Zeitschrift, pp. 56-62, JAN 2004.

[3] S. Saxena und I. D. Bedoya, „Fundamental phenomena affecting low temperature combustion and HCCI engines, high load limits and strategies for extending these limits," PROGRESS IN ENERGY AND COMBUSTION SCIENCE, pp. 457-488, OCT 2013.

[4] R. D. Reitz und G. Duraisamy, „Review of high efficiency and clean reactivity controlled compression ignition (RCCI) combustion in internal combustion engines," PROGRESS IN ENERGY AND COMBUSTION SCIENCE, Volume: 46, pp. 12-71, FEB 2015.

[5] A. B. Dempsey, N. R. Walker, E. Gingrich und R. D. Reitz, „COMPARISON OF LOW TEMPERATURE COMBUSTION STRATEGIES FOR ADVANCED COMPRESSION IGNITION ENGINES WITH A FOCUS ON CONTROLLABILITY," COMBUSTION SCIENCE AND TECHNOLOGY, Volume: 186, Issue: 2, pp. 210-241, Feb 2014.

[6] J. Eichmeier, Kombinierte Verbrennung brennraumintern gemischter Kraftstoffe mit unterschiedlichen Zündwilligkeiten untersucht am Beispiel von Benzin und Diesel, Berlin: Logos Verlag, 2012.

[7] F. Bach, Modellbasierte Verbrennungsregelung und Emissionspotential eines homogenen Tieftemperatur-Zweistoffbrennverfahrens in einem Mehrzylindermotor, Berlin: Logos Verlag, 2014.

[8] S. L. Kokjohn, R. M. Hanson, D. A. Splitter und R. D. Reitz, „Fuel reactivity controlled compression ignition (RCCI): a pathway to controlled high-efficiency clean combustion," INTERNATIONAL JOURNAL OF ENGINE RESEARCH, Volume: 12 Issue: 3, pp. 209-226, JUN 2011.

Numerical Investigation of Homogenous Charge Compression Ignition Operating Range Using Onion-Skin Multizone Model

J.M. Garcia-Guendulain[1], J.M. Riesco-Avila[2], A.E. Mendoza-Rojas[3] and O. Rodriguez-Abreo[1], F. Elizalde-Blancas[2]

[1]Universidad Politécnica de Querétaro. Carretera Estatal 420, CP 76240 El Marqués, Querétaro, Mexico.

E-mail: recepcion@upq.mx
Telephone: +(52) 442 101 9000

[2]Departamento de Ingeniería Mecánica, Universidad de Guanajuato. Carretera Salamanca-Valle de Santiago km 3.5+1.8, CP 36885, Comunidad de palo Blanco, Salamanca, Guanajuato, Mexico.

E-mail: webugto@ugto.mx
Telephone: +(52) 464 647 9940

[3]Facultad de Ingeniería, Universidad Autónoma de Querétaro. Carretera Chichimequillas S/N, CP 76140, Ejido Bolaños, Querétaro, Querétaro, Mexico.

E-mail: campus.aeropuerto@uaq.mx
Telephone: +(52) 442 192 1200

Abstract. In this work an evaluation of operating range in a HCCI engine with an onion skin multizone model has been developed. The present model can estimate the effect from physical and chemical processes inside combustion chamber with low computational resources. It is possible to simulate consecutive cycles with low computational time compared with other models (CFD models). This work analyses a single cylinder engine fueled with iso-octane (iC8H18). Good agreement with experimental data allows analyzing the effect of high temperature exhaust gasses recirculation as regulator agents of temperature of the mixture and dilution to delay the Ringing effect. Results allow identifying an operational range for HCCI, which abnormal combustion regions can be identified as a function of equivalence ratio and internal exhaust gas recirculation.

Notation

B	*Bore.*
C_p	*Specific heat at constant pressure.*
C_v	*Specific heat at constant volume.*
k	*Conductivity.*
$\mathcal{K}$	*Von Kármán constant.*
m	*Mass.*
MW	*Molecular weight.*
P_{cyl}	*In-cylinder pressure.*
Pr	*Prandtl number.*
Q_{cond}	*Conduction heat transfer.*
Q_{conv}	*Convection heat transfer.*
r_n	*Dimensionless distance in the normal direction*
R_u	*Universal gas constant.*
S	*Stroke.*
T	*Temperature.*
u	*Specific internal energy.*
U	*Internal energy.*
u_z	*Mean piston velocity.*

J.M. Garcia-Guendulain, J.M. Riesco-Avila, A.E. Mendoza-Rojas, O. Rodriguez-Abreo, F. Elizalde-Blancas

V Volume.
Y mass fraction.
y^+ Dimensionless distance from the cylinder wall

Greek Symbols

r Density.
m Viscosity.
$\dot{\omega}$ Production rates.

1. Introduction

Nowadays, internal combustion engines (ICE) operating regimes promise to improve the efficiency vs. emissions of conventional engines (spark-ignited and compression ignited engines). Homogenous charge compression ignition (HCCI) engines has been widely studied due to (1) high efficiency resulting from high compression ratio, lean operation and unthrottled intake [1–5], and (2) low NOx and PM emissions due to high levels of dilution leading to low temperature, fuel lean combustion [6].

Unlike to conventional engines, a control mechanism for start of combustion is necessary in HCCI engines, due to HCCI engines require the right temperature and composition at intake valve closing (IVC) instead a spark plug or injector (which are used in conventional engines). The uncontrolled start of combustion can result in rapid heat release leading to high in-cylinder pressure and the ringing problem (also known as knock), it can produce severe engine damage. Therefore, a detailed analysis of HCCI combustion is necessary to guide engine designers toward practical solutions. In this way some models have emerged and can be classified as zero-dimensional (single zone), multi-dimensional (CFD), and quasi-dimensional (multizone).

Single zone models may predict ignition timing with very low computational resources. However, in-cylinder thermal stratification cannot be predicted and therefore an overprediction of in-cylinder pressure, temperature, and NOx emissions is obtained.

Multidimensional models (CFD models) have demonstrated good agreement with experimental data [7,8]. However, a challenge emerges due to computational cost limits applicability to meshing processes and/or reduced/skeletal chemical kinetic mechanisms with hundreds rather than thousands of species to obtain operational region of the engine.

Multizone models can consider thermal stratification and chemical kinetics at much reduced computational expense vs. CFD, and therefore provide a versatile tool for accurate and computationally efficient analysis of HCCI combustion. This is especially true when the combustion process involves large molecules modeled with chemical kinetic mechanisms including thousands of species, or when hundreds of runs are necessary for determining optimum regions of operation. Improved methodologies can increase computational advantage even more, enabling rapid execution of hundreds of cases well within the computational capability of today's desktop or laptop computers rather than supercomputers.

In this paper a multizone model has been programmed and used for simulation of engine at several operating conditions with less computational resources than multidimensional models (CFD models). With this model, operational points of operation for a HCCI engine can be generated, where combustion control achieved by adjusting equivalence ratio and exhaust gas recirculation (EGR). Here, calculation of IVC temperatures have been obtained by coupling multizone model with methodologies extracted from literature [9–11], it allows to generate an operating optimal range from the influence of EGR and equivalence ratio. The description of the model and main results obtained are in next sections.

2. HCCI modelling

In the quasi-dimensional multi-zone modeling approach, the content of the cylinder is split on multiple reactors or zones and the way in which they interact, defines the type of multi-zone model to be used. In a balloon-type model, the zones can be considered as deformable control volumes with constant mass and typically they do not exchange heat or mass between them. Every zone losses heat toward cylinder walls in a predetermined way based on the volume or area of each region.

Generally, overall heat transfer is predicted using empirical correlations as that proposed by Annand [12], Woschni [13], Hohenberg [14] and their variations. The heat lost is distributed between the zones generating a thermal stratification during the mixture compression stage. This method generally assumes a uniform pressure on all the zones in each simulation time step. The aim of having a

temperature distribution is to reproduce the thermal stratification developed in the engine before ignition. This thermal stratification produces a sequential autoignition on several areas or charge regions (reactive mixture) in the cylinder. The rate at which the sequential autoignition occurs, which is related with the thermal stratification level, it is what determines the burning time and the pressure gradients increase during combustion.

Andreatta [15] developed one of the first balloon-type multi-zone combustion models. Woschni [13] correlation was used for estimating the heat loss in each zone, where heat transfer was calculated based on the temperature for each zone instead of an average in-cylinder temperature. Aceves et al. [16–18] and Babajimopoulos et al. [19] also developed a sequential multi-zone model for HCCI engines, by using CFD simulations to calculate the temperature distribution up to a predefined point of the compression stage, after which a solver of the chemical kinetics was used under balloon-type approach by initializing each zone based on the thermal distribution predicted by CFD simulations. The reason for using CFD for the no-reactive section for the cycle was to reach an adequate description of thermal stratification before ignition. Kodavasal et al.[20] in a similar way, used CFD to calculate thermal stratification in a single simulation, the advantage of this methodology consists on the speed at which results can be obtained due to the use of a preconditioner developed by McNenly et al. [21], this methodology is denominated Accelerated Multi-zone for Engine Cycle Simulation (AMECS). Easley et al. [22] developed a multi-zone model that describes crevices regions as well as the internal and external parts of the cores and adiabatic zones. In this model, only the external region, the boundary and the crevices are allowed to exchange mass with the aim of keeping a uniform pressure in the combustion chamber. Ogink y Golovitchev [23] used a similar model but coupled with software for simulation of consecutive cycles. Noda y Foster [24] also developed a balloon-type multi-zone model to analyze strategies on the control for combustion duration in hydrogen fueled HCCI engines. They noted that the effect of thermal stratification is more significant than fuel stratification for combustion duration. Sharma y Dhar [25] used a balloon-type model to analyze hydrogen combustion in a HCCI engines, however, a considerable difference on in-cylinder pressure and start of combustion prediction is obtained when compared with experimental data. Xu et al. [26] compared a single zone model and a multi-zone model with experimental data of a HCCI engine. They emphasized the need to use a multi-zone model for a better prediction of ignition and combustion duration.

In onion-skin model, the volume of combustion chamber is split on several concentric volumes where heat and mass transfer can exist between them, where thermal stratification is strongly defined by the heat exchange between the external zone and cylinder walls and crevices zones. Komninos et al. [27] developed an onion-skin model for zones with constant thickness, where empirical correlation by Annand [12] was implemented for the heat transfer towards cylinder walls. On the other hand, Komninos y Kosmadakis [28] implemented a heat transfer model that unlike to traditional models which are based on an average in-cylinder temperature, it is based on the external zone temperature. Kongsereeparp y Checkel [29] developed a multi-zone with an approach that allows a better geometrical description of the temperature in the boundary avoiding the need to adjust initial conditions. Godiño et al. [30] used an onion-skin model to analyze combustion for HCCI engines with good agreement with experimental data for in-cylinder pressure as well as for CO emissions. Multi-zone onion-skin models have been used to analyze the performance of HCCI engines fueled with alternative fuels [31–34]. Neshat y Saray [35] developed an onion-skin model where internal zones have the same height, which change with crank angle and a wall model was used for the heat transfer. Bissoli et al. [11] used a multi-zone model considering a wall function to estimate the heat transfer between the external zone and cylinder walls, which is adjusted by two constants that depended on the engine geometry and they have been originated from CFD simulations, validation with other geometrical conditions has been realized showing good agreement with experimental data, even for the evolution of some species with relation to crank angle. Another kind of multi-zone models are based on the probability density function (PDF), where the zones are created in a chemical space instead of a physical space [36–39].

In this work an onion-skin multizone model is demonstrated and validated with experimental results for an engine running on primary reference fuel (PRF) 90 (90% iso-octane by mass and 10% n-heptane by mass). An exploration on operating space for an HCCI engine controlled by regulating equivalence ratio and internal EGR was realized, demonstrating optimum regions of operation.

3. Multizone model

In this study the multizone model with detailed chemical kinetics was used to solve species, temperature, and pressure in transient conditions. The operation was simplified to closed cycle between inlet valve closing (IVC) and exhaust valve opening (EVO), for each incremental angle position between IVC and EVC.

The cylinder was split into several homogenous zones in terms of temperature, pressure, and species concentrations; however, these values can be stratified amongst zones. Heat transfer is obtained between zones by conduction heat transfer, and convection heat transfer is obtained at the first zone (near to walls).
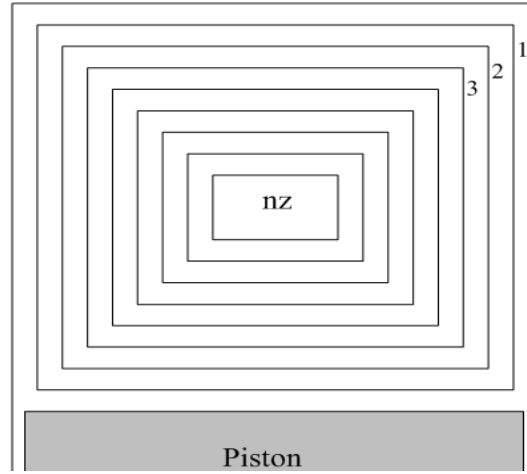
Fig. 1. Scheme of zone distribution for multizone onion-skin model.

For each j-th zone the first law of thermodynamics can be express as equation 1:

$$\frac{dU_j}{dt} = \frac{dQ_j}{dt} - \frac{dW_j}{dt} \tag{1}$$

$$\frac{dU_j}{dt} = m_j C_{v,j} \frac{dT_j}{dt} + u_j \sum_{i=1}^{ns} u_i \frac{dY_i}{dt} + \sum_{i=1}^{ns} u_i Y \frac{dm_i}{dt} \tag{2}$$

$$\frac{dW_j}{dt} = P_{cyl} \frac{dV_j}{dt} \tag{3}$$

$$\frac{dQ_j}{dt} = \frac{dQ_{j,cond}}{dt} + \frac{dQ_{j,conv}}{dt} \tag{4}$$

$$\frac{dQ_{j,cond}}{dt} = -k_{tot} A \frac{\partial T}{\partial x} \tag{5}$$

The terms in equation (1) are defined in equations (2) to (4), where Q is the heat transfer for each zone, which can be obtained by convection (6) and/or conduction (5). For convection heat transfer the Amsden [40] formulation is used.

$$\frac{dQ_{conv,2}}{dt} = \frac{\mu_{L,2} C_{p,2} F\left(T_2 / T_w\right)}{\text{Pr}_{L,2} \, r_{n,2}} A_w \tag{6}$$

$$F \begin{cases} 1.0 & y^+ \leq 11.05 \\[2em] \dfrac{\left(\dfrac{y^+ \text{Pr}_{L,2}}{\text{Pr}_T}\right)}{\dfrac{1}{\mathcal{K}} \ln\left(y^+\right) + B + 11.05\left(\dfrac{\text{Pr}_{L,2}}{\text{Pr}_{T,2}} - 1\right)} & y^+ > 11.05 \end{cases}$$

$$y^+ = \frac{\rho c_w u_z r_n}{\mu_L}$$

$$\frac{dY_{i,j}}{dt} = \frac{\dot{\omega}_{i,j} MW_i}{\rho_j} \tag{7}$$

$$V_j = \frac{\pi}{4}\left[B_j^2 S_j - B_{j+1}^2 S_{j+1}\right] \tag{8}$$

$$P_{cyl} = \frac{1}{V_{cyl}} \sum_{j=2}^{nz} \frac{m_j R_u T_j}{MW_j} \tag{9}$$

Species evolution for each zone is calculated in equation (6), and volume for each zone is calculated in equation (8). The overall pressure is assumed to be constant and is obtained with equation (9). All the equations are solved numerically using CANTERA package for calculations of chemical kinetics and thermodynamic properties.

4. Validation

Multizone model has been validated by comparison with CFD results obtained from a single cylinder HCCI engine fueled with iso-octane (iC_8H_{18}), 90% by mass and n-heptane (nC_7H_{16}) 10% by mass mixture (PRF90). Table 1 shows geometrical and operational conditions for the engine [20]. Intake temperature was set to maintain 50% of heat release at TDC (Figure 2). The multizone model is limited to closed cycle (from IVC to EVC), and a mechanism with 252 species and 1038 reactions were used [41]. An analysis of dependence on number of zones is shown in Figure 2, where with 11 zones, the maximum temperature (equation 10) and pressure (equation 11) differences are less than -1 K and 0.2%, respectively. The number of zones used here are agree with those shown in literature [11,32,34].

$$\Delta T_{\max} = T_{\max,i} - T_{\max,i-1} \tag{10}$$

$$\Delta P = \frac{P_{cyl,\max,i} - P_{cyl,\max,i-1}}{P_{cyl,\max,i}} \times 100 \tag{11}$$

J.M. Garcia-Guendulain, J.M. Riesco-Avila, A.E. Mendoza-Rojas, O. Rodriguez-Abreo, F. Elizalde-Blancas

Table 1. Engine specifications and operating conditions.

Displacement	0.540 liters
Bore	86 mm
Stroke	94.3 mm
Connecting rod length	152.2 mm
Compression ratio	12.25:1
Valves	4
Speed	2000 rpm
Intake pressure	100 kPa (absolute)
IVC	130° BTDC
EVO	148° ATDC

Figure 3 compares experimental pressure with multizone predictions. Good agreement is obtained for all cases. The figure shows the increase in peak cylinder pressure as the intake pressure increases due to more intense heat release. Here, maximum difference obtained here was 7% (200kPa) and a minimum of 1% (100kPa), which are similar to those shown in literature [7,8]. Figure 4 shows trends in heat release rates (HRR) for both CFD data [20] and present multizone model, which are reproduced with good agreement in terms of peaks value. However, choppy profiles are still obtained in multizone model (which is a characteristic of this kind of models).
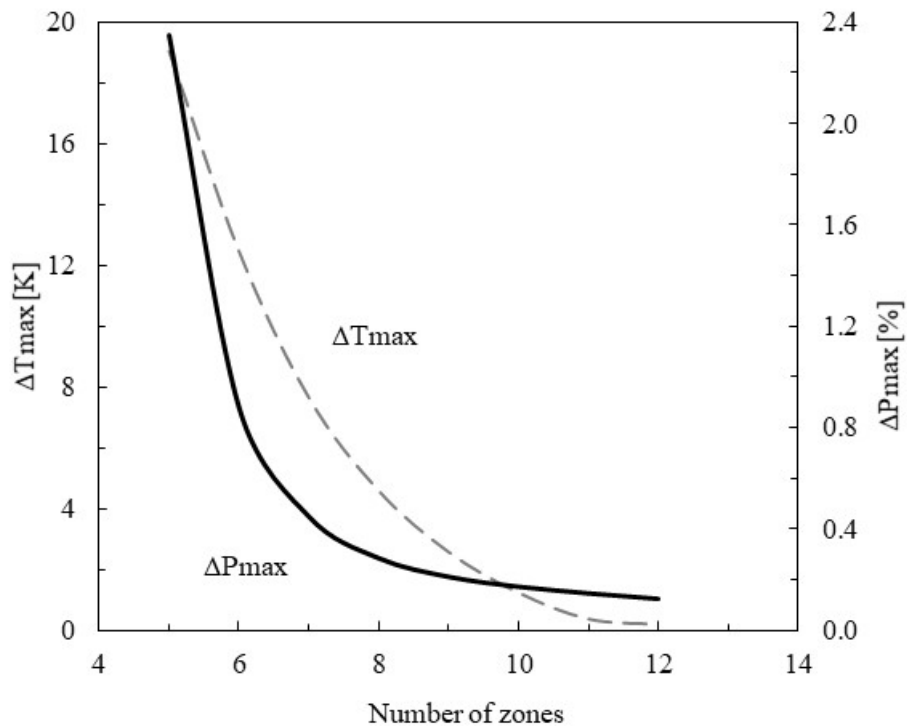
Fig. 2. Effect of the increase on number of zones in maximum temperature and pressure differences.
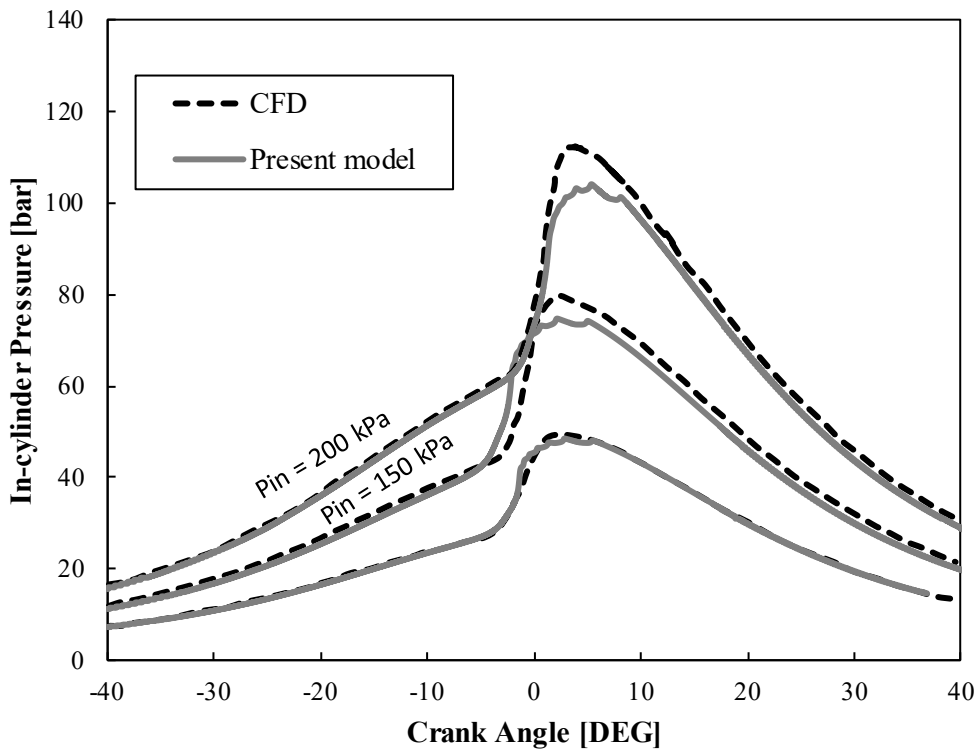
Fig. 3. Comparison of pressure profile obtained from CFD data (dashed lines) vs. multizone model (solid lines) results for the engine described in Table 1 running on PRF90.
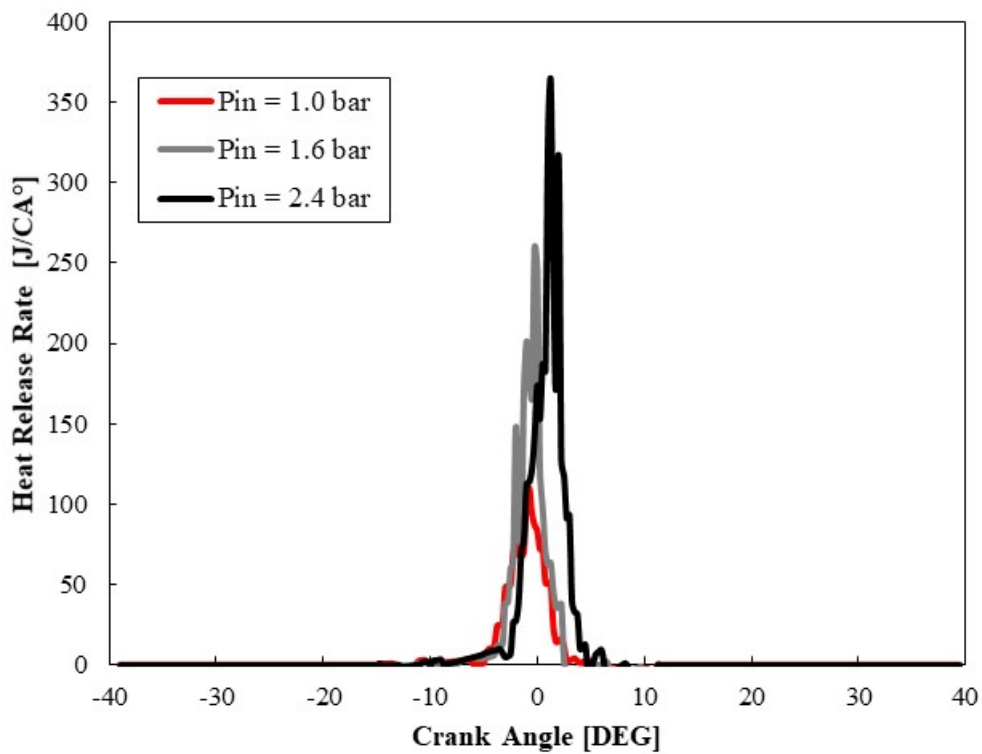
a)

Fig. 4. HRR trends obtained from a) CFD data (dashed lines) and b) multizone model (solid lines) results for the engine described in Table 1 running on PRF90.
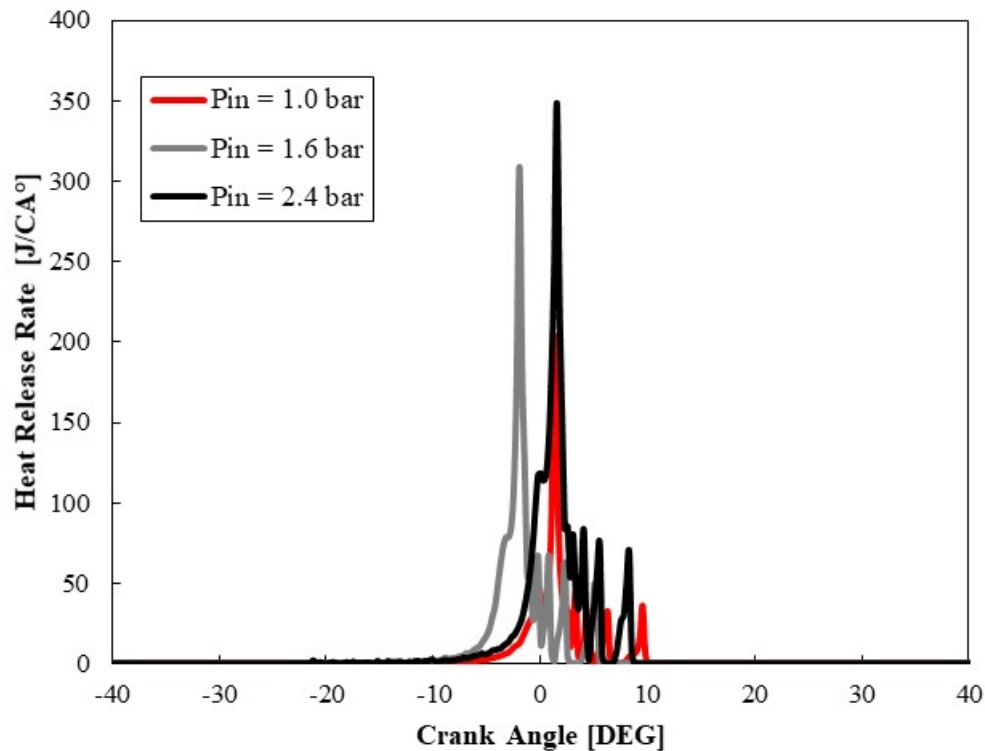
b)

Fig. 4. Continuation.

The accuracy of this validation increases our confidence for broad applicability to other fuels and engines. However, further validation is still necessary to test the limits and determine ranges of validity of the approach and model assumptions.

5. HCCI Operation with Equivalence Ratio and Internal EGR

HCCI engine control is a challenge due to strong dependence on chemical kinetics. In transportation a rapid change on load is necessary, therefore, the engine controller must be capable of rapidly responding to maintain efficient operation without knock or misfire. The analysis was conducted with following assumptions:

- Intake conditions at 300 K and 1 bar.
- Analysis limited to a single speed (2000 rpm).
- Closed cycle (from IVC to EVC)
- Calculation of IVC temperatures (with EGR) have been obtained by coupling multizone model with methodologies obtained from literature [9–11].

The HCCI operational map is generated by running the multizone model over 100 operating conditions to produce an engine performance map identifying regions of acceptable operation. The zones in the Figure 5 are defined as:

1. **No combustion:** Cases where the mixture doesn't ignite due to the in-cylinder temperature is not high enough to produce auto ignition are grouped in this zone. Lower intake temperature is required with higher equivalence ratios to ignite the in-cylinder mixture. At least 30% EGR is necessary for satisfactory HCCI combustion.
2. **Misfire:** Cases where combustion fails under conditions with high EGR are classified in this zone. In these cases, autoignition of in-cylinder mixture in some regions was presented, the mixture ignites but does not burn to completion due to very slow rate of reaction caused by very high dilution of the relatively small amount of fuel present.

3. **Ringing:** For rich mixtures, once mixture auto ignition starts, high pressure gradients are presented due to the fast heat release by combustion. In-cylinder pressure gradients produce vibrations (energy) transmitted through the engine structure, which could produce severe damage as a consequence of high in-cylinder overpressures. The Ringing (RI) parameter proposed by Eng [42] was used to measure the intensity of the pressure gradients. A limit value of RI = 5 MW/m2 was set, above which the transmitted vibrations through the engine structure are harmful for the combustion and engine integrity. EGR dilution helps to reduce ringing intensity, and high ϕ (0.9) can be reached within the ringing limit if EGR is increased to 60% (Figure 5).

4. **Partial combustion**: Cases where combustion efficiency is lower than 85% are classified in this zone. These cases correspond to high EGR and low equivalence ratios, which produces in-cylinder regions with unburned mixture.
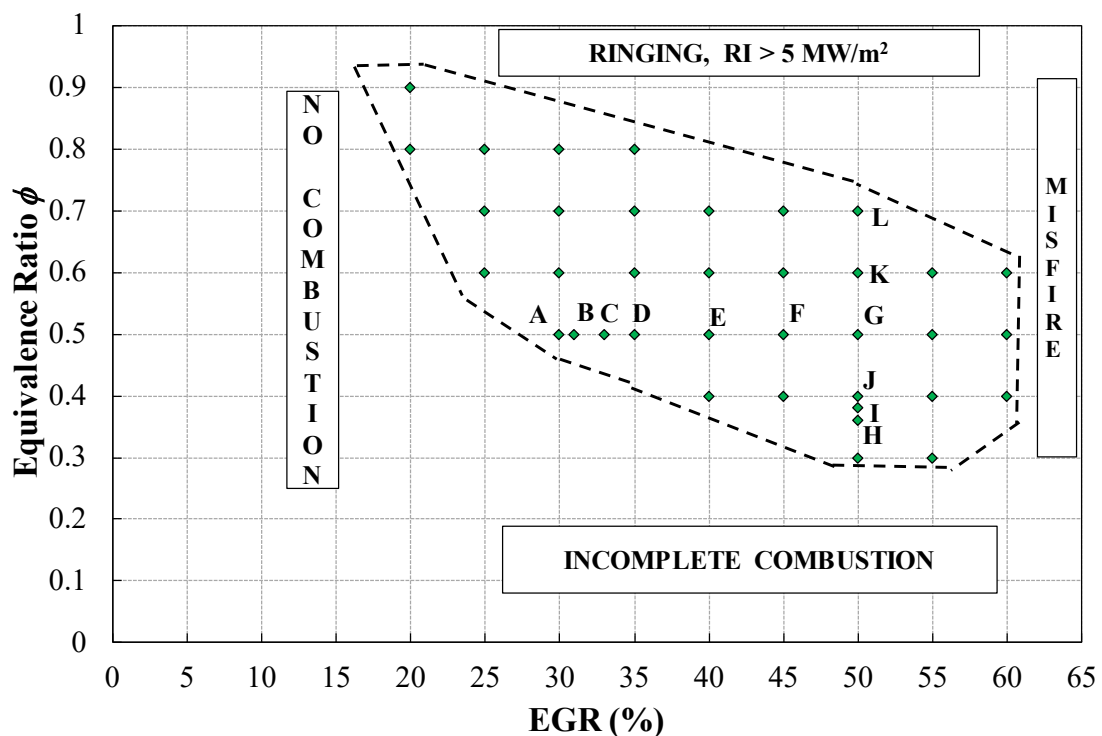
Fig 5. Equivalence ratio-EGR map showing region of acceptable HCCI operation (dashed contour) limited by four regions of abnormal combustion: no combustion, misfire, ringing, and partial combustion for the egine geometry of Table 1 running at Tin = 300 K and Pin = 100 kPa.

An acceptable region has been obtained; however, it is necessary to evaluate all points and identify the optimal operating region by analyzing the cumulative heat release for several points. An example can be represented by points identified with letters A-L (Figure 5). A sweep In the EGR direction (Figure 6) and equivalence ratio direction (Figure 7) were made.

Figure 6 shows some of the points within the acceptable HCCI operating region (D-G) have early combustion which lead to inefficient operation. Points A, B and C demonstrate near optimum combustion timing leading to high efficiency, where CA50 (50% of heat release) is reached at 10°, 5.8° and 0° ATDC, respectively.

Figure 7 shows the sweep in the EGR direction. Inefficient and early heat release are obtained, which can produce damage in the engine. Case H and I appears to be optimum due to heat release centered close to TDC. This point is very close to partial combustion limit and therefore a high precise controller is necessary for maintaining high combustion efficiency. It can be seen a higher power in point J than I, is generated (but inefficiently) due to high equivalence ratio, however, the same power could be obtained for a reduced EGR because lower EGR increase specific heat ratio and hence the indicated thermal efficiency (ITE).
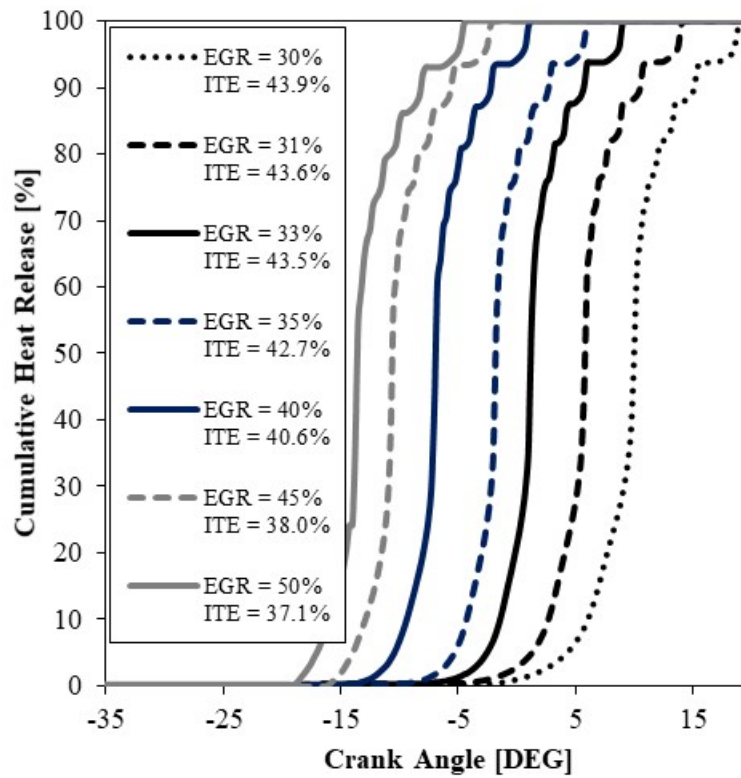
Fig 6. Cumulative Heat Release as a function of crank angle and indicated thermal efficiency (ITE) for points A-G.
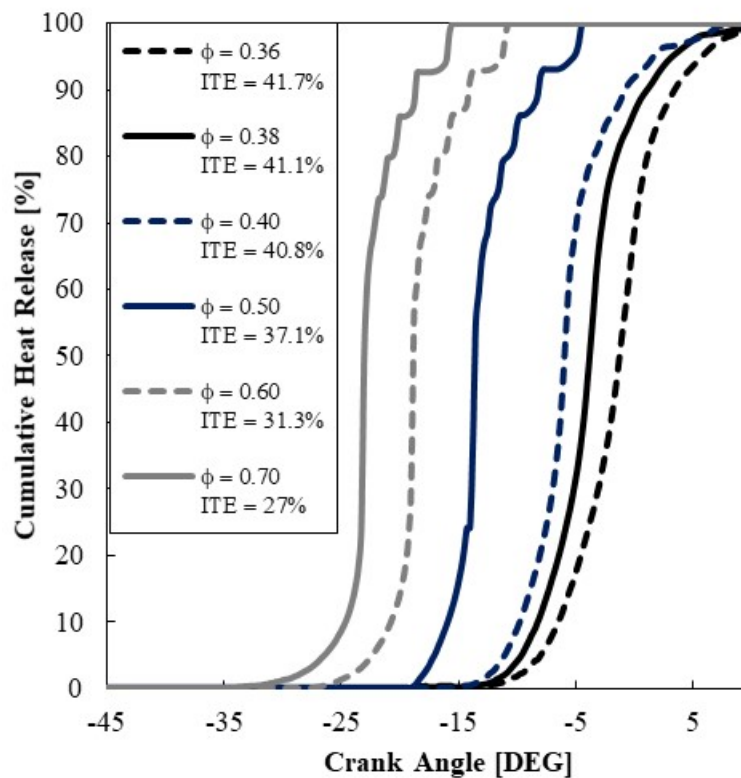
Fig 7. Cumulative Heat Release as a function of crank angle and indicated thermal efficiency (ITE) for points G-L
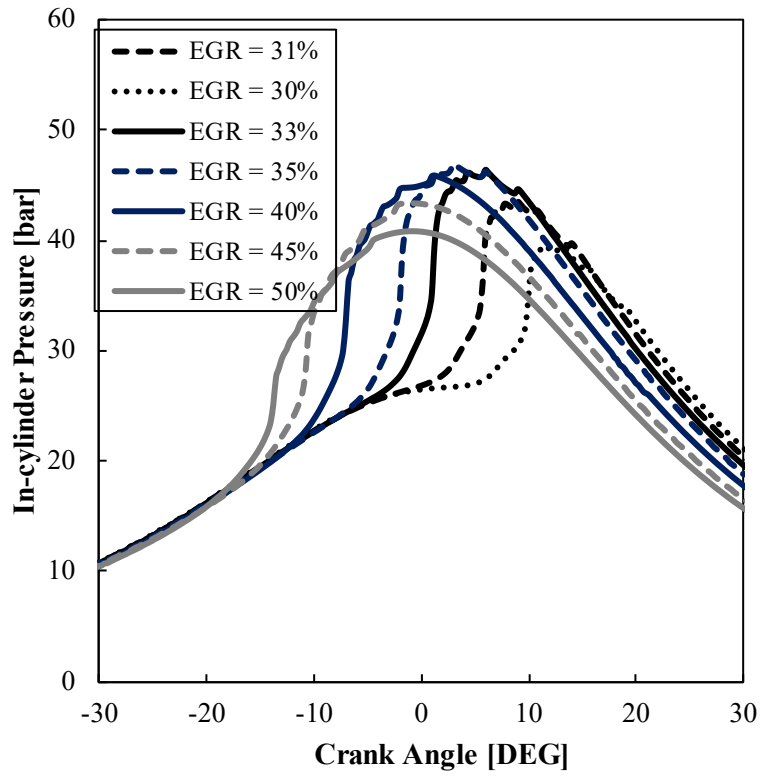
Fig 8. Pressure profiles for points A-G (Figure 7) obtained from multizone model
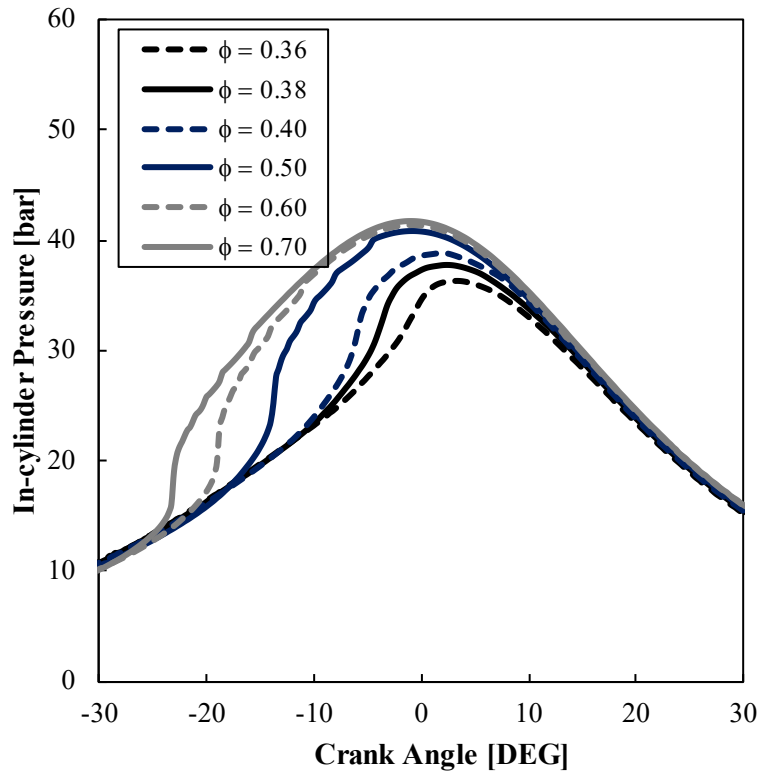
Fig 9. Pressure profiles for points G-K (Figure 7) obtained from multizone model

Figure 8 and 9 shows in-cylinder pressure traces for points obtained by sweeps on equivalence ratio direction and EGR direction, respectively. Again, very early and sudden combustion for points J-L and D-F is demonstrated.

Figures 6 and 7 show some points have early combustion, then they are not considered as acceptable operation region. Now, it is necessary to identify all points in the region of acceptable combustion (Figure 5), an optimal operating region is obtained where combustion timing is most appropriate for efficient combustion. This optimal operating region is shown in Figure 10. Very Careful mixture control is therefore necessary for maintaining efficient combustion while avoiding the risk of reduced combustion efficiency leading to poor operation.
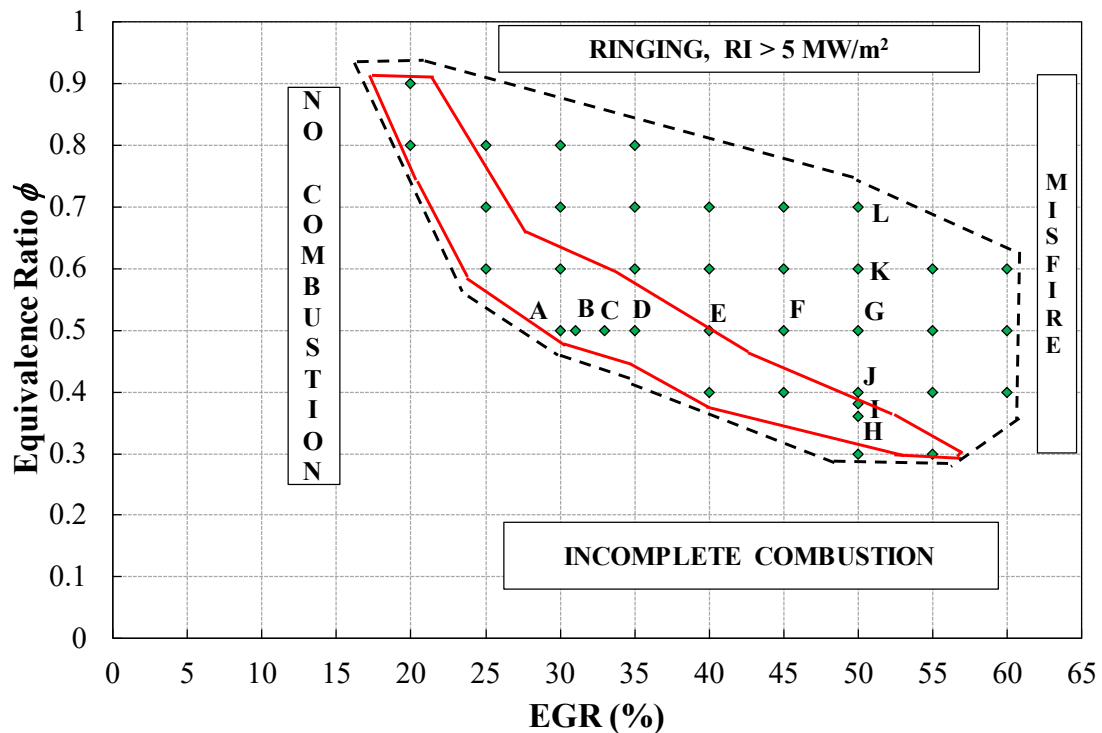
Fig 10. Optimal operation region with maximum efficiency due to the best appropriate combustion phasing

6. Conclusions

In this work an acceptable and optimum region for an HCCI engine using EGR and equivalence ratio as a combustion control has been developed. The multizone model is based on onion-skin approach and, which has the advantage of reduced computational time compared with multidimensional models and several operating conditions can be simulated in a relative short time. This multizone model can capture thermal stratification, which is very important to simulate HCCI engines, due to strong dependence of chemical reactions on temperature and the coupling with other models allow to evaluate the effect of EGR in closed cycle (form IVC to EVC). Main achievements are listed below.

- Onion-skin multizone model have been validated with CFD simulations obtained from literature. Good agreement is obtained, specially at atmospheric intake pressure (condition used in all simulations presented in this work), here maximum and minimum difference, in higher peak of pressure, with CFD data were 7% and 1% respectively, which are similar to literature.

- Combustion control based on adjusting EGR and equivalence ratio is characterized by several runs of multizone model. It was possible to obtain an acceptable HCCI operation region limited by abnormal combustion: Ringing effect, misfire, partial combustion, and no combustion.

- With acceptable region defined, an optimal region is also obtained. In this region high combustion efficiency is maintained together with combustion timing centered at TDC.
- Careful mixture control has a big role for maintaining efficient and smooth combustion while avoiding the risk of reduced combustion efficiency leading to poor operation.

References

[1] Dec JE, Sjöberg M. A Parametric Study of HCCI Combustion - the Sources of Emissions at Low Loads and the Effects of GDI Fuel Injection. Warrendale, PA: SAE International; 2003. https://doi.org/10.4271/2003-01-0752.

[2] Dec JE. A Computational Study of the Effects of Low Fuel Loading and EGR on Heat Release Rates and Combustion Limits in HCCI Engines. Warrendale, PA: SAE International; 2002. https://doi.org/10.4271/2002-01-1309.

[3] Sjöberg M, Dec JE, Cernansky NP. Potential of Thermal Stratification and Combustion Retard for Reducing Pressure-Rise Rates in HCCI Engines, Based on Multi-Zone Modeling and Experiments. Warrendale, PA: SAE International; 2005. https://doi.org/10.4271/2005-01-0113.

[4] Machrafi H, Cavadiasa S. An experimental and numerical analysis of the influence of the inlet temperature, equivalence ratio and compression ratio on the HCCI auto-ignition process of Primary Reference Fuels in an engine. Fuel Processing Technology 2008;89:1218–26. https://doi.org/10.1016/j.fuproc.2008.05.019.

[5] Yao M, Zheng Z, Liu H. Progress and recent trends in homogeneous charge compression ignition (HCCI) engines. Progress in Energy and Combustion Science 2009;35:398–437. https://doi.org/10.1016/j.pecs.2009.05.001.

[6] Duret P, Gatellier B, Monteiro L, Miche M, Zima P, Maroteaux D, et al. Progress in Diesel HCCI Combustion Within the European SPACE LIGHT Project. Warrendale, PA: SAE International; 2004. https://doi.org/10.4271/2004-01-1904.

[7] Yousefzadeh A, Jahanian O. Using detailed chemical kinetics 3D-CFD model to investigate combustion phase of a CNG-HCCI engine according to control strategy requirements. Energy Conversion and Management 2017;133:524–34. https://doi.org/10.1016/j.enconman.2016.10.072.

[8] Poorghasemi K, Saray RK, Bahlouli K, Zehni A. 3D CFD simulation of a natural gas fueled HCCI engine with employing a reduced mechanism. Fuel 2016;182:816–30. https://doi.org/10.1016/j.fuel.2016.06.005.

[9] Heywood JB. Internal Combustion Engine Fundamentals. Second Edition. New York, USA: McGraw-Hill; 1988.

[10] Sjöberg M, Dec JE. An Investigation of the Relationship Between Measured Intake Temperature, BDC Temperature, and Combustion Phasing for Premixed and DI HCCI Engines. Warrendale, PA: SAE International; 2004. https://doi.org/10.4271/2004-01-1900.

[11] Bissoli M, Frassoldati A, Cuoci A, Ranzi E, Mehl M, Faravelli T. A new predictive multi-zone model for HCCI engine combustion. Applied Energy 2016;178:826–43. https://doi.org/10.1016/j.apenergy.2016.06.062.

[12] Annand WJD. Heat Transfer in the Cylinders of Reciprocating Internal Combustion Engines. Proceedings of the Institution of Mechanical Engineers 1963;177:973–96. https://doi.org/10.1243/PIME_PROC_1963_177_069_02.

[13] Woschni G. A Universally Applicable Equation for the Instantaneous Heat Transfer Coefficient in the Internal Combustion Engine. Warrendale, PA: SAE International; 1967. https://doi.org/10.4271/670931.

[14] Hohenberg GF. Advanced Approaches for Heat Transfer Calculations. Warrendale, PA: SAE International; 1979. https://doi.org/10.4271/790825.

[15] Andreatta DA. The Use of Reformed Natural Gas as a Fuel for Reciprocating Engines. University of California, Berkeley; 1995.

[16] Aceves SM, Flowers DL, Westbrook CK, Smith JR, Pitz W, Dibble R, et al. A Multi-Zone Model for Prediction of HCCI Combustion and Emissions. Warrendale, PA: SAE International; 2000. https://doi.org/10.4271/2000-01-0327.

[17] Aceves SM, Flowers DL, Martinez-Frias J, Smith JR, Westbrook CK, Pitz WJ, et al. A Sequential Fluid-Mechanic Chemical-Kinetic Model of Propane HCCI Combustion. Warrendale, PA: SAE International; 2001. https://doi.org/10.4271/2001-01-1027.

[18] Aceves SM, Martinez-Frias J, Flowers DL, Smith JR, Dibble RW, Wright JF, et al. A Decoupled Model of Detailed Fluid Mechanics Followed by Detailed Chemical Kinetics for Prediction of Iso-Octane HCCI Combustion. Warrendale, PA: SAE International; 2001. https://doi.org/10.4271/2001-01-3612.

[19] Babajimopoulos A, Lavoie GA, Assanis DN. Modeling HCCI Combustion With High Levels of Residual Gas Fraction - A Comparison of Two VVA Strategies. Warrendale, PA: SAE International; 2003. https://doi.org/10.4271/2003-01-3220.

[20] Kodavasal J, McNenly MJ, Babajimopoulos A, Aceves SM, Assanis DN, Havstad MA, et al. An accelerated multi-zone model for engine cycle simulation of homogeneous charge compression ignition combustion. International Journal of Engine Research 2013;14:416–33. https://doi.org/10.1177/1468087413482480.

[21] McNenly MJ, Havstad MA, Aceves SM, Pitz WJ. Integration Strategies for Efficient Multizone Chemical Kinetics Models. SAE Int J Fuels Lubr 2010;3:241–55. https://doi.org/10.4271/2010-01-0576.

[22] Easley WL, Agarwal A, Lavoie GA. Modeling of HCCI Combustion and Emissions Using Detailed Chemistry. Warrendale, PA: SAE International; 2001. https://doi.org/10.4271/2001-01-1029.

[23] Ogink R, Golovitchev V. Gasoline HCCI Modeling: An Engine Cycle Simulation Code with a Multi-Zone Combustion Model. Warrendale, PA: SAE International; 2002. https://doi.org/10.4271/2002-01-1745.

[24] Noda T, Foster DE. A Numerical Study to Control Combustion Duration of Hydrogen-Fueled HCCI by Using Multi-Zone Chemical Kinetics Simulation. Warrendale, PA: SAE International; 2001. https://doi.org/10.4271/2001-01-0250.

[25] Sharma P, Dhar A. Development of chemical kinetics based hydrogen HCCI combustion model for parametric investigation. International Journal of Hydrogen Energy 2016;41:6148–54. https://doi.org/10.1016/j.ijhydene.2015.12.021.

[26] Xu H, Liu M, Gharahbaghi S, Richardson S, Wyszynski M, Megaritis T. Modelling of HCCI Engines: Comparison of Single-zone, Multi-zone and Test Data. Warrendale, PA: SAE International; 2005. https://doi.org/10.4271/2005-01-2123.

[27] Komninos NP, Hountalas DT, Kouremenos DA. Development of a New Multi-Zone Model for the Description of Physical Processes in HCCI Engines. Warrendale, PA: SAE International; 2004. https://doi.org/10.4271/2004-01-0562.

[28] Komninos NP, Kosmadakis GM. Heat transfer in HCCI multi-zone modeling: Validation of a new wall heat flux correlation under motoring conditions. Applied Energy 2011;88:1635–48. https://doi.org/10.1016/j.apenergy.2010.11.039.

[29] Kongsereeparp P, Checkel MD. Novel Method of Setting Initial Conditions for Multi-Zone HCCI Combustion Modeling. Warrendale, PA: SAE International; 2007. https://doi.org/10.4271/2007-01-0674.

[30] Godiño JAV, García MT, Jiménez-Espadafor Aguilar FJ, Trujillo EC. Numerical study of HCCI combustion fueled with diesel oil using a multizone model approach. Energy Conversion and Management 2015;89:885–95. https://doi.org/10.1016/j.enconman.2014.10.041.

[31] Visakhamoorthy S, Tzanetakis T, Haggith D, Sobiesiak A, Wen JZ. Numerical study of a homogeneous charge compression ignition (HCCI) engine fueled with biogas. Applied Energy 2012;92:437–46. https://doi.org/10.1016/j.apenergy.2011.11.014.

[32] Visakhamoorthy S, Wen JZ, Sivoththaman S, Koch CR. Numerical study of a butanol/heptane fuelled Homogeneous Charge Compression Ignition (HCCI) engine utilizing negative valve overlap. Applied Energy 2012;94:166–73. https://doi.org/10.1016/j.apenergy.2012.01.047.

[33] Neshat E, Saray RK, Hosseini V. Effect of reformer gas blending on homogeneous charge compression ignition combustion of primary reference fuels using multi zone model and semi detailed chemical-kinetic mechanism. Applied Energy 2016;179:463–78. https://doi.org/10.1016/j.apenergy.2016.06.150.

[34] Neshat E, Saray RK, Parsa S. Numerical analysis of the effects of reformer gas on supercharged n-heptane HCCI combustion. Fuel 2017;200:488–98. https://doi.org/10.1016/j.fuel.2017.04.005.

[35] Neshat E, Saray RK. Effect of different heat transfer models on HCCI engine simulation. Energy Conversion and Management 2014;88:1–14. https://doi.org/10.1016/j.enconman.2014.07.075.

[36] Maurya RK, Akhil N. Development of a new reduced hydrogen combustion mechanism with NOx and parametric study of hydrogen HCCI combustion using stochastic reactor model. Energy Conversion and Management 2017;132:65–81. https://doi.org/10.1016/j.enconman.2016.11.021.

[37] Maurya RK, Akhil N. Numerical investigation of ethanol fuelled HCCI engine using stochastic reactor model. Part 2: Parametric study of performance and emissions characteristics using new reduced ethanol oxidation mechanism. Energy Conversion and Management 2016;121:55–70. https://doi.org/10.1016/j.enconman.2016.05.017.

[38] Kraft M, Maigaard P, Mauss F, Christensen M, Johansson B. Investigation of combustion emissions in a homogeneous charge compression injection engine: Measurements and a new computational model. Proceedings of the Combustion Institute 2000;28:1195–201. https://doi.org/10.1016/S0082-0784(00)80330-6.

[39] Maigaard P, Mauss F, Kraft M. Homogeneous Charge Compression Ignition Engine: A Simulation Study on the Effects of Inhomogeneities. J Eng Gas Turbines Power 2003;125:466–71. https://doi.org/10.1115/1.1563240.

[40] Anthony A. Amsden. KIVA-3V A block-structured program for engines with vertical or canted valves. Los Alamos, New Mexico: Los Alamos National Laboratory; 1997.

[41] Mehl M, Chen JY, Pitz WJ, Sarathy SM, Westbrook CK. An Approach for Formulating Surrogates for Gasoline with Application toward a Reduced Surrogate Mechanism for CFD Engine Modeling. Energy Fuels 2011;25:5215–23. https://doi.org/10.1021/ef201099y.

[42] Eng JA. Characterization of Pressure Waves in HCCI Combustion. Warrendale, PA: SAE International; 2002. https://doi.org/10.4271/2002-01-2859.

DNS and Experimental Investigation of Ignition and Transition to Premixed Flame Propagation in Operating Conditions Representative of Modern High Efficiency Spark Ignition Engines

D. Jikadia[1], A. Dulbecco[1], C. Mehl[1] and F. Foucher[2]

[1] IFP Energies nouvelles, 1 et 4 avenue de Bois-Préau, 92852 Rueil-Malmaison, France; Institut Carnot IFPEN Transports Energie.

E-mail: alessio.dulbecco@ifpen.fr
Telephone: +33 (0)1 47 52 72 24

[2] Université d'Orléans, INSA-CVL, PRISME, EA 4229, F45072, Orléans, France.

E-mail: fabrice.foucher@univ-orleans.fr
Telephone: +33 (0)2 38 49 43 68

Abstract. The present social context imposes drastic reductions of transport greenhouse gases and pollutant emissions. To tackle this demand, car manufacturers adopt technologies such as engine down-sizing and diluted combustion processes. In this context, an efficient ignition of mixtures is crucial to ensure a high heat release. To get to a deeper understanding about the physics governing early stages of premixed combustion, the University of Orléans, in the framework of the French government research project ANR MACDOC, generated a consistent experimental database to study ignition and flame propagation processes in a constant volume vessel. This allows to have a detailed description of the flame dynamics of an air / isooctane / diluent mixture as a function of the thermochemical properties of the mixture and the nature of the diluent, as well as of the spark ignition energy. With the same aim, Direct Numerical Simulations (DNS) accounting for species differential diffusion and complex chemistry were performed at IFP Energies nouvelles (IFPEN). The simulation approach integrates a specific Adaptive Mesh Refinement (AMR) algorithm, able to track the flame front into the domain, to reduce the computational cost. This investigation is instrumental in obtaining a deeper insight in experimental results and evaluate the concurrent influences of chemical kinetics, flame stretch and ignition energy on the establishment of the premixed flame propagation. Investigation was pushed up to non-self-sustained ignition processes, leading to combustion extinction. The influence of the stretch on flame propagation was modelled using a non-linear formulation, function of the mixture Markstein number. The simulation results showed the capability of the numerical approach to reproduce the theoretical formulation of the problem, valid for thermodynamic equilibrium conditions, and experimental results. The present study is a necessary step to model ignition of next generation Spark Ignition engines operating under steady and transient conditions.

1. Introduction

One of the most important factors in premixed combustion modelling, and in particular for those based on flamelet approaches, is the laminar flame speed [1, 2, 3, 4, 5]. This variable can be measured experimentally and it varies depending on the fuel nature, mixture temperature, pressure, equivalence ratio, dilution rate and dilution type. In literature, several mathematical correlations fitting experiments are available for unstretched laminar flames [6, 7, 8]. Nevertheless, the most extremes operating conditions attainable experimentally are quite far from the conditions found in Internal Combustion Engine (ICE), especially in terms of pressure and temperature. Furthermore, in engines, flames are stretched and it is known that stretched laminar flames velocities can be quite different from the corresponding unstretched values [9]. Experimental works available in literature on the determination of the laminar flame speeds come from different research teams all around the world [10, 11, 12, 13, 14, 15]. These works refer to different thermochemical conditions, attaining extremes conditions of 20 bar in terms of pressure [10], and 450 K in terms of temperature [11], mainly relative to isooctane fuel. Regarding the impact of the stretch on the laminar flame speed, the above-mentioned works consider a linear dependence between the two variables. This assumption is controverted in the literature especially when dealing with diluted

mixtures [16]. Nowadays, it is common to use numerical simulation to be able to go beyond the limitations encountered in experimental works. This allows to determine the behaviour of laminar flame speed of different fuel compositions [17] and investigate more severe thermochemical conditions, by extrapolating the understanding of experiments. When coupled with complex chemistry, numerical simulation allows to determine species reaction rates of chemical mechanism accounting for hundreds of species and thousands of reactions [18]; nevertheless, this approach remains an approximation, as the chemical mechanisms are themselves validated on intervals of pressure and temperature which are quite far from real conditions inside ICE combustion chambers. Furthermore, in ICEs, flame propagates in highly turbulent flow fields and flame is wrinkled by turbulence. Usually, in literature, when dealing with turbulent flame propagation, flame stretch is commonly not accounted for. In [19], the ignition process, with a focus on the ignition-independent phase of flame propagation, was investigated, and an approach for 0D/QD modelling, giving a consistent description of the effective flame speed behaviour accounting for stretch for laminar and turbulent propagating conditions, was proposed.

The goal of this paper is to better understand the very beginning of flame propagation after the ignition process, the ignition-dependent one, to extract useful features to enrich the phenomenological modelling of the early flame propagation. In fact, this is a process that becomes crucial in highly diluted (up to 40% of Exhaust Gas Recirculation (EGR)) or ultra-lean (dilution ratio higher then $\lambda = 2$) mixture combustion. In details, after a short remind regarding premixed flame propagation theory, the experimental setup, and the generated database and major observations justifying this work are presented [8, 20, 21]. Then, the numerical technique and setup to perform complex chemistry DNS of expanding spherical flames, capable to account for the flame stretch impact on laminar flame propagation is presented. After that, the numerical-investigated database is introduced and the major results are discussed.

2. Experimental study

The experimental facility and methods used in this article are those described in [22], a brief description is given below. Investigations of laminar flame velocities and Markstein lengths in the present article were conducted in a high-pressure and high-temperature spherical combustion chamber with an inner volume of 4,2 L (200 mm inner diameter). The vessel can be heated to a maximum temperature of 473 K. The initial pressure inside the combustion chamber is limited to 10 bar. The device is equipped with a vacuum pump to achieve a residual pressure lower than 0.003 bar before the chamber is filled with the different gases. Synthetic air (79.1 vol% N_2 and 20.9 vol % O_2) was used for the experiments. Iso-octane was injected through a Coriolis mass flow meter (Bronkhorst mini CORI-FLOW 30 g/h) and volumes of air and diluent were introduced with thermal flow meters (Brooks 5850S, 2 NL/min for air and 0.5 NL/min for diluent). The air/diluent flow was directed to the exit of the Coriolis flow meter to convey the injected liquid. The inlet valve of the fuel/oxidant/diluent mixture was heated to 473 K to ensure the complete vaporization of isooctane. To obtain a perfectly homogeneous premixed mixture, a fan was installed inside the chamber to mix the gases. The fan is stopped 10 s before ignition, in order to avoid any perturbation during the flame propagation experiments. A piezoelectric pressure transducer and a type-K thermocouple were used to check, respectively, the pressure level and the temperature before ignition. The maximum deviation between the effective initial pressure inside the combustion chamber and the required initial pressure was about 3%. The temperature fluctuation of the prepared mixture was within 2 K with respect to the target initial temperature. Two tungsten electrodes (diameter 1.5 mm), with a 1 mm gap, linked to a conventional capacitive discharge ignition system, were used for spark production at the center of the chamber. A larger gap between the electrodes would provide a more efficient ignition under lean conditions, but the electrodes must be fairly close to create and maintain the electric arc. In all experiments, the minimum discharge energy required for spherical flame initiation was supplied to the spark gap in order to minimize the ignition-dominated phase [16]. To determine the minimum discharge energy, the charge time of the ignition coil was increased until spherical flame initiation, Fig. 1. The minimum discharge energy was then deduced from the temporal measurements of the voltage and the current intensity at the secondary winding of the ignition coil, using a Tektronix P6015A probe and a Stangenes 0.5-0.1W, respectively. This process was repeated for each operating condition. Depending on the initial pressure and temperature, the equivalence ratio, and the dilution rate, the discharge energy required for spherical flame initiation was varied between 2.5 and 51 mJ. As shown in Fig. 1, by observing the flame propagation dynamics, two phases can be distinguished: one, starting just after spark timing, impacted by the ignition energy value, the other, starting in the figure from a radius of about 6 mm, insensitive to the supplied energy. While the second was investigated in detail in previous works [19, 20, 23], the first one need to be deeply understood. Figure 2 and Fig. 3 show that flame propagation dynamics is also dependent on the mixture composition, characterized by the

presence of different rates of synthetic stoichiometric EGR and by a variation of equivalence ratio, ϕ, respectively; experiments shown in the figure were done by supplying the same ignition energy. Figure 2 compares experiments to non-linear modeling results of the ignition-independent flame propagation speed. Figure 3 shows that by varying the mixture equivalence ratio, the Markstein length used by the model is strongly impacted, leading for high equivalence ratio values to a variation of its sign, implying a very different impact of stretch on flame propagation speed: a negative Markstein length implies an increasing of the flame propagation speed with the increasing of K, with respect to the unstretched value.
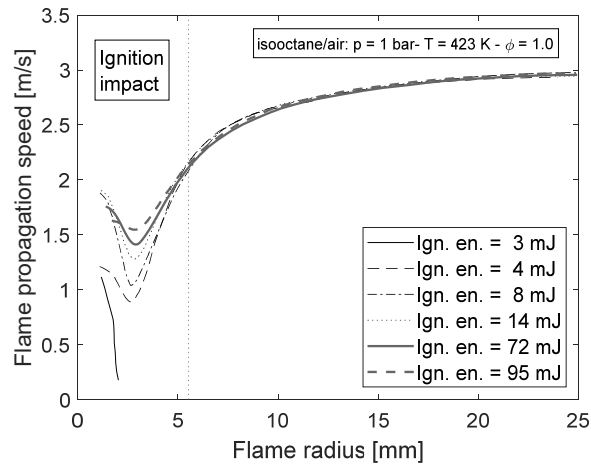
Fig. 1. Experimental results of the influence of the ignition energy on combustion process initiation and flame propagation speed [20]. Ignition energies and operating conditions are given in the figure
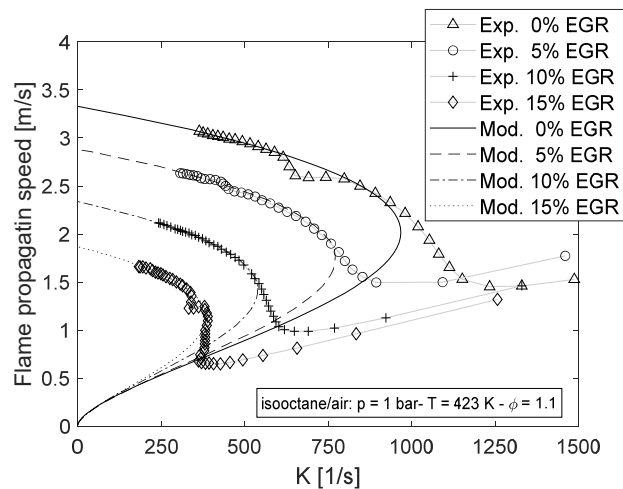
Fig. 2. Flame propagation speed as a function of the flame stretch, K, for different values of EGR dilution rate. Experiments and flame-to-stretch-dependence non-linear modeling results are compared [23]. Diluent rates and operating conditions are given in the figure
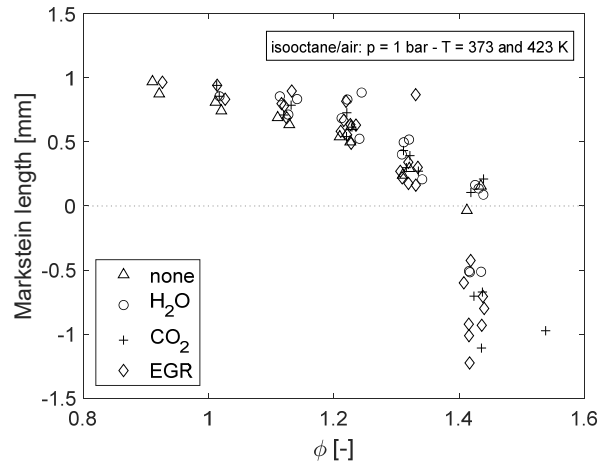
Fig. 3. Experimental data representing the Markstein lengths of isooctane/air/diluent mixtures as a function of the mixture equivalence ratio [23]. Diluent types and operating conditions are given in the figure

In the interest of developing detailed ignition models, it is important to understand which is the physical phenomenology holding the behaviors highlighted above

3. Numerical setup

To get a deeper insight about the physics holding the experiment described in Section 2, a virtual test-bed, representative of the experimental facility, was setup. To consider both fluid-dynamics, thermodynamics and chemical aspects of the problem, 3D Computational Fluid Dynamics (CFD) DNS accounting for complex chemistry were performed. To reduce the computational time, an ad hoc local-refinement mesh technique within the flame front was used. As an order of magnitude, each 3D simulation, running on 1 node accounting of 36 cores of the HPC ENER440 machine, took 46 hours computing time. Details about all these aspects are given in what follows.

3.1 Setup description

The ignition study is performed by computing ignition of unburned gases and subsequent flame propagation in a 3D cubic box with side L = 0.06 m. The base mesh consists of cubic cells having an edge length of 1 mm. Within this domain, at the centre, a 1.35 mm radius sphere and a second one, concentric the first, of 0.3 mm radius were specified as embedded mesh refinement regions presenting one and two levels of refinement[1], respectively, this is necessary to correctly represents the ignition process which involves high fluxes of energy in small temporal and spatial scales. Pressure Dirichlet boundary conditions are imposed at the boundaries of the domain. Initial conditions are homogeneous in the domain. Energy is deposited at the centre of the domain between times t_{ign}^{i} and t_{ign}^{f}. The total energy E_{ign} is prescribed and deposited at a constant rate. The heat release rate due to ignition, $\dot{\omega}_{ign}$, then reads:

$$\rho\dot{\omega}_{ign} = \rho\frac{E_{ign}}{t_{ign}^{f} - t_{ign}^{i}}$$

(1)

where ρ is the mixture density. Variations of E_{ign} in simulations were performed adjusting t_{ign}^{f}, as it was the case in experiments, $\dot{\omega}_{ign}$ was set equal to 5 W. Chemical processes are described by a mechanism including 33 species and 114 reactions, further reduced from a skeletal mechanism [24] using a Directed Relation Graph with Error Propagation and Sensitivity Analysis (DRGEPSA) [25]. Figure 4 shows that the unstretched laminar flame speed of the reduced mechanism closely matches the reference values

---

[1] Here a level of refinement corresponds to dividing the sides of a computational cell by two in order to convert the original cell into eight new ones.

at the conditions under investigation in this paper. Species diffusivities are computed using a mixture-averaged approach and differential diffusion effects are thus taken into account. The CONVERGE commercial CFD software [26] is selected in this work to carry out the simulations. Transport equations are solved using a Pressure Implicit with Splitting of Operators (PISO) method [27]. The spatial discretization scheme is second-order accurate with central differencing to minimize dissipation and the time integration is performed with a second order semi-implicit scheme. CONVERGE uses orthogonal grids which are generated using a modified cut-cell method. In particular, the solver includes an AMR algorithm, which refines the grid dynamically where needed.
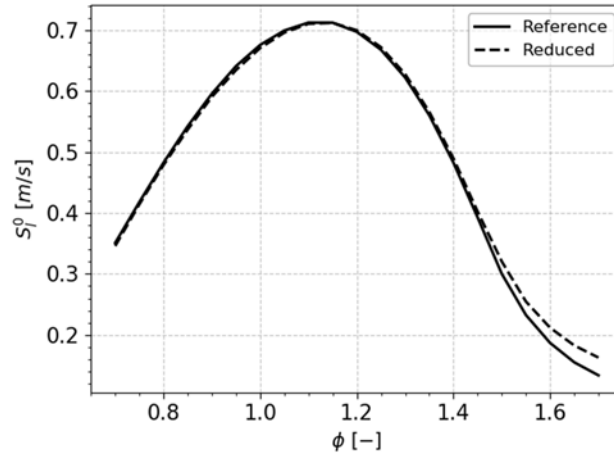
Fig. 4. Unstretched laminar flame speed for the reference (solid line) and the reduced (dotted line) mechanism, over a range of equivalence ratio at T = 423 K and p = 1 bar

3.2 TFM-AMR modeling approach

As flame thickness in the present conditions is small and flame propagates in the domain over time, an accurate description of the flame would require to uniformly refine the mesh in the whole domain using small cells. This, in turn, would lead to prohibitive computational costs. A strategy to reduce the computational cost while keeping the same resolution of the flame front is to use an AMR technique. AMR enables to track the moving flame front, and thus prevents from defining a uniform fine mesh. When considering AMR, a method needs to be specified to detect the flame front and consequently refine it at an adequate grid resolution. The detection of the flame front is here performed using a flame sensor-function which was introduced in the context of the Thickened Flame Model (TFM) [28]. The flame is first detected by defining a function S which locates the fuel reaction rate peak:

$$S = \max\left(\min\left(\beta \frac{|\dot{\omega}_{fuel}|}{\dot{\Omega}_{fuel}} - 1, 1 \right), 0 \right) \qquad (2)$$

where $\dot{\Omega}_{fuel}$ is the maximal fuel reaction rate, tabulated from 1-D laminar premixed flame computations as a function of the equivalence ratio, and $\dot{\omega}_{fuel}$ is the actual fuel reaction rate computed in the simulation. β is a parameter controlling the flame sensor sensitivity. The sensor-function S is then filtered using the methodology described in [29], not detailed here for brevity. This filtering technique broadens the sensor region and ensures that the flame front is properly detected and solved. The refinement is performed following the TFM-AMR methodology [30], which consists in activating AMR when $\hat{S} > 1$ (where $\hat{S}$ is the filtered sensor-function). The cell size is selected to ensure a sufficient number of points n_{res} in the flame front. The cell size Δ_x^{AMR} in the flame is thus:

$$\Delta_x^{AMR} = \frac{\delta_l^0}{n_{res}} \qquad (3)$$

where δ_l^0 is the laminar flame thickness, tabulated from the simulation of 1-D propagating premixed flames, prior to the 3-D simulation. In the present study, n_{res} is set at a value of six, which ensures a proper flame-propagation computation [29]. The CONVERGE solver used in this study involves Cartesian grids, which implies that cell size is inversely proportional to a power of two according to the following equation:

$$\Delta_x^{AMR} = \frac{\Delta_x^{base}}{2^{n_{AMR}}} \tag{4}$$

where n_{AMR} is the AMR level. Accordingly, in order to reach the desired AMR cell size, it is computed, by combining Eqs 3 and 4, as:

$$n_{AMR} = \mathrm{int}\left(\frac{1}{\log(2)} \log\left(\frac{n_{res} \Delta_x^{base}}{\delta_l^0} \right) \right) \tag{5}$$

where Δ_x^{base} is the resolution of the uniform mesh is the domain. Note that as the AMR level is an integer, the cell resolution takes discrete values. In practice, the closest resolution to δ_l^0 / n_{res} is used. In order to illustrate the approach, a representative evolution of the mesh in time is shown in Fig. 5.
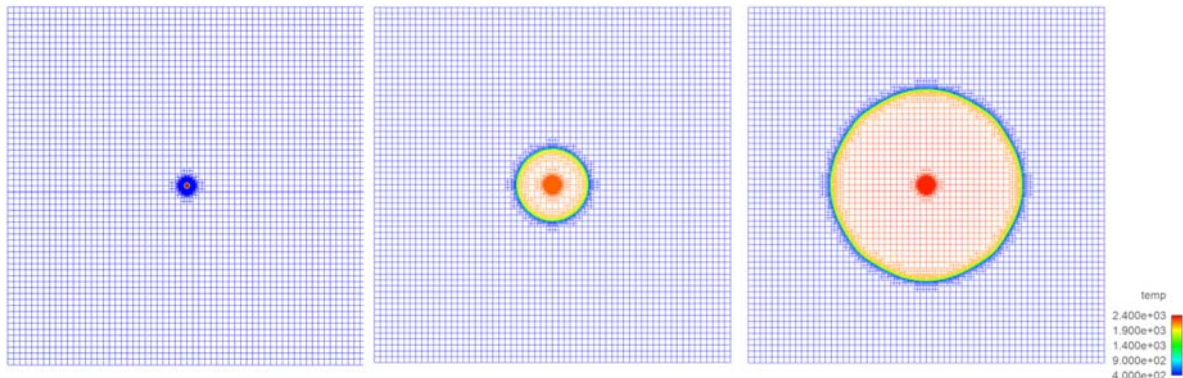
Fig. 5. Computational mesh evolution, colored by the mixture temperature variable, during the combustion process simulation. Images, refer to the following combustion times: 0.04 ms (left), 3.3 ms (center) and 6.3 ms (right). The operating conditions correspond to those of case 2 in Table 1

In the context of this study, for simulation results processing purposes, it was interesting to get access to properties related to Unburned Gas (UG) and Burned Gas (BG) mixtures. For this, a simple logical test on the temperature of the computational cell, T_{cell}, was introduced to discriminate between UG and BG cells:

$$T_{cell} \leq \left(T_u + \Delta T \right) \rightarrow UG \tag{6}$$
$$T_{cell} > \left(T_u + \Delta T \right) \rightarrow BG$$

where ΔT is an arbitrary offset to add to the unburned gas temperature, T_u, which is known for each cell, to identify the desired UG/BG threshold temperature. In this study a ΔT = 300 K was retained.

4. Numerical results

To study the phenomena highlighted in Section 2 related to expanding spherical laminar premixed flames, according to the available experimental database, several operating conditions were identified and retained for numerical investigation. The retained conditions are reported in Table 1. Two base operating conditions with and without dilution, case 1 and case 2 in Table 1 respectively, were identified to investigate the ignition energy impact on the combustion process, from extinction to high levels. The non-diluted case was then retained as the base operating condition to investigate variations of mixture equivalence ratio and to go further in the understanding of the early ignition phase, by means of a detailed thermodynamic analysis. The abovementioned topics are discussed in the following subsections. It is worth to point out the fact that, in this work, there was not the pretention to study neither the electric discharge process between electrodes, nor the formation of plasma (and its complex chemistry) and the establishment of shock waves. All these phenomena induce losses in the process transforming electric energy into heat to be transferred to the gas. To account for all these aspects in a global manner, empirically, variations of ignition energy were performed to reach flame extinction conditions. These limit conditions allow to bridge experimental energies, as those presented in Fig. 1, to numerical heat source terms, used in this work. As anticipated in Section 3, to correctly identify the mixture flame-intrinsic-properties, such as laminar flame speed, s_l, thickness, δ_l, and maximum reaction rate, Ω_{max}, required to parameterize the TFM-AMR model used in 3D computations, 1D flame computations were performed.

Table 1. Considered operating conditions for simulation. For each operating condition, variations with respect to the corresponding baseline case are highlighted in bold. Flame properties are also specified for each operating condition

	Case	Pressure [bar]	Temperature [K]	ϕ [-]	Diluent type	Dilution [%]	Ignition energy [mJ]	ΔT for BG detection [K]	s_l [m/s]	δ_l [mm]
Ref.	1	**1**	**423**	**1**	**CO_2**	**5**	**0.8**	**300**	0.50	0.42
Ref.	2	**1**	**423**	**1.1**	**-**	**-**	**0.2**	**300**	0.71	0.32
Case 1 ignition energy variation	3	1	423	1	CO_2	5	**0.4**	300	0.50	0.42
Case 1 ignition energy variation	4	1	423	1	CO_2	5	**1.6**	300	0.50	0.42
Case 1 ignition energy variation	5	1	423	1	CO_2	5	**3.2**	300	0.50	0.42
Case 2 ignition energy variation	6	1	423	1.1	-	-	**0.1**	300	0.71	0.32
Case 2 ignition energy variation	7	1	423	1.1	-	-	**0.4**	300	0.71	0.32
Case 2 ignition energy variation	8	1	423	1.1	-	-	**0.8**	300	0.71	0.32
Case 2 ignition energy variation	9	1	423	1.1	-	-	**1.6**	300	0.71	0.32
Case 2 ignition energy variation	10	1	423	1.1	-	-	**3.2**	300	0.71	0.32
Case 2 ϕ variation	11	1	423	**1.3**	-	-	0.2	300	0.62	0.34
Case 2 ϕ variation	12	1	423	**1.4**	-	-	0.2	300	0.48	0.41
Case 2 ϕ variation	13	1	423	**1.6**	-	-	0.2	300	0.18	0.93
Case 2 ΔT variation	14	1	423	1.1	-	-	0.2	**500**	0.71	0.32
Case 2 ΔT variation	15	1	423	1.1	-	-	0.2	**750**	0.71	0.32
Case 2 ΔT variation	16	1	423	1.1	-	-	0.2	**1100**	0.71	0.32

4.1 1D adiabatic constant pressure laminar premixed flame simulation

1D laminar flame computations were performed to identify unstretched laminar premixed flame intrinsic properties such as s_l, δ_l, $\Omega_{max.}$, Fig. 6 (not all properties are shown in the figure). In details, at each time step, starting from the computed temperature profile, Fig. 6 (bottom) in grey scale, the maximum value of the temperature gradient profile was identified, Fig. 6 (middle), and used to determine the approximated temperature profile, Fig. 6 (bottom) in red, whose approximated flame thickness, $\delta_{l,approx.}$, was computed according to the following equation [1]:

$$\delta_{l,approx.} = \frac{T_b - T_u}{\left.\dfrac{\partial T}{\partial x}\right|_{max}} \tag{7}$$

where T_b is the burned gas temperature. Starting from the approximated profiles, it was then possible to identify the number of computational cells within it, Fig. 6 (top). The laminar flame speed was then computed by tracking in time the spatial-coordinate, x, of a given temperature value belonging to the flame temperature profile, in this work 1275 K, according to the following equation:

$$s_l = \frac{\left. x \right|^{t+\Delta t}_{T_{track}} - \left. x \right|^{t}_{T_{track}}}{\Delta t} \tag{8}$$
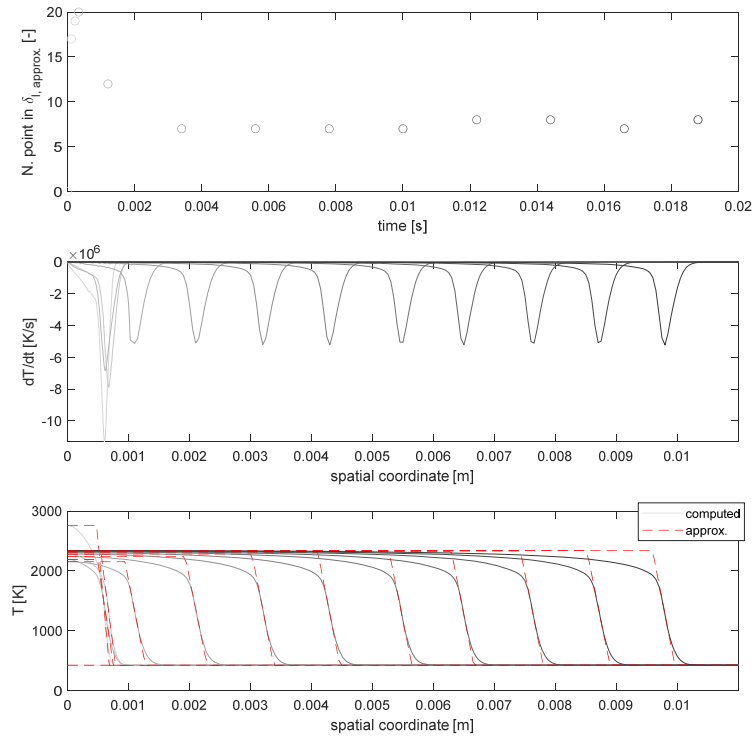
Fig. 6. 1D flame computation exploitation to extract intrinsic flame parameters required to feed the TFM-AMR model used in 3D computations. Operating conditions refer to case 2 of Table 1. The number of computational cells within the approximated temperature profile, in time (top); temperature gradient profile, for the time instants indicated in the top diagram; computed and approximated temperature profiles, for the time instants indicated in the top diagram. A grey scale code is used to relate the time instants to the different profiles

It is worth to note that, after a short transient phase, required to the establishment of the fluid dynamic equilibrium after ignition, the flame structure stabilises. The oscillations on the number of computational cells within the flame profile, varying between 6 and 7, is due to discretization issues and it is a pure, statistical phenomenon, indicating that, in average, the value is in between the two. The values of s_l and δ_l for the different operating conditions are reported in Table 1.

4.2 Theoretical modeling approach for stretch impact on flame propagation speed

Different definitions of flame velocity can be given to deal with laminar flame speed [1, 31]. The absolute velocity, S_b, represents the flame front velocity with respect to the burned gas coordinate system, which stays immobile. S_b is defined as:

$$S_b = \frac{dR_b}{dt} \tag{9}$$

where R_b is the burned gas volume radius, here supposed as being a spherical region. This is an interesting variable as it can be directly compared to experimental observations obtained by means of techniques such as shadowgraph [22], Schlieren [32], Raman [33] or tomography [32], both by following an iso-value of temperature or density, or the maximum value of the derivative of temperature or density. The displacement velocity, S_d, represents the flame velocity with respect to the local flow field:

$$S_d = S_b - \vec{u} \cdot \vec{n} \tag{10}$$

where $\vec{u}$ is the gas velocity and $\vec{n}$ is the flame front surface normal-vector pointing towards the unburned gas. For a spherical diverging flame, as it is the case in this work, this variable is very hard to measure because unburned gas is moving and the flow field is accelerated by the flame front. According to [1] by means of the continuity equation, it is possible to write the displacement velocity as the product of the absolute velocity and the ratio of burned and unburned gas densities, respectively ρ_b and ρ_u:

$$S_d = S_b \frac{\rho_b}{\rho_u} \qquad (11)$$

The consumption velocity, S_c, represents the speed at which reactants are consumed. For a spherical flame configuration, it holds:

$$S_c = -\frac{1}{\rho_u Y_{F_u} R_b} \int_0^{R_b} \dot{\omega}_F r^2 dr \qquad (12)$$

where Y_{F_u} is the fuel mass fraction in unburned gas and $\dot{\omega}_F$ is the fuel reaction rate. By knowing S_c, it is possible to compute the evolution of the burned gas mass, m_b, in time by mean of the relation below [31]:

$$\frac{dm_b}{dt} = 4\pi \rho_u S_c R_b^2 \qquad (13)$$

where:

$$m_b = \int_0^{V_b} \rho_b dV_b \qquad (14)$$

in which V_b represents the burned gas volume. For infinitely thin flame fronts and a burned gas density which does not vary in time, it holds:

$$S_c = S_d = \frac{\rho_b}{\rho_u} \frac{dR_b}{dt} \qquad (15)$$

This flame velocity is also called laminar flame speed, s_l. The burning velocity of a free planar flame is called unstretched laminar flame speed, s_l^0. The theoretical modelling approach used in this work to express the impact of stretch on the laminar flame speed is the one proposed in [34]. The stretch, K, is defined by the fractional rate of change of the flame surface, A:

$$K = \frac{1}{A} \frac{dA}{dt} \qquad (16)$$

In the specific case of a spherical flame configuration of radius R_b and volume V_b, $V_b = \frac{4}{3}\pi R_b^3$, the stretch expression holds:

$$K = \frac{2}{R_b} \frac{dR_b}{dt} = \frac{2}{R_b} S_b \qquad (17)$$

The influence of the stretch on the laminar flame speed, s_l, is defined by means of the Markstein length, L_b. This influence is expressed by means of a non-linear relation associating the stretched flame speed, S_b, to the stretch as:

$$\left(\frac{S_b}{S_b^0}\right)^2 \ln\left(\left(\frac{S_b}{S_b^0}\right)^2\right) = -\frac{L_b}{S_b^0} K \qquad (18)$$

where S_b^0 is the unstretched flame speed.

4.3 Impact of ignition energy on early flame propagation phase

The impact of the ignition energy on the mixture ignition process is discussed in this section. Figure 7 refers to operating conditions corresponding to case 1 in Table 1. Simulation results are compared to experimental results relative to the ignition independent flame propagation phase: despite not a perfect match between simulation and experiments, probably due to the impact of chemical kinetics description, simulation and experiments together fairly represent the expected evolutions of the shown variables. In details, as shown in Fig. 7 (middle), the obtained simulation results well represent the flame propagation speed evolution as shown in Fig. 1. The critical ignition energy is here somewhere in between 0.4 and 0.8 mJ. It can also be noticed that an increase of the ignition energy shortens the ignition phase, Fig. 7 (top), speeding up the growth of the burned gas region. Finally, observing Fig. 7 (bottom), it can be seen that the evolution of the flame speed with stretch follows a non-linear path, as the one described by the model detailed in Section 4.2, this result being in agreement with what shown in Fig. 2.

Fig. 7. Ignition energy variation impact on flame propagation: evolution of the flame radius in time (top), evolution of the flame propagation speed as a function of the flame radius (middle), evolution of the flame propagation speed as a function of the flame stretch (bottom). Simulation results, lines, are compared to different experimental realizations, markers. Operating conditions, referred to Table 1, are specified in the figure

Figure 8 refers to operating conditions corresponding to case 2 in Table 1. The critical ignition energy, between 0.1 and 0.2 mJ, is about an order of magnitude lower than the one showed in Fig. 1: this is in part due to the fact that ignition process losses are neglected in this study and in part to the fact that the mixture equivalence ratio is more propitious to ignite. According to Fig. 7, an increase of the ignition energy shortens the ignition phase, Fig. 8 (top and middle); nevertheless, this trend seems to tend towards an asymptote portraying that, over a given value, ignition energy is no more a lever to

speed up the combustion. Figure 8 (bottom) supports the fact that the flame propagation speed impacted by flame stretch follows a non-linear trajectory.
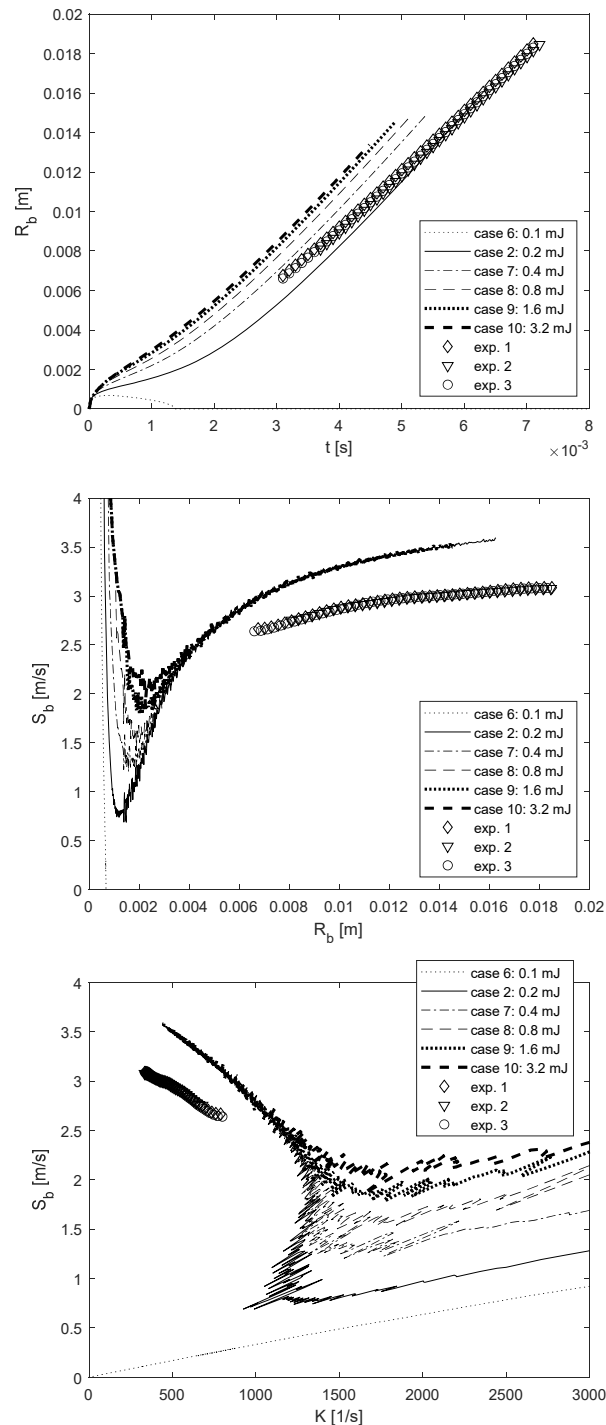
Fig. 8. Ignition energy variation impact on flame propagation: evolution of the flame radius in time (top), evolution of the flame propagation speed as a function of the flame radius (middle), evolution of the flame propagation speed as a function of the flame stretch (bottom). Simulation results, lines, are compared to different experimental realizations, markers. Operating conditions, referred to Table 1, are specified in the figure

Looking at Fig. 7 and Fig. 8, by comparing flame propagation evolutions referring to case 1 and case 2 of operating conditions having the same ignition energy, it is possible to observe that an increasing of the dilution rate has an impact on the ignition-dependent phase of the flame propagation process similar to the one caused by a decreasing of the ignition energy, i.e. makes it approaching to its critical ignition path; this fact is also validated from results shown in Fig. 2.

4.4 Impact of equivalence ratio on early flame propagation phase

The impact of an equivalence ratio variation on the ignition process of the reactive mixture detailed in case 2 of Table 1, ϕ = 1.1, is here discussed. The corresponding variations corresponds to values of ϕ up to 1.6. According to experimental evidences shown in Fig. 3, the Markstein length of an isooctane/air mixture changes from positive to negative moving from ϕ = 0.9 to ϕ = 1.6, the crossing point being around ϕ = 1.4. Figure 9 shows the simulation results. As a general remark, it can be seen in Fig. 9 (middle) that an increasing of ϕ corresponds to a decreasing of the unstretched flame speed.

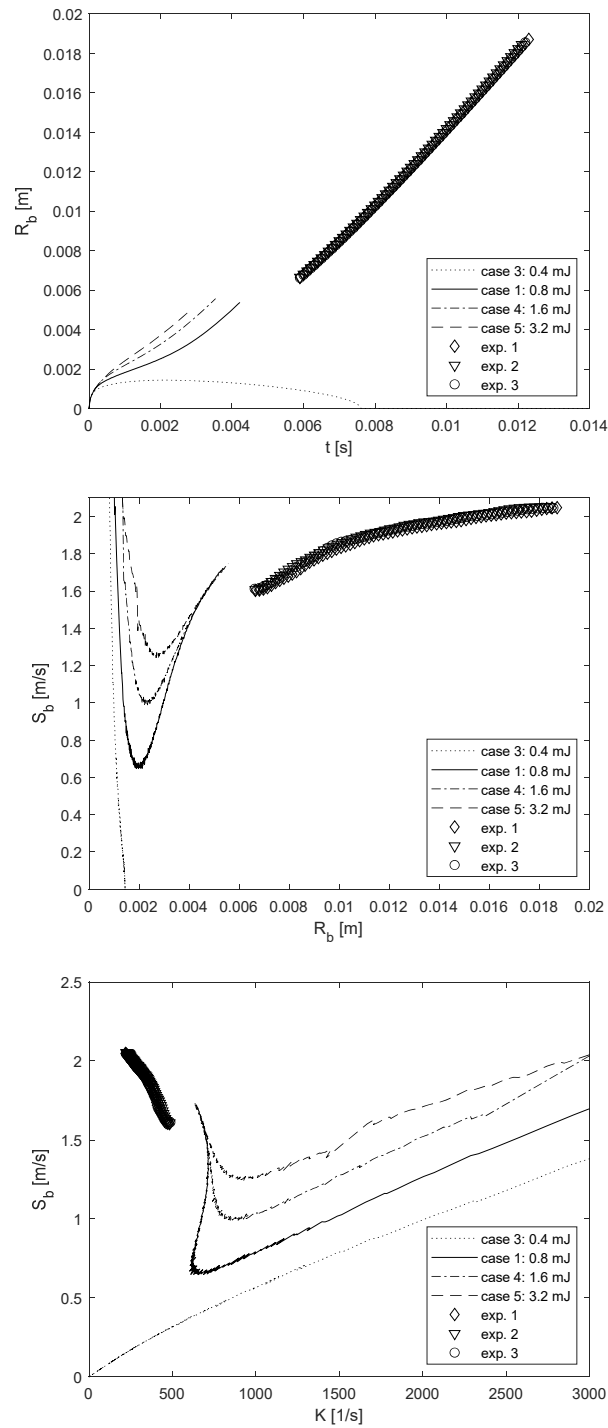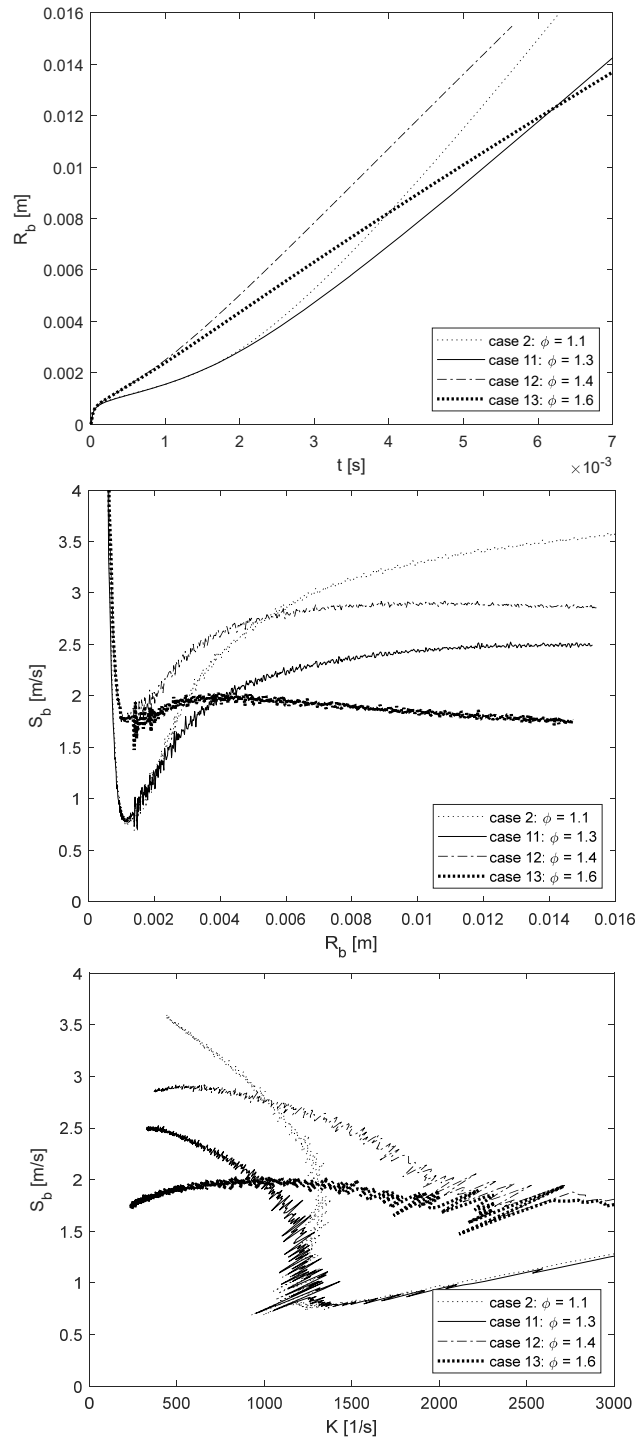**Fig. 9**. Mixture equivalence ratio variation impact on flame propagation: evolution of the flame radius in time (top), evolution of the flame propagation speed as a function of the flame radius (middle), evolution of the flame propagation speed as a function of the flame stretch (bottom). Operating conditions, referred to Table 1, are specified in the figure

Nevertheless, it can also be noticed that the flame radius evolution varies, somehow, in an unexpected way, in Fig. 9 (top). By passing from ϕ = 1.1 to ϕ = 1.3, combustion initiation almost does not change, Fig. 9 (middle and bottom), only in a second time, the mixture at ϕ = 1.1 burns faster because of the higher flame speed, Fig. 9 (middle). Differently, by passing from ϕ = 1.3 to ϕ = 1.4, the Markstein number becoming negative, an acceleration of the combustion initiation process can be noticed, Fig. 9 (middle and bottom); the fact that the Markstein number becomes negative is pointed out by the fact that for K < 500 s^{-1} the flame propagation speed decreases with the decreasing of K, Fig. 9 (bottom). Nevertheless, in a second time the mixture burning at ϕ = 1.3 experience a faster increasing of the burning rate, due to the higher flame speed. Finally, by passing from ϕ = 1.4 to ϕ = 1.6, combustion initiation almost does not change, Fig. 9 (middle and bottom), and in a second time, the mixture at ϕ = 1.4 burns faster because of the higher flame speed, Fig. 9 (middle). The case ϕ = 1.6, shows a more pronounced reduction of the flame speed with the decreasing of the stretch, Fig. 9 (bottom), indicating a still lower Markstein number.

4.5 Thermodynamic analysis of ignition phase

In this section, a thermodynamic analysis of the ignition process is performed, in order to clarify which variables influence the very first growth of the burned gas region and identify the driving factors allowing to improve the ignition process. In this sense, as a first step, in order to evaluate a potential impact on the results of the hypothesis done on the identification of the burned gas region, that is the choice of adopting ΔT = 300 K, a sensitivity study was performed. Different offsets were considered, varying from ΔT = 300 K up to ΔT = 1100 K, Fig. 10.
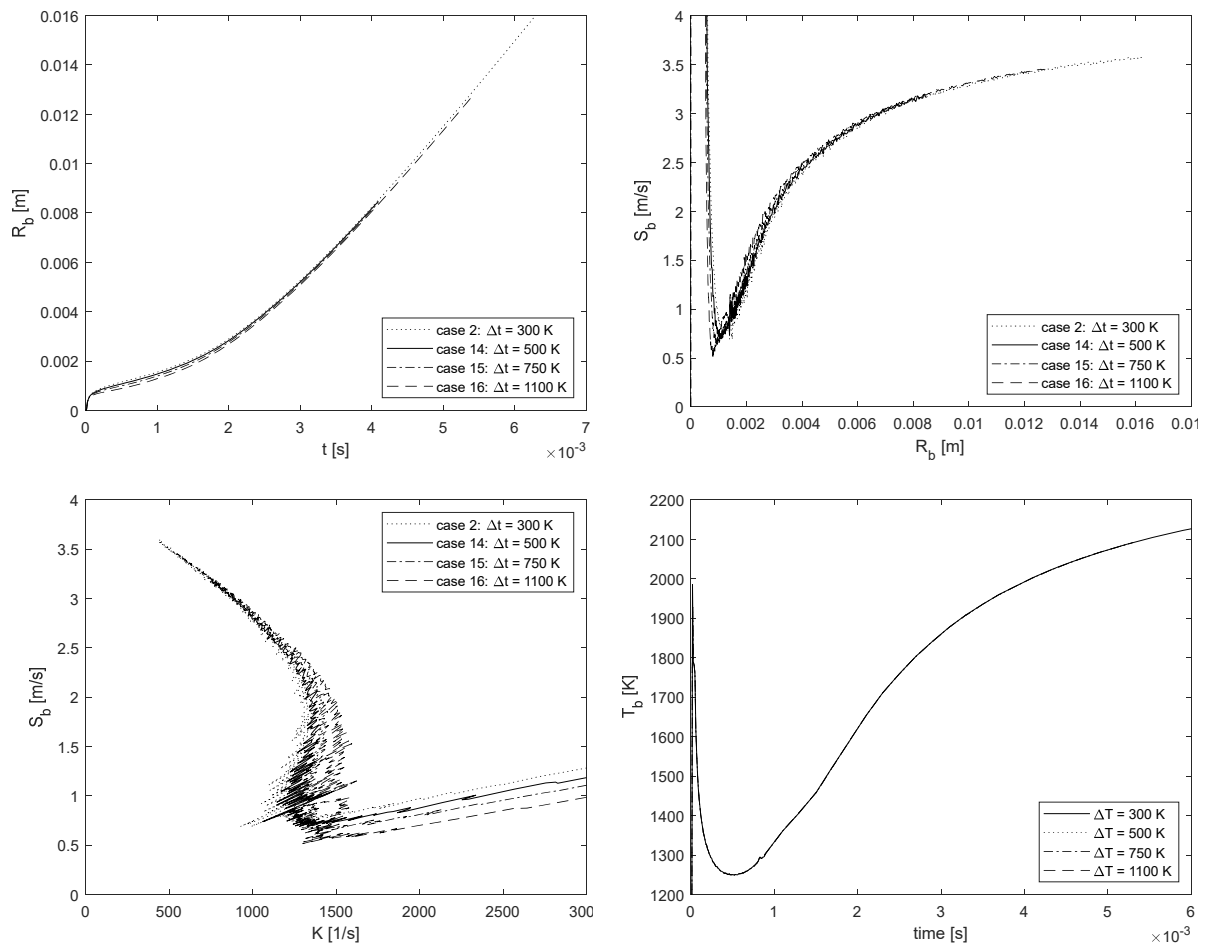
Fig. 10. Influence of the ΔT parameter choice on combustion process visualization and burned gas properties computation: evolution of the flame radius in time (top-left), evolution of the flame propagation speed as a function of the flame radius (top-right), evolution of the flame propagation speed as a function of the flame stretch (bottom-left), evolution of the burned gas temperature (bottom-right). Operating conditions, referred to Table 1, are specified in the figure

As shown in Fig. 10, even if some differences can be noticed at the very beginning of the combustion process in the plot representing the flame propagation speed as a function of the flame stretch, Fig. 10 (bottom-left), as the stretch is computed according to Eq. 17 where the burned gas zone radius is at the denominator, the choice of a different ΔT would not imply any substantial difference in the analysis of this study. To go further into the analysis of the ignition energy impact on the first phase of the flame propagation dynamics, the burned gas temperature evolution was investigated; the investigation concerns the case 2 baseline operating conditions of Table 1. As a first step, the T_b value relative to a developed unstretched flame was determined by means of 1D flame computations, as depicted in Fig. 11.
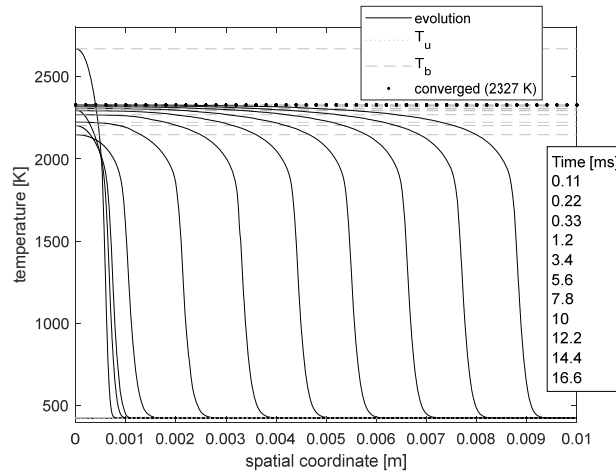
Fig. 11. 1D flame computation: evolution of the temperature profile in time relative to case 2 in Table 1; for each profile, Tu and Tb are shown; the converged value of Tb is highlighted by means of dot markers. The time instants corresponding to the profiles are shown in the table on the right

Figure 12 represents the evolution of T_b in time, as a function of the different ignition energies; the converged value of T_b, corresponding to the constant pressure adiabatic flame temperature, is also plotted. As shown, T_b in the burned gas region, never reach the converged value.
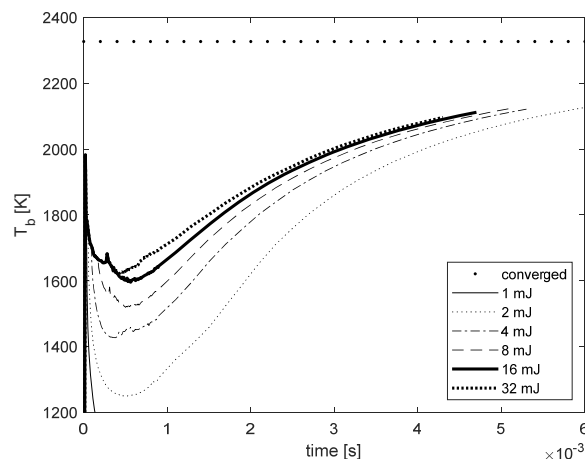
Fig. 12. Impact of an increasing of the ignition energy variable on burned gas temperature, converged curve refers to steady 1D computation; curves refer to cases 6, 2 and 7 to 10 of Table 1, respectively

This means that the stretched flame burned gases are under-adiabatic, which implies a less sustained flame propagation. As shown in Fig. 12, at the beginning of combustion T_b decreases. That means the balance between heat supply due to ignition and production due to combustion is lower than heat transfer. In this phase, ignition energy plays an important role in the ignition process as it allows to heat the mixture and maintain high temperatures, necessary to guarantee fast chemical kinetics. Accordingly, another factor that have an influence in this first phase is the mixture composition and in particular its heat capacity, as it influences the heat up process of the gases. That is one of the reasons,

together with the fact that dilution reduces chemical activity, why a diluted mixture requires higher ignition energies to ignite, Fig. 7 and Fig. 8. Then, it is the heat released by chemical reactions that sustains flame propagation, and so combustion. To conclude this analysis, Fig. 13 highlights the key-instants of ignition and flame propagation dynamics under different viewpoints.

In Fig. 13 (top-left) it is shown that the burned gas region radius increases very fast after spark timing, 0→A. In the phase A→B, flame speed reaches its minimum value, Fig. 13 (top-right). During this phase stretch reduces, Fig. 13 (bottom-left), in a first time due to the increasing of the flame radius and the lowering of temperature, but then, from 0.5 ms, temperature starts to increase again, Fig. 13 (bottom-right), equilibrating the stretch variation, leading to an equilibrium reached in B. In the phase B→C, stretch increases due to the intense chemical activity, whose contribution to stretch overcomes the increasing of R_b, Eq. 17. Finally, in the phase C→D, there is once again an inversion of relative contributions of the increasing flame speed and radius, resulting a reduction of stretch, Fig. 13 (bottom-left).
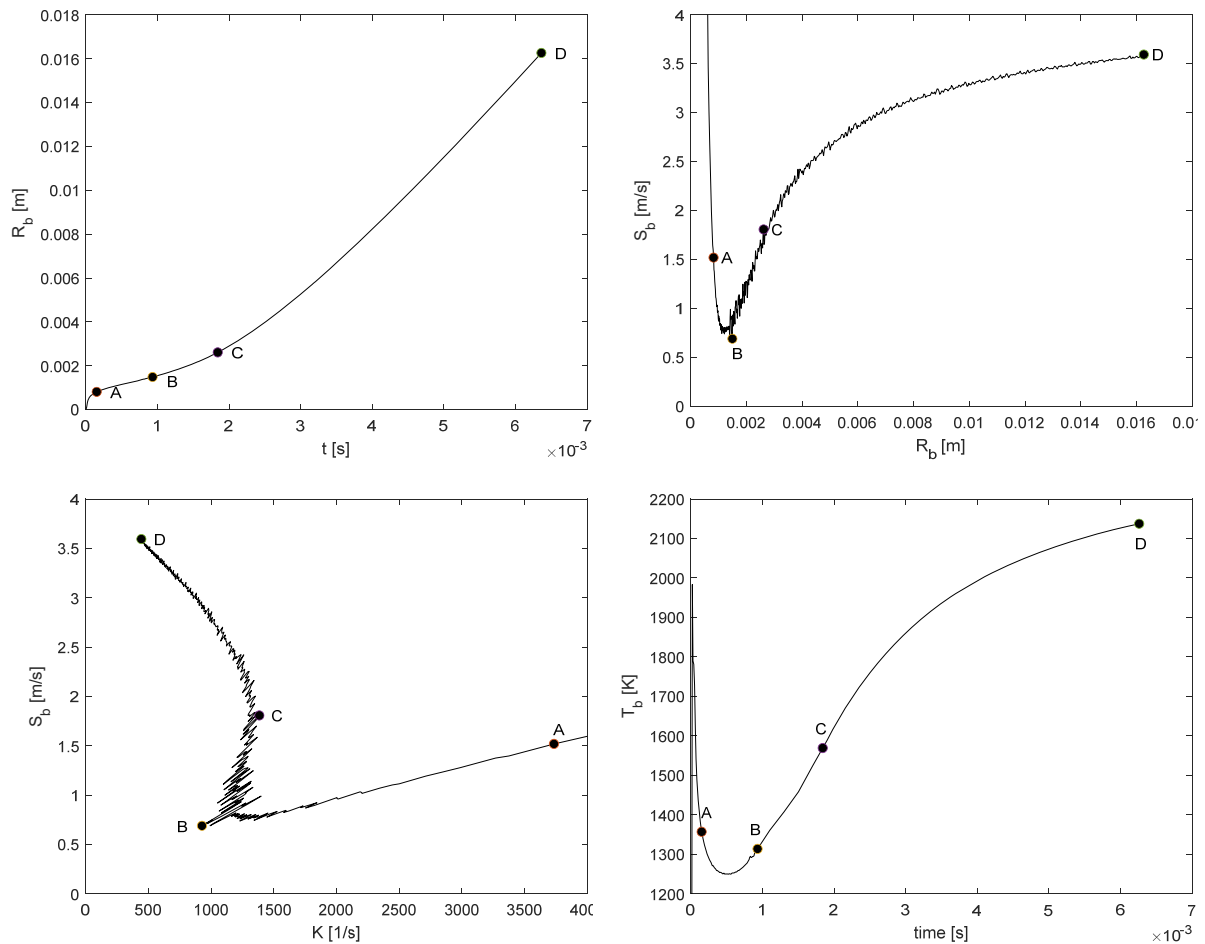
Fig. 13. Identification of the key points on the evolution of the burned gas volume during the mixture ignition process

5. Conclusion

This study, based on the experimental database generated by the University of Orléans in the framework of the ANR MACDOC project, aimed to get a deeper understanding about the physics governing early stages of premixed mixture combustion, process that becomes crucial in highly diluted or ultra-lean mixture combustion. For this, Direct Numerical Simulations (DNS) accounting for species differential diffusion and complex chemistry were performed at IFP Energies nouvelles (IFPEN). The simulation approach integrates a specific Adaptive Mesh Refinement (AMR) algorithm, called TFM-AMR, able to track the flame front into the domain, to reduce the computational cost. It was shown that the used numerical technique allowed to reproduce experimental results and in particular to account for the flame stretch impact on laminar flame propagation. In a first time, the impact of the ignition energy on the initial phases of combustion was evaluated; the investigation was pushed up to non-self-sustained ignition

processes, leading to combustion extinction. This study showed that ignition energy is important at the very beginning of the process by sustaining chemical activity, maintaining an adequate level of temperature. This justified the fact that diluted mixtures require higher ignition energies, as inert gas, heating up, reduces the temperature increasing. Furthermore, the obtained simulation results contributed to support the theory stating a non-linear dependence of laminar flame speed on the mixture Markstein number. In the following, variation of equivalence ratio of the mixture from $\phi = 1.1$ to $\phi = 1.6$ were performed, showing that simulation results, according to experiments, well captured the Markstein number sign change from positive to negative, leading to the overturning of the influence of the stretch on flame propagation. Finally, the flame propagation dynamics was deeply investigated to identify the different physical phenomena that, together, generate the flame dynamics observed in experiments. This last study allowed to obtain a deeper insight in experimental results and evaluate the concurrent influences of chemical kinetics, flame stretch and ignition energy on the establishment of the premixed flame propagation, but also it was a necessary step for modeling activities of next generation Spark Ignition engines operating under steady and transient conditions.

Acknowledgments

References

1. T. Poinsot and D. Veynante. Theoretical and numerical combustion. T. Poinsot, 2011.

2. A. Onorati, G. Montenegro. 1D and Multi-D Modeling Techniques for IC Engine Simulation. SAE International, 2020.

3. F. Bozza, A. Gimelli, S. Merola and B. Vaglieco. Validation of a fractal combustion model through flame imaging. SAE Paper 2005-01-1120, 2005.

4. S. Richard, S. Bougrine, G. Font, F.-A. Lafossas and F. Le Berr. On the Reduction of a 3D CFD Combustion Model to Build a Physical 0D Model for Simulating Heat Release, Knock and Pollutants in SI Engines. Oil & Gas Science and Technology – Rev. IFP, Vol. 64 - No. 3, pp. 223-242, 2009.

5. R.J. Blint. The relationship of the laminar flame width to flame speed, Combustion Science Technology, 49: 79–92, 1986.

6. M. Metghalchi and J. Keck. Burning Velocities of Mixtures of Air with Methanol, Isooctane, and Indolene at High Pressure and Temperature. Combustion and Flame, 48 (1982): 191-210.

7. O.L. Gulder. Burning velocities of ethanol-isooctane blends. Combustion and Flame, 56(3):261-268, 1984.

8. C. Endouard, F. Foucher and F. Halter. Effects of CO2, H2O and EGR dilution on laminar burning velocities and Markstein lengths of isooctane/air mixtures. Ninth Mediterranean Combustion Symposium, Rhodes, Greece, 2015.

9. O. Colin and K. Truffin. A spark ignition model for large eddy simulation based on an FSD transport equation (ISSIM-LES). Proc. Combust. Inst., 33(2):3097 – 3104, 2011.

10. S. Jerzembeck, N. Peters, P. Pepiot-Desjardins, and H. Pitsch. Laminar burning velocities at high pressure for primary reference fuels and gasoline: Experimental and numerical investigation. Combust. Flame, 156(2):292 – 301, 2009.

11. D. Bradley, R A Hicks, M Lawes, C G W Sheppard, and R Woolley. The Measurement of Laminar Burning Velocities and Markstein Numbers for Isooctane / Air and Isooctane/ n- Heptane / Air Mixtures at Elevated Temperatures and Pressures in an Explosion Bomb. Combust. Flame, 144:126–144, 1998.

12. G. Broustail, P. Seers, F. Halter, G. Moreac, and C. Mounaim-Rousselle. Experimental determination of laminar burning velocity for butanol and ethanol isooctane blends. Fuel, 90(1):1–6, January 2011.

13. X. Wu, Q. Li, J. Fu, C. Tang, Z. Huang, R. Daniel, G. Tian, and H. Xu. Laminar burning characteristics of 2,5-dimethylfuran and isooctane blend at elevated temperatures and pressures. Fuel, 95:234–240, 2012.

14. J.T. Farrel, R.J. Johnston, and I.P. Androulakis. Molecular Structure Effects On Laminar Burning Velocities At Elevated Temperature And Pressure. SAE Paper 2004-01-2936, 2004.

15. A.P. Kelley, A.J. Smallbone, D.L. Zhu, and C.K. Law. Laminar flame speeds of C5 to C8 n-alkanes at elevated pressures: Experimental determination, fuel similarity, and stretch sensitivity. Proc. Combust. Inst.,, 33:963–970, 2011.

16. A.P. Kelley and C.K. Law. Non-linear effects in the extraction of laminar flame speeds From expanding spherical flames. Combust. Flame, 156(9):1844–1851, 2009.

17. R. Bounaceur, O. Herbinet, R. Fournet, P.-A. Glaude, F. Battin-Leclerc, A. Pires da Cruz, M. ya-hyaoui, K. Truffin, and G. Moreac. Modeling the Laminar Flame Speed of Natural Gas and Gasoline Surrogates. SAE Technical Paper 2010-01-0546, pages 1–16, 2010.

18. R. J. Kee, F. M. Rupley, J. A. Miller, M. E. Coltrin, J. F. Grcar, E. Meeks, H. K. Moffat et al. CHEMKIN Collection, Release 3.6, Reaction Design, Inc., San Diego, CA, 2000.

19. A. Dulbecco, G. Font, F. Foucher and P. Brequigny. Experimental Investigation and Modeling of Early Flame Propagation Stages in Operating Conditions Representative of Modern High Efficiency Spark Ignition Engines. SAE Int. J. Adv. & Curr. Prac. in Mobility 2(2):567-585, 2020, https://doi.org/10.4271/2019-24-0073.

20. B. Galmiche. Caracterisation experimentale des flammes laminaires et turbulentes en expansion. PhD thesis, Université d'Orléans, 2014.

21. C. Endouard, F. Halter, C. Chauveau, F. Foucher, Combust. Sci. Technol. 188 (2016) 516–528.

22. B. Galmiche, F. Halter, and F. Foucher. Effects of high pressure, high temperature and dilution on laminar burning velocities and Markstein lengths of isooctane/air mixtures. Combust. Flame, 159:3286–3299, 2012.

23. C. Endouard. Etude expérimentale de la dynamique des flammes de prémélange isooctane/air en expansion laminaire et turbulente fortement diluées. PhD thesis, Université d'Orléans, 2016.

24. Y. An, Y. Pei, J. Qin, H. Zhao, S. Teng, B. Li and X. Li. Development of a PAH formation model for gasoline surrogates and its application for GDI engine CFD simulation. Energy, Vol. 94, 2016, pp. 367-379.

25. M. Raju, M. Wang, P.K. Senecal, S. Som and D.E. Longman. A reduced diesel surrogate mechanism for compression ignition engine applications. ASME 2012 Internal Combustion Engine Division Fall Technical Conference, 2013, pp. 711–722.

26. Convergent Science Inc., W. Madison. Converge CFD Software, Version 2.4, 2017.

27. R. Issa. Solution of the implicitly discretized fluid flow equations by operator-splitting. Journal of Computational Physics, Vol. 62, 1986, pp. 40–65.

28. O. Colin, F. Ducros, D. Veynante and Poinsot. A thickened flame model for large eddy simulations of turbulent premixed combustion. Phys. Fluids, Vol. 12, No. 7, 2000, pp. 1843–1863.

29. T. Jaravel. Prediction of pollutants in gas turbines using large eddy simulation. Ph.D. thesis, 2016.

30. C. Mehl, S. Liu, Y.C. See, O. Colin. Les of a stratified turbulent burner with a thickened flame model coupled to adaptive mesh refinement and detailed chemistry. AIAA Joint Propulsion Conference pp. AIAA 2018–4563 (2018).

31. A. Bonhomme, L. Selle, and T. Poinsot. Curvature and confinement effects for flame speed measurements in laminar spherical and cylindrical flames. Combust. Flame, 160:1208–1214, 2013.

32. D. Bradley, M. Lawes, K. Liu, and M.S. Mansour. Measurements and correlations of turbulent burning velocities over wide ranges of fuels and elevated pressures. Proc. Combust. Inst., 34(1):1519–1526, 2013.

33. D.M. Mosbacher, J.A. Wehrmeyer, R.W. Pitz, C.J. Sung, and J.L. Byrd. Experimental and numerical investigation of premixed tubular flames. Proc. Combust. Inst., 29(2):1479–1486, 2002.

34. F. Halter, T. Tahtouh and C. Mounaïm-Rousselle. Nonlinear effects of stretch on the flame front propagation, 157, 1825, 2010.

A Study of Cyclic Combustion Variations at Lean SI Engine Operation Using High-Speed In-Cylinder CO_2 Measurements

A. U. Bajwa[1], T. Linker[1], M. A. Patterson[1, 2], G. Beshouri[2] and T. J. Jacobs[1]

[1]Texas A&M University, College Station. USA

E-mail: abdullahbajwa@tamu.edu, tlinker@tamu.edu, tjjacobs@tamu.edu

[2]Advanced Engine Technologies Corporation. USA

E-mail: mark.patterson@aetco.com

Abstract. Engines operating at high levels of dilution experience significant combustion instabilities that produce cyclic variations in engine performance. In order to enhance the understanding of combustion variations at these operating conditions so that the efficiency and emissions benefits of diluted operation can be fully exploited, high-speed in-cylinder CO_2 data is used to study cycle resolved combustion behavior in a lean-burn, two-stroke engine at an unstable operating point. Post combustion CO_2 concentration along with IMEP data is used to categorize the recorded cycles into five groups, namely – misfires, post-misfire-high-pressure cycles, normal cycles, weak partial fires, and strong partial fires. It is found that substantial improvements in IMEP, engine stability, and thermal efficiency can be realized by avoiding non-normal cycles during engine operation.

Combustion characteristics of each cycle type are then studied by using a chemical kinetics-based solver to calculate cycle-resolved laminar flame speed (LFS) and ignition delay (ID) at various times during combustion. Post-misfire cycles, which are richer than other cycles, are found to have significantly faster combustion despite having long ID and high residual gas fraction. High LFS resulting from high equivalence ratio and combustion temperatures is responsible for the fast combustion. On the other hand, partially firing cycles have much lower LFS and as a result, undergo much slower combustion which is susceptible to premature extinction during the rapid expansion phase of the power stroke. At the end, the strong influence of LFS variations on flame initiation and propagation is demonstrated by comparing LFS and combustion phasing results. The influence is found to be strongest during the early stages of combustion.

Notation

CAD	*Crank angle degrees*
ID	*Ignition delay*
IMEP	*Indicated mean effective pressure*
LFS	*Laminar flame speed*
LoPP	*Location of peak combustion pressure*
MF	*Misfiring cycle*
mfb	*Mass fraction burned*
PF	*Partially firing cycle*
PP	*Peak combustion pressure*
ST	*Spark timing*
TER	*Trapped equivalence ratio*
TRF	*Trapped residual fraction*

1. Introduction

Lean and diluted operation of spark ignited internal combustion engines offers many advantages for emissions and performance. Dilution levels can be increased by increasing the fraction of residual combustion products in the combusting mixture through exhaust gas recirculation (EGR) or advanced exhaust valve closing. Diluted lean combustion offers emissions benefits in two ways; first, by improving the engine's thermal efficiency resulting from lowering of combustion temperatures and increase in specific heat ratio of the trapped mixture [1] (according to [2], 23% to 58% improvements in fuel economy can be realized by operating in lean regimes.), and second, by reducing NO formation during combustion because of cooler combustion temperatures. Another benefit of enhanced dilution (particularly for cooled EGR cases) is a reduction in the engine's propensity to knock [3]. The anti-knocking benefits can support engine downsizing efforts that are often limited by knocking. There are limits to the extent of dilution, beyond which combustion becomes unstable and produces partially firing cycles that have limited heat release (less than 70% of nominal according to [4]), or misfiring cycles that have no sensible heat release [5]. Such cyclic variabilities undo the efficiency gains achieved through dilution and cause fluctuations in the engine's torque output, adversely affecting vehicle drivability. An engine is deemed unacceptably unstable when the coefficient of variation (CoV) of indicated mean effective pressure (IMEP) is over 10% [6]. Modern automotive engines have CoV of IMEP less than 5%. In addition to drivability problems, unstable engine operation also negatively impacts the fuel conversion efficiency (fuel economy) as well as hydrocarbon and CO emissions because of a decrease in combustion efficiency.

In spark-ignited engines, the process of combustion starts with a spark discharge event which triggers a series of self-sustaining exothermic reactions that produce a flame which spreads radially outwards; entraining unburned gases (comprising air, fuel, and residual species) and then burning the entrained mixture to release heat. Initially, the surface of the flame (the flame front) is a smooth sphere, but as the flame front convects out and interacts with turbulent cylinder gases, wrinkles begin to appear on its surface to form a turbulent flame 'brush' [7]. This turbulence induced wrinkling of the flame front is critical for successful combustion at all engine speeds for engines undergoing pre-mixed combustion because turbulent wrinkling, which trends with the mean piston speed, increases the surface area of the flame front and consequently the flame entrainment rate. The combustion process can be divided into the flame initiation period and the flame propagation period. The flame initiation period is often described by the flame development angle: spark timing (ST) to 10% fuel mass fraction burned (mfb) angle.

Numerous theoretical models [7, 8, 9] have been proposed to simulate the effects of turbulence on flame entrainment rate. These models are based on the assumption that SI engine combustion falls in the reaction-sheet (and not the distributed reaction) regime, where cylinder flows are moderately turbulent and the turbulent flame burns locally at the laminar flame speed (LFS). LFS is the flame-front-relative velocity at which a quiescent mixture, at a given temperature and pressure, approaches the flame. It is an intrinsic property of the fuel-air-residual mixture and depends on the mixture's temperature (directly), pressure (inversely), and composition. The mixture composition is characterized by its equivalence ratio, which is a measure of the mixture's 'flammability' [10] (direct relation with LFS), and the residual gas fraction, which is a measure of the mixture's dilution (inverse relation with LFS). Dilution by recirculation or retention of combustion products reduces LFS more (almost twice as much) compared to the same amount of dilution by the addition of fresh air. LFS affects both flame initiation and propagation. At the start of combustion, the smooth nascent flame entrains unburned gases at LFS; and later during the combustion process, the turbulent flame burns locally at LFS, i.e. LFS determines the characteristic reaction timescale for combustion. Another fundamental combustion parameter that governs pre-mixed combustion is the ignition delay (ID), which is the time needed by a mixture to initiate self-sustaining combustion at a given temperature and pressure. In the context of IC engines, ID effects are mostly limited to the flame initiation stage.

Under diluted operating conditions, LFS decreases and the ignition delay is prolonged. This can produce both flame initiation and propagation problems. Longer ignition delays can hinder the formation of a stable flame kernel by delaying the start of combustion after the spark fires. Because of the delay, the flow (e.g. squish) around the spark plug responsible for moving the kernel away from the spark plug electrodes to avoid quenching by excessive heat loss to the electrodes might have already passed. Thus, leading to flame initiation failure. Flame propagation depends on the reacting mixture's ability to carry the flame in a timely manner through the entire combustion chamber. In diluted mixtures with low LFS, combustion is slow and the flame can quench prematurely during rapid expansion ('bulk quenching' [11]) without having traversed the required length of the combustion chamber. This results in partially firing cycles that have poor combustion efficiency and high unburned hydrocarbon emissions. Ayala and Heywood [8] reported that if the LFS dropped below a critical value (15 cm/s in their case), the accompanying increase in the eddy burn-up time caused the CoV of IMEP to increase rapidly. Misfires usually

signal a flame initiation failure and partial fires indicate a flame propagation failure. Retarded ST operating points are generally restricted by partial fire limits while advanced ST cases are restricted by misfire limits [10].

Some cyclic instability mitigating strategies for lean engine operation include: (1) enhanced turbulence levels to accelerate flame entrainment and speed up eddy burning by decreasing the turbulent eddy length-scales [8]; excessive turbulence, however, can quench the flame kernel in its infancy by convectively removing too much heat from it, (2) increased mixture reactivity (increasing LFS and decreasing ID) by dosing combustion mixture with more reactive fuels like H_2 [12] or ethane [13], (3) advancing spark timing to compensate for slower combustion, (4) 'fast-burn' combustion chambers to geometrically compensate for slower moving flames by decreasing the flame travel distance [6], (5) novel control strategies, e.g. controlling for combustion milestones like location of 50% mfb (CA_{50}) and location of peak combustion pressure by adjusting spark advance and EGR levels [14], or using information theory based control schemes to eliminate known problematic sequences of various cycle types [15], and (6) intensified ignition energy release by using hotter spark plugs having higher energy spark discharge [10], or using multiple (normally, two) plugs to increase the likelihood of successful flame initiation, or through turbulent jet ignition generated by pre-combustion chambers, which can provide up to one million times the ignition energy of a standard spark plug [16].

To support cyclic variability mitigation efforts at diluted engine operation, the current study attempts to enhance the understanding of combustion under diluted engine operation by investigating LFS and ID for various cycle types encountered to identify causes of combustion instabilities. By characterizing various cycle types based on their combustion signatures, targeted control solutions can be developed to sequester cycles with undesirable characteristics. Time-resolved in-cylinder CO_2 concentration and pressure measurements are used to study cyclic variations in a lean-burn, two-stroke engine under unstable operation. Fig. **1** shows measured pressure traces at three different spark timings (retarding rightwards) at part load operation to demonstrate the unstable nature of combustion in the engine being studied. These cases have high dilution levels (over 15% trapped residual fraction) because of the inefficient nature of combustion product removal in piston-scavenged two-stroke engines. Post combustion CO_2 concentration and IMEP data for an unstable operating point (Fig. **1**(a)) are then used to identify different kinds of cycles and the combustion characteristics of each cycle type are studied using cycle-resolved LFS and ID values calculated using a chemical kinetics based solver.
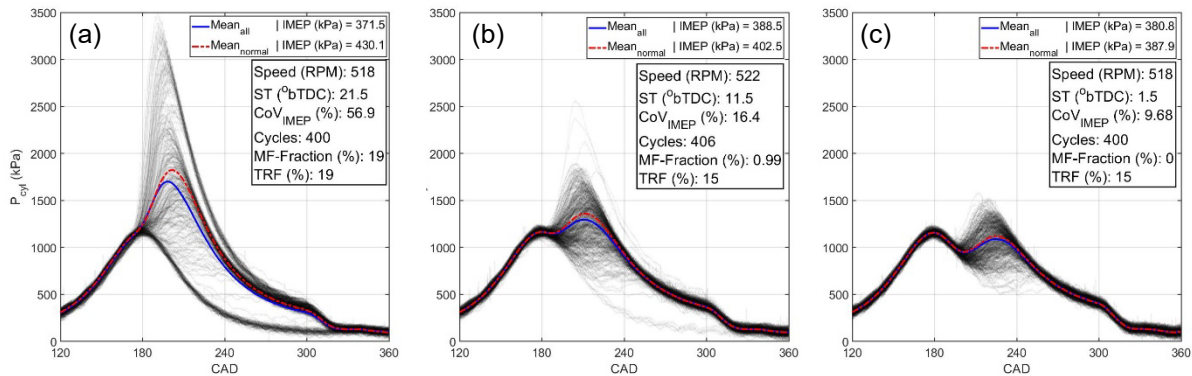
Fig. 1. Individual and average pressure traces (for all and normal combustion cycles) at three spark retard settings (a: -10ºR, b: 0ºR, c: +10ºR) at high-speed, part-load engine operation. Thin translucent curves are individual cycle traces

2. Experimental Setup

An Ajax E-565, single-cylinder, cross and piston scavenged, naturally aspirated, natural-gas-fueled, spark-ignited, two-stroke engine is used for this study.

Table **1** provides some technical specifications of the engine and Fig. **2** shows a schematic of the test setup with all relevant sensors listed.

The engine is equipped with cylinder and manifold pressure transducers, manifold temperature sensors, a fuel flow meter and a quadrature angular encoder. The exhaust from the engine goes to a 5-gas emissions analyzer (MEXA-7100D) that measures CO, CO_2, NO_x, THC and O_2 concentrations on a dry basis. Additional high-speed nondispersive infrared (NDIR) CO_2 sensors (NDIR-500 made by Cambustion Ltd.) are used to measure cylinder and exhaust concentrations on a time-resolved basis. Only

cylinder high-speed CO_2 results are presented herein. Cylinder gas is sampled through a port in the spark plug. More details of the engine test setup can be found in previous publications involving the same engine [17, 18].

Table 1. Specifications of the Ajax E-565 engine

Parameter	Units	Value
Bore	cm	21.6
Stroke	cm	25.4
Displacement	L	9.3
Compression ratio (geometric)	--	8:1
Compression ratio (effective)	--	6:1
Rated continuous power	kW	29.8
Spark timing	CAD (BTDC)	11.5
Exhaust Port Opening	CAD (ATDC)	120.4
Intake Port Opening	CAD (ATDC)	138.1
Air induction system	Naturally aspirated piston scavenged	
Fuel induction system	Hydraulically actuated valve in cylinder head	
Scavenging ports arrangement	Cross	
Fuel	Natural Gas (95 vol% CH_4, 2.2 vol% C_2H_6, 1.8 vol% N_2)	

1. Piezoresistive pressure transducer-1
2. Piezoelectric pressure transducer
3. Piezoresistive pressure transducer-2
4. Slow speed thermocouple-1
5. Slow speed thermocouple-2
6. High speed thermocouple
7. Angular encoder
8. Spark timing control (magnetic pickup)
9. Flow meter
10. Cambustion NDIR head-1
11. Cambustion NDIR head-2
12. MEXA five gas analyzer
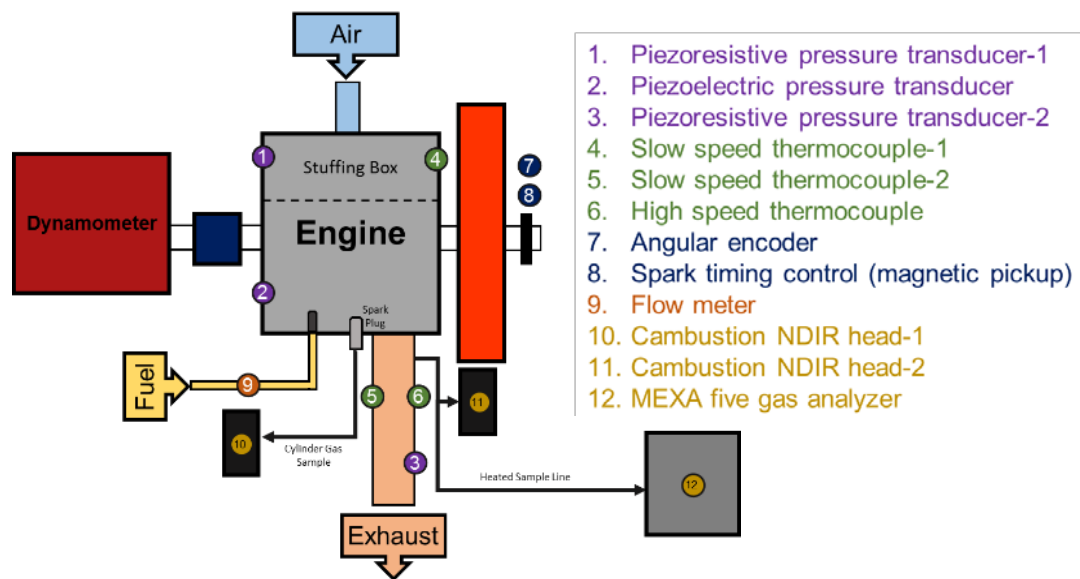
Fig. 2. Test bed schematic with all available sensors labelled

3. Cycle Characterization

In order to systematically study combustion for various cycle types encountered in diluted SI combustion, a characterization methodology based on high-speed cylinder pressure and CO_2 measurements is developed. IMEP is used as a cycle-resolved pressure metric and post-combustion CO_2 concentration is used as a cycle-resolved measure of combustion product concentration. Post-combustion CO_2 concentration is selected because any signature of combustion will be sensed as an increase in CO_2 concentration; and at a given operating point, the extent of this increase will be proportional to the strength of combustion for the corresponding cycle. Using IMEP, which is the displacement volume normalized area enclosed by the P-V curve (work), as an indicator of combustion strength has its limitations, whereby cycles with sensible combustion pressure rise during compression can incorrectly suggest the absence of combustion or the existence of weak combustion. Another possible pressure-based combustion indicator could be the peak combustion pressure (PP). PP values by themselves can be misleading as well because for slow burning cycles, PP could be indistinguishable from that of a misfiring cycle. Therefore, it is difficult to get a complete picture of the nature of combustion by using only IMEP or PP. Heuristic approaches that supplement pressure measurements with location of peak combustion pressure (LoPP)

data to predict the shape of the pressure curve (e.g. [19]) can offer better pressure based cycle-characterization for control applications. However, such methods require a reference database of pressure traces for different cycle types and can be computationally expensive.

A combined IMEP-CO_2 based cycle characterization approach is used for the current study as it is deemed to be an acceptable compromise between computational cost and cycle categorization accuracy; and can, therefore, serve as a controller-friendly method of diagnosis. Fig 3 shows the post-combustion CO_2 concentration as a function of IMEP for 400 consecutive cycles at the unstable operating point being studied (Fig. **1**(a): nominal torque - 548 Nm, nominal speed - 518 RPM), with different marker types showing different types of cycles identified by the IMEP-CO_2 characterization method. The following five different types of cycles are identified: complete misfires (MF), cycles with high peak cylinder pressure and IMEP immediately following misfiring cycles (MF+1), weak and strong partially firing cycles (PF$_{weak}$ and PF$_{strong}$, respectively), and nominal or normal operating cycles. Each cycle type can be thought of as samples from different statistical populations; each population representing engine behavior under distinct combustion regimes, e.g. negligible combustion regime produces misfiring cycles, advanced start of combustion caused by an anomalously rich trapped mixture produces high peak pressure cycles, and normal combustion results in nominal cycles. The histograms at the bottom of Fig 3 show the distribution of CO_2 (left) and IMEP (center) for all cycles, irrespective of their classification. The histogram on the right shows the IMEP distribution for only the normal cycles. The distribution using the entire data-set is tri-modal (one mode each for misfiring, post-misfiring, and normal cycles) and that for the normal cycles is Gaussian-like, indicating the absence of non-stochastic influences.
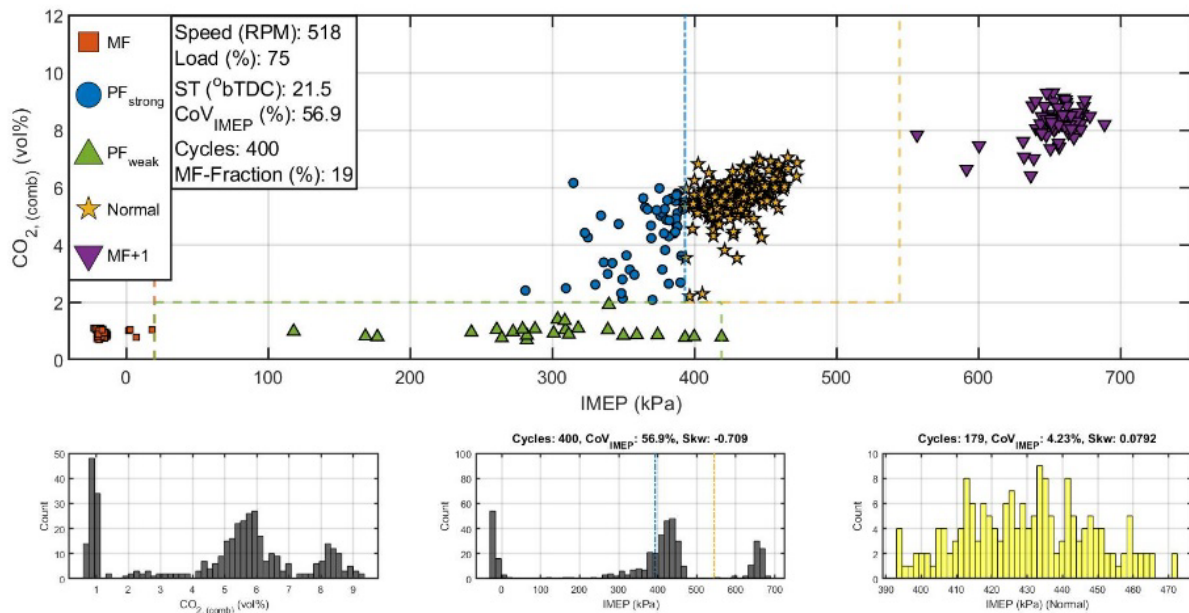
Fig 3. Top: Different kinds of cycles on an IMEP-CO2 map - dashed lines show borders for different cycle types; Bottom: histograms showing the distribution of CO2 (left) and IMEP (center) for all cycles, and IMEP for normal cycles (right)

Prior to discussing the methodology used to segregate cycles into the five types, for the sake of completeness, corresponding CO_2 maps are shown for PP and LoPP in Fig. **4**(a) and Fig. **4**(b), respectively. It can be seen from Fig. **4**(a) that, barring a few PF$_{weak}$ and normal cycles, post-combustion CO_2 concentration rises monotonically with PP, and asymptotically approaches a maximum value of around 10 vol%. Moreover, the PP distribution of normal cycles is Gaussian-like. The LoPP map shows that there is a substantial spread in the cycle data, especially for slow burning partially firing cycles and that the distribution for normal cycles is again Gaussian-like. It can also be seen that PPs for the MF+1 cycles are significantly higher and their location is, on average, slightly advanced compared to normal cycles.
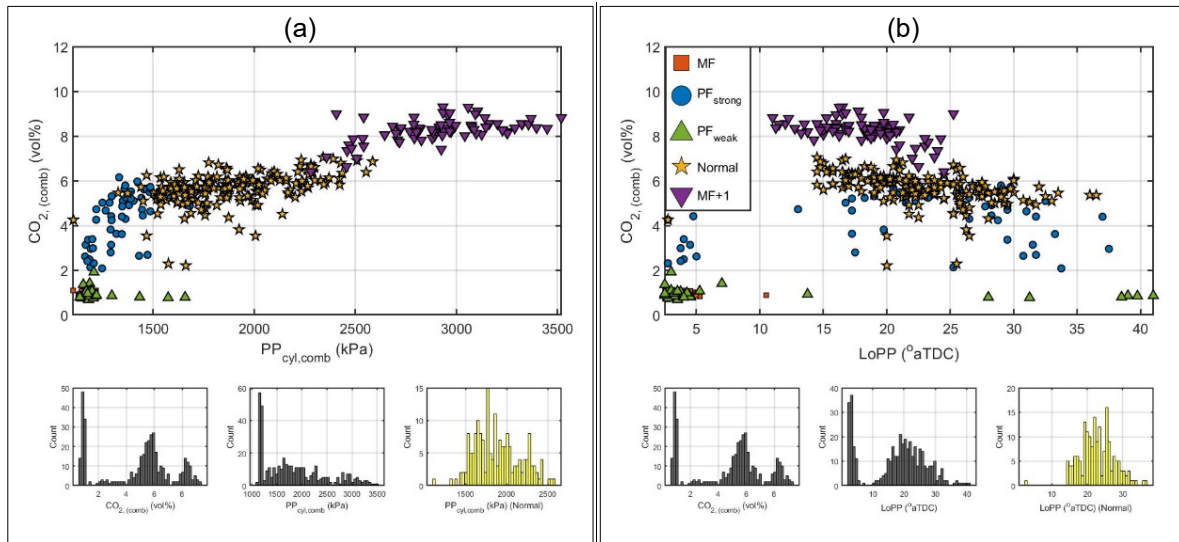
Fig. 4. Different kinds of cycles on (a) PP-CO$_2$ and (b) LoPP-CO$_2$ maps similar to Fig 3

A brief description of how the five cycle types shown on the CO$_2$-IMEP map (Fig 3) are identified is provided below. The method is somewhat subjective in nature and the bounds defined below might need to be adjusted for use with other engines. The taxonomy, however, is consistent with previous work done on two-stroke engine characterization [20, 21].

1. **Misfiring cycles** (squares): These are the cycles where both the pressure and CO$_2$ signatures point to the failure of combustion. The IMEP is around 0 and the post-combustion CO$_2$ concentration is less than 2 vol%, which is selected to be the lower post-combustion CO$_2$ concentration threshold for firing cycles. The CO$_2$ concentration values for the misfiring cycles range between 1.7 and 2.7 vol%. This is higher than ambient CO$_2$ concentration (~0.4 vol%) because of residual CO$_2$ in the cylinder from previous cycles. The selection criteria for misfiring cycles is:

$$\text{Cycle}_N \in [\text{MF}] \text{ if } \{\text{IMEP}_N \leq 20 \text{ kPa}\}$$

2. **Post-Misfiring cycles** (downward facing triangles): The cycles succeeding misfiring cycles have unusually high combustion pressures, and as a result, very high IMEPs. This increased combustion pressure is attributed to the burning of a richer-than-usual trapped mixture produced by residual fuel from the preceding misfiring cycle. According to [11], after a MF, only 20-30% of the delivered fuel mass is detected as HC emissions in the exhaust; implying that majority of the delivered fuel stays back as residual gas. The selection criteria for post-misfiring cycles is:

$$\text{Cycle}_N \in [\text{MF} + 1] \text{ if } \{\text{Cycle}_{N-1} \in [\text{MF}]\}$$

3. **Weak partial fires** (upward facing triangles): There are some cycles where evidence of combustion is only seen in the pressure data since the IMEP is higher than the 20 kPa misfiring threshold but the post-combustion CO$_2$ concentration is less than the combustion threshold. These cycles are labeled weak partially firing cycles, or weak partial fires for short. The absence of a combustion signature in the CO$_2$ data is attributed to the relatively weak nature of combustion that does not produce sufficient CO$_2$ to homogenously increase the cylinder CO$_2$ composition. As a result, for the case of weak partial fires, the cylinder gas sample analyzed by the CO$_2$ sensor does not have high enough CO$_2$ composition to indicate the existence of combustion. If larger samples had been drawn for these cases, some CO$_2$ rich strata would probably have made their way to the analyzer and CO$_2$ composition data would show combustion. Doing so would, however, deteriorate the time-response of the analyzer and the removal of substantial amounts of cylinder gas would affect regular engine behavior. For engine scavenging studies [22, 23, 24] with intermittent cylinder gas sampling using electronic or cam-actuated valves, upwards of 20% of the engine volume was sampled to get reliable data and around 20 cycles following a sampling cycle had to be skipped to let the engine recover from the cylinder gas donation.

Rate of heat release analysis is carried out to rule out that partial oxidation of fuel to CO instead of CO_2 is not responsible for the lack of sensible CO_2 rise. The results confirm that these cycles represent a sensor limitation. Therefore, weak-partial fires are not used in LFS based combustion analysis discussed in section 5. Henceforth, 'partial fires' will refer to strong partial fires unless qualified by a subscript. The selection criteria for weak partial fires is:

$$\text{Cycle}_N \in [\text{PF}_{\text{weak}}] \text{ if } \{\text{IMEP}_N > 20 \text{ kPa \& } [CO_2] \leq 2\text{vol\%}\}$$

4. **Strong Partial Fires** (circles): These are cycles that carry signatures of combustion both in the pressure and CO_2 data, but are characterized as partial fires because the IMEP falls in the range where there is a possibility of CO_2 not crossing the combustion threshold, indicating that the increase in CO_2 quantity is not large enough to guarantee a sensible increase in the cylinder CO_2 composition. These cycles can be thought of as partial fires where the sampled cylinder gas had a CO_2-rich stratum. The selection criteria for strong partial fires is:

$$\text{Cycle}_N \in [\text{PF}_{\text{strong}}] \text{ if } \{20 \text{ kPa} < \text{IMEP}_N < 90^{\text{th}} \text{ percentile IMEP of PF}_{\text{weak}}, \& [CO_2] > 2\text{vol\%}\}$$

The top tenth percentile IMEP for the weak partial fires is ignored in setting the upper bound for strong partial fires to avoid removing too many normal cycles (discussed next) because of a few high-IMEP weak partial fires.

5. **Normal Cycles** (stars): The cycles that don't fall in any of the four aforementioned categories are the normal cycles (complement of the union of [MF], [MF+1], [PF$_{\text{strong}}$], and [PF$_{\text{weak}}$]). The normal cycles are not influenced by misfiring cycles and have strong combustion signatures that are consistently sensed by pressure and CO_2 sensors. The selection criteria for normal cycles is:

$$\text{Cycle}_N \in [\text{Normal}] \text{ if } \{\text{Upper IMEP}_{[\text{PF}_{\text{weak}}]} \text{ bound} < \text{IMEP}_N < \min(\text{IMEP}_{[\text{MF}+1]}), \& [CO_2] > 2\text{vol\%}\}$$

It can be reasoned that the "normal" cycles represent nominal engine behavior at an operating point and should thus be used for validating engine simulations that do not have the ability to capture combustion instability effects. A comparison of average pressure traces obtained by using normal cycles versus all cycles is shown in Fig. **1** for three part-load operating points. Fig. **5** shows average pressure traces for five cycle types along with average apparent heat release rate curves for the case being
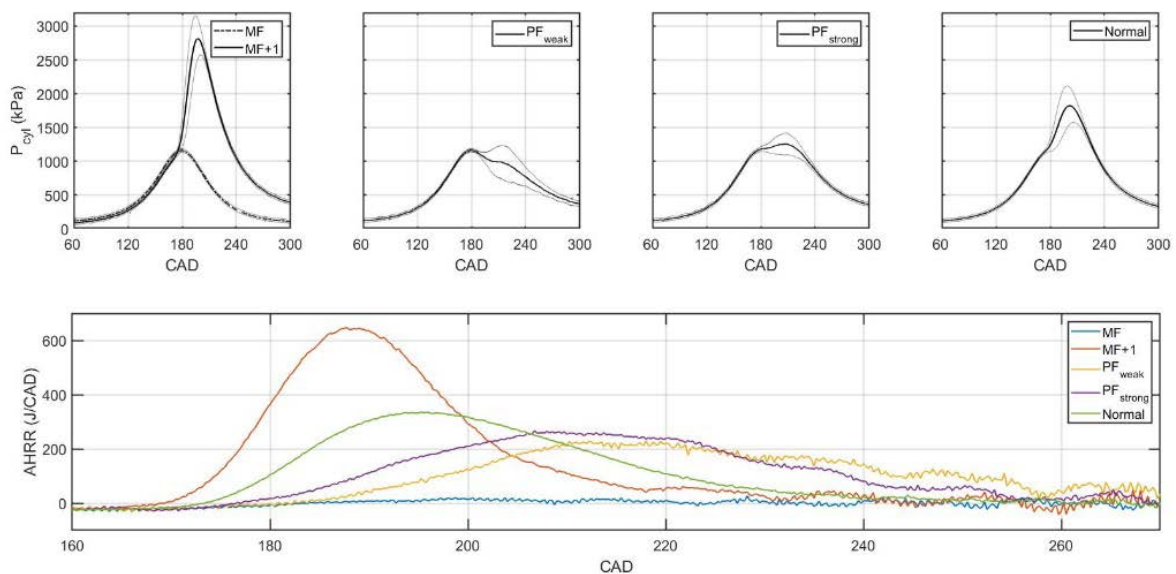
Fig. 5. Average pressure traces (top) for the five cycle types identified and their apparent rates of heat release (bottom), which have been slightly filtered for clarity. The translucent lines surrounding each pressure curve are the $\pm$ 1 standard deviation envelope about the mean

studied. The pressure traces show that each cycle type is notably different from the others and more importantly, from the normal cycle type. Therefore, including non-normal cycles (MF, MF+1, and PFs) in the calculations for determining the average pressure at an operating point can contaminate the normal cycle average with influence from non-representative cycles. The compression curve for the MF+1 cycles is lower than that of MF cycles because the trapped mixture, which is made richer and hotter by the large residual gas fraction, (1) has a lower specific heat ratio and (2) loses more heat to the walls. It can be seen from the heat release curves that the MF+1 cycles have the most advanced heat release and the accumulated heat release (area under the curve) is the highest (14.8 kJ). This is because of richening by residual fuel from the preceding MF. Partial firing cycles have the slowest heat release and their accumulated heat release is comparable to that of normal cycles (10.8 kJ).

Fig. **6** shows how the fraction of different engine cycle types changes across 36 operating points as the engine becomes increasingly unstable. Engine stability is quantified by the CoV of IMEP. At stable operating points 100% of the cycles comprise normal cycles with no misfiring of partially firing cycles. As the engine becomes more unstable, the share of misfires increases while that of normal cycle decreases, eventually going to less than 5% at very unstable cases. The share of partial fires increases initially and then falls as MF and MF+1 (not shown in Fig. **6**) become the dominant cycle types. The bottom sub-plot shows the increase in the difference between total and normal cycle averaged IMEP as a function of engine stability. The normal cycle averaged IMEP can be up to 100 kPa higher than the total averaged IMEP. From a controls application perspective, this difference can be thought of as an opportunity to improve the engine's IMEP by 100 kPa if a control system capable of removing all non-normal cycles in real-time can be developed. IMEP improvements would be accompanied by improvements in torque output, engine stability, thermal efficiency, and emissions; particularly hydrocarbon emissions from the elimination of MF and PF cycles and NO_x emissions from the elimination of high combustion temperature possessing MF+1 cycles. For the cycle being studied, the IMEP increases from 371 kPa to 429.7 kPa, the CoV of IMEP decreases from 56.9% to 4.23%, and (assuming the same fuel flow rate) the fuel conversion efficiency increases from 28.8% to 33.4%. A similar idea is proposed in [15], in which Shanon entropy-based heat release analyses are used to identify and quantify the strength of cyclic 'memory', i.e. the number of consecutive cycles across which the effects of a cycle (in the form of non-stochastic repeating patterns) can be felt. The number came out to be 5-6 for PFI SI engines and 10-11 for GDI engines. Up to 7.1% improvements in IMEP, 115% in CoV of IMEP, and 6.9% in indicated thermal efficiency were realized by removing problematic sequences at a 17% EGR level for a GDI engine. It is worth mentioning over here that for the current study, the mechanical governor that controls fueling to the engine was deactivated to maintain constant fuel flow during experiments. In regular engine operation, after a low IMEP cycle (MF, PF), the governor would add extra fuel to make up for lost power and keep IMEP constant. This would increase the intensity of MF+1 and PF+1 cycles and create the potential for catastrophic failure. Therefore, reduced IMEP fluctuations would also improve engine safety in addition to thermal efficiency and emissions.
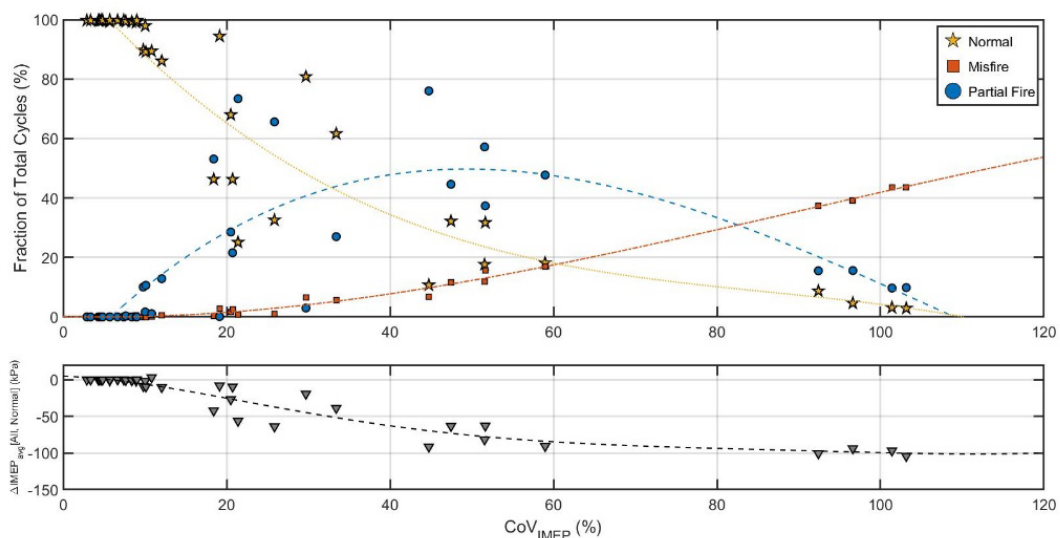
Fig. 6. (top) Cycle type fractions of the total recorded cycles and (bottom) difference between total and normal averaged IMEP as a function of CoV of IMEP for 36 operating points; dashed curves are trend lines

4. Effects of Cyclic Variability on Combustion Phasing, Trapped Residual Fraction and Equivalence Ratio

The characterization method described above is used to investigate changes in the trapped[1] residual fraction (TRF), trapped equivalence ratio (TER), and combustion phasing for various cycle types. TRF and TER results are shown using box-plots for the same operating point as before. The boxes represent the interquartile range, the horizontal lines in the boxes mark the sample median and the diamonds the sample mean. In the literature [4, 20], "return maps" (sometimes also called bifurcation plots) are occasionally used to relate cycles to those preceding them. Box plots were deemed better suited for the current study to probe the connection between different kinds of cycles. For the sake of completeness, some return maps are presented in the appendix.

TRF is calculated by using in-cylinder CO_2 as a tracer for combustion products. High-speed CO_2 measurements are used to extract cycle-resolved concentration data before and after gas-exchange, which are then used to calculate TRF using a calculation method similar to [22]. The original method has been modified to account for decrease in cylinder CO_2 concentration after exhaust port closing because of fuel injection. The resulting TRF expression for cycle 'N' is shown in equation 1. 'y_{fuel}' is the mole fraction of fuel in the pre-combustion mixture. An ambient CO_2 concentration of 400 ppm is used for TRF calculations. Cycles following weak-PFs are removed prior to analysis because the '$[CO_2]_{pre-EPO,N-1}$' values for such cycles corresponded to post-combustion concentration for weak-PFs, which, as discussed earlier, are unreliable and lead to unrealistically high TRF values for the following cycle.

$$\text{TRF}_N = \frac{[CO_2]_{post-inj,N} - [CO_2]_{Air}}{[CO_2]_{pre-EPO,N-1} - [CO_2]_{Air}} + \frac{[CO_2]_{Air}\, y_{fuel}}{[CO_2]_{pre-EPO,N-1} - [CO_2]_{Air}} \qquad (1)$$

Fig. 7. TRF for different cycle types (right), and breakdown of MF-1 cycles into its constituents (left). Numbers on the top of box-plots show the number of cycles for each type. Boxes show the interquartile range, diamonds represent the mean, horizontal lines within boxes are the median, and the whiskers are the fences beyond which data points are considered outliers

Fig. **7** (right) shows TRF results for various cycle types. Average TRF for normal, PF, and MF cycles falls in the 12% - 15% bracket. Cycles following MF cycles have very high TRF because of poor scavenging in misfiring cycles. The MF+1 cycles are primarily responsible for the operating-point-averaged TRF being 18.5%, which is significantly higher than that of normal cycles. This additional dilution

---

[1] Trapped refers to that portion of the two-stroke cycle when all ports are closed, i.e. from EPC to EPO.

might be partly responsible for the engine instability, as an increase in TRF decreases LFS and increases ID. This can lead to both flame initiation and propagation problems, which produce MF and PF cycles, respectively. To investigate the influence of cycles preceding MF (i.e. MF-1 cycles) on MF cycles, MF-1 cycles have also been plotted and their makeup is shown in the left sub-plot. The makeup is as follows: 35% MF+1, 42% normal, 0% MF, and 23% partial fires. The MF-1 cycles have high average TRF because of the sizable share of MF+1 type cycles in its constitution. Even though the TRF results do not point at the root cause of misfires, they do suggest that the high amount of trapped residuals for the cases when a misfiring cycle is preceded by a MF+1 cycle might be responsible for increasing the frequency of misfires and preventing the engine from recovering from a misfire. It can be argued that in the current example, the engine would have had 25 fewer misfires had the post-misfiring cycles not been anomalously rich. These misfires can potentially be avoided by reducing (or cutting off completely) the fuel supply, or adjusting the spark timing and/or EGR rate (if available) after a misfire has been detected to compensate for LFS changes caused by fuel enrichment and increased TRF. The TRF data is silent on the cause of the remaining 60% of the misfires. Similar reasoning can be extended for the role of pre-PF cycles (PF-1) in causing the PFs. The makeup of these cycles (50% normal, 29% MF+1, 0%, MF, 21% PF) has fewer MF+1 and more normal cycles, thereby making it impossible to predict a PF from its preceding cycle half of the time.

TER is calculated by assuming that the measured post-combustion CO_2 concentration represents the mole fraction of CO_2 in the products of the lean combustion reaction of methane shown below (equation 2). Combustion inefficiencies and dissociation effects are neglected. The oxidizer in TER calculations is fresh air only. To emphasize the fact that the calculated TER captures only those fuel molecules that are oxidized to form CO_2 and are subsequently sensed by the CO_2 analyzer, the TER is subscripted with 'combustion'. N_r in the following reaction is the number of moles of residual gas particles present at the start of combustion.

Equation (2):

$$N_r \left[CO_2 + 2H_2O + 2(3.76)N_2 + \left(\frac{2}{TER_{combustion}} - 2 \right)(O_2 + 3.76N_2) \right] + CH_4 + \frac{2}{TER_{combustion}}(O_2 + 3.76N_2)$$

$$\downarrow$$

$$(1 + N_r)CO_2 + 2(1 + N_r)H_2O + 7.52 \left(\frac{N_r}{TER_{combustion}} + 1 \right)N_2 + 2 \left(\frac{1}{TER} - 1 \right)(O_2 + 3.76N_2) + 2N_r \left(\frac{1}{TER_{combustion}} - 1 \right)O_2$$

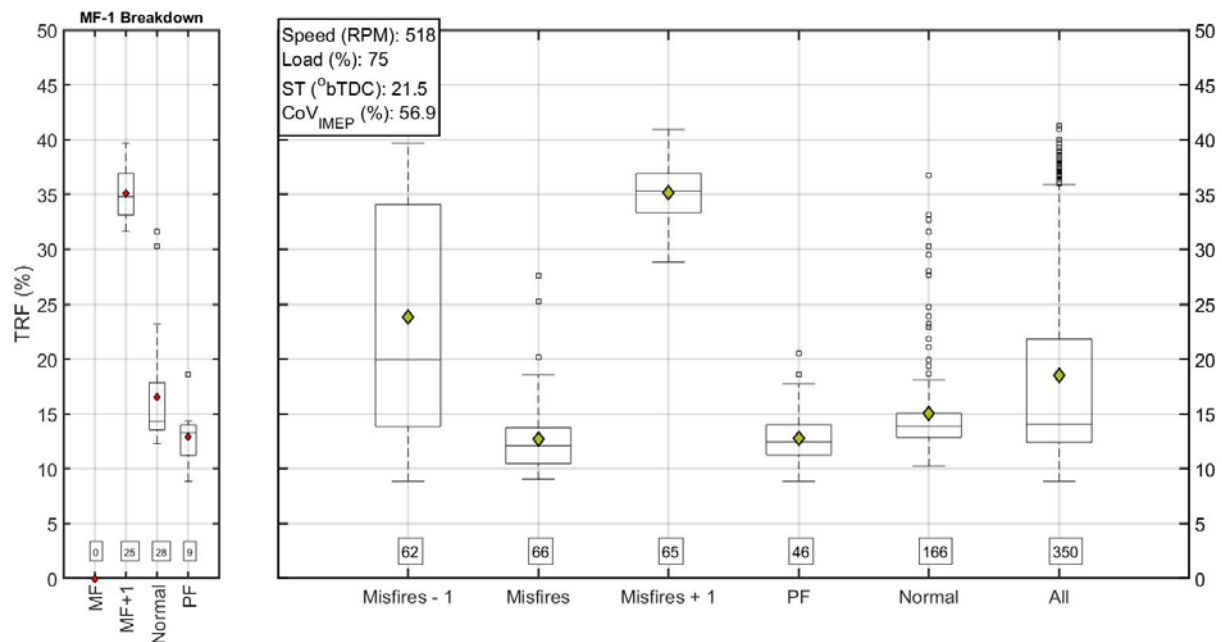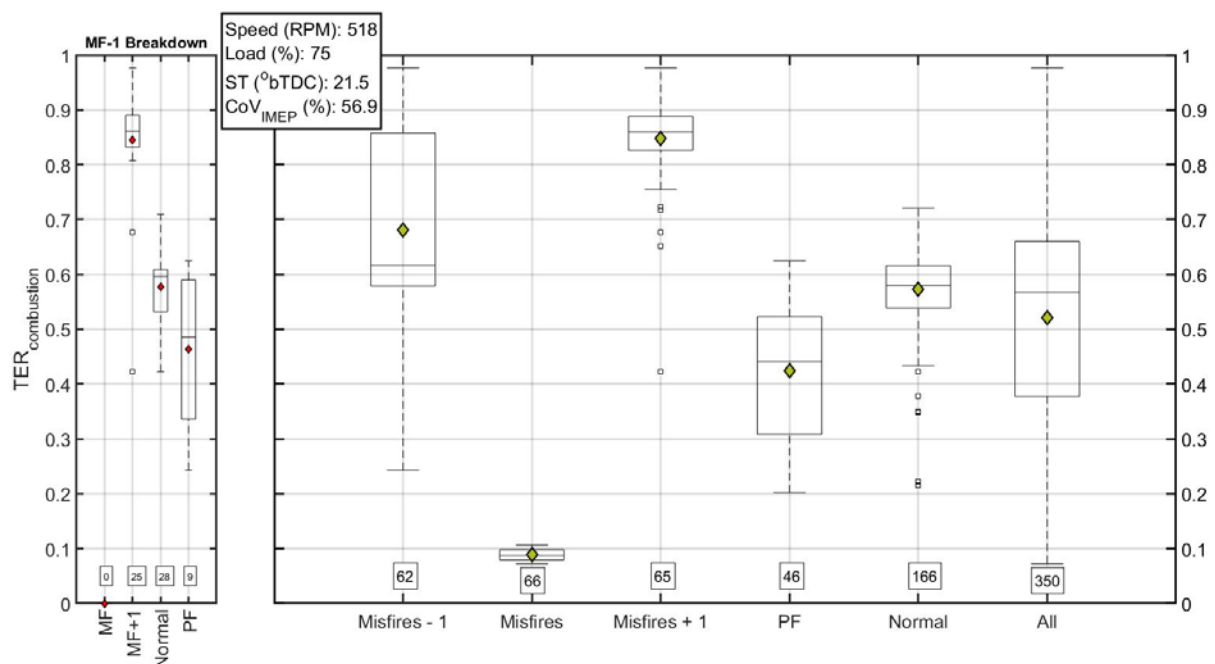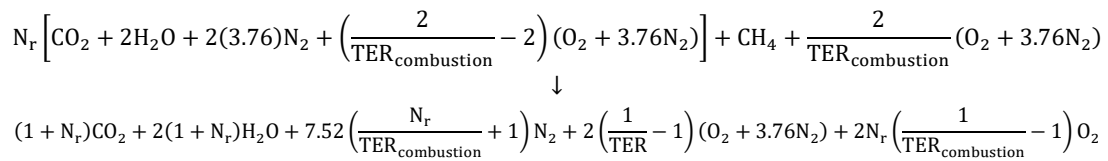**Fig. 8.** Combustion TER for different cycle types (right), and breakdown of MF-1 cycles into its constituents (left). Numbers on the top of box-plots show the number of cycles for each type. Boxes show the interquartile range, diamonds represent the mean, horizontal lines within boxes are the median, and the whiskers are the fences beyond which data points are considered outliers

Fig. **8** shows combustion TER for various cycle types. As expected, the MF+1 cycles are significantly richer than all other cycles, suggesting that their corresponding LFS would be higher and ID shorter. PF cycles are leaner than normal cycles, which could explain their slow burning nature. MF cycles appear to be extremely lean, but this is only so because combustion failed in these cycles and no combustion signal in the form of CO_2 concentration increase was sensed. The true TER based on the actual amount of fuel present in the cycle is probably much higher. Similar to TRF (Fig. **7**), the breakdown of MF-1 cycles' TER is presented as a separate sub-plot (Fig. **8** – left).

Rate of heat release analysis results are used to calculate the duration of various combustion stages namely, 0% mfb (ST) to 10% mfb, 50% mfb, and 70% mfb for the three combustion cycles. The average duration of these events is shown in Fig. **9** as an overlaid bar graph. The results corroborate the inferences about ID and LFS drawn from the TER results, i.e. (1) fuel-rich MF+1 cycles have the fastest combustion as evidenced by shorter flame development angle (CA_{0-10}) and combustion duration, defined as the number of crank angle degrees needed beyond the 10% mfb point to burn 70% of the fuel, and (2) PF cycles burn the slowest. Normal cycles fall in between the two abnormal combustion cycles. 70% mfb is selected for representing combustion duration to help with comparison across different cycle types since many PF cycles do not reach 80% mfb, let alone 90%.

The combustion phasing results are shown in a different manner in Fig. **10** to emphasize the connection between flame initiation (represented by CA_{0-10}) and propagation (represented by CA_{0-70} and CA_{10-70}) stages. Fig. **10**(a) shows that the effects of an increase in the flame development angle are felt throughout the combustion process and as a result, the time from ST to 70% mfb increase monotonically. It is worth noting that the rate of this increase is about 1.8 times the corresponding flame development prolongation. In other words, initial combustion variations, not only persist throughout the combustion process, but their speeding up or slowing down effects on the overall combustion process become more pronounced as combustion progresses. Fig. **10**(b) plots the increase in combustion duration (10% mfb to 70% mfb) as a function of the flame development angle to isolate the contribution of flame development angle in the slowing down of combustion. The results show that most of the increase in total combustion duration comes from the faster flame initiation process. The slope of the CA_{10-70} curve is only 0.81. The transmission of initial variations to the entire combustion process have been reported in [8] and attributed to variability in eddy burning times at very diluted conditions. The eddy burning time variations are brought on by variations in LFS and turbulent microscale. These results are explained using LFS calculations in the next section.
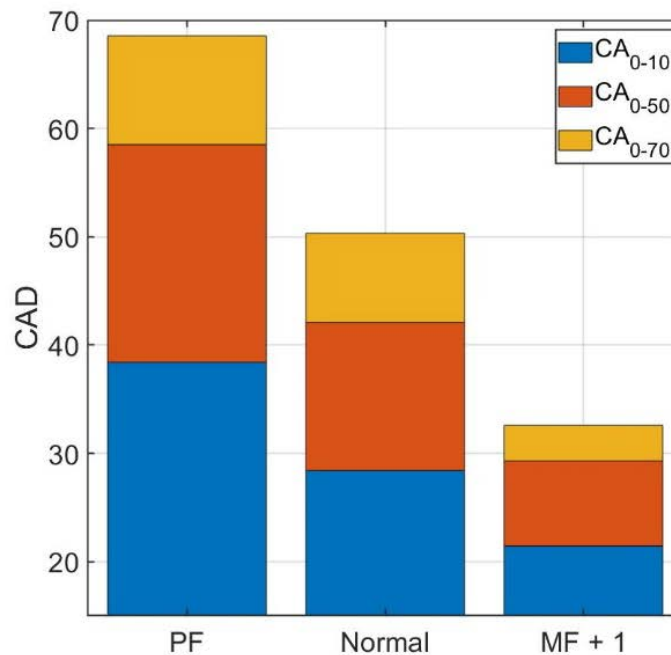
Fig. 9. Overlaid bar graph showing average crank angle degree duration for 10%, 50%, and 70% mass fraction burned
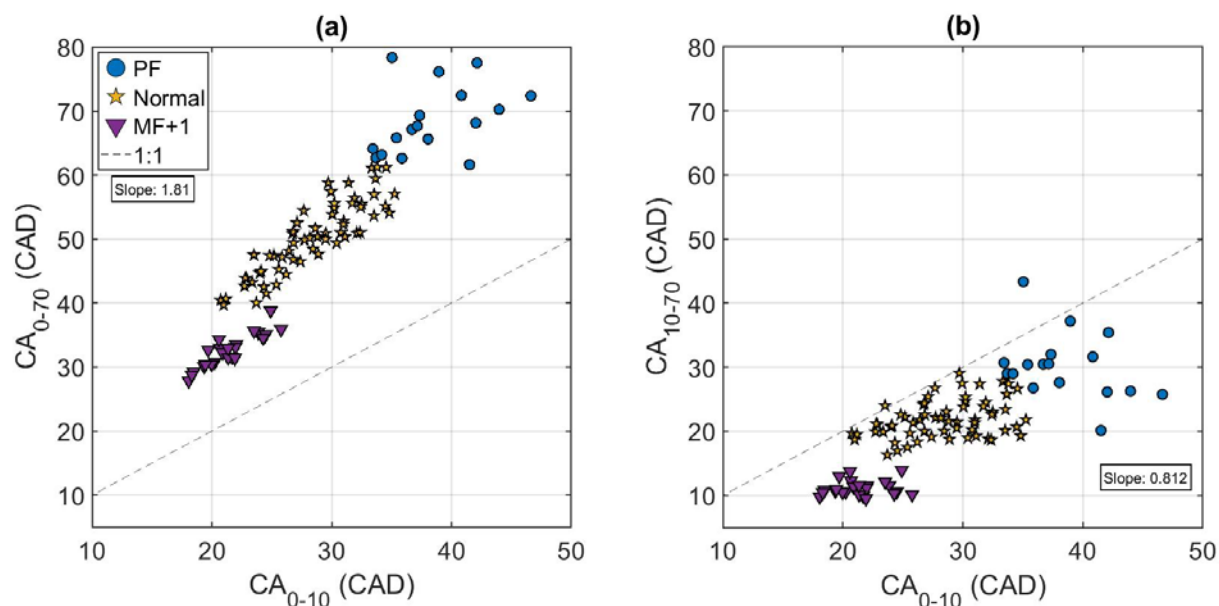
Fig. 10. (a) CA_{0-70} and (b) CA_{10-70} as a function of the flame development angle (CA_{0-10}) for the three combustion cycle types

5. Dissecting Cyclic Combustion Variations Using Laminar Flame Speed and Ignition Delay

The $TER_{combustion}$ and TRF results discussed above are used, along with cylinder temperature and pressure values, to calculate LFS and ID using a chemical kinetics solver. The solver code, developed and validated in previous works [25, 26], uses Cantera libraries called from a Python program. This code first initializes a fuel-air mixture at the user-defined temperature, pressure, equivalence ratio, residual fraction, and fuel composition. The initialized mixture is then passed to a 1D free flame object for LFS calculation or to a 0D homogeneous constant volume reactor object for ID calculation. In the case of LFS calculation, solutions are attempted three times: first with heat transfer disabled, second with heat transfer and grid refinement enabled, and third with multicomponent diffusion. The resulting LFS is the speed of the flow into the free flame at node one. ID is determined with the 0D constant volume reactor by detecting the time at which there is an inflection point in the formation of OH in the reactor. The combustion mechanism used is referred to as nc5_49 and is a natural gas oxidation mechanism containing 293 species and 1,588 reactions [27].

Fig. **11** shows the laminar flame speed results for the three combustion cycle types at five different times during the expansion stroke, starting at TDC. The average CA10, CA50, and CA70 timings have also been marked. The pressure and temperature values used in LFS calculations are shown in Fig. **12**. Temperature needed for the LFS computations is calculated from experimental cylinder pressure measurements by assuming that the trapped mass is present at the intake (scavenging chamber) density. The MF+1 cycles consistently have the highest LFS, followed by the normal and the PF cycles. MF+1 cycles have two LFS enhancing influences in the form of high TER and high combustion temperatures, and two LFS diminishing influences in the form of high TRF and high combustion pressure. The LFS enhancing factors, most notably TER, cause their LFS to be significantly higher than that of normal and PF cycles that have leaner trapped mixtures (Fig. **8**). Another thing worth noting is the trajectory of the LFS curves. LFS in MF+1 cycles rises very rapidly after combustion with the peak located around 36° aTDC. Normal cycle LFS appears to peak around 48° aTDC, while the PF LFS is still rising at 48° aTDC. Because of these differences in LFS, which affect both flame initiation and propagation, combustion phasing is significantly advanced for the MF+1 cycles compared to the other two combustion cycles, e.g. at 12° aTDC, the MF+1 cycles have burned 70% of the fuel, normal cycles have burned around 20%, and PFs have not even burned 10% of the fuel mass. The slow burning PF cycles might not reach complete combustion because when rapid expansion starts as the BDC-bound piston picks up speed, the flame might be quenched prematurely while there is still a significant amount of unburned fuel left in the cylinder. This can lead to high unburned hydrocarbon emissions. From a controls perspective, if the goal is to have LFS profiles similar to the normal profile, then the MF+1 cycles should either have higher dilution or lower amount of trapped fuel; and the PF cycles should have lower dilution or more trapped

fuel. The application of this strategy might, however, present some challenges because, as stated earlier, PF events are difficult to predict from the PF-1 cycles.
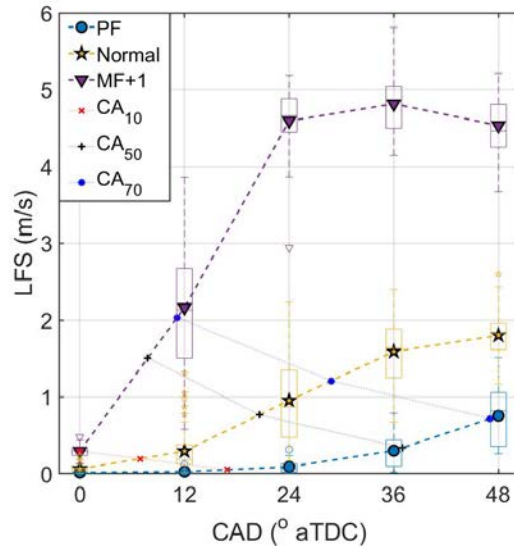
Fig. 11. LFS for different cycle types at different times during the expansion stroke. Boxes show the interquartile range, filled markers represent the mean, horizontal lines within boxes are the median, and the whiskers are the fences beyond which data points are considered outliers and represented by hollow markers
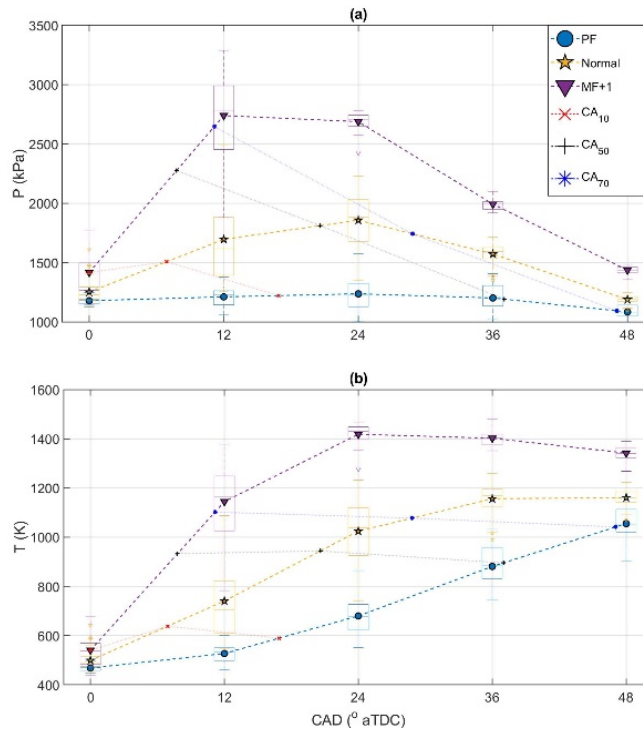
Fig. 12. Cylinder (a) pressure and (b) temperature for different cycle types at different times during the expansion stroke. Boxes show the interquartile range, filled markers represent the mean, horizontal lines within boxes are the median, and the whiskers are the fences beyond which data points are considered outliers and represented by hollow markers

To emphasize the strong influence of TER on LFS, cycle resolved LFS results at 50% mfb points are plotted in Fig. **13** as a function of combustion TER. The strong increasing relationship between the two is evident, especially for PF and normal cycles. The apparent deviation in the increasing trend for the MF+1 cycles is because of the extraordinarily high TRF values for these cycles. Had the residual fraction been comparable to that of normal and PF cycles, the LFS for the rich MF+1 would have been
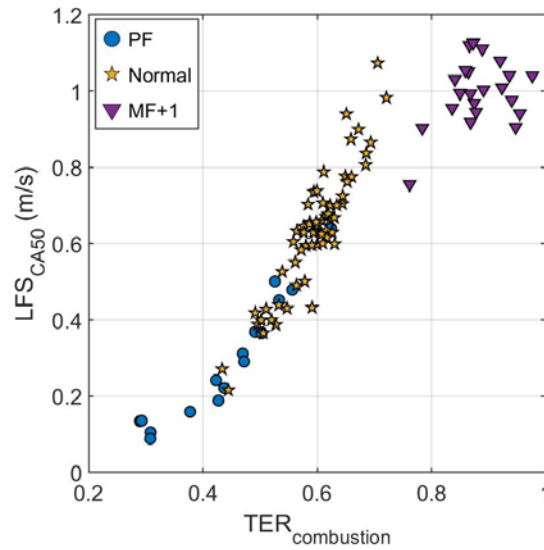
Fig. 13. LFS at CA50 as a function of TER$_{combustion}$ for the three combustion cycle types

even higher, likely following the PF and normal cycle trend. These results show that large amounts of residuals can even cause a noticeable decrease in the LFS of cycles with relatively rich trapped mixtures.

To explain the combustion phasing results shown in Fig. **10**, various combustion event durations are shown as a function of LFS at TDC in Fig. **14**. TDC is selected as a reference because it precedes most combustion milestones and can be considered a time datum within the flame initiation period. The slope and correlation coefficients of the combustion event duration and LFS results are also shown. These are used to highlight the average magnitude of combustion event duration shortening as LFS increases and the strength of LFS in driving these changes, respectively. Going from Fig. **14**(a) to Fig. **14**(c), the slope, which is the CAD-reduction in combustion event duration for every m/s increase in LFS, increases in magnitude by over 100%. This confirms that the effects of combustion variations on the overall comb ustion rate become more pronounced as combustion progresses.
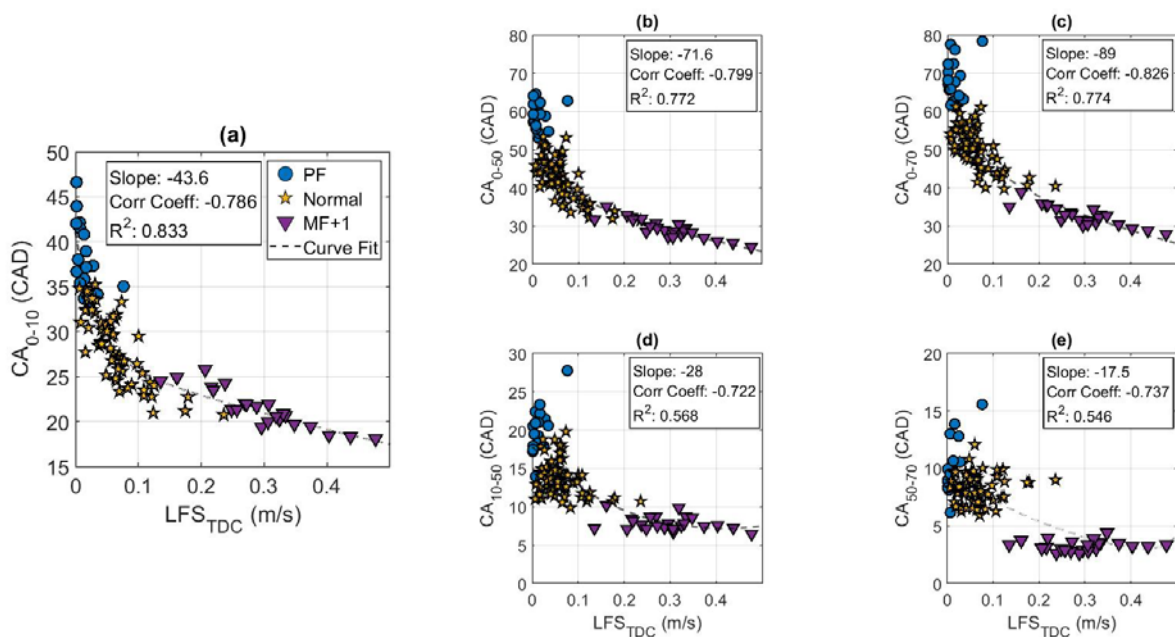
Fig. 14. Effects of LFS on combustion progression from (a) ST to 10% mfb, (b) ST to 50% mfb, (c) ST to 70% mfb, (d) 10% mfb to 50% mfb, and (e) 50% mfb to 70% mfb. Curve fit lines are of the type: y=ae^{bx} + ce^{dx}

Moreover, the strong positive correlation between LFS and combustion event durations indicate that variations in the flame initiation (Fig. **14**(a)) and propagation (Fig. **14**(b, c)) periods are caused by LFS changes. Fig. **14**(d) and Fig. **14**(e) show the isolated effects of LFS at TDC on CA_{10-50} and CA_{50-70}. The small combustion event shortening rate values (slopes) indicate that the effect of LFS increase on combustion rate increase becomes less pronounced during the later stages of combustion.

   Ignition delay results are calculated only at the conditions present at spark timing since the implications of ID are likely limited to the flame initiation period. The results, shown in Fig. **15**(a), are calculated using a constant temperature of 1200 K, which is the assumed flame kernel temperature. The temperature choice is based on iterative calculations to match ID and CA_{0-10} using the chemical ID solver and a simple conservation of energy based spherical flame kernel model. Results show that ID of the fast-burning MF+1 cycles is actually longer than that of the other two cycles. The longer ID means that the fast-burning nature of the MF+1 cycles, as observed from the heat release analysis results (Fig. **9**), result from faster LFS and not shorter ID. As mentioned in the introduction, in addition to influencing flame propagation, LFS also affects flame initiation for pre-mixed SI combustion by influencing the flame-entrainment rate. Therefore, for the case being studied, the faster LFS overpowers the combustion-speed-slowing effects of the longer ID during the flame initiation period. ID is longer for the richer MF+1 cycles because (1) ID is not as sensitive to TER as LFS [28], and (2) the end-of-compression pressures are noticeably lower for the MF+1 cycles (Fig. **15**(b)). High TRF for the MF+1 cycles might also be responsible for the longer ID.
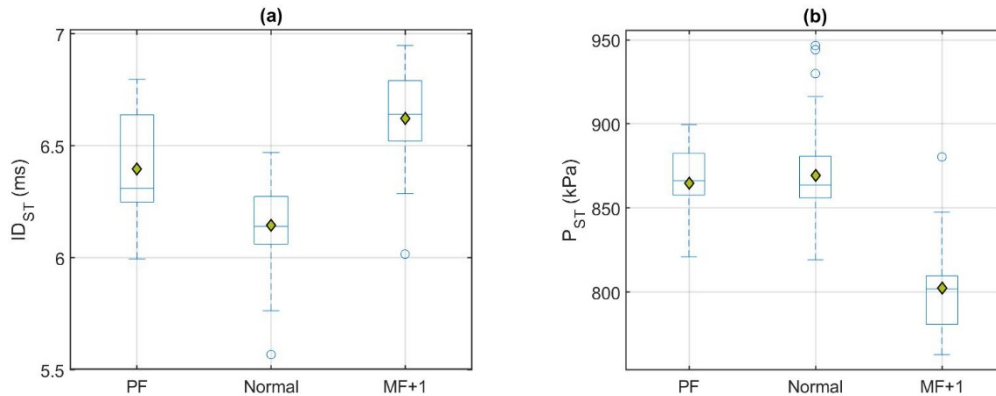
Fig. 15. Ignition delay and the corresponding pressure at spark timing for the three combustion cycle types. Boxes show the interquartile range, diamonds represent the mean, horizontal lines within boxes are the median, and the whiskers are the fences beyond which data points are considered outliers

6. Conclusions

High speed in-cylinder CO_2 data at an unstable operating point with high dilution levels was used with IMEP data to characterize engine cycles into different cycle types (MF, PF, Normal, and MF+1). Combustion characteristics of each cycle type were then studied using a chemical kinetics-based solver to calculate LFS and ID. Major conclusions from the cycle characterization and combustion analysis exercises are listed below:

1. MF+1 cycles, which are richer than PF and normal cycles, have higher LFS because of high TER and combustion temperatures, despite having high TRF and combustion pressures. The high LFS is responsible for the noticeably faster combustion observed in these cycles.
2. ID during the flame initiation period is longer for the fast-burning MF+1 cycles compared to the other two combustion cycle types because of high TRF and low compression pressures. Therefore, the fast paced MF+1 combustion is supported only by the high LFS.
3. PF cycles have significantly slower LFS compared to normal and MF+1 cycles, which results in slower combustion that is susceptible to premature extinction during the rapid expansion phase of the power stroke (bulk quenching). Any control solution for avoiding PF cycles should be able to first, detect PFs from their signatures in PF − 1 cycles and then lower dilution or increase TER to increase LFS for the would-be PF cycle. Break down of PF-1 cycles shows that it is difficult to predict PFs as half of all PF-1 cycles are normal cycles.

4. Variations in the early combustion stages, not only persist throughout the combustion process, but their effects on the overall combustion rate become even more pronounced as combustion progresses. These variations in the flame initiation period are likely caused by LFS changes.

5. A real-time control system capable of avoiding all non-normal cycles can substantially reduce IMEP fluctuations (improve engine stability); and consequently improve thermal efficiency, unburned hydrocarbon and NO_x emissions, and engine safety.

References

[1] J. A. Caton, "The Thermodynamic Characteristics of High Efficiency, Internal-Combustion Engines," *Energy Conversion and Management,* vol. 58, pp. 84-93, 2012.

[2] G. A. Lavoie, E. Ortiz-Soto, A. Babajimopoulos, J. B. Martz and D. N. Assanis, "Thermodynamic Sweet Spot for High-Efficiency, Dilute, Boosted Gasoline Engines," *International Journal of Engine Research,* pp. 260-278, 2013.

[3] T. Alger, J. R. C. Gingrich and B. Mangold, "Cooled Exhaust-Gas Recirculation for Fuel Economy and Emissions Improvement in Gasoline Engines," *International Journal of Engine Research,* pp. 252-264, 2011.

[4] B. Maldonado, A. Stefanopoulou, R. Scarcelli and S. Som, "Charactersitics of Cycle-to-Cycle Combustion Variability at Partial-Burn Limited and Misfire Limited Spark Timing Under Highly Diluted Conditions," in *AMSE ICEF Technical Conference*, Chicago, 2019.

[5] J. B. Heywood and E. Sher, The Two-Stroke Cycle Engine, Philadelphia: Taylor and Francis, 1999.

[6] J. Cha, J. Kwon, Y. Cho and S. Park, "The Effect of Exhaust Gas Recirculation (EGR) on Combustion Stability, Engine Performance and Exhaust Emissions in a Gasoline Engine," *KSME International Journal,* pp. 1442-1450, 2001.

[7] J. B. Heywood, Internal Combustion Engine Fundamentals, New York: McGraw-Hill, 1988.

[8] F. A. Ayala and J. B. Heywood., "Lean SI Engines: The Role of Combustion Variability in Defining Lean Limits," *SAE Technical Paper,* no. 2007-24-0030, 2007.

[9] N. C. Blizard and J. C. Keck., "Experimental and Theoretical Investigation of Turbulent Burning Model for Internal Combustion Engines," *SAE Transactions,* no. 740191, pp. 846-864, 1974.

[10] A. A. Quader, "What Lmits Lean Operation in Spark Ignition Egines—Flame Initiation or Propagation?," *SAE Transactions,* no. 760760, pp. 2374-2387, 1976.

[11] T. D. Fansler, D. T. French and M. C. Drake, "Individual-Cycle Measurements of Exhaust-Hydrocarbon Mass from a Direct-Injection Two-Stroke Engine," *SAE Transactions,* no. 980758, pp. 946-966, 1998.

[12] Ž. Ivanič, F. Ayala, J. Goldwitz and J. B. Heywood., "Effects of Hydrogen Enhancement on Efficiency and NOx Emissions of Lean and EGR-Diluted Mixtures in a SI Engine," *SAE Transactions,* no. 2005-01-0253, pp. 138-149, 2005.

[13] T. Linker and T. J. Jacobs, "Variable Fuel Effects on Legacy Compressor Engines, Phase V - Engine Control Enhancement," Pipeline Research Council International, 2020.

[14] B. Maldonado and A. Stefanopoulou, "Linear Stochastic Modeling and Control of Diluted Combustion for SI Engines," *IFAC Proceedings,* vol. 51, pp. 99-104, 2018.

[15] B. Kaul, R. Wagner and J. Green., "Analysis of Cyclic Variability of Heat Release for High-EGR GDI Engine Operation with Observations on Implications for Effective Control," *SAE International Journal of Engines,* pp. 132-141, 2013.

[16] D. B. Olsen, J. L. Adair and B. D. Willson., "Precombustion Chamber Design and Performance Studies for a Large Bore Natural Gas Engine," in *ASME ICES Technical Conference*, Chicago, 2005.

[17] A. U. Bajwa, M. Patterson, T. Linker and T. J. Jacobs, "A New Single-Zone Multi-Stage Scavenging Model for Real-Time Emissions Control in Two-Stroke Engines," in *ASME ICEF Technical Conference* , Chicago, 2019.

[18] A. U. Bajwa, A. Mashayekh, M. Patterson and T. Jacobs, "Interactions among 3D, 1D and 0D Models for Natural Gas Fueled Two-Stroke SI Engines," in *THIESEL*, Valencia, 2018.

[19] G. Beshouri and B. Goffin, "Starting Damage on Legacy Pipeline Engines," Pipeline Research Council International , 2018.

[20] M. Dettwyler and G. Beshouri, "Analysis of Large Bore Gas Engine Instability by the Use of Pressure Sensors in the Cylinder and Manifold," in *Gas Machinery Conference*, 2007.

[21] M. Huschenbett, M. Brunner, G. Beshouri and M. Dettwyler, "Analysis and Application of Advanced Balancing Techniques to PCC Fitted Pipeline Engines," in *Gas Machinery Conference*, Albuquerque, 2008.

[22] B. J. Tobis, R. Meyer, J. Yang, D. D. Brehob and R. W. Anderson, "Scavenging of a Firing Two-Stroke Spark-Ignition Engine," *SAE Transactions,* no. 940393, pp. 535-546, 1994.

[23] H. Z. Foudray and J. B. Ghandhi., "Scavenging Measurements in a Direct-Injection Two-Stroke Engine," *SAE Transactions,* no. 20034381, pp. 2195-2204, 2003.

[24] M. Nuti and L. Martorano., "Short-Circuit Ratio Evaluation in the Scavenging of Two-Stroke SI Engines," *SAE Technical Paper,* no. 850177, 1985.

[25] J. Hedrick and T. Jacobs, "Variable Natural Gas Composition Effects in LB 2S Compressor Engines Phase 1- Engine Response Final Report," Pipeline Research Council International, 2015.

[26] K. Fieseler, "Simulation Development of a Large Bore Two Stroke Integral Compressor Engine to Study Variable Natural Gas Composition Effects," Texas A&M University (MS Thesis), College Station, 2018.

[27] D. Healy, C. A. Kalitan, E. Petersen, G. Bourque and H. Curran, "Oxidation of C1 - C5 Quinternary Natural Gas Mixtures at High Pressures," *Energy & Fuels,* vol. 24, pp. 1521-1528, 2010.

[28] K. Fieseler, T. Linker, M. Patterson, D. Rem and T. J. Jacobs, "Estimating Laminar Flame Speed and Ignition Delay for a Series of Natural Gas Mixtures at IC Engine-Relevant Conditions," *ASME Journal of Energy Resources Technology,* vol. 142, no. 6, pp. 1-8, 2019.

Appendix: Return Maps
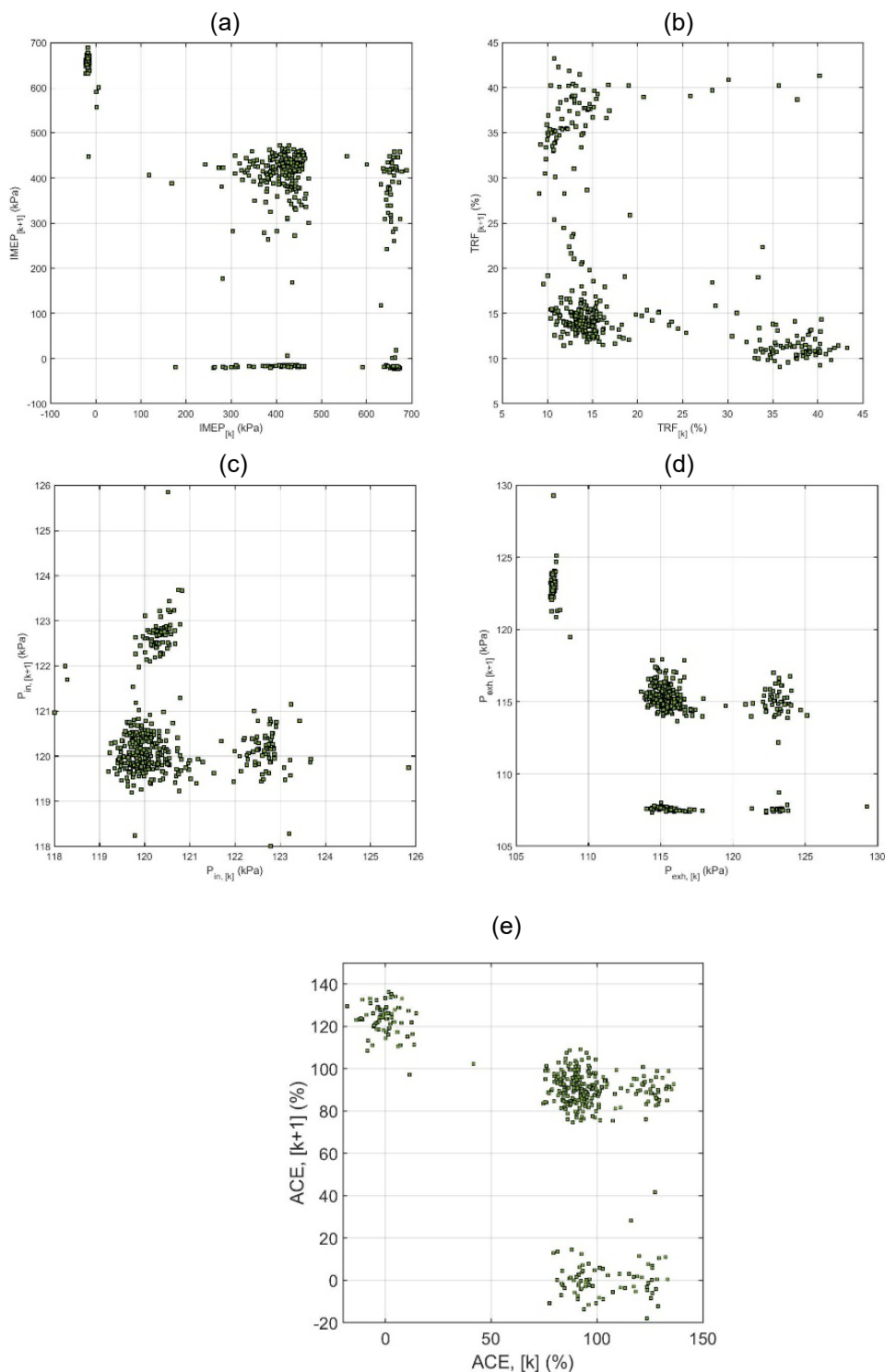
Return maps showing performance of a cycle vs. the previous cycle for (a) IMEP, (b) trapped residual fraction, (c) exhaust pressure, (d) intake pressure, and (e) apparent combustion efficiency (accumulated heat release normalized by the energy content of the delivered fuel, assuming constant fuel mass for all cycles)

Advanced Measurement Techniques for the Characterization of GDI Injector Tip Wetting and a Phenomenological Model of the Wetting Process

G. Dober, K. Karimi, B. Lemaitre, C. Majerus and N. Guerrassi

Delphi Technologies – Bascharage, Luxembourg

E-mail: gavin.dober@delphi.com
Telephone: +(352) 5018 7005

Abstract. Gasoline Direct Injection (GDi) fuel injectors are subject to tip wetting during the injection event. This wetting is a contributing factor towards tip deposit formation which can have a negative impact on engine performance. Deposits can modify the nozzle hole geometry which can alter the fuel flow rate, spray formation and generate controllability issues. Deposits can also lead to a diffusion flame after the main combustion event which significantly increases engine-out particulate emissions. To date, methods to characterize injector tip wetting have been largely qualitative and limited to the surface of the nozzle tip.

A new quantitative technique for the assessment of injector tip wetting is proposed using a Tip Residual Fuel (TRF) measurement device. The main principle of the TRF is to pass heated air over the injector tip, which evaporates the fuel present and then measure the concentration of the evaporated fuel using a flame ionization detector. The technique is highly sensitive and reliable. It can measure at tip temperatures of up to 120°C and is able to characterize both clean and dirty injector tips. The test and post-processing methods to measure tip leakage, the amount of sac residuals and to discriminate the surface wetting that occurs during injection from that occurring at the end of injection are described.

The TRF measurements are compared with an advanced optical measurement technique for tip wetting. The technique uses Laser Induced Fluorescence (LIF) with Ethanol as the working fuel, and Rhodamine 6G as a tracer to isolate the liquid wetting alone. High speed microscopic visualization of the wetting, both during and after the injection event is then made. The results allow for the identification of several key mechanisms involved in tip wetting.

These measurement techniques are applied to a number of GDi nozzle tips with different geometries. The results have then been used to build a basic model of the main phenomena involved in the tip wetting process for typical GDi nozzles with stepped holes (flow holes and counterbores).

Notation

CB	Counterbore
d	Nozzle exit diameter.
D_{10}	Arithmetic mean diameter of droplets.
E10	Euro6 E10 gasoline fuel
EOI	End of Injection
FID	Flame Ionisation Detector
FSOF	First Sight of Fuel
GDi	Gasoline Direction Injection
HC	Hydrocarbon
IMEP	Indicated Mean Effective Pressure
l/d	length/diameter ratio of the injector holes
LIF	Laser Induced Fluorescence
TRF	Tip Residual Fuel (Measurement Device)

1. Introduction

1.1. Background

Gasoline Direct Injection (GDi) fuel injectors are subject to tip wetting during the injection event. Depending on the injection strategy, the engine operating condition and a number of other factors, the liquid may partially or fully evaporate prior to the combustion event. If liquid fuel remains on the tip during the combustion event, then deposits can form on the tip, and a diffusion flame can be generated after the main combustion event in the vicinity of the nozzle tip (*Fig.* **1**). This diffusion flame contributes to a large increase in particulate mass and number from the engine [1, 2]. The formation of deposits can also have several other negative effects. It can modify the nozzle hole geometry which can change the injector static flow rate, the spray shape and generate combustion controllability issues [3]. Furthermore, the amount of deposits can be correlated with the size of the diffusion flame after the main combustion event which also correlates with the level of engine-out particulate emissions [1].
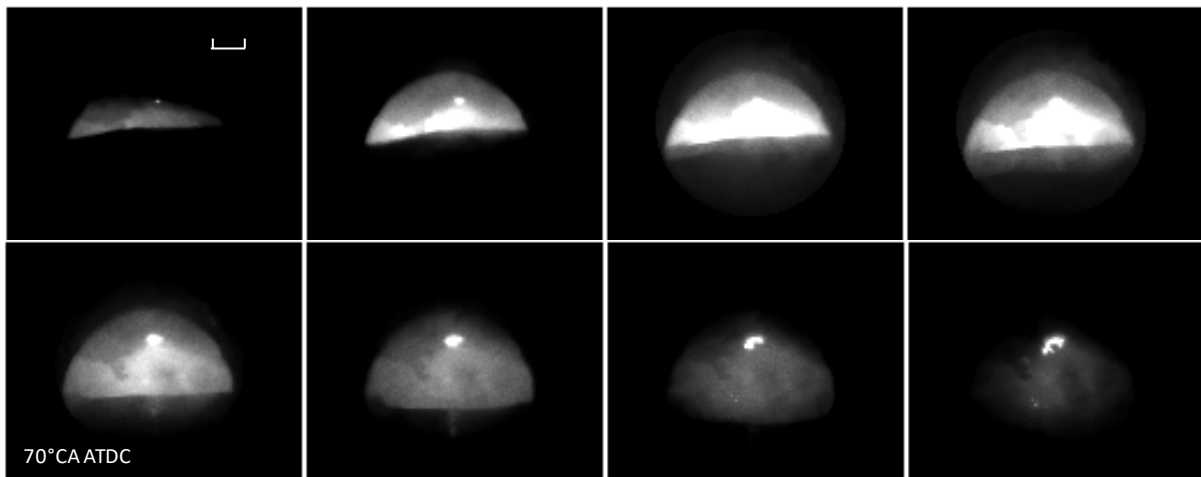
Fig. 1: Image sequence through a combustion event in a GDi engine at 2500rpm, 7bar IMEP. The main combustion event is initially visible, but then a diffusion flame is seen near the injector nozzle tip as the fuel stored on the tip is entrained into the hot burnt gases after the main combustion event

Consequently, it is desired to reduce the injector tip wetting in order to control the aforementioned problems. The design of the injector hole geometry is an important area of study for fuel injection equipment manufacturers in order to control tip wetting and hence engine out emissions over lifetime (**Fig. 2**). To date, significant uncertainties exist regarding key phenomena involved in injector tip wetting. Furthermore the experimental methods and data for the study of injector tip wetting are limited. Most studies have been phenomenological and have not been able to cover the full range of temperatures or pressure conditions that are experienced in the engine by working injectors.
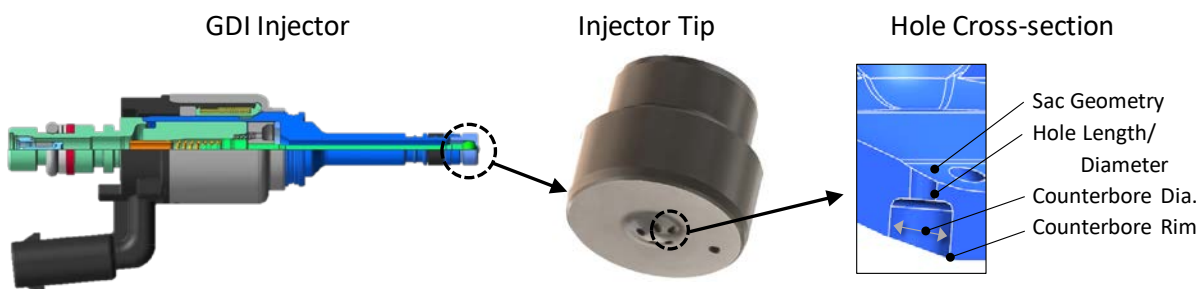
Fig. 2: Geometry of GDi Injector, Tip and Hole

1.2. Existing Techniques for the characterization of injection Tip Wetting

Within the application of GDi internal combustion engines, wetting investigations were historically focused on generic surface wetting with a view to understanding wetting and drying occurring through-

out the combustion chamber, for example on piston or valve surfaces. These techniques have used Laser Induced Fluoresence (LIF) either directly of Gasoline type fuels, or with tracers added [4, 5, 6]. The techniques can be calibrated to get a good understanding of both the wetted area and thickness of the fuel film. Together this information can be used to estimate the quantity of fuel on the surface and the rate at which it evaporates.

It is also possible to observe wetting without Fluorescence, using the different reflective properties of a curved fuel film on a wetted surface. However, the fuel film usually, rapidly becomes smooth and optically transparent as it spreads on the surface. An example of this type of test, using high speed photography may be seen in *Fig.* **3**. This test typically shows that the injector tip is dry during injection, but at the end of injection, the tip becomes wet due to the action of the final injected fuel. The flow phenomena at the end of injection can also be captured showing how the fully developed spray breaks down into ligaments and droplets. In this example, the spray degenerates into either a single solid ligament, or a liquid sheet (70µs EOI) flowing along the counterbore surface driven by the vorticity of the flow inside the spray hole [7]. Surface tension effects are relatively large and important at the end of the injection event when the spray momentum is low and are able to redirect the final ligaments onto the surface of the injector. While this phenomena is interesting, the performance of the injector under these cold atmospheric conditions is not representative of the wetting performance in the engine. The tip and fuel temperature and the gas density have a significant impact on both the fuel properties and the spray formation, and hence lead to a very different wetting process under realistic engine conditions.
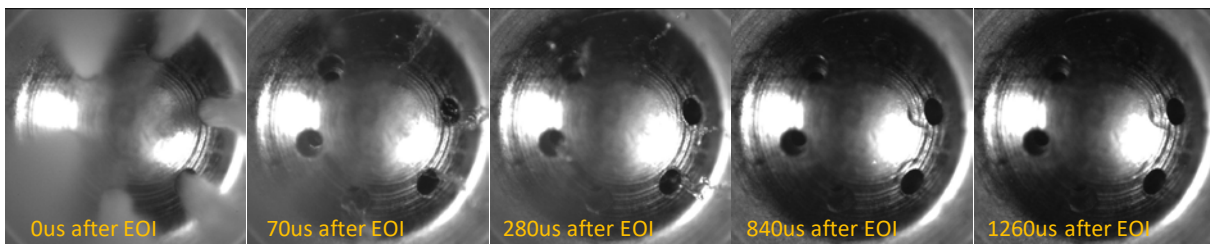
Fig. 3: Image sequence at the end of injection using high speed optical visualization of tip wetting on an atmospheric temperature/pressure chamber, 100bar, Illumination by Flash-lamp.

The LIF wetting measurements have recently been extended to investigate injector tip wetting with the aid of long distance microscopy [5, 8]. However, due to the complex shape of the injector nozzle tip, it becomes more difficult to accurately calibrate this type of measurement to estimate the quantity of fuel. Nevertheless, it has been possible to estimate the wetted area on the nozzle tip surface, at least the part which is visible to interrogation (excluding the sac, the holes and much of the hole counter-bores). Such techniques, while not addressing all questions are still useful for the purposes of injector nozzle tip development.

To date, most efforts to characterize injector tip wetting have been phenomenological or at best semi-quantitative. This paper attempts to address these shortcomings with a new quantitative measurement technique for tip wetting. In conjunction, to simultaneously observe and understand the wetting phenomena, an experiment was also developed, using LIF with a tracer and high speed microscopic photography of the injector tip. The experiment was designed to give a clear view of the phenomena of wetting, both during the injection event and after the end of the injection event. The two techniques are complementary and together provide the information necessary to guide nozzle geometry optimisation for low tip wetting.

1.3. Paper overview

This paper is structured in the following way. After the introduction, detailed descriptions of the quantitative measurement technique and then of qualitative technique are presented covering both the equipment design and the test methodology. Next, results from the two techniques are presented showing the impact on tip wetting of temperature and fuels, injector tip deposits and finally nozzle geometry. The paper is then concluded with the development of a phenomenological model of tip wetting which helps to understand the link between the control parameters and the observed wetting.

2. Experimental Apparatus : TRF

2.1. Objectives of the design

The design objective for the Tip Residual Fuel (TRF) test equipment is to quantitatively assess the amount of injector tip wetting after the end of an injection event. Given the evidence in the literature [9] of the influence of temperature and flash boiling on the wetting process, the device needs to be capable to assess the impact of fuel temperature. For simplicity a variation in the gas back-pressure was not considered. The rig was designed to accept all fuel types, at injection pressures of up to 350bar. This criteria was very important as generally optical techniques are limited to specific test fuels with particular optical properties. Given the rapid evaporation of the fuel at high temperatures, it is necessary to make the wetting assessment of the injector as soon as possible after the injection event, but still after all the droplets and ligaments have exited the nozzle and cleared the vicinity of the injector tip. Visualisation of the end of injection event shows that this process is variable and most sensitive to tip & fuel temperature with faster clearing of the tip at higher temperatures. Regardless of the condition, the injector tip region is typically clear of free droplets after ~2ms.

2.2. Design

The main principle of the TRF is to pass heated air over the injector tip, which evaporates the fuel present and then measure the concentration of the evaporated fuel using a flame ionization detector (FID). Such measurement techniques are already used for the characterisation of tip leakage [10], but to the knowledge of the authors have not yet been used for an investigation of injector tip wetting during an injection event. The evaporated fuel is sampled only after the end of injection using a high speed probe which is rapidly inserted under the injector tip. The probe takes approximately 20ms to travel to a position where it can begin to sample hydrocarbons (HC's) from under the injector tip. Close control is taken of the flow of air to evaporate the HC from the tip. Three separate gas flows are controlled around the tip to ensure that all the fuel evaporating from the tip, and none of the injected fuel is sampled by the FID.

The injector is mounted into a heated block which is temperature controlled. Due to long residence times of the fuel in the injector, prior to injection, it may be assumed that the metal of the injector tip and the fuel temperature reach an equal pre-determined value. A thermocouple is used to measure the injector nozzle body external surface temperature. This temperature was correlated against the injector tip temperature measured using a specific injector with a thermocouple embedded into the metal of the injector tip.

Fuel pressure is supplied using a piston based pressure amplifier which is fed by standard compressed air and a regulator. This solution provides a pressurization system which is not dependent on the fuel properties, ie. compressibility, lubricity etc. Thus allowing virtually all test fuels to be considered.

Automatic electronic control is implemented for the injection timing, duration and number and the probe movement. These can be combined into test sequences, which also consider purging of the injection system and settling time for the thermal management of the test apparatus.

2.3. Design Details

The main details of the TRF design are illustrated in **Fig. 4**. The injector is mounted vertically in the green heated block. The injector sprays into the purple exhaust funnel and immediately after the end of the injection event, the probe is moved into place underneath the nozzle tip. While the probe is in place, the fuel on the tip is evaporated and the concentration of HC is measured using a flame ionisation detector. Three air flow streams are managed in order to control and separate the HC source from the wet tip from the injected fuel. A sampling air flow is directed into the gap between the injector nozzle and the heated block. This air flows over the nozzle tip and is then completely captured by the sampling tube when sampling is taking place. In a ring around the sampling flow, an air curtain is provided whose purpose is to prevent a recirculation of droplets and spray into the vicinity of the tip during the injection events. This also provides sufficient extra clean air flow to make up the required sampling gas flow. Finally, additional air is drawn from the test room into the TRF device via the gap between the heated block and the exhaust funnel. This flow is managed by generating a depression on

the exhaust funnel and ensures that no HC's escape into the test room, and that all HC measurements are sourced directly from the tip wetting.
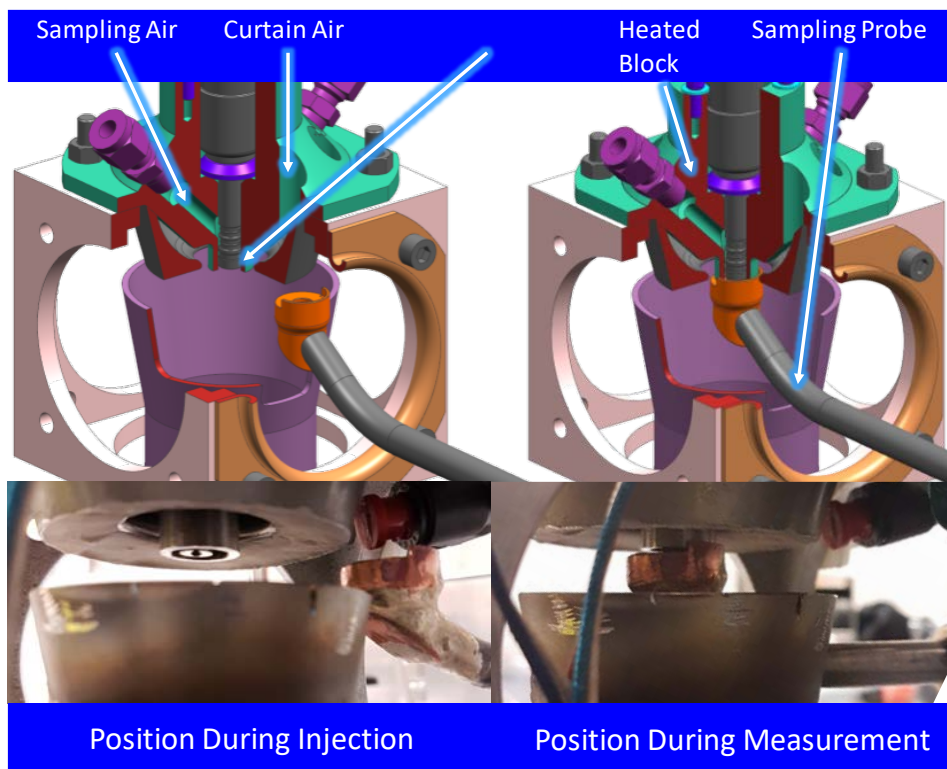
Fig. 4: Model of the TRF device showing the probe position during the injection event (left) and during the tip wetting sampling measurement (right).

As the residual fuel is subject to evaporation after the end of the injection event, the measurement probe must be moved as quickly as possible under the tip. The actuator to move the probe is capable of a maximum speed of approximately 0.6m/s. Given that the probe must be 10mm away from the spray during the injection event, it takes ~20ms to move the probe under the nozzle tip and to begin to collect the evaporating fuel. A sequence of images of the injection event and sample probe movement may be seen in **Fig. 5**.
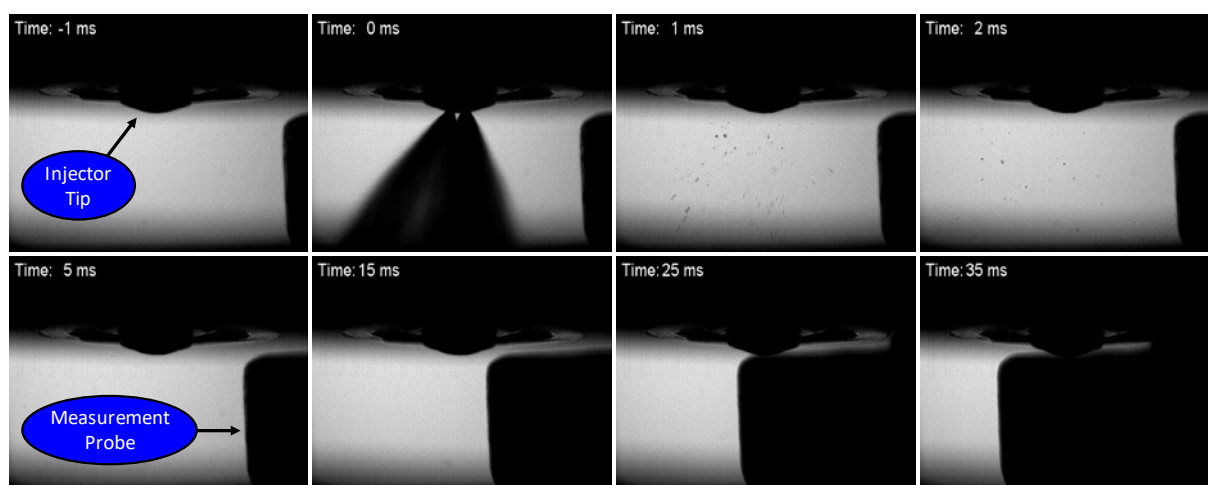
Fig. 5: Image sequence throughout a measurement, showing the injection and the movement of the probe under the nozzle tip after the end of injection

It is noted that because of the time delay to insert the probe underneath the nozzle tip after the end of injection, some of the fuel on the surface will have evaporated prior to the tip wetting measure-

ment beginning (**Fig. 6**). The proportion of fuel which is lost varies according to the temperature of the tip and the fuel properties. Consequently this technique does not give the exact wetted quantity at the end of the injection event, but measures the amount of wetting at ~20ms after the end of injection. Nevertheless, providing the methodology for measurement is kept consistent then all parts are impacted by this post injection drying in the same way and the technique is still useful to compare different nozzle designs.
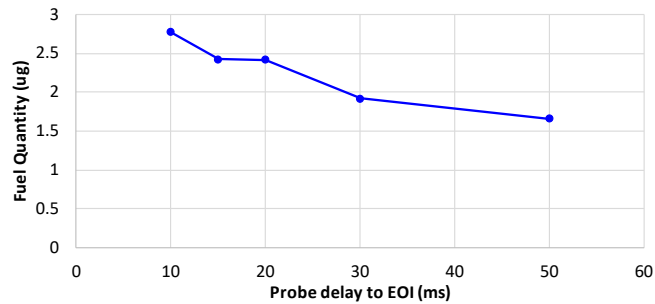
Fig. 6: Influence of probe delay time on the measured fuel quantity (90°C, Nheptane)

2.4. Test and Processing Methodology

The basic test methodology is illustrated graphically in **Fig. 7** and may be described by the following steps:

1. Wait for the tip to be completely dry (>120seconds from previous injections);
2. Insert sampling probe
3. Measure HC concentration of "dry tip" (reference sample for 6seconds);
4. Remove probe;
5. Make injections;
6. Re-insert probe;
7. Measure HC concentration of "wet tip" (measurement for 120seconds)
8. Remove probe

The integral of the signal after the injection event (**Fig. 7** - green) gives the mass of fuel remaining on the tip and in the sac. As tip leakage (**Fig. 7** - orange) can also contribute to the signal received it must be removed from this signal. It is noted that the example given has a relatively high tip leakage, and the majority of normally functioning nozzles have leakage rates less than 10% of that shown. The initial sample taken before the injection event allows a reference value for the leakage to be gathered. This may be compared to the signal value at the end of the main measurement (~120s) after the end of the injection event when all fuel on the tip should have been evaporated. It is noted that the leakage can add significant noise to the measurement of tip wetting. Ideally parts with low leakage should be used for wetting measurements, but where this is not possible, it is also useful to minimise the period over which the tip wetting signal is integrated.
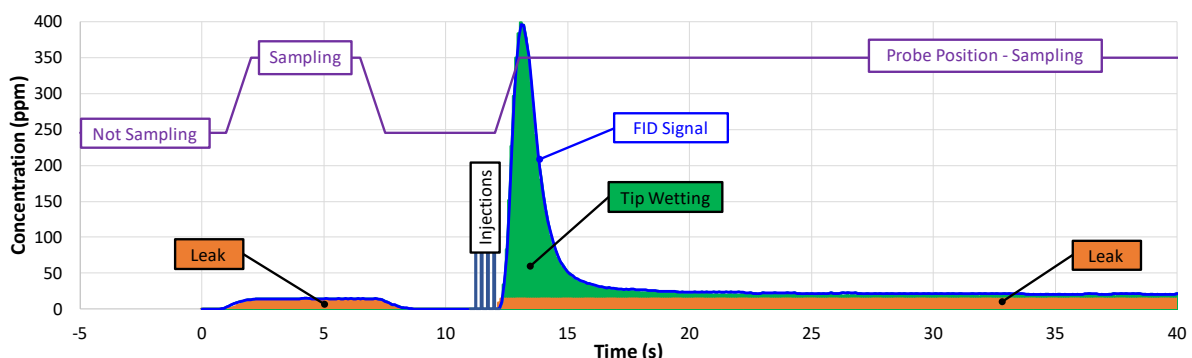
Fig. 7: Basic test sequence showing the timing of the sampling probe movement, the injections and the test signal generated by the FID. 4injections, Fuel pressure: 100bar, Tip temperature: 60°C

The required integration period is dependent on the time to evaporate the fuel on the tip which is dependent on temperature, fuel composition and nozzle geometry. It is noted that the process re-

quiring the most time for evaporation is for the fuel remaining within the nozzle sac, as it is not directly exposed to the drying air-flow. However as the purpose of the rig is to test a variety of different geometries it is not convenient to set the test methodology dependent on the nozzle geometry. Instead, a reference geometry with negligible leakage was selected to measure the evaporation time and a margin chosen to account for geometric differences between nozzles. As may be expected, higher nozzle temperatures lead to more rapid evaporation rates. An example of the impact of temperature on the evaporation time for E10 Gasoline is given in *Fig.* **8**. On the left, the FID signal may be observed. On the right, the time at which the smoothed signal returns to the background level +1ppm. The actual chosen integration window was set at two times the reference value, to account for tip geometry differences.
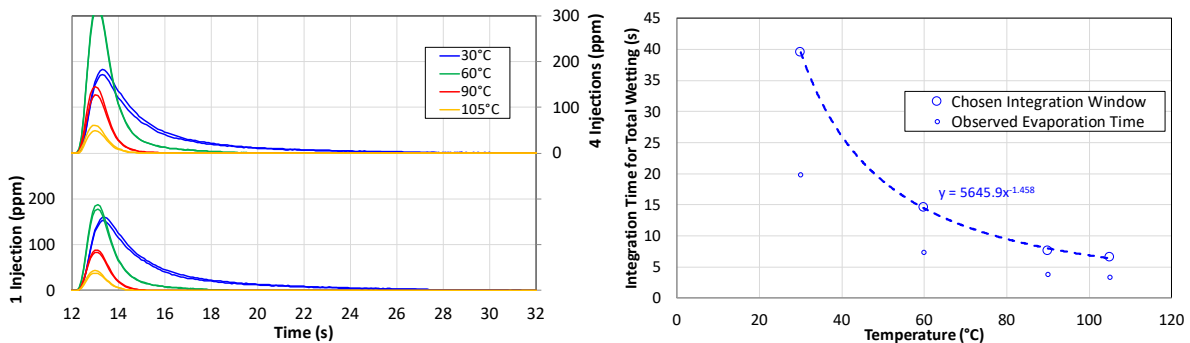
Fig. 8: Impact of tip temperature on evaporation time with E10 fuel. FID signal with 1 and 4 injections (left); Observed evaporation time compared plotted against temperature (right)

In order to understand the different sources of wetting on the tip, two different test sequences were developed. A pulse number variation test, and a pulse duration variation test. The pulse number variation test makes a different number of 1ms injections at 200Hz. This injection frequency was chosen to minimize the time between injection events but nevertheless keep the injections far enough separated, that hydraulic or electrical interactions between injection events are small. Example results for this test are given in **Fig. 9**. The number of injection used were chosen as: 1, 2, 4, 6 and 8. This pattern repeats 3 times over the complete test. For each injection train, the signal is integrated to calculate the wetted quantity. The results are plotted in **Fig. 9** on the right, and a line of best fit is plotted through the measurement points. Assuming that the amount of fuel remaining in the sac at the end of all of the injection events is independent of the number of injections, but the amount of fuel on the surface is dependent, then the y-intercept of this curve can be interpreted to measure the sac residual fuel quantity. The gradient of the curve will also indicate the injector tip external surface wetting from each injection event. The curvature observed in the line is a result of the increase in the time for evaporation of the first injection events compared to the last injection events. Consequently the calculation of the gradient of the curve to estimate wetting per injection is calculated at the position of 1 injection event where evaporation has had the least impact.
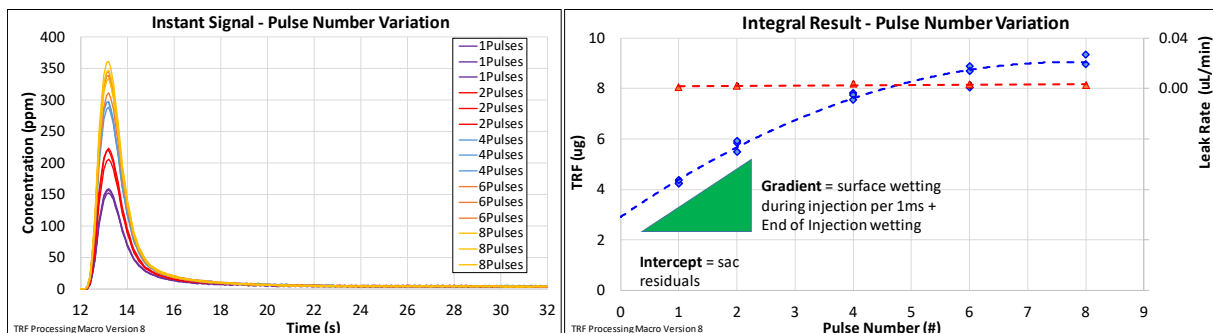
Fig. 9: Pulse number variation test. Fuel Pressure: 100bar, Tip temperature: 60°C. Instantaneous FID signal (left); Integral results (right)

In order to differentiate between wetting during injection and at the end of injection, a second test varying the pulse duration of a single injection event is made and shown in **Fig. 10**. The tested pulse durations were: 0.6ms, 1.0ms, 2.0ms, 3.0ms and 4.0ms. As before, this pattern of tests was repeated 3 times, each signal integrated to calculate the wetted fuel quantity and a fitted line drawn

through the measurement points. The y-intercept now represents the sac residuals + an end of injection quantity, and the gradient represents the wetting during injection per ms of injection. A comparison of the results from both tests allows quantitative measurements of the sac residual fuel mass, the fuel mass added to the surface during injection, and the fuel mass added to the surface at the end of injection. As with the pulse number test, a small amount of curvature is evident in the fitted line. Again, this effect is due to increased evaporation time before measurement with longer injection durations. However, as the time difference is smaller, the effect is also smaller, and a linear curve is fitted to the data, in order to avoid overfitting the data when tip wetting during injection is small. The main test conditions used for data presented within this paper are summarised within Table 1.
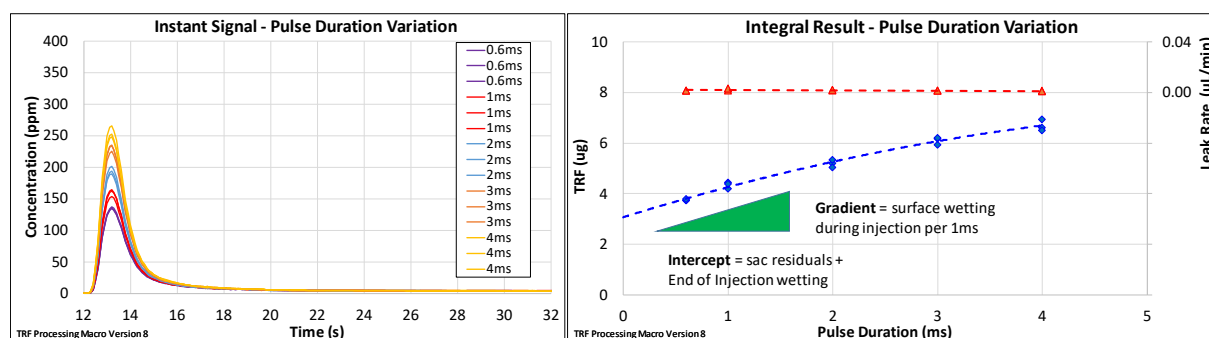
Fig. 10: Pulse duration variation test. Fuel pressure: 100bar, Tip temperature: 60°C.
Instantaneous FID signal (left); Integral results (right)

Table 1: List of TRF test conditions used for data presented in this paper

Test Condition	Value
Test Sequences	Injection number variation, Injection duration variation
Tip Temperature	30→105°C (60°C typical)
Injection pressure	100bar
Fuels	N-heptane, E10 Gasoline
Injection Frequency	200Hz
Probe travel time	20ms
FID sampling duration	10→120seconds (calibrated function of fuel and temperature)

2.5. Calibration, Measurement Repeatability & Accuracy

The device is calibrated for each fuel type using a micro-pipette to inject a known quantity of fuel directly into the FID measurement tube. The signal recorded on the FID is then integrated in the same way as the normal measurement signal in order to estimate a calibration value in ug/(sec*ppm). The FID is calibrated daily with span and zero reference gases to ensure its sensitivity does not drift.

During the device development, a significant effort was made to ensure good stability and consistency between measurements. It was found to be very important to ensure an accurate and stable control over the air flow rates, air pressures and purity of the 3 different air streams (sample, curtain and purge). Consequently the measurements are highly repeatable and very sensitive. It may be observed during an automated test measurement (**Fig. 9**), when each test condition is repeated 3 times, the measurement profiles are very similar.

To better quantify the accuracy of the measurement technique including the post-processing method, several clean parts were measured and fully analysed multiple times. These parts had various different nozzle tip geometries, but were all multi-hole GDi injectors with counterbores. They represented a range of performances, in both leak, sac and surface wetting. Between each of the measurements, the parts were disassembled from the device at least once, and tests were run over at least 2 days. The number of measurements, the average results and the standard deviation of those results was calculated for each of the parts, and are presented in Table 2.

From this data it may be observed that the standard deviation of the measurements for tip wetting are approximately 0.2µg. This standard deviation includes both the performance variation of the

actual part, as well as the accuracy of the measurement technique itself. As may be expected the size of the variation is greater when the amount of wetting is larger which is likely to be because of an increase in the part performance variability.

Table 2: Average and standard deviation over multiple tests for 6 parts using the pulse duration and pulse number tests to calculate: leakage, sac residuals and wetting both during and at the end of injection. Tip temperature: 60°C, E10 fuel.

	PART A			PART B			PART C			PART D			PART E			PART F			AVERAGE		
	#	Avg	Stdev	#	Avg	Stdev	#	Avg	Stdev	#	Avg	Stdev	#	Avg	Stdev	#	Avg	Stdev	Avg	Stdev	S/N Ratio
Leakage (uL/min)	6	0.0046	0.0020	4	0.0126	0.0015	5	0.0023	0.0026	6	0.0157	0.0029	4	0.001	0.0004	4	0.0502	0.0106	0.0123	0.0033	3.7
Sac & Hole Residuals (ug)	6	4.402	0.389	4	2.842	0.486	5	2.890	0.114	6	4.654	0.188	4	2.977	0.034	4	3.789	0.186	3.079	0.233	13.2
Surface Wetting during injection (ug/ms)	6	0.313	0.084	4	0.916	0.077	5	0.700	0.116	6	0.110	0.173	4	0.292	0.109	4	0.933	0.274	0.466	0.139	3.4
Surface Wetting at EOI (ug/inj)	6	0.273	0.128	4	0.555	0.136	5	0.205	0.200	6	0.465	0.189	4	0.089	0.071	4	1.709	0.241	0.471	0.161	2.9

The leakage measurements may also be observed to have a standard deviation of around 0.003µL/min compared to an average signal of 0.01µL/min, showing good sensitivity to very low leakage levels. It is noted that all these parts have low leakage levels. A high leakage typically increases the measurement noise for the other wetting values. For example, the standard deviation of the surface wetting measurements on Part F (with the highest leakage rate), is also the highest. The reason for this effect is the long time scale (120s) of the device measurement event, which is more than 1000 times longer than a typical engine cycle. The consequence is to magnify the signal from the constant leakage of the injector compared to the discrete wetting over a single injection event. So even at relatively modest levels of leakage the tip wetting signal can be swamped.

In summary, these results indicate that the device is capable of measuring tip wetting, and differentiating the type of tip wetting with an accuracy of ~0.2µg.

3. Experimental Apparatus: Optical

3.1. Objectives of the test Design

The purpose of the optical tests was to investigate the main phenomena involved in tip wetting both during and at the end of the injection process. In order to account for the expected strong influence of flash boiling on the wetting process, the test device needed to be capable of varying the fuel temperature over a wide range. The measurement method needed to be particularly sensitive to liquid wetting and insensitive to the presence of fuel vapour. Good microscopic optical visualisation of the injector tip surface was required.

3.2. Experimental Setup

A constant flow spray visualisation chamber was developed which had the possibility of controlling the fuel temperature, air temperature and air pressure. The air velocity in the chamber was kept to a minimum, less than 0.5m/s to avoid any influence on the emerging spray, and consequently, any side force
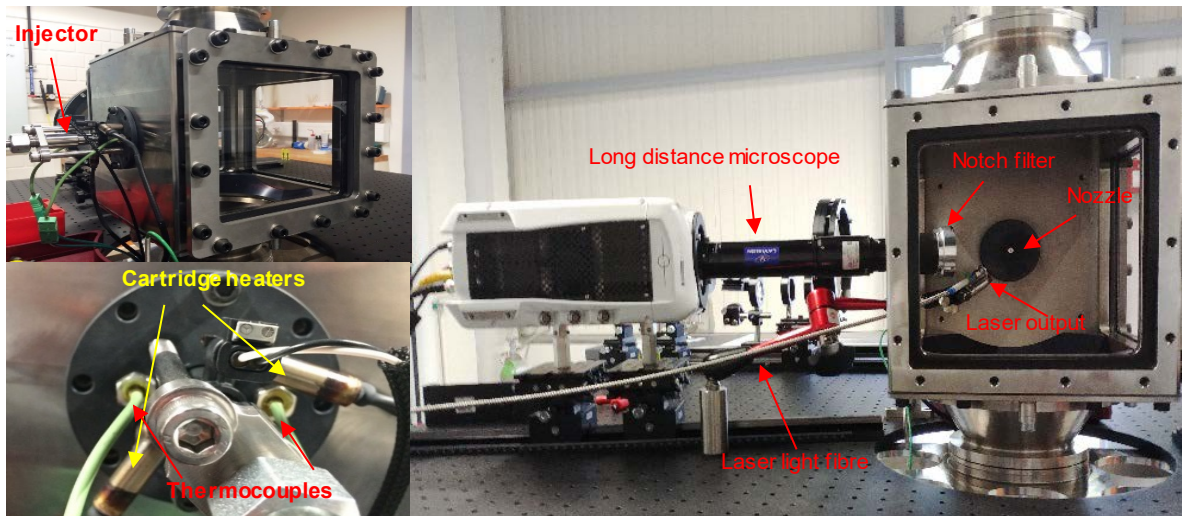
Fig. 11: Gasoline constant flow chamber and nozzle cartridge heater arrangements

or undesired injector tip wetting. For the results presented in this paper the gas pressure and temperature were kept at ambient.

A special injector holder (**Fig. 11**) which also housed two cartridge heaters in addition to two thermocouples was also utilized. The optical setup is also shown in the same figure. A dedicated controller regulated the cartridge heaters output power according to the desired temperature, via two thermocouples. This ensured the desired tip temperature was reached.

The relationship between the injector holder temperature and the injector tip temperature was calibrated using the same thermocouple instrumented GDi injector, as was utilized on the TRF.

With a dedicated injection controller, the working fuel was a mixture of pure Ethanol and Rhodamine *6G* as a Fluorescence tracer at a concentration level of *2g* of Rhodamine to *1L* of Ethanol. The mixture, and thus the emerging spray out of the nozzle, was excited by a Solid State Litron laser at *532nm*.

This choice of fuel and tracer allowed the liquid fuel to be selectively illuminated and allowed excellent contrast and visualisation of surface wetting, both during and at the end of the injection event.

The excited mixture emits with a peak wavelength at circa *552nm* (*Fig.* **12***)*. A Notch filter allowing passage for all wavelengths, but blocking the laser wave length at *532nm* was positioned in front of a long distance microscope, attached to a high speed Phantom *V711* video camera. With the frame rate set to *49kHz,* the corresponding resolution was at *320 x 320 Pixels (Scaling 2.5µm / Pixel)*, the exposure time was set to *2µs,* and the recording time was over *10ms* to ensure, that both the evolution of the tip wetting and the fuel decay and evaporation from the tip were visualised. The Litron laser was synchronised to match the frequency of the camera at *49kHz* and the two were driven externally via a dedicated software. For each experimental condition presented, *10* repetitions were recorded for statistical analysis.
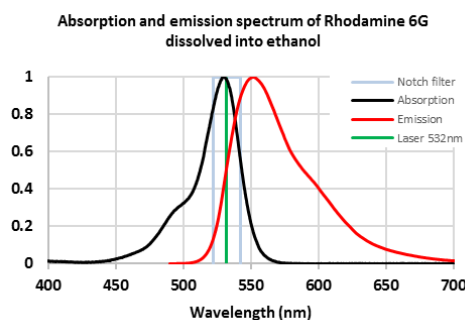
Fig. 12: Absorption and emission spectrum of Rhodamine mix, and the Notch Filter wavelength

3.3. Optical processing

The optical results were post-processed with an inhouse developed software based on MatLab [11]. The processing allowed a characterisation of the evaporation rate of the fuel from the surface of the nozzle after the end of the injection event through a measurement of the wetted surface area. The macro is based, on a binarization of the images with an automatically calculated threshold, using Otsu's method [12]. The images were masked for unwanted areas and a background subtraction was performed. The processing of the results was only applicable to the surface of the nozzle, and did not consider the inside of the injector hole or the counterbore.

4. Temperature & Fuels Sensitivity

Temperature has a significant impact on the tip wetting process due to the flash boiling phenomena. As the temperature of the nozzle increases and the amount of flash boiling increases, the spray opening angle at the nozzle hole exit increases. This trajectory change puts the droplets and ligaments in close proximity to the nozzle tip surface where they contribute to its wetting. The consequence is that experiments performed under cold conditions, frequently show very low amounts of surface wetting and are not indicative of the level of wetting at higher temperatures.

The influence of temperature on tip wetting results is illustrated in Fig. **13** using the visualisation method to identify the liquid fuel on the tip surface at 500µs after the end of injection. An increase in wetting may be observed up to ~90°C, after which the wetting appears to reduce again. This reduction is not due to a loss of the flash boiling phenomena but instead due to very rapid evaporation of any fuel which wets the surface. Another phenomena which may be observed at low temperatures is an increase in the amount and size of the droplets which are visible. This is related to the varying fuel properties such as viscosity and surface tension at low temperatures [13], leading to the formation of larger ligaments and droplets at the end of injection.

| 25°C | 60°C | 90°C | 110°C | 130°C |
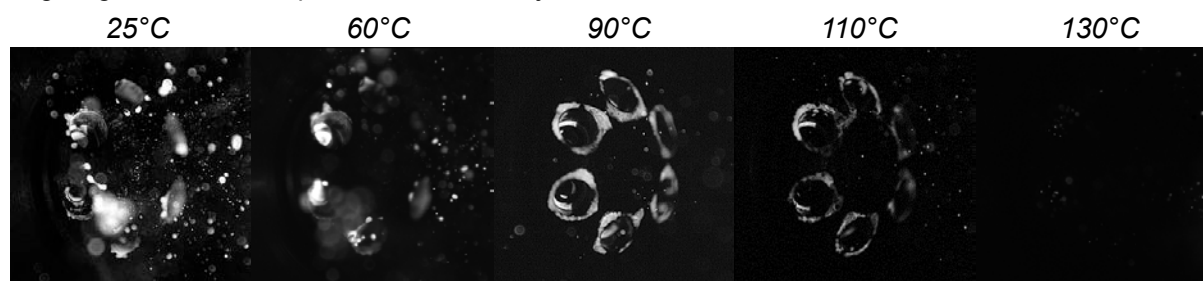
Fig. 13: Illustration of the impact of temperature on tip wetting at 350µs after the end of injection with tracer doped alcohol.

Conducting a similar experiment on the TRF device gives a similar influence of temperature on the wetting quantity (**Fig. 14**), for two different fuels: N-heptane; and E10 gasoline. Both fuels show a peak in the wetting signal at around 60°C, after which the signal strength quickly drops.

The key difference between the optical and the TRF measurement technique is that the optical measurement method is able to visualise the wetting both during and immediately at the end of the injection event, whereas the TRF cannot begin to measure the wet surface until ~20ms after the end of the injection event. Consequently, at high temperatures, surface evaporation is very rapid and may be well progressed before the probe arrives at the nozzle tip. Then the only fuel sampled is from evaporation of any fuel remaining in the sac of the injector tip.

An important benefit in the measurement is achieved by using a multi-component fuel. Such a fuel, has a wider range of temperatures over which flash boiling occurs, and slower evaporation rates for the heaviest components in the fuel. The amount of wetting from N-heptane fuel does not change significantly between 30 and 60°C, (it is simply measured over a shorter time period), and only at 90°C does the tip surface wetting increase due to flash boiling effects. At the same time, the integral of the signal has dropped significantly due to evaporation before sampling making the test condition uninteresting. For the E10 fuel, a significant increase in surface wetting at 60°C is observed together with a significant increase in the integral wetted quantity. Similar to N-heptane, at 90°C the integral tip wetted quantity has reduced significantly making this an impractical temperature at which to assess the wetting performance.
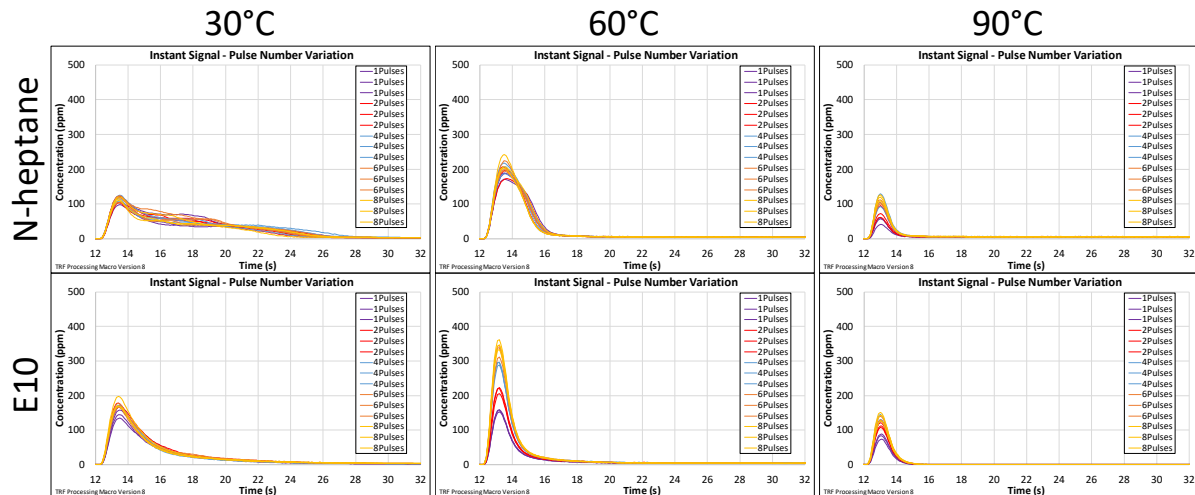
Fig. 14: Influence of fuel type on the measurement signal with respect to temperature.
Multi-component E10 fuel is compared to N-heptane

Even if the real surface wetting from an injection event is at a maximum at ~90°C, it is necessary to assess nozzles at a lower temperature on the TRF, to avoid that all the fuel is evaporated before the probe can be inserted into the measurement position. For the remainder of this paper, all measurements are presented at 60°C.

5. Impact of tip deposits

One of the premises of how injector tip deposits can lead to higher particulate emissions, is that the deposits cause an increase in the injector tip wetting [1], however, little direct evidence actually exists to confirm an increase in wetting with deposits. The TRF measurement method is not impacted by the presence of deposits on the tip surface and consequently has no trouble to measure how they affect injector tip wetting.

In order to investigate the impact of deposits on tip wetting, a nozzle was run on engine at constant speed (2500rpm) and load (7bar IMEP) and deposits were allowed to form. During the engine test the particulate mass emissions increased from <0.05mg/m^3 to ~1.0mg/m^3 or by a factor of 20 over ~8hours of run time. **Fig. 15** illustrates the tip wetting change for the nozzle in the fully coked and the fully cleaned state. An additional measurement was made with the deposits on the outside of the nozzle mechanically removed.

The deposits may be observed to increase both the internally retained sac residual fuel, and the fuel collected on the tip surface. The internal deposits were the dominant factor driving the increase in sac residuals, while the external deposits were the dominant factor driving the increase in wetting during injection. The wetting at the end of injection seemed to be strongly impacted by both internal and external deposits. It can also be seen that the wetting during injection on the clean nozzle is one of the smallest sources of wetting, while on the dirty nozzle it is the largest.
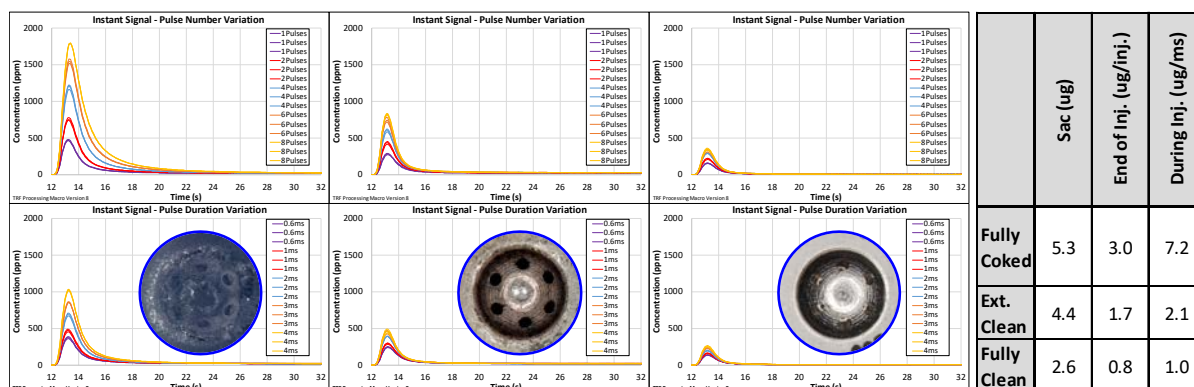
Fig. 15: Impact of injector tip deposits on residual fuel measurements, E10 fuel and tip temperature: 60°C. Pulse Number variation (top), Pulse duration variation (bottom). Table at right shows the calculated residual quantities using the post-processing method described in section 2.4.

6. Nozzle Design Effects

Nozzle geometry also has a strong influence on the injector tip wetting [5]. The internal flow impacts many phenomena leading to wetting, such as the opening angle and the atomisation characteristics of the spray, both during and at the end of the injection event. The main geometric parameters over which the injector designer has control are the size and shape of the sac, the hole l/d and the counter-bore diameter. Other influencing factors such as the spray targeting and nozzle static flow rate may not be freely chosen to minimise wetting but are typically imposed according to the combustion chamber design of the engine in which the injector is to be placed.

Variations in counterbore diameter, sac design and spray targeting are presented here.

6.1. Counterbore Diameter

Counterbore diameter (CB) has been observed to be one of the strongest influencing factors on tip surface wetting. The results for 3 similar nozzles, with the same sac, hole size and targeting, but with different counterbore diameters can be seen in **Fig. 16**. The same nozzles were measured on both the optical bench and on the TRF.

It is noted that small differences in the opening delay between the different injectors/nozzles, and the fact that the image frame timing is synchronised with the injector electrical drive pulse, mean that the initial image at first sight of fuel (FSOF) is taken at slightly different times after the actual start of injection (0→20μs). Due to the rapid movement of the injector needle during this period, a significant impact on the appearance of the spray in this initial image may be observed.

These results show a strong increase in the tip wetting as the CB diameter is increased. It can further be observed that the wetting increase is happening during the injection event, and that the wetting at the end of the injection event is insignificant, except for the smallest CB design.
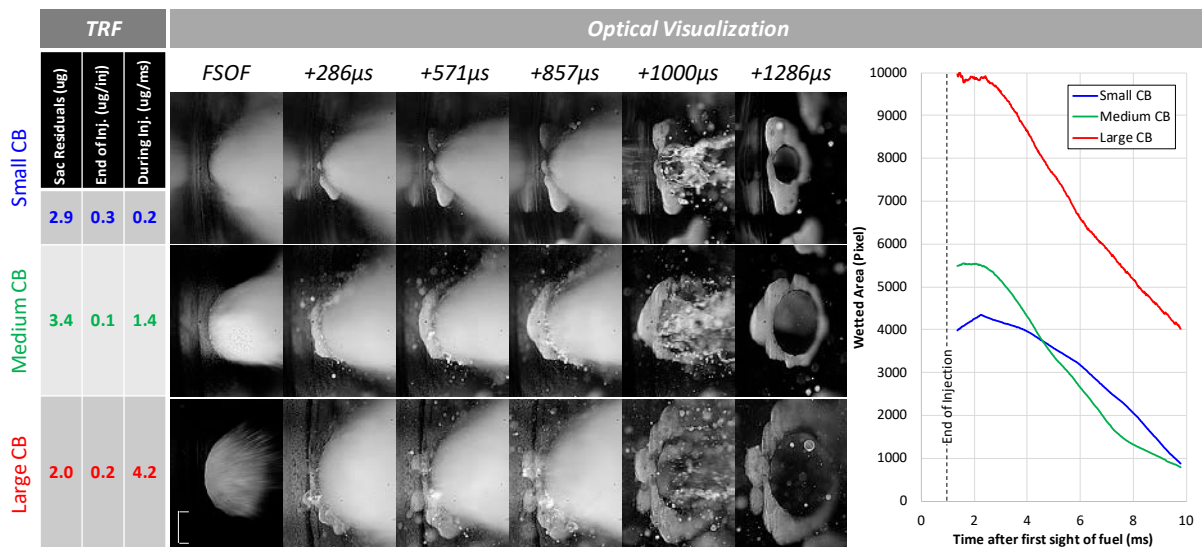
Fig. 16: Influence of CB diameter on tip surface wetting at 100bar for a 1ms injection event. TRF mass measurements (left), Visualisation of wetting through injection (middle), Wetted area after EOI (right)

It is noted that there is a very good correlation of the results between the optical measurements and the TRF measurements. They agree in their conclusion about the magnitude of wetting during and at the end of injection between the parts. It is also interesting to note the variation of the wetted area after the end of the injection event. The trends for the two larger CB's are different to the small CB indicating faster initial evaporation of this fuel film. A potential cause for this difference is the thickness of the film, however it may also be due to the surface film being partially replenished from fuel within the CB after the end of injection.

The sac residuals, which includes flow hole and CB residuals are also observed in the TRF measurements to vary significantly. The maximum sac residuals are actually with the medium CB design. Interestingly the final frame of the optical images also shows the largest amount of liquid within the CB for the medium CB design.

The reason for the increase in wetting with a larger CB, is at least in part due to the fact that the CB rim interface with the spray gets longer as the CB diameter increases. This therefore increases the potential for wetting to occur.

6.2. Sac Design

Sac design is also expected to have a strong influence on wetting, through its influence on the spray characteristics, as well as the volume and emptying characteristics of the sac. The results for 3 nozzles with the same holes and CB's, with two different sacs, one of which has two different depths and therefore volumes can be seen in **Fig. 17**. Sac_A_small is the same nozzle as presented in the previous section. As before, the same nozzles were measured on both the optical bench and on the TRF. These results show some significant differences, in particular in the balance of wetting during injection, at the EOI, and the sac residuals.

Even if the volume of the sac of Sac_B_small is low the sac residuals are relatively high which could indicate that this type of sac design has difficulty to fully empty itself of liquid. Conversely Sac_B_large is a much larger sac, but nevertheless has lower sac residuals. Sac_B_large is also subject to higher EOI wetting. This feature is consistent with the EOI wetting being influenced by the amount of final injected fuel at low velocity. The high EOI wetting with this sac design is also clearly visible within the optical visualisation.
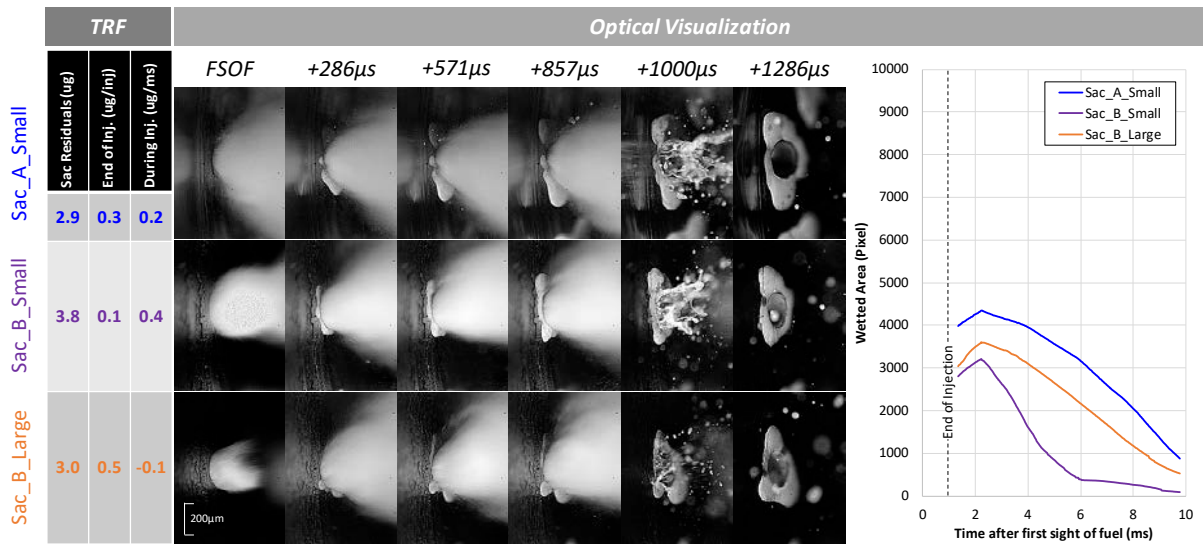
Fig. 17: Influence of sac design and volume on tip surface wetting at 100bar for a 1ms injection event. TRF mass measurements (left), Visualisation of wetting through injection (middle), Wetted area after EOI (right)

6.3. Spray Targeting

Finally, the spray targeting also has a clear influence on the pattern of injector tip wetting. For injectors which have a side mounting position in the engine, the spray pattern is usually very asymmetric. **Fig. 18** presents such a tip, after operation on engine and compares the coking pattern to low temperature
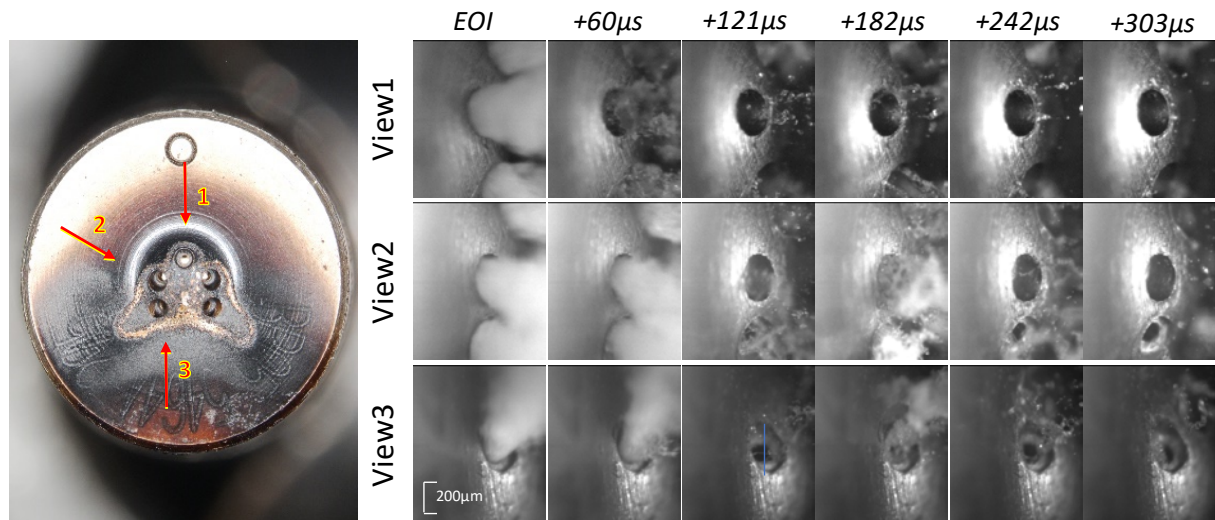
Fig. 18: Illustration of the impact of hole targeting angle on the surface wetting at the end of injection and deposit formation pattern. Hole number 3 makes a narrow angle with the injector tip surface which increases the chance to locally wet the surface

MIE scattering microscopic images of the spray. The coking pattern is indicating a wetted area in the vicinity of the holes, and prevalent to certain holes at the bottom of the image. These holes have spray plumes which have a trajectory which makes a narrow angle with the injector tip surface and puts the spray plume edge in close proximity to that surface. When droplets and ligaments are generated on the periphery of the spray, they then have a strong chance of wetting the surface. This is also true at the end of the injection event, as can be observed in the spray images.

7. Model of Wetting Phenomena

In order to better understand the main phenomena driving tip wetting, a detailed analysis was made of the high speed spray videos. It was possible through this analysis to directly observe several important wetting mechanisms taking place. From these observations a model of the tip wetting is then proposed.

The first point to make is that wetting during injection appears to dominate at typical injector engine operating temperatures. Except for sprays which have a low angle with respect to the tip surface, wetting during injection occurs almost exclusively at the counterbore rim.   Consequently the interaction of the spray and the CB rim is critically important for the wetting process.

As has already been mentioned, temperature has a strong impact on the level of tip surface wetting, but how this effect manifests is a more difficult question. **Fig. 19** illustrates the difference of a small change in temperature (at a temperature where wetting is very sensitive) mid-way through the injection process. We can observe that at higher temperatures:

- the spray is wider at the immediate nozzle hole exit
- the spray surface is less well defined, implying more atomisation and finer droplets
- there are significantly less droplets and ligaments visible
- typically the larger droplets and ligaments which exit the nozzle do so with a trajectory at a narrower angle from the nozzle surface, and can be observed in some instances to wet the surface directly.
- there is more surface wetted area
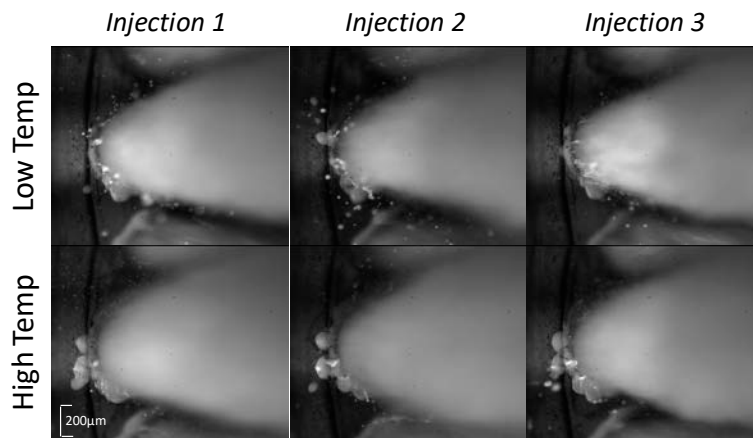
Fig. 19: A view of the spray and surface mid-way through injection for a small change in fuel temperature. A lower temperature leads to less flash boiling, a narrow spray & many ligaments and droplets. A higher temperature gives more flash boiling, a wider spray and higher surface wetting

With less flash boiling, the spray is narrower and the interaction of the spray and the counterbore rim is lower, leading to a gap between the spray and the rim. These gaps are not continuous but fluctuate as the injection progresses. Out of these gaps, low speed droplets and ligaments can exit the CB volume. The droplets and ligaments can even form into a completely separated jet as shown in **Fig. 20**.

The flapping of the jets and separation of the spray with the CB surface was also observed to occur preferentially at certain positions as illustrated in **Fig. 21**. At these positions, depending on the temperature, droplets and ligaments can be generated, or alternatively the surface is directly wet. The preferential location of the flapping and the wetting or ligament generation, implies a link to a minor feature in the hole geometry or a link to the internal flow field in the sac and the hole.   While not directly observed, it is speculated that the flapping could be a result of either partial hydraulic flip or intense localised vorticity within the hole flow.
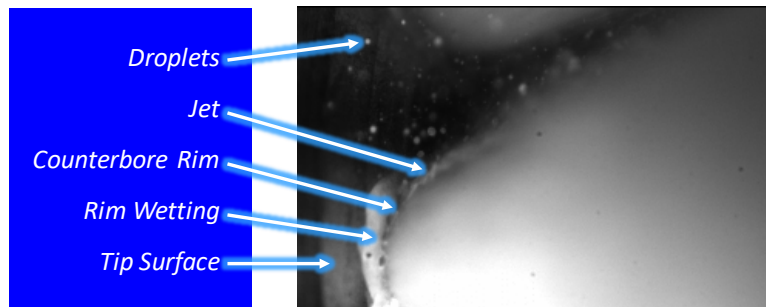
Fig. 20: Low speed jets on the spray surface, initiated at the CB rim break up into stray droplets which can strike and wet the nozzle surface
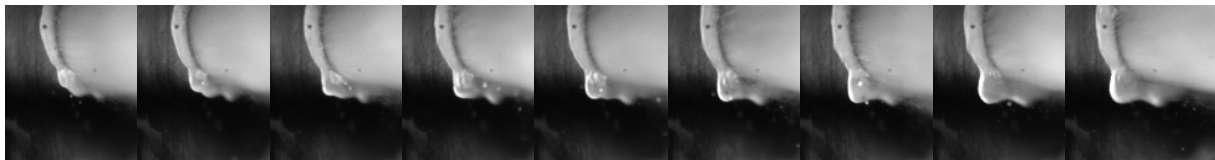
Fig. 21: View on the CB rim, mid-way through the injection. A flapping of jet may be observed where there is separation of the spray from the CB rim. Fuel from the CB cavity exits through this gap onto the nozzle surface.

Based on this analysis a phenomenological model of the wetting process was developed and is proposed in **Fig. 22**. The image illustrates a complex interaction of many different processes involved in tip wetting. It is noted that the experiments conducted did not show what was happening within the CB volume. It is expected that some fuel will collect in this cavity and must therefore exit the CB. The quantity of fuel collecting in this region, is also likely to be dependent on temperature and flash boiling as has been observed on the tip surface, and in the TRF measurements. How this fuel exits the CB must be dependent on the interaction of the main spray and the CB rim. The fuel can either be entrained into the main spray, ejected in jets or droplets separately from the main spray or forced onto the tip surface.
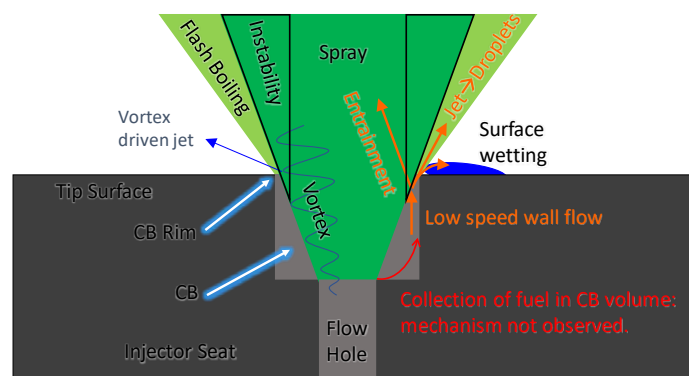
Fig. 22: Phenomenological Model of the wetting process

8. Conclusions

Two advanced techniques for the assessment of nozzle tip wetting have been developed at Delphi Technologies and presented in this paper. One of the techniques concentrates on the phenomena of nozzle tip wetting, and the other on the quantification of that wetting. These techniques were used to demonstrate the influence of some key nozzle tip control parameters on tip wetting. These techniques were also used to investigate the main phenomena at work during tip wetting and to develop a phenomenological model. Together such advanced tools offer the potential to improve our understanding

of tip wetting and to allow for further optimisation of GDi nozzle tip designs for minimum tip wetting, and therefore for maximum robustness and durability whilst operating on engine.

References

[1]   A. Berndorfer, S. Breuer, W. F. Piock and P. Von Bacho, "Diffusion Combustion Phenomena in GDi Engines caused by the Injection Process," in *SAE2013-01-0261*, 2013.

[2]   Y. Imaoka, Y. Hashizume, T. Inoue and T. Shiraishi, "A Study of Particulate Emission Formation Mechanism from Injector Tip in Direct-Injection Gasoline Engines," in *SAE2019-01-2244*, 2019.

[3]   P. R. Jamroz, Injector Deposit Formation in Gasoline Direct Injection Engines, Boston, USA: Massachusetts Institute of Technology, 2002.

[4]   F. Schulz, J. Schmidt and F. Beyrau, "Development of a sensitive experimental set-up for LIF fuel wall film measurements in a pressure vessel," *Experiments in Fluids,* no. 05/15, 2015.

[5]   H. Dageförde, A. Kiefer, W. Samenfink, W. Wiese and A. Kufferath, "Requirements for Spray and Tip Design of a Multi-hole Injector for DISI Engines," in *ICLASS*, Tainan, Taiwan, 2015.

[6]   N. Karwa, P. Stephan, W. Wiese and D. Lejsek, "Gasoline Direct Injection Engine Injector Tip Drying," in *19th Australasian Fluid Mechanics Conference*, Melbourne, Australia, 2014.

[7]   J. Shi, E. Gomez Santos, G. Hoffmann and G. Dober, "Large Eddy Simulation Tool for GDi Nozzle Development," *MTZ Worldwide,* vol. 10, pp. 58-63, 2018.

[8]   P. Leick, B. Bork and J. N. Geiler, "Experimental characterization of tip wetting in gasoline DI injectors," in *SAE2018-01-0286*, 2018.

[9]   K. Peterson and R. Grover, "Application of optical diagnostics and simulation to fuel injector tip wetting and soot production," in *11th International Symposium on Combustion Diagnostics*, Baden-Baden, Germany, 2014.

[10]   Moehwald/Bosch, "FLR1000 - Leakage test bench," 2020. [Online].

[11]   MATLAB, *version 9.5.0.944444 (R2018b),* Natick, Massachusetts: The MathWorks Inc., 2018.

[12]   N. Otsu, " A Threshold Selection Method from Gray-Level Histograms," *Automatica ,* vol. 11, no. 23-27, pp. 285-296, 1975.

[13]   P. Aleiferis and Z. van Romunde, "An analysis of spray development with Iso-octane, n-pentane, gasoline, ethanol, and n-butanol from a multi-hole injector under hot fuel conditions," *Fuel,* vol. 105, pp. 143-168, 2013.

Application of Deep Neural Networks to the Prediction of the Ignition Delay Time of Gasoline PRF and TRF Surrogates with the Addition of Oxygenates for CFD Engine Simulations

L. Pulga[1], G.M. Bianchi[1], G. Cazzoli[1], V. Mariani[1], C. Forte[2]

[1]UNIBO University of Bologna, Bologna, Italy

E-mail: leonardo.pulga2@unibo.it
Telephone: +(39) 051 2093306

[2]NAIS s.r.l., Bologna, Italy

Abstract. The engine knock is still one of the main limiting factors to the efficiency improvement of Spark Ignition engines. In order to predict its occurrence by means of Computational Fluid Dynamics tools under different loads and mixture conditions, standard empirical correlations are no longer accurate enough. To overcome this limitation, it is becoming increasingly common to refer to detailed chemical kinetics simulations computed at reference conditions and validated with experimental tests. Although this approach reduces the uncertainties in the prediction of the auto ignition occurrence, one factor that is still under active investigation with respect to the effect of physical and chemical conditions, is the definition of an appropriate gasoline fuel surrogate. The change in the definition of the surrogate formulation would require, however, a new computation of the Ignition Delay Times for the full map of physical and mixture properties combinations, which would be time consuming. In the present work, a complete methodology has been developed to generate a deep Neural Network capable of predicting the Ignition Delay Time of any surrogate from a palette of the three most common components used for gasoline surrogates (toluene, i-octane, n-heptane) and oxygenates (ethanol, methanol). The LLNL chemical kinetics mechanism has been adopted to generate the initial training dataset which is composed of 5 pure species, 78 mixtures and about 130000 data points. Before creating the training dataset, the LLNL has been validated against several experimental data available in literature for both pure fluids and gasoline surrogates. The same validation has been performed for the machine learning algorithm together with a sensitivity analysis comprehensive of the most important parameters. The machine learning algorithm achieved promising results with Mean Absolute Relative Error <2% and computing times reduced to a few seconds for any definition of the surrogate fuel.

Notation

AIT	*Auto-Ignition Temperature*
C	*Carbon*
CFD	*Computational Fluid Dynamics*
CO	*Carbon monoxide*
CPUh	*Computing hour for one core*
EGR	*Exhaust Gas Recirculation*
FFNN	*Feed-Forward Neural Network*
FFV	*Flex-Fuel Vehicle*
H	*Hydrogen*
IDT	*Ignition Delay Time*
LHV	*Lower Heating Value*
MARE	*Mean Absolute Relative Error*
MON	*Motor Octane Number*
NN	*Neural Networks*
NTC	*Negative Temperature Coefficient*
O	*Oxygen*
PI	*Pre-Ignition*
PM	*Particulate Matter*
PRFX	*Primary Reference Fuel (with X the vol% of i-octane)*
ReLU	*Rectified Linear Unit*
RON	*Research Octane Number*

L. Pulga, G. M. Bianchi, G. Cazzoli, V. Mariani, C. Forte

SI   Spark Ignition
T_b Normal boiling temperature
T_f Freezing temperature
TRFX   Toluene Reference Fuel (with X the RON value)
UHC   Unburned Hydrocarbon
ρ Density
ϕ Equivalence ratio

1. Introduction

The current public legislations regarding the topic of environmental impact have pushed the manufacturers of light-duty and heavy-duty vehicles to design engines with higher efficiency, reduced fuel consumption, and lower greenhouse gas emissions [1]. These targets are obtained by adopting ad hoc aftertreatment solutions and different control strategies.

The most common choices applied to enhance the engine efficiency are the adoption of smaller displacement units (downsizing) and slower turning engines (down-speeding), as well as optimized fuel injection strategies and variable valve lift and timing. At the same time, the continuous demand for higher torque and power has led to a significant increase of in-cylinder loads thanks to higher boost pressures, with challenges due to the relevant power density reached.

One of the main factors limiting the enhancement of the performance of modern Spark Ignition (SI) engines is the occurrence of abnormal combustion phenomena. When referring to abnormal combustion in SI engine operations, knock and Pre-Ignition (PI) are the most common events [2]. Knock is the self-ignition of the unburned end-gases (unburned mixture outside of the flame) where pressure and temperature have been increased by both the combustion process and compression due to the piston motion. This event produces a very fast chemical energy release causing a shock wave that generates a rapid increase of the cylinder pressure. The impulse caused by the shock wave excites a resonance in the cylinder at characteristic frequencies that depend on the cylinder bore diameter and the temperature inside the combustion chamber [3]. Thermo-mechanical damages to pistons, rings and exhaust valves can happen if sustained heavy knock occurs. PI, on the other hand, is a spontaneous mixture ignition generated by local hot spot-wall temperature or combustion chamber deposit, that can degenerate into a knock event especially when it happens before the spark ignition.

Many factors affect the occurrence of these abnormal combustion events and can be divided in three main groups: i) engine parameters, such as compression ratio, spark advance, air inlet temperature, boost pressure, combustion chamber geometry etc.; ii) fuel antiknock quality; iii) stochastics component due to the cycle to cycle variation.

A common approach in engineering practice used to investigate the auto-ignition event is the adoption of computational fluid-dynamic techniques, to simulate the combustion process that takes place within the cylinder using advanced numerical models. The choice of an adequate fuel surrogate is critical for the correct prediction of the auto-ignition behaviour of the mixture [4]; however, this holds true if the modelling approach is sensitive to the composition of the surrogate. While coupling a chemical kinetics solver to the main engine simulation would be sensitive to this choice, the use of tabulation and correlations for the Ignition Delay Time (IDT) of the fresh mixture, given thermodynamics conditions and composition, is still the mainstream choice due to computing time advantages [5]. Currently, the most common and simple fuel surrogate assumptions for representing commercial gasolines are the Primary Reference Fuels (PRFs), i.e. mixtures of i-octane and n-heptane, and the Toluene Reference Fuels (TRFs), i.e. mixtures of toluene, i-octane and n-heptane [6].

The classical correlations used for the IDT are the Arrhenius-based power laws e.g. the correlation elaborated by Douaud and Eyzat [7], who fitted an experimental dataset based upon the four-octane-number method used to characterize the knocking behaviour of the fuel and the engine. Del Vescovo et al. in [8] developed a correlation to predict the IDT of PRF blends with emphasis in capturing the Negative Temperature Coefficient (NTC) region profile.

The main advantages in the use of knock empirical models is their low computation cost and easy implementation, but they can hardly be considered accurate in the prediction of the IDT of new surrogate definitions or in extreme conditions such as for highly diluted mixtures or in presence of water vapour inside the mixture.

To overcome these limitations and maintaining low the computational costs of the model during the simulation, the use of pre-computed look-up tables of ignition delay times has become common [9].

Considering the vast range of the conditions that can be reached during engine operations (both thermodynamics and related to the mixture composition) and the level of refinement that the parameters

grid should have in order to capture the main gradients accurately, experimental data would be too expensive to generate. Therefore, the mainstream approach is based on the use of detailed chemical kinetics simulations performed in simplified domains, to populate the dataset, and eventually validate some of the results with experimental values. Even if more accurate than the correlation approach, and more time-efficient than the coupled solution of the chemical reactions, the generation of look-up tables performed with large kinetics schemes can still be time consuming, especially if the fuel surrogate is considered as a variable for the research campaign. At the same time, the generation of IDT results is an essential asset for the optimization of the fuel surrogate definition during the selection process.

It must be further considered that the blending of biofuels in gasolines is widely spreading: a) blends with 5%vol (E5 gasoline) and 10%vol (E10 gasoline) of ethanol can be operated without engine modifications [10]; b) Flex-Fuel Vehicles (FFV) can be fuelled with gasoline blends with 0-100% ethanol/methanol [11]. Despite the fact that those blends are characterized by reduced energy density (Lower Heating Value (LHV)) compared with traditional gasolines, they reduce the emission of carbon monoxide (CO), Unburnt Hydrocarbons (UHC), Particulate Matter (PM) [12]. Moreover, they contribute to improve the combustion speed and efficiency and are commonly employed as Octane boosters [13]. Therefore, including oxygenates (ethanol, methanol) in TRFs is a key aspect to capture the behaviour of future fuels.

The aim of this work is to present a methodology that employs an optimized deep learning workflow for the generation of a model capable of generating in a few seconds the values of the IDT at any relevant condition (pressure, temperature, air-fuel ratio, EGR) given the definition of the fuel surrogate. This integration between chemical kinetics simulations and machine learning or deep learning algorithms is more and more present in recent years' research and it has been proven to be a valuable tool in substitution to more traditional approaches [14, 15].

2. Methodology

2.1 Chemical kinetics simulations

The chemical kinetics simulations required to generate a sufficiently large training set for the NN have been performed using the Cantera [16] library in Python 3.7.2 [17], on a machine with 8 cores and 16 GB ram. The model adopted was a *zero-dimensional* perfectly stirred reactor at constant volume, to better emulate the conditions reached during the operation of an adiabatic shock tube [18], for which many experimental data are available. The implementation of the mixture formation in presence of EGR has been performed following the work of Cazzoli et al. [19]. The simulations are performed after initializing the reacting mixture at initial temperature and pressure and with the computed mass fractions of fuel, oxidizer, and EGR. The main properties used for the pure fluids selected for the fuel surrogate are reported in Tab. 1.

Table 1. Properties of the components of the pure fluids of the target fuel surrogates

Name	Toluene	i-Octane	n-Heptane	Ethanol	Methanol
Formula	C_7H_8	$i\text{-}C_8H_{18}$	$n\text{-}C_7H_{16}$	CH_3CH_2OH	CH_3OH
Group	Aromatics	i-Alkanes	n-Alkanes	Oxygenates	Oxygenates
w% C	92	84.9	84.6	52.6	37.8
w% H	8	15.1	15.4	13	12.5
w% O	0	0	0	34.4	49.7
ρ @298 K (kg/m^3)	862.24	687.9	679.6	785.13	786.61
T_b (°C)	110.13	98.74	97.94	78.09	64.21
T_f (°C)	-95	-107.4	-91	-114.1	-97.6
AIT (°C)	480	447	215	363	464
LHV (MJ/kg)	40.59	44.31	44.56	26.70	19.93
RON/MON (-)	121/107	100/100	0/0	108.6/89.7	108.7/88.6

After an initial screening based on literature results and internal validation, the complete LLNL chemical kinetics scheme [20] has been chosen for its completeness and overall good agreement with experimental data for TRF surrogates. The sensitivity of the chemical kinetics scheme to the composition of the surrogate has been evaluated with respect to the experimental data available in [21] for several pressures and temperatures. The LLNL mechanism shows an overall good agreement, and a correct sensitivity to the fuel composition at high and intermediate temperatures, while it displays a slight over-estimation of the ignition delay time for lower pressure of the ethanol containing surrogate presented in [22]. For sake of brevity, these results are shown in the results analysis together with the reference experimental data and the deep learning results.

2.2 Database generation

The complete LLNL scheme, which accounts for 1,387 reactions and 10,481 species, has been employed for the chemical kinetics simulations. The gasoline surrogate under test is defined with the volume fractions of the single species listed in Tab. 1 selected randomly (and constrained to have unity sum) and its stoichiometric air-fuel ratio is computed.

Besides the simulations for each single component of the palette, the surrogates for the database were formulated randomly for a total of 78 surrogates (reported in Fig. 1) with controls for ensuring the unity sum of all fractions.

The simulation grid is defined by different levels of pressure, temperature, equivalence ratio (i.e. operated fuel-air ratio / stoichiometric fuel-air ratio, Φ) and EGR. The pressure and the temperature levels are defined with a full factorial approach, whilst the equivalence ratio and the EGR are randomly taken in their given ranges, resulting in the following grid:

  a) 8 pressure unique points in the range 10-160 bar.
  b) 15 temperature unique points in the range 650-1400 K.
  c) 10 equivalence ratio unique points in the range 0.3-3.
  d) 4 EGR unique points in the range 0-30%.

The ranges of EGR, pressure and temperature were defined in order to cover a wide range of typical engine operating conditions. The range of Φ was defined according to engineering considerations. The rich limit accounts for rich pockets of mixture promoted by the liquid fuel late evaporation (wall film, crevice accumulation, residual droplets). The lean limit accounts for lean pockets of mixtures that might be present in the outer regions of the combustion chamber (e.g. squish volume) due to intense omega-tumble motions that transport the unburned mixture toward the end-gas.
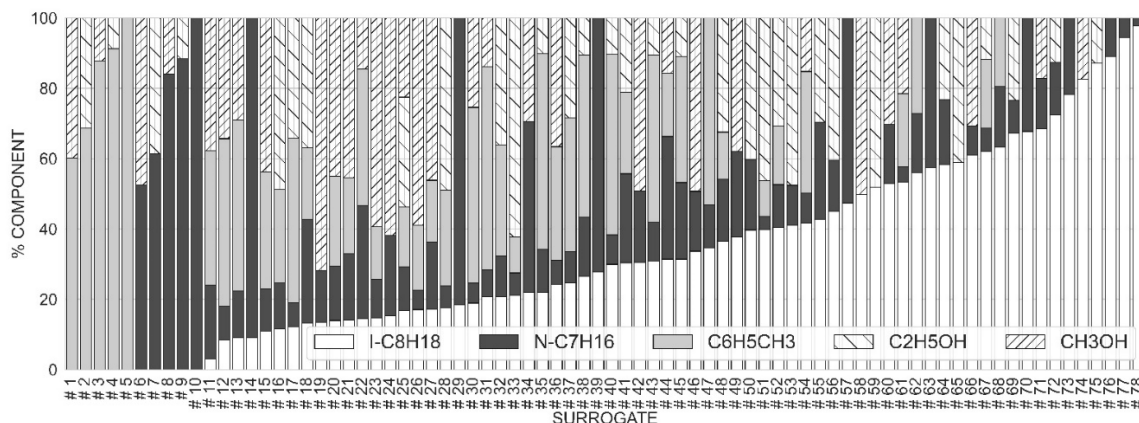
Fig. 1 Distribution of the dataset with respect to the surrogate components

2.3 Machine learning methodology

Neural Networks (NNs) and other machine learning algorithms applied to supervised problems are mainly used for classification (prediction of a category) or regression tasks (prediction of a continuous value), which is our case of application. Feed-Forward Neural Networks (FFNNs) are multi-layer inter-connected networks composed of base units called neurons, which transfer the information one-way layer by layer from the input to the output. The first layer (input layer) receives the input features, i.e. the parameters selected since they are correlated with the regression task. The last layer (output layer)

returns the inferred value transformed with a normal function. The other neurons between the input and the output layers form the hidden layers, which are the core of the NN model development, and their number, distribution and properties are the main optimization parameters.

The NNs developed in the present work are based on the implementation in *Python* 3.7.4 of the open-source software library Keras [23]. The output of the NN model is the IDT corresponding to that input fuel species fractions. The target value has been transformed with the log10 operation, in order to reduce the standard deviation of the distribution (based on the assumption of the classical Arrhenius shape). The input features of the NNs are the same parameters used to define the grid for the chemical kinetics simulation, namely fuel species fractions, pressure, temperature, equivalence ratio, EGR. The input features are all normalized in order to have mean value set to 0 and standard deviation to 1.

In addition, the input layer is combined with an extra layer that adds a white noise (Gaussian or GNoise) to the input features with the aim to prevent the trained network from overfitting, i.e. the data "memorization" during training that leads to a model with excellent predicting performances on the train set without being able to generalize to new data [24]. To further improve the robustness of the prediction, during the training phase, a kernel L2 regularization [24] is introduced in all the hidden layers.
The training algorithm for the NN's weights update was the Adam optimization algorithm [25] that iterates until a maximum number of 1E5 epochs is reached. The number of maximum iterations however is not expected to be reached because the training phase is limited by an early stop strategy that stops the optimization, retaining the best performing parameters, in case no better model is obtained on the train set after 100 consecutive repetitions.

The choice of the best architecture (i.e. number of layers and neurons per layer) and activation functions has been performed with a gaussian optimization approach [26] aimed at maximizing the prediction performance after a k-fold evaluation (with k=10), which consists in the iterative split of the full database into train set and test set. After the finalized architecture is defined, the NN is trained on 50% of the available dataset (train set) and evaluated on the remaining data, i.e. the test set, for further comparison with other methods in the predictions. By applying these strategies, the optimized neural network is expected to provide the best predictive accuracy on new 'unseen' points, and the results reported in the following sections have all been obtained with optimized network architectures.

2.4 Meta-learning approach

After an initial testing, the performance of the optimized neural network was analysed by performing a correlation analysis of the error committed on the test set with the input features. From this analysis, no significant correlation emerged, indicating that the model accuracy was evenly distributed within the domain, except for the temperature variable. It was noted that the model accuracy would degrade at temperatures outside of the 900-1200 K temperature region. Due to the NTC behaviour of paraffins, the prediction with NNs would naturally suffer from overfitting in that region since the larger part of the IDTs is distributed near the value of the NTC temperature range, resulting in the lack of representation for the higher/lower temperatures.

In order to compensate this modelling issue, this work proposes a meta-learning methodology, where multiple NNs are stacked in two consecutive levels. The workflow is based on the common approach of developing a prediction model for the ignition delay time by combining multiple correlations fitted with reference values from different temperatures intervals.

At the first level, during the training phase, the temperature range of the dataset (650-1400 K) is divided as follows: a) the low-temperature Arrhenius region (650-1000 K); b) the expected NTC region (900-1200 K); c) the high-temperature Arrhenius region (1100-1400 K). These regions were created with a slight temperature overlap between each other, in a manner to account for a similar number of points per region. The points in each region are provided to train three different and independent NNs, whose predictions will result in three different IDT values. In the second level, a larger NN is trained on the full database, but the input layer receives three additional features, namely the IDT values predicted by the three independent NNs at the first level, independently from their temperature. The second level FFNN is defined to receive as input features the physical and mixture properties and the 3 outputs from level 1.

For sake of illustration, Fig. 2 shows a schematic view of the meta-learning workflow and architecture.
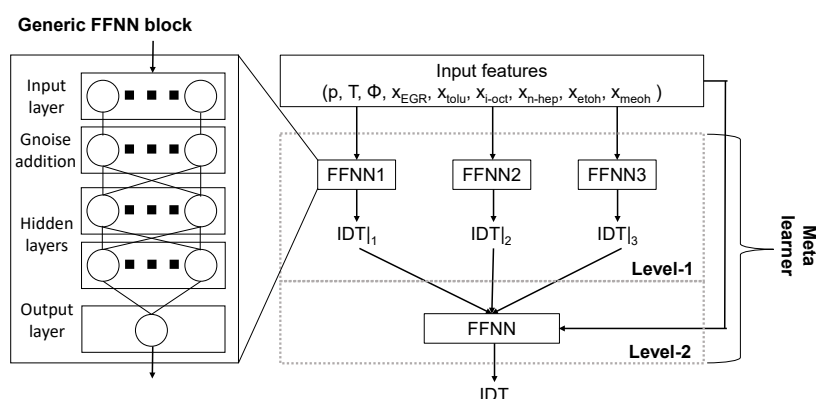
Fig. 2. Scheme of the meta learner workflow and architecture

3. Results

3.1 Metrics and objectives

To evaluate and compare the performance of the predictions achieved with the chemical kinetics simulations and the novel meta-learning methodology, different metrics have been applied. The first two metrics are the coefficient of determination (R^2, Eq. (1)) and the Mean Absolute Relative Error (MARE, Eq. (2)). In addition, a further metric was added, specifically for this case, based on the autoignition integral proposed by Livengood-Wu [27] and defined in Eq. (3) (Err_G) as the mean absolute error of the inverse of the ignition delay time. In Eqs. (1-3) y_i is the target value, f_i the prediction of the ith point (with N available cases) and $\bar{y}$ the mean target value. By considering this metrics, more importance is attributed to the conditions with shorter ignition delay times, whose correct prediction is of greater importance during the application in combustion simulations.

$$R^2 = 1 - \sum_i (y_i - f_i)^2 \bigg/ \sum_i (y_i - \bar{y})^2 \tag{1}$$

$$MARE = \sum_{i=1}^{N} |y_i - f_i|/y_i \cdot 100 \,/N \tag{2}$$

$$Err_G = \sum_{i=1}^{N} (1/y_i - 1/f_i) \bigg/ \sum_{i=1}^{N} (1/y_i) \cdot 100 \tag{3}$$

Besides the general performance on the whole database, the model is expected to predict accurately the effect of varying physical and chemical parameters and particularly the surrogate composition.

3.1 Performance on the dataset

According to the optimization process described in the previous section, one simple NN and the meta-learner have been optimized. The final simple NN is constituted by 2 hidden layers composed by 100 nodes with tanh activation function and 10 nodes with the ReLU activation function. The same structure has emerged for the first level of the meta-learner, while the second level of the meta-learner algorithm is constituted by a NN with 13 input nodes and 2 hidden layers composed by 130 nodes with tanh activation function and 13 neurons with the ReLU activation function. The performance of the one simple NN and that of the meta-learner are reported in Tab. 2 for both train and test set. The networks are compared with the performance of a reduced chemical kinetics scheme LLNL323 [28], which could represent an alternative approach because it would greatly reduce the computing time for the chemical kinetics simulations.

The performance of the meta-learner is further compared to that of the simple NN by focusing on the Mean Relative Error distribution at varying temperature reported in Fig. 3. Even if the mean values

are centred near 0% (0.1% for the meta learner and -1.8% for the NN), the evident advantage is the great reduction in the standard deviation of the error distribution at temperatures far from the NTC region. The standard deviation of the MARE has been chosen as an indicator for the distribution after performing the Shapiro-Wilk test for normality [29], considering the fact that the result of the statistics test for normality where the W statistics is computed as in Eq. (4), where z_i represent the ordered sample values from the smallest to the largest, a_i are constants generated from a normal distribution with the same mean, variance and covariance value.

$$W = \left(\sum_i a_i \cdot z_i\right)^2 \bigg/ \sum_i (z_i - \bar{z})^2 \qquad (4)$$

Table 2. Computing time and performance of the main computing approaches

Metrics	LLNL	LLNL323	NN	META-LEARNER
CPUh	100	10	0.0014	0.003
Err$_G$ TRAIN	-	6.453	6.92	4.563
MARE TRAIN	-	6.457	4.408	2.558
R^2 TRAIN	-	0.981	0.989	0.994
Err$_G$ TEST	-	6.132	6.21	4.045
MARE TEST	-	6.750	4.835	2.938
R^2 TEST	-	0.980	0.986	0.993
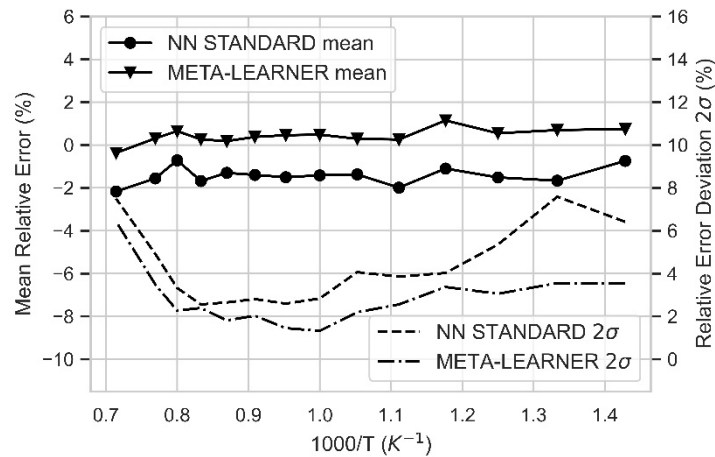
Fig. 3. Mean relative error as a function of temperature on the test set for the 2 different approaches

The results in terms of p-value (the probability of obtaining, assuming correct the target distribution, of presenting cases as extreme as the observed results) for the hypothesis are for both errors 0.0, while the statistics W is 0.91 for the standard NN approach and 0.95 for the meta-learner. The latter two show a high level of agreement with the normal distribution.

The performance of the meta-learner with respect to each single variable has been evaluated with a similar approach, but no significant correlation has been found between the error committed and the other variables, indicating that the performance is not expected to degrade with a variation in the mixture composition (surrogate definition, equivalence ratio and diluents' mass fractions) or with pressure. In particular, the sensitivity of the model to the addition of different fractions of oxygenates (both ethanol and methanol) has been deeply investigated. The results of the error distribution of the meta-learner are reported in Fig. 4 with respect to the addition of oxygenates. The mean relative error of the meta-learner and its distribution do not show any correlation with the oxygenate fractions on more than 30 different combinations in the test set.
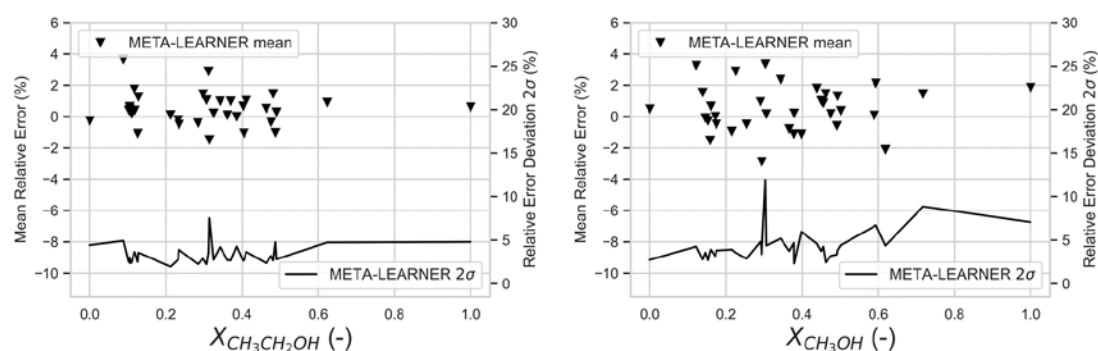
Fig. 4. Mean relative error as a function of the components' mass fractions

3.1 Performance on new surrogates

The train test split performed on the available dataset does not allow to evaluate specifically the predictive capacity of the model with respect to the fuel surrogate definition. This is due to the fact that the split is performed automatically in order to maintain similar distributions between the target values, independently from the distribution of the features. In order to evaluate the sensitivity of the surrogate definition, the two NN approaches (simple and meta-learner) were applied on surrogates that were not present inside the initial dataset, and whose composition is reported in Tab. 3. The RON value for these surrogates is estimated as the sum of the RON of the single components weighted on their molar fraction, which can be considered as a good approximation for TRF surrogates, as reported in [30].

As shown in Fig. (5), the model shows an overall good prediction capability with respect to the fuel surrogate definition, and almost no performance degradation with varying RON value of the surrogate. In Fig. (5, 6) is visible that the prediction performance with the LLNL (filled markers) and the meta-learner (dashed lines) are comparable on the three temperature regions. Therefore, when facing with new mixtures, the novel deep learning methodology allows to reach the same accuracy of detailed chemical kinetics simulations with strong reductions of the computing time (Tab. 2).

It must be underlined that the mismatch with experimental data shown in Fig. (6) for the ETRF, in particular for 10 bar and 30 bar, is due to the fact that the list of the significative reactions in mixtures comprising toluene and ethanol are currently under improving for detailed chemical kinetics. Thus, the high ethanol content in the ETRF (40%vol) in Fig. (6) is considered responsible for the predictive performance degradation of both the LLNL and the meta-learner.

Table 3. Composition of the surrogates adopted for validation

Surrogate [Reference]	vol% C_7H_8	vol% $i\text{-}C_8H_{18}$	vol% $n\text{-}C_7H_{16}$	vol% C_2H_6O	RON*	R^2
TRF70 [21]	21.29	42.48	36.23	0.0	70	0.978
TRF80 [21]	31.57	39.85	28.58	0.0	80.4	0.996
TRF91 [21]	44.10	36.58	19.31	0.0	91	0.996
TRF97.5 [21]	70.44	11.52	18.04	0.0	97.5	0.980
ETRF [22]	12.00	37.80	10.20	40.00	93.0	0.964
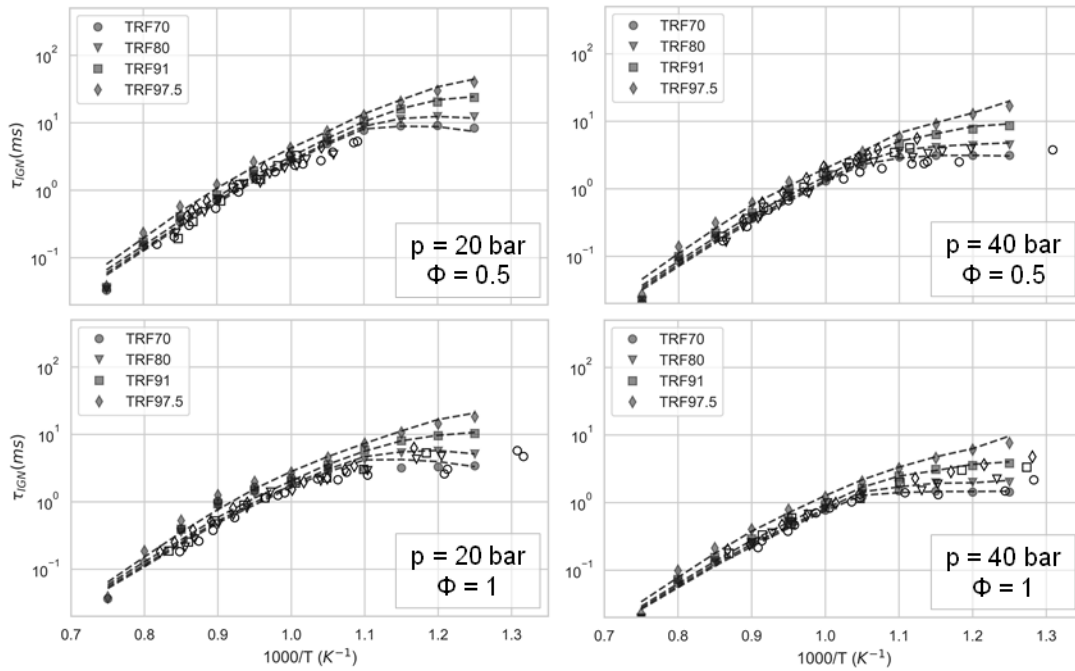
Fig. 5. Ignition delay time for four different TRF surrogates against temperature at different pressure and equivalence ratio. Empty markers=exp. data [21], filled markers=chemical kinetics, line=meta-learner
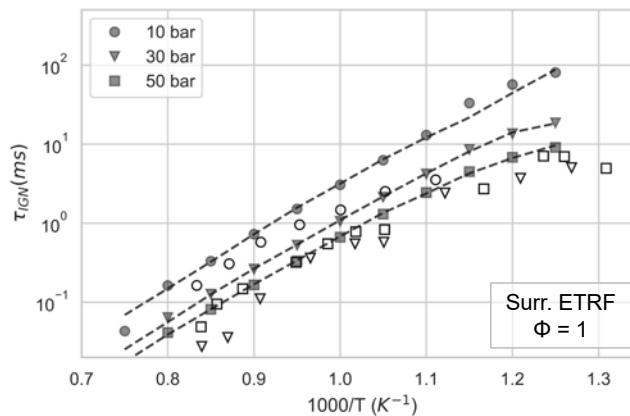
Fig. 6. Ignition delay time for the ETRF surrogate (40%vol ethanol) against temperature at different pressures and stoichiometric mixture. Empty markers=exp. data [22], filled markers=chemical kinetics, line=meta-learner

Conclusions

In the present work an innovative approach based on a modified Neural Network architecture has been described and validated, aimed at the prediction of the ignition delay time of any gasoline fuel surrogate represented by i-octane, n-heptane, toluene, ethanol and methanol. This approach consists in the stack of different interconnected Neural Networks called meta-learner. The performance of the model reveals to be higher than that provided by the classical neural networks, leveraging the known properties of the target variable. Comparing the classical Neural Network with the meta-learner on the dataset, the meta-learner achieved a reduced Mean Relative Error (from 2% to almost 0%) on the temperature range under review (650-1400 K). Furthermore, the meta-learner has shown an improved reliability by means of a reduced deviation of the error against the standard Neural Network. Maximum error deviation reductions around the 20% in the high temperature range and around the 30/50% in the low temperature and the Negative Temperature Coefficient ranges are reported. The final model is capable of populating look-up tables of ignition delay times for application in CFD codes in a few seconds with very accurate performance. At the same time, this model can be leveraged during the optimization of new gasoline

surrogates, providing an almost immediate evaluation of the ignition delay times to be compared with target values.

References

1. Stanton, D., "Systematic Development of Highly Efficient and Clean Engines to Meet Future Commercial Vehicle Greenhouse Gas Regulations", SAE Int. J. Engines 6(3):1395-1480, 2013, DOI: 10.4271/2013-01-2421.

2. Singh, E., Morganti, K., and Dibble, R., "Knock and Pre-Ignition Limits on Utilization of Ethanol in Octane-on-Demand Concept," SAE Technical Paper 2019-24-0108, 2019, DOI: 10.4271/2019-24-0108.

3. Corti, E., Forte, C., Cazzoli, G., Moro, D., Falfari, S., Ravaglioli, V., "Comparison of Knock Indexes Based on CFD Analysis", Energy Procedia, Volume 101, 2016, Pages 917-924, ISSN 1876-6102, DOI: 10.1016/j.egypro.2016.11.116.

4. Kim, N., Vuilleumier, D., Sjöberg, M., Yokoo, N. et al., "Using Chemical Kinetics to Understand Effects of Fuel Type and Compression Ratio on Knock-Mitigation Effectiveness of Various EGR Constituents," SAE Int. J. Adv. & Curr. Prac. in Mobility 1(4):1560-1580, 2019, DOI: 10.4271/2019-01-1140.

5. Truffin, K., Colin, O., "Auto-ignition model based on tabulated detailed kinetics and presumed temperature PDF – Application to internal combustion engine controlled by thermal stratifications", International Journal of Heat and Mass Transfer, Volume 54, Issues 23–24, 2011, Pages 4885-4894, ISSN 0017-9310, DOI: 10.1016/j.ijheatmasstransfer.2011.06.044.

6. Yuan, H., Chen, Z., Zhou, Z., Yang, Y., Brear, M., J., Anderson, J., E., "Formulating gasoline surrogate for emulating octane blending properties with ethanol", Fuel, Volume 261, 2020, 116243, ISSN 0016-2361, DOI:10.1016/j.fuel.2019.116243.

7. Douaud, A. M., Eyzat, P., "Four-Octane-Number Method for Predicting the Anti-Knock Behavior of Fuels in Engines". SAE Technical Paper, v87 780080, SAE, 1978.

8. DelVescovo, D., Kokjohn, S., and Reitz, R., "The Development of an Ignition Delay Correlation for PRF Fuel Blends from PRF0 (n-Heptane) to PRF100 (iso-Octane)," SAE Int. J. Engines 9(1):520-535, 2016, https://doi-org.ezproxy.unibo.it/10.4271/2016-01-0551. Erratum published in SAE Int. J. Engines 10(3):1383, 2017, DOI: 10.4271/2016-01-0551.01.

9. Knop, V., Michel, J., Colin, O., "On the use of a tabulation approach to model auto-ignition during flame propagation in SI engines", Applied Energy,Volume 88, Issue 12,2011,Pages 4968-4979,ISSN 0306-2619, DOI: 10.1016/j.apenergy.2011.06.047.

10. Omer, M., Yan, F., Luo, M., Turkson, R., "Spark Ignition Engine Combustion, Performance and Emission Products from Hydrous Ethanol and Its Blends with Gasoline", Energies. 9. 984. 10.3390/en9120984

11. De Melo, T.C.C., Machado, G.B., Belchior, C.R., Colaço, M.J., Barros, J.E., de Oliveira, E.J., de Oliveira, D.G., "Hydrous ethanol-gasoline blends-combustion and emission investigations on a flex-fuel engine" Fuel 2012, 97, 796–804

12. Rosdi, S., Mamat, R., Alias, A., Hamzah, H., Sudhakar, K., Hagos, F., "Performance and emission of turbocharger engine using gasoline and ethanol blends", IOP Conference Series: Materials Science and Engineering. 863. 012034, DOI: 10.1088/1757-899X/863/1/012034

13. Wang, C., Li, Y., Xu, C., Badawy, T., Sahu, A., Jiang, C., "Methanol as an octane booster for gasoline fuels", Fuel. 248. 76-84. DOI: 10.1016/j.fuel.2019.02.128.

14. Pulga, L., Bianchi, G., Ricci, M., Cazzoli, G. et al., "Development of a Novel Machine Learning Methodology for the Generation of a Gasoline Surrogate Laminar Flame Speed Database under Water Injection Engine Conditions," SAE Int. J. Fuels Lubr. 13(1):5-17, 2020, DOI: 10.4271/04-13-01-0001.

15. L. Pulga, G.M. Bianchi, S. Falfari, C. Forte, A machine learning methodology for improving the accuracy of laminar flame simulations with reduced chemical kinetics mechanisms, Combustion and Flame, Volume 216, 2020, Pages 72-81, ISSN 0010-2180, DOI: 10.1016/j.combustflame.2020.02.021.

16. Cantera: An object-oriented software toolkit for chemical kinetics, thermodynamics, and transport processes. http://www.cantera.org

17. Python Software Foundation. Python Language Reference. http://www.python.org

18. Lee, C., Vranckx, S., Heufer, A., Khomik, S., Uygun, Y., Olivier, H., Fernandes, R., "On the Chemical Kinetics of Ethanol Oxidation: Shock Tube, Rapid Compression Machine and Detailed Modeling Study", Zeitschrift für Physikalische Chemie. 226. 1-28. 10.1524/zpch.2012.0185.

19. Cazzoli, G., Bianchi, G., Falfari, S., Ricci, M. et al., "Evaluation of Water and EGR Effects on Combustion Characteristics of GDI Engines Using a Chemical Kinetics Approach," SAE Technical Paper 2019-24-0019, 2019, DOI: 10.4271/2019-24-0019.

20. Mehl M., Pitz, W., J., Westbrook, C. K., Curran, H. J., "Kinetic modeling of gasoline surrogate components and mixtures under engine conditions", Proceedings of the Combustion Institute 33:193-200

21. Javed, T., Lee, C., AlAbbad, M., Djebbi, K., Beshir, M., Badra, J., Curran, H., Farooq, A., "Ignition studies of n-heptane/iso-octane/toluene blends", Combustion and Flame, Volume 171, 2016, Pages 223-233, ISSN 0010-2180, DOI: 10.1016/j.combustflame.2016.06.008.

22. Cancino, L., Fikri, M., Oliveira, A., Schulz, C., "Ignition delay times of ethanol-containing multi-component gasoline surrogates: Shocktube experiments and detailed modelling", Fuel. 90. 1238-1244. DOI: 10.1016/j.fuel.2010.11.003.

23. Keras, Chollet,F. and others, 2015, keras.io

24. Kukačka, J., Golkov, V., Cremers, D., "Regularization for Deep Learning: A Taxonomy", arXiv:1710.10686

25. Kingma, D., P., Ba, J., "Adam: A Method for Stochastic Optimization", arXiv:1412.6980

26. Snoek, J., Larochelle, H., Adams, R., P., "Practical Bayesian Optimization of Machine Learning Algorithms", arXiv:1206.2944

27. Hu, Z., Somers, B., Cracknell, R., F., Bradley, D., "Investigation of the Livengood–Wu integral for modelling autoignition in a high-pressure bomb", 2016/01/02 DOI: 10.1080/13647830

28. Mehl M., Chen, J.Y., Pitz, W.J., Sarathy, S.M., Westbrook, C.K., "An Approach for Formulating Surrogates for Gasoline with Application Toward a Reduced Surrogate Mechanism for CFD Engine Modeling", Energy and Fuels, 25:5215-5223 (2011)

29. Shapiro, S., S., Wilk, M., B., "An analysis of variance test for normality (complete samples)", Biometrika, 52, 3

30. Pera, C., Knop, V., "Methodology to define gasoline surrogates dedicated to auto-ignition in engines", Fuel 2012;96:59–69. DOI: 10.1016/j.fuel.2012.01. 008. ISSN 0016-2361

Achieving Higher Brake Thermal Efficiency under Existence of Peak Firing Pressure Constraint with a HD Diesel Engine

N Uchida[1], K Watanabe[1] and K Enya[2]

[1]New ACE Institute. 2530 Karima Tsukuba-shi, Ibaraki Pref., 305-0822, Japan.

E-mail: n_uchida@nace.jp
Telephone: +(81) 29 856 1801

[2]Isuzu Advanced Engineering Center. 8 Tsuchidana, Fujisawa-shi, Kanagawa Pref., 252-0881, Japan.

Abstract. Further improvement in the brake thermal efficiency (BTE) of a diesel engine seems to be limited by a peak firing pressure (PFP) constraint, so that the Sabathe (limited-pressure or Seiliger) cycle is thought as an optimum ideal cycle under such a constraint. Therefore, if the higher PFP is allowed, combination of higher compression ratio, higher excess air ratio (boosting pressure), shorter combustion duration, and reduced in-cylinder cooling loss could have much potential to improve BTE. This study firstly investigated the potential for improvement in BTE by a higher PFP constraint (up to 35 MPa) with a single-cylinder HD diesel engine, and then on the effects of the measures to get over the PFP constraints. As one of the measures, cylinder offset was initially investigated. The results indicated that the cylinder offset resulted in slight deterioration in the indicated thermal efficiency (ITE) with the same compression ratio and heat release rate profile as expected by a numerical simulation. But it also has little potential for the further improvement in BTE even combined with shorter combustion duration which intended to improve degree of constant volume. Another measure, increase in the compression ratio is ambivalent toward PFP suppression. Nevertheless, it had much potential instead by combining with heat release rate profile control even under the existence of PFP constraint.

Notation

EGR   *Exhaust gas recirculation ratio.*
H   *Piston compression height.*
Ne   *Engine speed.*
P_{inj} *Fuel injection pressure.*
P_{in} *Intake pressure.*
Q, Q'   *Total fuel injection quantity, Cycle integral of apparent heat release rate.*
R   *Crank radius = Engine stroke / 2.*
T_{in} *Intake temperature.*
T_{cool} *Coolant outlet temperature.*
T_{oil} *Oil inlet temperature.*
W_i *Indicated Work.*
α   *crank angle degATDC.*
γ   *Specific heat ratio.*
δ   *Ratio of crank radius to connecting rod length.*
ε   *Compression ratio.*
$η_{gl}$ *Degree of constant volume (Gleichraumgrad).*
$η_{th}$ *Theoretical thermal efficiency.*
λ   *Excess air ratio.*
μ   *Ratio of cylinder offset (positive number for thrust side) to connecting rod length.*
ξ   *Cut-off ratio (volume at PFP / volume at TDC).*
ξ'   *2nd cut-off ratio (volume at end of after burning / volume at PFP).*
ψ   *Pressure ratio (pressure at end of constant volume combustion / pressure at start of combustion).*
ψ'   *2nd pressure ratio (PFP / pressure at the end of constant volume combustion).*

1. Introduction

For the improvement in BTE of a diesel engine, higher compression ratio, higher boosting pressure, shorter combustion duration, etc. should be effective. On the other hand, these measures all increase in PFP, and higher PFP could compensate BTE advantage by the higher friction loss estimated by the

traditional Chen-Flynn empirical equation [1]. Furthermore, current HD diesel engines should optimize the set of these parameters not to exceed the mechanical constraint for PFP. It might be an instance that no multiple-cylinder engines could achieve more than 48% of BTE without any waste heat recovery systems in the SuperTruck1 results [2].

For the maximization of indicated work under PFP constraint, Sabathe cycle is regarded as the most promising ideal cycle by a zero-dimensional engine model calculation [3]. To confirm this hypothesis, we introduced multiple-injector combustion system, which has more degrees of freedom to control heat release rate (HRR) profile only by adjusting each injection timing and quantity, as shown in Figure 1. The results indicated not only that BTE is the optimum with Sabathe-like cycle, but that the higher PFP is not always resulted in the higher friction loss. Furthermore, more rooms to improve BTE could be projected with higher PFP constraints [4].

In this study, the potential of BTE improvement by enhancing PFP limit was firstly experimentally confirmed with the Sabathe-like combustion cycle by utilizing the multiple-injector system. Then, we modified the target thermodynamic cycle from Sabathe-like cycle to the newly proposed cycle with higher HRR and shorter diffusion combustion period by allowing the higher PFP. However, the PFP constraint was still existed for further improvement in BTE by increasing compression ratio, boosting pressure, and HRR. As a measure to combine with other BTE improvement technologies by mitigating the PFP, the effect of cylinder offset and higher compression ratio were investigated.
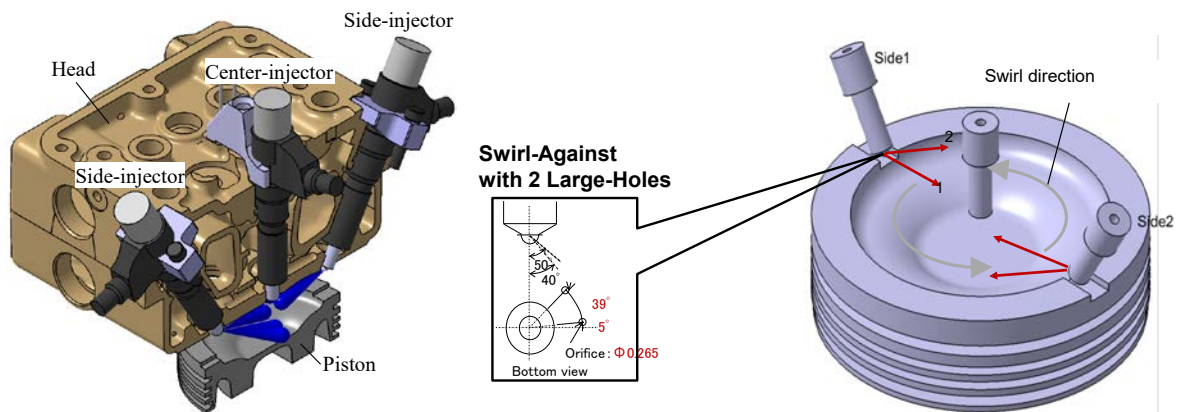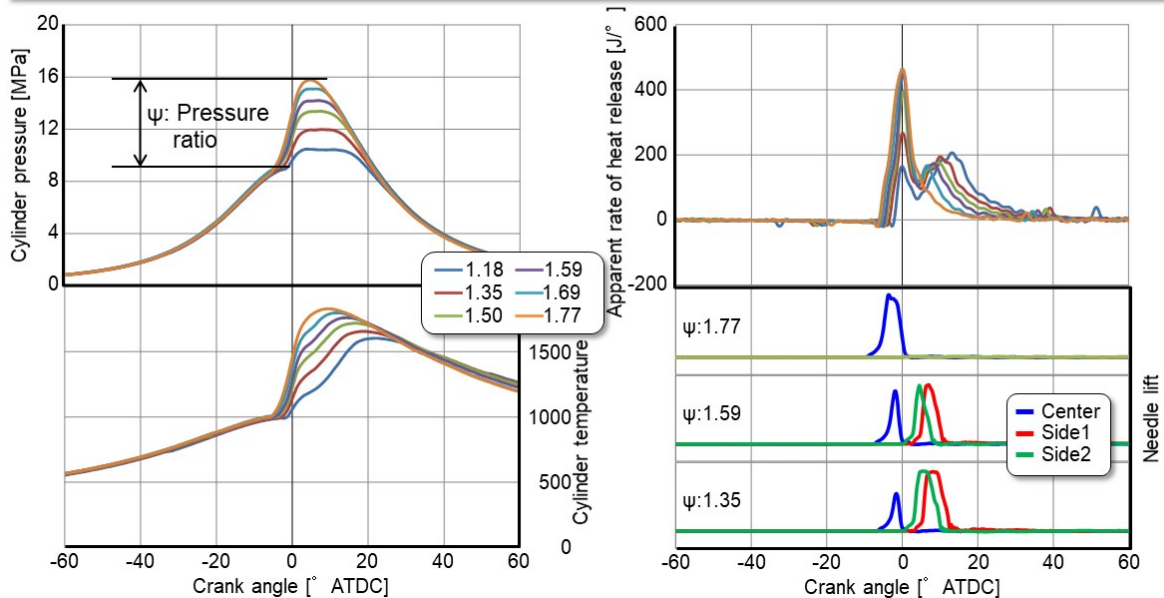
Fig. 1. Piston cavity design, injector orientation, spray direction and initial test results (nozzle specifications of side injectors were different from the current study; three orifices along the swirl) with the 140mm stroke engine and 18:1 of compression ratio [3]

2. Engine specifications, simulation models and schematics of experimental system

2.1 Engine specifications

Two single cylinder four-stroke direct-injection diesel engines with displacement volume of 2004cm^3 and 2147 cm^3 respectively were utilized for engine experiments. Detailed specifications of the engines are listed in Table 1. The 150mm stroke engine was designed to have a tolerance up to 35MPa of peak firing pressure. The compression ratio was slightly different even with the same pistons in both engines by the different engine displacement.

Table 1. Engines specifications

| Engine	Stroke: 140 mm (Only for Figure 3)	Stroke: 150 mm
Engine type	Single cylinder 4 stroke DI diesel	
Cylinder bore x Stroke	φ135 mm×140 mm	φ135 mm×150 mm
Engine displacement	2004 cm^3	2147 cm^3
Connecting rod length	250 mm	370.46 mm
Piston material	Forged steel (Monotherm)	
Top clearance	0.85 mm	
Compression ratio (same pistons)	18:1, 22:1	19.2:1, 23.5:1
Piston cavity type	Soup plate	
Valve system	Camless hydraulic VVA	
Fuel injection equipment	Common rail system (G4S modified)	
Maximum fuel injection pressure	300 MPa	
Nozzle orifice	Center: φ0.180 mm×9-150° Side: φ0.265 mm×2orifice×2	
Intake swirl ratio	0.9	
Peak firing pressure limit	30 MPa	35 MPa
Fuel	Diesel fuel JIS #2 (Japanese market fuel) Cetane number: 56.8, Density: 0.8271 g/cm^3 Sulfur content: 7 ppm (mass)	

The test engines simulate turbocharged and after-cooled heavy-duty diesel engines by an externally driven supercharger and exhaust throttling. A hydraulic variable valve actuation system (Sturman Industries, DHVVA) and an electronically controlled high-pressure common rail injection system (Denso G4S modified) which enable a maximum injection pressure of 300MPa were equipped in both engines. The nozzle orifice number and diameter of center injector nozzle was fixed at nine and φ0.180mm respectively. The geometric compression ratio of the baseline piston cavity was 18:1 (for the 140mm stroke engine, 19.2:1 for the 150mm stroke engine).

As shown in Figure 1, the system consists of one center mounted injector and two opposed side injectors per cylinder combined with a kind of soup plate type piston cavity. The center injector was vertically mounted at the center of the bowl, with the same nozzle orifice specification optimized for the conventional shallow dish combustion chamber, and the other two side injectors were slant-mounted to protrude their nozzle tip near the periphery of the piston cavity. Two nozzle orifices of opposed side injectors were directed against the swirl (clockwise from the top view). One of the orifices of the side injectors was directed inward the cavity, with the objective to reduce adjoined spray interference. These injectors were connected to the same common rail, so the injection pressure was identical in both the center and side injectors.

2.2 Schematics of experimental system

Figure 2 shows a schematic of the experimental apparatus. Intake boost pressure, exhaust back pressure, intake manifold temperature and EGR rate (EGR was not added as the parameter in this study) are widely controlled independently at any engine operating points. Intake boost pressure of up to 800kPa (abs.) is possible with an externally driven supercharger. Intake boost pressure and exhaust back pressure were made equal throughout the tests so that the external work done by the supercharging system could be ignored. The effect of variations in actual turbocharger efficiency and EGR cooler

efficiency on the engine performance and emission characteristics with boost pressure and EGR rate conditions were also excluded.
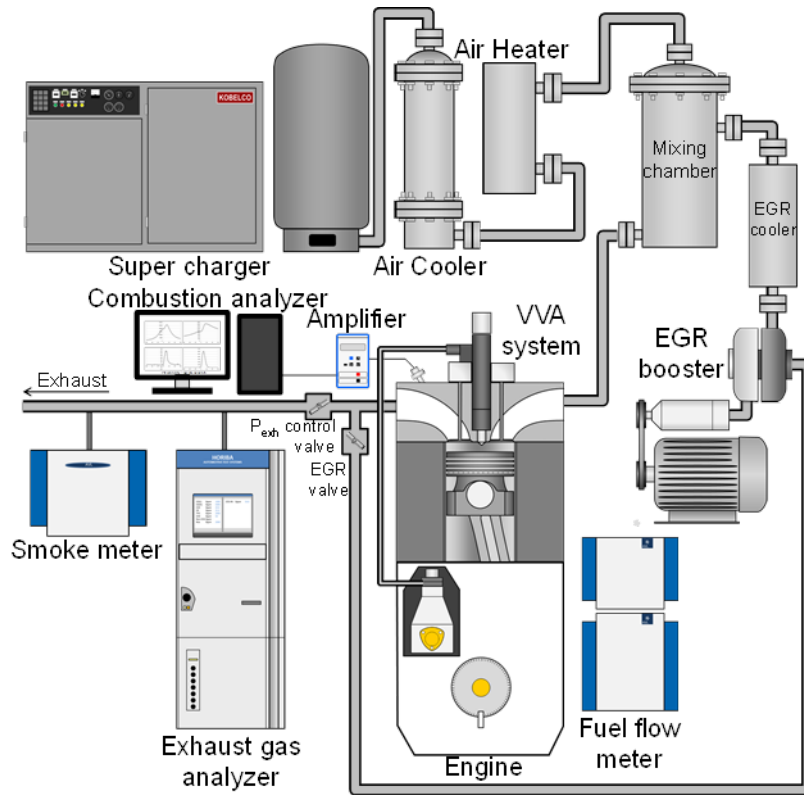
Fig. 2. Schematic of engine test system

3. Results and discussions

3.1 Effect of higher PFP on BTE

It is possible to modify the HRR only by adjusting each fuel injection timing and injection duration of the three injectors with the multiple-injector combustion system. If HRR for the constant volume combustion period was increased, PFP was also increased. It was experimentally confirmed as shown in Figure 3, higher PFP achieved by increasing HRR for the constant volume combustion phase resulted in the higher BTE without any significant increase in the cooling and mechanical loss. For the mechanical loss, it could be possible to project that the reduction of piston thrust side force in the expansion stroke should mostly affect in comparison with the friction at the bearings.

Therefore, it is assumed that shorter combustion duration than the Sabathe-like cycle by the higher HRR will increase BTE in case of allowing the higher PFP. However, higher in-cylinder pressure at very close to top dead center (TDC) will not result in the indicated work increase, because of rather slow volume change rate. Furthermore, from much air utilization view point, it could be better to increase in HRR after the in-cylinder volume is increased especially for higher compression ratio cases. From this knowledge, a new thermodynamic cycle is proposed as the better BTE potential than Sabathe cycle. Figure 4 compares the difference between Sabathe and the new cycle schematically. The new cycle shortens the combustion duration and increases the HRR in the late of combustion period. Pressure ratios ψ and ψ' refer to the pressure at states 2 and 3' relative to the pressure at state 1 and state 2, respectively. Cut-off ratios ξ and ξ' indicate the volume at states 3' and 4' relative to state 2 and state 3', respectively.
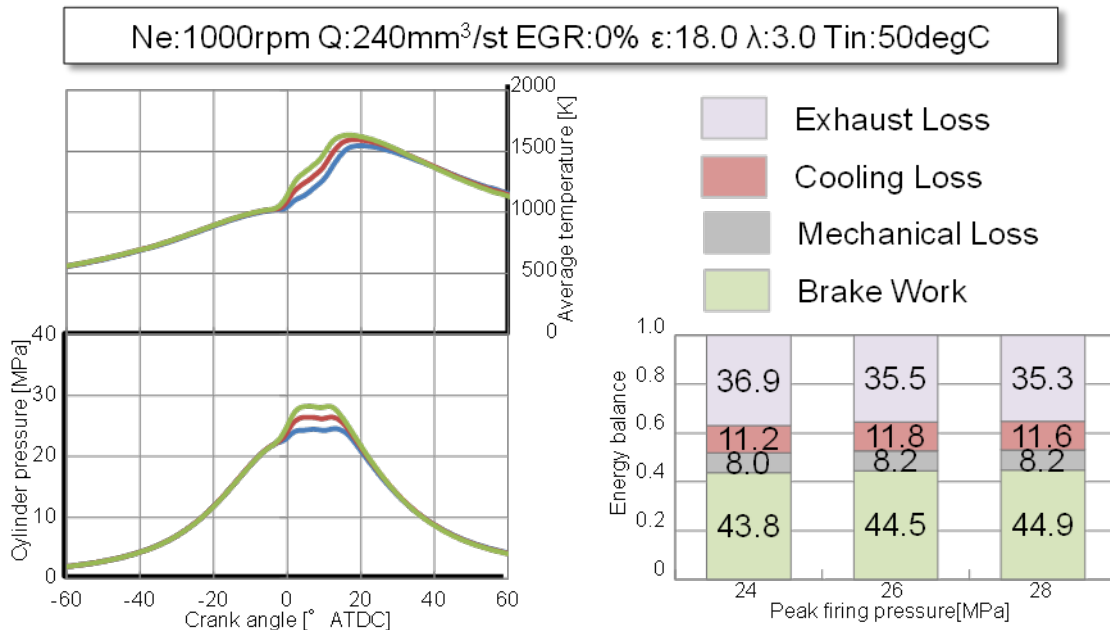
Fig. 3. Effect of higher PFP combustion with multiple-injector system on energy balance (Experimental results by utilizing 140mm stroke engine)

ξ: Duration from TDC to peak HRR
ξ': Duration of late combustion (after the end of injection)
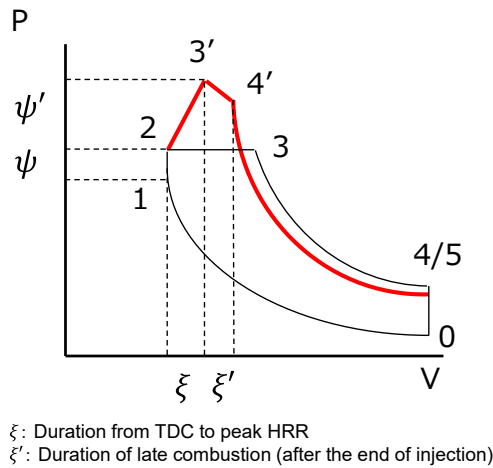
Fig. 4. Comparison of ideal pressure-volume diagram between baseline Sabathe cycle (black line: 0-1-2-3-4) and new thermodynamic cycle (red line: 0-1-2-3'-4'-5) allowing higher PFP than P_2 (or P_3)

As shown in Figure 4, the new cycle includes late combustion (after fuel injection period) phase (ξ'). It is not so easy to identify its combustion mode for the calculation of thermal efficiency during the late combustion phase (3' to 4'). In this model, the assumption of constant temperature expansion was chosen for late combustion phase. Theoretical thermal efficiency for the new cycle is therefore derived as equation (1). More detailed derived process is drawn in the published paper [5].

$$\eta_{th} = 1 - \frac{1}{\varepsilon^{\gamma-1}} \frac{\psi\psi'\xi^{\gamma}\xi'^{\gamma-1} - 1}{(\psi-1) + \psi(\psi'\xi-1) + \frac{1}{2}\psi(\psi'+1)(\xi-1)(\gamma-1) + \psi\psi'\xi(\gamma-1)ln\xi'} \quad (1)$$

By assuming the new thermodynamic cycle in a self-developed zero-dimensional engine model, ITE and PFP for various compression ratio (ε) and cut-off ratio (ξ) was calculated as shown in Figure 5. The zero-dimensional simulation based on the ideal cycle initially calculated the fuel energy consumption for each combustion period in Figure 4; from 1 to 2 determined by initial pressure ratio ψ (=1.1), from 2 to 3' (rest of heat release), from 3' to 4' determined by late combustion ξ' (20% of total fuel energy). The unknown parameter ψ' is automatically calculated by the parameter ξ. Woschni's empirical equation [6] was used to account for wall cooling loss. Once the HRR profile was achieved, ITE and

211

PFP were derived. Figure 5(a) indicates that a decrease in the cut-off ratio (or, increase in ψ' under the same energy input) has the same potential as an increase in the compression ratio to achieve higher ITE. That is, for a given PFP constraint, the potential ITE would be similar either way. On the other hand, at the high load condition, the increase in PFP with reduced cut-off ratio is more remarkable in order to achieve the same improvement in ITE as shown in Figure 5(b). Thus, careful control is necessary when decreasing the cut-off ratio under a PFP constraint.

(a) Middle load condition

(b) High load condition
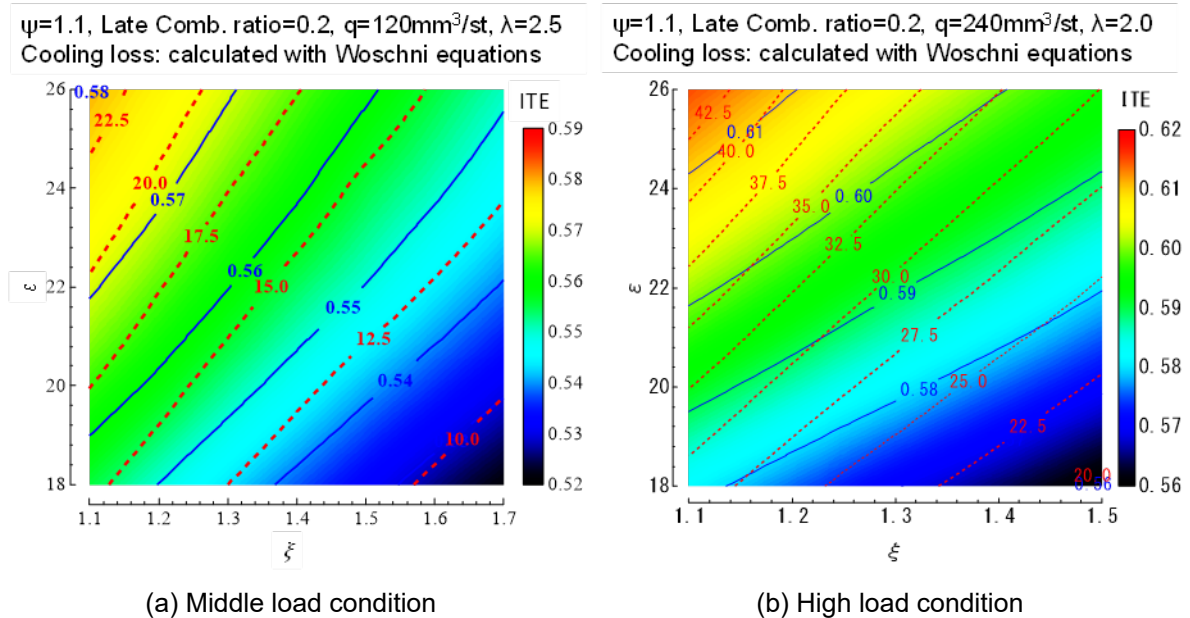
Fig. 5. Zero-dimensional thermodynamic calculation illustrating the effect of various compression ratios (ε) and cut-off ratios (ξ) on ITE (blue solid lines and color bar) and PFP in MPa (red dashed line)

Such PFP sensitivity difference between compression ratio and cut-off ratio in the high load condition are caused by higher volume change rate in the expansion stroke with higher compression ratio. That could compensate PFP increase under the same HRR profile.
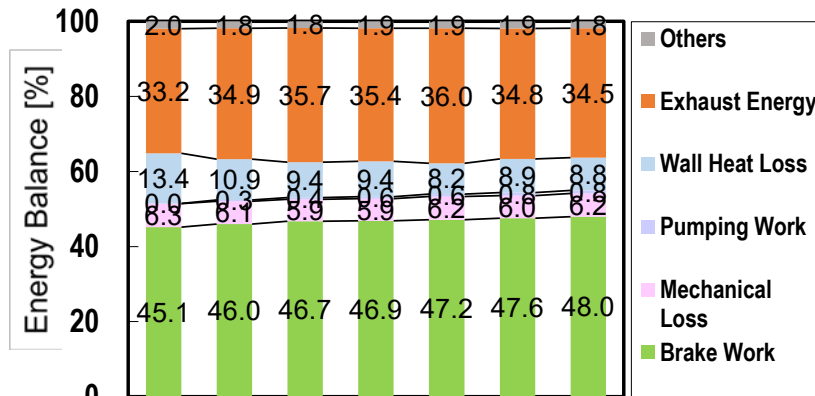
Tin [K]	323	291	←	←	←	←	←
λ	2.5	←	3.0	←	3.5	←	3.5
ξ	1.25 sabathe	1.23 sabathe	1.23 sabathe	1.17	1.17	1.16	1.16
Pinj [MPa] q [mm3/st]	200 240	← ←	← ←	← ←	← ←	← ←	211 256
IVC [deg.ATDC]	555	←	←	←	←	505	←

Fig. 6. Energy balance analysis for the single cylinder engine experiments by changing various parameters

Figure 6 shows the energy balance analysis (see Appendix 2 of [7] or [8]) for the experimental results to optimize BTE with the single cylinder engine by changing intake temperature, boosting pressure, combustion duration, fuel injection parameters and intake valve closing timing one by one. Again, any relationship between PFP and the mechanical loss was not clearly observed in this figure. Although the difference of each variant set of parameters were small, more than 0.2%pt difference in BTE and 0.5%pt difference in cooling loss are statistically significant. The three bars from the left show the results with Sabathe-like cycle, and the rest bars show with the new cycle by the higher HRR during the diffusion combustion period (ξ as in Figure 5). Even though the advantage was not so significant, third and fourth bars of the energy balance from the left indicated slight improvement in BTE of the new cycle over the baseline Sabathe-like cycle.

Figure 7 is the in-cylinder pressure and HRR at where the optimum BTE of 48% (ITE of 55%, the rightmost energy balance in the Figure 6) was achieved. These experiments were rather focused on the effect of reduced combustion duration by applying the new thermodynamic cycle from the baseline Sabathe-like cycle. PFP was already reached to 35 MPa (upper limit of this engine) even with the baseline (the lowest) compression ratio piston.

Ne:1000rpm Qin:256mm^3/st Prail:211MPa λ:3.5
Tcool=Toil:80degC EGR:0% Tin:18degC ε:**19.2:1**
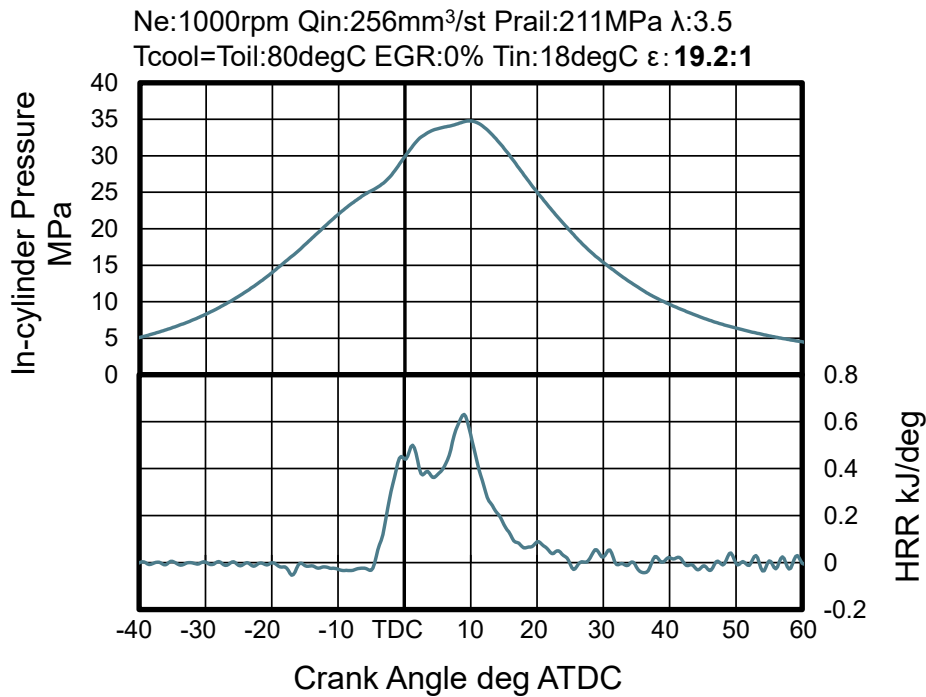
Fig. 7. Experimental result of in-cylinder pressure and heat release rate at point 48% of BTE (55% of ITE) by the single cylinder engine

3.2 Effects of cylinder offset on BTE under limited PFP

To modify parameters for BTE improvement with more degrees of freedom, PFP should be reduced from the current level. As the measure to suppress PFP during combustion period, cylinder offset was firstly selected to increase in the volume change rate early in the expansion stroke. Equation (2) shows the vertical height from the crank shaft center to the piston top; x.

$$x = R\left(\cos\alpha + \frac{1}{\delta}\sqrt{1-(\delta\sin\alpha-\mu)^2}\right) + H \qquad (2)$$

Figure 8 compares the variation of volume change rate near TDC for three cases, i.e. zero offset (baseline), 20mm offset to the anti-thrust side and zero offset with higher compression ratio as the reference. Although friction loss is commonly reduced with the cylinder offset to the thrust side, it is better to offset to the anti-thrust side for increasing the volume change rate near the TDC and in the expansion stroke. Increased top clearance was adjusted by changing the height of the fire deck from the center of

crank shaft. Fuel injection timing was not adjusted to the piston trajectory TDC basis, but kept to the crank shaft TDC basis. Form the equation 2, it is noticed that if the connecting rod length is smaller than the 150mm stroke engine, the piston trajectory TDC timing shift is much more. In comparison with the crank shaft TDC basis, the piston trajectory TDC basis has very little effects to increase the volume change rate in the expansion stroke at any rate. In other words, the effect of cylinder offset for the PFP is quite similar to that of retarded fuel injection timing.
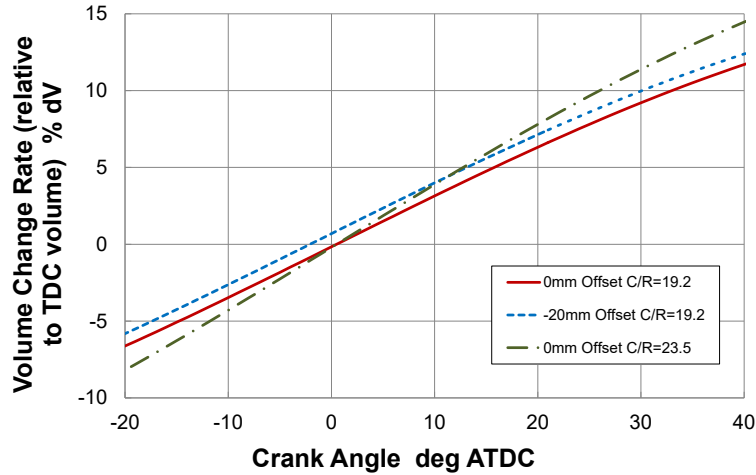
Fig. 8. Comparison of volume change rate with the baseline zero cylinder-offset case (150mm stroke engine)
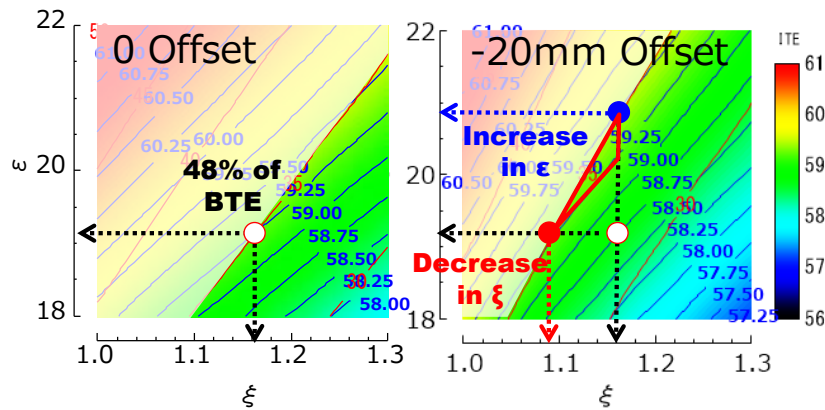
Fig. 9. ITE by zero-dimensional engine model calculation with and without cylinder offset

If cylinder offset to the anti-thrust side is applied, higher volume change rate after TDC could reduce in-cylinder pressure under the same HRR profile condition, resulted in the decrease in the indicated work. Therefore, the cylinder offset technique should be utilized in combination with other BTE and/or ITE improvement technologies. Figure 9 shows the simulated effects of cylinder offset to the anti-thrust side on ITE and PFP. The top-left masking area is above the current constraint; above 35 MPa of PFP. The white circle plot in the left figure and its operating parameters are the same as the result showing in Figure 7. In the right figure, the baseline white circle plot certainly shows the deterioration of ITE by the reduction of in-cylinder pressure with cylinder offset. In other words, more rooms for optimizing parameters are still existed. The red lined triangle in the right figure indicates the area where the higher ITE than the baseline conditions (as shown in Figure 7) is expected to achieve by modifying compression ratio: ε and/or cut-off ratio: ξ.

Figure 10 shows the experimental results with three different test conditions. In the right figure, blue plots indicated variation of ITE, BTE, and PFP for cylinder offsets with fuel injection based on the piston trajectory TDC. Injection timing and duration for each injector were the same as that for zero offset. As previously presumed, the results indicated no significant difference for blue plots both in BTE and PFP even with ±20 mm of cylinder offset. On the other hand, cylinder offset with fuel injection based on the crank shaft TDC has an effect to increase/decrease PFP with the baseline fuel injection strategy (green plots). BTE with the offset to the anti-thrust side was deteriorated by the decreased in-cylinder pressure as shown in the left figure. Deterioration of BTE with the thrust side offset could be caused by

the increase in the compression work for the advanced combustion phase. By advancing the side injection and the second center injection (a kind of after injection in the multiple injection strategy) timings, combustion duration was shortened and in-cylinder pressure was recovered in the anti-thrust side offset (red plots). Nevertheless, both ITE and BTE were not improved from the baseline condition. From the cycle efficiency viewpoint, it is necessary to increase theoretical thermal efficiency determined by compression ratio and specific heat ratio, and/or degree of constant volume (η_{gl}, see equation 3) for achieving higher BTE. However, η_{gl} only increased from 0.955 to 0.963 by the shorter combustion duration at 20mm of cylinder offset to the anti-thrust side, which could be one of the reasons why the thermal efficiency was not improved. This result corresponds to the zero-dimensional simulation in the right graph of Figure 9. Only reduced combustion duration, i.e. lower cut-off ratio: ξ, cannot achieve higher ITE than the baseline under the same PFP constraint.

$$\eta_{gl} = \frac{W_i}{\eta_{th(Otto\ cycle)} \times Q'} \qquad (3)$$

This figure also indicate that the cylinder offset to the thrust side based on the crank shaft TDC resulted in the increase in mechanical loss (difference between ITE and BTE), which is contradictory to the common knowledge. Nakamura et al. [9] reported no improvement in engine torque was experimentally observed which was caused by the lower transfer efficiency from reciprocating motion to rotating motion in low speed conditions, like these experiments, with the cylinder offset to the thrust side.
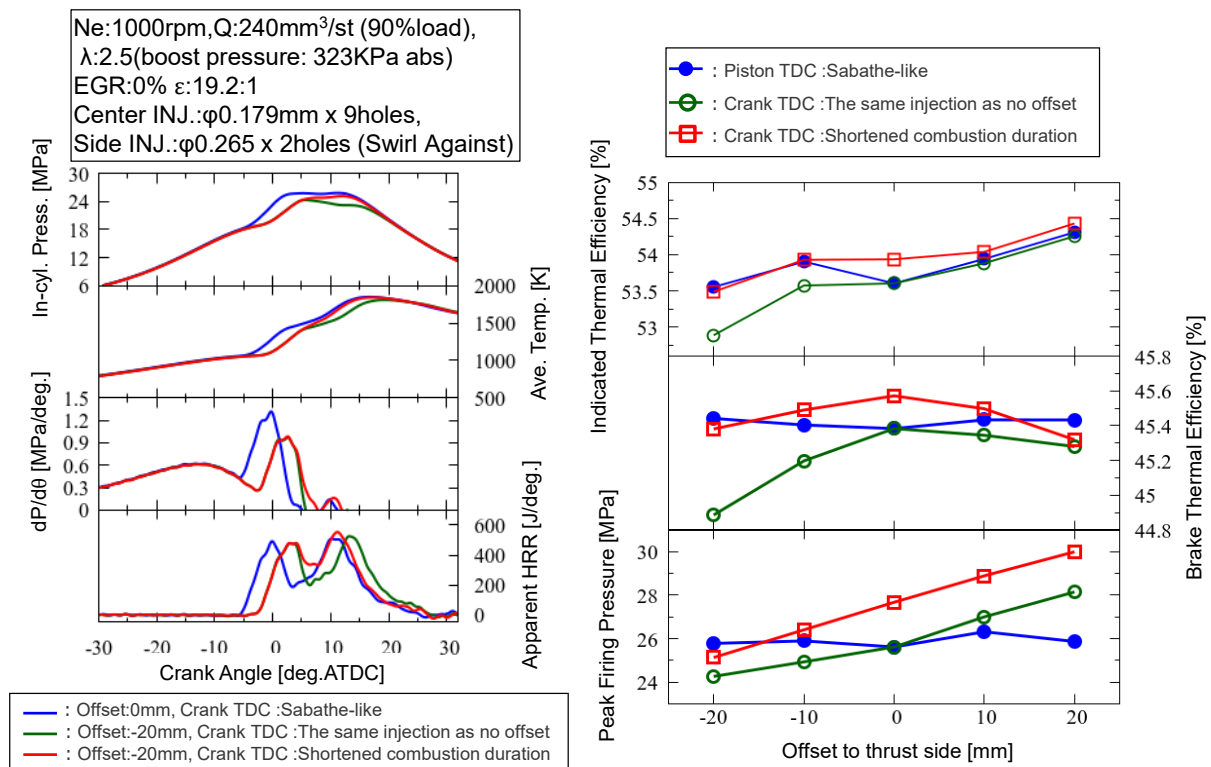
Fig. 10. Experimental results of the cylinder offset and additional combustion improvement effects on combustion characteristics and BTE

As suggested in Figure 8, the cylinder offset to the anti-thrust side based on the crank shaft TDC could be the similar effect as injection timing retard. This hypothesis was confirmed by the comparison of combustion characteristics with the injection timing retard and without cylinder offset. Figure 11 compares the 20 mm of cylinder offset results with the 2.6 degrees (interval between piston trajectory TDC and crank shaft TDC) of injection timing retard and no cylinder offset results. In-cylinder pressure and HRR were mostly identical.

Ne:1000rpm,Q:240mm³/st (90%load) λ:2.5
boost pressure: 323KPa abs EGR:0% ε:19.2:1
Center INJ.:φ0.179mm x 9, Side INJ.:φ0.265 x 2 (Swirl Against)

: Offset:0mm, Crank TDC :New cycle
: Offset:-20mm, Crank TDC :The same injection as no offset
: Offset:0mm, Crank TDC :2.6deg injection timing retard

Comb. Phasing	Base	Retard		Advance	
Offset	0[mm]	-20[mm]	0[mm]	+20[mm]	0[mm]
SOI	Base	Base	+2.6deg.	Base	-2.6deg.
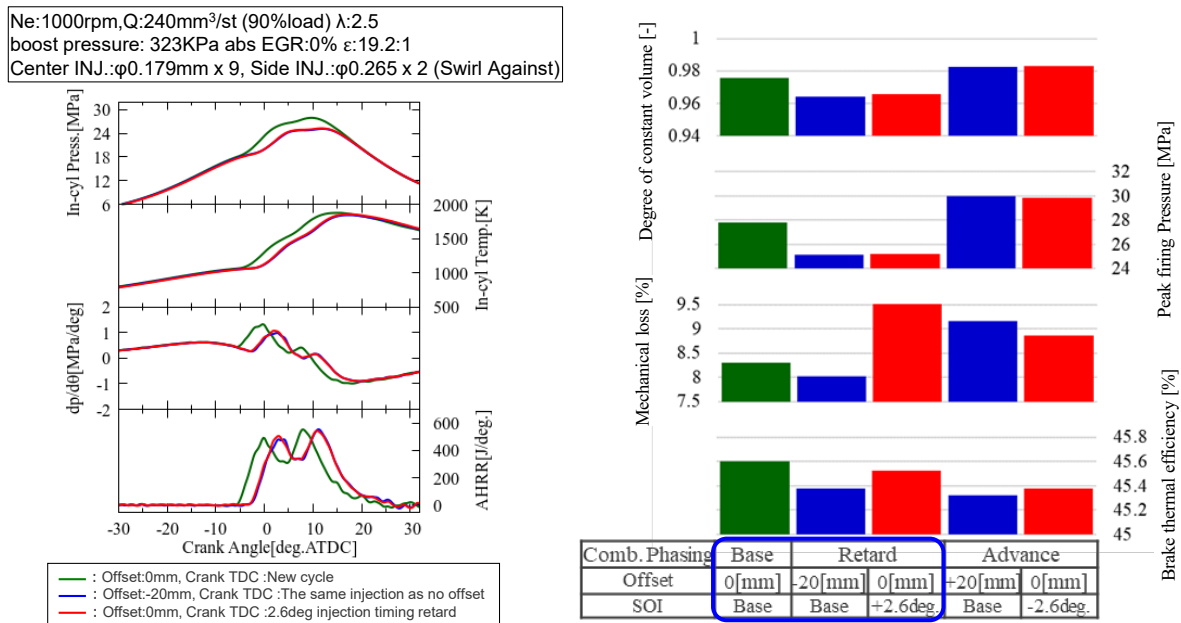
Fig. 11. Experimental comparison of combustion characteristics between cylinder offset and 2.6 degrees of injection timing retard without offset under the same injection strategy (green line and bars are for the baseline without any offset)

As can be seen in the right figure of Figure 11, BTE with the injection timing retard is slightly better than that with the cylinder offset and almost equal to that for the baseline condition even though the mechanical loss was the worst. The result indicates combustion phasing toward TDC is not prerequisite for achieving better BTE.

3.3 Effects of higher compression ratio on BTE under limited PFP

Reducing combustion duration significantly affected PFP increase, whereas no advantage in ITE improvement from the baseline was achieved in high load conditions. Therefore, it is worth carrying out the engine experiments with higher compression ratio, i.e. higher volume change rate, to determine the alternative direction of BTE improvement. However, because compression ratio directly affects not only PFP but fuel mixture formation and/or fresh air utilization in the cylinder, the practical improvement in BTE by the higher compression ratio will not be the same as the theoretical improvement in Figure 9. A new combustion chamber was utilized for the test as shown in Figure 12. Since the side injectors must be installed, the chamber diameter (squish area) is the same as baseline and the chamber must be much shallow to reduce the volume. This design has not been optimized yet, because 1) Spray flame interference to the wall could be increased, 2) Mixture formation and air utilization could be suppressed by the existence of wall much nearby the sprays.
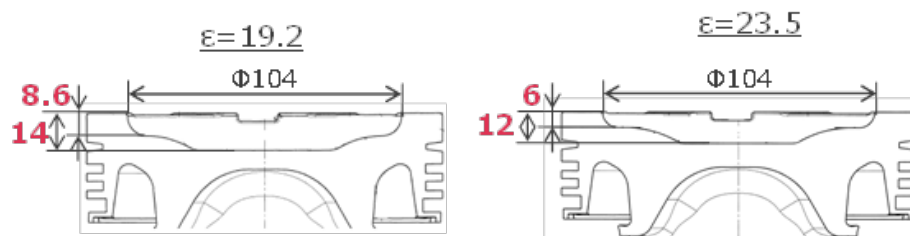
Fig. 12 Comparison of combustion chamber geometries for the different compression ratios (19.2:1 as baseline, 23.5:1 as a new chamber with higher compression ratio)

Increase in the compression ratio has not only the effect to improve theoretical thermal efficiency, but the effect to increase in the volume change rate during combustion period as shown in Figure 8. The latter effect much increases with the time from TDC. Therefore, the HRR especially in the later combustion phase should be increased to maintain the isobaric combustion of the Sabathe-like cycle. As shown in Figure 13, to aim at the Sabathe-like combustion cycle, HRR in the later part of combustion for the

higher compression ratio should be increased. Figure 14 shows the comparison of energy balance between the baseline and the higher compression ratio. Higher compression ratio resulted in about 1%pt of BTE improvement without any significant increase in mechanical and cooling losses even though PFP was 6.5 MPa increased.

Ne:1000rpm,Q:240mm³/st (90%load),
 λ:2.5(boost pressure: 323KPa abs), EGR:0%
Center INJ.:φ0.179mm x 9holes,
Side INJ.:φ0.265 x 2holes (Swirl Against)
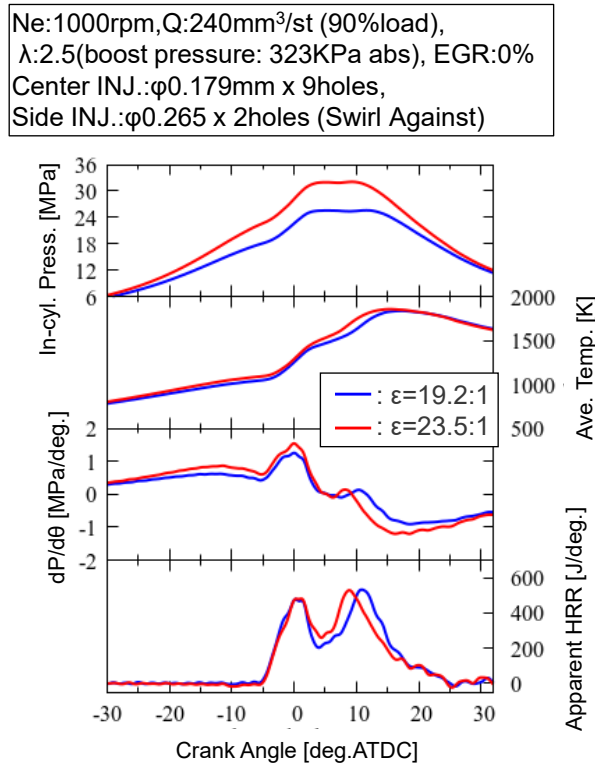
Fig. 13. Experimental comparison of combustion characteristics between ε=19.2:1 and 23.5:1 under Sabathe-like combustion

Ne:1000rpm,Q:240mm³/st (90%load), λ:2.5(boost pressure: 323KPa abs), EGR:0%
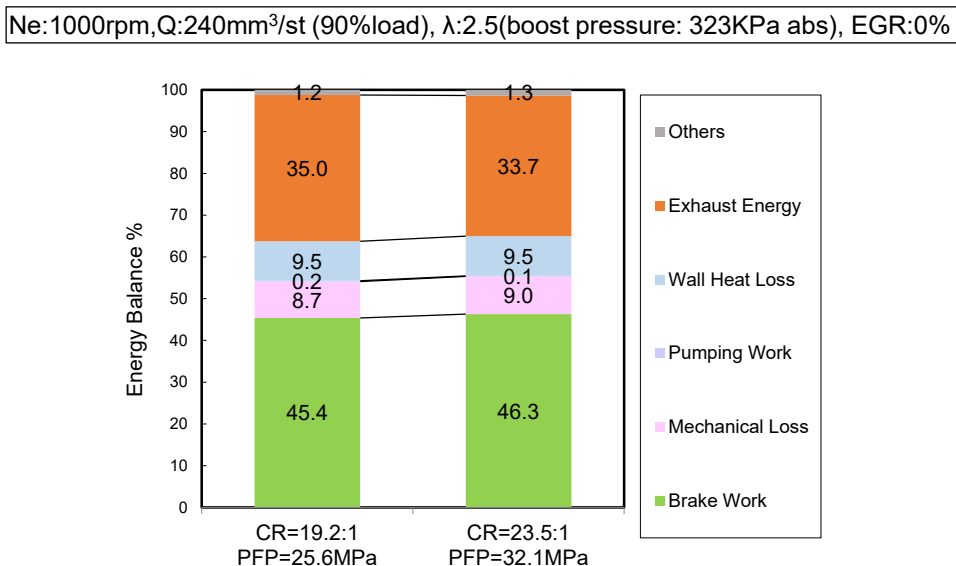
Fig. 14. Comparison of energy balance between ε=19.2:1 and 23.5:1 (the same data as Fig.13)

In general, theoretical thermal efficiency is higher for the combustion of much concentrated HRR around TDC. However, significant increase in PFP made it difficult. Looking back to Figure 8, volume change rate for the higher compression ratio is gradually increased and exceeds that for the cylinder offset at 10 degrees after TDC. To fully utilize the higher volume change rate with higher compression ratio, the HRR profile was tailored to it by modifying the injection strategy of three injectors. Furthermore, higher compression ratio has a potential to improve thermal efficiency itself, so it could be possible to

achieve significant improvement in ITE without any other technologies to recover the in-cylinder pressure. The result indicates that PFP increase was successfully suppressed (cooling loss was also reduced simultaneously) without any deterioration in BTE by offsetting HRR toward the timing in the expansion stroke where the volume change rate is higher than around TDC. That is, the TDC concentrated combustion is not necessarily effective to achieve higher BTE. And the optimum HRR profile for higher compression ratio resulted in the novel-thermodynamic-cycle-like combustion as shown in Figure 4.
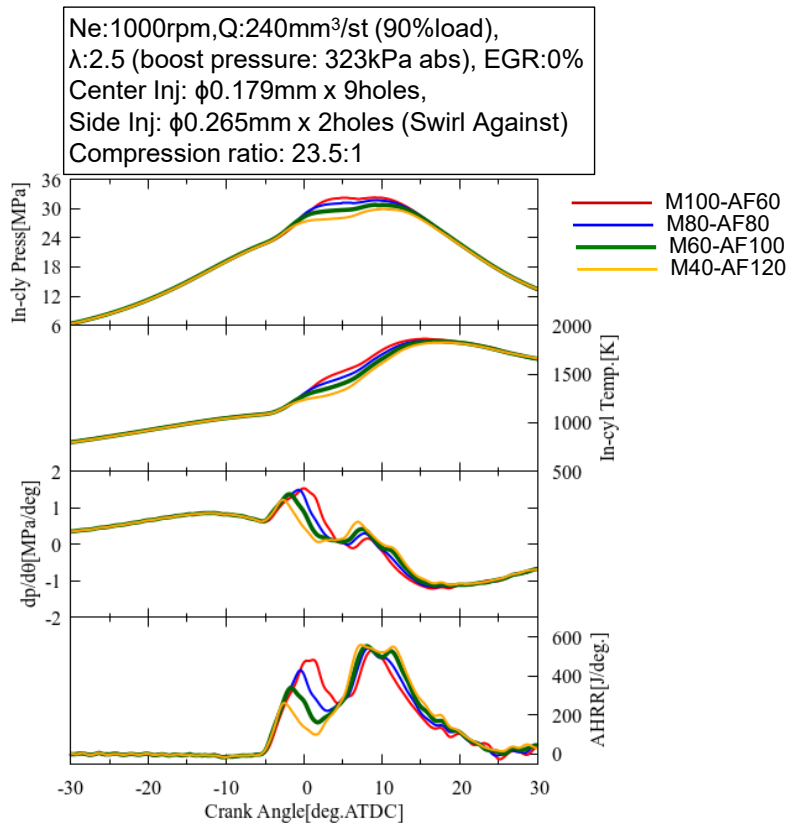
Fig. 15. HRR profile modulation by changing injection strategy of three injectors (Experiments)

Center injector: 160mm^3/st (M: Main, AF: After injection)
Side injector: 40mm^3/st each
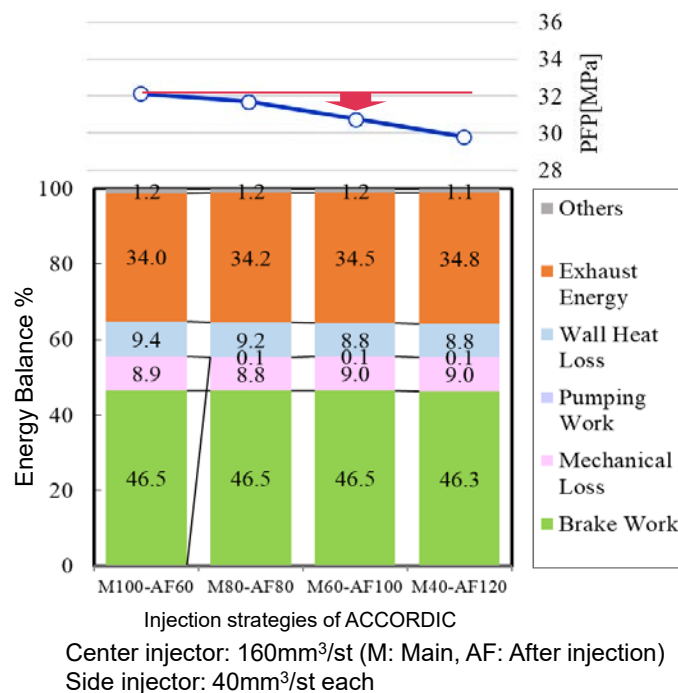
Fig. 16. Comparison of energy balance for modulated HRR profiles under ε= 23.5:1 (the same data as Fig.15)

Summary

It was experimentally confirmed that the higher PFP the more BTE can be achieved. From the optimum HRR control view point, modified Sabathe-like cycle was proposed, and experimentally confirmed increase in BTE by allowing slightly higher PFP in the expansion stroke than Sabathe-like cycle.

Then, to achieve further improvement in BTE under existence of PFP constraint, the effect of combination of the cylinder offset to the anti-thrust side and the shortened combustion period was investigated. Increase in volume change rate during diffusion combustion phase by the cylinder offset was anticipated to suppress the increase in PFP. The experimental results with the cylinder offset to the anti-thrust side showed the decrease in PFP as expected, however, the effect was no more than the delay of fuel injection timing for the interval between the crank shaft TDC and the piston trajectory TDC. Furthermore, increase in HRR (by shorten the combustion duration) to recover the deterioration of indicated work did not have further potential to improve both BTE and ITE from the baseline condition. That is, increase in η_{gl} under the existence of PFP constraint will not so effective for the thermal efficiency improvement, since it could be insensitive in such high load conditions.

By contraries, it is better to increase the compression and/or expansion ratio instead for achieving higher BTE even with the existence of PFP constraint. Furthermore, there should be more rooms to achieve lower PFP and improved cooling loss simultaneously with maintaining the optimum BTE by modulating HRR profile to be tailored to the timing, at where volume change rate is increased by the higher compression ratio.

Acknowledgements

References

[1] Chen SK and Flynn FK. Development of a Single Cylinder Compression Ignition Research Engine. SAE paper 650733, 1965.

[2] Delgado O and Lutsey N. The U.S. SuperTruck Program. ICCT White Paper, https://theicct.org/sites/default/files/publications/ICCT_SuperTruck-program_20140610.pdf (2014, accessed 28 Feb 2020).

[3] Uchida N, Okamoto T and Watanabe H. A new concept of actively controlled rate of diesel combustion for improving brake thermal efficiency of diesel engines: Part 1 - verification of the concept. *Int J Eng Res* 2018; 19(4):474–487.

[4] Uchida N and Watanabe H. A new concept of actively controlled rate of diesel combustion (ACCORDIC): Part II—simultaneous improvements in brake thermal efficiency and heat loss with modified nozzles. *Int J Eng Res* 2019; 20(1):34–45.

[5] Enya K and Uchida N. Enhancing Peak Firing Pressure Limit for Achieving Better Brake Thermal Efficiency of a Diesel Engine. SAE paper 2019-01-2180, 2019.

[6] Woschni G. A Universally Applicable Equation for the Instantaneous Heat Transfer Coefficient in the Internal Combustion Engine. SAE paper 670931, 1967.

[7] Uchida N, Galpin J, Watanabe K et al. Numerical and Experimental Investigation into Brake Thermal Efficiency Optimum Heat Release Rate for a Diesel Engine. SAE paper 2019-24-0109, 2019.

[8] Tsurushima T, Harada A, Iwashiro Y et al. Thermodynamic Characteristics of Premixed Compression Ignition Combustions. SAE Paper 2001-01-1891, 2001.

[9]   Nakamura M. A Study on the Effect of Crankshaft Offsetting on Fuel Economy in a Diesel Engine. JSAE paper 20164163 (in Japanese), *Trans JSAE* 2016; 47(2):313-318.

Mechanism of Thermal Efficiency Improvement in Twin Shaped Semi-Premixed Diesel Combustion

K. Inaba, Y. Zhang, Y. Kobashi, G. Shibata and H. Ogawa

Graduate School / Faculty of Engineering. Hokkaido University. N13, W8, Kita-ku, Sapporo, Japan.

E-mail: h-ogawa@eng.hokudai.ac.jp
Telephone: +(81) 11 706 6434

Abstract. Improvements of the thermal efficiency in twin shaped semi-premixed diesel combustion mode with premixed combustion in the primary stage and spray diffusive combustion in the secondary stage with multi-stage fuel injection were investigated with experiments and 3D-CFD analysis. For a better understanding of the advantages of this combustion mode, the results were compared with conventional diesel combustion modes, mainly consisting of diffusive combustion. The semi-premixed mode has a higher thermal efficiency than the conventional mode at both the low and medium load conditions examined here. The heat release in the semi-premixed mode is more concentrated at the top dead center, resulting in a significant reduction in the exhaust loss. The increase in the cooling loss is suppressed to a level similar to the conventional mode. In the conventional mode the rate of heat release becomes more rapid and the combustion noise increases with advances in the combustion phase as the premixed combustion with pilot and pre injections and the diffusive combustion with the main combustion occurs simultaneously. In the semi-premixed mode, the premixed combustion with pilot and primary injections and the diffusive combustion with the secondary injection occurs separately in different phases, maintaining a gentler heat release with advances in the combustion phase. The mechanism of the cooling loss suppression with the semi-premixed mode at low load was investigated with 3D-CFD. In the semi-premixed mode, there is a reduction in the gas flow and quantity of the combustion gas near the piston wall due to the suppression of spray penetration and splitting of the injection, resulting in a smaller heat flux.

Notation

CA50   *50% heat released crank angle*
EGR   *Exhaust gas recirculation*
IMEP   *Indicated mean effective pressure*
TDC   *Top dead canter*
η_{glh} *The degrees of constant volume heat release*
η_i *Indicated thermal efficiency*
η_u *Combustion efficiency*
ϕ_{ex} *Exhaust loss*
ϕ_p *Pumping loss*
ϕ_{other} *Other losses*
ϕ_w *Cooling loss*

1. Introduction

Premixed diesel combustion with a fuel injection relatively close to TDC, maintaining a sufficient ignition delay and ignition after the end of fuel injection with a large quantity of exhaust gas recirculation (EGR) has attracted much attention as a promising way for simultaneous reductions in nitrogen oxide (NOx) and particulate matter (PM) emissions as well as for achieving higher thermal efficiencies [1-9]. However, engine noise and limitations in the indicated mean effective pressure (IMEP) range due to the rapid combustion are serious issues impeding practical use. The rapid combustion can be suppressed with a large quantity of EGR, but carbon monoxide (CO) and total hydrocarbon (THC) emissions may increase with the increase in EGR, resulting in poorer thermal efficiency [7]. To overcome these disadvantages, there are several reports of the semi-premixed diesel combustion mode, with a first-stage premixed combustion of the primary injection and a second-stage spray diffusive combustion of the secondary injection suppressing the rapid first-stage premixed combustion, realizing a wider IMEP range with overall milder combustion [10 - 19]. The CO and THC formed in the first-stage premixed combustion are

oxidized with the second-stage spray combustion, resulting in the improvements in combustion efficiency. The authors have established efficient and clean semi-premixed diesel combustion mode with systematic investigations of the effects of operating parameters including intake gas and fuel injection conditions on the combustion characteristics over a wide operating range [17 - 19].

In this report, the energy balances and the exhaust gas emissions in the optimized semi-premixed diesel combustion mode and in the typical conventional diffusive diesel combustion mode mainly with diffusive combustion were compared to show the superiority of the semi-premixed mode and the mechanisms of the thermal efficiency improvements were analyzed with 3-D CFD analysis. The heat release of the semi-premixed mode can be more concentrated at the top dead center, expecting to realize a significant reduction in the exhaust loss and a higher thermal efficiency than the conventional diffusive diesel combustion mode.

2. Experimental Apparatus and Procedure

The experiments were conducted on a single cylinder, four-stroke cycle, supercharged, direct injection diesel engine with a common-rail fuel injection system and low pressure loop cooled EGR. The specifications of the engine are shown in Table 1. The stepped-lip re-entrant type combustion chamber shown in Fig. 1 was used, establishing a reduction in cooling loss due to weaker in-cylinder gas motion with squish. A piezoelectric injector (Denso G3P) and ordinary diesel fuel (JIS No.2) were used in all experiments.

Table 1. Engine specifications

Engine type	DI, single cylinder
Bore and stroke	$\phi 85 \times 96.9$ mm
Displacement	550 cm^3
Nozzle hole	0.104 mm $\times$ 10 - 156°
Compression ratio	16.3 : 1
Swirl ratio (ratio of swirl rpm to engine rpm)	1.6 : 1
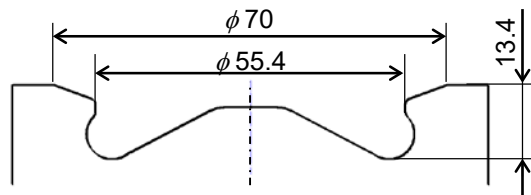
Fig. 1. The stepped-lip re-entrant type combustion chamber

Table 2 shows the engine operating conditions examined and detailed in section 4.1. A low load (IMEP ≈ 0.4 MPa, 1500 rpm) and a medium load (IMEP ≈ 0.7 MPa, 2000 rpm) were examined in the semi-premixed and the conventional diffusive diesel combustion modes. The total fuel injection quantity, Q_{total} at each load is fixed and the indicated mean effective pressures of the two modes are slightly different due to the change in thermal efficiency. The intake gas pressures were set with a supercharger driven by an electric motor and the exhaust gas pressure was adjusted to be equal to the intake gas pressure with a throttle valve, which modelled turbo-charged operation. The cooled EGR was realized with the exhaust gas passed through a diesel particulate filter (DPF) and an EGR cooler and the intake oxygen concentrations were set by adjusting the EGR quantity. The intake gas temperatures were set with an intercooler and a heater.

Figure 2 shows the fuel injection patterns and the typical rates of heat release in the semi-premixed diesel combustion mode and in the reference conventional diffusive diesel combustion mode at a medium load with the same total injection quantity. In the semi-premixed mode, the three-stage fuel injection with the pilot, primary, and secondary injections shown in (a) was used and the ignition timings and combustion phases were optimized for the indicated thermal efficiency [19]. The conventional mode, shown in (b), mainly consists in diffusive combustion with three-stage fuel injection including the pilot, pre, and main injections. This conventional mode is authorized by the Strategic Innovation Promotion

Program (SIP), "Innovative combustion technology" in Japan for reference and optimized in an engine for a commercial light duty vehicle with specifications similar to the engine in this experiment.

Table 2. Engine operating conditions in 4.1

Engine load	Low		Medium	
Engine speed [rpm]	1500		2000	
Total fuel injection quantity, Q_{total} [mg/cycle]	10		18	
IMEP [MPa]	≈ 0.4		≈ 0.7	
Intake gas pressure, P_{in} [kPa]	102 (N.A.)		120	
Intake oxygen concentration, O_{2in} [%]	15.5		16.5	
Intake gas temp., T_{in} [˚C]	60		40	
Combustion mode	Semi-premixed	Conventional diffusive	Semi-premixed	Conventional diffusive
Pilot injection quantity [mg/cycle]	3	1.5	4.5	1.5
Primary (pre) injection quantity [mg/cycle]	3	1.5 (pre)	4.5	1.5 (pre)
Secondary (Main) injection. quantity [mg/cycle]	4	7 (Main)	9	15 (Main)
Pilot injection timing [˚CA ATDC]	-13	-10	-10	-14
Primary (pre) injection Timing [˚CA ATDC]	-7	-2.75	-2.5	-3
Secondary (Main) injection timing [˚CA ATDC]	1.75	4	2.5	4.5
Fuel injection pressure [MPa]	100	100	200	135

The quantity and timing at each fuel injection stage are shown in the bottom half of Table 2. In both combustion modes three stage fuel injection was applied, but the quantities at the first and the second (pilot and primary) injections in the semi-premixed mode are much larger than the pre and pilot injections in the conventional mode to increase the premixed combustion and to decrease the diffusive combustion. In the experiments to investigate the effect of the combustion phase described in 4.2, the injection timings at all stages were simultaneously varied, maintaining the intervals and the quantities examined in 4.1.

The thermal efficiency related parameters were evaluated with the energy balance analysis. The energy balance during one cycle is described in Eq. (1).

$$\eta_i = \eta_u - \phi_{ex} - \phi_p - \phi_{other} \qquad (1)$$

η_i: The indicated thermal efficiency calculated with the fuel consumption per cycle and the in-cylinder pressure

η_u: The combustion efficiency calculated from the carbon monoxide (CO) and total hydrocarbon (THC) concentrations in the exhaust gas

ϕ_{ex}: The exhaust loss calculated from the change in enthalpy between the exhaust and intake gases considering the change in the specific heat with the temperature and gas compositions

ϕ_p: The pumping loss calculated with the in-cylinder pressure during the exhaust and intake strokes

ϕ_{other}: The other losses, calculated from Eq. (1), including the cooling loss as the main component and also the unburned fuel diluted into the lubricant oil

The pumping loss in this experiment can be considered negligible as the exhaust gas pressure was adjusted to be equal to the intake gas pressure with a throttle valve. Further, as both fuel injection timings in the first and second stages are set to be not far from the TDC, the fuel diluted into the lubricant oil is negligible in this experiment and ϕ_{other} is considered to be the cooling loss, ϕ_w, which is finally calculated from Eq. (1) as $\phi_w = \eta_i - \eta_u - \phi_{ex}$.
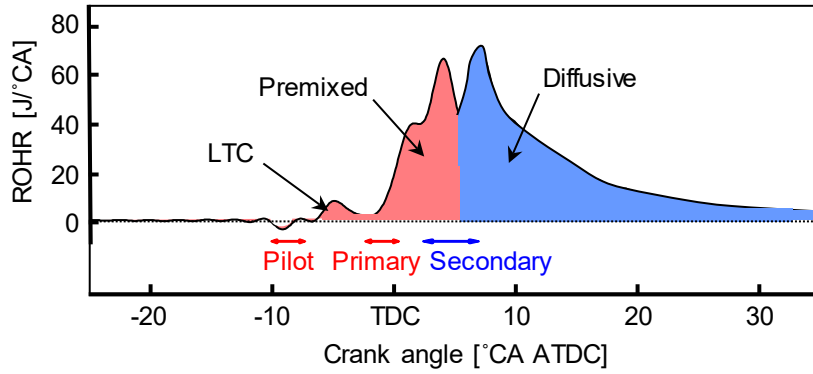
(a) Semi-premixed diesel combustion mode
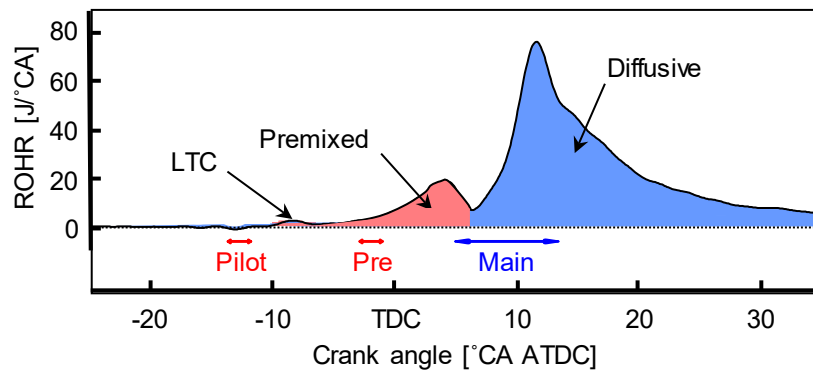
(b) Conventional diffusive diesel combustion mode

Fig. 2. Fuel injection patterns and the typical rates of heat release in the semi-premixed combustion and the reference conventional diffusive diesel combustion modes at a medium load with the same total injection quantity (The red and blue arrows show the timing and durations of the fuel injections)

3. Computational Mesh and Sub-models in CFD analysis

To investigate the combustion characteristics of the semi-premixed diesel combustion mode and the conventional diffusive diesel mode, numerical simulations were conducted using the 3-D CFD code AVL FIRE v2014. 1. Figure 3 shows the computational mesh of the stepped-lip re-entrant combustion chamber. To reduce the calculation time, a 36° sector mesh (corresponding to a single nozzle hole of the ten holes) was adopted. The average cell size is 0.5 mm and the total number of cells is around 172,000. Table 3 shows the sub-models for the spray [20], the turbulence [21], the mixture formation [22], the chemical reaction [23], and the heat transfer [24]. The fuel injection rates measured with the Bosch type rate of injection meter [25] in the experiments were applied for the simulations and the calculation was started from the IVC (intake valve closing).
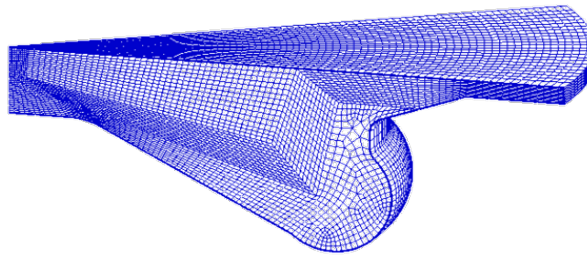
Fig. 3. Computational mesh of the stepped-lip re-entrant combustion chamber

Table 3. Sub-models in CFD code FIRE

Spray	Discrete droplet model
Evaporation	Dukowitz[20]
Breakup	KH-RT[20]
Turbulence	k-ζ-f model[21]
Turbulence interaction	PDF-Hybrid[22]
Chemical reaction	Tsurushima[23]
Heat transfer model	Han-Reitz model[24]

4. Results and Discussion

4.1 Comparison between the Semi-Premixed Diesel Combustion mode and the Conventional Diffusive Diesel Combustion mode

Figure 4 shows the in-cylinder gas pressure and the rate of heat release (ROHR) from the semi-premixed diesel combustion mode and the conventional diffusive diesel combustion mode at the low and medium load conditions. Here, the arrows under the curves indicate the timings and durations at the pilot, primary, and secondary fuel injections for the semi-premixed mode and at the pilot, pre, and main injections for the conventional mode. The combustion phases of the semi-premixed mode are around the top dead center, more advanced than of the conventional mode at both load conditions here. In the semi-premixed modes at both the low and medium loads, the heat release with low temperature oxidation from the pilot injection can be clearly seen before the primary injection and the first stage premixed combustion starts just after the end of the primary (second) injection, showing typical HCCI combustion.

(a) Low load (IMEP ≈ 0.4 MPa)

(b) Medium load (IMEP ≈ 0.7 MPa)
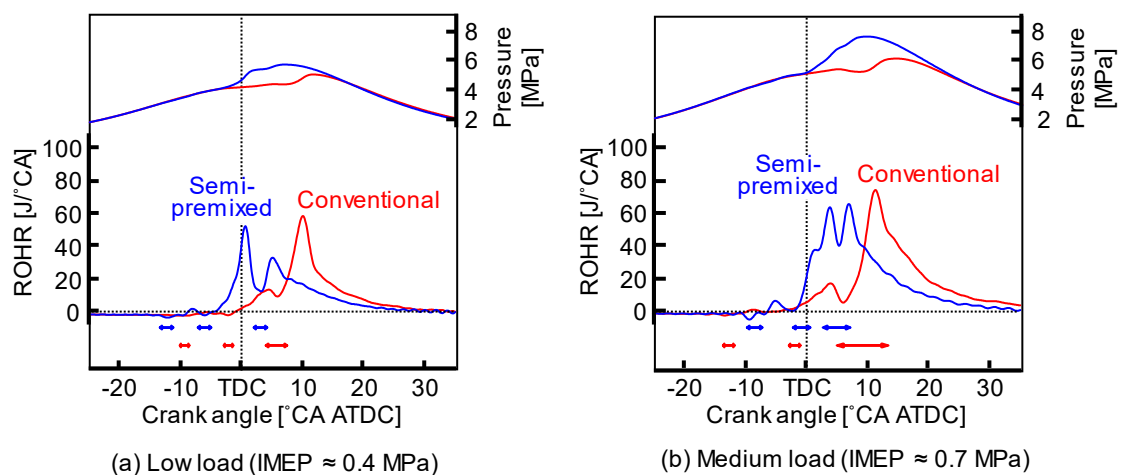
Fig. 4. The in-cylinder gas pressure and the rate of heat release (ROHR) from the semi-premixed diesel combustion and the conventional diffusive diesel combustion

Then, the second-stage diffusive combustion occurs just after the start of the secondary (third) injection. At the medium load, the two-stage premixed combustion with a shoulder shape just before the first peak due to the pilot and primary injections. The shoulder shaped part of the heat release is from the pilot injection and the first peak is mainly from the primary injection. The conventional modes at both loads also form two peaks; the first small peak is the premixed combustion from the pilot and pre injections and the second large peak is the diffusive combustion from the main injection. The quantities of the diffusive combustion of the semi-premixed modes are much smaller than in the conventional modes at both load conditions. Higher load operation than the medium load (0.7 MPa IMEP) was attempted with the semi-premixed mode, but the quantity of the primary injection cannot be increased due to the excessively large rate of pressure rise and the advantages at low and medium loads decreased.

Figure 5 shows the energy balances and the degrees of constant volume heat release, η_{glh} at the same conditions as in Fig. 4. The gross indicated thermal efficiencies, η_i in the semi-premixed diesel combustion modes are higher than in the conventional diffusive diesel combustion modes. This is due to smaller exhaust losses with improvements in the degrees of constant volume heat release mainly resulting from the advances in the combustion phases. Especially, at the medium load, there is a 2.5% improvement in the indicated thermal efficiency with reductions in the exhaust loss without increases in the cooling loss. The cooling losses from the semi-premixed mode with the early combustion phases are similar to the conventional mode with the later combustion phases at the low and medium loads. The cooling loss generally displays a trade-off relation to the exhaust loss and increases with advances in the combustion phase. However, the increases in the cooling losses are suppressed in the semi-premixed combustion mode.
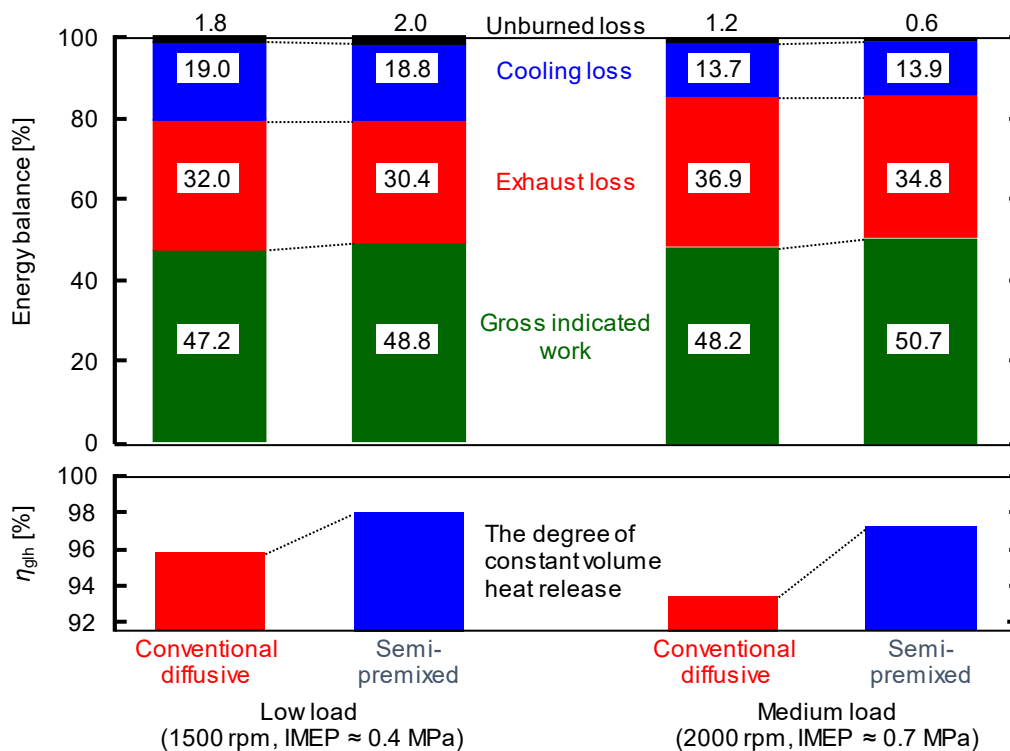
Fig. 5. The energy balances and the degrees of constant volume heat release, η_{glh} at the same conditions as in Figure 4

Figure 6 shows the maximum rate of pressure rise, $dP/d\theta_{max}$, the combustion noise, the NOx, and smoke emissions at the same conditions as in Fig. 4. In the semi-premixed diesel combustion modes, the maximum rate of pressure rise and the combustion noise are larger at both loads due to the earlier combustion phases than in the conventional diffusive diesel combustion mode with the retarded combustion phases. However, the differences in combustion noise between the semi-premixed mode and the conventional mode are only 2 dBA at the low load and 1 dBA at the medium load, minimizing the increases in the combustion noise by the dividing of the combustion. At the medium load the smoke emissions in the semi-premixed mode are much lower than in the conventional mode,

maintaining a similar low NOx level. At the low load the NOx and smoke emissions from the semi-premixed mode are sufficiently low, similar to the conventional mode.

To summarize the results so far, the semi-premixed diesel combustion mode has the potential to improve the indicated thermal efficiency without increases in the combustion noise and exhaust gas emissions. However, in the conventional diffusive diesel combustion modes compared so far, the combustion phases are more retarded than the optimum for the thermal efficiency to suppress the combustion noise, and the degree of constant volume heat release and the indicated thermal efficiency can possibly be improved by advancing the combustion phases. To evaluate such an advantage of the semi-premixed mode the influence of the combustion phases on the characteristics in the semi-premixed and the conventional modes are compared and discussed in the next section.
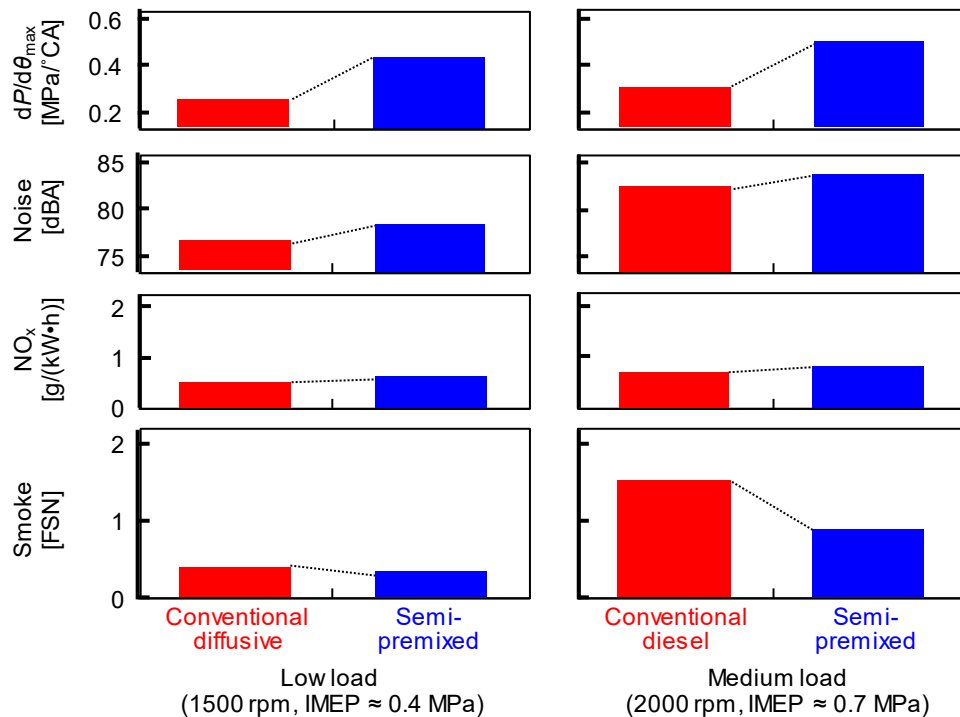
Fig. 6. The maximum rate of pressure rise, dP/dθmax, the combustion noise, the NOx and smoke emissions at the same conditions as in Fig. 4.

4.2 Influence of the Combustion Phase

Figure 7 shows the in-cylinder gas pressure and the rate of heat release (ROHR) for different combustion phases changed with the fuel injection timings in the semi-premixed and the conventional diffusive diesel modes at the low load condition (IMEP ≈ 0.4 MPa). Here, the arrows below the diagrams indicate the fuel injection timings and the durations at each stage. In the conventional mode the rate of heat release becomes more rapid with advances in the combustion phase as the premixed combustion with pilot and pre injections and the diffusive combustion with the main combustion occurs simultaneously. In the semi-premixed mode, the shapes of the rate of heat release are not significantly changed and maintain the mild heat release like the premixed combustion with pilot and primary injections and the diffusive combustion with secondary injection occurs separately in the different phases.

Figure 8 shows the influence of the combustion phase on the thermal efficiency related parameters (the indicated thermal efficiency, η_i, the combustion efficiency, η_u, the exhaust loss, ϕ_{ex}, and the cooling loss, ϕ_w) at the same conditions as in Fig. 7, with the combustion phase (50% heat released crank angle, CA50) as in the abscissa. Here, the solid symbols (blue: semi-premixed, red: conventional) are the results also shown in Fig. 4. As the combustion phase advances, the indicated thermal efficiencies improve, mainly due to decreases of the exhaust losses in both combustion modes. The exhaust losses in the semi-premixed mode are smaller than in the conventional mode at the same combustion phases, resulting in the higher indicated thermal efficiencies in the semi-premixed mode. The cooling loss in the conventional mode early in the combustion phase is larger than the other cases while there

is no increase with advancing combustion phasing in the semi-premixed mode. The larger cooling loss in the early conventional mode may be due to the rapid combustion as suggested by Fig. 7 (b), and a further reason for this will be discussed in 3.3 below.

Figure 9 shows the maximum rate of pressure rise, $dP/d\theta_{max}$ and the combustion noise at the same conditions as in Figs. 7 and 8. Here, the solid symbols (blue: semi-premixed, red: conventional) are the results also shown in Fig. 4. In both combustion modes the maximum rate of pressure rise and the combustion noise increase as the combustion phases advance. Particularly, the combustion noise from the conventional combustion in the advanced CA50 condition is larger due to the rapid combustion shown in Fig. 7.

(a) Semi-premixed

(b) Conventional diffusive
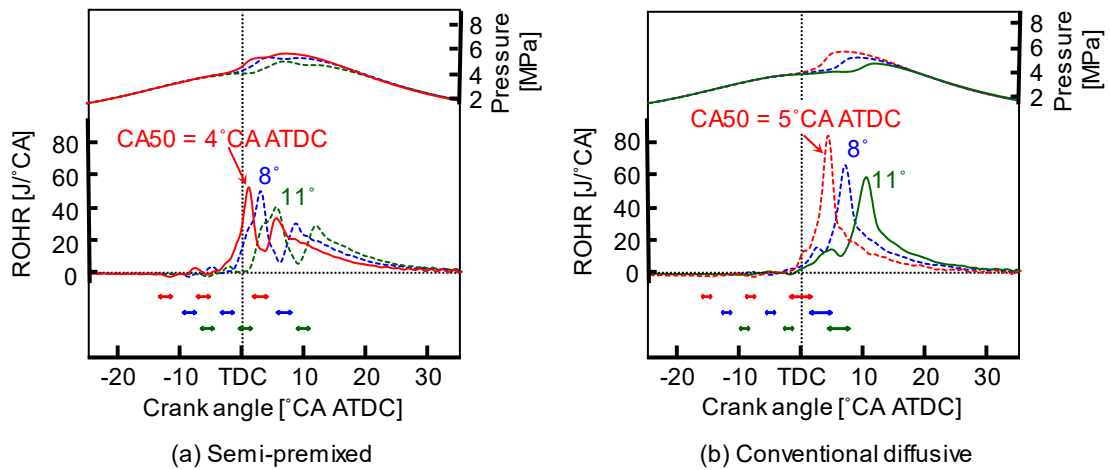
Fig. 7. The in-cylinder gas pressure and the rate of heat release (ROHR) for different combustion phases (IMEP ≈ 0.4 MPa)
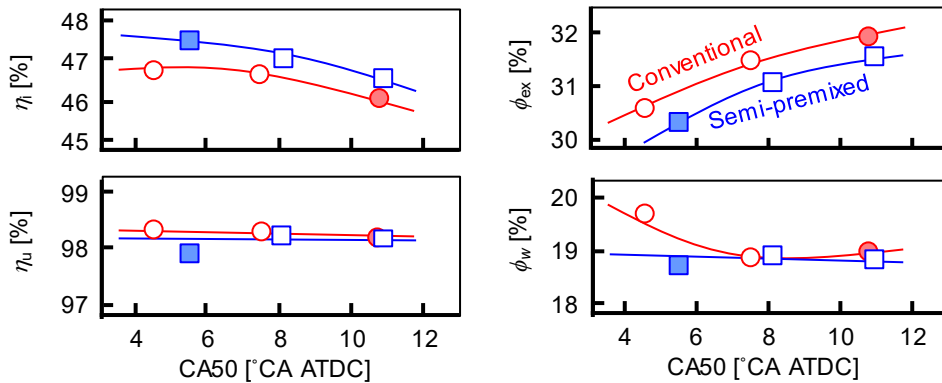
Fig. 8. The influence of the combustion phase on the thermal efficiency related parameters (indicated thermal efficiency, η_i, combustion efficiency, η_u, exhaust loss, ϕ_{ex}, and cooling loss, ϕ_w) at a low load (1500 rpm, IMEP ≈ 0.4 MPa)
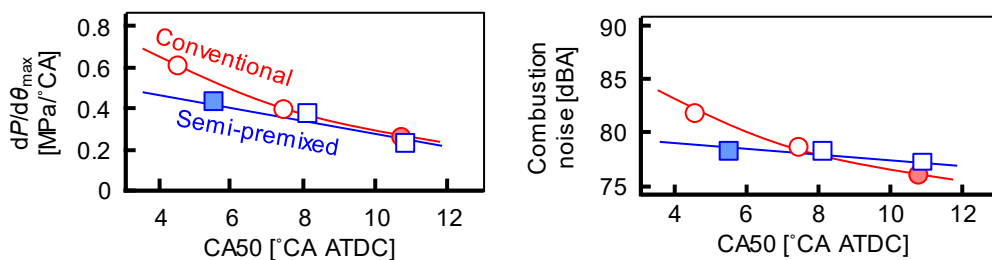
Fig. 9. The maximum rate of pressure rise, $dP/d\theta_{max}$, the combustion noise, and the exhaust gas emissions at a low load (1500 rpm, IMEP ≈ 0.4 MPa)

4.3 CFD Analysis on Mechanism of Thermal Efficiency Improvement in the Semi-pre-mixed Diesel Combustion

The experimental results so far have shown that the semi-premixed diesel combustion mode improves the thermal efficiencies mainly due to a reduction in the exhaust loss and without increasing the cooling loss. To elucidate the mechanism for this, the semi-premixed and conventional combustion modes were analyzed with the 3-D CFD code (AVL FIRE), mainly focused on the cooling loss.

Figure 10 shows the semi-premixed and the conventional modes with (a) the experiments and (b) the CFD for the analysis of the mechanism of thermal efficiency improvement with the semi-premixed combustion mode. The analysis here is for the semi-premixed mode in the red solid curves in Fig. 7 (a) and the conventional combustion in the red broken curves in Fig. 7 (b), which show the early combustion phases and are optimized for the thermal efficiency in both modes. The results with the CFD are very similar to the experiments, assuring a sufficient validity of the CFD.

(a) Experiments   (b) CFD
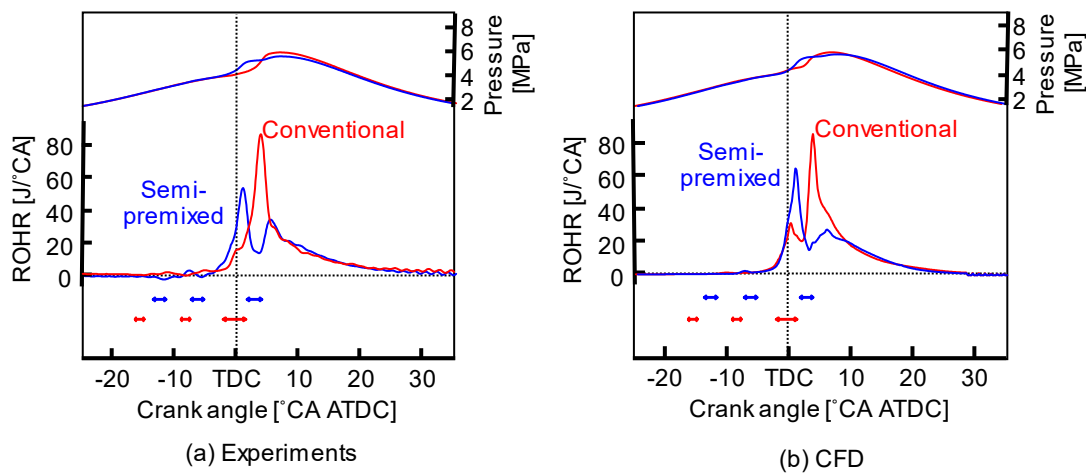
Fig. 10. The semi-premixed and the conventional modes for the analysis on mechanism of thermal efficiency improvement with the semi-premixed mode (1500 rpm, IMEP ≈ 0.4 MPa)

Figure 11 shows the rate of cooling loss, $dQ_w/d\theta$ and the integrated cooling loss normalized by the total energy supply, Q_w with the CFD analysis (the in-cylinder pressure and the rate of heat release are shown in Fig. 9 (b)). The percentages in the right panel show the calculated cooling loss differences from CA10 to CA50. In the conventional combustion mode, the rate of cooling loss rapidly increases just after the ignition and here the maximum rate of cooling loss is larger than in the semi-premixed combustion mode. The semi-premixed combustion mode shows the gentle increase of the rate of cooling loss with two stages and smaller $dQ_w/d\theta$, resulting in the much smaller cooling loss between CA10 and CA50.
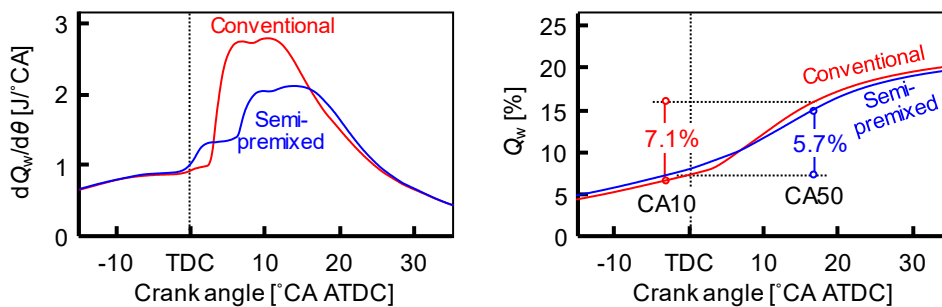
Fig. 11. The rate of cooling loss, $dQ_w/d\theta$ and the integrated cooling loss normalized by the total energy supply, Q_w with the calculation (1500 rpm, IMEP ≈ 0.4 MPa)

Figure 12 shows the plots of gas temperature, gas velocity, and heat flux along the piston top surface shown in Fig. 13. In the conventional mode at 4°CA ATDC the gas velocities are very fast and the high heat flux spreads widely on the lip of the combustion chamber where the fuel sprays impinge. In the semi-premixed combustion, there are also high temperature areas, but they are smaller and the gas velocities are much slower, resulting in the much smaller high heat flux areas despite the primary premixed combustion already having completed. This may be due to the slower impinging fuel spray on the piston wall and the decreases in the burned gas quantity near the piston wall due to the smaller fuel injection quantity per one stage and the suppression of fuel spray penetration with the dividing of the fuel injection. At 8°CA ATDC the high heat flux areas on the lip appears with the secondary combustion in the semi-premixed combustion, but the areas with high gas temperature, faster velocity, and high heat flux areas are smaller than in the conventional mode. At 12°CA ATDC the rates of heat release from both modes are similar as shown in Fig. 10, but the high heat flux area in the semi-premixed mode is still smaller than in the conventional mode and the rate of cooling loss is much smaller as shown in Figure 11.
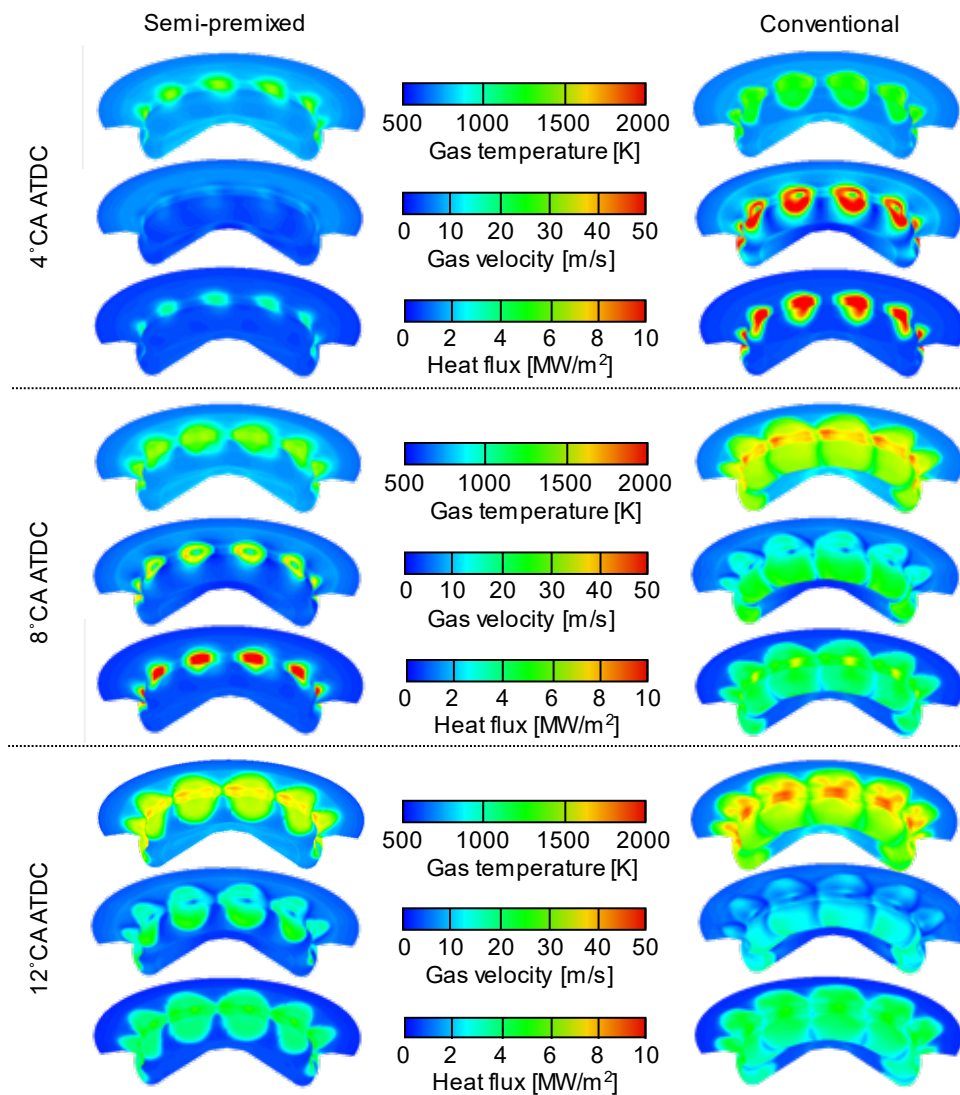
Fig. 12. Plots of gas temperature, velocity, and heat flux along the piston top surface (1500 rpm, IMEP ≈ 0.4 MPa)
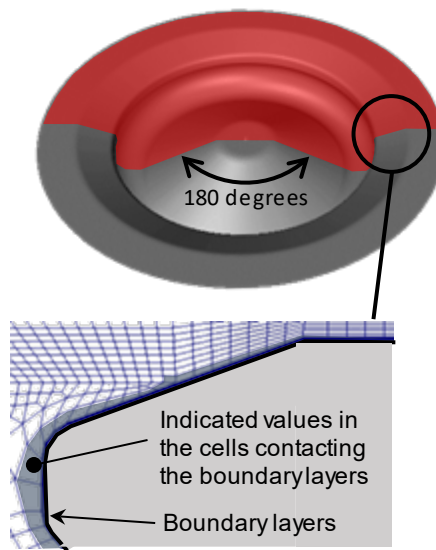
Fig. 13. Indicated area of piston surface in Fig.12

5. Summary

In this report, the twin shaped semi-premixed diesel combustion mode which releases half of the total heat with the premixed combustion and the conventional diesel combustion mode with mainly diffusive combustion were compared to show the superiority of the semi-premixed mode, and the mechanisms of the thermal efficiency improvements were analyzed with 3-D CFD analysis. The results may be summarized as follows:

1. The semi-premixed diesel combustion mode has a higher thermal efficiency than the conventional diffusive diesel combustion mode at both low and medium load conditions. The heat release of the semi-premixed mode is more concentrated at the top dead center, realizing a significant reduction in the exhaust loss with the higher degree of constant volume heat release. In the semi-premixed combustion with the optimized combustion phase, the cooling losses are also smaller than the conventional mode with the similar combustion phasing.

2. In the semi-premixed diesel combustion mode, the maximum rate of pressure rise and the combustion noise is slightly larger at both the low and medium load conditions due to the earlier combustion phases than in the retarded conventional diffusive diesel combustion mode. However, the increases in combustion noise from the retarded conventional mode are only 2 dBA at the low load and 1 dBA at the medium load, the combustion noise minimized by dividing the combustion.

3. At the medium load the smoke emissions in the semi-premixed mode are much lower than in the retarded conventional mode without significant increases in NOx emissions. At the low load the NOx and smoke emissions from the semi-premixed mode are sufficiently low and similar to the retarded conventional mode.

4. In the conventional mode the rate of heat release becomes more rapid with advances in the combustion phase as the premixed combustion with pilot and pre injections and the diffusive combustion with the main combustion occurs simultaneously. In the semi-premixed mode, the premixed combustion with pilot and primary injections and the diffusive combustion with secondary injection occur separately in the different phases, maintaining a gentle heat release with the advances in the combustion phase.

5. The CFD analysis showed that the cooling loss in the advanced conventional mode rapidly increases just after the ignition and that the maximum rates of cooling loss are much larger than in the semi-premixed combustion mode which shows a gentle increase with two stages, resulting in the much smaller cooling loss.

6. The range of high gas temperature and fast gas flows near the combustion chamber wall in the semi-premixed mode is smaller due to the smaller fuel injection quantity per injection stage when dividing the fuel injection than in the conditions of the advanced conventional mode, establishing the smaller heat flux and cooling loss.

Acknowledgments

References

1. Akihama, K., Takatori, Y., Inagaki, K. et al., "Mechanism of the smokeless rich diesel combustion by reducing temperature," SAE Technical Paper 2001-01-0655, 2001, doi:10.4271/2001-01-0655.

2. Hasegawa, R. and Yanagihara, H., "HCCI combustion in DI diesel engine," SAE Technical Paper 2003-01-0745, 2003, doi:10.4271/2003-01-0745.

3. Ickes, A. M., Bohac, S. V., and Assanis, N. D., "Effect of fuel cetane number on a premixed diesel combustion mode," Int. J. Engine Res. 10 (4): 251–263, 2009.

4. Li, T., Izumi, H., Shudo, T. et al., "Characterization of low temperature diesel combustion with various dilution gases," SAE Technical Paper 2007-01-0126, 2007, doi:10.4271/2007-01-0126.

5. Li, T., Suzuki, M., and Ogawa, H., "Effects of in-cylinder temperature and fuel air mixing quality on smokeless low temperature diesel combustion," Proc. COMODIA 2008; 135–142, 2008.

6. Li, T., Suzuki, M., and Ogawa, H., "Characteristics of smokeless low temperature diesel combustion in various fuel–air mixing and expansion of operating load range," SAE Technical Paper 2009-01-1449, 2009, doi:10.4271/2009-01-1449.

7. Ogawa, H., Li, T., and Miyamoto, N., "Characteristics of low temperature and low oxygen diesel combustion with ultra-high EGR," Int. J. Engine Res. 8 (4): 365–378, 2007.

8. Takeda, T., Nakagome, K. and Niimura, K., "Emission characteristics of premixed lean diesel combustion with extremely early staged fuel injection," SAE Technical Paper 961163, 1996, doi:10.4271/961163.

9. Ogawa, H., Xiong, Q., Obe, T. et al., "Improvements in Thermal Efficiency of Premixed Diesel Combustion with Optimization of Combustion Related Parameters and Fuel Volatilities," Int. J. Engine Res. 16 (1): 81–91, 2015.

10. Akagawa, H., Miyamoto, T., Harada, A. et al., "Approaches to Solve Problems of the Premixed Lean Diesel Combustion," SAE Technical Paper 1999-01-0183, 1999, doi:10.4271/1999-01-0183.

11. Hashizume, T., Miyamoto, T., Akagawa, H. et al., "Emission characteristics of a MULDIC combustion diesel engine: effects of EGR," JSAE Review; 23 (3): 428-430, 1999.

12. Horibe, N., Harada, S., Ishiyama, T. et al., "Improvement of premixed charge compression ignition based combustion by two-stage injection," Int. J. Engine Res. 10 (2): 71–80, 2009.

13. Kitamura, T. and Ito, T., "Mixing-Controlled, Low Temperature Diesel Combustion with Pressure Modulated Multiple-Injection for HSDI Diesel Engine," SAE Technical Paper 2010-01-0609, 2010, doi:10.4271/2010-01-0609.

14. Kuzuyama, H., Machida, M., Kawae, T. et al., "High Efficiency and Clean Diesel Combustion Concept Using Double Premixed Combustion: D-SPIA," SAE Technical Paper 2012-01-0906, 2012, doi:10.4271/2012-01-0906.

15. Fuyuto, T., Taki, M., Ueda, R. et al., "Noise and Emissions Reduction by Second Injection in Diesel PCCI Combustion with Split Injection," SAE Technical Paper 2014-01-2676, 2014, doi:10.4271/2014-01-2676.

16. Ikeda, H., Iida, N., Kuzuyama, H. et al., "An Investigation of Controlling Two-peak Heat Release Rate for Combustion Noise Reduction in Split-injection PCCI Engine Using Numerical Calculation," SAE Technical Paper 2014-32-0132., 2014, doi:10.4271/2014-32-0132.

17. Ogawa, H., Shibata, G., Sakane, Y. et al., "Semi-Premixed Diesel Combustion with Twin Peak Shaped Heat Release Using Two-Stage Fuel Injection," SAE Technical Paper 2016-01-0741, 2016, doi:10.4271/2016-01-0741.

18. Inaba, K., Ojima, Y., Masuko, Y. et al., "Thermal Efficiency Improvement with Super-charging and Cooled EGR in Semi-premixed Diesel Combustion with a Twin Peak Shaped Heat Release," Proc. THIESEL 2018, 2018.

19. Inaba, K., Masuko,Y., Zhang, Y., et al., "Thermal Efficiency Improvements with Split Primary Fuel Injections in Semi-Premixed Diesel Combustion with Multi-Peak Shaped Heat Release," SAE Technical Paper 2019-01-2170, 2019.

20. AVL FIRE VERSION 2014.1, Spray Module, 2014.

21. Hanjalic, K., Popovac, M., Hadziabdic, M., "A Robust Near-Wall Elliptic-Relaxation Eddy-Viscosity Turbulence Model for CFD," Int. J. Heat and Fluid Flow 25(6): 1047-1051, 2004, doi: 10.1016/j.ijheatfluidflow.2004.07.005.

22. AVL FIRE VERSION 2017, General Gas Phase Reactions Module, 2017.

23. Tsurushima, T. "A new skeletal PRF kinetic model for HCCI combustion," Proceedings of the Combustion Institute 32(2): 2835–2841, 2009, doi: 10.1016/j.proci.2008.06.018.

24. Han, Z., Reitz, R. D., "A Temperature Wall Function Formulation for Variable Density Turbulent Flows with Application to Engine Convective Heat Transfer Modeling," Int. J. Heat and Mass Transfer 40(3): 613-625, 1997, doi:10.1016/0017-9310(96)00117-2.

25. Bosch, W., "The Fuel Rate indicator: A New Measuring Instrument for Display of the Characteristics of Individual Injection," SAE 660749, 1966, doi:10.4271/660749

Predictive Thermal Load Analysis of an IC Engine Under Transient Operating Condition

A. Poredos[1], S. Gomboc[1], M. Kolaric[1], P.Sampl[2]

[1] AVL-AST d.o.o. Slovenia, Ulica Kneza Koclja 22, SI-2000 Maribor

Telephone: +(386) 2 229 45 29

[2] AVL List GmbH, Hans-List-Platz 1, 8020 Graz Austria

E-mail: hotline.austria@avl.com
Telephone: +(43) 316 787 555

Abstract. The internal combustion engine is facing one of the biggest challenges in its history, as the hunt for alternatives is more intense than ever. The competition is battery powered electric vehicles and fuel cell powertrains. However, it is anticipated, that with new technologies, further improving the efficiency of the combustion engine, in particular hybrid powertrains, will preserve the application of the ICE for the next decades as it has several advantages over the alternatives.

Compact and light weight designs with high specific power are the principal development directions for several years. Consequently, the engine components are being exposed to significantly higher mechanical and thermal loads, while on the other side increased thermal efficiency contributes directly to fuel savings and lower raw emissions. To balance performance parameters and durability, it is essential to understand the energy flows in the engine and to precisely evaluate the engines thermal load, as it helps preventing fatigue issues. Similarly, hybridized engines are exposed to potentially high alternating loads from zero to extreme within very short time periods. This again makes it necessary to predict structural temperatures under transient engine operating conditions accurately based on introduced combustion heat and heat dissipation through the cooling system. Only this way designing and calibrating of the engine and its cooling system can be done correctly, guaranteeing safe and failure-free operation.

In this paper the simulation workflow to determine the engine thermal load under transient operation is presented. It includes the use of a vehicle system model with all important sub-models such as engine model, cooling model and thermal network model. A 1D thermodynamic model provides boundary conditions for a 3D cylinder inner flow computation, which delivers the heat input to the engine structure and the 3D coolant flow simulation respectively. Unique models for fluid / structure heat transfer and their impact on simulation accuracy and engine design will be discussed. The 3D coolant flow simulation is being directly coupled with the thermal analysis of the structure within a single simulation. Simulation results have been validated against experiment on several use cases. Thus, the simulation methodology is applicable to all kind of combustion engines including gasoline, diesel and gas engines.

1. Introduction

The internal combustion engine has been primarily used as the undisputed enabler of individual mobility for decades. Now it is under enormous pressure in terms of increasing efficiency and performance while neutralizing its environmental impact in terms of pollutants and emissions. Designs are more and more compact and lightweight, whilst materials are exposed to a continuous increase of mechanical and thermal load.

As the industry is quickly moving towards electrification, the development time of the combustion engine should be even shorter and development costs shall to be continuously reduced.

This rush could lead to durability and reliability issues and an increase of warranty and maintenance costs, something that every OEM wants to avoid. Engineers are increasingly relying on simulations to fulfil these conditions as they are becoming more predictable and efficient. There are already several solutions available on the market for predictive IC engine thermal load analysis (Poredos et al. 2017, 2018). Two of the most frequently used methods are a decoupled CFD-FEA solution and a comprehensive closed coupled solution with simultaneous simulation of coolant flow and structural parts. Both methods are limited to simulation of stationary engine operating conditions.

In the new era of powertrain electrification and hybridisation, the IC engine can be exposed to even more extreme conditions. Due to the frequently alternating rotational speed and load, the components can undergo to even more fatigue-related failures and issues. Electrified powertrains lead to unfavourable operating profiles of the IC Engine – it runs more often under cold conditions under high load - a situation with is least desirable. Another critical scenario is the shutdown of the IC engine immediately at or shortly after very high loads are achieved (switching propulsion from IC engine to e-motor, uphill drive and immediate stop, pit stop during the race, …). To master these challenges, predictive simulations to compute the engines thermal load under steady but also transient conditions are very supportive.

This paper presents AVL's solution for simulating a complete combustion engine structural temperature under transient conditions. The solution is based on a system simulation model which provides boundary conditions for CFD simulations on component level. The target is to be predictive for all components of the vehicle with the focus on the combustion engine structural parts.

2. Vehicle Thermal Management Simulation

Let's assume a situation where during the vehicle development phase some IC engine structure overheating or thermal related fatigue appears. This can occur during road or chassis dyno testing, maybe even on an engine testbed. Investigation of the hardware itself is limited and difficult. However, a well calibrated simulation model can give an invaluable insight into the complete physical behaviour of the problematic component. In such cases, a multi-material closed coupled simulation of combustion, coolant flow and the structure can give an overview of the behaviour (Poredos et al. 2017, 2018) – hereinafter referred as a "Head Block Compound simulation" or "HBC simulation". It supports understanding of the phenomena to a great extent and provides the possibility of fast design optimisation by means of case studies considering different designs. Although the methodology is predictive and reliable, there is a big challenge of providing proper boundary conditions for such simulation. Simulation models can be prepared per component, but component models have to be connected. The most sophisticated comprehensive solution is to go on a big scale – a complete vehicle simulation.
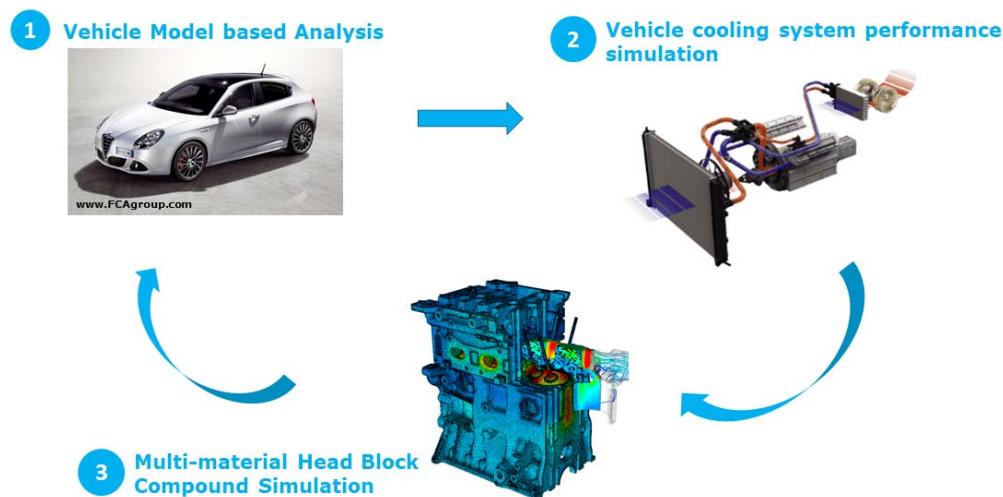
Fig. 1. Virtual thermal management system model

Fig. 1 presents the workflow used for obtaining most realistic boundary conditions required for the comprehensive Head Block Compound simulation. A vehicle thermal management system (VTMS) model is prepared and calibrated according to measurement data, if any hardware is already available. Such VTMS model also includes a sub-model of the engine cooling circuit, that can be used to obtain boundary conditions for HBC simulation. In return, simulation results of the HBC simulation, such as structural and coolant flow temperatures can be used to improve the accuracy of the complete VTMS in the next loop. Thereby, the predictability of the complete vehicle model is increased.

In the vehicle model all important vehicle parts like tires, braking systems, differentials (front, central rear, if existing), gearbox, clutch, and the complete powertrain (IC engine model in our case) are

modelled. The driver controller defines the current operating conditions of the vehicle, such as the vehicle velocity, engaged gear, engine load, etc.

The vehicle and engine model are connected and interact with each other. For example, the driver provides a load signal to the engine, generating a certain torque, which is applied to the drivetrain model. Based on the resistances defined in the powertrain model, a rotational speed is calculated and applied as the engine speed to the engine model. Based on the operation point of the engine (load and speed) and the current engine structure temperatures, heat and friction losses are evaluated and provided as a heat input for the thermal network model. In the thermal network model more accurate temperatures of the engine structure are calculated and applied to the engine model, where the heat and friction losses are evaluated for this new - improved set of temperature conditions. The VTMS model also includes sub-models of the engine cooling and lubrications circuits, which are connected to the thermal network model. This way, it is possible to continuously simulate the transfer of the generated heat during the combustion process through the engine structure and the coolant into the environment through the radiator and potentially other heat exchangers. Such system simulation models can be used to investigate the response and sensitivity of the entire system to a change introduced in one of the sub-systems. Every change on a component level results in a specific system response. The overview of the complete model, including heat and energy flow, is presented on Fig. 2.
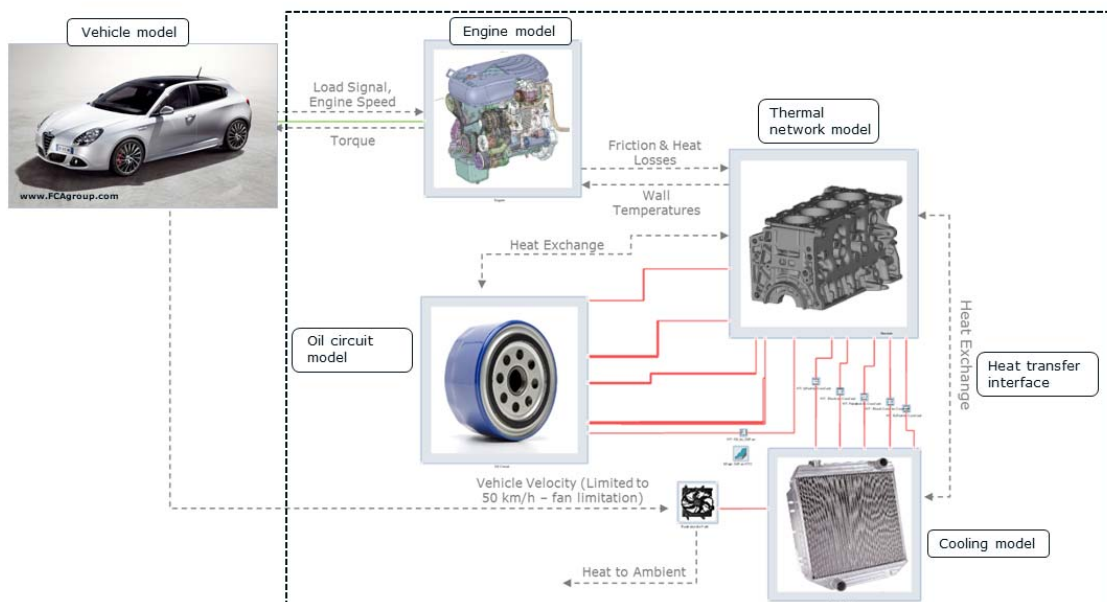
Fig. 2. VTMS model with all important heat flow related sub-models

VTMS models, such as the one in the Fig. 2, provides a comprehensive simulation solution for the complete vehicle. The simulation is performed with AVL CRUISE™ M. The model is calibrated to provide plausible results for the entire engine operating map (full load and various part-load conditions) and can therefore be used to simulate transient drive cycle scenarios. As such, the results obtained by this type of simulation can provide realistic boundary conditions for several different component level simulations (under-hood air flow simulation, head-block compound simulation, etc.). VTMS simulation results are usually used as a heat source and mechanical energy source for the transient drive cycle simulation, for example engine heat-up or cooldown simulation in extreme conditions.

On the other hand, VTMS simulations can also greatly benefit from component-level simulations. Some phenomena can only be observed in 3D simulations and these results can be used to recalibrate the VTMS model to improve its predictability. This way, many transient scenarios can be investigated with a reasonable degree of accuracy.

An engine model is presented in Fig. 3. The 0D air path includes the air cleaner, the compressor, the throttle and the intake manifold on the intake side, while the exhaust side includes the exhaust manifold, turbine, and the catalytic converter. The air path parts of the model provide the boundary conditions for the crank-angle resolved simulation of the combustion process. Such a model can be used to accurately compute, amongst other, the following flow variables:

- Time- (crank angle-) resolved conditions (mass-flow, fluid pressure and temperature, gas concentrations, …) at the intake and exhaust cylinder head flanges. These serve as boundary

conditions for 3D in-cylinder flow CFD simulations of the complete engine cycle. The extracted inner cylinder conditions from the 0D simulation serve as a reference data for combustion CFD simulations. In-cylinder CFD simulation results subsequently serve as a heat source for a complete engine structural thermal analysis (Poredos et. al 2017, 2018)

- Load-specific steady state coolant flow conditions - mass-flows and temperatures for all water-cooling jacket model inlets and outlets. These are used as boundary conditions for 3D coolant flow CFD simulations.
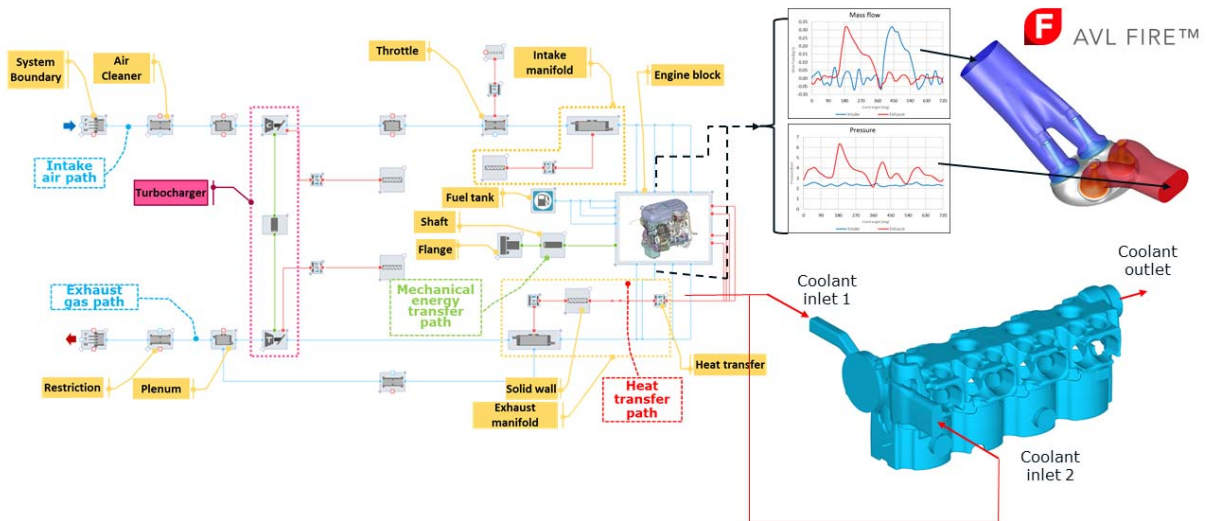
Fig. 3. Engine model

3. Multi-material modelling for engine thermal analysis

Increasing an engine's effective pressure induces higher thermal loads that can significantly reduce engine reliability, due to a higher risk of thermo-mechanical failures. Therefore, accurate prediction of the thermal field in the entire engine is a key for the subsequent thermal stress analysis which is employed to reveal and fix any potential design issues that might lead to abnormal combustion and engine failure.

The thermal analysis of an engine requires an integrated approach which begins with the in-cylinder simulation. The resulting wall heat transfer coefficients and gas temperatures are cycle-averaged in order to provide proper boundary conditions. Thermal boundary conditions, both convective and conductive, are pre-calculated with their spatial distributions based on the proper physical models. In addition, the heat generated by friction is determined (Poredos et al, 2017). Subsequently, all thermal boundary conditions together are applied to the entire component group (block, pistons, rings, pins) and the temperature distribution in the whole assembly, including the water-cooling jacket, is calculated by means of a multi-material (conjugate heat transfer) simulation.

The methodology is validated by analyzing the real engine (Table 1.) and utilizing the available temperature measurements. A complete in-cylinder analysis, which considers gas exchange, fuel spray injection and combustion simulation, is usually performed only for one cylinder. The transient results for near-wall gas temperature and the heat transfer coefficient (HTC) from cylinder inner flow simulations have to be time-averaged over one complete engine cycle and applied as convective boundary conditions to the structure. Note that the thermal inertia of the solid components facing the combustion chamber is relatively high and structural temperature oscillations within one engine cycle can be noticed just on very thin surface layer, thus justifying cycle-averaging of the thermal loads. Expecting that all cylinders have the same time-averaged gas temperatures and HTC distributions, the convective boundary conditions of one cylinder are mapped to the surface of all four cylinders of the structural model depicted in Fig. 4.

In the multi-material approach the coolant flow simulation is performed simultaneously with the structural thermal analysis. The simulation accounts for all important physical phenomena, such as nucleate boiling (Steiner et al. 2011), temperature dependent material properties and thermal contact resistances between different solid materials. At this point, it is worthwhile to point out the importance of the boiling phenomenon and the experimental investigations reported by Robinson et al. (2003) and

Hawley et al. (2004). Single-phase Boiling Departure Lift-off (BDL) model (AVL FIRE™, 2017) has been enhanced in line with the proposed composite convection model (Robinson et al., 2007).

Table 1. Investigated engine geometrical data and operating condition

Geometrical data	Bore	83mm
	Stroke	80.5mm
	Connecting rod length	148.5mm
	Compression ratio	9.5
	Number of cylinders	4
	Configuration	Inline - straight
Operating condition	Rotational speed	5500
	Engine load	100%
	Equivalence ratio	1.06
	Spark timing	5^0CA BTDC
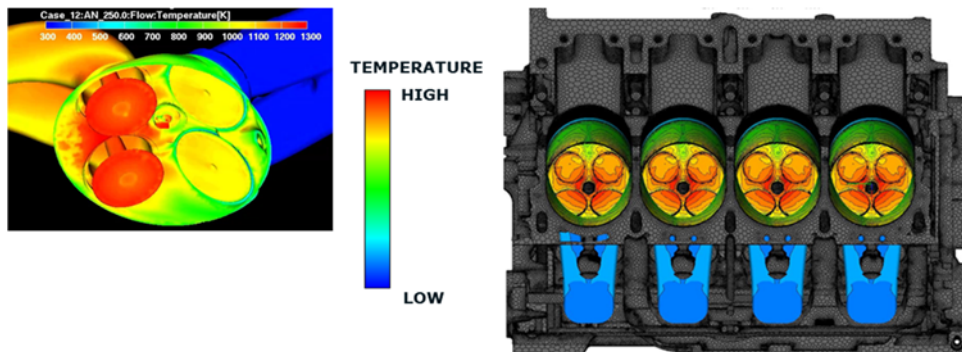
Fig. 4. Mapping of the gas side thermal boundary conditions
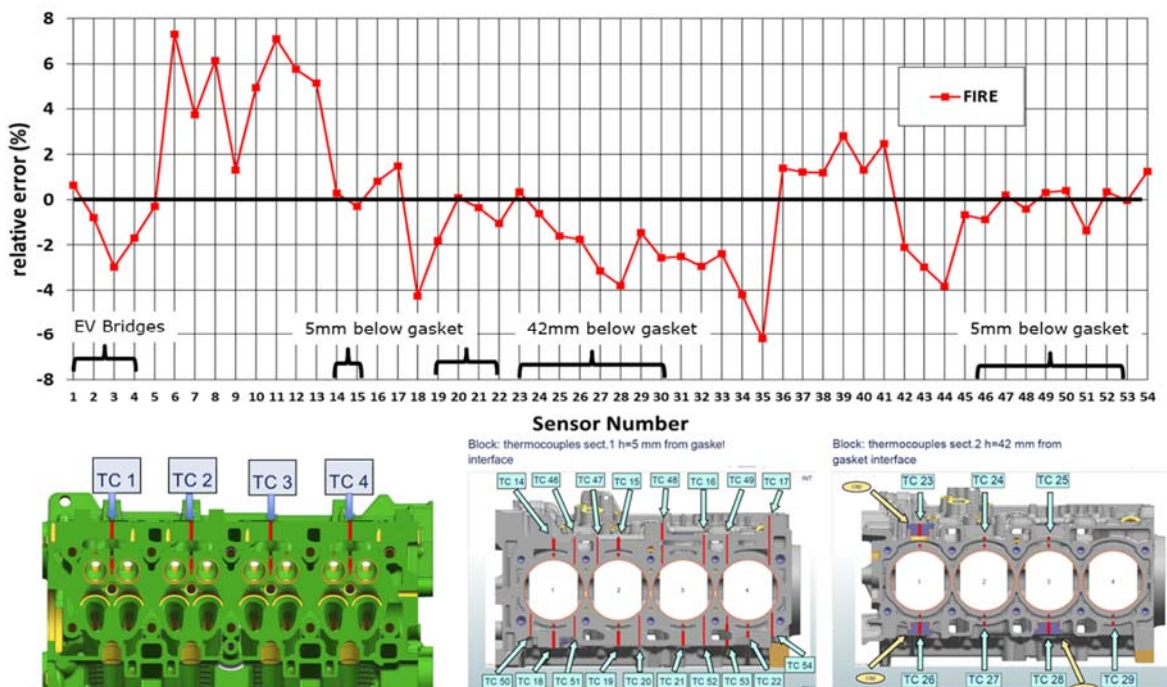
Fig. 5 The Relative error of the predicted temperatures against the thermocouple measurements at various locations in the cylinder head (#1-13) and the engine block (#14-54)

In total six million computational polyhedral cells were used, in a specific example, for a multi-material model consisting of 57 sub-domains and 9 different materials (incl. valves, valve seat inserts, valve guides, coolant fluid, aluminum alloy, liner etc.). The thermocouple measurements were performed at various positions in the cylinder head and cylinder block (detailed analysis is described in Poredos et al., 2017). A comparison between simulation results and measurements at the sensor locations for the cylinder head and the cylinder block is presented in Fig. 5. Although no estimate of uncertainty of the measured data is available, it is evident that the presented method yields accurate predictions of the local temperatures measured in the engine structure which are essential for the subsequent thermal stress analysis and serves as a good basis for the thermal structural analysis under transient engine operation.

Closer look to the thermo-couple distribution and the result quality reveals, that the locations closer to the cylinder gasket, show better agreement between simulated and measured values. These thermo-couples are located at the regions, where prescribed boundary conditions for the structural thermal analysis are provided by separately investigated simulations (like cylinder inner flow - combustion simulation). Locations closer to the outer engine surface and deeper towards the crankshaft, where structure is exposed to the empirically defined boundary conditions, show less accuracy in structural temperature prediction. All together it highlights the importance of the coupled simulations and the connections between them.

Special focus is required on analyzing critical areas, such as the exhaust valve bridges – thermo-couples 1 to 4. These locations showed the highest temperatures, which is a common critical area for every IC engine, resulting in a substantial boiling phenomena in the coolant flow and increased physical modeling complexity. With this, the underlining locations are extremely important from the stress and durability perspective. As illustrated, the temperature prediction at the critical locations was very good, increasing the value of the simulation method.

4. Thermal structural analysis under transient operating conditions

In Fig. 6. the simulation workflow chart for the transient engine cycle is presented on the left. The VTMS model must be prepared as described and the engine model should be part of it. As mentioned above, the latter provides boundary conditions for the cylinder inner flow (combustion) simulations, where one very high load (rated speed) and one very low load operating condition (idle) is investigated. A cylinder inner flow simulation of the complete engine cycle (720^0CA) needs to be executed for each operating condition separately. Results are cycle averaged and serve as a boundary condition for the structural thermal analysis, representing the main heat source load for the structure. In the next step a complete engine thermal analysis is done.
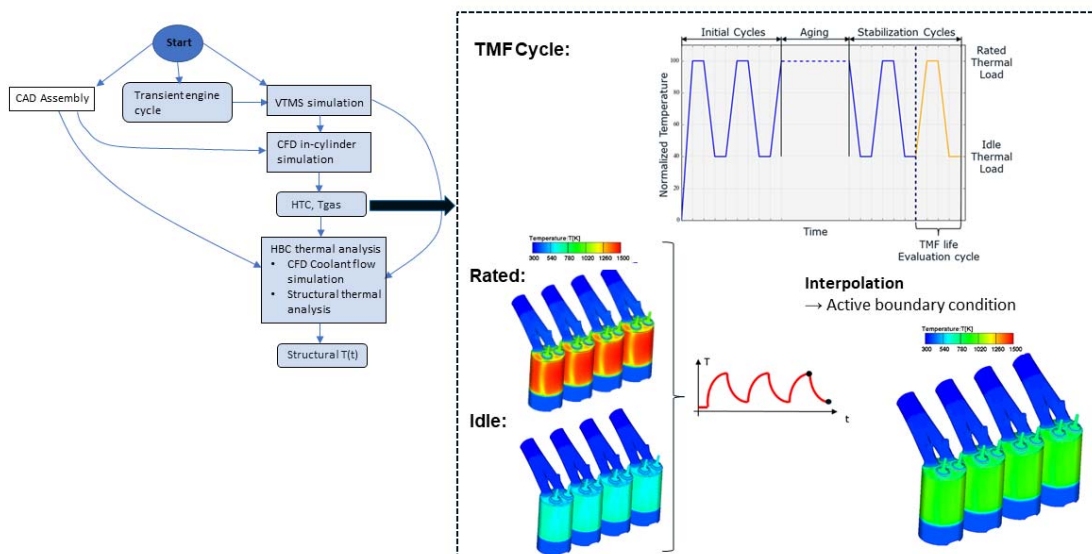
Fig. 6. Chart of simulation procedure for a transient cycle

The head-block compound simulation can also be run in transient mode. As already mentioned above, the thermal load resulting from the combustion simulation serves as a boundary condition and

can be varied with time. Time-dependent, so called "active boundary conditions" for the structural thermal analysis can be obtained by the interpolation between high and low load results.

On the right side of Fig.6. a typical cycle for a thermal material fatigue (TMF) simulation is shown. An alternating thermal load is applied to the structure and the number of cycles until fatigue appearance is calculated, which again serves as a basis for the life time prediction. Such simulation results provide very important input to the engine development process.

The right side of Fig.7. shows structural temperatures calculated for high (rated) and low (idle) load operating condition as a result of transient engine cycle simulation. For the TMF analysis the highest and the lowest thermal loads are the most important. Temperatures are calculated within AVL FIRE M™ multi-physics software by means of multi-material simulation described in the previous chapter. The structural thermal field is mapped to the finite element model (volume mapping). The structure is alternately exposed to high and low thermal loads. Based on that, a stress/strain analysis and a life time prediction simulation can be performed in the FEA software. With the new simulation method, the complexity of such simulations can be reduced to a great extent. The simulation workflow chart is illustrated on the left in Fig. 7.
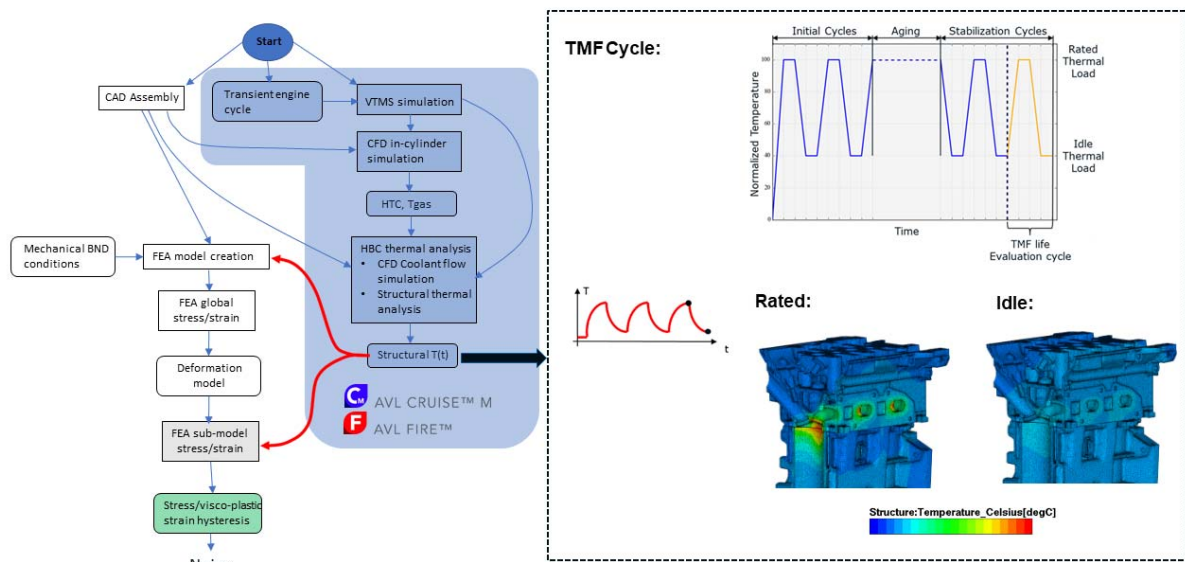
Fig. 7. Chart of simulation procedure for a TMF analysis

5. Example of transient engine operating condition simulation (uphill drive and stop)

Fig. 8 shows a simulation of an idle running engine which is suddenly exposed to an uphill drive. After engine start in cold conditions, it warms up under idle conditions (points 0-1). The acceleration
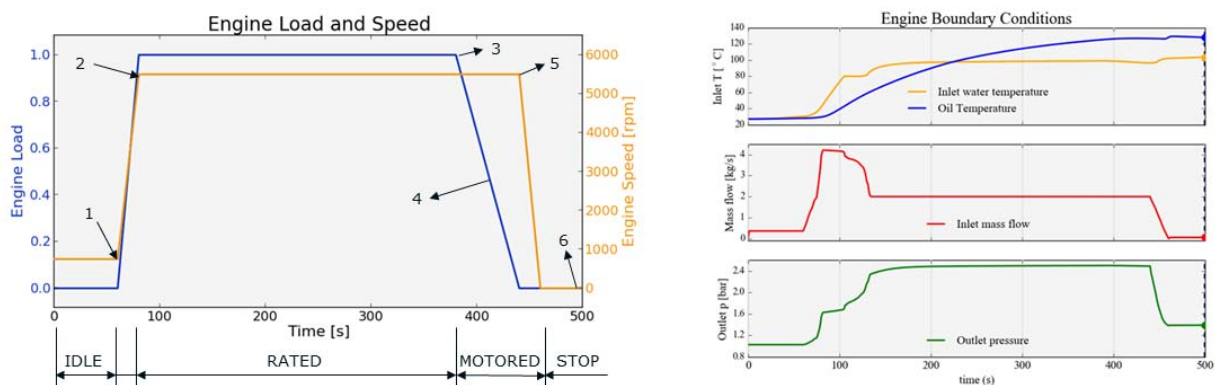
Fig. 8. Driving cycle example with corresponding WCJ BND conditions

phase to rated speed and load is relatively short (points 1-2). The vehicle moves uphill (points 2-3). After reaching the top of the hill, the engine load drops, but the vehicle keeps a constant velocity for a while, representing a short decent to the valley (points 3-4). This is reflected by maintaining maximal engine speed for some short time without any load (high idle motored conditions). After that the engine is turned off. The driving conditions are presented in the left diagram in Fig. 8. On the right side of the figure, the boundary conditions for the coolant flow are presented (obtained by a VTMS simulation). These reflect the engine speed and load conditions - as the engine load and rotational speed increases, the coolant flow temperature and mass-flow increase as well. Coolant mass-flow drops to zero after turning off the engine.
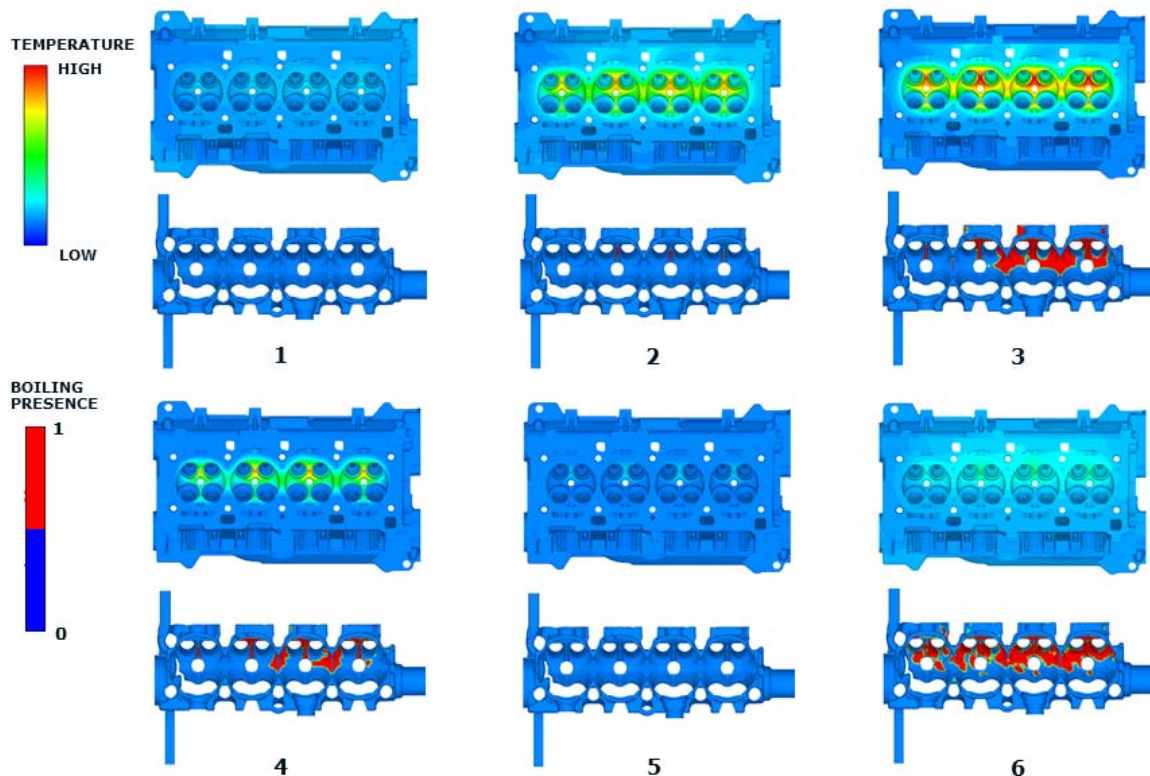
Fig. 9. Structural wall temperatures and boiling appearance at the coolant flow surface

Fig. 9. shows structural wall temperatures at different times of the driving cycle delineated in Fig. 8. The numbers points represent the characteristic points of the driving cycle:

- Point 1 represents structural temperature and boiling in the engine under idle conditions. Structural temperature is relatively low and no boiling effects can be noticed at the coolant flow surface.
- When the engine reaches the rated rotational speed and almost maximal load (Point 2), the structural temperature increases significantly and boiling in WCJ flow is barely noticeable at two of the exhaust valve bridges – an area which normally undergoes the highest load from the thermal point of view.
- After the engine is running at rated speed and power for some minutes (Point 3), the structural temperatures tend to reach the upper limit and the coolant experiences boiling conditions at a significant part of the wall area, impacting sensitive areas of the structure
- Point 4 in the diagram represents the conditions where the engine rotational speed is still at the maximum, but the load begins to drop. Structural temperature becomes lower and boiling intensity decreases.
- At Point 5 the engine still runs at the rated speed, but in motored conditions (no real load). Consequently, structural temperature is relatively low and there is no boiling in the coolant flow.
- The most critical conditions appear in point 6, when the structure is still not completely cold due to its heat capacity. With the engine and the water pump also convective heat transfer in the coolant stops. Heat conduction from the structure significantly heats up the coolant, which starts to boil again. This can lead to the critical conditions, causing the structural failure. Even in the best-case scenario, the situation is not harmless, as coolant flow deposits begin to be formed

(limescale) in the area where the coolant gets evaporated several times. Deposits as such have insulating effects, which leads to reduced cooling effectiveness and in long term further increases the possibility of structural failure.
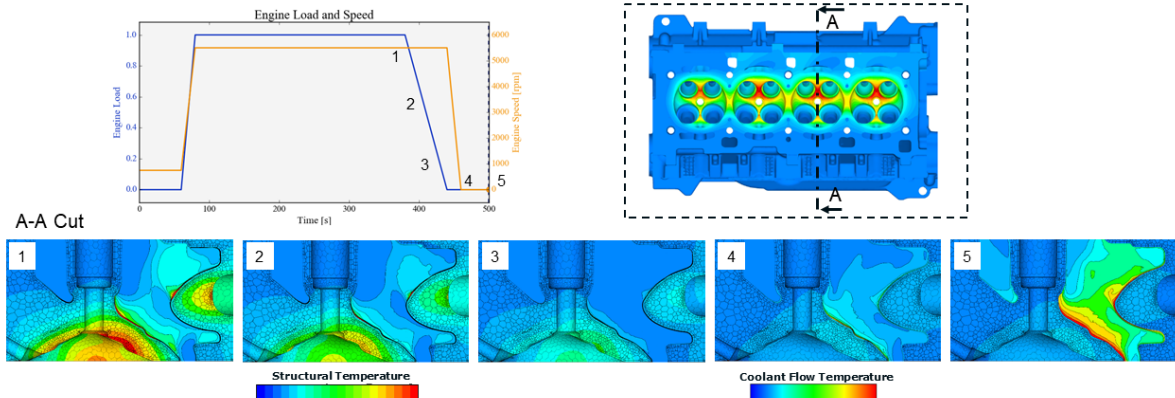
Fig. 10. Structural wall temperatures and boiling appearance at the engine model cross-section

In Fig. 10 the complete behavior of structural temperature, coolant flow boiling appearance in dependency of the engine rotational speed and load is presented in a cross-section through the complete engine structure and the coolant flow. The cross-section is positioned at the exhaust valve bridge – the region of the highest structural temperature in the complete model. Looking at specific locations usually provides more insight in the local conditions. For clearer and easier understanding, the temperature scaling has been adapted to reflect reference data for structural and coolant part of the model respectively.

To distinguish the different parts, the polyhedral computational mesh is displayed on the structural side, while the temperature field in the coolant flow is indicated by isolines.

- At Point 1 the structural temperature is high due to high load and high rotational speed.
- At Points 2 and 3 engine load is decreasing, while rotational speed is still high, therefore the structure and the coolant flow cool down. Both reach their lowest temperature at Point 4.
- Point 5 shows the situation when the structural temperature is relatively low, but still high enough to conduct heat into the coolant. Since the water pump has stopped operating, missing convective heat dissipation in the coolant causes excessive boiling. As already described above, such instances are critical and may lead to structural thermal failure.

The presented method is very versatile, therefore applicable to any transient engine operation mode. It serves as a solid basis for analysis, prediction and prevention of thermal structural failure which may appear under extreme, transient conditions.

Additionally, one of the biggest benefits of the presented comprehensive solution, consisting of a complete VTMS simulation coupled with a multi-material thermal analysis, is also a significantly simplified workflow for the TMF analysis (Fig. 7.)

6. Conclusions

This paper describes the AVL Solution for VTMS simulations with a focus on the FIRE™ M multi-material approach and recent related software development. The method is unique and offers a comprehensive solution for complete vehicle simulations. The VTMS model can provide reliable results for the entire engine operating map and can therefore be used to simulate transient drive cycles scenarios. As such, it provides the required boundary conditions for simulations on component level. When component simulations are done and calibrated, the complete VTMS model can benefit from that with respect to increased reliability and predictability. Subsequent VTMS simulation results are regularly used to provide the heat source and the mechanical energy source for transient drive cycle simulations, e.g. engine heat-up or cooldown simulations under extreme conditions. The workflow for simulating the thermal field in the entire engine structure including the coolant flow under transient operating conditions in a real driving cycle has been presented. The methodology can be used for simulating many different transient scenarios with a very high degree of accuracy.

References

Alkidas, A.C. and Myers, J.P.,1982:"Transient heat-flux measurements in the combustion chamber of a spark-ignition engine", J. Heat Transfer: T ASME Vol. 104, pp. 62-67, 1982

AVL List GmbH, 2019:"AVL FIRE™ manual, version 2019", Graz, Austria, 2019

AVL List GmbH, 2019:"AVL CRUISE™ manual, version 2019", Graz, Austria, 2019

Bovo, M., 2014:"Principles of Heat Transfer in Internal Combustion Engines from a Modeling standpoint", Ph.D. thesis, Chalmers University of Technology, Gothenburg, Sweden, 2014

Hawley, J. G., Wilson, M., Campbell, N. A. F., Hammond, G. P. and Leathard, M. J.,2004: "Predicting boiling heat transfer using computational fluid dynamics". Proceedings of the Institution of Mechanical Engineers, Part D: Journal of Automobile Engineering, 218 (5), pp. 509-520, 2004

Poredos, A., Kreuzwirth, G., Knaus, O. and Schwarz, W.,2017:"An Integrated Thermal Analysis Method for IC Engines", La simulation numérique au coeur de l'innovation automobile Congress, Paris, France, 2017

Poredos, A., Gomboc, S., Tomsic, M. 2018: "Heat Transfer Analysis for GDI Development", Computational methods for thermal problems, ThermaComp Conference, Bangalore, India, 2018

Robinson, K., Hawley, J. G. and Campbell, N. A. F.,2003:"Experimental and modelling aspects of flow boiling heat transfer for application to internal combustion engines". Proceedings of the Institution of Mechanical Engineers, Part D: Journal of Automobile Engineering, 217 (10), pp. 877-889, 2003

Robinson, K., Wilson, M., Leathard, M. J. and Hawley, J. G.,2007: "Computational modelling of convective heat transfer in a simulated engine cooling gallery". Proceedings of the Institution of Mechanical Engineers, Part D: Journal of Automobile Engineering, 221 (9), pp. 1147-1157, 2007

Steiner H., Brenn G., Ramstorfer F., Breitschaedel B.,2011:"Increased cooling power with nucleate boiling flow in automotive engine applications", New trends and developments in automotive system engineering pp 249-272, 2011

Šarić, S., Basara, B., and Žunič, Z.,2016:"Advanced near-wall modeling for engine heat transfer, Int. J. Heat and Fluid Flow", article in press, available online 26 July 2016

Šarić.S and Basara, B.,2015:"A Hybrid Wall Heat Transfer Model for IC Engine Simulations," SAE Int. J. Engines Vol. 8, No. 2, pp. 411-418, 2015

Tibaut, P. and Poredos, A., 2014 "Heat transfer analysis of an engine cylinder head", NAFEMS Multiphysics Simulation conference, Manchester, UK, 2014

Experimental Investigation of Wall Heat Transfer due to Spray Combustion in a High Pressure/High Temperature Vessel

K. Keskinen, W. Vera-Tudela, Y. M. Wright and K. Boulouchos

ETH Zürich, Aerothermochemistry and Combustion Systems Laboratory. Zürich, Switzerland

E-mail: keskinen@lav.mavt.ethz.ch
Telephone: +(41) 44 632 77 85

Abstract. Combustion chamber wall heat transfer is a major contributor to efficiency losses in diesel engines. In this context, thermal swing materials (adapting to the surrounding gas temperature) have been pinpointed as a promising mitigative solution. In this study, experiments are carried out in a high pressure/high temperature vessel to (a) characterize the wall heat transfer process ensuing through wall impingement of a combusting fuel spray, and (b) evaluate insulative improvements provided by a coating that promotes thermal swing. The baseline experimental condition resembles that of the Spray A from the Engine Combustion Network, while additional variations are generated by modifying the ambient temperature as well as the injection pressure and duration. Wall heat transfer and wall temperature measurements are time-resolved and accompanied by concurrent luminosity measurements. An uncoated investigation is carried out with several sensor locations around the stagnation point, elucidating sensor-to-sensor variability and setup symmetry. Surface heat flux follows three phases: (i) an initial peak, (ii) a slightly lower plateau dependent on the injection duration, and (iii) a slow decline. In addition to an uncoated reference case, the investigation involves a coating made of porous zirconia, an established thermal swing material. With a coated setup, the projection of surface quantities (heat flux and temperature) from the immersed measurement location requires additional numerical analysis of conjugate heat transfer. Starting from the traces measured beneath the coating, the surface quantities are obtained by solving a one-dimensional inverse heat transfer problem. The present measurements are augmented by CFD simulations supplied with recent rough-wall models. The surface roughness of the coated specimen is indicated to have a significant impact, offsetting the expected heat transfer benefit from the thermal swing material.

Notation

CFD	computational fluid dynamics
CMC	conditional moment closure
CVC	constant volume chamber
DNS	direct numerical simulation
ECN	Engine Combustion Network
ET	injector energizing time
IHCP	inverse heat conduction problem
PSZ	plasma-sprayed zirconia
RMS	root mean square
TBC	thermal barrier coating
TSM	thermal swing material
c	heat capacity
d	coating thickness
E	logarithmic law constant
F_V	soot volume fraction
G	roughness term in wall functions
J	error accumulation
k_{rms}	root mean square roughness
k_s	sand-grain equivalent roughness
L	line-of-sight luminosity
p	pressure
q	heat flux
Pr	Prandtl number

Pr_t turbulent Prandtl number
RA Reynolds analogy factor
RA_0 Reynolds analogy factor: ideal surface
RA_n normalized Reynolds analogy factor, scaled by RA_0
s_k skewness of the roughness probability density function
t time
T temperature
T^+ scaled near-wall temperature
ΔT temperature swing
u^+ scaled near-wall velocity
x position
X species volume fraction
y^+ scaled wall distance
Y species mass fraction
α thermal diffusivity
κ von Karman constant
λ thermal conductivity
ρ density

1. Introduction

In the ongoing task of CO2 emission reduction faced by the energy and transport sectors, diesel engine efficiency improvement is of utmost interest. In heavy-duty engines, contemporary trends of downsizing and lowered engine speeds contribute to higher in-cylinder temperatures and pressures. Such measures further increase heat transfer through combustion chamber walls, which already accounts for a large portion of engine efficiency losses [1].

Measures to reduce combustion chamber heat losses by thermal barrier coating (TBC) is a long-standing technique which began with the use of insulating materials designed to operate at high temperatures and is contemporarily pursued through thermal swing materials [2]. The problem in high-temperature insulators is that the advantages gained during expansion are countered by detriments during the gas exchange. In contrast, thermal swing materials (TSMs), adapting to the surrounding gas temperatures, aim to reduce heat losses both during the closed cycle by heating up, and during the gas exchange by cooling down. Materials promoting thermal swing ΔT have both low conductivity and low heat capacity, as indicated by the relationship $\Delta T \sim (\rho c \lambda)^{-1/2}$ where ρ is the density, c is the specific heat capacity and λ is the thermal conductivity [3, 4].

Studies in the past have reported both beneficial and detrimental impacts on heat transfer when applying in-cylinder insulation. Rationale to the detriments were hypothesized already in the 1980s: Furuhama et al. [5] found higher heat fluxes with coated pistons and suspected that this was due to enhanced near-wall combustion. Meanwhile, Woschni et al. [6] went so far as to dismiss combustion chamber wall insulation as a technique for efficiency improvements, suggesting to focus on lower temperature charges instead. More recently, the potential of TBCs has however been firmly recognised and also put to use: notably, the Toyota metal-based silica-reinforced porous anodized aluminium (SiRPA®) coating [2] was developed within the last decade. New, more extreme TSMs continue to be investigated: Andrie et al. [7] recently report marked efficiency gains with a thin layer of a material that possesses a conductivity and heat capacity nearly an order of magnitude smaller than plasma-sprayed zirconia (PSZ), a conventional TBC material. Porosity appears to be the key ingredient to such properties [4, 7], inherently resulting in open, rough surfaces. While sealed coatings were investigated in [7], promising options were not found, especially as the sealant increases the density of the coating. Andruzkiewicz et al. made both model-based investigations of thermal swing materials [4] as well as experiments using a anisotropic barium-neodynium-titanate coating [8], with properties close to that of PSZ. They reported that the permeable porous material resulted in increased heat losses (among other efficiency detriments), stating the utmost importance to maintain a sealed coating surface. Much of the losses were specifically attributed to porosity. While coated surfaces in [8] were also rough, no specific considerations were made for the role of roughness.

In comparison to more detailed discussion within the field of gas turbines, where TBCs are used to decrease underlying alloy temperatures [9], the role of surface roughness in TBC performance was comparatively neglected for some time in engines [10]. Negative impacts were recognized by Tree et al. in the 1990s [11], noting that rough surfaces promote combustion retardation, impacting efficiency.

More recently, Memme and Wallace [10] noted considerable improvements in engine performance when rough piston surfaces were smoothed. Moreover, the need to measure heat fluxes in the context of TBCs for better understanding was explicitly stated.

Rough-wall flows and heat transfer are evidently not a new field of study, having been in comprehensive engineering scrutiny since the early 1900s (e.g. [12]) – indeed, rough-wall effects are nowadays implemented into widespread tools such as the Moody diagram. However, many detailed aspects of near-wall flows have only recently been uncovered: through their experiments, Schultz and Flack [13] comprehensively described the behavior of flows from the smooth to the fully rough regime, also noting the structural similarity of such flows in regions outside of the immediate roughness element vicinity. Further, highly detailed insights into rough-wall flows have been made available through computational fluid dynamics (CFD) research, wherein use of the immersed boundary method has emerged as a popular approach [14]. The benefit of such methods is the ability to construct effective near-wall discretization for arbitrarily complex surface structures seen in industrial applications. As rough-wall effects are more prevalent at high Reynolds numbers, the evolution of modern high-performance computing (HPC) has been instrumental in managing the massive scale-separation present in such flows. Nevertheless, there are now even examples of fully resolved direct numerical simulations (DNS) where rough wall flow and heat transfer are investigated in realistic geometries [15, 16] or with conjugate heat transfer [17]. Besides increased understanding, the wealth of information in such studies can lead to improved models for engineering-scale CFD.

While computational efforts cannot be claimed to have been matured in diesel spray-induced wall heat transfer, experimental investigations thereof have been carried out for several decades in both cell and engine conditions (e.g. [18-22]). Main observations therein include that heat fluxes appear to be highest at or near the central impingement point, and that smaller nozzle-wall distance and higher spray velocity promote higher heat fluxes. Heat flux measurements for coated surfaces are however far less common. Coating effect analyses are often carried out in running engines; while this allows for a complete perspective on the effective outcome of coating application, the various components contributing to the result (such as heat transfer and combustion phasing) need to be separated.

1.1 Study objectives

In this study, reactive spray-wall impingement experiments are carried out in a quiescent, high pressure / high temperature cell while varying injection parameters (pressure, duration) and environmental aspects (wall material, chamber temperature). We aim to fill a research gap in the literature by investigating both uncoated and coated spray-wall heat transfer in a simplified setting resembling that of the Engine Combustion Network (ECN) Spray A. Such a configuration, while highly relevant to modern diesel engines, can also be replicated in future studies. Importantly, observations are focused directly on surface heat flux rather than on engine performance metrics. In this work, we put emphasis on the role of surface roughness as a potential coating-related detriment, and provide insight on the interplay between thermal swing benefits and roughness detriments using a fairly standard ceramic coating material. Experimental observations are augmented by a simplified numerical representation of the cell, constructed with the widespread Star-CD code using well-known numerical methodologies developed for diesel spray combustion. In addition to a one-dimensional conjugate heat transfer methodology, some of the latest outputs from recent rough-wall flow studies are introduced therein. The specific objectives of this work are as follows:

- Describe the temporal evolution of wall heat flux resulting from a combusting spray-wall impingement process and combine such measurements with concurrent optical diagnostics data
- Determine surface heat fluxes on a thermal swing material coating from measurements carried out beneath the coating
- Discuss the impact of coating surface roughness using CFD and literature-derived roughness models

The present paper is divided into sections as follows. In Sec. 2.1, the experimental methodology for cell operation, heat flux measurements and luminosity measurements is presented. The processing of coated measurements requires additional computations, which is elaborated in Sec. 2.2. The role of surface roughness in heat flux increase is discussed through CFD methodologies presented in Sec. 2.3. Results and related discussion are provided in a collated manner in Ch. 3, while conclusions are presented in Ch. 4.

2. Methodology

2.1 Experimental setup: optical imaging and heat flux measurements

The experiments have been performed in the high pressure / high temperature cell at the Aerothermo-chemistry and Combustion Systems Laboratory at ETH Zurich, which is a constant volume chamber (CVC) with a combustion chamber possessing a diameter of 110 mm and a depth of 60 mm. The CVC is equipped with a large frontal optical access of 90 mm diameter and four smaller side optical accesses, each with a diameter of 42 mm. These accesses provide an excellent opportunity for the application of various optical diagnostic techniques of sprays and jets. The cell body has six electrical heaters on the body and two valves for the inlet of fresh air and the outlet of exhaust gases. In the present case, the cell is operated with H2 pre-combustion. In this mode, the cell body is heated up to 500 K and filled up to 30 bar, after which an additional charge of air and hydrogen is injected into the chamber and ignited by a spark plug. The ensuing combustion causes the chamber pressure and temperature to rise to over 100 bar and 1000 K, respectively. The measurement conditions (pressure, temperature) are very well controlled and reproducible. Fig. **1** displays a schematic of the injection setup.
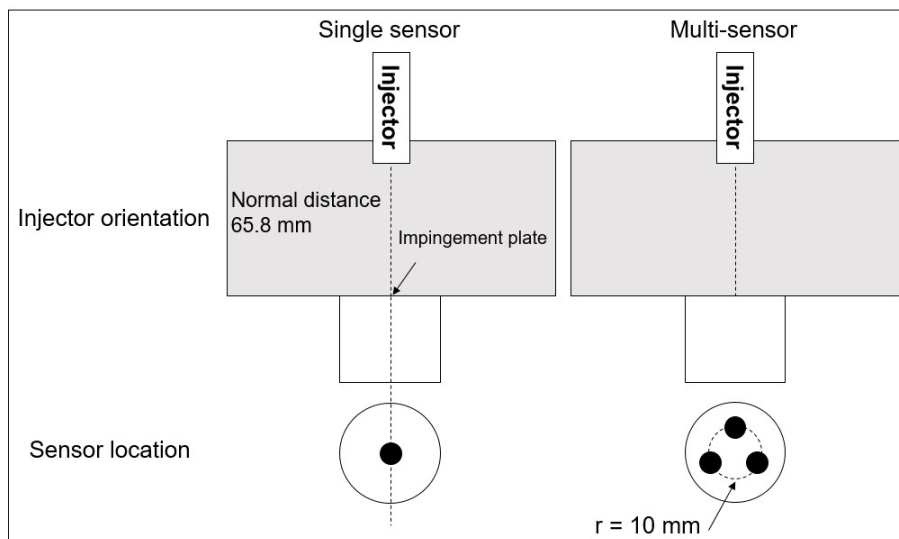
Fig. 1. Characteristic schematic of injection setups in the cell

The consumption of oxygen during the pre-combustion process was designed to obtain the oxygen concentration required for the investigations. After reaching its peak, pressure progressively decreases to the trigger pressure, and the injection is triggered at the correct instance. In this investigation, the trigger pressures are 60.7 bar and 52.9 bar that respectively represent gas-averaged temperatures of 900 K and 800 K at a density of 22.8kg/m^3. The oxygen concentration can be estimated by the consumption of hydrogen combustion. For these experiments the base conditions are 900 K of ambient temperature at a density of 22.8 kg/m3 and 15% (volume) of oxygen. For some cases, a variation in ambient temperature has been performed at 800 K while the density is kept constant.

A single-hole axial magnetic injector with a 90 μm nominal orifice diameter was used to inject n-dodecane into the combustion chamber. The nominal injection pressure was 1500 bar and the energizing time was set at 4 ms. For some conditions, variations in injection pressure were performed at 500 bar and 1000 bar, as well as a different energizing time of 1.5 ms and a temperature of 800 K. Table 1 summarizes the experimental cases of the present study. For each case, a minimum of 15 process repetitions were carried out.

Table 1. Experimental cases considered in the present work. In single-sensor cases, both uncoated and porous zirconia-coated variants are included.

Configuration	Coating	Injection	Chamber
Multi	Uncoated	p = 1500bar ET = 4ms	ρ = 22.8 kg/m^3 T = 900K
Single	Uncoated & Zirconia	p = 1500bar ET = 1.5ms	ρ = 22.8 kg/m^3 T = 900K
	Uncoated & Zirconia	p = 500bar ET = 1.5ms	ρ = 22.8 kg/m^3 T = 900K
	Uncoated & Zirconia	p = 500bar ET = 4ms	ρ = 22.8 kg/m^3 T = 900K
	Uncoated & Zirconia	p = 1000bar ET = 4ms	ρ = 22.8 kg/m^3 T = 900K
	Uncoated & Zirconia	p = 1500bar ET = 4ms	ρ = 22.8 kg/m^3 T = 900K
	Uncoated & Zirconia	p = 1500bar ET = 4ms	ρ = 22.8 kg/m^3 T = 800K

To quantify spray impingement-induced heat losses through the wall and variations in wall surface temperature, a special heat flux sensor was used. This sensor is designed by Dr. Müller Instruments GmbH for specific applications and is manufactured on demand [23]. The sensor measures variations in temperature, while the heat flux is inferred by assuming a semi-infinite body, with knowledge of the sensor material [23]. In order to mount the heat flux sensor in the combustion chamber, an impingement plate was designed to fit in place of one of the small optical accesses on the opposite side of the injector. This way, the spray would penetrate into the chamber and impinge on the plate after combustion has taken place. The impingement plate has a hollow design, allowing sensor mounting and removal while the plate is installed in the CVC. The plate also presents a flat surface so the sensor can be mounted flush on the plate. For coated scenarios, a porous spray-coated zirconia (ZrO2) layer with a thickness of 130 µm, manufactured by Fraunhofer IPK, is added on top of the impingement plate.

To visualise the diffusion flame and track the spray evolution inside the combustion chamber, luminosity from broadband radiation has been recorded. This technique visualizes flame advancement and its impingement on the plate. The recorded radiation mainly corresponds to soot thermal luminosity during the diffusion combustion phase. This type of radiation may have two kinds of contributions, chemiluminescence and incandescence. Under most operating conditions, the latter is the fundamental contribution as it depends on the amount of soot and its temperature. A qualitative indication of these metrics is therefore provided in the present analysis.

2.2 Coated heat flux measurements

Fig 2 elucidates the contrast between the physical situations of the uncoated and coated cases. While in the uncoated case the sensor is located at the gas-solid interface, the coated case has the sensor embedded within the solid surface.
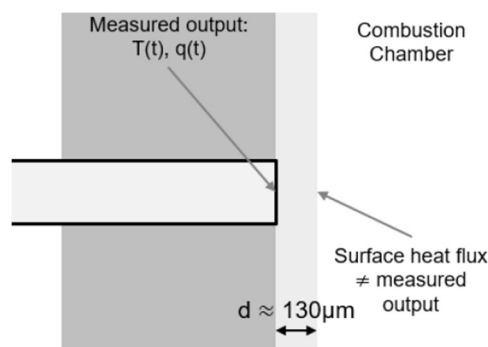
Fig 2. Coated case schematic description

Heat conduction in the coating domain is assumed to be governed by the one-dimensional heat equation:

$$\rho c \frac{\partial T}{\partial t} = \frac{\partial}{\partial x}\left(\lambda \frac{\partial T}{\partial x}\right) \tag{1}$$

where density ρ, specific heat capacity c and thermal conductivity λ are all functions of temperature T. Simplification to 1D from the full 3D equation is commonplace in spray-wall heat transfer, justified by the dominant magnitude of temperature gradients in the wall-normal direction [18]. Eq. (1) can be written in a more explicit form as

$$\frac{\partial T}{\partial t} = \alpha \left[\frac{\partial^2 T}{\partial x^2} + \frac{1}{\lambda}\frac{\partial \lambda}{\partial T}\left(\frac{\partial T}{\partial x}\right)^2\right] \tag{2}$$

where $\alpha = \lambda/\rho c$ is the thermal diffusivity. The problem at hand is formally an inverse heat conduction problem (IHCP) limited between $x \in [x_1, x_2]$ (where x_1 and x_2 are sensor and surface locations, respectively; see Fig 2) and $t \in [0, t_{end}]$, with an unknown temperature distribution $T(x,t)$ and unknown Neumann boundary condition $q(x_2, t)$. Measurement outputs include the time series for heat flux $q(x_1, t)$ and temperature $T(x_1, t)$ at the sensor location beneath the coating. Several distinct methods of solving IHCPs can be identified in the literature [24]. Here, we adopt a method where forward problems are iteratively modified. This selection is motivated by the ill-posed nature of the problem combined with the relatively significant amount of high-frequency noise in measurements. The error of a solution attempt J can be quantified based on the correspondence between simulated and experimental sensor temperatures as

$$J = \frac{1}{t_{end}} \int_0^{t_{end}} \left[T_{sim}(x_2, t) - T_{exp}(x_2, t)\right]^2 dt \tag{3}$$

and the problem reduces to a minimization of this error by modifying the unknown surface heat flux $q(x_2, t)$. The forward boundary value problem (Eq. (2)) is solved numerically by using the finite difference method in a Matlab solver. The initial temperature distribution is generated with a steady heat flux so that the initial sensor temperature is fulfilled, and spurious disturbances in the heat flux boundary condition prior to impingement are nullified. First and second spatial derivatives are approximated using central differences, while time integration is carried out using the classical explicit fourth order Runge-Kutta scheme (see e.g. [25]). The 130 µm 1D domain has a spatial resolution of 2 µm while a dynamic time step conforming to a diffusive Courant-Friedrichs-Lewy number of less than 0.5 is adopted. Thermodynamic properties of the used porous Zirconia material have been characterized by Fraunhofer IPK using differential scanning calorimetry and laser flash analysis for specific heat capacity and thermal diffusivity, respectively. Material properties were measured at temperatures between 20 and 600 degrees Celcius (Table 2). For computations, second-degree polynomial expressions were constructed from the measurements for $\alpha(T)$ and $\lambda(T)$, to provide a smooth expression for $\partial\lambda/\partial T$ in Eq. (2). Fig 3 shows an example of a reconstructed approximate solution to the problem.

Table 2. Measured thermodynamic properties of the porous zirconia applied in the coating (* indicates that the value was extrapolated).

Temperature	Specific heat capacity	Thermal diffusivity	Thermal conductivity
[°C]	J/gK	mm²/s	W/mK
20	0.45*	0.45	0.84
50	0.46	0.44	0.84
100	0.48	0.43	0.86
150	0.50	0.41	0.85
200	0.51	0.40	0.85
300	0.53	0.37	0.81
350	0.54	0.35	0.78
400	0.54	0.34	0.77
450	0.55	0.33	0.76
500	0.56	0.32	0.75
600	0.58	0.31	0.74
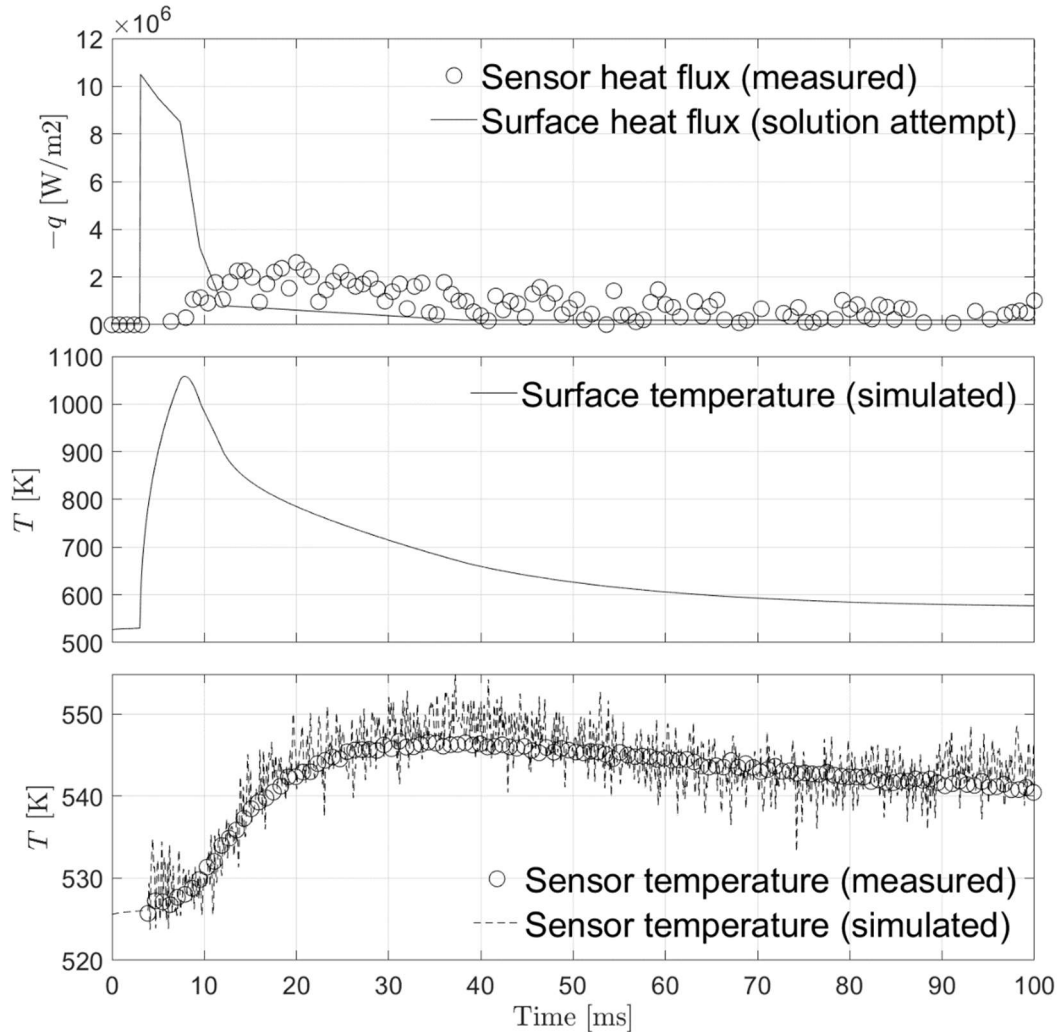
Fig 3. A reconstruction of the forward problem (Eq. 2), p = 500 bar, ET = 4 ms, T = 900 K. The heat flux boundary condition in the top frame (solid line) has been formed in a piecewise-linear manner, while the one at the sensor location (markers, every tenth shown) is given as a boundary condition by the measurement. The evolution of simulated surface temperature is visible in the central frame. The solution temperature at the sensor location (dashed line) adheres well to the measured temperature (markers; bottom), indicating that the present heat flux profile is a reasonable approximation of the solution.

2.3 Computational fluid dynamics simulation of the spray-wall impingement

Additional insight into the role of roughness in heat transfer increase is delivered here through a simplified CFD setup of the cell (based on [26]) using the Star-CD v.4.26 code (licensed by Siemens). The employed axisymmetric sector mesh (bulk and near-wall resolutions 0.5 mm and 0.1 mm, respectively, with gradual refinement) retains two main properties of the cell: a nozzle-to wall distance of 65.8 mm and a domain volume of 0.542 liters. The volume is initialized with quiescent conditions resembling the ECN Spray A: $T = 900$ K, $p = 60.7$ bar, $Y(O_2) = 0.1744$, $Y(H_2O) = 0.0624$, $Y(H_2O) = 0.7632$, $Y(CO_2) = 0.0936$. Simulations are carried out with the standard $k - \varepsilon$ turbulence model with $c_{\varepsilon 1} = 1.52$ to correct the round-jet anomaly [27] (causing underprediction of jet penetration), a common practice in diesel injection simulation [28]. The turbulent Prandtl number Pr_t is set to a constant value of 0.9. The utilized Bosch common-rail injector has been previously characterized in terms of outlet diameter and discharge coefficient (which is assumed constant), and the injection rate is approximated as a piecewise-linear profile with ramps of 110 µs. Spray modelling is based on a standard Lagrangian particle tracking (LPT) approach in Star-CD and employs gradient-based interpolation between the gas and liquid phases, a turbulent dispersion model and a droplet collision model. The Reitz-Diwakar model [29] is utilized for

aerodynamic droplet breakup modelling. For combustion, the conditional moment closure (CMC) model [30] is employed, having been previously validated in the present conditions [26, 28, 31].

Wall treatment is prescribed with a standard wall function approach which can be acknowledged lacking in the detailed description of heat flux in complex scenarios such as impinging flows [32]. It should be noted that wall model approximations are employed also in contemporary scale-resolving simulations of impinging sprays [33]. The goal of the present CFD work is to evaluate the predicted impact of roughness rather than to perform a high-fidelity computational investigation of spray-wall impingement. Hence, results are focused on the relative outputs between smooth and rough cases. As an additional component crucial to description of TSMs, a 1-D conjugate heat transfer model implemented in Star-CD is used in the coated simulations.

The impact of roughness on heat transfer can be approximated in two steps: (i) finding a suitable approximation for a rough-wall shear stress model, and (ii) determining a heat flux that corresponds to this stress prediction. The statistical impact of roughness on wall shear stress is usually expressed as a modified law of the wall:

$$u^+ = \frac{1}{\kappa}\log(Ey^+) - G \tag{4}$$

where $u^+ = u/u_\tau$ is the scaled velocity, $y^+ = \rho u_\tau y/\mu$ is the scaled wall distance, $E = 9.0$, and G is a function denoting the effect of roughness (when $G = 0$, the standard logarithmic law applies). As G increases, so does the wall shear velocity u_τ, describing the increase in wall shear stress due to roughness. Notably, G is commonly given as a function of scaled roughness $k_s^+ = \rho u_\tau k_s/\mu$ where k_s is a so-called sand-grain equivalent roughness [12]. As a generic rough surface cannot be directly measured in terms of k_s, a model is required to make such a description. Flack and Schultz [34] investigated various types of rough surfaces and their detailed surface quantities, developing a correlation to determine k_s:

$$k_s = 4.43 k_{rms}(1 + s_k)^{1.37} \tag{5}$$

where k_{rms} is the root-mean-square (RMS) roughness of the surface and s_k is the skewness of the displacement probability density function. While correspondence of Eq. (5) with the available experimental data was good in [34], it should be noted that the correlation was developed only for flows in the fully rough regime (corresponding to $k_s^+ > 15$ [35, 36]). Moreover, further investigation of pitted or eroded surfaces with negative s_k were highlighted as a means to improve Eq. (5). In the present work, Eq. (5) is used to characterize k_s of the coated Zirconia surface on the basis of surface measurements carried out according to the ISO 4287 standard [37]. The present surface has a RMS roughness of $k_{rms} = 20.5$ μm and a slightly positive skewness of $s_k = 0.099$, leading to an estimate of $k_s \approx 104$ μm.

Heat transfer increases induced by rough surfaces has been addressed with valuable literature contributions: Bons [38] investigated the applicability of the Reynolds analogy (i.e., analogous surface drag and heat transfer increases) in different flow conditions, including variations in streamwise pressure gradient, freestream turbulence, and surface roughness. A considerable portion of roughness-added drag is due to pressure drag, while a corresponding mechanism for heat transfer does not exist in the energy equation. Hence, the roughness-induced increase in wall heat transfer is generally lower than the respective increase in wall shear stress, and the Reynolds analogy does not apply.

Forooghi et al. [16] made a comprehensive and high-fidelity investigation of rough-wall heat transfer by DNS in both synthetic and realistic rough surface geometries. In their study, the lack of a Reynolds analogy reported by Bons [38] was replicated and quantified by a normalized Reynolds analogy factor $RA_n = RA/RA_0$, where $RA = |q_w|/\tau_w$ is the ratio of heat flux to shear stress, and RA_0 is such a ratio for an ideal, smooth surface. In CFD wall models, this ratio is typically prescribed by the turbulent Prandtl number Pr_t. From their simulation data, augmented by previous experimental results [38], Forooghi et al. [16] developed a correlation for RA_n, conveniently based on the scaled roughness:

$$RA_n = 0.55 + 0.45 \exp(-k_s^+/130) \tag{6}$$

Eq. (6) signifies that for smooth walls $RA_n = 1$, while for highly rough flows (with large k_s^+), the ratio approaches $RA_n = 0.55$. In the present work, eq. (6) is implemented for rough-wall heat transfer alongside the standard rough-wall functions for momentum and heat transfer in Star-CD:

$$u^+ = A + \frac{1}{\kappa} log\left(\frac{y^+}{k_s^+}\right) \tag{7}$$

$$T^+ = Pr_t(u^+ + P) \tag{8}$$

where $A = 8.5$ (based on [12]), $Pr_t = 0.9$, $P = \left[(Pr/Pr_t)^{3/4} - 1\right]\left[1 + 0.28\exp\left(\frac{-0.007Pr}{Pr_t}\right)\right]$, Pr is the molecular Prandtl number and $T^+ = c_p\rho u_\tau(T_w - T)/q_w$. Effectively, Eq. (6) simply modifies the heat flux prediction of the RA_0 case in eq. (8).

3. Results and discussion

First, sensor-to-sensor consistency and setup symmetry are examined using different sensor locations (cf. schematic in Fig. **1**) and sensor units. The results in Fig 4 show that heat flux readings are fairly consistent between different azimuthal measurement locations, although the values in location 10 mm-120° are slightly positively biased. A reason thereto may lie in the geometric positioning of the sensor, as location 10 mm-120° may be more sensitive to recirculating flow patterns. Overall, the sensor-to-sensor variance is however satisfactory. It is also notable that the central measurement location (at the intended stagnation point) yields results that are quite consistent with the surrounding radial points. The radial heat flux distribution is known to be affected by nozzle-to-wall distance, with higher proximity associated with a higher local stagnation maximum [33].

Fig 4 also provides a qualitative impression of the temporal heat flux evolution in both single and multi-sensor setups. Upon impingement, the heat flux rapidly reaches a maximum value, consistent with expectations from high plume tip temperatures [39] and prior heat flux experiments [40]. The initial peak is followed by a slightly lower, stabilized plateau with a time scale corresponding to the injection duration. As the large-scale temperature difference between the spray plume and the wall is in the order of 1500 K, the measured sensor temperature evolution (Fig 4, right) suggests only a small thermal swing impact on the heat flux. Finally, as injection is ceased, a progressive decline in heat flux is observed.
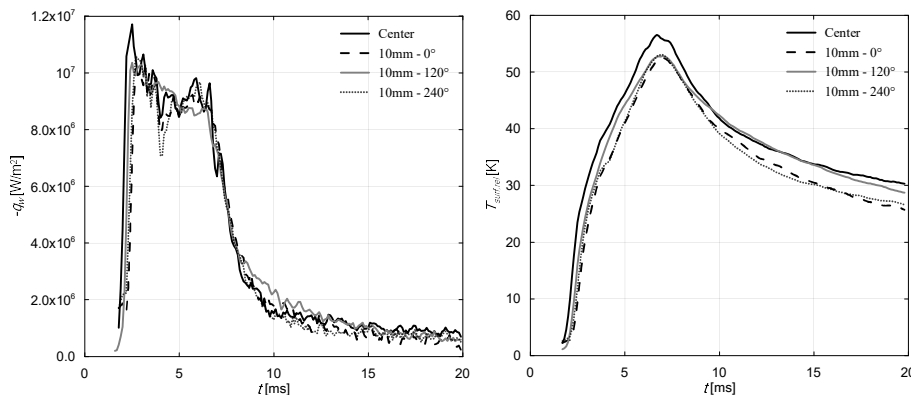
Fig 4. Heat flux (left) and relative temperature (right) evolution between sensors at different radial positions. Base conditions of 900 K, 22.8 kg/m³, 15% XO₂, 1500 bar, 4 ms.

Fig 5 (center) gives additional context to the heat flux description by displaying the flame-base and tip penetration from broadband radiation. The trend shows that the flame base stabilizes after ignition has started and only proceeds further downstream after fuel stops being injected. On the other hand, the flame tip continuously grows as the spray penetrates further into the chamber and stops only once it hits the impingement plate. In Fig 5 (bottom) it can be seen that the integrated intensity detected starts before the heat flux (Fig 5, top) begins. This is expected as the combustion starts far from the plate as seen in the flame-base and -tip evolution. The evolution of the intensity shows a rather stabilized behavior once the flame reaches a quasi-steady state. Once the injection event ends and the flame lifts from the nozzle vicinity, the flame area is reduced and the intensity drops. The flame base advancement timing corresponds closely with the decrease of the heat flux, implying that the gradual decrease is impacted by a decrease in spray momentum.
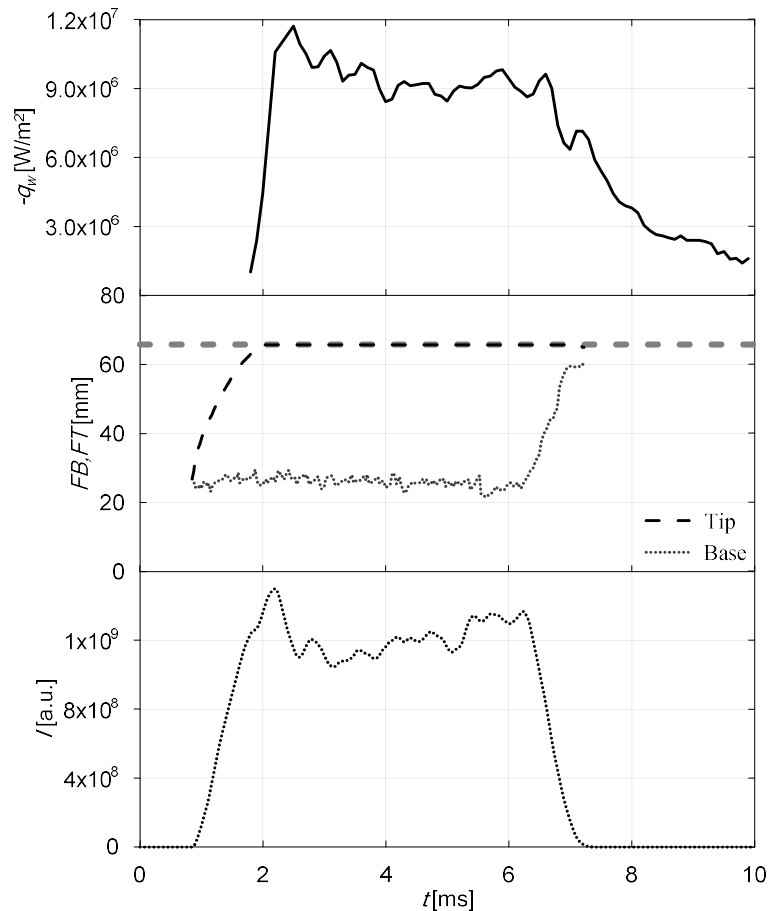
Fig 5. Heat flux (top) compared to flame-base and –tip (middle) and cumulative luminosity (bottom). Base conditions of 900 K, 22.8 kg/m^3, 15% XO_2,1500 bar, 4 ms. The dashed line indicates the impingement plate distance from the nozzle exit.

The effect of the ambient temperature variation of 800 K and 900 K is shown in Fig 6 (top-left) for the heat flux and in Fig 6 (bottom-left) for the surface temperature. It can be noted that the heat flux traces are very similar for both cases, the main difference is that the heat flux begins earlier for the case of 900 K. This is caused by acceleration of the flame tip due to the earlier combustion, which leads to the flame reaching the plate earlier than in the case at 800 K. For the temperature variation there is a constant offset between both cases, in which the case at 800 K presents a lower temperature increase than the 900 K case. This is expected as the lower ambient temperature will cause the flame to have a lower temperature. Although the peak of surface temperature seems to occur at a very similar time for both cases, around 7.5 ms (consistent with the end of the heat flux plateau), the rising slope also differs for the aforementioned reasons. Fig 6 (top-right) presents the heat flux and Fig 6 (bottom-right) the relative temperature for a combination of injection pressures and energizing times, 500 bar / 1.5 ms, 1500 bar / 1.5 ms, and 1500 bar / 4 ms. The cases at 1500 bar show a trend in which the longer injection dominates the stabilized phase caused by the diffusion flame. On the other hand, the case at 500 bar presents a peak at a much later time due to the lower tip velocity (induced by the lower injection pressure). This effect, combined with the short injection duration, causes the peak to be narrower and to have virtually no stabilized phase, as the injection stops approximately concurrently with the flame reaching the plate. The effect on the surface temperature is similar as in the previous cases, in which the peak of the temperature is reached at the end of the heat flux plateau. For the case at 500 bar, the temporal delay in heat transfer results from the lower spray velocity.
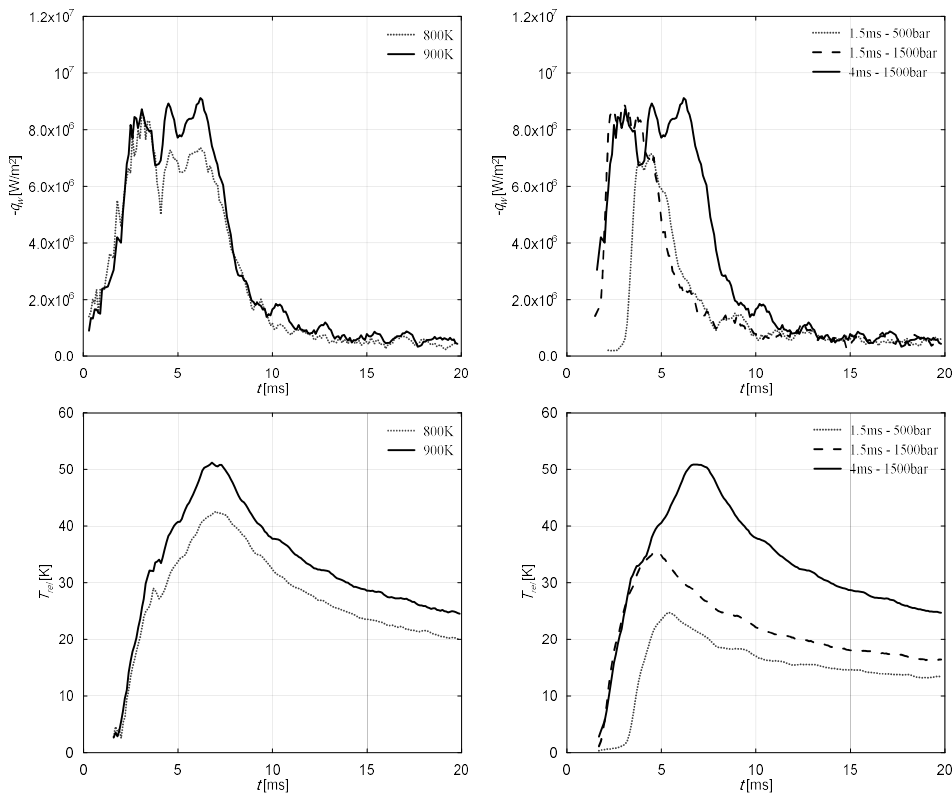
Fig 6. Heat flux (top) and relative temperature (bottom) evolution at different ambient temperatures (left) and different energizing times and injection pressures (right). Conditions of 800K/900K, 22.8kg/m^3, 15% XO$_2$,1500bar, 4 ms (left) and 900 K, 22.8 kg/m^3, 15% XO$_2$,500 bar/1500 bar, 1.5 ms/4 ms (right).

Fig 7 presents the heat flux (left) and relative temperature (right) variation between an uncoated and a zirconia-coated plate. We note that these are the results captured by the sensor, and not a surface heat flux comparison. The coated plate presents a much higher latency, in which the maximum heat flux is reduced to only a fraction of the uncoated reference, 2 MW/m^2 compared to 10 MW/m^2. A similar latency is noted with the sensor temperature.
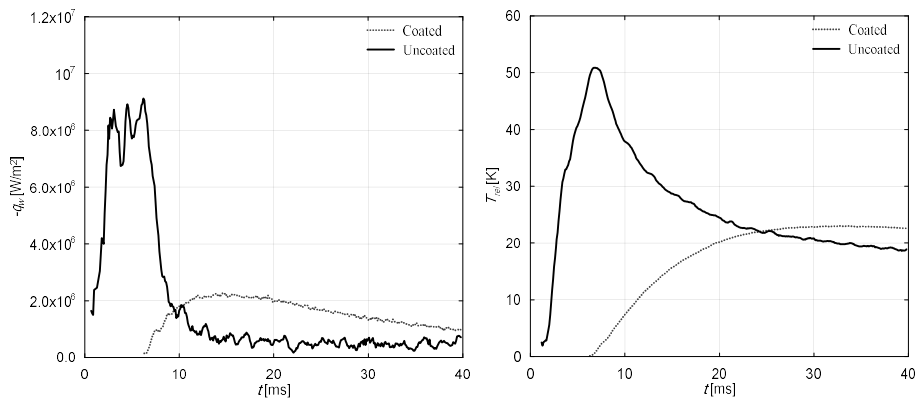
Fig 7. Heat flux (left) and relative temperature (right) evolution comparison for coated and uncoated plate. Base conditions of 900 K, 22.8 kg/m^3, 15% XO$_2$, 1500 bar, 4 ms.

Fig 8 shows a comparison of heat flux (left) and relative temperature (right) evolution under different conditions with the coated plate. Similar trends to those shown in Fig 6 can be seen, although the values are dampened by the effect of the coating. Reducing the ambient temperature leads to results consistent with the uncoated case. The combined effect of a lower injection pressure and a shorter injection duration leads to a later start of the heat flux, caused mainly by the lower injection velocity. Lower heat flux and temperature increases are also presented, which is a result of the smaller injected mass.
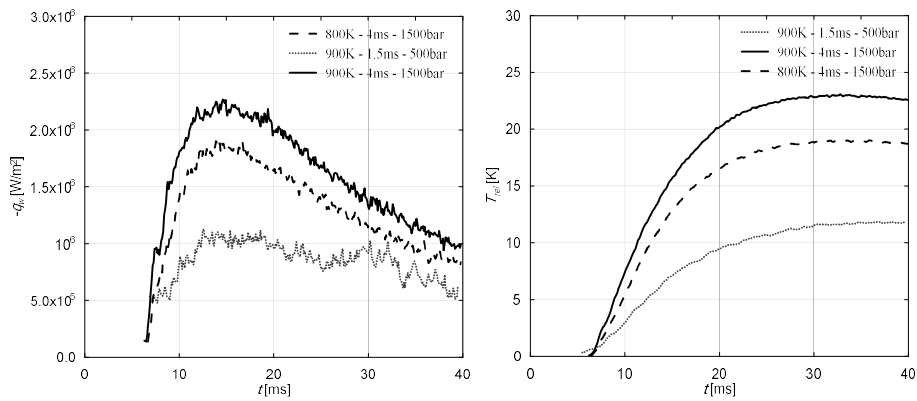
Fig 8. Heat flux (left) and relative temperature (right) evolution for the coated specimen at constant density 22.8 kg/m^3 and 15% XO$_2$ for different conditions: 800 K/900 K, 500 bar/1500 bar injection pressure and 1.5 ms/4 ms injection duration.

Observing only the raw coated results (Fig 7, Fig 8) is however misleading as the measurement location within the coating leads to a considerably different result in comparison to the surface heat flux. Hence, the techniques described in Fig 3 are employed in an attempt to recover the true surface heat flux.

Fig 9 shows comparisons between ensemble-averaged uncoated measurements and coated approximate results derived from the inverse problem. Throughout the various testing conditions, the indicated heat fluxes actually appear to be slightly higher in the coated cases, compared with the uncoated reference. Profile shapes, i.e. starting and ending points of high heat flux, as well as the gradual decline after end of injection, are very consistent with the uncoated measurement. This is to be expected as the timing and magnitude of thermal input (spray combustion) are not expected to strongly depend on the wall material. As in the uncoated cases, higher injection pressures that yield higher momentum sprays are indicated to lead to higher wall heat fluxes, consistent with the recent literature [22]. It appears however that in the cases with higher injection pressure, the increases are (proportionally) higher as well. A possible reason thereto is that the near-wall flow is of higher intensity, and the effect of roughness is hence more pronounced.
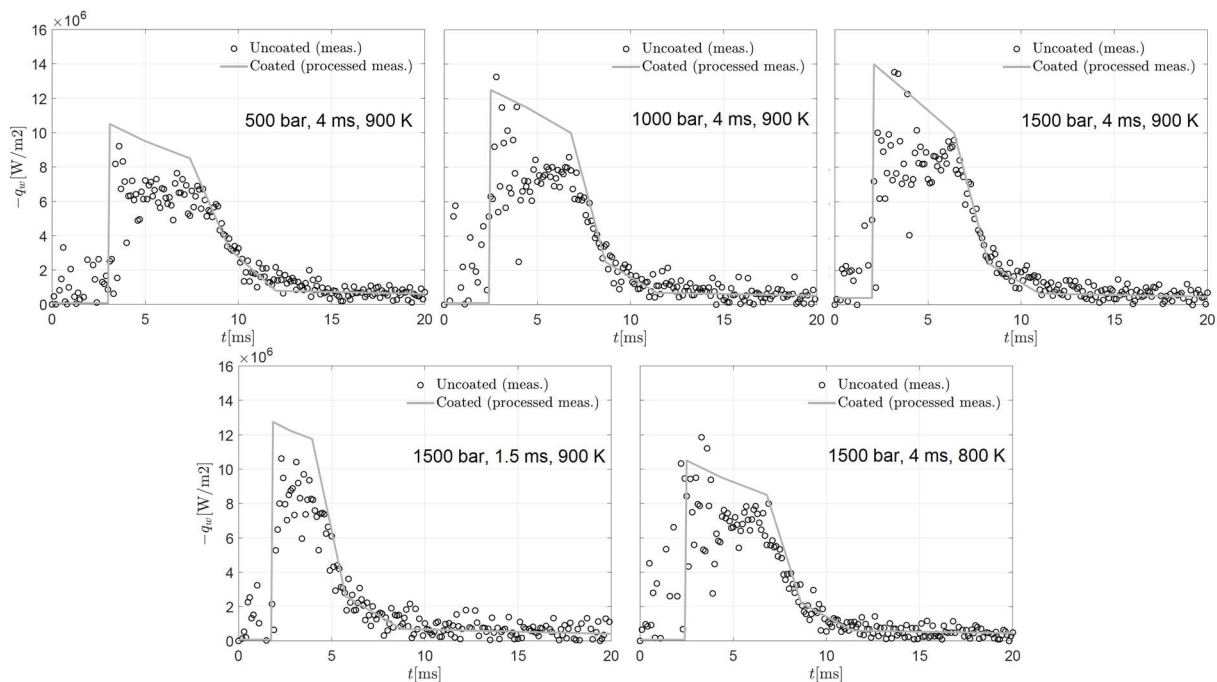
Fig 9. Measured uncoated heat fluxes (markers) and heat flux approximations of the coated inverse problem made via the finite difference solver (solid lines). The images show three variations of injection pressure, two variations of injection duration and two variations of cell temperature.

Now, it is important to discuss what can and cannot be stated based on the present approximation of the coated heat flux. We note that here such approximations are simple piecewise linear profiles.

The solution criterion for the coated cases pertains to the accumulated temperature difference (Eq. 3). Even small increments of some per cent of the heat flux profile impact this criterion clearly at the end of the simulation. Hence, the cumulative heat flux indicated by the profiles is a fairly confident result, keeping in mind sensitivities relating to inaccuracies of material properties and thickness. What is however much less certain is the exact, highly transient profile of heat flux during flame-wall impingement. Indeed, the results in Fig 9 should not be interpreted as entirely unique, and equivalent solution criteria can be obtained with slightly varying slopes (but similar mean levels during the period of high heat flux).

The obtained, reconstructed results naturally depend on input data provided to the problem. Here, we briefly analyze the sensitivity between the end-result and small deviations in problem parameters, (i) the exact coating thickness, and (ii) the measured material properties. The resulting profiles from 10 % variations in such quantities are shown in Fig 10.
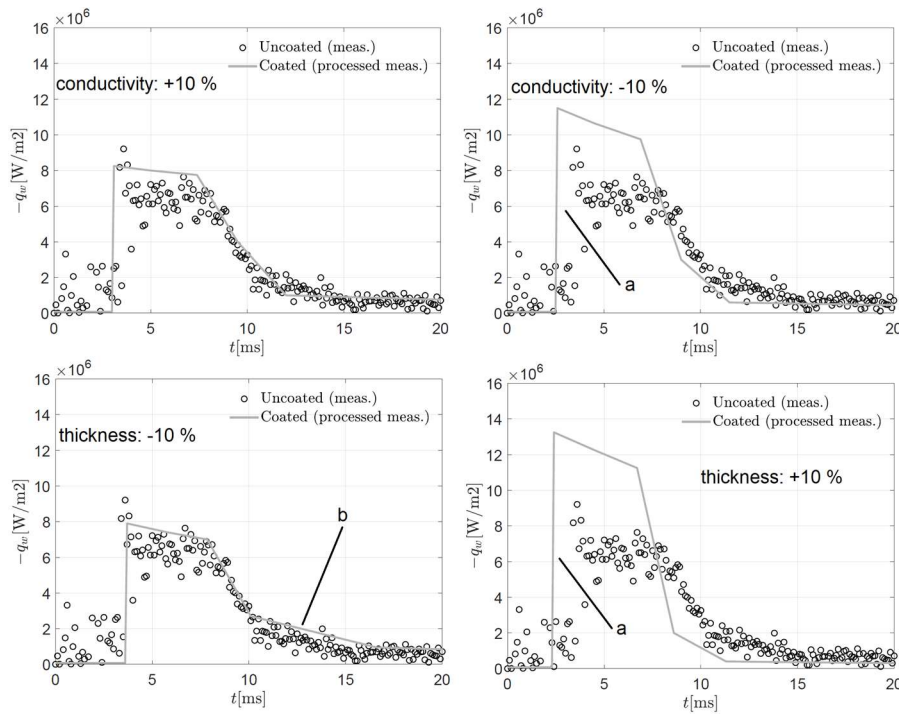
Fig 10. Sensitivity of processed, coated heat flux to variations in coating thickness and thermal conductivity (p = 500 bar, ET = 4 ms, T = 900 K). (a) and (b) refer to differences in heat flux timing and late-stage heat flux magnitude, respectively.

While in all cases the coated heat flux remains above that of the uncoated reference, the tested variations show that the amount of such excesses changes significantly, particularly with variations in the domain thickness. However, some of the variations may be more physically realizable than others. With the cases of higher thickness and lower conductivity, the heat flux phasing deviates from that of the uncoated case significantly (Fig 10, (a)). Moreover, with the -10 % thickness variation, it is noted that the peak heat flux is relatively similar to the uncoated case. With this in mind, it appears unlikely that during the decrease period (Fig 10, (b)) involving much less near-wall convection, the (hotter) coating would provide such a considerable increase in surface heat flux. It should be recalled however that the present observations cannot rule out the impact of phenomena such as fuel deposits trapped within the open pores.

Overall, the results presented here suggest that the expected benefits of the thermal swing material are not attained in the present case. Wall roughness is one of the detriments increasing heat transfer and hence its potential role is further investigated with the use of the CFD simulations. A qualitative comparison between the experimental and computational sprays is displayed in Fig 11. While the experimental image shows actual broadband luminosity, the simulated image has been processed according to a virtual line-of-sight luminosity L:

$$L(r,z) = \int_S f(r,z)ds \qquad (9)$$

where $f(r,z) = aF_V T^4$, a is a constant and F_V is the soot volume fraction. L is hence formed as line integrals through trajectories that penetrate the axisymmetric spray and its vicinity. A good qualitative correspondence is noted in the development of the luminous region from the emergence of luminosity to the developed, impinging spray flame.
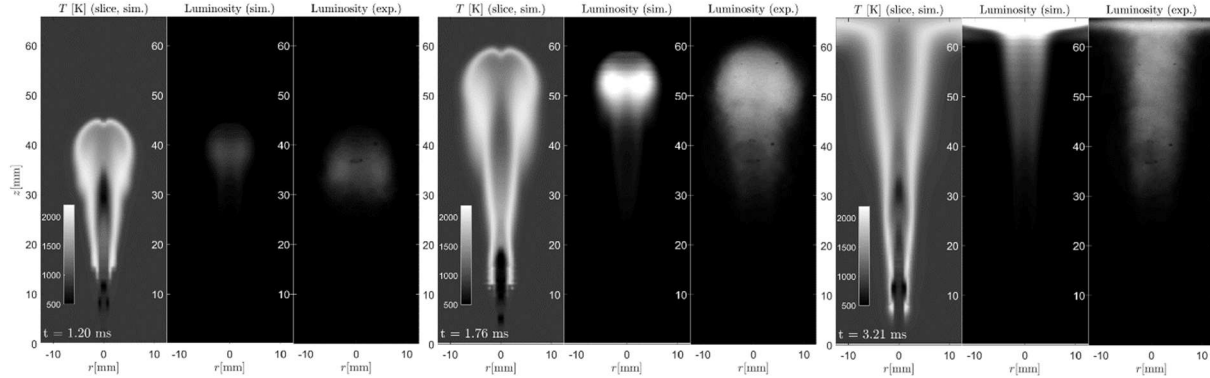
Fig 11. Spray evolution between simulation and experiment. Simulated temperature cutout contours (left frames), simulated virtual line-of-sight luminosity (central frames) and experimentally recorded luminosity (right frames) at 1.20 ms (left), 1.76 ms (center) and 3.21 ms (right).

Fig 12 displays traces of the stagnation point heat flux in both experiments and simulations. It is firstly noted that the heat flux level in the uncoated simulation is fairly close to that of the experiment. With the knowledge of uncertainties relating to wall-modelled CFD predictions of impinging flows, we do not infer this as an indication of computational fidelity, but rather consider that the result functions as a meaningful baseline for comparisons. In all CFD cases, the high heat flux duration is slightly shorter than in the experiments due to a difference in injection duration, which is likely to arise from the description of needle closing.

With an ideally smooth coating surface, the heat flux is initially similar to the uncoated case but begins an immediate decline due to the surface heating up. Eventually, a heat flux benefit of ca. 20 % is observed in the trace. With the rough coating, the situation is dramatically different, as a considerable
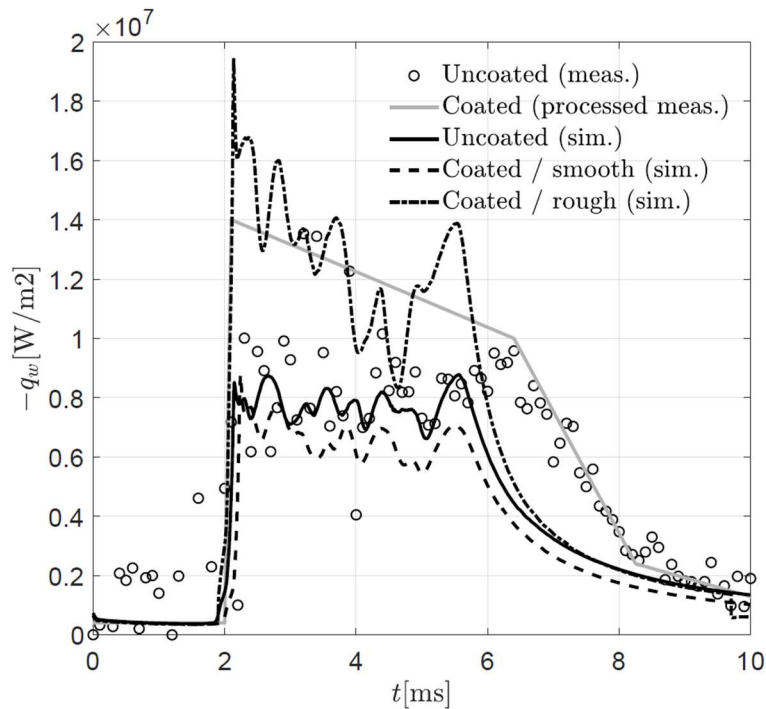
Fig 12. Stagnation point heat flux traces from both uncoated and coated experiments and simulations (p = 1500 bar, ET = 4 ms, T = 900 K). An ideal, smooth zirconia coating has been simulated in addition. Measurement results correspond to those in Fig 9.

heat flux increase is initially observed. As the surface heats up even quicker than in the smooth coated case and higher thermal swing is recorded, the heat flux trace gradually declines. Notably, there is fairly good agreement between the trends of the processed coating measurement and the coated simulation, coinciding on the observation that the present coated surface actually yields higher heat transfer in comparison to the smooth, uncoated counterpart. It should be noted that the employed rough surface models have not been developed specifically for impinging flows, which underlines the approximate nature of the CFD solution. Similar results are however noted for remote radial locations, where the boundary layer has experienced some development. To provide further validation to such comparisons in varying conditions, a simulation case with 500 bar injection pressure (Fig 13) displays a consistent relationship between smooth and rough-wall results. In this case, results are shown only up to 7 ms: shortly after the end of injection, the near-wall flow leaves the fully rough regime, to which the used correlations are not developed (and rough-wall modelling is discarded). Moreover, it should be noted that neglecting Eq. (6) would lead to even higher heat transfer predictions from the rough-wall CFD. Finally, it should be emphasized that that the magnitude of roughness effects is expected to be a function of the near-wall flow field. Hence, variations in injection parameters affecting the intensity of the impingement process (e.g. nozzle diameter and nozzle-wall distance) are likely to further influence comparisons between the present uncoated and coated scenarios.
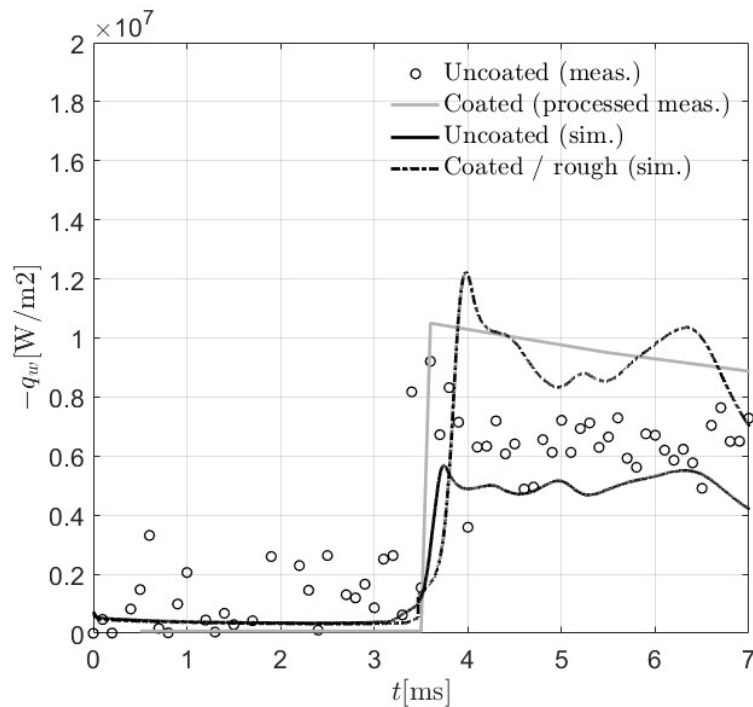
Fig 13. Stagnation point heat flux traces from both uncoated and coated experiments and simulations (p = 500 bar, ET = 4 ms, T = 900 K). Measurement results correspond to those in Fig 9.

4. Conclusions

The wall heat transfer due to spray combustion was studied in an engine-relevant environment. The high pressure/high temperature cell involved a combusting n-dodecane spray impinging on a plate, in which heat flux sensors were placed. Experiments were carried out in both uncoated and porous zirconia-coated scenarios, using conditions resembling those of the ECN Spray A. Coated measurements were analyzed by addressing an inverse heat transfer problem for the unknown surface heat flux, and auxiliary CFD simulations were carried out to approximate the impact of surface roughness on heat fluxes.

Uncoated measurements indicated surface heat fluxes ranging to about 10 MW/m² in the present configuration. Lower ambient cell temperatures led to lower flame temperatures and a lower peak heat flux. The onset of heat transfer is very rapid, and the measured heat fluxes traces typically show an initial maximum in the heat flux. After this peak, the heat flux decreases slightly and remains at a relatively constant plateau, depending on the injection duration. A short, low-pressure injection (1.5 ms

/ 500 bar) shows an exception to this trend: the small amount of fuel overmixes and ignites later than the other cases, and a stabilized phase in heat flux is not observed.

The coated measurement analysis indicates that heat fluxes from the gas to the solid were not reduced in accordance to expectations from the properties of the TSM. Based on (i) the coated, processed heat flux measurements, and (ii) auxiliary CFD computations with recently developed roughness correlations, it is argued that the surface roughness of the presently tested zirconia coating ($k_s \approx$ 104 μm) can alone offset the benefits provided by the surface temperature increase. It also appears likely that the roughness detriments are exacerbated in injections leading to more intense near-wall flows. A direct indication of the present study is hence to place increased research focus on thermal swing materials where relatively smooth surfaces can be attained.

Acknowledgments

References

1. Heywood, J.B., *Combustion engine fundamentals.* First edition. United States, 1988.
2. Kosaka, H., et al., *Concept of "temperature swing heat insulation" in combustion chamber walls, and appropriate thermo-physical properties for heat insulation coat.* SAE International Journal of Engines, 2013. **6**(1): p. 142-149.
3. Assanis, D.N. and E. Badillo, *Transient heat conduction in low-heat-rejection engine combustion chambers.* SAE transactions, 1987: p. 82-92.
4. Andruskiewicz, P., et al., *Analysis of the effects of wall temperature swing on reciprocating internal combustion engine processes.* International Journal of Engine Research, 2018. **19**(4): p. 461-473.
5. Furuhama, S. and Y. Enomoto, *Heat transfer into ceramic combustion wall of internal combustion engines.* SAE transactions, 1987: p. 38-53.
6. Woschni, G., W. Spindler, and K. Kolesa, *Heat insulation of combustion chamber walls—a measure to decrease the fuel consumption of IC engines?* SAE transactions, 1987: p. 269-279.
7. Andrie, M., et al., *Low heat capacitance thermal barrier coatings for internal combustion engines.* 2019, SAE Technical Paper no. 2019-01-0228.
8. Andruskiewicz, P., et al., *Assessing the capability of conventional in-cylinder insulation materials in achieving temperature swing engine performance benefits.* International Journal of Engine Research, 2018: p. 599-612.
9. Clarke, D.R. and S.R. Phillpot, *Thermal barrier coating materials.* Materials today, 2005. **8**(6): p. 22-29.
10. Memme, S. and J.S. Wallace. *The influence of thermal barrier coating surface roughness on spark-ignition engine performance and emissions*. in *ASME 2012 Internal Combustion Engine Division Fall Technical Conference*. 2012. American Society of Mechanical Engineers Digital Collection.
11. Tree, D.R., P.D. Wiczynski, and T.M. Yonushonis, *Experimental results on the effect of piston surface roughness and porosity on diesel engine combustion.* SAE transactions, 1996: p. 112-121.
12. Nikuradse, J., *Laws of flow in rough pipes.* 1950: National Advisory Committee for Aeronautics Washington.
13. Schultz, M. and K. Flack, *The rough-wall turbulent boundary layer from the hydraulically smooth to the fully rough regime.* 2007. **580**.
14. Piomelli, U., *Recent advances in the numerical simulation of rough-wall boundary layers.* Physics and Chemistry of the Earth, Parts A/B/C, 2019. **113**: p. 63-72.
15. Forooghi, P., et al., *DNS of momentum and heat transfer over rough surfaces based on realistic combustion chamber deposit geometries.* International Journal of Heat and Fluid Flow, 2018. **69**: p. 83-94.
16. Forooghi, P., M. Stripf, and B. Frohnapfel, *A systematic study of turbulent heat transfer over rough walls.* International Journal of Heat and Mass Transfer, 2018. **127**: p. 1157-1168.

17. Orlandi, P., D. Sassun, and S. Leonardi, *DNS of conjugate heat transfer in presence of rough surfaces.* International Journal of Heat and Mass Transfer, 2016. **100**: p. 250-266.

18. Arcoumanis, C. and J.-C. Chang, *Heat transfer between a heated plate and an impinging transient diesel spray.* Experiments in Fluids, 1993. **16**(2): p. 105-119.

19. Meingast, U., et al., *Analysis of spray/wall interaction under diesel engine conditions.* SAE transactions, 2000: p. 299-312.

20. Meingast, U., L. Reichelt, and U. Renz, *Measuring transient wall heat flux under diesel engine conditions.* International Journal of Engine Research, 2004. **5**(5): p. 443-452.

21. Huang, J.C. and G.L. Borman, *Measurements of instantaneous heat flux to metal and ceramic surfaces in a diesel engine.* SAE transactions, 1987: p. 66-81.

22. Mahmud, R., et al., *Characteristics of Flat-Wall Impinging Spray Flame and Its Heat Transfer under Diesel Engine-Like Condition: Effects of Injection Pressure, Nozzle Hole Diameter and Impingement Distance*. 2019, SAE Technical Paper.

23. *Coaxial Thermocouple MCT.* [cited 2020 02.04.]; Available from: https://mueller-instruments.de/en/temperature-sensors/heat-flux-thermocouple-mct-for-high-dynamic-tests/.

24. Alifanov, O.M., *Inverse heat transfer problems*. 2012: Springer Science & Business Media.

25. Vuorinen, V. and K. Keskinen, *DNSLab: A gateway to turbulent flow simulation in Matlab.* Computer Physics Communications, 2016. **203**: p. 278-289.

26. Pandurangi, S.S., et al., *Onset and progression of soot in high-pressure n-dodecane sprays under diesel engine conditions.* International Journal of Engine Research, 2017. **18**(5-6): p. 436-452.

27. Pope, S., *An explanation of the turbulent round-jet/plane-jet anomaly.* AIAA journal, 1978. **16**(3): p. 279-281.

28. Skeen, S.A., et al., *A progress review on soot experiments and modeling in the engine combustion network (ECN).* SAE International Journal of Engines, 2016. **9**(2): p. 883-898.

29. Reitz, R.D. and R. Diwakar. *Effect of drop breakup on fuel sprays*. 1986. SAE transactions.

30. Wright, Y., et al., *Simulations of spray autoignition and flame establishment with two-dimensional CMC.* Combustion and Flame, 2005. **143**(4).

31. Blomberg, C.K., et al., *Modeling split injections of ECN "Spray A" using a conditional moment closure combustion model with RANS and LES.* SAE International Journal of Engines, 2016. **9**(4).

32. Craft, T., et al., *A new wall function strategy for complex turbulent flows.* Numerical Heat Transfer, Part B: Fundamentals, 2004. **45**(4): p. 301-318.

33. Kawanabe, H., J. Komae, and T. Ishiyama, *Analysis of flow and heat transfer during the impingement of a diesel spray on a wall using large eddy simulation.* International Journal of Engine Research, 2018.

34. Flack, K.A. and M.P. Schultz, *Review of hydraulic roughness scales in the fully rough regime.* Journal of Fluids Engineering, 2010. **132**(4).

35. Schultz, M. and K. Flack, *The rough-wall turbulent boundary layer from the hydraulically smooth to the fully rough regime.* Journal of Fluid Mechanics, 2007. **580**: p. 381-405.

36. Demirel, Y.K., O. Turan, and A. Incecik, *Predicting the effect of biofouling on ship resistance using CFD.* Applied Ocean Research, 2017. **62**: p. 100-118.

37. ISO, E., *4287: 2009. Geometrical product specifications (GPS)-surface texture: profile method–terms, definitions and surface texture parameters (ISO 4287: 1997+ Cor 1: 1998+ Cor 2: 2005+ Amd 1: 2009)(includes Corrigendum AC: 2008 and Amendment A1: 2009)*. 2009.

38. Bons, J., *A critical assessment of Reynolds analogy for turbine flows.* J. Heat Transfer, 2005. **127**(5): p. 472-485.

39. Wehrfritz, A., et al., *Large eddy simulation of n-dodecane spray flames using flamelet generated manifolds.* Combustion and Flame, 2016. **167**: p. 113-131.

40. Arcoumanis, C. and P. Cutter, *Flow and heat transfer characteristics of impinging diesel sprays under cross-flow conditions.* SAE transactions, 1995: p. 798-812.

Performance of Direct Injected Propane and Gasoline in a High Stroke-to-Bore Ratio SI Engine: Pathways to Diesel Efficiency Parity with Ultra Low Soot

D. Splitter, V. Boronat, F. Chuahy, and J. Storey,

ORNL- Oak Ridge National Laboratory. 2360 Cherahala Blvd., 37932 TN, USA.

E-mail: splitterda@ornl.gov
Telephone: +(1) 865 341 1347

Abstract. This work explores pathways to achieve diesel-like, high-efficiency combustion with stoichiometric 3-way catalyst compatible combustion in a single-cylinder spark ignition (SI) research engine. A unique high stroke-to-bore engine design (1.5:1) with cooled exhaust gas recirculation (EGR) and high compression ratio (r_c) was used to improve engine efficiency by up to 30% compared with a production turbocharged gasoline direct injection spark ignition engine.

Engine experiments were conducted with both 91 RON E10 gasoline and liquified petroleum gas (LPG) (i.e., autogas) and were compared to legacy gasoline data on the production engine. Geometric compression ratio (**r_c**) of 13.3:1 was used for both fuels with additional experiments at 16.8:1 for LPG only. Measurements of exhaust soot particle size and number concentrations were made with both fuels. Significant reduction in soot particles across the whole particle size range were achieved with LPG due to the elimination of in-cylinder liquid films. The effects of EGR, late intake valve closing (IVC) and fuel characteristics were investigated through their effects on efficiency, combustion stability and soot production. Results of 47% gross thermal efficiency, and 45% net thermal efficiency at stoichiometric engine operation, at up to 17 bar IMEP and 2000 r/min with 16.8:1 r_c were achieved with LPG. Estimated brake efficiency values were compared to a contemporary medium duty diesel engine illustrating the benefits of the chosen path for achieving diesel efficiency parity.

1. Introduction

Achieving thermal efficiency parity with diesel engines is one of the major challenges of stoichiometric spark ignition (SI) engines, yet it is a promising path forward to reduce greenhouse gas emissions and simplify criteria pollution control through the use of three-way catalysts (TWC). Stoichiometric SI combustion presents major disadvantages when compared to diesel combustion. Primarily SI engine design is limited by knock, and thus r_c's of less than 12 are typical. Additionally, the need for a stoichiometric mixture for TWC operation eliminates the possibility of air dilution, a known strategy to improve combustion thermodynamic efficiency. Nevertheless, exhaust gas recirculation (EGR) can be used to mitigate this loss [1], while also reducing knock in naturally aspirated engines [2]. Mixture dilution in these engines is achieved with cooled EGR. Combustion stability, measured by cycle-to-cycle variations, limits the dilution level and thus the efficiency benefits that can be achieved. At high engine loads, cooled EGR becomes less effective at reducing knock and can even cause knock to increase [3]. At part load, SI engines require throttling to control the air fuel ratio of the mixture, introducing pumping losses. These losses can be reduced with flexible valve operating strategies like late intake valve closing [4], which

can be provide additional benefits when combined with cooled EGR [2]. Finally, SI engines are susceptible to stochastic pre-ignition (SPI) which can severely limit engine load and efficiency [5,6].

A major benefit of SI engines is that they allow the use of low carbon content fuels like methane and propane. Additionally, criteria pollutant control, like unburned hydrocarbons, carbon monoxide and nitrogen oxides (UHC, CO and NOx) is extremely efficient and does not require an additional reducer, as in selective catalytic reduction (SCR) systems, characteristic of diesel engines. Consequently, it is of interest to develop ways of closing the efficiency gap between diesel and stoichiometric SI engines combining the best characteristics of each system.

The control of criteria pollutants (UHC, CO and NOx) in stoichiometric SI engines has evolved quite substantially. Conversion efficiencies over a warm catalyst approaching 99.9% are common, reducing the challenge of emissions control to the first 30 seconds of a cold start. Additionally, precious metal loading in TWCs have been decreasing as thinner, lighter substrates with lower wash coat requirements are developed and thus substantially reduce aftertreatment cost [7,8].

At the same time, diesel engines are expected to meet significant technical barriers in being able to meet future NOx regulations. Recently the California air resources board (CARB) has announced its intention to reduce U.S. domestic NOx emission regulations for medium- and heavy-duty vehicles by an order of magnitude by 2027 [9]. While SCR systems are very effective at reducing NOx at steady state conditions, they require the use of urea as a reducer, which decreases the overall system fluid efficiency. Additionally, transient control requires complex control strategies to optimize urea consumption and formation of urea crystal deposits. The major challenge with upcoming MD/HD regulations is the requirement to maintain NOx control under extremely low engine loads. SCR systems currently cannot operate effectively below 170°C due to poor urea decomposition and low ammonia storage in the substrate. Currently, the deactivation of SCR systems at low temperatures is responsible for a large disparity between cycle-measured emissions during engine certification and real-world operation [10]. Current diesel NOx control research [11] which assesses the feasibility of meeting the proposed regulations showed that additional close-coupled catalysts and NOx traps may be required. These measures are expected to increase the cost of diesel aftertreatment system by as much as 100% [10]. The return on investment of the additional emissions control costs is duty-cycle dependent and may not be feasible for medium-duty vehicles with low annual mileage.

Currently, SI engines can achieve the criteria emissions regulation targets proposed for diesel engines by California Air Resource Board (CARB) [9,12]. However, due to their relatively low fuel efficiency, achieving phase 1 and phase 2 CO_2 emission regulations [13] is a challenge that is typically overcome by using fuels with higher hydrogen content (i.e., higher H/C ratio) than gasoline. While gasoline shows a marginal CO_2 improvement over diesel fuel for a given engine efficiency, liquefied petroleum gas (LPG) and compressed natural gas (CNG) can achieve significant reductions simply due to their lower carbon content. For engines with brake thermal efficiency (BTE) parity, LPG and CNG can reduce CO_2 emissions when compared to a diesel fuelled engine by 11.7% and 32.6%, respectively. Consequently, if an engine can achieve diesel-like efficiencies with LPG or CNG, there can be a simultaneous reduction in CO_2 emissions as well as a simplification, and cost reduction of the emissions control system. Both LPG and CNG exhibit high knock and pre-ignition resistance due to their high octane rating, which makes them great candidate fuels for high efficiency SI combustion. Their high volatility significantly reduce if not eliminate the formation of fuel films inside the cylinder during the injection process and likely results in reductions to soot and particulate matter emissions. Nevertheless, despite the potential advantages of both fuels, LPG offers significant advantages over CNG in terms of storage and delivery as it can be stored at relatively low pressures (~5 bar) and directly injected in common direct injection fuel systems with minor modifications. This makes it the more attractive choice for a simpler, cheaper system that could be rapidly adopted in the MD market. Consequently, the efficiency potential and particulate emissions of LPG in an SI direct injected (DI) engine will be a focus of the current work.

To achieve diesel-like efficiencies, loss mechanisms of stoichiometric SI engines must be identified and addressed. Additionally, technologies need to take advantage of the unique fuel properties to maximize engine performance. To that end, ORNL has recently commissioned a custom-built long stroke single-cylinder research engine (LSE) targeting high efficiency SI combustion, as first described in Boronat et al. [14]. To allow optimized control of mixture dilution, compression pressure and residual gases, the engine is fitted with EGR and a variable valve actuation system. The uniqueness of the platform comes in the form of a significantly larger stroke-to-bore ratio of 1.5:1 against a stock ratio of 1:1. The increase in stroke-to-bore ratio results in increased in cylinder turbulent kinetic energy (TKE), increasing turbulent flame speeds and reducing combustion durations. It is well documented that the use of "domed" pistons to achieve high compression ratio (r_c) is typically followed by increases in incomplete combustion due to flame quenching. The LSE avoids this limitation due to its increased piston

travel distance and naturally higher geometrical r_c, thus further increasing the potential for efficiency improvements.

The present work builds on previously reported LSE results [14] and explores in detail the mechanisms by which the LSE can improve efficiency and what opportunities are left for further improvement. Results with both gasoline and propane (surrogate for LPG) are shown and contrasted in terms of performance and efficiency. Detailed soot measurements including filter smoke number, photoacoustic measurements and scanning mobility particle sizing (SMPS) are used to characterize the soot emissions of the engine with both fuels. Results are contrasted against legacy data on a similar engine platform, and assessments of LPG engine efficiency are made.

2. Experimental set up

2.1 Engine platform

The LSE is a custom platform based on the General Motors (GM) Ecotec LNF family of engines, and was developed to operate under a wide variety of modes and engine operating conditions.

The LSE was developed on custom-built billet block, crankshaft and connecting rods. Figure 1 shows pictures and a schematic of the LSE. Custom components were combined with a stock cylinder

Fig. 1. LSE billet block, crankshaft and connecting rod. Cylinder head is equipped with a fully flexible valve actuation system by Sturman Industries. Engine was built for single cylinder operation. Custom crankshaft was built with two counterweights for overall engine balance.

Table 1. Stock LNF and LSE geometry information.

	LNF	LSE
Bore [mm]	86	86
Stroke [mm]	86	129
Connecting Rod [mm]	145	182.9
r_c [-]	9.2:1, 11.85, 13.8	13.3:1 (same piston as 9.2 LNF), 16.8 (same piston as 11.85 LNF)
Number of Valves	4	4
Displaced volume [l]	0.495	0.7493
Exhaust valve lift [mm]	10.2	9
Exhaust valve duration [°CA]	188	variable
Exhaust cam phasing authority [°CA]	-	variable
Inlet valve lift [mm]	10.2	9 (fixed in this study)
Intake valve duration [°CA]	200	variable
Intake cam phasing authority [°CA]	-	variable

head and piston assemblies. The stock valve actuation system was replaced by a fully flexible Sturmann variable valve actuation (VVA) system. The system enables variation of valve lift, opening time and duration of actuation, with independent control of each valve. The ballistic response of the valves in the system does not allow it to mimic the stock valve lift profile and maximum valve lift is limited to 9mm (vs. stock of 10.2mm). Detailed discussion of this system on can be found in [15,16,17,18]. Computational fluid dynamic studies showed that for matched valve opening events minimal differences were observed on the flow pattern and TKE profile of the engine as repotted in Boronat et al. [14], thus allowing direct comparisons to be made between the LSE and the stock LNF.

The production LNF coil on plug assembly is retained and can deliver 80mJ of spark energy. A spark plug two heat ranges colder replaces the stock spark plug to avoid hot-spot-run-away events while exploring high load conditions. Table 1 shows a summary of the production engine and the LSE geometries. Naturally the longer stroke required a longer connecting rod, and results in a higher r_c for a given piston when compared to the stock engine.

Figure 2 shows the two piston geometries used in the experiments. The stock LNF piston results in a r_c of 9.2 on the stock engine. When used in the LSE r_c is increased to 13.3 for the same top-dead-center (TDC) volume. A second piston bowl was modified to achieve a higher r_c of 11.8:1 on the stock engine while avoiding a "domed" configuration. When installed in the LSE the r_c is increased to 16.8. Further details can be found on previous reported work [15]
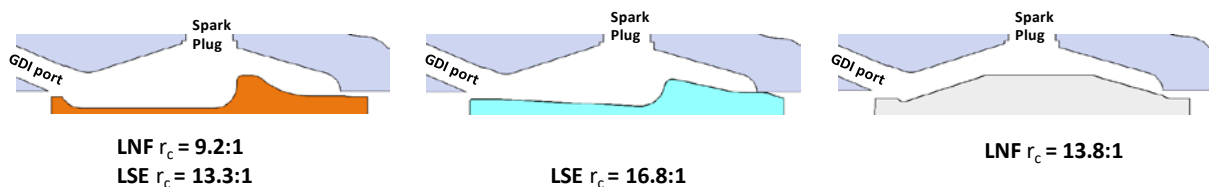
Fig. 2. Piston geometries used in the present work with r_c noted for each design and respective engine below image**.**

2.2 Experimental Setup and Testing Methodology

Engine control was managed by a National Instruments control software combined with the Combustion Analysis Toolkit (DCAT) package. In cylinder pressure traces were measured using a piezo-electric pressure transducer made by Kistler (6125C). Engine crank position was acquired by a shaft mounted encoder (2614C11) providing a crank angle resolution of 0.2 crank angle degrees. For all experimental conditions 2000 consecutive combustion cycles were recorded to generate ensemble metrics. Engine air supply was managed by an Alicat 2000SLPM air mass controller. Air intake temperature was controlled using a Sylvania Suremax 800 heater placed upstream of the intake plenum. Intake and exhaust surge tanks were installed to mitigate pressure pulsations, characteristic of single cylinder engines, which could affect boundary condition measurements. A cooled EGR loop was installed between the intake and exhaust surge tanks. An EGR cooler was used to keep the gas outlet temperature at a constant 40°C. EGR was adjusted by an electronic actuated valve in the EGR system and an engine back-pressure valve located downstream of the exhaust surge tank. Engine backpressure was adjusted to simulate a turbocharger with a combined efficiency of 40%, according to the calculation approach presented in [16].

Fuel supply was accomplished with six piston accumulators pressurized to 100 bar by nitrogen gas. Delivery pressure was finely controlled downstream of the accumulators by a TESCOM (ER3000SI-1) pneumatic pressure regulator. Fuel mass flow was measured by a Coriolis Micro-motion ELITE (CMF010P) flow meter. For all experimental conditions fuel injection timings were fixed at -280°CA aTDCf and spark timing was adjusted to achieve optimal thermodynamic efficiency while avoiding knock. Peak cylinder pressure was limited to 100bar. Combustion stability as measured by the coefficient of variation (COV) of the indicated mean effective pressure (IMEP) was kept below 3%.

2.3 Emissions equipment

Exhaust was sampled for criteria pollutants (CO, CO2, HC, and NOx) through a sampling line heated to 190 °C downstream of the surge tank and analyzed with a number of instruments including non-dispersive infrared (NDIR) for CO and CO2 detection, flame ionization detection (FID) for THC measurements, and chemiluminescence detection (CLD) for NOx.

Particulate matter (PM) was characterized through particle size and number measurements and carbonaceous soot measurements. Carbonaceous soot was measured through a photoacoustic sensor (AVL microsoot). Figure 3 shows a schematic of the particle size distribution (PSD) measurement apparatus. An ejector pump-based microdilution system was used to sample the exhaust downstream of the surge tank. The ejector pump was mounted directly on the probe to minimize line lengths. Total dilution ratio was measured by the CO_2 ratio of samples before and after dilution using a Fourier transform infrared spectrometer (FTIR) and ranged from 10:1 to 12:1. A scanning mobility particle sizer (SMPS, TSI Model 3936) was used to measure the particle size distribution of the diluted sample. Combined with a differential mobility analyzer (DMA, TSI model 3081) and a condensation particle counter (CPC, TSI model 3025) particle sizes from 9.8 to 429nm and quantities were measured.
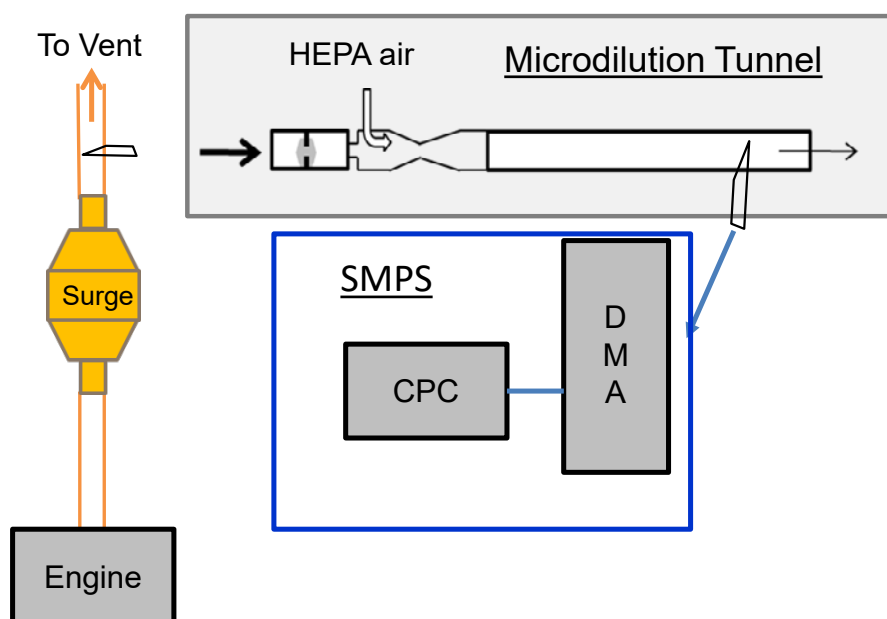
Fig. 3. Microdilution exhaust sampling system for particle size and particle number quantification.

2.4 Fuels

The engine was operated with propane (~96% propane balanced with ~2% butane and ~2% ethylene), and an 87 anti-knock index (AKI) gasoline with 10% ethanol by volume. Table 2 shows a summary of fuel properties and composition.

Table 2. Fuel properties

	87 AKI E0	87 AKI E10	LPG
RON (ASTM D2699)	90.2	90.9	112
MON (ASTM D2700)	83.9	83.4	97
S (RON – MON)	6.3	7.5	15
Boiling Point [°C]	N/A	N/A	-42
10% [°F] (ASTM D86)	97	52.3	N/A
50% [°F] (ASTM D86)	205	94.3	N/A
90% [°F] (ASTM D86)	316	325	
C wt% (ASTM 5391)	86.49	82.78	82.78
H wt% (ASTM 5391)	14.06	13.59	17.22
O wt% (ASTM 5599)	0	3.63	0
LHV [MJ/kg] (ASTM D240)	43.454	41.410	46.4
oxygenates % vol. (ASTM 5599)	0	9.87	0

2.5 Combustion analysis

Synchronous and asynchronous experimental data were processed by an in-house MATLAB based post-processing routine. Cylinder pressure traces were filtered using a zero-phase filter and combined with camshaft position feedback to calculate in-cylinder trapped mass on a cycle by cycle basis using the approach proposed by Cavina et al. [19]. Heat transfer losses were estimated using Woschni correlation [20] and crevice losses were calculated using the approach of Gatowski et al. [21]. Apparent heat release is calculated from filtered pressure traces and combined with heat transfer and crevice losses to derive total heat release. Engine TDC was adjusted using a magnetic proximity probe (AVL OT-Sensor 428) during motoring operation and TDC loss angle was adjusted based on the approach reported by Tunestål et al. [22].

3. Results

The results section will be divided into 4 sections spanning analysis of efficiency and particulate emissions.

3.1 LSE and fuel effects on combustion duration and combustion efficiency

Initial results of combustion duration and incomplete combustion are plotted for gasoline and LPG in Figure 4 A and B respectively. The results compare the LSE to the production LNF engine. Note that the gasoline LNF data in Figure 4 A was originally reported in Splitter et al. [16,17,18], which used the same valve timings, piston, and Sturman cylinder head as in the present work. The gasoline results in
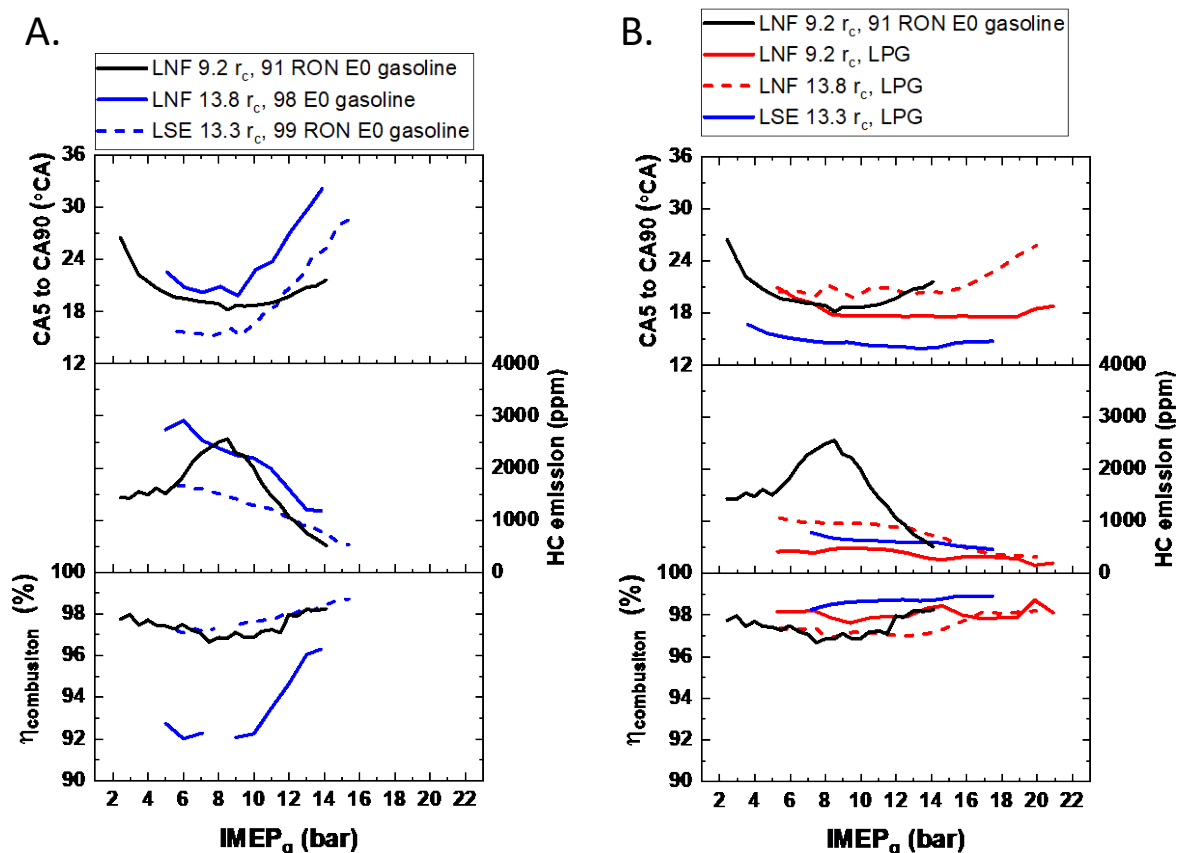
Fig. 4 Combustion efficiency, HC emissions, and combustion duration for (A.) Gasoline only with LNF at r_c=9.2 and r_c=13.8:1 ratios and LSE at r_c=13.3:1, and (B) LPG and gasoline reference with LNF at r_c=9.2 and propane with LNF with r_c=13.8:1 ratios and LSE with r_c=13.3:

Figure 4 A clearly highlight the advantages of the LSE platform with gasoline in a near r_c neutral analysis. Specifically, for a r_c of ~13.5:1 the LSE enables HC emissions equal to the production LNF engine (9.2 r_c) and thus reduced incomplete combustion losses. The source of these is attributed to the "dome" piston (Figure 2) needed in the LNF geometry to generate increased r_c. Clearly, the increased squish area in the dome design reduced combustion efficiency and increased combustion duration, effects that are well documented in the literature [23]. However, the approach used in the LSE offers high compression without increased quench and thus shows no effect to combustion efficiency; in fact combustion efficiency was seen to have increased with the LSE design, an effect attributed to increased charge motion. The increase in charge motion and reduction of quenching regions are evident on the combustion durations in Figure 4 A, where relative to the stock LNF, the dome piston showed increased combustion duration and the LSE showed reduced combustion duration. Note, that the increased r_c achieved through either the dome piston in the LNF or the stock piston in the LSE, result in earlier onset and more extreme knock, where the knock limited spark phasing effects on increasing combustion duration are also evident in the figure. Moreover, the similar r_c's in the dome piston and stock piston in the LSE result in the knock limit near the same load.

Interestingly when the fuel is changed from gasoline to LPG as shown in Figure 4 B, the trends in combustion duration of the LSE and dome piston continue, but the effects of quench on combustion efficiency are much less clear. For all r_c's and engine configurations tested it was observed that relative to gasoline, LPG offers improved combustion efficiency and reduced HC emissions. These effects are attributed to improved fuel vaporization from LPG compared to gasoline, and thus in-cylinder processes such as fuel films and injection strategy effects on mixing could be less pronounced with LPG than with gasoline. Interestingly the LSE still retains faster combustion than the LNF, and for a given engine configuration there is no appreciable combustion duration difference between LPG and gasoline (LNF 9.2 r_c). Note that with LPG there was virtually no knock onset observed in either engine at the tested conditions and combustion phasing was retarded only because of peak cylinder pressure limits being reached.

3.2 Long Stroke Engine Liquified Petroleum Gas Exhaust Gas Recirculation effects

The results in the previous section highlighted the combustion efficiency benefits that LPG offers over gasoline. Beyond these benefits, LPG also showed significantly improved EGR tolerance when compared to gasoline. Figure 5 shows that for all load conditions the COV of IMEP of LPG was overall lower than gasoline's and allowed a higher percentage of EGR before the COV limit was reached.

It is hypothesized that two main effects are responsible for the improved EGR tolerance performance of LPG; (1) Its laminar flame characteristics and (2) its flame stretch properties like Markstein length/number. As illustrated in the Borghi-Peters diagram [24] an increase in the laminar flame speed or reduction in the flame thickness of the fuel relative to turbulent velocity and length scales leads to a flame that is less prone to influences from the flow field. Flow field distortions of the flame kernel are believed to be one of the main components of cycle-to-cycle variation in spark ignition engines [25,26]. As EGR dilution is increased, the laminar flame speed of the fuel is reduced, and its flame thickness is increased. An increase in flame thickness makes the fuel more prone to influences from the flow field as turbulent eddies can corrugate the flame to a larger extent. LPG shows a lower thickening of the flame when EGR dilution is introduced, thus favoring its resistance to corrugation by turbulent eddies. LPG also shows a higher laminar flame speed than gasoline which allows it to have faster flame kernel formation and propagation, increasing the Dahmkoler number of the flame [27]. The second effect that contributes to LPG's higher EGR tolerance is related to its flame stretch properties. The Markstein length modifies the laminar flame speed of the fuel due to preferential diffusion effects. Under the conditions relevant to internal combustion engines the Markstein length is positive and relatively small, of the order of 0.1-0.2mm [28,29]. It is currently unknown how much these effects contribute to LPG's superior dilution tolerance in a real engine environment. Nevertheless, the Markstein length of propane is positive (i.e., stretch effects reduce the laminar flame speed of the fuel) and is smaller than the Markstein length for iso-octane, a surrogate for gasoline. As such, based on the available literature, LPG should be less susceptible to stretch effects. The effect of flame stretch is expected to increase the differences in laminar flame speed between LPG and gasoline. Flame stretch and preferential diffusion effects on flame kernel formation and effects on COV of IMEP is a topic that needs to be further explored to understand if the benefits of LPG can be extended by optimizing charge motion and turbulence.
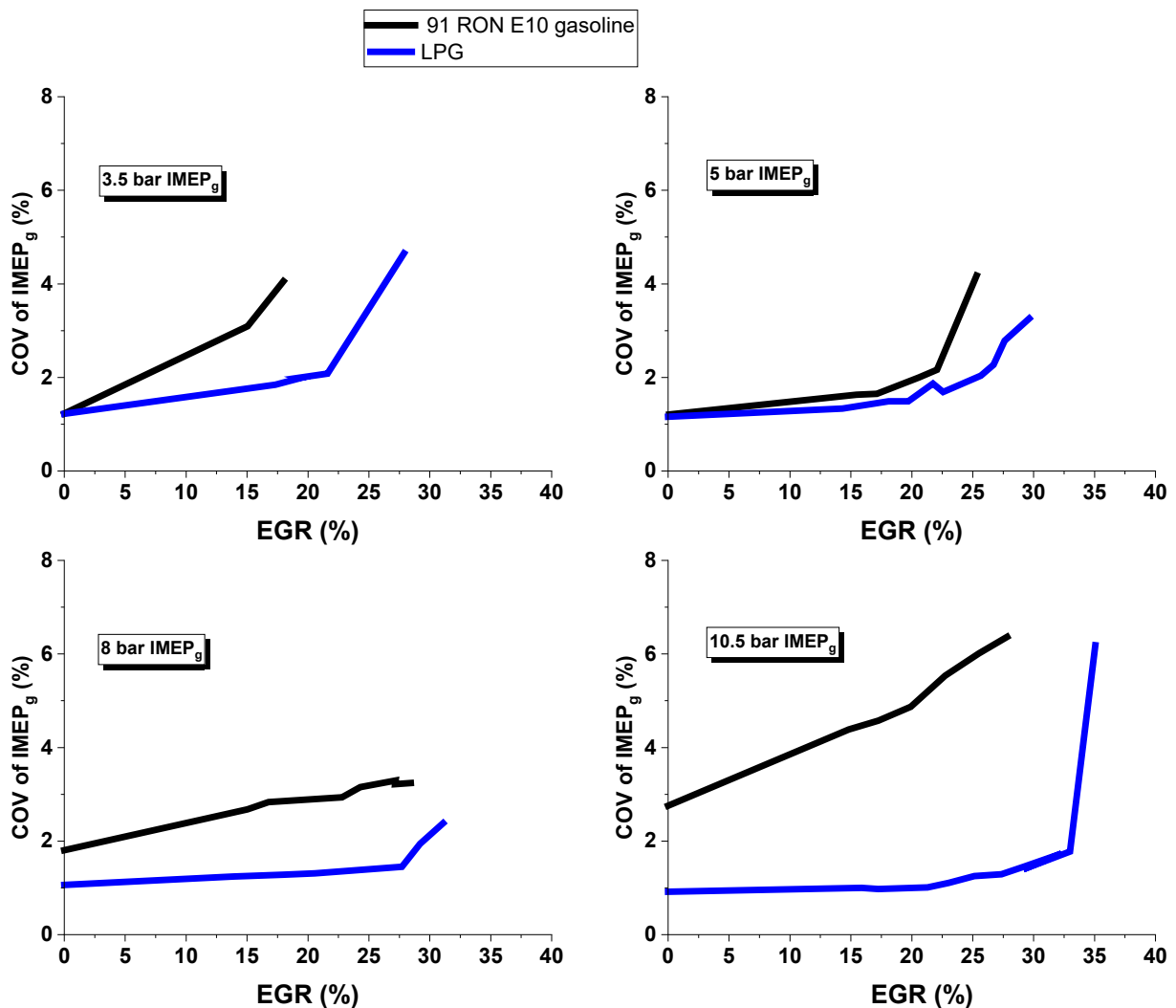
Fig. 5. COV of IMEP for DI gasoline (black) and LPG (blue) for four loads as a function of EGR at 2000 r/min.

3.3 Long Stroke Engine Liquified Petroleum Gas operating strategies for increased efficiency

The combined effects of LPG on engine efficiency were explored in a systematic approach. The LNF engine was operated in its stock form with LPG, and with the 13.8 r_c piston ("dome" piston). These experiments were conducted with 0% EGR and conventional cam timings. Results of the LNF (and LSE) with LPG are presented in Figure 6. Relative to gasoline with no changes to the engine r_c or operating conditions, LPG extends the load range significantly, but offers no significant efficiency benefits (green vs black lines in Figure 6); however, if r_c is increased then LPG can increase efficiency and simultaneously increase power density (blue vs black/green in Figure 6). At an 8 bar IMEP load, this results in approximately a 9.5% relative increase in efficiency compared to the baseline engine with either gasoline or LPG.

Using LPG but changing the engine from the LNF to the LSE offers further increase in efficiency observed (red vs green). These improvements are primarily due to reductions in heat transfer and combustion duration, as previously pointed out by Boronat et al. [14], there is also an increase in combustion efficiency which is minor but non-trivial. As shown in Figure 6, at an 8 bar IMEP load the LSE approach yields an approximate 16% relative improvement in efficiency compared to the baseline LNF. Although the LSE approach alone enabled good efficiency gain, the combination of EGR and even further increased r_c were also explored, which as shown in Figure 6, are where significant gains in efficiency can be realized. The high EGR rates possible with LPG were leveraged with late intake valve closing (110°CA bTDC vs 170°CA bTDC) and EGR. When used in tandem with 16.8 r_c this approach yielded

nearly a 30% improvement in efficiency compared to the baseline LNF engine. Moreover, the power density of the LSE with LPG is not fully represented here due to the flowrate limit of the stock fuel injectors. With increased flow rate injectors higher power density should be achievable. It should be noted that the efficiency and power density of the LSE SI LPG engine approach those of current medium duty diesel engines.
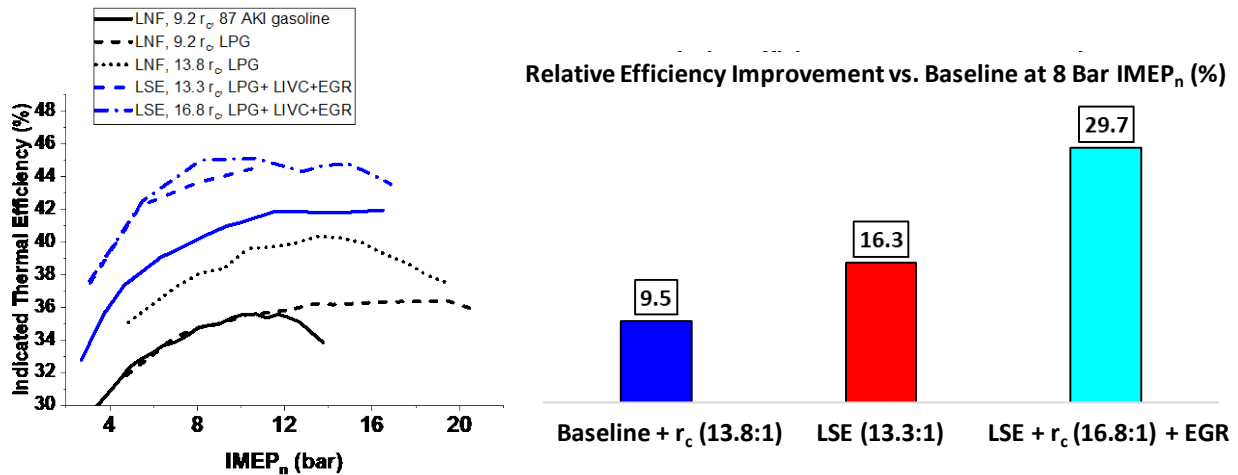
Fig. 6. Efficiency improvement pathway for ORNL LSE engine with LPG, pathway combined EGR and high r_c

3.4 LPG and gasoline FSN, Soot, and Particle Size Distributions comparisons

The previous section highlighted that that stoichiometric LPG offered significant improvements in efficiency, EGR tolerance, and combustion efficiency compared to stoichiometric gasoline, achieving efficiencies similar to diesel engine results. To further assess stoichiometric LPG engine operation, this section explores differences between LPG and gasoline particulate emissions.

Engine operation over a wide load range and several EGR levels were conducted. The LSE engine was operated with only the production LNF piston installed (Figure 2). The filter smoke numbers (FSN) of EGR sweep at four loads spanning the range of low-to-high load are plotted in Figure 7. Note that the 10.5 bar IMEPg load for gasoline was heavily knock limited and near its maximum spark retard while LPG was just becoming knock limited at this condition, so at the highest loads the combustion phasings were not matched, but at lower loads they are. At each load EGR was swept from 0% to the maximum possible until unstable engine operation occurred. The loads and conditions are the same as those presented in Figure 5, where COV of IMEP beyond 3 is where unstable operation existed.

Results in Figure 7 clearly show that LPG exhibits extremely low FSN values, effectively zero FSN for all EGR rates and loads ranging from 3.5 bar IMEPg to 10.5 bar IMEPg. TI is well known that fuel volatility and subsequent fuel wall wetting can be correlated with FSN and particulate emissions in SI DI engines. Szybist et al. [30] conducted several studies with DI in a GM LNF engine (i.e., the same engine the LSE in the present work is based on) and found that increased volatility fuels, like E20 and E85, and multiple injection events could be used to reduce particle emissions. That work and other simulation [31] and optical measurements [32], all support the hypothesis that the source of DI gasoline particulates is primarily form surface wetting.

These previous findings and the combined results further support the current hypothesis of reduced wall wetting with DI LPG compared to gasoline. The present results also show in Figure 7 that with LPG there is significantly reduced HC emissions, approximately 1/3 to 1/2 those of gasoline. These results are also observable with 0% EGR over a load sweep with several different engine configurations in Figure 4. The very low HC and effectively zero FSN with LPG regardless of load and EGR rate in Figure 7 combined with the similar findings regardless of engine configuration in Figure 4strongly suggest that DI LPG has very low surface wetting. Interestingly the results in Figure 7 also highlight that for gasoline, as EGR rate is increased FSN tends to be stable or decrease, with the latter prevalent at increased engine loads. Similar trends were also observed by Alger et al. [33] and Zhang et al. [34], where the latter work pointed out that as EGR rates increased the particle accumulation mode decreased and particles were primarily accumulation mode independent of fuel type used. In the present work similar processes appear to be occurring in gasoline, but at least for FSN there seems to be no

appreciable FSN from LPG entirely. Previous works attributed the accumulation mode to HC emissions; however, the present work observed an increase in HC emission in both gasoline and LPG with increased EGR rates, however, unlike gasoline, increased HC emission with LPG did not observe an increase in FSN. This suggests that with LPG, soot formation pathways from HC could eb different. To further explore the particles of LPG and gasoline further measurements and analysis were conducted.
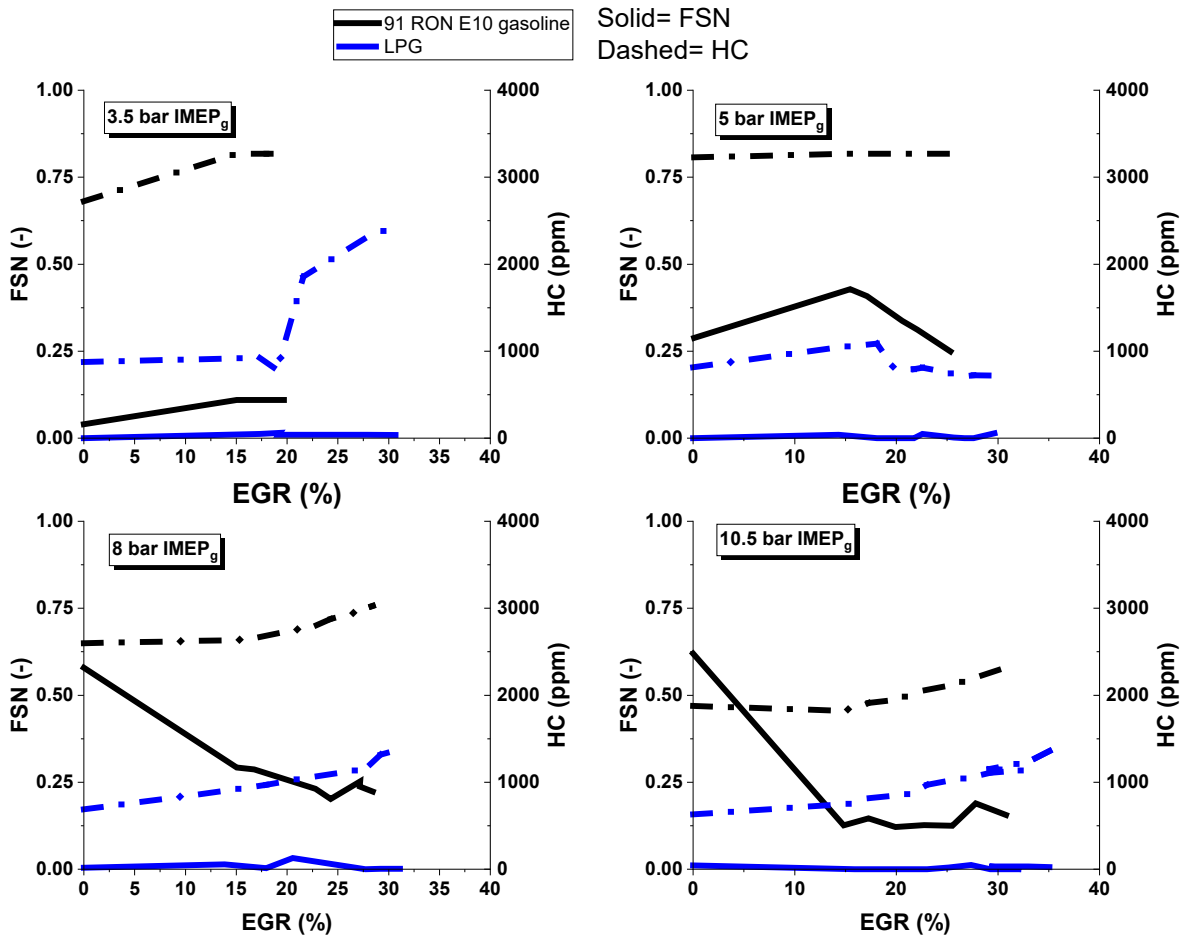
Fig. 7. FSN for DI gasoline (black) and LPG (blue) at four loads as a function of EGR at 2000 r/min.

To further analyze the particle emissions from DI LPG compared to gasoline, particle size distributions, and micro soot sensor (MSS) measurements were made. The results for a 0% EGR load sweep are plotted in Figure 8. Results show that like the EGR sweep (Figure 7), LPG has effectively zero FSN, but the results in Figure 8 also confirm that there is effectively zero soot for LPG as measured with a MSS. Likewise gasoline displayed similar trends in FSN and MSS measurements, which were low, but not an unmeasurable like those of LPG. Simultaneous acquisition of FSN, MSS< and SMPS particle measurements were made. The SMPS results for select loads are plotted in Figure 9, but the total particle number for the load sweep is displayed in Figure 8. Since measurements were conducted on a single cylinder engine, the total particle number (PN) was calculated on an IMEPn basis and corrected for dilution ratio. An average of 3 particle size measurements were made, where the dilution and load normalized average is plotted in Figure 8.

Interestingly despite the differences in soot and FSN between gasoline and LPG, the fuels have total PN that are of the same order and trend relatively well together. Gasoline operation at 13 and 15 bar IMEP was not possible due to knock limit of the fuel, but LPG displays a very interesting trend at these higher loads. Specifically, the total PN count is reduced by an order of magnitude.   It is thus hypothesized that most of the particles in both this engine for DI gasoline and LPG are occurring primarily from sources outside those of the fuels themselves, which could be lubricant or valve leakage
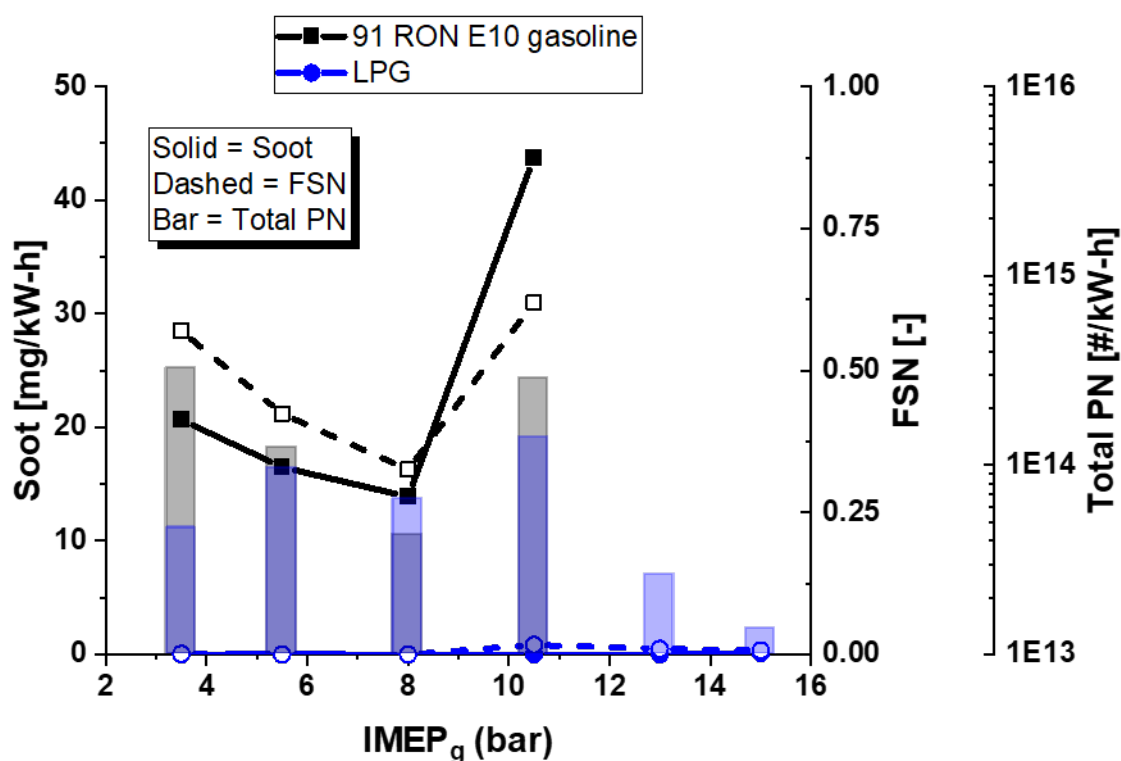
Fig. 8. Soot, FSN, and total particle number for DI gasoline (black) and LPG (blue) as a function of load at 2000 r/min with 0% EGR.

past exhaust valve seals from the hydraulic Sturman valve system. The sources of these are not directly known but elevated in-cylinder temperatures associated with higher engine loads could be responsible for at least part of the observed total PN reductions. Of particular note is that there is virtually no soot detected by the MSS for LPG whereas even the E85 resulted in measurable FSN in Szybist et al. [30] despite having lower particle numbers than the observed LPG results here. The lack of soot with LPG here is consistent with the idea that the particles observed with the SMPS are not soot carbon, but lubricant derived aerosols.

To further understand the sources of PM in the LPG engine the particle size distributions (PSD) are plotted in Figure 9. The shapes of the PSD of LPG compared to gasoline differ most when the particles are over approximately 100 nm diameter, with more of a pronounced log-normal distribution for the gasoline as compared to LPG. Unlike liquid fuels, the gaseous fuel is not likely to impinge on the walls or piston and result in pool fires or other sources of combustion particles, so the source of the particles is likely the lubricant and has more to do with the mechanics and temperature of lubricant aerosolization.

Consistent with this of lubricant as the primary source of LPG particles, the shapes of the PSD for the propane engine are plotted as a function of load with 0% and 15% EGR in Figure 10, where engine load is observed to reduce the particle size and total number. This is even more pronounced with 15% EGR, which is consistent with literature studies by others [33,34]. In contrast, broad particle size distributions are characteristic of DISI gasoline engines [35,36,37,38]. are not evident with LPG, suggesting that accumulation modes in general are very much reduced. Figure 10 illustrates that accumulation mode particles decay with load, where loads over ~10 bar IMEP show very limited accumulation mode particles (i.e., particles larger than ~30nm) with LPG. These findings combined with the efficiency results of Figure 6 suggest that DI LPG could be a viable opportunity for low emissions high efficiency engines like diesel engines that are common in medium duty applications.
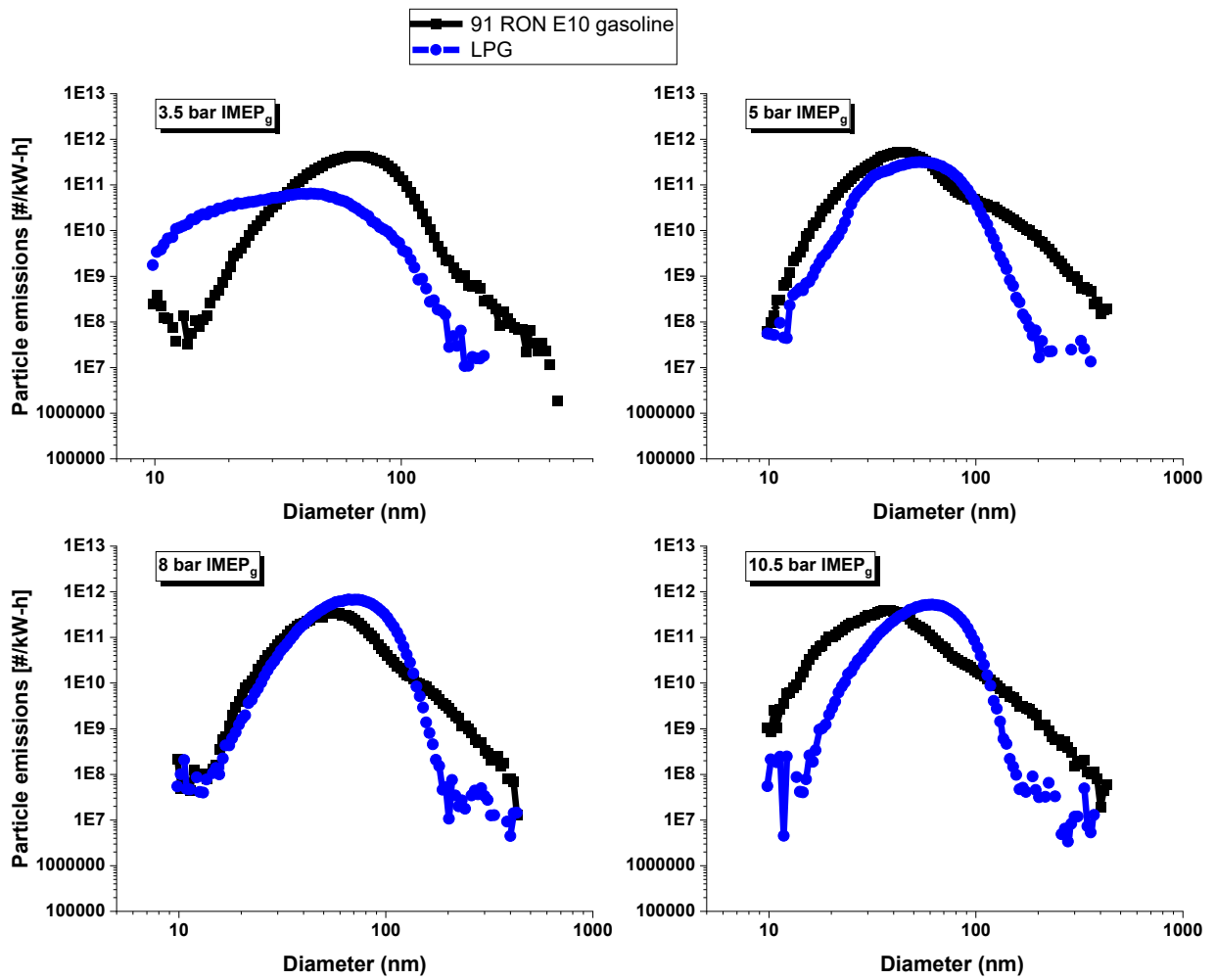
Fig. 9. Particle size distributions for DI gasoline (black) and LPG (blue) for four loads at 2000 r/min with 0% EGR.
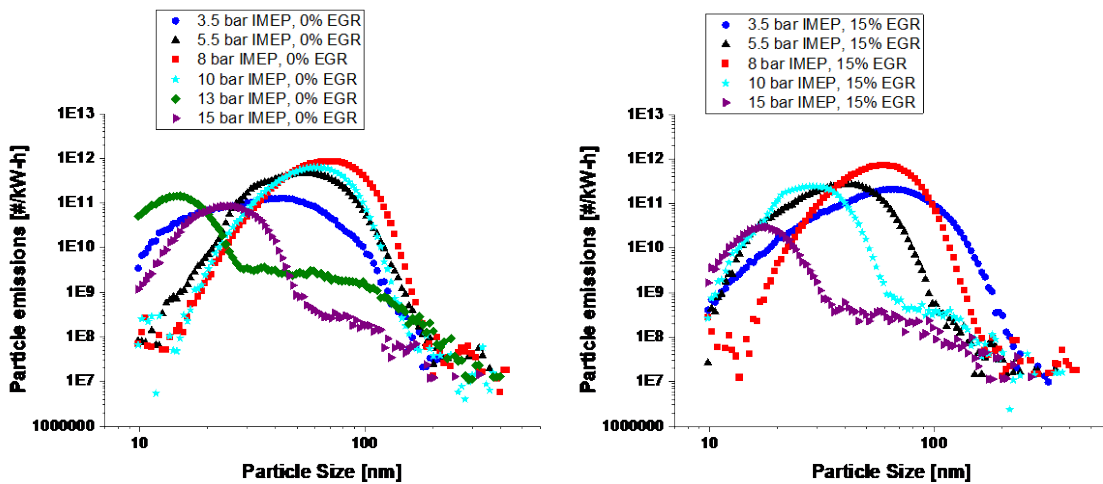
Fig. 10. Particle size distributions for LPG load sweeps with (A.) 0% EGR and (B.) 15% EGR

4. Discussion

The present results highlight that low PM and diesel like efficiencies are possible with DI LPG in a high r_c approach. The significance of this is directly applicable to the medium duty engine sector, which, in the United States, is primarily fueled by diesel and gasoline engines. In this sector it is common for 6-7L gasoline and diesel engines to be employed for a wide range of applications. One of the most prevalent engines is the Cummins ISB 6.7L diesel engine. The current results are demonstrated on a 0.75L single cylinder engine, and thus in a V8 configuration this would translate to a 6L total displacement design, which is highly relevant to the United States medium-duty sector.

Therefore, it is of interest to estimate what efficiency and performance of a LSE based LPG engine could be. Efficiency and load were corrected for friction using the default constants used in GT-power as explained in Boronat et al. [14] and Splitter et al. [17, 18]. Because the exact friction is unknown, the friction was estimated not as a direct number but a range. It was assumed that technologies to reduce friction could be applied to reduce friction up to 40% over default GT-Power values, which is relevant to what literature values have been reported by others [40]. The results of this analysis with the best efficiency LSE LPG results are plotted in Figure 11 and compared to the NHSTA reported values of the 2019 Cummins ISB, which are used for certification purposes. Clearly the results of DI LPG very closely approach those of the ISB in terms of brake thermal efficiency (BTE) and output (BMEP). Note that the load sweep with the LPG engine was prematurely stopped because the fuel injection system was unaltered form the stock engine and the injector duration needed for high load was beyond the safety limits imposed by the control software. A LPG specific injector design with increased flowrate would likely be required for further load expansion demonstration.
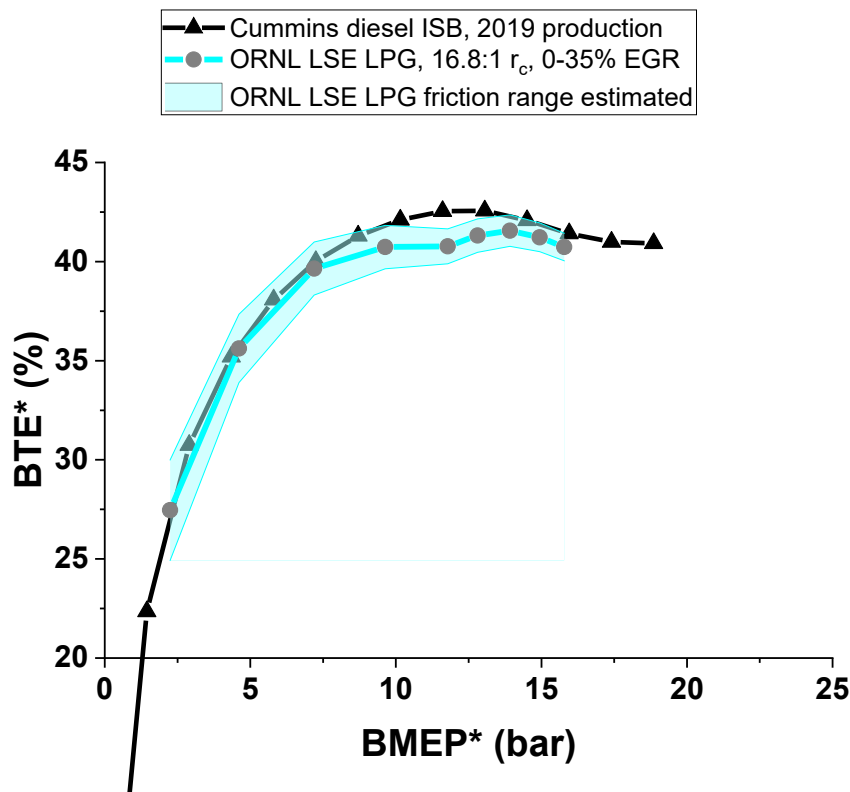
Fig. 11. ORNL LSE derived BTE numbers compared to 2019 production Cummins ISB diesel.

The ramifications of the efficiency illustrated in Figure 11 become apparent when examined form the perspective of pending 2027 emissions and efficiency regulation in the United states, which will regulate CO2 emissions in medium duty vehicles. Specifically, the 2027 standards are 457 [gCO_2/bhp-hr] and 535 [gCO_2/bhp-hr] in the SET cycle and FTP cycles respectively [39]. Since the emissions regulations are on a vehicle CO2 basis and not a, efficiency basis there are great potential opportunities for reduced carbon intensity fuels like LPG.

According to a national LPG survey by the Propane Education and Research Council (PERC) from 2017 and 2018 [41], LPG is between 91–96% on average propane, with the balance species of ethane (0.5–6.5%) and combinations of butane and its isomers (up to 7.5%). The significantly increased

H/C ratio of LPG ~2.67:1 is attractive for reducing CO_2 emissions by ~12% (energy basis when compared with diesel fuel) in a stoichiometric SI engine if engine brake thermal efficiency (BTE) parity with diesel is achieved, presenting a pathway to beyond 2027 compliance.

The results in the present work and that of Boronat et al. [14] illustrate that an engine design that exploits LPG's unique properties, greatly improves efficiency, and enables significantly higher r_c is possible. As shown in Boronat et al. [14], and Figure 6 and Figure 11 of the present work, diesel engine efficiency parity to the 2019 Cummins ISB is possible. Similar work has been conducted by Rengarajan et al. [42], in a multi cylinder engine but with lower efficiency than the present work due to reduced compression ratio and reduced stroke-to-bore ratio. The 2019 ISB is certified at 488 [gCO2/bhp-hr] (SET steady-state) and 525 [gCO2/bhp-hr] (FTP transient) [43], translating to 40.7% SET and 37.8% FTP cycle-averaged efficiency.

The present work highlights proof-of-concept results as illustrated in Figure 11 that DI LPG can approach or meet the Cummins 2019 ISB efficiencies. Thus, a similar SET and FTP transient efficiency to the ISB might be possible with DI LPG using an approach like the LSE. With further optimization and development, a target of 41% SET average with DI-LPG might be possible while meeting all applicable 2027 criteria emissions regulations as three-way catalyst of this program is highly possible as highlighted by previous work by others [44]. Achieving the such a cycle efficiency with LPG would result in cycle CO_2 emissions of 430gCO2/hp.hr, a 6% reduction from 2027 Phase 2 greenhouse gas (GHG) regulations and illustrate a pathway for SI engine approaches to meet or exceed 2027 emission regulation using DI LPG.

5. Conclusions

The present work illustrated performance and emissions of DI LPG and gasoline in a novel lone stroke engine (LSE). The major findings of the present work are outlined as the following.

1. Regardless of liquid petroleum gas (LPG) or gasoline fueling the LSE engine exhibited significantly improved combustion durations, which were ~20% faster than the production GM LNF engine, when using the same piston and TDC geometry. When using the similar compression ratios (i.e. a "dome" piston in the LNF was required), the LSE exhibited even further combustion duration benefits. These differences were attributed to significantly increased turbulence from the LSE's increase stroke

2. With gasoline the LSE was found to offer significantly improved HC and combustion efficiency improvements when high compression ratio was used. This was again attributed to the combustion chamber improvment for a given compression ratio with the LSE compared to the LNF. However, with DI LPG the advantages were reduced as HC emissions were extremely low with LPG overall.

3. LPG was found to enable increased EGR rate compared to gasoline (20-50% relative increase depending on load). The results were attributed to fundamental flame dynamics and combustion properties such as flame stretch differences of LPG vs. gasoline when EGR is used.

4. A combination of DI LPG with LIVC (110°CA bTDC$_f$), EGR (~30%) and high r_c (16.8:1) was found to yield in excess of 45% NTE with diesel like power density. This was an improvement of ~30% relative to the production engine with DI LPG.

5. DI LPG was found to have effectively zero measurable FSN and soot, but similar PN to gasoline. Particle size distribution (PSD) as a function of load showed that as load increased regardless of 0% or 15% EGR, DI LPG exhibited smaller diameter and lower number counts of particles. This translated to reductions in total PN overall. These combined results were postulated to be an effect of significantly reduced wall wetting with DI LPG as compared to gasoline.

6. Efficiency results were compared to a conventional MD diesel engine in the form of the 2019 Cummins ISB. Brake thermal efficiency of the single-cylinder LSE was estimated by a friction correlation and compared very favorably to the efficiency of the Cummins engine and power density. The results show promise for pathways of low GHG/CO2 fuels to meet future emissions regulation with SI TWC compatible combustion.

Acknowledgements

References

1. Wissink, M.L., Splitter, D.A., Dempsey, A.B., Curran, S.J., Kaul, B.C. and Szybist, J.P., 2017. An assessment of thermodynamic merits for current and potential future engine operating strategies. *International Journal of Engine Research*, *18*(1-2), pp.155-169.

2. Alger, T., Mangold, B., Roberts, C. and Gingrich, J., 2012. The interaction of fuel anti-knock index and cooled EGR on engine performance and efficiency. *SAE International Journal of Engines*, *5*(3), pp.1229-1241.

3. Szybist, J.P., Wagnon, S.W., Splitter, D., Pitz, W.J. and Mehl, M., 2017. The reduced effectiveness of EGR to mitigate knock at high loads in boosted SI engines. *SAE International Journal of Engines*, *10*(5), pp.2305-2318.

4. Szybist, J.P., Youngquist, A.D., Barone, T.L., Storey, J.M., Moore, W.R., Foster, M. and Confer, K., 2011. Ethanol blends and engine operating strategy effects on light-duty spark-ignition engine particle emissions. *Energy & Fuels*, *25*(11), pp.4977-4985.

5. Jatana, G.S., Splitter, D.A., Kaul, B. and Szybist, J.P., 2018. Fuel property effects on low-speed pre-ignition. *Fuel*, *230*, pp.474-482.

6. Chapman, E.; Davis, R.; Studzinski, W.; Geng, P. (2014). "Fuel Octane and Volatility Effects on the Stochastic Pre-Ignition Behavior of a 2.0L Gasoline Turbocharged DI Engine". *SAE Int. J. Fuels Lubr*. **7** (2): 379–389. doi:10.4271/2014-01-1226.

7. Craig, A., Warkins, J., Aravelli, K., Moser, D. et al., "Low Cost LEV-III, Tier-III Emission Solutions with Particulate Control using Advanced Catalysts and Substrates," *SAE Int. J. Engines* 9(2):1276-1288, 2016, https://doi.org/10.4271/2016-01-0925.

8. Johnson, T., "Vehicular Emissions in Review," *SAE Int. J. Engines* 9(2):1258-1275, 2016, https://doi.org/10.4271/2016-01-0919.

9. CARB "California Air Resources Board Staff Current Assessment of the Technical Feasibility of Lower NOx Standards Associated Test Procedures for 2022 and Subsequent Model Year Medium-Duty and Heavy-Duty Diesel Engines", accessed 02/20/2020.

10. Posada, F., Badshah, H., Rodriguez, F. (2020). In-use NOx emissions and compliance evaluation for modern heavy-duty vehicles in Europe and the United States. Retrieved from The International Council on Clean Transportation website: https://theicct.org/publications/inuse-nox-hdvs-us-eu, accessed 06/01/2020.

11. Neely, G., Sharp, C., and Rao, S., "CARB Low NOx Stage 3 Program - Modified Engine Calibration and Hardware Evaluations," SAE Technical Paper 2020-01-0318, 2020, https://doi.org/10.4271/2020-01-0318.

12. Rao, S., Sarlashkar, J., Rengarajan, S., Sharp, C. et al., "A Controls Overview on Achieving Ultra-Low NOx," SAE Technical Paper 2020-01-1404, 2020, https://doi.org/10.4271/2020-01-1404.

13. Dieselnet, "United States: Heavy-Duty Vehicles: GHG Emissions & Fuel Economy", accessed 02/20/2020, https://dieselnet.com/standards/us/fe_hd.php#co2

14. Boronat, V., Splitter, D., and Dal Forno Chuahy, F., "Achieving Diesel-Like Efficiency in a High Stroke-to-Bore Ratio DISI Engine under Stoichiometric Operation," SAE Technical Paper 2020-01-0293, 2020, doi:10.4271/2020-01-0293.

15. Szybist, J.; Foster, M.; Moore, W.; Confer, K. Investigation of Knock Limited Compression Ratio of Ethanol Gasoline Blends. SAE Technical Paper 2010-01-0619; 2010; DOI: 10.4271/2010-01-0619.

16. Splitter, D.A. and Szybist, J.P., 2014. Experimental investigation of spark-ignited combustion with high-octane biofuels and EGR. 2. Fuel and EGR effects on knock-limited load and speed. *Energy & Fuels*, *28*(2), pp.1432-1445.

17. Splitter, D.A. and Szybist, J.P., 2014. Experimental investigation of spark-ignited combustion with high-octane biofuels and EGR. 1. Engine load range and downsize downspeed opportunity. *Energy & Fuels*, *28*(2), pp.1418-1431.

18. Splitter, D. and Szybist, J., 2014. Intermediate alcohol-gasoline blends, fuels for enabling increased engine efficiency and powertrain possibilities. *SAE International Journal of Fuels and Lubricants*, *7*(1), pp.29-47.

19. Cavina, N., Siviero, C., Suglia, R., "Residual Gas Fraction Estimation: Application to a GDI Engine with Variable Timing and EGR". SAE Int Engines. 2004-01-2943.

20. Woschni, G., " A Universally Applicable Equation for the Instantaneous Heat Transfer Coefficient in the Internal Combustion Engine," SAE Transactions, Vol. 76, 1967, p. 3065.

21. Gatowski, J. A., En N. Balles, Kwang Min Chun, F. E. Nelson, J. A. Ekchian, and John B. Heywood. "Heat release analysis of engine pressure data." SAE transactions (1984): 961-977.

22. Tunestål, Per. "TDC offset estimation from motored cylinder pressure data based on heat release shaping." Oil & Gas Science and Technology–Revue d'IFP Energies nouvelles 66, no. 4 (2011): 705-716.

23. Caris, D. F., and E. E. Nelson. "a new look at High Compression Engines". No. 590015. SAE Technical Paper, 1959. https://doi.org/10.4271/590015

24. Peters, N. (1999). The turbulent burning velocity for large-scale and small-scale turbulence. Journal of Fluid Mechanics, 384, 107-132

25. Enaux, B., et al. (2011). "LES study of cycle-to-cycle variations in a spark ignition engine." Proceedings of the Combustion Institute 33(2): 3115-3122.

26. Zhao, L., et al. (2017). "Examining the role of flame topologies and in-cylinder flow fields on cyclic variability in spark-ignited engines using large-eddy simulation." International Journal of Engine Research 19(8): 886-904.

27. Mounaïm-Rousselle, C., et al. (2013). "Experimental characteristics of turbulent premixed flame in a boosted Spark-Ignition engine." Proceedings of the Combustion Institute 34(2): 2941-2949.

28. T. Kitagawa, Y. Togami, K. Harada, T. Ogawa, Effects of Pressure on Unstretched Laminar Burning Velocity, Markstein Length and Cellularity of Propagating Spherical Laminar Flames, Transactions of the Japan Society of Mechanical Engineers Series B 70 (2004) 2197-2204.

29. B. Galmiche, F. Halter, F. Foucher, Effects of high pressure, high temperature and dilution on laminar burning velocities and Markstein lengths of iso-octane/air mixtures, Combustion and Flame 159 (2012) 3286-3299.

30. Szybist, J.P., Youngquist, A.D., Barone, T.L., Storey, J.M., Moore, W.R., Foster, M. and Confer, K., 2011. Ethanol blends and engine operating strategy effects on light-duty spark-ignition engine particle emissions. *Energy & Fuels*, *25*(11), pp.4977-4985.

31. Moore, W.; Foster, M.; Lai, M.-C.; Xie, X.-B.; Zheng, Y.; Matsumoto, A. Charge motion benefits of valve deactivation to reduce fuel consumption and emissions in a GDi, VVA engine. SAE [Tech. Pap.] 2011, DOI: 10.4271/2011-01-1221.

32. Sabathil, D.; Koenigstein, A.; Schaffner, P.; Fritzsche, J.; Doehler, A. The influence of DISI engine operating parameters on particle number emissions. SAE [Tech. Pap.] 2011, DOI: 10.4271/2011-01-0143.

33. Alger, T., Gingrich, J., Khalek, I.A. and Mangold, B., 2010. The role of EGR in PM emissions from gasoline engines. *SAE International Journal of Fuels and Lubricants*, *3*(1), pp.85-98.

34. Zhang, Z., Wang, T., Jia, M., Wei, Q., Meng, X. and Shu, G., 2014. Combustion and particle number emissions of a direct injection spark ignition engine operating on ethanol/gasoline and n-butanol/gasoline blends with exhaust gas recirculation. *Fuel*, *130*, pp.177-188.

35. Storey, JME, Lewis, SA, Szybist, JP., Thomas, JF., Barone, T.L., Eibl, MA, and Kaul, B, "Novel Characterization of GDI Engine Exhaust for Gasoline and Mid-Level Gasoline-Alcohol Blends," SAE Int. J. Fuels Lubr., vol. 7, pp. 1-8, 2014.

36. Storey, JME, TL Barone, JF Thomas, and SP. Huff, 2012. "Exhaust Particle Characterization for Lean and Stoichiometric DI Vehicles Operating on Ethanol-Gasoline Blends," SAE Technical Paper Series 2012-01-0437, 2012.

37. Barone, TL, JME Storey, AD Youngquist, and JP Szybist. 2012. "An analysis of direct-injection spark-ignition (DISI) soot morphology," Atmospheric Environment 49, 268-274.

38. Koczak, J., Boehman, A., and Brusstar, M., "Particulate Emissions in GDI Vehicle Transients: An Examination of FTP, HWFET, and US06 Measurements," SAE Technical Paper 2016-01-0992, 2016, https://doi.org/10.4271/2016-01-0992.

39. Dieselnet, "United States: Heavy-Duty Vehicles: GHG Emissions & Fuel Economy", accessed 02/20/2020, https://dieselnet.com/standards/us/fe_hd.php#co2

40. Delgado, O. and Lutsey, N., 2014. The US SuperTruck Program. Washington DC.

41. Reinhart, T.E., 2015. Commercial medium-and heavy-duty truck fuel efficiency technology study-Report# 1 (No. DOT HS 812 146).

42. Rengarajan, S., Liu, Z., Lerin, C., Stetter, J., Narang, V. and Lana, C., 2020. LPG Direct Injection Engine for Medium Duty Trucks (No. 2020-01-5008). SAE Technical Paper.

43. EPA, "Annual Certification Data Vehicles, Engines and Equipment", accessed 04/24/2020, https://www.epa.gov/compliance-and-fuel-economy-data/annual-certification-data-vehicles-engines-and-equipment

44. Zigler, Bradley T, Toops, Todd, Krishnan, Sundar, and Srinivasan, Kal-yan. Direct Injection 4.3 L Propane Engine Research, Development, and Test-ing. United States: N. p., 2019. https://www.nrel.gov/docs/fy19osti/73876.pdf

Why Can Miller Cycle Improve the Overall Efficiency of Gasoline Engines?

M. Perceau[1,2], P. Guibert[2], S. Guilain[1], F. Segretain[2] and T. Redlinger[1]

[1]Renault – Guyancourt, France.

E-mail: marcellin.perceau@renault.com
Telephone: +(33) 144279563

[2]Sorbonne Université, Institut Jean le Rond d'Alembert, France

Abstract. New emissions regulations tend carmakers to get more interested in over-expanded cycle and therefore to leave the classical Otto cycle aside. The Miller cycle, using an early inlet valve closing, can significantly improve the overall efficiency of a turbocharged spark ignition engine. To do so, its size needs to be increased while maintaining the same effective compression ratio, this is known as the "rightsizing" concept. This new engine can also follow a more aggressive Miller cycle during partial load operations. The shorter valve intake event minimizes the need for throttling the air and so reduces the pumping losses, this method is known as "dethrottling". Indeed, the use of a variable valve timing system makes it possible to combine two different cam profiles in an engine, one for the full load operations and one for the partial loads. The benefits of this strategy will be explored using a new 0D model. This model includes a heat transfer submodel based on Woschni's coefficient and a friction submodel that will take the engine size changing into account. The shorter intake event in the Miller cycle induce in-cylinder aerodynamic losses and so a lower level of the turbulent speed at the top dead center. This increases the combustion duration and affect directly the overall efficiency. Therefore, the link between a turbulence loss and the increase of the combustion time will be studied. In comparison to the Otto cycle, the Miller cycle leads up to 4% consumption advantages according to the choice of the inlet valve closing and volumetric compression ratio.

Notation

V	In-cylinder volume
P	Pressure
r	mass-specific gas constant
T	Temperature
m	In-cylinder mass
X_{in}	Incoming values
X_{out}	Outgoing values
X_u	Unburned quantities
X_b	Burned quantities
blf	Backflow
u	Specific internal energy
h	Specific enthalpy
h_c	Convective heat transfer coefficient
A	Surface area

BDC	Bottom Dead Center
TDC	Top Dead Center
IVC	Inlet Valve Closing
$EIVC$	Early Inlet Valve Closing
$LIVC$	Late Inlet Valve Closing

1. The Miller Cycle

1.1 Context

The transportation sector was the source of 18% of the CO_2 released in the atmosphere in 2016 but 15% in 1990 [1]. This increase combined with global warming has prompted the European Parliament to restrict exhaust emissions by imposing the Euro 6 standard on car manufacturers. Despite the emergence of electric vehicles, the internal combustion engine still has a future. In 2035, in a scenario of high environmental regulations, 77.2% of vehicles sold worldwide will be gasoline engines, only 11.9% will be fully electric and 0.1% will be fuel cell powered [2]. The sector is therefore evolving and many innovations are being introduced to improve internal combustion engines.

Vehicles will tend to be electrified [3], [4] by switching to a 48V system, that will for example allow the use of e-turbo [5], or by a more complete hybridization. New components that will allow engines to operate optimally over a wider range of operating conditions will be introduced [6]. We can talk about variable compression ratio with, for example, a modification of the classic connecting rod and crank system. The system can be almost completely modified, as is the case with the MCE-5 engine [7], the crank section can also be redesigned, as the Infinity VC-turbo engine [8], and the connecting rod can vary its stroke while being integrated into the engine without major modifications [9], [10]. Conventional turbocharger are likely to be equipped with a variable turbine section [11]. The timing and lift of the valves can be modified by different systems during engine operation [12], [13]. The number of cylinders in operation may also vary according to the required load [14], [15]. Fluid properties can be altered to achieve better performance by injecting water and working on EGR systems [16], [17]. For example, water, injected during compression, cools the mixture by evaporation, which limits knocking and allows the use of higher compression ratios. The work done to reduce mechanical friction is revealed in most articles featuring new engines. Engineers are also experimenting new combustions by testing new fuels [18]–[20] and new types of ignition, such as Mazda's HCCI Skyactiv engine, which ignites the air-gasoline mixture at a high compression ratio [21], and a microwave ignition system that replaces traditional spark plugs [22]. Energy recovery by combined cycle is also studied, for example the heat extracted downstream of the catalytic converter can be used in a Rankine cycle where the turbine will drive the crankshaft [23].

The application of over expanded cycles such as the Atkinson and Miller cycles allows high efficiencies to be achieved, can be coupled with the above solutions [20], [24]–[26] and generally requires only minor engine modifications. Changes will be made mainly to the intake valve timing and to elements useful for internal aerodynamic, which will be described later.

1.2 Presentation of the Cycle

The Miller cycle is part of the over-expanded cycle family. Its expansion stroke is longer than its compression one. In this paper, we'll make the distinction between the compression ratio $r_c = V_{IVC}/V_{TDC}$ and the expansion ratio $r_e = V_{BDC}/V_{TDC}$. Where V_{IVC} is the cylinder volume when the inlet valve is closing, V_{TDC} is the top dead center volume and V_{BDC} the bottom dead center.

James Atkinson, a British engineer, was the first to work on over expanded cycle. He wrote three patents on engines working with complex connecting rods. The first one was written in 1886 and describes an opposed piston engine in which the volume at the end of the intake stroke is lower than the volume at the end of the expansion [27]. The second one is a four stroke engine presented in 1887 [28]. It's Atkinson's most famous engine and the most frequently presented one when talking about Atkinson cycle, Fig. 1. The volume at the end of the expansion stroke is twice as large as the one at the end of the compression stroke. According to the author, this leads to an engine that is more economical than any other gas-engine built before.

Atkinson wrote a patent, in 1892, about an over-expanded cycle engine closer to the classical four stroke internal combustion engine. However, few engines were produced so information about it can't be easily found. For more details about this engine, the reader can refer to Marshall's paper on the history of Atkinson's machines [29].

An over-expanded cycle engine with such a complex connecting rods system is not actually used in a vehicle. Yet, research has been made on the subject, we can mention BMW [30] and Honda with the EXlink engine [31], [32]. The major disadvantages are friction losses, inertia of the extra parts and the bigger space needed. The interest for this kind of system seems to grow when they allow variable compression ratio like, for example, MCE-5 engine [7] and Nissan's VC-turbo [8]. We can also add that Honda is working on its EXlink engine and tends to variable compression [34].
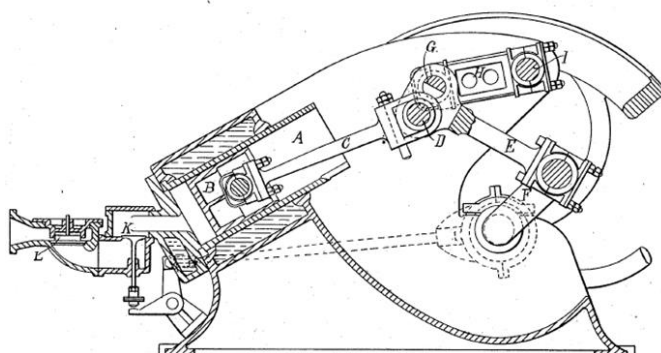
Fig. 1 : Atkinson « Cycle Engine » 1887 [28]

Another way to unlink the compression and the expansion stroke is to act on the time when the inlet valves are closing. When closing the valves before or after the bottom dead center the compression stroke is shorter than the expansion one. For an early inlet valve closing (EIVC), before the BDC, we have $V_{IVC} < V_{BDC}$ and so $r_c < r_e$. For a late inlet valve closing (LIVC), after the BDC, part of the fluid inside the cylinder is pushed back into the intake manifold. This leads to the same situation as before with a fluid volume smaller than what the cylinder could have contained, Fig. 2.
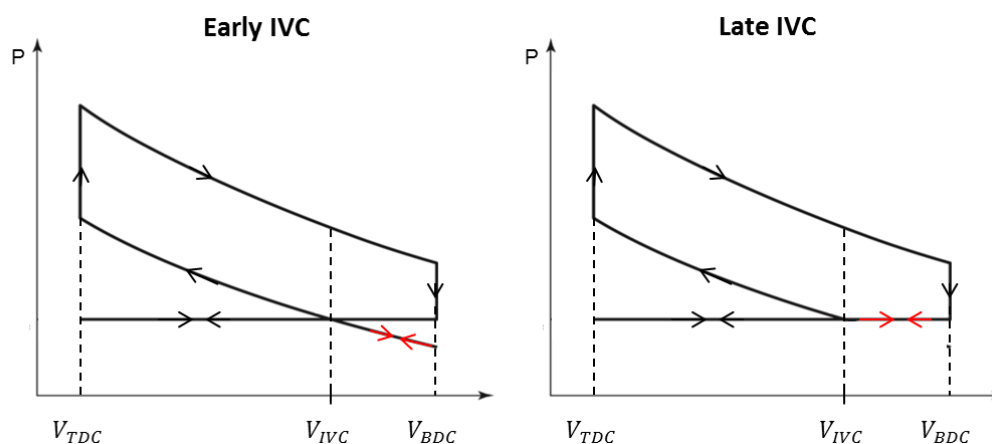
Fig. 2 : PV diagram : (Left) EIVC – (Right) LIVC

This method has been for the first time used by American engineer Ralph Miller. He invented a way to move forward or delay the intake valves closing progressively with the increase of the engine load, the main objective being to avoid knocking. He worked on a compression ignited engine, a spark ignited one and a two-stroke engine in three patents respectively deposited in 1954 [35], 1956 [36] and 1957 [37].

The name Miller cycle is most of the time linked to an early inlet valve closing (EIVC) whereas the name Atkinson cycle is related to late inlet valve closing (LIVC).We'll use this convention for this paper.

1.3 Application Strategy

1.3.1 Full Load : "Rightsizing"

Recent years have seen the arrival of a new concept in the world of internal combustion engines: "downsizing". The aim is to reduce the size of engines by reducing the volume of the cylinders or, for example, by using three cylinders instead of four. These engines are also equipped with a turbocharger, allowing them to deliver the same power as a larger-displacement engine. Direct fuel injection has also improved their performance. This reduction in size reduces mass and friction, and thus reduces fuel consumption.

Manufacturers' interest in the Miller cycle seems to have stopped this trend. Indeed, the term "rightsizing" is starting to appear in automotive journals. Manufacturers use a "downsized" engine from their line of products and design a larger displacement engine, the increase in size coming from the extended expansion of the Miller cycle. Examples include Opel's Ecotec engines [39], [40], Volkswagen's TSI engines [41], Audi's TFSI [42] and also BMW's boxer engine for motorcycles [43].

The increase in displacement is mainly achieved by increasing the piston stroke. The low dead volume of the combustion chamber is therefore maintained, which allows keeping the compression ratio at the maximum before knocking and thus does not degrade the engine's efficiency.

The benefit obtained by running a Miller cycle on an engine whose expansion has been extended compared to a reference engine following an Otto cycle, with the same compression ratio, is a gain in mechanical work. Therefore, there is an increase in thermal efficiency, Fig. 3 illustrates this principle. The reference engine follows the classic phases of intake (1 → 2), compression (2 → 3), combustion (3 → 4), expansion (4 → 5) and exhaust (5 → 1). The Miller extended expansion (4 → 5') engine follows the same compression phase (2 → 3), it has the same effective compression ratio as the reference engine. Assuming that the combustion is the same for both engines, using the same amount of fuel, the gain in mechanical work (zone: 5-5'-6-2) implies a better thermal efficiency for the Miller engine.
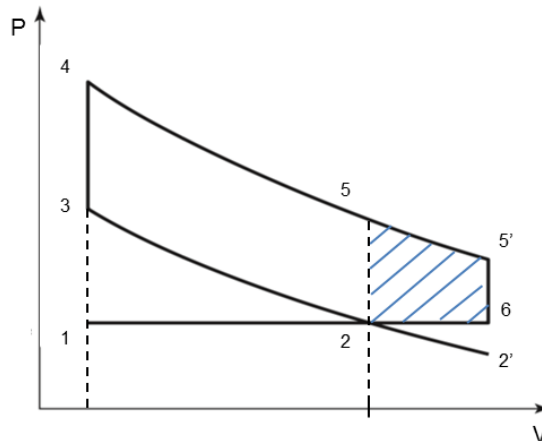
Fig. 3 : PV diagram showing Miller cycle gain at equal compression ratio

It should be noticed that the friction losses induced by the longer expansion phase are largely compensated by the gain in work [42]. Furthermore, engine manufacturers pay particular attention to reducing friction on moving parts by working on segmentation, cylinder surface treatment, bearings, type of oil used, etc.

We can take as an order of magnitude Volkswagen's figure that shows a 10% gain in consumption on its 1.5L engine compared to its previous model and Opel's figure for its 1.0L Ecotec engine that gains 6% in consumption. Audi gains 5% fuel consumption on its new TFSI engine. The IFPEN gives an indicated efficiency higher than 42% on a good part of the engine map, this figure being the result of an experimental study on a single cylinder engine [44]. These figures should be taken with care, as they correspond to the gains obtained on a new version of an engine from the manufacturers' range, and are therefore not equal in terms of on-board technology, taking the evolution from the former version into account. These benefits are hence not exclusively due to the application of the Miller cycle.

1.3.2 Part Load : "Dethrottling"

We have seen that the Miller cycle provides better thermal efficiency by increasing mechanical work when compared to a reference engine with the same compression ratio. Another advantage of the Miller cycle is that it can be used to reduce pumping losses, we can use the term "dethrottling". These are the pressure losses introduced by the throttle valve when working at part load, during the intake stroke. The idea is not new and dates back to the 1980s [45], but advances in variable lift and valve timing systems have democratized its use. The comparison is made here with a reference engine of the same displacement.
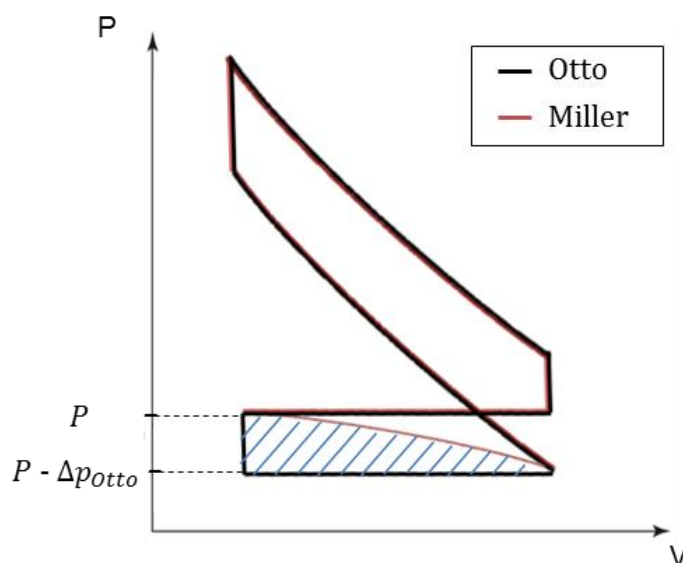
Fig. 4 : « Dethrottling » strategy

The comparison here is made at constant load and therefore at equal mechanical work. The benefits come from the quantity of fuel injected. During the throttle cycle, pressure losses require more air to be admitted into the engine to produce the same amount of mechanical work. The throttle cycle therefore consumes more fuel and is less efficient.

The control of the amount of air required for operations is no longer carried out by the throttle valve but by a system that varies the lift law of the intake valves. Different systems exist [12]. They can vary the duration of valve opening, the maximum opening and shift the law by a certain angle. To reduce the amount of air admitted by the engine, the intake valves will have to be open for a shorter period of time. Engines in production mainly use two cams, one with low lift for low loads and one with high lift for full load. The camshaft is also equipped with a phase shifter that allows the law to be shifted and therefore the valve closing time to be chosen in order to control the mass of air intake more precisely. We can mention Audi's Valvelift [46], BMW's ShiftCam [43] and Porsche's VarioCam [47] systems.

A numerical simulation study, using GT-Power, comparing a Miller cycle with a total lift of 170°CA and a standard cycle with a total lift of 240°CA of a 4-cylinder 1.8L engine shows that fuel consumption gains can be as high as 11% [48]. The figures announced by the manufacturers are lower. Honda announces a benefit of around 2% [49], Mercedes 5% [50] and Porsche 4% [51]. These figures should also be taken with care. Indeed, profits depend strongly on the valve timing and lift used, which is generally not informed.

1.3.3 Miller Cycle Limitations

Because of the shorter intake event, the Miller cycle leads to internal aerodynamic losses. The tumble movement is less intense, which leads to lower levels of turbulent kinetic energy at the top dead center. It's well known that turbulence, by wrinkling the flame front, accelerates combustion and improves its stability. Aerodynamic deterioration has therefore a strong impact on engine efficiency. The combustion duration, linked to the turbulent kinetic energy level, is an important parameter to consider when studying the Miller cycle.

2. Method to Compute the Efficiency

In this paper, we'll use a 0D/1D model to compute the overall efficiency of the Miller cycle. This model is based on the conservation laws of mass and energy in which the system is discretized in homogeneous volumes. During the phases of intake, compression, combustion, expansion and exhaust of the engine cycle, quantities like the pressure, the volume and the mass inside the cylinder will be computed to determine overall efficiency at the end of the cycle.

During non-combustion phases, which are the intake, compression, expansion and exhaust phases, the model considers one homogeneous volume. The fluid, being a mixture of burned and unburned gases, has the same properties in the whole cylinder. Quantities depend on the crank angle, which is an image of the time for a known speed rotation, so we'll use the term 0D model. All of them are computed according to the ideal gas law and the conservation of mass and energy. They are written as following [52]:

$$V \frac{dP}{dt} + P \frac{dV}{dt} = rT \frac{dm}{dt} + mr \frac{dT}{dt} \tag{1}$$

$$\frac{dm}{dt} = \frac{dm_{in}}{dt} + \frac{dm_{out}}{dt} + \frac{dm_{in}^{bfl}}{dt} + \frac{dm_{out}^{bfl}}{dt} \tag{2}$$

$$\frac{d(m.u)}{dt} = -P \frac{dV}{dt} + \frac{dQ_{wall}}{dt} + h_{in} \frac{dm_{in}}{dt} + h_{cyl} \left(\frac{dm_{out}}{dt} + \frac{dm_{in}^{bfl}}{dt} \right) + h_{out} \frac{dm_{out}^{bfl}}{dt} \tag{3}$$

During the combustion phase, the model considers two homogeneous volumes, one central volume containing the burned gases, which are the exhaust products, and the other one containing the fresh gas composed of fuel, air and residual gases. The pressure is supposed to be the same in both sides. Quantities will be calculated using the same laws as for the non-combustion phases and will be applied in both regions. There is flame front propagation that introduces a notion of length, we will then use the term 1D model. Wiebe's law described the energy release curve, where $x_b = m_b/m_{u,init}$ is the fraction of energy release [53], [54] :

$$x_b(\theta) = 1 - \exp \left[-a \left(\frac{\theta - \theta_{ign}}{\Delta \theta_{comb}} \right)^{m+1} \right] \tag{4}$$

Where θ_{ign} is the ignition crank angle, $\Delta \theta_{comb}$ is the combustion duration, m is the form factor and a the efficiency factor. The parameters of the correlation will be studied in a range that simulates the effect of combustion duration. The conservation of mass, combined with the conservation of volume, can then be used :

$$0 = \frac{dm_u}{dt} + \frac{dm_b}{dt} \tag{5}$$

$$\frac{dV}{dt} = \frac{dV_u}{dt} + \frac{dV_b}{dt} \tag{6}$$

The ideal gas law equation remains the same and is to be applied for both zones, to the unburned and the burned quantities. The conservation of energy in both sides is written as follow :

$$\frac{d(m_u u_u)}{dt} = -P \frac{dV_u}{dt} + \frac{dQ_{wall}^u}{dt} + h_u \frac{dm_u}{dt} \tag{7}$$

$$\frac{d(m_b u_b)}{dt} = -P\frac{dV_b}{dt} + \frac{dQ^b_{wall}}{dt} - h_u\frac{dm_u}{dt} \tag{8}$$

Kinematic is an important key for Miller and Otto cycles comparisons. The cylinder volume can be calculated, for each crank angle, according to geometrical parameters introducing $\lambda = l/a$ the ratio of the connecting rod length l and the crank radius a. Valve lift is also known for each crank angle according to the opening angle, the closing angle, and the maximum lift L_{max}. Therefore, a change in the inlet valve closing (IVC) will be well represented. Flows through valves depend on upstream and downstream conditions. The mass flow rates differ from the ideal values by introducing a discharge coefficient that is linearly dependent on the valve lift. These flows can also be choked if the upstream and downstream conditions are critical [53]. Moreover, the flow is considered as an ideal compressible fluid with thermodynamic properties changing according to the composition and the temperature. The fuel is considered to be isooctane and the air excess ratio is equal to 1.

During operations of the engine, thermal energy Q_{wall} is exchanged at the j walls :

$$\frac{dQ_{wall}}{dt} = \sum_j h_c(P,T).\left(T_j - T(t)\right)A_j \tag{9}$$

Exchanges at the cylinder head, piston, valves and cylinder liner are simulated. The model uses the Woschni formula to determine the transfer coefficients [55]. A friction sub-model allows us to assess the losses generated by different mechanical elements. It generates one fmep per cycle which is subtracted from the indicated work generated by the main model. For more details on this sub-model, the reader may refer to the "Friction and Lubrication" chapter in Ferguson's book [53]. Pumping losses are already managed by the mass transfer sub-model and will therefore not be included in this model. These two sub-models allow us to take into account an increase in the stroke and its effect on the overall efficiency.

3. Presentation of the Gains

This chapter outlines the gains that could be obtained by using the Miller cycle on a spark ignition engine compared to a conventional Otto cycle. It will focus on the "Rightsizing" approach. The efficiency will be computed as a function of intake valve closing time (IVC) and the benefits will be evaluated with respect to a reference engine.

The chosen reference engine consists of three cylinders, with four valves per cylinder with a bore diameter of 72.2mm and a stroke of 73.1mm. It has the following distribution: IVO=5°CA, IVC=210°CA, EVO=511°CA and EVC=715°CA. Calculations will be made at full load, throttle fully open, and at 2000 rpm.

The first part will deal with the sizing of Miller engines according to their IVC, a second part will deal with the choice of the ignition time and the last will study the effect of a variation in the combustion duration.

3.1 Sizing according to the IVC

The new engine must maintain the same effective compression ratio as the reference engine and therefore suck the same mass of air while closing its intake valves before BDC. This condition involves the same combustion energy. The model must therefore be able to recalculate the engine size according to the IVC chosen as an input parameter. We assume an optimal downsized reference engine, i.e. with a maximum permissible compression ratio before knocking. Rightsizing's approach is to apply the Miller cycle, choosing an IVC of less than 180°CA (EIVC), to an engine that is larger than the reference engine. The cylinder capacity will be increased by acting on the stroke, the cylinder diameter and the top dead volume are kept fixed in order to keep the supposed ideal volume of the combustion chamber.

The calculation of the new displacement is carried out by examining the mass of fresh air admitted into the cylinder. Knowing the mass of air admitted by the reference engine, the stroke of the Miller engine is increased until it admits the same amount of air. These iterations are performed over

complete engine cycles. Since the air mass is proportional to the amount of fuel injected, they allow a comparison of results with the same combustion energy.   Table 1 shows the evolution of the engine size as a function of the choice of intake valve closing angle IVC. The stroke is the average of the strokes calculated for several combustion durations, the cylinder capacity is calculated according to this average stroke. When IVC is 160°CA, the engine stroke is increased by about 5mm to admit the same amount of air as the reference configuration increasing its displacement from 0.90L to 0.96L. This corresponds to an increase of about 7% of the cylinder capacity. The engines are named in the left-hand column, we'll use these names for the rest of this paper.

Table 1 : Evolution of engine size according to the IVC choice

Engine	IVC (°CA)	Stroke (mm)	Capacity (L)
Ref	210	73,10	0,898
M170	170	75,01	0,921
M160	160	78,13	0,960
M150	150	82,48	1,013
M140	140	88,27	1,084
M130	130	95,87	1,177

As the comparison is made with the same combustion energy, benefits in the overall efficiency are mechanical work gains. Fig. 5 presents the PV diagram of two cycles, the reference one and a Miller cycle with an IVC at 130°CA. The shaded area represents the gains of the reference cycle over the Miller cycle and the light blue area represents the gains of the Miller cycle over the reference cycle. Because the blue area is greater than the grey area, the Miller cycle is more efficient than the reference cycle. It is clear that the gains are due to the prolonged expansion. A second advantage of the Miller cycle can also be observed. The maximum pressure is lower, which implies a lower sensitivity to knock for the Miller cycle. The compression ratio can therefore be increased in order to gain efficiency. This is due to the different kinematics between the two engines.
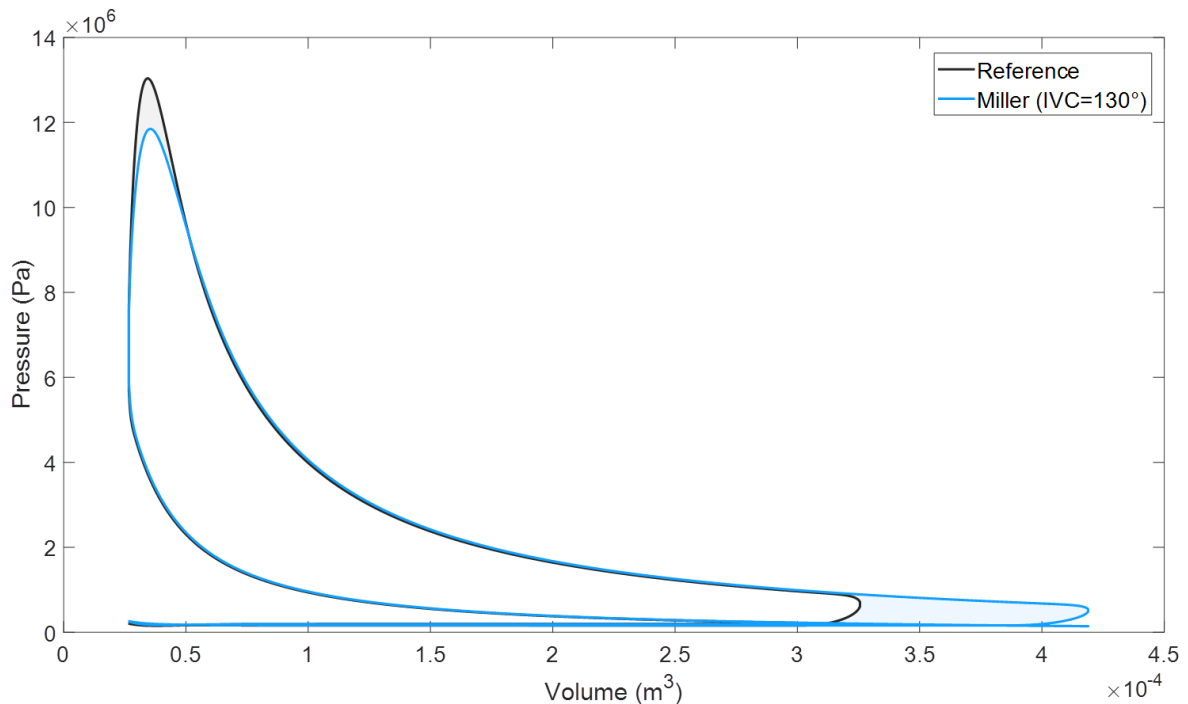
Fig. 5 : PV diagram – benefits with a Rightsizing approach

Fig. 6 shows the cumulative friction losses. On the left side there is the reference fmep, at an IVC of 210°CA, on the right side the friction losses in terms of energy are presented for the reference IVC and an IVC of 130°CA. Increased losses to the piston and auxiliaries are visible as the stroke length increases (decrease in IVC). The losses due to crankshaft rotation (Journal bearing) remain constant and those due to the valve train also increase, but the variation is too small to be observed on this graph. For an IVC of 210°CA the friction losses, when compared with the indicated work, are about 8.5%, whereas when the stroke is maximum, for IVC=130°CA, the total losses reach about 10%.
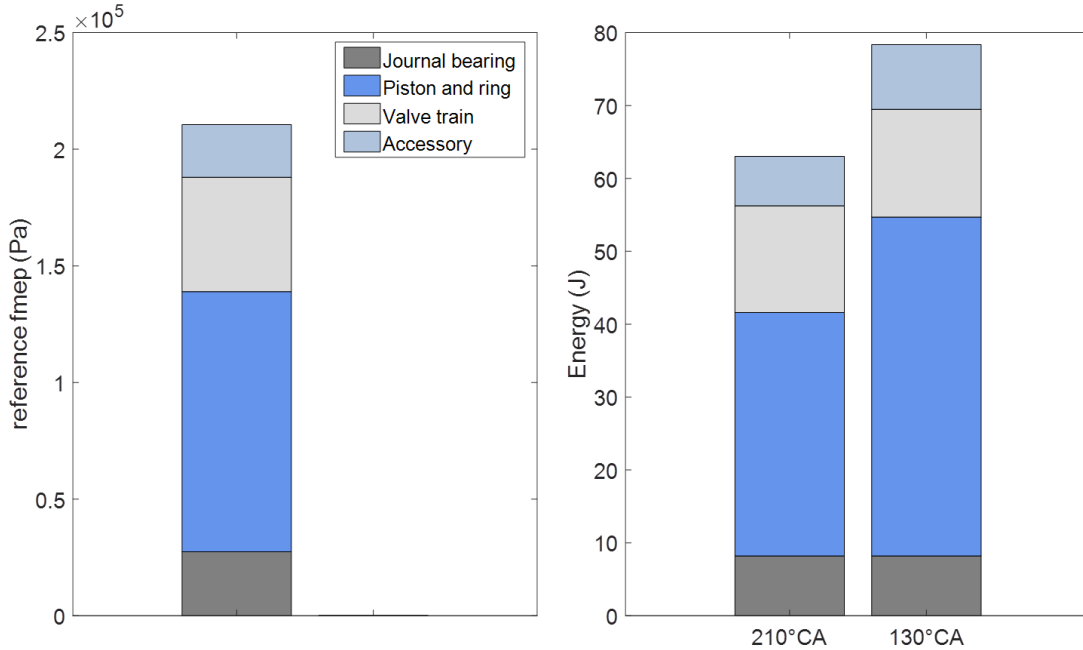
Fig. 6 : Cumulative friction losses. $\theta_{ign} = 350°CA$ – combustion duration $40°CA$ - $N = 2000 \, tr.min^{-1}$
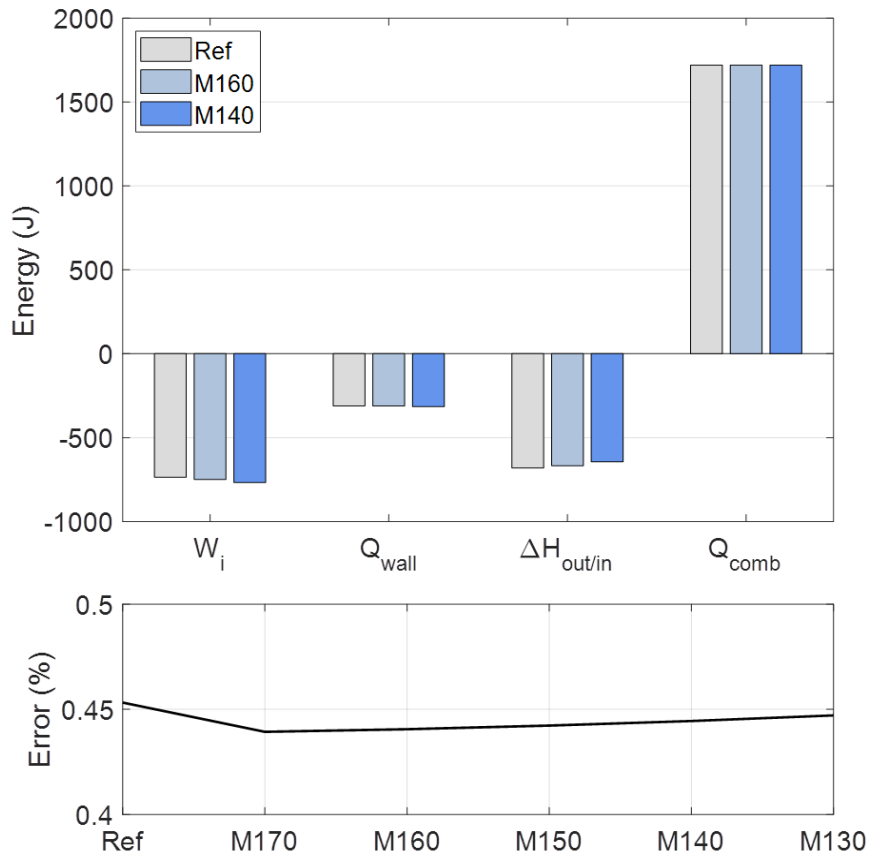
Fig. 7 : Model energy balance (Up) Contribution of each energy – (Down) Balance error

The energy balance calculation is used to check the correct operation of the model. Let's call W_i the indicated work, Q_{wall} the thermal energy lost from the walls, $\Delta H_{out/in}$ the enthalpy difference between the exhaust and the intake flow and Q_{comb} the energy produced by combustion. The contribution of each energy is plotted in upper Fig. 7 for the Ref, M160 and M140 engines. We can observe an increase in indicated work when IVC decreases due to the extended expansion of the Miller cycle. The increase in stroke increases the exchange at the walls but the variation is too small to be observed on the graph. The enthalpic flux decreases and is the result of a better recovery of expansion energy during the extended stroke of the Miller cycle. The combustion energy is constant, which confirms that the displacement of the Miller cycle for each IVC has been calculated properly. Lower Fig. 7 shows the percentage difference between the energy entering the system and the energy leaving the system for each engine. The average deviation is about 0.45% for each engine and is equivalent to about 7.5 Joules. This difference is very small and must come from approximations of some quantities such as the value of molar masses used in calculations.

3.2 Choice of the ignition time

The ignition time θ_{ign} is a parameter of the combustion law. Its optimization is made with a constant combustion duration fixed for this example at 40°CA. It is a good approximation according to authors [53], [54]. Wiebe's law needs two other parameters that are the form factor m and the efficiency factor a. The parameters $a = 5$ and $m = 2$ are generally chosen to represent the combustion of gasoline [53], [54]. We choose to keep $a = 5$ constant to compare engine with the same combustion efficiency. The form factor $m = 2$ is used and the impact of a variation around this value will be studied.

The efficiency of the reference engine and the five Miller engines, defined in the previous section, is calculated as a function of the ignition time for different form factor m. The left-hand side of Fig. 8 shows the efficiency for $m = 2$, which as we said, is usually used to represent the combustion of gasoline. We can observe that the lower the IVC, the higher the efficiency. These curves present a maximum for $\theta_{ign} = 350°CA$. The right-hand side of Fig. 8 shows the efficiency for form factors from 0.5 to 5 for each engine according to the 50 percent burn angle (CA50). This representation allows to show a maximum efficiency when $CA50 \approx 370°CA$. The engine therefore operates at optimum performance when 50 percent of the burnt mass is 10° after TDC. The optimum ignition angle θ_{ign} can then be deduce with Wiebe's law for each type of combustion represented by the form factor m. For $m = 2$ the calculation leads to $\theta_{ign} = 350°CA$. We can observe, for each type of combustion, when m is constant that a lower IVC leads to greater efficiency. We can also point out that the bigger m is, the higher the efficiency.
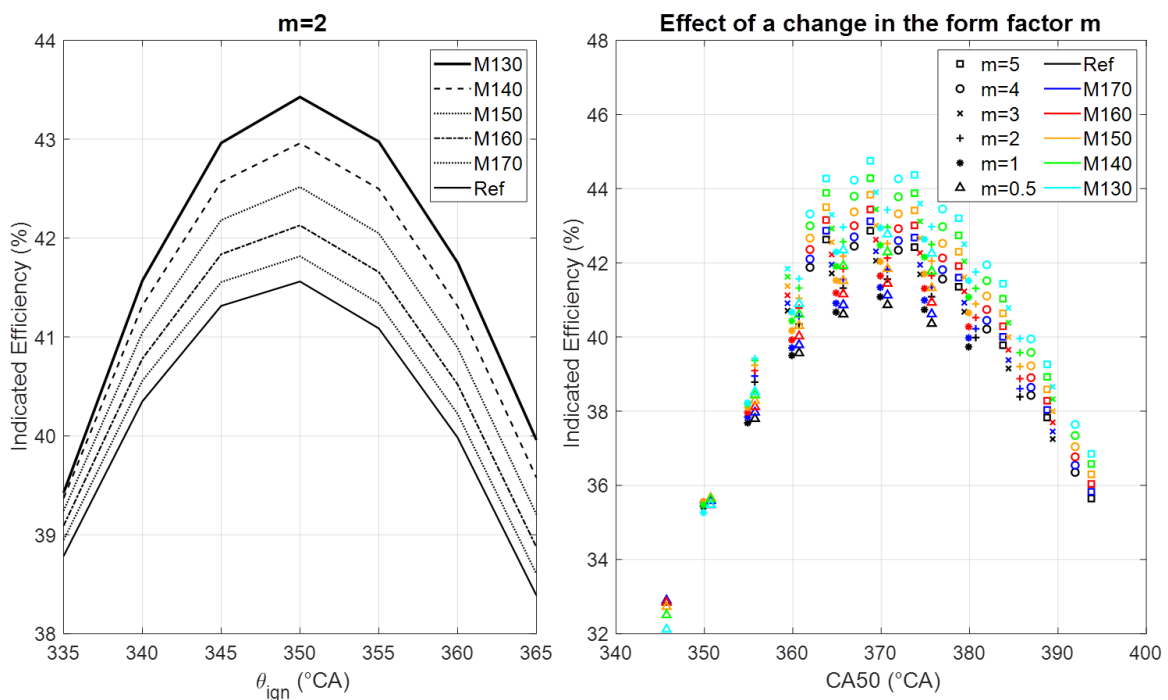
Fig. 8 : Effect of a change in $\boldsymbol{\theta_{ign}}$ over the indicated efficiency: (Left) $\boldsymbol{m = 2}$ - (Right) Variation in $\boldsymbol{m}$

This is due to a form factor representing faster combustion.

For the following part of this study, the ignition angle will be fixed at 350°CA and we will keep $m = 2$ constant.

3.3 Effect of a variation in the combustion duration

We will now study the effect of a variation in the combustion duration, which is an important parameter related to internal aerodynamics. Fig. 9 shows the six efficiency curves for the six engines in the previous figure, this time as a function of combustion duration. The ignition time is now set at 350°CA. The lower the IVC is, the greater the benefits are. We can observe a gain of up to 1.5 efficiency points. It can also be seen that at this optimum ignition angle, short combustion duration implies a higher efficiency. For example, for an IVC of 130°CA, an increase of about 3 efficiency points occurs when the combustion time is reduced from 60° to 40°CA. This is equivalent to a 7% gain in consumption. We know that the application of the Miller cycle degrades the level of turbulence at the end of compression and increases the combustion time. Working on the improvement of internal aerodynamics is therefore necessary in order to equal the aerodynamic performance obtained when applying a standard cycle.
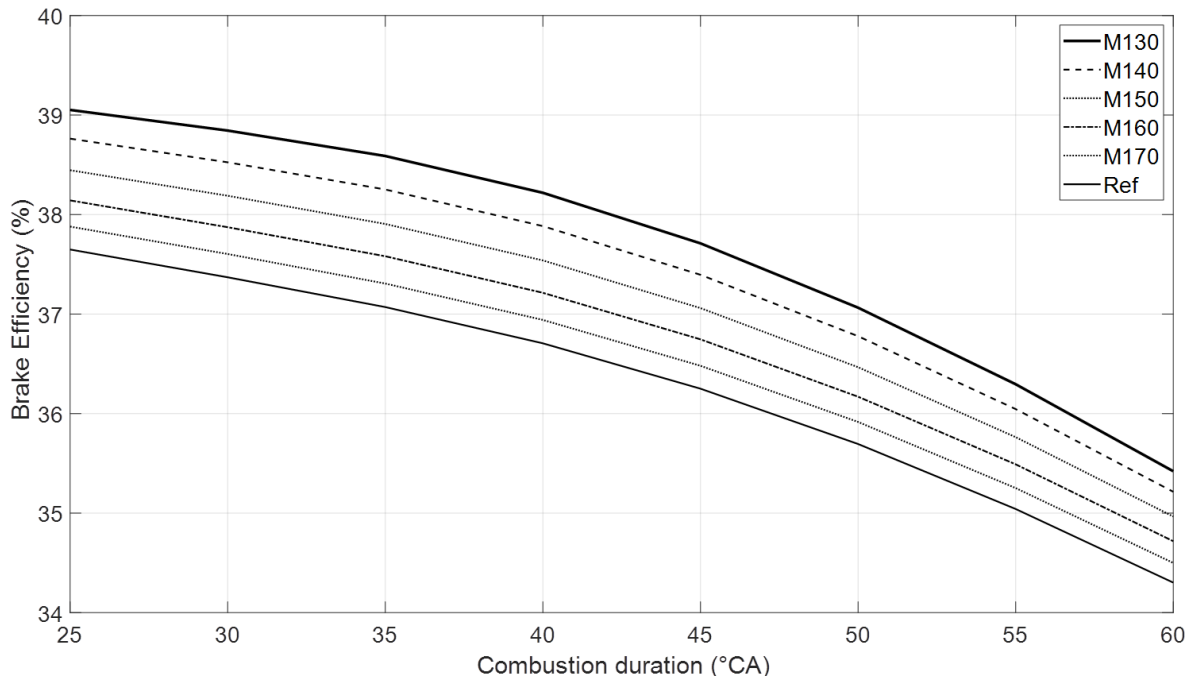
Fig. 9 : Effect of a $\Delta\theta_{comb}$ variation with $\theta_{ign} = 350°CA$

Fig. 10 now shows the gains obtained when applying the Miller cycle compared to the reference engine with a particular combustion duration. It is composed of three windows, the first window is for a reference with $\Delta\theta_{comb} = 35°CA$, the second for 40°CA and the last one for 45°CA. The left y-axis is for the benefits obtained when applying the Miller cycle relative to the reference. The right y-axis is for the Miller engine efficiency. Benefits are calculated as follows :

$$G_\% = 100.\frac{\eta_{Miller}(\Delta\theta_{comb}) - \eta_{ref}}{\eta_{ref}} \tag{10}$$

The blue squares are positioned on the curves IVC=140 and 160°CA. They indicate, as an example, the percentage gains obtained when the Miller cycle combustion time is equal to the reference. For a Miller cycle at IVC=140°CA the consumption gains are more than 3% and at IVC=160°CA they reach about 1.4%. Note that an extended burning time of less than 10°CA cancels the gains obtained by applying the Miller cycle at IVC=140°CA. One can also notice that for a decrease in the combustion duration compared to the reference, it could be possible to increase even more the impact of the Miller cycle benefits. It is therefore necessary to reinforce the aerodynamic movements in order to achieve a sufficiently fast combustion speed.
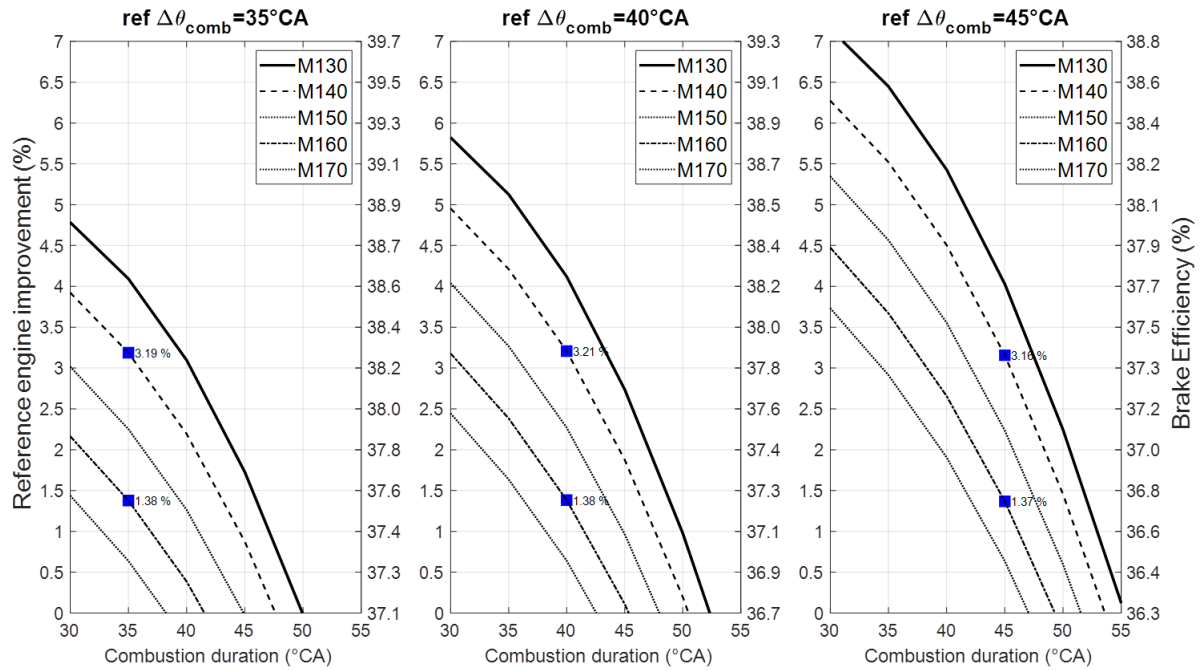
Fig. 10 : Benefits over the reference with a fixed combustion duration

4. Combustion duration and Turbulence

The flow motion improves combustion through the turbulence produced close to the end of the compression stroke. As the flow is compressed into the combustion chamber, the rotating vortices (tumble and swirl) that make the circular movement, tend to break into smaller structures and their kinetic energy is gradually converted into turbulent kinetic energy (TKE). In SI engines, this turbulence wrinkles the flame front and thus increases the exchange surface of the chemical reactions. Therefore, increasing the in-cylinder turbulence intensity improves the turbulent flame speed and combustion rate. Decreasing the combustion duration and reducing the time required for the flame front to reach the walls, reduces the heat losses and leads to higher efficiency.

This chapter presents a link between the combustion duration and the turbulence. The connection is made by using a turbulent flame speed formula [56] :

$$\frac{S_T}{S_L} = 1 + \frac{u'}{S_L} \tag{11}$$

Where S_T is the turbulent flame speed, S_L the laminar flame speed and u' is the root mean square of the velocity fluctuations. S_T represents the distance D covered by the flame over a certain period of time t_{comb}. The previous equation can then be written as follows :

$$u'(t_{comb}) = \left(\frac{D}{t_{comb} S_L} - 1 \right) S_L \tag{12}$$

The first section of this chapter presents a method to compute the flame radius that will then be used to determine the distance D. The second section shows laminar flame speed calculations and the last one presents the effect of a turbulent loss on the combustion duration.

4.1 Flame radius calculation

We consider combustion by flame front propagation. This flame front is assumed to be spherical with ignition centered on the roof of the combustion chamber. During its advance, it will meet the borders of the domain. It can come into contact with the piston and the liner. There are two possible developments, which are shown in Fig. 11. The first case represents the beginning of combustion, when the volume of the burned gases is semi-spherical and not constrained by the walls. It can then either come into contact with the piston (case 2) or come into contact with the liner (case 3). The end of combustion occurs when the volume is in contact with the piston and the liner (case 4).
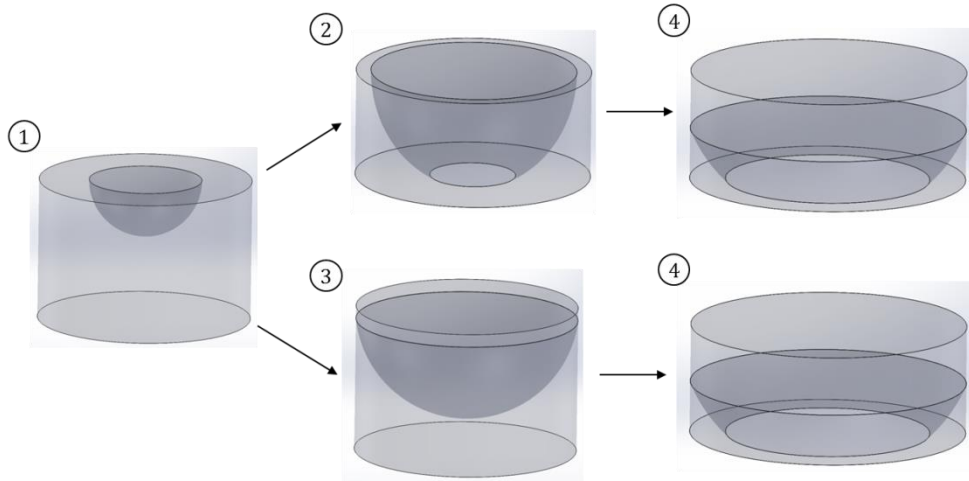
Fig. 11 : Flame front propagation

For each case, an analytical expression of the volume of gas burned was determined based on the geometric data. The radius r_f can then be determined as a function of the instantaneous stroke and the volume of burned gas. The expressions for the volume are written as follows :

$$\begin{cases} V_{bg,1} = \dfrac{2}{3}\pi r_f^3 \\[2mm] V_{bg,2} = \dfrac{\pi(r_f^2 - h^2)h}{3} + \dfrac{2}{3}\pi r_f^2 h \\[2mm] V_{bg,3} = \dfrac{2}{3}\pi r_c^2 h_f + \dfrac{2}{3}\pi r_f^3\left(1 - \dfrac{h_f}{r_f}\right) \\[2mm] V_{bg,4} = \dfrac{2}{3}\pi r_c^2 h_f + \dfrac{\pi(r_f^2 - h^2)h}{3} + \dfrac{2}{3}\pi r_f^2(h - h_f) \end{cases} \tag{13}$$

Where h is the distance between the roof and the piston, $h_f = \sqrt{r_f^2 - r_c^2}$ and r_c is the cylinder radius.

Fig. 12 shows the evolution of the flame radius where the volume of gas burned is given by Wiebe's law. Calculations have been made for several engines, defined by the rightsizing approach, and for several combustion durations. The graph on the left shows the evolution of the flame radius, normalized by the radius of the cylinder, as a function of the crank angle. The graph on the right side shows the evolution of the normalized flame radius as a function of the fraction of burned mass (MFB). Taking the average suggests the flame radius at 10, 50 and 90 percent burn angles (CA10, CA50 and CA90) to be, respectively, $0.483 r_c$, $0.865 r_c$ and $0.999 r_c$.
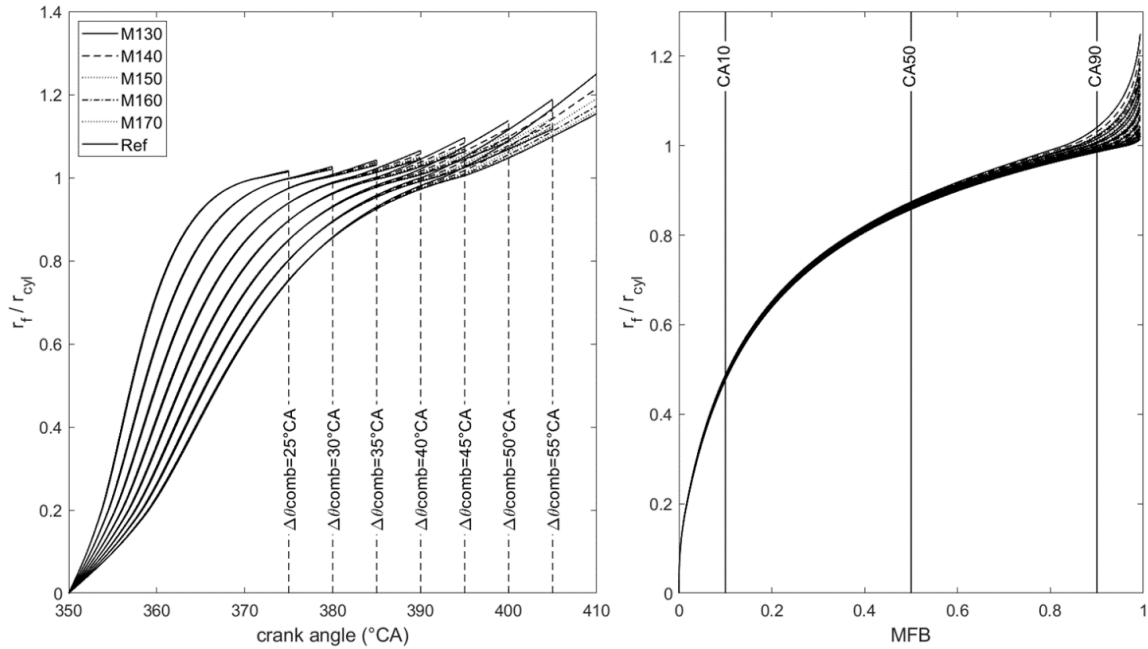
Fig. 12 : Normalized flame radius evolution

It is well known that, before reaching a certain scale, the flame is not enhanced by turbulence. At the end of combustion, the level of velocity fluctuations is generally low and the flame evolution is mainly disturbed by the expansion of the cylinder's volume. Therefore, the choice has been made to use the turbulent flame speed formula, presented in the introduction, between 10 and 90 percent burn angles. Over the period of 10 and 90 percent burn angles, the flame travels the distance $D = r_{f,90} - r_{f,10}$ during the time $t_{comb} = BD_{1090}$. So the turbulent flame speed over this period writes as follows:

$$S_{T,1090} = \frac{r_{f,90} - r_{f,10}}{BD_{1090}} \tag{14}$$

The flame radius is known for each engine and for combustion duration from 25°CA to 60°CA by 5°CA steps. Therefore, $S_{T,1090}$ is known for every combustion time from 25°CA to 60°CA by interpolation.

4.2 Laminar flame speed

The laminar flame speed is calculated with the following formula where all the constants are taken for gasoline conditions. The coefficients can easily be found in the literature [53]–[55] :

$$S_L = S_{L0} \left(\frac{T_u}{T_0}\right)^{\alpha} \left(\frac{P}{P_0}\right)^{\beta} \tag{15}$$

Fig. 13 shows the evolution of the laminar flame speed. On the left side, S_L is plotted for several combustion durations on one engine (IVC=160°CA). The shorter the burning time is, the higher the maximum speed is. This is caused by higher values of T_u and P when the combustion time is shorter. On the right side, S_L is plotted for several engines, defined by the rightsizing approach, the evolutions are almost the same.

The laminar flame speed is known for each engine and for every combustion duration from 25°CA to 60°CA by interpolation of the previous results. The mean value of S_L over the period of 10 and 90 percent burn angles is noted $S_{L,1090}$.
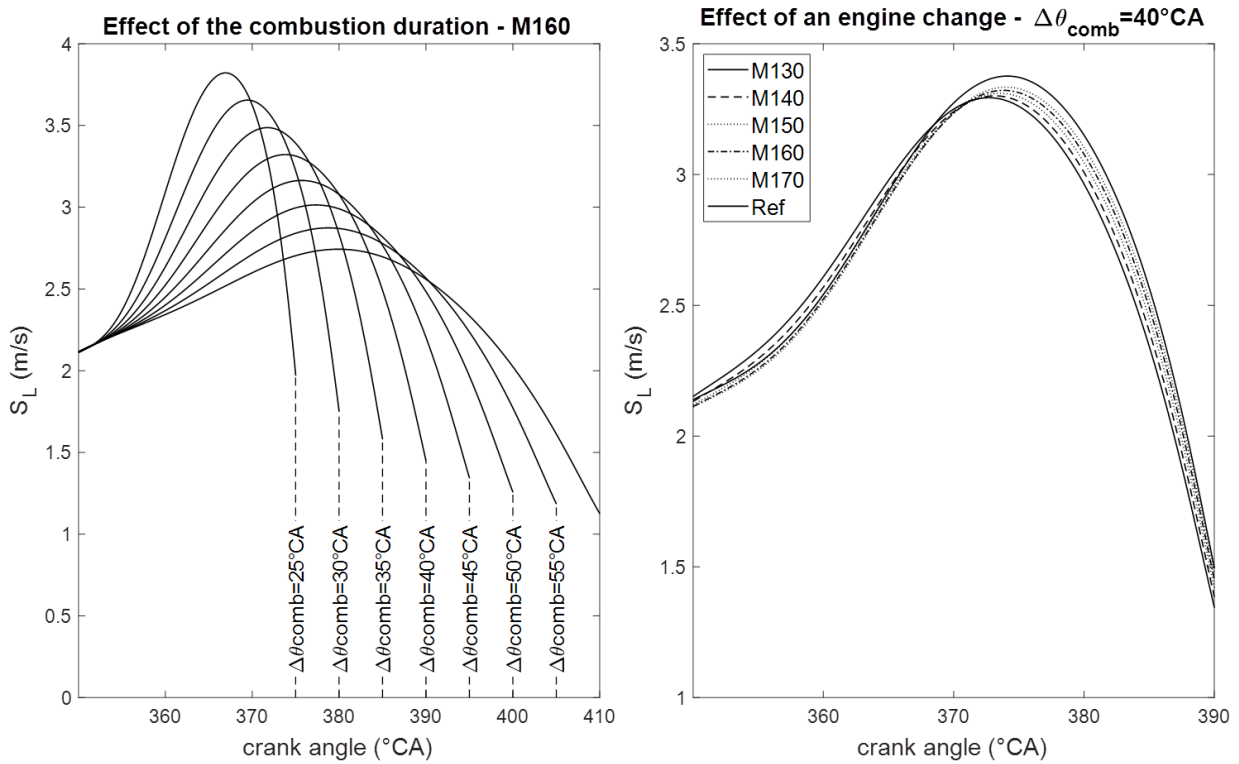
Fig. 13 : Evolution of the laminar flame speed

4.3 Effect of a turbulence loss on the combustion duration

Let's introduce the coefficient p representing a loss of turbulence in percent and rewrite the equation presented in introduction:

$$\left(1 - p(\Delta t_{comb})\right).u'_{ref}\left(\Delta\theta_{comb,ref}\right) = \left(\frac{S_{T,1090}(\Delta t_{comb})}{S_{L,1090}(\Delta t_{comb})} - 1\right)S_{L,1090}(\Delta t_{comb}) \qquad (16)$$

Where $u'_{ref}\left(\Delta\theta_{comb,ref}\right)$ is a velocity fluctuation reference at the reference combustion duration $\Delta\theta_{comb,ref}$ and Δt_{comb} the increase in combustion duration.

Fig. 14 shows the effect of a loss of turbulence on the combustion duration. Three reference combustion durations are represented $\Delta\theta_{comb}$ =35°CA, 40°CA and 45°CA, the associated reference turbulence speed u'_{ref} is respectively around $8.2\ m.s^{-1}$, $7\ m.s^{-1}$ and $6.1\ m.s^{-1}$ for each engine. The blue squares are positioned on the curves of the engines M140 and M160, like for Fig. 10. They indicate the loss of turbulence in percent for which the Miller cycle benefits are canceled compared to the reference engine. For example, on Fig. 10 we can read that for an increase of 5°CA (M160 ; $\Delta\theta_{comb} = 40°CA$) in combustion duration, the gains of the Miller cycle are canceled, Fig. 14 shows that this increase in combustion duration corresponds to a loss of 12.9% in the turbulent speed u'.

With the results from the "Rightsizing" section, we can conclude that a loss of turbulence of approximatively 13% cancels the benefits of using the Miller cycle with an IVC=160°CA, for an IVC of 140°CA the benefits are canceled with a loss of velocity fluctuation of about 22%. To make the most of the advantages of the Miller cycle, great attention must be paid to improve internal aerodynamics.
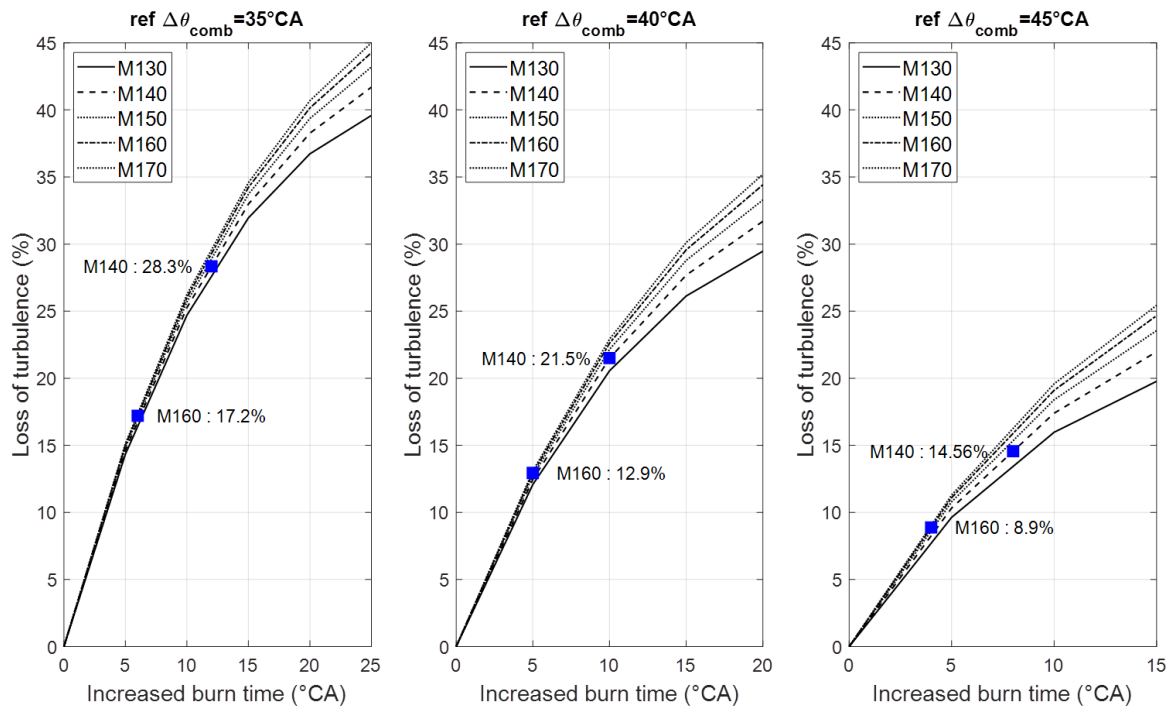
Fig. 14 : Loss of turbulence associated with an increased burn duration

Conclusions

The Miller cycle can improve the efficiency of internal combustion engines. A 0D model was developed to calculate the benefits of such a cycle. In summary :

- In a Rightsizing approach : benefits can be between 1 and 4% according to the choice of the IVC, with 1.4% for an IVC=160°CA and 3.2% for IVC=140°CA

- These results are for the same combustion duration, so the same level of turbulent velocity fluctuations. We exposed that for an increase of 5°CA of the combustion duration the benefits of the Miller cycle are canceled for IVC=160°CA, this corresponds to a turbulent loss of about 13%. For an IVC=140°CA, the turbulent losses that can cancel the advantages of the Miller cycle are approximatively 22%.

The in-cylinder aerodynamic is the key factor to be able to control the combustion process and reduce pollutant emissions of internal combustion engines. That's why many studies have been conducted to understand the flow generation process during the intake stroke and its development during the compression stroke before combustion. In particular in spark ignition engine, the turbulence generated at the end of the compression stroke has a great impact on the flame front development. The initial kernel development is affected by the turbulence level, which also impacts flame-front propagation and the time duration of the combustion process. This turbulence level results from the initial flow structure and is influenced by the engine geometry. Thus, intake ports and combustion chamber design influence the combustion efficiency and pollutant emissions. Moreover, the flow field varies from cycle to cycle resulting in cyclic variations of the combustion efficiency. It is necessary to find a geometry that reduces cyclic variation of the flow. However, it seems difficult to adapt the design for the whole engine operating range and specifically for a Miller Cycle. So, a possible solution remains in adapting the intake geometry to the operating point. For spark ignition engines, main studies consist of adapting the intake port design to maximize tumble ratio. Introducing a baffle which hides a part of the inlet port, or design artifacts as an active control to generate a swirling or tumbling effect, increases the overall level of turbulence in the combustion chamber without penalizing the filling of the engine. The needs of experiments and simulation to validate the Miller concept may be necessary.

References

[1]   IEA, « CO2 Emissions from Fuel Combustion 2018 », 2018.

[2]   PFA, « Contribution des véhicules légers et lourds à la réduction de la demande énergétique et des émissions de CO2 à horizon 2035 dans le monde », 2018.

[3]   M. Vogler, A. Konigstein, et N. Fuhrmann, « Combustion Engines for Electrified Powertrains », *MTZ worldwide*, 2019.

[4]   M. Ziegler, « Making Progress with Electrification », *MTZ worldwide*, 2019.

[5]   M. Rode, T. Suzuki, G. Iosifidis, et T. Scheuermann, « Electric Turbocharger Concept for Highly Efficient Internal Combustion Engines », *MTZ Worldw*, vol. 80, n° 7, p. 120‑125, juill. 2019.

[6]   R. Backhaus, « The Gasoline Engine Spark Ignition Remains », *MTZ worldwide*, 2019.

[7]   V. Collée, C. Constensou, F. Dubois, et L. Guilly, « Variable Compression Ratio for Future Emission Standards », *MTZ Worldw*, vol. 78, n° 4, p. 52‑57, avr. 2017.

[8]   S. Kiga, K. Moteki, et S. Kojima, « The New Nissan VC-Turbo with Variable Compression Ratio », *MTZ Worldw*, vol. 78, n° 11, p. 42‑49, nov. 2017.

[9]   W. Schoeffmann *et al.*, « Dual Mode VCS – Vehicle Integration of a Modular VCR-System », présenté à SIA Powertrain and Electronics, Paris, 2019.

[10]   C. Jung, A. Mudra, et D. Schulze, « Connecting rod for internal combustion engine with variable compression eccentrical element adjustment device », US10100725B2, oct. 16, 2018.

[11]   N. Morand, G. Agnew, N. Bontemps, et D. Jeckel, « Variable Nozzle Turbine Turbocharger for Gasoline" Miller" Engine », *MTZ worldwide*, vol. 78, n° 1, p. 40–45, 2017.

[12]   W. Hannibal, R. Flierl, L. Stiegler, et R. Meyer, « Overview of Current Continuously Variable Valve Lift Systems for Four-Stroke Spark-Ignition Engines and the Criteria for their Design Ratings », SAE International, Warrendale, PA, SAE Technical Paper 2004-01‑1263, mars 2004. Consulté le: juill. 31, 2019. [En ligne]. Disponible sur: https://www.sae.org/publications/technical-papers/content/2004-01-1263/.

[13]   N. Zsiga, A. Omanovic, P. Soltic, et W. Schneider, « Functionality and Potential of a New Electrohydraulic Valve Train », *MTZ Worldw*, vol. 80, n° 9, p. 18‑27, sept. 2019.

[14]   R. Koenen et J. Hansen, « Cylinder deactivation for a multiple cylinder engine », US20190107062A1, avr. 11, 2019.

[15]   T. Konrad, W. FIMML, et A. Bernhard, « Method for smoothly connecting a load during an activated cylinder deactivation process of an internal combustion engine », US20180128195A1, mai 10, 2018.

[16]   F. Hoppe, M. Thewes, H. Baumgarten, et J. Dohmen, « Water injection for gasoline engines: Potentials, challenges, and solutions », *International Journal of Engine Research*, vol. 17, n° 1, p. 86‑96, janv. 2016.

[17]   S. Zhu *et al.*, « A review of water injection applied on the internal combustion engine », *Energy Conversion and Management*, vol. 184, p. 139‑158, mars 2019.

[18]   R. Dauphin, D. Serrano, F. Guerbet, et L. Serve, « Fuel Formulations Based on RON Synergistic Effects for Better Fuel Economy and Lower CO2 Emissions », présenté à SIA Powertain and Electronics, Paris, 2019.

[19]   M. Ziegler, « There is no alternative to this strategy », *MTZ Worldw*, vol. 80, n° 7, p. 54‑57, juill. 2019.

[20]   W. Demmelbauer-Ebner, Jö. Theobald, Jö. Worm, et P. Scheller, « The new 1.5-l EA211 TGI evo », *MTZ Worldw*, vol. 79, n° 9, p. 16‑21, sept. 2018.

[21]   I. Hirose et M. Hitomi, « Mazdas way to more efficient ICE », *MTZ worldwide*, 2016.

[22]   « MWI Micro Wave Ignition AG – Mikrowellen-/ Raumzündungssysteme ». https://mwi-ag.com/.

[23]   W. Bou Nader, Y. Cheng, S. Houille, S. A. Belmedrek, et C. Dumand, « Methodology for the Optimization of the Overall Efficiency of a Combined Cycle: Internal Combustion Engine Coupled to Steam Rankine Cycle on Series Hybrid Electric Vehicles », présenté à SIA Powertrain and Electronics, Paris, 2019.

[24]   E. Ortiz-Soto et M. Younkins, « Advanced Cylinder Deactivation with Miller Cycle », *MTZ worldwide*, 2019.

[25]   N. Neumann, N. Freisinger, G. Vent, et T. Seeger, « Experimental investigation of Miller cycle combustion technology with water injection », in *19. Internationales Stuttgarter Symposium*, 2019, p. 599‑611.

[26]   M. E. S. Martins et T. D. M. Lanzanova, « Full-load Miller cycle with ethanol and EGR: Potential benefits and challenges », *Applied Thermal Engineering*, vol. 90, p. 274‑285, nov. 2015.

[27]   J. Atkinson, « Differential Engine », US336505A, févr. 16, 1886.

[28]   J. Atkinson, « Cycle Engine », US367496A, août 02, 1887.

[29]   E. L. Marshall, « The Quest for Thermodynamic Efficiency: Atkinson Cycle Machines Versus Ot-to Cycle Machines », *The International Journal for the History of Engineering & Technology*, vol. 79, n° 1, p. 6‑33, janv. 2009.

[30]   O. Dumbock, E. Schutting, H. Eichlseder, et W. Hubner, « Increasing the Efficiency of the Inter-nal Combustion Engine through Extended Expansion », *MTZ worldwide*, 2018.

[31]   « Honda Global | Exlink - Picture Book ». https://global.honda/innovation/technology/power/Exlink-picturebook.html.

[32]   S. Watanabe, H. Koga, et S. Kono, « Research on Extended Expansion General-Purpose En-gine Theoretical Analysis of Multiple Linkage System and Improvement of Thermal Efficiency », *SAE Transactions*, vol. 115, p. 1124‑1131, 2006.

[33]   « MCE5 VCRi », *MCE-5*. https://www.mce-5.com/vcri-taux-compression-variable-economie-carburant-reduction-co2-polluants/.

[34]   Y. Yamada, « Engine of compression-ratio variable type », US6820577B2, nov. 23, 2004.

[35]   R. Miller, « High-pressure supercharging system », US2670595A, mars 02, 1954.

[36]   R. Miller, « High expansion, spark ignited, gas burning, internal combustion engines », US2773490A, déc. 11, 1956.

[37]   R. Miller, « Supercharged engine », US2817322A, déc. 24, 1957.

[38]   S. Shuai, X. Ma, Y. Li, Y. Qi, et H. Xu, « Recent Progress in Automotive Gasoline Direct Injec-tion Engine Technology », *Automot. Innov.*, vol. 1, n° 2, p. 95‑113, avr. 2018.

[39]   T. Johnen, « "Rightsizing" A Strategic Customer Interest », *MTZ Worldw*, vol. 77, n° 6, p. 90‑90, juin 2016.

[40]   J. Sporleder, M. Alt, et T. Johnen, « The Efficient Gasoline Engines in the New Opel Astra K », *MTZ Worldw*, vol. 77, n° 2, p. 28‑33, févr. 2016.

[41]   W. Demmelbauer-Ebner, K. Persigehl, M. Gorke, et E. Werstat, « The New 1.5-l Four-cylinder TSI Engine from Volkswagen », *MTZ Worldw*, vol. 78, n° 2, p. 16‑23, févr. 2017.

[42]   R. Budack, R. Wurms, G. Mendl, et T. Heiduk, « The New Audi 2.0-l I4 TFSI Engine », *MTZ Worldw*, vol. 77, n° 5, p. 16‑23, mai 2016.

[43]   S. Kallich, H. Graf, K. V. Schaller, et S. Ritter, « The New BMW Motorrad Boxer Engine with ShiftCam Technology », *MTZ worldwide*, vol. 80, n° 4, p. 32‑39, avr. 2019.

[44]   P. Anselmi, X. Gautrot, O. Laget, M. Ritter, et C. Lechard, « Swumble In-Cylinder Fluid Motion: a Pathway to High Efficiency Gasoline SI Engines », présenté à SIA Conference, Paris, 2019.

[45]   H. P. Lenz, K. Wichart, et D. Gruden, « Variable Valve Timing—A Possibility to Control Engine Load without Throttle », *SAE Transactions*, vol. 97, p. 652‑658, 1988.

[46]   R. Huber, P. Klumpp, et H. Ulbrich, « Dynamic Analysis of the Audi Valvelift System », *SAE In-ternational Journal of Engines*, vol. 3, n° 1, p. 839‑849, 2010.

[47]   C. Brüstle et D. Schwarzenthal, « VarioCam Plus - A Highlight of the Porsche 911 Turbo En-gine », SAE International, Warrendale, PA, SAE Technical Paper 2001-01‑0245, mars 2001. Consulté le: août 26, 2019. [En ligne]. Disponible sur: https://www.sae.org/publications/technical-papers/content/2001-01-0245/.

[48]   Y. Wan et A. Du, « Reducing Part Load Pumping Loss and Improving Thermal Efficiency through High Compression Ratio Over-Expanded Cycle », SAE International, Warrendale, PA, SAE Technical Paper 2013-01‑1744, avr. 2013. doi: 10.4271/2013-01-1744.

[49]   T. Niizato, M. Shibata, M. Fischer, et U. Reinschmidt, « New 1.0-l Three-cylinder Gasoline En-gine from Honda », *MTZ Worldw*, vol. 79, n° 1, p. 16‑23, janv. 2018.

[50]   M. Mürwald, R. Kemmler, A. Waltner, et F. Kreitmann, « The new four-cylinder gasoline engines from Mercedes-Benz », *MTZ Worldw*, vol. 74, n° 11, p. 4‑11, nov. 2013.

[51]   T. Wasserbäch, T. Brandl, et R. Schmidt, « The Six-cylinder Boxer Engines in the Porsche 911 », *MTZ Worldw*, vol. 80, n° 7, p. 16‑23, juill. 2019.

[52]   P. GUIBERT, « Modélisation du cycle moteur Approche zérodimensionnelle », *Techniques de l'ingénieur Combustion dans les moteurs thermiques et environnement*, vol. base documen-taire : TIB166DUO., n° ref. article : bm2510, 2005.

[53]   C. R. Ferguson et A. T. Kirkpatrick, *Internal Combustion Engines: Applied Thermosciences*. John Wiley & Sons, 2015.

[54]   J. Heywood, *Internal Combustion Engine Fundamentals*. McGraw-Hill Education, 1988.

[55]   P. GUIBERT, « Modélisation du cycle moteur Moteurs à allumage commandé », *Techniques de l'ingénieur Combustion dans les moteurs thermiques et environnement*, vol. base documen-taire : TIB166DUO., n° ref. article : bm2511, 2005.

[56]   T. Poinsot et D. Veynante, *Theoretical and Numerical Combustion*. R.T. Edwards Inc., 2005.

Experimental Investigation on an Innovative Additive Manufacturing-Enabled Diesel Piston Design to improve Engine-out Emissions and Thermal Efficiency beyond Euro6

G. Di Blasio[1], R. Ianniello[1], C. Beatrice[1], F. C. Pesce[2], A. Vassallo[2] and G. Belgiorno[2]

[1]CNR – Istituto Motori. Viale Marconi,4, 80125 Naples, Italy

E-mail: g.diblasio@im.cnr.it
Telephone: +(39) 081 7177221

[2]Punch Torino S.p.A., Corso Castelfidardo, 36, 10129 Torino TO, Italia –
formerly General Motors Global Propulsion Systems

E-mail: francesco_concetto.pesce@punchtorino.com
Telephone: +(39) 011 438 2437

Abstract. In recent years the research on Diesel thermodynamics has been increasingly shifting from performance and refinement, obtained thanks to advanced fuel injection and charging technologies, to ultra-low emissions and efficiency. The last two attributes are key factors for the powertrain competitiveness in the automotive electrified future, especially in the European market where the pollutant emissions are approaching the Euro6D RDE step2 level and the CO_2 the value of 95g/km fleet average. In this framework, the present paper describes a research study conducted in cooperation between GM and Istituto Motori, exploring how the application of the most recent additive manufacturing technologies allow complex combustion bowl features enabling optimized combustion process to a level that was not compatible with standard manufacturing technologies. An innovative highly reentrant-sharp-stepped profile featuring radial-lips has been studied and fully characterized by means of a proper designed test rig and experimental campaign. A 0.5l single-cylinder engine coupled to a state of art fuel injection system has been developed, with the objective to demonstrate the potential of optimized fuel stratification and spray separation enabled by the radial mixing zone concept. The results show an important reduction of the engine-out smoke emissions in comparison to the Euro6B design with no detrimental effects on the efficiency when advanced compact injection patterns and optimized calibration are applied at partial loads. To this aim, sensitivity studies have been conducted to understand the optimal injection protrusion, spray indexing to the ribs and fuel injection parameters. Moreover, the prototype additive manufactured steel piston did not highlight durability concerns after an extensive experimental campaign at partial load conditions.

Notation

AM	Additive Manufacturing
aTDC	after Top Dead Center
BMEP	Brake Mean Effective Pressure
BSFC	Brake Specific Fuel Consumption
BSx	Brake Specific Emissions
CA	Crank Angle
CFD	Computational Fluid Dynamics
CNC	Computer Numerical Control
CO	Carbon Monoxide
CO$_2$	Carbon Dioxide
CR	Compression Ratio

DMLS	Direct Metal Laser Sintering
DoE	Design of Experiment
EC	Energizing Current
FIS	Fuel Injection System
HC	Hydrocarbons
HRR	Heat Release Rate
IMEP	Indicated Mean Effective Pressure
ISFC	Indicated Specific Fuel Consumption
ISx	Indicated Specific Emissions
MBF90-10	Combustion duration
MBF50	Crank Angle of 50% of the total heat released
NEDC	New European Driving Cycle
NOx	Nitrogen Oxides (NO, NO_2)
NTP	Nozzle Tip Protrusion
NVH	Noise Vibration and Harshness
O_{2_exh}	Oxygen concentration in the exhaust gases
OEM	Original Equipment Manufacturer
p_{cyl}	In-Cylinder Pressure
p_{rail}	Rail Pressure
pfp	Peak Firing Pressure
PM	Particulate Matter
SCE	Single-Cylinder Engine
SCR	Selective Catalytic Reduction
RDE	Real Driving Emissions
RMZ	Radial Mixing Zone
SLM	Selective Laser Melting
SoI	Start of Injection
TDC	Top Dead Center
WLTP	World Harmonized Light Vehicles Test Procedure
WT	Weight Thickness
η_{comb}	Combustion efficiency
η_{mech}	Mechanical efficiency
η_{therm}	Thermal efficiency

1. Introduction

After enjoying a roughly two-decades-long "golden age", in the last few years, the Diesel powertrain has undergone significant challenges, especially for passenger car applications [1]. The main reason can be routed back to concerns about the nitrogen oxides emissions gap between real-world and official certification ratings, before the Euro6D-temp and RDE Step1 legislation took place starting in September 2017 [2].

In the meantime, valuable efforts from industry and academia have been made to overcome the concerns in respecting emission targets under real driving conditions currently in place worldwide. In this framework, the OEMs have already introduced new diesel cars featuring conformity factors well below the Euro 6D-temp and RDE Step1 standard [3,4].

This huge achievement, which seemed unrealistic just a few years ago, leads to the reasonable conclusion that, in the short-medium term and in parallel with the electrification, Diesels will still play an important role in the transportation sector at least for as long as alternative solutions provide the flexibility and range expected by customers. However, the challenge for Diesel engines is to keep competitiveness in the CO2-cost tradeoff in comparison to other propulsion systems.

To this aim, research in Diesel engines is exploring every opportunity provided by mechanics and thermodynamics to reduce the fuel consumption effectively, and topics considered even as marginal not so many years ago are now moving to the forefront. Among the different technologies under development in order to further improve the Diesel nitrogen oxides and CO_2 emissions, the combustion system design (including by extension the charging and fuel injection systems) still represent the cornerstone. As it is well known, until about 2015 the optimization of turbocharging, EGR, intake ports, piston bowl profile and injection system has been primarily directed to increasing performance, reaching notable milestones as documented in [5-7].

More recently, by leveraging capable aftertreatment systems SCR-based, the fuel economy has been greatly improved by tuning of the thermodynamics and mechanics efficiencies [8, 9]. Nevertheless, the continuous reduction in tailpipe emissions under every operating condition (ambient temperature, altitude, driving style, vehicle load and mileage…) has made necessary a further significant improvement of engine-out emissions even in combination with the most sophisticated aftertreatment systems, with no compromise to fuel economy or performance [10].

In this context, advancements in Diesel combustion understanding enabled by state-of-art CFD and optical techniques [11-13], as well as in piston bowl design enabled by sophisticated additive manufacturing technologies [14, 15], are opening new possibilities in the tailoring of the combustion process. The present work describes some early results achieved employing a state-of-the-art 2500 bar fuel injection system capable of compact injection patterns (already used in [6, 7, 9, 10], now coupled to novel bowl profiles featuring advanced spray-guiding geometries. In particular, the bowl profiles studied encompass the most recent trends in light and heavy-duty (HD) Diesels, including sharp-stepped piston top, highly-reentrant bowl and radial lips (also called waves).

As shown in [14] on a HD Diesel engine, the in-cylinder flow during interactions between adjacent flames (flame-flame events) has a large impact on late-cycle combustion. To modify the flame-flame, a new piston bowl shape with a protrusion (wave) was designed to guide the near-wall flow. This design significantly reduced soot emissions and increased engine thermodynamic efficiency. The wave's main effect was to enhance late-cycle mixing, as demonstrated by apparent rate of heat release after the termination of fuel injection. Combustion simulations showed that increased mixing is driven by enhanced flow re-circulation, which produces a radial mixing zone (RMZ). The leading edge of the RMZ extends toward the center of the piston bowl, where unused ambient gas is available, promoting oxidation. The wave also enhances mixing in the trailing edge of the RMZ when it detaches from the wall, accelerating the burn-out of the RMZ.

A similar concept has been employed in [15], where the concept of the advanced piston bowl design is to align the bowl layout along with each fuel jet. Consequently, the piston bowl is not rotationally symmetric and forms something like a housing around the fuel jet. With the advanced piston bowl layout, the free spray penetration length is increased by 25% compared to conventional designs. Besides, the bowl contour has been adapted to improve the squish flow and mixture formation.

The present work builds on top of these results, by further modifying the combustion chamber and incorporating novel elements that optimize the thermodynamics of combustion process over a wide range of operating conditions, as will be described in the next section.

2. Additive-Manufacturing-Enabled Innovative Diesel Piston

The novel piston design concept that has been conceived and studied in the present paper builds upon 3 elements (Fig. 1):
- Sharp-Step feature: at high load, increases air utilization and performance;
- Inner bowl with high reentrancy: at low load, reduces heat losses and improves spray backward motion
- Radial lip feature (in the inner bowl only): at low load, further reduces heat losses (lowers air motion); at high load, separates the sprays combustion avoiding over-rich combustion and lowering PM production.

3) Radial lip feature (in inner bowl only)
At low load, further reduces heat losses (lowers air motion).
At high load, separates the sprays combustion thus avoiding over-rich combustion and lowering PM production.

1) Sharp-Step feature
At high load, increases air utilization and performance

2) Inner bowl with high reentrancy
At low load, reduces heat losses and improves spray backward motion
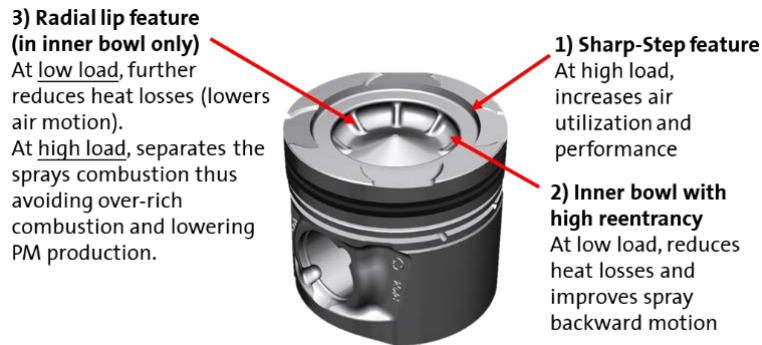
Fig. 1. Prototype bowl features

Details of the profile optimization and mechanisms of an operation via 3D-CFD of such a complex profile are presented in [20]. To the scope of this paper, it is worthwhile to recall that fuel sprays should be targeted at the middle of each cavity among two waves or lips, and therefore that there is a direct connection among the number of sprays and the number of cavities (which go hand-in-hand), and the angle sector among two lips reduces as the number of injector holes increases (Fig. 2).

| 8 lips 45° sector | 9 lips 40° sector | 10 lips 36° sector |
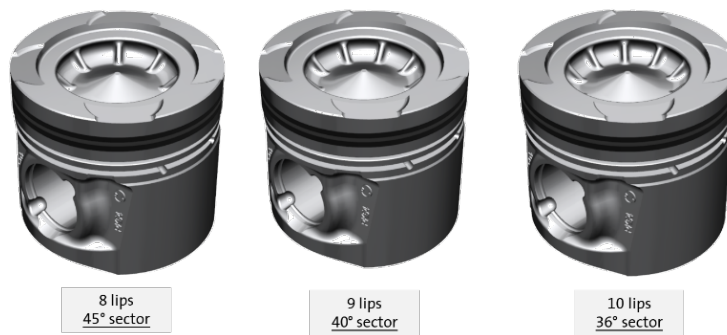
Fig. 2. Bowl matching with 8-9-10 sprays.

This paper is focused on the mechanical optimization of such a profile and its realization with steel-based additive manufacturing. In fact, while the realization of such a complex reentrant profile can be done on an aluminum piston blank using a 5-axes CNC, the durability necessary on modern Diesel engines requires a steel-based approach, especially due to high thermal stress on the lips (Fig. 3).

Fig. 3. Prototype steel piston left and side view (comparison with forged steel piston is provided, to show same compression height and top land).

2.1 Piston Design

The Additive Manufacturing (AM) piston design work has been conducted looking at the best compromise between "classic" piston design features that should ensure the piston functionality in the engine

and the new contents derived by the combination of the complex bowl shape features and the new opportunities opened by AM technology.

Conventional production processes like aluminum casting or steel forging would not easily allow the creation of undercut features as required by the highly-reentrant combustion bowl. With CNC machining, long cycle execution time and tool wear could become a concern, especially if a high strength material is chosen/required. The complex and sharpen bowl features would result in quite high local stress concentration that only a steel-based material could be able to withstand. Summing up the above needs with the exponential progress of AM processes from the last couple of years, the decision to proceed with the AM fabrication process using a steel-based material has been chosen. An "AM oriented" piston design work started consequently.

This has been a challenging task for several reasons. The AM material mechanical properties for this specific application and design are not fully known in the literature, especially concerning thermomechanical fatigue resistance, thermal expansion and dimension tolerances, and must be deeply verified.

Besides, AM required an "open mind" approach, avoiding influences by standard design methodologies and to revisit and design every feature - including the most classic ones - for the true function(s) they need to exhibit. As said, with AM there is freedom of geometry and any features can be realized "for free" independently from its complexity. In the specific our case, this means undercuts are possible not a problem, and complex piston bowls with ribs and reentrant step shape can be produced without the necessity to use a 5-axis milling CNC machine. Based on the information available, the best trade-off of each size of every single feature has been investigated trying to predict what would have been the behavior of material never used to produce a Diesel piston.

It is important to note that some of the key design dimensions were known based on project application/testing equipment chosen:

- Bore x Stroke (hence cylinder displacement)
- Compression Ratio and height
- Injector spray displacement
- Piston pin offset and diameter

There were instead some design parameters whose benchmark / best practices would be well known in case of a conventionally manufactured piston, but needed instead to be completely re-evaluated for the AM technology:

- Pin profile
- Skirt profile
- Lands
- Roughness
- Tolerances
- Ring groves

It is important now to consider that the AM piston will be printed by the powder bed-based SLM (Selective Laser Melting) technology, which needs supports made out of the material used for the part itself to avoid the not self-supported features to collapse during the printing process and the final part to warp due to residual stresses. The design for AM approach aimed to reduce the number of such supports because too many supports would have meant an increase of printing time affecting the overall costs as well as the inability to remove the supports themselves within unreachable areas.
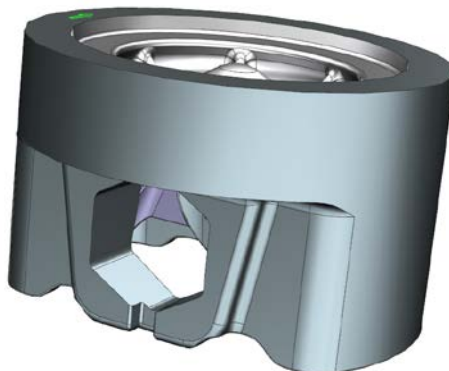

Fig. 4. Raw piston. Diamond shape for pin hole.

According to the above strategy, it should be noticed that the number of horizontal surfaces has been reduced by favouring the surfaces inclined at 45°. Such design guideline enables self-supporting walls to be printed out by the SLM process and can be perceived at the ribs of the skirt, the oil gallery or the raw pin hole where a diamond shape was chosen to avoid supports (Fig. 4) completely.

The oil gallery itself presents the so-called lattice structure, which can combine high strength, low mass, good energy absorption and thermal conductivity properties.

Different kinds of lattice structure can be printed out by SLM, ranging from honeycomb structures to open or closed cell frames. Each one of them has a different set of mechanical and thermal properties and reacts in a proper way and direction to the external loads. For this application, an open-cell frame has been eventually selected, in order to avoid metal supports within the oil gallery showing an optimal trade-off between light-weighting and oil circulation (Fig. 5).
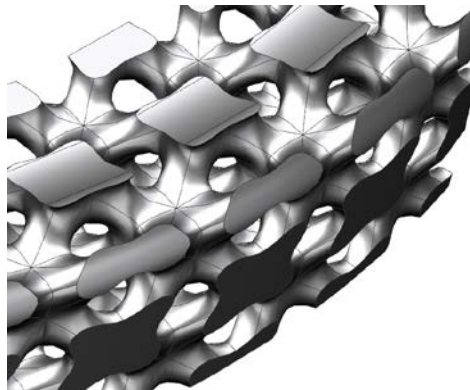
Fig. 5. Oil gallery open-cell lattice structure.

Most of the AM design-oriented practices were applied to the "raw part" design, and the final piston was then machined out of these raw parts using standard machining processes. As far as the structural design is concerned, the inner area of the piston has been topologically optimized (Fig. 6) based on the different load cases and constraints scenarios acting on the part during the combustion cycle. The target was to guarantee the proper mechanical strength related to the applied loads by gathering information about the correct material location. The methodology has considered the "design", the one optimized by the software, and the "non-design" spaces definitions. The design space has been created considering the supports avoidance guidelines (> 45° angles) as well as the oil inlet/outlet accesses. The final complex shape is manufacturable exclusively out of AM.

The choice of stock material (or machining allowance) ranges from a minimum of 1 mm, according to printing tolerances and expected roughness (skirt side), to a maximum of 2 mm in the internal area or of the pin hole, and they have been chosen based on the tolerances of the printing process. Final machining operations have also been defined to not compromise the topologically-optimized shape and its functionalities. Piston top and the whole bowl face has been then polished only (as can be noticed in Fig. 3).
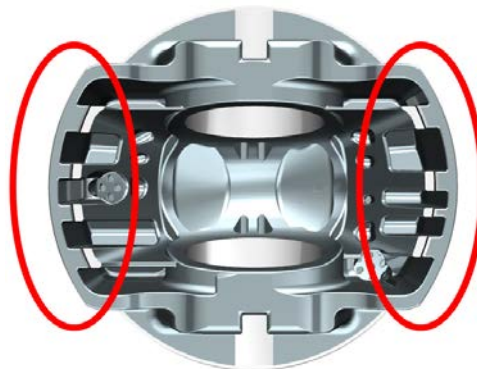
Fig. 6. Lower and inner skirt topology optimization and machining. Feature to handle the piston during machining operations.

Several modeling software toolkits have been used: Siemens NX 11.0 for standard modeling, Altair INSPIRE for topology optimization and AUTODESK Netfabb for Design for AM and printing simulation of parts (such as the oil gallery and skirt inner area). Finally, a set of views of the AM realized, and fully machined piston are reported in Fig. 7, including (top to bottom): top view, isometric view (highlighting the valve pockets areas in green and blue colors) and piston cross-section orthogonally to pin axis.

Fig. 7. Set of views of the AM realized and fully machined piston. Top to bottom: top view, isometric view and piston cross-section orthogonally to pin axis.

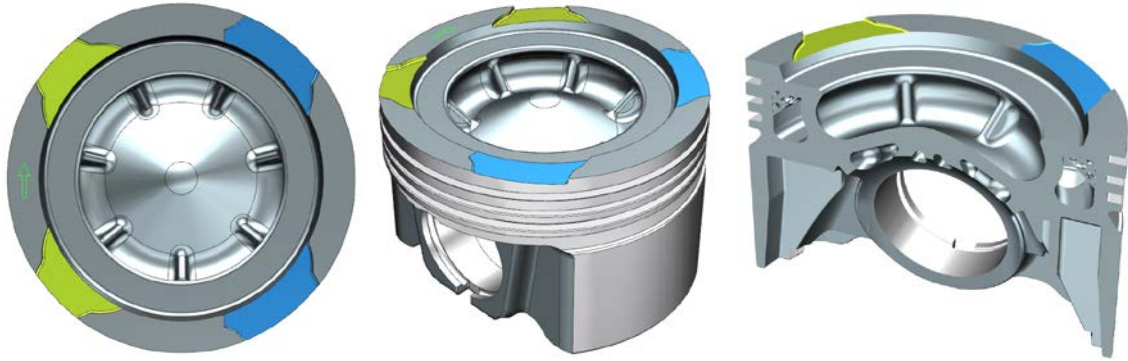## 2.2 Prototype Piston Manufacturing with Additive Technology

As introduced in the previous paragraph, the piston prototype manufacturing has been made out of an Additive powder bed-based technique which is the so-called SLM (Selective Laser Melting) or DMLS (Direct Metal Laser Sintering). That technique uses a laser source to melt consecutive layers of metal powder each other, and additively creates the final part. The process needs metal supports to avoid collapses during the printing phase, and distortions after the parts are removed from the printing platform, they are integral with. Some pictures of the layers melting process and of the metal supports creation are reported in Fig. 8.

The major decision was related to the Additive material choice since the technology shows a currently limited portfolio related to steels. The most common steels used for conventional pistons were not available into such a portfolio, so the best choice was the 316L stainless steel which has different properties the conventional ones mechanically and thermally wise (Table 1).

Table 1. Mechanical and thermal properties comparison.

Mechanical / Thermal properties	SS 316L (AM stress relief)	Baseline (Conventional)
0,02% Yield (MPa)	492	650
Ultimate tensile (MPa)	588	875
Elongation (%)	40	12
Hardness (HB)	165	275
Thermal Conductivity [W/mK]	13-15	35-40
CTE [micron/mmC]	19	13

This difference has been considered during the design, and topological optimization runs. However, the printed 316L stainless steel fulfilled the material requirements needed for this prototype phase testing combined with the proper cost trade-off as well as a potential future serial production investigation.

The printing orientation is crucial for an Additively manufactured piston since it affects the mechanical strength as well as the roughness. The metal process leads to a slight anisotropy due to the layer by layer melting by the laser source, and the weakest direction is the Z-axes. As far as the roughness is concerned, the SLM process cannot still achieve net shape as-built parts but a range of Ra 8-10μm on the top surfaces and Ra > 10μm on the side and bottom ones. According to that above the orientation chosen was to print the part with the piston bowl on the top to achieve the best trade-off as far as the post-processing operations as well. The as printed roughness of the bowl was around Ra 8μm also due to a tight set up of the printing parameters and even if acceptable a light polishing was needed.

A stress relief heat treatment was needed to avoid a risky distortion of the piston when removed from the build plates due to residual stresses caused by the laser source high power curing the part locally. The heat treatment helped to achieve a more relaxed microstructure, theoretically leading to the needed durability and fatigue requirements for the testing. This aspect must be deeper investigated in the future.

Post-processing operations were needed as a light polishing of the piston skirt and the bowl with high attention to not compromised the ribs shape and functionality.

The final machined piece and a clear understanding of the surface quality reached within the bowl are visible in Fig. 8.

Fig. 8. Set of views of the AM pistons during the printing process: from the first layers to the final rough pieces. The last picture shows the final part and bowl surface quality after the full machining.

3. Experimental Setup

The measurement program for the present study was conducted on a single-cylinder engine (SCE), with a displacement of 0.5 l, which integrates the main combustion system components of an advanced four-cylinder diesel engine. The engine is capable of meeting the EU-6d NOx emission target thanks to charge air cooling and high-pressure exhaust gas recirculation (EGR) without the application of any after-treatment system. In particular, the employed test engine is of modular and variable design to be flexible in the use of different engine configurations. The SCE represents the optimal tool for testing prototype components for time-consuming and costs savings benefits and without losing quality in comparison to multi-cylinder applications [8]. Once defined a proper correlation procedure [6], the results obtained for the test rig used in this study can be directly used as they are for the calculation of specific results for the 4-cylinder application.

The fuel injection system (FIS) is close to series production and capable of rail pressures up to 2500 bar using a solenoid injector. The injection pattern, as well as the rail pressure, can be adjusted freely as desired in order to compensate for fuel effects. The combustion system is rated at 70-75 kW/l and is capable of withstanding peak firing pressures up to 200 bar. All other engine components and auxiliary systems were properly designed and assembled. An in-house developed supervisory system, based on a C-RIO 9081 National Instrument platform, is deputed to control and monitor the test cell and engine control parameters. Detailed information on this engine can be found in various publications [6,

8], and the key engine specifications are summarized in Table 2. Furthermore, a detailed layout of the used single-cylinder engine can be found in Fig. 9.

Table 2. Hardware specifications for the prototype diesel engine

Parameters	Units	Specifications
Specific displacement	l/cyl	0.5
Bore x Stroke	mm	83 x 90.4
Compression Ratio	-	16.0
Valves per cylinder	-	4
Nozzle hydraulic flow rate	cm^3/30s	440
Nozzle hole number	-	7
Nozzle cone opening angle	deg	155
Piston Radial-lips	-	7
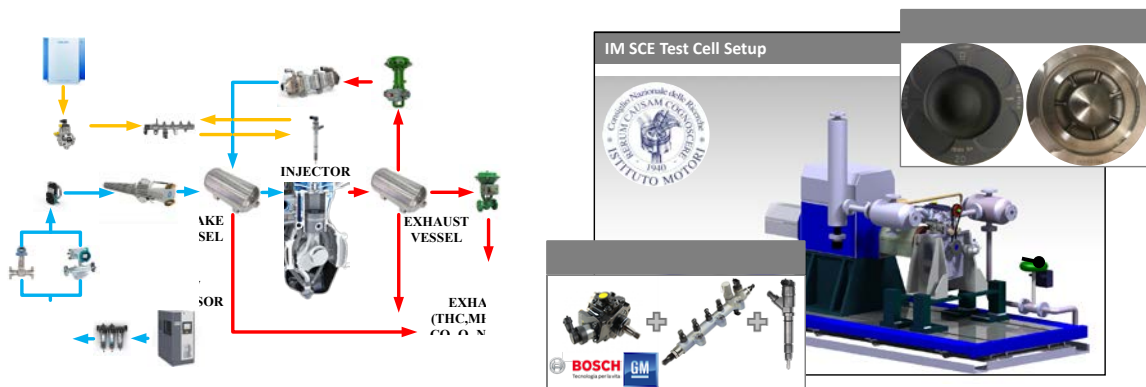
Fig. 9. Test cell layout (left). Engine and FIS technologies content and integration (right).

The engine has been fully instrumented with air flow meters, pressure, and temperature transducers to monitor, acquire, and save the electrical, thermal, fluidynamic, and mechanical states of each of the engine subsystems. The combustion metrics (indicating) are measured and calculated using the pressure signal of a flush-mounted piezoelectric pressure sensor installed in the glow-plug hole. The fuel injection system is characterized by using an ammeter for the electrical command and piezo-resistive pressure and temperature sensors placed along the high-pressure fuel line. At the same time, the in-cylinder gas-exchange phase (pumping loop) is characterized by piezo-resistive pressure sensors located in the intake and exhaust manifolds. The engine torque, speed, and actual crankshaft position are acquired employing an AVL encoder (engine side) and HBM T12 Torque meter (dynamometer side).

4. Test Methodology

The experimental activity is devoted to characterize and optimize the new defined combustion system and to robustly compare it to the conventional reference one, in terms of both emissions and thermal efficiency. To this goal, a simplified design of experiments (DoE) was agreed. Four steady-state engine operating key-points are examined. They include engine operating conditions of a C-class passenger car vehicle during the execution of the NEDC/WLTC cycles. Fig. **10** shows the relative speed-load engine map delimited by the full load curve, the cycle operating areas, and the selected partial load test points. As mentioned before, it is worth underlining that, dealing with an SCE, to make a fair calculation of the SCE "brake-quantities" in comparison to those of the real multi-cylinder engine, a validated friction correlation procedure reported in [6, 21] has been adopted. It considers a base engine design with a maximum peak firing pressure (pfp) of 180 bar.

Fig. 10. Test points delimited by the NEDC, WLTP engine operating areas of a C-class engine.

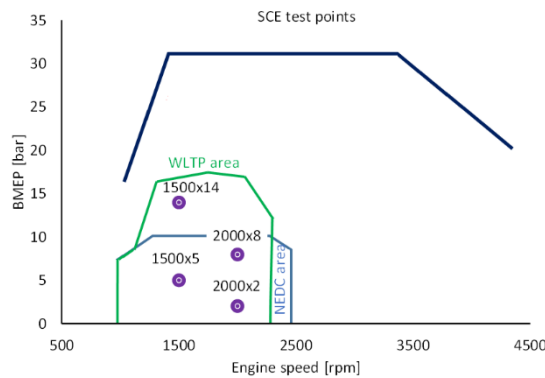The DoE based test campaign has required a preliminary parametric nozzle tip protrusion (NTP) investigation, to define the optimal spray targeting in relation to the piston bowl, concerning the effect on emissions and performance. These tests, for a fair comparison among all, were performed at fixed combustion barycenter (MBF50) and engine-out NOx emissions by varying the start of the injection (SOI) and the EGR rate, respectively. The Euro 6B NOx target levels are summarized in each chart of Fig. 11, and are 0.5 and 0.8 g/kWh, for 2000x2 and 2000x8, respectively [6, 8]. The fuel injection pressure (p_{rail}) was kept constant. An advanced injection pattern (pilot quantities, dwell times, number of injections) has been set as for the conventional steel piston. The NTP was varied using different washer thicknesses. The resulting optimal Washer Thickness (WT) was 1 mm, based on a deep investigation for different k-points, as reported in [8]. As part of this study, Fig. 11a shows the WT variation effect, between 0.5 mm and 2 mm, at 2000x8 only, on the emitted particulate matter (PM) and compared to the conventional piston value. The WT of 1 mm presents an indicated specific particulate-matter (isPM) reduction of about 50% without penalties on gaseous emissions and efficiency and then chosen as the best compromise among those tested. Then, further optimization of the injection pattern with the optimal NTP has been conducted, adopting a simplified approach with few factors and levels.
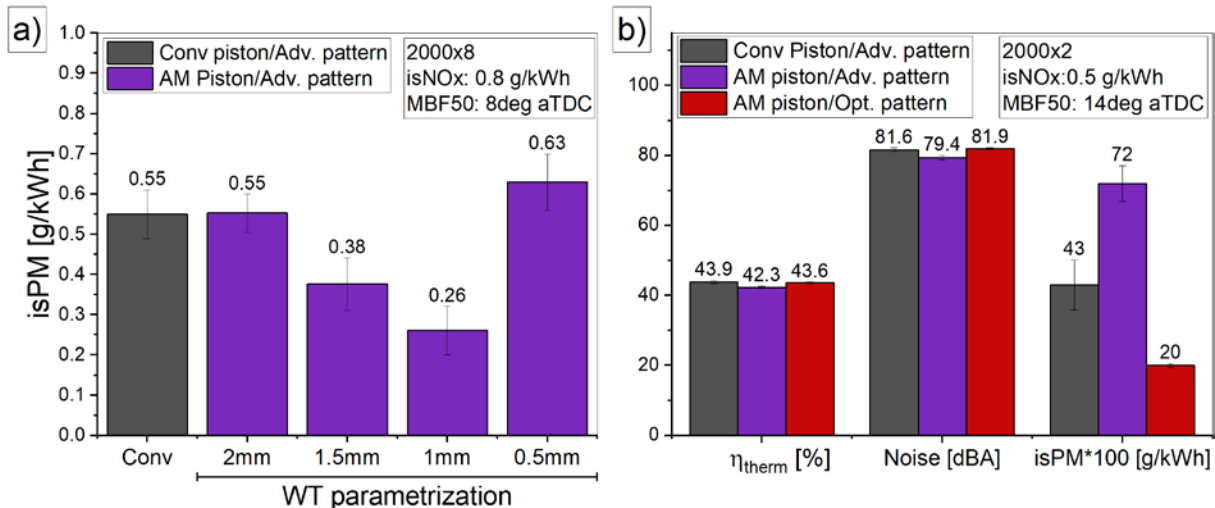
Fig. 11. Washer thickness parametrization at constant NOx: a) isPM trend at 2000x8 for AM piston varying the WT and referenced to the conventional one; b) Effect of the optimized AM Injection pattern at 2000x2 and WT=1mm referenced to the conventional piston one [8].

Fig. **11**b reports the pattern optimization results at 2000x2 and WT 1mm; it is the only point where the optimization became necessary. For the other test points, the same advanced injection patterns were employed. The figure compares the results of the optimized AM pattern with the conventional one. Indeed, the combination of AM piston and the advanced pattern shows comparable efficiency performance with a worsening of the PM of about 50%, and for this reason, it was required a further optimization in terms of PM by means of the injection pattern. Therefore, a variation of the dwell times, pilot quantities and number of pulses have been applied. As a result, a more compact injection pattern and combustion shape at constant MBF50, NOx emissions (0.5 g/kWh), and p_{rail} have been achieved. The

optimization has led to a significant PM reduction, about 50%, with slight differences in terms of thermo-dynamic efficiency and combustion noise compared to the conventional piston. A summary of the injection patterns for all the test points is schematized in Fig. 12.
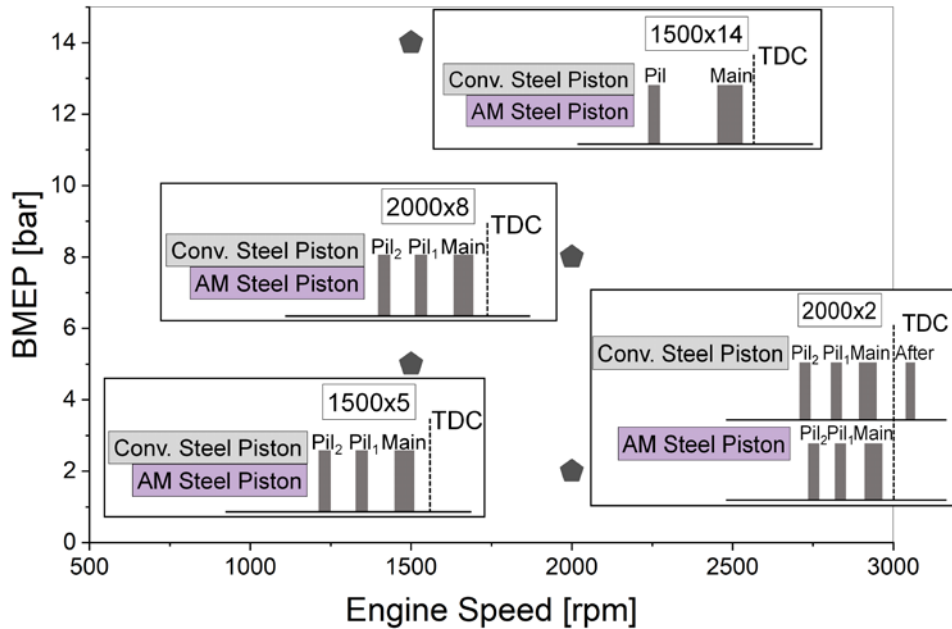
Fig. 12. Schematic of the optimized injection patterns adopted for both pistons.

Once defined the optimal WT and injection patterns, the statistical DoE approach was applied to optimize the emissions further efficiencies and emissions. It is worth underlining that this approach reduces the number of experiments without losing resolution on the response of the system [15]. Indeed, the DoE defines "factors" as the independent parameters that influence the dependent variable defined as "response" of the analyzed process. The DoE approach assesses the single and combined effect of the factors on the engine response quantifying the interaction of the factors and predicting the system response to factor setting and variation [16, 17].

After the preliminary parametric optimization of the injection pattern variables, only two factors, MBF50, and p_{rail}, were needed and have been selected as factors, and for each of them, three levels of variation have been applied. The main calibration parameters are summarized in Table 3, along with the EU 6b NOx target levels. For some sweeps, three levels were not enough to identify the minimum or maximum values. In those cases, the MBF50 sweep was extended toward higher or lower values. These points are evidenced in parentheses in Table 3.

Table 3. Test matrix of the MBF50 and p_{rail} parametric analysis performed for both pistons. Additional MBF50 values considered for the sweeps are in parentheses.

[rpm]x[bar]	NOx [g/kWh]	p_{rail} [bar]	MBF50 [deg aTDC]
2000x2	0.5	400	10-12-14
		500	10-12-14
		600	10-12-14
1500x5	0.6	500	8-10-12
		600	(4-6)-8-10-12
		700	(4-6)-8-10-12
2000x8	0.8	600	8-10-12
		700	(6)-8-10-12
		800	(6)-8-10-12
1500x14	2.0	1200	8-10-12
		1300	(4-6)-8-10-12
		1400	8-10-12

Finally, after selecting the best compromises, among the optimal points (Pareto front), in terms of ISFC and emission trends, in each of those points, EGR sweeps were performed to evaluate the emission trade-offs (NOx-PM, NOx-CO).

5. Results and Discussions

This section is divided into three parts. The first part analyses the effects of the factors on the global engine response to find the optimal engine parameters calibration (through the DoE method) and adopting the AM piston. Next, the optimal points comparison is presented in terms of ISFC, combustion noise, and emissions. Finally, a trade-off emission analysis carried-out through the EGR sweep is shown for all the optimal key-points between the two-piston bowls.

5.1 Design of Experiments

This section provides an overview of the results of the DoE, applied to the new piston configuration, on the global performances. As mentioned before, the aim is defining the optimal engine calibration for improving the spray-piston bowl interaction obtained with this prototype piston. In order to have reliable and consistent results, also considering the novelty of the system tested, each operating point has been repeated at least three times, and the graphed scatter bands represent the normalized standard deviation.

In Fig. 13, the effects of p_{rail} and CA50, at constant engine-out NOx emissions, on the response ISFC, PM, and combustion noise are assessed. For the sake of brevity, 1500x5 and 2000x8 parametrizations are reported. The same approach applied to the other test points provides similar trends. The variation range of the factors is reported in Table 3. The sweeps reported in Fig. 13 show that the AM piston configuration brings to improvements in terms of PM, ISFC, and noise at equal variables set-up. As highlighted in the previous authors' work, the combustion duration tends to be reduced, getting advantages on thermodynamic efficiency with benefits on fuel consumption [8]. The reduction is the consequence of the presence of the radial lips, which help in redirecting the fuel jets towards the centre of the combustion chamber, so reducing the spray momentum losses related to the collisions between adjacent jets and allowing a better air utilization in areas that are richer in oxygen. This is fully consistent with literature results demonstrating significant enhancement of the recirculating flow with more efficient late-cycle mixing and oxidation [18]. In Fig. 13, the soot emissions generally decrease with increasing injection pressure (increase the fuel kinetic energy). For all key-points, the benefits of using the AM piston are evident; the trend confirms a reduction in PM, confirmed also at higher-pressure levels tested, in the range 10-35% and 20-50% for 1500x5 and 2000x8, respectively. A further PM significant reduction can be achieved advancing the combustion phasing (MBF50), and justifying the choice of additional sweeps towards more advanced values. Similar ISFC values are detected at 1500x5, while at 2000x8 and higher-pressure levels slight advantages, and of about 1-2%, are evidenced in comparison to the conventional piston. The differences in terms of combustion noise are negligible except for the more advanced MBF50 settings (4 and 6 deg after top dead centre). According to this approach, the selection of the optimal point is based on achieving the best compromise in terms of PM and combustion noise trade-off.
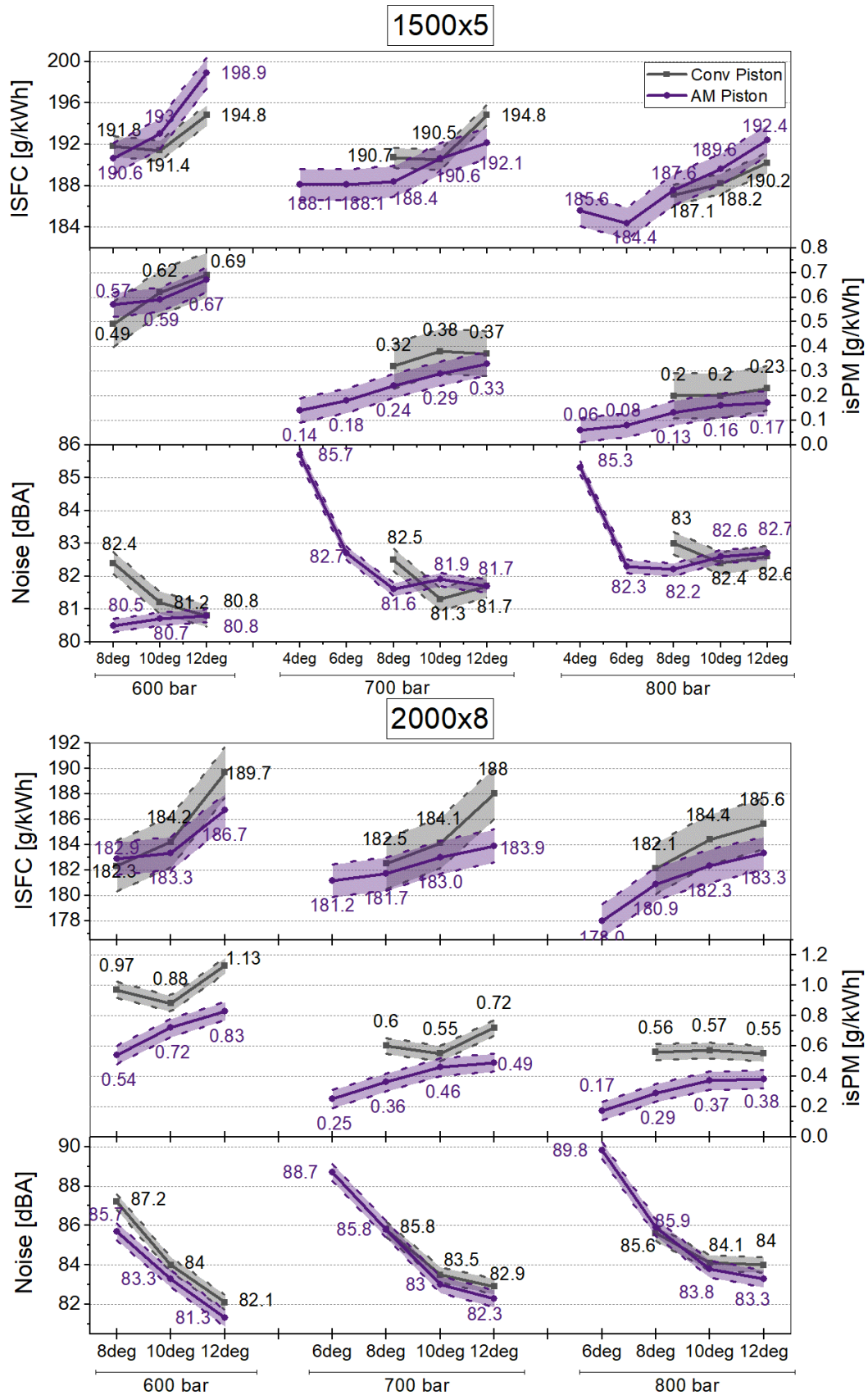
Fig. 13. MBF50 and p_{rail} sensitivities on ISFC, isPM, and noise at 1500x5 and 2000x8 for both pistons and at constant NOx emissions.

5.2 Optimized Engine Calibration

The optimal engine calibration parameters, in terms of p_{rail} and MBF50, for both pistons are reported in Table 4. Indeed, the sweeps have allowed identifying the optimal configuration of the spray-bowl interaction using AM piston.

Table 4. Optimal engine calibration parameters for high efficiencies and low emissions (NOx and PM) for AM piston referenced to the conventional one.

	MBF50$_{AM}$ [deg]	MBF50$_{CONV}$ [deg]	p_{rail_AM} [bar]	p_{rail_CONV} [bar]
2000x2	12	14	500	500
1500x5	6	10	700	600
2000x8	8	8	800	800
1500x14	6	8	1300	1400

Indeed, Fig. 14 reports a cross-section of the combustion chamber across the cylinder axis, including the modelled fuel sprays. The picture is a sketch of the relative spray-piston layout with the piston at TDC. It is representative of the situation near the end of hydraulic injection for operating point 1500x5 when the inner bowl with radial lips contains a large part of the fuel, and the RMZ mechanism can fully exhibit its potential in reducing soot formation during the spray reversion as explained in [8,14]. In this regard, the AM piston shows globally better performance when adopting an advanced MBF50 for all test points, as reported in Table 4, except for 2000x8.
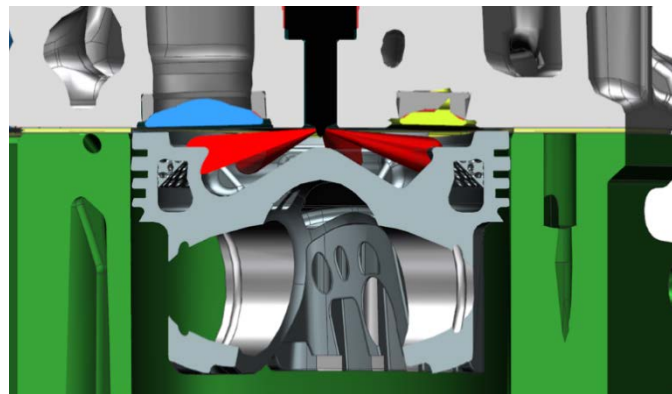
Fig. 14. Combustion chamber layout with the piston at TDC (near the end of hydraulic injection for operating point 1500x5) [8].

To investigate the combined effect of different engine calibration strategy and piston bowl shape, the in-cylinder pressure, HRR, and injection pattern are shown in Fig. 15, at 1500x5. A shorter combustion duration (Fig. 16) and a more pronounced pilot combustion phase are observed when the piston shape is changing from the conventional to the new piston design at the same calibration setup. However, when wall-interactions occur, which normally take place both during and after the fuel injection period, the combustion system geometry plays an important role in how the flow-field develops. According to Fig. 15, there are effects of the piston bowl geometry both during high temperature and late-cycle soot oxidation. The late-cycle reactions include oxidation of local pockets with rich mixtures and soot [20]. These processes are particularly sensitive to the geometry that may change the distribution of soot, remaining fuel, and oxidants. The main effect of the wave-piston geometry is an improved flow in the jet-jet region leading to enhanced mixing late in the cycle [20, 24].

Concerning the AM optimal calibration, an earlier combustion phasing (MBF50) and a similar combustion process are observed to the conventional one; the combustion shape shows a quasi-disappeared pilot combustion phase, which evolves almost entirely into the main combustion phase with similar combustion duration, but with benefits in thermodynamic efficiency (1.3%, Fig. 16). The advanced combustion phasing significantly improves the fuel/air mixing quality promoting the combustion rate due to the combined effects of the radial lips and interferential interactions [23,24].
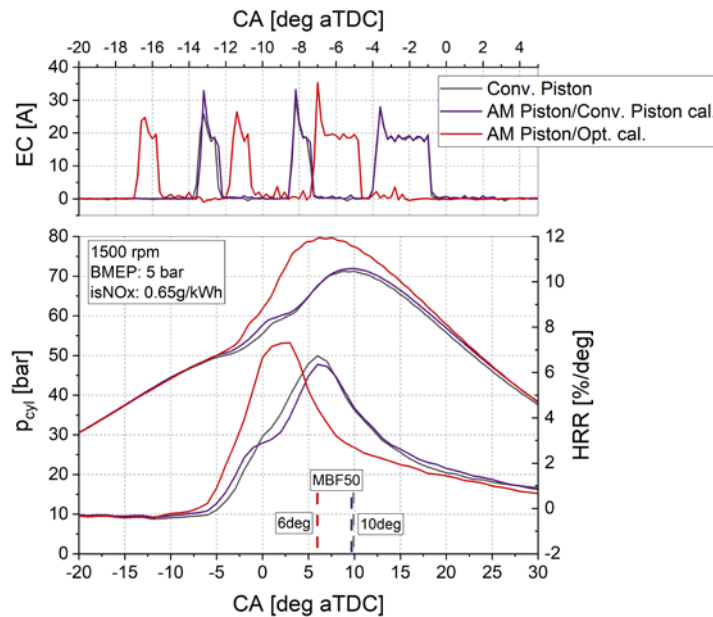
Fig. 15. In-cylinder pressure, injection pattern, and HRR for different engine calibration settings for both pistons, at 1500x5, and constant NOx emissions.
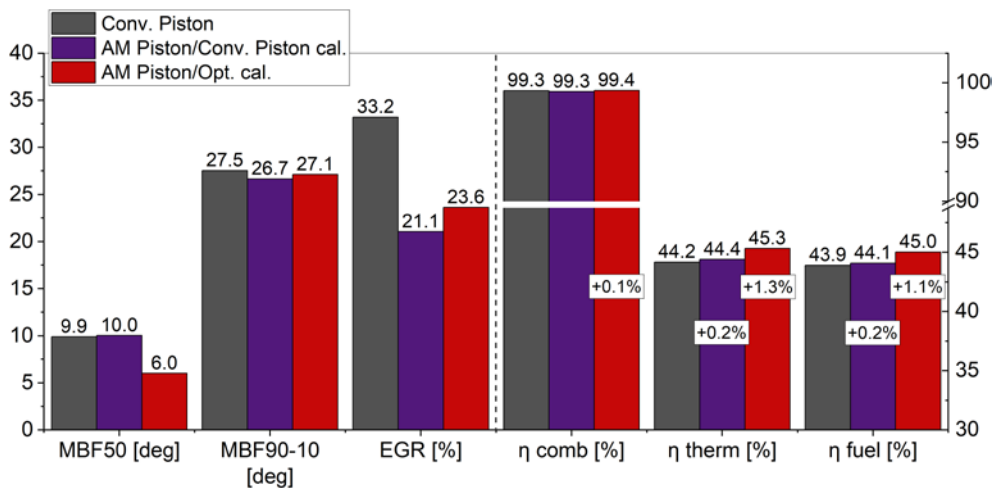
Fig. 16. Comparison of combustion indicators (a) and efficiencies (b) for both pistons and different injection calibration strategies at 1500x5 and constant NOx emissions.

Fig. **16** shows that the innovative piston bowl design and the optimized calibration strategy allow a further reduction in the EGR level of about 10%, at the same engine-out NOx emissions. In general, at 1500x5 (not all points are reported for brevity), the efficiency gain is mainly correlated to the thermodynamic efficiency improvement (shorter combustion duration and closer to the TDC) rather than the mechanical one worsening, taking into account the higher pfp and p_{rail} (Table 4).

Based on the discussion above, Fig. 17 shows the overall brake-quantities, in all the operating points, in terms of emissions and specific fuel consumption, applying the friction correlation deeply discussed in previous authors' studies [10]. This approach makes possible the use of the results obtained by the single-cylinder tests, reflecting the actual conditions of the multi-cylinder engine realistically. The noise values are also reported. The normalized values of the AM piston (optimal engine calibration) are referenced to those of the conventional one, except for the noise for which the absolute values are reported. All the comparisons are at constant Euro-6b engine-out NOx emissions based on an engine-out target allocation study and already reported in Table 3.

The radar plots in Fig. 17 show the bsFC gain in the range 0-2% and depending on the engine operating point, for all tested points. In general, at partial load, no significant changes can be detected for CO emissions, while at higher load, an increase of HC was captured. Even if this increase could

appear pretty significant in percentage, it is also true that at so high loads and warm conditions, the HC absolute values are very low and perfectly within the tolerance range. On the other side, a root-cause of this small degradation can be explained as a typical wall wetting phenomenon very probably due to the visible roughness low quality reached as the first attempt within the AM piston bowl, as shown in Fig. 8. A further improvement in surface quality will be investigated in the next future.

As general considerations, the overall performance of the AM piston is similar to the conventional one. The greatest benefits by using the innovative AM bowl is in terms of PM reduction, as clearly captured by plots. The reduction varies in the range of ~30-80%, confirming significant advantages obtainable by using such innovative bowl combustion concepts.
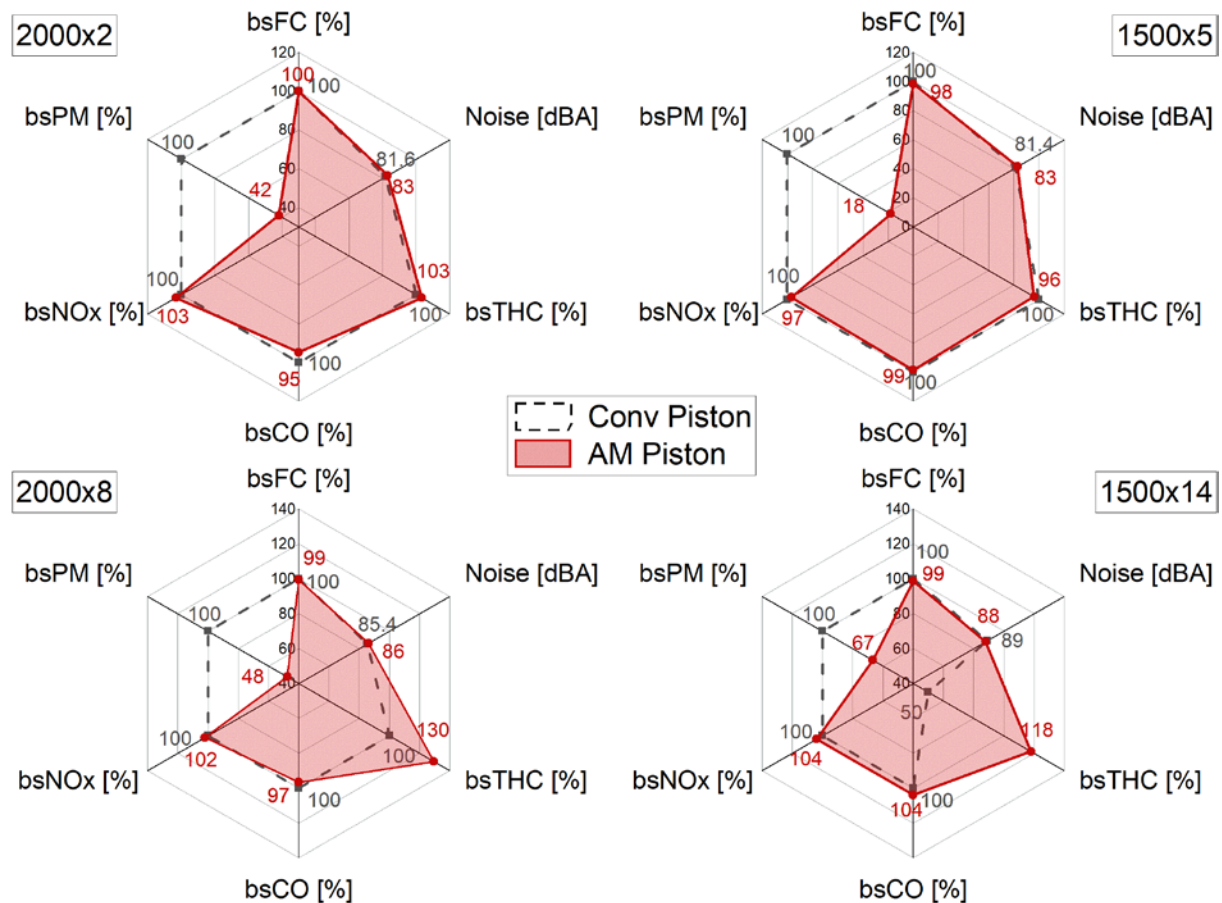
Fig. 17. Comparison of bsFC, combustion noise, and specific brake emissions for both pistons and all operating points.

5.3 EGR Trade-offs

Fig. **18** shows the EGR sweep results for all the key-points for both AM and conventional piston bowl configurations. For both, only the optimal injection pattern and engine parameter calibration were applied and based on the DoE results described above. The trade-offs refer to the specific indicated NOx-PM emissions. The grey area for each plot indicates the typical range of engine-out variation, which is expected stretching targets from EU6b to EU6d and beyond, considering that the major improvements will come from the medium-high load area, consistently with [25].

Again, EGR sweeps show how the benefits in terms of PM of the AM piston bowl are kept moving along the NOx reduction path. This is generally valid for all the tested points. Notwithstanding the general low PM levels for the test point 2000x2, the AM piston bowl is very effective, presenting a practically flat PM trend and practically not sensitive to NOx variation. At high load (1500x14), PM benefits for stretched calibrations appear less evident but still valuable to properly play in favor of a lower soot loading in the exhaust line. In general, at low-medium loads and stretched engine-out targets, the advantages by using the AM piston bowl still remain consistently in the 50-60% range.
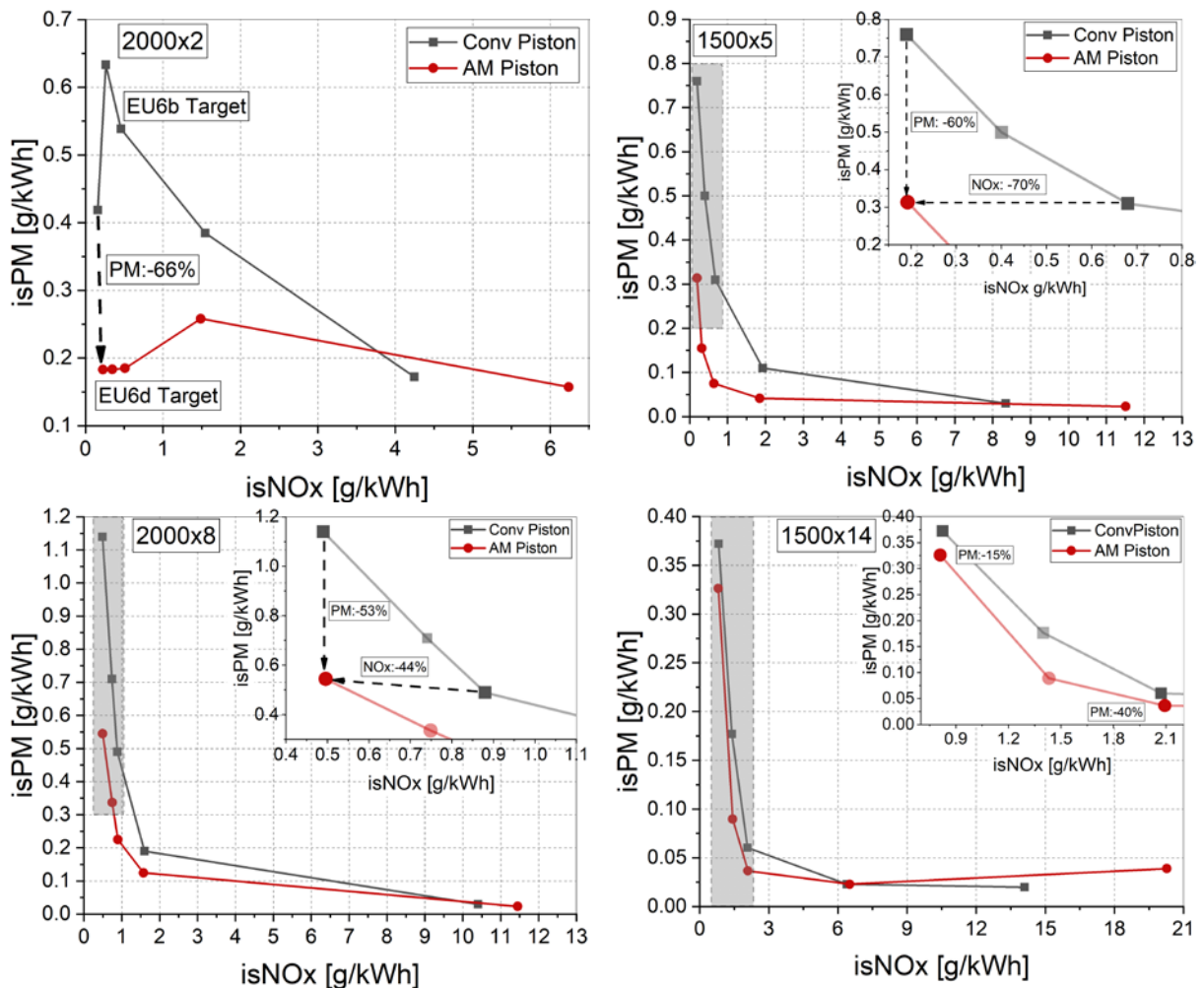
Fig. 18. Comparison of NOx-PM trade-offs for both pistons and optimal engine parameters settings. The NOx and PM reduction margins are highlighted in the high EGR and sooting points.

6. Conclusions

The paper reports the results of a project aimed at exploiting the potential of innovative diesel combustion systems by modifying the combustion chamber. An innovative highly-reentrant sharp-stepped profile featuring radial-lips has been studied on a specific developed single-cylinder engine test rig.
The prototype AM piston has been made out of an additive powder bed-based technique, which is the so-called SLM, and the approach is unique in its kind.

Sensitivity studies have been conducted to define the optimal injection protrusion varying the WT. The results demonstrated the full potential of improved fuel stratification and spray separation enabled by the radial mixing zone concept. Indeed, they confirmed an excellent reduction of engine-out smoke emissions with no deterioration on indicated efficiency when optimized injection patterns are applied.

The combination of innovative bowl piston design and advanced injection patterns brought to significant smoke improvements at partial load conditions. Indeed, the PM gain was in the range of 40-75% at constant NOx. Very low NOX targets have been achieved by stressing the NOx control through high EGR levels.

The overall results on emissions and engine performance concerning the potential of applying innovative combustion chamber geometries in combination with advanced injection patterns provide new and valuable information to define the development guidelines of future diesel engines.
In this regard, future activities will be conducted to further investigate on the spray indexing and combustion radial lips configurations, in order to balance excellent PM-NOx trade-off at partial load, and high performance at full load conditions.

Acknowledgments

References

1. "2020-2021 Automobile Industry Pocket Guide", European Automobile Manufacturers Association (ACEA), June 2019.

2. Baldino C., Tietge U., Muncrief R., Bernard Y., and Mock P., "Road Tested: Comparative Overview of Real-World Versus Type-Approval NOx and CO2 Emissions from Diesel Cars in Europe," ICCT White Paper, accessed September 2017, https://www.theicct.org/sites/default/files/publications/ICCT_RoadTested_201709.pdf.

3. Kufferath, A., Krüger, M., Naber, D., Mailänder, E., and Maier, R., "The Path to a Negligible NO$_2$ Immission Contribution from the Diesel Powertrain," Vienna Motoren Symposium, 2018.

4. Avolio, G., Brück, R., Grimm, J., Maiwald, O., Rösel, G., Zhang, H., "Super Clean Electrified Diesel: Towards Real NOx Emissions below 35 Mg/Km," in 27th Aachen Kolloquium Automobile and Engine Technology, 2018.

5. Steinparzer F., Nefischer P., Stütz W., Hiemesch D. and Kaufmann M., "The New BMW Six-Cylinder Top Engine With Innovative Turbocharging Concept", 37th Vienna Motoren Symposium, 2016.

6. Di Blasio, G., Beatrice, C., Ianniello, R., Pesce, F. et al., "Balancing Hydraulic Flow and Fuel Injection Parameters for Low-Emission and High-Efficiency Automotive Diesel Engines," SAE Technical Paper 2019-24-0111, 2019, https://doi.org/10.4271/2019-24-0111.

7. Di Blasio, G., Beatrice, C., Belgiorno, G., Pesce, F. et al., "Functional Requirements to Exceed the 100 kW/l Milestone for High Power Density Automotive Diesel Engines," SAE Int. J. Engines 10(5):2017, doi:10.4271/2017-24-0072. https://doi.org/10.4271/2017-24-0072

8. Belgiorno, G., Boscolo, A., Dileo, G., Numidi, F., Pesce, F. C., Vassallo, A., ... & Di Blasio, G. (2020). Experimental Study of Additive-Manufacturing-Enabled Innovative Diesel Combustion Bowl Features for Achieving Ultra-low Emissions and High Efficiency (No. 2020-37-0003). SAE Technical Paper, https://doi.org/10.4271/2020-37-0003.

9. Verdino, V., Vassallo, A., et al., "The New General Motors 3.0l Duramax Diesel Engine: a Technology Milestone Combining State-of-art Efficiency, Emissions, Performance and Refinement", Proceeding of Diesel Powertrains 3.0, 2019.

10. Beatrice, C., Di Blasio, G., Pesce, F., Vassallo, A. et al., "Key Fuel Injection System Features for Efficiency Improvement in Future Diesel Passenger Cars," SAE Int. J. Adv. & Curr. Prac. in Mobility 1(3):1084-1099, 2019, https://doi.org/10.4271/2019-01-0547

11. Tanov, S., Pachano, L., Andersson, Ö., Wang, Z. et al., "Influence of Spatial and Temporal Distribution of Turbulent Kinetic Energy on Heat Transfer Coefficient in a Light Duty CI Engine Operating with Partially Premixed Combustion," Appl. Therm. Eng. 129:31-40, 2018, doi:10.1016/j.applthermaleng.2017.10.006.

12. Garcia-Oliver, J.M., Garcia, A., Gil, A., and Pachano, L., "Study of Air Flow Interaction with Pilot Injections in a Diesel Engine by Means of PIV Measurements," SAE Int. J. Engines 10(3):740-751, 2017, doi:10.4271/2017-01-0617.

13. Miles, P.C., Hildingsson, L., and Hultqvist, A., "The Influence of Fuel Injection and Heat Release on Bulk Flow Structures in a Direct-Injection, Swirl-Supported Diesel Engine," Exp. Fluids 43(2-3):273-283, 2007, doi:10.1007/s00348-007-0281-7.

14. Eismark, J., Andersson, M., Christensen, M., Karlsson, A. et al., "Role of Piston Bowl Shape to Enhance Late-Cycle Soot Oxidation in Low-Swirl Diesel Combustion," SAE Int. J. Engines 12(3):233-249, 2019, https://doi.org/10.4271/03-12-03-0017.

15. Montgomery, D.C. 'Design and Analysis of Experiments' (8th Edition). John Wiley and sons, 2008.

16. Knafl, A., Hagena, J. R., Filipi, Z., & Assanis, D. N. (2005).Dual-use engine calibration (No. 2005-01-1549). SAE Technical Paper.

17. Brooks, T., Lumsden, G., and Blaxill, H., "Improving Base Engine Calibrations for Diesel Vehicles Through the Use of DoE and Optimization Techniques," SAE Technical Paper 2005-01-3833, 2005, doi:10.4271/2005-01-3833.

18. Y. Chen, X. Li, X. Li, W. Zhao, e F. Liu, «The wall-flow-guided and interferential interactions of the lateral swirl combustion system for improving the fuel/air mixing and combustion performance in DI diesel engines», *Energy*, vol. 166, pagg. 690–700, 2019.

19. Dolan, R., Budde, R., Schramm, C., and Rezaei, R., "3D Printed Piston for Heavy-Duty Diesel Engines", 2018 NDIA GROUND VEHICLE SYSTEMS ENGINEERING AND TECHNOLOGY SYMPOSIUM POWER & MOBILITY (P&M) TECHNICAL SESSION, August 7-9, 2018 - NOVI, MICHIGAN, https://events.esd.org/wp-content/uploads/2018/07/3D-Printed-Piston-for-Heavy-Duty-Diesel-Engines.pdf

20. Millo, F., Piano, A., Bianco, A., Pesce, F., and Vassallo, A., "Numerical Assessment of an Innovative Piston Bowl Concept in a Light-duty Diesel Engine", to be presented at SIA Powertrain 2020, Rouen, 2020

21. Di Blasio, G., A. Vassallo, F. C. Pesce, C. Beatrice, G. Belgiorno, and G. Avolio. 2019. "The Key Role of Advanced, Flexible Fuel Injection Systems to Match the Future CO2 Targets in an Ultra-Light Mid-Size Diesel Engine." SAE International Journal of Engines 12 (2). doi:10.4271/03-12-02-0010

22. Mendez, S. and Thirouard, B., "Using Multiple Injection Strategies in Diesel Combustion: Potential to Improve Emissions, Noise and Fuel Economy Trade-Off in Low CR Engines," SAE Int. J. Fuels Lubr. 1(1):662-674, 2009, https://doi.org/10.4271/2008-01-1329.

23. O'Connor, J., & Musculus, M., Effects of exhaust gas recirculation and load on soot in a heavy-duty optical diesel engine with close-coupled post injections for high-efficiency combustion phasing. International Journal of Engine Research, 2014, 15(4), 421–443.

24. J. Eismark, M. Christensen, M. Andersson, A. Karlsson, I. Denbratt, Role of fuel properties and piston shape in influencing soot oxidation in heavy-duty low swirl diesel engine combustion, Fuel 254 (2019) 115568, https://doi.org/10.1016/j.fuel.2019.05.151.

25. Recker, P., Gheorghe, M., Menne, C., Xenakis, L., Lilley, A., and Maugham, R., "Investigations for the Extension of the LP-EGR Operation Area at the Background of RDE", 25th Aachen Colloquium Automobile and Engine Technology 2016.

Assessment and Design of Real World Driving Cycles Targeted to the Calibration of Vehicles with Electrified Powertrain

S. Doulgeris[1], Z. Toumasatos[1], M.V. Prati[2], C. Beatrice[2] and Z. Samaras[1]

[1]Laboratory of Applied Thermodynamics, Department of Mechanical Engineering, Aristotle University of Thessaloniki, 54124, Greece.

E-mail: lat@eng.auth.gr, zisis@auth.gr
Telephone: +(30) 2310 996014

[2]Istituto Motori CNR, Viale Marconi, 4, 80125 Napoli, Italy

E-mail: m.v.prati@im.cnr.it, c.beatrice@im.cnr.it
Telephone: +(39) 0817177211

Abstract. Vehicles' powertrain electrification is one of the key measures adopted by manufacturers in order to develop low emissions vehicles and reduce the CO_2 emissions from passenger cars. Increased complexity of electrified powertrains increases the demand of cost-effective tools that can be used during the design of such powertrain architectures. The aim of the study presented in the current paper, is the design of a series of real-world velocity profiles that can be used for the virtual platform. To that aim a combined experimental and simulation approach is followed in order to derive generic real-world cycles used for the evaluation of the overall energy efficiency of electrified powertrains. The outcome of the study is specific driving cycles and a methodology for real world data analysis and evaluation, along with the assessment of the impact of different operational parameters to the total electrified powertrain.

1. Introduction

1.1 Background and Objectives

Vehicles' powertrain electrification is one of the key measures adopted by manufacturers in order to develop low emissions vehicles and reduce the CO_2 emissions from passenger cars. To that aim, hybrid (HV) and plug-in hybrid vehicles (PHEV) are powertrain configurations that appear to have the lowest CO_2 emissions performance compared to conventional vehicles, Fig. 1. Furthermore, HEVs and PHEVs should be representing the most important market in Europe in the next decades (Harrison and Thiel, 2017).

Although HEVs or PHEVs are based on existing vehicle architectures, the integration of the electric components and control modules increases the complexity of the powertrain remarkably and therefore the need of cost-effective tools that can be used during the design of such vehicles. To that aim vehicle simulation platforms could be used during the development and calibration of electrified powertrains. Given that the main focus currently is on the real world testing, due to the new European regulation, several operating conditions are imposed by on-road testing. As a result it is essential to identify specific driving mission profiles that address to the key aspects electrified powertrains and that can be used for vehicle calibration, reducing the development time and cost. To that aim the current study presents a combined experimental and simulation approach for the identification of such representative real-world cycles.

The current paper summarizes the activities conducted, in relation to the identification of representative real-world cycles. The main objective of the work described in this paper is the selection of representative real-world mission profiles that will be applied during the calibration of vehicles equipped with electrified powertrains. The target of the study is to propose a methodology to derive generic driving cycles that will be used for the evaluation of the electrified powertrains, in terms of the overall energy efficiency.
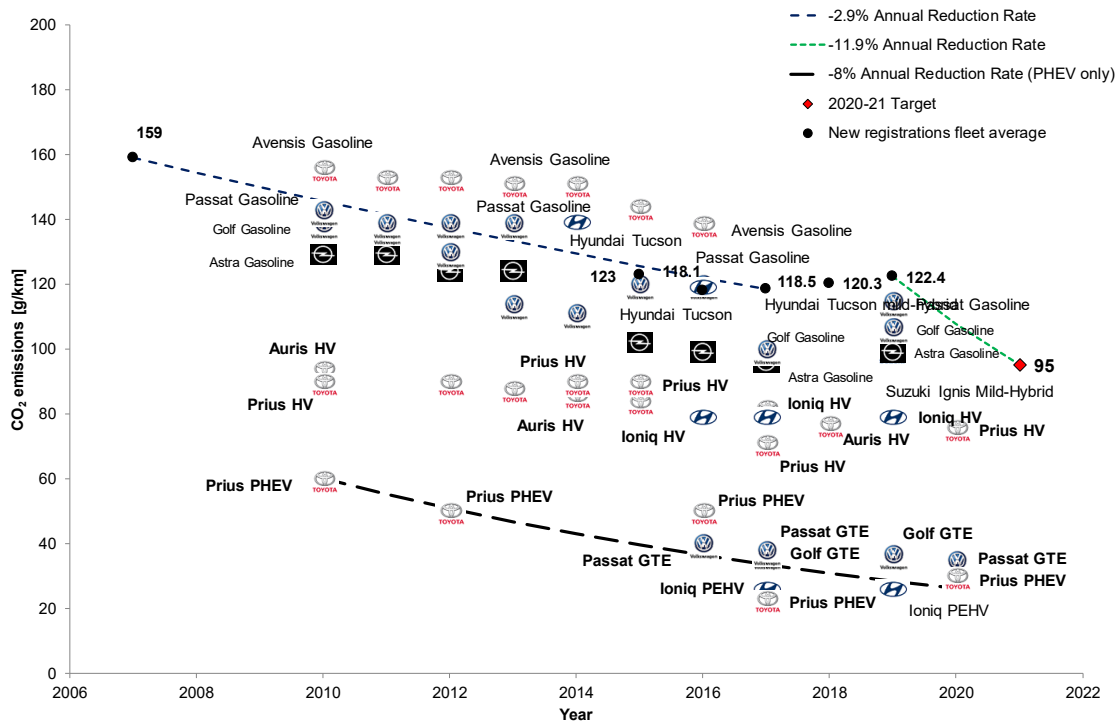
Fig. 1. CO_2 emissions evolution of passenger cars and annual reduction rate. Source: EEA (European Environmental Database), Monitoring of CO_2 emissions from passenger cars – Regulation (EC) No 443/2009

The definition of the representative real world mission profiles aims to investigate which driving conditions put a particular stress on the different components of the electrified powertrains. The main guideline is to propose a series of real world cycles that will cover the evaluation of the aspects and operational parameters (such as electric range, cold start, component limits, energy/fuel consumption and pollutant emission performance) of vehicles with electrified powertrains.

Main focus is to propose cycles that are considered as generic therefore it is aimed to be applicable to all the different hybrid and plug-in hybrid vehicles. Additionally they are considered as representative since they are derived from a series of actual real world test cases that include different driving conditions. Thus, the proposed velocity profiles, as derived from the analysis, can be used in different stages of the powertrain design, like for example during the component size selection to the system calibration and serve as the basis for virtual/simulation based development or assessment of electrified vehicles.

2. Methodology

For the purposes of the study, the methodology followed is based on a combined experimental and simulation approach. Based on the experience of previous experimental campaigns the test cases and the test protocols were designed according to the needs of the study. The tests were performed in order to identify the level of impact of the driving conditions on the operation of vehicles with electrified powertrains. Target was to reveal the critical parameters of such powertrains that need to be given attention. In addition to the experimental campaign, the investigation of the representative real-world velocity profiles is enhanced with simulation activities. Vehicle simulation models are calibrated on the basis of the experimental data and used to evaluate the effect of the variation of the operational parameters that were not covered during the experimental campaign. The use of the vehicle simulation models served to enhance the experimental activities. Thus, additional cases of real world mission profiles that were not covered or were not possible to replicable with experiments, as an effort to cover and include in the cycle evaluation a wider range of possible operating and driving conditions. The activities described in this paper are mainly focused on the energy management, power and fuel consumption of plug-in hybrid vehicles, although pollutant emissions performance was also evaluated during the experimental campaign and data post-processing.

2.1 Experimental campaign

The first part of the methodology was addressed to an experimental campaign with PHEVs (Plug-in hybrid vehicles) was performed. The testing sequence included both laboratory (chassis dynamometer), and on-road tests. The latest were realized under different driving mission profiles, i.e. driving cycles or real-world routes, respectively.

The experimental campaign was conducted with three D-segment plug-in hybrid vehicles with the two of them being different cars of the same make and model, main specs of which are shown in Table 1. The two vehicle models selected for the experimental campaign have different powertrain architectures as shown in Fig. 2. Vehicles 1 and 2 have a power split and Vehicle 3 a parallel hybrid configuration. Both vehicles have similar energy management strategy. The high voltage battery with the 8.8-8.9 kWh nominal capacity provides enough electric energy for a pure electric range of 30-50 km

Table 1. Specifications of the vehicles used during the experimental campaign

Vehicle	Vehicle 1 & 2	Vehicle 3
Engine		
Type	4-cylinder, Atkinson cycle engine	4-cylinder, Atkinson cycle engine
Fuel/Injection	Gasoline/PFI	Gasoline/DI
Displacement [cm^3]	1798	1580
Max. power [kW] @ engine speed [rpm]	72@5200	72@5700
Max. torque [Nm] @ engine speed [rpm]	142@3600	147@4000
Emissions standard	Euro 6b	Euro 6b
Powertrain		
Type	Power split	Parallel
Transmission		
Type	e-CVT	AT 6-speed Dual Clutch
Electric motor		
Max. power [kW]	53	44.5
Max. torque [Nm]	163	169
Electric generator		
Max. power [kW]	37	-
Max. torque [Nm]	35	-
High voltage Battery		
Capacity [kWh]	8.8	8.9
Nominal voltage [V]	352	360
Vehicle weight [kg]	*1530*	*1606*
Vehicle payload [%]	*55(V$_1$) & 78(V$_2$)*	*65*

Vehicle 1 & 2   **Vehicle 3**

ICE: Internal Combustion Engine   HSG: Hybrid Starter Generator
EM: Electric Motor   DCT: Dual Clutch
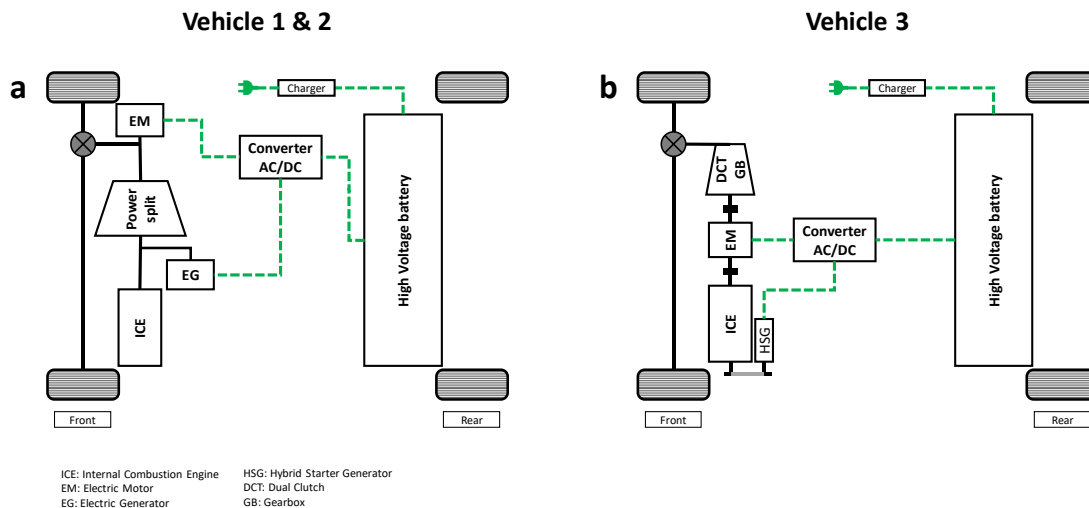EG: Electric Generator   GB: Gearbox

Fig. 2. Vehicles' powertrain architecture layout schematic, (a) Vehicles 1 & 2, (b) Vehicle 3

(charge depleting mode) and the electric motor is the main propulsion device. After the depletion of the battery vehicle operation enters to charge sustain mode, where a synergy between the thermal engine and the electric motor is imposed by the energy management strategy. For the vehicle with the power split configuration during charge sustain mode the vehicle is propelled by the internal combustion engine (ICE) and the electric motor, while simultaneously the generator connected to the ICE is generating electric power in order to ensure optimal efficiency of the ICE. For the vehicle with the parallel configuration, during charge sustain mode the ICE is propelling the vehicle while the electric machine is either used as a motor (assisting the ICE) or generator so that optimal operating point of ICE is achieved.

2.1.1 On-road testing

On-road testing was conducted on public roads in the region of Thessaloniki Greece and Napoli Italy, following pre-defined routes. The routes followed were designed in order to include urban, rural and motorway sections the distance of which comply with Real Driving Emissions (RDE) regulation European Commission (2017a) and (2017b). The RDE test is divided to three main sections, the pre-test, the main test and the post test. During the pre-test, calibration of all measurement devices is performed, as required prior to the main test. For the main test, according to the regulation vehicles' pollutant emissions performance (CO, NO_x and PN) is certified under on-road tests following a route that strictly follows urban, rural and motorway sequence, and complies to certain limits regarding driving dynamics and ambient conditions. Finally, to ensure validity of the measurement, a series of calibration checks are performed during post test procedure. The routes followed along with the velocity profile are illustrated in Fig. 3.
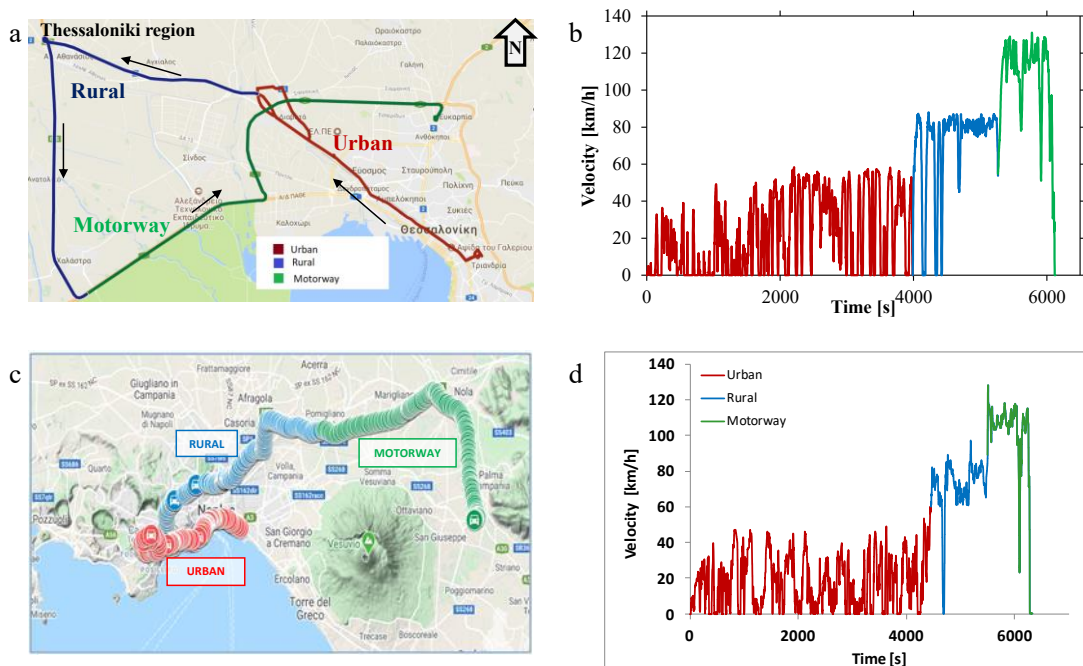

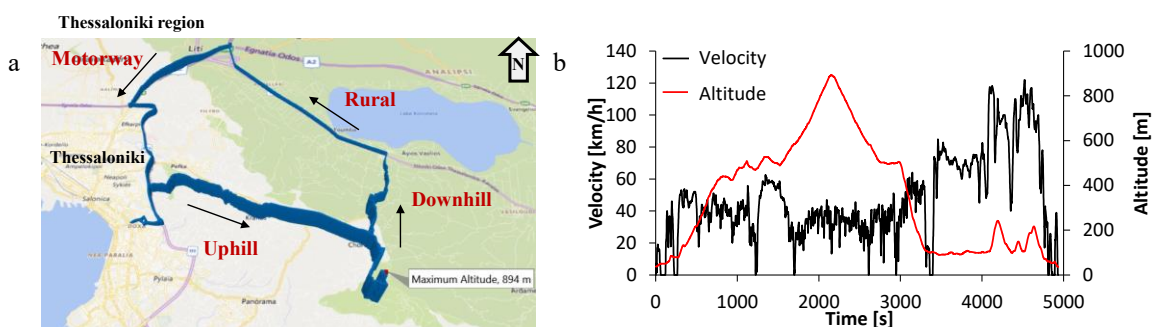**Fig. 3.** RDE routes followed during the experimental campaign

Fig. 4. Route that includes uphill and downhill driving

317

In addition to the RDE compliant routes, during the experimental campaign, a different route that includes uphill and downhill driving (road grade variation) was also followed. Velocity and altitude profile of this route are illustrated in Fig. 4.

The vehicles were tested at the routes presented above with different driving conditions and different levels of initial battery state of charge (SOC) or vehicle modes. Table 2 presents the test conducted during the experimental campaign with each vehicle. Each test is named as Vx – Ty, where x and y indicates the vehicle (V) number (see Table 1) and the test (T) sequential number respectively.

During the experimental campaign, a test was considered as a cold start when it started after vehicle soaking at 20-25°C (overnight or minimum 6 hours) and with initial engine coolant and catalyst temperature same as the soaking temperature, whereas in all other cases the test was considered as hot start. Additionally normal and aggressive driving is identified via the 95th percentile of the product of vehicle speed (V) per positive acceleration (a) (V*a 95th), for urban, rural and motorway driving compared to the limits defined by the RDE regulation (EC 2017a, 2017b). Thus normal driving is considered when V*a 95th for all parts (urban, rural and motorway) is below the RDE limits, and aggressive driving style is considered when V*a 95th for all parts is close or above the limits. Finally EV (electric vehicle) mode that appears in Table 2, is the operation that when selected, the vehicle will move purely electric (charge depleting mode) until battery reaches a low threshold and thermal engine turns on propelling the vehicle (charge sustain mode).

Table 2. Tests conducted during experimental campaign

	Mission profile	Altitude profile	Driving style	ICE start conditions	Battery initial SOC	Ambient temperature °C	EV mode
Vehicle 1							
V₁-T₁	RDE compliant	Flat road	Normal	Cold start	82.8%	30.8	ON
V₁-T₂	RDE compliant	Flat road	Aggressive	Cold start	81.9%	34.5	ON
V₁-T₃	RDE compliant	Flat road	Normal	Hot start	13.7%	37.1	ON
V₁-T₄	RDE non-compliant	Uphill – downhill	Normal	Hot start	15.7%	32.3	ON
V₁-T₅	RDE non-compliant	Uphill – downhill	Eco – driving	Cold start	82.4%	21	ON
V₁-T₆	RDE non-compliant	Uphill – downhill	Normal	Cold start	82.8%	30.7	ON
Vehicle 2							
V₂-T₁	RDE compliant	Flat road	Normal	Cold start	81.6-81.8%	30	OFF
V₂-T₂	RDE compliant	Flat road	Normal	Cold start	81.80%	31	ON
V₂-T₃	RDE compliant	Flat road	Normal	Cold start	82-82.6%	21	OFF
V₂-T₄	RDE compliant	Flat road	Normal	Cold start	80-82%	20	ON
V₂-T₅	RDE compliant	Flat road	Normal	Cold start	15.6-16%	21	ON
V₂-T₆	RDE non-compliant	Uphill – downhill	Normal	Cold start	60-81.6%	20	ON
Vehicle 3							
V₃-T₁	RDE compliant	Flat road	Smooth	Cold start	92%	22.6	ON
V₃-T₂	RDE compliant	Flat road	Smooth	Cold start	92.9%	26.7	ON
V₃-T₃	RDE compliant (reverse order)	Flat road (uphill during motorway)	Smooth	Cold start	93.7%	25.2	ON
V₃-T₄	RDE non-compliant	Uphill – downhill	Smooth	Cold start	94.1%	17.2	ON
V₃-T₅	RDE compliant	Flat road	Aggressive	Cold start	19.2%	25.1	ON

2.1.2 Measurement equipment

Real world measurements were conducted with a Portable Emissions Measurement System (PEMS) that was installed on the tested vehicles as illustrated in Fig. 5. The exhaust mass flow was measured through a mass flow meter (EFM) connected to the vehicle tailpipe. Exhaust sample was taken from the flow tube to measure tailpipe CO_2, CO and NO_x concentrations and PN emissions. Additionally, a GPS device was installed on the vehicle, connected to the PEMS device to record vehicle position (longitude and latitude), altitude and, as an indirect measurement, vehicle velocity. Vehicle operating parameters provided by the On-board Diagnostics (OBD) port were also recorded with the PEMS device.

Fig. 5. Installation of PEMS on the vehicles used for the experimental campaign
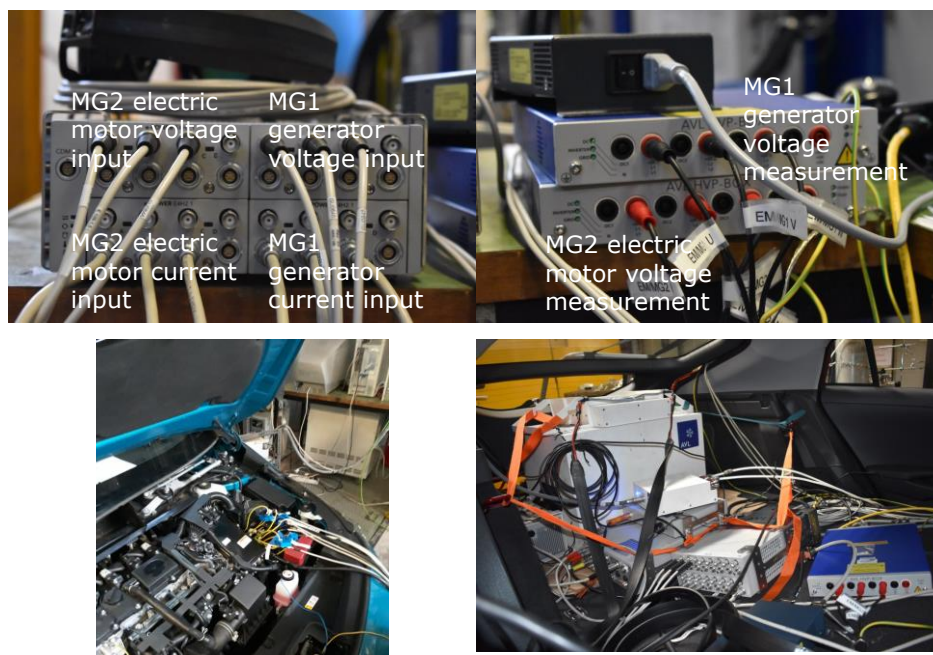
Fig. 6. Power analyser and installation on the vehicles

For the purposes of the study, during the experimental campaign, special attention was given to the measurement of the power flow within the different components of the powertrain. For that reason, a power analyser, AVL X-ion, was installed on the vehicles (Vehicle 1 was tested with the power analyser only in the laboratory, whereas Vehicle 3 was measured with the power analyser during both RDE and dyno tests). This device allows measuring the current (using current clamps) and voltage from the electric motors and the high voltage battery. The data acquisition software is calculating on real time the power of each different device, thus sampling rate is in the order of magnitude of kHz. The power analyser and the installation on the vehicles are presented in Fig. 6.

The instrumentation described above constitutes the complete experimental set up applied during the test campaign.

Table 3 summarizes the signals recorded during the tests. The data obtained create a complete data set that forms the basis for the evaluation of operation of these vehicles.

Table 3. Signals and data recorded during the tests

| Device	Signal/Data recorded
GPS	Altitude
	Route followed (longitude & Latitude)
	Velocity
PEMS	Emissions species CO_2, CO, NO_x & PN
	Ambient conditions (temperature, pressure & humidity)
	Exhaust mass flow
OBD recording device	Vehicle velocity
	Engine speed
	Engine coolant temperature
	Intake mass flow
	Intake air temperature & pressure
	Catalyst temperature
	Equivalence ratio
	High voltage battery state of charge
Power analyzer	Electric machines' current (3 phases)
	Electric machines' voltage (3 phases)
	Electric machines' power (calculated)
	Electric machines' speed (calculated)

2.2 Simulation approach

Parallel to the experimental campaign, a vehicle simulation model for the tested vehicle is developed and calibrated based on the test results. In order to implement the energy management strategy of the vehicles, user defined functions were developed, and a rule based supervisory control approach was applied. For the development of the simulation models the AVL Cruise software was used. As an example, accuracy of the model for vehicle 3 is presented in **Fig. 7**a. Simulated fuel consumption is very close to measured, while electric energy consumption shows a deviation of 0.8 kWh. Additionally, the instantaneous performance of the model is illustrated in **Fig. 7**b.
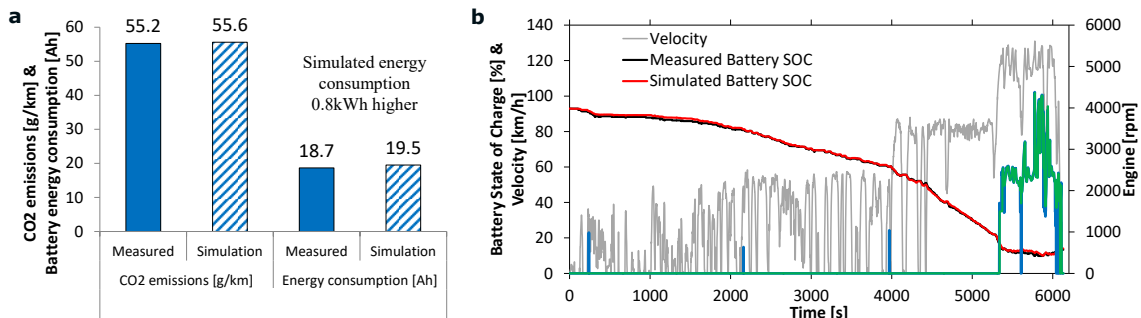
Fig. 7. Comparison between measurement and simulation for vehicle 3 over an RDE compliant route

Aim of the development of the simulation model was to conduct virtual tests in order to investigate the behaviour of the simulated vehicle under these cases that were not covered from the experimental campaign. For instance all RDE tests of Vehicle 3 conducted with fully charged battery were

performed with a normal/smooth driving style, whereas an aggressive driving style was selected for the RDE test with low initial battery SOC. As a result the simulation model was used to evaluate CO_2 emissions performance and electric range of the vehicle under an RDE route with aggressive driving style. Furthermore virtual tests with rural, urban and motorway sequence and with two levels of battery SOC (full and empty) were performed, since during the experimental campaign only regular RDE and RDE with reverse order (motorway, rural and urban) tests, with fully charged battery were conducted.

3. Results and discussion

The analysis of the experimental data obtained from the experimental campaign aim to reveal the points of interest from each different test case. Post processing of the test results indicates the correlation between driving conditions and operating parameters of the vehicles tested. Furthermore, virtual tests conducted with the developed simulation models to evaluate velocity profiles and vehicles operation for not tested cases, with a focus on energy management and fuel consumption.

3.1 Experimental data analysis and results

The analysis of the experimental set up and the evaluation were conducted according to specific guiding principles and parameters, listed below:

- Electric range for pure electric mode
- Energy and fuel consumption
- Energy management strategy and usage of different energy sources (fuel or battery)
- After treatment system operation and pollutant emissions performance
- Drivability or response to aggressive driving
- Powertrain components' limits

Target of the post processing of the results is to identify which cycle of those realized during the experimental campaign will be the most suitable to address the evaluation of the parameters mentioned above.

Starting the analysis from the RDE compliant trips that started with high initial battery SOC, it is easy to distinguish the two basic operations of the vehicles, charge depleting and charge sustain mode. From these tests it is possible to extract the real-world electric range of the tested vehicles. In Fig. 8 tests from Vehicle 1 and 3 starting with high initial SOC are presented. As indicated in the figure, the electric range of vehicle 1 is almost 34 km and includes mostly urban driving, whereas for vehicle 3 the electric range is approximately 51 km including urban and rural driving. From the evaluation of at all the tests performed with fully charged battery, it is concluded that the route followed, and the driving style influence the electric range. Specifically, for vehicle 1 electric range at tests V_1-T_1 and V_1-T_2 that were performed with the same driving style under the same route, electric range is in the order of magnitude of 30 km. For vehicle 2 at tests V_2-T_2 and V_2-T_3, that were conducted under the same route, electric range is for all cases electric range is in the order of magnitude of 45 km. The difference in electric range observed between vehicle 1 and 2 is due to different driving dynamics. Similarly, for vehicle 3 electric range under the same route (tests V_3-T_1 and V_3-T_2) is 51 km, whereas for test V_3-T_4 electric range is reduced to 21 km due to high power demand during uphill driving. Thus, the main factors affecting the electric range are the power demand and the driving style. For all cases examined in this study as electric range is defined the distance until battery reaches the low SOC threshold and internal combustion engine is selected as the primary source of propulsive power. Additionally, from the tests started with fully charged battery, real world electric energy consumption is evaluated. The real word electric energy consumed calculated during full electric mode is between 130-200 Wh/km. Outcome of this evaluation is that an RDE trip which is intended to be used for the evaluation of the electric range needs to have total distance higher than the expected electric range (for modern PHEVs higher than 60 km).

Furthermore, battery usage during each phase of RDE compliant tests can be evaluated. For example, most of battery energy is consumed during urban driving, approximately 30-50% of the total energy. During rural phase 20-40% of the battery is consumed depending on the driving condition, whereas during motorway the thermal engine is always enabled. In contrast, for the reverse RDE test the battery is fully depleted during motorway part and the ICE is operating partly during rural and urban part. Given that all electric range for reverse RDE was reduced compared to the regular RDE and that the strategy of these vehicles impose a charge depleting mode when battery is fully charge, it is concluded that sequence of urban, rural and motorway section and therefore power demand, affect

the electric power consumption (or battery depletion rate) and thus the electric range. Although for the reverse RDE CO_2 emissions are comparable to those at regular RDE, using the battery during motorway is not considered beneficial because this leads to extensive usage of the ICE in urban areas (in case of motorway, rural, urban sequence).
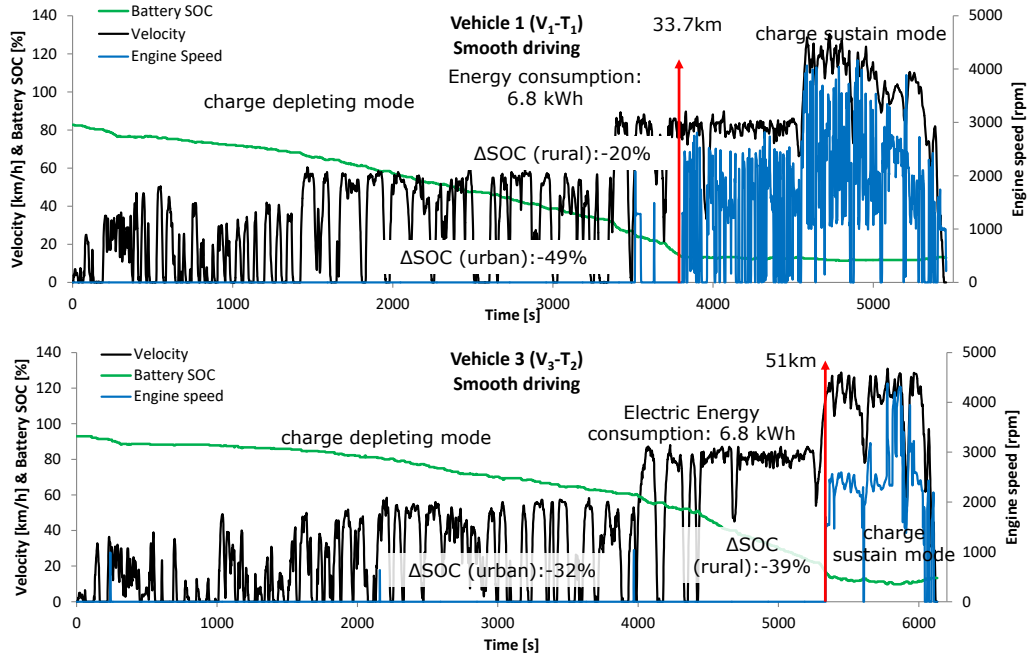
Fig. 8. Experimental results for RDE compliant tests with fully charged battery at the start, V_1-T_1 (upper) and V_3-T_2 (bottom)
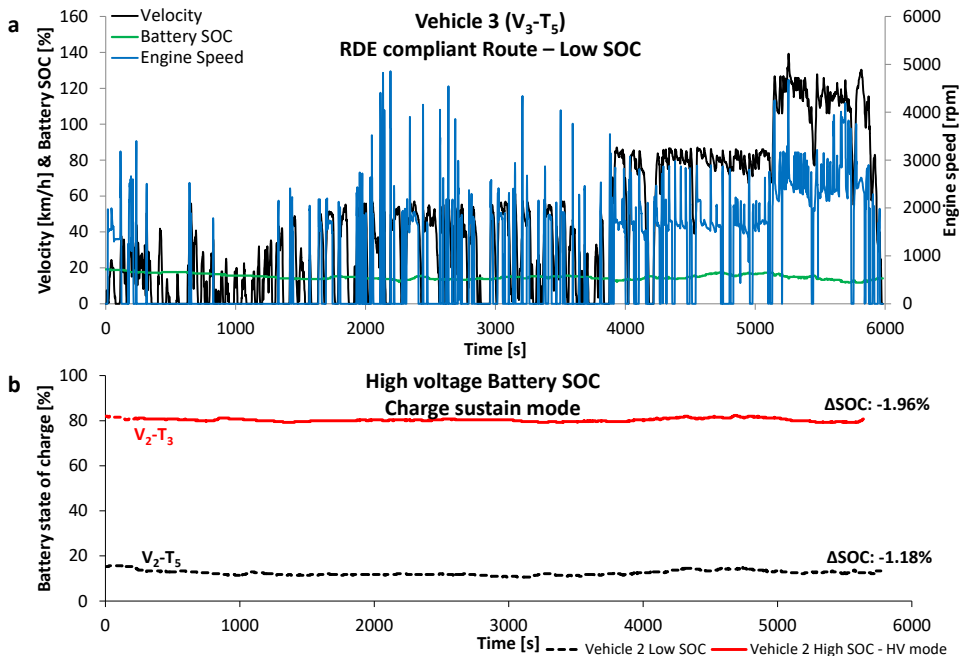
Fig. 9. (a) Test V_3-T_5 with low initial SOC and (b) Evolution of battery SOC under charge sustain mode Test V_2-T_3 with EV mode OFF and Test V_2-T_5 with low initial SOC

The second test that was examined and has a particular interest is the one with low initial battery SOC (depleted battery). During these tests the vehicle is constantly in charge sustain mode keeping the battery charge at a certain level (approximately around 15%-20%). However, this behaviour was also observed when hybrid mode (or EV mode was OFF) was selected and test started with fully charged battery. With this mode enabled, the thermal engine is selected as the primary device used for propulsion and charge sustain mode is enabled, meaning that the vehicle keeps battery SOC

around a certain value (i.e. the initial SOC). A test from vehicle 3 with low initial SOC is presented in Fig. 9a (test V_3-T_5) and the evolution of battery SOC from tests with hybrid mode enabled Test V_2-T_3 (solid line) and low SOC Test V_2-T_5 (dashed line) of vehicle 2 are illustrated in Fig. 9b.

Looking at the main outcomes of the Fig. 8 and Fig. 9, it can be concluded that for both vehicles, a SOC of 15-20% (1.3-1.8 kWh) represents the sufficient level of battery charge to assure that the hybrid mode will work in a proper way. This means that the amount of energy kept in the high voltage battery during charge sustain mode, ensures that synergy between ICE and electric motor (torque assist or charging) will lead to the optimal operating point of the powertrain. As a result, extensive usage of ICE for battery charging (with high fuel consumption) or extreme battery depletion are avoided. Furthermore, to ensure long life and durability of the high voltage battery, the control strategy will not allow SOC to drop below a 15-20% low SOC threshold.

During charge sustain or hybrid mode, the vehicle propulsion is mostly based on the thermal engine thus during those cycles it is possible to evaluate pollutant emissions performance. Aggregated test results of the emissions measurements are presented in Fig. 10. In this figure also emissions performance for tests with high initial SOC are included to reveal the strong relation with the initial battery charge condition and the RDE sequence. A second important parameter that effects the pollutant emission performance is the number of engine starts and the time that the thermal engine is not working. Particularly, for vehicle 3 the higher NO_x emissions are observed at tests V_3-T_3 and V_3-T_4, the route that includes uphill and down hill driving and the reverse RDE respectively. For V_3-T_3, the high NO_x emissions were observed at the engine starts indicated in Fig. 12c, points where catalyst temperature was lower than 300°C. In case of the reverse RDE (V_3-T_4) high NO_x emissions were observed at points where catalyst temperature was also lower than 300°C and particularly at motorway part where ICE power demand was high. It is worth mentioning that for both vehicles and for all cases, except V_3-T_5 test, low CO emissions are achieved against high NOx emissions. In contrast, for test V_3-T_5 that was performed in charge sustain mode and with aggressive driving, a substantial increase of CO was observed while NO_x emissions were lower than the rest of the tests. From instantaneous data analysis of V_3-T_5 test, frequent fuel enrichments were observed at vehicle accelerations.
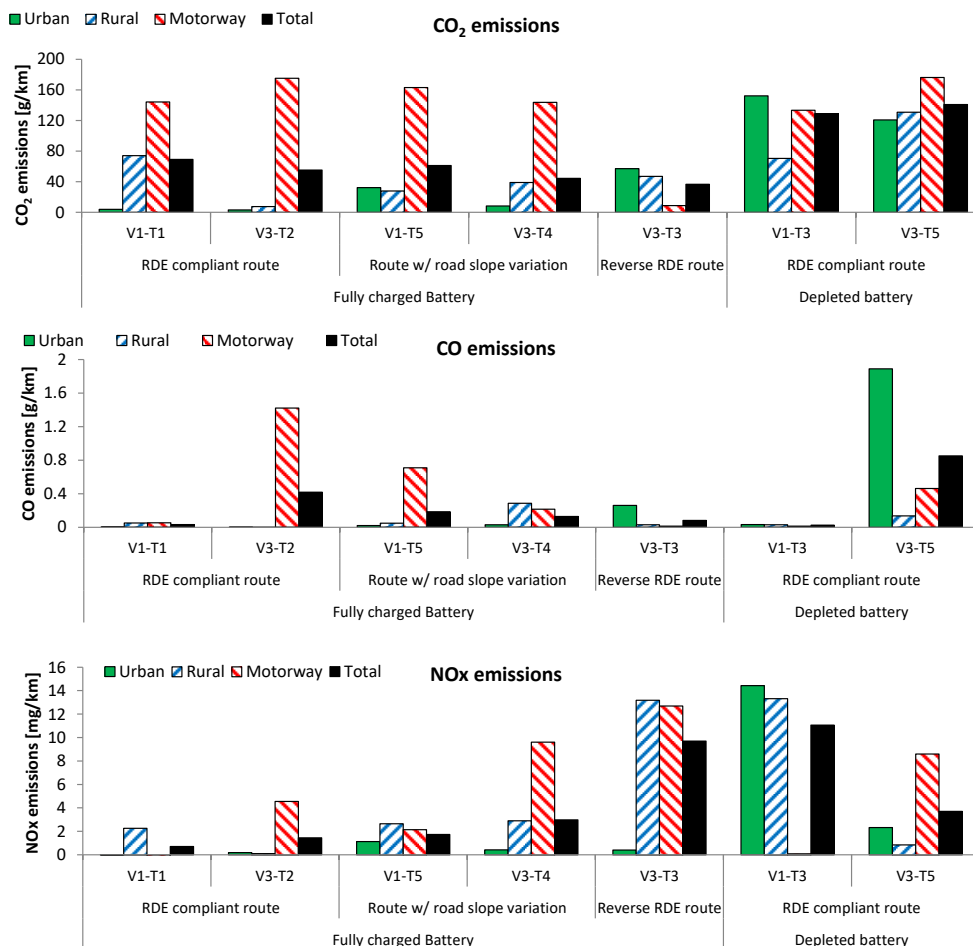

Fig. 10. Emissions performance results for tests with high & low initial battery SOC

With low initial battery SOC tests it also possible to evaluate the energy management strategy and the usage of the thermal engine or the electric machines. The share between electric and hybrid mode is presented in Fig. 11a. With the installed power analyser, it is possible to distinguish the portion of the time where the electric machine is used as a generator or motor. Analysis of the data obtained via the power analyser reveal also the usage of each powertrain component; example is presented in Fig. 11b. It is worth mentioning that Vehicle 2, due to its powertrain architecture, has the ability to use electric machines for propulsion and battery charging simultaneously, something that is not applicable in the Vehicle 3. As a result, for Vehicle 2 torque assist from the electric machines is included to engine ON phase.
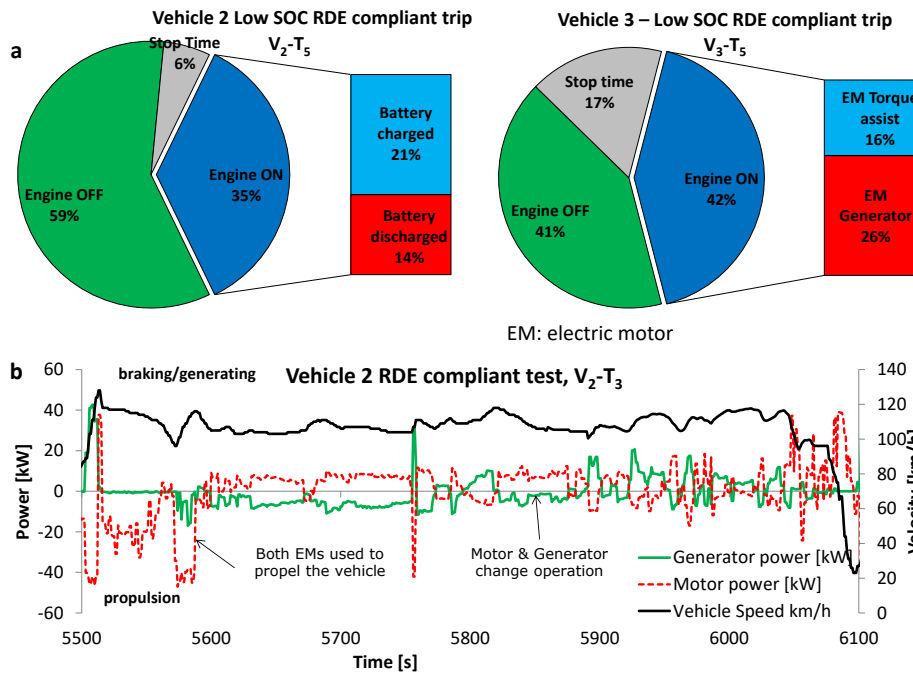

Fig. 11. (a) share between electric (engine OFF) and hybrid mode (engine ON) for tests with low initial SOC (left V_2-T_5, right V_3-T_5), (b) example of operation change between motor and generator, positive power means generating and negative power stands for propulsion, Test V_2-T_3

A special test case is the one conducted at the route which included uphill and downhill driving. During these tests the main observations made are:

- the high depletion rate of the battery due to high power demand during uphill driving
- the regenerative braking performance and the energy recuperated during downhill driving
- the cooling of the catalyst due to long time intervals between engine ON events.

In Fig. 12a, the evolution of battery SOC during a test from this route is presented. During uphill driving the battery depletion rate is high, leading to a decreased (compared to the RDE compliant routes) electric range. During downhill driving the long period of regenerative breaking leads to significant battery charging, with an increase of 27% of battery SOC. Driving conditions of this trip are proved to put particular stress to the high voltage battery since an of its temperature was observed, as shown in Fig. 12b.

During this trip it is possible to identify three main engine starts that occur with time difference between 600 and 1200 seconds, leading to a significant decrease of catalyst temperature, as shown in Fig. 12c.

From the presented results is can be concluded that this kind of tests may be suitable to evaluate specific points for a PHEV such as:

- the thermal management of the exhaust gas aftertreatment system
- the regenerative braking efficiency and the usage of the mechanical brakes
- the charge or discharge limits of the high voltage battery as they are related to temperature
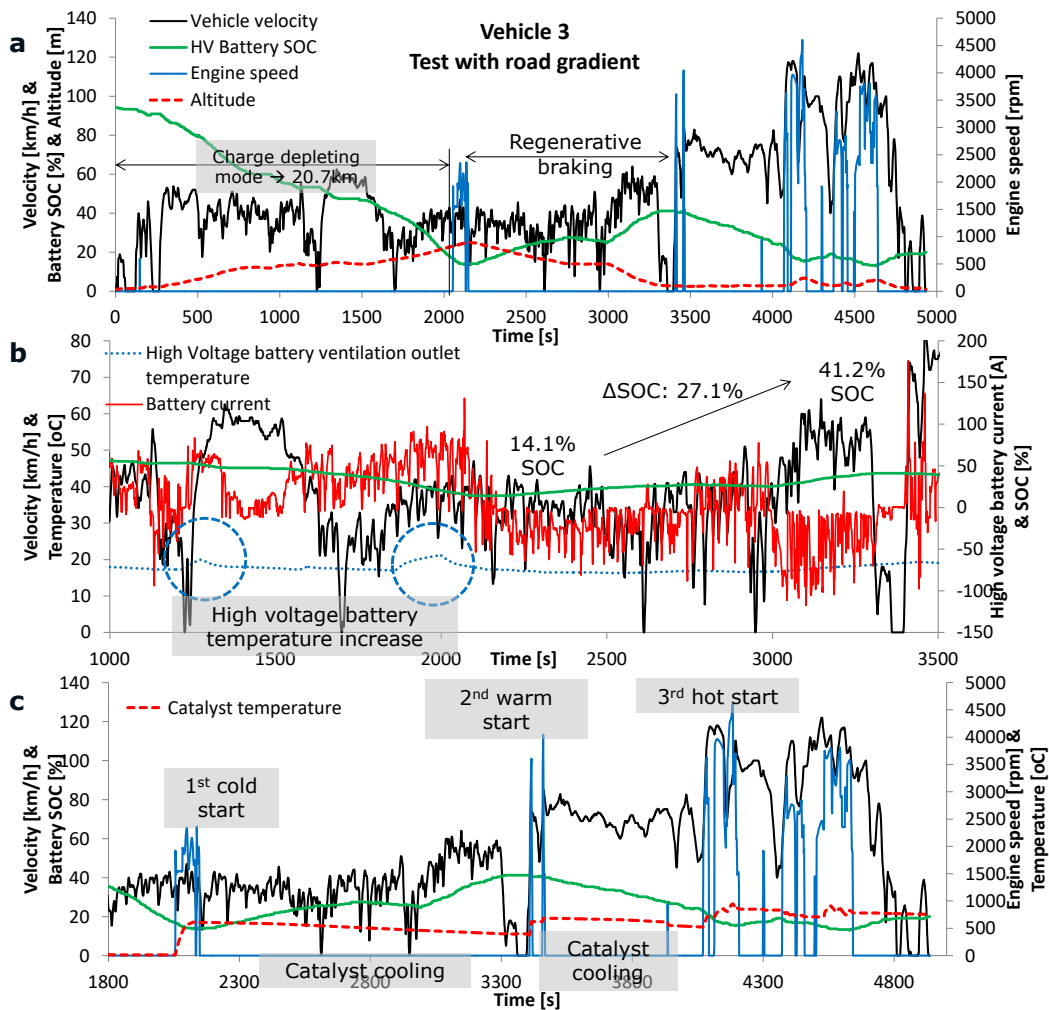
Fig. 12. Experimental results for Vehicle 3 tested at the route with road gradient variation, Test V_3-T_4

Finally, evaluation of the tests where the car was driven with an aggressive driving style, that includes frequent accelerations and decelerations which leads to a transient velocity profile Fig. 13a, showed that it is possible to cover a large area of the operating range of the vehicle in EV mode. As it is shown in Fig. 13b the operating area of the electric motor covered during the aggressive driving test is wider than the respective test with normal/smooth driving.
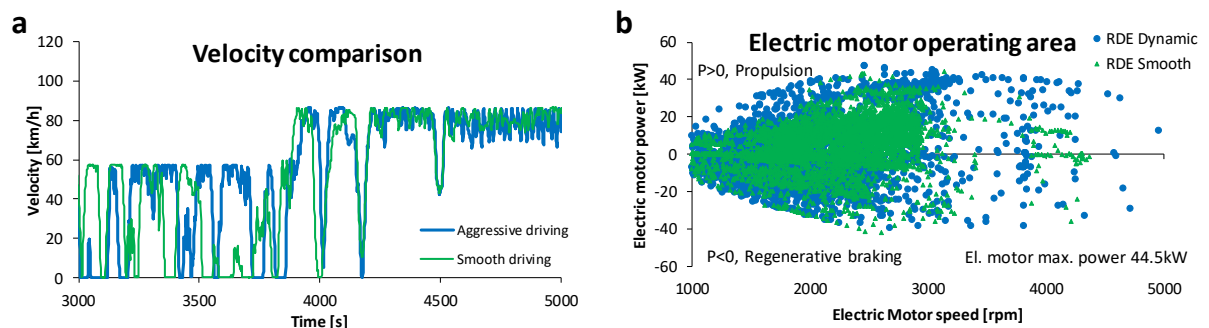
Fig. 13. Vehicle velocity (a) and electric motor operating points (b) comparison between aggressive/dynamic and smooth/normal driving

3.2 Simulation results analysis

Simulation model were used for a preliminary analysis to evaluate the performance of vehicle 2 under a series of different cases. A test case that was not considered but evaluated with the simulation model is an RDE velocity profile with different order of urban, rural and motorway part. Additionally, CO_2

emissions and energy consumption performance for a cycle with aggressive driving, mentioned as eDynamic (the representative cycle shown in Fig. 15b) were evaluated. Finally, the same cycles were simulated also with medium (30%) initial battery SOC. Results from the preliminary simulation based assessment are presented in Fig. 14.
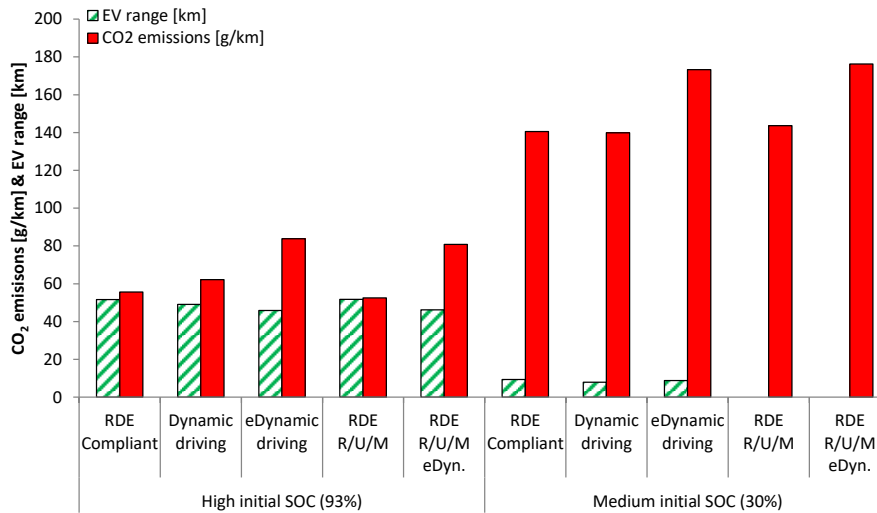
Fig. 14. Initial results from simulation activities (R/U/M: Rural/Urban/Motorway)

Fig. 14 shows that with a high initial battery SOC (93%), both compliant and dynamic RDE cycles exhibit very low CO_2 emissions values, all below the 2021 target of the 95 g/km (Regulation (EU) 2018/1832); whereas for the eDynamic test only, the CO_2 emissions value is close to the 2021 target. On the contrary, as expected, the use of the vehicle with a relatively low initial SOC (e.g 30%) produces much more CO_2, up to 80-90% more emissions observed for the eDriving cycle.

Looking at the eDynamic data, it is evident the great influence of the driving style. For the test with the most aggressive driving test an increase of about 30% and 20% in CO_2 emissions compared to the RDE compliant cycle was observed for the tests with initial SOC of 93% and 30%, respectively.

Another interesting remark is related to the comparison between different sequence of the driving phases (Urban, Rural and Motorway). Fig. 14 data indicate that a different sequence of the phases does not affect the CO_2 emission significantly, confirming the data of Fig. 8 where an almost constant charge depleting rate of the battery is showed for both urban and rural phases. In the future, through new simulation tests, it will be interesting to enrich such database with additional different sets of the non-compliant RDE cycles (e.g. R/M/U sequences or different duration of the phases etc.).

4. Conclusions

In the study presented an experimental evaluation of three plug-in hybrid vehicles under real world driving tests was performed. Analysis of the test results provide the functionalities of vehicles with heavy electrified powertrains that can be evaluated from selected RDE mission profiles. The analysis is also supported with simulation activities.

The proposed real-world driving profiles considered as representative aim to cover the evaluation of electrified powertrains during calibration. The selection is made so that all the parameters mentioned in section 3.1 are covered. As a result, the outcome of the study is a series of real world mission profiles, which were developed on the basis of the data gathered from the performed tests.

The first cycle that proposed as representative is a typical RDE compliant with normal driving; an example of such cycle is presented in Fig. 15a. The second cycle that is considered as representative is also an RDE trip driven with an aggressive driving style. An example is provided in Fig. 15b. The last representative real world mission profile is the one that includes road grade variation and uphill/downhill driving. An example is presented in Fig. 15c. The mission profile examples presented in the three figures (Fig. 15a, Fig. 15b and Fig. 15c) are derived directly from the tests as the measured velocity over the entire trip. The range of the basic specifications of these cycles are included in Table 4. Results of this study are considered representative of the operation of heavy electrified powertrains and the observations made are expected to occur also to other PHEVs. Thus, any real world driving cycle that has basic specifications within those presented above in Table 4 (given the variations due to different routes and traffic conditions) could be considered during the evaluation of PHEVs. For exam-

ple, an RDE compliant route can be used to evaluate the electrical power and fuel consumption, the pollutant emissions performance and the energy management strategy. Repetition of such test with different initial battery SOC could reveal the behaviour and the performance of such vehicles in relation with the battery conditions. Furthermore, aggressive driving under all the proposed cycles, and especially under a route that includes altitude variations, can be conducted in order to stress the battery in terms of thermal behaviour or assess the drivability of the vehicle. Finally, a hilly route similar to the proposed one can be used to evaluate the regenerative braking performance and the mechanical brakes usage. For example, during the experimental campaign Vehicle 3 proved to apply a more aggressive regenerative braking than Vehicle 1 as it recuperated more energy at the same downhill.

Table 4. Basic specifications of selected representative cycles

|	RDE compliant	Aggressive driving	Slope variation
Average Velocity [km/h]	36-50	47-52	48-53
Max. Velocity [km/h]	125-130	135-140	125-135
Average Acceleration [m/s^2]	0.2-0.3	0.3-0.34	0.21-0.31
Average Deceleration [m/s^2]	0.22-0.28	0.28-0.38	0.22-0.31
Trip Duration [s]	5500-6200	5500-6200	4500-5000
Urban/Rural/Highway Share [%]	33-36/32-35/29-34	33-36/32-35/29-34	53-55/20-24/22-31
Total trip length [km]	65-75	65-76	60-65
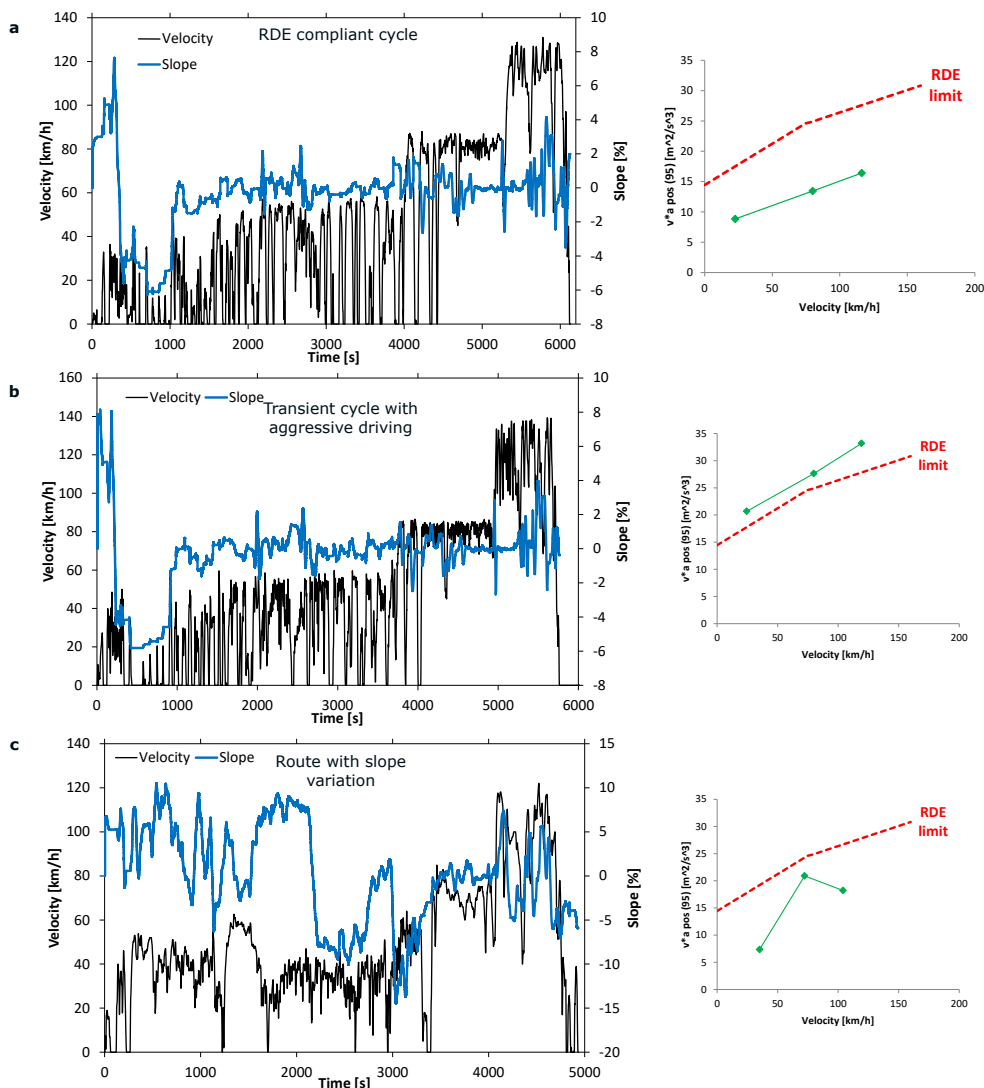
Fig. 15. Examples of the representative cycles

The study has also evidenced the useful of the vehicle simulation tools for design and calibration activities of the electrified vehicles. With the simulations performed it was possible to investigate the electric range and CO_2 emissions over RDE compliant and non-compliant (with different sequence of urban, rural and motorway driving) routes with fully charged and depleted battery and with different driving styles. As a result, the developed simulation models offer a good basis for the expansions of this study, to investigate the sensitivity of individual parameters and driving conditions on the operation of the whole powertrain or specific components, taking advantage of the repeatability of the simulations.

Acknowledgements

References

AVL, 2020. AVL Cruise - Vehicle System and Driveline Analysis, https://www.avl.com/cruise; [accessed on March 2020].

Doulgeris, S., Tansini, A., Dimaratos, A., Fontaras, G., Samaras, Z., 2019. Simulation-based assessment of the CO_2 emissions reduction potential from the implementation of mild-hybrid architectures on passenger cars to support the development of CO2MPAS. 23th International Transport and Air Pollution Conference (TAP),15-17 May 2019, Thessaloniki, Greece.

Ekstrom, F.B., Rolandson, O., Eriksson, S., Odenmarck, C. et al., "A Mild Hybrid SIDI Turbo Passenger Car Engine with Organic Rankine Cycle Waste Heat Recovery," SAE Technical Paper 2019-24-0194, 2019, doi:10.4271/2019-24-0194.

Engbroks, L., Knappe, P., Goerke, D., Schmiedler, S. et al., "Energetic Costs of ICE Starts in (P)HEV – Experimental Evaluation and Its Influence on Optimization Based Energy Management Strategies," SAE Technical Paper 2019-24-0203, 2019, doi:10.4271/2019-24-0203.

European Commission. Regulation (EU) 2017/1151. 2017a

European Commission. Regulation (EU) 2017/1154. 2017b

European Commission. Regulation (EU) 2018/1832. 2018

Harrison G. and Thiel C., "An exploratory policy analysis of electric vehicle sales competition and sensitivity to infrastructure in Europe", Technological Forecasting and Social Change, Volume 114, 2017, Pages 165-178, https://doi.org/10.1016/j.techfore.2016.08.007.

Guzzella, L., Sciarretta, A., (2013). Vehicle Propulsion Systems, Springer

Heywood, J. B. (1988). Internal Combustion Engines Fundamentals. New York, NY: McGraw-Hill.

Ichikawa, S., Takeuchi, H., Fukuda, S., Kinomura, S. et al., "Development of New Plug-In Hybrid System for Compact-Class Vehicle," SAE Int. J. Alt. Power. 6(1):2017, doi:10.4271/2017-01-1163.

Kapadia, J., Kok, D., Jennings, M., Kuang, M. et al., "Powersplit or Parallel - Selecting the Right Hybrid Architecture," SAE Int. J. Alt. Power. 6(1):2017, doi:10.4271/2017-01-1154.

Kato, S., Ando, I., Ohshima, K., Matsubara, T. et al., "Development of Multi Stage Hybrid System for New Lexus Coupe," SAE Int. J. Alt. Power. 6(1):2017, doi:10.4271/2017-01-1173.

Liu, Z., Ivanco, A., and Filipi, Z., "Impacts of Real-World Driving and Driver Aggressiveness on Fuel Consumption of 48V Mild Hybrid Vehicle," SAE Int. J. Alt. Power. 5(2):2016, doi: 10.4271/2016-01-1166

Samaras, Z., Tsokolis, D., Dimaratos, A., Ntziachristos, L., Doulgeris, S., Ligterink, N., Vonk, W., Cuelenaere, R., 2018. A Model Based Definition of a Reference CO_2 Emissions Value for Passenger Cars under Real World Conditions. SAE Tech. Pap. 2018-May, 1–9. https://doi.org/10.4271/2018-37-0031

VISION-xEV public web-page: www.vision-xev.eu

Winklhofer, E., Hirsch, A., Philipp, H., Trifterer, M. et al., "Powertrain Calibration Techniques," SAE Technical Paper 2019-24-0196, 2019, doi:10.4271/2019-24-0196.

Young, K., Jones, R., Hamley, A., Stoddard, J.et al., "Development of a Catalytic Converter Cool-Down Model to Investigate Intermittent Engine Operation in HEVs," SAE Int. J. Alt. Power. 7(2):139–153, 2018, doi:10.4271/08-07-02-0009.

Prediction of Gaseous Pollutant Emissions from a Spark-Ignition Direct-Injection Engine with Gas-Exchange Simulation

S. Esposito[1], L. Diekhoff[2] and S. Pischinger

Institute for Combustion Engines (VKA), RWTH Aachen University
Forckenbeckstrasse 4, D-52074, Aachen, Germany.

E-mail: s.esposito@itv.rwth-aachen.de
Telephone: +(49) 241 80 94877

Abstract. With the further tightening of emission regulations and the introduction of real driving emission tests (RDE), the simulative prediction of emissions is becoming increasingly important for the development of future low-emission internal combustion engines. In this context, gas-exchange simulation can be used as a powerful tool for the evaluation of new design concepts. However, the simplified description of the combustion chamber can make the prediction of complex in-cylinder phenomena like emission formation quite challenging. The presented work focuses on the prediction of gaseous pollutants from a spark-ignition (SI) direct injection (DI) engine with 1D-0D gas-exchange simulations. The accuracy of the simulative prediction regarding gaseous pollutant emissions is assessed based on the comparison with measurement data obtained with a research single cylinder engine (SCE). Multiple variations of engine operating parameters – e.g. load, speed, air to fuel ratio, valve timing – are taken into account to verify the predictivity of the simulation towards changing engine operating conditions. Regarding the unburned hydrocarbon (HC) emissions, phenomenological models are used to estimate the contribution of the piston top-land crevice as well as flame wall-quenching and oil-film fuel adsorption-desorption mechanisms. Regarding CO and NO emissions, multiple approaches to describe the burned zone kinetics in combination with a two-zone 0D combustion chamber model are evaluated. In particular, calculations with reduced reaction kinetics are compared with simplified kinetic descriptions. At engine warm operation, the HC models show an accuracy mainly within 20%. The predictions for the NO emissions follow the trend of the measurements with changing engine operating parameters and all modelled results are mainly within ±20%. Regarding CO emissions, the usage of the simplified kinetic models is not capable to predict CO at stoichiometric conditions with errors below 30%. With the usage of a reduced kinetic mechanism, a better prediction capability of CO at stoichiometric air-to-fuel ratio could be achieved.

Notation

α_{EVC}	Crank angle at exhaust valve closing / ° CA aTDC$_F$	p_{mi}	Indicated mean effective pressure / bar
α_{IVO}	Crank angle at intake valve opening / ° CA aTDC$_F$	Pe_Q	Peclet number / -
λ	Relative air-to-fuel ratio / -	R_{mix}	Gas constant of fuel air mixture / J/(kg·K)
A_{CO}	Coefficient CO kinetic model / -	s_L	Laminar flame speed / m/s
B_{CO}	Coefficient CO kinetic model / -	T	Temperature / K
D_m	Diffusion coefficient of the mixture / m²/s	T_{crev}	Temperature in crevices / K
d_Q	Quench distance / m	T_{head}	Wall temperature of cylinder head (gas side) / K
k_{fCO}	Forward coefficient CO oxidation / m³/(kmol·s)	T_{liner}	Wall temperature of cylinder liner (gas side) / K
l_F	Laminar flame thickness / m	T_{piston}	Wall temperature of piston (gas side) / K
m_{crev}	Mass in crevices / m	V_{crev}	Volume of crevices / m³
n_E	Engine speed / 1/min	x_b	Burned fuel mass fraction / -
p_{cyl}	In-cylinder pressure / Pa	Y	Mole fraction / -

---

[1] Currently at Institute for Combustion Technology (ITV), RWTH Aachen University, Templergraben 64, D-52062 Aachen, Germany.

[2] Currently at ISATEC GmbH, Rathausstrasse 10, D-52072 Aachen, Germany.

1. Introduction

Virtual engine development is a very valuable tool for new engine concepts. Regarding 1D-0D simulation, major applications have been connected in the last years to engine concept and design, turbocharger matching, optimization of engine technologies for fuel consumption targets, design of the peripheries, and pressure losses analysis. In the past, the topic of pollutant emissions in the development of new SI engines was not of highest priority (Morcinkowski et al., 2020) due to the availability of an exhaust after-treatment system like the three-way-catalyst, which was able with some calibration effort to meet the emission regulations. However, the current and future emission regulations, under consideration of the RDE, require a higher degree of virtual development and optimization of engine raw emissions. The possibility to predict engine emissions in a concept phase is of crucial importance for a fast and cost-effective development of new low-emission vehicle concepts (hybrid, range-extenders, etc.). Indeed, it allows the optimization not only of the engine itself, but also of the operating strategy of the entire vehicle. This possibility allows the evaluation of different vehicle concepts and supports the decision on hardware and system components already in the concept phase.

Up to now, however, the prediction of raw emission levels with thermodynamic simulation has been avoided also because of its complexity and the high modeling and computational effort required. Indeed, pollutant emission simulation requires the modeling and consideration of multiple physical phenomena that happen in the combustion chamber like mixture formation, spray-wall interaction, chemical kinetics, charge motion, which are transient and include complex geometry. 3D-CFD simulation is a tool that in principle give the possibility to take into account the majority of the aspects involved. However, the consideration of all these aspects results in a very high computational effort. For this reason, the 3D-CFD simulations are more suitable for investigation of specific aspects or component investigations (Morcinkowski et al., 2020).
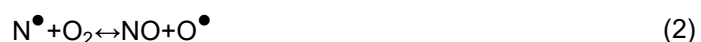
Maps of engine raw emissions are often required to simulate vehicle RDE cycles and evaluate the conformity to the regulation. For this scope, 0D-1D simulation is the best tool to verify the engine performance in the whole operating range and under different boundary conditions. However, the simplified description of the combustion chamber (normally 0D) can be a limiting factor for the predictivity of the models and can require additional modeling effort.

This work focuses on the prediction of gaseous pollutant emissions (NO, CO, HC) in 0D-1D environment with the commonly used commercial software GT-POWER. The study is based on emission measurement performed on a SI DI SCE, in order to have more suitable data for the validation of the emission models. Multiple kinetic approaches are verified regarding the prediction of NO and CO in a 0D two-zone combustion chamber model, while phenomenological models for HC have been implemented and validated (Esposito, 2020). The scope is to investigate the predictivity of the models in 0D-1D environment and to understand the limitations of the environment and, in case, the aspects that require further modeling effort.

2. Emission formation mechanisms in SI engines

2.1. Nitrogen oxides (NO$_x$)

The most relevant formation path in combustion engines is the thermal-NO mechanism. This derives from the dissociation of molecular oxygen that forms the radical O$^\bullet$ that attacks the molecular nitrogen to initiate a chain reaction (Liberman, 2008). This mechanism, known as the (Extended) Zeldovich Mechanism (EZM), can be described by a set of highly temperature-dependent reactions (Fenimore, 1971)(Hochgreb, 1998; Lavoie et al., 1970; Zeldovich, 1946):

$$O^\bullet + N_2 \leftrightarrow NO + N^\bullet \tag{1}$$

$$N^\bullet + O_2 \leftrightarrow NO + O^\bullet \tag{2}$$

$$N^\bullet + OH^\bullet \leftrightarrow NO + H^\bullet \tag{3}$$

Zeldovich (Zeldovich, 1946) first postulated (1) and (2). Lavoie, Heywood and Keck (Lavoie et al., 1970) extended the mechanism by including (3). The rate limiting step of the EZM is reaction (1) because the strong triple bond in the N$_2$ molecule requires a very high activation (Warnatz et al., 2006). Temperatures above 2000 K are prerequisites for the formation of NO via thermal-path. The highest NO production is observed for slightly lean mixtures in the hot gases behind the flame front (Hochgreb, 1998). Therefore, the highest NO engine emissions are observed at slightly lean conditions. The thermal-NO mechanism accounts for the majority of NO formed in internal combustion engines (Flagan and Seinfeld, 1988).

At lower temperatures and in fuel-rich conditions, the NO concentrations cannot be explained only by thermal-NO formation. Fenimore (Fenimore, 1971) introduced an alternative mechanism that forms NO from the intermediate radical species $CH^{\bullet}$, mainly on the flame front. This mechanism was called prompt-NO since the formation of nitric oxide is relatively fast due to aggressive HC radicals in comparison to thermal-NO (Flagan and Seinfeld, 1988). Fenimore identified the reaction:

$$CH^{\bullet}+N_2 \leftrightarrow HCN^{\bullet}+N^{\bullet} \tag{4}$$

as the rate-limiting step. The contribution of the prompt mechanism in stoichiometric laminar flames has been estimated in the order of 5-10% (Drake and Blint, 1991; Hochgreb, 1998). Lavoie and Blumberg (Lavoie and Blumberg, 1973; Lavoie and Blumberg, 1980) calculated that prompt-NO contribution in engines becomes important under high air-fuel mixture dilution (Hochgreb, 1998).

Additionally, the NO formation can be obtained through the N_2O mechanism. This is relevant especially at low temperature conditions in lean mixtures (Warnatz et al., 2006), where the thermal-NO formation is too low and the $CH^{\bullet}$ radical concentration not significant.

The NO_x formation in combustion engines is commonly modeled with kinetic approaches. Indeed, since the NO chemical reaction scales are quite slow compared to the engine process (Flagan and Seinfeld, 1988; Warnatz et al., 2006), the calculation with only equilibrium chemistry would lead to wrong results (Heywood, 1988; Warnatz et al., 2006). In the majority of cases, the EZM is used as main mechanism. Different parametrizations of the Arrhenius-like reaction rates for reactions according to (1), (2) and (3) can be found in the literature (Baulch et al., 1994; Heywood, 1988; Smith et al; Warnatz et al., 2006). Miller et al. (Miller et al., 1998) have further extended the EZM in a Super EZM (SEZM) that consists of 13 species and 67 reactions including the N_2O production path.

In combination with fuel reaction mechanisms, prompt-NO reactions can be additionally accounted since the HC radical $CH^{\bullet}$ concentrations are calculated (Anderlohr et al., 2009; Drake and Blint, 1991; Moskaleva and Lin, 2000). In the absence of a fuel oxidation mechanism, the $CH^{\bullet}$ concentration needs to be estimated to calculate the rate of reaction (4) (Dodge et al., 1998; Soete, 1975).

In general, temperature and air-fuel ratio of the burnt mixture are the most important factors determining the rate of NO formation (Hochgreb, 1998). The above-mentioned approaches are applied to the modeled combustion chamber and depend from the 0D (single-, two- or multi-zone) or multi-dimensional combustion chamber formulation. The two-zone model was actually developed for the better prediction of NO emissions in the field of 0D modeling (Merker, 2006) and represents a necessary requirement to achieve acceptable predictions of NO in 0D approaches. Examples for the usage of multi-zone models, which increase the detail in the description of mixture temperature and composition, can be found in (Arsie et al., 2003; Bhat and Tamma, 2014; Bhave and Kraft, 2004; Cao et al., 2008; Holly et al., 2016). However, the increase in complexity and model parametrization could overcome the benefit in accuracy prediction.

The two-zones approach demonstrated to deliver good results in combination with EZM models (Dodge et al., 1998; Mehrnoosh et al., 2012; Merker, 2006; Merker and Teichmann, 2014). Additionally, engine with high tumble ports are expected to achieve a high homogeneity in the mixture and to be better approximated by a 0D two-zone description. For these reasons, the 0D two-zone approach has been selected for this study.

2.2. Carbon monoxide (CO)

The fuel combustion process can be described as the conversion of the primary fuel to progressive smaller intermediate hydrocarbons, followed by oxidation to aldehydes or ketones, and finally to CO, which is then oxidized to CO_2 (Hochgreb, 1998). The reactions that involve fuel oxidation up to CO are relatively fast at typical combustion temperatures in SI engines, resulting in fast formation of CO, while the CO oxidation is in comparison relatively slow (Bowman, 1975). The CO oxidizes predominantly by reacting with $OH^{\bullet}$ according to the following reaction:

$$CO+OH^{\bullet} \leftrightarrow CO_2+H^{\bullet} \tag{5}$$

According to partial-equilibrium calculations (Flagan and Seinfeld, 1988), during combustion, CO levels are close to equilibrium concentrations, while during expansion, CO diverge from the equilibrium concentration and CO oxidation stops. The faster the cooling and expansion processes are the higher is the temperature at which CO starts to deviate from equilibrium concentrations. This happens because the recombination reactions are then unable to provide the needed radicals for maintaining CO equilibrium. In rich conditions, CO oxidation is in competition with the oxidation of H_2 that proceeds with the following reaction:

$$H_2+OH^\bullet+M\leftrightarrow H_2O+H^\bullet \tag{6}$$

While reaction (6) is found practical in equilibrium, reaction (5) is kinetically controlled. In other words, reaction (6) is substantially faster than (5) and a strong increase of CO is observed in rich conditions (Heywood, 1988). Due to these fast reactions in rich conditions, the deviation between equilibrium chemistry and kinetics is relatively small (Merker, 2006). In the stoichiometric range, the reactions (6) and (5) can be approximated via the gross reaction known as Water Gas Shift (WGS):

$$CO+H_2O\leftrightarrow CO_2+H_2 \tag{7}$$

In this case, it proceeds near to equilibrium because the chain propagators $H^\bullet$ and $OH^\bullet$ are not limited (Merker, 2006). In the lean range, CO oxidation is not in competition with H_2 oxidation anymore, but proceeds rather together with the following reaction:

$$O_2+H^\bullet\leftrightarrow OH^\bullet+O^\bullet \tag{8}$$
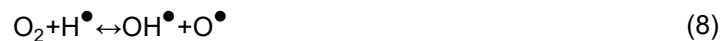
During expansion, more $H^\bullet$ than $OH^\bullet$ is available due to lack of equilibrium of reaction (5) and the CO oxidation is slow. Due to the very slow kinetics, a rough estimation of the CO concentration corresponds approximately to the equilibrium value at 1700 K (Merker, 2006).

All these considerations apply for locally homogeneous mixtures in the combustion chamber. Due to the sensitivity of the CO formation to the relative air-to-fuel ratio (λ), the CO emission from combustion engines are extremely sensitive to mixture formation.

The simplest model for the calculation of CO emissions consists in the usage of the WGS reaction (7). The limits of a chemical equilibrium approach are bound to the homogeneity limits. In internal combustion engines, the hypothesis of a homogeneous mixture can be more or less realistic (depending on the type and timing of fuel injection, charge motion), but in most cases it is not sufficient for CO modeling. For this reason, the usage of a chemical equilibrium approach results often in a calibrated threshold temperature necessary to meet the measured emission levels. In the literature, threshold temperatures for CO oxidation freezing range between 1000 and 1900 K (Grill, 2006).

The usage of a fuel oxidation mechanism allows the integration of all the above-mentioned reactions (5), (6), (8) with kinetics. Without fuel oxidation chemistry, the estimation of CO formation is quite difficult, especially because it was demonstrated that (5) has not an Arrhenius-like behaviour (Dryer et al., 1971). Bowman (Bowman, 1975) proposed the following expression for the rate of reaction (5) based on experimental data:

$$k_{f_{CO}}=A_{CO}\cdot 6.76\cdot 10^7\cdot e^{T/(B_{CO}\cdot 1102)} \tag{9}$$

with A_{CO} and B_{CO} equal to 1 and $k_{f_{CO}}$ expressed in m³/(kmol·s).

Flagan and Seinfeld (Flagan and Seinfeld, 1988) reported a detailed investigation of CO oxidation with a semi-kinetic approach in which the kinetics of reaction (5) are considered only for the forward rate, while the equilibrium rate coefficient is assumed for the backward reaction. They took into consideration the involved radicals ($H^\bullet$, $O^\bullet$, $OH^\bullet$) recombination reactions in a kinetic way too. They showed as the quenching of CO oxidation is influenced not only by the temperature, but alsodepends on the cooling rates. The CO oxidation modeling in a kinetic way shows then to rely greatly on the kinetics of the radicals involved in the relevant reactions. Chindaprasert et al. (Chindaprasert et al., 2006) used a reduced kinetic mechanism (83 species and 516 reactions) in combination with a two-zone thermodynamic model to predict CO emissions. They showed a relevant improvement from 48% average deviation to 25% with the kinetic approach in comparison to the chemical equilibrium. Due to the above-mentioned relative air-to-fuel ratio (λ) -sensitivity of the CO formation, multi-zone approaches that take into account the λ -distribution can aim to a better prediction of CO emissions. However, their parametrization may require a great deal of effort and can be highly dependent on the engine and/or the operating point.

2.3. Unburned hydrocarbons (HC)

Like the CO emissions, the emissions of unburnt hydrocarbons are resulting from incomplete fuel oxidation. In contrast to carbon monoxide, the equilibrium levels are very low and the oxidation reactions are very fast (Flagan and Seinfeld, 1988). Therefore, HC emissions result predominantly from regions where the fuel escape complete combustion. Many different sources of hydrocarbons have been identified and quantified in numerous literature studies (Alkidas, 1999a, 1999b; Amano and Okamoto, 2001; Cheng et al., 1993; Dorsch et al., 2016; Hochgreb, 1998; Janssen, 2010). The main sources of HC are (Dorsch et al., 2016):

- Combustion chamber crevices: narrow zones in the combustion chamber in which the flame does not proceed. Major crevices are piston-ring pack, valves seats, spark plug, and cylinder head gasket. However, the contribution of the piston top-land crevice alone is estimated around 40-90% (Dorsch et al., 2016).
- Flame quenching at the walls (5-7%), partial burn not at the walls (<10%).
- Oil-film fuel adsorption-desorption (5-30%): due to the solubility of fuel in oil, the oil-layer can adsorb fuel before combustion (concentration of fuel in the air-fuel mixture higher than in the oil-layer) and desorb it during expansion (concentration of fuel in the oil higher than in the burned mixture). Additionally, some fuel can be directly introduced into the oil-layer if the injected fuel hits the cylinder walls. However, this strongly depends on the operating conditions.
- Fuel-film (5-45%): film of liquid fuel formed as a result of the injection, which normally does not burn completely because of the local lack of oxygen and increases the HC emissions.

Additionally, combustion chamber deposits are considered a source of HC (~10%) because they can adsorb and desorb fuel. Nevertheless, the amount of deposits in the combustion chamber varies depending on the use and ageing of the engine and is therefore difficult to estimate. Lastly, the leakage of gases through the piston ring into the crankcase, known as blow-by, has an impact on the HC emission balance. Also, in this case the quantification can be very challenging.

The quantification of the single HC-mechanism contribution present in the literature is very variable and can be also very wide. All these sources are indeed influenced by the engine design, fuel injection targeting, fuel type, operating mode, engine state, etc. In general, the process that determines the final HC-emission level can be differentiated in "formation" and "post-oxidation". "Formation" refers to the process in which fuel or air-fuel mixture escapes the main combustion process or is released in the combustion chamber after the main combustion process. "Post-oxidation" represents the chemical process in which the previously formed HC can be oxidized during the expansion or the exhaust phases, if the temperature is high enough and sufficient oxygen is available. Cheng et al. (Cheng et al., 1993) suggest an estimation of the post-oxidation within the cylinder that is about one third of the HC from fuel sources (e.g. oil-film, deposits) and about two thirds of the HC from mixture sources (e.g. quenching, crevices). Eng (Eng, 2005) estimated the global HC oxidation in the expansion phase as approximately 70%.

Due to the heterogeneous source of the HC-emissions, the post-oxidation and the difficult quantification of the individual sources, the validation of HC-emission models is generally very challenging. The most commonly modeled sources of HC in 1D/0D models are the combustion chamber crevices due to their strong contribution to total HC emissions (D'Errico et al., 2002; Dorsch et al., 2016; Frølund and Schramm, 1997; Janssen, 2010; Min and Cheng, 1994, 1995; Oliveira and Hochgreb, 1999; Schramm and Sorenson, 1990; Sodré and Yates, 1997; Trinker et al., 1993). In multiple studies only the volume corresponding to the piston top-land crevice is considered and the ideal gas law is used to estimate the mixture content on the basis mainly of pressure and of temperature (mostly taken as equal to the wall temperature).

Many studies presented the modeling of the fuel adsorption-desorption of the oil-film. The fuel concentration in the oil-layer is commonly described (Albuquerque et al., 2011; D'Errico et al., 2002; Dorsch et al., 2016; Frølund and Schramm, 1997; Huang et al., 1996; Ihsan Karamangil et al., 2014; Janssen, 2010; Schramm and Sorenson, 1990; Sodré and Yates, 1997; Trinker et al., 1993; Yildirim et al., 2006; Yu and Min, 2002) with the 2nd Fick's law, which requires the 1D description of the fuel concentration trend over the oil-layer thickness. Some studies (Dent and Lakshminarayanan, 1983; Dorsch et al., 2016) presented a 0D approximation of the Fick's law, which gave similar plausible trends of the oil-film HC emissions with engine operating conditions.

Due to the limited contribution of the quenching-HC mechanism to the total HC emissions (5-7% (Dorsch et al., 2016), 3-12% (Lorusso et al., 1983)), relatively few literature sources concentrate on the modeling of wall-quenching HC for 0D/1D simulation. Dorsch et al. (Dorsch et al., 2016) estimated the quenching distance as a multiple of the laminar flame thickness according to Peters (Peters, 2010) in combination with a spherical flame propagation model to estimate the quenching contribution in a quasi-dimensional combustion chamber modeling.

Literature approaches to model post-oxidation can be divided mainly into (Janssen, 2010) threshold approaches (Dent and Lakshminarayanan, 1983; Janssen, 2010), one-step kinetics (Da Silva and Nigro, 2000; D'Errico et al., 2002; Dorsch et al., 2016; Heywood, 1988; Janssen, 2010; Lavoie, 1978; Schramm and Sorenson, 1990; Sodré, 1999; Sodré and Yates, 1997; Tinaut et al., 1999), and the use of detailed reaction mechanisms. In order to calculate the post-oxidation with detailed reaction mechanisms, a corresponding modeling depth is required, which also covers the intermediate products of the

oxidation. For this reason, kinetic mechanisms are required and kinetics solution on the base of particular thermodynamic boundary conditions is performed. However, these approaches are difficult to implement within a 0D/1D environment. Even if in comparison to the threshold approach the Arrhenius-like one-step chemistry is supposed to be more predictive, the variety of the parameters found in literature (Dorsch et al., 2016; Janssen, 2010) is subject to a certain calibration requirement, again a difficult validation for the individual HC sources.

3. Experimental methodology

3.1. Measurements at the SI DI research SCE

3.1.1 Engine

The measurement data used as basis for the model validation have been obtained with a DI SI research single cylinder engine (SCE). The specific experimental setup has already been described in other publications from the authors (Esposito et al., 2019; Esposito et al., 2020). The main technical data of the SCE are listed in Table 1.

Table 1. Hardware specification of the research SCE.

Characteristic / Unit	Value
Displacement / cm³	400
Bore / mm	75
Stroke / mm	90.5
Compression ratio / -	11.84:1
Valves per cylinder / -	4
Fuel injection pressure / bar	200
Injection timing / ° CA aTDC$_F$	-280
Intake & exhaust valve angle / °	17.5
Intake & exhaust event length (1 mm) / ° CA	186
Intake & exhaust cam phasing range) / ° CA	55

Both the DI injector and the spark plug are centrally located in the combustion chamber and the intake ports are symmetrical and high-tumble ports.

The investigations have been performed with a conventional RON95E5 market fuel as well as a Toluene Reference Fuel (TRF, mixture of iso-octane, n-heptane and toluene) surrogate with the addition of ethanol (TRF+E). The surrogate fuel composition targeted the relevant chemical properties of the RON95E5 gasoline (Esposito et al., 2020) and its composition in mass (%), after the real mixing, was $X_{iC_8H_{18}}$= 51.8%, $X_{nC_7H_{16}}$= 13.3%, $X_{C_7H_8}$= 28.8%, $X_{C_2H_5OH}$= 6.1%. In (Esposito et al., 2020), the authors showed that this TRF+E could accurately reproduce the behaviour of the market RON95E5 fuel regarding global combustion and gaseous emission behaviour. Due to the simpler composition, the measurement results with surrogate fuels are taken into account in this work.

3.1.2 Measurement devices

As far as the thermodynamic measurements are concerned, the cylinder pressure was measured with two Kistler 6045B pressure transducers, flush mounted in the combustion chamber roof. Sampling was performed via Kistler 5064 charge amplifiers and an FEV Indication System (FEVIS) within a resolution of 0.1° CA. Dynamic intake and exhaust gas pressures were measured with Kistler 4045 A5 pressure transducers and sampled at 0.1° CA resolution too. In total, 500 consecutive cycles were recorded for every operating point. Measurements of static pressures and temperatures were performed with conventional pressure transducers and thermocouples during an averaging interval of 30 s. The engine oil

and coolant were conditioned at a constant temperature of 90 °C. The intake air was conditioned at 25 °C upstream of the electronically controlled throttle flap. A pressure of 1.013 bar was imposed upstream of the throttle flap and in the exhaust manifold during throttled operation. For boosted operation, the exhaust pressure was set equal to the intake boost pressure to simulate turbocharging. The engine was coupled to an eddy-current brake and an electric dynamometer, which allowed to keep the speed at the selected value with an accuracy of ±1 1/min. The intake air mass flow was measured with an ultrasonic mass flow meter and the fuel flow with a Coriolis-type mass flow sensor.

In this specific measurement campaign, multiple emission measurement devices for gaseous emissions have been applied in different positions, as reported in (Esposito et al., 2019; Esposito et al., 2020). Relevant for this study are the average gaseous emission measurement performed with conventional emission analyzers. These standard measurements have been performed with a FEV Emission Rate (FEVER) device. The main specification of the devices included are reported in Table 2.

Table 2. FEVER devices specification. Abbreviations: CLD = Chemiluminescence Detector, NDIR = Non-Dispersive Infrared Detector, PMD = Para-Magnetic Detector, FID = Flame Ionization Detector, THC = Total-HC.

Characteristic	FEVER device					
	CLD	NDIR			PMD	FID
Sensed species	NO_x	CO		CO_2	O_2	THC
		Low	high			
Measuring range	0-10000 ppm	0-5000 ppm	0-10%	0-20%	0-25%	10-10000 ppm_{C3}
Accuracy	1% of measured value					
Linearity	2% of measured value					

The FEVER measurement sampling position considered for this study was located in the exhaust runner, about 13 cm downstream the exhaust valves. A schematic of the SCE and of the FEVER emission measurement position is reported in Figure 1.
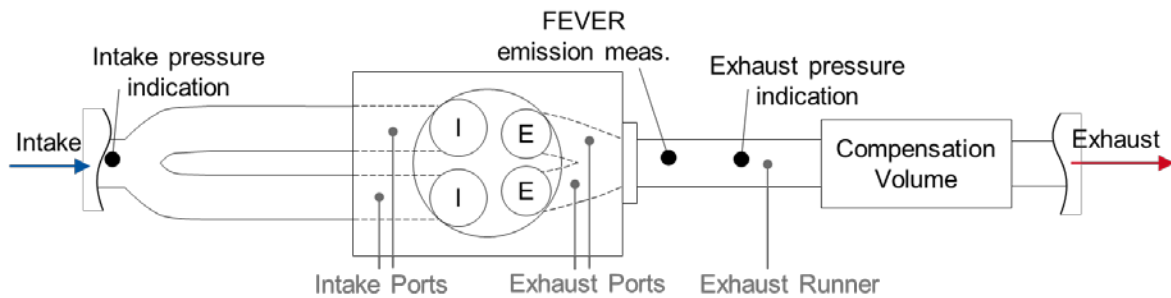

Fig. 1. Schematic of SCE with positions of FEVER emission measurement and low pressure indication.

3.1.3 Test plan

The operating points selected for comparison between measurement and simulation include variations of indicated mean effective pressure (p_{mi}) relative air-to-fuel ratio (λ), intake valve opening (α_{IVO}) and exhaust valve closing (α_{EVC}), at different speeds n_E. All operating points have been measured with an engine oil and coolant temperature of 90 °C and an intake air temperature of 25 °C. All the operating points considered in this work are schematized in Figure 2.
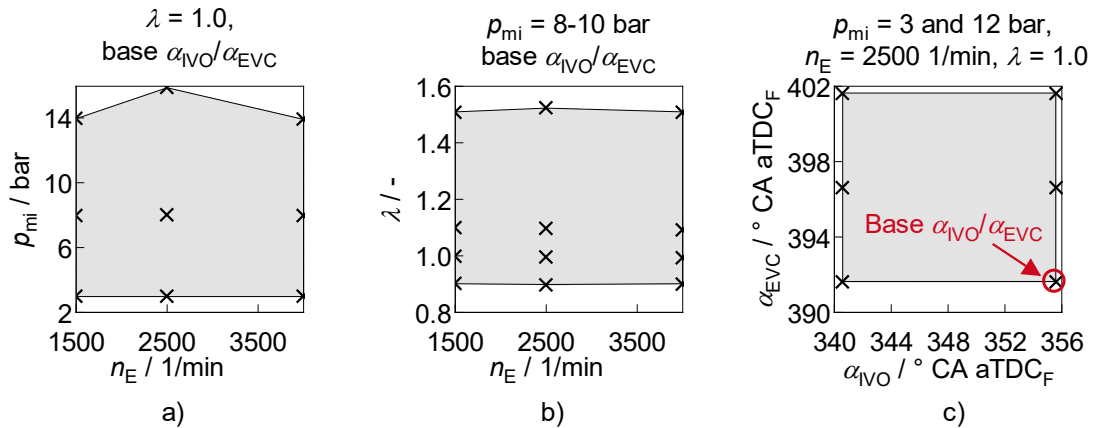
Fig. 2. Operating points (indicated with crosses) considered in this work, in total 33 points.
a) p_{mi} - n_E variations in stoichiometric conditions (9 points); b) λ - n_E variations at p_{mi} between 8 bar (for n_E = 1500 1/min) and 10 bar (12 points); c) valve timings variations performed at two different operating points at n_E = 2500 1/min, p_{mi} = 3 and 12 bar (6 points x2).

4. Simulation methodology

4.1. 1D/0D-simulation model

The 1D-simulation model used to validate the emission modeling was implemented within the software GT-POWER (Gamma Technologies, 2018). It includes the engine geometry between the low pressure indications on the intake and exhaust side (see Figure 1). At the model boundaries, the measured instantaneous pressure and average temperature conditions are imposed in order to eliminate the inaccuracy that could result from the modeling of intake and exhaust. In this way, major attention could be given to the combustion system.

In order to concentrate on the emission modeling, a non-predictive combustion model is adopted for the simulation. In particular, the burning profiles (x_b) evaluated by means of a Three-Pressure-Analysis (TPA) (Gamma Technologies, 2018) of the measured pressure traces (intake, exhaust, in-cylinder) are imposed for each operating point. The selected heat transfer model is a modified Woschni model without swirl according to Heywood (Heywood, 1988), identified in GT-POWER as "WoschniGT" (Gamma Technologies, 2018), with the standard parametrization. The combustion chamber is described with a two-zone model which enables the evaluation of the temperatures in the burned and unburned zones. Due to the early injection angle (-280° CA aTDC$_F$), the high-tumble engine concept and the central spark position, the 0D two-zone approach is considered a good approximation of the reality for this engine. The wall temperatures are specified in function of engine load p_{mi} and engine speed n_E, as shown in Fig. 3.
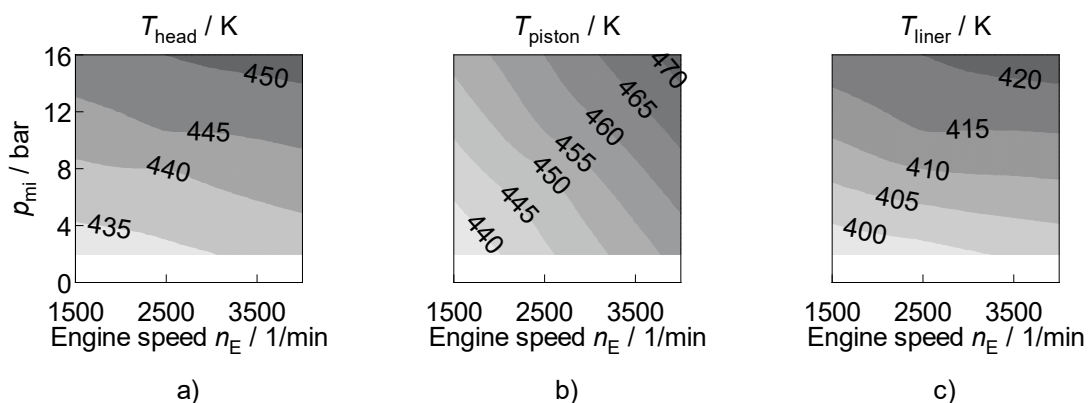

Fig. 3. Specified combustion chamber wall temperatures of the GT-POWER model.
a) cylinder head, b) piston, c) cylinder liner.

The resulting agreement of the simulation model regarding in-cylinder peak pressure was mainly within 5%, as depicted in Figure 4.
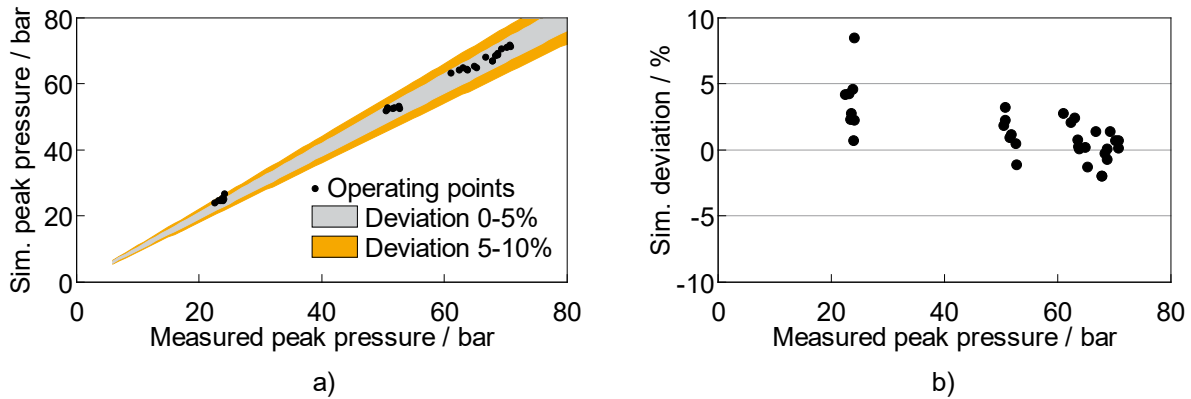
Fig. 4. GT-POWER simulation model accuracy regarding peak pressure. a) Correlation between simulated and measured pressures; b) Relative deviation of the simulation results vs measured peak pressure.

4.2. Burned zone kinetics modeling

In order to calculate the CO and NO emissions, a kinetic description in the burned zone of the combustion chamber is necessary. Regarding the modeling of the burned zone kinetics, mainly two approaches have been followed in this work: the usage of a reduced fuel oxidation mechanism and the usage of simplified kinetic models.

4.2.1 Chemical equilibrium calculations in GT-POWER

For the simplified kinetic models, an approximation of the species concentration needs to be performed in order to estimate the radical concentrations needed for NO and CO calculations. In absence of a specific kinetic mechanism, the basic approximation of the basic species concentrations (N_2, O_2, CO_2, CO, H_2, $N^\bullet$, $O^\bullet$, $H^\bullet$, NO, $OH^\bullet$, SO_2, Ar) are performed according to (Olikara and Borman, 1975).

4.2.2 Nitrogen oxide (NO) kinetic models

Multiple parametrization of the rate coefficients of the EZM are available in the literature. In this work, the reaction rates from Heywood (Heywood, 1988) (basic model in GT-POWER), GRI mechanism (Smith et al.), and Baulch et al. (Baulch et al., 1994) were applied. Table 3 reports the coefficient sets for the considered EZM models.

Table 3. Forward rate coefficients of the considered EZM models as a function of temperature (T) in K.

Reaction	Forward rate coefficient in m³/(kmol·s)		
	Heywood (GT-P)	GRI	Baulch et al.
(1)	$7.6 \cdot 10^{10} \cdot e^{-38000/T}$	$5.44 \cdot 10^{10} \cdot T^{0.1} \cdot e^{-38020/T}$	$1.8 \cdot 10^{11} \cdot e^{-38248/T}$
(2)	$6.4 \cdot 10^{6} \cdot T \cdot e^{-3150/T}$	$9.0 \cdot 10^{6} \cdot T \cdot e^{-3273/T}$	$9.0 \cdot 10^{6} \cdot e^{-3247/T}$
(3)	$4.1 \cdot 10^{10}$	$3.36 \cdot 10^{10} \cdot T \cdot e^{-194/T}$	$2.8 \cdot 10^{10}$

4.2.3 Carbon Monoxide (CO) kinetic models

The basic GT-POWER CO kinetic model adopts the approach from Bowman (9) for the calculation of the forward reaction of CO oxidation, while the backward reaction is determined on the basis of the chemical equilibrium calculations from Olikara and Borman (Olikara and Borman, 1975).

Preliminary investigations have shown an underestimation tendency of this simplified kinetic approach and within this work an empirical calibration of this model has been undertaken. In particular, the expression in the function of engine speed (n_E) and relative air-to-fuel ratio (λ) has been derived in

order to improve the agreement between simulated and measured CO for the selected points. The calibration resulted in the change of the coefficients of (9) to:

$$A_{CO} = 0.08^{\lambda} \qquad\qquad B_{CO} = 8 \cdot \left(\frac{1000}{n_E}\right)^{1.65} \qquad\qquad (10)$$

4.2.4 Reduced kinetic mechanism

The reduced mechanism used within this work is a reduced version of the mechanism from Cai et al. (Cai et al., 2019) for TRF+E surrogates (Esposito et al., 2020b). In particular, the low temperature kinetics of the long-chain hydrocarbons (iso-octane and n-heptane) has been removed to improve the computational time, since the auto-ignition chemistry was not relevant for the burned zone kinetics. The mechanism consists of 239 species and 1068 reactions. The reaction mechanism includes the detailed NO_x formation mechanism from (Lamoureux et al., 2010), which contains the EZM plus detailed prompt-NO mechanism as well as the N_2O path. This oxidation mechanism has been implemented in the burned zone kinetics of the cylinder object within the GT-POWER model. In this way, the concentration of all the species content in the burned zone is calculated with the cylinder pressure, air-to-fuel ratio and burned temperature.

An important aspect to note is that this reduced kinetic mechanism implemented in the burned zone chemistry requires more than 100 times longer computational time than the simplified kinetic mechanisms (verified on a test case with GT-POWER v2019). The selected implicit solver was the "DVODE" from the "ODEPACK" from Lawrence Livermore National Laboratory (Gamma Technologies, 2019).

4.3. Unburned hydrocarbons (HC) phenomenological models

The selection of the HC-sources to be modeled in this work has been based on the importance of the source itself for the total HCs, on the modeling feasibility within the 0D/1D environment and on the possibility to extend the models to other engines.

The modeled HC-sources in this work are: piston-ring crevice, flame wall-quenching, and oil-film adsorption-desorption mechanisms. Fuel-film HC-source can have also a relevance for DI engines. However, its contribution is strongly dependent on 3D effect bound to fuel injection and fuel-film formation, highly variable with operating conditions. For this reason, the modeling of the fuel-film contribution requires likely a high calibration effort within 0D/1D and it is of difficult generalization and transferability to other engines. Similarly, combustion chamber deposits depend on engine state and history and their contribution can be very variable, therefore of difficult modeling.

4.3.1 Piston top-land crevice model

For the piston-top land crevice HC emissions, the common approach followed in literature (D'Errico et al., 2002; Dorsch et al., 2016; Frølund and Schramm, 1997; Janssen, 2010; Min and Cheng, 1994; Oliveira and Hochgreb, 1999; Schramm and Sorenson, 1990; Sodré and Yates, 1997; Trinker et al., 1993) of calculating the mixture in a certain volume with the ideal gas law has been adopted. The volume considered corresponds to the piston top-land up to the first compression ring and is approximately 0.2% of the engine displacement and about 2.3% of the compression volume. The calculation of the mass in the crevices m_{crev} is performed as following:

$$m_{crev} = \frac{V_{crev} \cdot p_{cyl}}{R_{mix} \cdot T_{crev}} \qquad\qquad (11)$$

In which p_{cyl} is the cylinder pressure, R_{mix} is the gas constant of the air-fuel mixture, and T_{crev} is the crevice temperature assumed as a weighted average between the unburned gas temperature (calculated from GT-POWER, 70%) and the liner and piston wall temperatures (30%). The relative air-to-fuel ratio λ in the crevices is assumed as 5% richer than the one in the main combustion chamber. Both the crevice temperature and the air-fuel ratio hypotheses have been based on 3D-CFD simulations of the same engine.

4.3.2 Flame wall-quenching model

The estimation of the contribution of the wall flame-quenching to the HC emissions is based on the the estimation of the quenching distance d_Q. This is performed with a correlation with the laminar flame thickness l_F, as:

$$d_Q = l_F \cdot Pe_Q = \frac{D_m}{s_L} \cdot Pe_Q \qquad (12)$$

In which D_m is the diffusion coefficient of the mixture and s_L the laminar flame speed, while Pe_Q is the Peclet number for the flame quenching, which has been found to be in the range of 5-10 (Amano and Okamoto, 2001; Heywood, 1988; Lavoie et al., 1970; Peters, 2010).

In this work, the correlation from (Suckart et al., 2017) has been selected, with an average Pe_Q of 7.7. The calculation of the laminar flame speed s_L for the TRF+E surrogate has been performed according to the work from (Hesse et al., 2018) and the diffusion coefficient D_m according to the approach of (Smooke and Giovangigli). Both calculations are performed at each time step depending on the actual cylinder pressure and the temperature in the unburned zone.

For the calculation of the surfaces that are contacted by the flame, a simplified geometric spherical propagation model has been included in the simulation model.

4.3.3 Oil-film adsorption-desorption model

The calculation of the HC contribution from oil-film adsorption-desorption is performed according to the work of (Dent and Lakshminarayanan, 1983), also applied from (Dorsch et al., 2016). This formulation simplifies the one dimensional Fick's law solution by considering an effective penetration length of the fuel in the oil. In this way, by calculating the mass transfer coefficient of the gas and the oil, the mass flux of the fuel into the oil can be calculated at each time step on the basis of the fuel concentration in the mixture and in the oil film, taking into account the Henry constant of the fuel components in the oil. The Henry constant for the TRF fuel components has been taken from the data of (Schramm and Sorenson, 1991) regarding the solubility in oil SAE 10W-40 (used on the test-bench), while the Henry constant for ethanol has been estimated based on the work of (Lima Ribeiro and Sodré, 2015).

4.3.4 HC post-oxidation model

Instead of using threshold temperature or one-step chemistry approaches to describe the post-oxidation of the HC in the expansion stroke, a model based on 0D chemistry calculation has been developed. Multiple 0D constant volume reactor calculations have been performed with the kinetic mechanism from (Cai et al., 2019). The simulation matrix included multiple pressure, temperature and composition (air-to-fuel ratio and residual gas) data. For the crevice and quenching HC sources, the oxidation of an unburned mixture composition is calculated, whereas for oil-film HC the desorption of only fuel in burned mixture is taken into account.

The results of the 0D calculations are translated in a C-atom equivalent oxidation ratio and implemented in form of tables in the GT-POWER model. The input temperature for the tables is an assumed near-wall temperature for crevice and quenching HC (30% wall temperature and 70% burned temperature, based on 3D-CFD simulations). While for the oil-HC the burned temperature is taken as reference.

For the quenching HC, the oxidation ratio calculated with the 0D reactor is reduced by means of a factor (constant for all the operating points) in order to take into account the diffusion resistance of the HC in the quenching layer from the boundary layer.

At each time step, the mass of HC generated from the single HC models is then multiplied for the oxidation ratio depending on the actual simulation time step (the oxidation in one single time step is considered). The HC mass emitted with the HC-models is then converted in a molar concentration C_3 equivalent at EVC and used for comparison with the measurement data.

5. Results

In the following, the results of the above-mentioned models are shown. It is important to note that the results are the sole prediction of the models without further calibration.

5.1. Nitrogen oxide (NO)

Figure 5 depicts the measured NO emissions for the operating points of Figure 2 and the relative deviation from simulation to measurement for all different NO models considered in this work: three EZM parametrizations and the reduced kinetic mechanism.

Regarding the predictions in stoichiometric operation on the p_{mi}- n_E map (see Figure 5 e, i, m, q), overall differences of ±15% can be seen. The Heywood EZM parametrization shows a tendency to underestimate NO at low loads, whereas with GRI EZM underestimations of over 15% occur of at low speeds and high loads. The EZM from Baulch et al. gives the best predictions on the p_{mi}- n_E plane, slightly better than the reduced kinetic mechanism because all the points show deviations below 15%.

Regarding the λ variations at different speeds (see Figure 5 f, j, n, r), all models show a tendency to underestimate the NO emissions in lean operation. The EZM from Heywood and GRI show again a stronger underestimation tendency than the other models. This applies to GRI also in rich operation. The results of the Baulch EZM and of the reduced kinetic mechanism show again a similar behaviour, with deviations below 15% up to λ = 1.2. The reduced kinetic mechanism shows a better agreement in lean operation at high speeds probably due to the more detailed NO mechanism. Additionally, the speed dependency of the prediction deviation of the reduced kinetic mechanism can be bound to the mixture homogeneity in the combustion chamber. Indeed, at higher speeds, the mixture homogeneity is higher due to a high charge motion level. Hence, the 0D description of the combustion chamber therefore is a better approximation of the reality than at low speeds.

The reduced kinetic mechanism, due to its detailed chemistry, seems to be more speed dependent than simplified kinetic models (as it will be seen also for the CO predictions in Figure 6).

Regarding valve timing variations at low loads (see Figure 5 g, k, o, s), all the models with exception of the Heywood EZM show similar trends, with an overestimation of NO maximum at the largest valve overlap. All the simulation models show an increase of NO with increasing valve overlap, due to an increase in intake pressure needed to keep the load constant, while the measurements show an opposite trend. This deviation can be caused by the impossibility of the 0D model to describe the 3D in-cylinder phenomena of the gas exchange in the cylinder and then to determine the correct composition of the internal residual gases for a high valve overlap. At high load, not throttled anymore (see Figure 5 h, l, p, t), the measurements are relative insensitive to the valve timing and this is predicted from the models too.
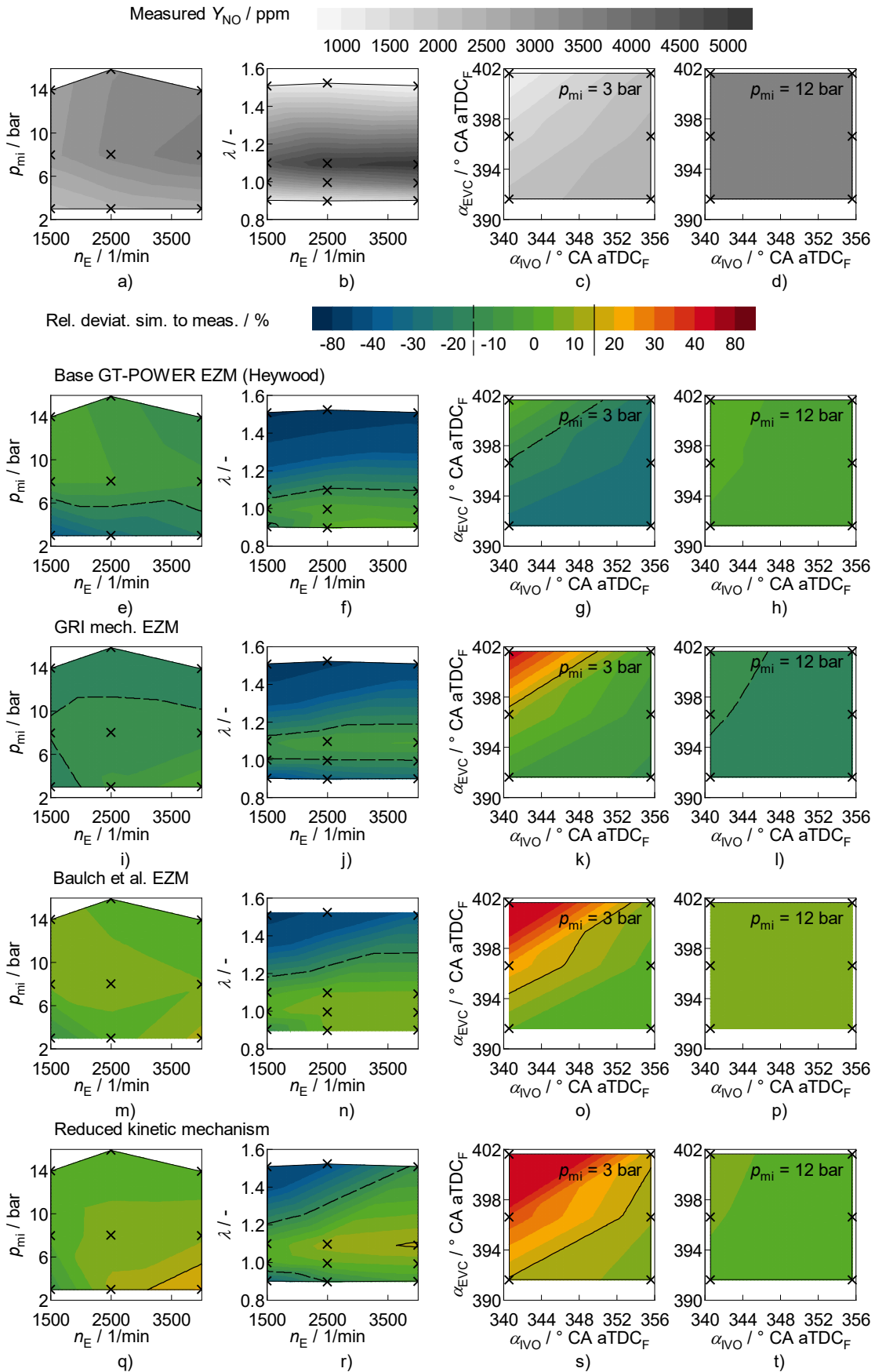
Fig. 5. Measured NO emissions (a-d) and relative deviations of the models: (e-h) Heywood, (i-l) GRI EZM, (m-p) Baulch et al. EZM, (q-t) reduced kinetic mechanism. Operating points from Figure 2.

5.2. Carbon monoxide (CO)

Figure 6 reports the measured CO emissions for the operating points of Figure 2 and the relative deviation of simulation to measurement for all the different CO models considered in this work: Bowman's kinetic approach in the base GT-POWER implementation and in a calibrated form as well as the reduced kinetic mechanism.
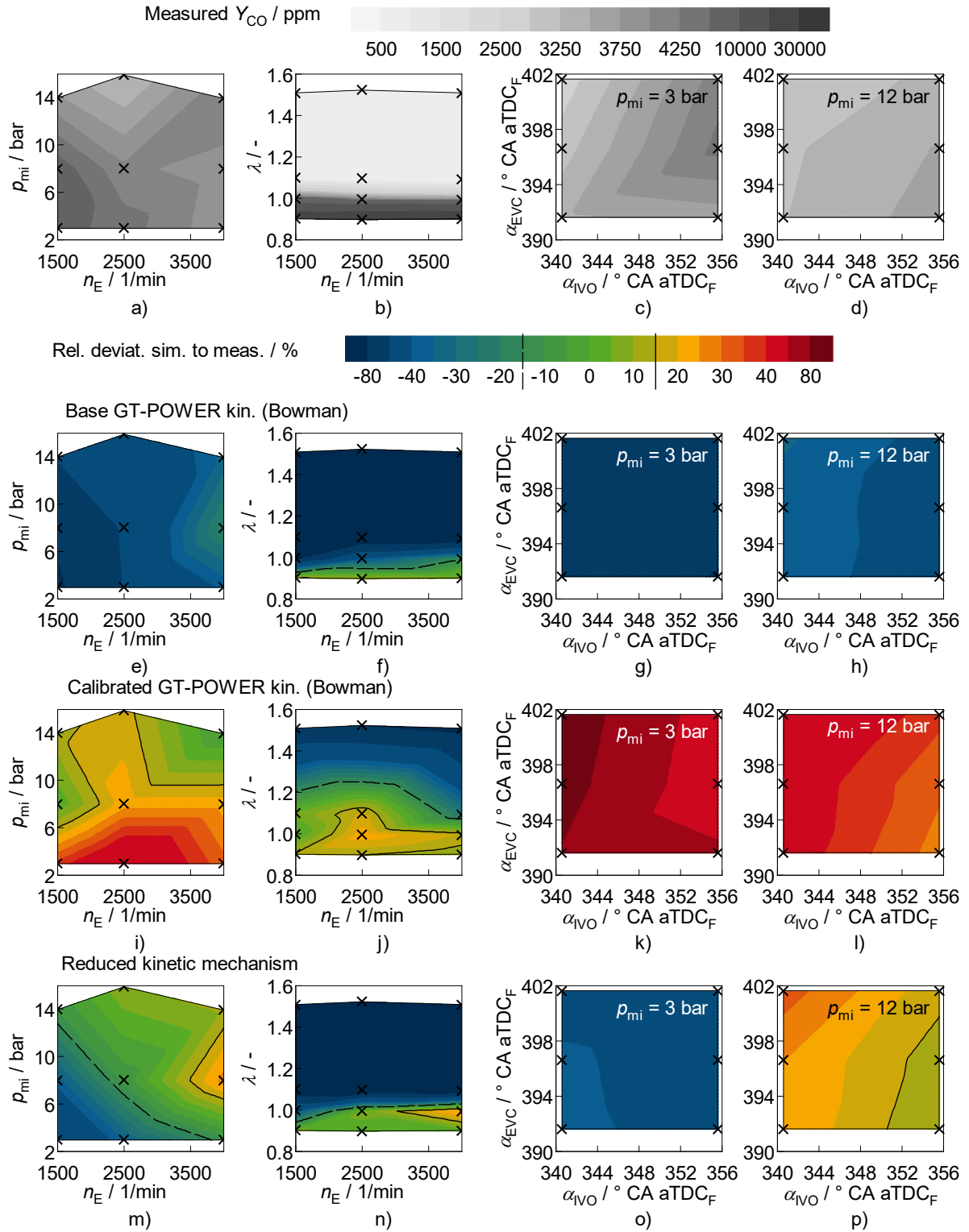

Fig. 6. Measured CO emissions (a-d) and relative deviations of the models: (e-h) base GT-POWER (Bowman), (i-l) calibrated Bowman (see (10), (m-p) reduced kinetic mechanism. Operating points from Figure 2.

In comparison to the NO prediction deviations, it can be seen that overall the deviations for the CO emissions are higher. There are high overestimations and underestimations and only relatively small areas present with differences below 15%. As anticipated at page 9, the basic implementation of the CO kinetic model of Bowman in GT-POWER results in a strong underestimation of the CO emissions (see Figure 6 e-h), with acceptable predictions only at rich operation. The calibrated version of this model (see Figure 6 i-l), allows a better prediction especially at slightly lean operation and at high loads. However, at low loads and with increased valve overlap strong overestimations result.

As far as the CO predictions of the reduced kinetic mechanism are concerned, more than half of the points in the p_{mi}- n_E map (see Figure 6 m) present deviations below 15%. Here, a strong speed-load dependency is visible. Due to the strong sensitivity of the CO emissions to mixture homogeneity, it is likely that the prediction of 0D simulations are better at higher speeds and loads at which the cylinder charge is better mixed. Regarding the predictions at different air-fuel ratios, a strong underestimation is observed at lean conditions. These 0D models are fundamentally incapable to predict CO emissions in lean operation because in these conditions CO does not originate from the burned zone, but from secondary phenomena like the late oxidation of the HCs expanding from the crevices.

To verify this aspect, the sensitivity to late HC oxidation of the CO emissions have been verified based on the input from 3D-CFD simulations with reaction kinetics (same reduced mechanism as the one used in GT-POWER for burned zone kinetics). The 3D-CFD geometry considers the piston-top land crevice geometry and for this reason it predicts the late oxidation of the HC from these crevices. The top plot of Fig. 7 compares the fuel mass fraction burned predicted with 3D-CFD with the one from TPA for a lean operating point. Even if the burning functions look very similar, the 3D-CFD simulation determines a slower fuel oxidation of the last ~1.5%. In the bottom plot of Figure 7, the effect of the burning function differences on the CO concentration in the cylinder is evaluated. The TPA burning function leads to a significantly lower CO values, since the CO is rapidly oxidized as soon as the heat release stops.

With the 3D-CFD burning function, the additional late fuel oxidation results in a further increase in CO and to substantially higher predicted CO values. The CO formation in the combustion chamber from the 3D-CFD simulation is different from the one in 1D-simulation, mainly because a non-zero CO concentration from residual gases is present at the start of the cycle. However, also the CO concentration in the 3D-CFD reveals an increase after 40° CA after TDC$_F$. This is qualitatively similar to what is observed in GT-POWER with the same burning function. Thus, the correct prediction of the last few percent of fuel burnt (linked to a crevice-HC post-oxidation model) is of crucial importance for a more realistic estimation of the CO emissions in lean operation within the 1D-simulation, although it is almost negligible for the matching of engine performance.
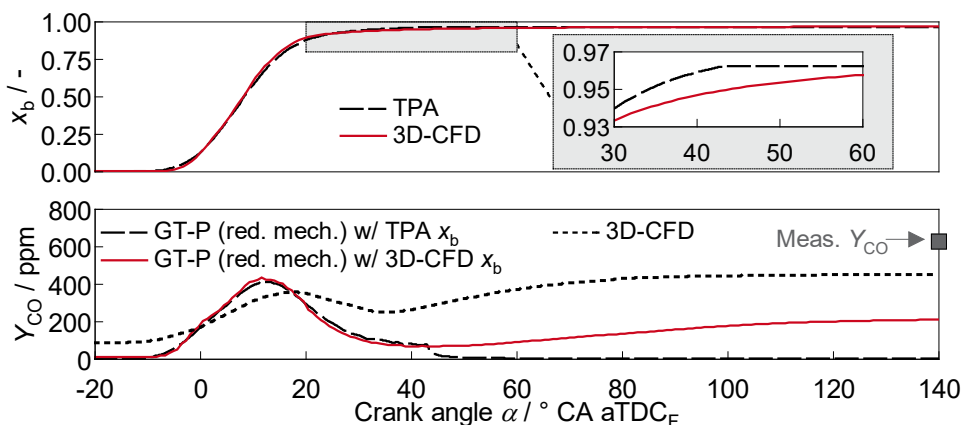

Fig. 7. Effect of burning function (x_b) on CO emission prediction in lean operation. Operating point: $n_E = 2500$ 1/min, $p_{mi} = 10$ bar, $\lambda = 1.5$. Top: comparison between the TPA burning function and the one calculated by means of 3D-CFD with reaction kinetics, which takes into account late oxidation of HC from the crevices. Bottom: in-cylinder predicted CO concentration with the different burning functions in GT-POWER with the reduced kinetic mechanism compared to 3D-CFD simulation.

5.3. Unburned hydrocarbons (HC)

Figure 8 reports the measured HC emissions for the operating points of Figure 2 and the relative deviation of the implemented phenomenological models to the measurements. Overall, it can be observed

that, despite the complexity of the HC mechanisms and the simplifications adopted in the modeling, in the majority of the operating points a deviation below 15% resulted.
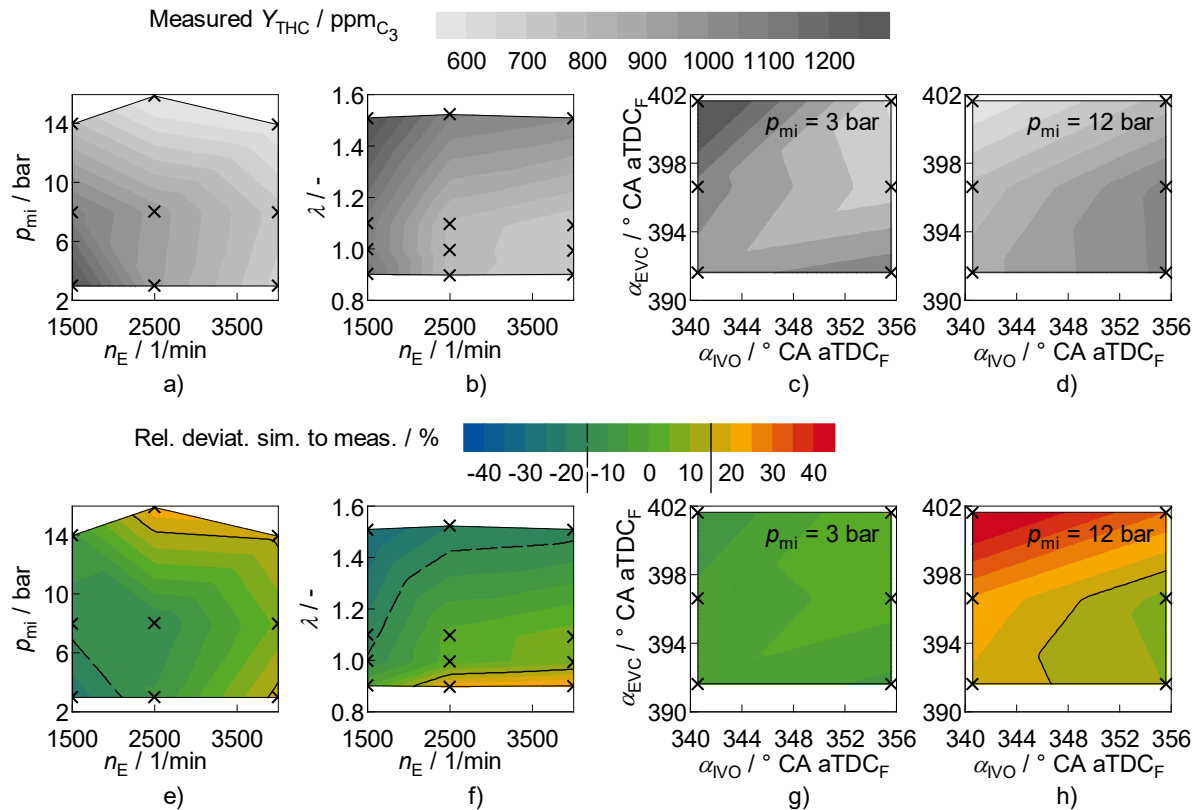

Fig. 8. Measured total HC emissions (a-d) and relative deviations of the HC-models (e-h). Operating points from Figure 2

The results are mainly influenced by the crevice-HC mechanism which contributes for over 90% to HC emissions at medium to high loads and stoichiometric operation, about 85% at low loads and up to 75% at lean operation. The oil-film HC contribution is almost constant at around 4-7%, while the quenching HC contributions are higher than 5% only at low loads (~10%) and in lean operation (up to 20%).

The underestimation at low loads and low speeds (see Figure 8 e) can be bound to mixture inhomogeneity, richer mixture in the crevices, partial burn effects, and formation of a fuel-film. These phenomena are not accounted for in the implemented model. The HC overestimation at high engine loads and speeds (see Figure 8 e) may be due to a reduction of the piston top-land crevice resulting from the piston thermal expansion. This is also currently not considered in the simulation model.

The underestimation at low loads and lean operation (see Figure 8 f) can again be bound not only to additional 3D phenomena regarding mixture formation and fuel, but also to incorrect estimation of the contribution of quenching-HC (especially post-oxidation). The HC-overestimation at rich operation and higher speeds (see Figure 8 f) can be bound to a faster HC oxidation in reality than what is predicted.

While at low loads the effect of valve overlap is correctly predicted (see Figure 8 g), at high loads (see Figure 8 h) the effect of the valve overlap is not correctly described by the HC-models. Indeed, the measurements show a reduction of HC with increasing valve overlap coming probably from the longer residence time of the HC in the combustion chamber that favours the HC post-oxidation. The simulation shows to be relative insensitive to this aspect due to the fact that the actual HC post-oxidation model is based on single time-steps and does not take into account the case in which a certain HC mass is oxidized over a longer residence time.

6. Conclusions

The present work shows the implementation and validation of predictive models for gaseous emissions from SI engines. The different approaches have been extensively validated and compared on over 30 operating points with varying engine speed, load, air-fuel ratio, and valve timing.

Multiple kinetic approaches have been used for the description of the CO and NO formation within the burned zone of the 0D two-zone combustion chamber description in GT-POWER.

The models for NO formation show overall a good predictivity with deviations in stoichiometric operation mainly within 20%. A general underestimation tendency of NO in lean operation is observed for all the models. This is probably due to the limits of the mixture homogeneity description of the 0D combustion chamber. Bound to the limitations of the 0D model is also the NO overestimation tendency with increasing valve overlap at low loads for the majority of the models. The best Extended Zeldovich Model (EZM) parametrization resulted to be the one from (Baulch et al., 1994), which shows the overall best results at stoichiometric conditions. However, the reduced kinetic mechanism shows comparable results in stoichiometric operation, but better predictivity in lean operation due to the presence of more complex NO mechanism. The outcome regarding the different kinetic descriptions is supposed to be extendable to 0D multi-zone approaches for the description of other combustion concepts (e.g., stratified mixture, pre-chamber, etc.).

The prediction of the CO emissions in a 0D environment resulted to be more challenging than the NO prediction. The usage of simplified kinetic approaches in combination with quite simplified equilibrium chemistry calculations is not sufficient to predict emissions with less than 30% deviation, even with additional calibration. The usage of a reduced fuel oxidation kinetic mechanism seems to improve the general description of the chemistry. However in stoichiometric operation, the effect of local mixture inhomogeneity is verifiable in the results. An increasingly better agreement is observed at higher engine speeds and loads due to higher mixture homogeneity in reality. This is better approximated with the 0D description. The prediction of CO at lean operation requires an accurate determination of the late fuel oxidation which is mainly linked to the crevice-HC mechanism. On this point, the coupling of the HC oxidation model with the calculated burning function can be a further development of the presented methodology and a possible outlook of this work.

Regarding HC prediction, phenomenological models have been implemented to account for the contributions of piston top-land crevice, wall flame-quenching, and oil-film fuel adsorption-desorption. The models overall show deviations mainly within 20%. Overestimation at high loads can be due to the reduction of the piston top-land crevice resulting from the thermal expansion of the piston during real fired operation. While underestimation at low loads and low speeds can be linked to not modeled phenomena like fuel-film or partial burn. The HC post-oxidation model could be further developed in order to take into account longer residence times in the combustion chamber, which may have an impact in case of increased valve overlap at high loads. Only the wall flame-quenching model is specifically implemented for SI combustion and a spherical flame propagation. The other models could be applied to other combustion concepts as well.

Acknowledgements

References

Albuquerque PCC de, Andrade Ávila RN de, Barros Zárante PH, et al. (2011) Lubricating oil influence on exhaust hydrocarbon emissions from a gasoline fueled engine. *Tribology International* 44(12): 1796–1799.

Alkidas AC (1999a) Combustion-chamber crevices: The major source of engine-out hydrocarbon emissions under fully warmed conditions. *Progress in Energy and Combustion Science* 25(3): 253–273.

Alkidas AC (1999b) The Effects of Head Gasket Geometry on Engine-Out HC Emissions from S.I. Engines. *SAE Technical Paper 1999-01-3580*. DOI: 10.4271/1999-01-3580.

Amano T and Okamoto K (2001) Uuburned Hydrocarbons Emission Source from Engines. *SAE Technical Paper 2001-01-3528*. DOI: 10.4271/2001-01-3528.

Anderlohr J, Bounaceur R, Piresdacruz A, et al. (2009) Modeling of autoignition and NO sensitization for the oxidation of IC engine surrogate fuels. *Combustion and Flame* 156(2): 505–521.

Arsie I, Pianese C and Rizzo G (2003) An Integrated System of Models for Performance and Emissions in SI Engines: Development and Identification. *SAE Technical Paper 2003-01-1052*. DOI: 10.4271/2003-01-1052.

Baulch DL, Cobos CJ, Cox RA, et al. (1994) Compilation of rate data for combustion modeling. Supplement I. *Journal of Physical and Chemical Reference Data* 23: 847.

Bhat V and Tamma B (2014) Development of Multi-Zone Phenomenological Model for SI Engine. *SAE Technical Paper 2014-01-1068*. DOI: 10.4271/2014-01-1068.

Bhave A and Kraft M (2004) Partially Stirred Reactor Model: Analytical Solutions and Numerical Convergence Study of a PDF/Monte Carlo Method. *SIAM Journal on Scientific Computing* 25(5): 1798–1823.

Bowman CT (1975) Kinetics of pollutant formation and destruction in combustion. *Progress in Energy and Combustion Science* 1(1): 33–45.

Cai L, Ramalingam A, Minwegen H, et al. (2019) Impact of exhaust gas recirculation on ignition delay times of gasoline fuel: An experimental and modeling study. *Proceedings of the Combustion Institute* 37(1): 639–647.

Cao L, Su H, Mosbach S, et al. (2008) Studying the Influence of Direct Injection on PCCI Combustion and Emissions at Engine Idle Condition Using Two Dimensional CFD and Stochastic Reactor Model. *SAE Technical Paper 2008-01-0021*. DOI: 10.4271/2008-01-0021.

Cheng WK, Hamrin D, Heywood JB, et al. (1993) An Overview of Hydrocarbon Emissions Mechanisms in Spark-Ignition Engines. *SAE Technical Paper 932708*. DOI: 10.4271/932708.

Chindaprasert N, Hassel E, Nocke J, et al. (2006) Prediction of CO Emissions from a Gasoline Direct Injection Engine Using CHEMKIN. *SAE Technical Paper 2006-01-3240*. DOI: 10.4271/2006-01-3240.

Da Silva LLC and Nigro FEB (2000) Modeling of Hydrocarbons Formation and Emission in Gas Engines. *SAE Technical Paper 2000-01-2038*. DOI: 10.4271/2000-01-2038.

Dent JC and Lakshminarayanan PA (1983) A Model for Absorption and Desorption of Fuel Vapour by Cylinder Lubricating Oil Films and Its Contribution to Hydrocarbon Emissions. *SAE Technical Paper 830652*. DOI: 10.4271/830652.

D'Errico G, Ferrari G, Onorati A, et al. (2002) Modeling the Pollutant Emissions from a S.I. Engine. *SAE International*. DOI: 10.4271/2002-01-0006.

Dodge LG, Kubesh JT, Naegeli DW, et al. (1998) Modeling NOx Emissions from Lean-Burn Natural Gas Engines. *SAE International*. DOI: 10.4271/981389.

Dorsch M, Neumann J and Hasse C (2016) Application of a Phenomenological Model for the Engine-Out Emissions of Unburned Hydrocarbons in Driving Cycles. *Journal of Energy Resources Technology* 138(2): 22201.

Drake MC and Blint RJ (1991) Calculations of NOx Formation Pathways in Propagating Laminar, High Pressure Premixed CH4/Air Flames. *Combustion Science and Technology* 75(4-6): 261–285.

Dryer F, Naegeli D and Glassman I (1971) Temperature dependence of the reaction CO + OH = CO2 + H. *Combustion and Flame* 17(2): 270–272.

Eng JA (2005) The Effect of Spark Retard on Engine-out Hydrocarbon Emissions. *SAE Technical Paper 2005-01-3867*. DOI: 10.4271/2005-01-3867.

Esposito S (2020) Analysis of Gaseous Pollutant Emissions from Spark-Ignition Engines. Ph.D. thesis, RWTH Aachen University.

Esposito S, Cai L, Günther M, et al. (2020) Experimental comparison of combustion and emission characteristics between a market gasoline and its surrogate. *Combustion and Flame* 214: 306–322.

Esposito S, Mally M, Cai L, et al. (2020b) Validation of a RANS 3D-CFD Gaseous Emission Model with Space-, Species-, and Cycle-Resolved Measurements from an SI DI Engine. *Energies* 2020, 13, 4287. DOI: 10.3390/en13174287.

Esposito S, Mauermann P, Lehrheuer B, et al. (2019) Effect of Engine Operating Parameters on Space- and Species-Resolved Measurements of Engine-Out Emissions from a Single-Cylinder Spark Ignition Engine. *SAE Technical Paper 2019-01-0745*. DOI: 10.4271/2019-01-0745.

Fenimore CP (1971) Formation of nitric oxide in premixed hydrocarbon flames. *Symposium (International) on Combustion* 13(1): 373–380.

Flagan RC and Seinfeld JH (1988) *Fundamentals of air pollution engineering*. Englewood Cliffs, NJ: Prentice Hall.

Frølund K and Schramm J (1997) Simulation of HC-Emissions from SI-Engines - A Parametric Study. *SAE Technical Paper 972893*. DOI: 10.4271/972893.

Gamma Technologies (2018) *GT-SUITE 2018: Engine Performance Application Manual*.

Gamma Technologies (2019) *GT-SUITE 2019.: Engine (GT-POWER) reference templates*.

Grill M (2006) Objektorientierte Prozessrechnung von Verbrennungsmotoren. Ph.D. thesis, Universität Stuttgart.

Hesse R, Beeckmann J, Wantz K, et al. (2018) Laminar Burning Velocity of Market Type Gasoline Surrogates as a Performance Indicator in Internal Combustion Engines. *SAE Technical Paper 2018-01-1667*. DOI: 10.4271/2018-01-1667.

Heywood JB (1988) *Internal combustion engine fundamentals*. New York: McGraw-Hill.

Hochgreb S (1998) Combustion-Related Emissions in SI Engines. In: Sher E (ed.) *Handbook of Air Pollution From Internal Combustion Engines:* Elsevier, pp. 118–170.

Holly WE, Lauer T, Schuemie HA, et al. (2016) Prediction of the knocking combustion and NOx formation for fuel gases with different methane numbers. *International Journal of Engine Research* 17(1): 35–43.

Huang Z, Pan K, Li J, et al. (1996) An Investigation on Simulation Models and Reduction Methods of Unburned Hydrocarbon Emissions in Spark Ignition Engines. *Combustion Science and Technology* 115(1-3): 105–123.

Ihsan Karamangil M, Sürmen A and Yenice S (2014) Mathematical modeling of hydrocarbon emissions from oil film for different fuels. *Fuel* 115: 818–825.

Janssen C (2010) Möglichkeiten zur Prädiktion von unverbrannten Kohlenwasserstoffen in einem direkteinspritzenden Ottomotor. Ph.D. thesis, Universität Rostock.

Lamoureux N, Desgroux P, El Bakali A, et al. (2010) Experimental and numerical study of the role of NCN in prompt-NO formation in low-pressure CH4–O2–N2 and C2H2–O2–N2 flames. *Combustion and Flame* 157(10): 1929–1941.

Lavoie G and Blumberg PN (1980) A Fundamental Model for Predicting Fuel Consumption, NO x and HC Emissions of the Conventional Spark-Ignited Engine. *Combustion Science and Technology* 21(5-6): 225–258.

Lavoie GA (1978) Correlations of Combustion Data for S. I. Engine Calculations - Laminar Flame Speed, Quench Distance and Global Reaction Rates. *SAE Technical Paper 780229*. DOI: 10.4271/780229.

Lavoie GA and Blumberg PN (1973) Measurements of NO Emissions From a Stratified Charge Engine: Comparison of Theory and Experiment. *Combustion Science and Technology* 8(1-2): 25–37.

Lavoie GA, Heywood JB and Keck JC (1970) Experimental and Theoretical Study of Nitric Oxide Formation in Internal Combustion Engines. *Combustion Science and Technology* 1(4): 313–326.

Liberman MA (2008) *Introduction to Physics and Chemistry of Combustion*. Berlin Heidelberg: SpringerVerlag.

Lima Ribeiro K de and Sodré JR (2015) Henry's constants for ethanol, iso-octane and gasoline absorption in engine lubricants. *Lubrication Science* 27(4): 231–239.

Lorusso JA, Kaiser EW and Lavoie G (1983) In-Cylinder Measurements of Wall Layer Hydrocarbons in a Spark Ignited Engine. *Combustion Science and Technology* 33(1-4): 75–112.

Mehrnoosh D, Asghar HA and Asghar MA (2012) Thermodynamic model for prediction of performance and emission characteristics of SI engine fuelled by gasoline and natural gas with experimental verification. *Journal of Mechanical Science and Technology* 26(7): 2213–2225.

Merker GP (2006) *Simulating combustion: Simulation of combustion and pollutant formation for engine-development*. Berlin, New York: Springer.

Merker GP and Teichmann R (eds) (2014) *Grundlagen Verbrennungsmotoren*. Wiesbaden: Springer Fachmedien Wiesbaden.

Miller R, Davis GC, Lavoie G, et al. (1998) A Super-Extended Zel'dovich Mechanism for Nox Modeling and Engine Calibration. *SAE Technical Paper 980781*. DOI: 10.4271/980781.

Min K and Cheng WK (1994) In Cylinder Oxidation of the Piston-Crevice Hydrocarbon in SI-Engines. *International Symposium COMODIA 94*.

Min K and Cheng WK (1995) Oxidation of the Piston Crevice Hydrocarbon During the Expansion Process in a Spark Ignition Engine. *Combustion Science and Technology* 106(4-6): 307–326.

Morcinkowski B, Adomeit P, Mally M, et al. (eds) (2020) *Emissionsvorhersage in der Entwicklung ottomotorischer EU7-Antriebe*.

Moskaleva LV and Lin MC (2000) The spin-conserved reaction CH+N2→H+NCN: A major pathway to prompt no studied by quantum/statistical theory calculations and kinetic modeling of rate constant. *Proceedings of the Combustion Institute* 28(2): 2393–2401.

Olikara C and Borman GL (1975) A Computer Program for Calculating Properties of Equilibrium Combustion Products with Some Applications to I.C. Engines. *SAE Technical Paper 750468*. DOI: 10.4271/750468.

Oliveira IB and Hochgreb S (1999) Effect of Operating Conditions and Fuel Type on Crevice HC Emissions: Model Results and Comparison with Experiments. *SAE Technical Paper 1999-01-3578*. DOI: 10.4271/1999-01-3578.

Peters N (2010) *Combustion Theory: CEFRC Summer School Princeton June 28th - July 2nd*.

Schramm J and Sorenson SC (1990) A Model for Hydrocarbon Emissions from SI Engines. *SAE Technical Paper 902169*. DOI: 10.4271/902169.

Schramm J and Sorenson SC (1991) Solubility of gasoline components in different lubricants for combustion engines determined by gas—liquid partition chromatography. *Journal of Chromatography A* 538(2): 241–248.

Smith GP, Golden DM, Frenklach M, et al. GRI-Mech 3.0. Available at: http://www.me.berkeley.edu/gri_mech/.

Smooke MD and Giovangigli V Formulation of the premixed and nonpremixed test problems. In: *Reduced Kinetic Mechanisms and Asymptotic Approximations for Methane-Air Flames.:* pp. 1–28.

Sodré JR (1999) Further Improvements on a HC Emissions Model: Partial Burn Effects. *SAE Technical Paper 1999-01-0222*. DOI: 10.4271/1999-01-0222.

Sodré JR and Yates DA (1997) An Improved Model for Spark Ignition Engine Exhaust Hydrocarbons. *SAE Technical Paper 971011*. DOI: 10.4271/971011.

Soete GG de (1975) Overall reaction rates of NO and N2 formation from fuel nitrogen. *Symposium (International) on Combustion* 15(1): 1093–1102.

Suckart D, Linse D, Schutting E, et al. (2017) Experimental and simulative investigation of flame–wall interactions and quenching in spark-ignition engines. *Automotive and Engine Technology* 2(1-4): 25–38.

Tinaut FV, Melgar A and Horrillo AJ (1999) Utilization of a Quasi-Dimensional Model for Predicting Pollutant Emissions in SI Engines. DOI: 10.4271/1999-01-0223.

Trinker FH, Cheng J and Davis GC (1993) A Feedgas HC Emission Model for SI Engines Including Partial Burn Effects. *SAE Technical Paper 932705*. DOI: 10.4271/932705.

Warnatz J, Maas U and Dibble RW (2006) *Combustion: Physical and chemical fundamentals, modeling and simulation, experiments, pollutant formation*. Berlin, New York: Springer.

Yildirim AM, Gul MZ, Ozatay E, et al. (2006) Simulation of Hydrocarbon Emissions from an SI Engine. *SAE International Journal of Engines*. DOI: 10.4271/2006-01-1196.

Yu S and Min K (2002) Effects of the oil and liquid fuel film on hydrocarbon emissions in spark ignition engines. *Proceedings of the Institution of Mechanical Engineers, Part D: Journal of Automobile Engineering* 216(9): 759–771.

Zeldovich YB (1946) The oxidation of nitrogen in combustion and explosions,. *Acta Physiochimica, USSR*(Vol. 21): 577–628.

Sub-23 nm Particle Emissions from Internal Combustion Engines for Future Certification and Evaluation of Calibration Methods

P. Kreutziger[1], Y. Otsuki[1], L. Japs[1], M. Rieker[1], A. Pérez Martínez[2] and S. Paz Estivill[2]

[1]HORIBA Europe GmbH, Hans-Mess-Str. 6, 61440 Oberursel, Germany

E-mail: philipp.kreutziger@horiba.com
Telephone: +(49) 6172 1396-0

[2] IDIADA Automotive Technology SA, L'Albornar E-43710, Santa Oliva (Tarragona), Spain

Abstract. On-road motor vehicles are important sources of ultra-fine particulate matter (PM) emissions, which present acknowledged health and environmental risks. The Horizon 2020 PEMS4Nano project (www.pems4nano.eu) is providing a contribution to future regulations on emissions in laboratory environment as well as real driving conditions due to a current lack of certification methods. To detect the smallest size of the particles below 23 nm, with a threshold from at least 10 nm onwards, two different systems have been optimized according to the targets. Due to higher particle losses for sub-23 nm particles inside of the stationary system and portable emission measurement system (PEMS), it is observed that the differences in calibration methods can cause higher deviations between these instruments. However, the systems show a good agreement during exhaust measurement tests and similar tendencies against conventional particle number measurement systems, as current legislation requires. Within this study, different vehicle types and sampling positions have been evaluated and a comparison regarding the different calibration methods is done.

Notation

CAST	*Combustion Aerosol STandard*
CPC	*Condensation Particle Counter*
CS	*Catalytic Stripper*
CVS	*Constant Volume Sampling*
D_{50}	*Lower detection limit (Particle Diameter) where the detection efficiency equals 50%*
ET	*Evaporation Tube*
FCAE	*Faraday-Cup Aerosol Electrometer*
GDI	*Gasoline Direct Injection*
GPF	*Gasoline Particle Filter*
ICE	*Internal Combustion Engine*
LDV	*Light Duty Vehicle*
NO_2	*Nitrous Dioxide*
NO_x	*Nitrous Oxide*
PAO	*Poly-Alpha-Olefin*
PCRF	*Particle Concentration Reduction Factor*
PEMS	*Portable Emission Measurement System*
PEMS-10	*PEMS for sub-23 nm measurement (threshold 10 nm)*
PM	*Particulate Matter*
PMP	*Particle Measurement Programme*
PN	*Particle Number*
PNC	*Particle Number Counter*
RDE	*Real Driving Emission*
SPCS	*Solid Particle Counting System*
SPCS-10	*SPCS for sub-23 nm measurement (threshold 10 nm)*
SPCS-AVACS	*Automated Validation and Calibration System for SPCS and PEMS use*
UNECE	*United Nations Economic Commission for Europe*
VPR	*Volatile Particle Remover*
WLTC	*Worldwide harmonized Light duty driving Test Cycle*

P. Kreutziger, Y. Otsuki, L. Japs, M. Rieker, A. Pérez Martínez and S. Paz Estivill

1. Introduction

Atmospheric pollution levels are not decreasing in Europe, especially components like Nitrogen Dioxide (NO₂) and Particulate Matter (PM), even though the emission regulations in the automotive industry are getting stricter (Weiss et al. 2001). PM measurement methodology utilizing gravimetric mass determination is approaching its detection limit, therefore the Particle Measurement Programme (PMP), under United Nations Economic Commission for Europe (UNECE), has developed the PN measurement methodology and the desired testing protocols for the PN emissions certification for vehicles at the chassis dynamometer (UNITED NATIONS 2015). The PMP system consists of the Volatile Particle Remover (VPR) and the Particle Number Counter (PNC). The cut-off diameter is defined as the particle diameter of 50% detection efficiency (D_{50}). For current certification methods the D_{50} is defined with ±12% at 23 nm and in addition the PNC requires a detection efficiency ≥90% at 41 nm (ISO/TC 24/SC 4 2015). The draft regulation for sub-23 nm considers at 10 nm a detection efficiency at 65% with ±15% and at 15 nm ≥90%. In addition, PN PEMS must meet these targets also to fulfill the Real Driving Emission (RDE) regulation (EUROPEAN COMMISSION 2017).

As there are differences in the system configurations and calibration procedures between a laboratory PMP system and PN PEMS, the detection efficiencies of these instruments are not perfectly matching. Especially when many small particles are emitted in the area of the D_{50}, these differences can cause significant disagreements in laboratory measurement and on-board measurements (Otsuki et al. 2019).

A contribution of the Horizon 2020 project PEMs4Nano is to evaluate the feasibility of future regulation and calibration methods to drive the implementation of sub-23 nm measurements. The purpose of this paper is to evaluate and validate the observed differences between portable and laboratory systems on engine exhaust measurements with gasoline vehicles equipped with and without Gasoline Particle Filter (GPF).

2. Calibration of Solid Particle Number Measurement Systems

Measurement differences between stationary and on-board PN measurement systems are observed due to a lot of influencing factors and due to the diverse application and use case of these devices. Apart from all other influencing factors there is the potential to observe variations in the results of the PN concentration due to the different calibration procedures (Otsuki et al. 2019).

It is also challenging to generate enough small particles for the calibration and to detect small particles as the European emission regulation might require in the future. This is caused by the higher particle losses in sub-23 nm regime (Otsuki et al. 2014), especially in the case of PN PEMS.

In the following sections the currently used sub-23 nm calibrations of the systems used in the experiment (Solid Particle Counting System with a threshold of at least 10 nm – SPCS-10 and Portable Emission Measurement System for PN with a threshold of at least 10 nm – PEMS-10) are explained and the differences between the systems are compared.

2.1 SPCS

To accurately calibrate the stationary SPCS according to the PMP procedure following the Regulation No. 83 for Light Duty Vehicle (LDV) a two-step approach is considered (UNITED NATIONS, 2015).

First, the Condensation Particle Counter (CPC) must be calibrated against a reference device, here by a Faraday-Cup Aerosol Electrometer (FCAE). The aerosol which is used is a Poly-Alpha-Olefin (PAO) also known as Emery Oil. The detection efficiency has been evaluated for the particle sizes of 10 nm, 23 nm, 41 nm and 55 nm (Horn 2017). To adjust the cut-off curve and the particle size dependency, the temperatures in the instrument can be adjusted and a correction factor is applied. Here the Temperature of the Saturator (T_S) has been set to 39°C and the Condenser (T_C) to 19°C. A correction factor of 1,07 (defined as k-factor) has been applied.

Second, the system is calibrated against the particle losses. The main factor which will be measured and calculated here is the Particle Concentration Reduction Factor (PCRF). The usual procedure to calculate the PCRF (f_r) is shown by Eq. 2. For the particle sizes of 30 nm, 50 nm and 100 nm the losses are measured (United Nations 2015). N_{in} and N_{out} are PN concentrations at the inlet and outlet of the VPR, respectively.

$$f_r(d_p) = \frac{N_{in}}{N_{out}} \qquad (1)$$

$$f_r = \frac{f_r\,(30nm) + f_r\,(50nm) + f_r\,(100nm)}{3} \qquad (2)$$

In this study, the PCRF has been calculated in addition for 15 nm and 23 nm, however, these values are only there for comparison reasons and will not be implemented to the correction method, to maintain the comparability between commercial available 23 nm measurements systems and future sub-23 nm measurement systems (Maier 2018).

2.2 PEMS

To accurately calibrate a PN PEMS, at the end, it requires a system efficiency of the desired measurement equipment. As the device to calibrate consists of a CPC the two-step approach from sub-section 2.1 is followed.

First, the condensation particle counter has been calibrated with thermally treated Combustion Aerosol STandard (CAST) soot particles to a detection efficiency slightly above 50% at 10 nm. The temperatures of the CPC have been adjusted to $T_S = 36°C$ and $T_C = 20°C$ (Horn 2018).

Second, the losses within the system are measured and afterwards they are corrected. There is not such a definition for the PCRF like in Eq. 2. For that reason, it has been decided to measure the particle losses at a particle diameter of 200 nm to determine the PCRF (here called C_0-factor). After applying this factor, the system efficiency is measured (Kreutziger 2018).

2.3 Comparison of sub-23 nm calibration procedures

The main differences of the calibration of sub-23 nm devices are dependent on the detection efficiency of the condensation particle counters. However, the compensation of particle losses and correction factors are differently applicated. For laboratory systems, the CPC and the system are evaluated separately, and correction factors are applicated independent. The PCRF is calculated according to Eq. 2, because it can be measured against the same reference CPC. For a PN PEMS, only one correction factor is used at 200 nm, even though, this factor is size-dependent. Due to the simplicity of the instrument, the factor cannot be measured before and after the VPR with the same CPC, so it is mandatory to measure in the plateau region of the instrument under test and the reference CPC.

3. Experiments and Results

3.1 Calibration Results

The detection efficiency of the SPCS-10 CPC is higher due to initial calibration and k-factor correction. To achieve an efficiency greater than 50% with soot-like CAST aerosol, the target at 10 nm was set to 70% efficiency (Horn 2017). The results of the CPC calibration are shown in Fig. 1.
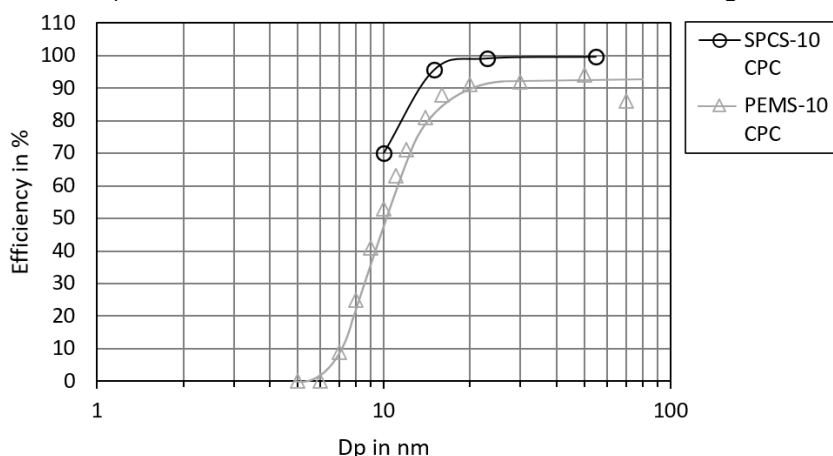

Fig. 1. Size dependent detection efficiency for CPC used in SPCS-10 (k-factor corrected) and in PEMS-10

Once the CPC has been calibrated the particle losses within the system are evaluated. The increase of particle losses (normalized to 100 nm particles for the SPCS-10 and normalized to 200 nm particles for the PEMS-10) is shown in Fig. 2. These losses of PEMS and SPCS are relatively comparable at particle sizes from 30 nm to 200 nm. Below 30 nm, especially in the sub-23 nm regime, the PEMS-10 device performance shows less detection efficiency of these particles due to the higher simplicity of its design and lower flow rates. At 15 nm the increase in particle losses is more than twice as much as in the SPCS-10, with a value above 200% in comparison to 200 nm particles.
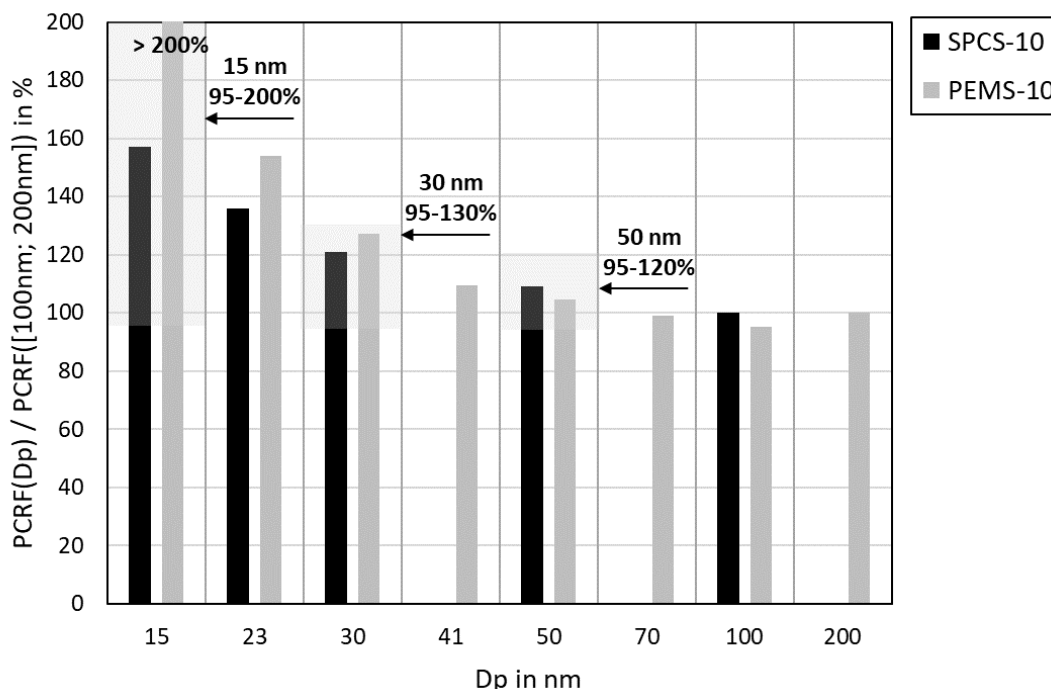
Fig. 2. Size dependent PCRF in SPCS-10 and PEMS-10

The overall detection efficiency (here system efficiency) has been evaluated with the applied correction factors (calculated for SPCS-10 and measured for PEMS-10). Shown in Fig. 3, it is visible that the overall particle system detection efficiency of the SPCS-10 is always > 5% for particle sizes between 30 nm to 100 nm. Below 30 nm, especially in the sub-23 nm regime, the detection efficiency of these particle sizes drifts even more apart. At 15 nm, there is already a deviation of around 30% noticeable. The general offset between the two instruments can be explained by calibration, but the higher deviation at smaller particle sizes can be caused by different amounts of particle losses, in example by diffusional losses due to a more simplified design in the PEMS as well as lower flows.
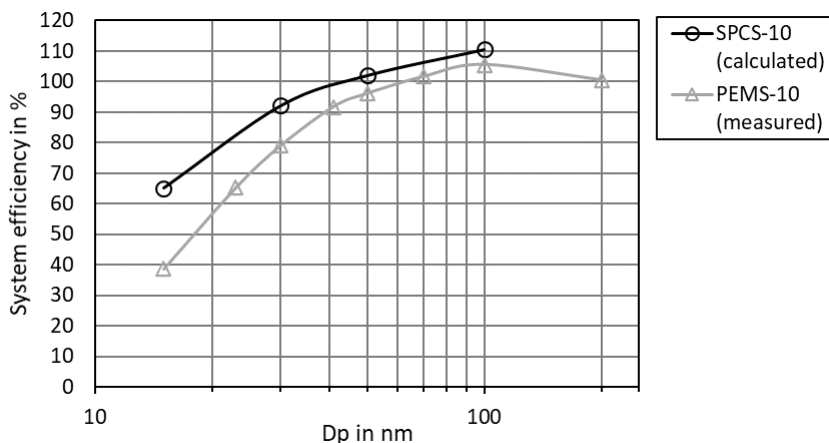

Fig. 3. Size dependent system efficiency in SPCS-10 and PEMS-10

3.2 Validation of Calibration Results with SPCS-AVACS

The validation measurements of the initial calibration have been performed with the Solid Particle Counting System – Automated Validation and Calibration System (SPCS-AVACS) according to the schematic shown in Fig. 4.
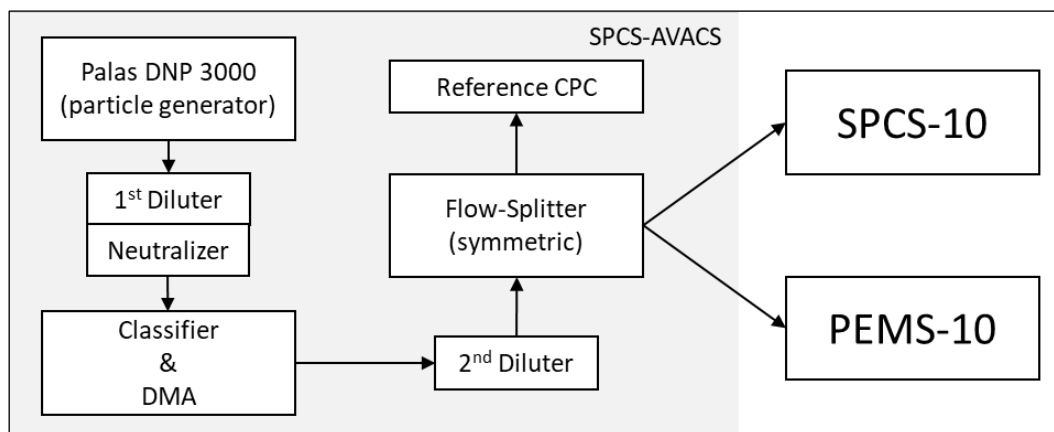

Fig. 4. Measurement setup for validation of particle penetration investigation with SPCS-AVACS

In Figure 5 the results of the SPCS-AVACS measurements are shown and the differences in comparison to Fig. 3 are as expected, relatively similar. However, looking more deeply in the area of the sub-30 nm regime, the system efficiency for both instruments decrease slightly. A difference in total PN (P/km) for the chassis dynamometer tests is expected, which can be explained by the maintaining gap between the detection efficiencies of SPCS-10 and PEMS-10. The concentration for the PEMS-10 device is lower.
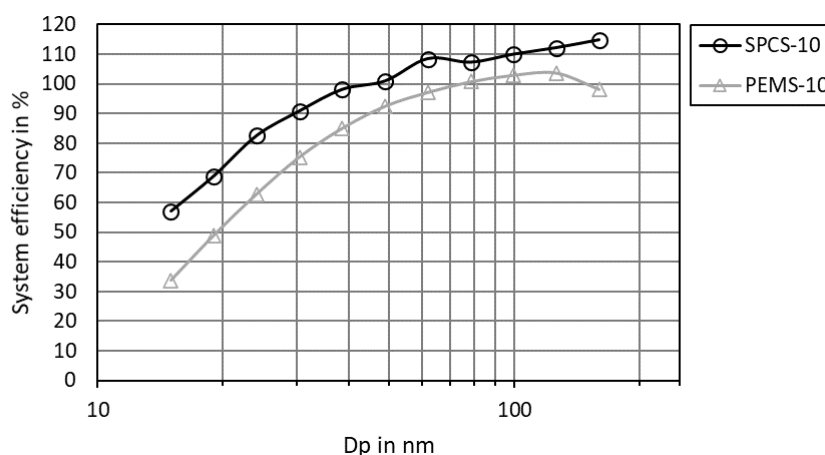
Fig. 5. Size dependent measured system efficiency in SPCS-10 and PEMS-10 for validation with SPCS-AVACS

3.3 Results at Chassis Dynamometer

The amount of the difference between PEMS-10 and SPCS-10 during chassis dynamometer testing cannot be determined with a simple offset (in example by 10%) due to differences of the particle size distributions of several engine technologies. Engine and aftertreatment technologies are responsible for the emitted number of particles in the desired size range. In general Gasoline Direct Injection (GDI) vehicles have bigger amounts of particles in the size range of 40 nm to 60 nm, but also have a higher contribution in the sub-23 nm regime. By applying a GPF, the amount of sub-23 nm particles is reduced significantly (Kassel et al. 2013). It is expected that the GPF equipped GDI's have less measurement differences between PEMS-10 and SPCS-10 because of the minor number of particles in the sub-23 nm regime. At these vehicle classes, the particle penetration differences in the measurement systems are not significantly influencing the measurement results. However, this behavior can be influenced by other factors like the connection of the measurement devices at different sampling positions at the CVS

tunnel, or by using the method of sampling from the tailpipe, where the exhaust mass flow of the vehicle needs to be calculated.

In Figure 6 the general schematic of the locations of the test equipment (PEMS-10 and SPCS-10) is shown. For comparison reasons, it is suggested to apply the PEMS-10 and the SPCS-10 at the Constant Volume Sampling (CVS) tunnel to avoid any influences of the measurement caused by other effects, in example by pressure pulsation or the need to read the exhaust mass flow at tailpipe. It is expected, that the particle number concentration of a PEMS at the tailpipe is lower than in comparison to the measurement at the CVS tunnel (Stanard 2018).
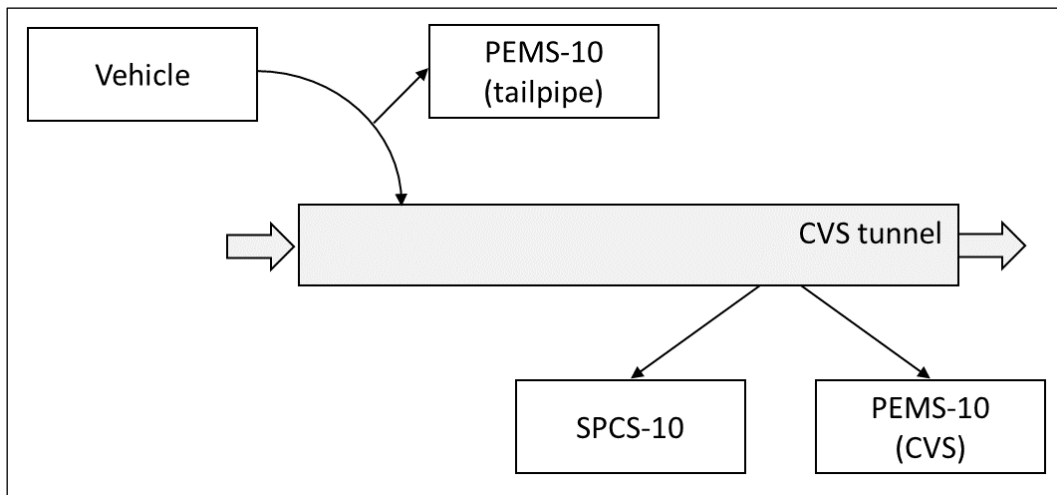
Fig. 6. Measurement setup for exhaust PN of vehicles with and without GPF

The tests carried out in this study are different from the ones carried out in the certification method, whereas the vehicle without GPF (vehicle 1) has to meet a PN target of 6×10^{12} P/km during the New European Driving Cycle, and the vehicle with GPF (vehicle 2) has to meet a PN target of 6×10^{11} P/km during the Worldwide harmonized Light duty driving Test Cycle (WLTC). For comparison reasons, both vehicles have been tested according to WLTC procedure at 23°C on a chassis dynamometer (UNITED NATIONS 2015). Vehicle 1 has been tested at HORIBA Testcenter in Oberursel (Germany) and vehicle 2 at IDIADA in Santa Oliva (Spain). The results of these tests are shown in Fig. 7.
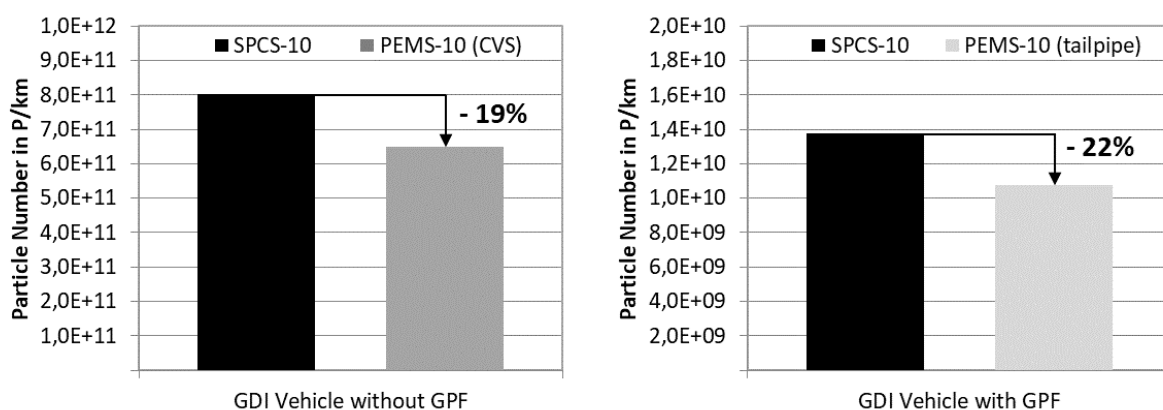

Fig. 7. WLTC measurements of GDI vehicles (left without GPF; right with GPF) at different positions

A huge influence on the implementation of a GPF is visible by looking at the total particle concentration between the 2 figures, as the particle concentration during the test cycle decreases from vehicle 1 to vehicle 2 by almost two orders of magnitude.

Between the two instruments SPCS-10 and PEMS-10 there is a difference of 19% in particle detection for vehicle 1 observed, where the PEMS-10 is measuring less. This trend has also been confirmed at the chassis dyno at IDIADA, where the PEMS-10, located at the CVS tunnel as well, was measuring 13% less particles in a specific test. This vehicle was not equipped with a GPF and had similar engine specifications than vehicle 1.

Regarding Vehicle 2, there is a 22% difference observed, which is higher than the two vehicles without GPF shown in the above paragraph. According to Fig. 6, here the PEMS-10 was connected at the tailpipe of the vehicle, where further influencing factors are considered which can lead to an increase of the gap in particle concentration measurement. The correlation of the SPCS-10 to PEMS-10 becomes more accurate to a level of smaller than 10% when the PEMS-10 is connected to the CVS tunnel instead of tailpipe with a GPF equipped vehicle (Pérez and Paz 2019).

4. Discussion

In this study both, stationary and on-board, PN measurement systems, which are capable to detect particles smaller than 23 nm as the future regulation requires, have been evaluated against their calibration methods.

The validation of the SPCS-10 and the PEMS-10 shows a good comparison according to the calibration data of the instruments. There are minor differences in the sub-23 nm regime observed. This may be caused by the setup of the SPCS-AVACS, as this device has been originally developed to characterize the equipment for current certification and engine dynamometer particle counting systems with a threshold of 23 nm onwards. Anyways, it is observed that it can be used for sub-23 nm measurements to detect instrument failures or efficiency drifts caused by deterioration of the alcohol storage capability of the wick inside the CPC.

Even though the calibrations of the devices are different, they showed a good agreement during the exhaust measurement tests with a value below 25% deviation. Moreover, both systems concertedly showed similar tendency against conventional systems which follows current regulatory requirements (Stanard 2018).

5. Conclusions

This study first assessed the influence of the different calibration procedures between stationary and on-board PN measurement systems for sub-23 nm particles. Different tendencies have been observed depending on the vehicle types. With a low amount of PN emissions in the sub-23 nm regime, both systems show minor differences, even though the particle losses in the PEMS-10 are much higher than in the SPCS-10. On the other hand, the differences of both measurement equipment stay below the level of 25% in example, when a GDI was tested without a GPF.

There is the possibility that PEMS-10 devices can have higher deviation due to several influencing factors, which are not considered in this study. The conformity factor (caused by instrument variability) of 50% between laboratory and PEMS should be kept in the future for sub-23 nm measurement devices. Further studies should evaluate the influence of other types of vehicles as well as it must be considered that there are further influencing factors when comparing PEMS-10 and SPCS-10 according to the certification method (tailpipe measurement and CVS tunnel measurement).

All in all, this sub-23 nm evaluation showed that the measurement technology with the desired calibration is as robust as current 23 nm systems for GDI vehicles with and without GPF. Further studies must be considered to evaluate different engine technologies like Diesel, Compressed Natural Gas or Hybrids. So far, there are no problems detected and it is promising that these devices are ready to be introduced into the market in the near future.

Acknowledgements

References

EUROPEAN COMMISSION, "COMMISSION REGULATION (EU) 2017/1154 of 7 June 2017 amending Regulation (EU) 2017/1151 supplementing Regulation (EC) No 715/2007 of the European Parliament and of the Council on type-approval of motor vehicles with respect to emissions from light passenger and commercial vehicles (Euro 5 and Euro 6) and on access to vehicle repair and maintenance information, amending Directive 2007/46/EC of the European Parliament and of the Council, Commission Regulation (EC) No 692/2008 and Commission Regulation (EU) No 1230/2012 and repealing Regulation (EC) No 692/2008 and Directive 2007/46/EC of the European Parliament and of the Council as regards real-driving emissions from light passenger and commercial vehicles (Euro 6)," 2017.

Horn, H. G., "Calibrated CPC with D50 ≤ 10 nm for laboratory use - together with the documented calibration procedure" PEMs4Nano Technical Report D2.02, 2017

Horn, H. G., "Calibrated CPC with D50 ≤ 10 nm for PEMS use" PEMs4Nano Technical Report D2.05, 2018

ISO/TC 24/SC 4, "Aerosol particle number concentration – Calibration of condensation particle counters," ISO 27891:2015, 2015.

Kassel, R., Couch, P., Conolly, M. and Hammer-Barulich, A., "Ultrafine Particulate Matter and the Benefits of Reducing Particle Numbers in the United States", Gladstein, Neandross & Associates, MECA, 2013

Kondo, K., Kojima, K., Kusaka, T., and Otsuki, Y., "Influence to the PN Emissions in Calibration Procedure for Portable and Stationary Solid Particle Number Measurement Systems," SAE Technical Paper 2019-01-2196, 2019.

Kreutziger, P., "Calibrated PEMS particle counting system and calibration procedure," PEMs4Nano Technical Report D2.07; 2018.

Maier, T., "Calibrated laboratory particle counting system and calibration procedure," PEMs4Nano Technical Report D2.04; 2018.

Otsuki, Y., Nakamura, H., Kojima, K., Kondo, K. et al., "Investigation in Calibration Procedures for Portable and Stationary Solid Particle Number Measurement Systems," SAE Technical Paper 2019-01-1187, 2019, doi:10.4271/2019-01-1187

Otsuki, Y., Takeda, K., Haruta, K., and Mori, N., "A Solid Particle Number Measurement System Including Nanoparticles Smaller than 23 Nanometers," SAE Technical Paper 2014-01-1604, 2014, doi:10.4271/2014-01-1604.

Pérez, A., Paz, S., "Testing for final validation and robustness evaluation of the equipment developed" PEMs4Nano Technical Report D4.3; 2019.

Stanard, A., "Light Duty PEMS Validation / Chassis Dynamometer Correlation", CRC Report No. E-122, 2018

UNITED NATIONS, "Concerning the Adoption of Uniform Technical Prescriptions for Wheeled Vehicles, Equipment and Parts which can be Fitted and/or be Used on Wheeled Vehicles and the Conditions for Reciprocal Recognition of Approvals Granted on the Basis of these Prescriptions," Addendum 82: Regulation No. 83, Revision 5, 2015.

Weiss, M., Bonnel, P., Hummel, R., Manfredi, U. et al. "Analyzing on-road emissions of light-duty vehicles with portable emission measurement systems," JRC Scientific and Technical Reports EUR 24697 EN, 2011.

Exhaust Gas Recirculation Combined with Regeneration Mode in a Compression Ignition Diesel Engine Operating at Cold Conditions

J. Galindo[1], V. Dolz[1], J. Monsalve-Serrano[1], M.A. Bernal[1] and L. Odillard[2]

[1]CMT – Motores Térmicos. Universitat Politècnica de València. Camino de Vera s/n, E-46022 Valencia, Spain.

E-mail: vidolrui@mot.upv.es
Telephone: +(34) 963 877 650

[2]Valeo – Systèmes Thermiques. La Verrière, France.

E-mail: laurent.odillard@valeo.com
Telephone: +33 (0) 130135225

Abstract. Internal combustion engines working at cold conditions lead to the production of excessive pollutant emission levels. The use of the exhaust gas recirculation could be necessary to reduce the nitrogen oxides emissions, even at these conditions. This paper evaluates the impact of using the high-pressure exhaust gas recirculation strategy while the diesel particulate filter is under regeneration mode on a Euro 6 turbocharged diesel engine running at low ambient temperature (-7ºC). This strategy is evaluated under 40 hours of operation, 20 of them using the two systems in combination. The results show that the activation of the high-pressure exhaust gas recirculation during the particulate filter regeneration process leads to a significant nitrogen oxides emissions reduction of 50% with respect to a reference case without exhaust gas recirculation. Moreover, the modification of some engine parameters compared to the base calibration, as the exhaust gas recirculation rate, the main injection advance and the post injection quantity, allows to optimize this strategy by reducing the carbon monoxide emissions up to 60%. Regarding the hydrocarbons emissions and fuel consumption, a small advantage could be observed using this strategy. However, the activation of the high-pressure exhaust gas recirculation at low temperatures can produce fouling deposits on the engine components (valve, cooler, etc.) and can contribute to reach saturation conditions on the particulate filter. For these reasons, the regeneration efficiency is followed during the experiments through the filter status, concluding that the use of small high-pressure exhaust gas recirculation rates in combination with the regeneration mode also allows to clean the soot particles from the particulate filter. These soot depositions are visualized and presented at the end of this work with a brief analysis of the soot characteristics and a quantitative estimation of the total soot volume produced during the experimental campaign.

Notation

$\dot{m}$	*Mass flow.*
P	*Pressure.*
T	*Temperature.*
η_{vol}	*Volumetric efficiency.*
η_{comb}	*Combustion efficiency.*
n	*Engine speed.*
R	*Gas constant.*
T	*Temperature.*
V_{eng}	*Engine volume.*

1. Introduction

Launch of current vehicles homologation regulations has challenged car manufacturers and research institutions to fulfil more stringent regulatory conditions. Limited fuel consumption, altitude changes, real driving emissions and cold start operation are considered guidelines in the current and future legislations

(Yang et al. 2020). Furthermore, the consequent reduction in the pollutant emissions levels is a second challenge to achieve for the automotive industry. Apart from the imperative reduction in carbon dioxide (CO_2) emissions, the nitrogen oxides (NO_x) emissions reduction in diesel engines will be a major concern in future regulatory stages. In order to fulfil these regulations, the internal combustion engine architecture is continuously studied and improved, testing different strategies and systems that allow to reduce the impact of these pollutant emissions in the environment (Torregrosa et al. 2017).

In this context, a widely known strategy used and improved during the last several years is the exhaust gas recirculation (EGR), even in its two configurations, one of them called low pressure (LP) EGR with a more complex architecture and a second one more simple and conventional called high pressure (HP) EGR (Desantes et al. 2013). However, these strategies are presented as an effective solution to reduce the NO_x emissions levels in different engine operating points, even working at cold conditions, when the pollutant emissions are largely critical. For these reasons, the use of EGR could be mandatory to comply with the current and future approval regulations (Luján et al. 2015, 2018).

The conventional HP EGR circuit, where the EGR rates are limited by the pressure difference among the inlet and outlet manifolds, is a low cost and effective solution due to its simple architecture and high potential to reduce NO_x emissions (Zamboni and Capobianco 2012). Taking this into account, the evaluation of this strategy, in combination with other engine working conditions, as per example, the Diesel Particulate Filter (DPF) regeneration, is a necessary study point. The DPF regeneration is a process controlled by the Electronic Control Unit (ECU) that aims to clean and remove the particulate matter (PM) collected in the engine after treatment system (Guardiola et al. 2018). For this reason, a possible scenario in which the engine is working at cold conditions, while activating the HP EGR to reduce the NO_x emissions and the DPF regeneration strategy due to reaching saturation conditions in the filter, is necessary to be evaluated from the experimental point of view.

Nevertheless, the use of HP EGR to reduce the NO_x levels presents some issues, as per example condensation and fouling depositions resulted of a degraded combustion, specially working at low temperatures (Galindo et al. 2020a, 2020b; Luján et al. 2019). The soot particles can affect the main components of the EGR line (i.e. EGR valve, EGR cooler, intake manifold) reducing its life span (Abarham et al. 2013). In addition, it could contribute to accelerate the DPF loading, thus affecting its normal operation (Fang et al. 2019). A group of researchers, (Lapuerta et al. 2012, 2014) have investigated the effect of soot accumulation in a DPF of a common rail diesel engine on the combustion process and pollutant emissions, reproducing a New European Driving Cycle (NEDC). The investigation concluded that performing a DPF regeneration without controlling the injection settings parameters and the EGR ratio could increase the NO_x emissions around 60% and the fuel consumption around 4%. This is caused due to the higher back pressure and the higher temperature of the re-circulated gas, which modifies the combustion process and moves the engine operation away from its optimum conditions.

Afterwards, the authors carried on evaluating these issues and presented some strategies for the active DPF regeneration modifying the engine control parameters. The selected parameters to be studied were the injection timing, exhaust gas recirculation and amount of post injected fuel. In this case, the work was performed at steady-state conditions at 2000 rpm of engine speed and 94 Nm of torque, a representative point of the New European Driving Cycle. The relevant findings of the authors were that eliminating the EGR during the regeneration process is an optimal option for a fast DPF regeneration and reduced fuel consumption. However, low values of EGR could contribute to avoid uncontrolled regeneration in the cases of very high soot load at the DPF and to reduce NO_x emissions. Regarding the injection timing and the amount of post injected fuel, it was concluded that keeping the optimal temperature conditions is essential for an efficient DPF regeneration.

Regarding the impact of fouling depositions in the EGR line components and its characterization, several studies have been performed in the literature. (Arnal et al. 2015) presented the characterization of five different types of diesel soot, which were collected from several high pressure EGR coolers working at different conditions (engine bench and vehicle). The authors highlight the fact that the fouling depositions on EGR components as EGR coolers and valves, decreases its thermal efficiency and increases the pressure drop producing the malfunctioning of the device, implying the non-compliance of the NO_x standard regulations. In addition, these depositions are composed of adsorbed compounds like lube oil and unburned fuel that could aggravate this issue.

According to the previous paragraphs, in this work, the impact of using the HP EGR while the DPF is under regeneration process in a 4-cylinder diesel engine working at cold conditions (-7ºC) is evaluated. The results of the study are divided into two main sections. The first section presents the effect of using HP EGR together with the regeneration mode on the regulated diesel emissions, NO_x and soot, as well as on the combustion engine efficiency is assessed. In addition, the DPF loading is evaluated. In the second section, a brief analysis of the fouling phenomena observed on the HP EGR

line components is also presented. This analysis includes an approximated estimation of the soot mass and volume collected from the HP EGR line during the experimental campaign.

2. Experimental setup and methodology

2.1 Test bench description and configuration

In order to perform this theoretical-experimental work, an in-line 4 cylinders, 1.6 liter, turbocharged, diesel engine was used. Table 1 summarizes the technical features of the engine used. To carry out the experiments at cold conditions, the engine was installed in a climatic test bench, where the temperatures of the test bench air, fuel and coolant are under control. The test bench is instrumented to measure the torque, speed, temperatures and pressures at different engine points. The injected fuel mass flow and the intake air mass flow are also measured. Figure 1 shows the engine configuration and its instrumentation.
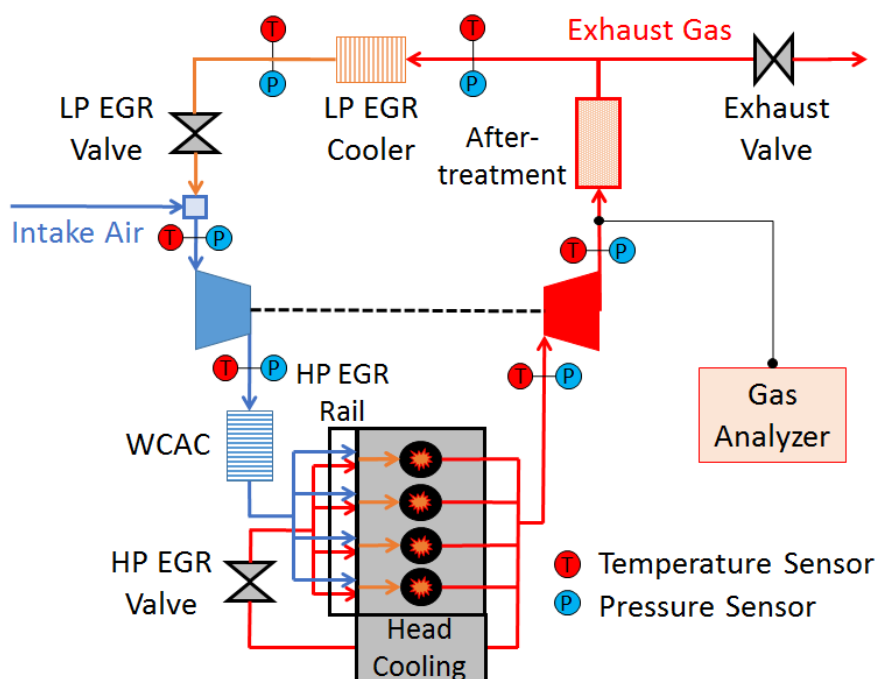
Fig. 1. Engine configuration

The engine has two EGR circuits. The first one is the LP EGR circuit, in which the exhaust gas pass through the catalyst and the DPF, and then are redirected into the turbo compressor. The second circuit is the HP EGR. In this case, the exhaust gas is directly cooled in the cylinder head and mixed with the fresh air that comes from the intake line. This circuit consists of an internal duct that guides the exhaust gases coming from the exhaust manifold through a compact section of the cylinder head (without EGR cooler) to reduce its temperature, a HP EGR valve controlled by the ECU of the engine, and a HP EGR rail, where the exhaust gases are driven and distributed to the engine intake manifold and mixed with the air at the intake of the four cylinders. The Water Charge Air Cooler (WCAC) is activated with a constant regulation in order to control the engine intake temperature due to the higher temperatures reached during the DPF regeneration mode.

Table 1. Engine specifications

Number of cylinders	4	Maximum torque (Nm/rpm)	320/1750
Number of valves	16	Compression ratio	15.4 : 1
Bore x stroke (mm)	80 x 79.5	Fuel injection system	CDI
Total displacement (cc)	1598	EGR system	HP and LP
Maximum power (kW/rpm)	96/4000	Intake cooling system	WCAC

Several engine parameters were measured to assess the engine performance and to analyze the impact of the proposed configuration. The measured parameters together with the sensors features are presented in Table 2.

Table 2. Instrumentation accuracy

Sensor	Variable	Accuracy [%]	Range
Thermocouples type K	Temperature	1	-200 to 1250ºC
Pressure sensor	Pressure	0.3	0 to 10bar
Gravimetric fuel balance	Fuel mass flow	0.2	0 to 150kg/h
Hot wire meter	Air mass flow	1	0 to 720kg/h
Dynamometer brake	Torque	0.1	0 to 480Nm

The air mass flow through the intake line of the engine was measured by means of a hot wire anemometer with a measurement error of 1%. The fuel consumption during the cycle was measured with an AVL fuel balance, which has a measurement error of 0.2%. A Horiba Mexa 7100 DEGR was used to measure O2, CO2, CO emissions using a non-dispersive infrared analyzer, and unburned hydrocarbons (HCs) with a chemiluminescent detector. The error of the gas analyzer is in the range of 2%. The measurement point is located upstream of the after-treatment system.

The EGR rate was not possible to obtain from CO_2 measurement in exhaust and intake manifolds due to the complexity of the HP EGR line to be instrumented. Instead of, the HP EGR rate was mathematically estimated using the engine volumetric efficiency as it will be explained in the methodology subsection.

2.2 Methodology and strategies

The ambient temperature inside the climatic chamber was set at -7ºC. Tests are performed in steady-state conditions with an engine speed of 2000 rpm and 4 bar of brake mean effective pressure (BMEP). The engine working condition was defined as a representative point for the DPF regeneration, comparable to a real engine operation on a highway at 120km/h with medium load.

For this experimental work, the engine has been running during 40 hours at -7ºC activating the HP EGR, 20 of them activating the regeneration mode together. Figure 2 shows the process to carry out each test. First, the engine warm-up process is performed in standard conditions (without EGR and without regeneration) until the engine coolant temperature reaches 60ºC, then, a 20% of HP EGR rate is activated by the ECU and the regeneration mode is forced manually. A post injection is enabled in this mode with the aim of increasing the exhaust gas temperature and burn the soot particles bonded on the DPF. This condition is maintained along 30 minutes and then the regeneration mode is deactivated, returning to the standard engine calibration. To hold fouling conditions on the DPF at the end of each test is the aim of working with the base calibration (only HP EGR performed), this methodology allows to check the DPF regeneration process during the first 30 minutes of the test. This procedure is repeated continuously until reaching a testing time of two hours per day.

To achieve an efficient regeneration process of the DPF, some relevant variables are followed during the experiments. The post injected fuel quantity and turbine inlet temperature are verified. These parameters allow to control a key condition to conduct a DPF regeneration, as the exhaust gas temperature. In order to check the DPF loading process, two reading calibration variables are recorded. First, the pressure difference (ΔP) between the DPF inlet and outlet, as an indicator of the back pressure generated in the engine exhaust line that could modify the HP EGR rate performed and as a consequence the engine intake temperatures. And second, the particulate filter soot mass estimated by the ECU, as a reference parameter to check the DPF loading conditions. This estimated value is an internal calculation, based on the DPF status and several variables calculated and measured by the ECU, as per example, DPF pressure difference, upstream and downstream temperatures, engine working conditions, DPF diagnosis, etc.
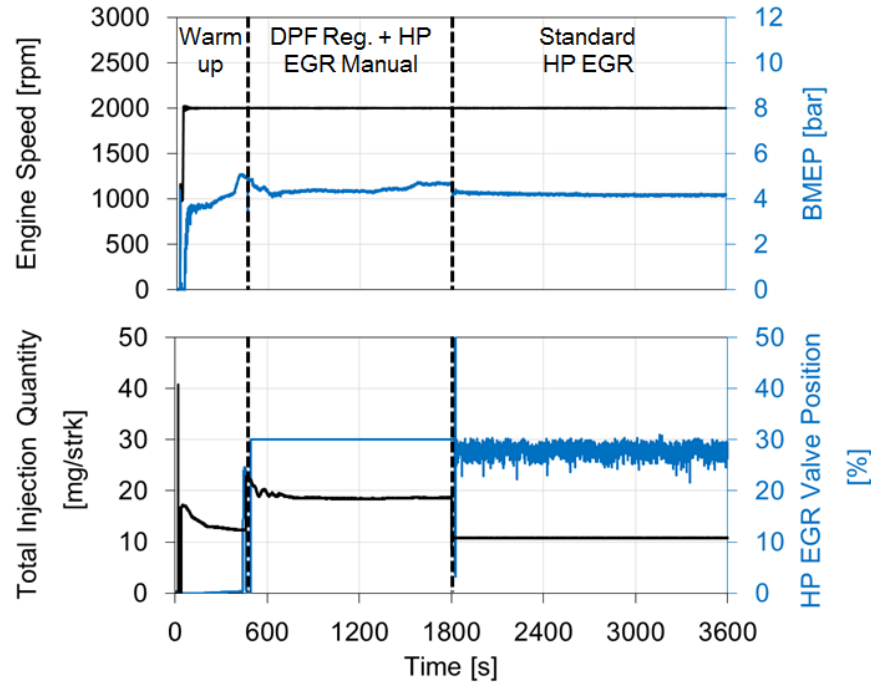
Fig. 2. Profile of the tests performed

Due to the abovementioned impossibility to obtain an EGR rate estimation from CO_2 measurement, it was necessary to estimate the engine volumetric efficiency for this engine configuration. Equation 1 shows this efficiency as a function of the air mass flow, the engine parameters, the boost pressure and the intake temperature. When the volumetric efficiency is assessed, it is consider this value as a constant value and it is possible to obtain the EGR rate as a relation between the air mass estimated theoretically by using the volumetric efficiency (Eq. 2) and the air mass flow measured. Equation 3 shows the HP EGR rate estimation.

$$\eta_{vol} = \frac{\dot{m}_{air}}{\frac{P_{boost}}{R\,T_{intake}} \cdot V_{eng}.\,n.\,i} \qquad (1)$$

$$\dot{m}_{theor} = \eta_{vol} \cdot \frac{P_{boost}}{R\,T_{intake}} \cdot V_{eng}.\,n.\,i \qquad (2)$$

$$EGR_{rate} = \frac{\dot{m}_{theor} - \dot{m}_{air}}{\dot{m}_{theor}} * 100 \qquad (3)$$

Finally, to visualize the impact of performing HP EGR combined with the DPF regeneration at cold conditions (-7°C) on the engine components, some of them (i.e. HP EGR valve, HP EGR Rail, WCAC) has been disassembled and cleaned before starting with the experimental work.

3. Results and discussion

In order to present how the use of the HP EGR combined with the regeneration mode could affect the engine behavior and its performance under cold operating conditions, this section is divided into two different parts. In the first subsection, the impact of this configuration on the engine thermal behavior, DPF regeneration efficiency, pollutant emissions and fuel consumption is presented. In the second subsection, the fouling phenomena evolution inside the EGR line components is presented.

3.1 Impact of the HP EGR combined with regeneration mode on the engine behavior

Perform HP EGR while the DPF is being regenerated leads to a higher temperature in the engine intake line as expected. In order to show the main results of this work in terms of repeatability and dispersion between tests, a group of eight tests is selected. First, a reference test performed at -7ºC activating the regeneration mode at the end of the engine warm-up (500 s) and only performing HP EGR in standard engine conditions after second 1800. Later, a group of five tests using HP EGR with the regeneration mode activated between second 500 and second 1800 and finally, two tests where the DPF reached saturated conditions under similar working conditions. Figure 3 shows the engine intake temperature measured in the intake manifold. Comparing the reference test with the tests performing HP EGR together with regeneration mode, it can be observed how the intake temperature increases approximately by 30ºC. Thanks to keep the same WCAC regulation between tests, in the figure it can be observed how the engine intake temperature increases progressively with regard to the reference test due to the HP EGR activation. These higher temperatures could increase the in-cylinder temperature improving the engine combustion efficiency.
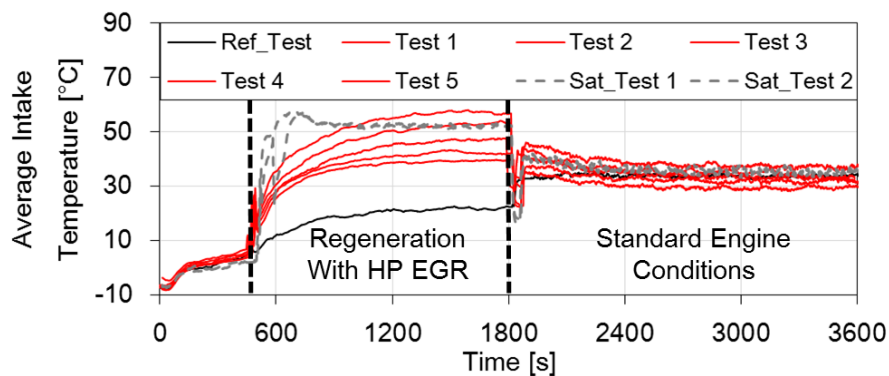
Fig. 3. Engine intake temperature
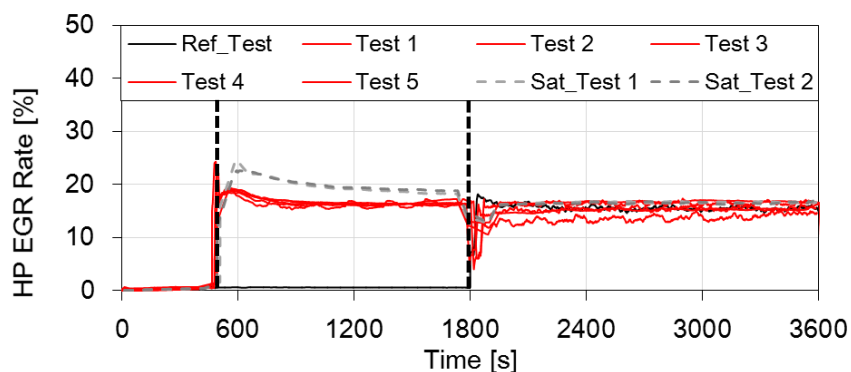
Fig. 4. HP EGR rate performed

Figure 4 shows the HP EGR rate. It is a mathematical estimation using the Eq. 3 abovementioned. The HP EGR rate performed together with the regeneration mode is a similar rate than the used by the ECU in standard engine conditions. The EGR rate remains approximately constant at 20%. However, the saturated tests present an EGR rate higher than 20% due to a possible DPF saturation or soot accumulation in the HP EGR line.

The DPF saturation is followed through the difference pressure and the soot mass estimation performed by the ECU. Figure 5 shows the DPF ΔP as a reference to identify if there are clogging conditions on the DPF. It can be observed how performing HP EGR while the DPF is under regeneration allows to reduce the pressure difference below the reference test, indicating that the regeneration process is efficient. Soot mass variable recorded from the ECU confirmed this statement. Nevertheless, under standard engine conditions (right of the figure) to perform only HP EGR and to operate under cold conditions could produce a DPF saturation increasing this ΔP value. It is important to highlight that the exhaust gases carried through the high pressure circuit are not cleaned in the engine after treatment system and could affect the combustion process considerably. For this reason, the control of the EGR rate, the EGR line temperatures and the engine intake temperature is a key factor to ensure a reliable DPF regeneration process.

Regarding the saturated tests, the higher EGR rate due to a higher pressure difference, it is an evidence of the soot accumulation on the DPF and the consequence of a higher intake temperature. This fact, under control, could improve the combustion efficiency but without control could affect the thermal efficiency of the components (i.e. EGR valve and EGR cooler) affecting its normal operation.
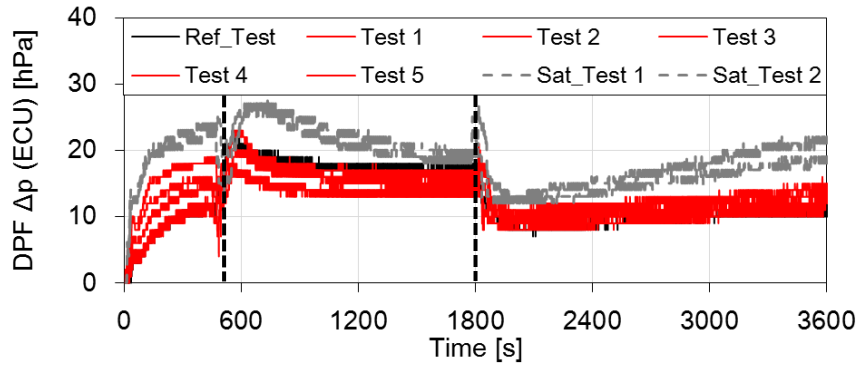

Fig. 5. DPF difference pressure

3.1.1 Pollutant emissions

Measured values of NOx, HC and CO emissions measured upstream the after-treatment system are presented in Fig. 6. The aim of performing EGR is to obtain a significant NOx emissions reduction under cold operating conditions. Nevertheless, one disadvantage of this strategy is the combustion degradation, increasing the unburned HCs and PMs. The top graph of Fig. 6 shows the measured values of NOx emissions. With the standard calibration at cold conditions, the engine is prepared to perform HP EGR and keep a NOx values of approximately 2.5 g/kWh. During the DPF regeneration mode in combination with the HP EGR this value is reduced to approximately 1.25 g/kWh. This value represents a reduction of 50%. In terms of HC emissions, a significant increase is observed compared to the standard calibration due to the additional post injected fuel used during the DPF regeneration. However, comparing the DPF regeneration with and without HP EGR, it could be observed that the proposed configuration could help to reduce this issue thanks to a small reduction in the post injected fuel.
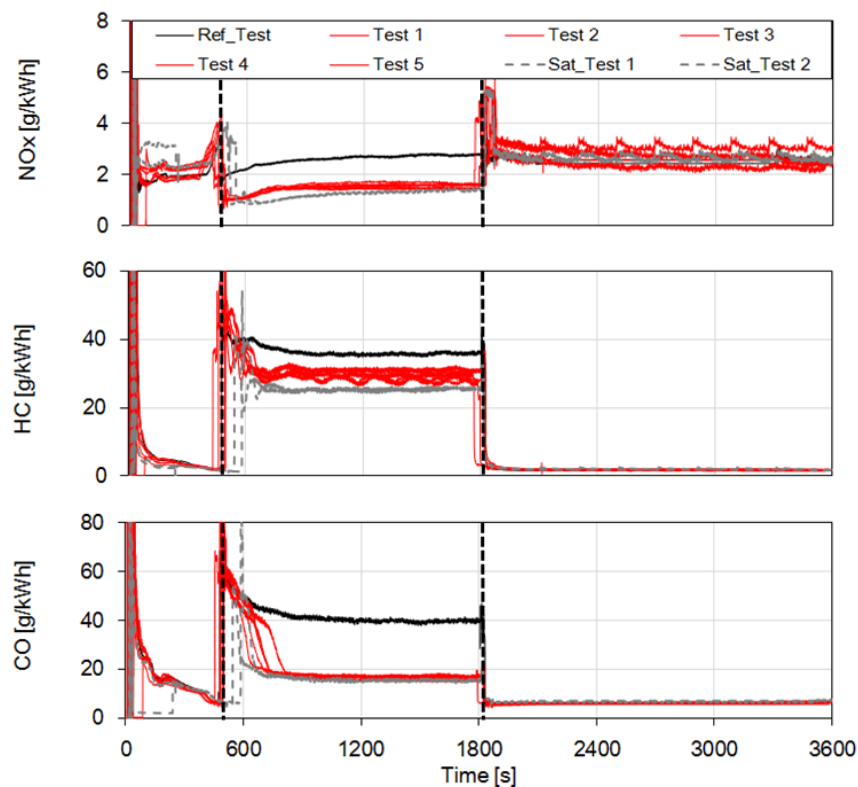

Fig. 6. Raw pollutant emissions measurements

Finally, activating the HP EGR during a regeneration process, keeping an appropriate main injection advance and thanks to the higher intake temperature reached with this proposed configuration the CO emissions could be reduced significantly, as it can be observed by comparing the use of the HP EGR or not. It is possible to estimate an approximate reduction of 60%. This reduction allows to reach close values to the values performed under the standard engine calibration, besides, the after treatment system could also reduce significantly these values.

3.1.2 Combustion efficiency and fuel consumption

Figure 7 shows the combustion efficiency and the brake specific fuel consumption (BSFC) for the different tests. The combustion efficiency estimates the quantity of fuel burned during the combustion process and it is calculated by means of the engine-out emissions measurements, as is shown in the Eq. 4.

$$\eta_{comb} = 1 - \frac{\dot{m}_{HC}(\dot{m}_{air} + \dot{m}_{fuel})}{\dot{m}_{fuel}} - \frac{\dot{m}_{CO}(\dot{m}_{air} + \dot{m}_{fuel})}{4\,\dot{m}_{fuel}} \qquad (4)$$

As mentioned above, during the first minutes of an engine cold start there are instabilities and degradations in the combustion. In Figure 7, it can be observed how the combustion efficiency increases progressively with the engine warm-up until the 500 s approximately. Performing a DPF regeneration could affect the combustion process due to the additional fuel injected when the post injection is activated. By this reason, it can be observed how the reference test without EGR presents the lower efficiency. Activating the HP EGR together with the regeneration mode a slight improvement in the combustion efficiency is denoted. This improvement is due to a higher intake temperature and a quite reduction in the post injected fuel during the regeneration mode, the consequent higher in-cylinder temperature promotes a better combustion process. In addition, a brake specific fuel consumption reduction is coherent with this behavior.

Working with the standard engine calibration, both, combustion efficiency and BSFC present optimal values, taking into account that this operation is at low ambient temperature (-7ºC).
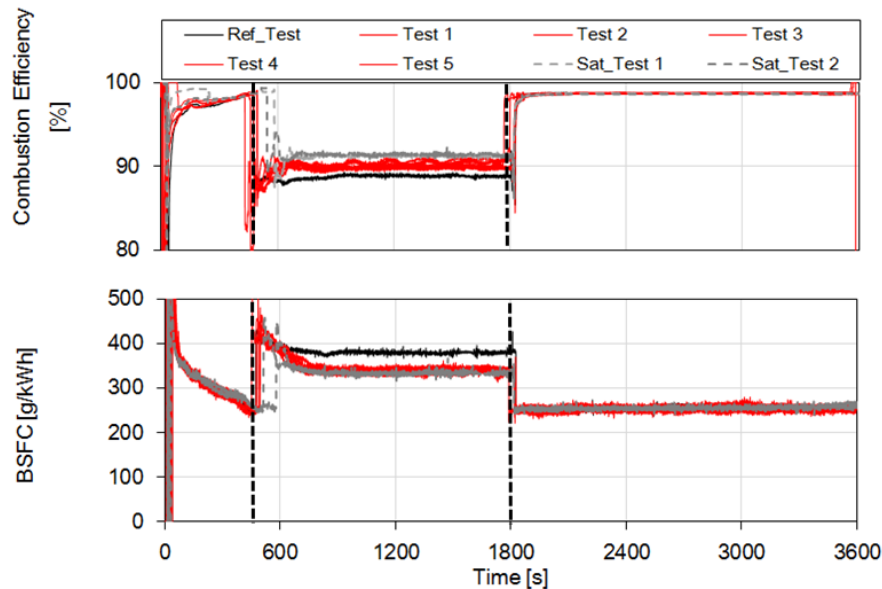

Fig. 7. Combustion efficiency and BSFC

3.2 Impact of the HP EGR combined with regeneration mode on the engine components

The second aim of this experimental work is a brief analysis of a known event presented when an IC engine is operating with exhaust gas recirculation (EGR) at very low ambient temperatures. These are the fouling deposits, which could affect the EGR systems due to unburned HC and PM depositions on its principal components (i.e. EGR valve and EGR cooler).

After 40 hours performing HP EGR at cold conditions, fouling depositions on the HP EGR line components are observed. Figure 8 shows an images of the initial and final conditions of the HP EGR valve of the circuit. It can be observed a black soot on the actuator surface comparing the reference (initial condition) with the final condition. This is a typical soot as found in EGR circuits of IC engines, with similar features, like matte black color, carbon texture and rough surface.

Initial Condition	Final Condition
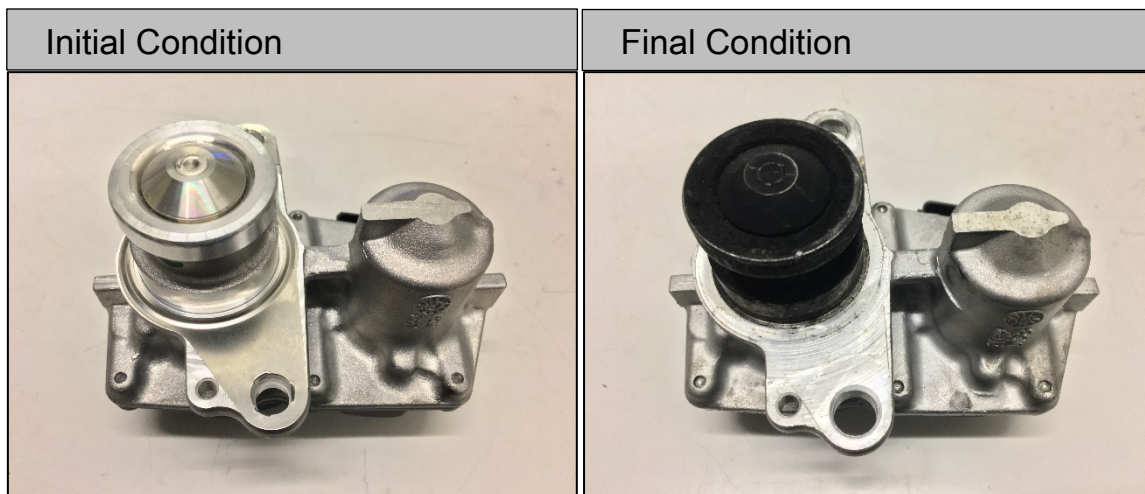
Fig. 8. Fouling observed on the HP EGR valve

In order to obtain a quantitative estimation of the amount of soot produced during this experimental campaign, approximately 50% of the soot particles has been removed and collected from the HP EGR components (i.e. EGR valve, ducts, rail and intake manifold). To perform this estimation, the layer of soot observed on the surface of the elements is consider as a geometrical area with the same shape of the element. For example, the EGR valve actuator observed in Fig. 8 is considered as a tube with cover. Then, measuring the thickness of the soot layer the soot volume is calculated. Furthermore, to know the mass of soot, the particles collected from each element are weighed in a precision scale. In this way, the estimated quantity of soot and the known mass of soot could give some relevant information about the density of the particles observed in this study.

Approximately, 30 cm^3 of soot equivalent to a 6 gr of soot mass has been estimated after 40 hours performing HP EGR and DPF regeneration at cold conditions. This calculated value can be considered as an acceptable amount of soot produced when exhaust gas recirculation is used. Typical saturation values in diesel engines to conduct DPF regeneration are close to 20 gr of soot.

Conclusions

In this experimental work, the advantages, disadvantages and impacts of performing HP EGR together with the DPF regeneration mode during engine cold operating conditions have been studied. The impact in regeneration efficiency, pollutant emissions and fuel consumption were presented. Besides, a brief analysis of the impact of fouling depositions on the engine components have been performed.

The main objective of performing HP EGR at cold conditions (-7°C) is to reduce the NO_x emissions thanks to the oxygen concentration reduction of the working fluid in the combustion chamber. In this work, a noticeable NO_x emissions reduction of approximately 50% with respect to a reference case without HP EGR during a DPF regeneration process has been achieved. Regarding HC and CO emissions, another advantages were found with this proposed configuration. A significant CO emissions reduction of 60% was achieved performing HP EGR and fixing a main injection advance of -10°crk. In terms of HC emissions, a reduction of 15% was observed due to the improvements in combustion efficiency and fuel consumption. During the DPF regeneration, the additional fuel injected in the post injection affected the combustion efficiency due to the late combustion of this fuel during the exhaust stroke.

A quite benefit could be observed due to a slight improvement in the combustion temperature when the HP EGR is activated.

On the other hand, performing HP EGR without the regeneration mode at cold conditions could contribute to the DPF saturation and degradation, the accumulation of soot increases the pressure difference in the DPF and as a consequence an increment in the EGR rate performed and in the EGR temperatures was registered.

In order to avoid previous conclusion, the regeneration efficiency was evaluated through the DPF difference pressure, the soot mass estimated by the ECU, the HP EGR rate and the engine intake temperature. It was found that to activate only the HP EGR at cold conditions with EGR rates beyond 20% contributed to increase the soot depositions and to saturate the DPF early. By this reason, if the purpose is to activate the HP EGR to reduce NO_x emissions, the EGR rate and the intake temperatures must be controlled and limited. The LP EGR could be presented as another option to decrease this impact. However, performing a low HP EGR rate in combination with the regeneration mode could reduce the post injected fuel and the exhaust gas temperature, but anyway continue keeping the regeneration efficiency in acceptable values. This was confirmed verifying the DPF status through the ECU variables (DPF ΔP and soot estimation). It allowed to obtain the noticeable NO_x emission reduction abovementioned.

The second aim of this research work is the analysis and visualization of fouling phenomena produced by the HP EGR activation at cold conditions. After 40 hours of tests, soot particles were found on the HP EGR line of the engine. These particles match with typical fouling observed in IC engines. A fouling quantity of 30 cm^3 and 6 gr was estimated, observing that the principal components where soot is deposited were the HP EGR rail and the engine intake manifold.

Acknowledgements

References

Abarham, Mehdi, Tejas Chafekar, John W. Hoard, Ashwin Salvi, Dan J. Styles, C. Scott Sluder, and Dennis Assanis. 2013. "In-Situ Visualization of Exhaust Soot Particle Deposition and Removal in Channel Flows." *Chemical Engineering Science* 87:359–70.

Arnal, Cristina, Yolanda Bravo, Carmen Larrosa, Valentina Gargiulo, Michela Alfè, Anna Ciajolo, María Ujué Alzueta, Ángela Millera, and Rafael Bilbao. 2015. "Characterization of Different Types of Diesel (EGR Cooler) Soot Samples." *SAE International Journal of Engines* 8(4):2015-01–1690.

Desantes, José M., José M. Luján, Benjamín Pla, and José A. Soler. 2013. "On the Combination of High-Pressure and Low-Pressure Exhaust Gas Recirculation Loops for Improved Fuel Economy and Reduced Emissions in High-Speed Direct-Injection Engines." *International Journal of Engine Research* 14(1):3–11.

Fang, Jia, Zhongwei Meng, Jiansong Li, Yuheng Du, Yuan Qin, Yuan Jiang, Weilian Bai, and George G. Chase. 2019. "The Effect of Operating Parameters on Regeneration Characteristics and Particulate Emission Characteristics of Diesel Particulate Filters." *Applied Thermal Engineering* 148(November 2018):860–67.

Galindo, José, Vicente Dolz, Javier Monsalve-Serrano, Miguel Angel Bernal Maldonado, and Laurent Odillard. 2020. "Advantages of Using a Cooler Bypass in the Low-Pressure Exhaust Gas Recirculation Line of a Compression Ignition Diesel Engine Operating at Cold Conditions." *International Journal of Engine Research* 1468087420914725.

Galindo, Jose, Roberto Navarro, Daniel Tarı, and Francisco Moya. 2020. "Development of an Experimental Test Bench and a Psychrometric Model for Assessing Condensation on a Low- Pressure Exhaust Gas Recirculation Cooler."

Guardiola, Carlos, Benjamin Pla, Pau Bares, and Javier Mora. 2018. "An On-Board Method to Estimate the Light-off Temperature of Diesel Oxidation Catalysts." *International Journal of Engine Research*.

Lapuerta, Magín, Juan J. Hernández, and Fermín Oliva. 2014. "Strategies for Active Diesel Particulate Filter Regeneration Based on Late Injection and Exhaust Recirculation with Different Fuels." *International Journal of Engine Research* 15(2):209–21.

Lapuerta, Magín, José Rodríguez-Fernández, and Fermín Oliva. 2012. "Effect of Soot Accumulation in a Diesel Particle Filter on the Combustion Process and Gaseous Emissions." *Energy* 47(1):543–52.

Luján, José Manuel, Héctor Climent, Santiago Ruiz, and Ausias Moratal. 2018. "Influence of Ambient Temperature on Diesel Engine Raw Pollutants and Fuel Consumption in Different Driving Cycles." *International Journal of Engine Research*.

Luján, Jose Manuel, Vicente Dolz, Javier Monsalve-Serrano, and Miguel Angel Bernal Maldonado. 2019. "High-Pressure Exhaust Gas Recirculation Line Condensation Model of an Internal Combustion Diesel Engine Operating at Cold Conditions." *International Journal of Engine Research*.

Luján, José Manuel, Carlos Guardiola, Benjamín Pla, and Alberto Reig. 2015. "Switching Strategy between HP (High Pressure)- and LPEGR (Low Pressure Exhaust Gas Recirculation) Systems for Reduced Fuel Consumption and Emissions." *Energy* 90:1790–98.

Torregrosa, A. J., A. Broatch, P. Olmeda, J. Salvador-Iborra, and A. Warey. 2017. "Experimental Study of the Influence of Exhaust Gas Recirculation on Heat Transfer in the Firedeck of a Direct Injection Diesel Engine." *Energy Conversion and Management* 153(June):304–12.

Yang, Zhiwen, Yao Liu, Lin Wu, Simon Martinet, Yi Zhang, Michel Andre, and Hongjun Mao. 2020. "Real-World Gaseous Emission Characteristics of Euro 6b Light-Duty Gasoline- and Diesel-Fueled Vehicles." *Transportation Research Part D: Transport and Environment* 78(January):102215.

Zamboni, Giorgio and Massimo Capobianco. 2012. "Experimental Study on the Effects of HP and LP EGR in an Automotive Turbocharged Diesel Engine." *Applied Energy* 94:117–28.

Model-Based Calibration: Using Machine Learning Algorithms and Virtual Control Unit Approaches

J. Julià, M. Alonso, S. Shigemoto

NTCE-S – Nissan Technical Center Europe, Spain

E-mail: jordi.julia@nissan-europe.com
Telephone: +(34) 933 618 594

Abstract. In recent years, stringent new emissions legislations impact on Automotive Industry had accelerated the necessity for the implementation of new Powertrain Development Methodologies to achieve new targets, while minimizing the impact on the already highly challenging economic and timing development constraints present in Automotive Industry.

At the same time, recent important improvements in the field of Machine Learning (hereunder ML) based on higher Computational Capabilities has allowed ML to become a candidate for many Technological Industries and has already been consolidated by sectors as Image Processing and Computer Writing. Additionally, for the Automotive Industry, important progress for Virtual Control Units has been achieved based on higher Computational Capabilities.

Using ML and Virtual Control Units for Automotive Powertrain Development purpose, focusing respectively on Engine Performance (Fuel Consumption/Emissions) and Control Units Software modelling, makes it possible to obtain a good Models Accuracy/Development Time trade-off, becoming a useful methodology specially for Engine Control Unit Calibration purposes such as Control Software and Engine Hardware Definition (related to its Performance Optimization).

As data source for ML Models Training and its Validation as well as for Virtual ECU models, a wide and efficient portfolio of Testing Capabilities become essential, focusing always in the most efficient test to obtain the required data for ML training and the optimisation of the Model Accuracy/Development Time trade-off.

This paper presents methodology developed by Nissan for Petrol Engines Particulate Mass and GPF Market Performance in terms of Software Control Strategies Definition based on ML technologies and Virtual ECM modelling approach. The importance of Testing Capabilities to obtain accurate models with short development time requirements is highlighted as well.

Notation

ML	*Machine Learning*
ECU	*Electronic Control Unit*
GPF	*Gasoline Particulate Filter*
ECM	*Engine Control Module*
CO2	*Carbon Dioxide*
ADAS	*Advanced Driver Assistance Systems*
DoE	*Design of Experiments*
GP	*Gaussian Processes*
AGP	*Advanced Gaussian Processes*
RNN	*Recurrent Neuronal Networks*
MiL	*Model in the loop*
SiL	*Software in the loop*
PN	*Particulate Number*
PM	*Particulate Mass*

CVT	Continuous Variable Transmission
NARX	Nonlinear Autoregressive with Exogenous input structure
$m(x)$	Mean Function
$K(x,x')$	Covariance function
$f(-)$	Underlying function defining the system under study
x	Input vector
w	Vector of parameters of the linear model
y	Observed target value
ε	Gaussian noise
σ_n^2	Variance
Σ_p	Covariance Matrix
$N(\mu,\Sigma)$	Gaussian distribution with mean vector μ and covariance matrix Σ
$D = \{x_i,y_i|i=1,\dots,m\}$	Input-Output pairs used for training
I_m	m x m identity matrix
$k_{SE}(x_i,x_j)$	Squared Exponential Covariance function
$\Lambda=diag([l_1^2,\dots,l_d^2])$	d x d Diagonal Matrix of elements l12,…,ld2
$\log p(y|\theta)$	log marginal likelihood
$O(-)$	Computational Complexity
WLTC	Worldwide harmonized Light vehicles Test Cycles
PRC	People's Republic of China
CPU	Central Processing Unit
O2	Dioxygen
CAFE	Corporate Average Fuel Economy

1. Introduction and motivation

Automotive Industry situation has severely changed in the recent years due to several circumstances such as the implementation of new Emissions and CO2 Targets, Society Technological Transformation, Vehicles Access Restrictions into the Cities and the evolution of Internal Combustion Engines to Electrified Systems.

Under these new requirements the implementation of fields such as Artificial Intelligence and Machine Learning [1] into Automotive Industry has rapidly increased. Advanced Driver Assistance Systems (ADAS) or the implementation of improved Testing and Powertrain Development Methodologies [2, 3] are examples of the usage of these fields.

As well as a consequence from the new requirements, improvement of control logics of all engineering systems has become necessary based on the increment of specific control units and logics. Due to this increment on the amount of software and control units, the usage of Virtual Control Unit Software [4] or Software Development Simulation Platforms [5] to improve software development processes and secure associated timings and costs has become essential.

In such scenario, mindset for innovation and improvement must always be present in all engineering facets. In this document it is shared the usage of simulation platforms based on the combination of "*Efficient Testing Methodologies + Machine Learning Algorithms + Virtual ECM*" for Powertrain Advanced Engineering and Calibration Development purposes. Extensive portfolio of capabilities from each of these fields (i.e. diverse testing approaches such as Global DoE or Dynamic DoE, diverse types of algorithms like Gaussian Processes or Recurrent Neuronal Networks and diverse Virtual ECM approaches such as Software in the Loop or Software Functions Model in the Loop) combined together make possible to efficiently build remarkably capable simulation platforms for almost any powertrain system (e.g. gasoline or hybrid powertrain systems).

As example, it is described how this approach is being used for prediction of Gasoline Particulate Filter Performance in the Market from an early stage of powertrain development and with the purpose of defining most suitable hardware and software for Gasoline Particulate Filter system. This case can be considered as a continuation for the "*Efficient Testing Methodologies + Machine Learning Algorithms + Virtual ECM*" approach development started in the past based on diesel engines [6].

2. Methodology Description

2.1 Overview of Simulation Platform

Simulation Platform (hereunder referred as GPF Performance in the Market) purpose is to predict Gasoline Particulate Filter system Performance in the Market and in particular risk of GPF clogged occurrence.

To this purpose, simulation platform is comprised by Vehicle, Engine Performance (ML Regression) and Virtual ECM Models. For the training of ML Regression Models, data from GPF Vehicle Test Campaign is used. For the prediction of Market Performance, vehicle speed from a comprehensive Customer Database for market understudy is used. Overview of simulation platform is provided below (figure 1). Further detail for each model is provided in the following chapters.
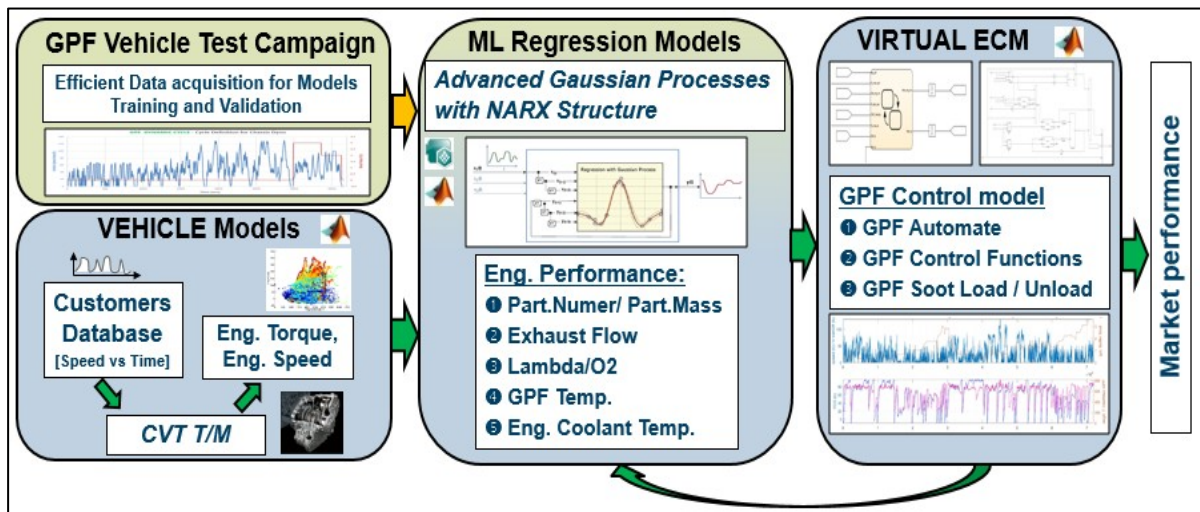
Fig. 1. Simulation Platform Overview

Due to their relevance on the simulation platform purpose, Engine Out Particulate Number and Mass models accuracy are essential. To capture impact of ambient temperature [-10, 0, 10, 20ºC] and engine [Cold Start&Warm-up/Hot] conditions on PN/PM amount generation, specific model is used for each condition as described below (figure 2)
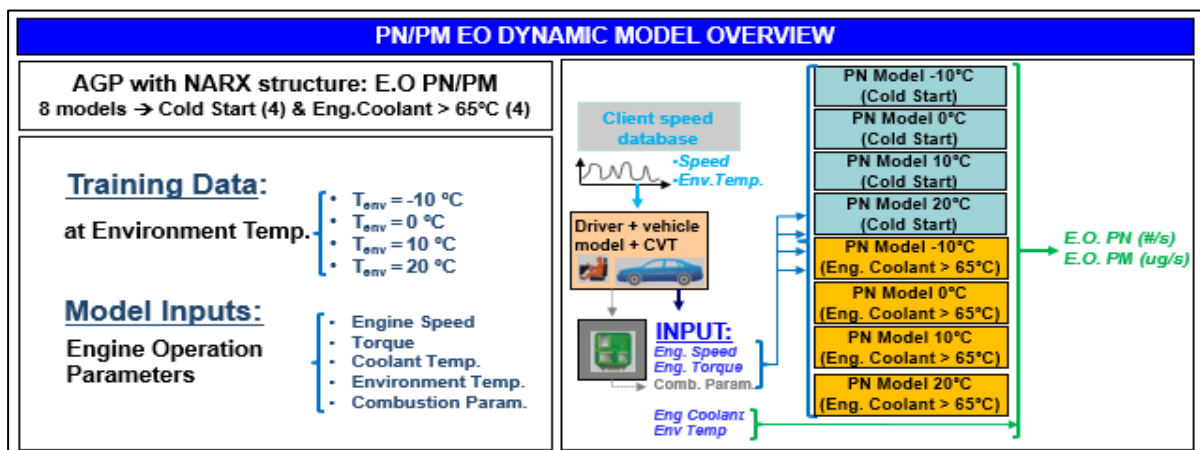
Fig. 2. PN/PM Dynamic Models Overview

For the rest of Engine Performance dynamic models used in this simulation platform, behaviour can be estimated based on only 1 model, differentiation based on ambient and engine conditions is not required.

2.2 Description of Virtual ECM Model (Model-In-the-Loop for Application Layer GPF Functions)

In this study Virtual ECM part is implemented based on Model-In-the-Loop (hereunder MiL) approach in Matlab Simulink, functions implemented belonging to ECM software Application Layer functions related to GPF control (e.g. GPF Automate). MiL is built up by assembly of all required functions, each function available in Simulink model and assembly performed based on Alliance Renault-Nissan-Mitsubishi virtualization process [5]. Finally MiL model is assembled with CVT and ML Dynamic Models (detail for both provided in following chapters). For simulation, MiL GPF functions operation is based on feedback from CVT and ML Dynamic Models.

As example of the type of functions implemented in the MiL in MATLAB Simulink, below (figure 3) it is provided an overview of a part of one of the functions in charge of GPF management implemented.
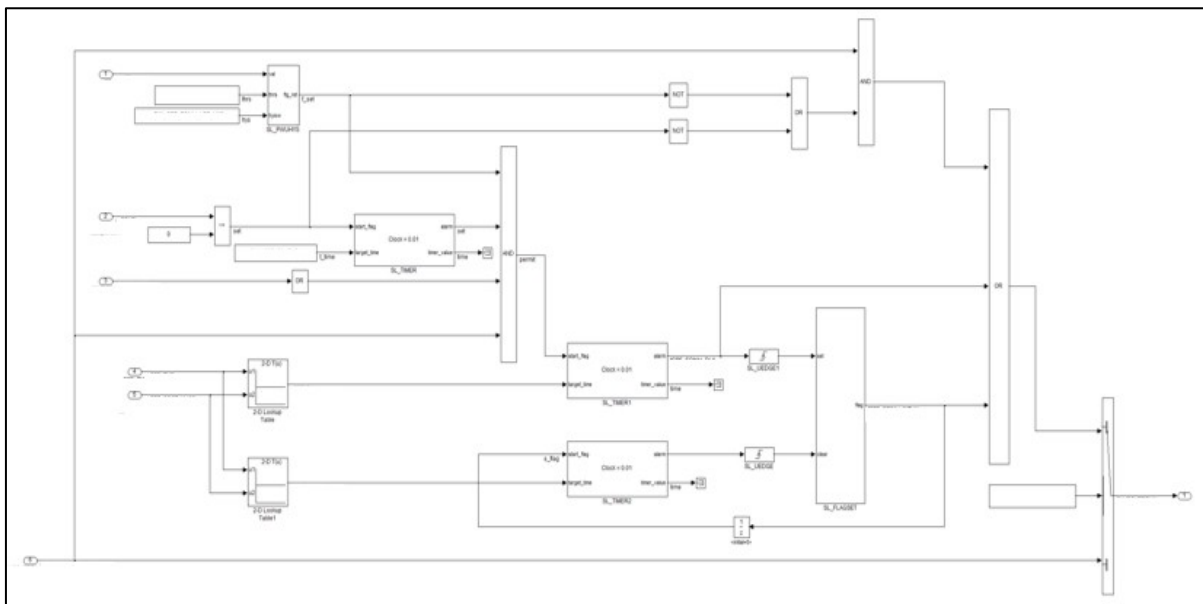
Fig. 3. Overview of ECM Function implemented in MiL Model for GPF System Control

2.3 Description of Continuous Variable Transmission Model

Continuous Variable Transmission (CVT) is powertrain transmission type used in this study. Therefore, specific model is required to implement CVT laws behaviour. As shown below (figure 4) CVT model is comprised by following parts:

- Calculation of Required Power based on Vehicle Load set and Target Speed.
- Calculation of Engine Speed based on Vehicle Speed and Accelerator Pedal Position
- Calculation of Engine Torque based on Required Power and Engine Speed
- Calculation of Accelerator Pedal Position based Engine Speed and Engine Torque
- Engine Status Off/On is considered
- Limitation of Maximum Engine Power (Torque and Speed) according to Full Load Performance
- Correction of Engine Speed during overrun condition
- Correction of Engine Speed and Torque at Fast Idle condition
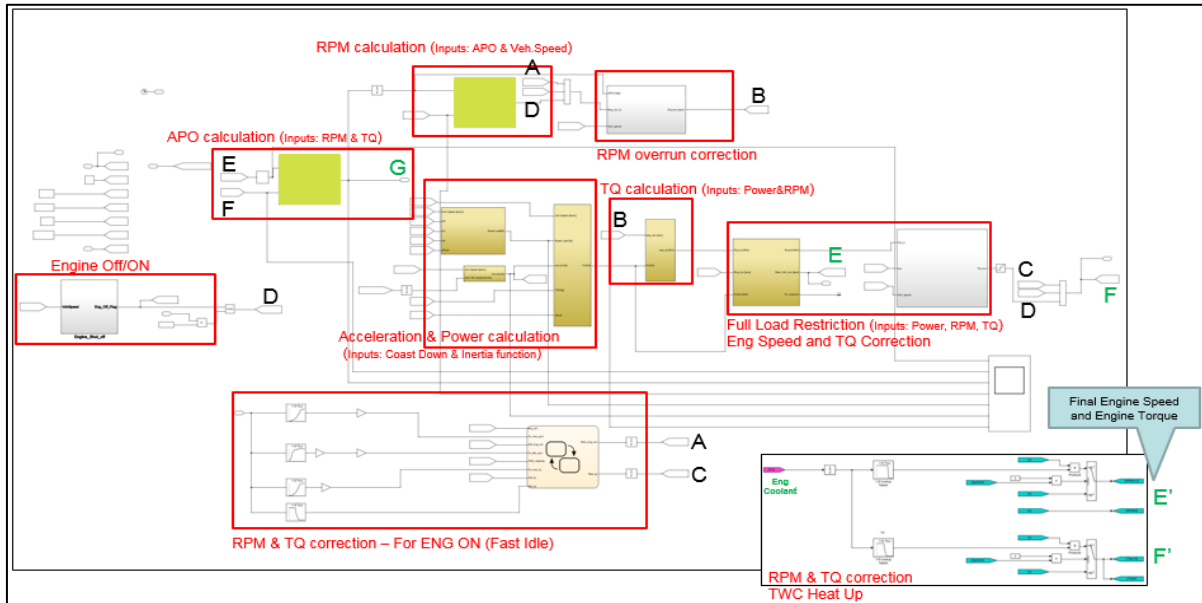- Correction of Engine Speed and Torque during Three-Way Catalyst Heat-Up condition

Fig. 4. Overview of Continuous Variable Transmission

As reference, below (figure 5) there is comparison between vehicle data and CVT model for WLTC test:

Fig. 5. CVT model behaviour for WLTC

As shown in comparison data, even implementation of corrections, factors and filters, behaviour differences are present at some peaks in transient conditions and some stabilized conditions between vehicle test data and CVT model data. Additionally, CVT torque converter Lock-up off condition at low vehicle speed condition (~<15km/h) cannot be appropriately included in this model.

To overcome these differences on Engine Speed and Torque between CVT vehicle and model behaviours, it is decided to use CVT model estimated Engine Speed and Torque as input for training of Dynamic Models. Therefore from vehicle speed and load set conditions from real vehicle test, it is calculated Engine Speed and Engine Torque values from CVT model. Then these new CVT model Engine Speed and Torque values are used together with vehicle test data to train the dynamic models. This post processing operation for Engine Speed and Torque values allows to minimize impact of CVT model differences in Dynamic Models.

2.4 Description of Dynamic Models

2.4.1 Overview of Advanced Gaussian Processes with NARX structure for Dynamic Models

Gaussian Processes (hereunder GP) belonging to Bayesian models type provide a probabilistic and non-parametric approach to learn from data based on kernel machines (in case of GP, based on Covariance functions). Use of GP for Machine Learning purposes has been comprehensively studied and demonstrated in [7]. Additionally, an extensive literature of successful application cases can be found (e.g. [8, 9, 10])

As fundamentals background referent to the type of models used in this study, a short overview of some GP properties for ML is provided here. This overview is focused at first on GP usage for Regression and Supervised Learning* models and secondly on inclusion of Dynamic modelling capabilities based on NARX approach.

Generally speaking a GP can be defined as a collection of random variables any finite number of which have a joint Gaussian distribution. Therefore a GP is completely specified by its mean function $m(x)$ and its covariance function $K(x, x')$

$$GP(m(x), K(x, x')) \tag{1}$$

For regression and supervised learning purposes, normally it is considered a standard linear regression with additional Gaussian Noise such as

$$f(x) = x^T w, \quad y = f(x) + \varepsilon \tag{2}$$

Where f represents the underlying function defining the system under study, being considered a GP with mean function m(x) and covariance function K(x,x'), x the input vector, w the vector of parameters of the linear model, y the observed target value and ε a Gaussian noise with mean 0 and variance σ_n^2

$$f(x) \sim GP(m(x), K(x, x')), \quad \varepsilon \sim N(0, \sigma_n^2) \tag{3}$$

Previous to progress further based on Bayesian analysis and consider any training data for model regression purpose, according to Bayesian approach it is required to consider a prior definition over the function parameters w. From [7] normally it can be defined as mean 0 and covariance matrix Σ_p

$$w \sim N(0, \Sigma_p) \tag{4}$$

Due to w prior consideration, at this point the prior of function $f(x)$ is considered as mean 0 and covariance matrix $K(x, x')$

From previous considerations and based on the probabilistic framework and the usage of training data, the following predictive distribution can be obtained for regression models as demonstrated in [7]:

$$p(y_* | x_*, D) = N(\mu_*(x_*), \sigma_*^2(x_*)), \text{with} \begin{cases} \mu_* = k_*^T(K + \sigma_n^2 I_m)^{-1} y \\ \sigma_*^2 = \sigma_n^2 + k_{**} - k_*^T(K + \sigma_n^2 I_m)^{-1} k_* \end{cases} \tag{5}$$

Where D = $\{x_i, y_i | i = 1, ..., m\}$ are the m input-output pairs used for training, $k_* \in R^{mx1}$ the vector of covariance between the latent function value $f(x_*)$ at the test point x_* and the training function values, $K \in R^{mxm}$ the covariance matrix of the training function values, I_m the m x m identity matrix, $y \in R^{mx1}$ the vector of training outputs and $k_{**} = k(x_*, x_*)$ the prior variance of $f(x_*)$

(*)Supervised Learning understood as the task of learning from empirical data differentiated between inputs and outputs and Regression as the ability to predict continuously an output or target, normally defined as y, from a set of inputs normally defined as a vector x.

In the case of k_* and K these are built using the covariance functions as

$$k_* = \begin{bmatrix} k(x_1, x_*) \\ \vdots \\ k(x_m, x_*) \end{bmatrix} \; and \; K = \begin{bmatrix} k(x_1, x_1) & \cdots & k(x_1, x_m) \\ \vdots & \ddots & \vdots \\ k(x_m, x_1) & \cdots & k(x_m, x_m) \end{bmatrix} \tag{6}$$

Being the covariance functions usually parametrized by a set of hyperparameters. In this study the Squared Exponential Covariance function is used, based on its smoothness characteristic. This covariance function can be described as

$$k_{SE}(x_i, x_j) = \sigma_0^2 \exp\left(-\frac{1}{2}(x_i - x_j)^T \Lambda^{-1}(x_i - x_j)\right) \tag{7}$$

With $\Lambda = \text{diag}([l_1^2, \dots, l_d^2])$ where l_i are the characteristic length-scales, being d the input dimensionality, (the amount of input parameters in each x_i) and σ_0^2 the variance of the latent function f. As demonstrated in [1] these hyperparameters values can be learned from the training data by maximizing the log marginal likelihood described here as

$$\log p\,(y|\theta) = -\frac{1}{2}y^T(K + \sigma_n^2 I_m)^{-1}y - \frac{1}{2}\log|K + \sigma_n^2 I_m| - \frac{m}{2}\log 2\pi \tag{8}$$

Additionally, in the case of the Advanced GP, to overcome the limitations that may come from the linear regression approach, it has been demonstrated that the inputs and/or outputs can be projected into some more suitable higher or different feature space based on a set of basis functions independent from parameter w. Then the presented linear regression model and probabilistic approach can be applied directly into this new feature space. Identification of this most suitable feature space and projections can be learnt in supervised or unsupervised manners as presented in [11, 12]

For the purpose of Dynamic Modelling, it is additionally required the use of a Nonlinear Autoregressive with Exogenous input (NARX) structure [13, 14]. The use of this structure allows to expand the input space with additional feedback from the past inputs and output and to transform the dynamic identification problem into a quasi-stationary relationship with the new input vector $\tilde{x}(k)$

$$y(k) = f_{NL}(\tilde{x}(k)) = f_{NL}\left(x_1(k), \dots, x_1(k - n), x_2(k), \dots, x_2(k - n), y(k - 1), \dots, y(k - n)\right)$$

Where k indicates a discrete time-step and n the maximum input and output delay used.

However for GP, computational complexity scales as $O(m^3)$ due to the matrix inverse in (5). This situation becomes even worse in the case of dynamic models with large amount of training and NARX structure. As a result data computational complexity may become infeasible from resources capabilities. To solve these issues it is required the use of more efficient Sparse GP approach [15, 16].

2.4.2 Description of Training Data Generation – Efficient Testing

To efficiently train ML Dynamic Models, data from synthetic cycles is used. Synthetic cycles are defined to obtain the data required to fully characterise the system understudy with the minimum testing resources. In this study for GPF System, several synthetic cycles plus some specific urban driving conditions cycles are used. All tests are performed based on vehicle and climatic chassis dyno facility at different ambient temperature conditions (i.e. -10 ºC, 0 ºC, 10 ºC and 20ºC).

As example of one of the synthetic cycles used, below are shown vehicle speed, road slope, engine speed and engine torque characteristics for synthetic cycle *GPF Dynamic Cycle*. From ML training point of view, this cycle of 1h of duration provides as much data as 6h of standard cycles would provide.
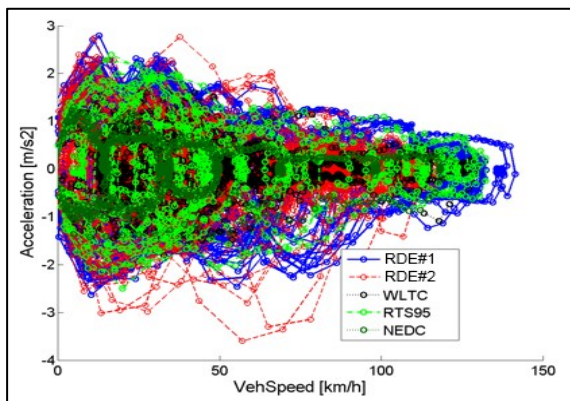
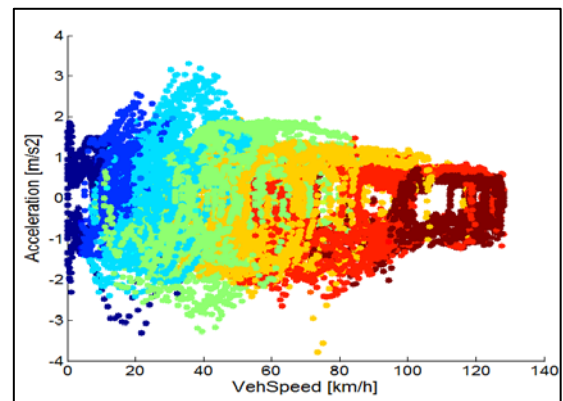**Fig. 6.** Veh. Accel,&Speed Range from Ref. Cycles

Fig. 7. Veh. Accel.&Speed Range from Synth. Cycle
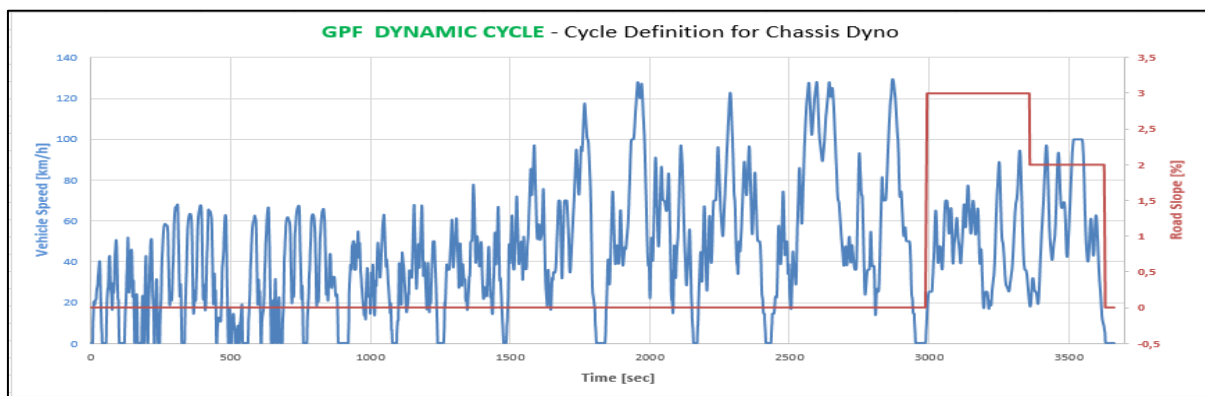

Fig. 8. Synthetic Cycle Speed, Road Slope and Duration Overview
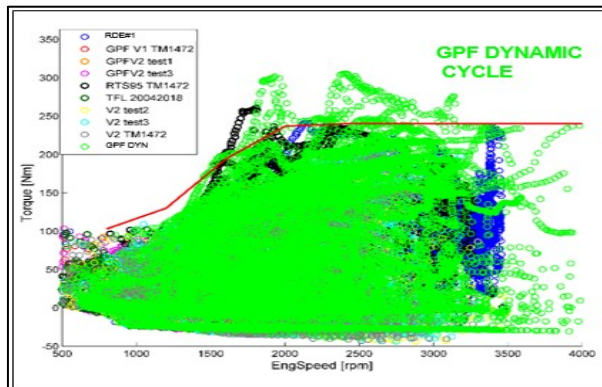

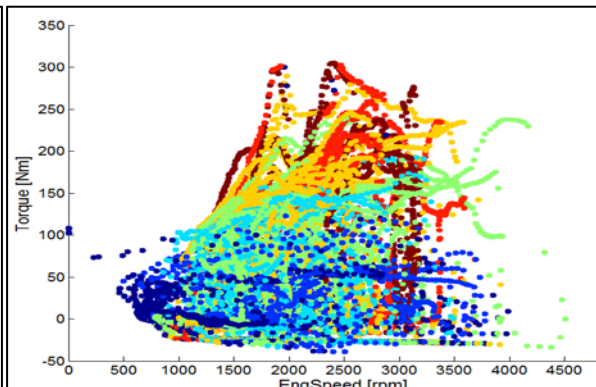**Fig. 9.** Synth. Cycle Eng. Speed and Tq Comparison

Fig. 10. Synth. Cycle Eng. Speed and Torque Range

2.4.3 Overview of Dynamic Models Training Behaviour

As previously described, Advanced Gaussian Processes with NARX structure are used for ML Dynamic Models used in this study. This type of models has been used for Engine Out Particulate Number (PN EO), Exhaust Flow and GPF Temperature. PN EO model is based on engine out measurement with HORIBA MEXA-SPCS2000 and ADDAIR PEGASOR PPS-M, Exhaust Flow model is based on Engine Control Unit internal model previously calibrated and GPF Temperature is based on temperature sensor instrumented at GPF center position.

As example of NARX AGP regression capabilities for Dynamic data, below is shown training behaviour for WLTC cycle at 20ºC for the models involved on GPF performance (i.e. PN EO, Exhaust Flow and GPF Temp). In the case of PN EO model, it is comprised by Cold and Hot engine conditions models.
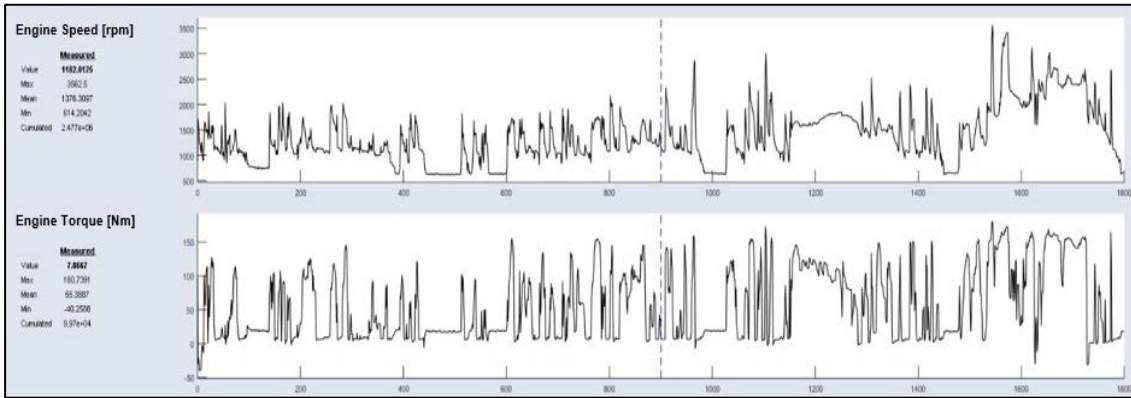
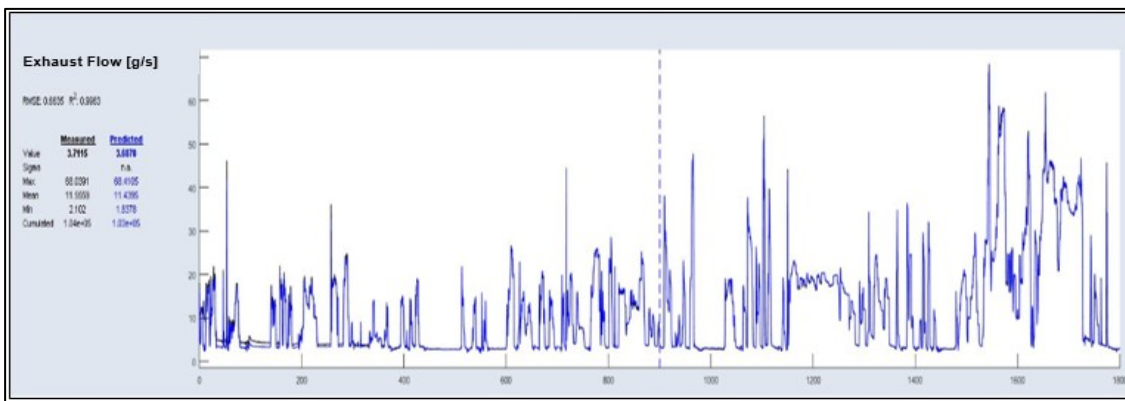**Fig. 11.** Engine Speed and Engine Torque Inputs for WLTC

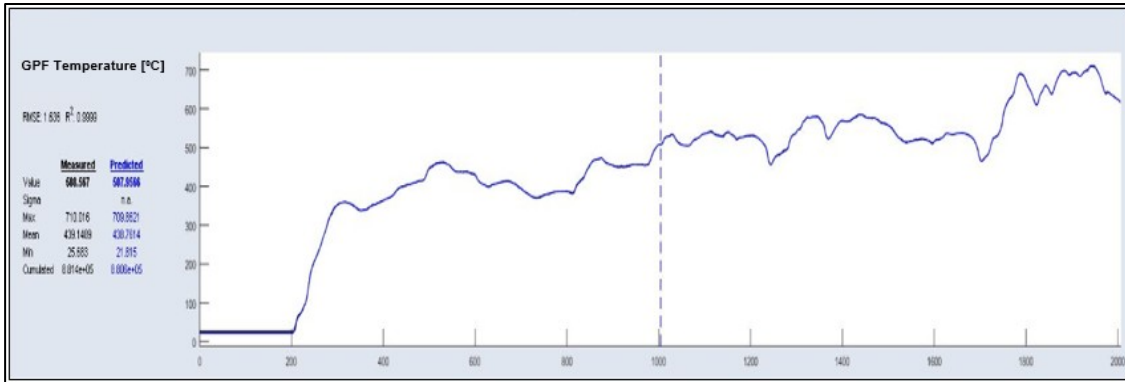**Fig. 12.** Exhaust Flow Model Training behaviour for WLTC 20ºC

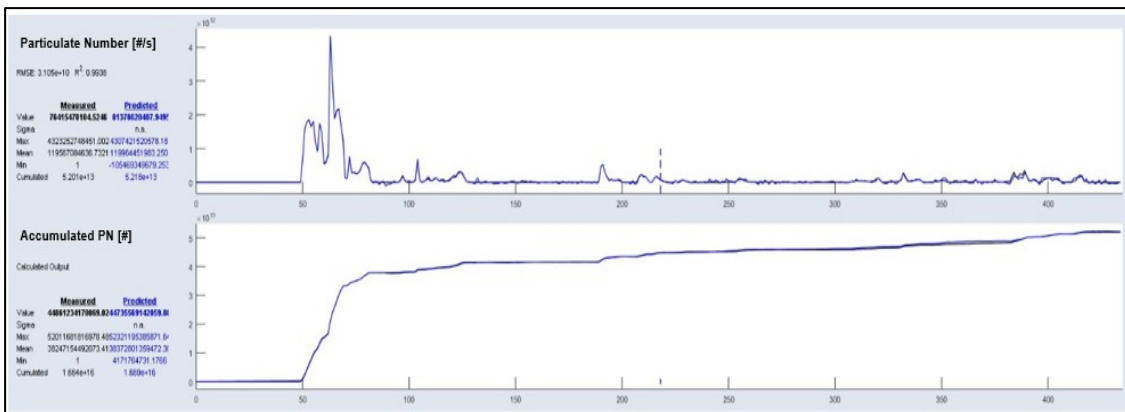**Fig. 13.** GPF Temperature Model Training behaviour for WLTC 20ºC

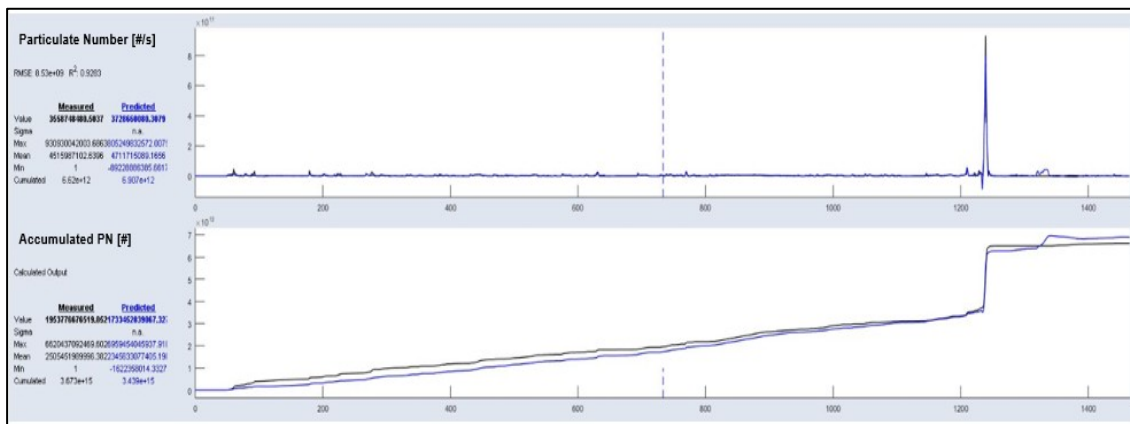**Fig. 14.** PN Model (Cold Engine) Training behaviour for WLTC 20ºC

Fig. 15. PN Model (Hot Engine) Training behaviour for WLTC 20ºC

2.4.4 Overview of Dynamic Models Validation Behaviour – CVT + Virtual ECM + ML Dynamic Models

GPF Performance in the Market model is validated based on the analysis of vehicle speed and acceleration operation ranges from customer's database for market understudy. Due to the differences between Cold Start/Warm-Up and Hot Engine phases for Soot mass generation, operation range analysis is differentiated between Cold and Hot Engine (figure 16)

To be able to efficiently validate the model based on data from vehicle testing, it has been identified the minimum number of customers and which parts of their driving profile are required to be tested to cover the whole operation range from customer's database. Additionally, to limit the time and number of tests to be performed, identification is focused on most critical conditions for GPF soot burn, it means urban and rural driving conditions. As a result, 4 customers have been identified with 2 driving parts from each to be tested, each part being of approximately 1h of duration (i.e. ~8h of vehicle testing in total). To collect required data for Cold Start/Warm-Up phases validation, each test was started after vehicle soaking preconditioning. To validate models behaviour for different ambient temperatures, identified cycles were tested at -10ºC and 20ºC of Ambient Temperature condition.
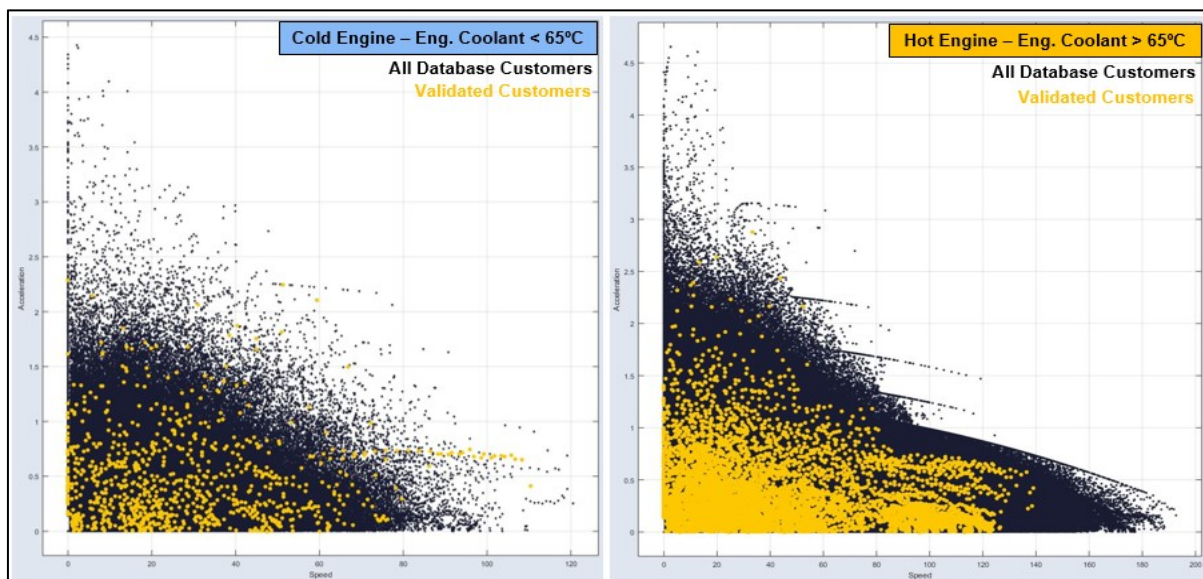

Fig. 16. Veh. Speed and Accel. Range from Market Customer Database. Differentiated by Cold and Hot Engine

Following is shown the behaviour of 2 validation cycles, referred as part#1 and part#2 from customer#1. The model validation (i.e. CVT + Virtual ECM + ML Dynamic Models referred as Simulation Data) is compared to test data from vehicle physical test (referred as Test Data). These parts have been

selected as they are representative of model behaviour for worst conditions for soot burn purpose, low urban vehicle speed.

- Customer #1, part #1 – Ambient Temp. 20ºC. Urban Driving with No Soot Burn opportunity.
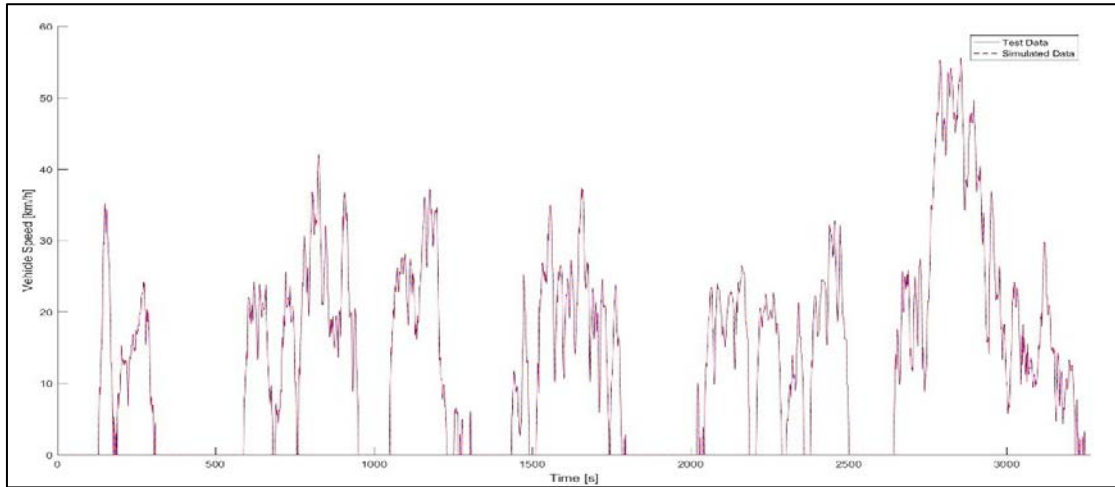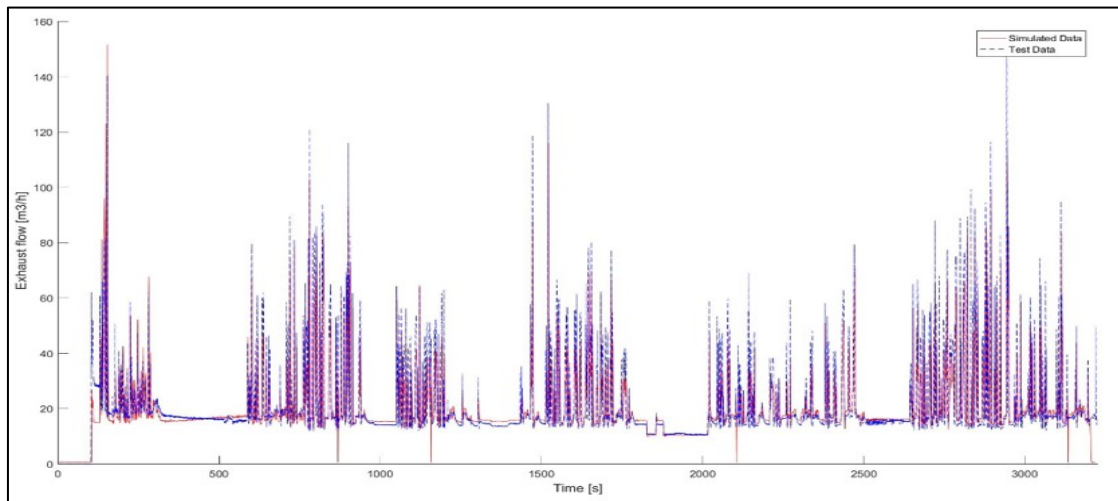

Fig. 17. Vehicle Speed [km/h]

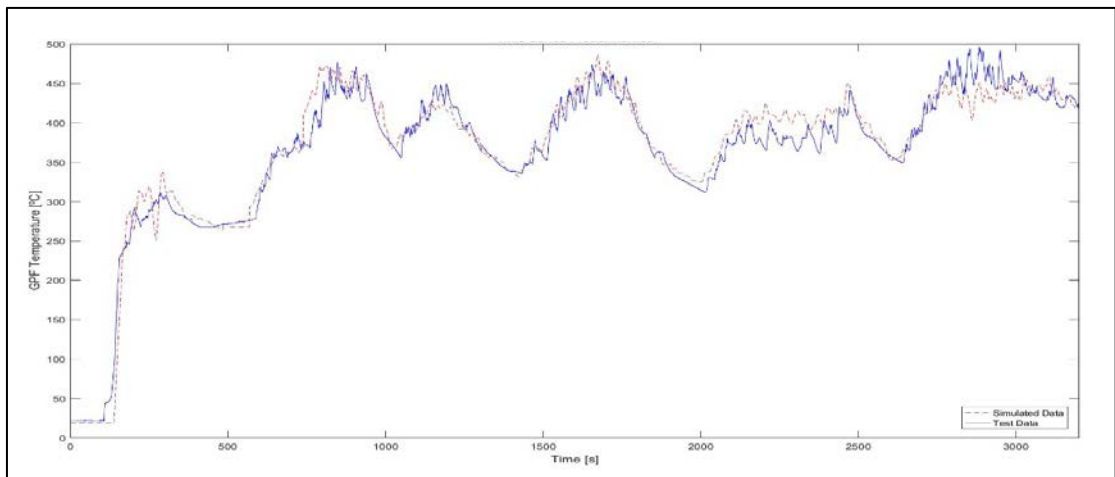
Fig. 18. Engine Exhaust Flow [kg/h]
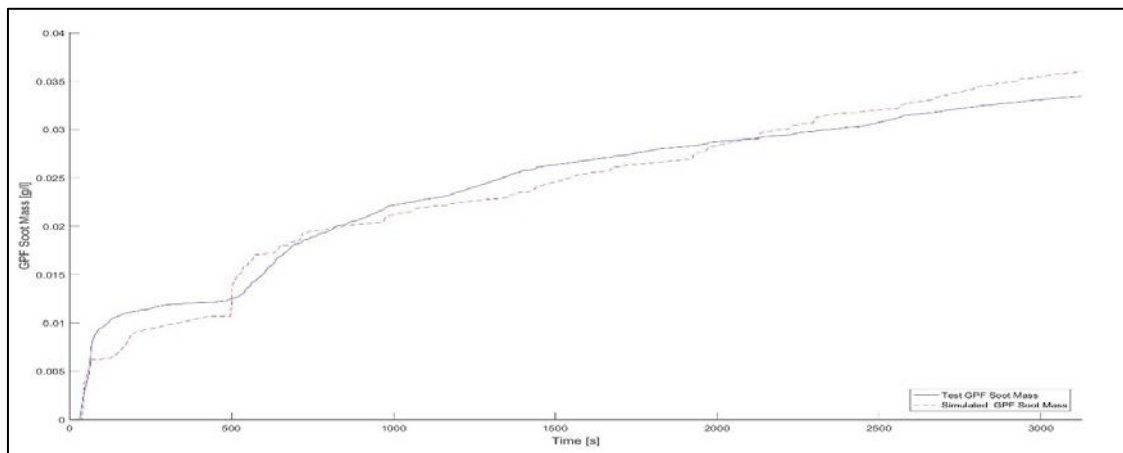

Fig. 19. GPF Temperature [ºC]

Fig. 20. GPF Soot Mass [g/l]

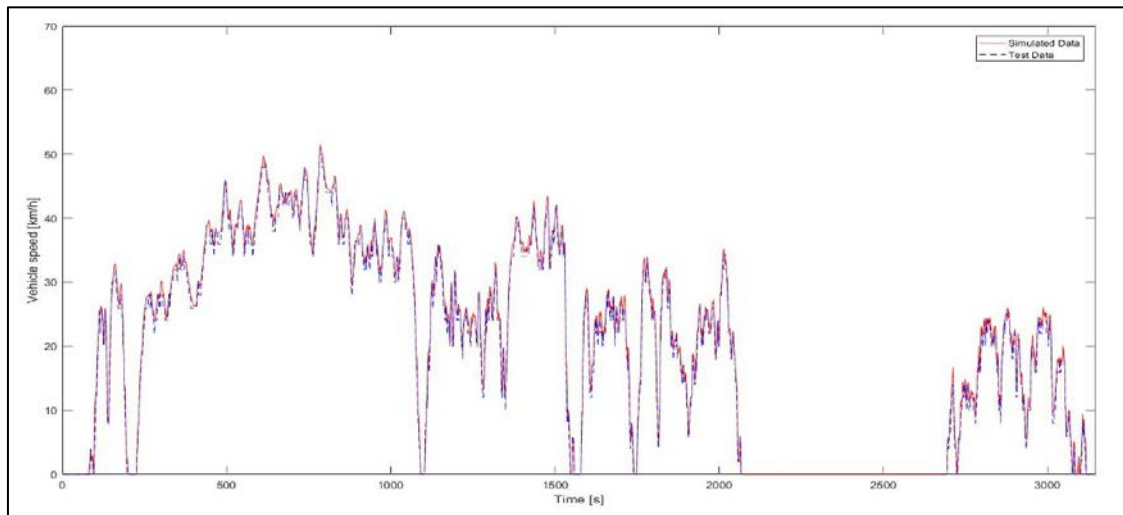• Customer #1, part #2 – Ambient Temp. -10ºC Urban Speed with Soot Burn opportunity.

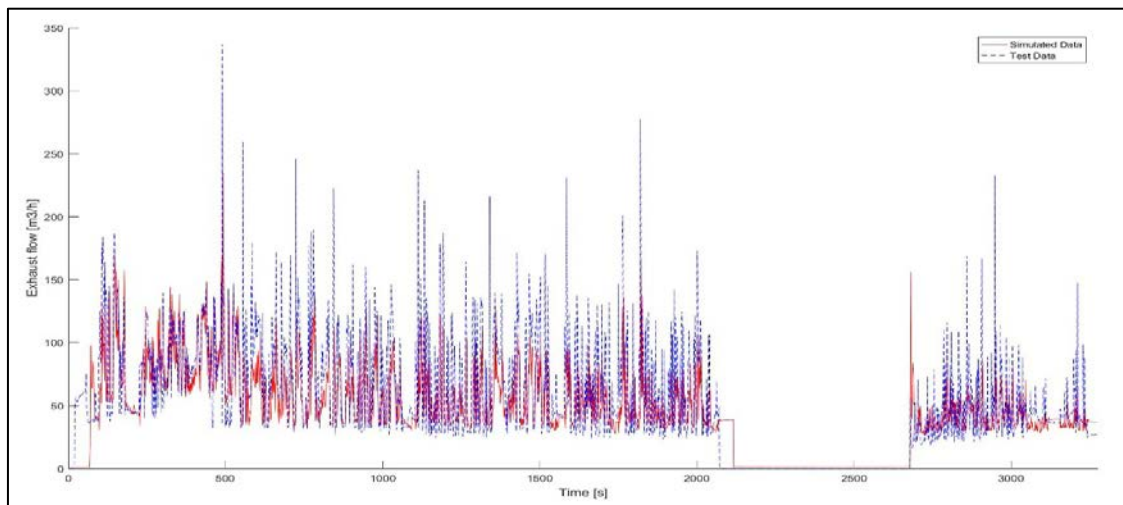**Fig. 21.** Vehicle Speed [km/h]

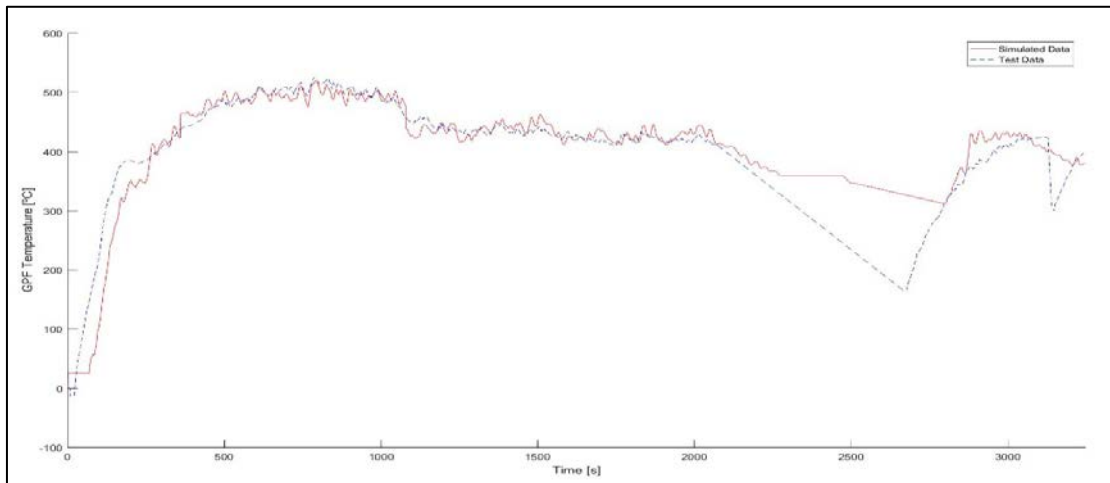**Fig. 22.** Engine Exhaust Flow [kg/h]
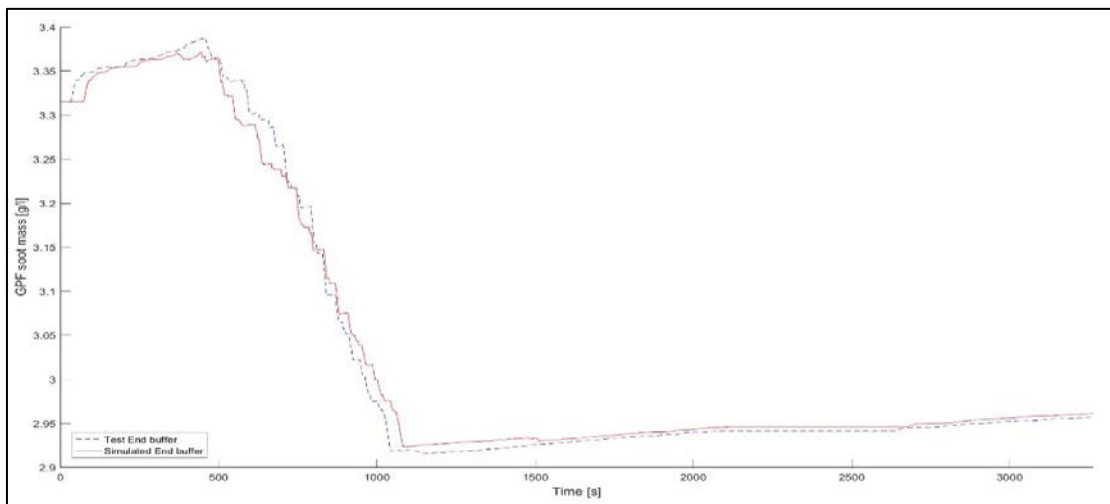
Fig. 23. GPF Temperature [°C]

Fig. 24. GPF Soot Mass [g/l]

As shown in these images, model validation for market customer's predictions has been proved good enough so to accept GPF Performance in the Market Simulation results as representative of market condition. Therefore, GPF Performance in the Market simulation results have been used for definition of GPF Hardware (Position and Volume) and Control Logic (GPF Automate) and confirmation of GPF Performance in the worst market condition as describe in chapter 3.

2.5 Description of Customer Database and Weekly Average Temperature

One direct way to validate market performance is to base simulation predictions on actual market information. For this scenario, having the relevant information from market, in this case the inputs used by the simulation platform and data representative of all market conditions, being especially important those conditions considered as worst scenario for the system understudy, is essential to get reliable conclusions from simulations. In this study a comprehensive database according to all relevant requirements for the GPF system simulation is available. Therefore it has been possible to make market performance predictions based on actual vehicle speed profile data from a comprehensive market customer's database.

Additionally to Vehicle Speed and Engine on/off conditions, ambient temperature is required as input for the simulation platform due to its impact on the amount of soot particles generated, especially in the cold starts and during the warmup phases of the engine (from cold start up to ~65°C of Engine Coolant temperature).

The People's Republic of China (PRC) is the case considered in this study. This is a very severe market due to the extensive range of driving patterns and ambient temperatures to be considered. In the case of driving conditions, as previously explained predictions are based on a comprehensive database of all conditions to be found in the market. Regarding ambient temperature, it is based on weekly average temperature (figure 1) from some of the most populated cities in PRC selected based on their different ambient temperature conditions: Cold Area (Harbin❶, yearly average temp ~4ºC), Mid Area (Shanghai❷, yearly average temp ~16ºC) and Hot Area (Shantou❸, yearly average temp ~22ºC)
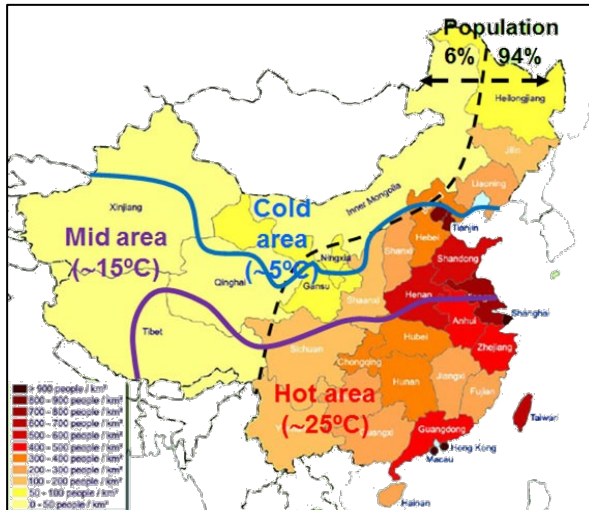
Fig. 25. PRC Population Distribution by Area
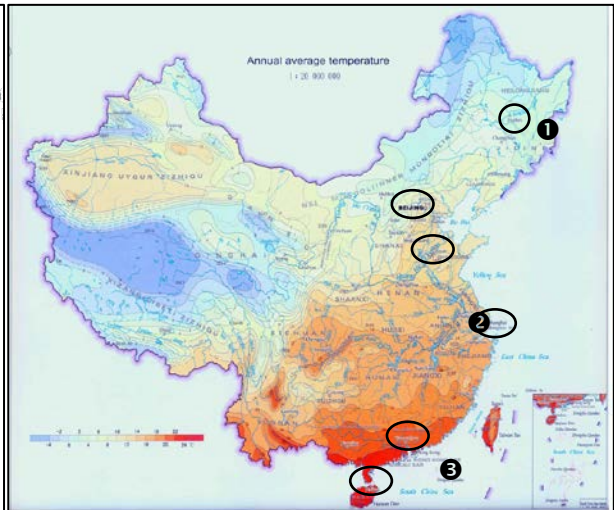
Fig. 26. Harbin❶, Shanghai ❷ and Shantou ❸
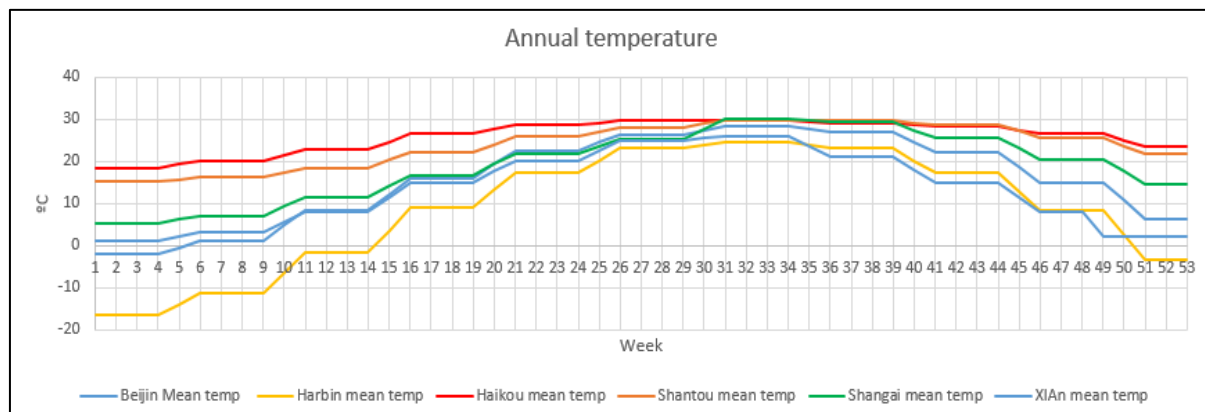
Fig. 27. PRC Weekly Average Ambient Temperature per city (Harbin, Shangai and Shantou)

2.6 Description of Parallel Computing Use

Due to the amount and duration of the cases to be simulated, it is required the use of Parallel Computing Capabilities. Parallel Computing is based on the use of High Performance Computer with 88 cores of CPU@[2,2GHz; 3,6GHz] and 512 GB of RAM. From software point of view, simulations are managed in parallel by MATLAB Parallel Computing Toolbox. As represented below (figure 28), each customer simulation is run in parallel based on the assignation of different CPU core. Simulations common database, parameters and results from each Simulink simulation are managed by MATLAB.

As reference of the benefit of using this approach, simulations take ~3days based on Parallel Computing use. Without Parallel Computing, simulations would take ~60days, which would be not acceptable from the requirements of the GPF Performance on the Market Simulation Platform.
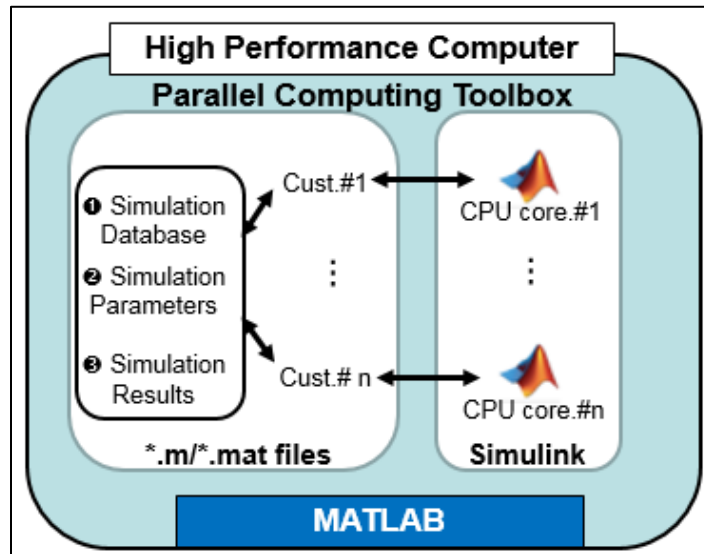
Fig. 28. MATLAB Parallel Computing Overview

2.7 Description of Results

For each customer it is calculated the GPF Soot evolution over 2 weeks' time based on vehicle speed. Maximum Soot and Final Soot in the GPF are computed in each case. (e.g. GPF Soot evolution for 2 customers and different initial soot conditions, figures 29 and 30).

- Ambient Temp: -10ºC; Initial Soot in GPF: 0g/l; Max. Soot in GPF: 1,22g/l; Final Soot in GPF: 0,16g/l
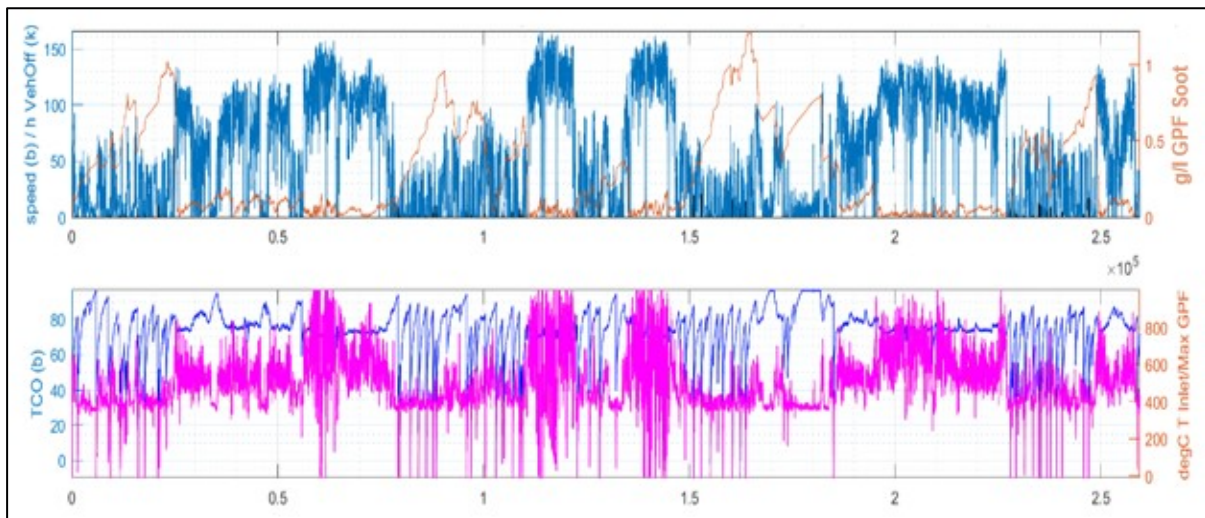
Fig. 29. 2 weeks of GPF soot evolution, example 1. Vehicle Speed, Coolant Temp. and GPF Temp. also plotted

To cover all the expected conditions in the market, a comprehensive set of simulations based on different Initial Soot Mass in the GPF and different Ambient Temperature conditions are calculated for each customer. Different Initial Soot Mass and Ambient Temperature are representative of different GPF Automate Operation Areas (i.e. different system behaviour to manage soot amount depending on the area being present) and different regions and seasons of the Market understudy (e.g. -10ºC/0ºC/10ºC/20ºC for PRC Market).

Then GPF Soot evolution results from all simulation cases previously calculated are combined based on Ambient Weekly Average Temperature, as described in chapter 3.5. Based on this calculation, GPF Soot yearly evolution is estimated and risk of GPF Clogged issues in the market is probabilistically estimated.

- <u>Ambient Temp</u>: -10ºC; <u>Initial Soot in GPF</u>: 3g/l; <u>Max. Soot in GPF</u>: 3,37g/l; <u>Final Soot in GPF</u>: 2,16g/l
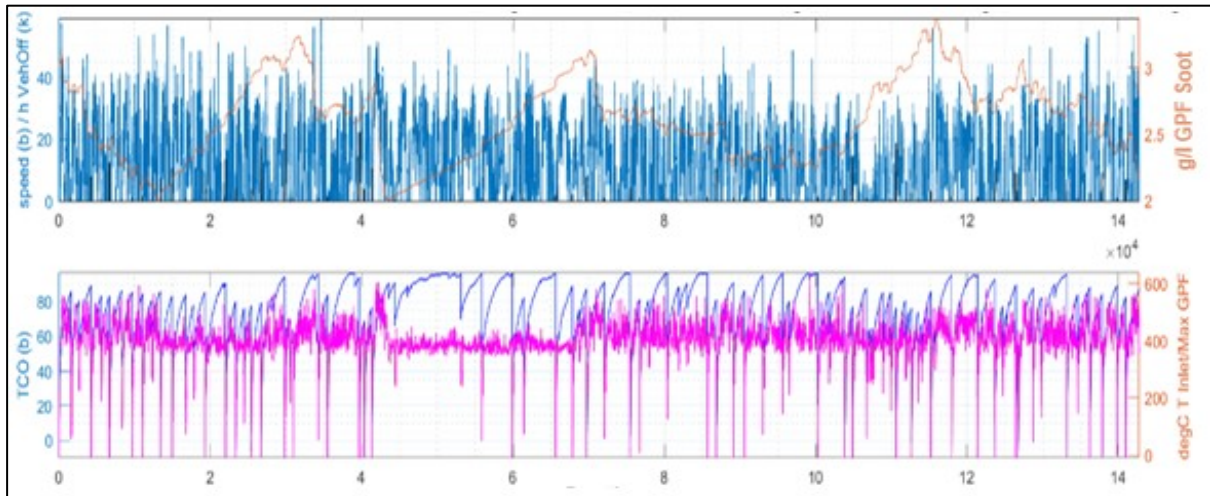
Fig. 30. 2 weeks of GPF soot evolution, example 2. Vehicle Speed, Coolant Temp. and GPF Temp. also plotted

3. Application Cases for GPF Market Performance Simulation Platform

Hereunder it is described some of the applications cases the simulation platform is being used for:

1. Definition of GPF Hardware (Position and Volume)
2. Definition of Engine Control Unit Software for GPF control (GPF Automate)
3. GPF Performance in Worst Market Condition (Coldest Regions and Low Speed Profile Customers)

Following it is provided additional detail for each of these cases.

3.1. Definition of GPF Hardware (Position and Volume)

For GPF position and volume definition many aspects from engine and vehicle layout design need to be considered. Normally GPF systems are introduced to evolutions of engine and vehicle definitions previously designed. Therefore, it is necessary to find the best GPF definition capable of fulfilling all functions required by a GPF system while respecting all Engine and Vehicle layout constraints.

In the example shown below, due to engine and vehicle layout constraints GPF underfloor definition was necessary. In this case, definition of GPF position and volume are of high relevance due to the lower exhaust gas temperature conditions at the GPF compared to a closed coupled definition.
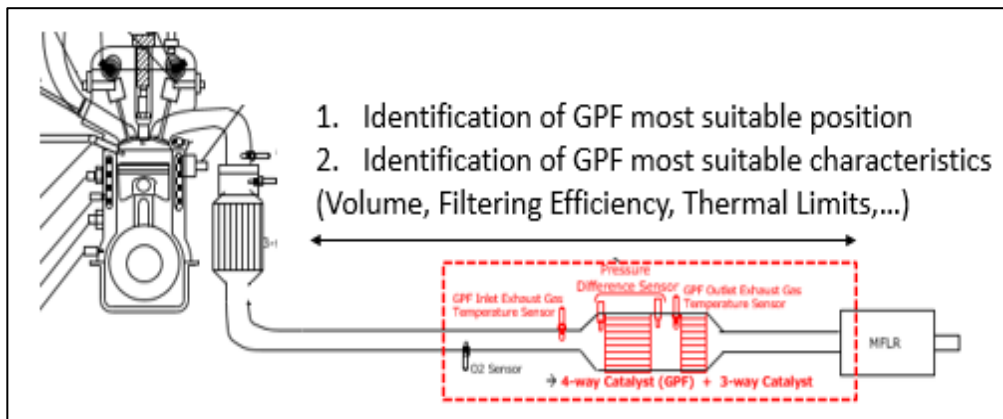
Fig. 31. Identification of Hardware best design

Altogether with the rest of engineering groups whose performance is related with the implementation of the GPF system (i.e. Combustion, Emissions, Powertrain and Vehicle Designers, Drivability, Engine Noise and Thermal Risk groups among others) a set of potential technical definitions was identified. Then based on GPF Performance in the Market forecast from simulation platform it was selected the best Volume and Position definition to guarantee no GPF clogged occurrence in the market while fulfilling all requirements from the rest of performances (figure 31).

3.2 Definition of ECU Software for GPF Control (GPF Automate)

As important as hardware it is the definition of the required software design. In the case of GPF system, software operation is based on a set of models implemented in the Engine Control Module so to continuously characterise GPF status (e.g. GPF Internal Temperature, Soot amount trapped in the GPF, O2 flow through the GPF, etc.). These models are used as inputs of the GPF Automate which is in charge of managing actions related to GPF control.

From calibration point of view, all models must be calibrated according to accuracy requirements defined so to guarantee the appropriate management of the GPF system. Once all the required models behave appropriately, it can be considered that the GPF performance in the market mainly depends on how the GPF is managed by the GPF Automate. Therefore availability of methodologies as GPF Performance in the Market Simulation platform to define appropriate GPF Automate characteristics becomes essential.

Following is mentioned GPF Automate characteristics that have been defined or validated according to GPF Performance in the Market Simulation Platform results:

* Definition of required GPF Maximum Soot Storage Capacity to avoid risk of GPF clogged for any driving condition

* Definition of Engine Combustion Minimum Temperature achievement to guarantee no GPF clogged occurrence in any condition (e.g. urban driving with always low average speed)

* Validation of no GPF clogged in any conditions due to the maximum acceptable GPF temperatures for soot burn limitations defined by GPF designers to secure no risk of damage for GPF part

* Definition of use of GPF related lamps on vehicle combi meter in case customer notification about GPF system status may be required (e.g. Visit to Vehicle Dealer is required)

GPF Automate resulting from all mentioned definitions has allowed to guarantee Market satisfaction based on achievement of expected GPF performance and fulfilment of all requirements from the rest of powertrain and vehicle performances (e.g. Fuel Consumption, Emissions, Drivability, etc.)

3.3 GPF Performance in Worst Market Condition (Coldest Regions and Low Speed Profile Customers)

For GPF System, worst conditions correspond to high amount of soot generation from engine combustion together with low GPF temperature. Normally highest amounts of soot are generated during engine cold start and warm-up phases and lowest GPF Temperatures are achieved in urban driving conditions. In this conditions it may be difficult to burn GPF soot and avoid any GPF clogged risk in the market.

In the case here described, worst conditions were identified in the coldest regions of PRC (i.e. from chapter 3.5, Harbin region with yearly average temp ~4ºC and coldest of ~-20ºC) and in those customers with always urban driving conditions with low average speed (e.g. ~30km/h average speed) and many engine cold starts. This behaviour can be described as the repetition of the following pattern:

Engine On (Cold start-High PM Generation) → *Urban Low Speed (No opportunity for soot burn)* → *Engine Off (long soaking, Engine Cooled-down to Ambient Temperature, ~ [-20ºC;0ºC])* → …

In these worst conditions, GPF Market Performance Simulation becomes a very powerful tool to identify which Hardware and Software definitions are required to avoid any risk of GPF clogged issues in the market.

As shown below (figures 32 and 33), for worst conditions soot burn is only possible based on the use of GPF Heat-Up combustion. Therefore GPF Heat-Up performance must be set up so to guarantee soot burn opportunities for these conditions. Additionally, minimization of combustion soot amount generation at engine cold start and warm-up phases must be considered to avoid too high frequency of GPF Heat-Up combustion due to its impact on Fuel consumption.

- Ambient Temp: -10ºC; Initial Soot in GPF: 0gpl; Max. Soot in GPF: 2,82gpl; Final Soot in GPF: 2,76gpl
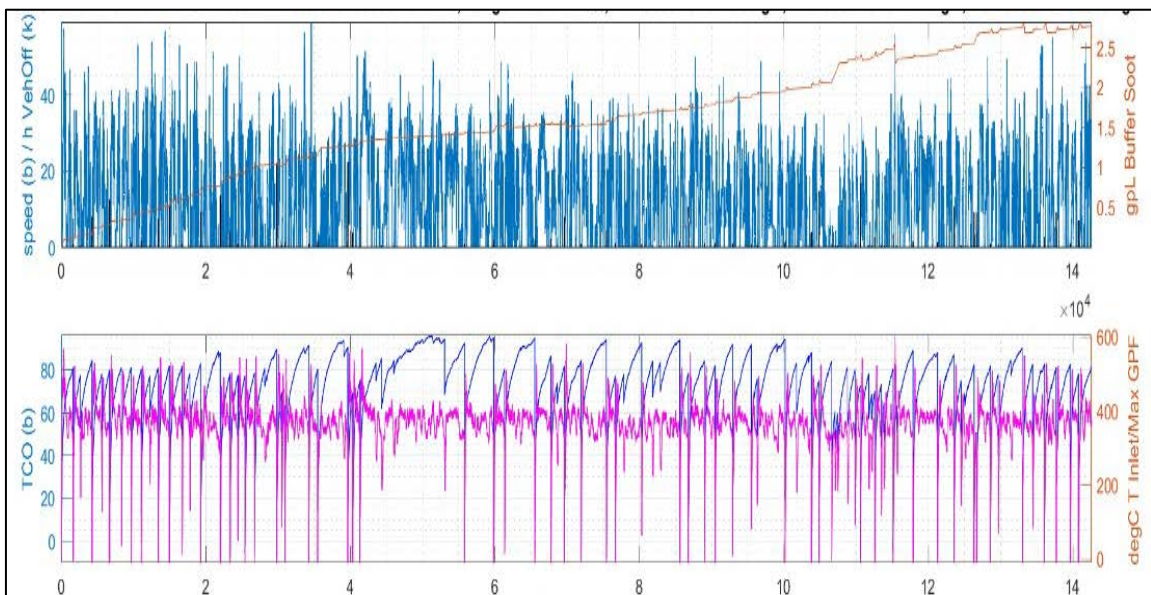

Fig. 32. 2 weeks' time of GPF Soot evolution for Worst Market Condition without Heat-Up Combustion

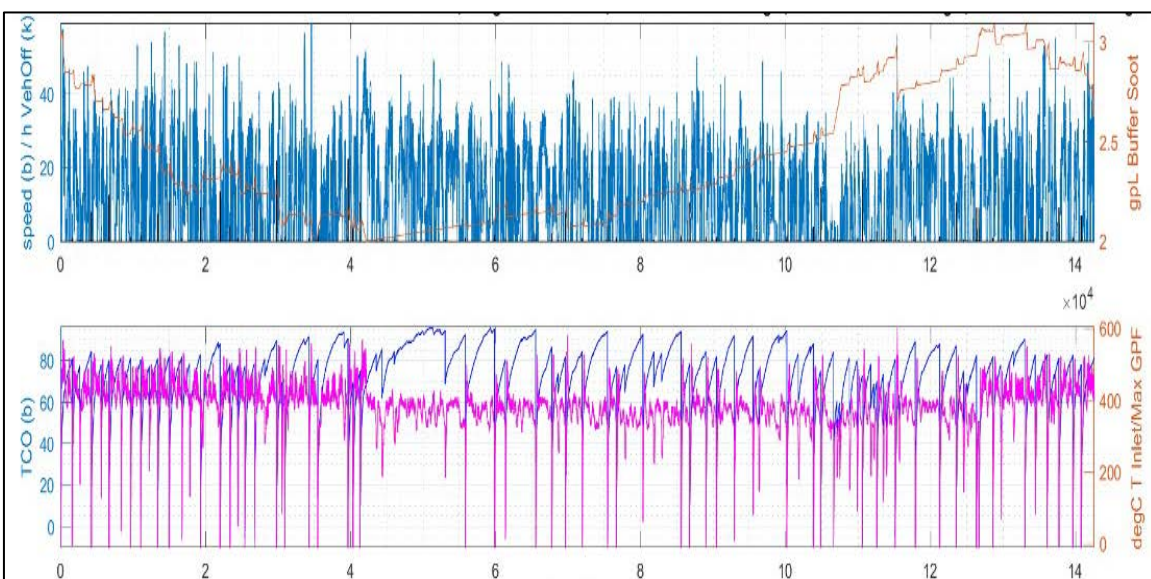- Ambient Temp: -10ºC; Initial Soot in GPF: 3gpl; Max. Soot in GPF: 3,10gpl; Final Soot in GPF: 2,75gpl

Fig. 33. 2 weeks' time of GPF Soot evolution for Worst Market Condition with Heat-Up Combustion

In the case that GPF operation strategies available cannot avoid all risks of GPF clogged in the market, GPF Performance Simulation Platform allows to estimate the expected amount of customers that will be required to visit the vehicle company dealer for GPF Service Regeneration purpose and their frequency.

4. Conclusions

During the last years the Automotive Industry has become even more demanding with the introduction of new Emissions Legislations, the implementation of new automotive technologies and the society technological changes. Nowadays it is established this demand will continue to increase in the years to come with the introduction of new Euro 6e/7 Emissions Legislations, CAFE CO2 targets and the implementation of Autonomous Driving, Powertrain Electrification and efficient Energy Management technologies. In this strongly challenging scenario, mindset willing to find the most suitable methodologies to improve efficiency and quality in all aspects while minimizing costs must always be present.

In the case of Advanced Engineering and Control Unit Calibration for Powertrain Systems, identification of best Systems Design (e.g. engine hardware and engine control software) and optimal Engine Control Module Calibration Settings from early development phases are essential to guarantee achievement of best market quality standards and secure project development timings requirements while keeping minimum costs.

To that purpose, as briefly described in this material, Nissan has been working in the last years in the development of efficient simulation platforms for Powertrain Definition and Control Unit Calibration based on "*Efficient Data Generation + Machine Learning Algorithms + Virtual ECM + Parallel Computing*" approach. Based on expertise and strong engine and vehicle testing facilities capabilities, testing methodologies have been put in place to efficiently generate accurate data (i.e. related to the system understudy) to be used to train the Machine Learning Algorithms (e.g. Gaussian Processes with NARX structure or Recurrent Neuronal Networks) that are used together with related Control Unit Software functions implemented based on Virtual models. As well as for the Gasoline Particulate Filter Performance in the Market described in this material, this approach has been used in the recent years for Diesel Engine Systems Definition and Validation such as Fuel Consumption/Emissions optimization and NOx validation for worst RDE conditions.

The combination of "*Efficient Data Generation/Efficient Testing + Machine Learning Algorithms + Virtual ECM + Parallel Computing*" presented in this study has been proven as a powerful approach from efficiency, quality and costs reduction points of view for Automotive Powertrain Systems Definition and Control Units Calibration Development. Additionally it is considered this approach will become even more powerful in the years to come based on the continuous and increasing improvement pace of Testing, Machine Learning, Virtual Control Units and Computers capabilities resulting from the Automotive and other engineering fields.

Acknowledgments

References

1. Stuart J. Russel, Peter Norvig, "Artificial Intelligence: A Modern Approach"
2. Klar, H., Klages, B., Gundel, D., Kruse T., Huber, R. and Ulmer, H., "New processes for efficient, model-based engine calibration", presented at Proceedings of the 5th Symposium on Development Methodology 2013, Germany, October 22-23, 2013

3. Thewes, S., Lange-Hegermann, M., Reuber, C. and Beck, R., "Advanced Gaussian Process Modeling Techniques" presented at International Conference – Design of Experiments (DoE) in Powertrain Development 2015, Germany, June 11-12, 2015

4. Mauss, J., Pfister, F., "Digital Transformation of RDE Calibration Environments: The Quest for Networked Virtual ECUs and Agile Processes", , presented at International Conference on Calibration Methods and Automotive Data Analytics, 2019

5. Jordan, Y., von Wissel, D., Dolha, A., Mauss, J., "Full Virtualization of Renault's Engine Management Software and Application to System Development", presented at Embedded Real Time Software and Systems (ERTS) 2018

6. Alonso, M., "Model Based Calibration: A Challenge for Optimal Emissions, 6th International Exhaust Emissions Symposium, Poland, 2018

7. Rasmussen, C.E. and Williams, C., K., I.: "Gaussian Processes for Machine Learning (Adaptive Computation and Machine Learning)", Cambridge, USA, The MIT Press, 2005, ISBN: 026218253X

8. Kruse, T., Huber, T., Kleinegraeber, H., Deflorio, .N, "Optimizing Gaseous and Particle Emissions of a GDI Engine by Coupling a Dynamic Data Based Engine Model with ECU Injection Structures", presented at MBC III of International Conference on Calibration Methods and Automotive Data Analytics, 2019

9. Gutjahr, T., Ulmer, H., and Ament, C., "Sparse Gaussian Processes with Uncertain Inputs for Multi-Step Ahead Prediction" IFAC Proceedings Volumes 45(16):107-112,2012, doi:10.3182/20120711-3-BE-2027.00072

10. Schillinger, M., Hartmann, B., Jacob, M., "Dynamic Safe Active Learning for Calibration" presented at International Conference on Calibration Methods and Automotive Data Analytics, 2019

11. Snelson, E., Rasmussen, C.E., Ghahramani, Z.: "Warped Gaussian Processes". In *NIPS* 2004

12. Calandra, R., Peters, J., Rasmussen, C.E.: "Manifold Gaussian Processes for Regression"

13. Sjöberg, J., Zhang, Q., Ljung, L., Benveniste, A., Delyon, B., Glorennec, P.-Y., Hjalmarsson, H., and Juditsky, A., "Nonlinear Black-Box Modeling in System Identification: a Unified Overview" In Automatica, volume 31, Elsevier, 1995

14. Nelles, O., "Nonlinear System Identification: From Classical Approaches to Neural Networks and Fuzzy Models" Springer, 2001

15. Quiñonero-Candela, J., Rasmussen, C.E., Williams, C.K.I.: "Approximation Methods for Gaussian Process Regression" May, 2007

16. Schreiter, J., Nguyen-Tuong, D., Toussaint, M., "Efficient sparsification for Gaussian process regression". In: Neurocomputing 192, June 2016

Neutral Air Quality Impact Vehicle for Urban Areas: NMHC and NH$_3$ Adsorption during Cold Start for ICE Based Powertrains

C. Norsic[1], G. Bourhis[2], M. Lecompte[3], K. Barbera-Italiano[3], E. Laigle[4] and C. Chaillou[4]

[1] EMC France, 4 Allée de la Rhubarbe, Achères, 78260, France

E-mail: christophe.chaillou@aramcooverseas.com
Telephone: +(33) 7 60 31 74 49

[2] IFP Energies nouvelles, 1 et 4 avenue de Bois-Préau, 92852 Rueil-Malmaison Cedex - France, Institut Carnot IFPEN Transports Energie

[3] IFP Energies nouvelles, Rond-point de l'échangeur de Solaize, BP 3 - 69360 Solaize - France, Institut Carnot IFPEN Transports Energie

[4] Aramco Fuel Research Center, 232 Avenue Bonaparte, Rueil-Malmaison, 92852, France

Abstract. For several decades, the transportation sector has been improving pollutant emissions to reduce its environmental impact. An innovative approach is conducted, integrating different aspects related to pollutant emission levels: fuel, powertrain, After-Treatment Systems (ATS) and atmospheric pollutant evolution. The objective is to develop a Neutral Air Quality Impact Vehicle with a nearly zero impact emission technology to get a neutral or positive effect on urban Air Quality (AQ). A technical solution, based on an innovative complete exhaust system architecture for hybrid-gasoline powertrains, allows reducing pollutants when common ATS are not efficient. The paper discusses about a part of this solution which introduces different sorbents placed at the tailpipe, after the core ATS as a way to mitigate cold start related emissions.

Dedicated materials, with a potential to adsorb and convert the different pollutants, are selected and evaluated on a Synthetic Gas Bench (SGB), reproducing the conditions in the exhaust line (temperature, gas composition and residence time) with complex gas mixtures. Simple gas mixtures are also tested to characterize the performance of each material. Despite the low partial pressure, large storage capacities are obtained with some molecules, especially for Non-Methanic-Hydrocarbons (NMHC) and NH$_3$.

A 0D-model, involving each material calibrated with SGB data, is developed to perform system optimization at the vehicle level. The optimization aims at determining the system configuration maximizing ATS conversion efficiency. Projection of specific combination of materials, especially dedicated to NMHC and NH$_3$, showed a reduction of more than 99% of NMHC present downstream of the Three Way Catalyst (TWC) during the cold start phase of 100 seconds and 100% storage efficiency for ammonia. Further investigation are on-going for the other pollutant emissions and for the warm operations.

Notation

AC	Activated Carbon
ADS	Adsorbent
AFR	Air Fuel Ratio
AQ	Air Quality
ASC	Ammonia Storage Catalyst
ATS	After-Treatment System
CAQI	Common Air Quality Index
CC	Close Coupled
CH$_4$	Methane
CO	Carbon monoxide

CO_2	Carbon dioxide
Cu	Copper
Cu-X	Copper based zeolite
DOC	Diesel Oxidation Catalyst
DPF	Diesel Particulate Filter
Ds	Downstream
FAER	Fuel Air Equivalent Ratio
FID	Flame Ionization Detector
GC	Gas Chromatograph
GDI	Gasoline Direct Injection
GPF	Gasoline Particulate Filter
HC	Hydrocarbons
HD	Heavy Duty
H_2O	Water
ICE	Internal Combustion Engine
IR	Infra-Red
LD	Light Duty
LEZ	Low Emission Zone
MOF	Metal Organic Framework
NAQIV	Neutral Air Quality Impact Vehicle
NH_3	Ammonia
NL	Normal Liter
NMHC	Non-Methanic-Hydrocarbons
NO	Nitrogen monoxide
NO_X	Nitrogen oxides
NO_2	Nitrogen dioxide
N_2O	Nitrous oxide
N_2	Nitrogen
O_3	Ozone
PF	Particulate Filter
PFI	Port Fuel Injector
PM	Particulate Matter
PM_{10}	Particulate Matter with diameter < 10 μm
PN	Particulate Number
PNA	Passive NO_X Adsorber
SCR	Selective Catalytic Reduction
SGB	Synthetic Gas Bench
SOA	Secondary Organic Aerosol
SO2	Sulfur dioxide
THC	Total Hydrocarbons
TPD	Temperature Programmed Desorption
TWC	Three Way Catalyst
UF	Underfloor
Us	Upstream
VOC	Volatile Organic Compound
WAQI	World Air Quality Index
WLTC	Worldwide harmonized Light vehicles Test Cycle
WLTP	Worldwide harmonized Light vehicles Test Procedure

1. Introduction

The Air Quality (AQ) has improved in the last two decades but the regulated limitations are still not met in various locations [1] and mainly in large urban areas. The source of emissions is very diverse: heating systems, industries, transport sector, agricultural … [2]. Depending on the molecule considered (HC, CO, NO_X …), the main emitting source could differ. Also, immission level is conditioned both by imported pollution (from remote geographical zones) and local pollutant sources [2]. To reduce the air pollution levels and improve the air quality, large cities, such as Amsterdam, London, Paris, Berlin or Madrid, started to introduce, more than 10 years ago [3], Low Emission Zones (LEZ). The objective of these restrictions is to limit the pollution from the transport sector and mainly the road traffic. Their impact

seems to be limited to a few percent of reduction and not always statistically significant for PM$_{10}$ (Particulate Matter < 10 μm), due to background concentrations [4]. For NO$_2$, the impact of LEZ implementation seems more controversial with studies showing low impact [4] or positive impacts up to an average of 40% reduction on the urban background concentrations [5]. Independently of the impact of the LEZ, the objective of this approach is to develop technologies able to reduce the road transport pollutant emissions and make their contribution negligible compared to other sources.

Transport sector, which includes the Light Duty (LD), Heavy Duty (HD) road transportation, marine transportation, train, subway, aviation transportation, etc. shows a large variety of emissions sources: exhaust emissions and non-exhaust emissions. The non-exhaust emission, related to the brakes, tires, road wear and the resuspension of road dust, are mainly emitting particulates [6], regulated, in the light duty sector, as Particulate Number (PN) or Particulate Matter (PM), according to respectively number or mass concentration. The exhaust emission of an Internal Combustion Engine (ICE) are mainly composed of Hydrocarbons (HC), Carbon Monoxide (CO), NO$_X$ and in a smaller amount the NH$_3$ or Nitrous Oxide (N$_2$O).

A global innovative approach, called Neutral Air Quality Impact Vehicle (NAQIV), has been initiated by Aramco to reduce the amount of direct and indirect pollutants, and to minimize the impact of ICE based vehicles on the AQ. This global approach includes studies of fuels, powertrain technologies, both conventional and innovative After-Treatment System (ATS) and AQ. AQ investigation is key to point out the main molecules that impact, directly or indirectly the ambient air quality [7], including Secondary Organic Aerosol (SOA) formation. The main objective of this approach is to build a vehicle able to have neutral impact on the AQ, meaning that the operation of such a fleet of vehicles would not affect the AQ. This paper will deal only with the ATS part of the global NAQIV approach.

In order to reduce the impact of the transport sector on the direct and indirect emissions, different technologies are conventionally used in Gasoline and Diesel powertrains, lumped in the common term "After-Treatment System". Three Way Catalyst (TWC), Diesel Oxidation Catalyst (DOC), Selective Catalytic Reduction (SCR), Gasoline Particulate Filter (GPF), Diesel Particulate Filter (DPF), Ammonia Slip Catalyst (ASC), Passive NO$_X$ Adsorber (PNA) constitute a non-exhaustive list of systems that reduce the engine out emissions with high efficiency.

This study is considering a hybrid-gasoline powertrain. The lambda one gasoline-based powertrains are all equipped with a TWC and the most up-to-date Euro 6d-temp Gasoline Direct Injection (GDI) based powertrain are equipped with a GPF. The main function of TWC is to convert simultaneously HC, CO and NO$_X$. Cold start is defined as the first seconds of running of an engine after few hours of stop. During a cold start, all the engine parts are at room temperature, generally considered between 23 ±5°C as defined by the European regulated procedures and Worldwide harmonized Light-duty vehicles Test Procedures (WLTP) [8]. During the cold start phase, the combustion is not stable due to the fuel vaporization and the cold wall of the combustion chamber and piston. Therefore, the Air/Fuel ratio (AFR) needs to be adapted to improve the combustion stability and ensure a stable engine running. Due to incomplete combustion and the AFR increase, the engine out emissions are typically high during the cold phase. TWC global efficiency is also typically low at ambient temperature despite sorbent presence to mitigate the low temperature activity. The light-off efficiency, defined as 50% of conversion efficiency, is around 250-300°C [9] for the considered molecules HC, CO and NO$_X$. So, double-effect of high amount of engine-out and low conversion efficiency results in high level of HC/CO/NO$_X$ pollutant emissions during the cold start phase of an engine. This cold start phase may have different durations depending on the engine powertrain technology, the ATS architecture – Close Coupled (CC) or Underfloor (UF), the catalyst, the type of cycle or road trip (slow or fast), the use of heater (burner or electric) and powertrain strategies. Different durations are typically considered but they range generally between 40 and 100 seconds [10]. More than 50 to 90 percent of the cumulated mass of the HC, CO and NO$_X$ pollutants are emitted during the cold start phase (Figure 1) of a Worldwide harmonized Light vehicles Test Cycle (WLTC).

On the other hand, NH$_3$ is mainly produced by the TWC during the transition phase of lean-to-rich mixture [11] with low AFR and is well spread along the cycle. This study will focus mainly on the cold start phase of the system and on NMHC and NH$_3$ molecules.

Different strategies allow to reduce cold start pollutant emissions. This study will develop a technology based on two chemical principles: adsorption and oxidation catalysis but only the adsorption system will be discussed in the paper. Adsorption is a physico-chemical phenomenon, well adapted to cold start pollutant abatement because of the relatively high partial pressure of pollutants [12]. A lower concentration will reduce the adsorption driving force. Indeed, during the cold-start, peaks of emissions of ten to twenty seconds are observed (Figure 1).
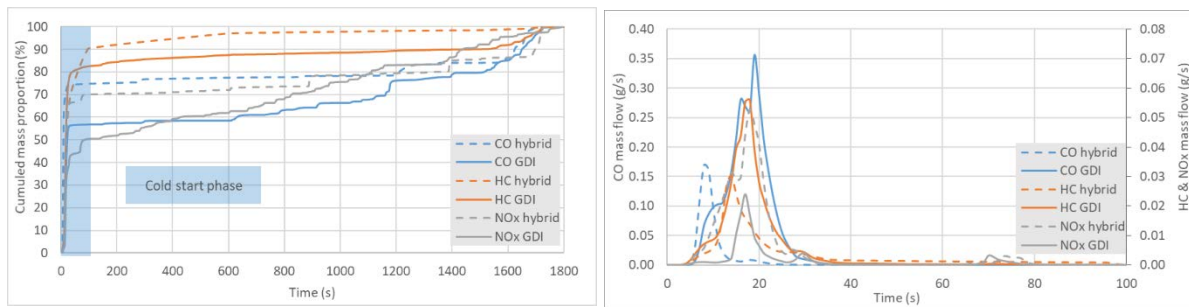
Fig. 1. Cumulated mass proportion (left) and mass flow (right) of CO, HC and NO_X for GDI and hybrid powertrains for a cold start WLTC

When averaging over 100s, this reduces the average concentration and therefore the adsorption efficiency. A lot of different storage materials exist: metal oxides, Metal Organic Frameworks (MOF), zeolites, Activated Carbons (AC) [13]. Based on an extensive open literature screening a number of different sorbents have been selected, and different characteristics were evaluated:

- the global efficiency allowing to determine the remaining quantities at the exhaust pipe
- the storage capacity to determine the volume of sorbent
- the desorption when the concentration/partial pressure is reduced or when the temperature increases
- the compatibility with the exhaust gas composition including mainly the water and CO_2 that largely affect the efficiency of adsorption materials

The first three above mentioned characteristics are linked to the operating temperature. Sorbent materials are well known to be efficient at low temperature but have low efficiency when the temperature increases [14]. Although the lowest temperature of the exhaust line is close to the tailpipe, the temperature is still higher than the desorption temperature when driving on road or highway (Figure 2). During the 100 seconds of the cycle, the tailpipe temperature is around room temperature and allows to select 25°C for the cold start temperature reference.
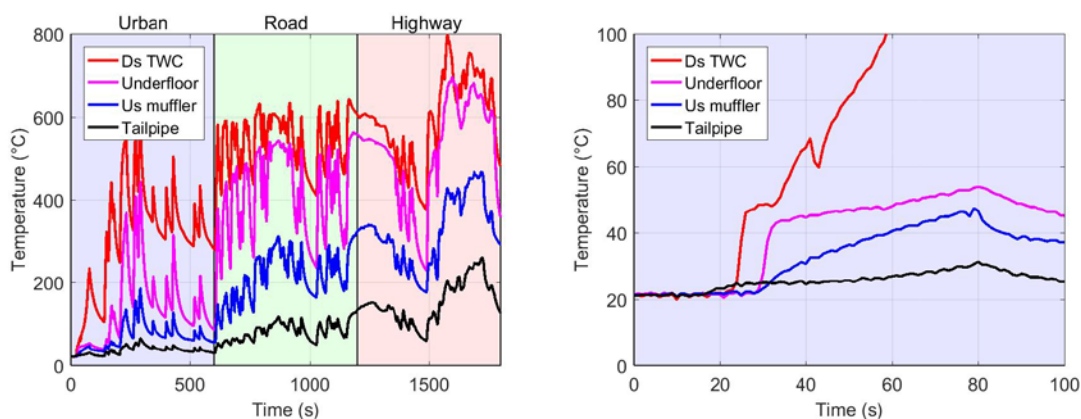
Fig. 2. Exhaust temperature for different locations (Downstream (Ds) TWC, middle UF, Upstream (Us) muffler and tailpipe) for entire WLTC for a hybrid powertrain (left) and zoom on the first 100 seconds (right)

In order to ensure a low temperature level and to determine the operating conditions, the system will be located in a bypass, close to the tailpipe (Figure 3) of the exhaust line. The system and location will allow to have an efficient adsorption and a large storage capacity. To manage the durability and lifetime of the system, two options are currently investigated: a cartridge system with a maintenance period or a regenerative system.
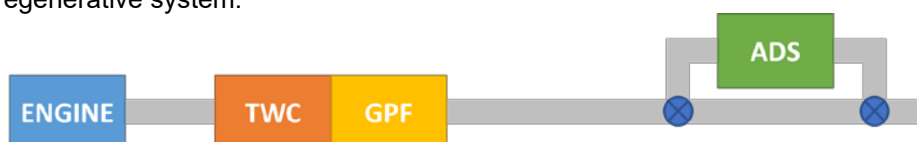
Fig. 3. Architecture of the sorbent bypass close to the tailpipe of the exhaust line

Materials have been tested on a Synthetic Gas Bench (SGB) to extend the assessment of their reported performance for simplified exhaust gas compositions of a gasoline powertrain. This test campaign allows to get the different material characteristics with one or two different samples.

A model has been developed to simulate the expected behavior of material combination for a hybrid powertrain, for more than two materials, on the storage capacity and efficiency of multiple molecules.

This paper will first present the experimental apparatus used to test the selected materials. Then, a description of the model characteristics and the calibration process will be presented. The results part will disclose the adsorption performance for the materials and demonstrate the potential of adsorption efficiency and storage capacity. The second part of the results is dedicated to the modelling of the different materials. The last part of the article will present the projection of the efficiency of a material combination to demonstrate the high potential of reduction of emissions of HCs and NH_3.

2. Experimental setup

2.1 SGB description

SGB experiments were carried out in a tubular flow reactor under atmospheric pressure (Figure 4). To operate at residence times representative of a typical automotive exhaust system, a total volumetric flow rate of 4.94 NL/min was chosen and 430 mg of fresh, i.e. never used, adsorbent (powder form) was used for each adsorption test. All gases were fed to the reactor via Bronkhorst mass flow controllers. The reactor is composed of a quartz tube placed in an electrically heated oven. The temperature was controlled by two thermocouples placed upstream and downstream of the adsorbent bed. Several analyzers were used to measure the pollutants concentrations at the reactor outlet. The adsorbed/desorbed stream composition was on-line analyzed by IR laser (for CO_2, NO, NH_3, N_2O, H_2O), and a Non Dispersive-IR (for CO), while the total amount of HCs was quantified by a Flame Ionization Detector (FID) coupled with a µGC to follow the adsorption/desorption profile of each hydrocarbon. Due to the long sampling period of the µGC (340s) compared to FID (1s), the temporal evolution of each hydrocarbon is reconstructed built using both gas analysis systems.
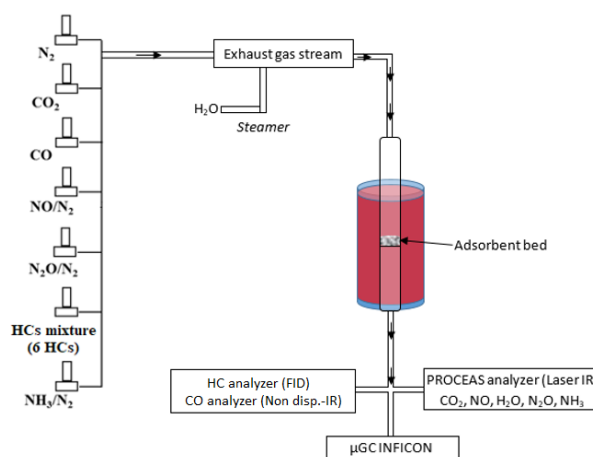
Fig. 4. Experimental setup for present experiments

The compositions of both GDI (Euro 6d temp) and a hybrid gasoline powertrain, using a PFI (Port Fuel injector) engine, exhaust gas surrogates (mixtures of a limited number of gas components representative of the real exhaust gas composition) were determined from previous chassis dynamometer bench tests. For SGB tests, only the composition of the GDI powertrain is tested. Hybrid powertrain composition will be used for projections. Cold start WLTC cycles were performed during these tests. The concentrations used in this study are presented in Table 1 and are determined from these WLTC. Two different mixtures were tested for adsorption experiments: a mixture representative of an average « cold start » (100 seconds) composition at the tailpipe, and a mixture representative of the average concentrations over a distance of 5 km (the first 5 km of a WLTC are typical of automotive trips in urban areas). A wide diversity of hydrocarbons were measured at the exhaust of the vehicles. However, to simplify the preparation of the synthetic exhaust gas blend, a surrogate gas has been defined, containing one compound selected to represent each chemical family. Toluene, ethylene, i-pentane and n-pentane

stand respectively for aromatics, alkenes, branched alkanes and linear alkanes. Aldehydes are not represented in this mixture due to their low concentration.

Table 1. Inlet mole fractions (in ppmV) and water (in %) of the synthetic exhaust gas in the tubular flow reactor for a GDI powertrain

Species	"Cold start" mixture	"5 km" mixture
N-pentane	100	20
I-pentane	50	10
Toluene	50	10
Ethylene	200	40
Acetylene	20	4
CH_4	75	15
CO	3 000	750
NO	75	20
N_2O	10	5
NH_3	50	20
CO_2	100 000	100 000
H_2O	1.5%	5%
N_2	balance	balance

The adsorption tests were realized at different temperature (25, 50 and 150°C) until reaching saturation for each molecule of pollutant present in the gas stream. Then, the adsorbent was flushed under a N_2 flow of 4.94 NL/min, to ensure the purge of residual pollutants in the lines and to measure the desorption with zero partial pressure. Finally, the Temperature Programmed Desorption (TPD) was run under the same N_2 flow at a heating rate of 10°C/min, from adsorption temperature to 600°C, to perform the complete desorption and to clean the material.
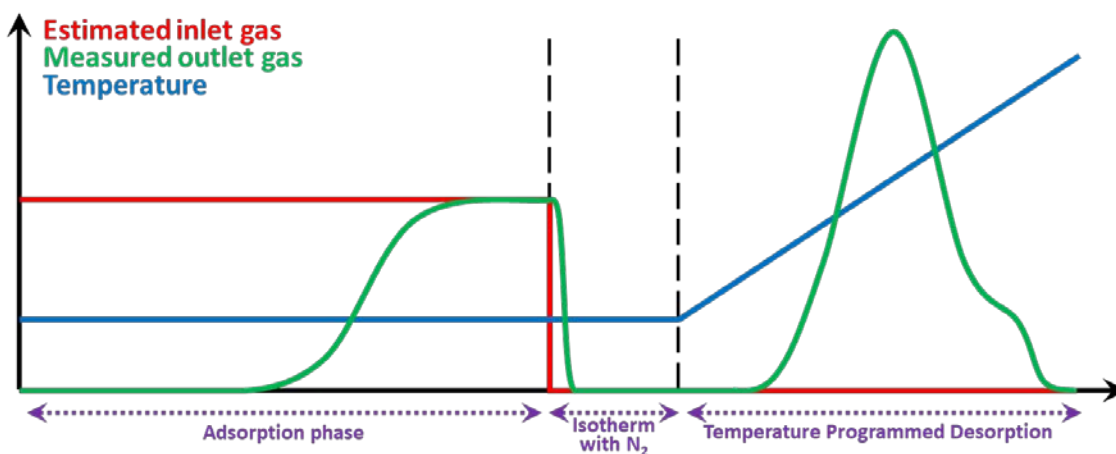
Fig. 5. Test process at SGB

2.2 Materials & test matrix

Different adsorbents were tested in this study (Table 2). The Cu-ZSM5, Cu-β, Fe-β and NH_4-β zeolites were provided by Clariant. The 5A, HY and 13X molecular sieves were purchased at Sigma Aldrich as well as the ZIF-8 (MOF). Activated carbons come from NORIT. The particular AC GCN3070 has been produced from coconut shell by using steam physical activation, while the RO 3515 is made from steam-activated peat. The surface areas are 1514 and 796 m^2/g respectively.

Several parameters of the adsorbents as well as the adsorption tests matrix are presented in Table 2. All adsorbents were tested at 25°C, and only those with the best efficiencies were tested at higher temperature but are not presented in this paper.

Table 2. Adsorbent properties and tests matrix

Adsorbents	Material type	SiO2/Al2O3 molar ratio (-)	Pore size (Å)	Metal content (wt.%)	Adsorption temperature		
					25°C	50°C	150°C
Cu-ZSM5	Zeolite	30	~6	4.5 (Cu)	×	×	×
Cu-β	Zeolite	30	~7	4.5 (Cu)	×	×	×
Fe-β	Zeolite	30	~7	>3 (Fe)	×		
NH4-β	Zeolite	30	~7	-	×		
HY	Zeolite	30	~7.4	-	×		
5A	Zeolite	2	~5	-	×		
13X	Zeolite	2.4	~13	-	×		
GCN3070	Activated carbon	-	12	-	×	×	×
RO3515	Activated carbon	-	-	-	×		
ZIF8	MOF	-	11.6(3.4)	-	×		

3. Numerical Modelling setup

3.1 Model description

The storage model is zero dimension (0D), considering the reactor as one single point and neglecting convective transport, mass and heat transfers. It has been developed using Matlab/Simulink, running with a fixed time-step of 0.1s. That is sufficient to resolve the temporal evolution of concentration over the whole experiment.

It is assumed that each storage site is linked to a single molecule, as all experiments are performed in the same conditions (fixed HC ratio for "cold start" and "5 km" mixtures, sorbent initially empty). Any competitive reaction processes or possible inhibition phenomena are neglected.

For a given species j, assuming there are several storage sites on a given material, storage is modelled following a Langmuir kinetic formalism by computing at each time step the following usual equations [15]:

- Raw adsorption rate for the site i :
$$v_{ads\,raw_i} = k_{0_{ads_i}} P_j (1 - \theta_i)$$
  - $k_{0_{ads_i}}$ is the rate constant for adsorption of site i
  - P_j is the partial pressure of specie j
  - θ_i is the surface coverage of site i

- Final adsorption rate for the site: if the total adsorption rate is above the inlet flow concentration Q_j, adsorption rates are normalized to avoid over-consumption.
$$v_{ads_i} = \begin{cases} if \; \sum_i v_{ads\,raw_i} > Q_j & v_{ads_i} = Q_j \cdot \dfrac{v_{ads\,raw_i}}{\sum_i v_{ads\,raw_i}} \\ if \; \sum_i v_{ads\,raw_i} < Q_j & v_{ads_i} = v_{ads\,raw_i} \end{cases}$$

- Desorption rate for the site i follows a Temkin-type rate expression:
$$v_{des_i} = k_{0_{des_i}} e^{-\frac{E_{a_{des_i}}(1-\alpha_i\theta_i)}{RT}} \theta_i$$

  - $k_{0_{des_i}}$ is the rate constant for desorption of site i
  - $E_{a_{des_i}}$ is the activation energy for desorption of site i
  - α_i is a constant to describe the dependence of the activation energy of desorption from the surface coverage θ_i of site i
  - R is the ideal gas constant
  - T is the reactor temperature

- Molar quantities stored on the whole material N_{tot} and for each site N_i:
$$N_{tot} = \sum_i N_i \qquad N_i = \int v_{ads_i} - v_{des_i}$$

- Surface coverage for the site i, assumed to be locally homogeneous, and defined as ratio of quantity stored and total molar capacity $N_{i_{max}}$

$$\theta_i = N_i / N_{i_{max}}$$

Heat balance is herein neglected due to the high dilution of pollutants in the diluent gas.

To calibrate the model, the first step is to determine how many sites are required to correctly represent the material behavior. Then, five parameters totally define each site: the storage capacity, the adsorption and desorption rates, the activation energy for desorption and the constant to link the surface coverage and the activation energy of desorption.

3.2 Calibration process

Each material has been characterized with the adsorption phase using gas mixtures and TPD. Using those tests, it is possible to calibrate the storage model with the following steps:

1. Determine the number of sites analyzing the desorption profile for every storage temperature.
2. Evaluate the total storage capacity during storage and TPD phases, and then storage capacity of each site.
3. Calibrate the desorption parameters of each site: $E_{a_{des_i}}$, α_i and $k_{0_{des_i}}$. If available, values from literature can be used, or an algorithm has been developed to find the most accurate values for fitting the desorption curve.
4. Calibrate the adsorption related parameter: $k_{0_{ads_i}}$

Example 1: desorption calibration for NH₃ stored on Cu-ZSM5

Cu-ZSM5 is a well-known zeolite and it has been widely studied. Many models found in the literature [16] show that Cu-ZSM5 can be described with four storages sites: physisorption, weak acid, strong acid and metallic. Values for $E_{a_{des_i}}$ and α_i are also available and are used for the model calibration.

For this model, the assumption is a full coverage of active sites at the end of storage phase and before the start of the TPD phase.

It can be noticed, with the analysis of the TPD at different storage temperatures (Figure 6), that curves at 50°C and 150°C are very similar while the 25°C desorption is different from the others below 300°C.
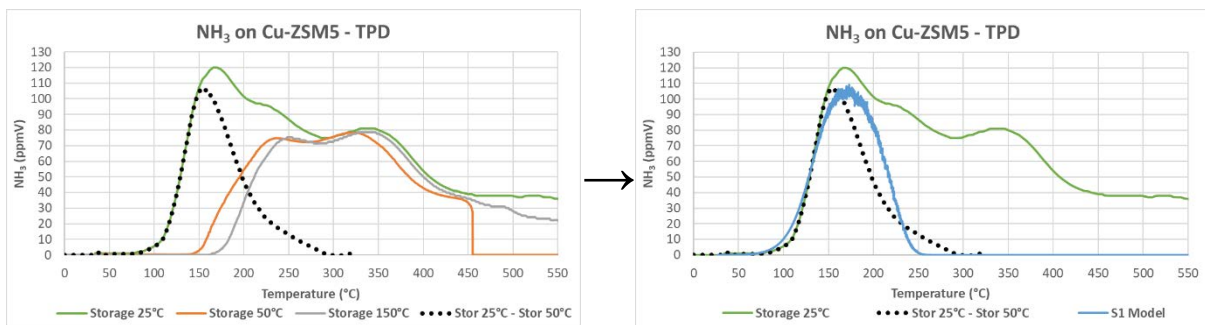
Fig. 6. Concentration of NH₃ during TPD for different storage temperature (25, 50 & 150°C), for the difference between storage at 25°C & 50°C and for the site 1 of the model for Cu-ZSM5

The difference between 25°C and 50°C (black dots) highlights the desorption of physisorbed ammonia, which has the lowest activation energy. This storage site, named S1 in the figure, is only available for storage at 25°C and not for the other temperatures.Using that curve, storage capacity of this site can be estimated. As $E_{a_{des}}$ and α are known, $k_{0_{des}}$ is determined to fit the model with the experimental curve. The first storage site is now calibrated.

The three other sites are calibrated using an iterative process: storage capacities and rate constants are manually chosen to fit the total desorption curves (Figure 7).

The model fits accurately the desorption curves for every storage temperature (*Expe* and *Model total* curves in Figure 7).
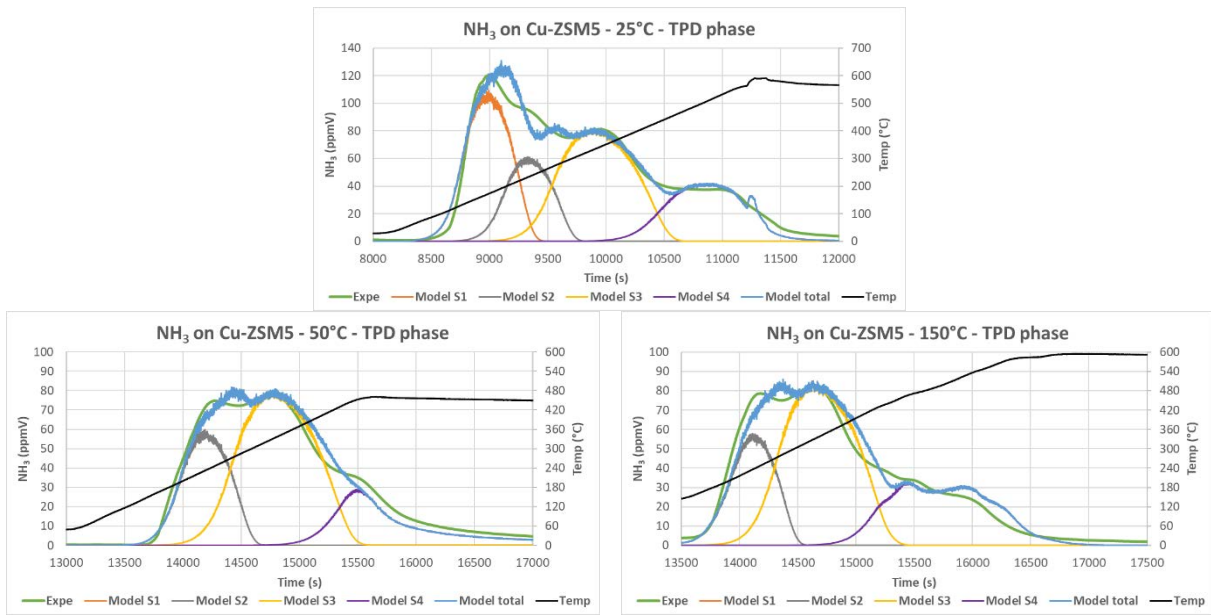
Fig. 7. Concentration of NH3 during TPD for different storage temperatures (25, 50 & 150°C) and associated desorption deconvolution for four sites for Cu-ZSM5

Example 2: adsorption calibration for NH$_3$ on Cu-ZSM5

All parameters have been previously calibrated except adsorption rate constants. Literature values are first used for storage profiles at 25°C, 50°C and 150°C and then, if necessary, values are manually adjusted to fit the experimental curves [17] (Table 3).

Inlet gas concentration is determined with downstream analysis when the material is saturated. For 50°C and 150°C, the model represents correctly the phase where NH$_3$ is fully stored and also the transient phase up to the material saturation (Figure 8). At 25°C, the model over-predicts the adsorption efficiency at the beginning of the transient phase.

Table 3. Comparison of adsorption rate constants from literature and calibrated for NH$_3$ on Cu-ZSM5

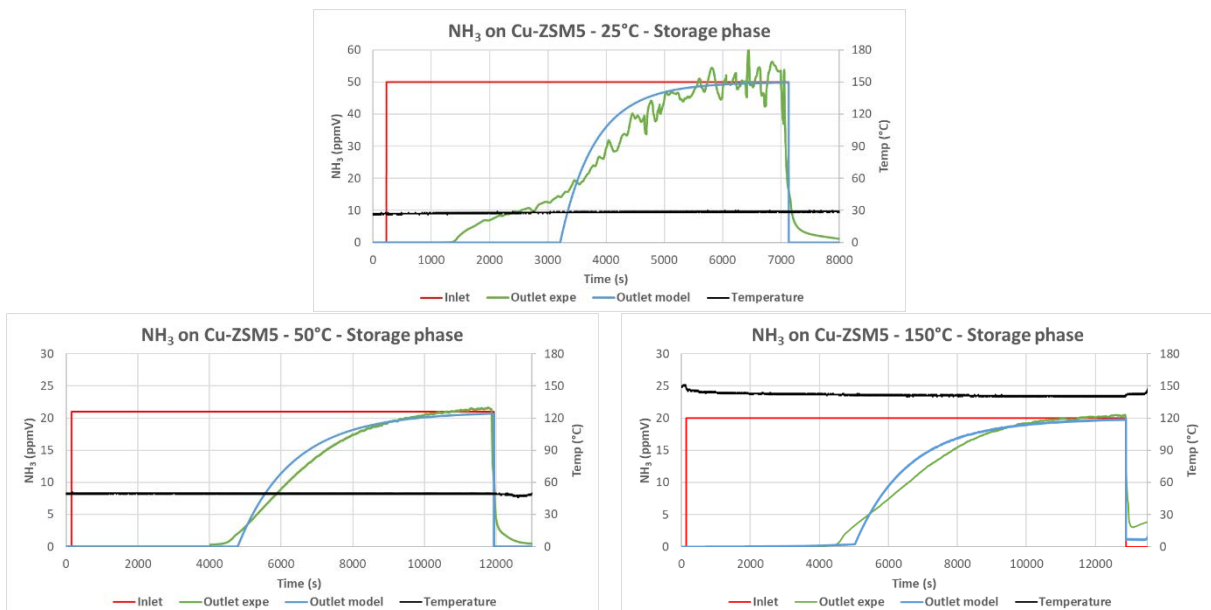|	S1	S2	S3	S4
Literature rate constants (mol/(s.kg$_{mat}$))	9.9 10^{-4}	5.8 10^{-4}	7.8 10^{-4}	4.1 10^{-4}
Calibrated rate constants (mol/(s.kg$_{mat}$))	9.9 10^{-4}	7.4 10^{-4}	7.8 10^{-4}	4.1 10^{-4}
Ratio literature/calibrated values (-)	1.00	0.78	1.00	1.00

Fig. 8. Concentration of NH$_3$ during adsorption phase for different temperatures (25, 50 & 150°C) for Cu-ZSM5

Example 3: adsorption calibration for toluene on AC (Activated Carbon NORIT GCN3070)

Calibration procedure is applied to model the desorption of toluene on AC. Starting from storage at 150°C, where only one peak is observed, one site is added for each temperature 50°C and 25°C.The model shows very good results for the three storage temperatures (Figure 9).

Adsorption rates are adapted to fit the experimental curves, starting from the rate of 150°C site, then calibrate the rate of 50°C site, and finally the rate of 25°C site (Figure 10).
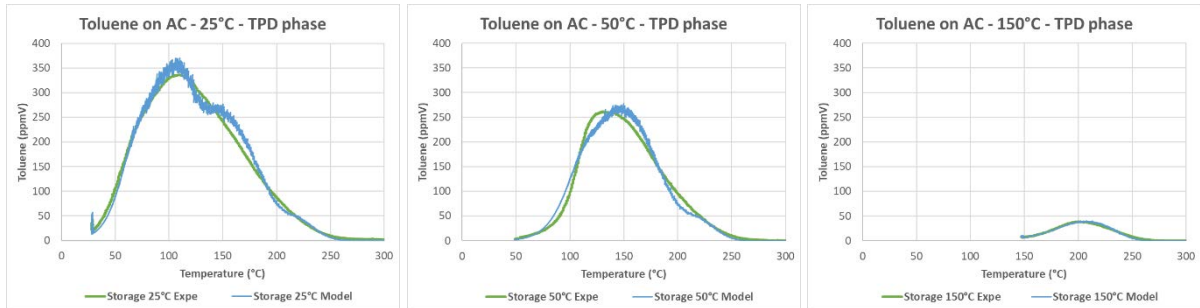
Fig. 9. Concentration of toluene during TPD for different storage temperatures (25, 50 & 150°C) for AC
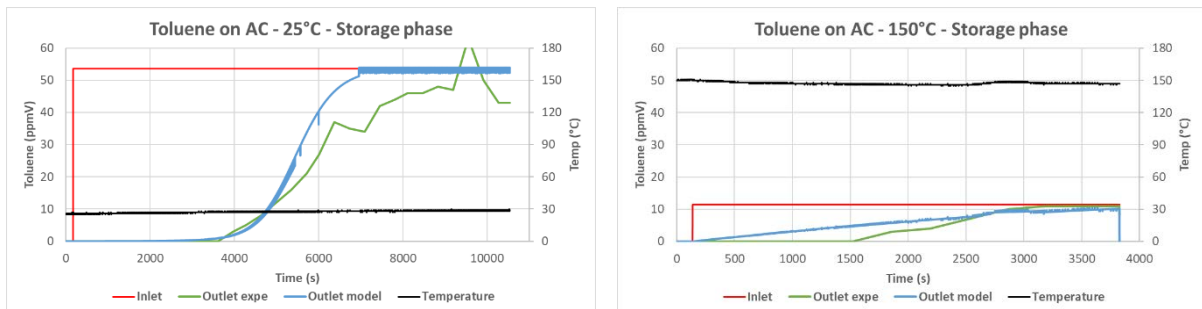
Fig. 10. Concentration of toluene during adsorption phase for different temperatures (25 & 150°C) for AC

For 25°C, the model correctly represents the full adsorption and the transient phase up to full saturation of AC with toluene, particularly the transition between both is well modelled. For 150°C, the model is less representative of the experimental results.

To further validate the model on AC, additional tests have been performed a posteriori. First, as desorption is observed at 25°C due to weak adsorption, a storage phase followed by a long isotherm under N_2 is run. Another test performed an alternation of gas mixture injection and isotherm under N_2, to confirm if the model can capture this transient behavior (Figure 11). The model slightly over-predicts overall adsorption efficiency but fairly represents the transient behavior of toluene on AC with only three storage sites.

Fig. 11. Concentration of toluene during adsorption and desorption phases (25°C)

4. Results and discussion

4.1 SGB

Most of the pollutant present at the exhaust are emitted during cold start. In order to reduce these emissions, different adsorbents were tested in this study. The objective of these tests was to develop a system placed in a by-bass at the end of the exhaust line to store pollutants during the first 100s.

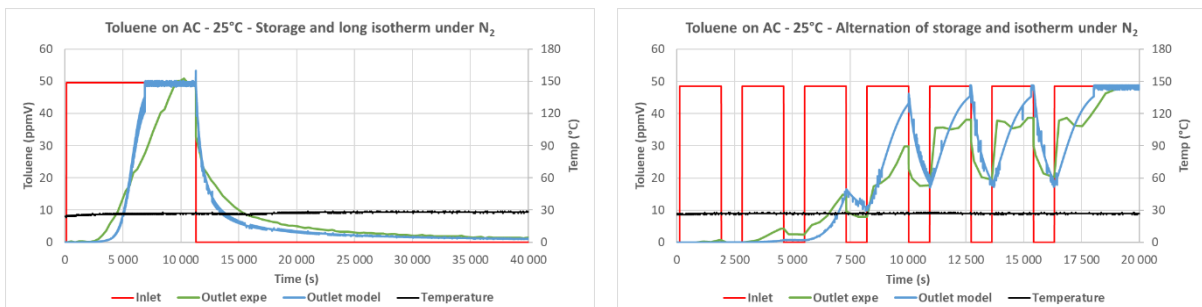Figure 12 shows the adsorption capacity per catalyst mass of the different materials for total hydrocarbons (THC) at 25°C. Activated carbons are very efficient for HC adsorption. However, this material only allows to store toluene, i-pentane and n-pentane. Ethylene, acetylene and methane are indeed not captured by activated carbon. Methane is a molecule which is difficult to remove by adsorption and no adsorbent tested in this study demonstrated significant potential. The best materials to adsorb ethylene and acetylene are copper-exchanged zeolites, but their efficiency is still low. These zeolites also showed the best results for NH$_3$ adsorption (Figure 13).

Cu-β and Cu-ZSM5 are efficient for the adsorption of NH$_3$ whatever the temperature and the gas mixture (Figure 13). These materials are however more rapidly saturated with the "cold start" mixture than with the "5 km" mixture. At 25°C with the "cold start" mixture, the adsorption capacities are 26 and 32 mg/g respectively. With the Cu-β a decrease of the efficiency is observed with the increase in temperature (50 and 150°C with same gas mixture), while the Cu-ZSM5 does not appear to be affected.
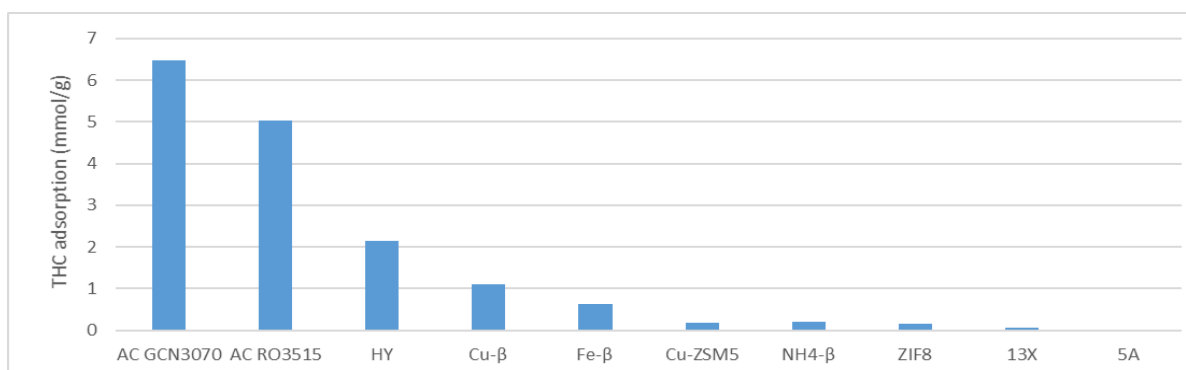
Fig. 12. Hydrocarbons adsorption capacity per catalyst mass of the different materials at 25°C and with the "cold start" mixture
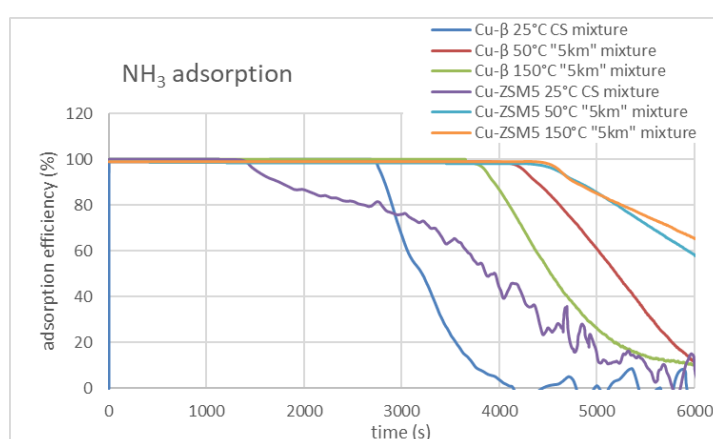
Fig. 13. NH3 adsorption efficiency of the cupper zeolites at 25, 50 and 150°C with "cold start" or "5km" mixture

The adsorption capacities are similar at 50 and 150°C for this material (21 mg/g). This zeolite could allow to adsorb NH$_3$ emitted throughout the vehicle trip if it is located at the end of the exhaust line.

Among the materials studied, some have shown interesting properties for NMHC or NH$_3$ adsorption. Synergetic effects have already been observed by combining materials in series [18]. In our case study by combining several adsorbents, it seems also possible to store an important quantities of NMHC and NH$_3$ during the first 100s.

Figure 14 shows the adsorption efficiencies at 25°C for NMHC by virtually combining activated carbon GCN3070 (430mg) and Cu-ZSM5 (430mg). With this combination 100% of toluene, n-pentane and i-pentane are stored for the first 100s. Ethylene is 100% adsorbed for about ten seconds thanks to the Cu-ZSM5. However, additional tests using an increased quantity of Cu-ZSM5 sorbent materials showed an increase capacity of storage of ethylene with a higher duration with 100% of adsorption efficiency. Conversely, acetylene seems hardly adsorbed by these combined materials.
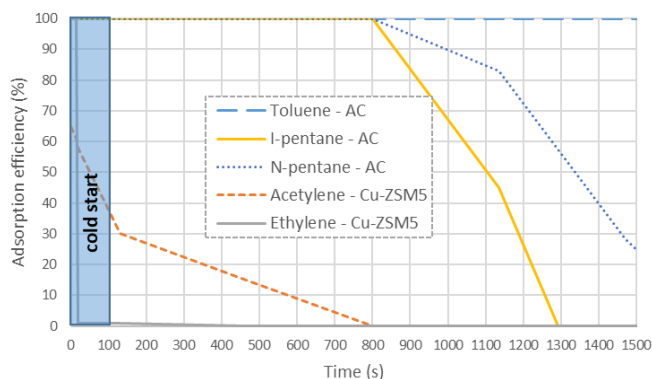
Fig. 14. NMHC adsorption during cold start at 25°C by combining activated carbon GCN3070 and Cu-ZSM5
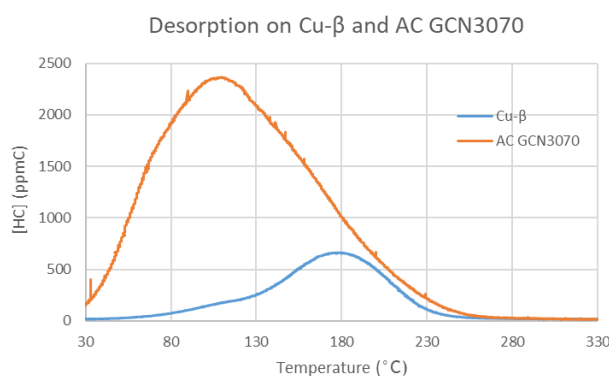
Fig. 15. Temperature Programmed Desorption of HC with AC GCN3070 and Cu-β

Another interesting combination is AC GCN3070 with Cu-β. Indeed, activated carbon has the greatest adsorption capacity for HC but desorption energies seem lower than those of Cu-β as shown on Figure 15.

The adsorption sites being rather weak, the activated carbon desorbs at a low temperature and a slow desorption of the HCs under N_2 flow can be observed, unlike the Cu-β. The sorbent material combination allows a large adsorption capacity and could avoid pollutant emissions before ATS activation. In the next part, the combination of different materials will be modelled.

4.2 Modelling

First, a comparison of the model prediction is performed for the adsorption efficiency at 25°C for activated carbon, Cu-ZSM5 and Cu-β. Each material is exposed to the "cold start" mixture. The model has been calibrated for each HC and NH_3 (Figure 16).

- Toluene: AC has the largest storage capacity, followed by Cu-β and finally Cu-ZSM5. The model correctly predicts the full adsorption efficiency and the transient phase up to saturation.
- NH_3: AC does not adsorb readily ammonia. Cu-β has the greatest storage capacity compared to Cu-ZSM5 and the model is predictive on the whole adsorption profile, except for Cu-ZSM5 where the model over-predicts the full efficiency phase.
- I-pentane and n-pentane: AC is the most promising material in terms of storage capacity, followed by Cu-β and then Cu-ZSM5 (same ranking as for toluene). The model matches correctly the experimental curves regarding the full-efficiency and the transient phase.
- Ethylene: only Cu-ZSM5 exhibits affinity for ethylene, but it is very small. The model is predictive.

- Acetylene: only Cu-ZSM5 has shown a storage capacity and at the beginning of the gas mixture injection, the adsorption efficiency is only partial. The model fits the experimental curve.
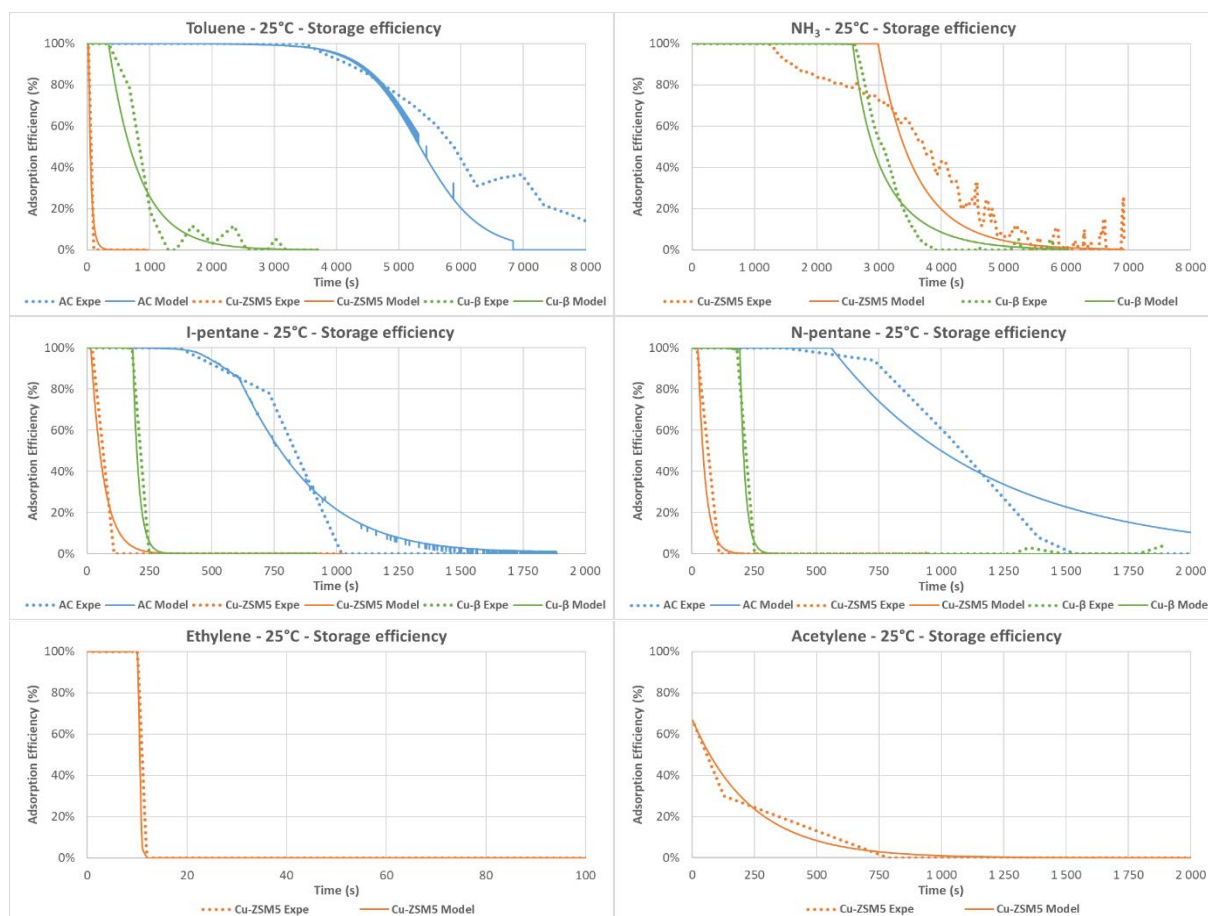
Fig. 16. Comparison of experimental and modelled adsorption efficiencies at 25°C for AC, Cu-ZSM5 and Cu-β

4.3 Projections

As the model correctly predicts the adsorption, it will be used to determine the optimal sequence of sorbents to have the highest efficiency of adsorption for the longer period. As the NH$_3$ storage capacity on Cu-zeolites is very large, it is not a sizing criteria and projections of tailpipe emissions are only focused on NMHC storage. A constant concentration of pollutants has been considered reflecting the SGB performed tests.

Those projections were performed using the average emissions of a hybrid gasoline vehicle (Euro 6d-temp) during the first 100s (Table 4). These concentrations were measured during WLTC (cold start) on chassis dynamometer bench. A specific compound has been selected to represent each chemical family.

Table 4. NMHC emitted during cold start (100s) for GDI and hybrid gasoline powertrain

Species	GDI	Hybrid gasoline
	[ ] (ppmV – ppmC)	[ ] (ppmV – ppmC)
Aromatics – toluene	50 – 350	20 – 140
Alkenes – ethylene	200 – 400	3 – 6
Linear alkanes – n-pentane	100 – 500	37 – 185
Branched alkanes – i-pentane	50 – 250	34 – 170
Alkynes – acetylene	20 – 40	2.5 – 5
NMHC	. – 1540	. – 506

To determine the optimal sequence of sorbents, different scenarios were simulated:

- The system is made of two sorbents in a row and each sorbent mass is 430mg (as experimental setting to calibrate the model)
- Those sorbents are located in a bypass close to tailpipe so the system temperature is 25°C.
- The inlet gas profile is a repeated sequence of two phases:
  - 100s of gas mixture injection, representative duration of an engine cold-start after a TWC.
  - 50s with flow but without pollutants injection, assuming that sorbents are exposed to flow longer that cold-start duration as it is not possible to exactly know when the TWC is fully activated. This will lead to small desorption of toluene, i-pentane and n-pentane.

The desorption profiles for those three molecules are presented in Figure 17 with the hybrid gasoline gas mixture.
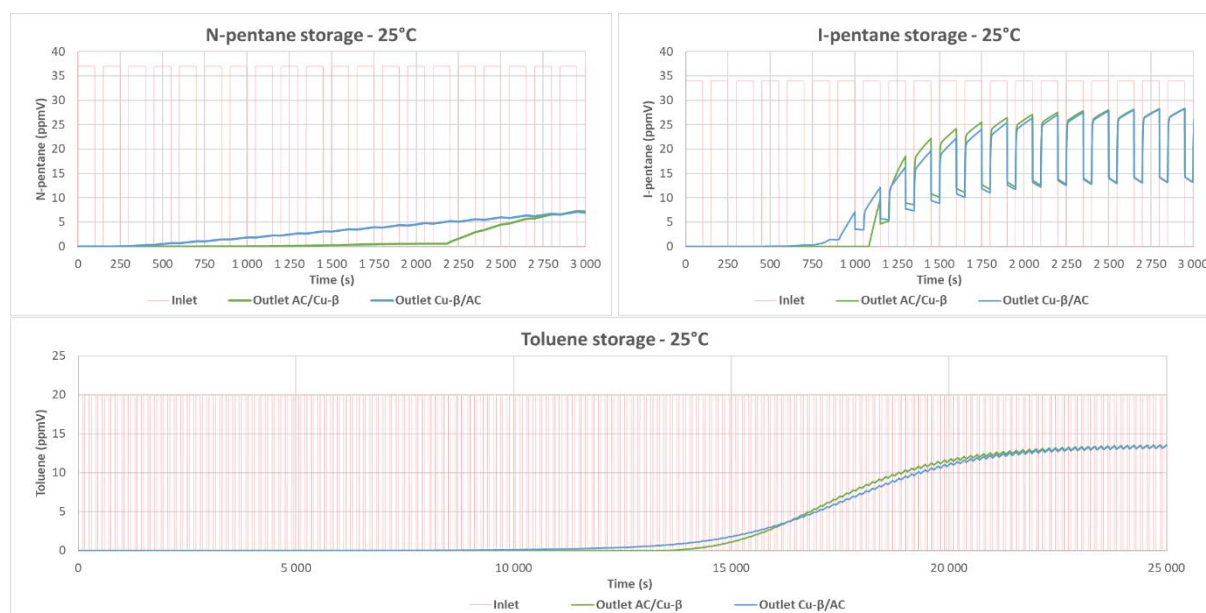
Fig. 17. Comparison of desorption for n-pentane, i-pentane and toluene for a series AC/Cu-β and Cu-β/AC sorbents association

Two combinations were simulated: an AC sorbent followed by a Cu-β sorbent (green curves) and the reverse (blue curves). The combination AC/Cu-X is the optimal solution to maximize the full storage phase and avoid desorption. Activated carbon has the largest storage capacity but can easily desorb the physisorbed HC at very high storage levels. Cu-X have lower capacities but strongly store HC.

Another interesting combination is AC GCN3070 with Cu-ZSM5. In addition to Cu-β, as ethylene and acetylene are only stored by Cu-ZSM5, this sorbent has to be a part of the device to ensure the highest efficiency regarding HC.

Other simulations have been performed to determine the optimal sequence between AC / Cu-ZSM5 / Cu-β and AC / Cu-β / Cu-ZSM5 using a large number of materials. Even if the results are quite similar, it appears that AC / Cu-ZSM5 / Cu-β is the optimal solution to reach the longest full storage efficiency.

To optimize the device efficiency, a large set of simulations has been performed to get the best ratios between sorbents for one SGB sorbent mass of 430mg. As storage capacities of NH_3 are very large compared to HC, the best ratio is determined considering an instantaneous storage efficiency above 99% for NMHC. Two inlet profiles are simulated:

- An ideal bypass closing-strategy: once the cold-start is over, the bypass is closed and no desorption due to flow can be observed. The optimal setup of sorbent material corresponds to 20wt.% of AC, 50wt.% of Cu-ZSM5 and 30wt.% of Cu-β.
- A more realistic bypass closing-strategy: the bypass is open longer than cold-start to be sure to get all pollutants coming from TWC, desorption due to flow on AC is possible but should be limited by Cu-ZSM5 and Cu-β. The optimal architecture of sorbent material is now 20wt.% of AC, 40wt.% of Cu-ZSM5 and 40wt.% of Cu-β.

The two optimized architectures of sorbent material do not differ much from each other with the same AC quantity of 20% and closed quantity of copper zeolites. This specific combination of materials can reduce up to 99% of Non-Methanic-Hydrocarbons (NMHC) present downstream of the Three Way Catalyst (TWC) of a hybrid vehicle during cold start (Figure 18).

The optimized sequence has an instantaneous NMHC storage efficiency above 99% for almost two cold-start events. Ethylene is the first HC observed downstream the sorbent material, followed by i-pentane.
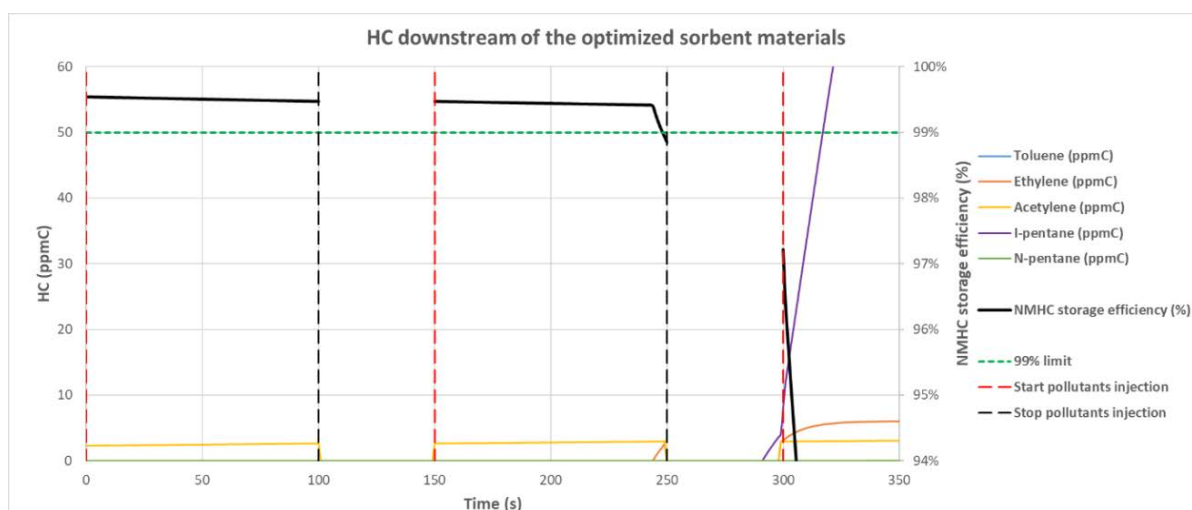

Fig. 18. HC downstream of the optimized sorbent materials and storage efficiency estimation for 20wt.% of AC, 40wt.% of Cu-ZSM5 and 40wt.% of Cu-β

5. Conclusions

Investigations have been performed to initiate the development of a system able to reduce the exhaust tailpipe pollutant emissions of a hybrid gasoline powertrain engine. A part of the system is composed of a bypass in the exhaust, close to the tailpipe, to store pollutants during the cold start. Sorbent materials have shown good storage capacities at low temperatures. A large screening of materials allows to select the most promising ones to be tested on synthetic gas bench with representative mixtures of gasoline engine exhaust gas composition. Through modelling and projections, different combinations of material locations and material quantities have been evaluated. Indeed, the efficiency of conversion for NMHCs has been determined for a cold start application.

Among more than 10 selected sorbents, some of them demonstrate very low storage efficiencies and storage capacities. Activated Carbon shows high storage capacities and high efficiency for three main HC molecules: toluene, n-pentane & i-pentane. Other HCs molecules have high adsorption with copper based zeolites. Copper zeolites also have high storage capacities for ammonia. Two combinations of the same materials have been tested showing differences of behavior during the isotherm desorption phase and showing the importance of location and order of the materials. The combination with AC first, followed with copper zeolites, demonstrates the maximum storage capacity with 100% efficiency and avoid desorption.

Modelling of the sorbent has shown a high level of accuracy for the main adsorption and desorption phenomena. Even with the presence of four different storage sites for the NH$_3$ storage, the modelling was able to fit the real test. Despite of that, some additional functions, like the molecules competition, need to be investigated to improve the model representativity.

The projection of the emissions of a hybrid gasoline powertrain has been performed to estimate the storage efficiency over a cold start phase of 100 seconds. For NMHCs, a high level of adsorption efficiency is obtained with more than 99%. Even if ethylene & acetylene are not completely stored, the high efficiency can be reached during a long time with combination of 20wt.% of activated carbon and a 40wt.% of each copper zeolites: Cu-β and Cu-ZSM5

The developed adsorbent model is necessary to optimize the system by determining the best architecture and the optimal sorbent combination. Further studies are planned to confirm these projections including a complete scale-up of the system to be tested in a multi-cylinder engine bench to validate the system in more realistic and dynamic conditions (concentrations, temperature, mass flow rates…). Finally, additional technologies are considered, in combination with the sorbent, to provide an overall optimized ATS able to reduce all the other pollutant emissions (CO, NO_x …) of an ICE based powertrain for both cold start and warm operations.

References

1. Pollution de l'air. origines, situation et impacts, 05/05/2020, https.//www.ecologique-solidaire.gouv.fr/pollution-lair-origines-situation-et-impacts

2. Seinfeld, John H., and Spyros N. Pandis. Atmospheric Chemistry and Physics. From Air Pollution to Climate Change. Hoboken, N.J.. J. Wiley, 2006

3. Pavlos Panteliadis, Maciej Strak, Gerard Hoek, Ernie Weijers, Saskia van der Zee, Marieke Dijkema, Implementation of a low emission zone and evaluation of effects on air quality by long-term monitoring, Atmospheric Environment, Volume 86, 2014, Pages 113-119, ISSN 1352-2310, https.//doi.org/10.1016/j.atmosenv.2013.12.035.

4. Anaïs Pasquier, Michel Andre. Decomposition of Low emission zone strategies into mechanisms and methodology for assessing their impacts on air pollution. Journal of Earth Sciences and Geotechnical Engineering, Scienpress LTD, 2017, 7 (1), pp. 241-261. hal-01467083

5. Degraeuwe Bart, Pisoni Enrico, Peduzzi Emanuela, De Meij Alexander, Monforti-Ferrario Fabio, Bodis Katalin, Mascherpa Alessandro, Astorga-Llorens Maria, Thunis Philippe, Vignati Elisabetta, Urban NO2 Atlas, EUR - Scientific and Technical Research Reports, ISSN 1018-5593, doi.10.2760/538816

6. Thorpe, A., Harrison, R., 2008. Sources and properties of non-exhaust particulate matter from road traffic. a review. Sci. Total Environ. 400 (1e3), 270-282.

7. Kawsar Mehsein, Caroline Norsic, Christophe Chaillou, André Nicolle, Minimizing secondary pollutant formation through identification of most influential volatile emissions in gasoline exhausts. Impact of the vehicle powertrain technology, Atmospheric Environment, Volume 226, 2020, 117394, ISSN 1352-2310, https.//doi.org/10.1016/j.atmosenv.2020.117394.

8. Worldwide harmonised Light-duty vehicles Test Procedure (WLTP) and Real Driving Emissions (RDE), Regulation (EU) 2017/1151

9. G. Mahadevan, S. Subramanian, Experimental investigation of cold start emission using dynamic catalytic converter with pre-catalyst and hot air injector on a multi cylinder spark ignition engine, Technical Paper 2017-01-2367, ISSN 0148-7191. https.//doi-org.proxy.lib.umich.edu/10.4271/2017-01-2367 (Published October 8, 2017 by SAE International in United States).

10. Hedinger, Raffael & Elbert, Philipp & Onder, Christopher. (2017). Optimal Cold-Start Control of a Gasoline Engine. Energies. 10. 1548. 10.3390/en10101548.

11. Rolf Wunsch, Christof Schön, Marcus Frey, Dana Tran, Sophie Proske, Tim Wandrey, Maria Kalogirou, Jochen Schäffner, Detailed experimental investigation of the NOx reaction pathways of three-way catalysts with focus on intermediate reactions of NH3 and N2O, Applied Catalysis B. Environmental, Volume 272, 2020, 118937, ISSN 0926-3373, https.//doi.org/10.1016/j.apcatb.2020.118937

12. C. Blaker et al., Microporous and Mesoporous Materials 241 (2017) 1-10; Z. Han et al., Process Safety and Environmental Protection 135 (2020) 273-281

13. Teresa Gelles, Anirudh Krishnamurthy, Busuyi Adebayo, Ali Rownaghi, Fateme Rezaei, Abatement of gaseous volatile organic compounds. A material perspective, Catalysis Today, 2019

14. L. Jiang, et al., Applied Thermal Engineering 169 (2020) 114973; Z. Han et al., Process Safety and Environmental Protection 135 (2020) 273-281

15. Stavros A. Skarlis, David Berthout, André Nicolle, Christophe Dujardin, Pascal Granger, Modeling NH3 storage over Fe- and Cu-zeolite base, Urea-SCR catalysts for mobile Diesel engines, Transport Research Arena – Europe 2012

16. Stravros A. Skarlis, IR spectroscopy based kinetic modeling of NH3-SCR on Fe-zeolites. application for Diesel engines aftertreatment system simulation, 2013, 59-67

17. Sjövall H., Blint R.J. and Olsson L. (2009), Detailed Kinetic Modeling of NH3 and H2O adsorption, and NH3 oxidation over Cu-ZSM-5, The Journal of Physical Chemistry C, 113, 1393-1405

18. Dimitrios Karamitros, Grigorios Koltsakis, Model-based optimization of catalyst zoning on SCR-coated particulate Filters, Chemical Engineering Science 173 (2017) 514–524

Real-time NOx Estimation in Light Duty Diesel Engine with In-cylinder Pressure Prediction

Youngbok Lee, Seungha Lee and Kyoungdoug Min

Advanced Automotive Research Center, Seoul National University, 1 Gwanak-ro, Gwanak-gu, Seoul 08826, South Korea.

E-mail: kdmin@snu.ac.kr
Telephone: +(82) 2 880 1661

Abstract. Recently, there have been numerous efforts to cope with automotive emission regulations. Various strategies to reduce engine-out NOx emissions and proper after-treatment systems, such as selective catalytic reduction (SCR) and lean NOx trap (LNT), have been taken into account in the engine research field. In this study, an engine-out NOx prediction model was established where NO and NO_2 are estimated separately. During the procedure for estimating NO and NO_2 (NOx), a real-time prediction model of in-cylinder pressure was applied so that the inputs to the NOx prediction model could be provided only by the data acquired from the engine control unit (ECU). This implies that an in-cylinder pressure sensor is not necessarily required to properly predict the engine-out NOx in real time. The real-time NOx estimation model was validated through the worldwide harmonized light-duty vehicle test cycle (WLTC) without a pressure sensor, and the total NOx error during the mode was comparable with the total NOx error of the portable NOx sensor. This real-time NOx estimation model can ultimately contribute to minimizing tail-pipe NOx emissions by influencing both emission calibration at the engine design stage and the management of NOx after-treatment systems where NOx conversion efficiency is heavily affected by the NO_2/NO ratio.

Notation

θ	*Instantaneous crank angle*
θ_0	*Crank angle when combustion starts*
$\Delta\theta$	*Duration of combustion*
$\Delta\theta_{norm}$	*Normalized duration of combustion*
Φ	*Phi, global fuel-air equivalence ratio*
$[\ ]_e$	*concentration of equilibrium state*
$[\ ]_{exh}$	*concentration at exhaust gas*
k	*Specific heat ratio*
m_{pilot}	*Fuel mass of pilot injection*
$m_{main+post}$	*Fuel mass of main and post injections*
n	*Polytropic index*
P	*In-cylinder pressure*
P_{SOC}	*In-cylinder pressure at start of main combustion*
P_{max}	*Maximum in-cylinder pressure caused by main combustion*
P_{mfb50}	*In-cylinder pressure at MFB50 timing*
Q_{loss}	*Heat loss from the in-cylinder gas to outside during the combustion process*
Q_{main}	*Heat release of main combustion*
Q_{pilot}	*Heat release of pilot combustion*
Q_{norm}	*Normalized heat release*
T	*In-cylinder temperature*
T_{max}	*In-cylinder maximum burned gas temperature*
$T_{unburned}$	*In-cylinder unburned gas temperature*
T_{avg}	*Average temperature between T_{max} and exhaust gas temperature*
V	*In-cylinder volume*
A/F	*Air-Fuel ratio*
BMEP	*Brake Mean Effective Pressure*
EGR	*Exhaust Gas Recirculation*

EVO   *Exhaust Valve Open timing*
IVC   *Intake Valve Close timing*
LHV   *Lower Heating Value*
LNT   *Lean NOx Trap*
MFB x   *Timing when x % of the fuel is burned. It is the same expression with widely used CA x.*
RDE   *Real Driving Emission*
SCR   *Selective Catalyst Reduction*
SOC   *Start of Combustion timing*
SOI   *Start of Injection timing*
WLTC   *Worldwide harmonized Light-duty vehicle Test Cycle*

1. Introduction

To cope with more stringent emission regulations, many researchers in the internal combustion engine field are struggling to reduce engine emissions while reducing fuel consumption. The main emissions from a diesel engine are particulate matter (PM) and NOx. More than 90% of the PM included in engine-out exhaust gas can be captured physically by a diesel particulate filter (DPF) [1], the most widely used device for PM reduction in diesel engines. There has also been significant research to minimize tailpipe-out NOx emissions in various ways. Most conventional diesel engines adopt an exhaust gas recirculation (EGR) system to reduce engine-out NOx emissions by lowering the combustion temperature [2, 3]. Research studies have focused on controlling the EGR system for NOx emission optimization by considering smoke emission spikes [4] to counteract transient operating conditions. However, it is not enough to just reduce engine-out NOx emissions to meet stringent emissions regulations. Therefore, most vehicle manufacturers adopt additional after-treatment systems, such as lean NOx trap (LNT) and selective catalytic reduction (SCR). Some manufacturers have even considered using both after-treatment systems [5, 6] to cope with the harsh test conditions of the real driving emission (RDE) test.

To establish a strategy for minimizing engine-out NOx emissions, it is necessary to know the real-time engine-out NOx if real-time feedback control is desired, and a NOx sensor that is physically inserted at the exhaust gas pipe can be helpful for the control. However, there can be cost problems with a portable NOx sensor. Therefore, there have been many studies to estimate engine-out NOx emissions without an additional NOx sensor. Andersson et al. modeled NOx estimation aiming to address a real-time calculation based only on a single injection [7]. Arrègle et al. studied a NOx model for on-board applications and conducted sensitivity analysis. They found that NOx prediction is critically dependent on the accuracy of the in-cylinder air mass and the total mass [8, 9]. Guardiola et al. established a NOx predictive model oriented to engine control. This model is based on in-cylinder pressure for calculating an instantaneous heat release rate and an adiabatic flame temperature [10]. Finesso et al. developed a real-time combustion model that was used for evaluating in-cylinder temperature, heat release rate and NOx emissions. The combustion model is based on a three-zone thermodynamic model where the combustion chamber is divided into a fuel zone, an unburned zone and a stoichiometric burned zone [11]. These studies of NOx estimation have some room for improvement. Some studies propose a model that is too complex to compute rapidly for application in real-time estimation, and others have too many calibration coefficients and a lack of physics. Most models predict just NO or NOx emissions without distinguishing NO and NO_2. It is important to know the NO_2/NO ratio because the efficiency of the after-treatment systems can be affected by the engine-out NO_2/NO ratio [12, 13]. Devadeas et al. proposed that the maximum DeNOx was found for $NO_2/NO=1$, but under conditions where the ammonia dosage was limited to 10 ppm, the $NO_2/NO=1/3$ ratio showed the best DeNOx efficiency [12]. Therefore, information about the NO_2/NO ratio can be helpful to minimize tailpipe-out NOx by maximizing the efficiency of the after-treatment system under given NO_2/NO conditions, and the dosage of ammonia can also be optimized.

Most NOx prediction models that are based on the extended Zeldovich mechanism need in-cylinder pressure data. The characteristic temperature for the NOx formation equation can basically be calculated from data on in-cylinder conditions such as pressure and volume. Additionally, in-cylinder pressure data are necessary when calculating the heat release rate, which is widely used for the characteristic index of combustion. However, there is a problem with the cost aspects because of the relatively expensive in-cylinder pressure sensor. Many research studies have attempted to calculate the in-cylinder pressure or the heat release rate without the sensor. Finesso et al. simplified the fuel injection rate in a triangular wave and calculated the heat release rate based on the fuel injection rate [14]. The

Wiebe function approximates the cumulative heat release rate with a form of a continuous random variable normal distribution. The Wiebe function is the most widely used tool for internal combustion engine applications [15]. In this paper, the Wiebe function was also adopted for in-cylinder prediction [16, 17].

Over the years, the authors have tried to estimate the engine-out NOx, and engine-out NO and NO$_2$ models have been established at steady-state conditions [18, 19]. The NOx models require the in-cylinder pressure information as necessary input data. Therefore, we also developed an in-cylinder pressure model at steady-state conditions [16, 17]. Finally, study in this paper tried to estimate engine-out NOx in real time using only ECU data without a pressure sensor. Based on an NO prediction model [19, 20], NOx could be estimated with the additional NO$_2$ model [18]. The NO$_2$ model consists of both formation and decomposition mechanisms and considers the dominant pathways and reactions for each mechanism. The pressure estimation procedure could be conducted in 3 steps [16, 17], where the 1st step is assumed to be a polytropic process until there is a combustion reaction in the chamber and the 2nd and 3rd steps calculate the in-cylinder pressure during the pilot and main combustion periods, each using the Wiebe function. This pressure estimation was applied to the NO and NO$_2$ models, which require in-cylinder pressure information. Therefore, this semi-physical NOx prediction model is capable of real-time calculation of NOx while separating NO and NO$_2$ by using data from the engine control unit without a pressure sensor. As a result, NO and NO$_2$ estimations without a pressure sensor were validated through the WLTC (Worldwide harmonized Light-duty vehicles Test Cycle) mode, and the total NOx error of the model during the mode was comparable with the total NOx error of a portable NOx sensor.

2. Experimental setup

2.1 Test engine

The test engine used for this study is a 1.6-liter 4-cylinder light-duty CI engine, which has a compression ratio of 17.3 and a displacement volume of 1582 cc with a single-stage variable geometry turbocharger. The test engine has a common rail system with a solenoid-type injector. Other detailed specifications of the engine are listed in   Table 1.

Table 1. Specifications of the test engine

Engine type	1.6-liter 4-cylinder Euro5 CI engine
Displaced volume	1582 cc
Bore x Stroke	77.2 mm x 84.5 mm
Connecting rod	140 mm
Compression ratio	17.3
Turbocharger	Single-stage VGT
Fuel injection system	Common rail injection (solenoid)
Nominal rated power and torque	94 kW @ 4000 RPM 26.5 kg·m @ 1900~2750 RPM

2.2 Test cell setup

The test engine was installed in an 'AVL test system-340 kW AC dyno controller', as shown in Fig. 1. This dynamometer system allows for not only steady-state testing but also transient-state testing, so the WLTC mode was conducted for validation of models during transients. Fig. 1 shows a schematic diagram of the whole system for estimating engine-out NO and NO$_2$ emissions. For the prediction models, an in-cylinder pressure sensor (Kistler 6056A, piezoelectric type) measures the pressure of cylinder #1, and the signal of the sensor is amplified by a Kistler Kibox amplifier. Finally, an ETAS ES1000 device acquires the pressure data from the Kibox and other data that are necessary for the NO and NO$_2$ prediction models from the engine control unit (ECU). Therefore, the ES1000 can calculate the real-time NO and NO$_2$ emissions using the data and ASCET software, where the logic of the models is imported. In the case of predicting NO and NO$_2$ emissions without the pressure sensor, the ES1000 additionally calculates the pressure prediction model using data from the ECU instead of obtaining the pressure signal from the sensor.

An exhaust gas analyzer 'HORIBA MEXA 7100 DEGR' and portable NOx sensor 'Continental UniNOx' were used to measure engine-out NO and NOx. A 'JEILSYSCOM fast 2200-Fourier Transform Infrared (FTIR) Spectrometer' also measured engine-out NO_2 directly for NO_2 modeling.
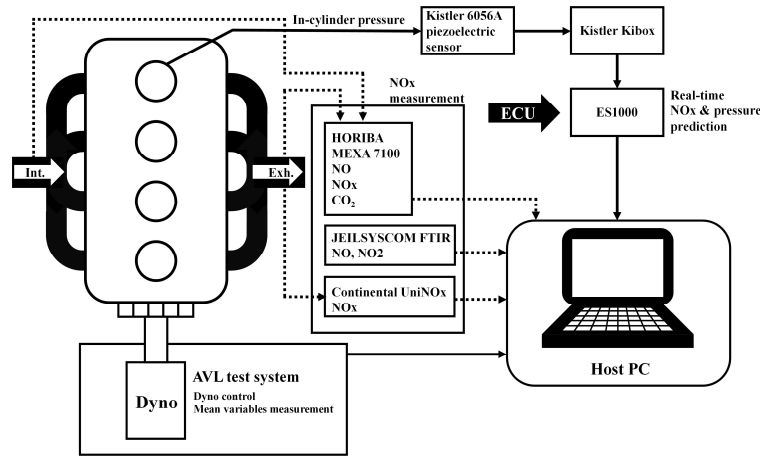

Fig. 1. Test cell setup schematic.

3. Experimental conditions

The experimental conditions used for establishing the models are described in this section. Fig. 2 shows the steady-state experimental conditions. The pressure estimation model [16] was established with the same steady-state conditions (220 cases) used for the NO prediction model [19, 20]. Those operating points are represented by black circle, red triangle and blue square marks in the figure and include not only base points but also swing points. Base points were selected from the originally mapped points of the ECU, and swing points were conducted by changing the engine demand parameters from the original ECU map to check the robustness of the models. The swept parameters are the air mass (EGR ratio), main injection timing, rail pressure and boost pressure. The green diamond marks in the figure represent experimental points (74 cases) for modeling NO_2 prediction [18] and also include swing points with several parameters – air mass (EGR ratio), main injection timing, rail pressure and swirl ratio at BMEP 4-bar conditions over the whole engine speed range. These experimental points were selected because they can cover the WLTC operating points marked in Fig. 2.
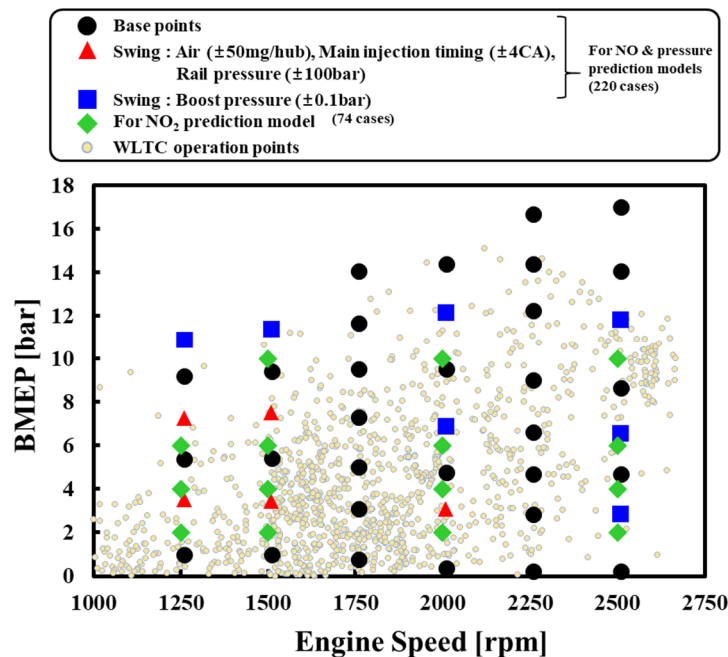

Fig. 2. Steady-state experimental conditions

To validate the real-time application potential of the models, a transient-state experiment was conducted, and the WLTC mode, which is one of the emission test cycles, was selected for the test. This emission cycle consists of low, middle, high and extra-high phases that can cover a wide range of vehicle speeds. Therefore, the models can be verified through a wide range of operation points. Engine speed and torque data that are matched with the velocity during the WLTC are imported to the ALV test system dyno controller to conduct a transient test with the test engine.

4. NOx prediction

In this study, the engine-out NOx prediction model consists of two models. One model is the NO prediction model, which is based on and simplifies the extended Zeldovich mechanism [19, 20]. The other model is the NO_2 model, which is dependent on NO emissions [18]. These emission models require representative temperature values, which can be calculated from the in-cylinder pressure.

4.1 NO model

The NO prediction model [19, 20] is described in this section. As inputs of the model, in-cylinder pressure and other data from the ECU are used. Based on the extended Zeldovich mechanism, some simplifications are adopted to make it possible to calculate the engine-out NO emissions as fast as it can be conducted within a cycle-by-cycle period. The basic NO formation mechanism (extended Zeldovich) is described by equation 1. The maximum burned gas temperature (T_{max} [k]) is selected as a representative temperature in the equation because it was found that the average NO formation rate is proportional to the maximum NO formation rate [19, 20]. The notation '[ ]' in the equation denotes the mole fraction.

$$NO\ [ppm] = \int \left(\frac{dNO}{dt}\right)_{max} dt = \int \frac{A}{T_{max}^{1/2}} \exp\left(\frac{-69090}{T_{max}}\right) [O_2]^{1/2}[N_2]\ dt$$

(1)

However, equation 1 just considers NO formation at the highest temperature location of combustion gas. Therefore, the total NO formation area should be additionally considered, as expressed by equation 2. In this equation, the duration of NO formation is also considered instead of integrating the NO formation rate. One assumption was introduced to simplify the NO formation mechanism (Equation 2). This assumption is that the 'NO formation area × duration' is proportional to the fuel quantity [mg/cycle·cylinder] injected into the cylinder, and this assumption is applied to equation 3. The engine speed [rpm] in equation 3 is used as a compensation parameter to correct the absolute time of the duration of NO formation.

$$NO\ [ppm] = \text{Maximum NO formation rate at the highest temperature location} \times \text{formation area} \\ \times \text{duration}$$

(2)

$$NO\ [ppm] = \frac{A_1}{T_{max}^{\frac{1}{2}}} \exp\left(\frac{-69090}{T_{max}}\right) [O_2]^{\frac{1}{2}}[N_2] \times \text{Fuel quantity/rpm}$$

(3)

NO is formed mainly in the burned zone, and equation 3 can calculate the concentration of NO formed only in the burned zone. To calculate the NO concentration of the total in-cylinder volume, we should also consider the unburned zone. Therefore, a concentration correction factor (CCF) was adopted to compensate for the NO concentration considering the unburned zone volume (Equation 4). The PHI (∅) in the equation indicates the global fuel-air equivalence ratio for the operating conditions.

$$NO\ [ppm] = \text{Maximum NO formation rate at the highest temperature location} \times \text{fuel quantity/rpm} \times \text{CCF}$$

$$= \frac{A_2}{T_{max}^{\frac{1}{2}}} \exp\left(\frac{-69090}{T_{max}}\right) [O_2]^{\frac{1}{2}}[N_2] \frac{\text{Fuel quantity}}{\text{rpm}} \times \text{PHI}(\emptyset) \times \frac{T_{max}}{T_{unburned}}$$

(4)

Not only the NO formation mechanism but also the NO decomposition mechanism occurs during the combustion process in the cylinder, especially under high-EGR conditions [7, 9, 21]. However, equation 4 expresses only the NO formation mechanism. Finally, the rate constant (33050) of the exponential term was changed as expressed by equation 5 to consider the decomposition mechanism. The value of the constant could be obtained from the empirical result. A_n in equations 1~5 are fitting coefficients.

$$NO \ [ppm] = \frac{A_3}{T_{max}^{\frac{1}{2}}} \exp\left(\frac{-33050}{T_{max}}\right) [O_2]^{\frac{1}{2}}[N_2] \times \frac{Fuel \ quantity}{rpm} \times PHI(\emptyset) \times \frac{T_{max}}{T_{unburned}}$$

(5)

4.2 NO₂ model

The NO₂ model consists of formation and decomposition mechanisms [18]. In the formation mechanism, NO₂ can be formed only by conversion from NO, and equation 6 shows the dominant path of NO₂ conversion in the combustion process [22].

$$NO + HO_2 \rightarrow NO_2 + OH$$

(6)

Then, equation 7 describes the rate of NO₂ formation, reflecting the above reaction path with the assumption of the equilibrium condition and with the initial condition of $[NO_2]/[NO_2]_e \ll 1$, and k_1 is the reaction rate coefficient.

$$\frac{d[NO_2]}{dt}_{formation} = k_1[NO]_e[HO_2]_e = A \times \exp\left(\frac{240}{T}\right)[NO]_e[HO_2]_e$$

(7)

Equation 8, which governs the reaction pathways of NO₂ decomposition in the cylinder, can derive the rate of NO₂ decomposition [23], as expressed in equation 9.

$$NO_2 + H \rightarrow NO + OH, \quad NO_2 + O \rightarrow NO + O_2$$

(8)

$$\frac{d[NO_2]}{dt}_{decomposition} = k_2[NO_2]_e[H]_e + k_3[NO_2]_e[O]_e$$

$$= B \times \exp\left(\frac{-180}{T}\right)[NO_2]_e[H]_e + C \times \exp\left(\frac{-30970}{T}\right)\frac{[O_2]_e^{0.5}}{T^{0.5}}[NO_2]_e$$

(9)

The net NO₂ concentration can be calculated using the above NO₂ formation and decomposition rates by multiplying each characteristic time (τ), as described by equation 10.

$$[NO_2]_{net} = \frac{d[NO_2]}{dt}_{formation} \times \tau_{formation} - \frac{d[NO_2]}{dt}_{decomposition} \times \tau_{decomposition}$$

(10)

To compute the NO₂ concentration in real time using the above equations, we should select proper parameters, especially for the characteristic time, temperature and concentration of radicals in the equations.

As Hori's previous study determined [24], NO₂ conversion from the NO reaction can occur in a relatively wide range of temperatures. Therefore, the characteristic time of NO₂ formation can be represented by the duration from the start of the main combustion (SOC) timing to the exhaust valve opening (EVO) timing on an absolute time scale [ms] . The average temperature (T_{avg} [k]), which has a value of the middle point between the maximum temperature and exhaust gas temperature, is selected as a characteristic temperature for this formation reaction considering the NO₂ formation period.

For the rate of NO₂ formation (Equation 7), the concentration of engine-out NO emissions was selected, and the equilibrium value of the HO₂ radical concentration could be formulated as a function of phi and the averaged temperature.

In the case of NO$_2$ decomposition reactions, the reactions are active in a high temperature range [23]. Therefore, the in-cylinder maximum temperature was selected as a characteristic temperature. The NO$_2$ decomposition time was characterized by parameters – fuel quantity [mg/cycle·cylinder], engine speed [rpm] and swirl ratio [-]. The lasting period of the high temperature (combustion) region where NO$_2$ decomposition reactions are active is proportional to the fuel quantity, and the engine speed is inversely proportional to the duration, considering the absolute time scale. The decomposition time can also be shortened by some cooling effects through the flow in the cylinder. The parameters that can affect the cooling effect through fast air flow are the swirl ratio and the engine speed.

For the rate of the NO$_2$ decomposition reaction (Equation 9), the H radical was replaced with the exhaust H$_2$O concentration, which is the source of the H element and becomes stable after combustion [18]. The other species, O$_2$ and NO$_2$, were replaced by the exhaust O$_2$ concentration and the formed NO$_2$ concentration, respectively [18]. Therefore, equation 11 expresses the final form of the NO$_2$ model.

$$
\begin{aligned}
[NO_2]_{net} = {} & A \times \exp\left(\frac{240}{T_{avg}}\right)[NO] \times f\big(phi, T_{avg}\big) \times main\ SOC\ to\ EVO \\
& - [NO_2]_{formation}\left[B \times \exp\left(\frac{-180}{T_{max}}\right)[H_2O]_{exh} + C \times \exp\left(\frac{-30970}{T_{max}}\right)\frac{[O_2]_{exh}{}^{0.5}}{T_{max}{}^{0.5}}\right] \times \frac{fuel}{rpm \cdot swirl^{0.43}}
\end{aligned}
$$

$$(11)$$

5. Pressure estimation

The NO and NO$_2$ models explained in the previous section require an in-cylinder pressure sensor to calculate the representative temperature and other values. However, it is possible to predict the NOx emissions without the pressure sensor when an in-cylinder pressure estimation model is applied. This section describes the developed in-cylinder pressure model, which is divided into three steps: a compression process, pilot combustion process and main combustion process [16, 17]. These processes are presented in Fig. 3. As shown in the figure, the prediction of the in-cylinder pressure was conducted through 3 steps. A polytropic relation was applied during the compression, and Wiebe functions were used during the pilot and main combustion phases.
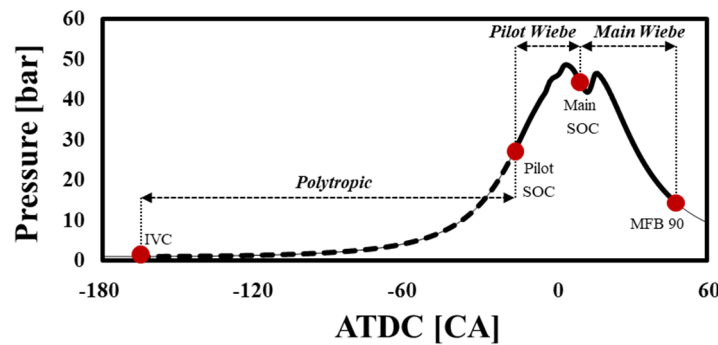
Fig. 3. Construction of pressure estimation procedures, including the polytropic process during the compression stroke and the Wiebe functions during the pilot and main combustion processes [16]

5.1 Polytropic process

The in-cylinder pressure during the compression phase is represented as a polytropic process (Equation 12), which shows the relation among the in-cylinder pressure (P), volume (V) and polytropic index (n). The initial pressure in this compression period was acquired from a boost pressure sensor, which is a basic accessory of the experimental engine. The cylinder volume changes can be calculated from the geometry of the cylinder. Therefore, finally, the pressure at the end of the compression process can be calculated through the polytropic relation (Equation 12).

$$PV^n = constant$$

$$(12)$$

The polytropic index (n) plays an important role when estimating the pressure during the compression process, and a variable polytropic index was applied in this study, reflecting various engine operating conditions to predict a more accurate in-cylinder pressure at the end of the compression [16, 17]. The polytropic index was fitted as a function of in-cylinder gas composition and intake manifold temperature [25].

5.2 Wiebe function

The Wiebe function is a cost-effective mathematical function for approximating the burning rate (heat release) in internal combustion engines. We also adopted the Wiebe function for estimating pressure after the pilot SOC to 90% of fuel burned (MFB 90) timing in the combustion phase [16, 17]. Equation 13 shows the basic forms of the Wiebe function, where $\Delta\theta$ and θ_0 indicate the duration and start of combustion, respectively, in the crank angle unit. This Wiebe equation represents normalized heat release ($Q_{norm.}$). The burned fraction with respect to the duration is also dependent on the constant coefficient C. The shape factor, m, is the combustion characteristic exponent, which determines the shape of the burning rate.

$$Q_{norm.} = 1 - \exp\left[-C\left(\frac{(\theta - \theta_0)}{\Delta\theta}\right)^{m+1}\right]$$

(13)

When the pilot fuel is injected into the cylinder, the combustion reaction does not occur immediately after the injection, and ignition occurs after the end of the injection in conventional diesel engines because of the relatively low in-cylinder temperature and pressure conditions compared with the conditions when the main fuel is injected. Pilot fuel combustion can be regarded as premixed combustion. Therefore, a single Wiebe function (Equation 14) was used to describe the normalized burning rate during the period from pilot injection timing to the main SOC timing [16, 17]. Otherwise, the main combustion of the conventional diesel engine always shows a diffusion phase and a premixed phase that is the result of mixing between the fuel and air during the ignition delay period. Therefore, a single Wiebe function is not an appropriate method for approximating the burning rate of the diesel main combustion, which does not consist of one phase. Therefore, the normalized heat release of the main combustion was described by a double Wiebe function by superposing two Wiebe functions, as shown in equation 15 [16, 17].

$$Q_{pilot\ norm.} = 1 - \exp\left[-a\left(\frac{\theta}{\Delta\theta_{pilot,norm}}\right)^{b+1}\right]$$

(14)

$$Q_{main\ norm.} = c\left\{1 - \exp\left[-d\left(\frac{\theta}{c\Delta\theta_{main,norm}}\right)^{e+1}\right]\right\} + f\left\{1 - \exp\left[-d\left(\frac{\theta}{f\Delta\theta_{main,norm}}\right)^{g+1}\right]\right\}$$

(15)

To simplify the model considering real-time application, the Wiebe coefficients (a~g) in equations 14 and 15 were set in one set in such a way that the Wiebe equations were fitted by the normalized heat release in all experimental cases [16, 17].

After the coefficients of the main and pilot Wiebe functions representing the normalized pilot and main heat release (Equations 14 and 15, respectively) were determined, the fuel mass (m_{pilot} and $m_{main+post}$) and lower heating value (LHV) were multiplied to obtain the heat release of the pilot and main combustion (Q_{pilot} and Q_{main}), as shown in Equations 16 and 17, respectively. In the main Wiebe (Equation 17), 'c' and 'f' indicate the proportion of the premixed and the diffusion combustion during the total main combustion period, respectively, therefore, the sum of 'c' and 'f' has a value of nearly 1. Diffusion combustion typically occupies a larger portion than premixed combustion in a general diesel engine [17]. In the case of the main heat release (Equation 17), the actual heat release is lower than the heat generated by the chemical energy of the fuel because of heat loss (Q_{loss}). Therefore, the heat loss was subtracted from the heat energy term calculated from the fuel mass and LHV before multiplying the energy term by the normalized main Wiebe function (Equation 17). However, the heat loss was not

considered when calculating the pilot heat release (Equation 16) due to the relatively lower fuel mass than the mass of the main fuel. To complete the Wiebe functions, the ignition delay (to determine the SOC), main combustion duration (from main SOC to MFB90) and heat loss (Q_{loss}) were additionally modeled [16, 17, 26] with the parameters from the engine control unit. These subordinated models were applied to equations 16 and 17. And   Table 2 shows the subordinated models to be calibrated and objective of the models at each step of the pressure estimation.

$$Q_{pilot} = m_{pilot} \times LHV \times \left\{ 1 - \exp\left[-a\left(\frac{\theta}{\Delta\theta_{pilot}} \right)^{b+1} \right] \right\}$$

(16)

$$Q_{main} = (m_{main+post} \times LHV - Q_{loss}) \times \left\{ c\left\{ 1 - \exp\left[-d\left(\frac{\theta}{c\Delta\theta_{main}} \right)^{e+1} \right] \right\} + f\left\{ 1 - \exp\left[-d\left(\frac{\theta}{f\Delta\theta_{main}} \right)^{g+1} \right] \right\} \right\}$$

(17)

Table 2. Summary of the sub-models consisting the pressure estimation

step	compression	pilot combustion	main combustion
Sub models	- Polytropic index: To derive the variable polytropic index during the compression process at different operation conditions	- Pilot Wiebe function: To represent pilot combustion burning rate - Ignition delay: To detect pilot and main SOC which is also used for calculating pilot combustion duration	- Main Wiebe function: To represent main combustion burning rate - combustion duration: It is used in the main Wiebe - Heat loss during main combustion: It is used in the main Wiebe

6. Results and discussion

6.1 NO and NO₂ prediction under steady state

Through steady-state experiments including not only base points but also swing points, NO and NO_2 estimations were modeled, and Fig. **4** shows the result [18, 19]. The result shows the accuracy of the R-square 0.982 in NO prediction and R-square 0.834 in NO_2 prediction. Result of NO_2 prediction might seem to be inaccurate. However, this model that considers the chemical reactions of the formation and decomposition mechanism can show a higher predictability than the previously proposed models [22, 27] especially under low ppm conditions, and has fewer constant coefficients that should be tuned. These proposed models will be applied to real-time NOx calculation through combining with in-cylinder pressure model.
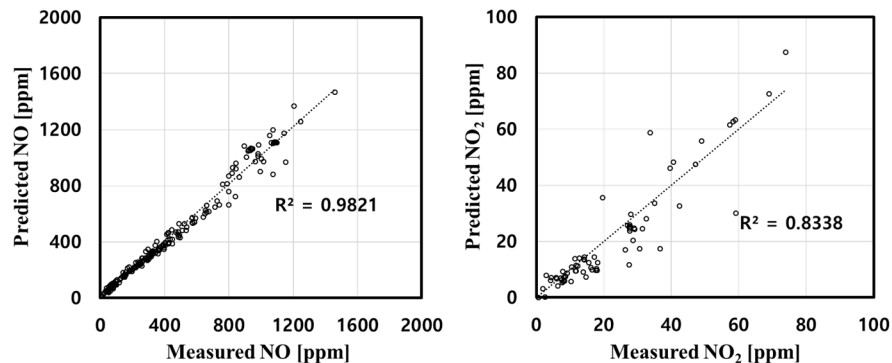

Fig. 4. Steady-state result of NO and NO2 prediction with proposed models [18, 19]

6.2 Pressure prediction under steady state

The pressure estimation could be conducted in 3 steps using the polytropic process and the Wiebe functions, and this model used only data from ECU [16, 17]. Fig. 5 shows the pressure estimation for some cases of steady-state experiments. Graphs on the Fig. 5 represent the results at different engine speeds and BMEP conditions, and it could be found that the estimated pressure can describe the tendency of the measured pressure well at the various engine speeds and BMEP conditions.

Fig. **6** shows the results of pressure prediction at all steady-state conditions (220 cases), comparing estimated pressure and measured pressure at SOC timing (P_{soc}) and when they have a peaked value by the main combustion (Generally, the value of the second peak at the pressure profile graph, P_{max}). These two pressure parameters are most important when applied to the NOx prediction model, because the two pressure values should be used for calculating the maximum temperature, which is used for the characteristic temperature of the NO formation equation [19, 20].

P_{soc} and P_{max} are the results of the pilot Wiebe and the main Wiebe functions and P_{soc} could be estimated with good accuracy (R-square, 0.979). A relatively small quantity of pilot fuel and a low deviation of the pilot fuel quantity between experimental cases might lead to this result with high accuracy, though the pilot Wiebe does not consider even heat loss.
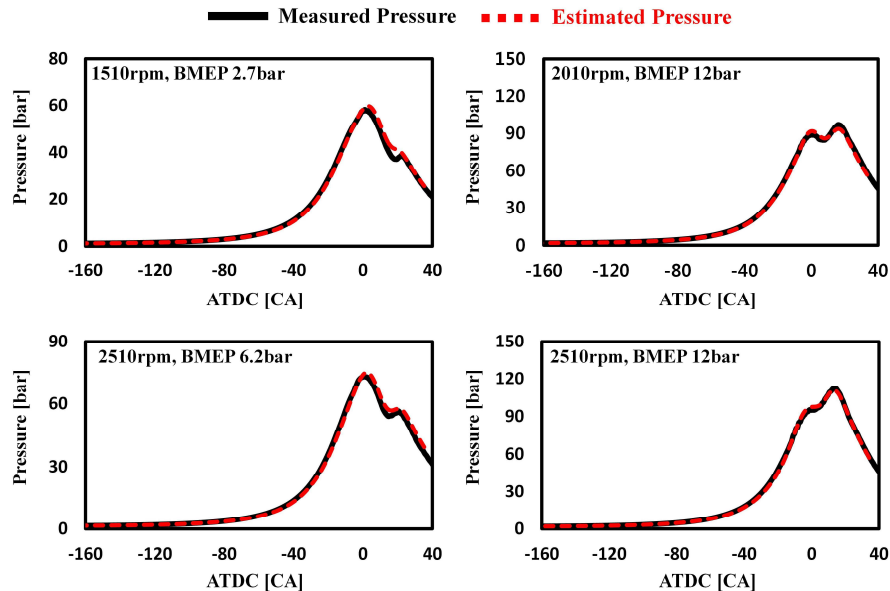

Fig. 5. Validation of pressure estimation with some steady-state experimental cases (1510~2510 rpm, BMEP 2.7~12 bar)

However, P_{max} was predicted with an accuracy of R-squared (0.96), which is lower than the accuracy of P_{soc}. This error might originate from the high deviation of the main fuel quantity between the experimental cases that have a wide range of BMEP conditions (0.2~17 bar). Other reasons for the errors are from the heat loss model and the combustion duration model, which were fitted with related parameters for simplification due to the purpose of real-time calculation [16, 17]. Step-by-step characteristics of the whole pressure prediction model can make the error worse in later steps because the input of the model at a specific step should be dependent on the result of the previous step. Therefore, it was found that the error increases when the later pressure is estimated as shown in the Fig. **6**.
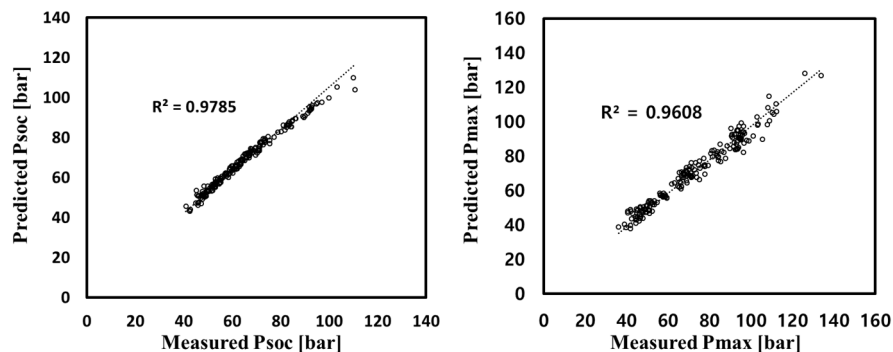

Fig. 6. Measured vs. predicted P_{soc} (left) and P_{max} (right) [17]

6.3 NOx prediction with a pressure sensor during transient conditions

The engine-out NOx was estimated during transient conditions (WLTC) by combining the evaluated NO and NO₂ models [18, 19], which were established through steady-state experimental data. As described in the '2.2 Test cell setup' section, the ETAS ES1000 device acquires the pressure data and other data from the ECU to calculate the NOx emissions during transient conditions. Then, the ES1000 can calculate the real-time NO and NO₂ emissions using the data and ASCET software, where the logic of the models is imported.

In the process of NOx estimation, it is important to calculate the accurate in-cylinder gas composition because the representative concentration of major species such as oxygen and nitrogen is determined by the in-cylinder gas composition. Therefore, acquiring the right values of the lambda and EGR rate is necessary. When establishing the NO and NO₂ models during steady-state conditions, a lambda sensor and an exhaust gas analyzer (HORIBA MEXA 7100 DEGR) were used to measure the lambda and EGR rate. The lambda sensor, which is inserted at the exhaust manifold, can also be used to measure the lambda during a transient test. However, it was impossible to measure the EGR rate using the exhaust gas analyzer during transient conditions due to the delay caused by the relatively long length of the sampling line. Therefore, the EGR rate during transient conditions was calculated from the temperatures at the intake manifold, downstream of the intercooler and downstream of the EGR cooler using a fast response hot wire [28].

Finally, the instantaneous NOx emissions calculated from the model were compared with the engine-out NOx measured by the 'HORIBA MEXA 7100 DEGR' and the 'Continental UniNOx' portable NOx sensor, as shown in Fig. **7**. During the whole cycle (1800 sec), the estimated NOx follows the behavior of the measured NOx well according to the figure. In the results of the Fig. **7**, we took into account the delay of both the 'HORIBA MEXA 7100 DEGR' and the 'Continental UniNOx' portable NOx sensor because the two sensors have different response time. Therefore, as a reference signal, we also measured NO during the transient using CAMBUSTION FAST FTIR device. This real-time device enables cycle by cycle measurement. Then, we shifted NOx signal from the HORIBA MEX7100 DEGR and portable NOx sensor by matching with the NO signal from the real-time NO measurement device.

Fig. **8** shows the NO and NO₂ predictions separately in the middle of the WLTC mode using the in-cylinder pressure sensor. The figure also shows the NO₂/NO ratio, lambda and fuel quantity during the operation. The Lambda in the Fig. **8** is global lambda which came from the engine control unit (ECU) data and was measured by lambda sensor. The NO₂/NO ratio increases when lambda increases because there is enough oxygen for NO-NO₂ conversion under high-lambda conditions. Additionally, high-lambda conditions are created by the load (fuel quantity) decreasing region, as shown in Fig. **8**. Therefore, a low in-cylinder temperature during combustion caused by low load conditions also increases NO₂ formation (Equation 11). On the other hand, less NO is produced due to the low temperature. Therefore, the NO₂/NO ratio is high at the point where NO is low.
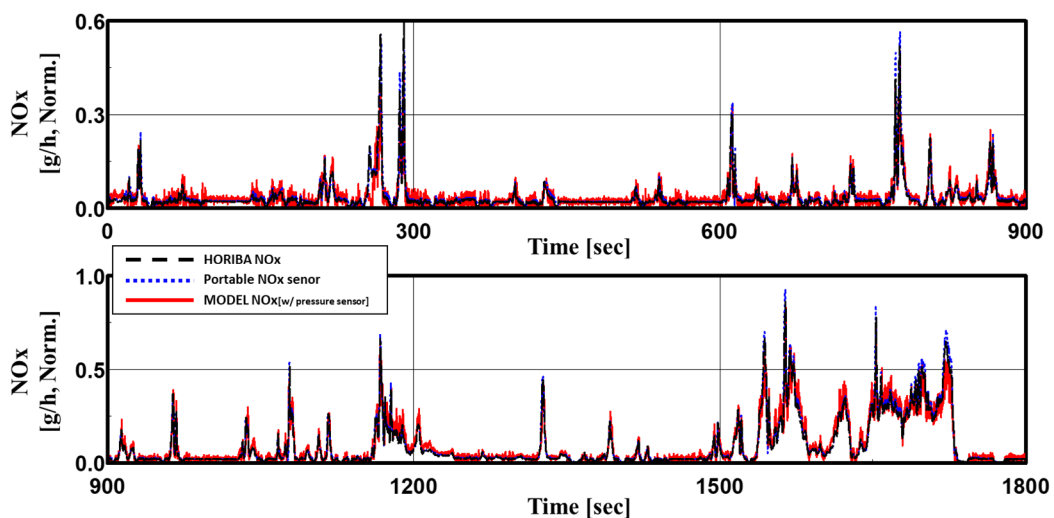

Fig. 7. Transient-state results of NOx prediction using the pressure sensor with the proposed models [18, 19]
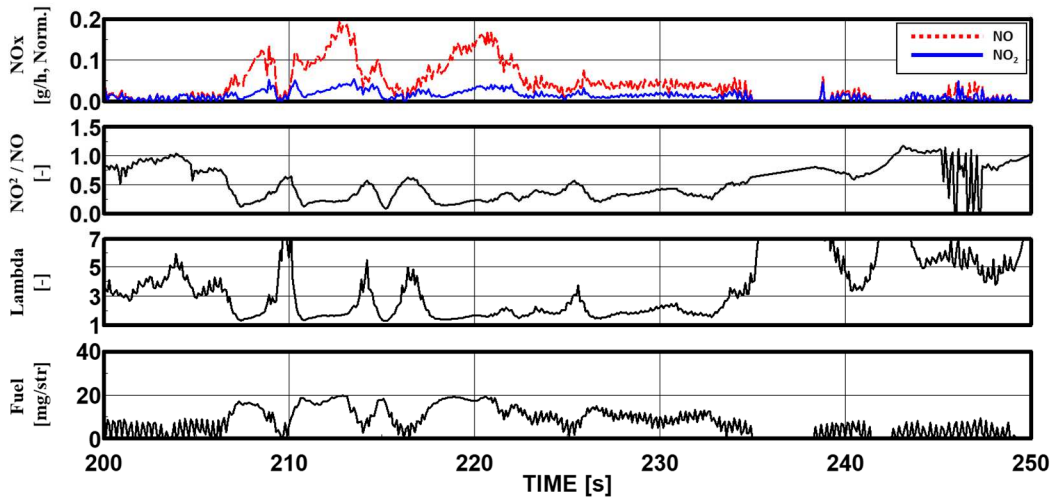
417

Fig. 8. Transient-state results of NO and NO$_2$ prediction in the middle of the WLTC mode

6.4 Validation of pressure prediction during transient conditions

In the previous section (6.3), the engine-out NOx was estimated using the in-cylinder pressure sensor during the transient state. Then, if the in-cylinder pressure can be estimated during the transient state, it is possible to predict the engine-out NOx emissions using just ECU data without an in-cylinder pressure sensor in real time.

Therefore, to verify the potential of the established pressure prediction model [16, 17] for NOx estimation in real time, the model was validated for transient conditions. Fig. 9 represents the results of the pressure estimation in the middle of the WLTC mode, which are applied to the NO and NO$_2$ prediction models. To show the potential for wide use of the model, the figure shows the behavior of P$_{soc}$ and P$_{mfb50}$ (pressure value at MFB 50 timing). P$_{mfb50}$ is one of the most important pieces of information from the pressure data for combustion control [29, 30]. The figure shows that the estimated pressure follows the measured value well, although there is some overestimation of P$_{mfb50}$ when the injected fuel quantity decreases rapidly. This is because of underestimation of the heat loss during the main Wiebe calculation process.
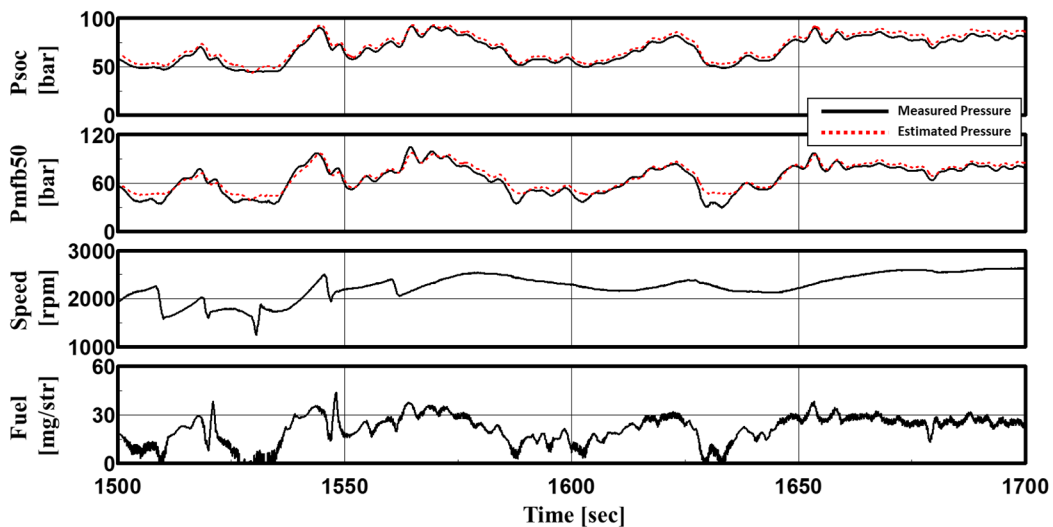

Fig. 9. Pressure (P$_{soc}$ and P$_{mfb50}$) estimation in the middle of the WLTC mode

6.5 NOx prediction without a pressure sensor during transient conditions

The pressure prediction was finally applied to the NO and NO$_2$ prediction model. Therefore, the results of the NOx prediction without a pressure sensor during the WLTC mode are described in Fig. 10. The

results show the behaviors of the estimated NOx (in two cases: the case with the pressure sensor and the case without the pressure sensor) and the measured NOx, and it could be found that the estimation values match well with the behavior of the measured values.
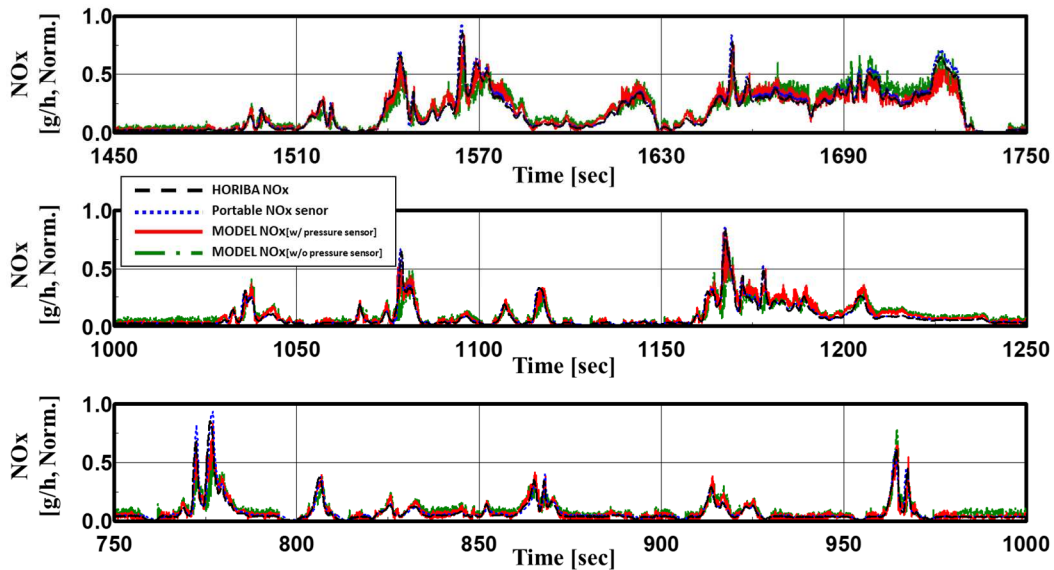

Fig. 10. Instantaneous NOx emissions and estimation in the middle of the WLTC mode.

However, as shown in Fig. 11, the NOx level was underestimated in the acceleration region. This error was caused by the EGR rate, which was calculated by the temperatures at the intake manifold, downstream of the intercooler and downstream of the EGR cooler using a fast response hot wire [28]. In the acceleration region, the fast response hot wire downstream of the EGR cooler measured the temperature of the remaining EGR gas, although the EGR valve was closed. This resulted in a higher EGR rate being calculated than the actual EGR rate. This higher EGR rate made the calculated NOx lower by decreasing the in-cylinder oxygen concentration and representative temperature values used in the NO and NO_2 models.

It was also found that the NOx estimated without the pressure sensor was lower than the NOx predicted with the pressure sensor in the acceleration region, according to Fig. 11. This was also due to the higher EGR rate being calculated. This made the calculated in-cylinder oxygen concentration lower, which prolonged the result of the main combustion duration model used in the main Wiebe function [16, 17]. Sensitivity analysis was conducted on the in-cylinder pressure model in the author's previous study [16]. The lengthened main combustion duration decreased the peak value of the main heat
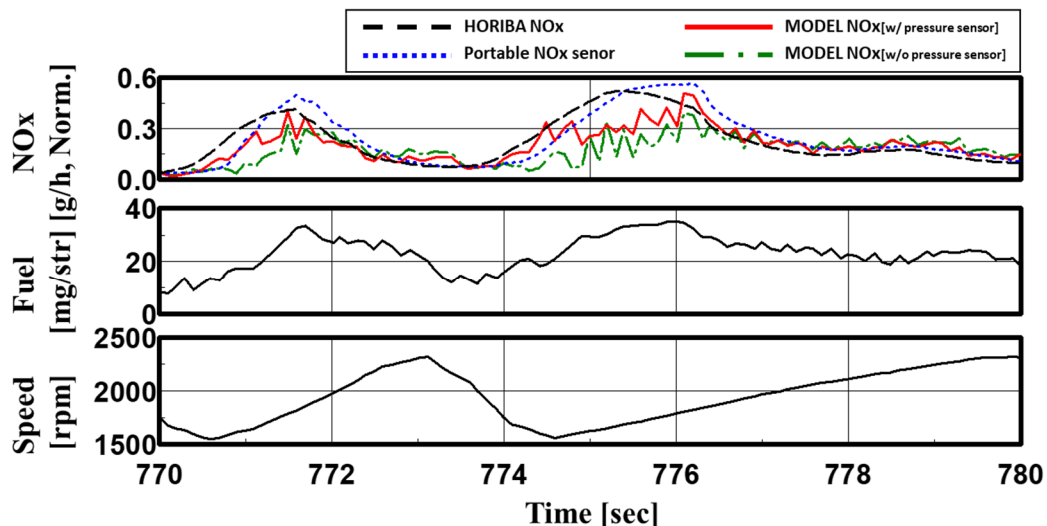

Fig. 11. Underestimated engine-out NOx in the acceleration region

release rate and the in-cylinder pressure. Therefore, in the acceleration region, the NOx calculation without the pressure sensor showed a lower value than the calculated NOx using the pressure sensor because the maximum pressure and temperature caused by the main combustion were decreased when using the in-cylinder pressure model. The underestimated engine-out NOx in the acceleration region implies that, in this real-time NOx model, it is critical to calculate the accurate EGR rate during transient conditions.

Fig. 12 shows the normalized accumulated NOx emissions and estimation during the whole WLTC period. Although the total error of the NOx estimation without the pressure sensor is larger than that in the case where the pressure sensor is used, the error does not exceed 10% when 'HORIBA MEXA 7100 DEGR' is selected as a reference. This level of error is comparable with the level of error of the portable NOx sensor that shows approximately 7% error during the WLTC mode (Table 3).
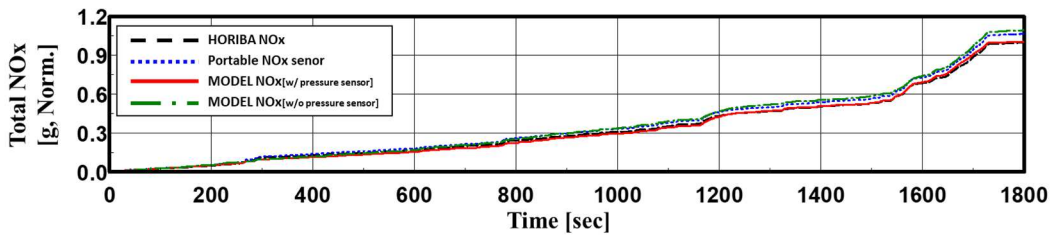

Fig. 12. Accumulated NOx emissions and estimation during the WLTC mode.

Table 3. Errors of accumulated NOx during the WLTC mode when HORIBA is selected as a reference device.

	Portable sensor	Horiba	Model [w/ sensor]	Model [w/o sensor]
Total NOx [g, Norm.] (Error %)	1.069 (6.9%)	1 (ref.)	1.009 (0.9%)	1.098 (9.8%)

Fig. 13 shows the reason why more cumulative NOx was calculated when the pressure sensor was not used. The region presented in Fig. 13 is the period where the cumulative NOx value difference between the NOx models (the model with the pressure sensor and the model without the pressure sensor) increases. In this period, the estimated pressure showed a higher value than the measured value. This is because of the underestimated subordinated models of the Wiebe function, such as the main combustion duration model and heat loss model [16, 17]. Underestimation of the heat loss during the main Wiebe calculation process in these engine operating conditions can lead to overestimation of the in-cylinder pressure. Additionally, the estimated in-cylinder pressure is highly sensitive to the combustion duration model used in the Wiebe function [16]. One of the variables in the combustion duration model is oxygen concentration, which can be calculated from the lambda and EGR rate. Therefore, to improve the real-time NOx model without a pressure sensor proposed in this paper, it is important not only to improve the accuracy of the subordinated models but also to apply the more correct EGR rate in real time.
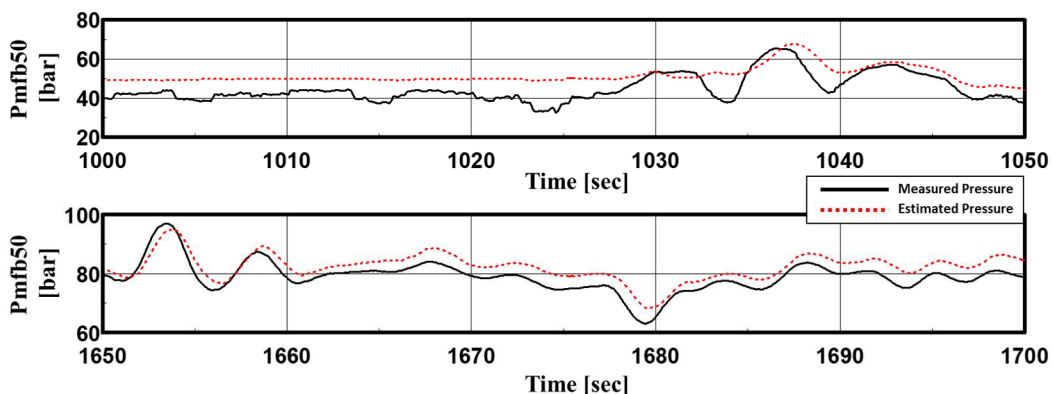

Fig. 13. Overestimated in-cylinder pressure in the middle of the WLTC mode

7. Summary and conclusion

In this study, the engine-out NOx emissions of a light-duty diesel engine were predicted in real time without using a pressure sensor. For the estimation, the established NO and NO$_2$ model acquires the in-cylinder pressure information from the pressure model to calculate the representative temperature values. The combined model was validated for transient conditions in the WLTC mode.

Based on the Zeldovich mechanism, an engine-out NO model was established with the key assumption that the 'NO formation area x duration' is proportional to the fuel mass. The NO$_2$ model consists of formation and decomposition mechanisms. Each mechanism takes the dominant reaction pathways of NO$_2$ formation and decomposition occurring with the in-cylinder conditions. Especially in the decomposition step, the cooling effect was considered, which can shorten the decomposition reaction by mixing the high-temperature region with low-temperature unburned gas.

Pressure prediction was conducted through three steps. First, the pressure was calculated for the polytropic process during the compression procedure, and a variable polytropic index, which is changeable with temperature and the in-cylinder gas composition, was adopted in this step. Then, the pilot combustion and main combustion phases were approximated using pilot Wiebe and main Wiebe functions, respectively, in these steps.

In the results, the NO and NO$_2$ models combined with the estimation of in-cylinder pressure were applied to real-time NOx prediction without a pressure sensor. The model was verified for the transient state (WLTC mode). The total estimated NOx error (9.8%) of the model is comparable with the total estimated NOx error of the portable NOx sensor. To reduce the errors of the mode, it is important not only to improve the accuracy of the subordinated models but also to apply the more correct EGR rate in real time.

This real-time NOx estimation model that predicts NO and NO$_2$ levels separately can contribute to the management of NOx after-treatment systems and real-time emission control strategies to minimize tail-pipe NOx emissions. Additionally, this real-time NOx estimation model without a pressure sensor can be applied when calibrating emissions in the stage of engine design.

Acknowledgements

References

1. Yang, J., Stewart, M., Maupin, G., Herling, D. et al. "Single wall diesel particulate filter (DPF) filtration efficiency studies using laboratory generated particles." *Chemical Engineering Science* 64(8):1625-34, 2009.

2. Zheng, M., Reader, G. T., and Hawley, J. G., "Diesel engine exhaust gas recirculation—a review on advanced and novel concepts." *Energy conversion and management* 45(6):883-900, 2004.

3. Alriksson, M. and Denbratt, I., "Low temperature combustion in a heavy duty diesel engine using high levels of EGR," SAE Technical Paper 2006-01-0075, 2006, doi:10.4271/2006-01-0075.

4. Yokomura, H., Kouketsu, S., Kotooka, S., and Akao, Y., "Transient EGR control for a turbocharged heavy duty diesel engine," SAE Technical Paper 2004-01-0120, 2004, doi:10.4271/2004-01-0120.

5. Theis, J. and Gulari, E., "A LNT+ SCR system for treating the NOx emissions from a diesel engine," SAE Technical Paper 2006-01-0210, 2006, doi:10.4271/2006-01-0210.

6. Theis, J. R., Dearth, M., and McCabe, R., "LNT+ SCR catalyst systems optimized for NO x conversion on diesel applications," SAE Technical Paper 2011-01-0305, 2011, doi:10.4271/2011-01-0305.

7. Andersson, M., Johansson, B., Hultqvist, A., and Noehre, C., "A predictive real time NOx model for conventional and partially premixed diesel combustion," SAE Technical Paper 2006-01-3329, 2006, doi:10.4271/2006-01-3329.

8. Arrègle, J., López, J. J., Guardiola, C., and Monin, C., "Sensitivity study of a NOx estimation model for on-board applications," SAE Technical Paper 2008-01-0640, 2008, doi:10.4271/2008-01-0640.

9. Arregle, J., López, J. J., Guardiola, C., and Monin, C. "On board NOx prediction in diesel engines: a physical approach." In *Automotive Model Predictive Control*, 25-36. Berlin, Heidelberg: Springer, 2010.

10. Guardiola, C., López, J., Martin, J., and García-Sarmiento, D., "Semiempirical in-cylinder pressure based model for NOx prediction oriented to control applications." *Applied Thermal Engineering* 31(16):3275-86, 2011.

11. Finesso, R. and Spessa, E., "A real time zero-dimensional diagnostic model for the calculation of in-cylinder temperatures, HRR and nitrogen oxides in diesel engines." *Energy Conversion and Management* 79:498-510, 2014.

12. Devadas, M., Kröcher, O., Elsener, M., Wokaun, A. et al. "Influence of NO 2 on the selective catalytic reduction of NO with ammonia over Fe-ZSM5." *Applied Catalysis B: Environmental* 67(3):187-96, 2006.

13. Malpartida, I., Marie, O., Bazin, P., Daturi, M. et al. "The NO/NO x ratio effect on the NH 3-SCR efficiency of a commercial automotive Fe-zeolite catalyst studied by operando IR-MS." *Applied Catalysis B: Environmental* 113:52-60, 2012.

14. Finesso, R., Spessa, E., Yang, Y., Alfieri, V. et al. "HRR and MFB50 estimation in a Euro 6 diesel engine by means of control-oriented predictive models." *SAE International Journal of Engines* 8(2015-01-0879):1055-68, 2015, doi:10.4271/2015-01-0879.

15. Ghojel, J., "Review of the development and applications of the Wiebe function: a tribute to the contribution of Ivan Wiebe to engine research." *International Journal of Engine Research* 11(4):297-312, 2010, doi:10.1243/14680874JER06510.

16. Lee, Y., Lee, S., Han, K., and Min, K., "Prediction of In-cylinder Pressure for Light-duty Diesel Engines," SAE Technical Paper 2019-01-0943, 2019.

17. Lee, Y., Lee, S., and Min, K., "Semi-empirical Estimation Model of In-cylinder Pressure for Compression Ignition Engines." *Proceedings of the Institution of Mechanical Engineers, Part D: Journal of Automobile Engineering*:0954407020916952, 2020.

18. Lee, Y., Lee, S., and Min, K., "Prediction of NOx considering NO and NO2 for a CI engine." *Applied Thermal Engineering, submitted* 2020.

19. Lee, S., Lee, Y., Kim, G., and Min, K., "Development of a Real-Time Virtual Nitric Oxide Sensor for Light-Duty Diesel Engines." *Energies* 10(3):284, 2017, doi:10.3390/en10030284.

20. Lee, S., Lee, Y., Han, K., Lee, K. M. et al. "Virtual NOx sensor for Transient Operation in Light-Duty Diesel Engine," SAE Technical Paper 2016-01-0561, 2016, doi:10.4271/2016-01-0561.

21. Mellor, A. M., Mello, J., Duffy, K. P., Easley, W. et al. "Skeletal mechanism for NOx chemistry in diesel engines," SAE Technical Paper 981450, 1998, doi:10.4271/981450.

22. Finesso, R., Misul, D., and Spessa, E., "Estimation of the engine-out NO2/NOx ratio in a EURO VI diesel engine," SAE Technical Paper 2013-01-0317, 2013, doi:10.4271/2013-01-0317.

23. Turns, S. R. *An introduction to combustion.* Vol. 287: McGraw-hill New York, 1996.

24. Hori, M., "Effects of Probing Conditions on NO2/NOx Ratios." *Combustion Science and Technology* 23(3-4):131-35, 1980.

25. Lee, Y. and Min, K., "Estimation of the Polytropic Index for In-cylinder Pressure Prediction in Engines." *Applied Thermal Engineering,* 158:113703, 2019, doi:10.1016/j.applthermaleng.2019.04.113.

26. Lee, Y., Lee, S., and Min, K., "Ignition Delay Model of Multiple Injections in CI Engines," SAE Technical Paper 2019.

27. Hsieh, M.-F. and Wang, J., "NO and NO2 concentration modeling and observer-based estimation across a diesel engine aftertreatment system." *Journal of Dynamic Systems, Measurement, and Control* 133(4):041005, 2011.

28. Lee, S., Lee, J., Lee, S., Kim, D. et al. "Study on reduction of diesel engine out emission through closed loop control based on the in-cylinder pressure with EGR model," SAE Technical Paper 2013.

29. Bengtsson, J., Strandh, P., Johansson, R., Tunestål, P. et al. "Closed-loop combustion control of homogeneous charge compression ignition (HCCI) engine dynamics." *International journal of adaptive control and signal processing* 18(2):167-79, 2004, doi:10.1002/acs.788

30. Shahbakhti, M. and Koch, C., "Characterizing the cyclic variability of ignition timing in a homogeneous charge compression ignition engine fuelled with n-heptane/iso-octane blend fuels." *International Journal of Engine Research* 9(5):361-97, 2008.

Electrical Modelling and Mismatch Effects of Thermoelectric Modules for Energy Recovery in Diesel Exhaust Systems

S. Ezzitouni, P. Fernández-Yáñez, L. Sánchez and O. Armas

Universidad de Castilla-La Mancha, Campus de Excelencia Internacional en Energía y Medioambiente, Escuela de Ingeniería Industrial y Aeroespacial de Toledo, Real Fábrica de Armas. Edif. Sabatini. Av. Carlos III, s/n, Toledo, 45071, Spain.

E-mail: octavio.armas@uclm.es
Telephone.: +34 926 295462

Abstract. Thermoelectric generators (TEG) typically used in automotive transport normally have the thermoelectric modules (TEM) longitudinally arranged with the exhaust gas flow. This leads to a thermal mismatch between the exhaust gas and the thermoelectric modules that is not constant throughout the generator length. In addition, the electrical connection of the TEMs also greatly affects the output electrical power of the whole TEG. Most published models consider the thermoelectric modules electrically isolated from each other, which does not reflect real working conditions and affects the outcome of the model. In this work, a computational model capable of predicting the electrical behavior of a TEG in any operating mode of the tested engine has been developed. In this case, the TEMs can be thermally and electrically arranged in different series-parallel configurations. The comparison of theoretical and experimental results shows a good precision of the model and the possibility of using it as a simulation tool. The root mean square error (RMSE) of the electrical power generated by the TEG is 1.10 W.

1. Introduction

The global energy balance of diesel engine shows that around a third part of the energy supplied by fuel, in light-duty vehicles, is wasted through the exhaust system (Ezzitouni et al. 2020). Increasing levels of environmental pollution and fuel economy has encouraged research upon ways to recover heat in internal combustion engines. One of the technologies used for waste thermal energy recovering is the thermoelectric generators (TEGs).

A thermoelectric module (TEM) is a system formed by pairs of n and p type semiconductors that converts thermal energy into electrical energy through the Seebeck effect as long as there is a temperature gradient between its two faces. The assembly of one or more thermoelectric modules in a single device is known as a thermoelectric generator.

In the automotive industry, thermoelectric generators are usually located in the exhaust system, taking advantage of the residual heat transferred by the exhaust gases through the exhaust pipe wall (as hot source) and the engine cooling water or the air (as cold source).

The purpose of this work is to develop a computational model to predict the electrical power generated by a TEG in a diesel engine under steady operation modes. Most published models consider the thermoelectric modules electrically isolated from each other, which does not reflect real working conditions and affects the outcome of the model. This study takes a further step and overcomes such issue. This model could help to state criteria for suggesting electrical configurations and connections of TEM is a determined TEG.

The model developed in this work, once validated, is intended to be used as a simulation tool to study the following three case scenarios: i) thermal mismatch among thermoelectric modules in the same electrical branch, ii) malfunction of some modules and iii) variation of the number of modules in a electrical branch.

2. TEG modelling

The proposed procedure is divided into two steps: firstly, heat transfer modelling from the exhaust gas to the thermoelectric modules and secondly is the electrical model itself, which models the interconnected modules (Fig. 1).
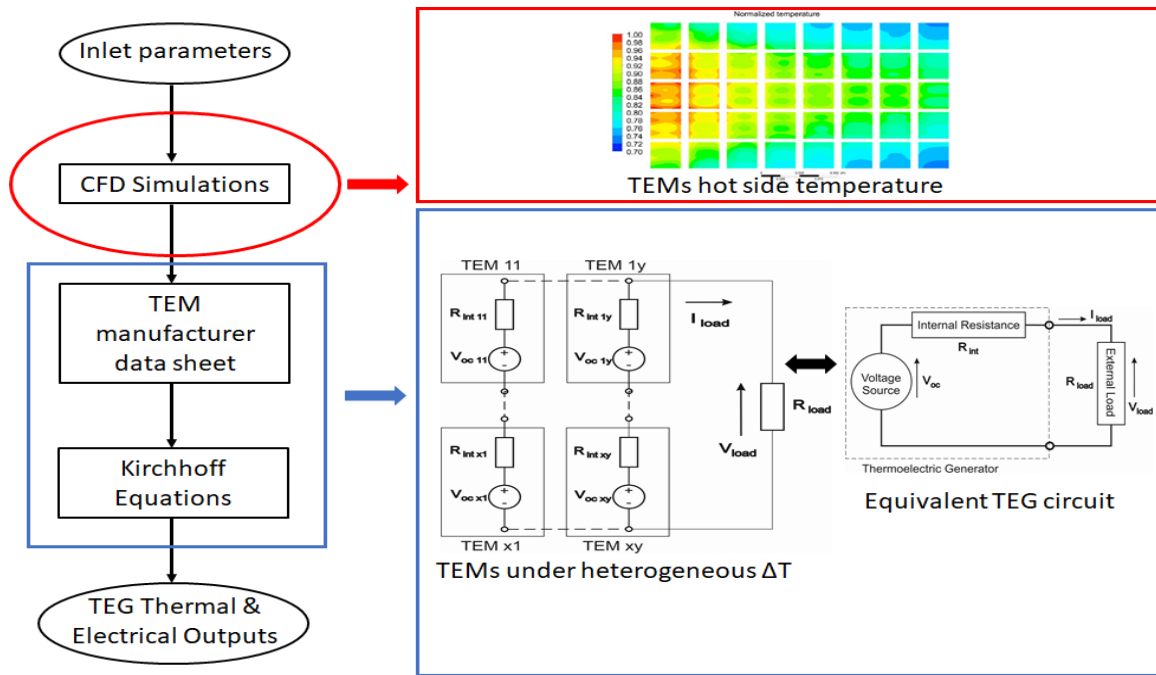
Fig. 1. Electrical model diagram of TEMs in series-parallel configuration under heterogeneous ΔT conditions

2.1 CFD simulations

The first part of the model consists of carrying out three different types of three-dimensional CFD simulations: gas-side heat exchanger, the whole TEG system and an on-site simulation of the TEG system including the upstream catalytic converter of the engine (Fernández-Yáñez et al. 2018). These simulations estimate the distribution of surface temperatures on both faces of each of the TEMs in the operating modes of the engine tested (Fig. 1).

2.2 Electrical model

The TEM can be electrically modelled as a voltage source (V_{oc}) in series with an internal resistance (R_{int}) (Fig. 1). It has been shown, theoretically and experimentally, that the Maximum Power Point is found when the array's terminals voltage is at half of the open-circuit value (Rowe and Min 1998). The TEMs are electrically arranged in series, parallel or in a mixed configuration according to the characteristics of the external load connected to the TEG in terms of voltage and current.

Applying Kirchhoff's Laws and Thévenin's Theorem, it is possible to determine the mathematical expressions that define the V_{oc} and R_{int} of the equivalent circuit of the complete TEG as a function of the electrical parameters of the TEMs (Eqs. 1 and 2).

$$V_{oc} = \left(\sum_{j=1}^{y} \frac{\sum_{i=1}^{x} V_{oc_{ij}}}{\sum_{i=1}^{x} R_{int_{ij}}} \right) \cdot \left(\sum_{j=1}^{y} \frac{1}{\sum_{i=1}^{x} R_{int_{ij}}} \right)^{-1} \qquad (1)$$

$$R_{int} = \left(\sum_{j=1}^{y} \frac{1}{\sum_{i=1}^{x} R_{int_{ij}}} \right)^{-1} \qquad (2)$$

From the data provided by the manufacturer of the TEMs, the relationship between each of the electrical parameters of the TEM and the temperature of the hot side has been modeled as a second-degree polynomial function (Eqs. 3 and 4).

$$V_{oc} = a_1 T_h{}^2 + a_2 T_h + a_3 \qquad (3)$$

$$R_{int} = b_1 T_h{}^2 + b_2 T_h + b_3 \qquad (4)$$

425

3. Experimental setup

The same experimental setup used in Ezzitouni et al. (Ezzitouni et al.2020), has been used in the present TEG model validation. The tested TEG houses in its central part and along its entire length, the modified section of the exhaust pipe (Fig. 2a). Over the two faces of the modified section 80 bismuth telluride commercial thermoelectric modules, 40 on each face, are placed. The cold sides of the thermoelectric modules are refrigerated with two water heat exchangers, one per side of the TEG.

The temperature of each of the 80 modules is different and, therefore, their electrical output too. The way they are electrically connected strongly affects the power output of the whole TEG system. For this reason, the TEMs, were electrically characterized. As example, the Fig. 2b shows qualitative results obtained under one of the engine operating modes tested (2400 rpm, 110 Nm). The TEMs are numbered (1-40) from hottest to coldest.

These results reveal the pattern of temperature distribution along the TEG. To avoid electric mismatch, the TEMs were sorted by temperature proximity into four different groups with the modules connected serial wise as shown in Fig. 2d.

4. Model validation

To evaluate the electrical TEG model, the operating modes chosen on the effective torque - engine speed map mainly cover the lower left quadrant of this map, as can be seen in Fig. 2c. This quadrant mainly corresponds to the urban driving conditions of the vehicle in which the engine is mounted.

The model developed in this work was validated by comparing the experimental data with the numerical data estimated by the model under the same conditions (Table 1). The precision lack between measured and calculated values is mainly due to the electrical energy losses in connection and measurement circuits of the electrical parameters. It can be seen how the values of the error decrease as the engine load increases. That is, the model is more accurate in motor operating modes where the TEG generates more electrical energy since the relative proportion of electrical energy losses becomes lower.
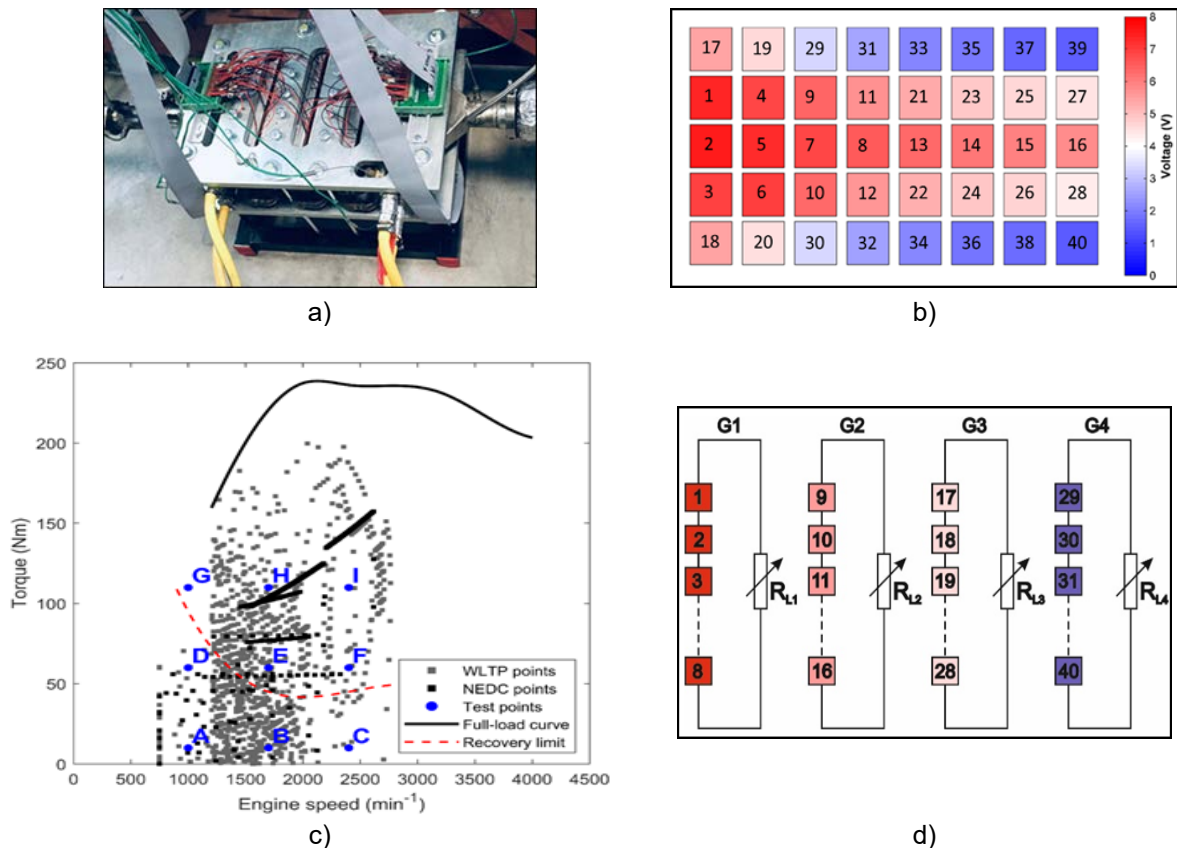

a)

b)

c)

d)

Fig. 2. a) Top view of the TEG coupled to the exhaust pipe, b) TEMs numbered from hotter to colder, c) Experimental test conditions and d) Sketch of the TEG and modules connection to the electrical charge circuit.

Table 1. Experimental values vs Theoretical values

Operating modes		A	C	E	F	G	H	I
Output Electrical power [W]	Experimental	0.30	3.40	10.20	25.80	15.70	31.70	56.70
	Modelled	0.35	3.94	11.78	27.02	16.56	32.77	58.20
Relative error [%]		16.67	15.88	15.49	4.73	5.48	3.38	2.65
RMSE [W]		1.10						

5. Simulation of possible scenarios

Results were obtained by simulation of the following three scenarios: i) thermal mismatch among thermoelectric modules in the same electrical branch, ii) malfunction of some modules and iii) variation of the number of modules in a branch.

In the first scenario, it is shown that the electrical connection of TEMs under conditions of thermal imbalance has a negative effect on the production of electrical energy (greater than 8%) in comparison with the energy generated by the same TEMs, but individually controlled.

The second scenario simulates the situation in which a TEM does not function properly and stops producing electrical power. However, its internal resistance continues to consume energy due to the Joule effect. In this case, the energy loss, due to the malfunction of a single thermoelectric module, is very important. Hence, the need to incorporate protective electronic components, for example, diodes.

In the third scenario, the most suitable electrical configuration for the TEG tested is investigated in terms of the number of TEMs in each branch. Many options, which go from connecting in series all the available TEMs to individually controlling each of the TEMs. The greater the number of groups of interconnected TEMs and the smaller the number of TEMs in each branch, the greater the electrical power recovered by the TEG. However, the control circuit will be more complicated and expensive due to the increase in the number of necessary converters. The most suitable configuration for this type of TEG is to find a balance between the number of converters and the number of TEMs connected to each converter.

6. Conclusions

In this work, a model capable of predicting the electrical behavior of a thermoelectric generator has been developed when their TEMs, electrically interconnected, are exposed to non-uniform temperature gradients. Before electrically arranging the thermoelectric modules, it is important to characterize each one of them in order to detect temperature mismatches or possible damaged modules. The results of the simulation of several scenarios allow to affirm that: i) The power lost by mismatched conditions can be very significant; ii) It is necessary to protect the electrical circuit against the possible non previously detected malfunction of some TEMs and; iii) A balance must be found between the number of converters and the number of thermoelectric modules connected to each converter.

Acknowledgements

References

Ezzitouni S, Fernández-Yáñez P, Sánchez L and Armas O (2020) Global energy balance in a diesel engine with a thermoelectric generator. Applied Energy: vol 269, 115139.

Fernández-Yáñez P, Armas O, Capetillo A and Martínez-Martínez S (2018) Thermal analysis of a thermoelectric generator for light-duty diesel engines. Applied Energy: vol 226: pp 690–702.

Rowe DM and Min G (1998) Evaluation of thermoelectric modules for power generation. J Power Sources: vol 73(2): pp 193–198.

Engine and Fuel Co-Optimization Platform using the Stochastic Reactor Model with Tabulated Chemistry

L. C. Gonzalez Mestre[1], A. Duggan[2], T. Franken[1], L. Seidel[3], K. P. Shrestha[1], A. Matrisciano[4] and F. Mauss[1]

[1]Brandenburg University of Technology Cottbus-Senftenberg, Cottbus, Germany.

E-mail: LauraCatalina.GonzalezMestre@b-tu.de
Telephone: +(49) 17634667363

[2]ESTECO North America, Detroit (MI), USA.
[3]LOGE Deutschland GmbH, Cottbus, Germany.
[4]Chalmers University of Technology, Goteborg, Sweden.

Abstract. A novel engine and fuel co-optimization platform is developed based on the Quasi-Dimensional Stochastic Reactor Model and tabulated chemistry. The co-optimization platform is applied for a multi-objective optimization campaign including fuel blends composed of the RON95E10 base fuel and Methanol, Ethanol, Toluene or Hydrogen as alternative fuel components. Experimental measurements of a single cylinder research engine operated at four different operating points with the RON95E10 base fuel are used to train and validate the simulation model. The results show the remarkable ability of a fast tabulated chemistry based co-optimization approach to find the best suitable engine operation set up for a range of fuel blends. Methanol, Ethanol and Hydrogen blends with optimized engine operating parameters show a great potential to reduce the fuel consumption, CO and CO_2 emissions.

1. The Engine and Fuel Co-Optimization Platform

The engine and fuel co-optimization platform workflow is shown in Fig. 1. First, the dual fuel tabulated chemistry model [1,2] composed of the alternative fuel component and the RON95E10 base fuel is selected. Following, the optimization of the four operating points is started. For each operating point (OP), the engine operating parameters and the fuel blend composition are optimized to minimize specific fuel consumption (ISFC), CO and CO_2 emissions. Thereby, the Quasi-Dimensional Stochastic Reactor Model (QD-SRM) [3]
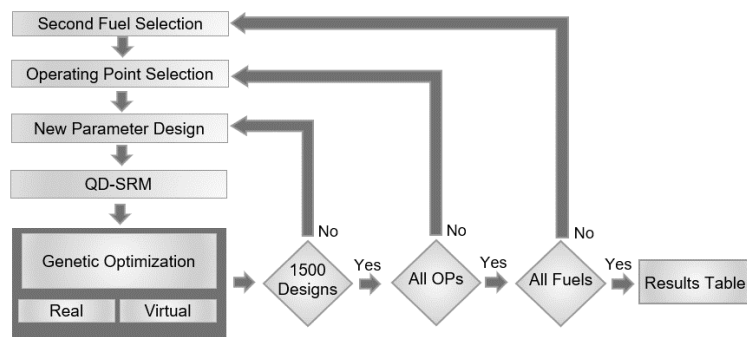

Fig. 1. Engine and fuel co-optimization platform workflow.

L.C. Gonzalez Mestre, A. Duggan, T. Franken, L. Seidel, K. P. Shrestha, A. Matrisciano, F. Mauss

with tabulated chemistry predicts the combustion process and emission formation. The genetic optimization incorporates the Non-Dominated Sorting Genetic Algorithm (NSGA-II), which has proven to be a robust algorithm for multi-objective optimization problems [4,5]. Additionally, a virtual optimization using metamodels is applied to refine the Pareto Front (FAST method) [6]. The new designs coming from the virtual optimization loop, are evaluated with the QD-SRM. The overall optimization loop is continued until the total design number reaches 1500. Then the next OP is evaluated following the same optimization strategy. When all OPs are finished, the next dual fuel tabulated chemistry model of the alternative fuel component is evaluated.

2. Numerical Test Cases

The four fired operating points used in this work, are measured at a single cylinder research engine fuelled with RON95E10 in the FVV project "Water Injection in SI Engines" [7] and used for the training and validation of the simulations. The Bore is 71.9 mm, Stroke 82 mm, Rod 137 mm and Compression Ratio 10.75.

2.1. Optimization Objectives

Three objectives should be minimized in the optimization: ISFC, specific CO_2 and specific CO emissions.

2.2. Optimization Input Parameters

In this study, six input parameters are selected considering their strong influence on the performance of the engine, the impact on autoignition in the end gas and emission formation. The parameters are changed in relation to the reference value. The compression ratio (CR) is changed between -1.0 and +7.0, the fuel fraction (FF) is changed between -0.5 and +0.0, the equivalence ratio (Φ) is changed between -0.5 and +0.5, the initial pressure (PIVC) is changed between -0.2 bar and +0.2 bar, the spark timing (ΘFP) is changed between -10 °CA and +10 °CA and initial temperature (TIVC) is changed between -20 K and
+40 K.

2.3. Optimization Constraints

The maximum value of the reactivity parameter (ε) and the minimum value of the resonance parameter (ξ) are used to constraint all QD-SRM simulations to subsonic autoignition (knock limit). A detailed description of the ε and the ξ parameters can be found in [8,9]. The Indicated Mean Effective Pressure (IMEP) constraint ensures that the engine load is kept constant and the Mass Fraction Burned (MFB) constraint forces the optimization to only accept designs with close to complete combustion.

3. Simulation Results

The feasible designs of each optimization are arranged into two clusters depending on its objective values. Designs with low CO_2 values are arranged in Cluster 1 and designs with low ISFC and CO values are arranged in Cluster 2.

3.1. Fuel Optimization Results

Figure 2 shows the mean cluster values of the optimization objectives and parameters for each fuel optimization. The reference case displays the values without optimization and the RON95E10 case shows the values of the optimization without adding a second fuel.
Table 1 presents the results for the optimized fuel blends of each cluster from the fuel blend optimization campaign. The reference case shows the fuel properties of the RON95E10 base fuel. The results for Methanol show Methanol fuel fraction between 11% (M11) and 29% (M29) with an increase in the indicated

efficiency from 3.5% points to 4.2% points. The results for Ethanol show Ethanol fuel fraction between 25% (E25) and 49% (E49) with an increase in the indicated efficiency from 4.1% points to 4.8% points. It becomes visible that less Methanol fuel fraction in the fuel blend is required to improve the indicated efficiency by a similar margin compared to Ethanol. Adding 45% (H45) Hydrogen fuel fraction to the fuel blend improves the indicated efficiency by 3.1% points but the gains are below the ones of the Methanol and Ethanol fuel blends. Increasing the Hydrogen fuel fraction in the fuel blend, increases the reactivity of the end gas in the engine and elevates the knock probability. Hence, further improvements in the engine operating parameters to improve the efficiency are limited. As discussed earlier, increasing the aromatic content in the fuel blend is not desirable and hence no optimized fuel blend is included in the table.
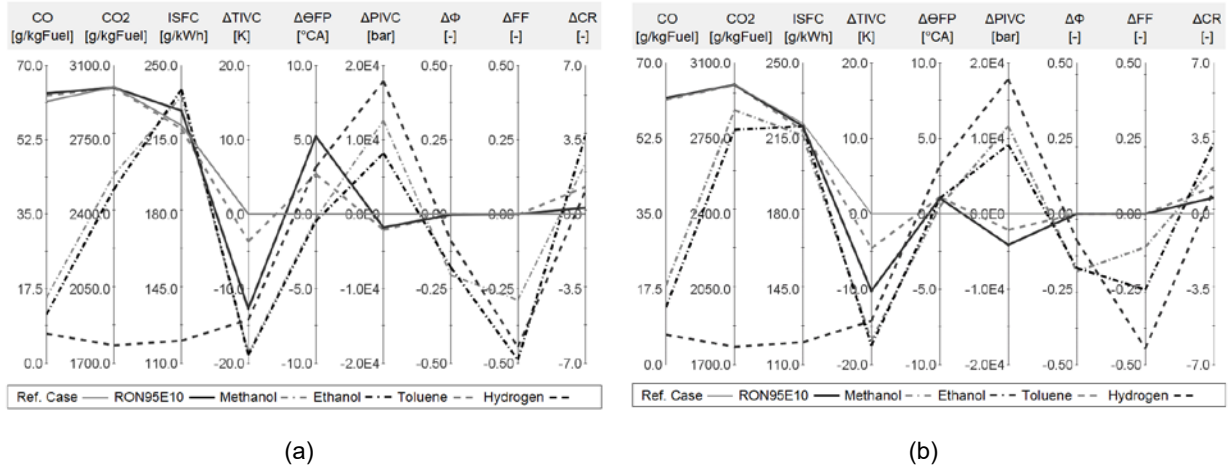

Fig. 2. Results of optimization objectives and engine parameters of different fuel blends at OP 1500rpm 15bar. (a) Cluster 1 (b) Cluster 2. The relative changes (Δ) of the reference case are zero.

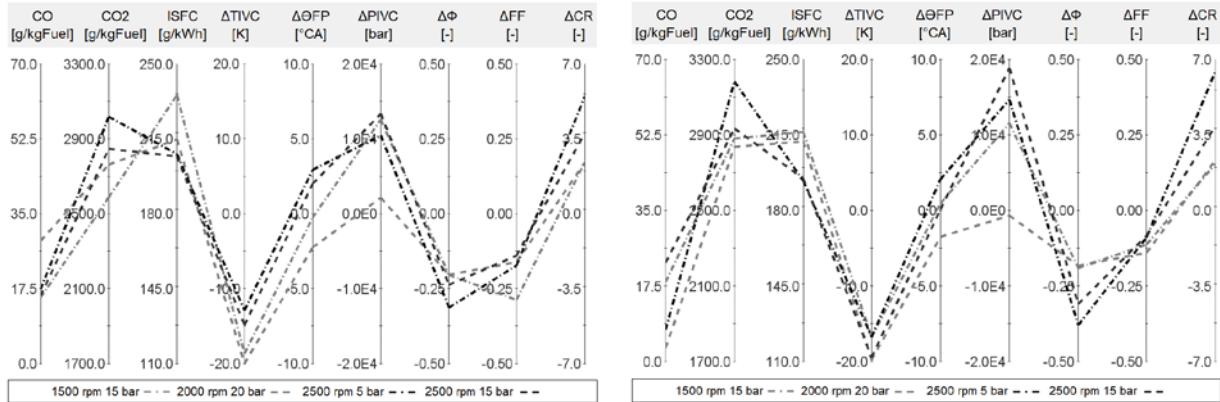**Table 1.** Fuel properties of the optimized fuel blends obtained from the fuel optimization campaign.

Cluster	Fuel	ρ_{norm} [kg/m^3]	ΔLHV [MJ/kg]	ΔLHV [MJ/l]	C:H:O	ΔRON [-]	ΔMON [-]	$\Delta\eta_i$ [%]
Ref.	RON95E10	756.25	41.16	31.13	6.3:11.7:0.2	96.7	87.4	39.40
1	M29	765.92	-6.1	-4.27	3.5:7.6:0.6	+4.7	+0.8	+4.17
1	E49	772.02	-7.07	-4.81	3.5:8.0:0.7	+9.3	+3.9	+4.83
1	H45	-	+35.16	-	-	-	-	+3.09
2	M11	759.97	-2.35	-1.63	4.9:9.7:0.4	+1.9	+0.3	+3.47
2	E25	764.39	-3.64	-2.45	4.6:9.4:0.5	+4.8	+2	+4.08
2	H45	-	+35.16	-	-	-	--	+3.09

3.2. Operating Point Optimization Results

It can be observed in Fig. 3 the results of the RON95E10 and Methanol fuel blend optimization for the four operating points (see Table 2).

Table 2 presents the fuel properties of the optimized fuel blends from the OP optimization campaign. In this campaign the second fuel is always Methanol. The reference case shows the fuel properties of the RON95E10 base fuel. The results of the OP 1500rpm 15bar shows Methanol fuel fraction between 11% (M11) and 29% (M29) with an increase in the efficiency from 3.5% points to 4.2% points. The OP 2000rpm 20bar shows Methanol fuel fraction between 14% (M14) and 16% (M16) with an increase in the efficiency around 4.4% points. These two operating points are knock limited, this is why the higher Methanol content is desired to reduce the knock probability. The OP 2500rpm 5bar presents 17% (M17) Methanol fuel fraction for Cluster 1 and 9% (M9) Methanol fuel fraction for Cluster 2. Their respective increase in the indicated efficiency is 5.6% points and 6.8% points. Finally, the OP 2500rpm 15 bar presents Methanol fuel fraction between 8% (M8) and 13% (M13) with an efficiency increase of 5.5% points and 4.1% points respectively.

The increment of the Methanol content in the fuel blend is found to be beneficial over the whole investigated engine operation range, increasing the efficiency by at least 3.5% points.

(a)   (b)

Fig. 3. Results of the optimization objectives and engine parameters of different operating points of optimized RON95E10 and Methanol fuel blends. (a) Cluster 1 (b) Cluster 2. The relative changes (Δ) of the reference case are zero.

Table 2. Fuel properties of the optimized fuel blends from the operating point optimization campaign.

OP	Cluster	Fuel Fraction	ρ_{norm} [kg/m^3]	ΔLHV [MJ/kg]	ΔLHV [MJ/l]	C:H:O	ΔRON [-]	ΔMON [-]	Δη$_i$ [%]
1500rpm 15bar	Ref.	RON95E10	756.25	41.16	31.13	6.3:11.7:0.2	96.7	87.4	39.40
	1	M29	765.92	-6.10	-4.27	3.5:7.6:0.6	+4.7	+0.8	+4.17
	2	M11	759.97	-2.35	-1.63	4.9:9.7:0.4	+1.9	+0.3	+3.47
2000rpm 20bar	Ref.	RON95E10	756.25	41.16	31.13	6.3:11.7:0.2	96.7	87.4	40.00
	1	M16	761.61	-3.41	-2.38	4.4:9:0.5	+2.6	+0.4	+4.42
	2	M14	760.9	-2.97	-2.07	4.6:9.3:0.5	+2.3	+0.3	+4.46
2500rpm 5bar	Ref.	RON95E10	756.25	41.16	31.13	6.3:11.7:0.2	96.7	87.4	40.53
	1	M17	762.02	-3.66	-2.55	4.3:8.8:0.5	+2.8	+0.5	+5.64
	2	M9	759.23	-1.90	-1.32	5.1:10:0.4	+1.5	+0.2	+6.79
2500rpm 15bar	Ref.	RON95E10	756.25	41.16	31.13	6.3:11.7:0.2	96.7	87.4	41.41
	1	M13	760.91	-2.96	-2.06	4.6:9.3:0.5	+2.3	+0.4	+4.13
	2	M8	758.99	-1.74	-1.21	5.2:10.2:0.4	+1.4	+0.2	+5.48

4. Conclusions

A novel co-optimization platform based on the QD-SRM, tabulated chemistry and genetic algorithms is developed and successfully applied for a multi-objective optimization campaign of RON95E10, Methanol, Ethanol, Toluene and Hydrogen fuel blends and different operating conditions to reduce the ISFC, CO and CO_2 emissions. The main conclusions of this study are listed below:

- It was found that adding up to 49% Ethanol, 29% Methanol or 45% Hydrogen fuel fraction in the fuel blend reduces the CO emissions by 50 g/kgFuel and the CO_2 emissions by 500 g/kgFuel.
- Hydrogen fuel blends show the highest reduction in ISFC, while the increased reactivity of the end gas could be problematic for safe engine operation.
- It is found that Toluene is not beneficial for improving the ISFC, CO and CO_2 emissions and further reduction of the aromatics content within the RON95E10 base fuel and replacing it with oxygenated components could be investigated.
- Increasing the Methanol fuel fraction in the fuel blend between 8% to 29% is beneficial for CO and CO_2 emissions reduction for all OPs.

- The lowest ISFC is found for the operating points 2500rpm 5bar and 2500rpm 15bar, while the operating points 1500rpm 15bar and 2000rpm 20bar could not be improved as much because of the knock limitation.
- The computer hardware used was: Five cores of Intel of i7-8700 CPU with Frequency equal to 3.20 GHz and the average CPU time running one optimization with 1500 designs was 4h 50 min. Hence, the method has shown that it can be effectively used on standard computers.

References

[1]   H. Lehtiniemi, F. Mauß, M. Balthasar, I. Magnusson, Modeling Diesel Spray Ignition using Detailed Chemistry with a Progress Variable Approach, Combust. Sci. Technol. 178 (2006) 1977–1997.

[2]   A. Matrisciano, T. Franken, C. Perlman, A. Borg, H. Lehtiniemi, F. Mauss, Development of a Computationally Efficient Progress Variable Approach for a Direct Injection Stochastic Reactor Model, SAE Tech. Pap. 2017-01-0512. (2017).

[3]   M. Pasternak, Simulation of the Diesel Engine Combustion Process Using the Stochastic Reactor Model, BTU Cottbus - Senftenberg, 2016.

[4]   A. Konak, D.W. Coit, A.E. Smith, Multi-objective optimization using genetic algorithms: A tutorial, Reliab. Eng. Syst. Saf. 91 (2006) 992–1007. https://doi.org/10.1016/j.ress.2005.11.018.

[5]   D.E. Goldberg, Genetic algorithms in search, optimization, and machine learning, Reading, MA Addison-Wesley. (1989).

[6]   ESTECO, modeFRONTIER 2018R1, (2018). https://www.esteco.com/modefrontier.

[7]   F. Mauss, M. Gern, M. Bargende, A.. Kulzer, Water Injection in SI Engines, FVV Final Report, Frankfurt am Main, (2020).

[8]   D. Bradley, C. Morley, X.J. Gu, D.. Emerson, Amplified Pressure Waves During Autoignition: Relevance to CAI Engines, SAE Tech. Pap. 2002-01 -2868. (2002).

[9]   X.J. Gu, D.. Emerson, D. Bradley, Modes of Reaction Front Propagation from Hot Spots, Combust. Flame. 133 (2003) 63–74.

Experimental and Numerical Analysis of Flow Distribution and NO$_x$ Sensors Layout Sensitivity in Close-coupled SCRoF Systems

I.F. Cozza[1], F. Feliciani[1], G. Buitoni[2], M. Tabarrini[2] and L. Postrioti[3]

[1]Punch Torino S.p.a, Italy
E-mail: ivan_flaminio.cozza@punchtorino.com; Telephone: +(39) 0

[2]Shot-to-Shot Engineering srl, Italy
E-mail: info@stse.eu; Telephone: +(39) 0753747523

[3]Dipartimento di Ingegneria, Università degli Studi di Perugia, Italy
E-mail: lucio.postrioti@unipg.it; Telephone: +(39) 0755853733

Abstract. Close-coupled aftertreatment systems (ATS) for automotive Diesel engines composed of DOC and SCR-on-Filter offer a significant potential in terms of pollutant emission control capability even with the introduction of more aggressive driving cycles and rigorous limits for type-approval tests. In particular, in low load conditions resulting in moderate gas flow rate and temperature in the exhaust system, the NOx conversion capability of the SCR system largely relies on both the UWS mixing device efficacy and on NOx sensors used to detect the actual NH3 slip and residual NOx concentration. As a consequence, developing experimental procedures and numerical tools for the analysis of the actual flow pattern and species concentration over peculiar sections of the exhaust system is crucial to support the ATS development process. In this work, a state-of the-art complete SCRoF-type ATS was analysed using a hot flow bench in steady operating conditions representative of type-approval key-points in terms of flow rate, temperature and upstream NOx concentration. During the tests, the overall system NOx conversion efficiency along with the NOx and NH3 distribution maps over the main flow section downstream the SCRoF were detected and compared with the corresponding distributions obtained by the 3D numerical analysis to support the design process of the entire system. Further, during the same tests the accuracy of three production, master-type NOx sensors positioned along the exhaust line downstream the ATS was compared with the flow bench mean measurements, evidencing how the NOx sensors actual position can significantly affect their accuracy particularly in low load operating conditions.

1. Introduction

In the global scenario, pollutants emissions and global warming effects on both the environment and human health are forcing the adoption of more efficient and clean technologies for mobility. In the automotive sector, these constraints are actuated via the adoption of more aggressive driving cycles and rigorous limits on CO$_2$ and pollutants emissions, that both represent a crucial task for OEMs, along with a progressive powertrain electrification. In this challenging frame, Diesel engine - eventually in a mild or plug-in hybrid powertrain - is still very attractive given its inherently high thermal efficiency and fun-to-drive attitude [1]. At the same time the adoption of effective NOx and PM emissions control technologies is the enabling factor to be compliant with the latest emission regulation procedures. In recent years, ATSs composed of oxidation catalyst (DOC), particulate filter (DPF) and SCR catalyst (eventually combined in a single SCRoF device) arranged in the so-called "close-coupled" configuration have proved to be an effective technical solution to control PM and NOx emissions [2-4]. Globally, PM reduction efficiency higher that 90% and simultaneously NO$_x$ emissions below 80 mg/km can be achieved in RDE tests.

Diesel ATSs efficacy in engine warm-up phases is largely based on both a proper thermal management of the SCR catalyst warm-up and on the design of an efficient UWS mixing system. The most complex tasks in the transients are promoting the urea-to-ammonia conversion process and evenly distributing NH$_3$ over the SCR inlet section, with moderate urea solid deposits and ammonia slip. To accomplish these tasks, a sophisticated ATS design is required, based on both CFD and experimental [5-8]. Further, an effective control system is required, based on both predictive models and on measurements, among which the NOx/NH$_3$ downstream the ATS. In the present paper, a prototype Diesel ATS in closed-coupled configuration is analyzed both numerically experimentally by a hot flow bench to deepen the

mixing section efficacy in terms global conversion efficiency and of ammonia distribution uniformity. In particular, a proprietary gas sampler was developed to investigate the local composition downstream the SCRoF. The comparison of species experimental distribution with the corresponding numerical results offers a deep insight in the mixer operation. Further, the sensitivity of production NOx/NH3 sensors to the measuring station was validated, offering a contribution to the robustness of the ATS control strategy.

2. Experimental Setup and main Hot Flow Bench output

The SCR efficiency analysis was carried out by the Hot Flow Bench (HFB), a regenerative test bench specifically designed for the analysis of automotive exhaust line components in realistic conditions. The HFB is used for the analysis of complete SCR converters efficiency and for the evaluation of ammonia uniformity downstream the SCR catalyst. To this end a proprietary apparatus - *STSe Local Gas Sampler (SLGS)*- was used. The HFB allows testing SCR systems in assigned operating conditions (air flow rate, temperature, NO/NO$_2$ concentration and UWS/NO$_x$ ratio). The bench (Fig.*1*) is composed of a blower, a laminar flow meter, a regenerative tube-and-shell heat exchanger, an electric heater and a re-configurable test section; operation with air mass flow rate and temperature up to 600 kg/h and 600 °C is possible. Independently from the air flow rate and temperature, pure NO and NO$_2$ flow rates are introduced in the air stream and regulated by hot-film flow controllers (Bronkhorst Mini Flow). The UWS injection is controlled as pressure, frequency and actuation time, with the mass flow rate monitored by a Coriolis flow meter (Sitrans MassFlow 3000). The NO, NO$_2$ and NH$_3$ concentration in the hot air flow is monitored by a QCL Horiba Mexa 1400 QL NX; the gas is sampled downstream the SCRoF. The HFB is managed by a control system developed in LabVIEW. The main standard test outcomes are defined.
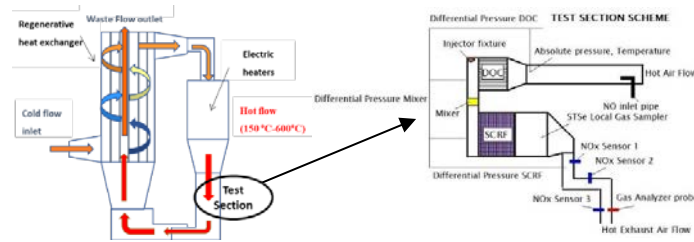

Fig.1.- TSe Hot Flow Bench and SCRF converter measuring positions scheme

NO$_x$ Conversion Efficiency evaluation – The system conversion efficiency curve is evaluated as:

$$Eff(\%) = 10 * \frac{\overline{NO_{x,in}} - \overline{NO_{x,out}}}{\overline{NO_{x,in}}} \qquad (1)$$

UWS solution is started after a proper stabilization period following the NOx insertion; the final efficiency is determined once stability criteria for the residual NO$_x$ and NH$_3$ are fulfilled.

NO$_x$ and NH$_3$ uniformity concentration map evaluation – The evaluation of the Uniformity Index (UI) both for the NH$_3$ and the NO$_x$ at the SCRF catalyst outlet section is obtained by the SLGS installed between the SCR catalyst and the ATS cap (Fig.2). Distribution maps were derived from the concentrations measured by the SLGS mobile probe connected to the bench gas analyzer; the probe was positioned along 81 stations over a plane 10 mm downstream the SCRF catalyst. The final UI is computed as:

$$[UI\ NO_x\ Slip]\ Uniformity\ Index\ NO_{x,slip}\ [\%] = (1 - \frac{\sum_{i=1}^{81} |NO_{x,i} - NO_{x,mean}| * A_i}{2 * NO_{x,mean} * \sum_{i=1}^{81} A_i}) * 100 \qquad (2)$$

$$[UI\ NH_3\ Slip]Uniformity\ Index\ NH_{3,slip}\ [\%] = (1 - \frac{\sum_{i=1}^{81} |NH_{3,i} - NH_{3,mean}| * A_i}{2 * NH_{3,mean} * \sum_{i=1}^{81} A_i}) * 100 \qquad (3)$$

Fig.2. ATS installed in STSe HFB equipped with STSe Local Gas Sampler

Production NO$_X$/NH$_3$ sensor position analysis - The bench was equipped with three NO$_x$/NH$_3$ individually-calibrated production sensors, installed in different positions along the exhaust line after the

ATS (Sensors #1, #2 ad #3 in Fig.*1*). By this setup, it was possible evaluating the sensor position influence on the sensor's readout with respect to the bench gas analyzer (sample in position #3). The single species concentrations measured by the bench analyzer were weighted with the individual sensors cross-sensitivity factor to obtain "virtual production sensor" data to be compared with sensors #1, #2 and #3:

$$Virtual\ Production\ Sensor_n = NO_{x,bench} + K_n * NH_{3,bench} \qquad (4)$$

3. Three-Dimensional CFD model description

CFD-3D analysis of the multiphase flow in ATSs is conducted using a coupled Eulerian-Lagrangian model (Star-ccm+). The Eulerian part is simulated solving the compressible Navier-Stokes equations on a 3D unstructured polyhedral mesh with prism layers in the near-wall region. Turbulence modeling is based on a RANS approach, using a k-Omega SST two-equation model. Wall modeling approach is based on all-y+ wall functions. The effect of cooling on the ATS walls has been modeled with a Conjugate Heat Transfer model of the solid walls around the gas. All the interface surfaces between gas and metal are modeled as conformal interfaces. The Lagrangian part is solved with a two-way coupled solver. In this work, the UWS has been approximated with pure water, and the Ammonia vapor concentration has been calculated as a post-processing step from the theoretical Urea dosing. The spray break-up model is based on a Reitz-Diwakar approach. The spray-wall interaction is modeled using Bai-Gosman based spray wall boundary conditions. The interaction between the UWS spray and the cool walls may lead to formation of liquid film. This is modeled with an evaporating- fluid film quasi-2D model, coupled with both the Eulerian and the Lagrangian solver. Both boiling and film stripping are accounted for. The UWS spray injector is modeled with a conical jet with imposed static mass flow rate, droplets diameters and velocity distribution. The diameter distribution is based on Rosin-Rammler distribution, while the velocity distribution is normal. All the spray properties are tuned against experimental spray data collected in spray bomb tests. All the simulations are transient and the UWS injection is pulsed. The pulse duration is calculated to inject the desired amount of Urea on the SCRoF. One single injection pulse is simulated.

4. Experimental and CFD results

An experimental test campaign was carried out spacing 12 different working points from 10% to 75% of engine full flow rate at different flow temperatures (from 180° to 350°), using NH_3/NO_x alpha ratio from stoichiometric value to 2. Conversion efficiency graph (*Fig. 3*, left) shows the comparison between efficiency
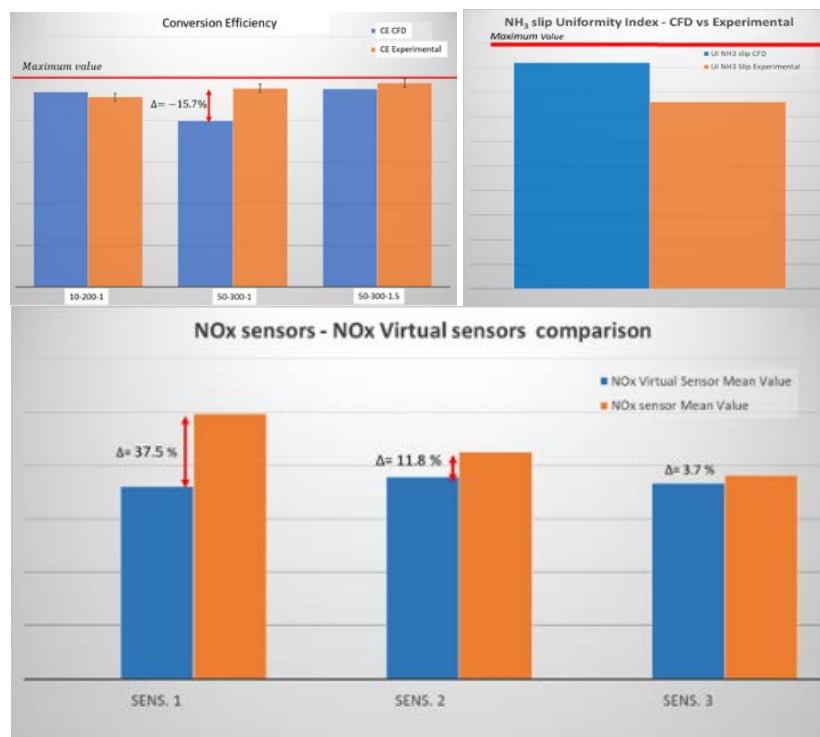

Fig.3. ATS NOx Conversion Efficiency and NOx-NH3 Uniformity Index (exp vs CFD)-NOx reading (virtual vs exp)

measured data and CFD model data for 3 working conditions, from 10% to 50% engine full flow rate, 200 and 300°C, NH_3/NO_x alpha ratio 1 and 1,5. Globally, the agreement among experimental and numerical results is encouraging, while for the 50% load, 300°C condition the CFD efficiency is underestimated.

NOx sensors reading values (Fig.3, right) show the gap between the reading values of the production sensors installed along the exhaust line with respect to the virtual reference sensor output. Sensors #1, #2 and #3, were located 25, 500 and 1250 mm downstream ATS outlet section, respectively. The graph shows the results taken at 50% engine full flow rate, 300°C, NH_3/NO_x ratio 1,5. The reading reliability of the production sensors is heavily affected by the position from the SCRoF, the mismatch being reduced from position #1 to #3 (from 3,7% to 37,5%). A similar behavior was observed in all operating conditions.
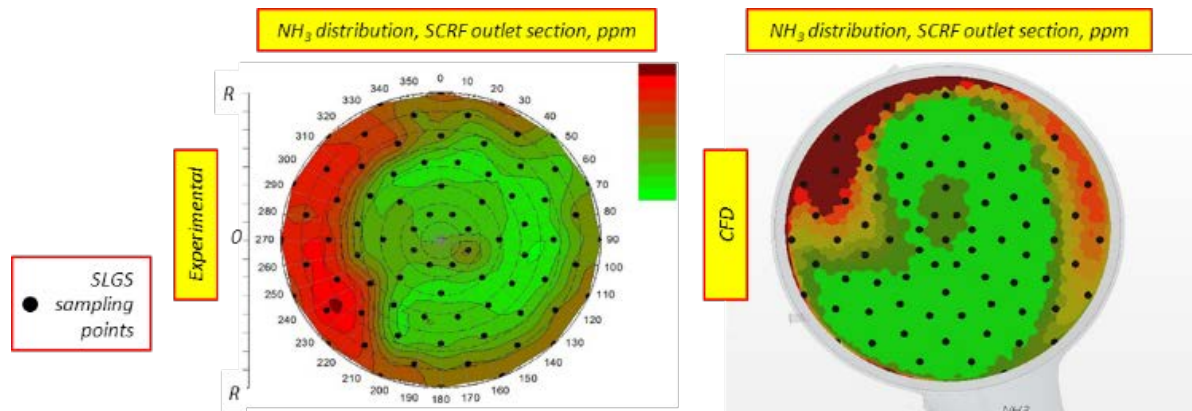

Fig. 4. NH3 slip concentration maps (exp vs CFD)

NH_3 distribution was evaluated in terms of uniformity index (*Fig.3*, center) and concentration maps on the outlet surface of the SCRoF catalyst (*Fig. 4*). Results are referred to the test case at 50% engine full flow rate, 300°C, NH_3/NO_x alpha ratio 1,5. The agreement among experimental and CFD results for NH_3 concentration maps is encouraging. In particular, it is evident a NH_3 accumulation on the periphery to be ascribed to the mixer operation.

5. Conclusions

In this paper, the study of the functional properties of an ATS coupled with the sensors that control it has been conducted. The study has been carried on with an innovative experimental methodology to study the internal flow distribution in the pipe, and it has been compared with 3D CFD simulations. The effect of the positioning of the NOx sensors on the monitoring quality is proven by the experimental results. For future developments, a more detailed CFD model will be applied and compared to the experimental data, to demonstrate the capability of simulation to be a viable substitute to experimental tests for ATS development.

References

1. Johnson, T. and Joshi, A., "Review of Vehicle Engine Efficiency and Emissions," *SAE Int. J. Engines* 11(6):2018-01–0329, 2018, doi:10.4271/2018-01-0329.

2. Eder, T., Lückert, P., Kemmner, M., and Sass, H., "OM 654 — Launch of a New Engine Family by Mercedes-Benz," *MTZ Worldw.* 77(3):60–67, 2016, doi:10.1007/s38313-015-0097-4.

3. Knirsch, S., Weiss, U., Möhn, S., and Pamio, G., "New Generation of the Audi V6 TDI Engine Part 2: Thermodynamics, Application and Exhaust Cleaning," *MTZ Worldw.* 75(10):22–27, 2014, doi:10.1007/s38313-014-0231-8.

4. Landsberg, D., Zink, U., Müller-Stach, T., Diego Albarracin Caballero, J., Robb, L., Wittka, T., Fiebig, M., Wilkes, T., and Schönen, M., "Emission Control System for RDE -Catalyst Technology and Application Requirements," 2018.

5. Way, P., Viswanathan, K., Preethi, P., Gilb, A., Zambon, N., and Blaisdell, J., "SCR Performance Optimization Through Advancements in Aftertreatment Packaging," 2009, doi:10.4271/2009-01-0633.

6. Quan, S., "Towards Quantitative Prediction of Urea Thermo- Hydrolysis and Deposits Formation in Exhaust Selective Catalytic Reduction (SCR) Systems," 1–9, 2019, doi:10.4271/2019-01-0992.Abstract.

7. Postrioti, L., Brizi, G., Ungaro, C., Mosser, M., and Bianconi, F., "A methodology to investigate the behaviour of urea-water sprays in high temperature air flow for SCR de-NO applications," *Fuel* 150:548–557, 2015, doi:10.1016/j.fuel.2015.02.067.

8. Birkhold, F., Meingast, U., Wassermann, P., and Deutschmann, O., "Modeling and simulation of the injection of urea-water-solution for automotive SCR DeNOx-systems," *Appl. Catal. B Environ.* 70(1–4):119–127, 2007, doi:10.1016/j.apcatb.2005.12.035.

9. Epling, W.S., Campbell, L.E., Yezerets, A., Currier, N.W., and Parks, J.E., "Overview of the Fundamental Reactions and Degradation Mechanisms of NOx Storage/Reduction Catalysts," *Catal. Rev.* 46(2):163–245, 2004, doi:10.1081/CR-200031932.

Cryogenic fluids for future transportation systems

M. Jaya Vignesh[1] G. Tretola[1] R. Morgan[1] G. De Sercey[1], A. Atkins[1,2], M. Heikal[1], K. Vogiatzaki *[1]

[1]Centre for Automotive Engineering, University of Brighton, United Kingdom

E-mail*:k.vogiatzaki@brighton.ac.uk

[2] Ricardo Innovations, United Kingdom

Abstract. Cryogenic fluids can serve as cost-effective energy vectors for transportation. They can expand considerably in volume when in contact with higher temperatures, and thus, can be used to move a piston even without combustion as in the case of liquid nitrogen engines. Also they are more easily transported from the production site in comparison to their gaseous fuel counterparts, as the case of natural gas for example, which makes them perfect candidates for being used as alternative fuels in cleaner and more efficient engines, considering that the liquification process can be done using renewable forms of energy. In this paper we investigate the thermophysical properties and the dynamics of cryogenic sprays at super-critical conditions, relevant to engine operation. The motivation of the work is to optimise the injection and vaporisation process of the cryogenic fluids in compression chambers.

1. Introduction

The need for sustainable and cleaner alternatives to fossil fuels has resulted in a new interest in the integration of cryogens in novel ultra-low emission transpiration systems. A cryogenic liquid is commonly defined as a liquid with a boiling point below –90°C. The most commonly used cryogens in transportation are liquified natural gas (LNG), nitrogen (LN_2) and hydrogen (LH_2) which will be investigated in our work. LNG is predominantly methane that has been cooled down (−162 °C) to liquid form. It can be considered as one of the most environmentally friendly fossil fuels. For an equivalent amount of heat, burning natural gas produces about 30% less carbon dioxide than burning petroleum. One of the main advantages of LNG, aside from the environmental aspect, is that LNG tanks are light and thus allow for larger fuel storage, making LNG ideal for long-haul trucks that carry heavy loads or travel long distances between stops[1]) LNG is also recommended for rail, marine, and off-road vehicles. An additional advantage of LNG is that the safety record of LNG carriers is also very good. In terms of volume-based energy density LNG is approximately 2.4 times that of CNG, it is comparable to propane and ethanol but is only 60 percent that of diesel and 70 percent that of gasoline.

LN_2 is nitrogen which has been cooled down (−195.79 °C) in liquid state. It is produced industrially by fractional distillation of liquid air. Liquid nitrogen vehicle designs have been suggested as early as 1902 (Liquid Air). A more recent example of such concept is the Dearman engine[2] which is a piston engine driven by the expansion of liquid nitrogen or liquid air, to produce power without the need of combustion. It is based on the Rankine cycle, (same cycle as the steam engines). The main advantage of liquid nitrogen vehicles is that the exhaust gas is simply nitrogen. This does not make it though completely pollution free, since energy is required to liquify the nitrogen in the first place, but that liquification process can be powered by a renewable energy source. Another recent high efficiency technology that combines combustion with LN_2 injection is the CryoPower engine, a recuperated split cycle engine developed by Dolphin N2 and the University of Brighton[3].In CryoPower, the compression and combustion strokes are performed in different cylinders. Intensive cooling of the compression stroke by the injection of liquid nitrogen directly into the chamber enables the recovery of waste heat from the exhaust between the compression and combustion cylinders. Brake efficiencies of RSCE over 50% have been reported without compression cooling, rising to 60% where the compression stroke is cooled by the injection of LN_2. The technology targets the heavy duty, long-haul sector where electrification is ineffective. This technology aside from the increased efficiency it also offers a 30% reduction in CO_2 emissions.

LH_2 is made from H_2 cooled down to −252.87 °C. It is a common rocket fuel, however more recently, has also been used as fuel for internal combustion engines or fuel cells. Various submarines (Type 212 submarine, Type 214 submarine) and hydrogen vehicles are using this form of hydrogen (see DeepC, BMW H2R). The advantage of LH_2 is that when it is burnt it mostly produces water and not carbon-based emissions. However, the issue with NOx is still present. Due to its similarity, equipment

can be shared with systems designed for LNG. One main issue though with LN$_2$ is its very low energy density in comparison to other fuels which also means that larger storage on board facilities are needed.

The pressure prevailing in the combustion or compression chamber for the above engines can reach up to 20 MPa, with the most efficient ones operating in the higher end of the pressure range. This results in the chamber pressure and temperature being supercritical to the injected cryogenic fluid at their critical point of operation. Therefore, in most of the applications above, the injected cryogenic fluids experience a sudden change in environment from subcritical to supercritical, which affects the jet/spray disintegration and evolution. As numerical simulations are increasingly being used in the development phase of new engines, it is necessary to accurately capture the underlying mechanical and thermodynamic mechanism driving the jet evolution and disintegration in such conditions to develop effective injection strategies. The injection process is pivotal to obtain the maximum efficiency possible from such engines through uniform dispersion of the cryogenic fluid when used as coolant in order to absorb the heat uniformly throughout the chamber and provide optimum air-fuel mixing when used as fuel source.

Table 1: Table of cryogenic properties relevant to the operation of internal combustion engines. For comparison, the properties of two other common fuels (Diesel and Gasoline) have been included

	LNG	LN$_2$	LH$_2$	DIESEL	GASOLINE
DENSITY (KG/L)	0.43	0.808	0.07	0.85	0.78
BOILING POINT (^{0}C)	-162	-195	-252.87	360	210
EXPANSION RATIO	1:600	1:848	1:694	14-1/25-1	9:1/12-1
AUTOIGNITION TEMPERATURE (^{0}C)	599	-	571	210	280
EXPLOSIVE LIMITS	5%-15%	-	4%-74.2%	0.6%-7.5%	1.4%-7.6%

2. Thermophysical Properties

One of the primary challenges in running simulations of cryogenic jets is the requirement for accurate thermophysical models to estimate density, heat capacity, viscosity and thermal conductivity of the fluids being simulated, especially as these fluids transition from sub- to super-critical conditions. The rapid change in these thermophysical properties around the critical temperature at supercritical
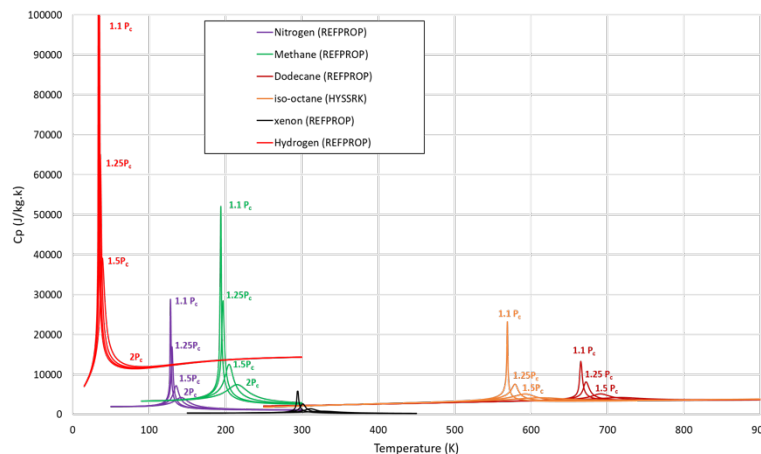

Fig. 1. Comparison of isobaric heat capacities of various cryogenic fluids and hydrocarbon-based fuels at supercritical pressures (1.1Pc, 1.25Pc, 1.5Pc and 2 Pc).

pressures renders the simple equation of states (EOS) and thermophysical models designed for fluids under atmospheric conditions problematic. At subcritical pressures, like any common fuels, cryogenic fluids vaporise on reaching the boiling temperature and the thermophysical properties instantly change from that of liquid to that of the gas. At supercritical pressures though, the transition from liquid to gas-like is rapid but continuous and the associated thermophysical properties change sharply from that of liquid to gas. This trend in thermophysical properties is not unique to cryogenic fluids alone. Any fluid at supercritical pressures possesses the same behaviour. **Fig. 1** presents the heat capacities of various cryogenic fluids and hydrocarbon-based fuels at various supercritical pressures. The supercritical pressures are presented in the reduced form ($P_r = P/P_c$). Though the trend is similar with spikes in heat capacity at supercritical pressures just above critical pressure and corresponding steep gradients in

other thermophysical properties, it can be observed that the fluids with lower molecular weight possess amplified heat capacity spikes when compared with higher molecular weight fluids. Since the common cryogenic fluids potentially useful in engine applications are of low molecular weight when compared against fuels used in the engines, the cryogenic fluids have a more drastic spike in heat capacity and steep gradients in other thermophysical properties.

In the simulations that will be presented in the current paper we use a polynomial fit of isobaric thermophysical properties (obtained from NIST). This method is simpler than programming and implementing a complete real gas EOS. In our previous work [4] we have also performed a comparison of existing cubic and empirical real gas EOS's concluding that an alternative could be the SRK EOS in terms of accuracy for the entire liquid to gas/supercritical fluid range and availability of associated and/or derived models to estimate other thermophysical properties.

3. Numerical Simulations

3.1 Simulated cases

Table 2. Table of cryogenic injection cases numerically simulated

Case	Injection			Chamber			
	Critical Pressure	Temperature	Velocity	Fluid	Pressure	Reduced Pressure	Temperature
LN_2-N_2	3.4 MPa	135 K	10 m/s	Nitrogen (N2)	6 MPa	1.7	298 K
					10 MPa	2.9	
					17 MPa	5	
LNG-N_2	4.6 MPa	135 K	10 m/s	Nitrogen (N2)	6 MPa	1.3	298 K
					10 MPa	2.2	
					17 MPa	3.7	
LH_2-N_2	1.3 MPa	30 K	10 m/s	Nitrogen (N2)	6 MPa	4.6	298 K
					10 MPa	7.7	
					17 MPa	13	

3.2 Model and Computational Details

We have developed a new compressible two fluid code based on OpenFOAM to simulate cryogenic fluids in varying pressure environment ranging from sub to super-critical conditions. The computational domain consists of a 3D cylindrical chamber with the dimensions given in **Fig. 2** The mesh is cylindrical and axi-symmetric. The cut section view of the mesh presented in **Fig. 2** displays the axial and radial discretisation.
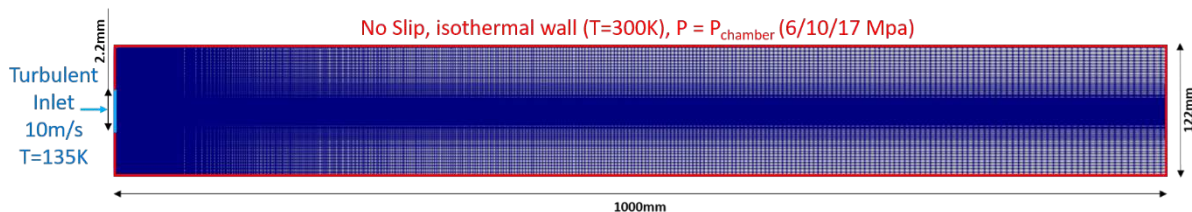

Fig. 2. Dimensions of the cylindrical chamber along with the boundary conditions implemented and the cut section of the mesh

3.3 Results

Fig. 3 shows the contour plots of temperature of LN2 and LNG injected in the same pressure (10MPa) environment. Given that the critical point of these two fluids is similar the reduced pressure is comparable as well (see Table 2) It can be seen that although the jets present a similar spreading in reality the

distribution of phases is different due to the different fluids. In the LN2 case the liquid becomes transitional upon the injection while the LNG remains liquid close to the nozzle. Also the surrounding fluid is gas exhibits different behavious. In the **Fig. 4** of LNG injected into N2 for pressures (10 and 17MPa), it can be observed that with increasing pressure the jet region consists more transitional phase.
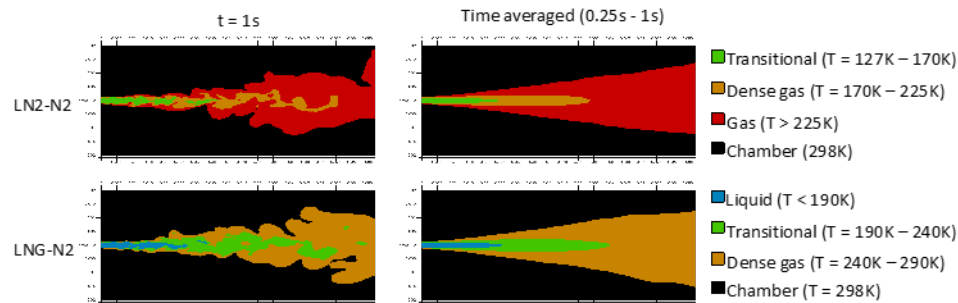

Fig. 3. Contour plots of temperature of LN2 (top) LNG (bottom) at 10MPa chamber pressure
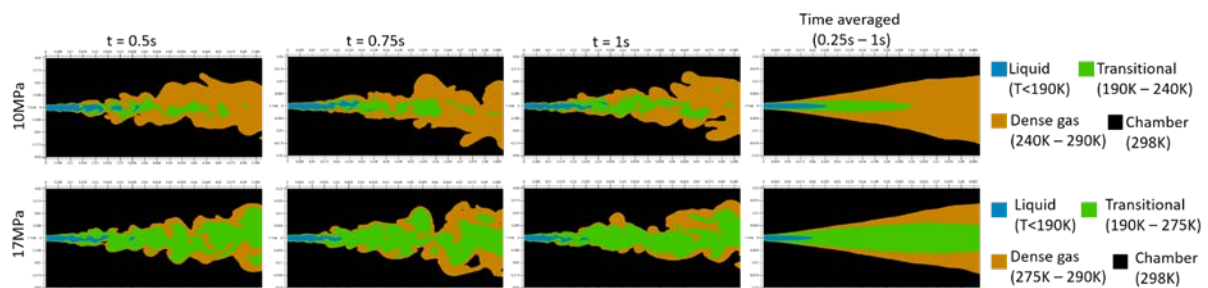

Fig. 4. Contour plots of temperature of LNG injection into N2 (LNG-N2) for three different time instances at 10MPa (top) and 17MPa (bottom) chamber pressure

4. Conclusions

A thorough understanding of cryogenic spray evolution and breakup has significant importance in engine applications. A better atomisation and dispersion of cryogenic fluid is necessary for efficient combustion (in the case of cryogenic fuels) and cooling (in the case of cryogenic coolants). In this paper we have demonstrated some of the important characteristics of the dynamic behaviour associated with the various phases (liquid like, gas like and transitional) of three cryogenic fluids, LNG, LH_2, LN_2 injected at different pressure environments

Acknowledgment

References

[1]   A. Boretti, "Advances in diesel-LNG internal combustion engines," *Applied Sciences (Switzerland)*. 2020.

[2]   "The Dearman Engine producing clean cold and power." .

[3]   J. M. Gopal, G. Tretola, R. Morgan, G. de Sercey, A. Atkins, and K. Vogiatzaki, "Understanding Sub and Supercritical Cryogenic Fluid Dynamics in Conditions Relevant to Novel Ultra Low Emission Engines," *Energies*, 2020 https://doi.org/10.3390/en13123038.

[4]   M. J. Vignesh *et al.*, "Use of cryogenic fluids for zero toxic emission hybrid engines," *Internal Combustion Engines and Powertrain Systems for Future Transport 2019: Proceedings of the International Conference on Internal Combustion Engines and Powertrain Systems for Future Transport,, December 11-12, 2019, Birmingham, UK*, 2020, p. 117.